# Analogue and Numerical Modelling of Crustal-Scale Processes

Edited by
S. J. H. Buiter and G. Schreurs

Geological Society
Special Publication 253

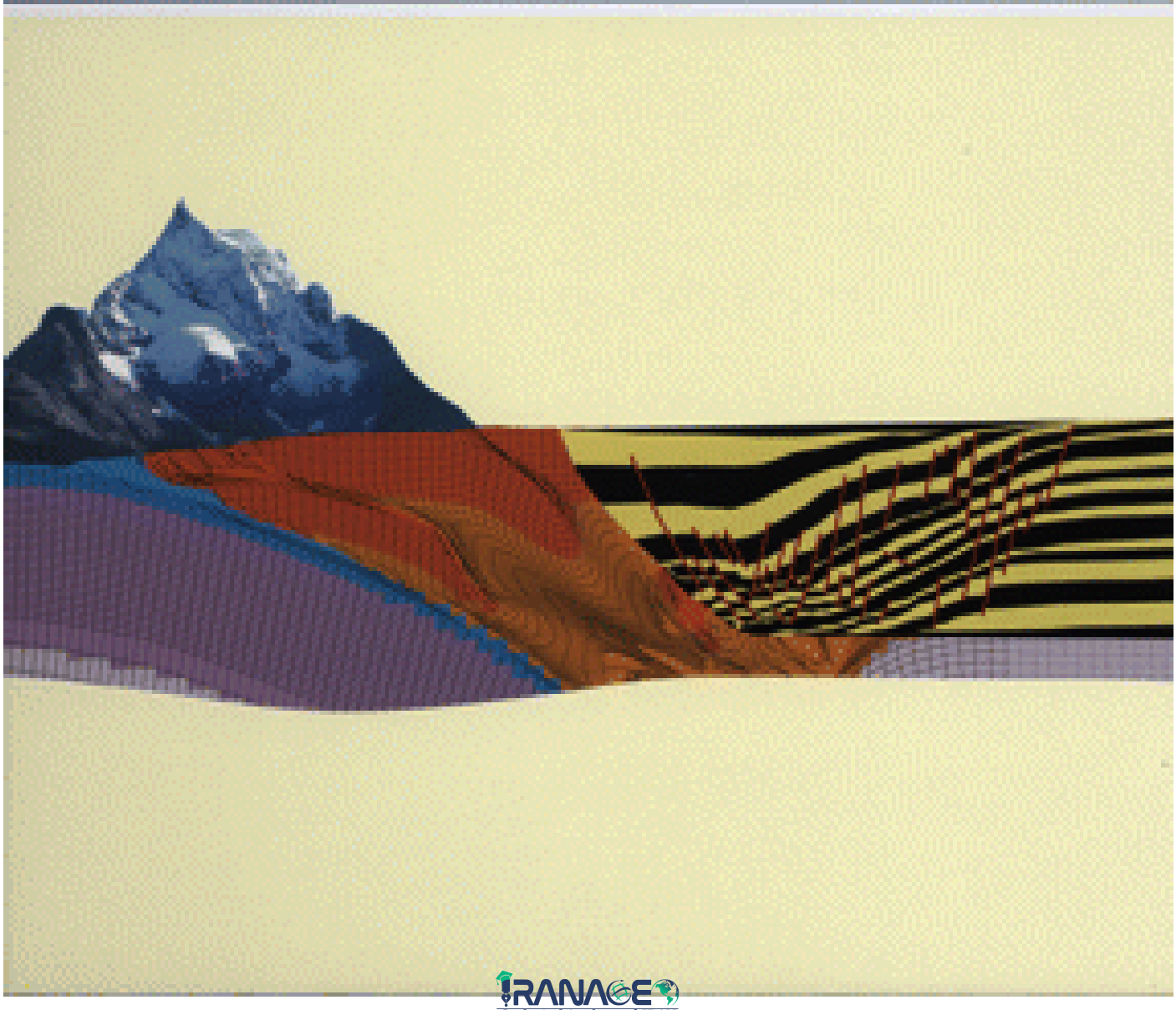

# Analogue and Numerical Modelling of Crustal-Scale Processes

Edited by
S. J. H. Buiter and G. Schreurs

Geological Society
Special Publication 253

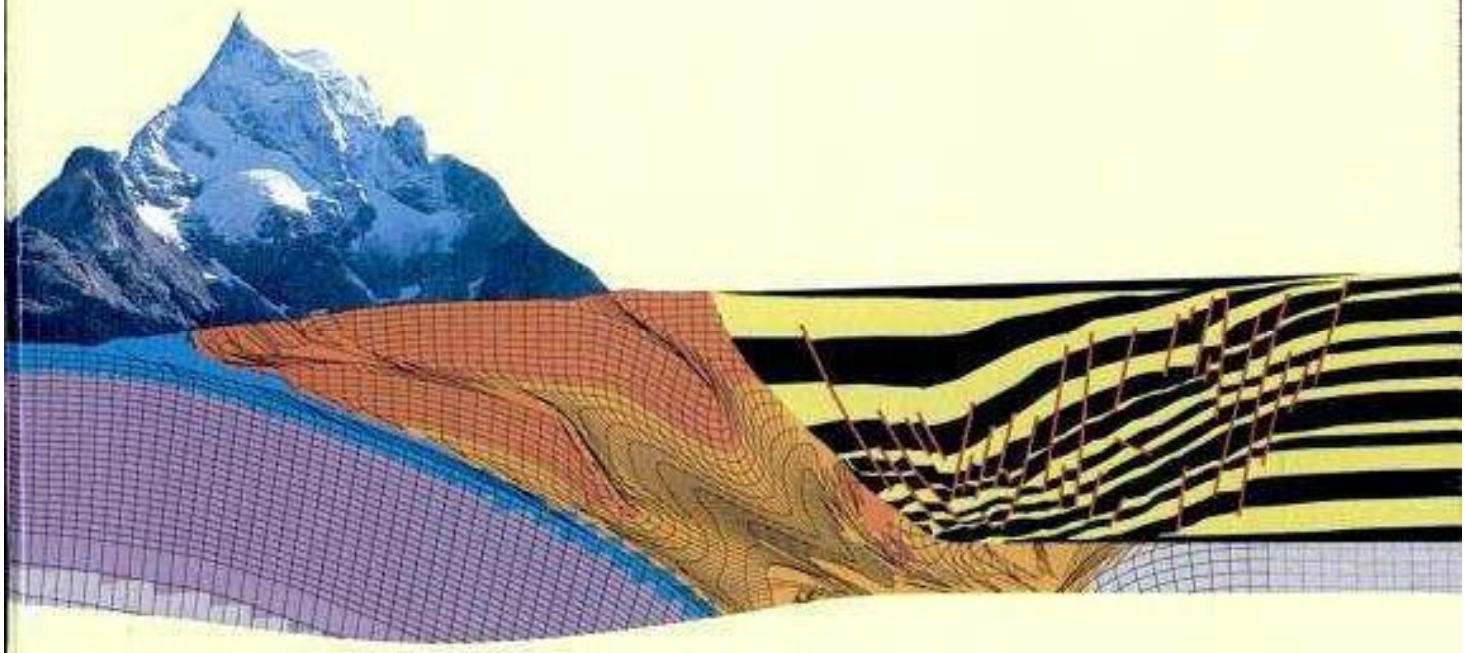

# Analogue and Numerical Modelling of Crustal-Scale Processes

## Geological Society books refereeing procedures

The Society makes every effort to ensure that the scientific and production quality of its books matches that of its journals. Since 1997, all book proposals have been refereed by specialist reviewers as well as by the Society's Books Editorial Committee. If the referees identify weaknesses in the proposal, these must be addressed before the proposal is accepted.

Once the book is accepted, the Society Book Editors ensure that the volume editors follow strict guidelines on refereeing and quality control. We insist that individual papers can only be accepted after satisfactory review by two independent referees. The questions on the review forms are similar to those for *Journal of the Geological Society*. The referees' forms and comments must be available to the Society's Book Editors on request.

Although many of the books result from meetings, the editors are expected to commission papers that were not presented at the meeting to ensure that the book provides a balanced coverage of the subject. Being accepted for presentation at the meeting does not guarantee inclusion in the book.

More information about submitting a proposal and producing a book for the society can be found on its web site: www.geolsoc.org.uk.

It is recommended that reference to all or part of this book should be made in one of the following ways:

BUITER, S. J. H. & SCHREURS, G. (eds) 2006. *Analogue and Numerical Modelling of Crustal-Scale Processes*. Geological Society, London, Special Publications, **253**.

REY, P. F. & HOUSEMAN, G. 2006. Lithospheric scale gravitational flow: the impact of body forces on orogenic processes from Archaean to Phanerozoic. *In*: BUITER, S. J. H. & SCHREURS, G. (eds) 2006. *Analogue and Numerical Modelling of Crustal-Scale Processes*. Geological Society, London, Special Publications, **253**, 153–167.

GEOLOGICAL SOCIETY SPECIAL PUBLICATION NO. 253

# Analogue and Numerical Modelling of Crustal-Scale Processes

EDITED BY

S. J. H. BUITER

Geological Survey of Norway, Trondheim, Norway

and

G. SCHREURS

University of Bern, Switzerland

2006
Published by
The Geological Society
London

# THE GEOLOGICAL SOCIETY

The Geological Society of London (GSL) was founded in 1807. It is the oldest national geological society in the world and the largest in Europe. It was incorporated under Royal Charter in 1825 and is Registered Charity 210161.

The Society is the UK national learned and professional society for geology with a worldwide Fellowship (FGS) of 9000. The Society has the power to confer Chartered status on suitably qualified Fellows, and about 2000 of the Fellowship carry the title (CGeol). Chartered Geologists may also obtain the equivalent European title, European Geologist (EurGeol). One fifth of the Society's fellowship resides outside the UK. To find out more about the Society, log on to www.geolsoc.org.uk.

**The Geological Society Publishing House** (Bath, UK) produces the Society's international journals and books, and acts as European distributor for selected publications of the American Association of Petroleum Geologists (AAPG), the American Geological Institute (AGI), the Indonesian Petroleum Association (IPA), the Geological Society of America (GSA), the Society for Sedimentary Geology (SEPM) and the Geologists' Association (GA). Joint marketing agreements ensure that GSL Fellows may purchase these societies' publications at a discount. The Society's online bookshop (accessible from www.geolsoc.org.uk) offers secure book purchasing with your credit or debit card.

To find out about joining the Society and benefiting from substantial discounts on publications of GSL and other societies worldwide, consult www.geolsoc.org.uk, or contact the Fellowship Department at: The Geological Society, Burlington House, Piccadilly, London W1J 0BG: Tel. +44 (0)20 7434 9944; Fax +44 (0)20 7439 8975; E-mail: enquiries@geolsoc.org.uk.

For information about the Society's meetings, consult *Events* on www.geolsoc.org.uk. To find out more about the Society's Corporate Affiliates Scheme, write to enquiries@geolsoc.org.uk.

Published by The Geological Society from:
The Geological Society Publishing House
Unit 7, Brassmill Enterprise Centre
Brassmill Lane
Bath BA1 3JN, UK

(*Orders*: Tel. +44 (0)1225 445046
Fax +44 (0)1225 442836)
Online bookshop: www.geolsoc.org.uk/bookshop



**British Library Cataloguing in Publication Data**

A catalogue record for this book is available from the British Library.

ISBN-10 1-86239-191-2
ISBN-13 978-1-86239-191-8

Typeset by Techset Composition, Salisbury, UK
Printed by MPG Books Ltd, Bodmin, UK

**Distributors**

*USA*
AAPG Bookstore
PO Box 979
Tulsa
OK 74101-0979
USA
*Orders*: Tel. +1 918 584-2555
Fax +1 918 560-2652
E-mail bookstore@aapg.org

*India*
Affiliated East-West Press Private Ltd
Marketing Division
G-1/16 Ansari Road, Darya Ganj
New Delhi 110 002
India
*Orders*: Tel. +91 11 2327-9113/2326-4180
Fax +91 11 2326-0538
E-mail affiliat@vsnl.com

*Japan*
Kanda Book Trading Company
Cityhouse Tama 204
Tsurumaki 1-3-10
Tama-shi, Tokyo 206-0034
Japan
*Orders*: Tel. +81 (0)423 57-7650
Fax +81 (0)423 57-7651
E-mail geokanda@ma.kcom.ne.jp

# Contents

**Models of sedimentary basins**



**Models of surface processes and deformation**



**Models of faults and fluid flow**

# Preface

As Earth's crust is the most accessible part of our planet, a wealth of information on its structure and composition is available from geological observations and geophysical measurements. Its shape and composition today are, however, the result of processes occurring at different scales in time and space, rendering study of the crust a complex and challenging undertaking. Field observations and seismic data, for example, confront us with the present day structures and must, for an in-depth understanding of their origin, be reconciled with the processes of deformation that created them. Reconstructing these processes in the past is commonly hindered by lack of continuous outcrop, limited depth resolution and little to no constraints on time. Analogue and numerical models may help improve our understanding of crustal-scale processes through their ability to simulate the birth and evolution of deformational structures at different scales. In this context, the link between theory and observations makes modelling a fundamental tool for the study of processes that alter the Earth's crust.

This volume presents new analogue and numerical model studies of natural processes contributing to the state of the Earth's crust. It shows the insights offered by models over a broad range of tectonic problems, in all cases carefully documenting the model approach used. By 'model' we mean an approximation of a physical process that will help further our understanding of the process itself, the measurable or observable structures that result from it, and the parameters that control it. Models allow us to set the boundary conditions, study the effects of parameter variations and perform sensitivity analyses. By their nature, they are, however, always a simplification of reality. As the words imply, an analogue model represents a scaled analogue of a natural structure, scaling not only the dimensions, but also the forces and material (for example, sand or clay) properties. A numerical model is a mathematical description of the natural situation, whereby aspects of processes are chosen that are of interest and can also feasibly be captured in equations. Both modelling techniques allow us to generate hypotheses regarding crustal-scale processes that can be tested against the results of field observations and geophysical studies.

The volume is divided into five sections:

- *Analogue and numerical sandbox models* tests the reproducibility of models between different laboratories and the suitability of different numerical solution methods for reproducing sandbox results.
- *Models of orogenic processes* describes processes influencing styles of orogenic deformation at convergent plate margins.
- *Models of sedimentary basins* discusses different aspects of extension, inversion and hydrocarbon migration within extensionally-formed sedimentary basins.
- *Models of surface processes and deformation* focuses on links between crustal-scale deformation and erosion processes at the Earth's surface.
- *Models of faults and fluid flow* discusses faults, important for short-term seismicity and their long-term effects on crustal strength, and fluid flow, which is crucial for oil reservoir studies.

The origin of this volume lies in GeoMod2004, an international meeting on analogue and numerical modelling of geological processes, held in Switzerland in June 2004. We would like to thank our co-organizers, Giovanni Bertotti and Paolo Ruffo, and all the participants of GeoMod2004, who provided the stimulus for editing this volume. Sixteen of the 23 papers in this book were presented or initiated at this conference. We thank the Geological Society Publishing House and especially Angharad Hills, Staff Editor, Helen Floyd-Walker, Production Editor, and Bob Holdsworth, Society Books Editor, for all their help in the publication of this book.

Susanne Buiter
& Guido Schreurs

# Acknowledgements

The editors thank the following colleagues and friends who kindly helped with the reviewing the papers submitted for this volume:

Jürgen Adam
Atilla Aydin
Andrey Babeyko
Maria E. Benardinelli
Antonio Benedicto
Paul Bons
Roger Buck
Douglas Burbank
Nestor Cardozo
Giacomo Corti
Dickson Cunningham
Olivier Dauteuil
Roberta de Franco
Alexander Densmore
Tim Dooley
Elizabeth Eide
Susan Ellis
Claudio Faccenna
Kevin Furlong
Denis Gapais
Lykke Gemmer
Muriel Gerbault
Rob Govers
Lyal Harris
Kes Heffer
Kaj Johnson
Hemin Koyi
Erik Lundin
Yvonne Martin
Othmar Müntener
Paul Nadeau
Thorsten Nagel
Dick Nieuwland
Marleen Nyst
Francis Odonne
Nick Oliver
Christophe Pascal
David Pedreira
Fred Pollitz
Russ Pysklywec
Antonio Ravaglia
François Roure
Mike Sandiford
Wouter Schellart
Fritz Schlunegger
Michael Seyferth
Guy Simpson
Rudy Slingerland
Blanka Sperner
Colin Stark
Randell Stephenson
Drew Stolar
Fabrizio Storti
Kurt Stüwe
Phaedra Upton
Ioannis Vardoulakis
Bruno Vendeville
John Walsh and
Martha Withjack.

The cost of color figures in this book were in part sponsored by Statoil ASA. Their support is kindly acknowledged.

# Analogue benchmarks of shortening and extension experiments

GUIDO SCHREURS[1], SUSANNE J. H. BUITER[2], DAVID BOUTELIER[3], GIACOMO CORTI[4], ELISABETTA COSTA[5], ALEXANDER R. CRUDEN[3], JEAN-MARC DANIEL[6], SILVAN HOTH[7], HEMIN A. KOYI[8], NINA KUKOWSKI[7], JO LOHRMANN[7], ANTONIO RAVAGLIA[9,*], ROY W. SCHLISCHE[10], MARTHA OLIVER WITHJACK[10], YASUHIRO YAMADA[11], CRISTIAN CAVOZZI[5], CHIARA DELVENTISETTE[12], JENNIFER A. ELDER BRADY[10], ARNE HOFFMANN-ROTHE[7], JEAN-MARIE MENGUS[6], DOMENICO MONTANARI[12] & FARAMARZ NILFOROUSHAN[8]

[1]*Institute of Geological Sciences, University of Bern, Baltzerstrasse 1-3, CH-3012 Bern, Switzerland (e-mail: schreurs@geo.unibe.ch)*

[2]*Centre for Geodynamics, Geological Survey of Norway, 7491 Trondheim, Norway*

[3]*Department of Geology, University of Toronto, 22 Russell St., Toronto, Ontario M5S 3B1, Canada*

[4]*CNR-Istituto di Geoscienze e Georisorse, Sezione di Firenze, via G. La Pira 4, I-50121 Firenze, Italy*

[5]*Dipartimento di Scienze della Terra, Università di Parma, Parco Area delle Scienze 157/A, I-43100 Parma, Italy*

[6]*Institut Français du Pétrole, 1 et 4 avenue de Bois Préau, F-92500 Rueil Malmaison, France*

[7]*GeoForschungsZentrum Potsdam, Telegrafenberg, D-14473 Potsdam, Germany*

[8]*Hans Ramberg Tectonic Laboratory, Department of Earth Sciences, Uppsala University, Villavägen 16, S-75326 Uppsala, Sweden*

[9]*Dipartimento di Scienze della Terra, Università di Pavia, via Ferrata 1, I-27100 Pavia, Italy*

[10]*Department of Geological Sciences, Rutgers University, Piscataway, NJ, 08854, USA*

[11]*Department of Civil and Earth Resources Engineering, Kyoto University, Kyoto 606-5801 Japan*

[12]*Dipartimento di Scienze della Terra, Università di Firenze, via G. LaPira 4, 1, I-50121 Firenze, Italy*

**Current address: Midland Valley Exploration Ltd., 14 Park Circus, Glasgow, G3 6AX, UK*

**Abstract:** We report a direct comparison of scaled analogue experiments to test the reproducibility of model results among ten different experimental modelling laboratories. We present results for two experiments: a brittle thrust wedge experiment and a brittle-viscous extension experiment. The experimental set-up, the model construction technique, the viscous material and the base and wall properties were prescribed. However, each laboratory used its own frictional analogue material and experimental apparatus. Comparison of results for the shortening experiment highlights large differences in model evolution that may have resulted from (1) differences in boundary conditions (indenter or basal-pull models), (2) differences in model widths, (3) location of observation (for example, sidewall versus centre of model), (4) material properties, (5) base and sidewall frictional properties, and (6) differences in set-up technique of individual experimenters. Six laboratories carried out the shortening experiment with a mobile wall. The overall evolution of their models is broadly similar, with the development of a thrust wedge characterized by forward thrust propagation and by back thrusting. However, significant variations are observed in spacing between thrusts, their dip angles, number of forward thrusts and back thrusts, and surface slopes. The structural evolution of the brittle-viscous extension experiments is similar to a high degree. Faulting initiates in the brittle layers above the viscous layer in

*From*: BUITER, S. J. H. & SCHREURS, G. (eds) 2006. *Analogue and Numerical Modelling of Crustal-Scale Processes*. Geological Society, London, Special Publications, **253**, 1–27.
0305-8719/06/$15.00 

close vicinity to the basal velocity discontinuity. Measurements of fault dip angles and fault spacing vary among laboratories. Comparison of experimental results indicates an encouraging overall agreement in model evolution, but also highlights important variations in the geometry and evolution of the resulting structures that may be induced by differences in modelling materials, model dimensions, experimental set-ups and observation location.

Geoscientists have used scaled experimental models (from here on also referred to as analogue models) for more than a century to gain insight into the kinematic and dynamic evolution of geological structures (e.g., Cadell 1888; Ramberg 1981; Koyi 1997). The ability to observe structures while they form is both attractive and insightful, and the ease with which model experiments can be performed has certainly contributed to their widespread application. Although many experiments have investigated similar geological processes, a direct comparison of experiments using the same prescribed set-up has until now been lacking. Testing the reproducibility of model results among different laboratories is important as it allows for documentation of the degree to which variations in model apparatus, modelling materials and experimental techniques can affect the outcome of experiments. Assessing the reliability of analogue models also has implications for comparisons between structures formed in experimental models, results of numerical simulations and natural field examples.

We present the results of two analogue 'benchmarks': a shortening experiment and an extension experiment. Ten modelling laboratories participated in these experiments. The experimental set-up, the construction technique, the viscous material (employed in the extension experiment) and the material covering walls and base were prescribed. Since each laboratory used its own frictional analogue material (sand, microbeads, wet clay) and experimental apparatus, our study is not a benchmark in its strictest sense. Our aims are to (1) indicate the degree of reproducibility of model results between different laboratories, (2) highlight the influence of material properties, model boundary conditions and experimental set-up, and (3) use our results to suggest further benchmark experiments.

The two experimental set-ups were designed to simulate upper-crustal processes, and can be placed among a wide range of laboratory experiments studying contractional and extensional deformation. Numerous studies document experiments of thrust wedges under normal gravity conditions (e.g., Davis *et al.* 1983; Malavieille 1984; Mulugeta & Koyi 1987, 1992; Mulugeta 1988; Colletta *et al.* 1991; Lallemand *et al.* 1994; Koyi 1995; Storti & McClay 1995; Mugnier *et al.* 1997; Gutscher *et al.* 1996, 1998; Storti *et al.* 2000; Schreurs *et al.* 2001; Turrini *et al.* 2001; Kukowski *et al.* 2002; Costa *et al.* 2004; Hoth *et al.* 2005). Deformation in these experiments occurs either by displacing a back wall or by pulling a basal sheet below a fixed wall. Such indenter-type or basal-pull-type models are not entirely equivalent, as we will discuss below. Parameters investigated in published thrust wedge experiments include basal friction, the presence of décollement layers, dip of the initial basal surface, surface slope, and the effects of erosion. In general, such models display a series of forward-propagating, in-sequence thrusts, whereby changes in, for example, basal friction or erosion may cause renewed hinterland activity. Many authors have investigated brittle-viscous extension in a normal gravity field (e.g., Tron & Brun 1991; Vendeville & Jackson 1992*a*, *b*; Brun *et al.* 1994; Keep & McClay 1997; Brun 1999; Gartrell 2001; Bahroudi *et al.* 2003). In these models, a viscous layer typically overlies a velocity discontinuity at the base of the model and is itself overlain by brittle materials. In all experiments the viscous basal layer exerts a strong control on fault nucleation and location.

In a companion paper, Buiter *et al.* (2006) present numerical equivalents of both analogue experiments and compare the results qualitatively and quantitatively. This study shows that numerical models employing different techniques (finite-element, finite-difference and distinct element methods) are able to reproduce results of analogue models successfully. The combination of analogue and numerical modelling methods may help establish the robust features of models of crustal-scale processes (e.g., Ellis *et al.* 2004; Pysklywec & Cruden 2004; Panien *et al.* 2006).

## Methods

### *Material properties*

We focus on experiments performed in a natural gravity field. In such experiments dry sand or wet clay are commonly used to simulate brittle rocks in the upper crust, and viscous materials to simulate salt or lower crustal rocks. In the shortening experiment, the models consisted of granular

materials (sand and glass microbeads) only, whereas for the extension experiment both brittle and viscous materials were used. All laboratories used the same polydimethylsiloxane (PDMS) as viscous material. This is a linear viscous material (silicone polymer) with a viscosity of $5 \times 10^4$ Pas at room temperature and at strain rates below $3 \times 10^{-3}$ $s^{-1}$ (Weijermars 1986; see also Ten Grotenhuis *et al.* 2002; Cruden *et al.* 2006). In contrast, each laboratory used its own brittle materials, which generally differed in density, frictional properties, grain sizes and grain shape (Table 1). Several laboratories measured the frictional properties of their granular materials using either a Hubbert-type shear box (Hubbert 1951), a ring-shear tester (Schulze 1994) or a Casagrande shear box (Casagrande 1932). Errors in ring-shear measurements are usually small (less than 1%). Measurements in Hubbert-type shear boxes are less precise, because of the larger uncertainty associated with the determination of the exact timing of the onset of shearing. As the Casagrande shear box measurements in this study employed higher normal loads than occur in the experiments, the measured values for cohesion are not considered representative for the experimental conditions.

Although experimental modellers have often assumed that their brittle materials deform according to the Coulomb failure criterion with constant frictional properties, several studies demonstrate that materials such as quartz sand, corundum sand and glass microbeads are characterized by elastic/frictional plastic behaviour with strain-hardening preceding failure (at peak strength) and subsequent strain-softening until a stable value is reached (Lohrmann *et al.* 2003; Panien 2004). Such mechanical behaviour is very similar to the one exhibited by experimentally deformed rocks (e.g., Jaeger & Cook 1979; Marone 1998; Barnhoorn *et al.* 2004). Values for the angle of internal friction (at peak strength) range from 33° to 45° for quartz sand and from 21° to 29° for microbeads (Table 1). These values are generally comparable to those determined experimentally for upper crustal rocks (Byerlee 1978). Strain-softening may be expressed as the percentage difference between peak friction and dynamic stable friction. For the materials used in this study, it varied from 4% to 20% for quartz sand and from 0% to 14% for microbeads (Table 1). In each case, strain softening in microbeads was lower than in sand. Cohesion values of granular materials display a wide range varying between −25 and 150 Pa. The negative values and the large variation in cohesion values may be related to uncertainties in the linear extrapolation of the failure envelope to very low normal stresses. At low normal stresses, the failure envelope is no longer a straight line, but has a convex-leftward shape with negligible cohesion (Schellart 2000). One laboratory (Piscataway) used wet clay instead of dry sand for the extension experiment. Their clay has an elasto-plastic rheology with an angle of peak friction of 27°.

To reduce the influence of the variable properties of sidewalls and base of the modelling apparatus, they were covered with a self-adhesive, transparent PVC foil (brand Alkor, article number 120010). The influence of this foil was investigated by measuring the friction between sand and the foil in the GeoForschungs Zentrum ring-shear tester. For fine-grained sand (20–200 μm) the angle of peak friction was 19.8° ± 0.1° and the angle of stable friction was 16.5° ± 0.3°. For coarser-grained sand (20–650 μm) the angles of peak and stable friction were 19.7° ± 0.1° and 16.7° ± 0.3°, respectively. This implies that the use of different sands in the experiments probably had only little influence on values of boundary friction, as long as Alkor foil was used on all sidewalls and the base.

Differences in frictional properties of the model materials may be attributed to the applied measuring technique (e.g., Casagrande shear box, Hubbert-type shear box or ring-shear tester), the filling technique and/or intrinsic material properties such as grain size distribution, grain shape and composition (Table 1). Variations in material properties may be important for differences in the evolution of experimental models. Lohrmann *et al.* (2003) found that the kinematics of thrust wedges are largely a function of their material properties. Adam *et al.* (2005) point out that the strength increase of the granular materials during the strain-hardening phase towards peak strength influences the localization and early development of faults. A detailed investigation of the exact causes of the differences in material properties is beyond the scope of our study, but it should be kept in mind that our modelling results are influenced by the use of different granular materials.

### *Scaling*

Our models aim at representing upper-crustal conditions and can be scaled up to natural dimensions by observing geometric, kinematic and dynamic similarity relationships (Hubbert 1937; Ramberg 1981). We assume that 1 cm in the models corresponds to 1 km in nature and that (dimensionless) angles of internal friction can

**Table 1.** *Material properties and grain characteristics*

| Laboratory | Density (kg m$^{-3}$) | C at $\phi_{peak}$ (Pa) | $\phi_{peak}$ (°) | $\phi_{stable}$ (°) | Strain soft. (%) | Grain size (μm) | Grain shape | Composition |
|---|---|---|---|---|---|---|---|---|
| *Bern* | | | | | | | | |
| Quartz sand* | 1560 | 21 ± 18 | 35.5 | 31.2 | 15 | 80–200 | angular | 99% $SiO_2$ |
| Corundum sand* | 1890 | 39 ± 10 | 37 | 32.2 | 16 | 88–125 | angular | 95% $Al_2O_3$ |
| Microbeads* | 1480 | 25 ± 4 | 22.3 | 20.6 | 8 | 70–110 | well-rounded | 72.5% $SiO_2$<br>13.8% $Na_2O$<br>8% CaO |
| *Florence* | | | | | | | | |
| Quartz sand | 1550 | 66 | 39 | n.d. | n.d. | <250 | rounded | n.d. |
| *Kyoto* | | | | | | | | |
| Quartz sand | 1390 | n.d. | n.d. | 34 | 9 | m = 203 | angular | 93% $SiO_2$<br>4% $Al_2O_3$ |
| Microbeads | 1420 | n.d. | n.d. | 25 | 0 | m = 193 | spherical | $Na_2O$–CaO–$SiO_2$ |
| *Parma* | | | | | | | | |
| Quartz sand† | 1500 | † | 34.1 | n.d. | n.d. | 60–250 | Sub-rounded | 99.8% $SiO_2$ |
| Microbeads | 1540 | n.d. | n.d. | n.d. | n.d. | m = 180 | rounded | n.d. |
| *Pavia* | | | | | | | | |
| Quartz sand† | 1500 | † | 33.2 | 32.1 | 4.1 | 60–250 | angular to sub-angular | 99.8% $SiO_2$ |
| Microbeads† | 1550–1600 | † | 26.4 | 26.2 | 1 | 150–250 | well-rounded | n.d. |
| *Piscataway* | | | | | | | | |
| Clay‡ | 1600 | ~40 | 27 | n.d. | n.d. | <100 | platy | Kaolinite + 40–50% $H_2O$ |
| *GFZ Potsdam* | | | | | | | | |
| Quartz sand* | 1740 | 94 ± 7 | 35.4 ± 0.3 | 28.2 ± 0.05 | 20.2 | 20–630 (m = 350) | well-rounded | 95% $SiO_2$ |
| Microbeads* | 1590 | −6 ± 19 | 29.1 ± 0.14 | 22.5 ± 0.04 | 13.6 | 300-400 | well-rounded | n.d. |

| | | | | | | | | |
|---|---|---|---|---|---|---|---|---|
| *IFP Rueil-Malmaison* | | | | | | | | |
| Quartz sand | 1500 | n.d. | 45 | 39 | 19 | m = 116 | angular | >98% $SiO_2$ |
| Corundum sand | 1880 | n.d. | 39 | 34 | 16.7 | m = 108 | angular | >98% $Al_2O_3$ |
| Microbeads | 1400–1600 | n.d. | n.d. | n.d. | n.d. | m = 121 | well-rounded | 72.5% $SiO_2$<br>13.8% $Na_2O$<br>8% CaO |
| *Toronto* | | | | | | | | |
| Quartz sand* | 1625 | 3 | 35.7 | 29.2 | 22.2 | 150–200 | angular | >98% $SiO_2$ |
| Microbeads* | 1575 | 41 | 25.5 | 23.4 | 9.2 | ~100 | rounded | n.d. |
| *Uppsala* | | | | | | | | |
| Quartz sand§ | 1350 | ~150 | 33 | 30 | 11 | 60–250<br>m = 125 | angular | 97% $SiO_2$ |
| Microbeads§ | 1440 | ~50 | 21 | 20 | 5 | 53–105 | rounded | 73 % $SiO_2$<br>12.5% $Na_2O$<br>8.5% CaO<br>4.5% MgO |

C = cohesion; m = median of grain size; $\phi_{peak}$ = angle of peak friction; $\phi_{stable}$ = angle of stable-dynamic friction; strain-softening is measured as the difference between coefficient of peak friction and coefficient of stable-dynamic friction divided by the coefficient of peak friction.
n.d. = not determined.
*Angles of peak friction, stable-dynamic friction and inferred cohesion determined with a ring-shear tester (Schulze 1994) at GFZ Potsdam.
†Angles of peak friction and stable-dynamic friction determined with a Casagrande shear box (Casagrande 1932) at high normal loads; these normal loads are much higher than those in the experiments. Values of cohesion obtained by linear regression of high normal stress Casagrande tests are questionable (Pavia: −686 Pa for microbeads, and 21378 Pa for sand; Parma: 12000 Pa for sand).
‡Angle of peak internal friction and inferred cohesion determined with a ring-shear tester (Sims 1993).
§Angles of peak friction, stable-dynamic friction and inferred cohesion determined with a Hubbert-type shear box (Hubbert 1951) at low normal loads comparable to those produced in analogue experiments presented here.

be taken to be equal at both scales. Then,

$$\frac{C_p}{\rho_p} = 10^5 \frac{C_m}{\rho_m} \quad (1)$$

where subscript $p$ denotes natural conditions, subscript $m$ analogue model conditions, $C$ is cohesion and $\rho$ is density. Using representative densities $\rho_m$ *c.* 1600 kgm$^{-3}$ and $\rho_p$ *c.* 2800 kgm$^{-3}$, a cohesion of 10 Pa in the model corresponds to around 2 MPa in nature. The scaling up of viscous properties depends on the assumed velocity $v$ ($v_m$ was prescribed in our experiments):

$$\frac{\eta_p v_p}{\rho_p} = 10^{10} \frac{\eta_m v_m}{\rho_m} \quad (2)$$

for viscosity $\eta$.

## Shortening experiment

### *Model set-up*

In the shortening experiment a thrust wedge was built in alternating layers of different strength. Six laboratories (Bern, Parma, Pavia, IFP Rueil-Malmaison, Toronto, Uppsala) deformed their model by moving the backwall (right-hand wall in our figures) of the apparatus towards the interior of the model (leftward). For ease of description these models are referred to as mobile back wall models (Fig. 1a). Two laboratories (Kyoto and GFZ Potsdam) produced shortening by pulling an underlying sheet horizontally beneath the vertical backwall. These models are referred to as fixed back wall models (Fig. 1b). The applied shortening rate varied between the models. This was not expected to influence the results as only rate-independent brittle model materials were used.

The model dimensions (length and width) varied between the laboratories (Table 2). The mechanical stratigraphy was the same in all models. A 5 mm thick layer of sand at the base of the apparatus was overlain by a 5 mm thick layer of weaker microbeads, which in turn was overlain by additional layers of sand (Fig. 1a, b). To visualize deformation, the sand layers above the microbeads were either coloured differently or alternated with corundum sand, which has similar mechanical properties to quartz sand (laboratories of Bern and IFP Rueil-Malmaison, Table 1). The total thickness of the layers was 3.5 cm. The granular materials were sieved from a height of 20 cm with a filling rate of approximately 250 grams/minute. The model was not pre-compacted before the onset of shortening. A wedge of sand, 10 cm long and with a 10° surface slope was sieved adjacent to the right-hand vertical wall to facilitate the build up of the thrust wedge. The base of the modelling apparatus remained horizontal.

As the Alkor foil created visualization problems across glass sidewalls, the laboratories of Kyoto, Parma and Pavia did not apply foil on the sidewalls, while GFZ Potsdam applied the foil only on the sidewall which was not used for visualization. Two laboratories (Kyoto and Parma) tested the sensitivity of the experimental results to the presence of Alkor foil on the sidewalls. For most laboratories no significant material loss through a gap at the base of the right-hand vertical wall was reported. In the two fixed back wall experiments (Kyoto and GFZ Potsdam) there was a small exit slot (<1 mm) above the conveyor belt. In the Toronto experiment, there was initially no slot below the right-hand mobile wall, but at the end of the experiment a small slot (<1 mm) appeared.

All laboratories monitored the cross-sectional evolution, either by photography through transparent sidewalls (GFZ Potsdam, Kyoto, Parma, Pavia, Toronto and initial stage of Uppsala) or by X-ray CT imaging through the centre of the model (Bern and IFP Rueil Malmaison) (Table 2). The laboratory from Uppsala monitored mainly the surface evolution of the model and cut a cross-section through the central part of the model at the end of the experiment.

### *Comparison of mobile back wall model results*

Figure 2 shows the cross-sectional structural evolution of the eight thrust wedge models after 0, 2, 6, 10 and 14 cm of displacement. A comparison of surface structures of three of the models (Fig. 3) shows a difference in drag of the structures along the sidewalls (walls parallel to the shortening direction). Thrusts are convex to the hinterland for the fixed back wall models and convex to the foreland for the mobile back wall models. Because the two shortening set-ups led to differences in structural evolution and given that the majority of the experiments were mobile back wall models, we only compared quantitative parameters related to the cross-sectional geometry for the six mobile back wall models.

To compare model results quantitatively, we measured the following parameters for up to 14 cm of displacement (Table 3, Figs 4 and 5): the amount of displacement at which forward thrusts form (Fig. 4a), their basal and upper dip

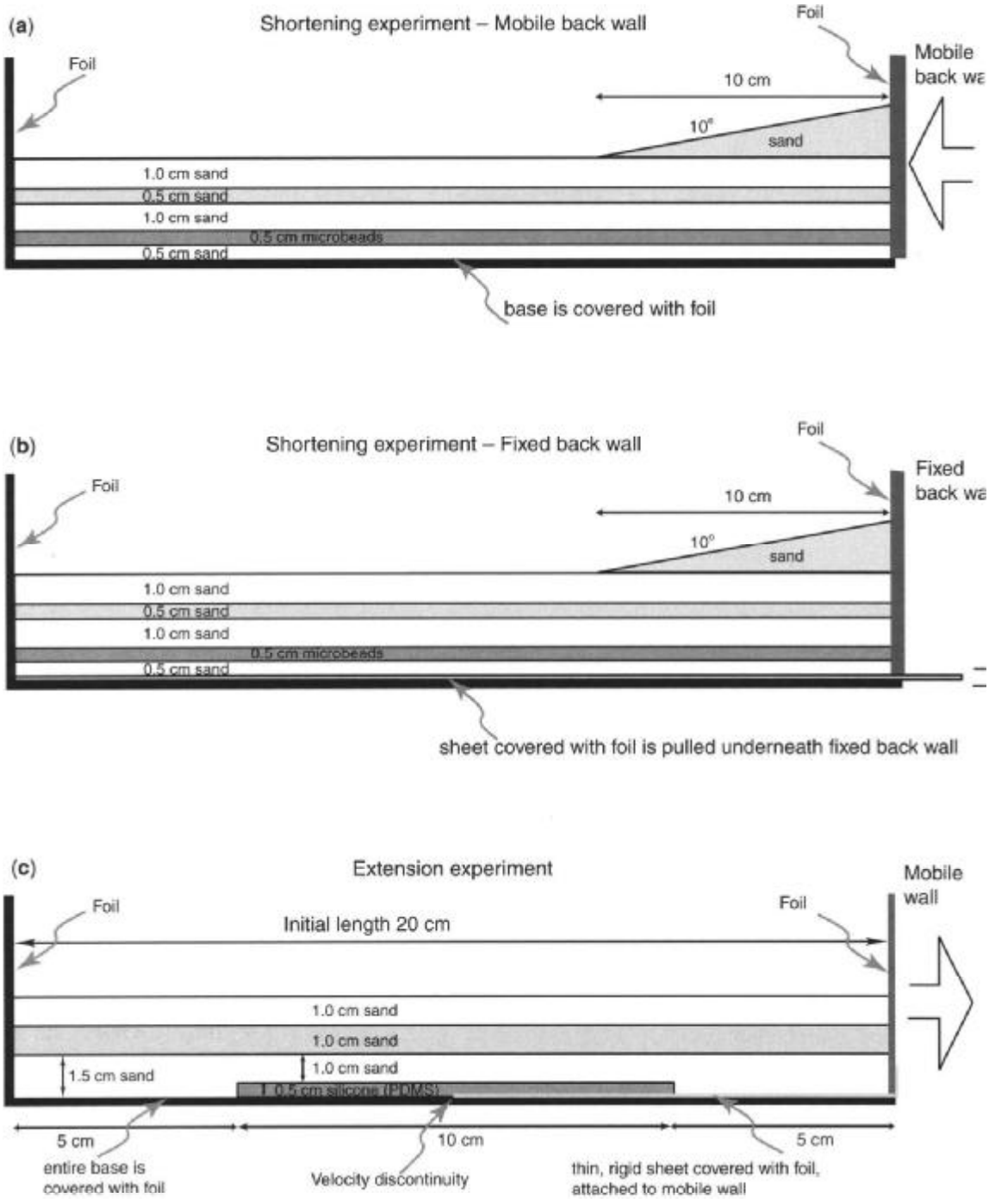


**Fig. 1.** (**a**) Setup of the shortening experiment with a mobile back wall. The mobile back wall moves leftward (towards the foreland). (**b**) Setup of the shortening experiment with a fixed back wall. Shortening is achieved by pulling a basal sheet below the fixed wall. (**c**) Setup of the extension experiment. A thin viscous slab of PDMS, 10 cm wide and 5 mm high, lies in the central part of the model. Half of the PDMS overlies the thin rigid sheet that is attached to the mobile wall. The mobile wall moves rightward.

angle (Figs 4b and c, respectively; see Fig. 4 for definition), the dip angle of back thrusts (Fig. 4d), the spacing between forward thrusts (measured as the distance to the previous thrust at the moment of initiation of a new thrust) (Fig. 4e), the surface slope of the wedge (Fig. 5), the amount of fault-controlled shortening, the displacement at which the microbeads layer was activated and the length of the detachment in the microbeads layer (Table 3). The amount of shortening accommodated by faults is determined from the offset of

**Table 2.** *Model dimensions and details of model set-up*

| Laboratory | Model dimensions* (cm) (shortening experiment) | Model dimensions* (cm) (extension experiment) | Fixed or mobile back wall (shortening experiment) | Alkor foil sidewalls parallel to displ. direction | Small exit slot (shortening experiment) | Thickness rigid basal sheet (extension experiment) | Monitoring method | Other changes with respect to prescribed set-up |
|---|---|---|---|---|---|---|---|---|
| Bern | 35.8 × 80 | 20 × 80 | Mobile | Yes | No | 0.5 mm | CT scan | |
| Florence† | n.a. | 20 × 90 | n.a. | Yes | n.a. | ? | Surface, | |
| | | 20 × 25 | | Yes | | | final sections | |
| Kyoto | 94 × 50 | n.a. | Fixed | No | 0.5 mm | n.a. | Surface, side | |
| | | | | Yes | | | | |
| Parma‡ | 60 × 33 | n.a. | Mobile | Yes | No | n.a. | Surface, side, | |
| | 60 × 33 | | | No | No | n.a. | final sections | |
| Pavia | 70 × 30 | n.a. | Mobile | No | No | n.a. | Surface, side | |
| Piscataway | n.a. | 20 × 61 | n.a. | No | n.a. | 0.2 mm | Surface, | Extension |
| | | | | | | | final sections | to 3 cm |
| GFZ Potsdam | 340 × 20 | n.a. | Fixed | No | 1 mm | 0.3 mm | Surface, side | |
| IFP Rueil-Malmaison | 37 × 78 | 20 × 78 | Mobile | Yes | No | 0.5 mm | CT scan | |
| Toronto | 41.9 × 45 | 29.2 × 45 | Mobile | Yes | Late stage, | 1.6 mm | Surface, side (short), | Initial width |
| | | | | | <1 mm§ | | final sections | ext. expt. |
| | | | | | | | | 29.2 cm |
| Uppsala | 41 × 30 | n.a. | Mobile | Yes | No | n.a. | Surface, | |
| | | | | | | | final sections | |

*Dimensions of model (length × width): length is measured parallel and width perpendicular to shortening or extension direction.
†Two extensional experiments were performed with different model widths.
‡Two shortening experiments were performed with and without Alkor foil on the sidewalls (see Fig. 4 for results with Alkor foil).
§A small exit slot (<1 mm) formed at the end of the experiment as the piston-wall was slightly uplifted.
n.a. = not applicable.

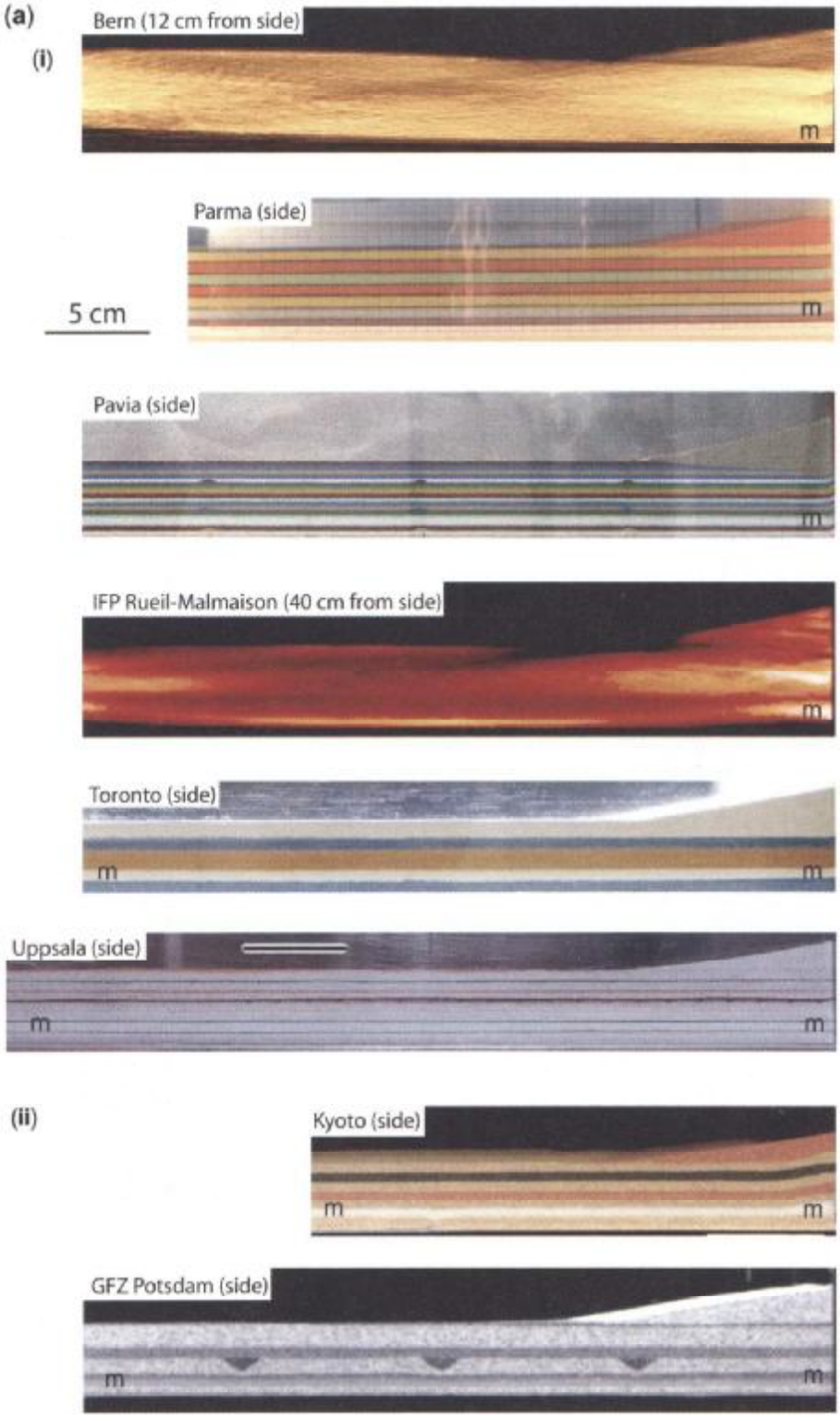


**Fig. 2.** Results for the shortening experiments for mobile back wall (i) and fixed back wall (ii) models. The microbeads layer is indicated by an 'm'. Model length is not shown completely for all laboratories (see also Table 2). Note slightly oblique views for the Toronto model. The microbeads layer is not well visible in CT images of the early stages of the Bern and IFP Rueil-Malmaison experiments. (**a**) Initial geometries. The locations of the cross-sections are indicated with the laboratory names.

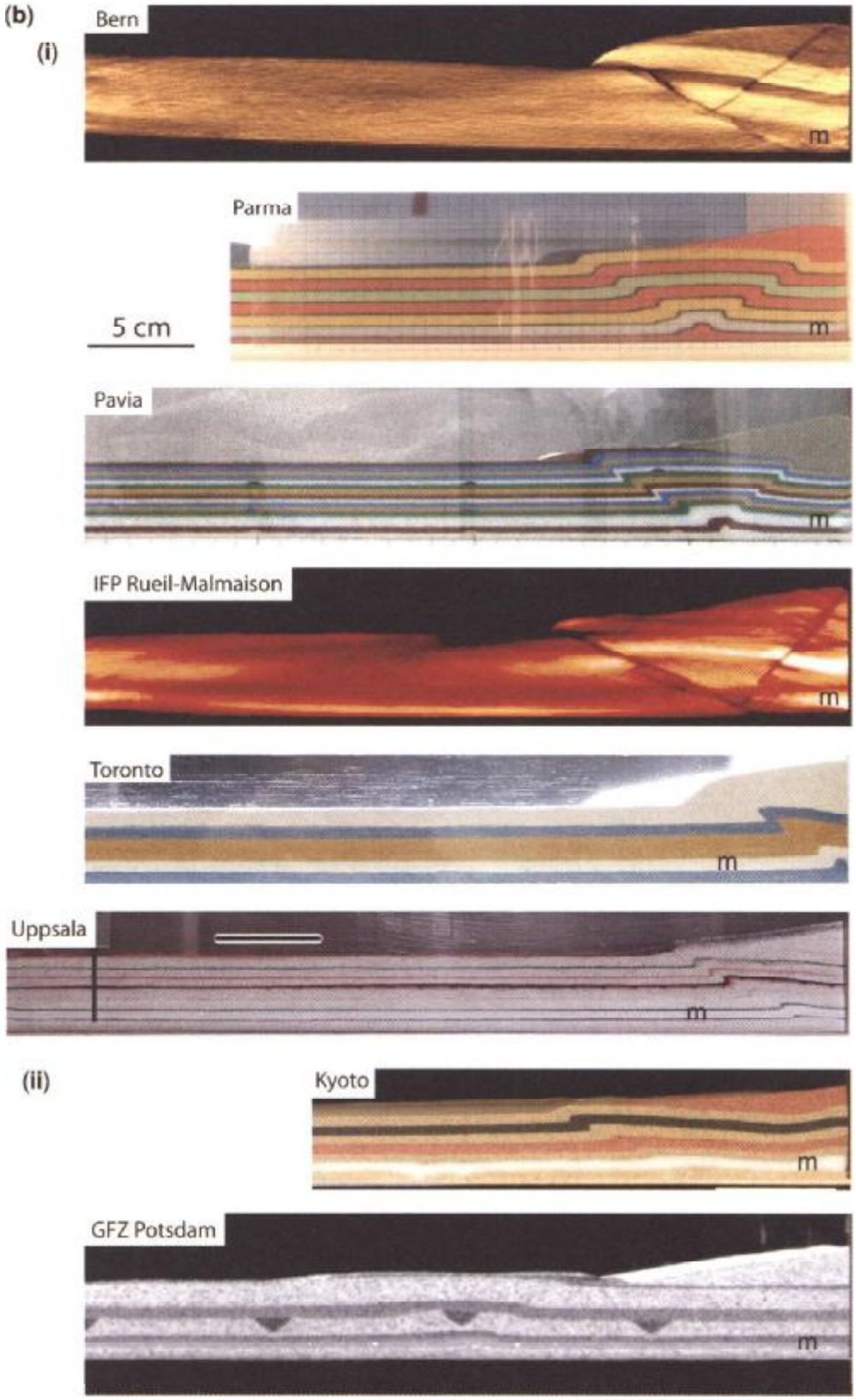


**Fig. 2.** (**b**) Geometries after 2 cm displacement.

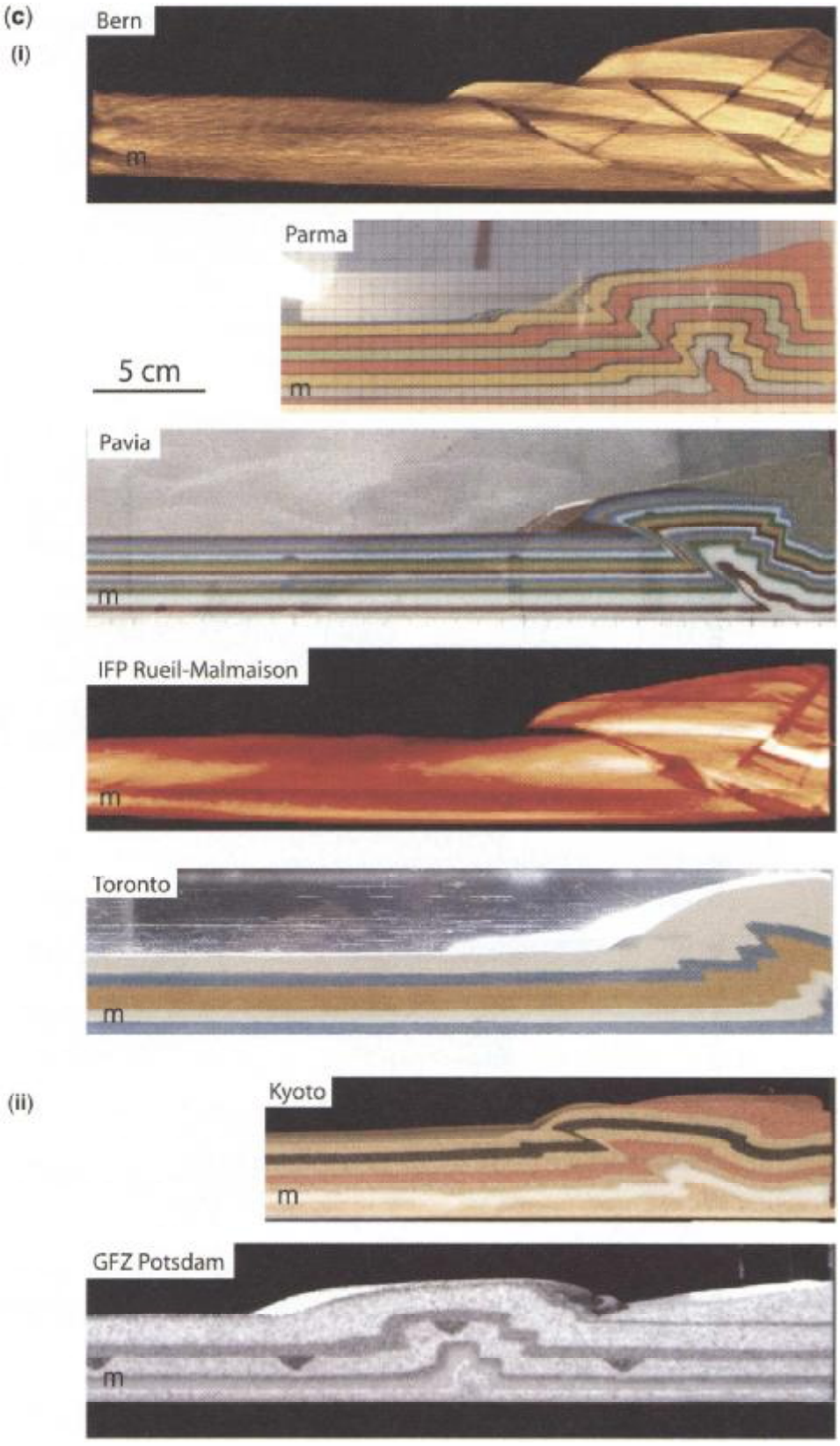


**Fig. 2.** (c) Geometries after 6 cm displacement.

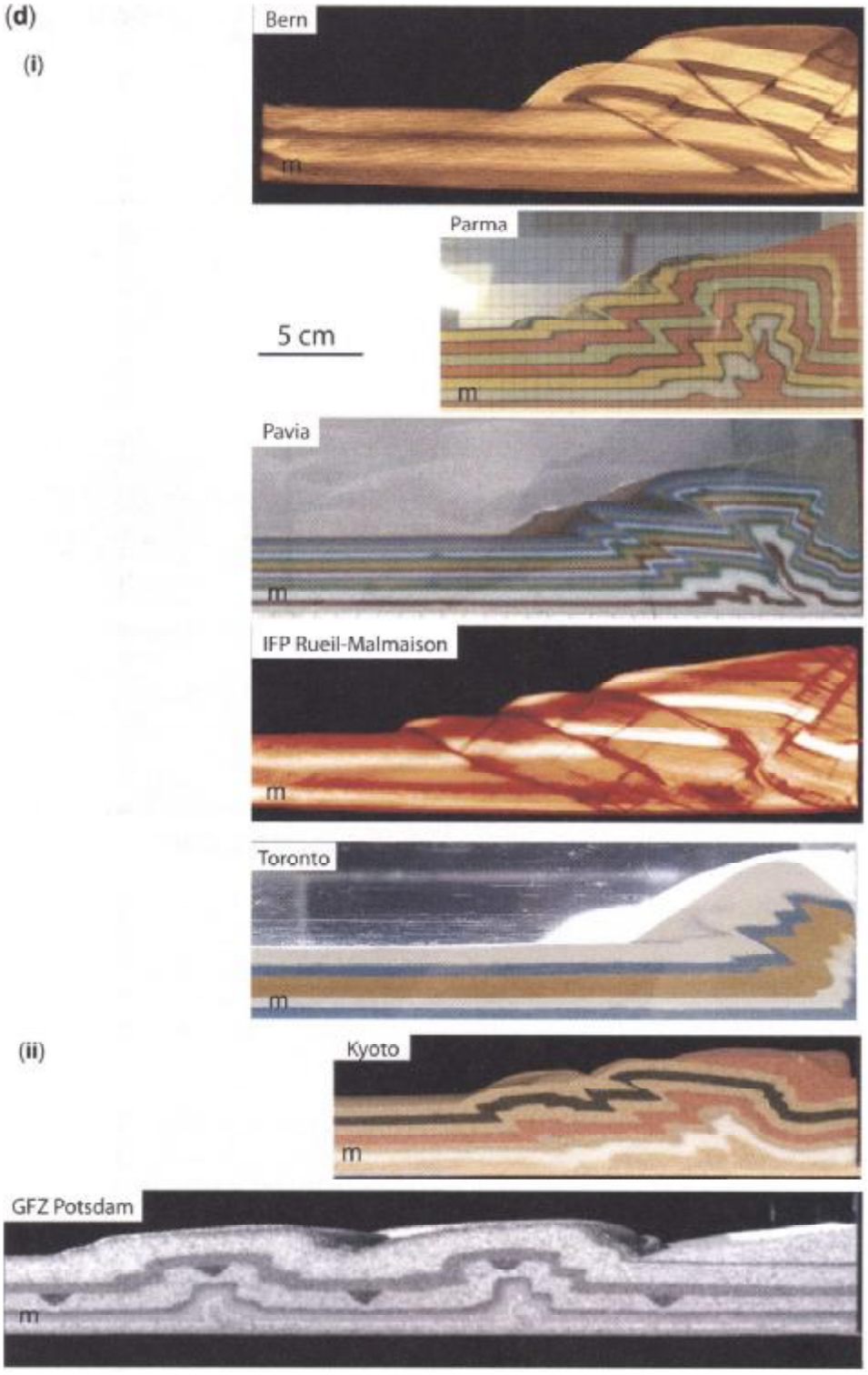


**Fig. 2.** (**d**) Geometries after 10 cm displacement.

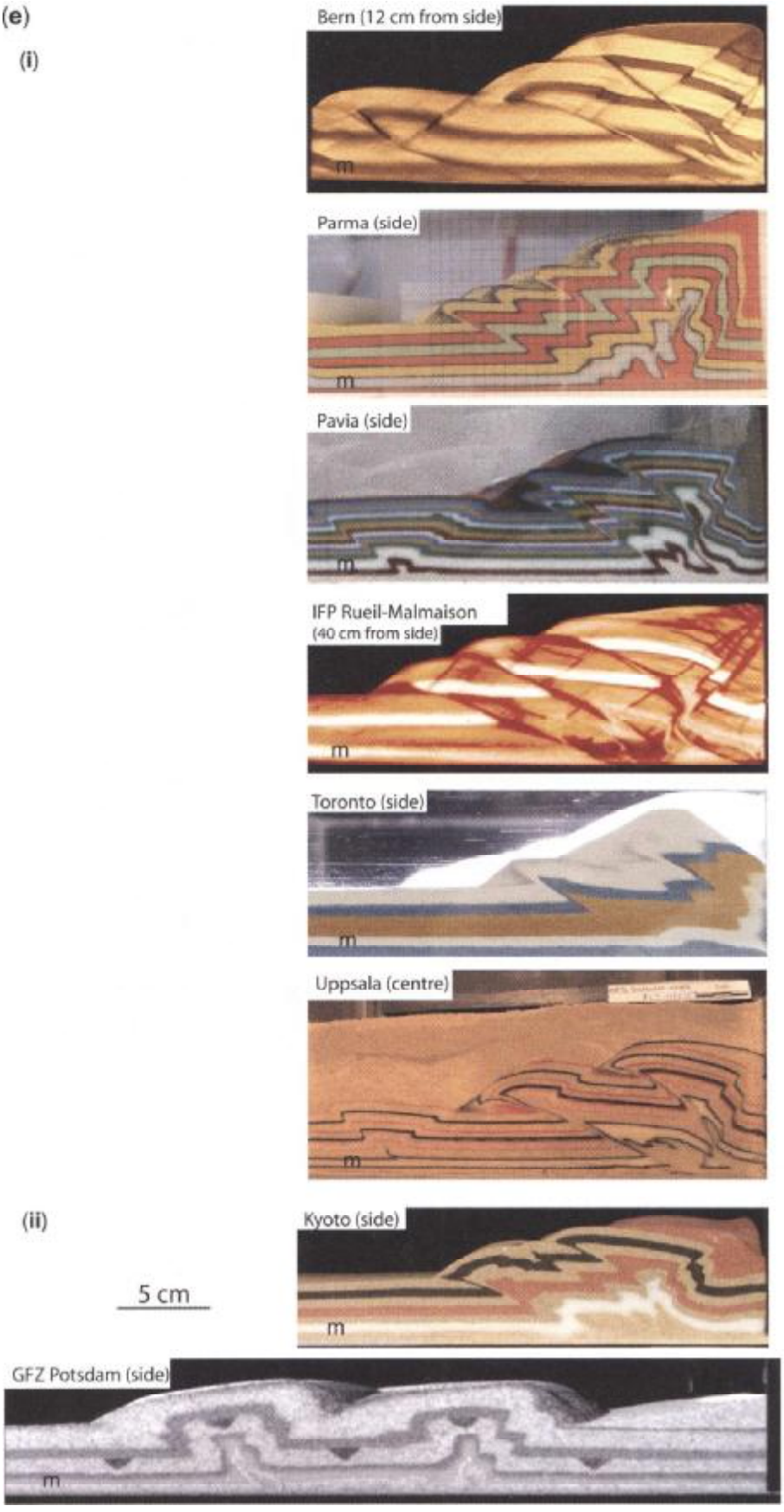


**Fig. 2.** (e) Geometries after 14 cm displacement. The Uppsala model has been covered with an additional sand layer before cutting of section.

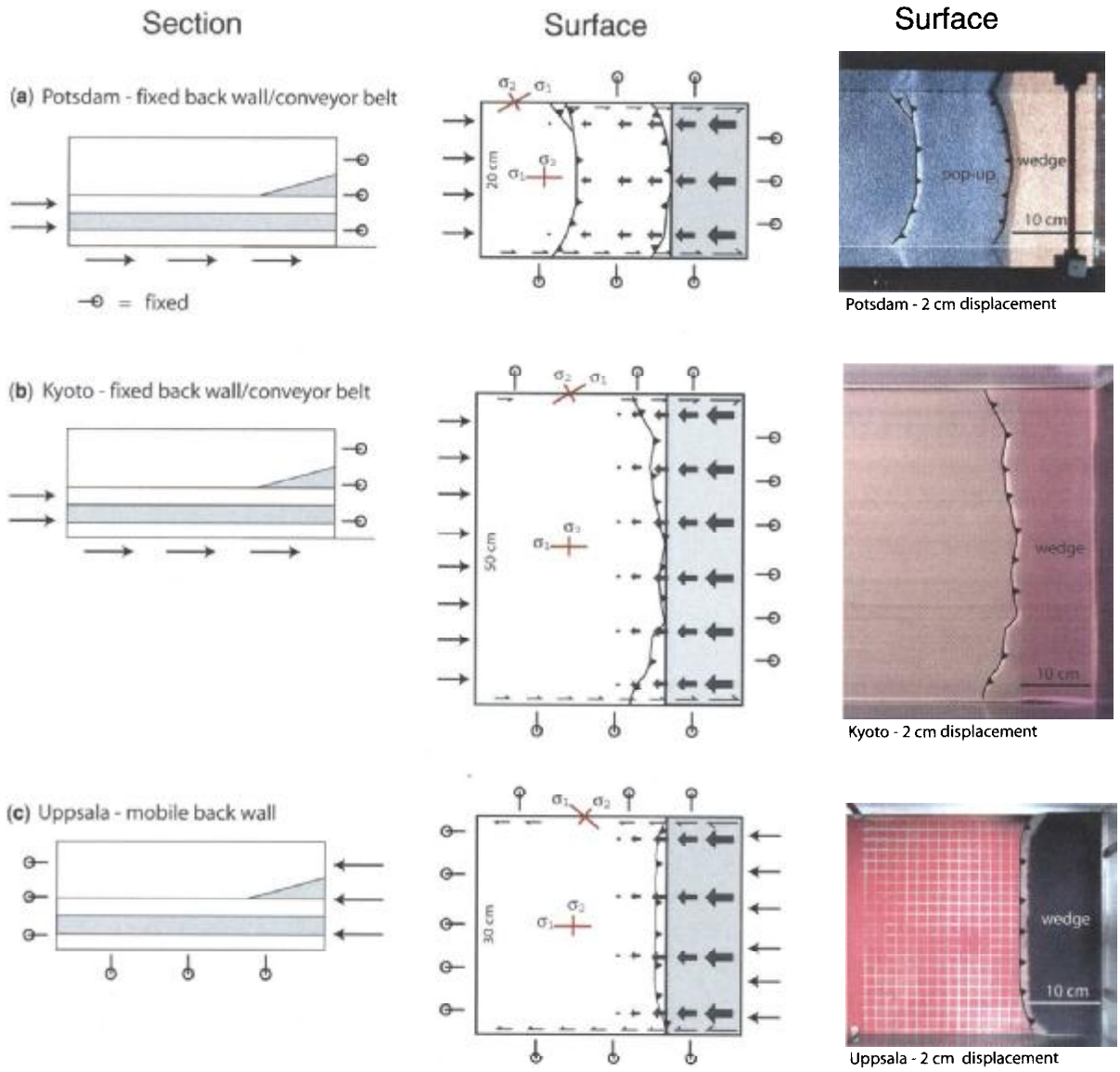


**Fig. 3.** Left-hand column: Cross sections of fixed and mobile back wall model set-ups. Middle column: Surface views with sense and relative magnitude of horizontal shear stresses acting at the base of the model (filled arrows) and shear stresses acting at depth along the lateral sidewalls (half arrows). The rotation of $\sigma_1$ from pure compression in the centre of the model to strike-slip at the sides explains the sense of curvature of the surface traces of the reverse faults. Right-hand column: Surface views of models after 2 cm displacement. (**a**) Fixed back wall model of Potsdam (model width 20 cm). (**b**) Fixed back wall model of Kyoto (model width 50 cm). (**c**) Mobile back wall model of Uppsala. Note the difference in drag of structures along the sidewalls between fixed and mobile back wall models. Grey-shaded area in column in the middle indicates the initial location of the sand wedge.

cut-off points of material layers by the faults. Quantitative analysis used sections along the lateral boundaries (Parma, Pavia and Toronto, initial stage of Uppsala) or through the centre of the model using X-ray CT images (Bern, IFP Rueil-Malmaison). Analysis of the Uppsala model was mainly done by monitoring the surface evolution and by cutting a section through the model at the end of deformation. Thus we could not measure all parameters for this experiment. As in the equivalent numerical models (Buiter *et al.* 2006), we found that the measurements were sensitive to the person measuring due to small differences in interpretation. Therefore, two people measured parameters for all experiments (using cross-sectional images taken at 1 cm increments of displacement) in the same manner and averaged the obtained values. In general the differences between the two measurers were small, with a maximum variation in fault dip angle values of 6°.

**Table 3.** *Quantification of mobile back wall shortening experiments*

| Laboratory | Fault shortening* at 4 cm (cm) | Microbeads layer | |
|---|---|---|---|
| | | Activated at (cm) | Detachment length (cm) |
| Bern | 2.85 | 5 | 6.6 |
| Parma | n.d.† | 11 | 2.2 |
| Pavia | 1.9 | no | – |
| IFP Rueil-Malmaison | 2.75 | no‡ | – |
| Toronto | 1.9 | 10.8 | 9.3 |
| Uppsala | n.d. | 12.3 | 12.7 |

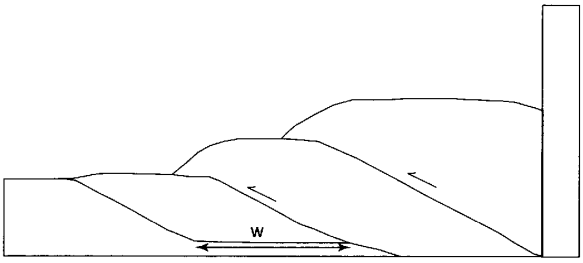


*Fault-controlled horizontal shortening determined by cut-off points between layers and the faults.
†In the model of Parma fault-controlled shortening was not determined as the faults are not narrow shear zones, but rather wide kink-like structures with deflection of layers towards the kink zones.
‡Reactivation of microbeads with a detachment length of 1.8 cm occurred along strike at 9 cm shortening.
Inset at bottom shows how detachment length (w) was measured.

The mobile back wall models share the following similarities: (1) Shortening is accommodated by forward thrusts, which propagate in-sequence towards the foreland, and by back thrusts (Fig. 2). (2) After 2 cm of displacement, an active forward thrust formed in all models (Fig. 2b). (3) The dip angles of this first forward thrust are fairly similar: 28° ± 4° for its lower dip and 29° ± 3° for its upper dip. Upper dip angles are generally slightly steeper (Figs 4b and c). (4) The dip angle of back thrusts is higher than the dip angle of forward thrusts (Fig. 4d).

From Figures 2, 4 and 5 and Table 3 it is also clear that variations in thrust wedge deformation occur among the models: (1) The number of forward thrusts that formed at a particular amount of displacement is variable (maximum difference of two thrusts) (Figs 2 and 4a). (2) Five experiments show the first thrust propagating upward from a point located to the left of the base of the back wall, whereas two experiments (Toronto, Fig. 2b and one model of Parma, Fig. 6a, b) show the forward thrust propagating from the corner at the base of the back wall. The reason for this difference is not entirely clear. A comparison of mobile back wall models whose evolution was monitored through glass sidewalls suggests that the presence of Alkor foil along the sidewalls could promote the formation of forward thrusts emanating from the lower right-hand corner. Cross-sections cut after 14 cm displacement located near or adjacent to the transparent sidewalls are shown in Figure 6 for the two models that applied Alkor foil to the sidewalls (one model of Parma and Toronto). In both models a large number of forward thrusts formed very close to the mobile wall. The absence of back thrusts close to the mobile wall for these models is in agreement with the formation of forward thrusts rooting at the basal right-hand corner, as this does not leave space for the formation of back thrusts propagating from the base. Alternatively, the variation in first thrust configuration could be caused by variation in sand properties. Shear zones may be located close to the mobile wall for sand in which peak strength is reached fast. Variations in friction along the back wall or in the height of the gap below the right-hand wall (however small) may also play a role.

(3) Four experiments (Bern, Parma, Pavia, IFP Rueil-Malmaison) show the formation of a back

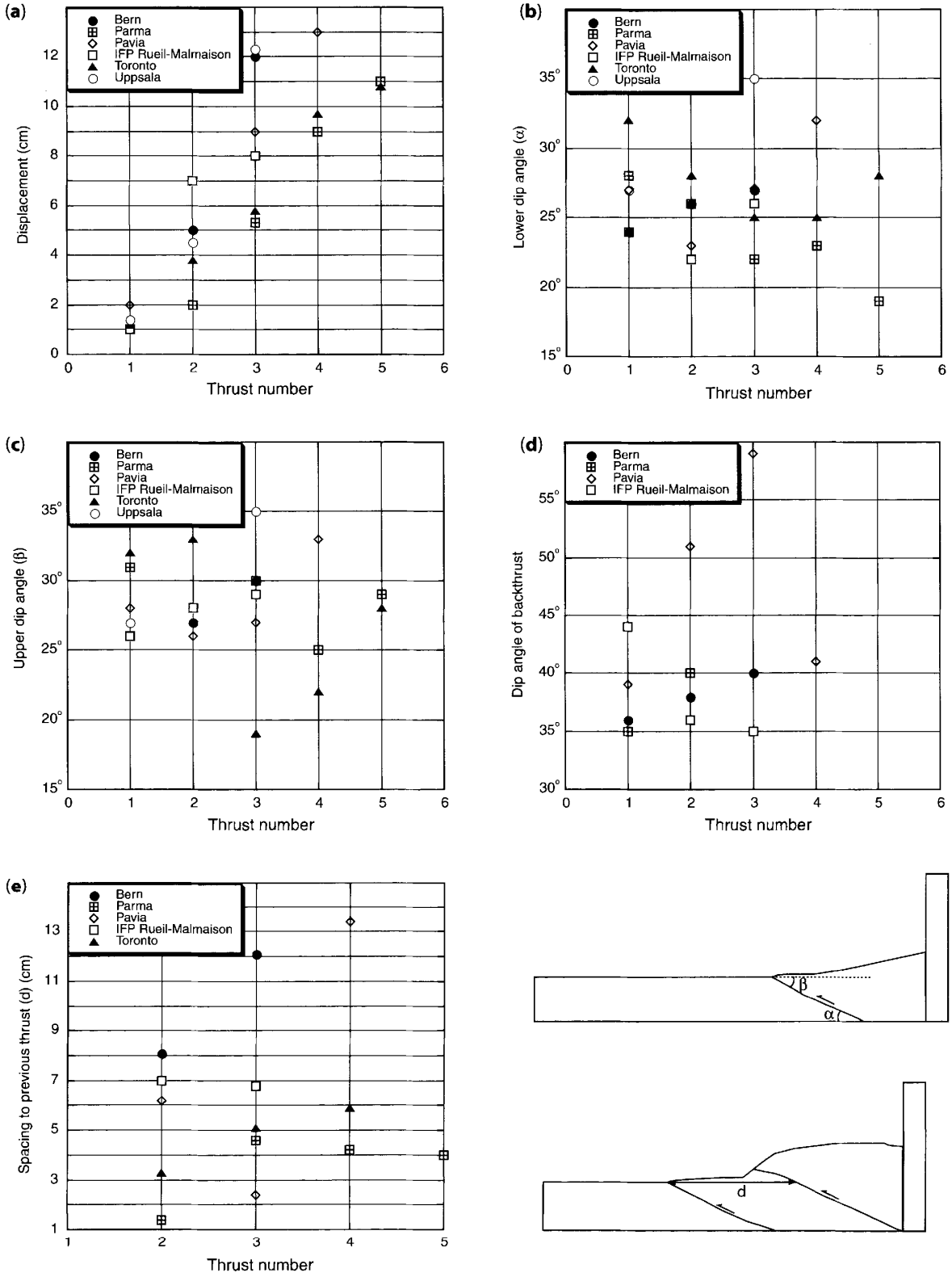


**Fig. 4.** Quantitative comparison of the six mobile back wall models. All values were measured at the moment a new fault initiated. (**a**) The amount of displacement at which a forward thrust forms. (**b**) Lower dip angle of forward thrusts. (**c**) Upper dip angle of forward thrusts. (**d**) Dip angle of back thrusts. (**e**) Spacing to previously formed forward thrust at the moment of initiation of a new forward thrust. Insets at right-hand lower corner show how lower dip angle ($\alpha$), upper dip angle ($\beta$) and thrust spacing (d) were measured.

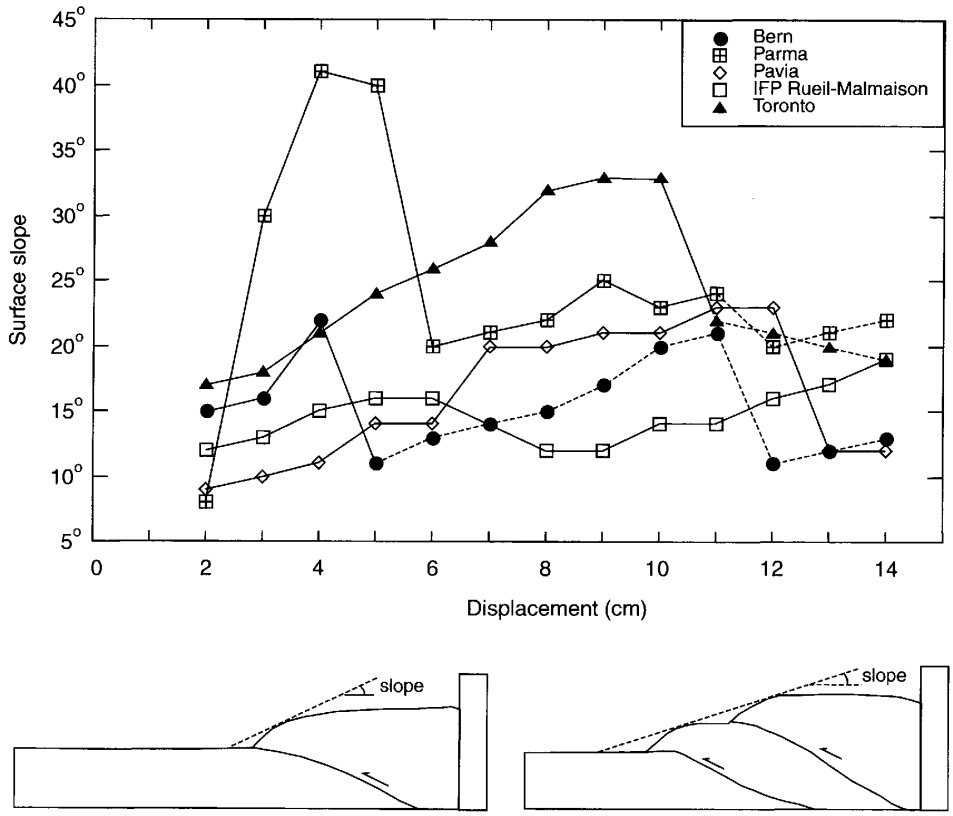


**Fig. 5.** Surface slope versus displacement for five mobile back wall models. Lines are solid when the microbeads layer has not been activated and dotted after activation of the microbeads layer. The insets show how surface slope was measured for one thrust (left) and for more than one thrust (right).

thrust related to the first thrust. In three of these experiments, the back thrust roots onto the base of the model and connects with the upper right-hand corner of the wedge. In the Bern experiment, however, the first back thrust roots at the top of the microbeads layer and does not connect with the upper right-hand corner of the wedge. In this experiment, CT images reveal that the back thrust forms later than the forward thrust. The back thrust rooting at the top of the microbeads layer suggests sensitivity to small variations in material properties (between sand and microbeads) for the Bern model (Fig. 2). In the Toronto experiment back thrusts did not form until 12 cm of displacement and are then related to the frontal thrust (Fig. 6f). (4) The distance between a newly formed thrust and the previously formed thrust is highly variable (Fig. 4e). (5) The microbeads layer was activated in four experiments (Bern, Parma, Toronto, Uppsala). In one experiment (IFP Rueil-Malmaison) activation of microbeads occurred along strike of the sections shown in Figure 2, based on CT scans. In the Pavia experiment, no activation took place (Table 3). (6) The length of the detachment in the microbeads layer is variable (Table 3).

(7) The surface slope of the wedge is also highly variable (Fig. 5). The high surface slope angles at 3 to 5 cm of displacement in the Parma experiment are the result of a second forward thrust that formed very close to the first one (with a thrust spacing of only slightly over 1 cm; Fig. 4e). Oscillations in surface slope angles occur as new thrusts form. The thrust wedges do not seem to reach a stable state. It may be that more displacement is needed before a stable field is reached (Lohrmann *et al.* 2003). Alternatively, alternating use of the embedded microbeads layer or the base of the model for forward thrust propagation may disturb stable surface slopes. The strength contrast between the microbeads layer and the base may be comparable, depending on the sand and microbeads used. Figure 6 shows no clear effect on surface slope of the first activation of the embedded microbeads layer. (8) Fault-controlled shortening at 4 cm of displacement varies between 48 and 71%, implying that diffuse deformation and deformation taken up by folding ranges from 29 to 52%.

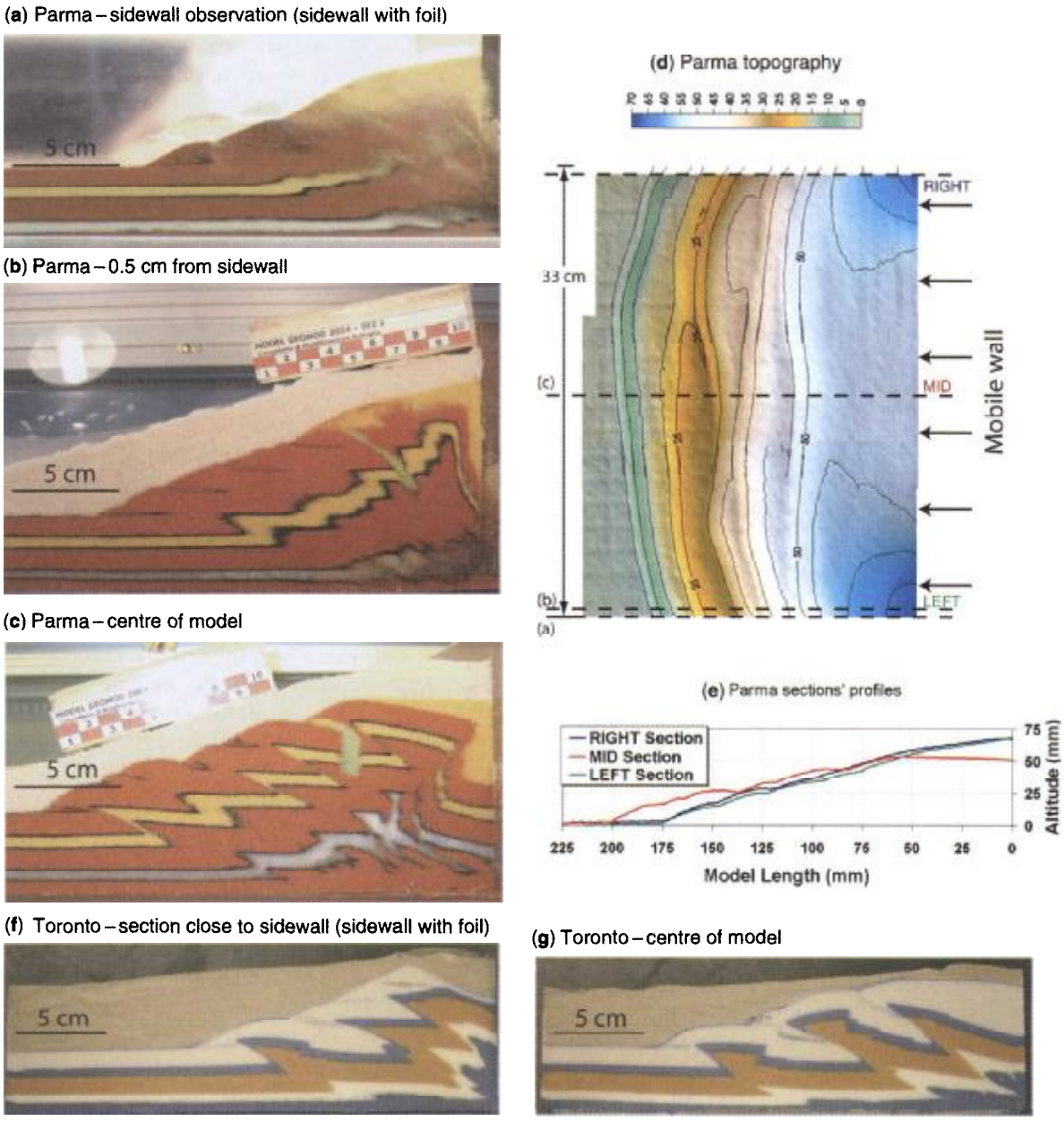


**Fig. 6.** Influence of lateral shear stresses illustrated in models of Parma (a–e) and Toronto (f and g). Structures are shown after 14 cm displacement. This model of Parma shown is with Alkor foil attached to the sidewalls (and is, therefore, different from the model in Fig. 2). The model of Toronto also has Alkor foil applied to the sidewalls (same model as in Fig. 2). (**a**) Cross section as observed through glass sidewalls. Note that Alkor foil partly obscures model visualization. (**b**) Cross section at 0.5 cm from sidewall. (**c**) Cross section through centre of model. (**d**) Contour map showing topography of deformed model, obtained by laser scanner; scale in cm above model base. (**e**) Topographic profiles 0.5 cm from sidewalls (right and left section) and through centre of model ('mid section'). (**f**) Cross section close to lateral sidewall. (**g**) Cross section through centre of model. Note that in (b), (c), (f) and (g) a sand layer was added on top of the model before cutting.

### *Effects of experimental set-up, material properties and boundary conditions*

The geometry and evolution of the structures in the shortening experiments reflects differences in experimental set-up, material properties and model dimensions.

The surface structures in Figure 3 show that thrusts are convex to the hinterland for fixed back wall models and convex to the foreland for mobile back wall models. Although the absolute magnitude of the basal and lateral shear stresses are not known, the curved geometry along the

sidewalls indicates differences in stress trajectories between fixed and mobile back wall models. The sense and relative magnitude of the basal shear stresses at the onset of shortening are the same for both fixed and mobile back wall models. The basal shear stresses are highest near the back wall and decrease away from it as a result of both decreasing wedge load and increasing distance from the back wall. The sense of the lateral shear stresses, however, is different for the fixed and mobile back wall models. The lateral shear stresses in the fixed back wall models are directed towards the fixed back wall, i.e., in a direction opposite to the basal shear stresses. In contrast, in the mobile back wall models the direction of the lateral shear stresses is the same as that of the basal shear stresses. The difference in sense of lateral shear stresses for fixed and mobile back wall models results in the difference in drag of structures near the sidewalls (compare Figs 3a and b with Fig. 3c). In both cases, the drag is in the same direction as the sense of the lateral shear stresses and can be understood from the rotation of the $\sigma_1$ (most compressive stress) direction from pure compression in the centre of the models towards strike-slip at the sides (Fig. 3).

In the fixed back wall model of Potsdam, a pop-up structure formed in front of the pre-existing wedge with the back thrust close to its toe (Figs 2b and 3a). The pre-existing wedge itself was not involved in the thrusting. The initial localization of deformation in front of the wedge in the Potsdam experiment (20 cm width) is similar to other fixed back wall model experiments with an initial wedge geometry and comparable initial thicknesses (Gutscher *et al.* 1996, 1998 (30 cm width); Konstantinovskaia & Malavieille 2005 (10 cm width)). In the mobile back wall models, a forward thrust or box fold structure forms close to the mobile wall and deforms the pre-existing wedge (Figs 2 and 3c). The fixed back wall model of Kyoto (Figs 2 and 3b) shows a structural evolution that is more similar to the mobile back wall models, with a forward thrust surfacing close to the toe of the wedge. A main difference between the Potsdam and Kyoto fixed back wall models is the width (measured perpendicular to shortening direction): the Potsdam model is 20 cm wide and 340 cm long, and the Kyoto model is 50 cm wide and 94 cm long. This suggests that model width has an important influence on the overall structural evolution of the thrust wedge. Comparisons of the Kyoto and Potsdam models (Figs 3a and b) suggest that the effect of lateral shear stresses on model structures is more important in narrow models. The width of a model apparatus needs careful attention, therefore, balancing between minimization of edge effects which occur in narrow models and minimization of heterogeneities due to, for example, hand sieving, which tends to be amplified in wide models.

The set-up of our shortening experiment required that at least 14 cm inward displacement could be accommodated without deformation reaching the back wall. Activation of the microbeads layer may cause thrusting to step further out than for a homogeneous sand layer, and a longer initial domain length will consequently be needed in that case. The region in front of the foremost thrust may, depending on the type of sand used, strain-harden upon shortening, and deformation of the wedge may be influenced if the strain-hardening front reaches the back wall. Adam *et al.* (2005) show that the region of diffuse strain accumulation in front of the wedge can have a length of approximately 15 cm (for a 3.5 cm high input layer). Some models in our study may in their late deformation stages have been affected by the length of the model apparatus, as deformation and/or the region of strain-hardening has reached the back wall. The length of the model apparatus should, therefore, also be considered carefully when designing an experiment.

The effects of lateral shear stresses on the shape of the thrust wedge during shortening are illustrated in Figure 6 for two mobile back wall models (Parma and Toronto). The cross-sectional wedge geometries at different locations (Figs 6a–c and 6f–g), the final model topography (Fig. 6d) and topographic profiles along different cross-sections (Fig. 6e) show that the thrust wedge shortens and steepens toward the sidewalls due to the shear stresses along the sidewalls. It is important, therefore, to evaluate the along-strike (perpendicular to the shortening direction) variation of model results. The effects of sidewall properties on model evolution could be tested by repeating the same experiment while varying only the materials of the walls.

As the properties of the granular materials varied significantly, it was not to be expected that all experiments would develop in an identical manner. The set-up of our comparison is, furthermore, not suitable to uniquely distinguish the effects of the differences in material properties from the influence of other variables such as model boundary conditions and dimensions. This can be tested by performing the same experiment in the same apparatus with different granular materials (Lohrmann *et al.* 2003).

*Implications of the shortening experiments*

The shortening experiments show that differences in material properties, boundary conditions (fixed back wall versus mobile back wall models) and model dimensions may result in significant differences in model results. Despite these differences, a comparison of the mobile back wall models demonstrates similar styles of deformation in which shortening is accommodated by both in-sequence forward propagation of thrusts and, in most models, by back thrusts. We consider this an encouraging result, which will help establish robust features in laboratory tectonic models. The variations in geometry and structural evolution among the mobile back wall models may be attributed to (1) differences in properties of the granular materials, (2) small variations in the exit slot below the mobile wall, (3) differences in the location of observation (at sidewall versus centre of model), (4) the properties of the walls (presence or absence of Alkor foil), (5) width of the box (due to influence of lateral shear stresses), (6) length of the model (for short domain lengths), and (7) set-up technique (for example, small variations may occur when sieving granular layers by hand and levelling of layers after sieving may lead to some compaction).

Our results indicate that care has to be taken when evaluating quantitative results from model experiments and applying them to natural systems. This is especially the case when results are obtained from measurements through transparent sidewalls (where lateral shear stresses are greatest). Although analogue models may be qualitatively used to interpret the mechanics of thrust wedges, limitations apply to quantifiable results such as thrust spacing, surface slope, length of detachment layer and the number of thrusts versus shortening.

## Extension experiment

*Model set-up*

The extension experiment tested the influence of a weak, basal viscous layer on fault localization in overlying brittle materials (Fig. 1c). Five modelling laboratories ran the extension experiment (Bern, Florence, Piscataway, IFP Rueil-Malmaison and Toronto). The initial length (measured parallel to the extension direction) was 20 cm in all models, except for Toronto, where it was 29.2 cm. The width of the model, measured perpendicular to the extension direction, was variable (Table 2). The Florence laboratory ran two experiments with different widths (25 and 90 cm). Alkor foil covered the base and sidewalls of the experimental apparatus. A thin sheet, also covered with Alkor foil, lay on the base of the apparatus. It extended from the centre of the apparatus to a mobile end wall (right-hand side in all figures) and was attached to it. Extension was produced by moving the mobile wall with the attached sheet outward at a constant velocity of 2.5 cm/hour. The edge of the mobile sheet acted as a velocity discontinuity. Total displacement was 5 cm, except for the Piscataway model where it was 3 cm.

A 10 cm long and 5 mm thick slab of viscous PDMS covered the central part of the apparatus. To minimize PDMS sticking to the sidewalls, Vaseline was applied over a height of 5 mm from the right end (mobile) wall to the left end of the PDMS layer. Four models used dry sand and one model (from Piscataway) used wet clay as the brittle analogue material (Table 1). Sand was sieved (from a height of 20 cm with a filling rate of approximately 250 grams/minute) or clay was placed adjacent to and on top of the basal PDMS slab. Multiple sand (or clay) layers had the same material properties (as much as possible), but different colours to help in visualizing deformation. The model was not pre-compacted before the onset of extension. The total height of the model was 3.5 cm. No sedimentation occurred during extension. Two laboratories (Bern and IFP Rueil-Malmaison) monitored the model cross-sectional evolution by X-ray CT imaging through the centre of the model and three laboratories (Florence, Toronto, Piscataway) by monitoring the surface evolution and by cutting a cross-section through the centre after the end of the experiment.

*Model results*

Figure 7 shows the cross-sectional evolution of the models Bern and IFP Rueil-Malmaison for four stages of displacement (0, 0.5, 1 and 2 cm). Figure 8 illustrates the final cross-sectional geometry of all five models. Surface views at 2 cm displacement are shown in Figure 9. We measured the following parameters for a quantitative comparison of the models: the amount of displacement at which the first faults formed and their fault dip angle (Table 4), the amount of fault-controlled extension (Table 4), the displacement at which faults formed at the edges of the silicone layer (Table 4), and the dip angle and migration of the first-formed normal fault to the right of the velocity discontinuity with increasing extension (Fig. 10). Due to different monitoring procedures not all

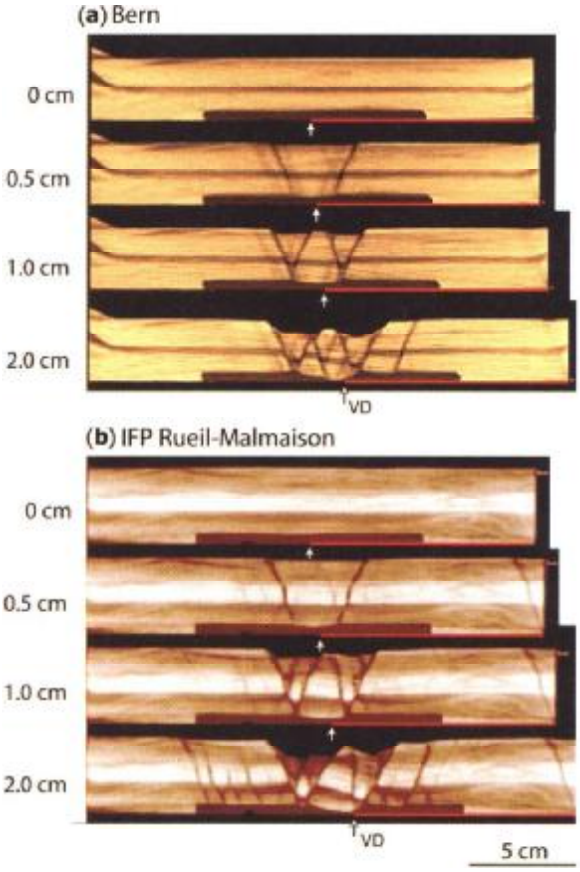


**Fig. 7.** Cross-sectional geometries of two extension experiments at 0, 0.5, 1 and 2 cm displacement. The horizontal red line indicates the position of basal thin sheet covered with Alkor foil. The tip of the basal sheet is indicated with a white arrow (VD = velocity discontinuity). (**a**) Model of Bern. The cross-section is taken 35 cm from the side (see Fig. 9). (**b**) Model of IFP Rueil-Malmaison. The cross-section is taken through the centre of the model.

parameters could be determined for all laboratories. The values were again measured by two people and then averaged.

Analysis of the qualitative and quantitative aspects of the experimental model results allows the following observations:

(1) After 1 cm of displacement, fault zones are visible in all models. In most models, faults formed near the centre of the model and with additional extension, the faulted zone broadened, with younger faults propagating towards the edges of the silicone layer (Fig. 7). In the narrow model of Florence (25 cm width), the model evolution differed (Fig. 9). The first faults nucleated onto the right-hand edge of the silicone layer and much of the subsequent extension was accommodated along these faults. In this narrow experiment, the velocity discontinuity had no influence on localizing initial deformation. With additional extension, most faulting concentrated in the brittle layers along the right-hand edge of the silicone layer and only minor faulting occurred in the centre and left-hand side of the model. In two other models (Toronto and Florence large-width model), early faulting also nucleated at the right-hand edge of the silicone, but nearly simultaneously with the development of faults near the central velocity discontinuity. Faulting in the central part of the model subsequently accommodated most of the continued extension. All sand-silicone models demonstrate that the rheological change between the viscous silicone layer and the brittle sand cover, combined with friction along the sidewalls, may result in the nucleation of faults along the edges of the silicone layer.

(2) All models show drag structures due to friction along the sidewalls (Fig. 9). The sense of the curvature of the surface views of the normal faults can be understood from the rotation of $\sigma_3$ (least compressive stress) from pure extension in the centre of the model towards strike-slip at the sides (see also Vendeville 1987).

(3) The first formed faults have dip angles of 60° to 69° in sand layers and dip angles of 55° to 58° in clay. These dip angles correspond closely to those expected for Mohr-Coulomb faults, for which the fault dip should be $45° + \phi/2$ (Coulomb angle).

(4) The cross-sectional evolution of the Bern and IFP Rueil-Malmaison models, obtained by X-ray CT imaging through the centre of the model, shares many similarities. Extension first leads to the formation of two main fault in the central part of the model on either side of the velocity discontinuity (Fig. 7; panels at 0.5 cm). These faults are initially symmetrically located with respect to the velocity discontinuity. However, the fault extrapolations do not root directly above the velocity discontinuity, but are offset laterally. This may be explained by more distributed thinning of the silicone layer, which smooths out the influence of the velocity discontinuity. Further displacement along the two main normal fault causes further thinning and sideways expulsion of the silicone layer and results in the formation of two conjugate fault sets (Fig. 7; panels at 1 cm). As displacement of the basal sheet continues, the initial symmetry of the first deformation structures is disrupted. The silicone continues to thin, the surface depression becomes wider and asymmetric in shape, and the faulted zone broadens outward.

(5) The dip angle of the first formed normal fault on the right side of the velocity discontinuity that dips away from the mobile wall decreases with continued extension (Fig. 10a). For larger amounts of displacement (5 cm), faults tend to

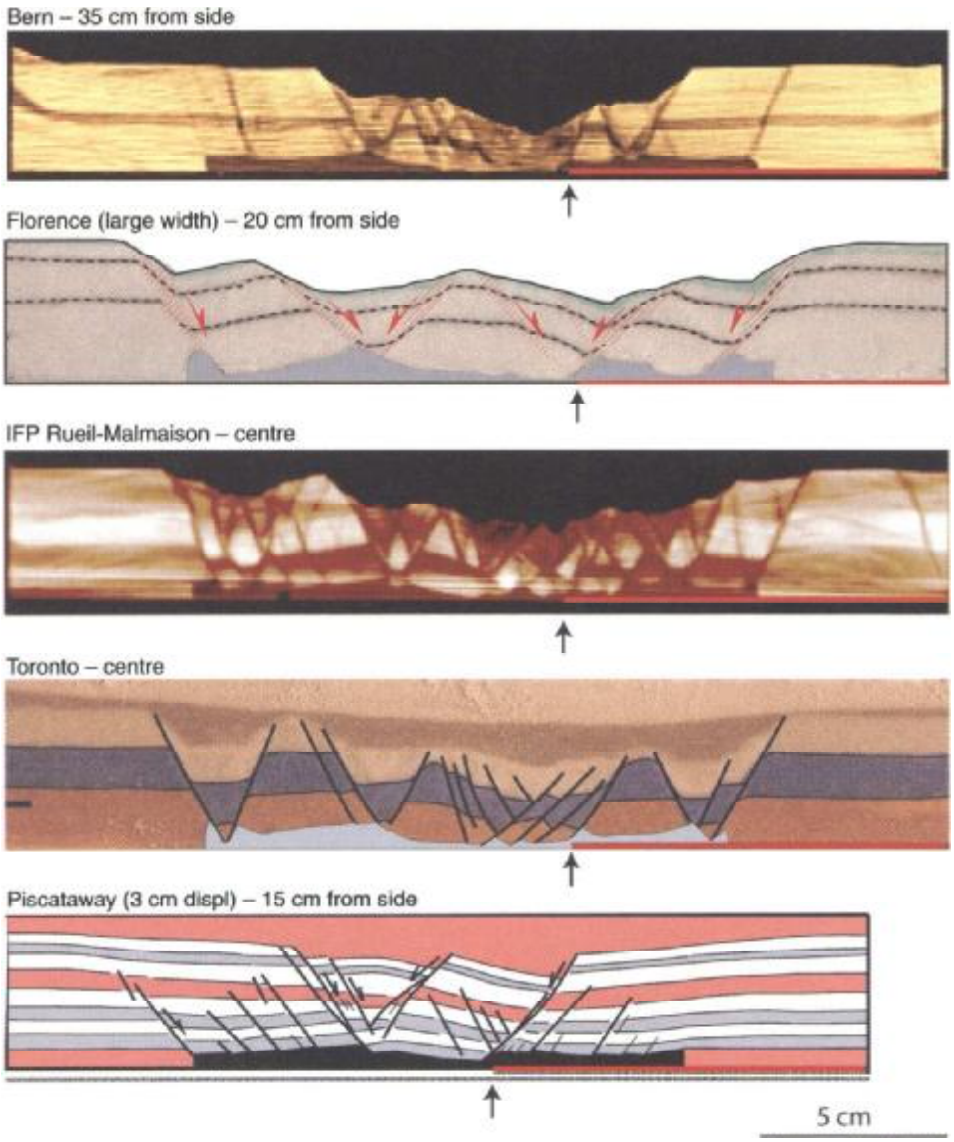


**Fig. 8.** Cross-sectional geometries at 5 cm displacement for the extension models of Bern, Florence (model of 90 cm width), IFP Rueil-Malmaison and Toronto. The Piscataway clay model is at 3 cm displacement (line-drawing after photograph). A sand layer has been added to the models of Toronto and Piscataway before cutting. The horizontal red line indicates the position of the basal thin sheet covered with Alkor foil. The tip of the basal sheet (the velocity discontinuity) is indicated with a small arrow.

become listric and block rotations become more pronounced.

(6) The first-formed normal fault on the right side of the velocity discontinuity (dipping away from the right end wall) moves to the right as the model is extended (Fig. 10b). In the models of Bern and IFP Rueil-Malmaison fault migration is similar and in both cases slower than the displacement velocity of the mobile wall because continued extensional deformation is also accommodated by the formation of new faults in the block located to the right of the first formed normal fault.

(7) The amount of fault-controlled extension at 2 cm could be measured in three experiments and ranges between 0.8 cm in the silicone-clay model and 0.9 to 0.95 in the silicone-sand models.

### *Implications of the extension experiments*

As in the shortening experiment, we find that the width of the model (perpendicular to the extension direction) may cause differences in model results. Lateral friction seems to have a larger influence on initial fault location and evolution

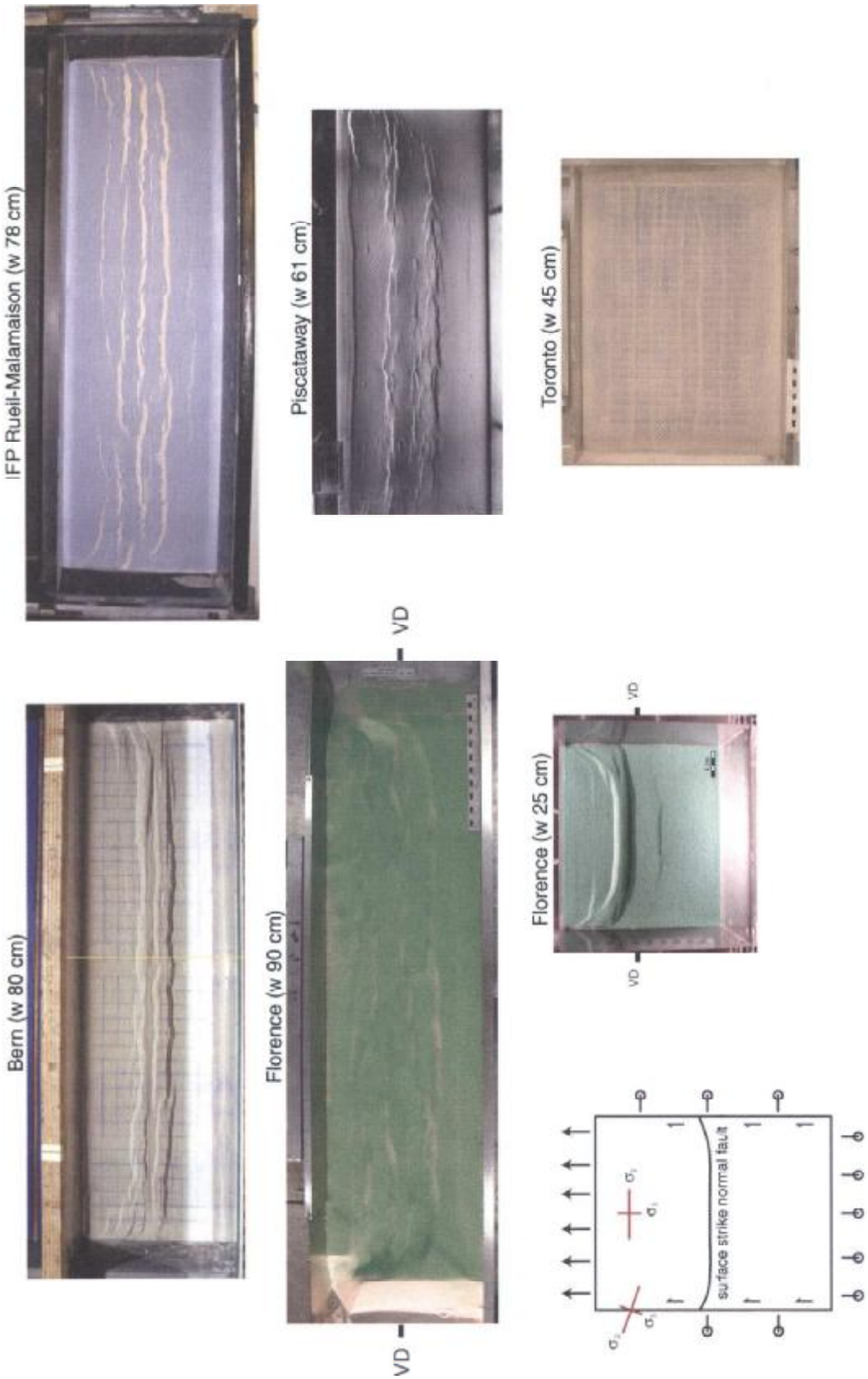


**Fig. 9.** Surface views of the extension models of Bern, Florence (25 cm and 90 cm wide models), IFP Rueil-Malmaison, Piscataway (57 cm of 61 cm width is shown) and Toronto at 2 cm displacement. The width of the models is indicated with the laboratory names at the top of each panel. The mobile wall is at the top of each panel. Inset shows how the rotation of $\sigma_3$ from pure extension in the middle of the model to strike-slip at the sides explains the direction of the drag structures at the sidewalls.

**Table 4.** *Quantification of extension experiment*

| Laboratory | Fault extension* at 2 cm (in cm) | Fault initiation at edges of PDMS (at cm of extension) | | First fault on left side of VD dipping toward mobile wall | | First fault on right side of VD dipping away from mobile wall | |
|---|---|---|---|---|---|---|---|
| | | Left | Right | Dip angle | At extension (cm) | Dip angle | At extension (cm) |
| Bern | 0.9 | never | 4–4.5 | 69° | <0.5 | 65° | <0.5 |
| Florence† | n.d. | 1 | 1 | 60°‡ | <0.5 | § | |
| Piscataway | 0.8 | 2 | never | 55°‖ | | 58°‖ | |
| IFP Rueil-Malmaison | 0.95 | never | 2–2.5 | 65° | <0.5 | 60° | <0.5 |
| Toronto | n.d. | 1.2 | 0.6 | 62° | 0.6–1.2 | 62° | 0.6–1.2 |

*Fault-controlled horizontal extension determined by cut-off points between layers and the faults.
†Results shown are for large-width (90 cm) model.
‡Fault dip measured at surface.
§First two faults that form both dip towards mobile wall.
‖Fault dip measured at surface; faults dip shallower towards bottom of model.
VD = velocity discontinuity.

in narrow models than in the wider models. A comparison between the Toronto model (29.2 cm length) and the other models (20 cm length) (Fig. 8) shows no clear indication for influence of the length of the model for this set-up. In wide models the main graben forms initially above the velocity discontinuity, as observed in the equivalent numerical models (Buiter *et al.* 2006). A comparison between these models shows a high level of agreement with respect to initial fault dip and graben location, graben broadening and decrease in fault dip with continued extension. However, variability in structural evolution does occur and includes differences in the number of normal faults that form and the timing with which faulting propagates to the edges of the viscous layer. The differences in evolution between the models may be attributed to (1) differences in material properties, (2) differences in model width, (3) possible small variations of initial silicone slab geometry, (4) variations in base and wall properties, and (5) differences in location of observation. Similar to the shortening experiment, our results indicate that caution is required when quantitative results such as the

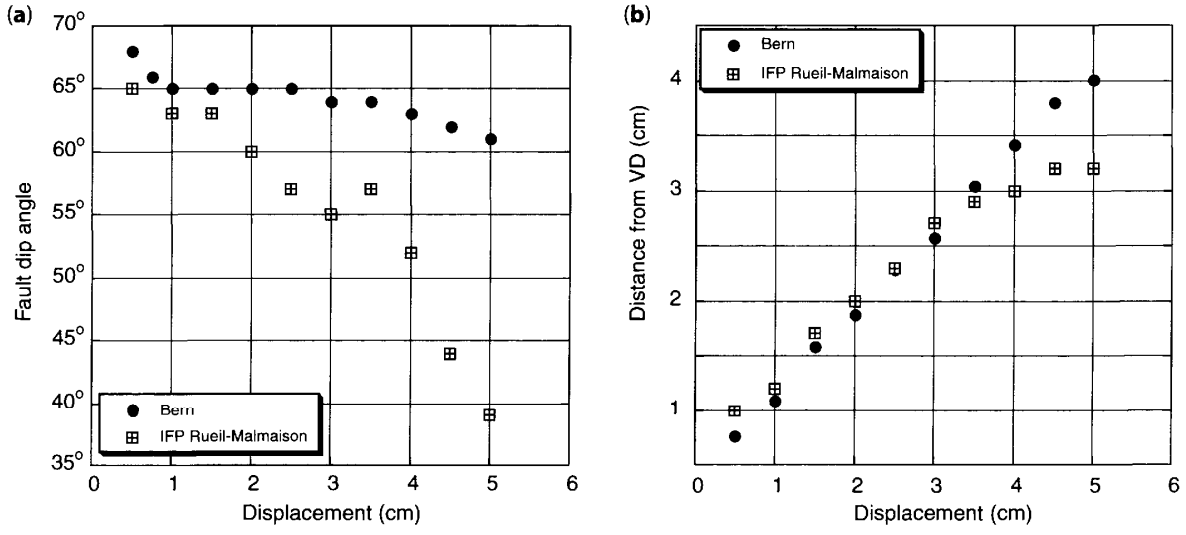


**Fig. 10.** (**a**) Dip angle versus displacement for the first formed normal fault on the right side of the velocity discontinuity and dipping away from the mobile wall. (**b**) Normal fault migration in the extension experiment. The migration of the first formed normal fault on the right side of the velocity discontinuity and dipping away from the mobile wall is measured relative to the velocity discontinuity (VD).

number and spacing of faults are extrapolated from analogue models to natural systems.

## Conclusions and outlook

We used two experimental set-ups to test the reproducibility of model results among different experimental modelling laboratories. We find that all models demonstrate a similar first order evolution. The differences among the models in our study may help to identify main focus points for future comparison studies.

A comparison of eight brittle thrust-wedge experiments shows that model evolution may differ in detail to a considerable extent. These differences may be related to: (1) differences in model set-up (i.e., two laboratories used a conveyor belt below a fixed back wall and six laboratories used a mobile back wall above a fixed horizontal base), (2) differences in model dimensions, (3) location of observation (i.e., at the transparent sidewall or in the centre of the model), (4) material properties of granular materials (angle of internal friction, cohesion and amount of strain softening and strain hardening), (5) mechanical properties along the walls (with or without Alkor foil), (6) small differences in the set-up technique used by individual experimenters ('the human factor'). All mobile back wall experiments show the development of a thrust wedge characterized by in-sequence forward thrusts and minor back thrusting. A large variability exists in quantitative parameters such as fault dip, thrust spacing, number of forward and back thrusts, and surface slope.

The evolution of wide extension models is highly similar. Normal faulting initiates in the brittle layers above the viscous silicone layer, near the basal velocity discontinuity. Fault dip angles tend to shallow with continued extension. Variations between laboratories occur for parameters such as fault dip angle and fault spacing. Reducing the variability in quantifiable parameters such as number of faults and fault spacing will be a challenge for future analogue benchmarks.

The present study is the first ever comparison of analogue experiments between different modelling laboratories and our results may be used as a guide for the design of future comparison studies. Future 'benchmarks' could focus on: (1) a simpler experimental design to minimize the number of differences in experimental set-up among the participating laboratories, (2) use of the same materials in comparison studies between different laboratories (to test the influence of model apparatus and experimenter), (3) measuring the properties of a sample of the same material in different shear testers in order to determine the influence of the measuring method, (4) additional tests of the influence of material properties for different materials and experimental set-ups (where the same experimenter repeats the same experiment in the same laboratory and modelling apparatus), following up on previous studies (e.g., Lohrmann *et al.* 2003; Atmaoui *et al.* 2005; Withjack & Callaway 2000), (5) having different experimenters perform the same experiment using one apparatus (in the same laboratory) to test the 'human factor', (6) testing the variability of quantifiable parameters obtained by one experimenter using one single apparatus and the same materials against the variability of these parameters among laboratories, and (7) testing the effects of the properties of walls and base of the modeling apparatus by performing the same experiment (with the same material and by the same experimenter) for different materials covering the base and walls.

The results of our benchmark study illustrate the importance for analogue experimental studies of a clear specification of modelling apparatus, set-up technique, material properties and boundary conditions, and may help in establishing the degree to which model results may be extrapolated to natural examples.

C. Beaumont, J.-P. Brun, and B. Colletta are thanked for providing constructive feedback on the design of the experiments, J. Adam and S. Ellis for help in determining the list of parameters to quantify, B. Vendeville for insightful discussions on the importance of boundary conditions and experimental procedures, and the participants of the GeoMod2004 pre-conference workshop for helpful discussions. We also thank J. Adam and B. Vendeville for their encouraging and helpful reviews. This study was supported by Swiss National Science Foundation Grant 2000-067952.02 (GS), the Natural Sciences and Engineering Research Council of Canada (ARC), Deutsche Forschungsgemeinschaft as part of SFB 267 (NK), and the Swedish Research Council, VR (HAK and FN).

## References

ADAM, J., URAI, J. L. *ET AL.* 2005. Shear localization and strain distribution during tectonic faulting – new insights from granular-flow experiments and high-resolution optical image correlation techniques. *Journal of Structural Geology*, **27**, 283–301.

ATMAOUI, N., KUKOWSKI, N., STÖCKHERT, B. & KÖNIG, D. 2005. Initiation and development of pull-apart basins with riedel shear mechanism: Insights from clay scaled experiments. *International Journal of Earth Sciences*. DOI: 10.1007/S00531-005-0030-1.

BAHROUDI, A., KOYI, H. A. & TALBOT, C. J. 2003. Effect of ductile and frictional décollements on

style of extension. *Journal of Structural Geology*, **25**, 1401–1423.

BARNHOORN, A. BYSTRICKY, M., BURLINI, L. & KUNZE, K. 2004. The role of recrystallization on the deformation behaviour of calcite rocks: large strain torsion experiments on Carrara marble. *Journal of Structural Geology*, **26**, 885–903.

BRUN, J.-P. 1999. Narrow rifts versus wide rifts: inferences for the mechanics of rifting from laboratory experiments. *Philosophical Transactions, Royal Society London A*, **357**, 695–712.

BRUN, J.-P., SOKOUTIS, D. & VAN DEN DRIESSCHE, J. 1994. Analogue modelling of detachment fault systems and core complexes. *Geology*, **22**, 319–322.

BUITER, S. J. H., BABEYKO, A. YU. *ET AL.* 2006. The numerical sandbox: Comparison of model results for a shortening and an extension experiment. *In*: BUITER, S. J. H. & SCHREURS, G. (eds) *Analogue and Numerical Modelling of Crustal-Scale Processes.* Geological Society, London, Special Publications, **253**, 29–64.

BYERLEE, J. 1978. Friction of rocks. *Pure and Applied Geophysics*, **116**, 615–626.

CADELL, H. M. 1888. Experimental researches in mountain building. *Transactions of the Royal Society of Edinburgh*, **1**, 339–343.

CASAGRANDE, A. 1932. Research on the Atterberg limits of soils. Public Roads, **13(9)**, 121–136.

COLLETTA, B., BALE P., BALLARD, J. F., LETOUZEY, J. & PINEDO, R. 1991. Computerized X-ray tomography analysis of sandbox models: Examples of thin-skinned thrust systems. *Geology*, **19**, 1063–1067.

COSTA, E., CAMERLENGHI, A. *ET AL.* 2004. Modelling deformation and salt tectonics in the eastern Mediterranean Ridge accretionary wedge. *Geological Society of America Bulletin*, **116**, 880–894.

CRUDEN, A. R., NASSERI, M. B. & PYSKLYWEC, R. 2006. Surface topography and internal strain variation in wide hot orogens from three-dimensional analogue and two-dimensional numerical vise models. *In*: BUITER, S. J. H. & SCHREURS, G. (eds) *Analogue and Numerical Modelling of Crustal–Scale Processes.* Geological Society, London, Special Publications, **253**, 79–104.

DAVIS, D., SUPPE, J. & DAHLEN, F. A. 1983. Mechanics of fold-and-thrust belts and accretionary wedges. *Journal of Geophysical Research*, **88**, B2, 1153–1172.

ELLIS, S., SCHREURS, G. & PANIEN, M. 2004. Comparisons between analogue and numerical models of thrust wedge development. *Journal of Structural Geology*, **26**, 1659–1675.

GARTRELL, A. P. 2001. Crustal rheology and its effect on rift basin styles. *In*: KOYI, H. A. & MANCKTELOW, N. S. (eds) *Tectonic Modeling: A volume in honor of Hans Ramberg*. Geological Society of America Memoir, **193**, 221–233.

GUTSCHER, M.-A., KUKOWSKI, N., MALAVIEILLE, J. & LALLEMAND, S. 1996. Cyclical behaviour of thrust wedges: Insights from high basal friction sandbox experiments. *Geology*, **24**, 135–138.

GUTSCHER, M.-A., KUKOWSKI, N., MALAVIEILLE, J. & LALLEMAND, S. 1998. Material transfer in accretionary wedges from analysis of a systematic series of analog experiments: *Journal of Structural Geology*, **20**, 407–416.

HOTH, S., ADAM, J., KUKOWSKI, N. & ONCKEN, O. 2005. Influence of erosion on the kinematics of bivergent orgens. Results from scaled sandbox simulations. *In*: WILLETT, S.D., HOVIUS, N., BRANDON, M.T. & FISHER, D. (eds) *Tectonics, Climate, and Landscape Evolution.* Special Paper **398**, Penrose Conference Series, The Geological Society of America, Boulder, CO, 201–225, DOI: 10.1130/2006.2398 (12).

HUBBERT, M. K. 1937. Theory of scale models as applied to the study of geological structures. *Geological Society of America Bulletin*, **48**, 1459–1520.

HUBBERT, M. K. 1951. Mechanical basis for certain geological structures. *Geological Society America Bulletin*, **62**, 355–372.

JAEGER, J. C. & COOK, N. G. W. 1979. *Fundamentals of rock mechanics.* John Wiley and Sons, New York, 585pp.

KEEP, M. & MCCLAY, K. R. 1997. Analogue modelling of multiphase rift systems. *Tectonophysics*, **273**, 239–270.

KONSTANTINOVSKAIA, E. & MALAVIEILLE, J. 2005. Erosion and exhumation in accretionary orogens: Experimental and geological approaches. *Geochemistry, Geophysics, Geosystems ($G^3$)*, **6**, Q02006, DOI 10.1029/2004GC000794.

KOYI, H. A. 1995. Mode of internal deformation in sand wedges. *Journal of Structural Geology*, **17**, 293–300.

KOYI, H. A. 1997. Analogue modelling: From a qualitative to a quantitative technique, a historical outline. *Journal of Petroleum Geology*, **20**, 223–238.

KUKOWSKI, N., LALLEMAND, S. E., MALAVIEILLE, J., GUTSCHER, M.-A. & RESTON, T. J. 2002. Mechanical decoupling and basal duplex formation observed in sandbox experiments with application to the western Mediterranean Ridge accretionary complex. *Marine Geology*, **186**, 29–42.

LALLEMAND, S. E., SCHNÜRLE, P. & MALAVIEILLE, J. 1994. Coulomb theory applied to accretionary and non-accretionary wedges: Possible causes for tectonic erosion and/or frontal accretion. *Journal of Geophysical Research*, **99**, B6, 12033–12055.

LOHRMANN, J., KUKOWSKI, N., ADAM, J. & ONCKEN, O. 2003. The impact of analogue material properties on the geometry, kinematics, and dynamics of convergent sand wedges. *Journal of Structural Geology*, **25**, 1691–1771.

MALAVIEILLE, J. 1984. Modélisation expérimentale des chevauchements imbriqués: application aux chaînes de montagnes. *Bulletin Societé Géologique de France*, **7**, 129–138.

MARONE, C. 1998. Laboratory-derived friction laws and their application to seismic faulting. *Annual Review of Earth and Planetary Sciences*, **26**, 643–696.

MUGNIER, J. L., BABY, P., COLLETTA, B., VINOUR, B., BALE, P. & LETURMY, P. 1997. Thrust geometry controlled by erosion and sedimentation: A view from analogue models. *Geology*, **25**, 427–430.

MULUGETA, G. 1988. Modelling the geometry of Coulomb thrust wedges. *Journal of Structural Geology*, **10**, 847–859.

MULUGETA, G. & KOYI, H. 1987. Three-dimensional geometry and kinematics of experimental piggy-back thrusting. *Geology*, **15**, 1052–1056.

MULUGETA, G. & KOYI, H. 1992. Episodic accretion and strain partitioning in a model sand wedge. *Tectonophysics*, **202**, 319–322.

PANIEN, M. 2004. Analogue modelling experiments of basin inversion using well-characterized granular materials and comparisons with numerical models. Ph.D. thesis. University of Bern, Switzerland.

PANIEN, M., BUITER, S. J. H., SCHREURS, G. & PFIFFNER, O. A. 2006 Inversion of a symmetric basin: Insights from a comparison between analogue and numerical experiments. *In*: BUITER, S. J. H. & SCHREURS, G. (eds) *Analogue and Numerical Modelling of Crustal-Scale Processes.* Geological Society, London, Special Publications, **253**, 253–270.

PYSKLYWEC, R. N. & CRUDEN, A. R. 2004. Coupled crust-mantle dynamics and intraplate tectonics: two-dimensional numerical and three-dimensional analogue modelling. *Geochemistry, Geophysics Geosystems G*$^3$, **5(10)**, DOI 10.1029/2004GC000748.

RAMBERG, H. 1981. *Gravity, deformation and the Earth's crust.* Academic Press, London.

SCHELLART, W. P. 2000. Shear test results for cohesion and friction coefficients for different granular materials: scaling implications for their usage in analogue modelling. *Tectonophysics*, **324**, 1–16.

SCHREURS, G., HÄNNI, R. & VOCK, P. 2001. Four-dimensional analysis of analog models: Experiments on transfer zones in fold and thrust belts. In: KOYI, H. A. & MANCKTELOW, N. S. (eds) *Tectonic Modeling: A volume in honor of Hans Ramberg*. Geological Society of America Memoir, **193**, 179–190.

SCHULZE, D. 1994. Entwicklung und Anwendung eines neuartigen Ringschergerätes. *Aufbereitungstechnik*, **35(10)**, 524–535.

SIMS, D. 1993. The rheology of clay: a modeling material for geologic structures: *EOS, Transactions, American Geophysical Union*, **74**, 569.

STORTI, F. & MCCLAY, K. 1995. Influence of syntectonic sedimentation on thrust wedges in analogue models. *Geology*, **23**, 999–1002.

STORTI, F., SALVINI, F. & MCCLAY, K. 2000. Synchronous and velocity-partitioned thrusting and thrust polarity reversal in experimentally produced doubly-vergent thrust wedges: Implications for natural orogens. *Tectonics*, **19(2)**, 378–396.

TEN GROTENHUIS, S. M., PIAZOLO, S., PAKULA, T., PASSCHIER, C. W. & BONS, P.D. 2002. Are polymers suitable rock analogs? *Tectonophysics*, **350**, 35–47.

TRON, V. & BRUN, J-P. 1991. Experiments on oblique rifting in brittle-ductile systems. *Tectonophysics*, **188**, 71–84.

TURRINI, C., RAVAGLIA, A. & PEROTTI, C. 2001. Compressional structures in a multilayered mechanical stratigraphy: Insights from sandbox modeling with three-dimensional variations in basal geometry and friction. *In*: KOYI, H. A. & MANCKTELOW, N. S. (eds) *Tectonic Modeling: A volume in honor of Hans Ramberg*. Geological Society of America Memoir, **193**, 158–178.

VENDEVILLE, B. C. 1987. *Champs de failles et tectonique en extension: modélisation expérimentale.* Ph.D. thesis, University of Rennes I.

VENDEVILLE, B. C. & JACKSON, M. P. A. 1992*a*. The rise of diapirs during thin-skinned extension. *Marine Petroleum Geology*, **9**, 331–353.

VENDEVILLE, B. C. & JACKSON, M. P. A. 1992*b*. The fall of diapirs during thin-skinned extension. *Marine Petroleum Geology*, **9**, 354–371.

WEIJERMARS, R. 1986. Flow behaviour and physical chemistry of bouncing putties and related polymers in view of tectonic laboratory applications. *Tectonophysics*, **124**, 325–358.

WITHJACK, M. O. & CALLAWAY, S. 2000. Active normal faulting beneath a salt layer; an experimental study of deformation patterns in the cover sequence. *AAPG Bulletin*, **84**, 627–651.

# The numerical sandbox: comparison of model results for a shortening and an extension experiment

SUSANNE J. H. BUITER[1], ANDREY YU. BABEYKO[2,8], SUSAN ELLIS[3], TARAS V. GERYA[4], BORIS J. P. KAUS[5], ANTJE KELLNER[2], GUIDO SCHREURS[6] & YASUHIRO YAMADA[7]

[1]*Centre for Geodynamics, Geological Survey of Norway, 7491 Trondheim, Norway (e-mail: susanne.buiter@ngu.no)*

[2]*GeoForschungsZentrum Potsdam, Telegrafenberg, 14473 Potsdam, Germany*

[3]*Institute of Geological and Nuclear Sciences, P.O. Box 30368, Lower Hutt, New Zealand*

[4]*Swiss Federal Institute of Technology, Sonneggstrasse 5, 8092 Zürich, Switzerland*

[5]*Department of Earth Sciences, University of Southern California, Los Angeles, USA*

[6]*Institute of Geological Sciences, University of Bern, Baltzerstrasse 1-3, 3012 Bern, Switzerland*

[7]*Department of Civil and Earth Resources Engineering, Kyoto University, Kyoto 606-5801, Japan*

[8]*Now at Institut für Meteorologie und Geophysik, J.W. Goethe Universität Frankfurt, Germany*

**Abstract:** We report results of a study comparing numerical models of sandbox-type experiments. Two experimental designs were examined: (1) A brittle shortening experiment in which a thrust wedge is built in material of alternating frictional strength; and (2) an extension experiment in which a weak, basal viscous layer affects normal fault localization and propagation in overlying brittle materials. Eight different numerical codes, both commercial and academic, were tested against each other. Our results show that: (1) The overall evolution of all numerical codes is broadly similar. (2) Shortening is accommodated by in-sequence forward propagation of thrusts. The surface slope of the thrust wedge is within the stable field predicted by critical taper theory. (3) Details of thrust spacing, dip angle and number of thrusts vary between different codes for the shortening experiment. (4) Shear zones initiate at the velocity discontinuity in the extension experiment. The asymmetric evolution of the models is similar for all numerical codes. (5) Resolution affects strain localization and the number of shear zones that develop in strain-softening brittle material. (6) The variability between numerical codes is greater for the shortening than the extension experiment.

Comparison to equivalent analogue experiments shows that the overall dynamic evolution of the numerical and analogue models is similar, in spite of the difficulty of achieving an exact representation of the analogue conditions with a numerical model. We find that the degree of variability between individual numerical results is about the same as between individual analogue models. Differences among and between numerical and analogue results are found in predictions of location, spacing and dip angle of shear zones. Our results show that numerical models using different solution techniques can to first order successfully reproduce structures observed in analogue sandbox experiments. The comparisons serve to highlight robust features in tectonic modelling of thrust wedges and brittle-viscous extension.

Numerical and analogue modelling methods represent two different techniques with which the evolution of geological structures, such as fold-and-thrust belts and sedimentary basins, can be investigated. The underlying assumption with both methods is that their results approximate the development of structures in the real Earth in a reasonable manner. We may then expect that the results of analogue and numerical models look similar when applied to the same

*From*: BUITER, S. J. H. & SCHREURS, G. (eds) 2006. *Analogue and Numerical Modelling of Crustal-Scale Processes*. Geological Society, London, Special Publications, **253**, 29–64.
0305-8719/06/$15.00 

set-up. This expectation motivated us to directly compare results of numerical models obtained with different codes and results of analogue experiments from different laboratories. The aims of our study are (1) to compare results from different numerical codes and (2) to test the similarity of numerical and analogue models, in order to help establish robust features of tectonic models on the scale of the upper crust.

The companion paper (Schreurs *et al.* 2006) presents the results of an analogue comparison study with ten participating modelling laboratories. Two experimental set-ups were tested: (1) a brittle convergent thrust wedge experiment and (2) a brittle-viscous extension experiment. The reproducibility of modelling results between the laboratories was found to be fairly high as shown by the same general trends in the results. Differences between the analogue models were found in, for example, number of faults, fault spacing and dip, and surface slopes. The study highlights the importance of (1) a careful determination of properties of the granular materials and (2) the effects of lateral side boundaries on resulting structures due to friction between model materials and sidewalls. A sandbox needs to be wide enough, therefore, to avoid such boundary effects, and structures should if possible be studied in sections well away from the sidewalls.

We present numerical equivalents of the two analogue experiments of Schreurs *et al.* (2006). The conditions of the analogue modelling apparatus and the analogue material properties are approached as closely as possible. We compare the numerical results to each other through determination of their qualitative (visual) and quantitative (measurements of, for example, surface slope and shear zone dip) similarities and differences. Our study is not a numerical benchmark in its strictest sense as this would require the use of the exact same initial setup, material properties, boundary conditions, mesh size and time step size (see for example the numerical convection benchmarks of Blanckenbach *et al.* 1989; van Keken *et al.* 1997). Instead, we show the variability in results obtained by using different solution methods (finite element method, finite difference method and distinct element method) and allowing variations in mesh and time step size and boundary conditions (e.g., implementation of boundary friction). With our approach, we test the code-independence of tectonic structures predicted by numerical models and our findings are, therefore, of direct relevance for studies in which numerical experiments are used to investigate geological processes. Eight numerical codes were used in our comparison: Abaqus/Standard, LAPEX-2D, I2ELVIS, Microfem, NISA/Static, PFC$^{2D}$, SloMo and Sopale. A description of these codes is given in the next section.

The combination of our study with the accompanying paper results in a series of numerical and analogue model experiments, which are compared in a qualitative and quantitative manner with each other. Our results can be used to evaluate how closely various numerical solution methods can reproduce analogue model conditions. Issues that should be considered carefully in the 'numerical sandbox' include the suitability of continuum methods (e.g., finite element method) in simulating the behaviour of discontinuous grains, the importance of dilatation and compaction in granular materials, and the representation of velocity discontinuities. Numerical modelling of sandbox experiments poses significant computational challenges requiring that numerical codes are able to (1) calculate large deformations, (2) represent complex boundary conditions, including frictional boundaries and free surfaces, and (3) include a complex rheology involving both viscous and frictional/plastic materials. These challenges reflect directly the state-of-the-art requirements for numerical modelling of large-scale tectonic processes.

The two experimental set-ups were designed to reflect set-ups commonly used in the study of upper-crustal tectonic processes. Convergent thrust wedges have been studied with analytical techniques (Davis *et al.* 1983; Dahlen 1984), analogue experiments (e.g., Mulugeta 1988; Gutscher *et al.* 1998*a*; Storti *et al.* 2000) and numerical models (e.g., Strayer *et al.* 2001; Burbridge & Braun 2002). Similarly, brittle-viscous extension has been investigated with analogue (e.g., Michon & Merle 2000; Bahroudi *et al.* 2003) and numerical (e.g., Behn *et al.* 2002; Wijns *et al.* 2003) methods. A few previous studies have combined numerical and analogue modelling methods for studying a tectonic process on the scale of the crust. Sassi *et al.* (1993) investigated the reactivation of pre-existing faults in a compressive regime and showed how the visualization of the stress field in the numerical results (obtained with a distinct element method) could help in the interpretation of the observed reactivation of some low angle faults. The models calculated with the distinct element method by Saltzer & Pollard (1992) of structures in sedimentary layers overlying basement normal faults show a high resemblance to deformation patterns typically observed in sandbox models. A high level of agreement between analogue and numerical models of

brittle and brittle-viscous thrust wedges was obtained by Ellis *et al.* (2004). Their results indicate that the continuum approximation of the finite element method does not necessarily need to be a strong limitation in modelling granular materials. An encouraging agreement between results from finite element and analogue models is also shown by Panien *et al.* (2006); Cruden *et al.* (2006) and Le Pourhiet *et al.* (2006).

Numerical and analogue modelling techniques share the advantages and disadvantages of trying to capture aspects of a geological process in a model. Both methods allow the evolution of structures to be observed, which can be helpful in generating ideas on the origin and development of structures observed in the field. With numerical and analogue models it is possible to vary model parameters easily and determine their relevance for the process under consideration. However, models are also only an approximation of the natural situation and their restrictions should be taken into account when interpreting their results. Advantages of the numerical method are the easy quantification of model results, including the possibility of tracking stresses, strain and strain-rates during the evolution of the model, and the relatively large freedom in choice of material properties (including a relatively easy implementation of temperature-dependent rheologies), boundary conditions and geometries. Some approaches lose accuracy when dealing with large deformation situations (due to remeshing, for example) or large viscosity contrasts. The resolution of 3D models is in general still quite low. Analogue models on the other hand are very suitable for studying the 3D evolution of structures with time. This makes it possible to evaluate the effects of, for example, lateral changes in material properties or oblique extension. The technique is limited in the application of temperature dependent rheologies, phase changes and variations in geometries. Numerical and analogue techniques are partly complementary and the combination of both methods may help establish the robustness of model results (see also Smart & Couzens-Schultz 2001).

## Modelling methods

### *Material properties*

The models contain three materials, which have properties resembling those of quartz sand, glass microbeads and polydimethylsiloxane (PDMS). In the analogue comparison, every laboratory used its own granular materials, which typically differ in frictional properties and density (see Schreurs *et al.* (2006) and Table 1). In the numerical experiments fixed values are used to allow the comparison of the numerical results to each other (Table 1). The material behaviour of the numeric brittle materials is characterised by a Coulomb failure-frictional criterion:

$$\sigma_t = \sigma_n \tan(\phi) + C \qquad (1)$$

where $\sigma_t$ denotes shear stress, $\sigma_n$ normal stress, $\phi$ the angle of internal friction and $C$ cohesion. Measurements of the properties of analogue granular materials show that deformation initially occurs through a combination of elastic and frictional strain-hardening behaviour until failure at peak strength ($\phi_{peak}$), followed by a strain-softening phase until a stable strength

**Table 1.** *Material properties*

| Material | Values in numerical models | | | | | Measured analogue properties* | | | | |
|---|---|---|---|---|---|---|---|---|---|---|
| | Density (kg m$^{-3}$) | C (Pa) | $\phi^{\dagger}_{peak}$ | $\phi^{\ddagger}_{stable}$ | $\eta$ (Pa s) | Density (kg m$^{-3}$) | C (Pa) | $\phi^{\dagger}_{peak}$ | $\phi^{\ddagger}_{stable}$ | $\eta$ (Pa s) |
| Sand | 1560 | 10 | 36° | 31° | | 1350–1740 | 3–150 | 33°–45° | 28.2°–39° | |
| Microbeads | 1480 | 10 | 22° | 20° | | 1400–1600 | −25–50 | 21°–29.2° | 20°–26.2° | |
| PDMS | 965 | | | | 5e4 | 965 | | | | 5e4 |
| Side friction | | 0 | 19° | 19° | | | | 20°§ | 16°–17°§ | |

*Values from Schreurs *et al.* (2006) for the materials used in the laboratories of University of Bern, IFP Rueil-Malmaison, University of Parma, University of Pavia and University of Toronto. Sand is sieved from 20 cm height with an approximate filling rate of 250 grams/minute. PDMS from Weijermans (1986).

†Angle of internal friction at peak strength.

‡Angle of internal friction at stable strength.

§GFZ sand measured by J. Lohrmann shows an angle of internal friction of 20° softening to 16° (fine-grained sand, 20–200 μm) or 17° (coarser sand, 20–650 μm).

($\phi_{stable}$) is reached (Lohrmann *et al.* 2003; Panien 2004; see also Jaeger & Cook 1979). Five of the eight numeric codes used in our study include elastic material behaviour. For sand, the elastic component is probably relatively small (J. Adam pers. comm.). Most of the numerical models (six of eight) have been run without dilatation and (de)compaction of the materials is, therefore, not automatically taken into account. The strengthening of material in the initial strain-hardening phase seen in analogue models (Adam *et al.* 2005) is in these cases not included. Strain-softening from peak strength to stable strength is assumed to be caused by dilatation of sand at yield and is explicitly prescribed in the numeric models that do not include dilatation. The softening is simulated by a linear decrease in the angle of internal friction over a finite strain interval of 0.5 to 1.0 (finite strain is total accumulated effective strain as measured by the square root of the second invariant of the strain tensor). The cohesion values of the analogue materials were determined using different measuring apparatus (see Schreurs *et al.* 2006) and show a large variation. Cohesion is obtained by extrapolation of the shear stress versus normal stress curve and is, therefore, likely to be an overestimate at low stress values where the stress curve is no longer a straight line, but has a convex-outward shape (Ranalli 1987; Schellart 2000). The boundary friction between sand and the sidewalls and base of the model (which are covered with an 'Alkor' foil in the analogue experiments) is approximately 20°, softening to 16°/17° (for fine sand with grain size 20–200 μm and coarse sand with grain size 20–650 μm, J. Lohrmann, pers. comm.) and a constant value of 19° has been used in the numerical experiments.

PDMS is a Newtonian material with a viscosity of $5 \times 10^4$ Pa s (at room temperature and strain rates below $3 \times 10^{-3}\ s^{-1}$, Weijermars 1986) and low Maxwell times. It is modelled as a linear viscous material: $\tau = 2\eta\dot{\varepsilon}$, for deviatoric stress $\tau$, viscosity $\eta$, and strain-rate $\dot{\varepsilon}$.

## Scaling

Some of the models are scaled up from the analogue sandbox-scale (cm) to upper-crustal scale (km). This scaling requires that dynamic similarity is observed (Hubbert 1937; see also Ellis *et al.* 2004). Dynamic similarity is maintained when force ratios and length ratios are constant. The models in this study can be scaled completely through the following three relationships: (1) geometric similarity:

$$\frac{l_n}{l_a} = \text{constant} \tag{2}$$

where $l_n$ and $l_a$ are the lengths in the numerical and analogue model, respectively; (2) constant ratio of gravitational force to viscous force between the numerical and the analogue model:

$$\frac{\rho g l^2}{\eta v} = \text{constant} \tag{3}$$

where $\rho$ density, $g$ gravitational acceleration, $\eta$ viscosity and $v$ velocity; and (3) constant ratio of frictional strength ($\sigma_y$) to lithostatic pressure:

$$\frac{\sigma_y}{\rho g l} = \text{constant} \tag{4}$$

The values for $\rho$, $\phi$ and $g$ in the numerical models are within the ranges of the analogue values (Table 1).

## Description of the numerical codes

In the following, only a brief description of the main features of the numerical codes is given and the reader is referred to the references provided for more detailed information. Specific assumptions concerning the boundary conditions for the experiments are discussed with the description of the model set-up for each experiment.

*Abaqus/Standard.* Results obtained with Abaqus/Standard are shown for both experiments and were provided by Susan Ellis. Abaqus is a Lagrangian Finite Element code with implicit time integration (Abaqus/Standard User's Manual 2003). Material behaviour is visco-elasto-plastic and materials deform elastically until plastic or viscous yield is reached, after which deformation continues on yield. Tests for the shortening experiment show that material quickly reaches plastic yield once it enters the deforming region. Plastic yielding is modelled using a non-associative plastic flow law with dilatation chosen as zero (to facilitate comparison with the other experiments). Strain softening is included. Boundary friction is implemented through an elastic-stick contact surface formulation. The experiments are scaled such that 1 cm equals 1 km in the numerical model.

*I2ELVIS.* Taras Gerya provided results from his I2ELVIS code (the successor of I2VIS, Gerya & Yuen 2003) for both experiments. I2ELVIS solves the Stokes equation for creeping

flows using the finite difference method on a Eulerian staggered grid combined with a marker-in-cell technique. Material behaviour is visco-elasto-plastic and incompressible (with, therefore, zero dilatation). Elasto-plastic deformation dominates for sand-like material due to the high background viscosity of $10^{12}$ Pa s, which results in a large visco-elastic relaxation time ($10^6$ s). In contrast viscous deformation dominates for PDMS-like material due to the low viscosity of $5 \times 10^4$ Pa s, which gives small visco-elastic relaxation times (0.05 s). Strain softening is included. Boundary friction is incorporated through frictional contact layers (4 elements wide at the sides and 2.5 elements high at the base). Free surface behaviour is obtained through a low viscosity 'air' layer on top of the model ($\eta = 1$ Pa s and $\rho = 1$ kg m$^{-3}$). The experiments are not scaled.

*LAPEX-2D.* Model results for LAPEX-2D were provided by Andrey Babeyko for both experiments. LAPEX-2D solves for balances of mass, momentum and energy through an explicit Lagrangian Finite Difference technique (FLAC-type) (Cundall & Board 1988; Poliakov *et al.* 1993; Babeyko *et al.* 2002). Material and history properties including full stress and strain tensors are tracked and updated by using particles. The material behaviour is visco-elastic with plastic yielding. Dilatation is zero. Strain softening is included. Boundary friction is implemented through explicitly added frictional forces at the boundary nodes (newly added feature for these experiments). The experiments are scaled whereby 1 cm equals 10 km in the numerical model.

*Microfem.* Susan Ellis also provided model results calculated with Microfem (Fullsack 1995) for both experiments. Microfem is a plane-strain arbitrary Lagrangian Eulerian finite element code. The Stokes equation for incompressible creeping flows is solved on a Eulerian grid on which material properties are tracked using a Lagrangian material grid. A free surface is achieved through vertical stretch or shortening of the Eulerian grid. Material behaviour is either viscous or plastic and incompressible (zero dilatation). Strain softening is included. The version used here is modified from the original code from the Dalhousie Geodynamics group. Frictional contacts are incorporated in a simple manner by allowing nodes to move unconstrained tangential to the boundary once frictional yield is exceeded (Ellis *et al.* 2004). The experiments are scaled such that 1 cm equals 1 km in the numerical models.

*NISA II/Static 12.0.* Results for the shortening experiment were provided by Antje Kellner. NISA/Static is a Lagrangian Finite Element code (NISA II User Manual 1997). It solves the equations of mechanical equilibrium for visco-elasto-plastic materials, but was used in an elasto-plastic mode for this study. Associated Mohr-Coulomb plasticity is used with a dilatation angle equal to the angle of internal friction. Strain softening is not included. Boundary friction is implemented through the contact element tool: For each frictional boundary two contact surfaces are defined. A contact element combines two contact surfaces facing each other. The experiment is not scaled.

*PFC$^{2D}$.* Results for the shortening experiment using the Distinct Element Method PFC$^{2D}$ (PFC$^{2D}$ User's Guide 1999) were provided by Yasuhiro Yamada. The model domain consists of discrete circular elements where only neighbours interact. Linear elasticity (force-displacement law; Cundall & Strack 1979) is incorporated through normal and shear forces at element contacts. The force in the normal direction and a pre-defined friction coefficient determine the inter-element friction in the shear direction. During deformation the size of each element is preserved and only the arrangement in the particle assembly is distorted. Dilatation is incorporated as a change in the inter-element porosity. Strain softening is not included. Boundary friction is incorporated in a similar manner as the inter-element friction. The experiments are scaled whereby 1 cm equals 300 m in the numerical model.

*SloMo.* Results for the extension experiment were provided by Boris Kaus. SloMo is a plane-strain finite element code (Kaus 2005) which solves the Stokes equations for incompressible materials. The rheology is visco-elasto-plastic with Mohr-Coulomb plasticity. A mixed formulation is employed, with linear, discontinuous, shape-functions for pressure and quadratic shape functions for velocity to avoid spurious pressures (Pelletier *et al.* 1989). Uzawa-type iterations are used to satisfy the incompressibility constraint (Cuvelier *et al.* 1986). In this work, the code has been used in a Lagrangian fashion, with regular remeshing to deal with large deformations (see also Poliakov & Podladchikov 1992). Iterations are performed for plasticity, to ensure that both the force balance and the plastic yield functions

are satisfied simultaneously. The interface between sharply varying material properties is tracked by marker-chains, whereas other material properties are stored on the integration points. Strain softening is included. Dilatation is zero. The experiment is not scaled.

*Sopale*. Model results for Sopale are shown for both experiments and were provided by Susanne Buiter. Sopale is a plane-strain arbitrary Lagrangian Eulerian finite element code (Fullsack 1995) and is the successor of Microfem. A more efficient tracking of material properties (whereby the Lagrangian particles are no longer only constrained to a regular grid and particle injection maintains a high particle density) allows a higher resolution. This version has been modified from the original code to allow horizontal stretch or shortening of the Eulerian grid (in addition to the vertical Eulerian grid modification for free surface behaviour). Strain softening is included. Boundary friction is implemented through the use of frictional contact layers (4 elements wide at the sides and 4 elements high at the base). The experiments are scaled such that 1 cm scales up to 1 km in the numerical model.

## Shortening experiment

### *Model set-up*

The shortening experiment follows a more or less classic set-up used to study fold-and-thrust belt evolution with analogue models. Shortening is achieved by moving the right-hand wall inward while the left wall and base are held fixed. The model consists of 'sand' layers with an embedded 0.5 cm thick layer of weaker 'microbeads' (Fig. 1a). Total height is 3.5 cm. The length of the models is variable (Table 2), but since deformation did not reach the left wall in any of the models, all were considered long enough. At the right side an initial wedge 10 cm long with 10° surface slope overlies the model. This wedge slope is in the stable field for a sand wedge (as calculated for this set-up from Dahlen 1984; Zhao *et al.* 1986). The two main problems with representing the analogue set-up numerically lie with the boundary conditions. First, different solutions were applied to simulate boundary friction (contact boundary friction or frictional boundary layers). Second, the mobile wall moving over the base of the sandbox represents a velocity discontinuity, which may lead to high pressures in this corner.

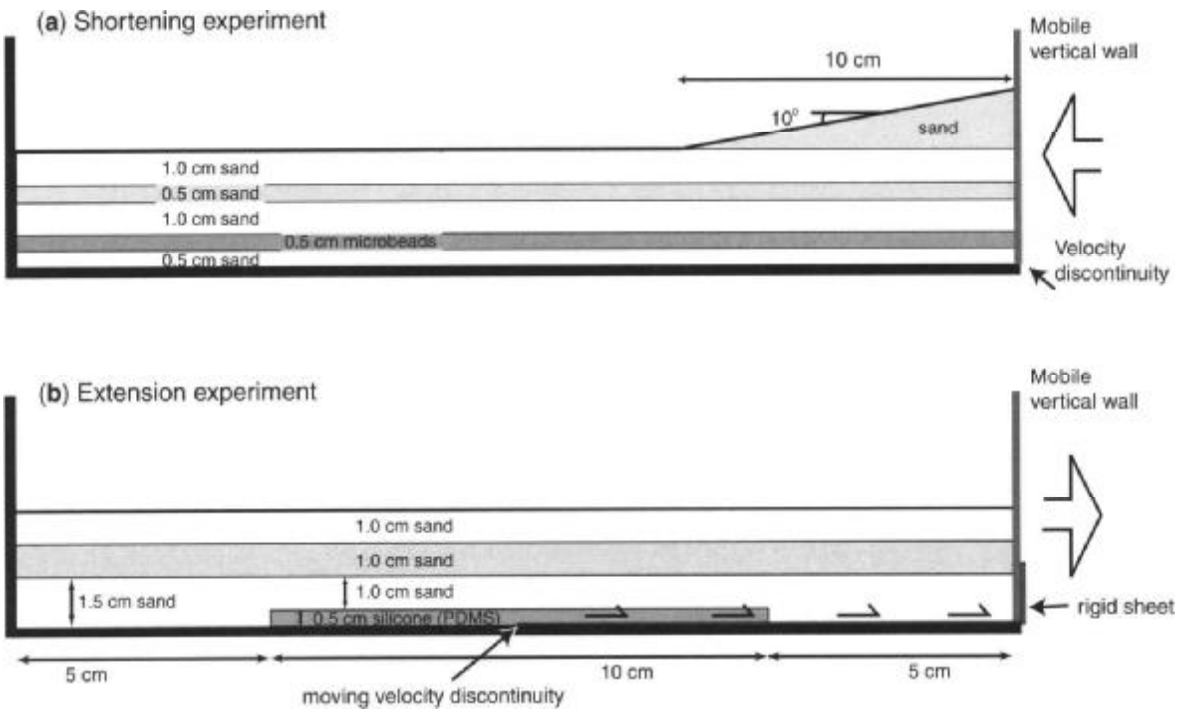


**Fig. 1.** (**a**) Set-up of the shortening experiment. Horizontal layers of 'sand' (which have the same properties and differ in colour only) with an embedded layer of weaker 'microbeads' are shortened through a mobile wall on the right-hand side which is pushed leftwards. (**b**) Set-up of the extension experiment. A viscous layer (PDMS, 10 × 0.5 cm) lies in the central part of the model on the base. The rest of the model consists of three 'sand' layers (only differing in colour). Extension is achieved by moving the right wall with the attached 10 cm long sheet outwards to the right.

**Table 2.** *Shortening experiments*

| Code | Method* | Nodes† | Track points | Domain length‡ | Norm. elem. size§ | E‖ (MPa) | $\nu^1$ | $\eta^2$ (Pa s) |
|---|---|---|---|---|---|---|---|---|
| Abaqus/ Standard | FEM | 301 × 36 | n.a. | 30 km/30 cm | 0.1 | 0.5 | 0.25 | 5e6 |
| I2ELVIS | FDM + MIC | 900 × 75 | 393750 | 45 cm | 0.05 | 3 | 0.50 | 1e12 |
| LAPEX-2D | FDM + MIC | 351 × 71 | 400000 | 400 km/40 cm | 0.075 | 0.1 | 0.125 | 4.5e10 |
| Microfem | ALE | 201 × 36 | 7236 | 28 km/28 cm | 0.17 | n.a. | n.a. | 4e13[3] |
| NISA/Static | FEM | 201 × 14/18 | n.a. | 50 cm | 0.25 | 0.5–1.0¶ | 0.25 | n.a. |
| $PFC^{2D}$/Kyoto | DEM | ~18000 | n.a. | 12 km/40 cm | 0.06 | n.a. | n.a. | n.a. |
| Sopale | ALE | 401 × 71 | 253411 | 40 km/40 cm | 0.08 | n.a | n.a. | 4.6e13 |

*FEM = Finite Element Method, FDM = Finite Difference Method, ALE = Arbitrary Lagrangian Eulerian, DEM = Distinct Element Method, MIC = Marker-in-Cell.
†Nodes in horizontal × vertical direction, or total number of nodes.
‡First value is for the numerical model, second value is its equivalent scaled down to the sandbox scale. Height is 3.5 (left-hand side) to 5.26 cm (top of wedge at right-hand side).
§Normalized element size is measured as the square root of element area, scaled to sandbox scale (cm).
‖Young's modulus, scaled to sandbox scale.
¶ 0.5 MPa for microbeads, 1.0 MPa for sand.
[1]Poisson ratio.
[2]Background viscosity, scaled to sandbox scale.
[3]Equivalent linear viscosity; a non-linear viscosity was used in the calculations.

The shortening experiment was run with seven numerical codes (Abaqus/Standard, I2ELVIS, LAPEX-2D, Microfem, NISA/Static, $PFC^{2D}$ and Sopale). Five experiments have zero dilatation, while NISA/Static and $PFC^{2D}$ are dilatational. Details of the set-up for each code are given in Table 2. The initial geometry for all numerical models is shown in Figure 2a. The following code-specific assumptions and explanations apply:

*Abaqus/Standard.* Because Abaqus/Standard uses a Lagrangian formulation and remeshing was not employed, the code cannot handle large deformations and fails to converge at an early step.

*I2ELVIS.* The rigid mobile wall (with a background viscosity of $10^{14}$ Pa s and a shear modulus of $10^2$–$10^4$ MPa) is moving inside the computational domain and is, therefore, not simulated through an external boundary condition. The right-hand side frictional boundary layer is limited in vertical extent. During shortening, part of the weak 'air' layer at the top of the model moves spontaneously to behind the mobile wall.

*LAPEX-2D.* Diffusive erosion (diffusion coefficient of the order $10^{-6}$ $m^2$ $s^{-1}$) is applied at the surface to avoid steep slope angles not supported by the current meshing technique.

*Microfem.* A small amount of surface smoothing is applied. Tests have shown that this does not significantly affect the dynamic evolution.

*NISA II/Static.* Because NISA/Static uses a Lagrangian approach without remeshing, the code cannot handle large deformations and fails to converge at an early step.

*$PFC^{2D}$.* The density of all materials is 1600 kg $m^{-3}$ and, therefore, differs slightly from the values used in the other experiments (Table 1). The radii size is randomized within 12–24 m (sand) and 5–10 m (microbeads). Shearing tests suggest a shear angle in bulk behaviour of 35° for sand and 25° for microbeads. The basal boundary condition has the same friction angle as sand and is, therefore, higher than the value used in the other experiments.

*Sopale.* To avoid numerical instabilities associated with an abrupt velocity change the mobile wall velocity is smoothed by extrapolating the applied velocity to 0 over the lowermost 200 m (equals 0.2 cm) of 'sand' (excluding the basal frictional layer). A minimal amount of diffusive erosion (diffusion coefficient $10^{-9}$ $m^2$ $s^{-1}$) is applied at the surface.

### *Model results*

The structural evolution of all models is shown in Figure 2 with plots of geometry and strain-rates after 2, 6, 10 and 14 cm of displacement (unless specified otherwise). Shear zones can readily be identified on the geometry plots, while the strain-rate plots visualize their propagation, moment of initiation and later abandonment.

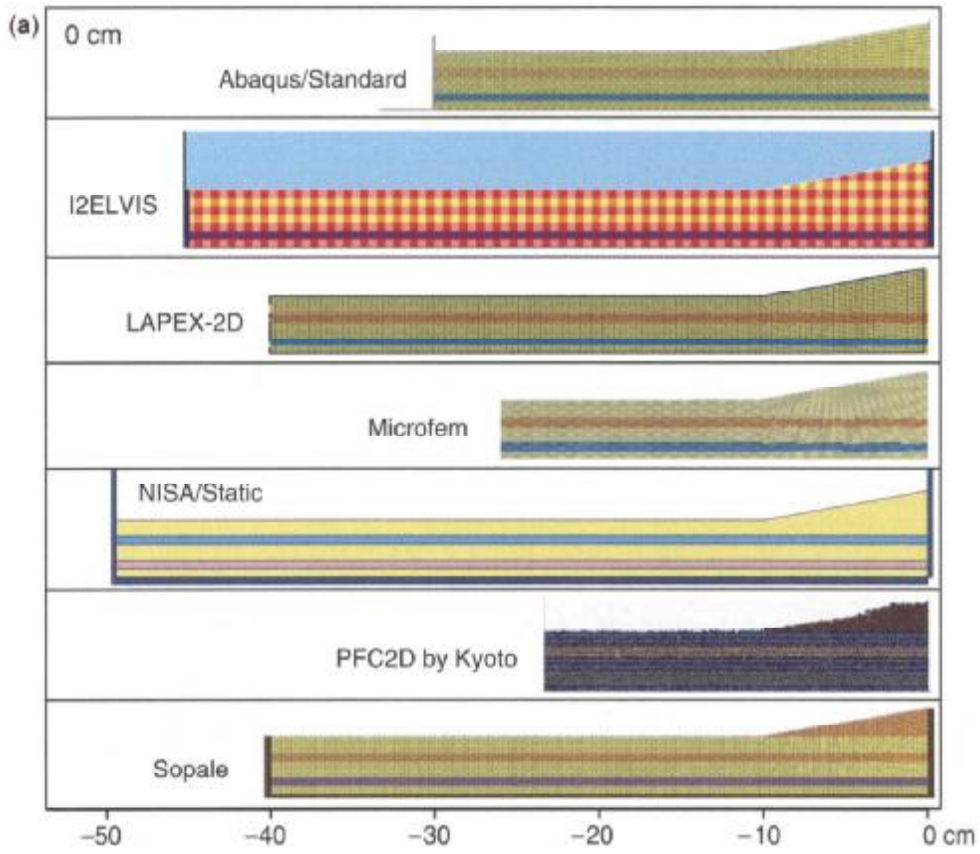


**Fig. 2.** Results for the shortening experiment. All quantities (including strain-rates) are scaled down to the sandbox scale. (**a**) Initial geometries. The grid of Abaqus/Standard is the calculation grid, while for LAPEX-2D, Microfem and Sopale the shown grid is (a subset of) the tracking grid.

The strain-rate plots also show when the weak embedded layer is utilized and whether shear zones propagate forward along the weak layer or along the base of the model. In continuum numerical models shear displacement is not accommodated along discrete fault planes, but rather along more distributed shear zones. For ease of comparison with the analogue models, we will, however, sometimes refer to 'faults' when describing numerical results.

In order to allow a comparison of all model results in a more quantitative manner we measured the following properties (Table 3, Figs 3 and 4): amount of displacement at which forward thrusts form, their dip angle, the spacing between thrusts, the amount of fault-controlled shortening, surface slope, when the embedded weak layer is activated, and the length of the detachment in this layer. We found, however, that our measurements were influenced by the measurer and subject to small differences in interpretation. The values reported here were, therefore, completely measured by two people, in the same manner, and subsequently averaged. A fault was considered to be initiated when deformation had clearly localized along it as shown by strain-rate maxima and small finite displacement of the deforming material. Dip angles were measured on the finite deformation plots and represent a dip angle for the whole shear zone (not differentiating between upper and lower dip angles). The variation in dip angle values between the two measurers was on average 2° (ranging between 0°–5°). Measurements of surface slope are rather inaccurate in the initial stages of shortening when only one thrust has formed (Fig. 4b), but improve substantially as soon as a second thrust has formed (Fig. 4c). From then on the difference between the values measured by the two measurers did not exceed 3°. Oscillations in surface slope angles occur just before or after the formation of a new thrust, depending on the degree to which a new thrust is incorporated into the wedge. To determine the amount of shortening accommodated by faults, we

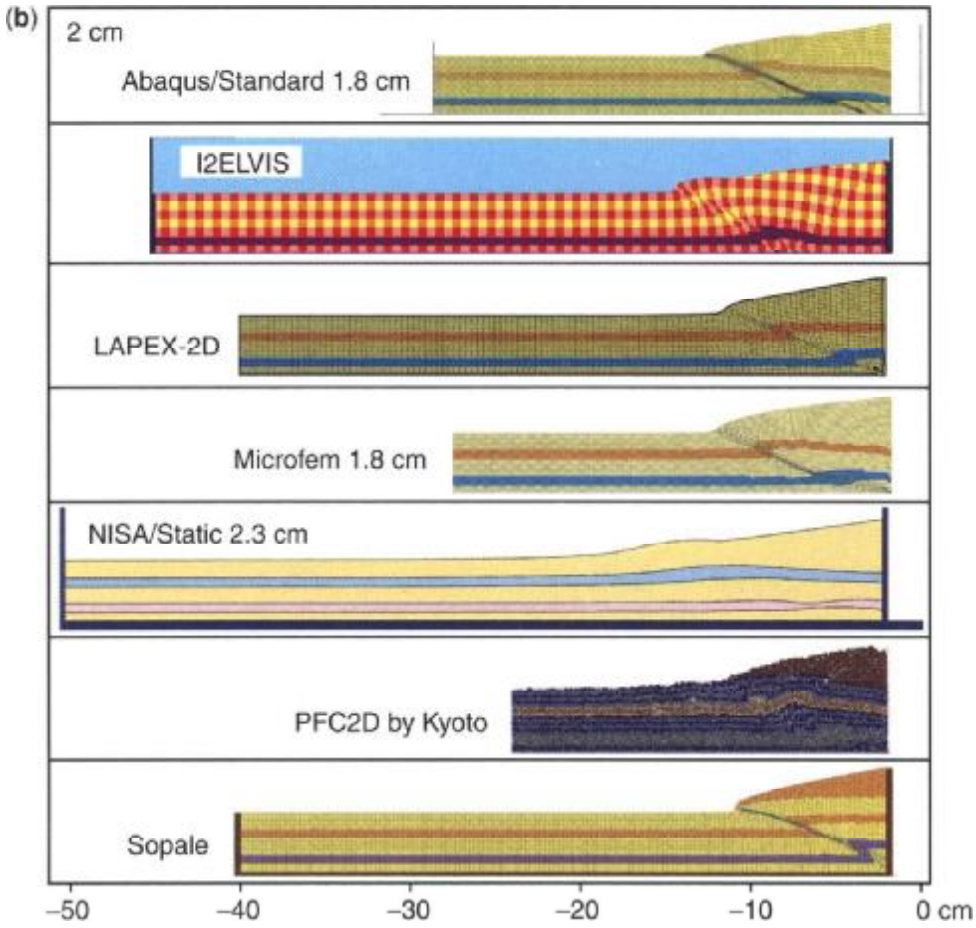


**Fig. 2.** (**b**) Geometries after 2 cm. Note that Abaqus/Standard and Microfem are shown after 1.8 cm and NISA/Static after 2.3 cm.

measured the offset of layers at a fault by using the cut-off points of the layers and the fault. Folding of layers towards a fault zone was classified as folding-controlled shortening. Fault-controlled shortening was in a number of cases difficult to determine accurately as the cut-off points of layers with faults were smeared out. The ranges in Table 3 reflect the differences between the two measurers.

The numerical models share many similarities: (1) Shortening is accommodated by in-sequence forward propagation of thrusts (Figs 2 and 3a). (2) The first-formed forward thrust roots at the base of the mobile wall in most of the experiments (Figs 2b and c). (3) By 2 cm of displacement an active forward thrust has formed in all models (Fig. 2b). (4) The location where the first-formed forward thrust reaches the surface is influenced by the surface wedge in almost all of the experiments (except maybe NISA/Static) (Fig. 2b). (5) The embedded weak layer accommodates shear displacement in almost all experiments when sufficient shortening has occurred to increase the surface wedge (Table 3) (the strain-rate plots for I2ELVIS show activity of the weak layer, but no finite strain accumulates here). (6) The surface slope remains in the stable field for critical taper theory (calculated from Dahlen (1984) and Zhao *et al.* (1986) for homogeneous sand) (Fig. 4). Activation of the embedded weak layer has no discernable effect on surface slope (Table 3 and Fig. 4). The stable taper field for a cohesive wedge building in 2.5 cm thick material above the weak layer is almost the same as the stable field shown in Figure 4.

Although the manner in which the models accommodate shortening leads to a similar style of deformation, it is also clear from Figures 2, 3 and 4, and Table 3 that variations exist among the models. Differences between the model results are: (1) The number of thrusts that have formed at a specified amount of displacement is variable (maximum two thrusts difference in the displacement range examined here) (Figs 2 and 3a). (2) The dip angle of the

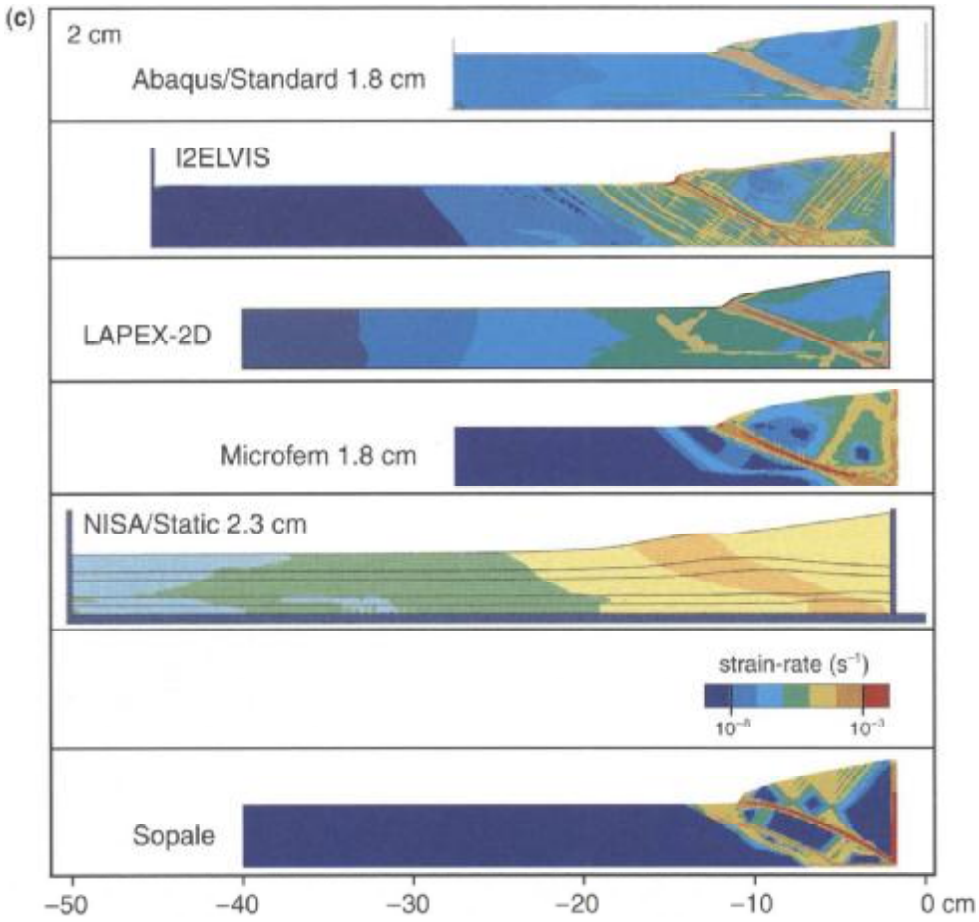


**Fig. 2.** (c) Strain-rates after 2 cm (Abaqus/Standard and Microfem after 1.8 cm, NISA/Static after 2.3 cm).

forward thrusts shows variations of up to 14°. The dip angle of the first thrusts is most likely influenced by the initial surface wedge. Later thrusts have dip angles between 45° (non-dilatational Roscoe angle) and $45° - \phi/2$ (Coulomb angle) (Vermeer 1990). (3) The distance between a newly formed thrust and the previously formed thrust is highly variable (Fig. 3c). (4) The embedded weak layer is first activated at different amounts of shortening (Table 3). (5) The amount of fault controlled shortening differs highly (Table 3).

### *Sensitivity analyses*

An important advantage of numerical models is the ease with which the sensitivity to model parameters can be investigated. We tested the variability of the numerical results to assumptions regarding the model set-up (mesh resolution and elasticity) and values of material properties (cohesion and basal friction). We found that the evolution of thrusts is influenced by the resolution of the calculation domain, which may provide a partial explanation of differences found between the numerical results. Figures 5a and b show the difference after 10 cm displacement for I2ELVIS caused by increasing the normalized element size (Table 2) from 0.05 to 0.1, thus reducing the resolution. A higher resolution tends to increase the number of shear zones, while the individual shear zones become more focussed. A similar trend can be seen when comparing the result from the two ALE-type codes Microfem (lower resolution) and Sopale (higher resolution). Studies using analogue sandbox experiments found that thrust spacing depends on layer thickness, basal friction and surface slope (Mulugeta 1988; Mulugeta & Koyi 1992; Gutscher *et al.* 1998*b*). However, as pointed out by Mulugeta (1988) changes in material layering may perturb a systematic thrust spacing and it may be, therefore, that the embedded weak ('microbeads') layer in our set-up partly contributes to the observed irregularity in thrust spacing. The sensitivity of shear zone width and spacing is discussed further with the results of the extension

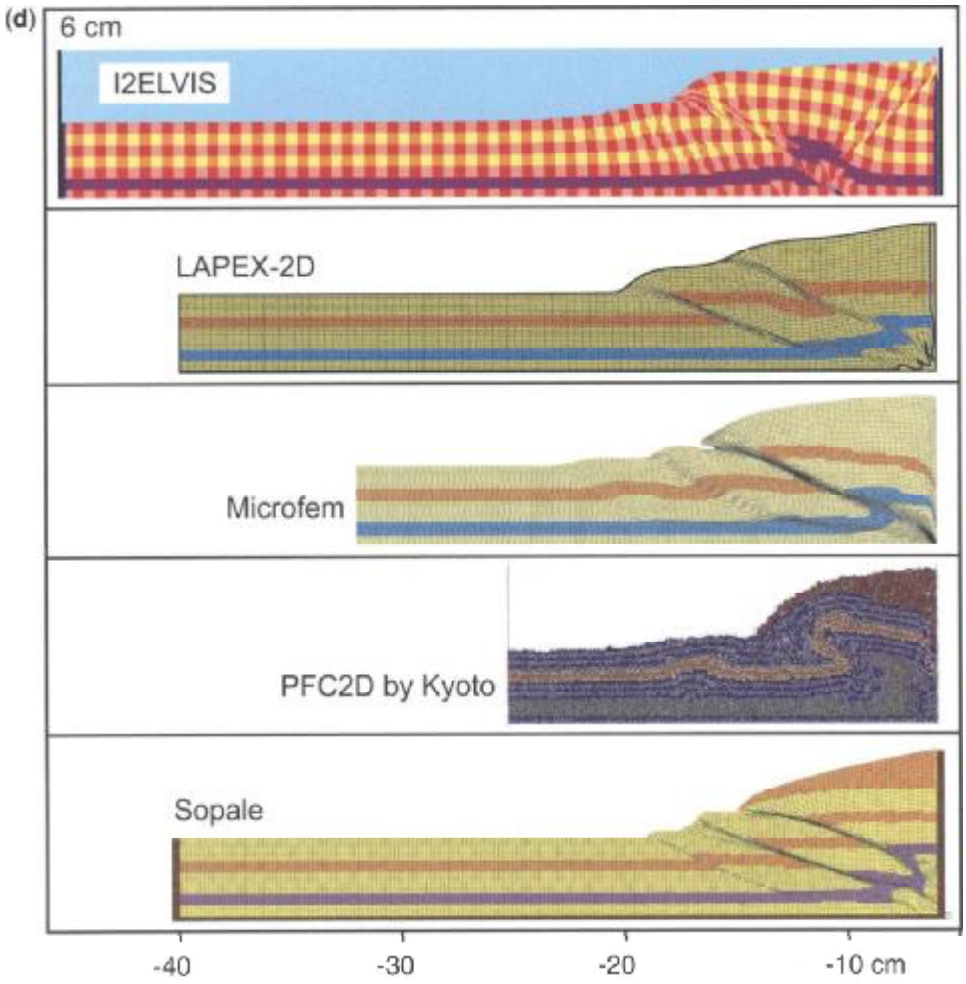


**Fig. 2.** (**d**) Geometries after 6 cm.

experiment (section on *Localization of shear deformation*).

We have assumed that in sandbox-type experiments the amount of finite strain that can be accommodated by elastic material behaviour is small. Abaqus/Standard, I2ELVIS, NISA/Static and LAPEX-2D include elastic behaviour and their deformation is essentially elasto-plastic in the shortening experiment, while Microfem and Sopale behave essentially rigid-plastic. A general comparison of the large-deformation results shows that the elastic component in material behaviour may lead to slightly more distributed deformation (as strain can also be accommodated between shear zones), but that overall the effect of elasticity is small for our set-up and material properties. In LAPEX-2D, effective elastic strain remains below approximately 2%.

Critical taper theory predicts that the strength of the frictional materials directly influences the taper angle that can be supported. With higher cohesion values the range of stable taper angles increases (from Zhao *et al.* 1986). Ellis *et al.* (2004) found in their thrust wedge experiments that surface slope increases with increasing cohesion, whereby the increase in surface slope mainly occurs at the toe of the material which has been thrust up. Tests with Sopale show that variations in the slope angle of the enveloping surface for cohesion variations from 0 to 100 Pa are limited (2° for displacements of 10 cm or more) without a clear trend towards higher slopes for higher cohesion. Higher cohesion material can support steeper edges of thrust sheets (Figs 5c, d and e). As the higher cohesion value was assigned to 'sand' and 'microbeads' alike, the strength contrast across the 'microbeads' layer is reduced and less shear displacement is consequently accommodated along it.

From Sopale experiments we find that a decrease in the basal friction angle (from 19° to 10°) reduces the surface slope (with around 8°

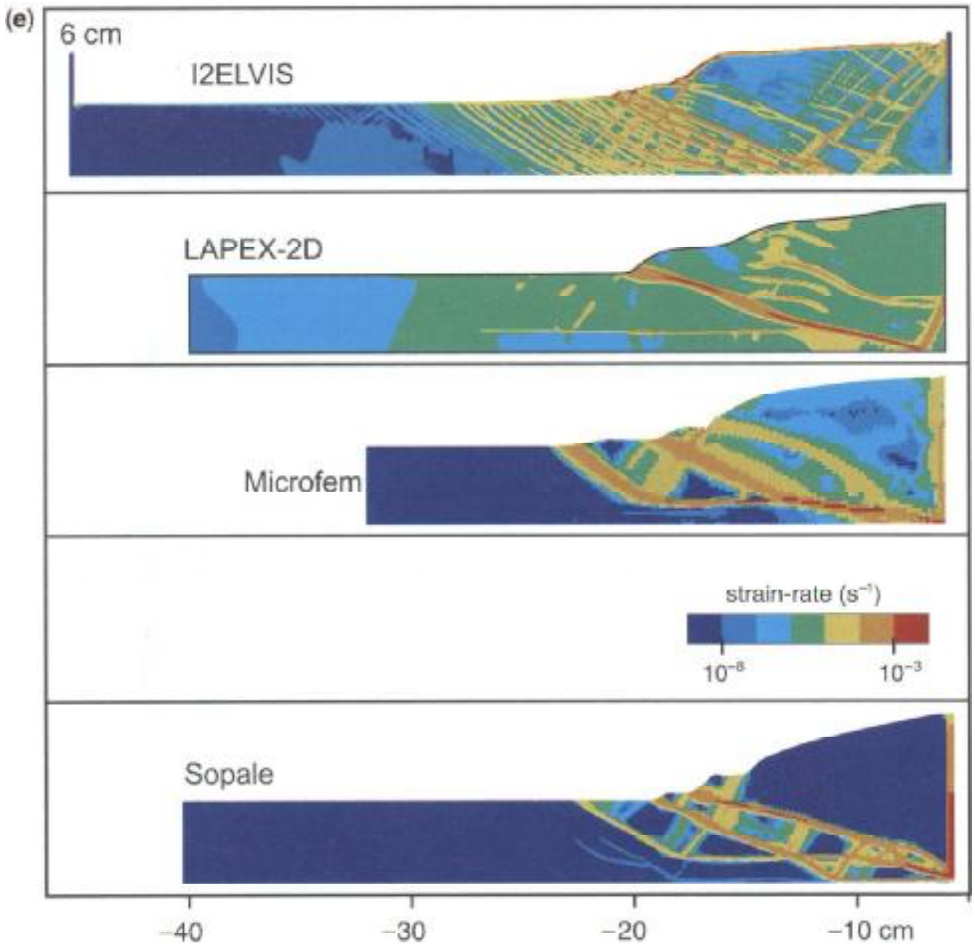


**Fig. 2.** (e) Strain-rates after 6 cm.

for the later shortening stages). This trend is in accordance with critical taper theory, which predicts lower critical taper angles for lower basal friction (Davis *et al.* 1983), and has also been found in other thrust wedge studies (Gutscher *et al.* 1998a; Vanbrabant *et al.* 1999). For low basal friction forward propagation of thrusts occurs faster.

### *Implications of the numerical experiments*

The numerical results for the thrust wedge experiment show similar deformation styles in which shortening is accommodated in a mainly rigid-plastic manner by in-sequence forward propagation of thrusts. Thrust wedge formation and propagation is, therefore, a robust feature of the seven models. However, despite the use of similar initial set-ups, material properties and boundary conditions, variability in structural evolution arises. These differences highlight the possible ranges in structural evolution and measurable quantities (e.g., surface slope) due to the application of different numerical codes, variable resolution and different implementation of boundary conditions. A fascinating unexpected result is the role of measurer bias in determining quantities such as dip and thrust spacing. Our results indicate that thrust spacing and the number of thrusts versus displacement should be considered carefully when evaluating results from numerical simulations and applying these (in a general manner) to natural systems. This implies that although numerical models may be used 'qualitatively' to interpret the mechanics of thrust wedges, limitations exist to the extent to which quantifiable measures such as thrust fault sequences may be compared at the present time. Future code comparisons may be helpful in reducing the differences between the numerical model results. Test experiments should preferably have a simplified set-up (avoiding abrupt changes in velocity boundary conditions which may require numerical smoothing), the same grid resolution, and material properties as similar as possible.

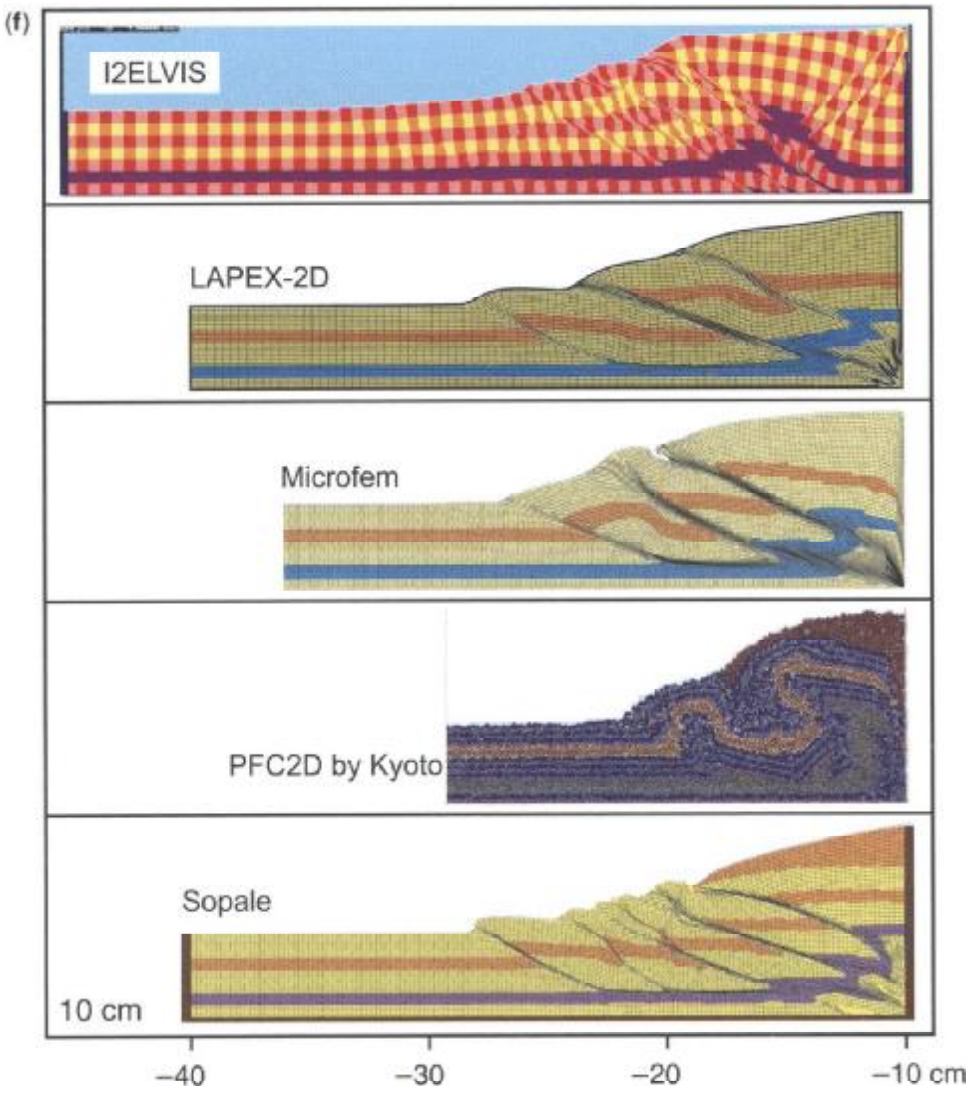


**Fig. 2.** (f) Geometries after 10 cm.

*Comparison to analogue results*

Figure 6 compares the numerical model geometries at 2 and 14 cm of displacement to results at equivalent stages from the analogue experiments of the laboratories of Bern, IFP, Parma, Pavia and Toronto (Schreurs *et al.* 2006). We have selected those analogue experiments that have the same set-up as our numerical experiments (i.e., no conveyor belt type experiments) and for which cross-sectional information was recorded. The properties of the granular materials used in the five analogue experiments are variable (e.g., sand: $\phi_{peak}$ between 33.2° and 45°, $\phi_{stable}$ 29.2°–39°; microbeads: $\phi_{peak}$ 22.3°–26.4°, $\phi_{stable}$ 20.6°–26.2°; the exact values can be found in Schreurs *et al.* (2006)) and this probably affected the analogue results. As the analogue granular materials are dilatational, they compact upon shortening. The strain-hardening effect this causes has not been included in most of the numerical experiments. Three analogue experiments were monitored through glass sidewalls (Parma, Pavia, Toronto) while two recorded internal deformation with X-ray CT tomography (Bern, IFP). In the accompanying paper (Schreurs *et al.* 2006) it is shown that edge effects may influence the deformational structures close to the lateral (observation) sidewalls. The extent of edge effects may be evaluated by surface monitoring and cutting of sections after the final stage of the experiment. The quantification of parameters in all analogue and numerical experiments was as much as possible done in the same manner. Ranges of parameters that were measured in the analogue

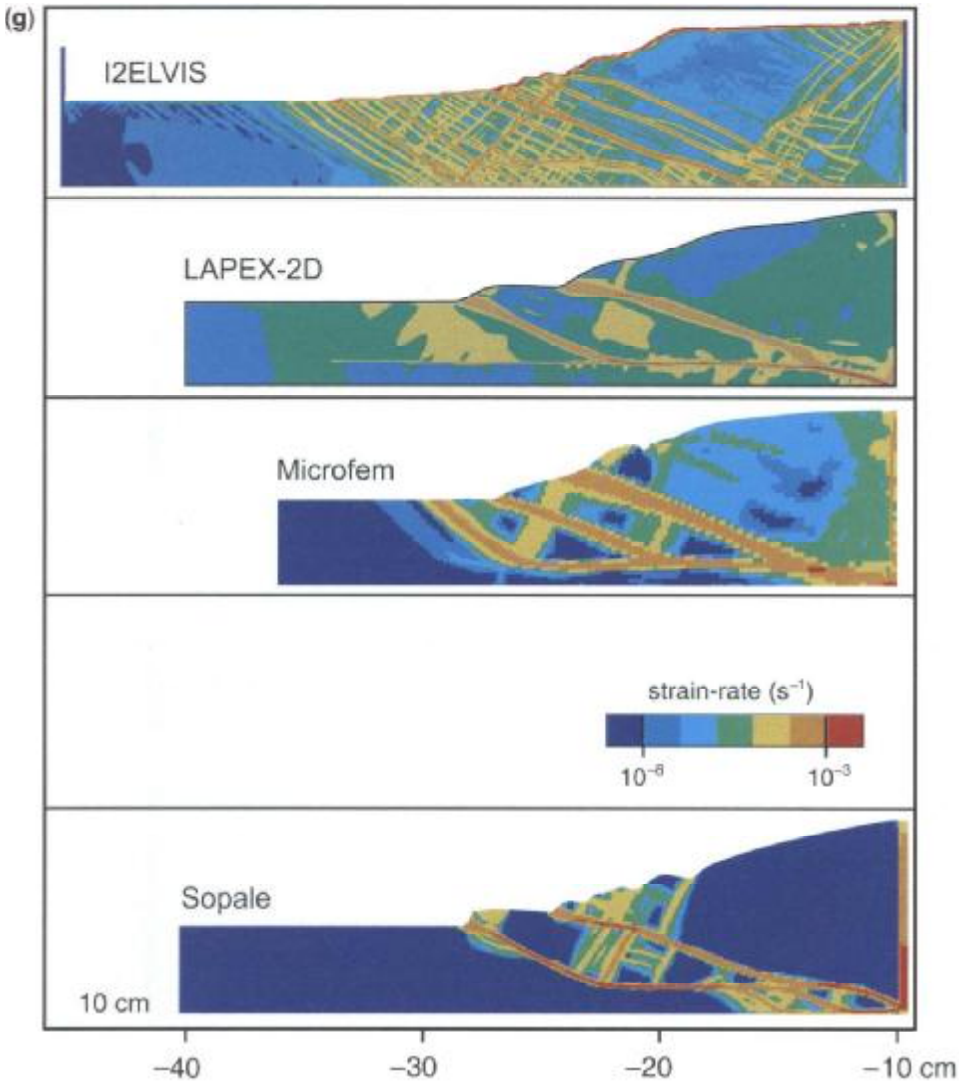


**Fig. 2.** (g) Strain-rates after 10 cm.

experiments (number of thrusts, dip angle, thrust spacing, fault-controlled shortening, microbeads layer activation and surface slope) are indicated in the figures and table which report the numerical values (Figs 3 and 4 and Table 3).

The comparison of our numerical results to the analogue models leads to the following observations: (1) The variability between numerical codes is about the same as the degree of variability between different analogue models. (2) The numerical codes produce the same overall structure and sense of forward-propagation seen in the analogue models. (3) Most of the analogue models show the forward thrust (at 2 cm displacement, Fig. 6a) propagating from a basal point located to the left of the lower right-hand corner, whereas most of the numerical models show the forward thrust propagating from this corner. This may reflect a difficulty in the numerical models of representing the velocity discontinuity at the corner. Panien *et al.* (2006) show that thrust localization near the mobile wall is sensitive to the exact implementation and smoothing of the applied velocity near the basal corner. Alternatively, the actual velocity discontinuity in the analogue models may not be so sharply defined as implied by the set-up (Fig. 1) and just a small exit slot may smooth the impact of the velocity discontinuity. (4) Most of the analogue models show a distinct backthrust at 2 cm displacement which is poorly represented in most of the numerical models (except in the results of I2ELVIS, in which the mobile wall is part of the computational domain and has a 0.05 cm high exit slot at the base) (Fig. 6a). The absence of the backthrust in the numerical models may link to the strong preference for the first forward thrust

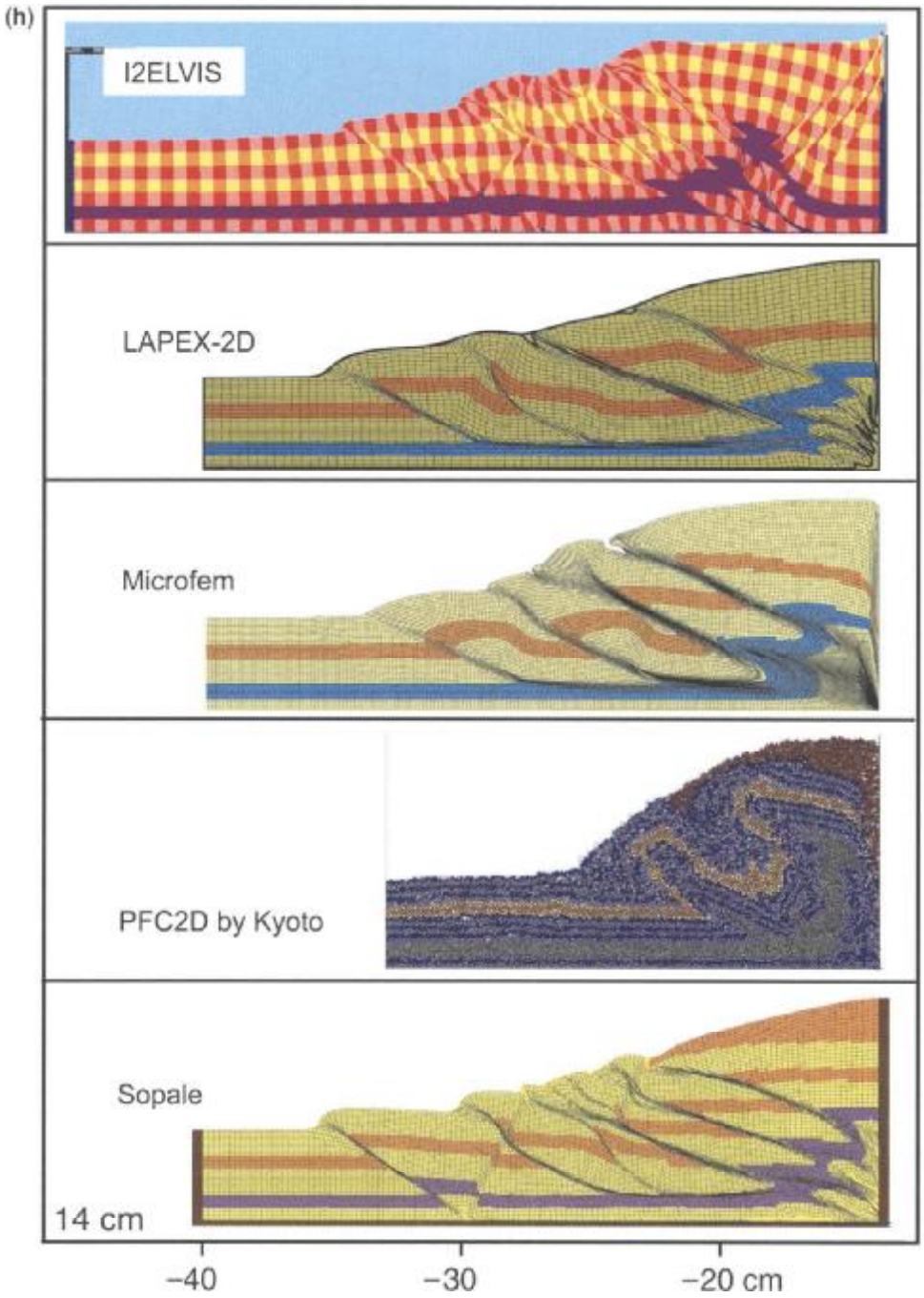


**Fig. 2.** (**h**) Geometries after 14 cm.

to initiate at the basal right-hand corner, as this configuration does not allow for a backthrust propagating up from the base. Interestingly, in the thrust wedge models of Ellis *et al.* (2004) (which were run with Microfem) a backthrust is visible and the first forward thrust roots to the left of the mobile wall. The exit slot below the mobile wall in these simulations may smooth the corner discontinuity, which suppresses the tendency for the thrust to localize in the basal corner and then allows a backthrust to form. Alternatively, the backthrust in these experiments could be due to the high angle of friction for the backstop. (5) The analogue models show the first thrust intersecting the surface to the left of the imposed wedge, as do the numerical models (Fig. 6a). (6) Localization of deformation in shear zones in the initial stages of shortening occurs slightly earlier in the numerical models than in the analogue models. The analogue

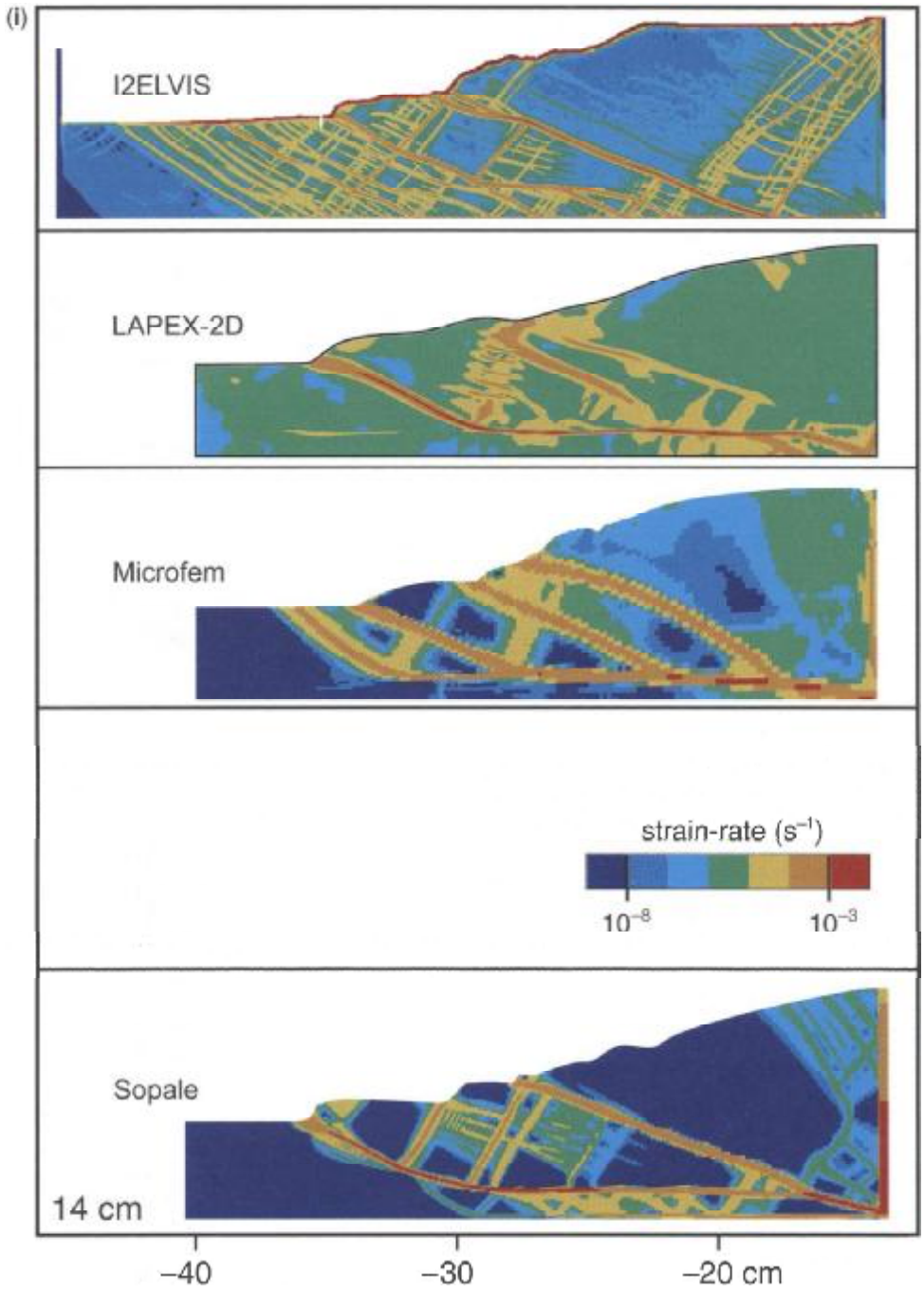


**Fig. 2.** (i) Strain-rates after 14 cm.

models accommodate up to 0.5 cm of shortening through lateral compaction before visible faults form. (7) The variation in the number of thrusts between different numerical codes is approximately the same as the variation between equivalent analogue models (Fig. 3a). (8) The spacing of thrusts is less variable between the numerical codes than between the analogue experiments (Fig. 3c). (9) The dip angles of the forward thrusts are generally slightly lower in the analogue experiments (between 19° and 33°) than in the numerical experiments (between 20° and 39°) (Fig. 3b). The analogue experiments follow the theoretical values for Coulomb dip angles (Vermeer 1990) quite closely, which for the frictional properties of these five analogue experiments range between approximately 23° and 29°. The predicted values for the numeric dip angles lie between 27° (Coulomb dip angle) and 45° (non-dilatational Roscoe dip angle).

**Table 3.** *Quantification of shortening experiments**

| Code | Fault short.† at 4 cm | 'Microbeads' layer | |
|---|---|---|---|
| | | Activated at | Detachm. length |
| Abaqus/ Standard | n.a. | n.a. | |
| I2ELVIS | 2.5–2.6 | never | |
| LAPEX-2D | 1.9–2.8 | 3 | 7.4 |
| Microfem | 1.5–2.3 | 4 | 6.2 |
| NISA/Static | n.a. | n.a. | |
| PFC$^{2D}$/Kyoto | 1.5–1.8 | 6 | 8.0 |
| Sopale | 2.0–2.8 | 4 | 5.0 |
| Analogue ranges‡ | 1.9–2.9 | 5.0–never | 2.2–9.3 |

*All values referred to sandbox scale in cm. Output stages typically available at 0, 0.5, 1, 2 and then every 2 cm of shortening.
†Fault-controlled horizontal shortening determined by cut-off points between layers and the faults.
‡Analogue values from experiments of University of Bern, University of Parma, University of Pavia, IFP Rueil-Malmaison and University of Toronto (Schreurs *et al.* 2006).

The first thrusts may be influenced by the surface wedge, leading to lower values for their dip angles. (10) The surface slopes measured for the numerical models plot around the lower ranges of the analogue surface slopes (Fig. 4). This is probably caused by the generally lower strength of the numerical materials in comparison with many of the analogue materials (Table 1).

Most of the differences between the numerical and analogue models may be attributed to the difficulty in representing the exact set-up of the analogue model and to differences in material properties. Despite these differences, the numerical models still produce a similar taper geometry and evolutionary style to the analogue models.

## Extension experiment

### *Model set-up*

The extension experiment examines the influence of a weak, basal viscous layer on normal fault localization and propagation in overlying brittle materials. The model is 20 cm wide and 3.5 cm high (Fig. 1b). It consists of three 'sand' layers (only coloured differently) and a 10 cm wide and 0.5 cm high layer of viscous PDMS, which overlies the central basal part of the model. A thin rigid sheet covering the base of the model extends from the middle to the right lateral wall and is attached to it. Extension is achieved by moving the right wall outward to

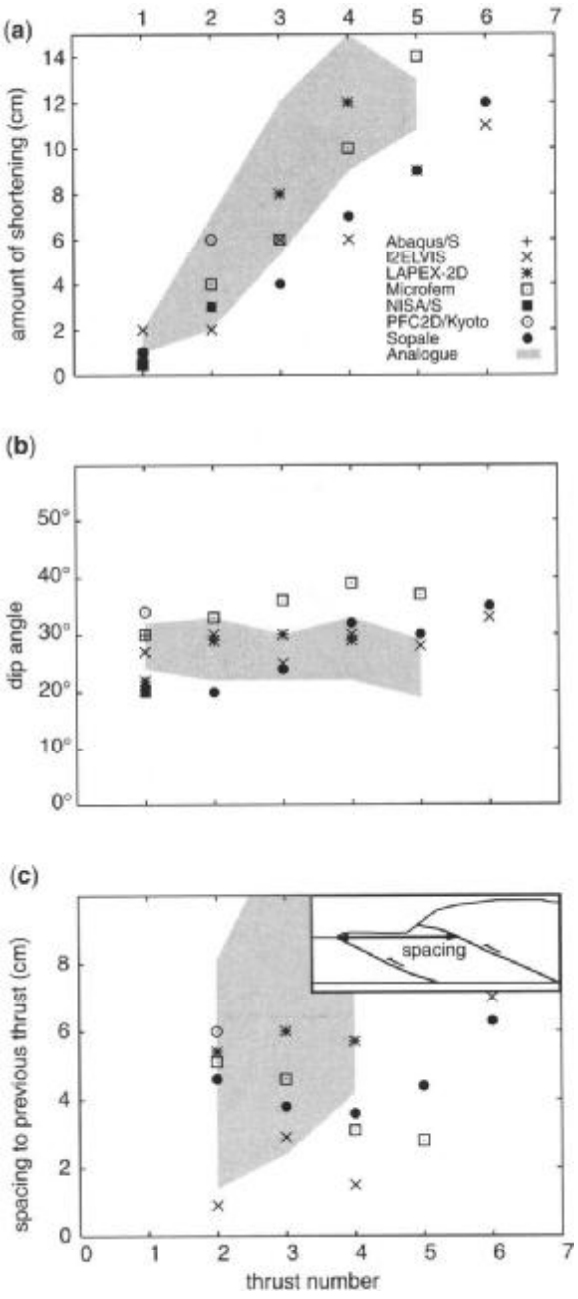


**Fig. 3.** (**a**) The amount of displacement at which a forward thrust forms shows that all experiments have forward propagation of thrust formation. (**b**) Dip angle of forward thrusts at the moment of their initiation. A dip angle of approximately 19° is expected for the first thrust if its location was entirely controlled by the initial wedge. (**c**) Spacing to the previous forward thrust measured at the moment of initiation of the new forward thrust. Inset shows how thrust spacing is measured. The quantities in (**b**) and (**c**) have been measured at the same stages of shortening as depicted in (**a**). The grey bands denote the range of values measured for the analogue experiments of University of Bern, IFP Rueil-Malmaison, University of Parma, University of Pavia and University of Toronto (see also Fig. 6 and Schreurs *et al.* 2006).

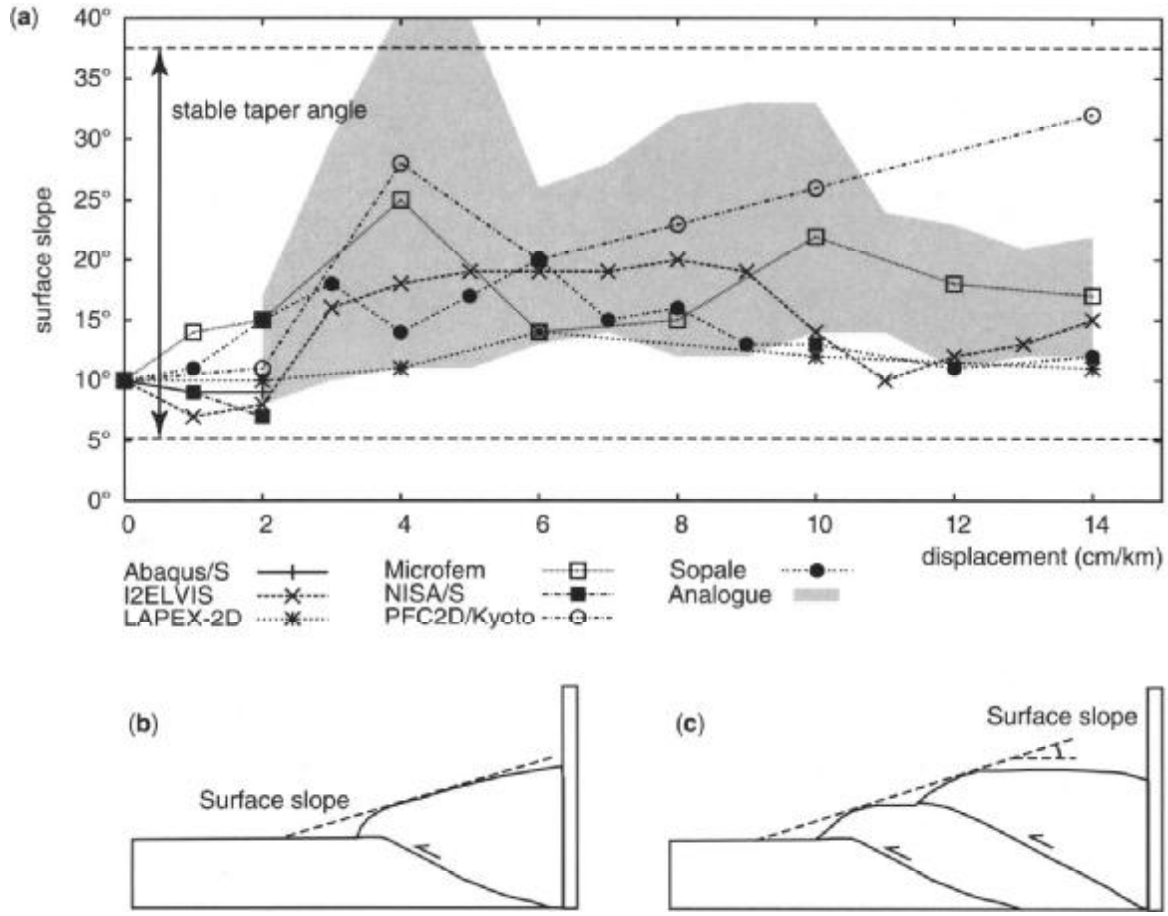


**Fig. 4.** (**a**) Surface slope versus amount of displacement. Surface slopes as measured in the analogue experiments of University of Bern, IFP Rueil-Malmaison, University of Parma, University of Pavia and University of Toronto (Schreurs *et al.* 2006) are shown as a grey band. (**b**) Schematic figure showing how surface slope has been determined for the early stages of shortening. It is clear that the initial surface slope angles are difficult to determine. (**c**) For two or more thrusts, the surface slope has been determined by drawing the enveloping surface.

the right at a rate of 2.5 cm/hr. This velocity is also transmitted to the right basal half of the model through the basal sheet. The tip of the basal sheet forms a migrating velocity discontinuity. The base of the model, the basal sheet and the sidewalls are again covered with Alkor foil (prescribed boundary friction is 19°). The boundary condition of silicone overlying this foil was treated differently in the models. The extension experiment was run with six numerical codes (Abaqus/Standard, I2ELVIS, LAPEX-2D, Microfem, SloMo and Sopale; Table 4), which were all non-dilatational for this experiment. The initial geometries are shown in Figure 7a. The following code-specific assumptions apply:

*Abaqus/Standard.* Basal friction is applied along the entire bottom boundary. The change in velocity at the basal velocity discontinuity is accommodated over 4 elements (0.4 km scaling to 0.4 cm). The model diverged after 1.5 cm of displacement.

*I2ELVIS.* Basal friction is applied along the whole bottom boundary. The rigid mobile wall and a 0.5 mm thin rigid plate (with a background viscosity of $10^{14}$ Pa s and a shear modulus of $10^{2}$–$10^{4}$ MPa) are included into the computational domain. During extension, part of the weak 'air' layer at the top of the model is spontaneously displaced from behind the mobile wall.

*LAPEX-2D.* Basal points above the moving sheet are assigned the velocity of the sheet, whereas basal points to the left of the moving sheet are held fixed. The change in velocity at the basal velocity discontinuity is accommodated over 4 elements (2.7 km scaling to 0.27 cm).

*Microfem.* Basal friction is applied along the entire bottom boundary. The change in velocity at the basal velocity discontinuity is smoothed over 3 nodes (0.25 km scaling to 0.25 cm). The domain width is 25 km (25 cm).

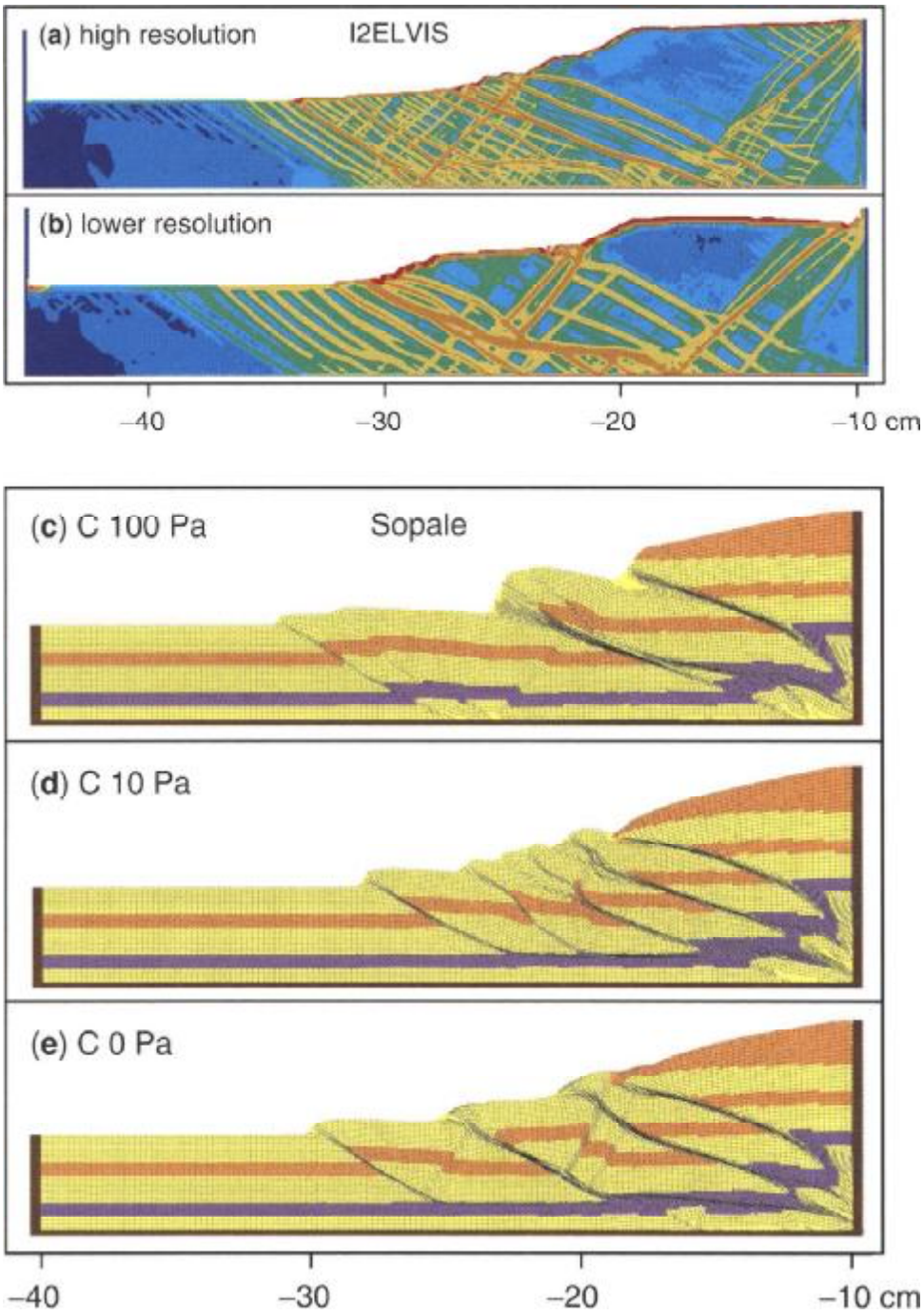


**Fig. 5.** Sensitivity tests for the shortening experiment. I2ELVIS strain-rates after 10 cm of displacement for (**a**) high resolution (normalized element size 0.05 as in Fig. 2) and (**b**) lower resolution (normalized element size 0.1). Sopale results after 10 cm of displacement for (**c**) a cohesion of 100 Pa (sandbox scale), (**d**) a cohesion of 10 Pa (as in Fig. 2), and (**e**) a cohesion of 0 Pa.

*SloMo*. Basal points above the moving sheet are assigned the velocity of the sheet, whereas points to the left are held fixed. The basal velocity discontinuity is accommodated by a linear decrease in velocity over 0.5 cm (10 elements).

*Sopale*. Basal points above the moving sheet are assigned the velocity of the sheet, whereas basal points to the left of the moving sheet are held fixed. The change in velocity at the basal velocity discontinuity is accommodated over 4 elements (0.2 km scaling to 0.2 cm). The vertical sides are held fixed (however, this boundary condition has no effect as deformation does not propagate to the lateral ends of the model).

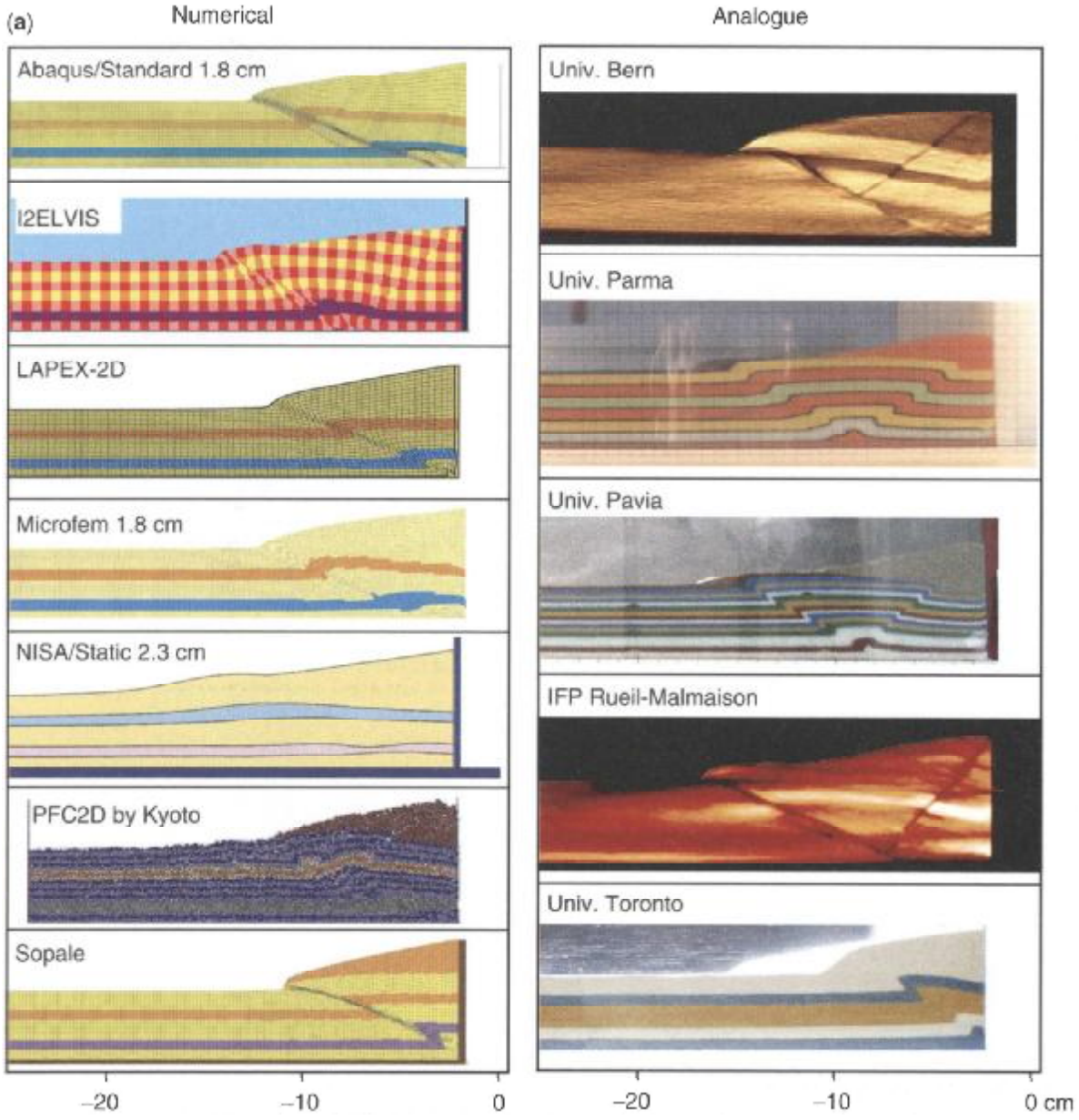


**Fig. 6.** Comparison of numerical and analogue results for the shortening experiment. (**a**) 2 cm of shortening (note that the model domain has been cropped on the left-hand side). (**b**) 14 cm of shortening.

*Model results*

The evolution of the six numerical models is shown in Figure 7 with plots of geometry and strain-rate (after 1, 2 and 5 cm of extension) and pressure (after 1 and 5 cm). Measurements of fault dip, location of fault initiation, fault-controlled extension and fault migration are shown in Table 5 and Figure 8. The measurement procedure was the same as for the shortening experiment. The initial set-up of the experiment is symmetric and the very first deformation structures should, therefore, be symmetric. The symmetry is disrupted as the basal sheet is pulled out from underneath the model.

Analysis of the numerical results allows the following observations (Figs 7 and 8, Table 5): (1) Extension first leads to the formation of two conjugate shear zones centred at the basal velocity discontinuity (the tip of the basal sheet) with a dip angle of 45° to 55° (Fig. 7b, Table 5). The dip angles are within the values expected for dynamic pressure-dependent non-dilatational Mohr-Coulomb shear zones, where predictions

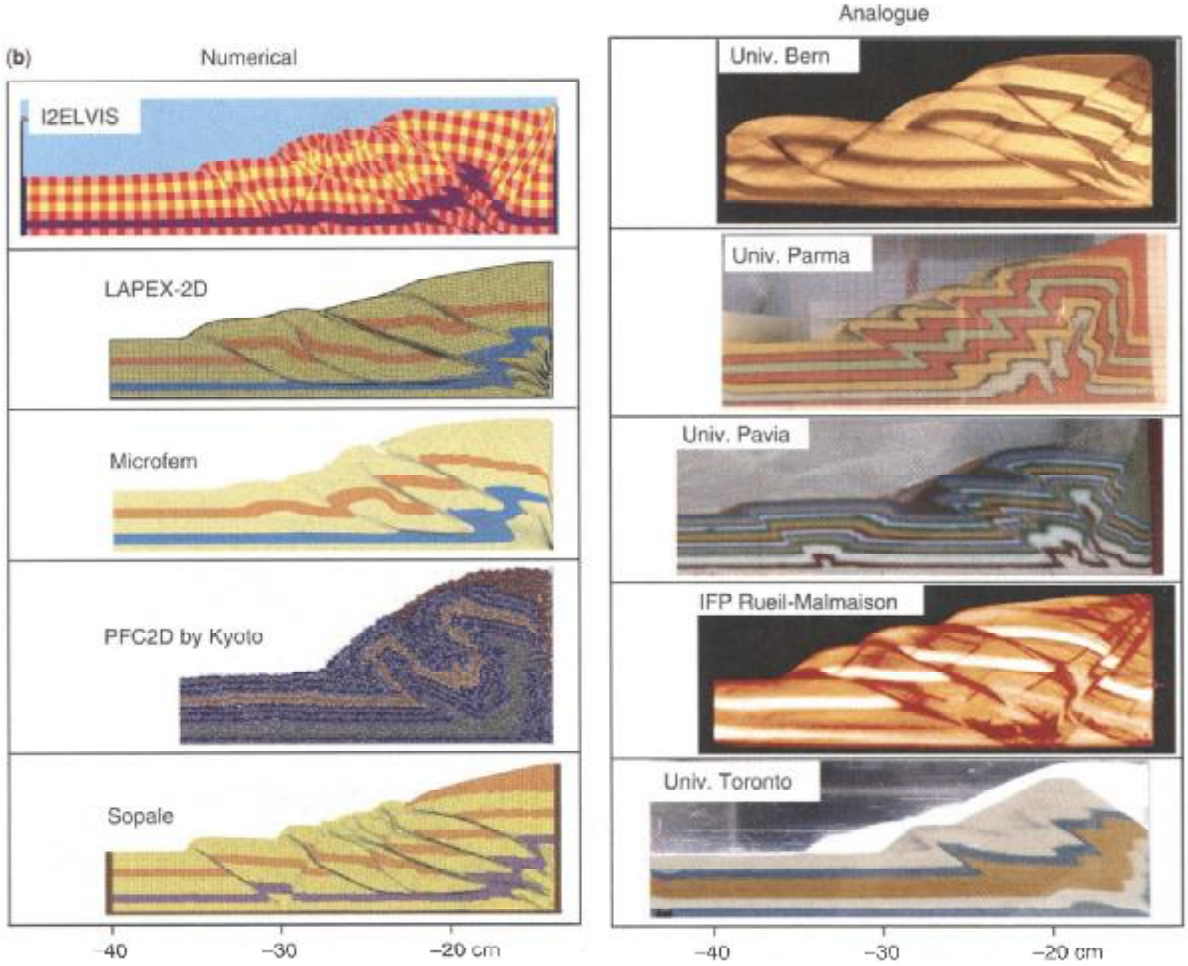


**Fig. 6.** *Continued.*

**Table 4.** *Extension experiments*

| Code | Method* | Nodes† | Track points | Norm. elem. size‡ | E§ (MPa) | $\nu$‖ | $\eta$¶ (Pa s) | $\Delta t$[1] | Veloc.[2] |
|---|---|---|---|---|---|---|---|---|---|
| Abaqus/ Standard | FEM | 201 × 36 | n.a. | 0.1 | 0.5 | 0.25 | 5e6 | varies | 2.2 cm/yr |
| I2ELVIS | FDM + MIC | 400 × 75 | 175000 | 0.05 | 3 | 0.50 | 1e12 | /0.008 h | 2.5 cm/hr |
| LAPEX-2D | FDM + MIC | 301 × 71 | 340000 | 0.0577 | 0.1 | 0.125 | 4.5e10 | 1 yr/1.4e-3s | 1 cm/yr |
| Microfem | ALE | 201 × 61 | 12261 | 0.1 | n.a. | n.a. | 4e13[3] | 700 yr/22.2s | 2.2 cm/yr |
| SloMo | FEM | 401 × 71 | 94500 | 0.05 | 0.005 | 0.50 | 1e9 | /5s | 2.5 cm/hr |
| Sopale | ALE | 401 × 71 | 253411 | 0.05 | n.a. | n.a. | 4.6e13 | 1000yr/7.2s | 0.5 cm/yr |

*FEM = Finite Element Method, FDM = Finite Difference Method, ALE = Arbitrary Lagrangian Eulerian, MIC = Marker-in-Cell.
†Nodes in horizontal × vertical direction.
‡Normalized element size is measured as the square root of element area, scaled to sandbox scale (cm).
§Young's modulus, scaled to sandbox scale.
‖Poisson ratio.
¶Background viscosity (for sand), scaled to sandbox scale. The numerical value for the viscosity of the silicone for the scaled experiments can be derived from the analogue viscosity value (5e4 Pa s), the numerical velocity and the scaling relationships (Equation 3).
[1]Time step used in the calculations. First value is for the numerical model, second value is its equivalent scaled to the sandbox scale.
[2]Velocity on sandbox scale is 2.5 cm/hr for all experiments.
[3]Equivalent linear viscosity; a non-linear viscosity was used in the calculations.

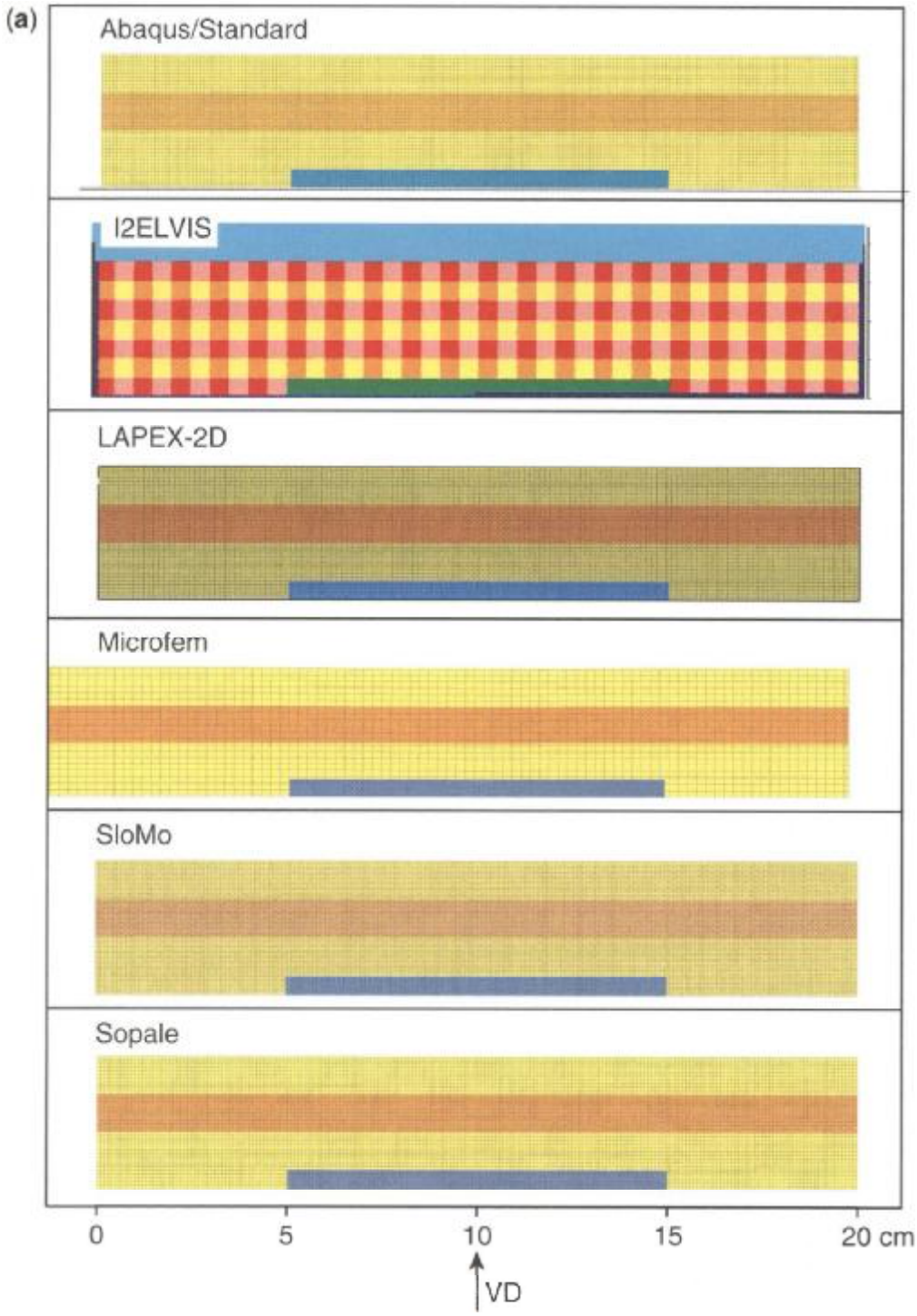


**Fig. 7.** Results for the extension experiment. All quantities (including strain-rates and pressures) are scaled down to the sandbox scale. (**a**) Initial geometries. The grid of Abaqus/Standard is the calculation grid, while for LAPEX-2D, Microfem, SloMo and Sopale the shown grid is (a subset of) the Lagrangian tracking grid.

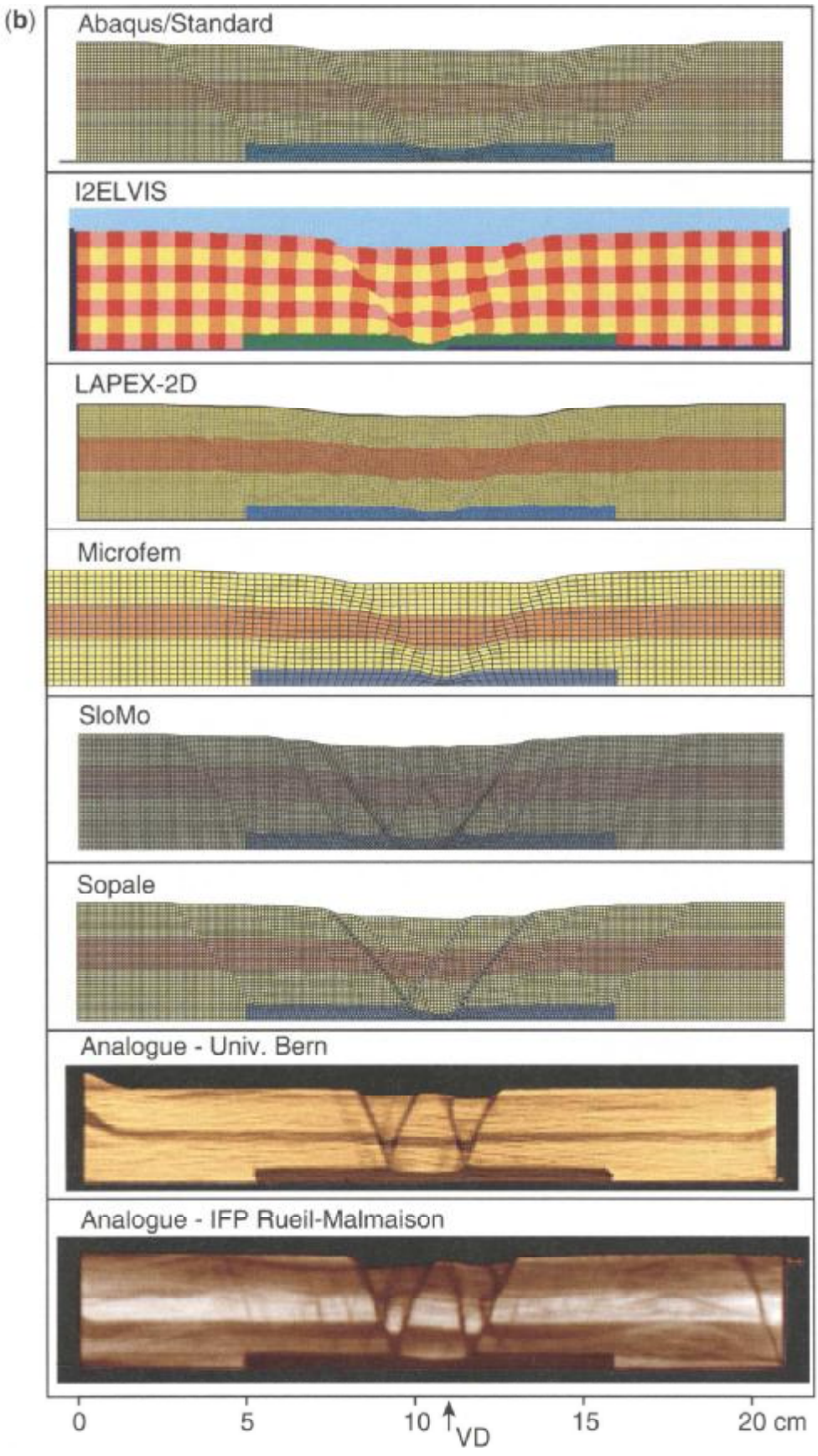


**Fig. 7.** (**b**) Geometries after 1 cm, including analogue examples of University of Bern and IFP Rueil-Malmaison. VD = velocity discontinuity.

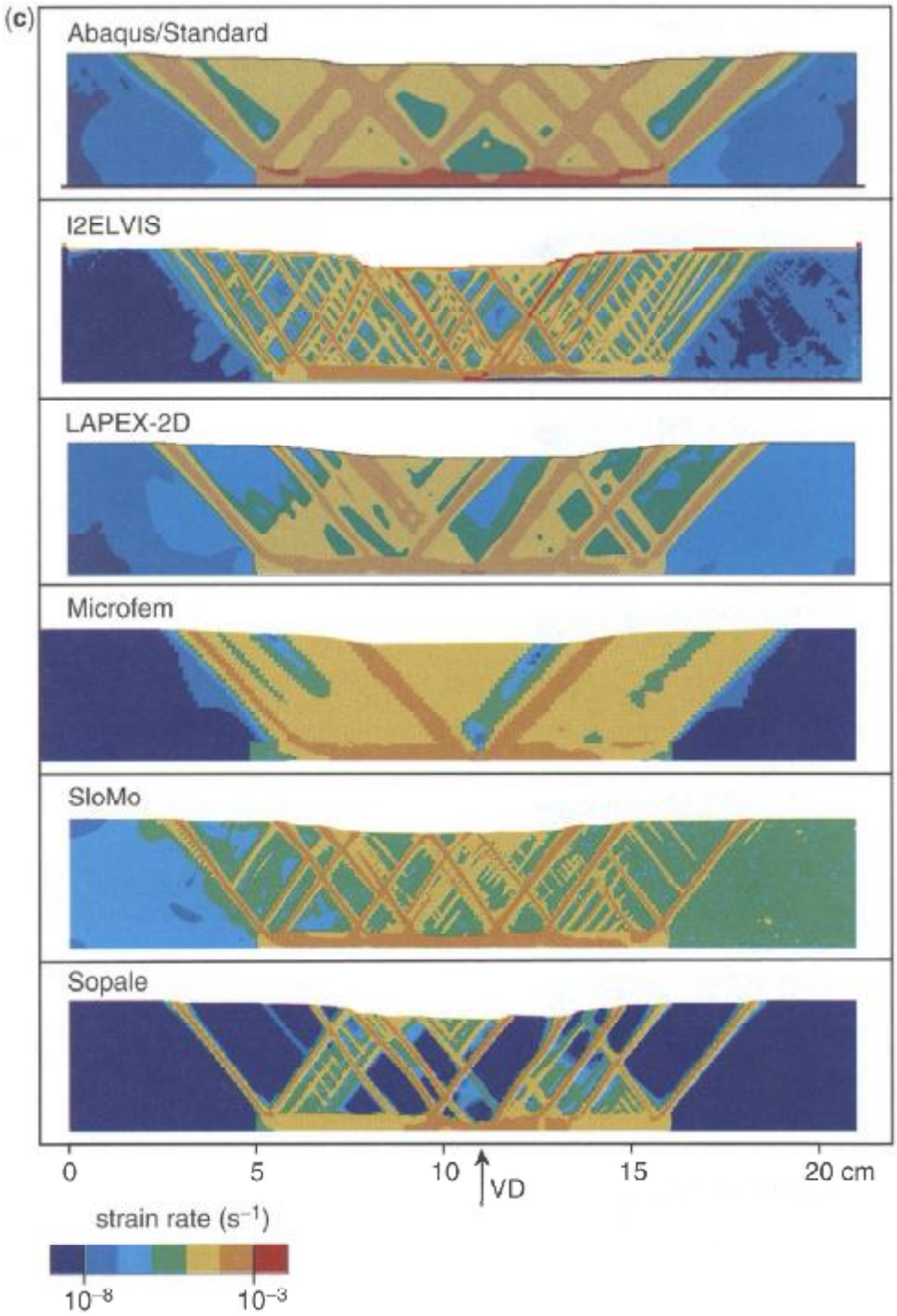


**Fig. 7.** (c) Strain-rates after 1 cm.

for fault inclination range between 45° (Roscoe angle) and $45° + \phi/2$ (Coulomb angle) (Vermeer 1990). The agreement in fault dip angles among the models is reflected in the similarity in dynamic pressures at 1 (and also 5 cm) of extension (Figs 7d and i). (2) The viscous layer distributes deformation quickly and at 1 cm of extension distributed shear zones are visible in all models (Fig. 7c). The left and right side edges of the viscous layer are found quickly (Table 5). (3) With continued extension, the shear zones migrate to the right, the silicone layer thins and the surface depression becomes wider and asymmetric in shape (Figs 7d–g). The structural evolution of all the large-deformation models is very similar, especially in light of the differences in basal boundary condition. This suggests that the basal contact is not

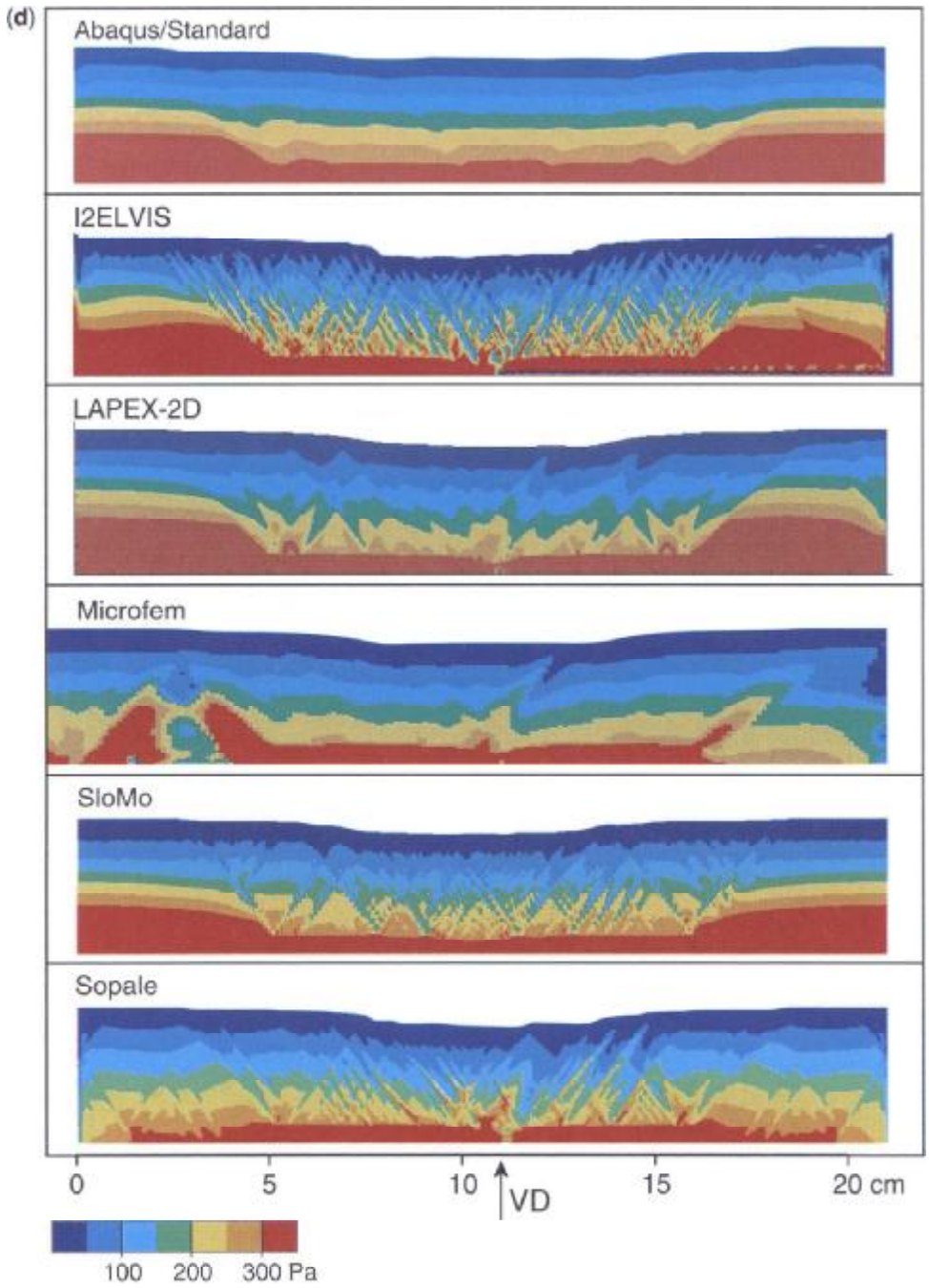


**Fig. 7.** (**d**) Dynamic pressures after 1 cm.

as important as the interaction between the moving velocity discontinuity and the viscous layer. (4) The evolution in dip angle of the first formed shear zone to the right of the velocity discontinuity is fairly similar for the different models (Fig. 8a). For larger amounts of extension (>5 cm), we find that block rotation becomes more pronounced and fault dip decreases. (5) The first formed shear zone moves to the right as the basal sheet is pulled out (Fig. 8b). A general trend is that fault migration is slower than the velocity with which the basal sheet is pulled because deformation is taken up by the block to the right of the first formed shear zone (e.g., through the formation of new shear zones). The differences between the numerical models are small and the effect on the resulting geometries is small as well. (6) The amount of fault-controlled extension is again highly variable (Table 5), as was observed for the shortening experiment. (7) The dynamic pressure field (Figs 7d and i) is more heterogeneous than the strain-rate field (Figs 7c and h) and visualizes both existing shear zones (currently or previously

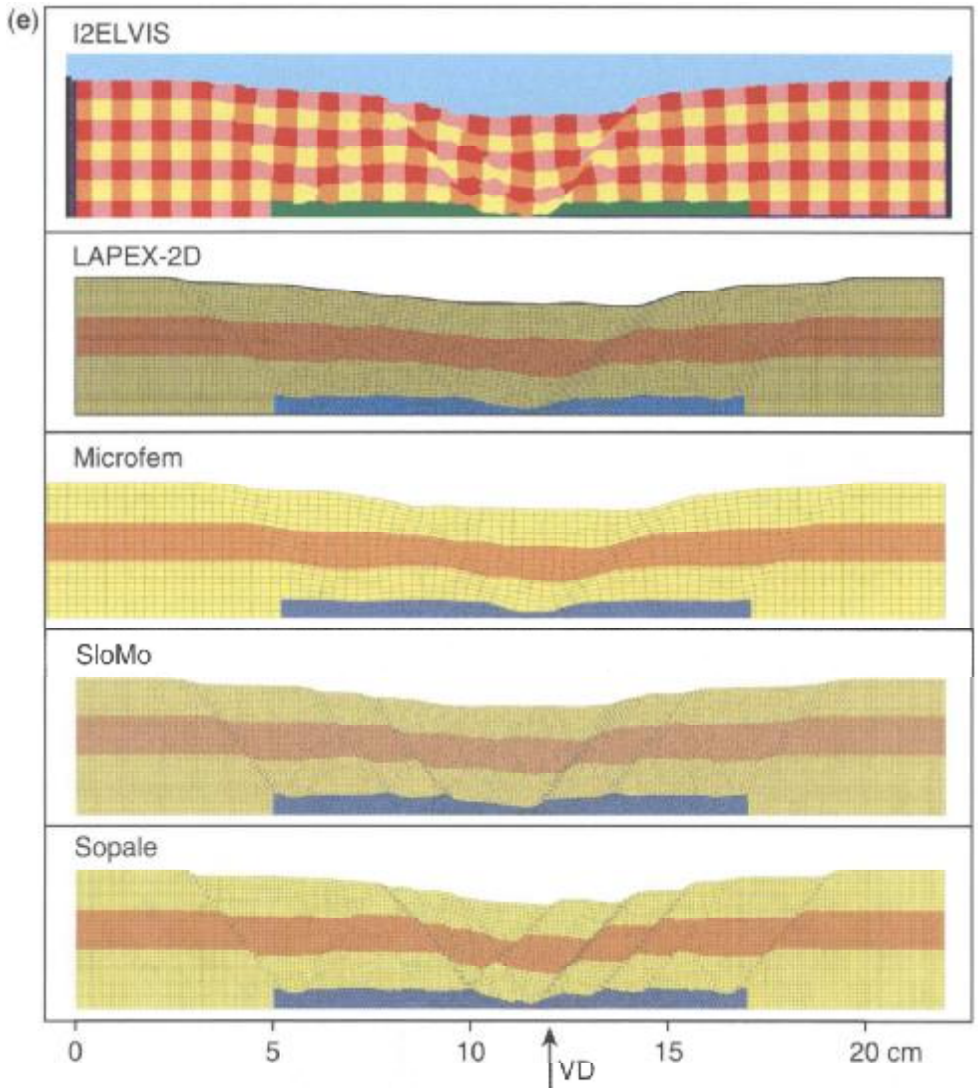


**Fig. 7.** (e) Geometries after 2 cm.

active) and potential shear zones (which are not necessarily activated). A comparison of the pressure fields for LAPEX-2D and Sopale shows that the seemingly rigid footwall blocks at the sides of the model behave in a different way in the two models. In Sopale the footwalls are at yield, whereas in LAPEX-2D they show an infinitesimal amount of elastic deformation ($10^{-5}$ approximately) and are not at yield. In a purely viscous-plastic code (such as Sopale) any amount of deformation in a high-viscosity limit brings the stresses immediately on yield. This is not the case for a visco-elasto-plastic code where the material has an additional freedom to deform elastically. The dynamic pressure for Abaqus/Standard is less well resolved due to the relatively low resolution of the model, which may perhaps also incorporate a certain degree of pressure smoothing. The pressure plots for Microfem show the effects of the stick-slip friction basal boundary condition. This creates a region of enhanced dynamic pressure in the left footwall block, which is not seen in the results for the other codes. However, the enhanced pressures do not have a large influence on deformation since the average strain-rates in this region are low.

### *Localization of shear deformation*

Comparison of the six experiments shows that the degree of focussing of deformation on shear zones may vary significantly (Table 5, Fig. 7). Results from I2ELVIS and Sopale demonstrate that both the degree of localization and the number of shear zones that form strongly

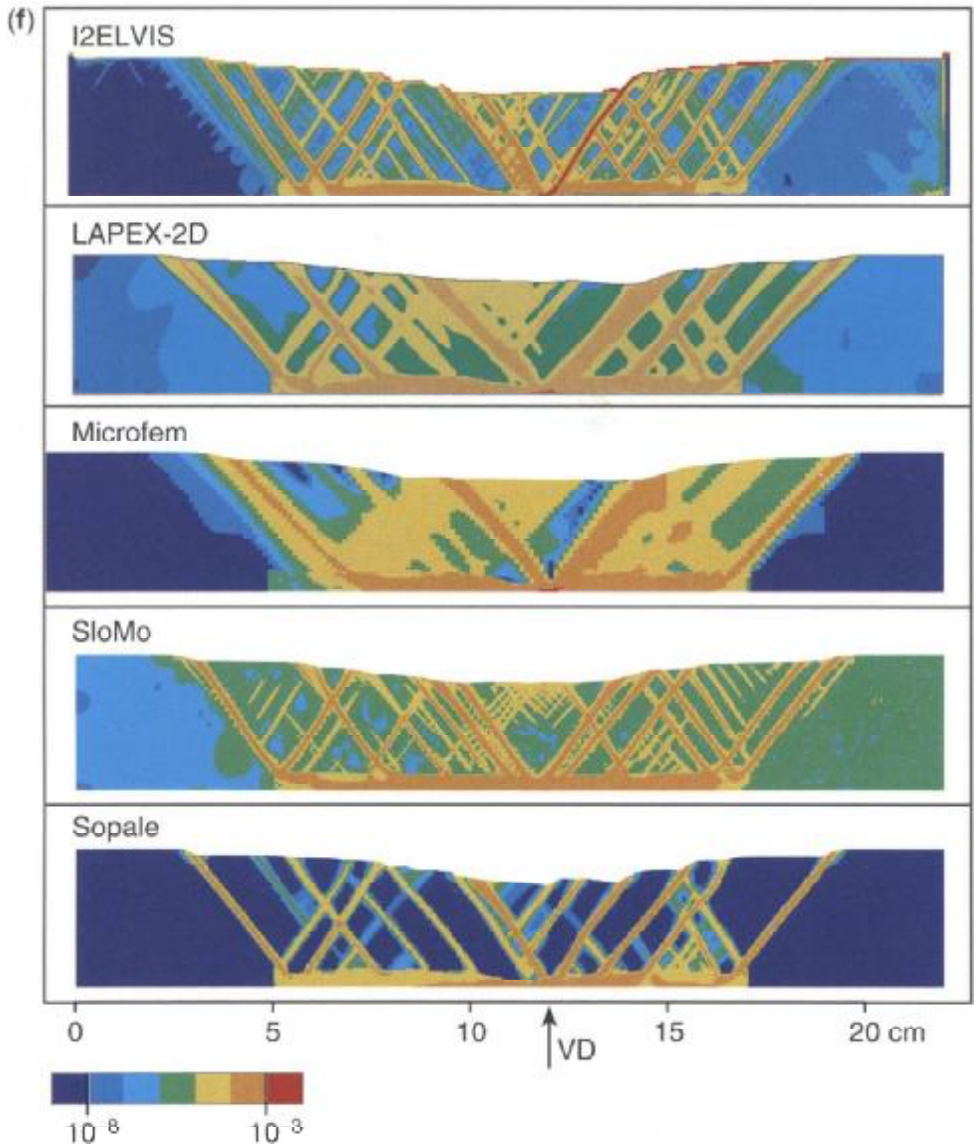


**Fig. 7.** (f) Strain-rates after 2 cm.

increase with increasing resolution of the numerical grid. This can also be seen from a comparison of the results from Microfem (lower resolution ALE code) and Sopale (higher resolution ALE code) (Fig. 7). According to Cundall (1990), the ratio of elastic bulk modulus to lithostatic pressure is an important parameter for fault spacing, whereby an increase in this ratio decreases fault spacing. In nature, the value of this dimensionless ratio is expected to vary over orders of magnitude (for example, between 17 and 4432, using an elastic modulus of $10^{10}$–$10^{11}$ Pa, $\rho$ 2300–3000 kg m$^{-3}$ and height 1–20 km) and the variation in this ratio for the four numerical experiments that include elastic material behaviour is of the same order (between 3 and 1867 using the elastic *shear* modulus, $\rho$ 1560 kg m$^{-3}$, height 3.5 km). However, in the set-up of our experiment, the viscous layer and the velocity discontinuity control the initial location of shear zones and this set-up is, therefore, not suitable for a systematic study of shear zone spacing.

The use of dynamic pressure in Mohr-Coulomb plasticity significantly increases the localization of deformation in shear zones (tests with I2ELVIS and Sopale, Fig. 9). A Von Mises model (no pressure dependence) with an equivalent strength and softening to the Mohr-Coulomb models shows a considerably lower degree of localization (Figs 9a and d). With a depth-dependent pressure (Fig. 9b) localization is still less than in the dynamic pressure case (Figs 9c and e). To be noted here is that the

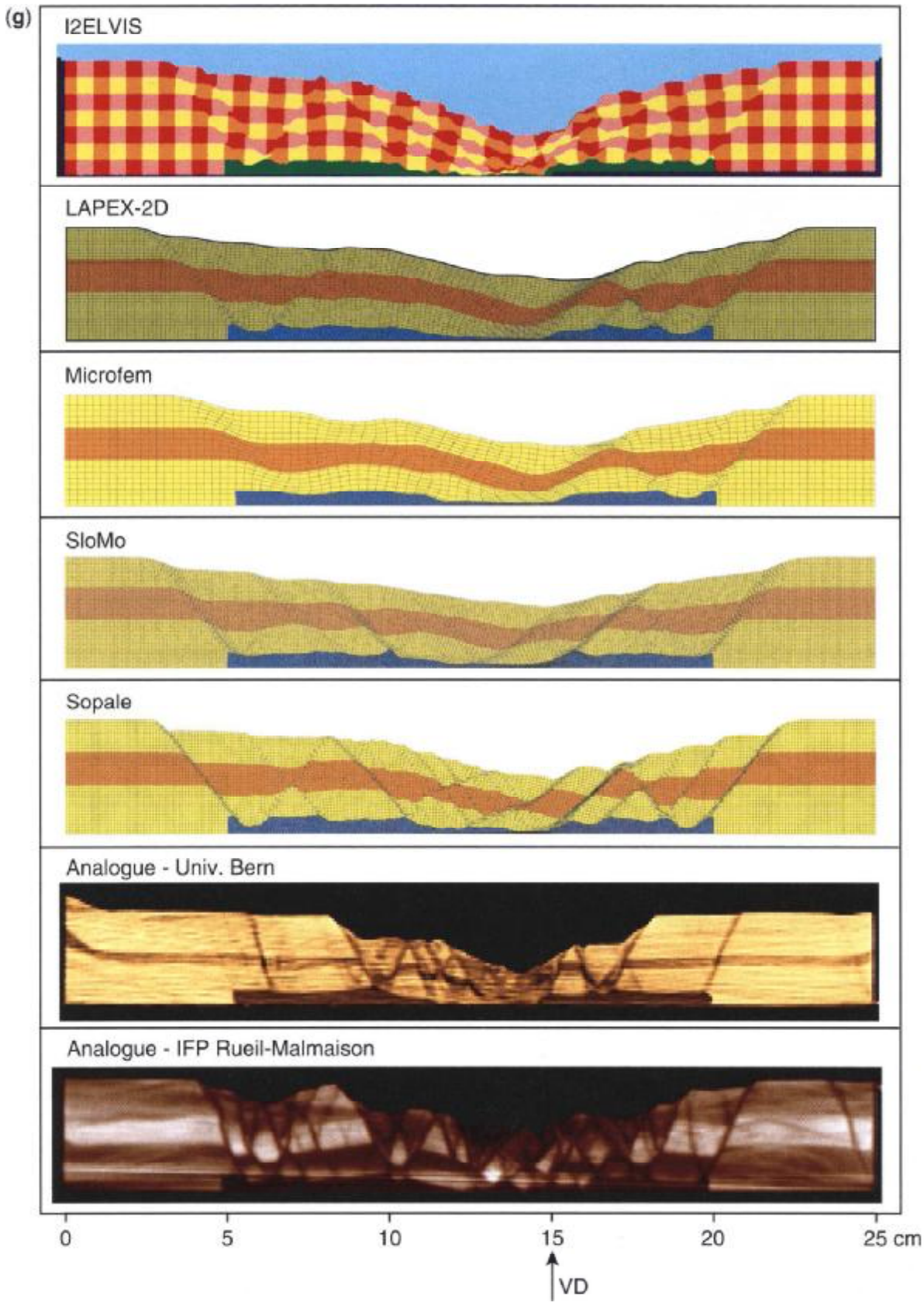


**Fig. 7.** (g) Geometries after 5 cm, including analogue examples of University of Bern and IFP Rueil-Malmaison.

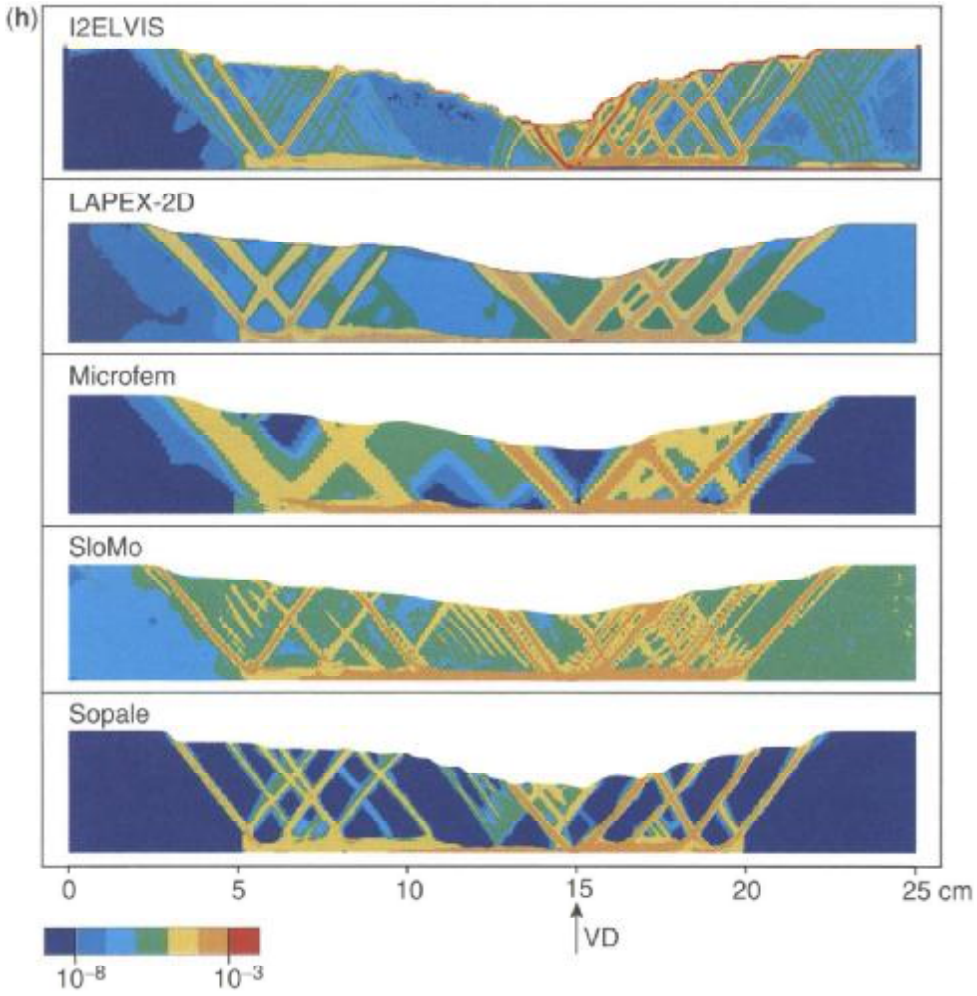


**Fig. 7.** (**h**) Strain-rates after 5 cm.

dynamic pressure is calculated differently in the two codes compared in Figure 9 (see also Figs 7d and i). Sopale (and also Microfem) calculate dynamic pressure through a penalty formulation with a high but finite penalty ratio (Fullsack 1995) which leads to quasi-incompressibility (or a slight compressibility). In I2ELVIS the purely incompressible continuity equation is solved. Our test calculations with I2ELVIS have also shown that for a marker-in-cell technique, the numerical width of shear zones depends strongly on the interpolation schemes which are used for strain rate, stress and viscosity: numerical diffusion due to the interpolation between nodes of the grid and the markers can cause strong (two- to fivefold) widening of shear zones leading to a decrease in strain-rate contrast. Finite element and finite difference codes have a tendency to reduce shear zone width with decreasing element size, implying that numerical shear zone width is mesh-dependent. Very fine meshes probably underestimate the width of localized shear zones in comparison with observed shear band widths in granular media (see also de Borst & Sluys 1991; Zervos *et al.* 2001).

### *Sensitivity analyses*

In the extensional models presented here, two different boundary conditions were applied at the base. In Abaqus/Standard, I2ELVIS and Microfem, boundary friction was applied along the whole bottom boundary, including along the viscous material. In LAPEX-2D, SloMo and Sopale, grid points on the basal sheet were assigned the velocity with which the sheet was pulled and points to the left of the sheet were held fixed. The high level of agreement between the modelling results of the six experiments shows that any effect of this variation in basal boundary condition is small. The tip of

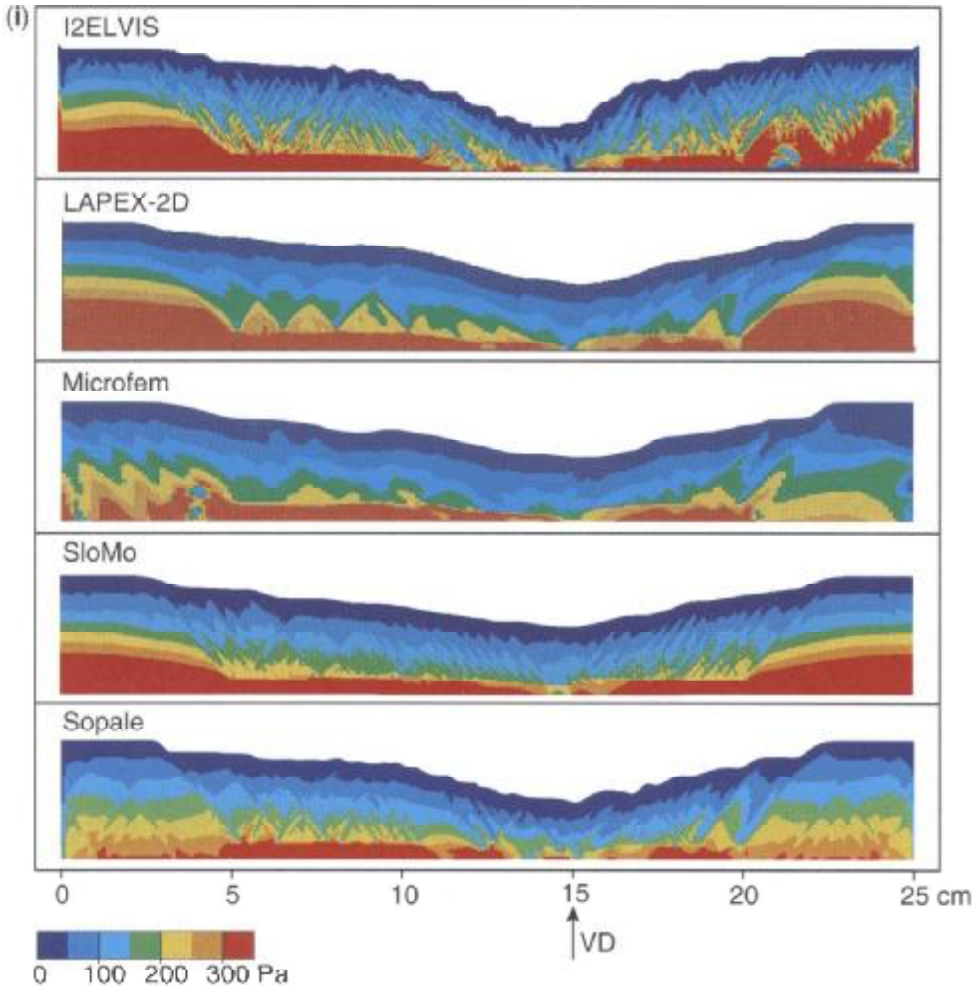


**Fig. 7.** (i) Dynamic pressures after 5 cm.

the basal sheet serves to initially localize deformation in a symmetric manner in the centre of the model. An experiment with a free slip base without basal sheet (run with Sopale) shows that in this case shear zones first form at the edges of the viscous layer and soon after in the centre of the model.

Experiments with I2ELVIS and Sopale show that a lower extensional velocity (which is equivalent to a lower viscosity for the viscous layer)

**Table 5.** *Quantification of extension experiments**

| Code | Fault ext.† at 2 cm | Fault initiation at ends of PDMS | | Fault on left side of VD | | Fault on right side of VD | |
|---|---|---|---|---|---|---|---|
| | | Left | Right | dip | when | dip | when |
| Abaqus/Standard | – | 0.5 | 0.5 | 45° | 0 | 45° | 0 |
| I2ELVIS | 0.9–1.2 | never | 2 | 51° | 1 | 52° | 1 |
| LAPEX-2D | 0.7–0.9 | 0.5 | 0.5 | 51° | 0.5 | 53° | 0.5 |
| Microfem | 0.5–1.2 | never | 1.5 | 46° | 0.5 | 48° | 0.5 |
| SloMo | 0.7–0.8 | 2 | 2 | 53° | 1 | 55° | 1 |
| Sopale | 1.1–1.3 | 0.5 | 0.5 | 50° | 0.5 | 52° | 0.5 |
| Analogue ranges‡ | 0.9–1.0 | never | 2–4.5 | 65°–69° | 0.5 | 60°–65° | 0.5 |

*All values referred to sandbox scale in cm. Output stages typically available at 0, 0.5, 1 and then every cm of extension.
†Fault-controlled horizontal extension determined by cut-off points between layers and the faults.
‡Analogue values from experiments of University of Bern and IFP Rueil-Malmaison (Schreurs *et al.* 2006).

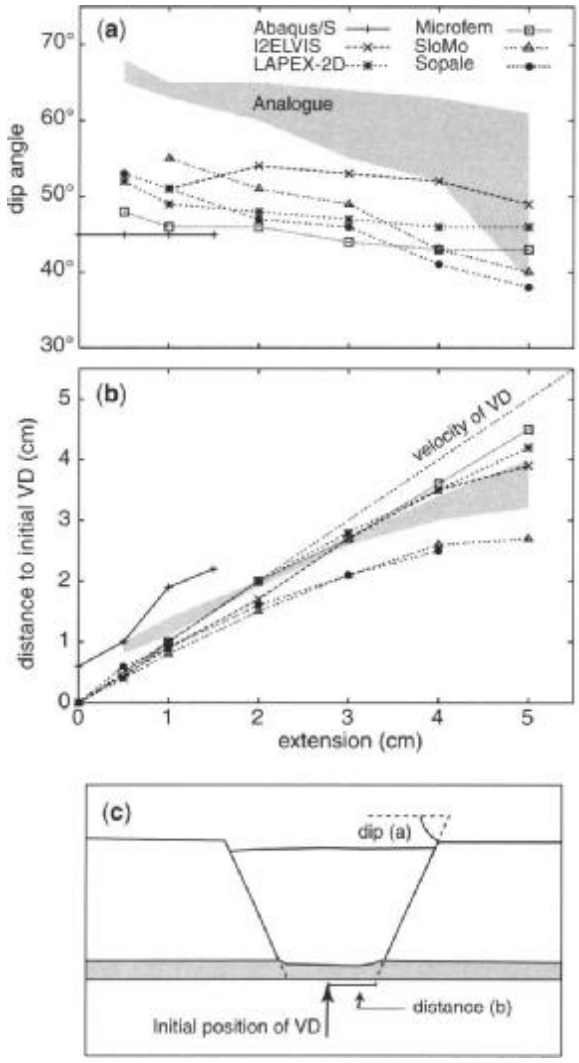


**Fig. 8.** (**a**) Dip angle of the first-formed normal fault on the right-hand side of the velocity discontinuity (the tip of the basal sheet) versus extension. (**b**) Migration of the same fault. The migration is measured relative to the initial position of the tip of the basal sheet. (**c**) Schematic drawing showing how the quantities in (a) and (b) were measured. The grey bands denote the range of values measured for the analogue experiments of University of Bern and IFP Rueil-Malmaison (see also Fig. 7 and Schreurs *et al.* 2006).

favours a more efficient outward propagation of shear zone development. The surface depression is less deep. A higher cohesion of the 'sand' material leads to locally steeper surface slopes, similar to our observations for the shortening experiment. We found that a reduction or increase in the strain softening range does not affect the results significantly. Tests with I2ELVIS and Sopale also showed that a higher resolution calculation grid (smaller element size) leads to the development of more shear zones which are better focussed, as discussed above. This can also be seen from a comparison of Microfem (lower resolution) to Sopale (higher resolution) results and is again similar to our observation for the shortening experiment.

### *Implications of the numerical experiments*

Comparison between the different numerical codes for the extension experiment shows a high level of agreement. All predict the same location of maximum thinning and show the same general evolution and stepping out of shear zones. High-resolution numerical codes (e.g., Sopale) predict rotation of shear zones with larger finite deformation. The extensional results show much less variation compared to the shortening experiment. Ellis *et al.* (2004) suggest that experiments involving weak viscous layers reduce the influence of boundary conditions on both analogue and numerical results, and instead pass control to rheological strength contrasts within the model domain. In our set-up, the weak viscous basal layer serves to reduce the effect of stress discontinuities due to the basal velocity discontinuity.

Although the overall dynamics and evolution of the different numerical codes are similar, differences in the number of shear zones that develop, the timing at which the ends of the viscous layer are activated and the shear zone dip can be seen. These differences partly appear to reflect differences in mesh resolution. As for the shortening experiment, we find that caution is required in interpretations from numerical results involving number of shear zones and shear zone spacing.

Our numerical experiments may also have important implications for the understanding of pressure distributions in large-scale tectonic processes involving the development of shear zones. As follows from our results, the dynamic pressure field (Figs 7d and i) in a medium subjected to brittle/plastic deformation deviates strongly from the lithostatic distribution often assumed in geosciences. These results are in line with other theoretical studies (e.g., Mancktelow 1995; Petrini & Podladchikov 2000; Burg & Gerya 2005) which predict significant underpressure and overpressure effects in orogenic processes. This, in turn, may have strong consequences for the pressure-temperature evolution of deformed rocks complexes composing the Earth's crust and lithospheric mantle.

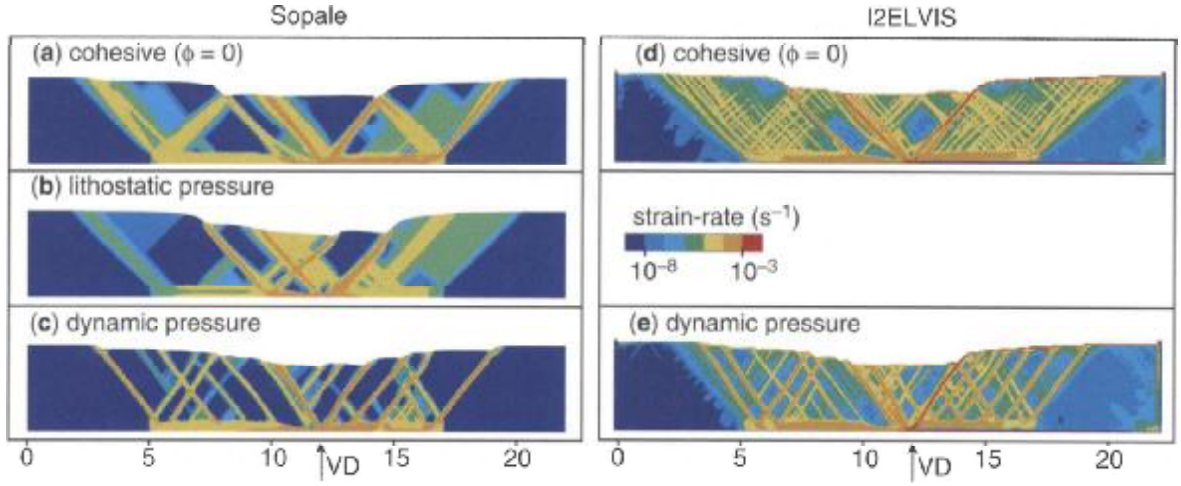


**Fig. 9.** A comparison of strain-rates for I2ELVIS and Sopale after 2 cm of extension shows the influence of the plasticity description. (**a**) and (**d**) Angle of internal friction $\phi = 0$. Cohesion softens from 170 Pa to 140 Pa (sandbox scale). These values mimic the same strength and strength reduction as for the frictional extension models. (**b**) Sopale for Mohr-Coulomb plasticity with depth-dependent pressure. (**c**) and (**e**) Mohr-Coulomb plasticity with dynamic pressure (standard case).

*Comparison to analogue results*

Only two analogue experiments documented cross-sectional information at different extension stages and could be used to compare the numerical results against. The analogue results of the University of Bern and IFP Rueil-Malmaison show an overall similar evolution, but differ in the velocity with which normal faults are distributed outwards (Schreurs *et al.* 2006). The geometries of the numerical and analogue experiments after 1 and 5 cm of extension are shown in Figures 7b and g. The dip angle and migration of the first formed shear zone to the right of the velocity discontinuity are compared in Figure 8. In the numerical experiments reported here the mobile wall velocity is directly applied to the right-hand side of the models. However, in the analogue sandbox the role of the mobile wall is likely only to prevent the sand from collapsing and does not provide a driving force. The extension is passed to the model by the moving basal sheet. Because there is a sufficient distance between the right-hand wall and the velocity discontinuity this is, however, not likely to affect the analogue-numerical comparison.

Comparison of the numerical results to the two analogue experiments shows that: (1) The numerical experiments predict the overall dynamics and evolution of the analogue system reasonably well. (2) In both analogue and numerical results, shear zones initiate at the basal velocity discontinuity and with increasing extension new shear zones develop outwards. (3) Both numerical and analogue results show a rotation of shear zones with shallowing dip angles for increasing extension. (4) The velocity with which the first formed normal fault to the right of the velocity discontinuity moves to the right is very similar between the two analogue results and the numerical models (Fig. 8b). (5) The main difference between the analogue and numerical results is the dip angle of the shear zones (Figs 7 and 8a). The dip angles in the analogue experiments are much steeper (between 60° and 69° initially) and follow Coulomb behaviour, with dip angles predicted by $45^\circ + \phi/2$ ($63^\circ$–$68^\circ$ for the material properties of the two analogue experiments). All numerical extension models assume zero dilatation and for dynamic pressure-dependent Mohr-Coulomb behaviour dip angles between 45° (Roscoe) and $45^\circ + \phi/2$ (Coulomb) are then to be expected (Vermeer 1990) ($45^\circ$–$63^\circ$ for our material properties). The observed initial dip angles ($45^\circ$–$55^\circ$) are in the lower range of the theoretical values. Assigning a non-zero dilatation angle, $\psi$, to 'sand' will increase the theoretical minimum dip angle value to $45^\circ + \psi/2$. Tests with I2ELVIS show that a non-zero dilatation angle indeed results in higher dip angles for the shear zones.

## The numerical sandbox

Our study presents a direct qualitative and quantitative comparison of numerical and analogue model results for two experimental set-ups aimed at simulating upper-crustal tectonic processes. Results from seven numerical codes are compared to results from five analogue

laboratories for a brittle thrust wedge experiment, while results from six numerical codes are compared to results from two analogue laboratories for a brittle-viscous extension experiment. The accompanying paper (Schreurs *et al.* 2006) shows additional analogue shortening and extension results, which could not be used in our comparison as either cross-sectional information was not recorded during the experiment or a different material (clay) was used.

A comparison of analogue experiments from different laboratories has to take into account that differences may occur in material properties (whereby properties may even slightly change due to storage conditions or small vibrations), modelling apparatus, model set-up (width and length) and in the set-up technique of individual experimenters. The effects of some variations can be tested by determining the reproducibility of each experiment in the same laboratory, but it is clearly of importance to determine the inter-laboratory reproducibility of analogue model results as well. The accompanying paper (Schreurs *et al.* 2006) shows an encouraging first order agreement of model results of different analogue laboratories, despite variability in model widths and in material properties.

In comparison, numerical experiments have the potential to be much more reproducible, since material properties, model set-up and boundary conditions can be specified exactly. However, set-ups between different experimenters may also vary in subtle ways depending on assumptions used, and even slightly different ways of interpreting and prescribing the initial set-up. The eight numerical codes used in our comparison differ with each other for the following properties and assumptions: (1) resolution, imposed element aspect ratios, and type of element; (2) time step (extension experiment); (3) smoothing of velocity discontinuities; (4) implementation of frictional boundaries; (5) material properties (dilatation and elasticity); (6) scaling; (7) calculation of dynamic pressure; and (8) surface smoothing (shortening experiment). Our results indicate that grid resolution, representation of boundary conditions (boundary friction and velocity discontinuities), calculation of dynamic pressure and dilatation require careful attention in sandbox-type experiments. In contrast, elastic material behaviour, scaling of the experiment and small amounts of surface smoothing appear to play only a minor role.

Our results highlight that different numerical solution methods (finite difference method, finite element method, distinct element method) can successfully be used to reproduce structures seen in analogue sandbox models. The numerical codes can do reasonably well in qualitatively predicting the dynamic evolution of the system in shortening and extension, shear zone (fault) formation, and taper geometry (shortening experiment). The level of variability between the numerical results is about the same as the degree of variability between the analogue results. Numerical codes show differences with each other, and the analogue experiments, for detailed location, dip and spacing of shear zones. As the initial set-up and material properties of analogue models can be relatively well constrained, their results can form a useful test for numerical models. Numerical models may, therefore, benefit from future studies focusing on the differences between analogue and numerical modelling results. Our results indicate that future experiments should preferably choose a simplified set-up that reduces the effects of boundary conditions and especially abrupt changes in boundary velocities, prescribe resolution and time step size, use material behaviour which is as similar as possible and, if possible, quantify results in an unambiguous manner.

Our results emphasize the importance of the following issues for numerical sandbox-type studies: (1) the ability to model large deformation structures; (2) the ability to represent boundary friction, velocity discontinuities and a free surface; (3) the representation of a composite (elasto)-visco-plastic rheology; (4) calculation with a relatively high resolution (important for shear zone evolution, for example); (5) minimization of numerical diffusion; and (6) consensus on the procedure for quantification of the results. These are important for studies in which numerical and analogue models are used in combination, but reflect at the same time requirements to study Earth tectonic processes.

## Conclusions

Two experimental set-ups inspired by settings from structural geology were used to compare eight numerical codes to each other. Despite differences in set-up and material behaviour between the individual experiments, the results are useful in showing that: (1) Numerical codes at the present time are capable of modelling the dynamic evolution of compressional and extensional settings, including shear-zone development, forward propagation of thrust wedges, and taper geometry of convergent wedges. The qualitative behaviour of the different codes is similar. (2) A quantitative analysis of the results of these codes shows a higher degree of variability, particularly in number of shear

zones that develop and their spacing and dip angle. (3) A comparison between the results of the numerical codes and equivalent analogue experiments shows agreement in the overall evolution of the system and in the localization of deformation onto faults/shear zones. The variability among the numerical results is of the same order as the variations among the analogue results. Differences with the analogue results are also apparent, for example, in dip angles of extensional shear zones, degree of localization, and the development of backthrusts in the shortening experiment. Reducing these differences represents an interesting challenge for numerical modellers.

We hope that the comparisons shown here are a useful guide to the structural geology community, in highlighting the degree to which numerical codes may be used to reproduce experiments in the sandbox and/or processes at the scale of the upper crust.

The figures of the analogue experiments were kindly provided by the laboratories of Bern (GS), IFP Rueil Malmaison (J.-M. Daniel, J.-M. Mengus), Parma (E. Costa, C. Cavozzi), Pavia (A. Ravaglia) and Toronto (D. Boutilier, A. Cruden). J. Lohrmann measured the angle of friction of (GFZ Potsdam) sand on 'Alkor' foil. C. Beaumont, J.-P. Brun and B. Colletta gave us helpful feedback on the design of the experiments. We thank the participants of the GeoMod2004 pre-conference workshop for their insightful discussions and Claudio Faccenna for sharing with us his introductory talk on analogue and numerical modelling which he presented at this workshop. We would like to thank N. Kukowski and the reviewers R. Buck and K. Furlong for their positive feedback, and Y. Podladchikov, S. Hoth and S. Medvedev for stimulating discussions. Microfem and Sopale were developed by P. Fullsack and the Geodynamics Group at Dalhousie University. Simulations by BK have been run at the USC high performance computing facilities. This work was supported by ETH Research Grant TH-12/04-1, RFBR grant #03-05-64633 and the RF President Program 'Leading Scientific School of Russia' (grant #03.5.1645) to TVG and project SFB-267 from the Deutsche Forschungsgemeinschaft for AYuB and AK.

## References

ABAQUS/STANDARD USER'S MANUAL 2003. Vol. 1 & 2, version 6.4. Abaqus Inc, Pawtucket, Rhode Island, USA.

ADAM, J. & URAI, J. L. *ET AL.* 2005. Shear localization and strain distribution during tectonic faulting – new insights from granular-flow experiments and high-resolution optical image correlation techniques. *Journal of Structural Geology*, **27**, 283–301.

BABEYKO, A. YU., SOBOLEV, S. V., TRUMBULL, R. B., ONCKEN, O. & LAVIER, L. L. 2002. Numerical models of crustal scale convection and partial melting beneath the Altiplano-Puna Plateau. *Earth and Planetary Science Letters*, **199**, 373–388.

BAHROUDI, A., KOYI, H. A. & TALBOT, C. J. 2003. Effect of ductile and frictional décollements on style of extension. *Journal of Structural Geology*, **25**, 1401–1423.

BEHN, M. D., LIN, J. & ZUBER, M. T. 2002. A continuum mechanics model for normal faulting using a strain-rate softening rheology: implications for thermal and rheological controls on continental and oceanic rifting. *Earth and Planetary Science Letters*, **202**, 725–740.

BLANKENBACH, B. & BUSSE, F. *ET AL.* 1989. A benchmark comparison for mantle convection codes. *Geophysical Journal International*, **98**, 23–38.

BURBIDGE, D. R. & BRAUN, J. 2002. Numerical models of the evolution of accretionary wedges and fold-and-thrust belts using the distinct-element method. *Geophysical Journal International*, **148**, 542–561.

BURG, J.-P. & GERYA, T. V. 2005. Viscous heating and thermal doming in orogenic metamorphism: numerical modelling and geological implications. *Journal of Metamorphic Geology*, **23**, 75–95.

CRUDEN, A. R., NASSERI, M. B. & PYSKLYWEC, R. 2006. Surface topography and internal strain variation in wide hot orogens from three-dimensional analogue and two-dimensional numerical vise models. *In*: BUITER, S. J. H. & SCHREURS, G. (eds) *Analogue and Numerical Modelling of Crustal-Scale Processes*. Geological Society, London, Special Publications, **253**, 79–104.

CUNDALL, P. A. 1990. Numerical modelling of jointed and faulted rock. *In*: ROSSMANITH, A. (ed.) *Mechanics of Jointed and Faulted rocks*. Balkema, Rotterdam, 11–18.

CUNDALL, P. A. & BOARD, M. 1988. A microcomputer program for modelling large-strain plasticity problems. *In*: SWOBODA, G. (ed.) *6th International Conference in Numerical Methods in Geomechanics*. A. A. Balkema, Brookfield, VT, 2101–2108.

CUNDALL, P. A. & STRACK, D. L. 1979. A discrete numerical model for granular assemblies. *Geotechnique*, **29**, 47–65.

CUVELIER, C., SEGAL, A. & VAN STEENHOVEN, A. A. 1986. *Finite Element Methods and Navier-Stokes Equations*. Reidel Publishing Company, Dordrecht, 483pp.

DAHLEN, F. A. 1984. Noncohesive critical Coulomb wedges: an exact solution. *Journal of Geophysical Research*, **89**, 10125-10133.

DAVIS, D., SUPPE, J. & DAHLEN, A. 1983. Mechanics of fold-and-thrust belts and accretionary wedges. *Journal of Geophysical Research*, **88**, 1153–1172.

DE BORST, R. & SLUYS, L. J. 1991. Localization in a Cosserat continuum under static and dynamic loading conditions. *Computer Methods in Applied Mechanics and Engineering*, **90**, 805–827.

ELLIS, S., SCHREURS, G. & PANIEN, M. 2004. Comparisons between analogue and numerical models of thrust wedge development. *Journal of Structural Geology*, **26**, 1659–1675.

FULLSACK, P. 1995. An arbitrary Lagrangian-Eulerian formulation for creeping flows and its application in tectonic models. *Geophysical Journal International*, **120**, 1–23.

GERYA, T. V. & YUEN, D. A. 2003. Characteristics-based marker-in-cell method with conservative finite-difference schemes for modelling geological flows with strongly variable transport properties. *Physics of the Earth and Planetary Interiors*, **140**, 293–318.

GUTSCHER, M.-A., KUKOWSKI, N., MALAVIEILLE, J. & LALLEMAND, S. 1998*a*. Material transer in accretionary wedges from analysis of a systematic series of analog experiments. *Journal of Structural Geology*, **20**, 407–416.

GUTSCHER, M.-A., KUKOWSKI, N., MALAVIEILLE, J. & LALLEMAND, S. 1998*b*. Episodic imbricate thrusting and underthrusting: Analog experiments and mechanical analysis applied to the Alaskan Accretionary Wedge. *Journal of Geophysical Research*, **103**, 10161–10176.

HUBBERT, M. K. 1937. Theory of scale models as applied to the study of geologic structures. *Bulletin of the Geological Society of America*, **48**, 1459–1520.

JAEGER, J. C. & COOK, N. G. W. 1979. *Fundamentals of Rock Mechanics*. John Wiley and Sons, New York, 585pp.

KAUS, B. J. P. 2005. *Modelling approaches to geodynamic processes*. PhD thesis, ETH Zürich.

LE POURHIET, L., MATTIONI, L. & MORETTI, I. 2006. 3D modelling of rifting through a pre-existing stack of nappes in the Gulf of Corinth (Greece): a mixed analogue/numerical approach. *In*: BUITER, S. J. H. & SCHREURS, G. (eds) *Analogue and Numerical Modelling of Crustal-Scale Processes*. Geological Society, London, Special Publications, **253**, 233–252.

LOHRMANN, J., KUKOWSKI, N., ADAM, J. & ONCKEN, O. 2003. The impact of analogue material properties on the geometry, kinematics, and dynamics of convergent sand wedges. *Journal of Structural Geology*, **25**, 1691–1771.

MANCKTELOW, N. S. 1995. Nonlithostatic pressure during sediment subduction and the development and exhumation of high pressure metamorphic rocks. *Journal of Geophysical Research*, **100**, 571–583.

MICHON, L. & MERLE, O. 2000. Crustal structures of the Rhine graben and the Massif Central grabens: An experimental approach. *Tectonics*, **19(5)**, 896–904.

MULUGETA, G. 1988. Modelling the geometry of Coulomb thrust wedges. *Journal of Structural Geology*, **10**, 847–859.

MULUGETA, G. & KOYI, H. 1992. Episodic accretion and strain partitioning in a model sand wedge. *Tectonophysics*, **202**, 319–333.

NISA II™ USER'S MANUAL VERSION 7.0, 1997. Engineering Mechanics Research Corporation, Troy, Michigan, USA.

PANIEN, M. 2004. *Analogue modelling experiments of basin inversion using well-characterized granular materials and comparisons with numerical models*. Ph.D. thesis. University of Bern, Switzerland.

PANIEN, M., BUITER, S. J. H., SCHREURS, G. & PFIFFNER, O. A. 2006. Inversion of a symmetric basin: Insights from a comparison between analogue and numerical experiments. *In*: BUITER, S. J. H. & SCHREURS, G. (eds) *Analogue and Numerical Modelling of Crustal-Scale Processes*. Geological Society, London, Special Publications, **253**, 253–270.

PELLETIER, D., FORTIN, A. & CAMARERO, R. 1989. Are FEM solutions of incompressible flows really incompressible? (Or how simple flows can cause headaches!) *International Journal of Numerical Methods in Fluids*, **9**, 99–112.

PETRINI, K. & PODLADCHIKOV, Y. 2000. Lithospheric pressure-depth relationship in compressive regions of thickened crust. *Journal of Metamorphic Geology*, **18**, 67–77.

PFC$^{2D}$ 1999. *User's Guide* Version 3.0. Itasca Consulting Group, Inc.

POLIAKOV, A. N. & PODLADCHIKOV, Y. Y. 1992. Diapirism and topography. *Geophysical Journal International*, **109**, 553–564.

POLIAKOV, A. N., CUNDALL, P. A., PODLADCHIKOV, Y. Y. & LYAKHOVSKY, V. A. 1993. An explicit inertial method for the simulation of the visco-elastic flow: an evaluation of elastic effects on diapiric flow in two- and three-layers models. *In*: STONE, D. B. & RUNCORN, S. K. (eds) *Flow and Creep in the Solar System: Observations, Modelling and Theory*. Kluwer Academic Publishers, 175–195.

RANALLI, G. 1987. *Rheology of the Earth: deformation and flow processes in geophysics and geodynamics*. Allen & Unwin Inc., Winchester, USA, 366pp.

SALTZER, S. D. & POLLARD, D. D. 1992. Distinct element modelling of structures formed in sedimentary overburden by extensional reactivation of basement normal faults. *Tectonics*, **11(1)**, 165–174.

SASSI, W., COLLETTA, B., BALÉ, P. & PAQUEREAU, T. 1993. Modelling of structural complexity in sedimentary basins: the role of pre-existing faults in thrust tectonics. *Tectonophysics*, **226**, 97–112.

SCHELLART, W. P. 2000. Shear test results for cohesion and friction coefficients for different granular materials: scaling implications for their usage in analogue modelling. *Tectonophysics*, **324**, 1–16.

SCHREURS, G. & BUITER, S. J. H. *ET AL.* 2006. Analogue benchmarks of shortening and extension experiments. *In*: BUITER, S. J. H. & SCHREURS, G. (eds) *Analogue and Numerical Modelling of Crustal-Scale Processes*. Geological Society, London, Special Publications, **253**, 1–28.

SMART, K. J. & COUZENS-SCHULTZ, B. A. 2001. Mechanics of blind thrusting: Comparison of numerical and physical modelling. *The Journal of Geology*, **109**, 771–779.

STORTI, F., SALVINI, F. & MCCLAY, K. 2000. Synchronous and velocity-partitioned thrusting and thrust polarity reversal in experimentally produced, doubly-vergent thrust wedges: Implications for natural orogens. *Tectonics*, **19(2)**, 378–396.

STRAYER, L. M., HUDLESTON, P. J. & LORIG, L. J. 2001. A numerical model of deformation and fluid-flow in an evolving thrust wedge. *Tectonophysics*, **335**, 121–145.

VANBRABANT, Y., JONGMANS, D., HASSANI, R. & BELLINO, D. 1999. An application of two-dimensional finite-element modelling for studying the deformation of the Variscan fold-and-thrust belt (Belgium). *Tectonophysics*, **309**, 141–159.

VAN KEKEN, P. E., KING, S. D., SCHMELING, H., CHRISTENSEN, U. R., NEUMEISTER, D. & DOIN, M.-P. 1997. A comparison of methods for the modelling of thermochemical convection. *Journal of Geophysical Research*, **102**, 22477–22495.

VERMEER, P. A. 1990. The orientation of shear bands in biaxial tests. *Geotechnique*, **40**, 223–236.

WEIJERMARS, R. 1986. Flow behaviour and physical chemistry of bouncing putties and related polymers in view of tectonic laboratory applications. *Tectonophysics*, **124**, 325–358.

WIJNS, C., BOSCHETTI, F. & MORESI, L. 2003. Inverse modelling in geology by interactive evolutionary computation. *Journal of Structural Geology*, **25**, 1615–1621.

ZERVOS, A., PAPANASTASIOU, P. & VARDOULAKIS, I. 2001. A finite element displacement formulation for gradient plasticity. *International Journal for Numerical Methods in Engineering*, **50**, 1369–1388.

ZHAO, W.-L., DAVIS, D. M., DAHLEN, F. A. & SUPPE, J. 1986. Origin of convex accretionary wedges: evidence from Barbados. *Journal of Geophysical Research*, **91**, 10246–10258.

# Interaction between normal faults and pre-existing thrust systems in analogue models

GIACOMO CORTI[1], SERENA LUCIA[2], MARCO BONINI[1], FEDERICO SANI[2] & FRANCESCO MAZZARINI[3]

[1]*CNR – Istituto di Geoscienze e Georisorse, Via La Pira, 4-50121 Firenze, Italy (e-mail: cortigi@geo.unifi.it)*

[2]*Dipartimento di Scienze della Terra, Università degli Studi di Firenze, Via La Pira, 4-50121 Firenze, Italy*

[3]*Istituto Nazionale di Geofisica e Vulcanologia, Via della Faggiola, 32-56100 Pisa, Italy*

**Abstract:** The influence of pre-existing thrusts on the development of later normal faults was investigated using scaled laboratory analogue models. Experiments consisted of a phase of shortening followed by extension at variable angles of obliquity ($\alpha$) to the shortening direction. Results suggest that the angle $\alpha$ has a major influence on the surface fault pattern and on the interaction between shortening-related structures and later extensional structures. Three different modes of interactions were identified depending upon the extension kinematics. (1) For orthogonal extension ($\alpha = 0°$), shortening-related fold and thrust structures strongly influence the development of normal faults: graben structures nucleate within anticlines and the normal faults reactivate thrusts at depth (*branching at depth mode of interaction*). (2) For highly oblique extension ($\alpha \geq 45°$), shortening-related structures exert no influence on normal faults as extension-related steeply-dipping faults (characterized by an oblique component of movement) displace early thrusts (*no interaction mode*). (3) For intermediate obliquity angles ($\alpha = 15°, 30°$), an *intermediate mode of interaction* characterizes the experiments, where the *no interaction* and *branching at depth* modes coexist in different regions of models. Modelling results can be used to infer regional extension directions as is shown for the Northern Appenines (Italy).

It has been shown that in many cases pre-existing thrust systems play an important role in controlling the architecture of superimposed normal faults. Mechanical theory suggests that the probability of reactivation of pre-existing thrust faults depends on their orientation with respect to the superimposed extensional stress field (e.g., Sibson 1985). The process was investigated in previous analogue models (Krantz 1991; Faccenna *et al.* 1995 and references therein), suggesting that the initial dip of thrust faults has a major control on the development of successive normal faults. Both studies started with a phase of shortening that resulted in progressively steeper thrust faults prior to extension. Model results suggested that three different types of interactions between pre-existing thrusts and successive normal faults may arise (e.g., Faccenna *et al.* 1995): (1) *No interaction* occurs in case of low-dip thrusts ($<32° \pm 1°$) and normal faults form independently, displacing pre-existing thrusts; (2) *branching at depth* of normal faults with thrusts is observed for intermediate dip angles ($32° \pm 1° - 41° \pm 1°$); (3) total reactivation occurs on thrusts dipping at angles higher than $41° \pm 1°$. These three basic mode of interaction between normal faults and thrust systems have been recognized and described in natural systems, such as the Central Apennines (Italy) and the North Sea region (Faccenna *et al.* 1995).

Active extensional structures interacting with early thrust systems have been also recognized in the Northern Apennines (e.g., Finetti *et al.* 2001). In this fold-and-thrust belt, the early compressive structures show a prominent curvature along strike and the successive normal faults display strong variations in terms of trend, arrangement and kinematics in different sectors of the chain (Fig. 1). In particular, where thrusts are orthogonal to the regional NE–SW extension direction (e.g., Mugello Basin; Fig. 1), normal faults are long and linear, display a mainly pure dip-slip kinematics and

*From*: BUITER, S. J. H. & SCHREURS, G. (eds) 2006. *Analogue and Numerical Modelling of Crustal-Scale Processes*. Geological Society, London, Special Publications, **253**, 65–78.
0305-8719/06/$15.00 

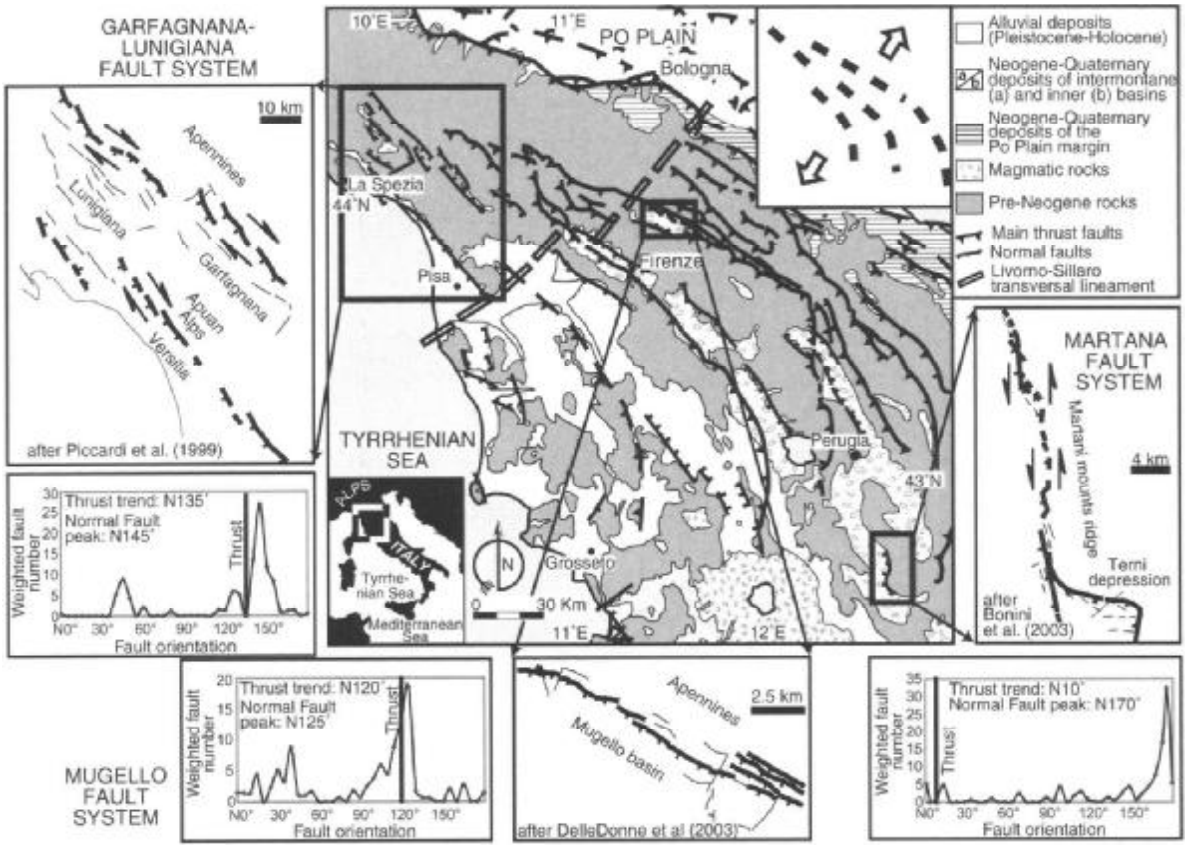


**Fig. 1.** Schematic structural map of the Northern Apennines (Italy), showing the location of the selected active normal fault systems. Inset shows the location of the investigated area. Graphs display fault orientation, with the weighted fault number plotted against the fault orientation (measured considering the north as the reference direction, i.e., 0°). The weighting factor for each fault is the ratio between the fault length and the minimum length of the whole data set, such that long faults have higher ratio (weight) than short ones. The frequency of the azimuth of a fault directly relates to this ratio; the longer the fault the higher its frequency. The thick black lines in the graphs indicate the thrust direction. The small inset on the map shows the orientation of the main thrust fronts (thick dashed lines) with respect to the roughly NE–SW extension direction. Active normal fault systems in the selected areas are from Piccardi *et al.* (1999), Delle Donne *et al.* (2003) and Bonini *et al.* (2003).

are subparallel to the early compressive structures (Delle Donne *et al.* 2003). Conversely, where thrusts are slightly oblique to the extension (Garfagnana-Lunigiana area; Fig. 1), normal faults are arranged en-echelon, are characterized by an oblique-slip kinematics and display a mean peak in distribution oriented at about 10° with respect to the earlier thrusts (Piccardi *et al.* 1999). In case of high obliquity (e.g., Martani Mounts-Terni Basin area; Fig. 1), normal faults are linear, are characterized by an important (locally dominant) strike-slip component of movement and form at an angle of 20° to the pre-existing structures (Bonini *et al.* 2003). These features suggest that the different orientation of thrusts with respect to the direction of extension may have exerted an important control on the pattern of successive extensional structures. This influence is investigated in this study by means of analogue models. We present a series of experiments on polyphase deformation, consisting of orthogonal shortening followed by extension at variable angles of obliquity.

## Analogue modelling

The experiments were performed at the Tectonic Modelling Laboratory of the CNR-IGG located at the Earth Science Department of Florence University (Italy) using the experimental apparatus shown in Figure 2. The models, with initial dimensions of 50 cm × 50 cm × 4 cm, were built over the metal base of the apparatus. Models consisted of a sand-pack overlying a ductile silicone layer. The models were confined on three sides by a mobile L-shaped wall and a fixed wall (Fig. 2). The right-hand frontal end remained unconfined (Fig. 2). Deformation was

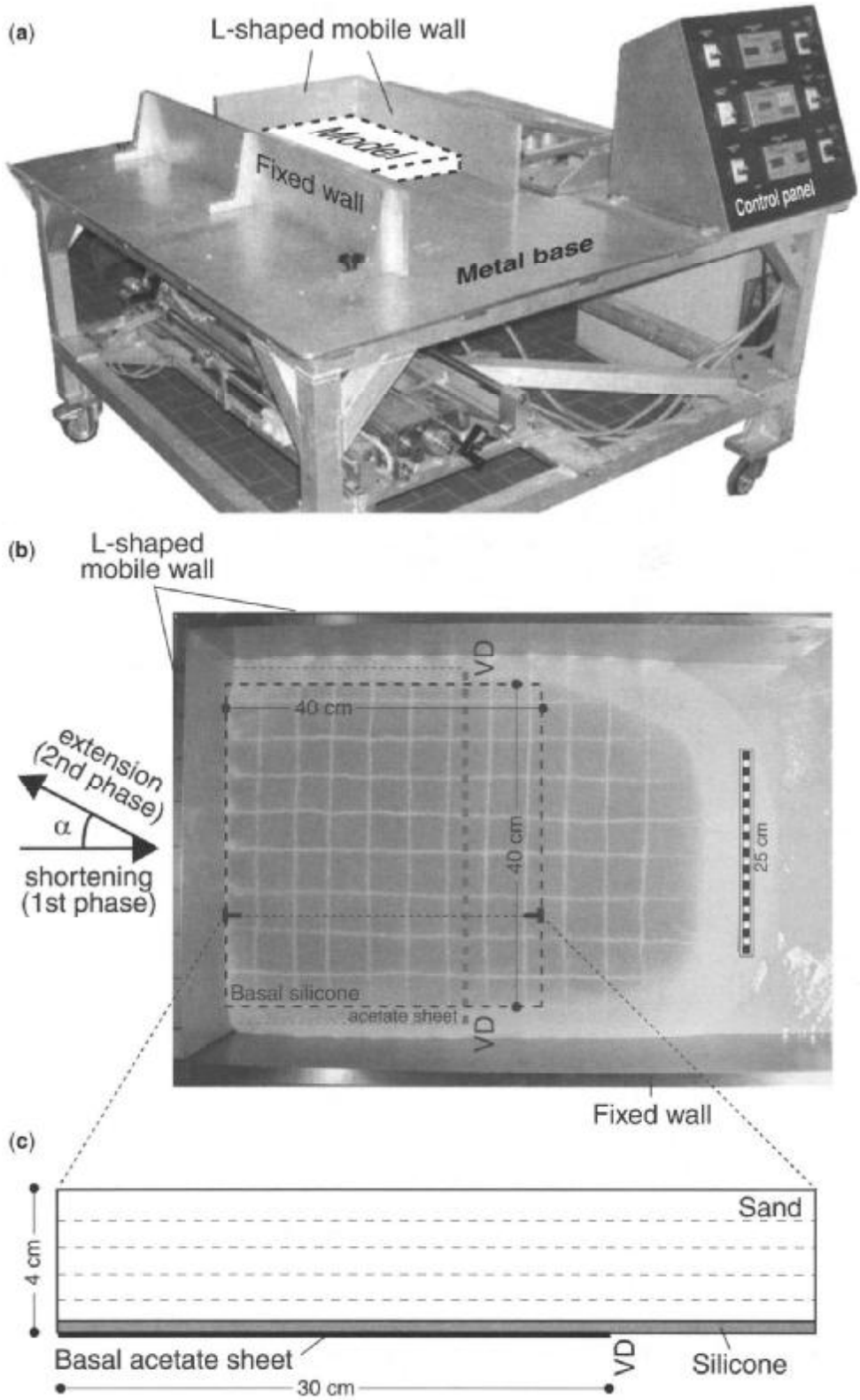


**Fig. 2.** Experimental set-up. (**a**) Photograph of the experimental apparatus. (**b**) Model top-view, with the two directions of deformation indicated. Angle of obliquity ($\alpha$) is the angle between the direction of shortening and extension. (**c**) Schematic model cross-section. See text for details.

achieved through displacement of the L-shaped wall, driven by two orthogonal stepper motors controlled by a central unit. In each experiment the shortening direction during the first phase of deformation was parallel to the long axis of the L-shaped wall (Fig. 2). Extension during the second phase was varied in different experiments in order to investigate the influence of the obliquity angle $\alpha$ (angle between extension and shortening direction; Fig. 2b) on the final structural pattern. Obliquity angles of 0°, 15°, 30°, 45° and 60° were investigated (Table 1). Deformation during the extensional phase was localized by a thin acetate sheet (*c.* 0.1 mm thick) at the base of the model and fixed to the L-shaped wall. The thin sheet created a central velocity discontinuity (VD), parallel to the short axis of the mobile wall (Fig. 2). In this set-up, displacement along the VD was transferred by viscous coupling at the base of the sand layer (see Tron & Brun 1991). In nature, the VD simulates a pre-existing discrete fabric at upper crustal levels (e.g., Faccenna *et al.* 1995; Morley 1999); in the case of the Northern Apennines, this may be a basement thrust reactivated during the extensional phase (e.g., Finetti *et al.* 2001).

Shortening occurred at a constant velocity of 40 mm/hr up to 25% bulk shortening, whereas extension took place at 6 mm/hr up to 10% bulk extension (Table 1). In order to improve visualization of surface fault patterns generated by extension, an evenly distributed thin layer (<1 mm) of coloured sand was added on top of the shortened models before the second phase of deformation.

### *Analogue materials*

In the models, a 3.5 cm-thick sand layer was used to simulate the brittle part of the sedimentary cover in nature. We used dry Fontainebleu sand, an almost pure quartz sand (>99% $SiO_2$) with a rounded grain shape, a grain size <250 μm and a density of *c.* 1550 Kg $m^{-3}$. Material properties were measured with a ring-shear tester and yielded a cohesion of *c.* 65 Pa and an angle of peak internal friction of *c.* 39°. In order to better visualize and analyse in detail the internal brittle deformation, different layers of coloured sand were introduced as horizontal passive markers within the sand-pack. A 40 cm × 40 cm × 0.5 layer of silicone (Mastic Silicone Rebodissant 29, produced by CRC, France) was placed at the base of the model in order to distribute deformation in the overlying sand-pack, as in the models by Faccenna *et al.* (1995). The silicone is characterized by a density of 1150 kg $m^{-3}$ and a viscosity of $1.6 \times 10^4$ Pa s (measured with a coni-cylindrical viscometer at a temperature of *c.* 23°C). The viscous layer simulates a décollement layer (e.g., an anhydritic evaporite horizon) underlying a brittle sedimentary cover, as occurring for example in the Northern Apennines stratigraphic column (Burano formation; e.g., Bonini & Sani 2002). This silicone layer also allowed to reduce the strong stress reorientation associated with a rigid VD (Morley 1999) and thus to avoid its excessive control on fault location (Faccenna *et al.* 1995).

### *Scaling*

Scaling of the models was obtained following the principles of dynamic similitude (e.g., Ramberg 1981). The models were intended to represent a length scale of $10^{-5}$, such that 1 cm in the model represents 1 km in nature. Dynamic-kinematic similarity was achieved through dimensionless ratios of forces (e.g., Ramberg 1981; Weijermars & Schmeling 1986). The scaling ratios of the different model and nature parameters are reported in Table 2. The viscosity ratio chosen is $1.6 \times 10^{-15}$, implying that silicone (with a viscosity of $1.6 \times 10^4$ Pa s) simulates a natural viscosity of $1 \times 10^{19}$ Pa s, which is a reasonable value for natural evaporitic layers in the Northern Apennines (e.g., Bonini & Sani 2002). The velocity scaling factor implies that deformation occurs at natural rates of

**Table 1.** *Parameters of model deformation*

| Model | Compression velocity (mm/hr) | Bulk compression (%) | Obliquity angle $\alpha$ | Extension velocity (mm/hr) | Bulk extension (%) |
|---|---|---|---|---|---|
| COM-EXT-01 | 40 | 23 | 0° | 10 | 10 |
| COM-EXT-02 | 40 | 25 | 15° | 13 | 10 |
| COM-EXT-03 | 40 | 25 | 30° | 13 | 10 |
| COM-EXT-04 | 40 | 25 | 45° | 13 | 10 |
| COM-EXT-05 | 40 | 25 | 60° | 13 | 10 |

**Table 2.** *Scaling parameters for brittle and ductile deformation*

| Parameter | Model | Nature | Model/Nature |
|---|---|---|---|
| Length, l (m) | 0.01 | 1000 | $1 \times 10^{-5}$ |
| Density brittle layer (kg $m^{-3}$) | 1500 | 2750 | 0.54 |
| Gravity, g (m $s^{-2}$) | 9.81 | 9.81 | 1 |
| Coefficient of friction, $\mu$ | 0.8 | *c.* 0.6–0.8 | *c.* 1 |
| Stress, $\sigma$ (Pa) | | | $5.4 \times 10^{-6}$ |
| Cohesion, c (Pa) | *c.* 50 | $1 \times 10^{7}$ | $5.4 \times 10^{-6}$ |
| Density ductile layer (kg $m^{-3}$) | 1100 | *c.* 2400 | *c.* 0.5 |
| Viscosity, $\nu$ (Pa s) | 16000 | $1 \times 10^{19}$ | $1.6 \times 10^{-15}$ |
| Strain rate 1st phase, $\varepsilon$ ($s^{-1}$) | $2.2 \times 10^{-3}$ | $6.5 \times 10^{-13}$ | $3.4 \times 10^{9}$ |
| Strain rate 2nd phase, $\varepsilon$ ($s^{-1}$) | $3.4 \times 10^{-4}$ | $10^{-13}$ | $3.4 \times 10^{9}$ |
| Time 1st phase, t (s) | $9 \times 10^{3}$ | $3.1 \times 10^{13}$* | $2.9 \times 10^{-10}$ |
| Time 2nd phase, t (s) | $2.3 \times 10^{4}$ | $8 \times 10^{13}$† | $2.9 \times 10^{-10}$ |
| Displacement velocity 1st phase, v (m $s^{-1}$) | $1.1 \times 10^{-5}$ | $3.2 \times 10^{-9}$‡ | $3.4 \times 10^{4}$ |
| Displacement velocity 2nd phase, v (m $s^{-1}$) | $1.7 \times 10^{-6}$ | $5 \times 10^{-11}$§ | $3.4 \times 10^{4}$ |

*corresponding to 1 Ma
†corresponding to 2.5 Ma
‡corresponding to 10 mm/a
§corresponding to 1.5 mm/a

*c.* 10 mm $a^{-1}$ and *c.* 1.5 mm $a^{-1}$ during the shortening and extensional phase, respectively.

## Modelling results

Orthogonal shortening during the first deformation phase resulted in regularly-spaced fore- and back-thrusts parallel to the mobile wall, defining well-developed anticlinal structures (Fig. 3). During shortening, the silicone flowed into the core of these anticlines, giving rise to a bulge in the ductile layer. For low amount of shortening, thrusts localized close to the moving wall, where the most prominent anticlines were observed. Subsequently, thrust structures propagated forward, affecting almost the whole model (Fig. 3). Boundary effects related to the movement of the L-shaped mobile wall and to the lateral confinement of the model resulted, in some cases (e.g., model COM-EXT 01; Fig. 3b), in a slight S-shaped surface strike of structures. However, these effects were restricted to a narrow area (generally <5 cm) and did not alter the geometry of shortening-related structures in the central part of the models.

The dip of thrusts was rather constant in the different experiments, being typically in the range of 32°–35°. Dip of thrusts lower than 25° were occasionally observed and were probably linked to the rotation of secondary structures during progressive displacement along major thrusts (e.g., Krantz 1991).

During the extensional phase, deformation was achieved through activation of the basal VD (Fig. 2). Extension was accommodated by a system of normal faults that nucleated at low bulk extension (*c.* 5–6%; Fig. 3c). Their orientation, arrangement and kinematics, as well as their relation with the early thrusts, was strongly controlled by the angle of obliquity, $\alpha$ (see below).

### *Orthogonal extension ($\alpha = 0°$)*

For orthogonal extension ($\alpha = 0°$; model COM-EXT 01), normal faults developed sub-parallel to the main thrusts and were distributed over a wide area in the left side of the model and mainly close to the moving wall (Fig. 4a). These faults were characterized by a pure dip-slip movement and mainly formed parallel to and within anticlines defined by fore- and back-thrusts. In particular, two major normal faults nucleated within the most prominent anticline, close to the moving wall. Model cross-sections show that normal faults formed above the bulge of the silicone layer, between conjugate couples of fore- and back-thrusts. The main extensional faults connected to and reactivated early back-thrusts at depth (Fig. 4a). The diagram of fault orientation (Fig. 4a) shows a main peak of the normal fault orientation coinciding with the early thrust

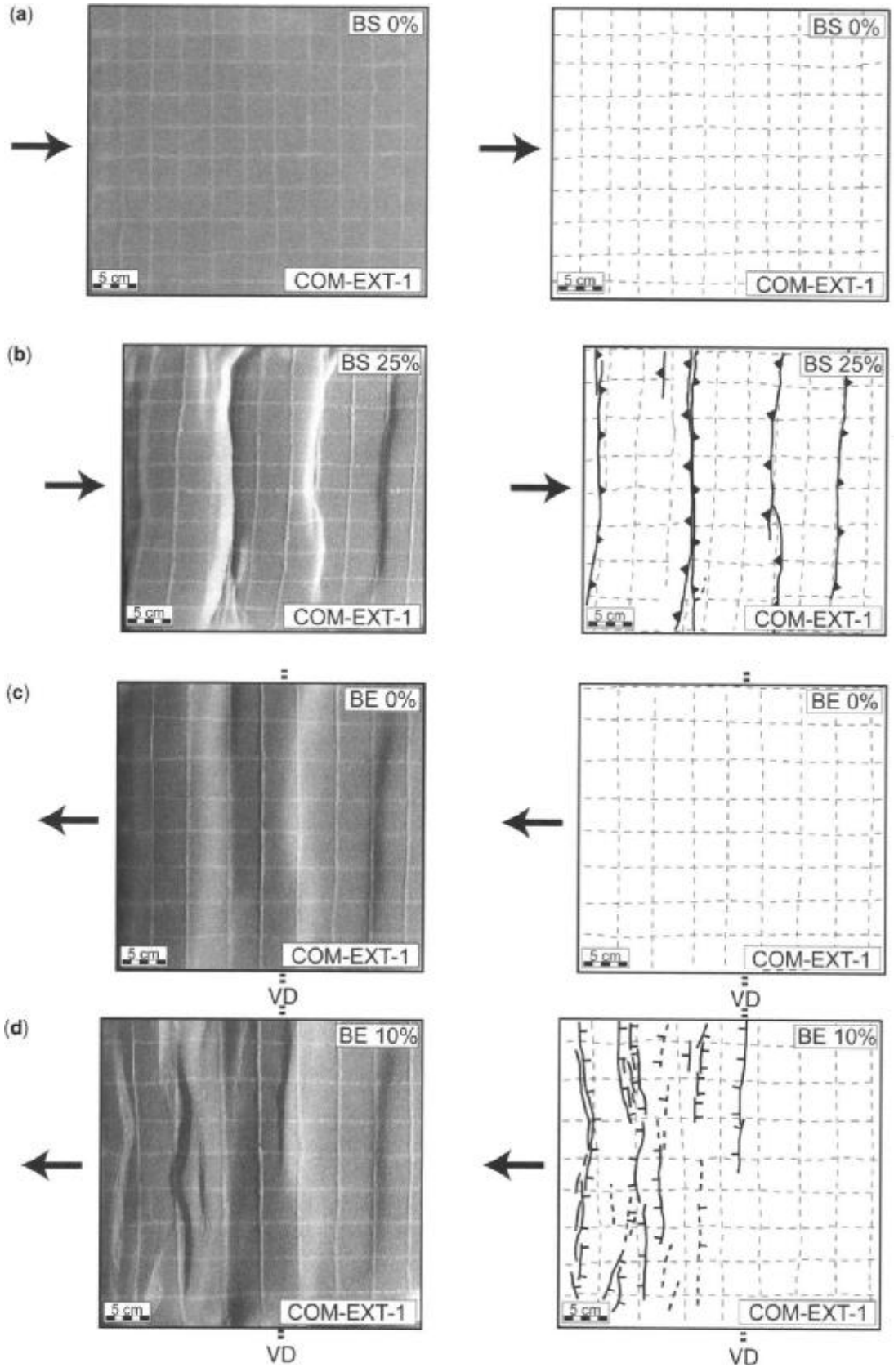


**Fig. 3.** Deformation of model COM-EXT-01 illustrated as top-view photos (left panels) and line drawings of structures (right panels). Only the portion of the model above the silicone layer is shown. The successive deformation stages are: (**a**) Onset of shortening, (**b**) end of shortening, (**c**) onset of extension, (**d**) end of extension. Note that in (c) the shortened model was covered by a thin layer of coloured sand to allow better observation of extension-related fault patterns.

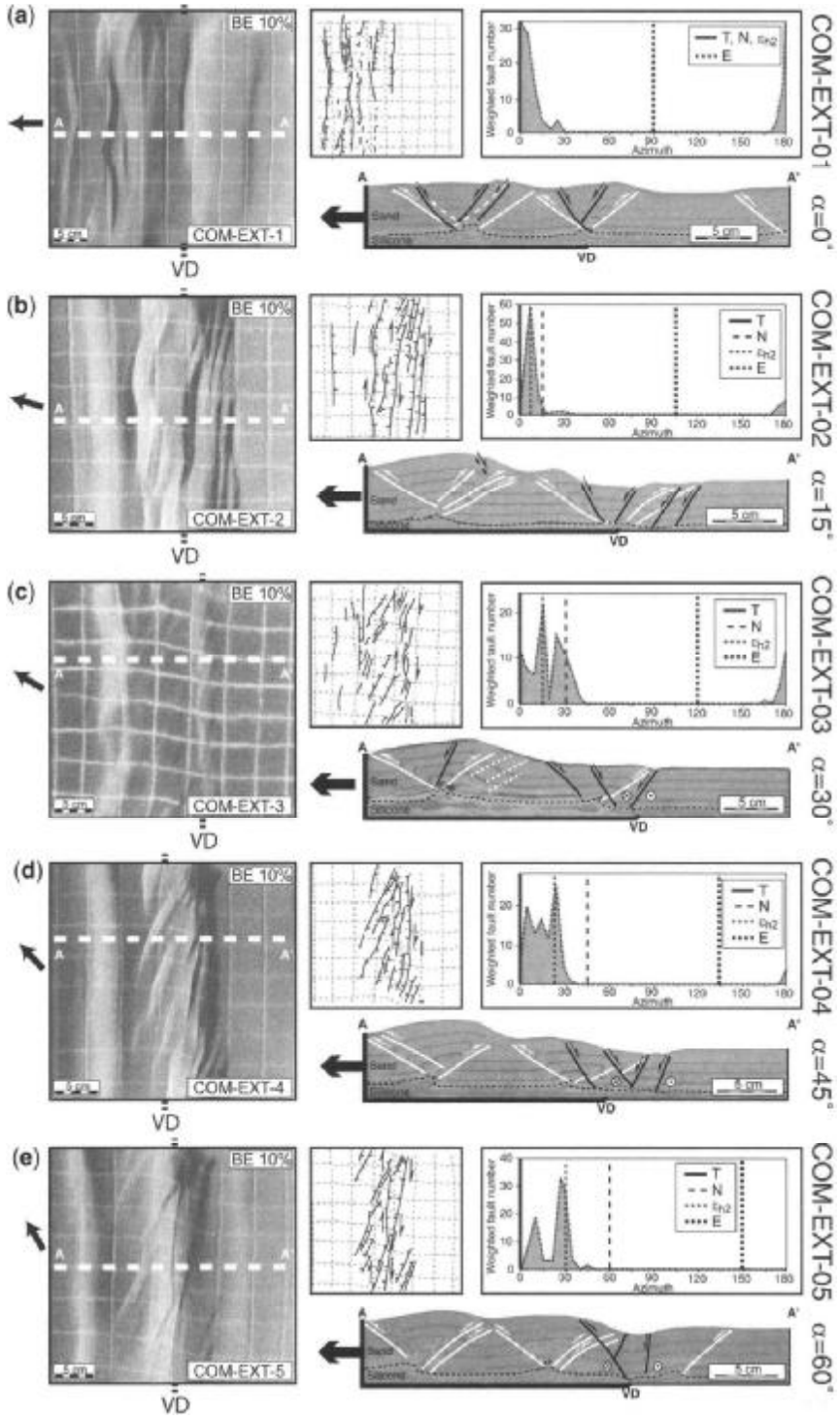


**Fig. 4.** Results of the experimental series illustrated as top-view photos (left), line drawings of surface deformation (top centre), graphs of fault orientation (top right) and longitudinal cross-sections (bottom centre-right). In the top-view photo, the light is from the right; the trace of the cross-section is indicated with the dashed white line on the model top-view. In the graphs of fault orientation, the azimuth of faults represents the angle (measured clockwise) that extensional structures form with respect to the short side of the mobile wall of the apparatus (i.e., with respect to the VD); the fault number is calculated as explained in Fig. 1. E is the extension direction; N is the perpendicular to the extension direction; T represents the thrust trend, which is parallel to the VD. $\varepsilon_{h2}$ indicates the direction of the secondary horizontal principal strain which is orthogonal to the direction of the maximum horizontal extensional strain, $\varepsilon_{hmax}$. In orthogonal extension, since no shear is involved in deformation, $\varepsilon_{hmax}$ and the extension direction coincide and consequently N and $\varepsilon_{h2}$ are parallel, their azimuths being 0°. During oblique rifting, extension and shear contribute to deformation. Analytical models (Withjack & Jamison 1986) have shown that the angle between $\varepsilon_{hmax}$ and the extension direction increases with increasing obliquity angles $\alpha$ and consequently the angle between $\varepsilon_{h2}$ and N increases from model COM-EXT 02 to model COM-EXT 05.

trend, indicating that most extensional structures formed parallel to shortening-related structures and perpendicular to the extension direction.

### *Low obliquity extension ($\alpha = 15°$, $30°$)*

Models of low obliquity angles (COM-EXT 02, $\alpha = 15°$; COM-EXT 03, $\alpha = 30°$; Figs. 4b, c) were characterized by more complex patterns of extensional structures, with the majority of normal faults oblique to the early structures and arranged en-echelon. Extensional faults sub-parallel to the thrusts were less common, but still observable in the portion of the model close to the mobile wall (Fig. 4b). Thrust-parallel faults were characterized by almost pure dip-slip kinematics, whereas oblique faults displayed a marked strike-slip component, as inferred from the displacement of the passive grid marker drawn on top of the models (Figs. 4b, c).

In cross-sections, normal faults either cross-cut or reactivate thrusts at depth (Figs. 4b, c). In model COM-EXT 02 ($\alpha = 15°$), the diagram of fault orientation shows a single main peak forming an angle of *c.* 7° to the thrust trend and *c.* 8° to the perpendicular to the direction of extension (Fig. 4b). This peak coincides with the direction of the secondary horizontal strain ($\varepsilon_{h2}$), which is orthogonal to the maximum horizontal extensional strain ($\varepsilon_{hmax}$). Note that, since oblique stretching combines both extension and horizontal shear, $\varepsilon_{hmax}$ does not coincide with the extension direction but forms an angle with this direction which is controlled by the obliquity angle $\alpha$ (Withjack & Jamison 1986); analogously, $\varepsilon_{h2}$ does not coincide with the normal extension direction (see Fig. 4).

Fault orientation of model COM-EXT 03 ($\alpha = 30°$) is characterized by three main peaks (Fig. 4c). The main peak corresponds to faults trending at *c.* 15° to the early thrusts and to the normal extension direction. Again, this main peak coincides with the orthogonal to the maximum horizontal extensional strain $\varepsilon_{h2}$. A secondary maximum relates to faults forming at an angle of *c.* 25° to the early thrusts, whereas a third peak correlates to thrust-parallel normal faults (Fig. 4c).

### *High obliquity extension ($\alpha = 45°$, $60°$)*

In models COM-EXT-4 ($\alpha = 45°$) and COM-EXT-5 ($\alpha = 60°$) the highly oblique extension was accommodated by the development of oblique faults with a prominent (locally dominant) strike-slip component (Fig. 4d, e). Fault nucleation near the central VD and the area affected by deformation was narrower with respect to previous low-obliquity and orthogonal extension models (see section below). Analysis of model cross-sections reveals that extensional faults displaced the early thrusts and that no reactivation occurred (Fig. 4d, e).

Graphs of fault orientation are characterized by three and two main peaks for model COM-EXT-4 ($\alpha = 45°$) and model COM-EXT-5 ($\alpha = 60°$), respectively. In model COM-EXT-4, the highest peak corresponds to faults developing at angles of *c.* 25° to the early thrust faults and at *c.* 20° to the normal extension direction (Fig. 4e). In model COM-EXT-5, oblique-slip faults develop at *c.* 30° to the pre-existing thrusts and to the normal extension direction (Fig. 4e). Both peaks roughly coincide with the direction orthogonal to the maximum horizontal extensional strain ($\varepsilon_{h2}$).

### *Parameters of deformation as a function of the obliquity angle $\alpha$*

Figure 5 summarizes the main parameters of model deformation in relation to the varying obliquity angle $\alpha$. Comparison of the different models suggests that an increase in the angle of obliquity leads to a decrease in width of the deformed zone (Fig. 5a) due to an increase in the dip of the main faults (Fig. 5b) that have a more prominent strike-slip component for high obliquity angles ($\alpha = 45°$, $60°$).

Fault density shows an almost linear decrease with increasing $\alpha$ (Fig. 5c), suggesting that for high-obliquity extension, deformation is accommodated by a few well-developed oblique-slip faults. This is exemplified by model COM-EXT-5, where deformation is mostly accommodated by three main oblique-slip faults extending for almost the entire width of the model (Fig. 4e).

Finally, fault length is characterized by high values for models with $\alpha = 0°$ and 15°; values then decrease, reaching a minimum for models with $\alpha = 30°$ and 45°; then a marked increase is observed for $\alpha = 60°$ (Fig. 5d). This suggests that for orthogonal or low obliquity ($\alpha = 15°$) extension, deformation is taken up by long faults, probably controlled by the pre-existing thrust faults. An increase to intermediate $\alpha$ values leads to patterns of faulting characterized by short, oblique faults. A further increase in $\alpha$ leads to the development of long, oblique slip faults with an important strike-slip component.

## Discussion: modes of interaction between pre-existing thrusts and successive normal faults

Our experiments investigated the development of extensional structures following a previous

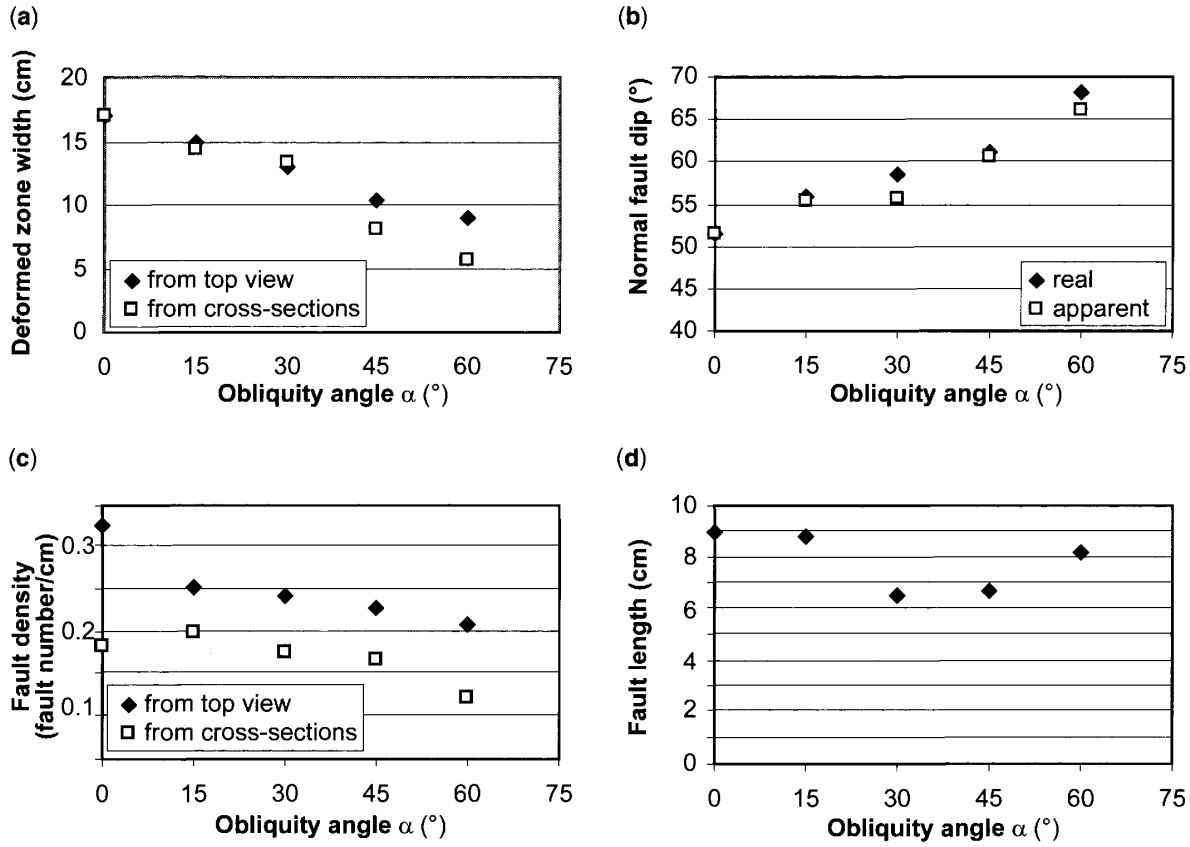


**Fig. 5.** Quantified parameters as a function of the angle of obliquity ($\alpha$). All parameters were calculated along three 25 cm-long regularly-spaced reference lines on the model surface and three cross-sections in the central part of the models. (**a**) Deformed zone width. (**b**) Mean dip of normal faults; note that since extensional structures may be oblique with respect to the model cross-section, both real and apparent dip have been reported. (**c**) Density of normal faults (calculated as fault number divided by the length of the reference line or cross-section). (**d**) Tip-to-tip fault length. The discrepancy in the measurements from model top-views or cross-sections is related to the presence of extensional structures characterized by low vertical displacement, which are difficult to recognize in model cross-sections.

contractional phase of deformation, and simulating the reactivation of a deep-seated pre-existing discrete fabric (e.g., a basement thrust simulated by the velocity discontinuity, VD) that is located below an evaporite layer at the base of a brittle sedimentary cover. Extensional reactivation of the discrete anisotropy is transferred through the viscous layer to the overlying brittle sandpack, which deforms by distributed faulting. The kinematics of the pre-existing fabric and in particular the obliquity of extension, which controls the ratio between the extensional and the strike-slip components of motion (e.g., Withjack & Jamison 1986), determine differences in the architecture of extensional structures, and their relations with previous thrusts. Three different main modes of interactions between pre-existing thrusts and later extensional faults are identified (Fig. 6).

(1) For $\alpha = 0°$, early shortening-related structures strongly influence the development of successive normal faults, giving rise to graben structures that nucleate within and dismember previous thrust anticlines (Fig. 6a). Normal faults are parallel to the early thrusts, are long and linear and display a pure dip-slip component. In this case, the master fault of the grabens joins the thrusts at depth, locally inverting the movement on these faults and thus reactivating their deepest portions. The location and geometry of the main normal faults is primarily influenced by both the presence of the silicone bulge between fore- and back-thrusts and the local stress-field influence exerted by the topography related to the presence of the anticlines (e.g., Gartrell 2001). However, reactivation of the lower portion of early thrusts by normal faults suggests that the drop in shear strength due to sand dilatancy along thrusts contributes (although it may not play a determining role) to the localization of subsequent extensional faults, as suggested by the experimental results

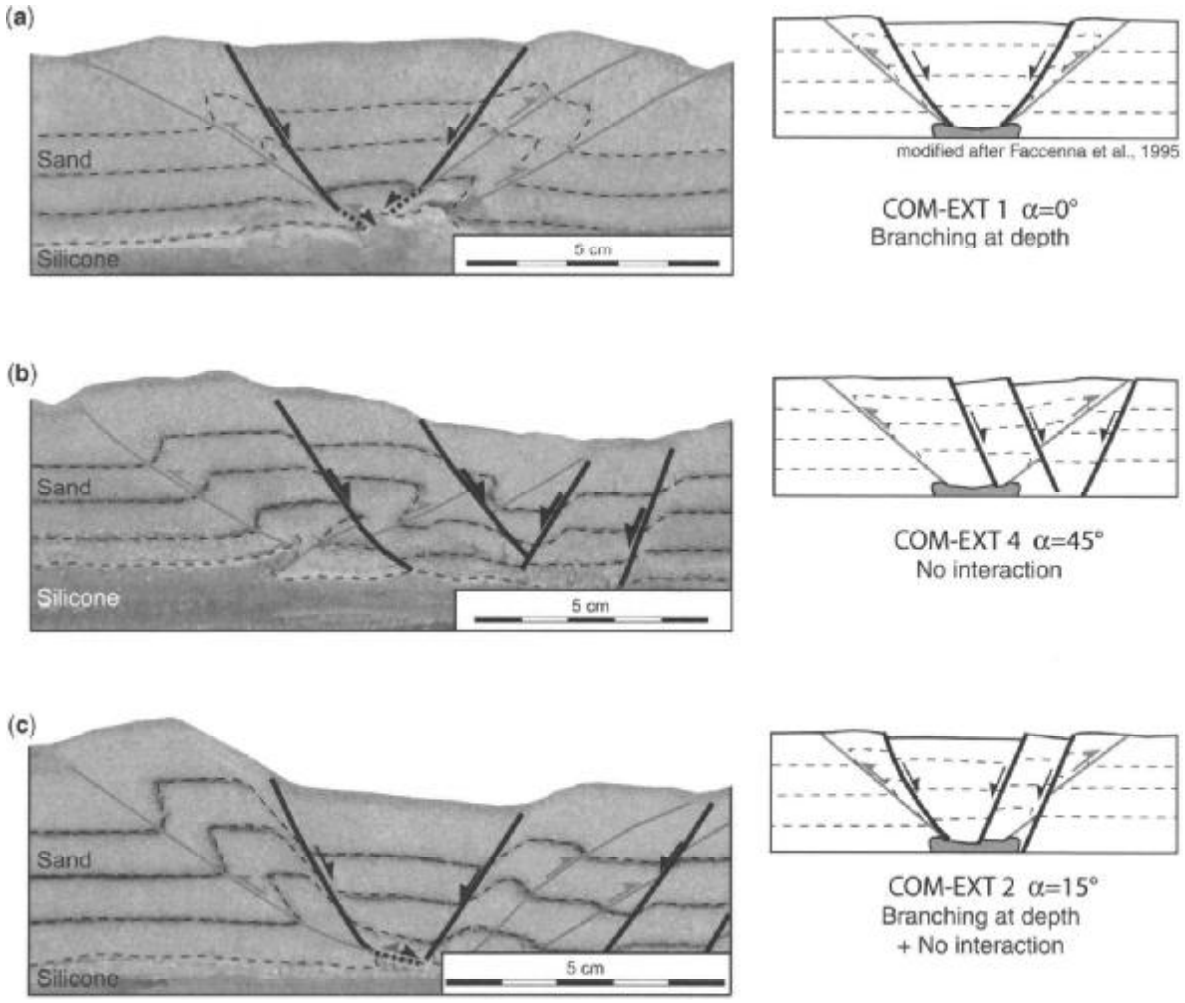


**Fig. 6.** Modes of interaction between normal faults and pre-existing thrust systems in the different experiments. A schematic representation of fault interaction is also shown. See text for details.

of Faccenna *et al.* (1995). The normal fault geometry is similar to the linked faults of Krantz (1991) and the mode of interaction between thrusts and later faults is equivalent to the *branching at depth mode* obtained by Faccenna *et al.* (1995) for similar initial thrust dips (32°–35°).

(2) For high obliquity angles ($\alpha \geq 45°$), no influence on later extension-related faults is exerted by compressive structures (Fig. 6b), in a similar fashion to the *no interaction mode* of Faccenna *et al.* (1995). Deformation is localized along a few long and steeply-dipping, oblique-slip normal faults that displace thrust faults and nucleate in a narrow zone above the VD. The oblique-slip faults have a large strike-slip component and show no relation with previous anticlinal structures (unlinked faults of Krantz 1991). Although the *no interaction mode* was suggested by Faccenna *et al.* (1995) to characterize models with initial thrust dips $<32° \pm 1°$, in the current models this behaviour is also obtained for slightly higher initial thrust dips in the range of 32°–35°.

(3) For intermediate obliquity angles ($\alpha = 15°$, 30°), an *intermediate mode of interaction* characterizes the experiments. The two beforementioned behaviours (*no interaction + branching at depth*) coexist in different regions of the model (Fig. 6c). Deformation is taken up by short, oblique-slip normal faults, often arranged en-echelon and characterized by an increasing component of strike-slip motion. The majority of faults are oblique to both the thrust (and VD) trend and orthogonal to the direction of extension. Most faults are indeed perpendicular to the maximum extensional horizontal strain (Withjack & Jamison 1986). Increasing the angle of obliquity in the models leads to: (i) the development of faults that are increasingly oblique with respect to the early thrusts, (ii) an almost linear decrease in the width of the

deformed zone, (iii) an increase in fault dip, and (iv) a decrease in fault density. Similar fault patterns were observed in previous sand-box models of oblique (Tron & Brun 1991; Corti *et al.* 2001) and polyphase rifting (Bonini *et al.* 1997; Keep & McClay 1997; Corti *et al.* 2003).

Our model results suggest that the mode of interaction between pre-existing thrusts and newly-formed normal faults is not only influenced by the initial dip of thrusts but also by the kinematics of the extensional phase, which in turn controls fault dip, length and kinematics of later faults. Reactivation of faults along their entire length (as seen in cross-section) was never observed in the models. This supports theoretical predictions from Mohr envelopes for reactivation of pre-existing faults in sand as well as observations by Krantz (1991) and Faccenna *et al.* (1995) that an initial thrust dip higher than *c.* 40° is required in order to have complete fault reactivation.

## Relevance of model results for evaluating the regional extension direction in nature: the case of the Northern Apennines

Analogue modelling results have been used in the past to infer the regional extension direction in natural examples (e.g., Withjack & Jamison 1986; Tron & Brun 1991; Dauteuil & Brun 1993; Harris *et al.* 1994; Bonini *et al.* 1997; Clifton *et al.* 2000) mainly on the basis of a statistical analysis of the surface fault pattern. In order to determine the regional extension direction, fault orientations for different angles of obliquity in the models are compared to faults in nature using the thrust trend as a reference direction. The extension direction in nature can be obtained by best fitting the main peaks in the fault orientation in nature with the statistical data from the models.

In the arc-shaped Northern Appenines fold-and-thrust belt extensional faults are superimposed on early thrusts. In different sectors of this chain, the younger normal faults display strong variations in terms of strike, arrangement and kinematics (Figs 1 and 7). These different fault patterns are compared to our analogue models in order to obtain a coherent regional extension direction.

The best fit of graphs of fault orientation suggests that the fault arrangement in the Garfagnana-Lunigiana area (in the northwestern part of the chain) is comparable (though more complex) to low obliquity models (specifically, $\alpha = 15°$). Given the local orientation of the pre-existing thrusts in the area (*c.* N135°), the correspondence in the main peak in fault orientation suggests a N60°-directed local extension (Fig. 7). Eastwards, the main peak in the graph of faults in the Mugello basin (in the central part of the chain; Figs 1 and 7) corresponds to the one characterizing the orthogonal extension model ($\alpha = 0°$), indicating a *c.* N30° direction of extension. Finally, the orientation of faults in the Martani Mounts-Terni Basin area is in good agreement with a high obliquity model ($\alpha = 60°$), indicating a *c.* N30° direction of extension.

Overall, extrapolation of model results to a regional kinematic scenario suggests a compatibility with a roughly NNE to NE-directed extension, consistent with analysis of Quaternary and active deformation in the area (e.g., Piccardi *et al.* 1997, 1999; Bonini *et al.* 2003; Jiménez-Munt *et al.* 2003; Mariucci & Müller 2003). Variations in the extrapolated regional direction of extension in the Garfagnana-Lunigiana area may be related to the influence of rheological anisotropies (as the Apuan Alps metamorphic core complex) that may have locally caused a stress re-orientation, thus contributing to modifications of fault orientations. Both in models and nature normal faults increase their obliquity with early thrusts and their strike-slip component increases with higher angles of obliquity (i.e., passing from the Mugello basin, $\alpha = 0°$, to the Garfagnana-Lunigiana area, $\alpha = 15°$ and to the Martani Mounts-Terni Basin area, $\alpha = 60°$). Fault-slip data collected along the major fault systems are in good agreement with the proposed kinematic scenario, indicating an almost pure dip-slip kinematics in Mugello (Delle Donne *et al.* 2003), a minor dextral component of oblique-slip in Garfagnana-Lunigiana (Bernini & Lasagna 1988; Bernini *et al.* 1991; Piccardi *et al.* 1999) and an important sinistral component of displacement along the Martana Fault System (Bonini *et al.* 2003; Fig. 1).

## Conclusions

Laboratory analogue models were used to investigate the influence of pre-existing thrust systems on the development of later normal faults. Experiments consisted of a first phase of shortening, followed by extension at variable angles of obliquity ($\alpha$). Model results suggest that the trend, arrangement and kinematics of faults are strongly influenced by the obliquity of extension, which also has a major effect on the interaction between normal faults and early thrusts. Three main modes of interactions were

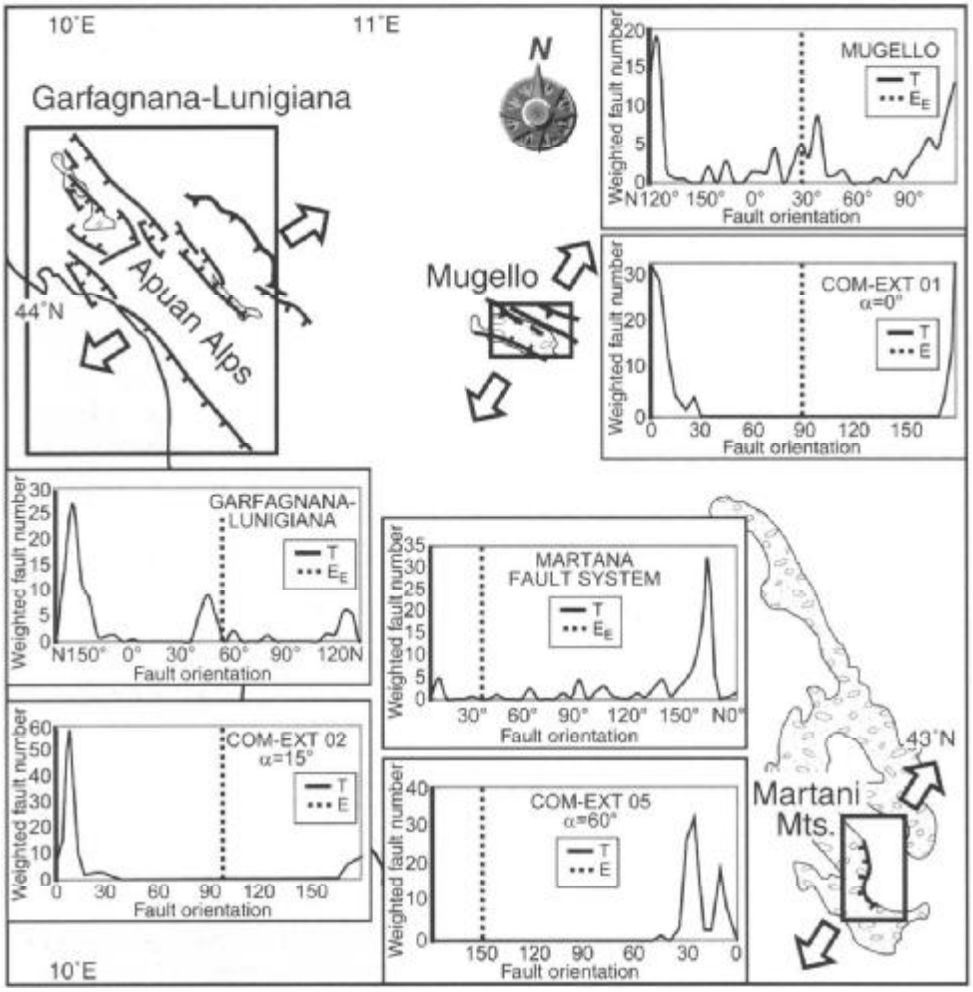


**Fig. 7.** Extrapolation of model results to nature. White arrows in the selected domains of the Northern Appennines indicate the extension direction as obtained by comparison between the graphs of fault orientation (insets). For this comparison, the reference direction is represented by the direction of early thrusts. Histograms of fault orientation in nature have been shifted in order to make the thrust trend coincide with the one in the model. For the Martana Fault System, the experimental histogram has been reflected horizontally in order to fit the dextral model kinematics with the sinistral deformation inferred in nature. Extension direction in nature was then obtained by best fitting the main peaks in the fault orientation with those of the different experiments. Note that minor peaks at N40°–45° in nature, not present in the graphs of models, correspond to *c.* NE–SW transverse structures reactivating pre-existing discontinuities (e.g., Boccaletti *et al.* 1977; Bemporad *et al.* 1986). E: extension direction; $E_E$: extension direction extrapolated from models to nature; T: thrust trend. Lithological symbols as in Fig. 1.

identified, depending on the kinematics of extension.

(1) For orthogonal extension ($\alpha = 0°$) normal faults nucleate within previous thrust anticlines reactivating thrust faults at depth (*branching at depth mode of interaction*).
(2) For high obliquity extension ($\alpha \geq 45°$), no relations between extension-related faults and early compressive structures is observed and extension-related steeply-dipping normal faults (characterized by an important and locally dominant strike-slip component) displace thrust faults (*no interaction mode*).
(3) For intermediate obliquity angles ($\alpha = 15°$, 30°), an *intermediate mode of interaction* characterizes the experiments, as the two behaviours described above (*no interaction + branching at depth*) coexists in different regions of the models.

A comparison of the fault orientations in our analogue models with natural examples of thrust belts that have undergone later extension may yield insights on the regional extension direction, as shown for the Northern Apennines.

We thank reviewers A. Benedicto and L. Harris and editor G. Schreurs for the detailed, constructive comments which helped to improve the manuscript. C. Del Ventisette and D. Montanari are warmly thanked for their support during the experimental work. D. Delle Donne is thanked for providing us data concerning the Mugello basin. We also express our gratitude to M. H. Dickson for improving the English text. Dr. Baldi of the Colorobbia Italia S.p.A. is thanked for providing us the quartz sand used in the experiments.

## References

BEMPORAD, S., CONEDERA, C., DAINELLI, P., ERCOLI, A. & FACIBENI, P. 1986. Landsat imagery: a valuable tool for regional and structural geology. *Memorie della Società Geologica Italiana*, **31**, 287–298.

BERNINI, M. & LASAGNA, S. 1988. Rilevamento geologico e analisi strutturale del Bacino dell'Alta Val di Magra tra M. Orsaro e Pontremoli (Appennino Settentrionale). *Atti della Società Toscana di Scienze Naturali, Serie A*, **95**, 139–183.

BERNINI, M., PAPANI, G., DALL'ASTA, M., LASAGNA, S. & HEIDA, P. 1991. The Upper Magra Valley extensional basin: a cross section between Orsaro Mt. and Zeri (Massa province). *Bollettino della Società Geologica Italiana*, **110**, 451–458.

BOCCALETTI, M., COLI, M. & NAPOLEONE, G. 1977. Nuovi allineamenti strutturali da immagini landsat e rapporti con l'attività sismica negli Appennini. *Bollettino della Società Geologica Italiana*, **96**, 679–694.

BONINI, M. & SANI, F. 2002. Extension and compression in the Northern Appennines (Italy) hinterland: evidence from the Late Miocene-Pliocene Siena-Radicofani Basin and relations with basement structures. *Tectonics*, **21(3)**, 10.1029/2001TC900024.

BONINI, M., SOURIOT, T., BOCCALETTI, M. & BRUN, J. P. 1997. Successive orthogonal and oblique extension episodes in a rift zone: laboratory experiments with application to the Ethiopian Rift. *Tectonics*, **16**, 347–362.

BONINI, M., TANINI, C., MORATTI, G., PICCARDI, L. & SANI, F. 2003. Geological and archaeological evidence of active faulting on the Martana Fault (Umbria-Marche Apennines, Italy) and its geodynamic implications. *Journal of Quaternary Science*, **18**, 695–708.

CLIFTON, A. E., SCHLISCHE, R. W., WITHJACK, M. O. & ACKERMANN, R. V. 2000. Influence of rift obliquity on fault-population systematics: results of experimental clay models. *Journal of Structural Geology*, **22**, 1491–1509.

CORTI, G., BONINI, M., INNOCENTI, F., MANETTI, P. & MULUGETA, G. 2001. Centrifuge models simulating magma emplacement during oblique rifting. *Journal of Geodynamics*, **31**, 557–576.

CORTI, G., BONINI, M., CONTICELLI, S., INNOCENTI, F., MANETTI, P. & SOKOUTIS, D. 2003. Analogue modelling of continental extension: a review focused on the relations between the patterns of deformation and the presence of magma. *Earth-Science Reviews*, **63**, 169–247.

DAUTEUIL, O. & BRUN, J. P. 1993. Oblique rifting in a low spreading ridge. *Nature*, **361**, 145–148.

DELLE DONNE, D., PICCARDI, L., SANI, F. & VANNUCCI, G. 2003. Active tectonics of the Mugello Basin (Northern Apennines, Italy). EGS-AGU-EUG Joint Assembly, Nice, France, April 2003, *Geophysical Research Abstracts*, **5**, 06229.

FACCENNA, C., NALPAS, T., BRUN, J. P., DAVY, P. & BOSI, V. 1995. The influence of pre-existing faults on normal fault geometry in nature and in experiments. *Journal of Structural Geology*, **17**, 1139–1149.

FINETTI, I. R., BOCCALETTI, M., BONINI, M., DEL BEN, A., GELETTI, R., PIPAN, M. & SANI, F. 2001. Crustal section based on CROP seismic data across the North Tyrrhenian-Northern Apennines-Adriatic Sea. *Tectonophysics*, **343**, 135–163.

GARTRELL, A. P. 2001.Crustal rheology and its effect on rift basin styles. *In*: KOYI, H. A. & MANCKTELOW, N. S. (eds) *Tectonic Modeling: A Volume in Honor of Hans Ramberg*. Geological Society of America, Memoirs, **193**, 221–233.

HARRIS, L. B., HIGGINS, R., DENTITH, M. C. & MIDDLETON, M. 1994. Analogue modelling of transtensional faulting applied to the structure of the Perth Basin, Western Australia. *In*: PURCELL, P. G. & PURCELL R. R. (eds) *The sedimentary basins of Western Australia*. Proceedings of the Petroleum Exploration Society of Australia Symposium, Perth, 801–810.

JIMÉNEZ-MUNT, I., SABADINI, R. & GARDI, A. 2003. Active deformation in the Mediterranean from Gibraltar to Anatolia inferred from numerical modeling and geodetic and seismological data. *Journal of Geophysical Research*, **108 (B1)**, 2006, DOI 10.1029/2001JB001544.

KEEP, M. & MCKLAY, K. 1997. Analogue modelling of multiphase rift systems. *Tectonophysics*, **273**, 239–270.

KRANTZ, R. W. 1991. Normal fault geometry and fault reactivation in tectonic inversion experiments. *In*: YIELDING, A. M. & FREEMAN, B. (eds) *The Geometry of Normal Faults*. Geological Society, London, Special Publication, **56**, 219–229.

MARIUCCI, M. T. & MÜLLER, B. 2003. The tectonic regime in Italy inferred from borehole breakout data. *Tectonophysics*, **361**, 21–35.

MORLEY, C. K. 1999. How successful are analogue models in addressing the influence of pre-existing fabrics on rift structures? *Journal of Structural Geology*, **21**, 1267–1274.

PICCARDI, L., CORTI, G. & BOCCALETTI, M. 1999. Oblique extension in the Tyrrhenian side of the Northern Apennines (Italy). Proceedings of the XXIV European Geophysical Society General Assembly, The Hague, 19–23 April 1999, *Geophysical Research Abstracts*, **1**, 82.

PICCARDI, L., SANI, F., BONINI, M., BOCCALETTI, M., MORATTI, G. & GUALTIEROTTI, A. 1997. Deformazioni quaternarie nell'Appennino centro-settentrionale: evidenze ed implicazioni. *Il Quaternario*, **10**, 273–280.

RAMBERG, H. 1981. *Gravity, deformation and the Earth's crust*. Academic Press, London.

SIBSON, R. H. 1985. A note on fault reactivation. *Journal of Structural Geology*, **7**, 751–754.

TRON, V. & BRUN, J.-P. 1991. Experiments on oblique rifting in brittle-ductile systems. *Tectonophysics*, **188**, 71–84.

WEIJERMARS, R. & SCHMELING, H. 1986. Scaling of Newtonian and non-Newtonian fluid dynamics without inertia for quantitative modelling of rock flow due to gravity (including the concept of rheological similarity). *Physics of the Earth and Planetaty Interiors*, **43**, 316–330.

WITHJACK, M. O. & JAMISON, W. R. 1986. Deformation produced by oblique rifting. *Tectonophysics*, **126**, 99–124.

# Surface topography and internal strain variation in wide hot orogens from three-dimensional analogue and two-dimensional numerical vice models

ALEXANDER R. CRUDEN, MOHAMMAD H. B. NASSERI & RUSSELL PYSKLYWEC
*Department of Geology, University of Toronto, 22 Russell Street, Toronto, Ontario M5S 3B1, Canada*

**Abstract:** The post-accretionary deformation of wide, hot orogens is characterized by pure-shear or transpressional shortening of relatively weak lithosphere (the orogen) between converging stronger blocks (the vice). We report on a series of analogue vice models and compare the resulting three-dimensional strain fields and surface topographies to equivalent two-dimensional numerical experiments. In the analogue models a rheologically stratified (frictional/viscous) weak orogenic lithosphere overlying a viscous asthenosphere is squeezed between converging strong lithospheric blocks. Ductile lower crust and mantle in the weak lithosphere is free to flow laterally, parallel to the orogen. The Argand number describes the model dynamics and strongly controls both the orogenic relief and the degree of lower crustal orogen parallel stretching in the analogue models. Cross sections of numerical and analogue experiments display consistent geometries in which upper crustal deformation is characterized by upright folding compared to apparently decoupled horizontal strains in the lower crust. The relative buoyancy and degree of orogen parallel flow in the lower crust of the analogue models has a dramatic influence on three-dimensional strain fields and the kinematics of upper crustal curvilinear shear zones. The analogue and numerical results demonstrate the importance of three-dimensional effects in determining the structure of natural orogens and compare favourably to field and geophysical observations of large hot orogens in the geological record.

Three-dimensional strain partitioning has long been recognized as a key phenomenon in the kinematic and dynamic evolution of convergent orogens (e.g., Oldow *et al.* 1989; Vauchez & Nicolas 1991; Royden 1996). A classic example is the partitioning between orogen-parallel strike-slip fault systems and ductile thickening in the Alpine-Himalayan chain (e.g., Tapponnier *et al.* 1982; Dewey *et al.* 1986; Davy & Cobbold 1988). Recent studies have documented decoupling between upper crustal and mid- to lower-crustal deformation in convergent magmatic arc, collisional orogen and post-orogenic collapse settings (e.g., Axen *et al.* 1998; Garde *et al.* 2002; Klepeis *et al.* 2004). A common expression of such decoupling is the observation of vertical orogen sub-parallel transpression zones, upright folding and cleavage development in the upper crust versus subhorizontal fabric development and lateral flow in the mid to lower crust, as documented by both field and seismic reflection studies in Archean to Mesozoic orogens (e.g., Collins & Vernon 1991; Gapais *et al.* 1992; Jackson & Cruden 1995; Hajnal *et al.* 1996; Moser *et al.* 1996; Royden *et al.* 1997; Axen *et al.* 1998).

The post-accretionary deformation of such wide, hot orogens (e.g., Superior, Grenville, Variscan, Cordilleran, Tibetan) has been attributed to pure-shear or transpressional shortening of relatively weak lithosphere (the orogen) between converging stronger blocks (the vice). In such 'vice models', the orogenic crust is weakened due to the properties of inherited accreted material or thermal/magmatic softening, and deformation is effectively decoupled from mantle dynamics (Ross *et al.* 1995; Ellis *et al.* 1998; Burg *et al.* 2002). The structural and topographic development of the resulting orogen depends on the vertical and lateral rheological structure of the lithosphere, the initial and final widths of the weak zone, surface erosion, and three-dimensional effects (e.g., lateral extrusion; Dewey *et al.* 1986; Ratschbacher *et al.* 1991; Mancktelow & Pavlis 1994; Royden 1996; Seyferth & Henk 2004).

The purpose of this contribution is to investigate the roles of orogen parallel flow and rheological stratification on the vertical and lateral

*From*: BUITER, S. J. H. & SCHREURS, G. (eds) 2006. *Analogue and Numerical Modelling of Crustal-Scale Processes.* Geological Society, London, Special Publications, **253**, 79–104.
0305-8719/06/$15.00 

development of structures in convergent settings. We describe a series of three-dimensional (3D) analogue model experiments and corresponding two-dimensional (2D) numerical models that investigate the structural and topographic response of a model orogenic lithosphere as it is compressed between converging blocks of significantly stronger lithosphere. The analogue experiments inherently permit flow of orogenic material orthogonal to the compression direction. Comparison of these experiments with 2D numerical models, together with detailed structural and topographic data from the model surface and serial sectioning allows us to evaluate the significance of such orogen parallel flow. We will highlight the influence of relative variations in the strength and density of the ductile crust, which dictate the degree of coupling within the crust and body forces, respectively.

## Experimental design

The basic design of both our analogue and numerical experiments follows the set up of the original vice models of Ellis *et al.* (1998) and is also similar to recent 3D numerical models of Seyferth and Henk (2004). Due to restrictions imposed by laboratory modelling techniques, our experiments are isothermal, which contrasts with those of Ellis *et al.* (1998) and Seyferth and Henk (2004). However, our focus is to explore the first-order effects of syn-convergent, orogen parallel flow rather than time-dependent phenomena due to variations in thermal and rheological structure. Hence the isothermal nature of our experiments is justified, and the results presented below are complementary to published 2D and 3D numerical thermomechanical models.

The basic configuration of our analogue and numerical experiments is summarized in Figure 1. In the 3D analogue models, a relatively weak model orogenic lithosphere composed of brittle material (upper crust) overlying viscous layers representing ductile lower crust and mantle lithosphere is squeezed between blocks (the vice) of model lithosphere of significantly greater total strength (Fig. 2). Both the vice and orogen float isostatically on a weaker model asthenosphere. Convergence is achieved by the motion of two pistons, which move inward at the same constant rate, driven by a step motor and screw gear assembly (Fig. 3). The vice-piston and vice-orogen boundaries are no-slip, as is the contact between asthenospheric material and the tank walls. The upper boundary in both the analogue and numerical models is a free surface.

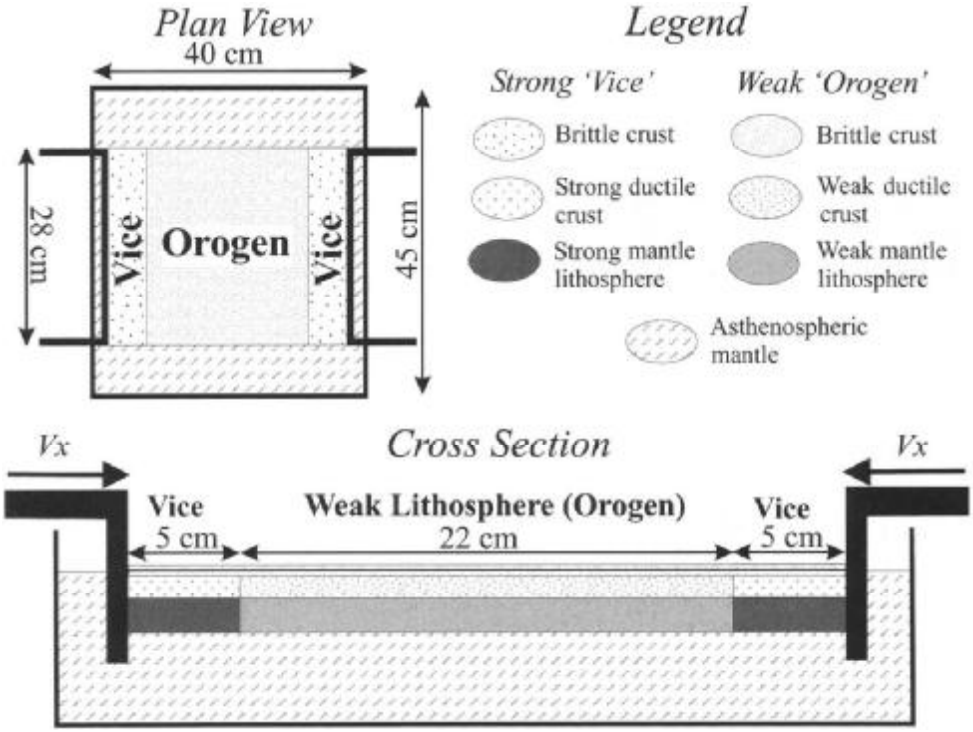


**Fig. 1.** Vice model set up. Top left is a plan view and bottom is a cross-sectional view of how each analogue experiment is constructed. With the exception of the rigid pistons (black) used to impose orogenic convergence in the analogue models, the cross-section also summarizes the set-up for the numerical experiments.

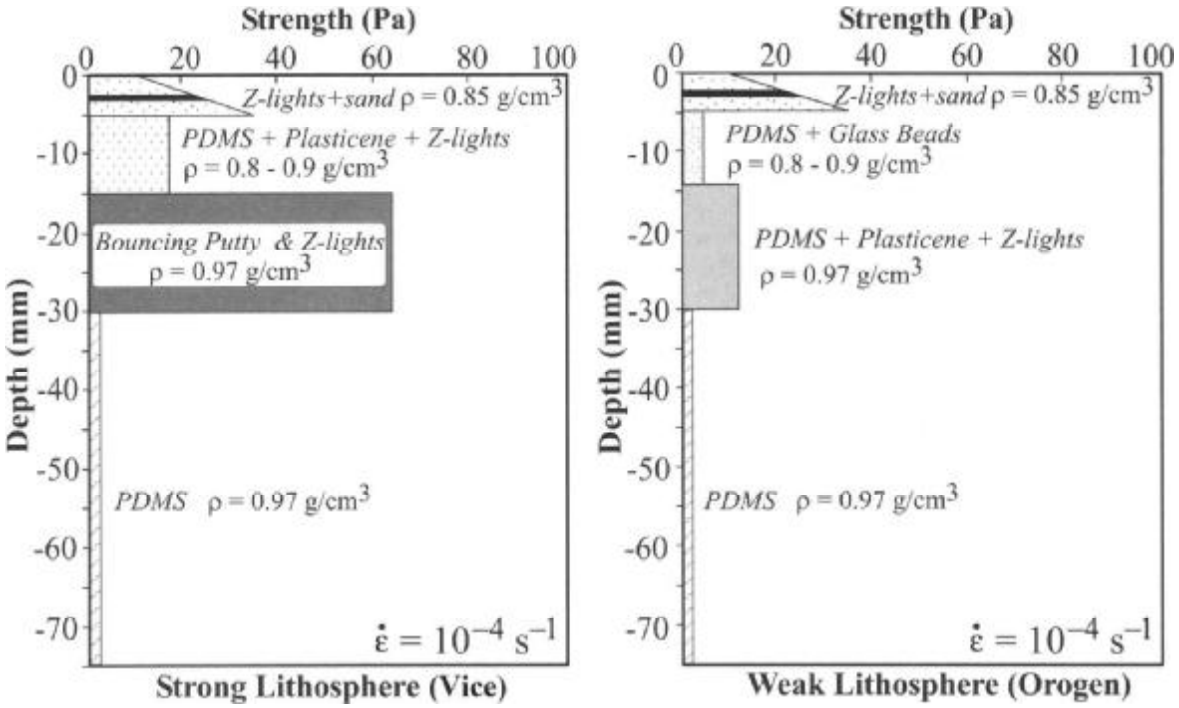


**Fig. 2.** Representative strength envelopes for the strong lithospheric blocks (vice) and weak orogenic lithosphere employed in the analogue experiments. See Table 1 for a complete summary of the physical properties of materials employed in the experiments.

Orogen parallel flow in the analogue experiments is achieved by constructing the model orogen such that it is unconfined at both ends (Figs 1 and 3). As such, the model orogen is free to flow outwards into a reservoir that is initially filled only with asthenospheric material. A similar approach has been used previously to model radially spreading nappes (Gilbert & Merle 1987; Merle 1989), and indentor (Davy & Cobbold 1988) and escape tectonics (Ratschbacher *et al.* 1991). In nature such unconfined boundaries might be represented by subduction zones, which retreat away from the orogen due to slab roll back (e.g., Schellart & Lister 2004). Lateral flow of model asthenosphere material in our simulated tectonic vice is illustrated in Figure 4. Deformation of a passive marker grid indicates that bulk orogen normal contractional and orogen parallel extensional strain is effectively homogeneous in the area of the models underlain by orogenic lithosphere. More complex strain fields develop adjacent to the lateral walls of the tank and at the corners of the pistons, outside the area of experimental interest. Because asthenospheric material is free to move around and under the pistons (Fig. 4), there is no change of volume or depth of this layer throughout the tank during the experiment.

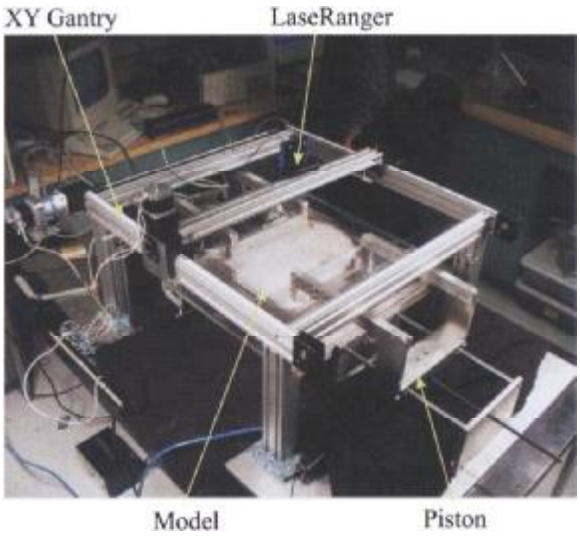


**Fig. 3.** Oblique view of the experimental apparatus and laser topography scanner. Both the piston and XY-gantry are propelled by computer-controlled stepper motors. Person and control computer in background for scale.

The 2D numerical models are set up with identical cross-sectional geometry and material properties to those of the analogue experiments. Our approach to modelling takes advantage of the relative strengths of laboratory and numerical approaches (e.g., Pysklywec & Cruden 2004).

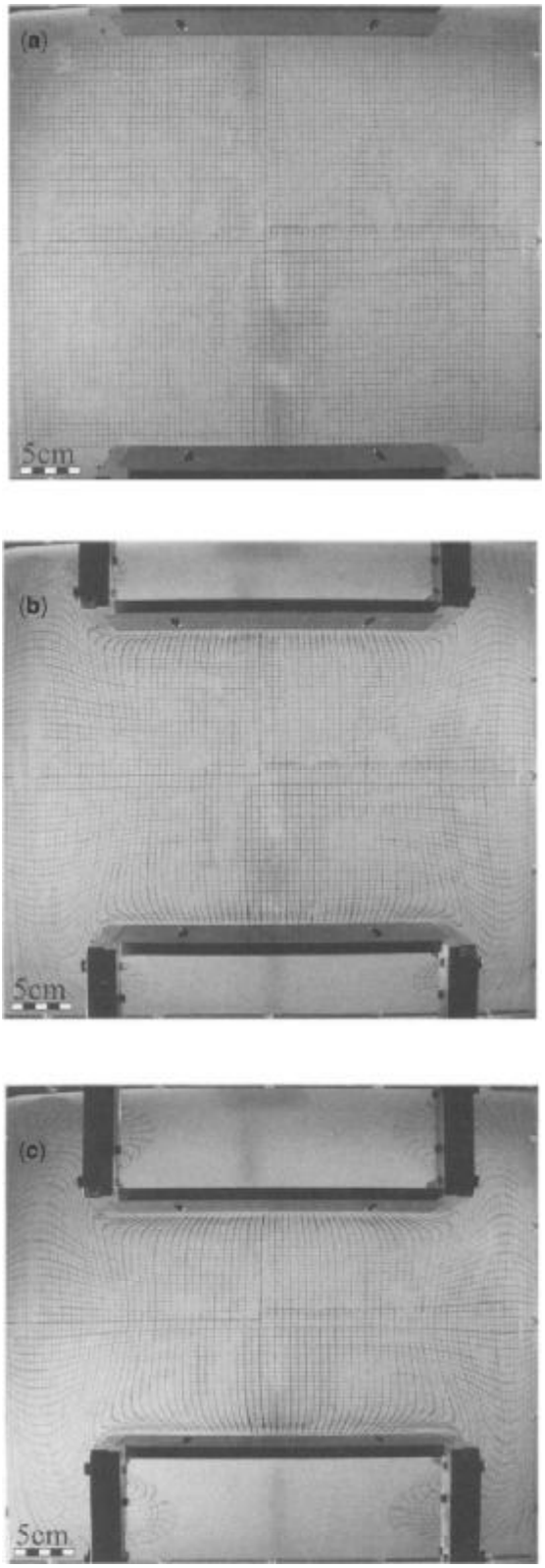


**Fig. 4.** Deformation of passive marker grid at top of asthenospheric material in response to convergence of pistons. The displacement of the passive grid gives an approximate illustration of the flow of model asthenosphere beneath fully constructed vice models.

In the vice experiments reported here, analogue models provide insights into the contribution of 3D orogen flow on the structural development of the orogen. The 2D numerical experiments act as a control on the laboratory experiments, by allowing for more variations in rheological parameters, and providing quantitative information on the evolving model orogen through time.

## Laboratory experiments

Scaling and the general construction of the laboratory experiments (Table 1; Figs 1 and 2) follows the approach for analogue modelling of lithospheric deformation at 1 g described by Davy and Cobbold (1988, 1991). The experiments are approximately scaled to nature by selection of appropriate dimensions (geometric similarity) and laboratory materials (dynamic and kinematic similarity). By necessity the scaling is only approximate because of practical considerations in the laboratory (limitations of model size, time and suitable materials) and uncertainties in the natural system (densities, rheologies, time dependence, etc.).

### *Materials and scaling*

In designing the laboratory experiments we used the physical properties of the asthenospheric mantle material and the length scale of the crust as our principal constraints. For practical purposes we define a length scale based on a model crustal thickness, $l_m =$ 1.5 cm, which for a natural continental crustal thickness $l_p = 40$ km gives a length scale ratio $L = l_m/l_p = 3.8 \times 10^{-7}$ (where the subscripts $m$ and $p$ refer to laboratory and natural prototype scales, respectively). As our working fluid to model asthenospheric mantle we use polydimethylsiloxane (PDMS), which is a transparent, high viscosity, high molecular weight silicone polymer that is frequently used in analogue modelling studies (e.g., Weijermars 1986; Pysklywec & Cruden 2004). PDMS has a density $\rho_m =$ 970 kg/m$^3$, which for a natural asthenospheric density of $\rho_p = 3100$ kg/m$^3$, sets a density scale of $P = \rho_m/\rho_p = 0.31$. In these experiments at 1 g the gravity scale ratio is $G = g_m/g_p = 1.0$.

The rheological properties of all ductile materials used in this study were measured over a range of strain rates relevant to the experiments with a rotary viscometer (based on a design by Cobbold & Jackson 1992), calibrated against a TA Instruments AR1000 rheometer. PDMS has a slightly non-Newtonian rheology

**Table 1.** *Parameters for laboratory vice models*

| | | $W$ (cm) | $L$ (cm) | $h$ (cm) | $\rho$ (kg/m$^3$) | $\eta_{eff}$ (Pas) | $\phi$ | $\sigma_o$ (Pa) | Material | $V_x$ (cm/hr) | $S$ (cm) | $F_t$ (Pa) | $F_b$ (Pa) | $Ar$ |
|---|---|---|---|---|---|---|---|---|---|---|---|---|---|---|
| **All Models** | | | | | | | | | | | | | | |
| *Asthenosphere* | Mantle | 32 | 45 | 4.5 | 970 | $2.50 \times 10^4$ | | | PS | | | *c.* 50 | *c.* 20 | *c.* 0.4 |
| *Vice* | Lower Crust | 5 | 28 | 1.0–0.8 | 900 | $3.20 \times 10^5$ | | | PS + Pl + Gb | | | | | |
| | Mantle Lithosphere | 5 | 28 | 1.5–2.0 | 970 | $>1.00 \times 10^7$ | | | BP + Zl | | | | | |
| **Individual Models** | | | | | | | | | | | | | | |
| *Experiment #27* | Upper Crust | 32 | 28 | 0.6 | 850 | | 28°–34° | 7–44 | S + Zl | 1.6 | 9.6 | 6.8 | 25.2 | 3.7 |
| | Lower Crust | 22 | 28 | 1 | 900 | $5.20 \times 10^4$ | | | PS + Zl | | | | | |
| | Mantle Lithosphere | 22 | 28 | 1.5 | 970 | $1.58 \times 10^4$ | | | PS + Pl + Zl | | | | | |
| *Experiment #29* | Upper Crust | 32 | 28 | 0.6 | 850 | | 28°–34° | 7–44 | S + Zl | 1.1 | 7.7 | 6.3 | 25.3 | 4 |
| | Lower Crust | 22 | 28 | 1 | 800 | $4.05 \times 10^4$ | | | PS + DF + Gb | | | | | |
| | Mantle Lithosphere | 22 | 28 | 1.5 | 970 | $1.68 \times 10^5$ | | | PS + Pl + Zl | | | | | |
| *Experiment #30* | Upper Crust | 32 | 28 | 0.4 | 850 | | 28°–34° | 7–44 | S + Zl | 1 | 7.5 | 4.1 | 16.8 | 4.1 |
| | Lower Crust | 22 | 28 | 1 | 900 | $4.10 \times 10^4$ | | | PS + DF + Gb | | | | | |
| | Mantle Lithosphere | 22 | 28 | 1.5 | 970 | $1.71 \times 10^5$ | | | PS + Pl + Zl | | | | | |
| *Experiment #32* | Upper Crust | 32 | 28 | 0.4 | 840 | | 28°–34° | 7–44 | S + Zl | 0.4 | 11 | 3.2 | 16.7 | 5.2 |
| | Lower Crust | 22 | 28 | 0.8 | 900 | $4.28 \times 10^4$ | | | PS + DF + Gb | | | | | |
| | Mantle Lithosphere | 22 | 28 | 2 | 970 | $2.00 \times 10^5$ | | | PS + Pl + Zl | | | | | |
| *Experiment #33* | Upper Crust | 32 | 28 | 0.4 | 840 | | 28°–34° | 7–44 | S + Zl | 0.4 | 11 | 3.2 | 16.8 | 5.2 |
| | Lower Crust | 22 | 28 | 0.8 | 800 | $4.11 \times 10^4$ | | | PS + DF + Gb | | | | | |
| | Mantle Lithosphere | 22 | 28 | 2 | 970 | $2.00 \times 10^5$ | | | PS + Pl + Zl | | | | | |
| *Experiment #34* | Upper Crust | 32 | 28 | 0.45 | 850 | | 28°–34° | 7–44 | S + Zl | 1.3 | 8.45 | 4.8 | 19 | 4 |
| | Lower Crust | 22 | 28 | 0.8 | 900 | $1.17 \times 10^4$ | | | PS + DF + Gb | | | | | |
| | Mantle Lithosphere | 22 | 28 | 2 | 970 | $1.64 \times 10^5$ | | | PS + Pl + Zl | | | | | |

$W$ = orogen perpendicular width; $L$ = orogen parallel length; $h$ = vertical thickness; $\rho$ = density; $\eta_{eff}$ = effective viscosity; $\phi$ = angle of internal friction; $\sigma_o$ = cohesion (maximum values); $Vs$ = convergence rate; $S$ = amount of shortening; $F_t$ = tectonic force (resistance); $F_b$ = Bouyancy force (gravity collapse); $Ar$ = Argand number = $F_b/F_t$.
PS = Polydimethylsiloxane (PDMS); Pl = Harbuts plasticene (blue/black); DF = Dow Corning 30,000 cSt Fluid; BP = Dow Corning Bouncing Putty; Gb = 3M Glass Bubbles; S = quartz sand; Zl = 3M Z-light ceramic microspheres.

defined by the flow law:

$$\sigma^n = \eta\,\dot{\varepsilon} \tag{1}$$

where $\sigma$ is stress, $\dot{\varepsilon}$ is strain rate, $\eta$ is a material constant and $n$ is the power law exponent. Because our modelling materials are slightly non-Newtonian ($n = 1.05$ to 1.2) for scaling purposes we define an effective dynamic viscosity $\eta_{\text{eff}} = \sigma/\dot{\varepsilon}$, which for our PDMS (Dow Corning Silastic 4-2901) at a laboratory strain rate of $10^{-5}\,\text{s}^{-1}$ is $2.5 \times 10^4$ Pa s. Assuming an effective viscosity of $[\eta_{\text{eff}}]_p = 10^{21}$ Pa s for the natural asthenosphere (Mitrovica & Forte 1997) defines a viscosity scale ratio $M = [\eta_{\text{eff}}]_m/[\eta_{\text{eff}}]_p = 2.5 \times 10^{-17}$. The time scale ratio for the experiments can now be defined as $T = M/[PLG] = t_m/t_p = 2.13 \times 10^{-10}$.

Thicknesses and properties of the crustal and mantle components of the model lithospheres follow from these scaling parameters and are summarized in Table 1 and Figures 1 and 2. Equivalent values of all experimental parameters are given in Table 2.

Variations in the both the density and effective viscosity of ductile mantle lithosphere and lower crust in the experiments are achieved by adding appropriate amounts of Harbut's plasticene (blue and black), low viscosity PDMS (Dow Corning 30,000 cSt Fluid) and solid fillers to PDMS. The effect of blending plasticene with PDMS is to increase both the density and effective viscosity of the mixture. Solid fillers employed in this study are 3M Z-lights ceramic microspheres and 3M Scotchlight Glass Bubbles, which have grain densities of 650 and 320 kg/m$^3$, respectively. Mixing different proportions of these fillers, which have average diameters *c.* 100 μm, to either pure PDMS or PDMS + Plasticene mixtures decreases the density and increases the effective viscosity of the material. Low viscosity PDMS can be added in small amounts to the above mixtures in order to lower their viscosity. Several different configurations of crustal density and effective viscosity structure were employed in our experiments (Table 1).

Brittle behaviour of the upper crust in the models is simulated by a layer of granular material, whose scaled thickness varies between models from 16 to 11 km. To acquire the desired average upper crustal density we alternated, in the appropriate proportion, layers of Z-light microspheres and quartz sand with bulk densities of 440 and 1570 kg/m$^3$, respectively. Ring shear tests on both materials in the normal stress range 500 to 2000 Pa determined internal friction angles $\phi = 28°$–$34°$ and (linearly extrapolated) cohesion values of $\sigma_o = 7$–$44$ Pa for Z-lights and quartz sand, respectively (J. Lohrmann, GeoForshungsZentrum, Potsdam, unpublished results 2005). Following Schellart (2000) we consider the cohesion values above to be upper bounds on the conditions in our experiments, in which normal stress values vary between 0 and 50 Pa. In this range, the cohesion of dry granular materials approaches 0 Pa (Schellart 2000), hence Z-lights and quartz sand are approximate analogues for modelling the macroscopic, frictional, behaviour of fractured upper crust (Davy & Cobbold 1991; Rossi & Storti 2003).

### *Model construction*

All laboratory experiments were run in a 40 cm (width) × 45 cm (length) × 10 cm (depth) Plexiglas tank (Figs 1 and 3). Models were constructed by sequential addition of asthenospheric and lithospheric layers, with sufficient relaxation time allowed to minimize the development of air bubbles, and to ensure the pre-deformed model achieved isostatic equilibrium. During model construction, lateral flow of ductile material was prohibited by the insertion of vertical sheet metal barriers at the margins of the model orogen. These were removed immediately before the pistons were activated. After removal of the barriers and activation of the pistons, model orogenic material was free to flow at right angles to the compression direction into the reservoir of PDMS. This experimental set-up is designed to maximize the effects of orogen parallel flow driven primarily by piston convergence. Apart from a minor adjustment that occurs when the side barriers are removed, in the absence of piston convergence orogen parallel flow driven by gravity alone would be minimal over the typical duration of our experiments (*ca.* 8 hours).

### *Observation methods*

Progress in all experiments was monitored by time-lapse digital photography from the side and top as well as by linear scanning of the surface topography (Fig. 3). A passive marker grid was imprinted on the top of the model by placing a rectilinear mask over the top surface and sprinkling a thin layer of fine grained white sand through it. Motion of this grid mapped progressive surface deformation in the evolution of the model. In the case of experiments employed to visualize the flow field in the asthenosphere, a passive marker grid was imprinted on the

**Table 2.** *Scaled natural equivalent parameters in vice models*

| | | $W$ (km) | $L$ (km) | $h$ (km) | $\rho$ (kg/m$^3$) | $\eta_{eff}$ (Pas) | $\phi$ | $\sigma_o$ (MPa) | $V_x$ (cm/yr) | $S$ (km) | $F_t$ (MPa) | $F_b$ (MPa) | $Ar$ |
|---|---|---|---|---|---|---|---|---|---|---|---|---|---|
| **All Models** | | | | | | | | | | | | | |
| *Asthenosphere* | Mantle | 853 | 747 | 120 | 3100 | $1.00 \times 10^{21}$ | | | | | *c.* 420 | *c.* 168 | *c.* 0.4 |
| *Vice* | Lower Crust | 133 | 747 | 21–27 | 2876 | $1.28 \times 10^{22}$ | | | | | | | |
| | Mantle Lithosphere | 133 | 747 | 40–53 | 3100 | $4.00 \times 10^{23}$ | | | | | | | |
| **Individual Models** | | | | | | | | | | | | | |
| *Experiment #27* | Upper Crust | 853 | 747 | 16 | 2717 | | 28°–34° | 59–286 | 8.0 | 256 | 57 | 212 | 3.7 |
| | Lower Crust | 587 | 747 | 27 | 2876 | $2.08 \times 10^{21}$ | | | | | | | |
| | Mantle Lithosphere | 587 | 747 | 40 | 3100 | $6.32 \times 10^{21}$ | | | | | | | |
| *Experiment #29* | Upper Crust | 853 | 747 | 16 | 2717 | | 28°–34° | 59–286 | 5.5 | 205 | 53 | 213 | 4 |
| | Lower Crust | 587 | 747 | 27 | 2557 | $1.62 \times 10^{21}$ | | | | | | | |
| | Mantle Lithosphere | 587 | 747 | 40 | 3100 | $6.72 \times 10^{21}$ | | | | | | | |
| *Experiment #30* | Upper Crust | 853 | 747 | 11 | 2717 | | 28°–34° | 59–286 | 5.0 | 200 | 34 | 141 | 4.1 |
| | Lower Crust | 587 | 747 | 27 | 2876 | $1.64 \times 10^{21}$ | | | | | | | |
| | Mantle Lithosphere | 587 | 747 | 40 | 3100 | $6.84 \times 10^{21}$ | | | | | | | |
| *Experiment #32* | Upper Crust | 853 | 747 | 11 | 2685 | | 28°–34° | 59–286 | 2.0 | 293 | 27 | 140 | 5.2 |
| | Lower Crust | 587 | 747 | 21 | 2876 | $1.71 \times 10^{21}$ | | | | | | | |
| | Mantle Lithosphere | 587 | 747 | 53 | 3100 | $8.00 \times 10^{21}$ | | | | | | | |
| *Experiment #33* | Upper Crust | 853 | 747 | 11 | 2685 | | 28°–34° | 59–286 | 2.0 | 293 | 27 | 141 | 5.2 |
| | Lower Crust | 587 | 747 | 21 | 2557 | $1.64 \times 10^{21}$ | | | | | | | |
| | Mantle Lithosphere | 587 | 747 | 53 | 3100 | $8.00 \times 10^{21}$ | | | | | | | |
| *Experiment #34* | Upper Crust | 853 | 747 | 12 | 2717 | | 28°–34° | 59–286 | 6.5 | 225 | 40 | 160 | 4 |
| | Lower Crust | 587 | 747 | 21 | 2876 | $4.68 \times 10^{20}$ | | | | | | | |
| | Mantle Lithosphere | 587 | 747 | 53 | 3100 | $6.56 \times 10^{21}$ | | | | | | | |

Scaling factors = model/prototype: Length, $L = 3.8 \times 10^7$; Velocity, $V = 1760$; Density, $P = 0.313$; Viscosity, $M = 2.5 \times 10^{-17}$; Stress, $\Sigma = 1.19 \times 10^{-7}$; Time, $T = 2.13 \times 10^{-10}$.

PDMS using a transfer method (Dixon & Summers 1983).

Surface topography measurement was made using a laser triangulation device (Aculux LaseRanger) that is translated linearly over the model surface by an XY-gantry system at a stand-off distance of *c.* 13 cm (Fig. 3). Between 5 (Expt. #27) and 34 (Expt. #34) scan lines were collected at 0.5 to 1 hour intervals during the experiments (the variation was due to improvements made to the speed of data acquisition over the duration of the experimental programme). Individual topographic measurements were made with a spacing of 1 mm along each scan line and the positional accuracy of the XY gantry was $\pm 0.1 \sim$ mm. The distance resolution of the laser device is $\pm 0.1$ mm, but due to gantry vibration and scattering effects of the model surface materials the nominal topographic resolution is $\pm 0.2 \sim$ mm.

The internal structure of models was examined after the end of each experiment. First, the granular layer over one third of the model surface was removed using a vacuum hose, and the exposed brittle ductile interface was photographed. Subsequently, the remaining granular material was saturated with water and the model was placed in a freezer at $-50°C$ (i.e., below the crystallization temperature of PDMS). After 12 hours, serial sections of the model were prepared using a band saw, and photographed. Some viscous relaxation of deformed layer interfaces probably occurs during the initial cooling of the models. However, as shown below, the wavelengths and amplitudes of folded interfaces in the sectioned analogue models are similar to those observed in numerical experiments, indicating that the effects of viscous relaxation are relatively minor.

## Numerical experiments

A suite of two-dimensional numerical experiments was conducted as a parallel comparison to the analogue models. The numerical models are scaled to the analogue experiments, and their initial configuration is shown in Figure 1.

The models assume incompressibility of the materials, and the governing equations for the system are:

$$-\nabla p + \nabla \cdot \sigma' + \rho g_z = 0 \qquad (2)$$

$$\nabla \cdot \mathbf{u} = 0 \qquad (3)$$

where $\mathbf{u}$ is the velocity field and $g_z$ is the vertical component of gravity. The full stress tensor $\sigma_{ij}$ has been divided into two components: $\sigma_{ij} = \sigma'_{ij} - p\delta_{ij}$ where $\sigma'$ is the deviatoric component of the stress tensor and $p$ is pressure ($p = -\frac{1}{3}\sigma_{ii}$ for an incompressible fluid). Viscous or plastic rheologies are imposed for the materials in the numerical model to simulate the behaviour of the analogue materials. For the viscous materials we adopt a power law constitutive relation (Eqn. 1), and for the brittle crust, a Coulomb-type yield criterion of the form $\sigma_y = p\sin\phi + \sigma_o$ was used (where $\sigma_y$ is the second invariant of the deviatoric stress).

The system of equations is solved using the arbitrary Lagrangian–Eulerian (ALE) finite element method (Hirt *et al.* 1974; Fullsack 1995). The solution space is discretized using a Eulerian resolution of $321 \times 81$ nodes and a Lagrangian resolution of $601 \times 151$ nodes, evenly distributed through the box. The numerical routine has been benchmarked rigorously with previous studies (Poliakov & Podladchikov 1992; Blankenbach *et al.* 1989; Houseman & Molnar 1997; van Keken *et al.* 1997) to verify its accuracy in computing viscous flow and surface topography.

The top boundary of the box is a free surface and all the other sides have an imposed zero tangential velocity (i.e., no slip). Material is not permitted to penetrate the lower boundary of the box. Deformation in the model is driven by buoyancy forces arising from material density variations and the imposed lithospheric 'vice' contraction. This contraction is simulated as a velocity boundary condition at the sides of the solution space; along the lithospheric portion of each side boundary new lithosphere material is introduced into the box at a horizontal velocity $V_x/2$. An outward flux of asthenospheric material is imposed along the sub-lithospheric portion of the sidewalls of the box in order to balance the mass of injected lithosphere.

### *Overview and dynamic analysis of experiments*

The six laboratory experiments reported here represent a range of orogenic conditions as dictated by rheological and density structure and boundary conditions (convergence rate, $V_x$). Variations in dynamics and body forces in the experiments can be quantified and direct comparison to nature can be made by considering the Argand number. The Argand number is defined as the dimensionless ratio of buoyancy forces to tectonic forces, $Ar = F_b/F_t$ (England & McKenzie 1982; Houseman & England 1986). For these experiments, the buoyancy

force is the static outward force per unit length that results in gravitational collapse of the model lithosphere over the asthenosphere. Following Benes & Davy (1996), the buoyancy force for a three-layer model is given by:

$$F_g = \rho_1 g\frac{h_1}{2} + \rho_1 g\frac{(z_2^2 - z_1^2)}{2} + \rho_1 g\frac{(z_3^2 - z_2^2)}{2} - g\frac{(\rho_1 h_1 + \rho_2 h_2 + \rho_3 h_3)}{2\rho_m} \quad (4)$$

where $\rho_1$, $\rho_2$, $\rho_3$ and $h_1$, $h_2$, $h_3$ are densities and thicknesses of the upper crust, lower crust and lithospheric mantle, respectively; $\rho_m$ is the density of the asthenosphere (PDMS); $z_1 = h_1$, $z_2 = h_1 + h_2$, and $z_3 = h_1 + h_2 + h_3$. Note that $F_g$ is calculated for the start of the experiment and therefore does not consider the buoyancy force caused by crustal thickness changes. $F_g$ is therefore a relative measure of the potential for the model lithosphere to flow laterally over the asthenosphere, and it is resisted by $F_t$, which is the vertically averaged stress required to deform the model lithosphere at a given strain rate.

The tectonic force in the models is calculated as:

$$F_t = \frac{h_1\sigma_o + (h_1^2/2\tan\phi) + h_2(\eta_2\,\dot{\varepsilon})^{1/n_2} + h_3(\eta_3\,\dot{\varepsilon})^{1/n_3}}{z_3} \quad (5)$$

where $\eta$ is the material constant, $n$ is the power law exponent (Eqn 1; subscripts 1, 2, 3 refer to model upper crust, lower crust and lithospheric mantle, respectively) and $\dot{\varepsilon} = V_x/W$ where $W$ is the width of the orogen measured parallel to the shortening direction. Note that because $V_x$ is constant, $\dot{\varepsilon}$ increases with time during each experiment. As with $F_g$, values of $F_t$ and $Ar$ reported here are for the start of each experiment (Table 1).

$F_t$ in the experimental orogen varies between 3.2 and 6.8 Pa, corresponding to natural values of 41 to 87 MPa (Tables 1 and 2). The main controls on $F_t$ in the model orogen are due to the thickness of the brittle crust, $h_1$, and the effective viscosity of the lower crust, $[\eta_{\text{eff}}]_2$. With the exception of Experiment #34, the model orogenic mantle lithosphere is only marginally stronger than the lower crust. This was mainly predicated by limitations imposed by available analogue materials at the time the experiments were carried out, and the resulting trade-off between maintaining the correct density for the mantle lithosphere layer (important for body force scaling), and its strength. Although the effective viscosity of mantle lithosphere material in the experiments would certainly be too low for modelling of stable continental lithosphere, its relative strength compared to crustal and asthenospheric material is consistent with materials used in other analogue model studies (e.g., Sokoutis *et al.* 2000). The scaled natural effective viscosity of the mantle lithosphere in the experiments (*c.* $7 \times 10^{21}$ Pa s; Table 2) is also consistent with experimental (e.g., Kohlstedt *et al.* 1995; Hirth & Kohlstedt 1996; Mackwell *et al.* 1998) and geophysics (e.g., Maggi *et al.* 2000) based estimates of the strength of upper mantle rocks in natural orogens, if the geothermal gradient is steep and conditions are relatively wet (e.g., $\eta_{\text{eff}} \sim 10^{21}$ to $10^{22}$ at strain rates of $10^{-14}$ to $10^{-15}\,\text{s}^{-1}$; Jackson 2002; Toussaint *et al.* 2004).

The strong lithospheric blocks (vice blocks) in the experiments have $F_t$ values that are $\sim$10 times greater than the model orogen. The bulk of the strength in these blocks resides in the mantle lithosphere layer (Fig. 2), which is composed of bouncing putty with finite yield strength (Dixon & Summers 1986) mixed with Z-light spheres to achieve the correct density. The effective viscosities of the mantle lithosphere and lower crust in the vices scale up to $>1 \times 10^{23}$ and *c.* $1 \times 10^{22}$ Pa s, respectively. These values are consistent with a dry upper mantle and granulitic lower crust (Kohlstedt *et al.* 1995; Mackwell *et al.* 1998), as could be expected in stable continental lithosphere. Hence the overall strength of the model orogenic and vice lithospheres and the details of their rheological structure are consistent with a hot orogen with a wet mantle lithosphere and quartz-dominated lower crust (e.g., Toussaint *et al.* 2004) being squeezed between blocks of cold cratonic continental lithosphere (Fig. 2; Table 2).

$F_b$ in the experiments varies between 16.7 and 25.2 Pa, resulting in values of $Ar$ from 3.7 and 5.2 (Fig. 5a; Table 1). Such values indicate that the orogenic lithosphere will tend to collapse if boundary conditions are suitable, and are consistent with conditions employed in previous numerical and analogue model studies of lithospheric convergence and extension (Houseman & England 1986; Benes & Davy 1996). Values of $Ar$ between 1 and 10 are considered to describe the balance of forces in wide, hot orogens such as the Himalaya, and $Ar \geq 3$ is required to develop orogenic plateaux such as the Tibetan plateau (England & McKenzie 1982; Dewey *et al.* 1986; England & Houseman 1986). In the vice blocks, $Ar \ll 1$, which describes the balance of forces expected in stable continental lithosphere, in which gravitational forces are expected to be significantly resisted by the tectonic strength.

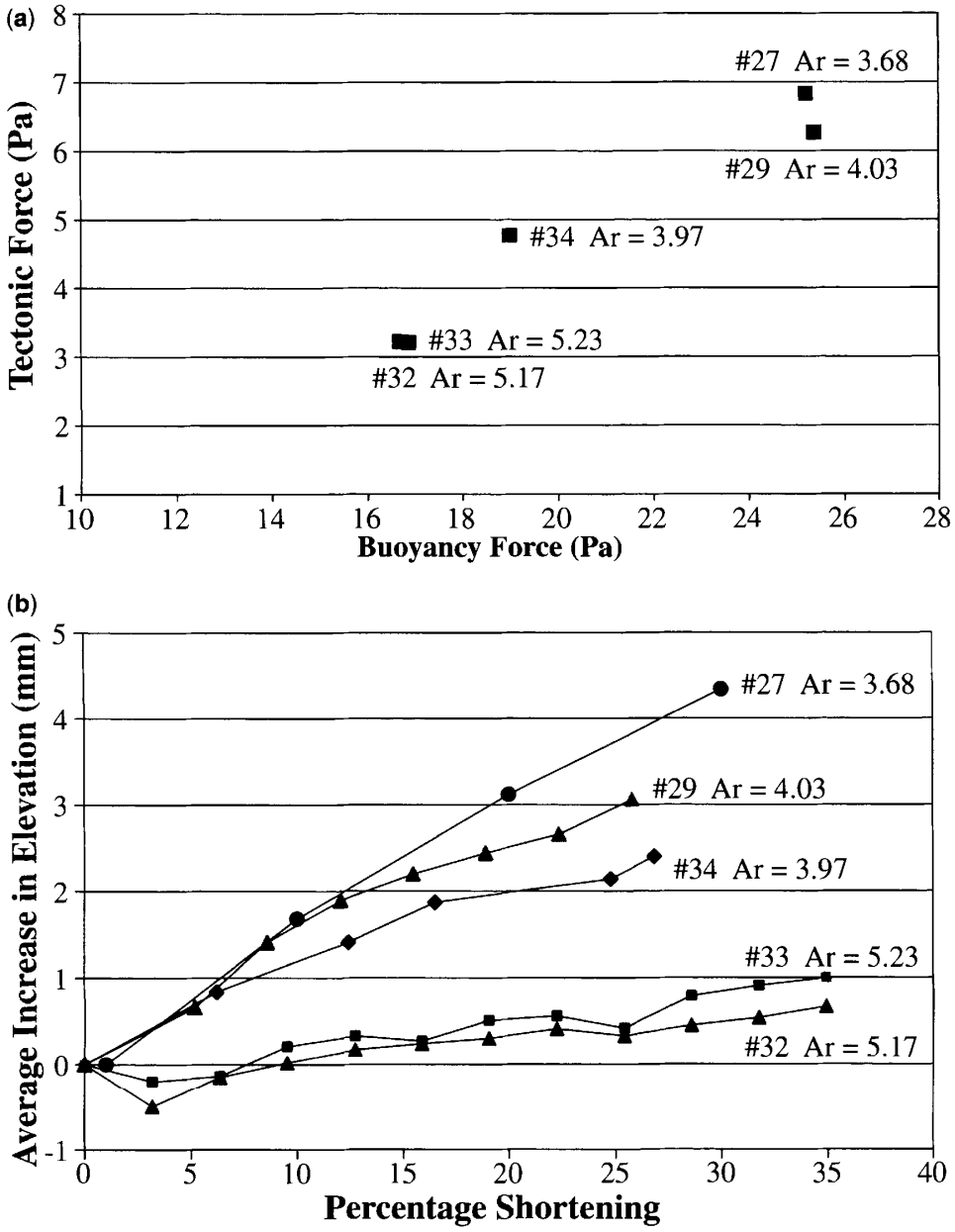


**Fig. 5.** (**a**) Comparison of tectonic forces ($F_t$) and buoyancy forces ($F_b$) in analogue experiments. (**b**) Increase of average surface elevation of orogenic crust in analogue vice models as a function of the amount (%) shortening and Argand number, *Ar*.

Because *Ar* in the experiments is in agreement with values estimated in nature, we can demonstrate approximate dynamic similarity between our vice models and wide, hot orogens. Kinematic similarity is satisfied by imposing model convergence rates of 0.4 to 1.6 cm/hr, which scale up to typical orogenic convergence rates of 2 to 8 cm/a. The model thicknesses and horizontal dimensions scale up to values expected in large orogenic systems (Table 2), which together with total scaled amounts of shortening of 200 to 300 km (25–35% shortening) also satisfy the requirements of geometric similarity.

The effect of *Ar* in the experiments can be evaluated by quantifying how elevation in the model orogen grows with time. Figure 5b plots the average elevation in the area confined between the vice blocks, determined by laser profilometry, as a function of the amount of shortening in each experiment. After an initial drop in elevation due to removal of the barriers at the edge of the model orogen, average elevation increases steadily. As expected, the

fastest elevation growth occurs in experiments with smaller *Ar* values. This is because orogenic thickening outstrips the rate of lateral orogenic collapse allowed by the strength of the model lithosphere. The average height attained in Experiment #27 corresponds to a scaled equivalent mean elevation of *c.* 11500 m, which seems excessive for terrestrial orogens. Experiments #29 and #34 have final scaled average elevations of *c.* 8000 and 6000 m, which is a reasonable fit for Earth, given the absence of erosion in the experiments. In the highest *Ar* experiments (#33 and #32), final scaled mean elevations are $\leq$2600 m and mean scaled elevations at times that correspond to the end of Experiments #29 and #34, are *c.* 1300 m.

In the presentation of the experimental results below, we will focus on the influence of *Ar* on the structural and topographic evolution of the model orogen, and examine the role of the relative buoyancy and strength of the lower crust. The attributes of the ductile crust of wide, hot orogens are important because the crust is likely to be weak due to the combined effects of high geothermal gradient, presence of water and quartz-rich composition (e.g., Toussaint *et al.* 2004). These conditions may also lead to partial melting over large areas (e.g., Meissner & Mooney 1998; Rey *et al.* 2001), resulting in a further lowering of the strength of the lower to mid-crust and, if the degree of melting is sufficient, to decrease its bulk density (e.g., Rey 1993; Teyssier & Whitney 2002). Experiments #29, #33 and #34 examine the situation of a weak, non-buoyant ductile crust; in Experiments #29 and #33, the ductile crust is weak and buoyant; and in Experiment #34 the ductile crust is non-buoyant, but significantly weaker than the other models.

## Results

Firstly, we consider the influence of lower crustal density on the evolution of the models, using representative experiments having a buoyant (#29) or non-buoyant (#34) lower crust. Secondly, the contribution of *Ar* on experimental outcomes and the differences between equivalent 3D analogue and 2D numerical experiments are discussed by focussing on results of Experiments #29, #32 and #34.

### *Buoyant lower crust experiments (#29 and #33)*

Surface deformation (analogue only), topography (analogue and numerical) and cross-sectional geometry (numerical only) of Experiment #29 at intermediate (12%) and late amounts (24%) of shortening are shown in Figure 6. Surface deformation in this experiment is characterized by early formation of a conjugate system of shear zones (Fig. 6a) that subsequently evolves into a localized, curvilinear orogen-subparallel zone of thrusting and folding (Figs 6a and 7a). Not evident in Figures 6a and d is the development of upper crustal folds, which are observed in the topographic profiles (Figs 6b and e) and serial sections (Fig. 8a). Overall, the amplitudes and wavelengths of the topographic features associated with these folds are very similar in the analogue and numerical runs. A notable feature in both the analogue and numerical runs of this experiment is the development of significant zones of overthrusting of the model orogen crust over the encroaching vice. A similar degree of overthrusting is also observed in Experiment #33, which also had a buoyant lower crust. Although upper crustal folding in Experiment #33 is more distributed than in Experiment #29, the formation of conjugate sets of upper crustal shear zones is also observed, particularly close to extruding margins of the model orogen.

In comparison to the experiments described below, overthrusting or 'overflow' parallel to the shortening direction at the vice margins, and the development of conjugate upper crustal shear zones within the orogen appear to be common attributes in models with buoyant ductile crust. We attribute the pronounced overflow of buoyant crust and overlying brittle material to be due to a 'water bed' effect. As postulated by Bailey (1999, 2001), a thickened, buoyant and weak ductile crust is gravitationally unstable. Under horizontal plane strain conditions, the resulting net outward force acts opposite to the shortening direction, and provided crustal strength can be exceeded at the orogen margins, overflow will occur (Bailey 2001). The effect of this overflow in our experiments is twofold. Firstly, as seen in the analogue and numerical cross sections (Fig. 8a), outwardly vergent thrust zones develop at the orogen-vice boundary zone. Secondly, upper crustal folding is suppressed because of orogen perpendicular extension caused by the overflow. In the analogue version of Experiment #29, folding in the orogen is confined to a central region, in which the folds are probably amplified by local gravitational instability between the upper and lower crust (Fig. 8a). In the equivalent numerical model, distributed upper crustal folds have significantly lower amplitude than in models with non-buoyant ductile crust. Formation of conjugate upper crustal shear zones in analogue Experiments #29 and #33 is consistent with

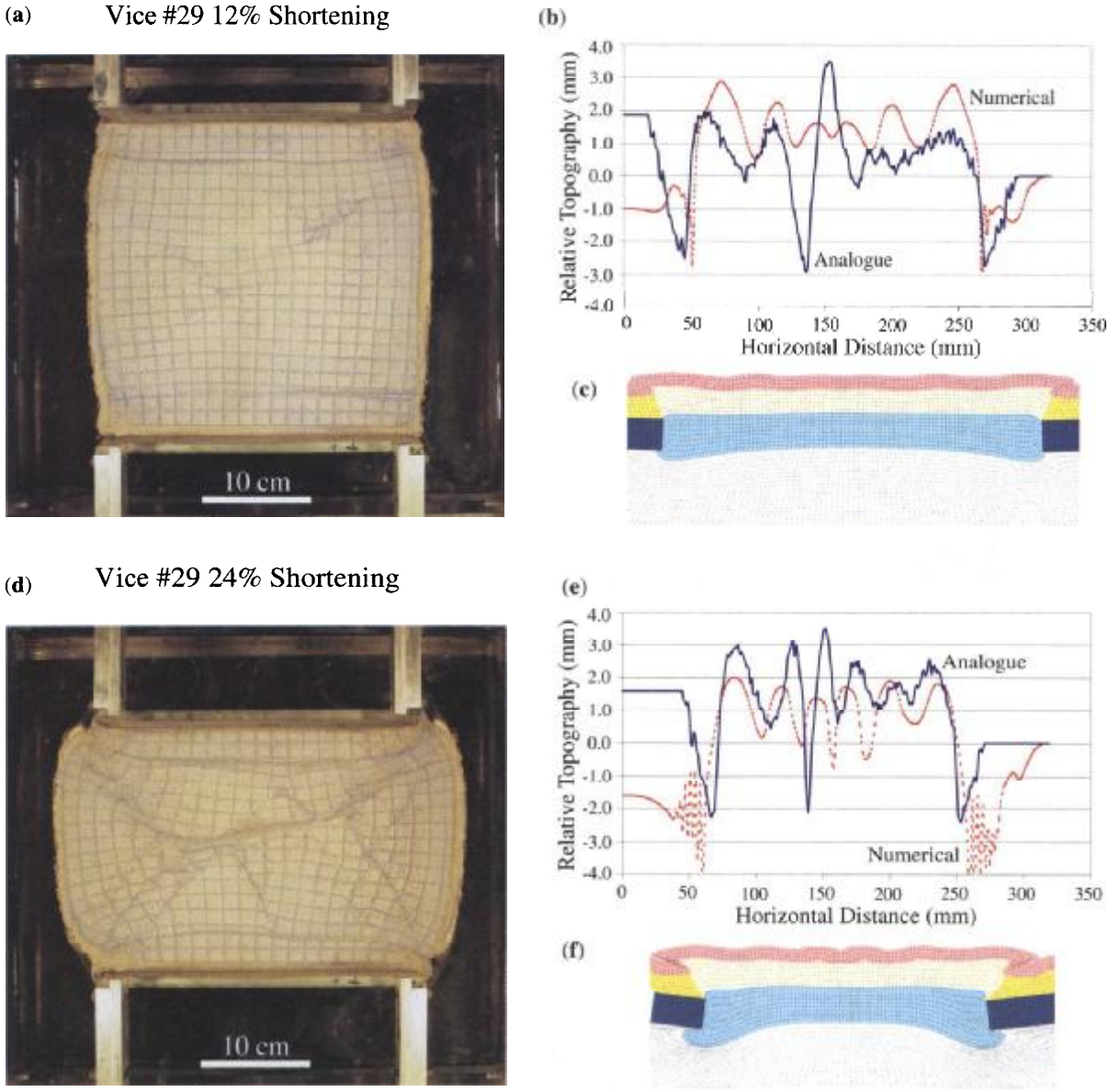


**Fig. 6.** Results for Experiment #29, with buoyant ductile crust. (**a**) and (**d**) Photographs of top surface after 12% and 24% shortening. (**b**) and (**e**) Comparison of central topographic profiles of analogue and numerical models after 12% and 24% shortening. Relative topography is the difference between the present and original elevation. The analogue and numerical results have been re-levelled for comparison purposes. (**c**) and (**f**) Cross-sections of numerical experiment at 12% and 24% shortening.

orogen parallel flow, driven both by the gravitationally unstable thickened ductile crust, and by orogen-parallel stretching exerted at the base of the model lithosphere by the asthenosphere (Fig. 4).

Due to the very high strength of the mantle lithosphere in the vice blocks, significantly weaker mantle lithosphere material in the model orogen has a tendency to underthrust the vice margins (Figs 6c, f and 8). This effect is observed in all experiments. We consider these features to be artefacts of the experimental boundary conditions and therefore do not ascribe any special tectonic significance to them. Their development does not appear to have a major influence on the formation of structures in the orogenic crust. However, the addition of extra dense material to the base of the vice lithosphere, together with a torque exerted on the strong vice upper mantle layer by the underthrusting of orogenic material, results in a net tilting of the vice blocks towards the interior of the model, as observed in both surface elevation data (Figs 6 and 9) and cross-sections (Fig. 8). Tilting of the

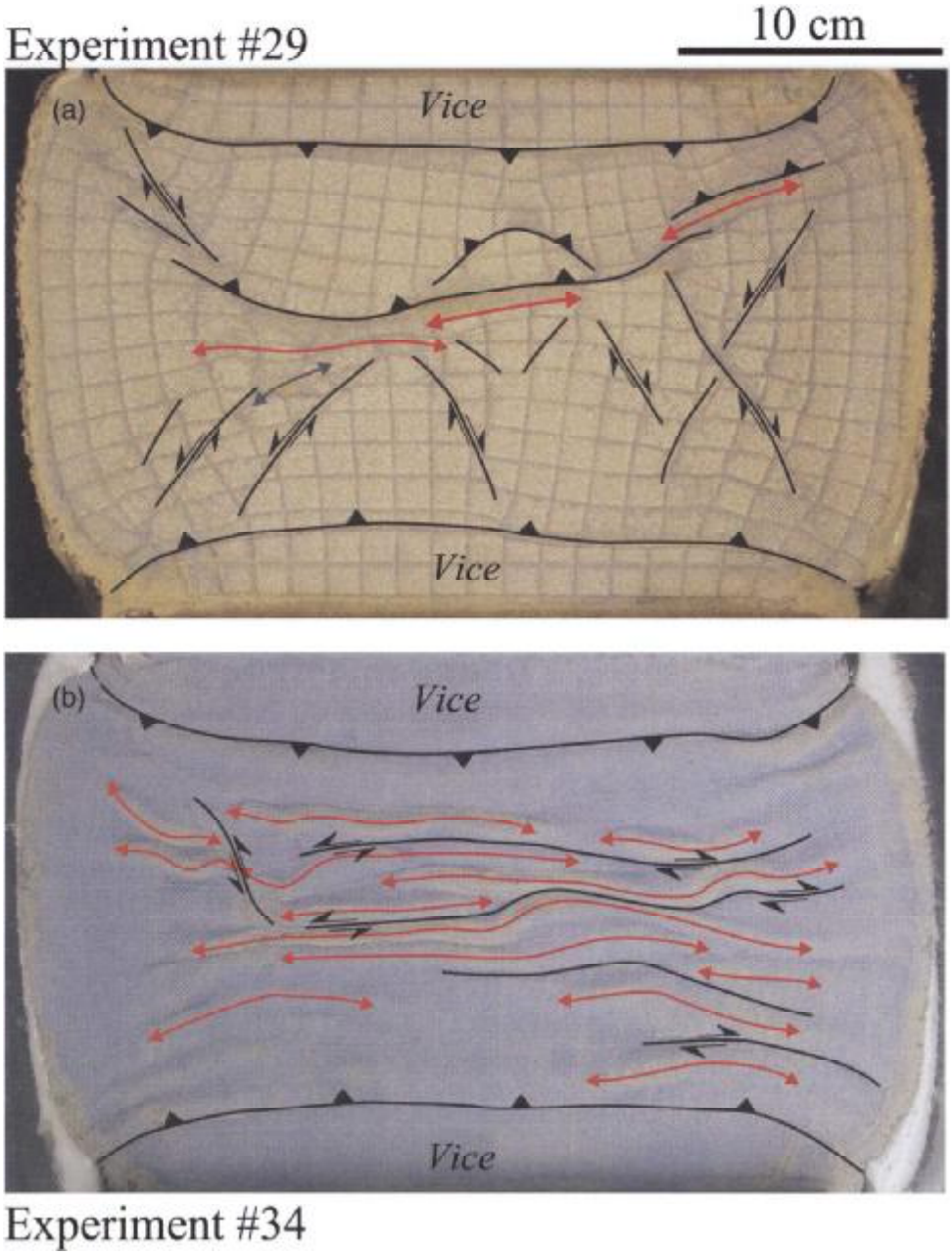


**Fig. 7.** Structural interpretations of Experiments #29 (**a**) and #34 (**b**), based on surface deformation patterns and serial sections. Red double headed arrows are axial traces of anticlines. Black lines are faults (barbs on hanging wall of thrusts, based on analysis of serial sections; sense of shear on vertical strike slip faults is indicated, based on deflection of marker grid).

vice blocks is more pronounced in the analogue models because of the finite width of the vice blocks over which this torque acts.

*Non-buoyant lower crust experiments (#27, #30, #32 and #34)*

Results for Experiment #34 are presented in Figures 7 to 9. Although the *Ar* numbers and general topographic growth behaviour are similar (Table 1, Fig. 5), upper crustal deformation in this experiment is markedly different to that in Experiment #29. Namely, the deformation is characterized by the formation of distributed orogen subparallel curvilinear folds from an early stage of the tectonic evolution (Figs 9a, b, c). As shortening progresses the folds lengthen and merge, and at late stages, orogen subparallel shear zones develop,

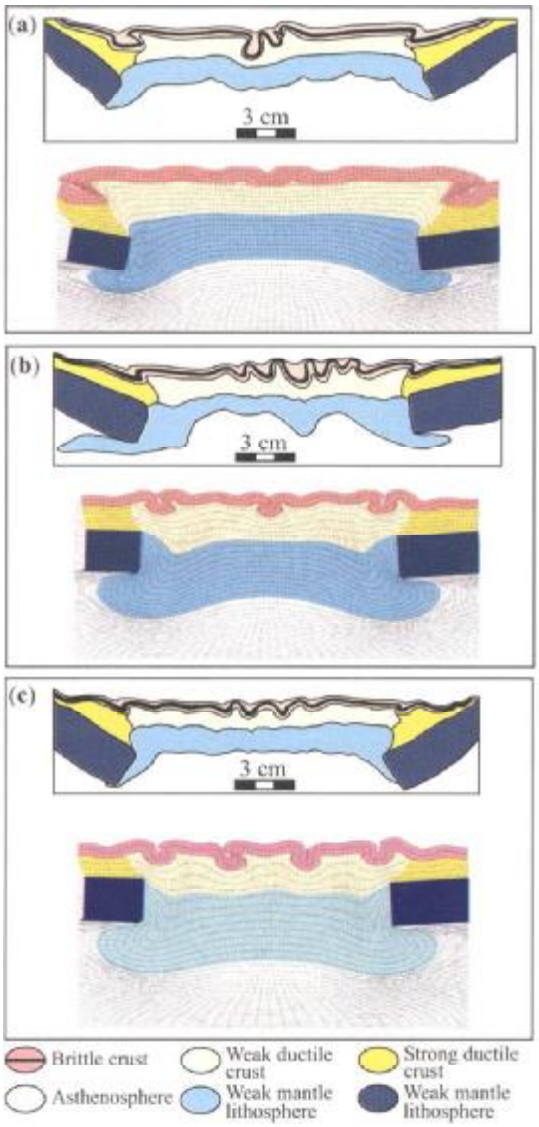


**Fig. 8.** Central cross-sections for analogue and numerical Experiments #29 (**a**), #34 (**b**) and #32 (**c**) after 32% shortening. Cross-sections of analogue experiments are line drawings traced from photographs of serial sections cut through the centre of the model after freezing.

typically in synclinal cores (Figs 7b and 9d). Conjugate shear zones are generally absent, except at the outer regions of the extruding orogen. The degree of overthrusting of orogenic crust over each vice is significantly less than in models with buoyant crust. Both the amplitude and wavelength of upper crustal folds, as determined from topographic profiles and cross-sections, are quite similar in the analogue and numerical runs.

In experiments with non-buoyant ductile crust, orogen parallel shear zones appear to be favoured in models with thicker brittle upper crust and lower *Ar*, being best developed in Experiment #27 and least well developed in Experiment #32. The geometry of folds at the brittle-ductile boundary also varies according to the effective viscosity of the lower crust. In Experiments #27, #30 and #32 both analogue and numerical runs are characterized by folds at the brittle-ductile interface that are cylindrical in cross-section, with a tendency to develop cuspate geometries in anticlinal cores (Fig. 8c). In Experiment #34, which had a ductile crust an order of magnitude weaker than the other models, anticlinal cores were markedly cuspate, resembling mullion structures in cross-section (Fig. 8b) (e.g., similar to the observations of Sokoutis 1990).

### *Effects of three-dimensional versus two-dimensional geometry*

As noted in the experimental results described above, both the topographic profiles and cross-sections for equivalent analogue and numerical experiments are qualitatively (e.g., fold shapes, vice margin structure; Fig. 8) and quantitatively similar (e.g., close correspondence in amplitude and wavelength of fold-related features on topographic profiles; Figs 6 and 9). However, significant differences between the 3D analogue and 2D numerical experiments are evident when surface deformation patterns are examined (Fig. 7) and in the topographic and internal characteristics of experiments with higher *Ar* numbers (Figs 8c and 10).

The upper crust of the numerical experiments responds to the imposed convergence by folding, and varying amounts of overthrusting at the vice margins. As noted previously, the upper crust of the analogue models is characterized by the development of folds *and* vertical shear zones, either in the form of conjugate arrays (Expts #29 & #33; Fig. 7a) or orogen parallel curvilinear shear zones (Expts #27, #30, #32, #34; Fig. 7b). Thrusts also develop at the vice margins and in some cases in association with pop-up structures formed in the interior of the orogen (e.g., Figs 7a and 8a).

While the lower occurrence of strain localization in the brittle crust of the numerical models can be attributed to choice of model rheology, the development of systems of vertical shear zones in the analogue experiments are due to both strain softening within the granular material *and* orogen-parallel flow. In the case of models with non-buoyant ductile crust, orogenic shortening is accommodated by distributed upper crustal folding and moderate overthrusting

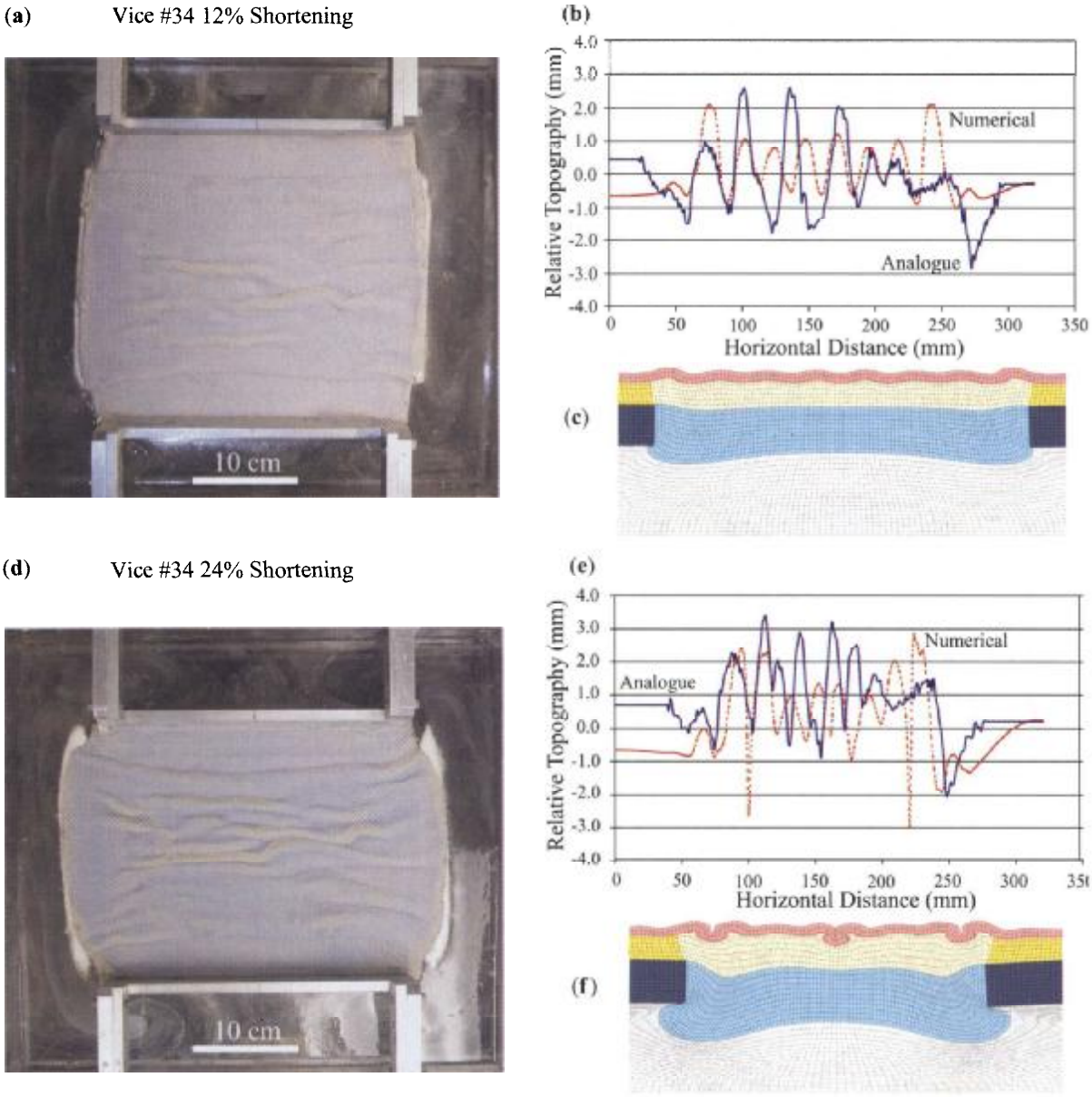


**Fig. 9.** Results for Experiment #34, with non-buoyant, weak ductile crust. (**a**) and (**d**) Photographs of top surface after 12% and 24% shortening. (**b**) and (**e**) Comparison of central topographic profiles of analogue and numerical models after 12% and 24% shortening. Relative topography is the difference between the present and original elevation. The analogue and numerical results have been re-levelled for comparison purposes. (**c**) and (**f**) Cross-sections of numerical experiment at 12% and 24% shortening.

at vice margins. Orogen-parallel extension in the upper crust of these experiments is taken up by a component of homogeneous stretching, parallel to fold axes and by displacements on orogen subparallel curvilinear shear zones (Fig. 7b). An interesting property of these shear zones is that their sense of shear changes along strike in response to the flow direction in the underlying ductile crust and upper mantle.

In models with buoyant ductile crust, the upper crust responds to convergence by significant overthrusting at vice margins and by localized folding and thrusting in the model interior. Orogen parallel extension in these cases is taken up by relative outward displacements and rotations of large blocks of brittle model upper crust bound by conjugate sets of shear zones, whose acute bisectors are parallel to the convergence direction (Fig. 7a). This style of deformation is attributed to the 3D nature of the 'water bed effect' discussed above. Because the upper crust is lifted up by the buoyant, thickening

ductile crust, it is relatively less confined than in experiments with non-buoyant ductile crust. With the exception of a central region of orogen parallel folds and thrusts, this allows the upper crust to break up into relatively undeformed blocks whose motion between conjugate shear zones is controlled by the flow of the underlying ductile crust and upper mantle (Fig. 7a).

In experiments with low to intermediate *Ar* number (#27, #29, #34) we observe a generally close correspondence between analogue and numerical runs in terms of cross-sectional geometry and topographic profiles, when compared to the central part of the models. However, in the analogue models the mean elevation, the amplitude of folds in cross-section and their surface expression decrease outward along the strike of the orogen, introducing significant differences with respect to the numerical results. These effects are due to the increasing importance of orogen-parallel flow on the geometry of upper crustal structure towards the free end of the models. A similar difference between analogue and numerical results is observed even in the central region of models with high *Ar* number (#32, #33). In these experiments both the amplitudes of folds in cross-section and their surface expression in topographic profiles are noticeably less in the analogue models (Figs 8c and 10). This is because in the analogue experiments with high *Ar* number, gravity driven orogen parallel flow can effectively keep up with the slow imposed convergence rate. In 3D this enhanced outward flow has the effect of suppressing the build up of relief and the amplitude of upper crustal folds, even in the central region of the models.

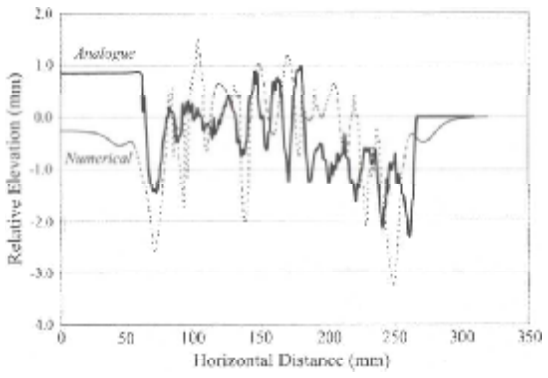


**Fig. 10.** Relative surface elevation profiles in analogue (central profile; heavy line) and numerical (thin dashed line) runs of Experiment #32. Re-levelled for comparison purposes.

### *Three-dimensional structure of the brittle-ductile interface*

The complex 3D structure of the brittle-ductile interface in the analogue experiments was observed by removal of the upper crustal granular layer with a vacuum hose at the end of each experiment (Fig. 11). Folds at this interface are typically doubly plunging and display an anastomosing pattern in 3D. Fold amplitude and wavelength decreases approaching the free end of the model orogen and the overall strain pattern is similar to that observed in viscous-only experiments (e.g., Fig. 4 and Gilbert & Merle 1987). Significant stretching parallel to fold axes in our experiments is evident from the observation of segmented (boudinaged) fold hinges (Fig. 11). Vertical upper crustal shear zones do not penetrate into the ductile crust, although some shear zones do root into linear zones of very short wavelength, short axial length arrays of en-echelon folds. The brittle-ductile interface therefore represents a decoupling horizon for shear zones, but not for folds, which are clearly continuous across it. However, cross-sections (Fig. 8) show that folding of the brittle ductile interface does not continue to the crust-mantle boundary, indicating that upright folds in the models are disharmonic at the crustal scale.

**Fig. 11.** Oblique view of the brittle-ductile interface (in foreground) of Experiment #27, after removal of upper granular layer (in background) with a vacuum hose. The width of the model between the vertical pistons is 9.6 cm. Strong vice ductile crust is pink, weak ductile crust is yellow.

*Three-dimensional bulk finite strains*

Comparison of the analogue and numerical experiments indicates that the centre profile cross-sectional area of the ductile crust and orogenic upper mantle in the analogue models has decreased over the duration of each set of runs. The change in cross-sectional area of these layers is an indication that material has flowed out of the section, parallel to the orogen, and is therefore a measure of orogen-parallel stretch in the models.

Using the coordinate system defined in Figure 12a, we employ the change in cross-sectional area of the ductile crust and orogenic upper mantle, together with known amounts of horizontal shortening, to estimate the bulk finite strain in the central portion of each analogue experiment. The principal strains $(1+e_x)$, $(1+e_y)$ and $(1+e_z)$ are defined to be oriented parallel to the shortening direction ($x$), the orogen ($y$) and normal to the model surface ($z$) and the principal strain ratios in this coordinate system are $R_{xy} = (1+e_x)/(1+e_y)$, $R_{xz} = (1+e_x)/(1+e_z)$ and $R_{yz} = (1+e_y)/(1+e_z)$ (Fig. 12a). The bulk principal strain measured parallel to the shortening direction is given by the known amount of convergence in each experiment, $(1+e_x) = [1+(W-W_o)/W_o]$ where $W$ and $W_o$ are the final and original widths of the orogen. The bulk principal strain measured parallel to the orogen can be estimated from the change in cross-sectional area of the unit in question as $(1+e_y) = A_o/A$ where $A_o$ and $A$ are the initial and final cross-sectional areas measured from digital images of serial sections. Assuming the model materials are incompressible, the vertical bulk principal strain is $(1+e_z) = 1/[(1+e_x)(1+e_y)]$, which can be checked against measurements of the change in vertical thickness of the unit from serial sections.

Values of $R_{yz}$ and $R_{xz}$ mantle lithosphere and ductile crust are plotted against $Ar$ in Figures 12b and c. Because of variations between strain ratios estimated for different serial sections, the values presented here are averages determined from bulk strains measured from serial sections in the inner two-thirds of the orogen (i.e., from profiles taken from the centre to two-thirds of the way out to the free edge). Data from the outer one-third has been omitted because strains in this region are highly variable and sensitive to the presence of the unconfined boundary.

The bulk strain ratios in Figure 12 provide a general view of the state of 3D finite strain within the models and therefore can be used to predict fabric elements in the ductile parts

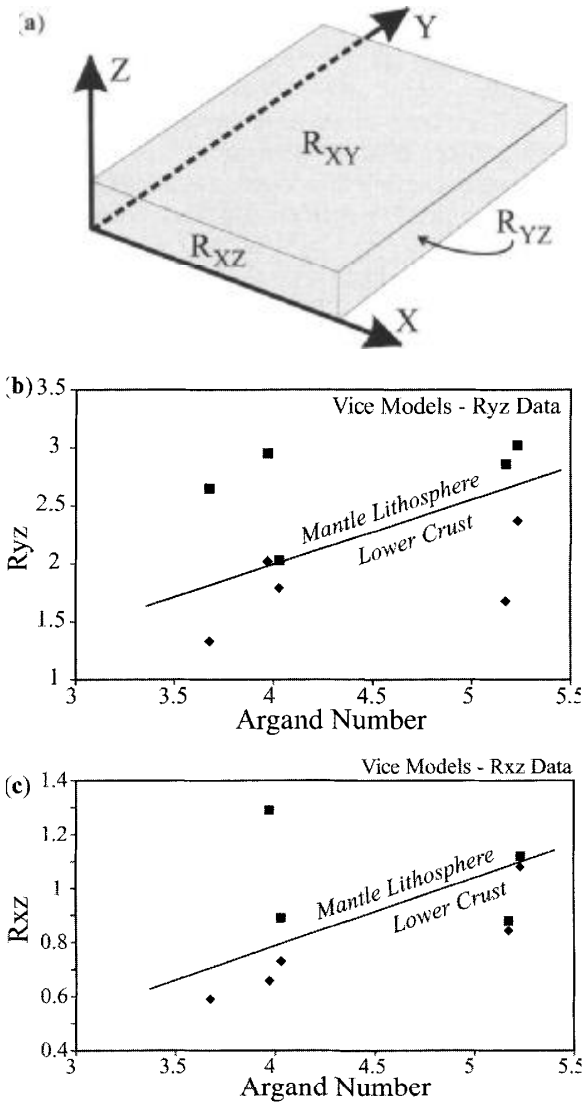


**Fig. 12.** (**a**) Coordinate system used for determination of bulk strains in analogue models. (**b**) $R_{xy}$ versus $Ar$ number for ductile crust and mantle lithosphere. (**c**) $R_{xz}$ versus $Ar$ number. Squares are bulk strain rations measured for mantle lithosphere, diamonds are ductile crust.

of natural vice orogens. Values of $R_{yz}$ increase with increasing $Ar$, reflecting the greater amount of orogen parallel flow in models with slower shortening rates and larger buoyancy forces (Fig. 12b). For each experiment, $R_{yz}$ is greater in the mantle lithosphere compared to the ductile crust. This reflects the presence of a vertical, orogen-parallel velocity gradient in the models, with the fastest rate of orogen parallel flow occurring at the base of the mantle lithosphere and the slowest at the brittle-ductile interface.

Values of $R_{xz} > 1$ indicate strain ellipsoids with horizontal $(1 + e_x)$ principal strains, while values $<1$ correspond to strain ellipsoids with vertical $(1 + e_z)$ principal strains. Because of the orogen parallel orientation of $(1 + e_y) > (1 + e_x)$, bulk flattening planes in the ductile crust and mantle lithosphere in the models are therefore either horizontal ($R_{xz} > 1$) or vertical and striking parallel to the orogen ($R_{xz} < 1$). In cases where $R_{xz} = 1$, the bulk strain ellipsoid will be prolate, with a long axis parallel to the orogen. $R_{xz}$ values increase with increasing $Ar$. This is because vertical thinning, $(1 + e_z)$, due to orogen parallel flow, becomes more important with increasing $Ar$. In individual experiments $R_{xz}$ is consistently greater in the mantle lithosphere than in the ductile crust, which again reflects the orogen-parallel vertical velocity gradient.

With exception of Experiment #33 ($Ar = 5.2$), comparison of $R_{xz}$ and $R_{yz}$ values indicates that bulk finite strains in the ductile crust are characterized by vertical orogen-parallel flattening planes with a strong orogen parallel stretch. In Experiment #33, which has the largest Ar number and a buoyant ductile crust, the bulk finite strain is close to prolate orogen parallel stretching in both the ductile crust and mantle lithosphere. Bulk finite strains in the mantle lithosphere in the other experiments vary from close to prolate with strong orogen parallel stretch to general flattening with a horizontal $xy$ plane. Bulk plane strains are not observed in any of the analogue models, in contrast to the 2D numerical experiments, which predict, by definition, plane strains.

### *Local variation in finite strain*

The above analysis is useful for predicting the bulk strain symmetry and intensity in the ductile crust and mantle lithosphere of laterally flowing vice orogens. However, examination of analogue model cross-sections (e.g., Fig. 8) and detailed local measurements of local thickness variations in these sections, indicate considerable heterogeneity in finite strain. Although the bulk finite strain in the ductile crust of most models is characterized by a vertical orogen parallel flattening plane, thickness variations indicate that local finite strain in this layer can vary between horizontal flattening and orogen parallel stretching to pure orogen parallel constriction. For example, $R_{xz}$ in Experiment #29 varies locally between 0.35 and 2.6, due entirely to strong vertical thickening (maximum $(1 + e_z) \sim 1.8$) and pronounced vertical thinning (minimum $(1 + e_z) \sim 0.23$) within an individual cross-section. Similar local finite strains are observed in all analogue experiments, indicating that deformation of the ductile crust and mantle lithosphere is characterized by strong across and along-strike variability.

## Summary of experimental findings

The major 3D structural characteristics of the vice models, as deduced by analysis of surface deformation patterns, topography data and cross-sections, are summarized in Figure 13. The major finding of the analogue and numerical experiments are as follows:

(1) 3D analogue models highlight the profound effect that syn-convergent orogen parallel flow can have on the development of structures at different levels of the crust (Fig. 13). The significance of these effects is highlighted by comparison to complementary 2D numerical experiments.

(2) Upper crustal deformation is decoupled from lower crustal strain. The boundary between these deformation regimes is transitional and occurs below the brittle-ductile interface in the models.

(3) Finite strain in the ductile crust and mantle lithosphere is characterized by orogen parallel stretching. Strain symmetries vary from horizontal flattening, to orogen parallel constriction, to vertical flattening normal to the shortening direction.

(4) Different upper crustal deformation styles are developed in models with non-buoyant versus buoyant lower crust. Due to the 'water bed' effect, models with buoyant lower crust display marked overflow of the orogenic crust over the bounding vice

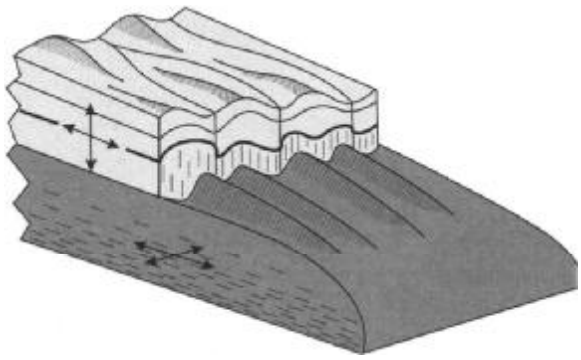

**Fig. 13.** Interpretation of the first order 3D structural characteristics of the vice experiments. Brittle upper crust is pale grey, ductile crust is dark grey. Arrows indicate orientation of bulk flattening strain ($xy$). Dashes indicate predicted orientation of metamorphic foliations.

blocks, while orogen parallel extension in the upper crust is accommodated by conjugate fracture systems and block rotations. Models with non-buoyant lower crust experience distributed upper crustal folding, and orogen parallel flow in the brittle crust is accommodated by a combination of homogenous stretching and displacements on vertical curvilinear transpression zones, whose kinematics are governed by the polarity of lower crustal flow, rather than the tectonic boundary conditions.

(5) The contribution of gravitational forces to the 3D evolution of the orogen increases with increasing *Ar* number. The *Ar* number controls the mean elevation attained by the orogen and the degree to which orogen-parallel flow will influence the cross-sectional geometry of the orogen. Comparison of analogue and numerical experimental results show that, in the central part of the orogen, amplitudes of folds and their surface expressions are similar in analogue and numerical models with lower *Ar*, while enhanced orogen-parallel flow in analogue models with higher *Ar* results in significant suppression or damping of these structures.

## Discussion

Implicit in the vice orogen concept is that the orogenic lithosphere is effectively decoupled from the mantle dynamics responsible for continued plate convergence (Ellis *et al.* 1998). Decoupling of the overriding orogen from the subducting plate appears to be favoured at late stages of collision, provided the orogenic crust becomes sufficiently weak due to the combined effects of thickening and build-up of radiogenic heat (Burg & Ford 1997; Ellis *et al.* 1998). Many large orogens record a similar evolution from initial accretion and collision leading to crustal thickening, followed by gravitationally driven collapse (Dewey *et al.* 1986; Malavieille 1993). In cases where radiogenic heating is great enough, partial melting of the mid to lower crust may occur, leading to enhanced decoupling and the possibility of local buoyancy effects due to the presence of low density felsic melts at depth (Rey 1993; Vanderhaeghe & Teyssier 2001). Hence, the structural and geophysical characteristics of many large orogens are dominated by boundary conditions and mechanical properties that developed at late stages of their history, rather than during the early subduction-related stages of accretion and initial thickening (e.g., Burg *et al.* 2002). The results of the vice model experiments reported above should therefore be evaluated in terms of their potential application to the late-stage structure and dynamics of large hot orogens. Key features of several natural vice orogens are reviewed below in light of the experiments.

### *The Superior vice: insights from project Lithoprobe*

The Superior Province of Canada is thought to have formed by progressive Neoarchean north to south accretion of juvenile volcanic arcs and continental crustal fragments onto a Mesoarchean nucleus (Williams 1990). The large-scale east-west belt structure of the Superior Province (Fig. 14), a variety of syn-accretionary plutonic and sedimentary rocks, together with the preservation of north dipping intra-crustal seismic fabrics and upper-mantle penetrating reflectors, records this *c.* 2720 to 2680 Ma accretionary history (e.g., Card & Ciesielski 1986; Calvert *et al.* 1995; White *et al.* 2003). The post-accretionary history of the Superior province is characterized by widespread granitic intrusion and the development of regional systems of upper crustal, vertical curvilinear shear zones (Fig. 14) (Leclair *et al.* 1993; Card & Poulsen 1998). This late (2660 to 2650 Ma) orogen-scale tectonothermal event coincides with final collision with a continental terrane in the south (Percival *et al.* 1994), thereby putting the entire Superior orogen into the jaws of a north-south vice.

Although generally interpreted in terms of a dextral transpressive regime (e.g., Williams *et al.* 1992), the regional-scale system of curvilinear shear zones have both dextral and sinistral horizontal displacements, depending on their orientation, and typically also record a strong zone normal flattening component (e.g., Wilkinson *et al.* 1999). Seismic reflection profiles indicate that the shear zones root into or are truncated by strong mid-crustal reflectivity fabrics (Jackson & Cruden 1995; Chroukroune *et al.* 1997; White *et al.* 2003). Field observations of tilted crustal sections indicate that mid-crustal reflectivity likely correlates with strong metamorphic fabrics and intrusive layering associated with an episode of east-west extensional flow under high temperature (amphibolite to granulite facies) conditions (Moser *et al.* 1996). U–Pb dating of metamorphic and igneous minerals associated with these fabrics and metamorphic mineral assemblages in upper crustal shear zones indicate that both mid-crustal extensional

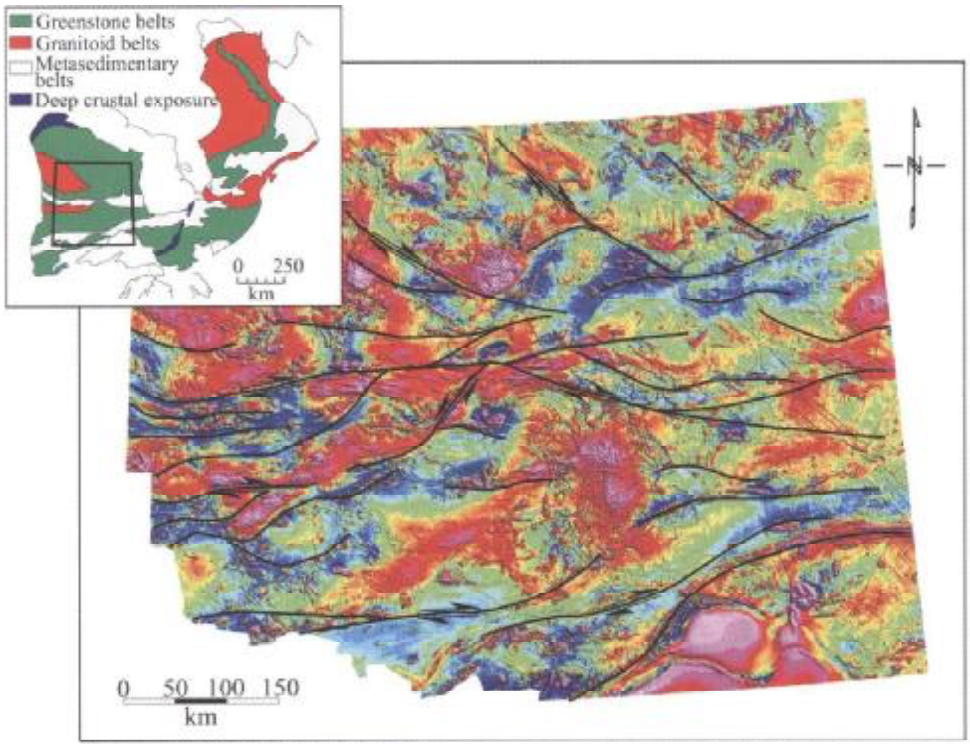


**Fig. 14.** Total field aeromagnetic map of the western part of the Superior Province (reprocessed after Gupta 1991). Blue tones are low magnetic intensity and red tones are high magnetic intensity. Major curvilinear shear zones, active in the late Archean (*c.* 2680–2650 Ma) are indicated with their sense of horizontal shear, where known. Inset: major subdivisions and location of the Superior Province with respect to the Great Lakes and Hudson's Bay. Box indicates location of the aeromagnetic map.

flow and upper-crustal deformation localized on transpressional shear zones were broadly contemporaneous at *c.* 2660 Ma (Moser *et al.* 1996; Wilkinson *et al.* 1999). Mid-crustal metamorphism continued episodically until *c.* 2600 Ma (Krogh 1993), suggesting that mid to lower crustal flow continued well after upper crustal deformation was locked in.

The geometry, kinematics and timing of upper crustal curvilinear shear zones in the Superior Province and their relationship to mid-crustal, orogen parallel extensional fabrics strongly resembles the characteristics of vice models with non-buoyant lower crust (Fig. 7b). The predominance of low pressure – low to medium temperature metamorphic assemblages within the Superior Province and the local preservation of prehnite-pumpellyite facies rocks indicate that orogenic relief and crustal thickening was likely suppressed. This scenario is most consistent with Experiment #33, which due to a high *Ar* number of 5.2 only increased in average elevation by *c.* 1 mm (equivalent to *c.* 2600 m) after 35% shortening (Fig. 5b), developed upper crustal curvilinear shear zones and upright folds, and experienced strong bulk mid crustal vertical flattening and orogen-parallel extensional strains (Fig. 12). Continued mid to lower crustal ductile flow in the Superior Province could be accounted for by top-down cooling (and stiffening) of a hot crust during continued orogen-parallel collapse.

### *Other Archean vice orogens*

The vice models also account for the structural features of other Neoarchean orogens. For example, the Yilgarn craton of Australia is also characterized by a system of orogen subparallel curvilinear shear zones that root into mid-crustal horizontal reflectors (e.g., Goleby *et al.* 2002). Structural studies indicate the shear zones are associated with orogen-parallel extension, triggered by weakening due to mid-crustal granite emplacement and subsequent gravitational collapse (i.e., increase in *Ar*) (Davis & Maidens 2003). The characteristics of Experiments #33 and #34 also best match those of the Yilgarn.

In contrast to the Superior and Yilgarn, late Archean deformation in the Dharwar craton, India, and Zimbabwe craton, Africa, are strongly

influenced by buoyancy effects in addition to the formation of upper crustal shear zones and folds (Choukroune *et al.* 1997; Treloar & Blenkinsop 1995). The structural style of the Dharwar craton is characterized by an anastomozing system of orogen sub-parallel shear zones which tend to be associated with synformal keels that wrap around elongate doubly plunging antiforms (domes) cored by granitic gneisses. Bouhallier *et al.* (1995) ascribe this strain pattern to lateral compression of thermally weakened lithosphere and simultaneous growth of gravity instabilities in the crust (diapirism). Such a scenario fits well with Experiment #32, which due to the combination of a buoyant lower crust and high *Ar* number, developed orogen sub-parallel shear zones that nucleated in syncline cores, and elongate anticlines cored and amplified by buoyant lower crustal material. Late Archean deformation of the Zimbabwe craton occurred due to compression caused by collision with the central zone of the Limpopo belt to the south (Treloar & Blenkinsop 1995). In contrast to the examples cited above, this led to the development of conjugate sets of regional NNE-striking sinistral and ESE-striking dextral shear zones that accompanied the intrusion of the Chilimanzi granites (Treloar & Blenkinsop 1995). This pattern is consistent with Experiment #29 (Fig. 7a) and suggests that the Chilimanzi granites were sufficiently voluminous to affect the bulk density of the mid crust. However, southward overflow at the Zimbawe craton–Limpopo belt margin is not observed, perhaps due to the protracted earlier tectonic history of this boundary (McCourt & Vearncombe 1992).

### *Proterozoic vice orogens*

Almost all Proterozoic orogens are wide (*c.* 500–1000 km), have significant restored length (>2000 km) and formed by convergence between older, strong Archean lithospheric blocks (e.g., Trans-Hudson orogen, White *et al.* 1999; Svecofennian orogen, Ehlers *et al.* 1993; East African-Antarctic orogen, Jacobs & Thomas 2004). As in the Archean, these orogens record an early history of accretionary tectonics, and are followed by a protracted latter stage of transpression under high temperature conditions (Gapais *et al.* 2005). Taking the Palaeoproterozoic Trans-Hudson orogen of Canada as an example, this late transpression is expressed by orogen sub-parallel curvilinear shear zones and pervasive metamorphic fabrics that record upper crustal vertical thickening and horizontal extension under ductile conditions. Seismic reflection data indicates that vertical upper crustal shear zones root into strong mid-crustal horizontal reflectivity (Hajnal *et al.* 1996). Seismic and structural studies of the eastern boundary of the Trans-Hudson with the Archean Superior Province indicate an early phase of outward thrusting (overflow), followed by steepening and overturning of the boundary zone (White *et al.* 1999). Although the latter feature is not observed in the vice models, the late orogenic structure of the Trans Hudson and other Proterozoic orogens fits well with experiments with non-buoyant lower crust. Given the development of higher pressure metamorphic assemblages and the longevity of high temperature thermal conditions (Gapais *et al.* 2005), Experiment #34 (Figs 7b and 9), with a lower *Ar* number and therefore greater thickening under more ductile lower crustal conditions, applies best to these orogens.

### *Phanerozoic vice orogens*

Elements of vice tectonics can also be recognized in many Palaeozoic to Recent orogenic systems. The original vice models of Ellis *et al.* (1998) were inspired by structural and geophysical features of the Newfoundland Appalachians, where weak lithosphere of the Dunnage zone is squeezed between the strong vice blocks of the Avalon and Humber zones. The Variscan orogeny of Europe developed in response to convergence between Laurentia and Gondwana in the late Palaeozoic (Vanderhaeghe & Teyssier 2001). This convergence led to the development of a major system of orogen sub-parallel curvilinear shear zones and associated sedimentary basins and well-developed mid-crustal horizontal reflectivity linked to partial melting, granite intrusion and extensional flow (Rey 1993; Malavieille 1994; Vanderhaeghe & Teyssier 2001).

Vice tectonics are also apparent in the Alpine-Himalayan system, particularly in Tibet and Anatolia, which are currently experiencing eastward and westward escape in response to collision between Asia with India and Arabia, respectively (Tapponier *et al.* 1982; Dewey *et al.* 1986). As in the vice orogens cited above, orogen parallel extension in the upper crust is accommodated by displacements on systems of curvilinear shear zones that based on available seismic data in Tibet, root into a mid-crust characterized by horizontal reflectivity and the presence of partial melts (Nelson *et al.* 1996; Vanderhaeghe & Teyssier 2001). Although much recent attention has been focussed on orogen perpendicular channel flow of mid-crustal material facilitated by erosion at the southern side of the Himalaya

(e.g., Beaumont *et al.* 2001), the larger scale response of the Tibetan plateau to vice-like convergence between India and Asia is similar to the models presented here and characterized by orogen parallel ductile flow of the lower crust and development of related vertical shear zones in the upper crust (Royden *et al.* 1997).

Likewise, the East Anatolia high plateau appears to be a particularly good example of an active vice orogen. Following an earlier Tertiary accretionary history, this region has experienced vice-like compression between stronger lithospheric blocks represented by the Rhodope-Pontide arc and Arabian plate for the last 11 Ma (Şengör *et al.* 2003). Slab break off at *c.* 11 Ma led to decoupling of the orogenic lithosphere from mantle dynamics as well as crustal weakening and magmatic activity (Keskin 2003). Continued convergence has resulted in the development of the East Anatolia high plateau (mean elevation *c.* 2 km; viz. Experiment #32), significant westward lateral extrusion of the Anatolian block, as well as the development of upper mantle shear wave splitting anomalies that are consistent with orogen parallel flow of the asthenosphere under East Anatolia (Dewey *et al.* 1986; Sandvol *et al.* 2003; Şengör *et al.* 2003).

### *Implications for fabric studies in orogens*

The discussion above focuses on the large-scale surface characteristics and cross-sectional structure of possible vice orogens. Our experiments also provide potential insight on the 3D distribution of strain, fabrics and mesoscopic structures in orogens. For example, field studies find that 'plane strain is more the exception than the rule' in ductilely deformed rocks in orogenic belts (Huddleston 1999) with finite strain measurements indicating a complete spectrum from L-, through L-S and S-tectonites (Ramsay & Huber 1987). The experiments reported here demonstrate that significant variations in finite strain can be achieved by local variation in the degree of vertical thinning or thickening combined with lateral variation in the amount of orogen parallel extension. In particular, they provide insight into the development of orogen parallel stretching lineations observed in the deeper, crystalline parts of some orogens (e.g., Gapais *et al.* 1992; Hatcher 2001) as well as the observation of extension along orogen parallel fold axes (Mancktelow & Pavlis 1994).

A significant feature of all the vice experiments reported here is a transition from upper crustal folding and vertical shear zone development to lower crustal, orogen parallel ductile flow (Fig. 13). The boundary between these regimes in the models is not a discrete detachment; rather it is gradational between the folded brittle-ductile interface and the underlying ductile crust. This is likely an artefact of the model construction: in nature the brittle-ductile transition occurs over a finite thickness of middle crust and field observations indicate that boundaries between 'partitioned' upper and lower crustal structural regimes (Oldow *et al.* 1989; Royden 1996) occur across well-defined detachment structures, often associated with discrete mechanical features such as lithological contacts or magmatic softening horizons (e.g., Collins & Vernon 1991; Axen *et al.* 1998; Klepeis *et al.* 2004).

The common observation of mid to lower crustal seismic reflectivity in orogens is predicted by the orogen parallel flow observed in the models (see also Meissner & Mooney 1998). Because of the weak rheology employed and the vertical velocity gradient observed in the models, orogen parallel stretching is greater in the mantle lithosphere of the experiments than in the ductile crust (Fig. 12b). Strong orogen parallel stretching in the mantle lithosphere and underlying asthenosphere of natural orogens may impart a sufficient degree of anisotropy to cause seismic shear wave splitting anomalies (e.g., Vauchez & Nicolas 1991; Sandvol *et al.* 2003).

## Conclusions

Simple vice models provide insight into how different strain regimes can develop at different levels of the crust, in response to boundary conditions, rheological structure and gravitational forces. The experiments provide a framework for the interpretation of a diverse array of structural and geophysical observations in Archean to Recent vice orogens (e.g., upper crustal vs. lower crustal structural regimes; finite strain variation, seismic reflectivity patterns; upper mantle seismic anisotropy). The results also illustrate how in some cases interpretation of local structures in the field (e.g., transpressive shear zones, deep crustal extensional fabrics) might lead to erroneous inferences about palaeotectonic boundary conditions (e.g., oblique convergence; post-orogenic collapse).

The University of Toronto Tectonic Laboratory has been funded by Discovery, Equipment and Lithoprobe Grant programs of the Natural Sciences and Engineering Research Council of Canada (NSERC). We are grateful to D. Boutelier and W. M. Schwerdtner for comments on a draft of the manuscript, and A. Babeyko, S. Ellis and W. Schellart for thorough and constructive reviews, all of which led to substantial improvements, clarifications and corrections. This is Lithoprobe contribution #1412.

## References


AXEN, G. J., SELVERSTONE, J., BYRNE, T. & FLETCHER, J. M. 1998. If the strong crust leads, will the weak crust follow? *GSA Today*, **8**, 1–8.

BAILEY, R. C. 1999. Gravity-driven continental overflow and Archaean tectonics. *Nature*, **398**, 413–415.

BAILEY, R. C. 2001. Dynamical analysis of continental overflow. *Journal of Geodynamics* **31**, 293–310.

BEAUMONT, C., JAMIESON, R. A., NGUYEN, M. H. & LEE, B. 2001. Himalayan tectonics explained by extrusion of a low-viscosity crustal channel coupled to focused surface denudation. *Nature*, **414**, 738–742.

BENES, V. & DAVY, P. 1996. Modes of continental lithospheric extension: experimental verification of strain localization processes. *Tectonophysics*, **254**, 69–87.

BLANKENBACH, B. & BUSSE, F. *ET AL.* 1989. A benchmark comparison for mantle convection codes. *Geophysical Journal International*, **98**, 23–38.

BURG, J.-P. & FORD, M. 1997. Orogeny through time: an overview. *In*: BURG, J.-P. & FORD, M. (eds) *Orogeny Through Time*, Geological Society Special Publication, **121**, 1–17.

BURG, J.-P., SOKOUTIS, D. & BONINI, M. 2002. Model-inspired interpretation of seismic structures in the Central Alps: crustal wedging and buckling at mature stage of collision. *Geology*, **30**, 643–646.

BOUHALLIER, H., CHARDON, D. & CHOUKROUNE, P. 1995. Strain patterns in Archaean dome and basin structures: the Dharwar craton (Karnakate, South India). *Earth and Planetary Science Letters*, **135**, 57–75.

CALVERT, A. J., SAWYER, E. W., DAVIS, W. J. & LUDDEN, J. N. 1995. Archaean subduction inferred from a mantle suture in the Superior Province. *Nature*, **375**, 670–674.

CARD, K. D. & CIESIELSKI, A. 1986. DNAG #1 subdivisions of the Superior Province of the Canadian Shield. *Geoscience Canada*, **13**, 5–13.

CARD, K. D. & POULSEN, K. H. 1998. Geology and mineral deposits of the Superior province of the Canadian Shield. *In*: LUCAS, S. B., ST. ONGE, M. R. (eds) *Geology of the Precambrian Superior and Grenville Provinces and Precambrian Fossils of North America*, Geological Society of America, **C1**, 13–204.

CHOUKROUNE, P., BOUHALLIER, H. & ARNDT, N. T. 1995. Soft lithosphere during periods of Archaean crustal growth or crustal reworking. *In*: COWARD, M. P. & REIS, A. C. (eds) *Early Precambrian Processes*, Geological Society Special Publication, **95**, 67–86.

CHOUKROUNE, P., LUDDEN, J. N., CHARDON, D., CALVERT, A. J. & BOUHALLIER, H. 1997. Archaean crustal growth and tectonic processes: a comparison of the Superior Province, Canada and the Dharwar Craton, India. *In*: BURG, J.-P. & FORD, M. (eds) *Orogeny Through Time*, Geological Society Special Publication, **121**, 63–98.

COBBOLD, P. R. & JACKSON, M. P. A. 1992. Gum rosin (colophony): a suitable material for thermomechanical modeling of the lithosphere. *Tectonophysics*, **210**, 255–271.

COLLINS, W. J. & VERNON, R. H. 1991. Orogeny associated with anticlockwise P-T-t paths: evidence from low-P, high-T metamorphic terranes in the Arunta Inlier, central Australia. *Geology*, **19**, 835–838.

DAVIS, B. K. & MAIDENS, E. 2003. Archaean orogen-parallel extension: evidence from the northern Eastern Goldfields Province, Yilgarn Craton. *Precambrian Research*, **127**, 229–248.

DAVY, P. & COBBOLD, P. R. 1988. Indentation tectonics in nature and experiment, 1. Experiments scaled for gravity. *Bulletin of the Geological Institute, University of Uppsala, New Series*, **14**, 129–141.

DAVY, P. & COBBOLD, P. R. 1991. Experiments on shortening of a 4-layer model of the continental lithosphere. *Tectonophysics*, **188**, 1–25.

DEWEY, J. F., HEMPTON, M. R., KIDD, W. S. F., SAROGLU, F. & ŞENGÖR, A. M. C. 1986. Shortening of continental lithosphere: the neotectonics of Eastern Anatolia – a young collision zone. *In*: COWARD, M. P. & RIES, A. C. (eds) *Collision Tectonics*, Geological Society Special Publication, **19**, 3–36.

DIXON, J. M. & SUMMERS, J. M. 1983. Patterns of total and incremental strain in subsiding troughs; experimental centrifuged models of inter-diapir synclines. *Canadian Journal of Earth Sciences*, **20**, 1843–1861.

DIXON, J. M. & SUMMERS, J. M. 1986. Another word on the rheology of silicone putty; Bingham. *Journal of Structural Geology*, **8**, 593–595.

EHLERS, C., LINDROOS, A. & SELONEN, O. 1993. The late Svecofennian granite-migmatite zone of southern Finland – a belt of transpressive deformation and granite emplacement. *Precambrian Research*, **64**, 295–309.

ELLIS, S., BEAUMONT, C., JAMIESON, R. A. & QUINLAN, G. 1998. Continental collision including a weak zone: The vise model and its application to the Newfoundland Appalachians. *Canadian Journal of Earth Sciences*, **35**, 1323–1346.

ENGLAND, P. & HOUSEMAN, G. 1986. Finite strain calculations of continental deformation 2. Comparison with the India-Asia collision zone. *Journal of Geophysical Research*, **91** (B3), 3664–3676.

ENGLAND, P. C. & MCKENZIE, D. P. 1982. A thin viscous sheet model for continental deformation. *Geophysical Journal of the Royal Astronomical Society*, **70**, 295–321.

FULLSACK, P. 1995. An arbitrary Lagrangian-Eulerian formation for creeping flows and its application in tectonic models. *Geophysical Journal International*, **120**, 1–23.

GAPAIS, D., PECHER, A., GILBERT, E. & BALLEVRE, M. 1992. Synconvergence spreading of the higher Himalaya crystalline in Ladakh. *Tectonics*, **11**, 1045–1056.

GAPAIS, D., POTREL, A., MACHADO, N. & HALLOT, E. 2005. Kinematics of long-lasting Palaeoproterozoic transpression within the Thompson Nickel Belt (Manitoba, Canada). *Tectonics*. **24**, TC3002, DOI:10.1029/2004TC001700.

GARDE, A., CHADWICK, B., GROCOTT, J., HAMILTON, M. A., MCCAFFREY, K. J. W. & SWAGER, C. P. 2002. Mid-crustal partitioning and attachment during oblique convergence in an arc system, Palaeoproterozoic Ketilidian orogen, southern Greenland. *Journal of the Geological Society, London*, **159**, 247–261.

GILBERT, E. & MERLE, O. 1987. Extrusion and radial spreading beyond a closing channel. *Journal of Structural Geology*, **9**, 481–490.

GOLEBY, B. R., KORSCH, R. J., FOMIN, T., BELL, B., NICOLL, M. G., DRUMMOND, B. J. & OWEN, A. J. 2002. Preliminary 3-D geological model of the Kalgoorlie region, Yilgarn Craton, Western Australia, based on deep seismic-reflection and potential-field data. *Australian Journal of Earth Sciences*, **49**, 917–933.

GUPTA, V. K. 1991. Shaded image of total magnetic field of Ontario, west central sheet. *Ontario Geological Survey*, Map **M2585**, scale 1:1,000,000.

HAJNAL, Z., LUCAS, S. B., WHITE, D. J., LEWRY, J., BEZDAN, S., STAUFFER, M. R. & THOMAS, M. D. 1996. Seismic reflection images of strike-slip faults and linked detachments in the Trans-Hudson Orogen. *Tectonics*, **15**, 427–439.

HATCHER, R. D. Jr. 2001. Rheological partitioning during multiple reactivation of the Palaeozoic Brevard Fault Zone, Southern Appalachians, USA. *In*: HOLDSWORTH, R. E., STRACHAN, R. A., MAGLOUGHLINE, J. F. & KNIPE, R. J. (eds) *The Nature and Tectonic Significance of Fault Zone Weakening*. Geological Society of London, Special Publications, **186**, 257–271.

HIRT, C. W., AMSDEN, A. A. & COOK, J. L. 1974. An arbitrary Lagrangian-Eulerian computing method for all flow speeds. *Journal of Computational Physics*, **14**, 227–253.

HIRTH, G. & KOHLSTEDT, D. L. 1996. Water in the oceanic upper mantle: implications for rheology, melt extraction and the evolution of the lithosphere. *Earth and Planetary Science Letters*, **144**, 93–108.

HOUSEMAN, G. & ENGLAND, P. 1986. Finite strain calculations of continental deformation 1. Method and general results for convergent zones. *Journal of Geophysical Research*, **91**(B3), 3651–3663.

HOUSEMAN, G. A. & MOLNAR, P. 1997. Gravitational (Rayleigh-Taylor) instability of a layer with non-linear viscosity and convective thinning of continental lithosphere. *Geophysical Journal International*, **128**, 125–150.

HUDLESTON, P. J. 1999. Strain compatibility and shear zones: is there a problem? *Journal of Structural Geology*, **21**, 923–932.

JACKSON, J. 2002. Faulting, flow, and the strength of the continental lithosphere. *International Geology Review*, **44**, 39–61.

JACKSON, S. & CRUDEN, A. R. 1995. Formation of the Abitibi greenstone belt by arc-trench migration. *Geology*, **23**, 471–474.

JACOBS, J. & THOMAS, R. J. 2004. Himalyan-type indenter-escape tectonics model for the southern part of the late Neoproterozoic-early Palaeozoic East African-Antarctic orogen. *Geology*, **32**, 721–724.

KESKIN, M. 2003. Magma generation by slab steepening and breakoff beneath a subduction-accretion complex: an alternative model for collision-related volcanism in Eastern Anatolia, Turkey. *Geophysical Research Letters*, **30**, 8046, DOI 10.1029/2003GL018019.

KLEPEIS, K. A., CLARKE, G. L., GEHRELS, G. & VERVOORT, J. 2004. Processes controlling vertical coupling and decoupling between the upper and lower crust of orogens: results from Fiordland, New Zealand. *Journal of Structural Geology*, **26**, 765–791.

KOHLSTEDT, D. L., EVANS, B. & MACKWELL, S. J. 1995. Strength of the lithosphere: constraints imposed by laboratory experiments. *Journal of Geophysical Research*, **100**, 17587–17602.

KROGH, T. E. 1993. High precision U-Pb ages for granulite metamorphism and deformation in the Archean Kapuskasing structural zone, Ontario: implications for structure and development of the lower crust. *Earth and Planetary Science Letters*, **119**, 1–18.

LECLAIR, A. D., ERNST, R. E. & HATTORI, K. 1993. Crustal-scale auriferous shear zones in the central Superior province, Canada. *Geology*, **21**, 399–402.

MACKWELL, S. J., ZIMMERMAN, M. E. & KOHLSTEDT, D. L. 1998. High-temperature deformation of dry diabase with application to tectonics on Venus. *Journal of Geophysical Research*, **103** (B1), 975–984.

MAGGI, A., JACKSON, J. A., MCKENZIE, D. & PRIESTLEY, K. 2000. Earthquake focal depths, effective elastic thickness, and the strength of the continental lithosphere. *Geology*, **28**, 495–498.

MALAVIEILLE, J. 1993. Late orogenic extension in mountain belts: insights from the Basin and Range and the late Paleozoic Variscan belt. *Tectonics*, **12**, 1115–1130.

MANCKTELOW, N. S. & PAVLIS, T. L. 1994. Fold-fault relationships in low-angle detachment systems. *Tectonics*, **13**, 668–685.

MCCOURT, S. & VEARNCOMBE, J. R. 1992. Shear zones of the Limpopo Belt and adjacent granitoid-greestone terranes: implications for late Archaean collision tectonics in southern Africa. *Precambrian Research*, **55**, 553–570.

MEISSNER, R. & MOONEY, W. 1998. Weakness of the lower continental crust: a condition for delamination, uplift and escape. *Tectonophysics*, **296**, 47–60.

MITROVICA, J. X. & FORTE, A. M. 1997. The radial profile of mantle viscosity: results from the joint inversion of convection of post-glacial rebound observables. *Journal of Geophysical Research*, **102**, 2751–2769.

MERLE, O. 1989. Strain models within spreading nappes. *Tectonophysics*, **165**, 57–71.

MOSER, D. E., HEAMAN, L. M., KROGH, T. E. & HANES, J. A. 1996. Intracrustal extension of an Archean orogen revealed using single-grain U-Pb geochronology. *Tectonics*, **15**, 1093–1109.

NELSON, K. D. and ZHAO, W. *ET AL.* 1996. Partially molten middle crust beneath southern Tibet:

synthesis of project INDEPTH results. *Science*, **274**, 1684–1688.

OLDOW, J. S., BALLY, A. W., Avé LALLEMANT, H. G. & LEEMAN, W. P. 1989. Transpression, orogenic float, and lithospheric balance. *Geology*, **18**, 991–994.

PERCIVAL, J. A., STERN, R. A., SKULSKI, T., CARD, K. D., MORTENSEN, J. K. & BÉGIN, N. J. 1994. Minto block, Superior province: missing link in deciphering assembly of the craton at 2.7 Ga. *Geology*, **22**, 839–842.

POLIAKOV, A. & PODLADCHIKOV, Y. 1992. Diapirism and topography. *Geophysical Journal International*, **109**, 553–564.

PYSKLYWEC, R. & CRUDEN, A. R. 2004. Coupled crust-mantle dynamics and intraplate tectonics: two-dimensional numerical and three-dimensional analogue modelling. *Geochemistry, Geophysics, Geosystems ($G^3$)*, **5**(10), Q10003, DOI 10.1029/2004GC000748.

RAMSAY, J. G. & HUBER, M. I. 1987. *The techniques of modern structural geology. Volume 2. Folds and Fractures.* Academic Press.

RATSCHBACHER, L., MERLE, O., PHILLIPE, D. & COBBOLD, P. 1991. Lateral extrusion in the Eastern Alps: Part I. Boundary conditions and experiments scaled for gravity. *Tectonics*, **10**, 245–256.

REY, P. 1993. Seismic and tectono-metamorphic characters of the lower continental crust in Phanerozoic areas: a consequence of post-thickening extension. *Tectonics*, **12**, 580–590.

REY, P., VANDERHAEGHE, O. & TEYSSIER, C. 2001. Gravitational collapse of continental crust: Definitions, regimes, mechanisms and modes. *Tectonophysics*, **342**, 435–449.

ROSS, G. M., MILKEREIT, B., EATON, D., WHITE, D., KANASEWICH, E. R. & BURIANYK, M. J. A. 1995. Palaeoproterozoic collision orogen beneth the western Canada sedimentary basin imaged by Lithoprobe crust seismic-reflection data. *Geology*, **23**, 195–199.

ROSSI, D. & STORTI, F. 2003. New artificial granular materials for analogue laboratory experiments: aluminium and siliceous microspheres. *Journal of Structural Geology*, **25**, 1893–1899.

ROYDEN, L. 1996. Coupling and decoupling of crust and upper mantle in convergent orogens: implications for strain partitioning in the crust. *Journal of Geophysical Research*, **101**(B8), 17679–17705.

ROYDEN, L., BURCHFIEL, B. C., KING, R. W., WANG, E., CHEN, Z., SHEN, F. & LIU, Y. 1997. Surface deformation and lower crustal flow in eastern Tibet. *Science*, **276**, 788–790.

SANDVOL, E. & TURKELLI, N. *ET AL.* 2003. Shear wave splitting in a young continent-continent collision: An example from Eastern Turkey. *Geophysical Research Letters*, **30**, 8041, DOI 10.1029/2003GL017390.

SCHELLART, W. P. 2000. Shear test results for cohesion and friction coefficients for different granular materials: scaling implications for their usage in analogue modelling. *Tectonophysics*, **324**, 1–16.

SCHELLART, W. P. & LISTER, G. S. 2004. Tectonic models for the formation of arc-shaped convergent zones and backarc basins. *In*: SUSSMAN, A. J. & WEIL, A. B. (eds) *Orogenic curvature: integrating palaeomagnetic and structural analysis*, Geological Society of America Special Paper, **383**, 237–258.

ŞENGÖR, A. M. C., ÖZEREN, S., GENÇ, T. & ZOR, E. 2003. East Anatolia high plateau as a mantle-supported, north-south shortened domal structure. *Geophysical Research Letters*, **30**, 8045, DOI 10.1029/2003GL017858.

SEYFERTH, M. & HENK, A. 2004. Syn-convergent exhumation and lateral extrusion in continental collision zones – insights from three-dimensional numerical models. *Tectonophysics*, **382**, 1–29.

SOKOUTIS, D. 1990. Experimental mullions at single and double interfaces. *Journal of Structural Geology*, **12**, 365–373.

SOKOUTIS, D., BONINI, M., MEDVEDEV, S., BOCCALETTI, M., TALBOT, C. J. & KOYI, H. 2000. Indentation of a continent with a built-in thickness change: experiment and nature. *Tectonophysics*, **320**, 243–270.

TAPPONNIER, P., PELTZER, G., LA DAIN, A. Y., ARMIJO, R. & COBBOLD, P. 1982. Propagating extrusion tectonics in Asia: New insights from simple experiments with plasticene. *Geology*, **10**, 611–616.

TEYSSIER, C. & WHITNEY, D. 2002. Gneiss domes and orogeny. *Geology*, **30**, 1139–1142.

TOUSSAINT, G., BUROV, E. & JOLIVET, L. 2004. Continental plate collision: unstable vs. stable slab dynamics. *Geology*, **32**, 33–36.

TRELOAR, P. J. & BLENKINSOP, T. G. 1995. Archaean deformation patterns in Zimbabwe: true indicators of Tibetan-style crustal extrusion or not? *In*: COWARD, M. P. & REIS, A. C. (eds) *Early Precambrian Processes*, Geological Society Special Publication, **95**, 87–108.

VANDERHAEGHE, O. & TEYSSIER, C. 2001. Partial melting and flow of orogens. *Tectonophysics*, **342**, 451–472.

VAN KEKEN, P. E., KING, S. D., SCHMELING, H., CHRISTENSEN, U. R., NEUMEISTER, D. & DOIN, M. P. 1997. A comparison of methods for the modeling of thermochemical convection. *Journal of Geophysical Research*, **102**, 22477–22496.

VAUCHEZ, A. & NICOLAS, A. 1991. Mountain building: strike-parallel motion and mantle anisotropy. *Tectonophysics*, **185**, 183–201.

WEIJERMARS, R. 1986. Flow behaviour and physical chemistry of bouncing putties and related polymers in view of tectonic laboratory. *Tectonophysics*, **124**, 325–358.

WHITE, D. J., JONES, A. G., LUCAS, S. B. & HAJNAL, Z. 1999. Tectonic evolution of the Superior boundary zones from coincident seismic reflection and magnetotelluric profiles. *Tectonics*, **18**, 430–451.

WHITE, D. J., MUSACCHIO, G., HELMSTAEDT, H. H., HARRAP, R. M., THURSTON, P. C., VAN DER VELDEN, A. & HALL, K. 2003. Images of a lower-crustal oceanic slab: direct evidence for tectonic accretion in the Archean western Superior province. *Geology*, **31**, 997–1000.

WILKINSON, L., CRUDEN, A. & KROGH, T. 1999. Timing and kinematics of post-Timiskaming deformation within the Larder Lake-Cadillac deformation zone, SW Abitibi greenstone belt, Ontario, Canada. *Canadian Journal of Earth Sciences*, **36**, 627–647.

WILLIAMS, H. R. 1990. Subprovince accretion tectonics in the south-central Superior Province. *Canadian Journal of Earth Sciences*, **27**, 570–581.

WILLIAMS, H. R., SCOTT, G. M., THURSTON, P. C., SUTCLIFFE, R. H., BENNET, G., EASTON, R. M. & ARMSTRONG, D. K. 1992. Tectonic evolution of Ontario: Summary and Synthesis. In: *Geology of Ontario*, Special volume **4**, part 2, Ontario Geological Survey, Canada, 1255–1332.

# Relative importance of trenchward upper plate motion and friction along the plate interface for the topographic evolution of subduction-related mountain belts

ANDREA HAMPEL & ADRIAN PFIFFNER
*Institute of Geological Sciences, University of Bern, Baltzerstr 1, 3012 Bern, Switzerland (e-mail: andrea@geo.unibe.ch)*

**Abstract:** We present finite-element models that investigate the relative importance of both trenchward motion of the upper plate and interplate coupling for the development of topography at convergent margins. Commonly, the role of a trenchward moving continental plate for the growth of topography is neglected in both modelling and field studies. Instead, forces exerted by the downgoing plate on the continental plate as well as interplate coupling are thought to be responsible for the deformation of the upper plate. Our model set-up includes an oceanic plate, which is in contact with a continental plate along a frictional plate interface and driven by slab pull. Both lithospheres have an elasto-visco-plastic rheology. The models demonstrate that friction along the plate interface can only lead to a high topography if the upper plate is moving toward the trench. Without such a trenchward advance, no high topography is generated, as the upper plate subsides owing to the drag exerted by the subducting plate. Increasing the coefficient of friction only amplifies the drag and increases the amount of subsidence. Our findings imply that trenchward motion of the continental plate plays a key role for the development of mountain belts at convergent margins; subduction of an oceanic plate even with high interplate coupling cannot explain the formation of Andean-type orogens.

The growth of topography at convergent margins like the Andean subduction zone has commonly been explained from a point of view that centres on the nature and behaviour of the subducting oceanic plate (Jordan *et al.* 1983; Bott *et al.* 1989; Dewey & Lamb 1992; Shemenda 1993; Willett *et al.* 1993; Gephart 1994; Huang *et al.* 1998; Stern 2002; Lamb & Davis 2003; Nicol & Beavan 2003). In particular, the age and buoyancy of the oceanic plate, its angle of subduction or the ratio between the velocity of plate convergence and of subduction have been drawn upon to explain different styles of deformation in the upper plate (e.g., Molnar & Atwater 1978; England & Wortel 1980; Royden 1993). Furthermore, the material flow in the wedge of mantle between the slab and the overriding plate as well as the viscosity of the mantle wedge have been inferred to modify the topography of the upper plate (Wdowinski *et al.* 1989; Billen & Gurnis 2001). This view assigns a passive role to the overriding plate, which is assumed to react to the forces exerted by the oceanic plate, and neglects the motion of the continental plate.

The use of a framework with an oceanic plate actively moving away from a spreading ridge and sliding down a fixed subduction slot beneath a continent has been criticized by Hamilton (1995, 2003), who emphasizes that oceanic plates subduct because their slabs sink into the mantle owing to their higher density. Hence, the slab pull force acts only in the vertical direction and generally leads to rollback of the slab (e.g., Forsyth & Uyeda 1975; Hamilton 2003). As a consequence, subduction zones (like other plate boundaries) are not stationary and, moreover, downgoing oceanic plates cannot compress their associated upper plates and induce intraplate shortening (Hamilton 1995, 2003). In Jarrard's (1986) comprehensive statistical analysis of the relations between subduction parameters, this is manifested in a poor correlation between the upper plate's strain regime, and the age and other characteristics of the downgoing plate. In contrast, a high correlation exists between the upper plate's strain regime and its absolute motion, which suggests that among the independent subduction parameters the motion of the upper plate is a first-order parameter to control the deformation of the upper plate (Jarrard 1986; Heuret & Lallemand 2005). Likewise, other studies inferred a close relation between the absolute motion

*From*: BUITER, S. J. H. & SCHREURS, G. (eds) 2006. *Analogue and Numerical Modelling of Crustal-Scale Processes*. Geological Society, London, Special Publications, **253**, 105–115.
0305-8719/06/$15.00 

of the overriding plate and backarc extension or shortening (Chase 1978; Uyeda & Kanamori 1979; Ruff & Kanamori 1980; Scholz & Campos 1995; Conrad *et al.* 2004).

Another first-order factor discussed as relevant for mountain building in the upper plate is the degree of interplate coupling (e.g., Dmowska *et al.* 1996; Cattin *et al.* 1997; Wang & He 1999; Bevis *et al.* 2001; Husson & Ricard 2004; Yanez & Cembrano 2004). In fact, the topographic profile of the upper plate has been used to *infer* high coefficients of friction and shear stresses along a plate interface, for example for the Andes (Lamb & Davis 2003) or northeast Japan (Huang *et al.* 1997). While Lamb & Davis (2003) and Huang *et al.* (1997) ultimately link the high interplate coupling to the subduction of the oceanic plate, other studies point out the close correlation between high seismic coupling and the trenchward advance of the upper plate (Uyeda & Kanamori 1979; Ruff & Kanamori 1980; Conrad *et al.* 2004). Numerical modelling studies on the influence of friction on topography also reached different conclusions about the role of friction in a subduction system (Cattin *et al.* 1997; Hassani *et al.* 1997; Buiter *et al.* 2001). Hassani *et al.* (1997) constructed finite-element models and assigned an effective elastic thickness to the lower and upper plate. Their upper plate was fixed, while a horizontal velocity and a slab pull force were imposed on the ridgeward and trenchward ends of the oceanic plate, respectively. The models were calculated with friction coefficients of $\mu = 0$, 0.1, 0.2 and 0.5. For all friction coefficients, Hassani *et al.* (1997) found that friction drags the upper plate down with the subducting plate, thereby inhibiting the growth of high topography. These results have been confirmed by Buiter *et al.* (2001) for a friction coefficient of $\mu = 0.1$ in a similar set-up; in another model run with a frictionless plate interface, Buiter *et al.* (2001) observed an upward vertical displacement for a trenchward advancing upper plate. In contrast to Hassani *et al.* (1997) and Buiter *et al.* (2001), Cattin *et al.* (1997) used a model in which the ocean plate subducts with a prescribed velocity and slab curvature beneath an elasto-visco-plastic upper plate, which moves toward the trench at a constant velocity. They concluded that friction coefficients of $\mu \leq 0.2$ are required to create and maintain high topography in the upper plate; only friction coefficients of $\mu > 0.2$ tend to drag the upper plate down. The contrary predictions of the different models with respect to interplate coupling, upper plate motion and the development of topography are not easily resolved, since Cattin *et al.* (1997) incorporate a trenchward moving overriding plate but do not account for slab pull, whereas the models of Hassani *et al.* (1997) and Buiter *et al.* (2001) consider slab pull but in a setting with a moving oceanic and fixed upper plate. The differences in the set-ups and results point, however, to the critical role that the delicate interaction between slab pull, interplate coupling, and motion of the upper plate might play for the deformation and the topographic evolution of the overriding plate.

Our study aims to evaluate the role of two parameters, trenchward upper plate motion and interplate coupling, for the growth of topography in the upper plate. We use finite-element models that include an oceanic plate which is driven by slab pull, and is in contact with a continental plate along a frictional plate interface. Following Cattin *et al.* (1997), Hassani *et al.* (1997), and Buiter *et al.* (2001), we represent the sub-lithospheric mantle by applying a basal boundary condition because this allows to study the interaction of the oceanic and continental lithospheres in a numerically feasible way. Two sets of models, in which the upper plate is fixed or moves toward the trench, will be presented. The models are not intended to represent any specific subduction zone but to shed light on the relative importance of the two parameters, upper plate motion and interplate coupling.

## Model set-up

The model consists of a 4000 km-long oceanic plate with a thickness of 80 km and a 2000 km-long continental lithosphere, which is divided into a 30 km-thick crust and a 70 km-thick lithospheric mantle (Fig. 1). Both the oceanic and the continental lithospheres have an elasto-visco-plastic rheology, with a depth-independent Von-Mises yield stress and a temperature-independent linear viscosity. The values of the material properties (*cf.* Turcotte & Schubert 2002; $\rho$ density, E Young's modulus, $\nu$ Poisson's ratio, $\sigma_y$ Von-Mises yield stress, $\eta$ viscosity) are given in Figure 1. At the bottom of the model linear spring and dashpot elements, which mimic the behaviour of an asthenosphere with a density of $\rho = 3200$ kg/m$^3$ and a viscosity of $\eta = 10^{20}$ Pa s, are applied to account for isostatic effects. In addition, a lithostatic pressure equivalent to the overburden is applied to the bottom of the two plates (oceanic plate: 2.6 GPa, continental plate: 3 GPa). The representation of the sub-lithospheric mantle by boundary conditions means that corner flow in the mantle wedge is neglected.

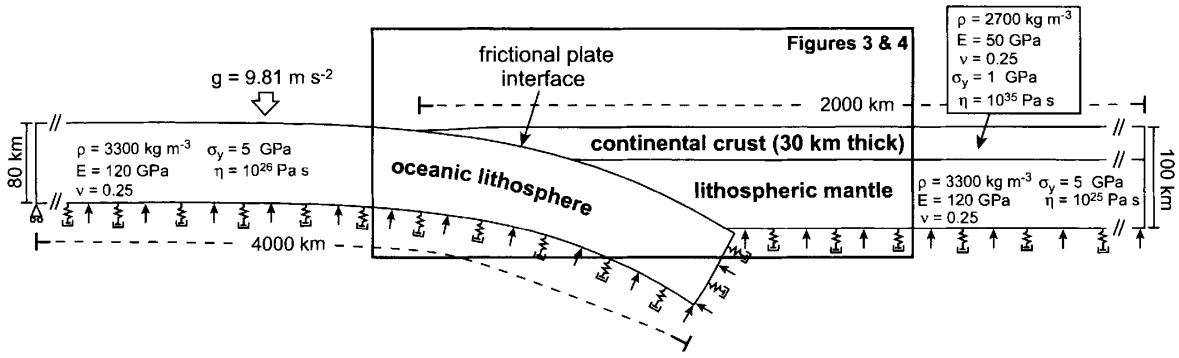


**Fig. 1.** Model set-up with separate oceanic and continental lithospheres that are in contact along the plate interface. Slip on the plate interface is controlled by a Coulomb criterion. The left end of the oceanic lithosphere is free to move in the horizontal direction and fixed in the vertical direction; the right end of the continental plate may not move in the vertical direction and is either fixed (Figs 2a, 3, 5a and 6a) or moves trenchward (Figs 2b, 4, 5b and 6b). Bending stresses in the oceanic plate are calculated separately and imported as pre-stress field (*cf.* Hibbitt *et al.* 2002). In order to include isostatic effects, lithostatic pressure as well as linear spring and dashpot elements that mimic the asthenosphere are applied at the bottom of both plates. See text for explanation of the material properties.

The plate interface is modelled as the contact zone between the two separate meshes of the oceanic plate and the continental plate. Relative tangential motion of the contacting element surfaces is governed by a Coulomb failure criterion with a critical shear stress ($\tau_{max}$) and a coefficient of friction ($\mu$) (*cf.* ABAQUS, 2002). In the models presented below, the coefficient of friction is increased stepwise from $\mu = 0$ to $\mu = 0.3$. A higher value of the friction coefficient is unrealistic for subduction systems, as indicated by heatflow data and palaeo-geothermal gradients of high-pressure/low-temperature metamorphic rocks (Molnar & England 1990; Kao & Chen 1991; Tichelaar & Ruff 1993).

The calculations have been performed with the ABAQUS/Standard software (ABAQUS, 2002), which uses a Lagrangian formulation and solves the following equation

$$\vec{\nabla}\bar{\bar{\tau}} + \rho\vec{g} = 0$$

where $\bar{\bar{\tau}}$ is the stress tensor, $\rho$ density, and $\vec{g}$ gravitational acceleration. The elements have an average size of 10 × 10 km and 5 × 5 km for the oceanic and continental plate, respectively; no remeshing is applied. In a first step, the bending stresses in the oceanic plate, which is downflexed owing to a vertical force of $8 \times 10^{13}$ N/m applied to its right edge, are calculated in the absence of the overriding plate (*cf.* Buiter *et al.* 2001; Funiciello *et al.* 2003). In the second step, the continental plate is added and contact is established along the plate interface (this stage of the model is shown in Fig. 1); the system is then allowed to reach isostatic equilibrium again. This procedure avoids the explicit implementation of subduction initiation and allows starting the experiments at a stage at which a slab has already formed. In the third step, the oceanic plate subducts, driven solely by slab pull, which is generated by its own weight and the force applied during the initial phase. No velocity or density anomalies or any additional forces are prescribed on either end of the subducting plate, which is free to move in the horizontal direction. The only boundary condition applied is that the far left edge of the oceanic plate is fixed in the vertical direction. In other words, the subduction velocity of the oceanic plate as well as the curvature of the slab may evolve freely during the main phase of the experiments. The subduction velocity in all models is of the order of a few centimeters per year. The right end of the continental plate is held fixed in the vertical direction. In the first model set presented below, the right edge of the upper plate is fixed in the horizontal direction as well (Figs 2a, 3, 5a and 6a). In the second model set, the boundary condition is such that the upper plate moves toward the trench owing to a displacement of 100 km prescribed at its right edge (Figs 2b, 4, 5b and 6b).

## Results

### *Models with right end of the continental plate fixed*

Figure 3 shows the finite vertical displacement fields for the first set of models, in which the right end of the upper plate is not allowed to move in the horizontal direction. All experiments are run until 200 km of relative slip are reached

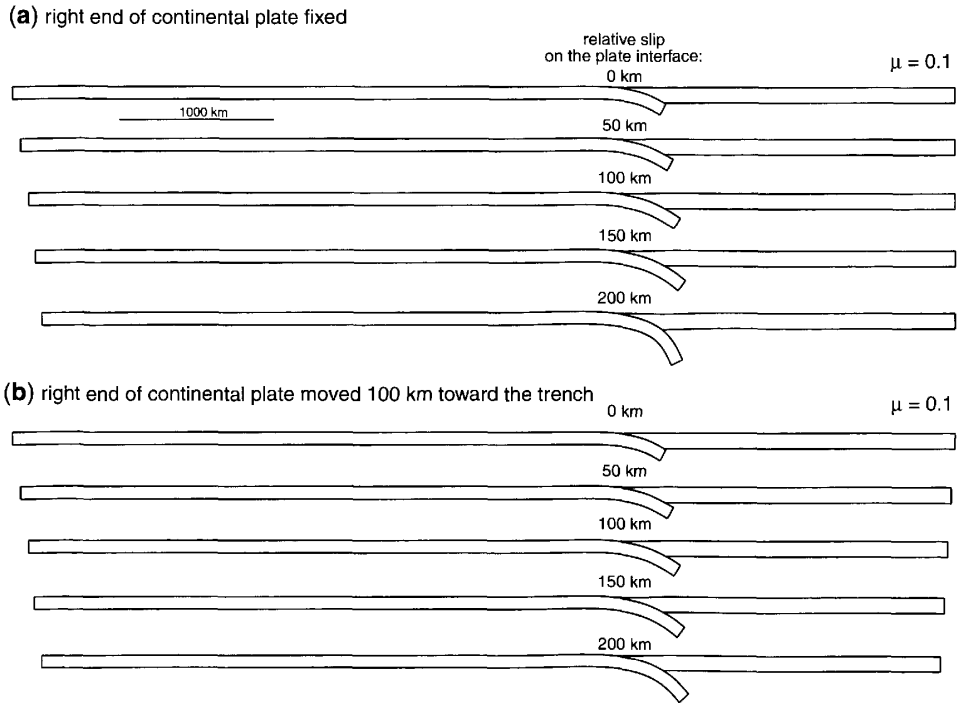


**Fig. 2.** Different stages of the experiments with a friction coefficient of $\mu = 0.1$ (**a**) without and (**b**) with trenchward motion of the upper plate.

on the plate interface; the slip is distributed uniformly on the plate interface. In order to illustrate the development of the entire model, different stages of the experiments performed with $\mu = 0.1$ are shown in Figure 2. For the frictionless case and for a coefficient of friction of $\mu = 0.05$, a broad zone of upward vertical motion develops landward of the intersection between the base of the continental lithosphere and the top of the subducting plate (region C in Fig. 3a, b). For coefficients of friction of $\mu \geq 0.1$, this zone strongly subsides by up to 9 km (regions C in Fig. 3c–e). In contrast, the frontal part of the overriding plate, within a distance of 30–40 km from the trench, is uplifted by *c.* 2 km regardless of the friction coefficient applied (regions A in Fig. 3). Between the uplifted and strongly subsiding regions A and C the upper plate experiences a moderate amount of subsidence of 1–2 km in all models (regions B).

The strong influence of the friction coefficient on the evolution of the models is also revealed in a comparison of their initial and final topographic profiles (Fig. 5a). For $\mu \leq 0.05$, a broad zone, in which the topography is higher than at the initial stage, has developed, whereas in the case of $\mu \geq 0.1$ the upper plate subsides over a wide region, with the width increasing with higher friction coefficients. Note that in all experiments, including the ones with upper plate motion (presented below), the topography evolves continuously from the initial to the final stage.

With respect to the stress field, the subsiding part of the upper plate is associated with a region of curved trajectories of the principal stresses $\sigma_1$ and $\sigma_3$ (shown in the upper panel of Fig. 6a for the model with $\mu = 0.1$). The maximum principal stress is vertical near the base of the lithosphere and perpendicular to the plate interface in its lower part. In the lower left corner of the upper plate, the minimum principal stress attains negative values (lower panel of Fig. 6a). This pattern of the principal stresses indicates that the lower left part of the upper plate is dragged down by the subducting plate. At the surface of the subsiding segment, the maximum principal stress has a horizontal orientation and is higher than in neighbouring regions, which is an expression of the upper plate's flexure resulting from the downward drag induced by the oceanic plate.

### *Models with a trenchward-moving continental plate*

In the second set of experiments, the upper plate moves trenchward by 100 km. The finite vertical displacement fields after 200 km of slip are

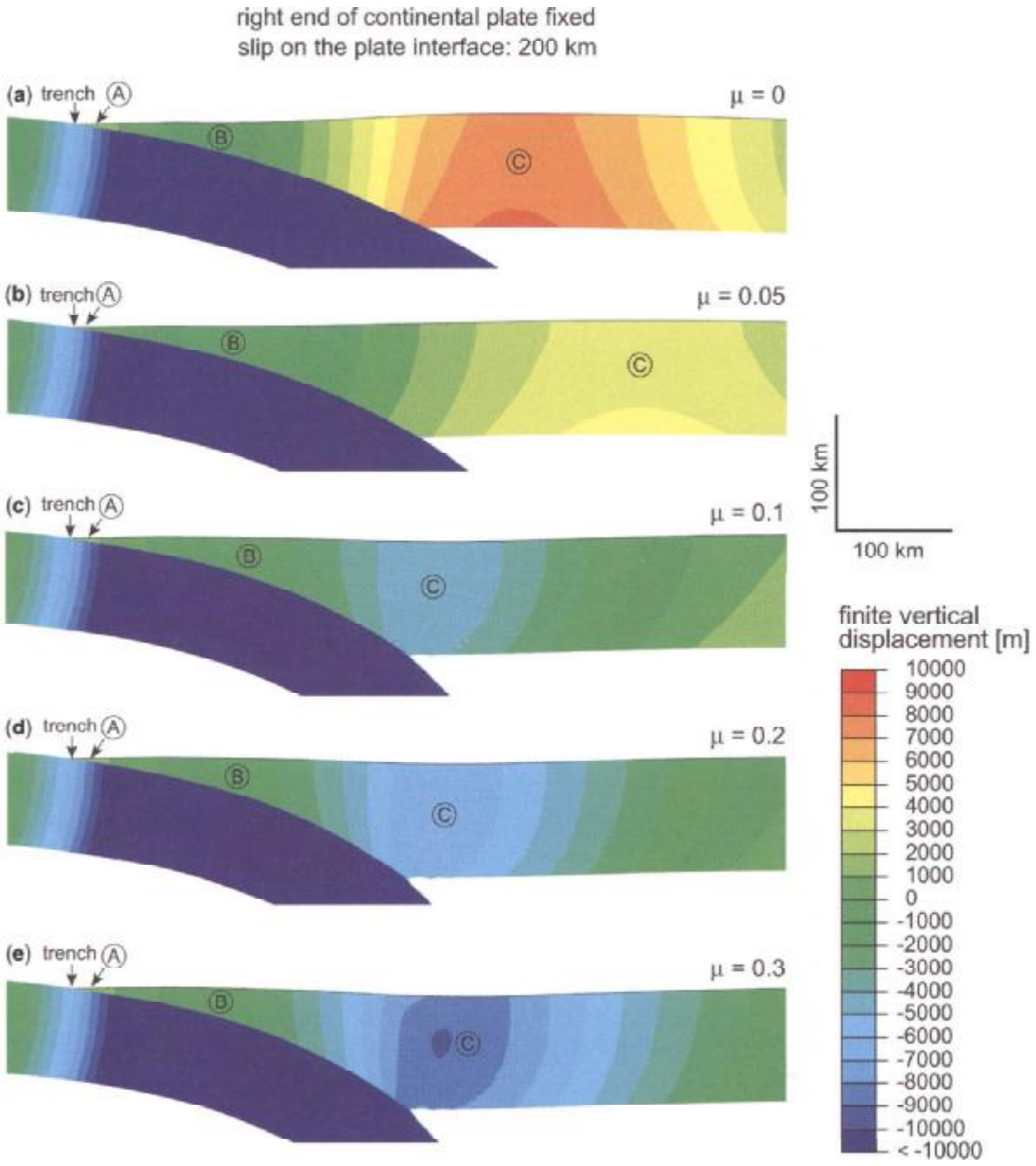


**Fig. 3.** Finite vertical displacement fields after 200 km of slip on the plate interface for the models with the right end of the continental plate fixed in the horizontal direction. Circles at the bottom of the model mark the spring and dashpot elements. Note that friction coefficients of $\mu \geq 0.1$ lead to strong subsidence of the upper plate (regions C) and inhibit the formation of a mountain belt. The frontal part of the upper plate (A) is uplifted; the adjacent part marked by B experiences moderate subsidence by 1–2 km.

depicted in Figure 4. For all coefficients of friction, the overriding plate experiences uplift, however, the uplift pattern differs for low and high friction values. In the presence of a frictionless plate interface, the distribution of uplift is similar to the one observed in the first model set except that the amount of uplift (Fig. 4a) and the final topography (Fig. 5b) is considerably higher. A maximum of ca. 9 km of uplift is reached slightly landward of the intersection of the base of the continental lithosphere and the top of the subducting oceanic plate (region C in Fig. 4a). For $\mu = 0.05$ and $\mu = 0.1$, the zone of highest uplift broadens and lower maximum

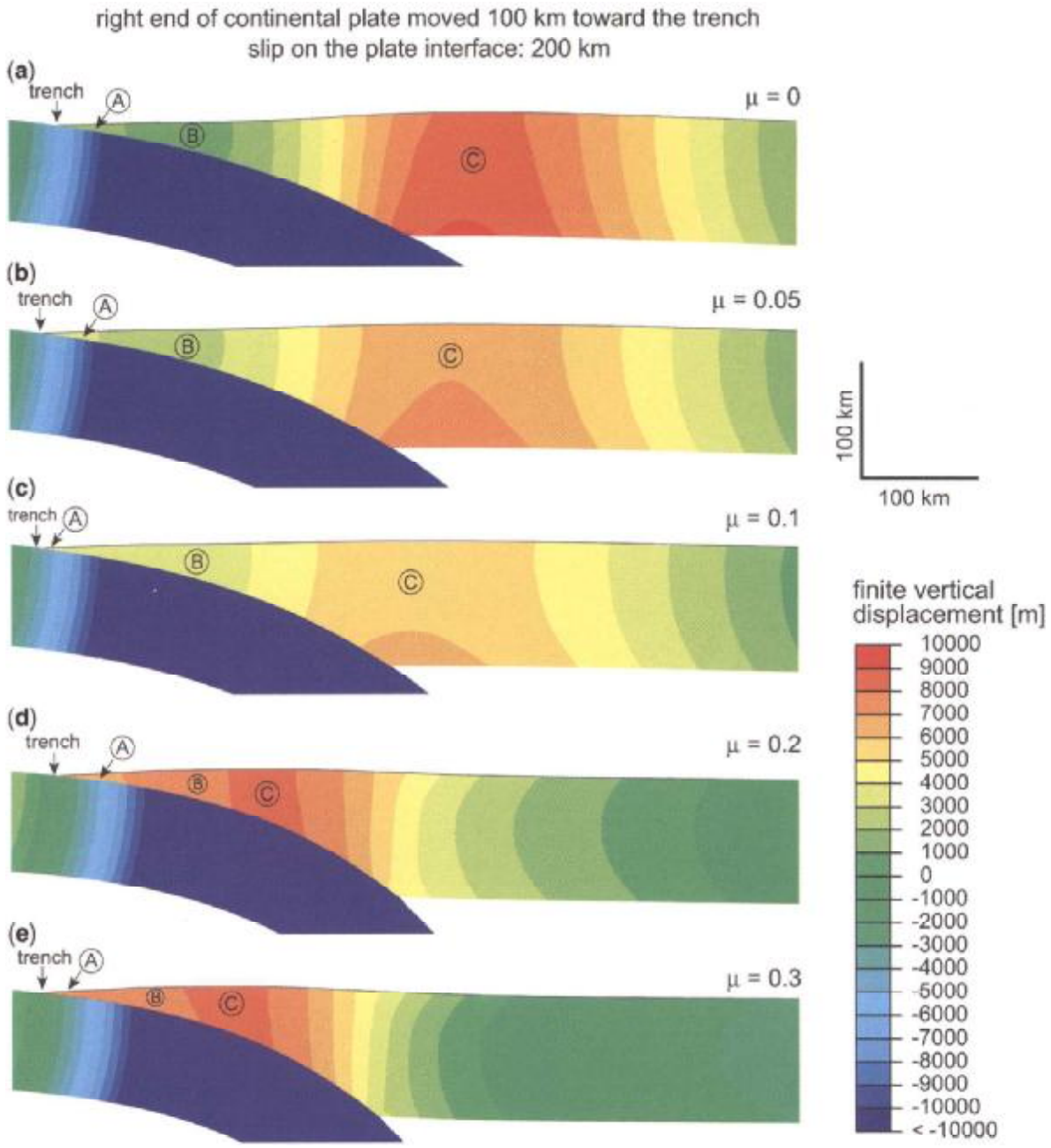


**Fig. 4.** Finite vertical displacement fields after 200 km of slip on the plate interface for the models with the continental plate advancing 100 km toward the trench. Note that for all coefficients of friction, high topography develops in the upper plate, regardless of the coefficient of friction (regions C). In the models with $\mu \leq 0.1$, the frontal part of the upper plate (A) experiences higher uplift than the adjacent region (B). For friction coefficients of $\mu > 0.1$, uplift in the overriding plate localizes above the plate interface (C in d, e).

values of 5–7 km are observed (regions C in Fig. 4b, c). In the three models with $\mu \leq 0.1$, the frontal part of the upper plate (A) is more strongly uplifted than the adjacent region B. The difference between the maximum and minimum upward displacement observed in regions C and B, decreases from 8 km ($\mu = 0$) to 2 km ($\mu = 0.1$) (Fig. 4a, c). For friction coefficients of $\mu > 0.1$, the uplift pattern changes dramatically: the zone of maximum uplift narrows and shifts toward the trench to a position above the centre of the plate interface, where a maximum vertical displacement of 8–9 km is reached (region C in Fig. 4d, e). The trenchward shift of the region with maximum vertical displacement is associated with a shift

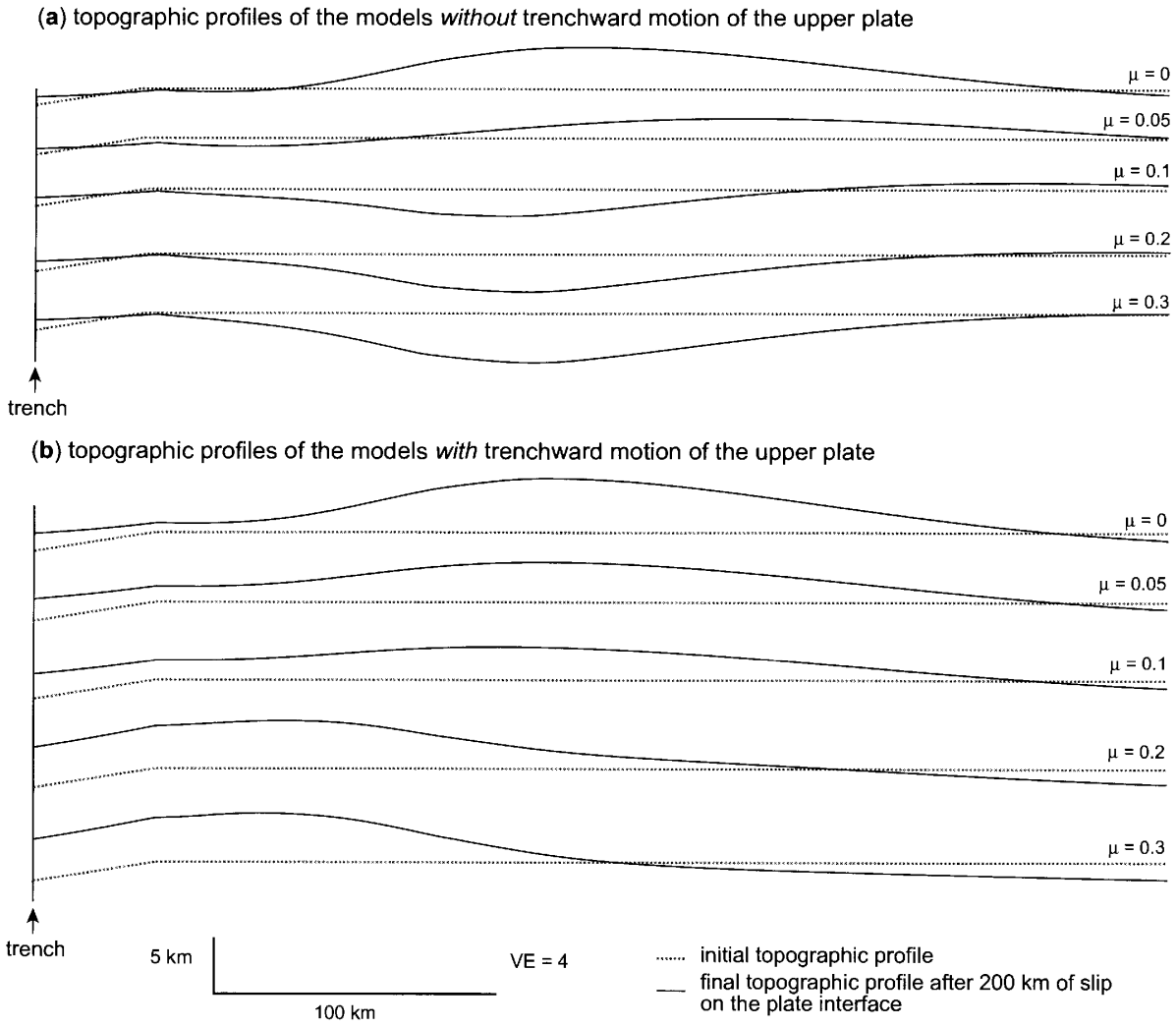


**Fig. 5.** Topographic profiles of the two model sets (**a**) without and (**b**) with trenchward motion of the upper plate. The dotted grey line marks the initial topography (Fig. 1), while the black line indicates the final topographic profile after 200 km of slip on the plate interface.

of the highest topography toward the trench (Fig. 5b). In the models with $\mu \geq 0.1$, the amount of uplift increases continuously from the trench to the region of maximum uplift (C), i.e., region B experiences stronger uplift than the frontal part of the continental plate (A).

The stress field obtained for the models with upper plate motion differs considerably from the one observed for a stationary upper plate (Fig. 6b). The orientation of the principal stresses indicates that the continental plate is under horizontal compression throughout, with the highest values of the maximum principal stress occurring at the lower left corner of the upper plate. With increasing friction, this region of high compressive stresses becomes larger (not shown in Fig. 6).

## Discussion and conclusions

The results of our experiments reveal the crucial role of the upper plate's behaviour for topographic evolution at convergent margins. If the overriding plate remains stationary, the pull of the subducting plate tends to drag it down; this effect is amplified with increasing interplate coupling (Figs 3c–c and 6a). This observation agrees with the modelling results of Hassani *et al.* (1997) and Buiter *et al.* (2001). High topography in the upper plate develops in two cases: (1) if the upper plate remains fixed and the plate interface is frictionless, which is in accordance with Buiter *et al.* (2001), and (2) for $\mu > 0$, if the upper plate advances trenchward. In the latter case, the motion of the overriding plate

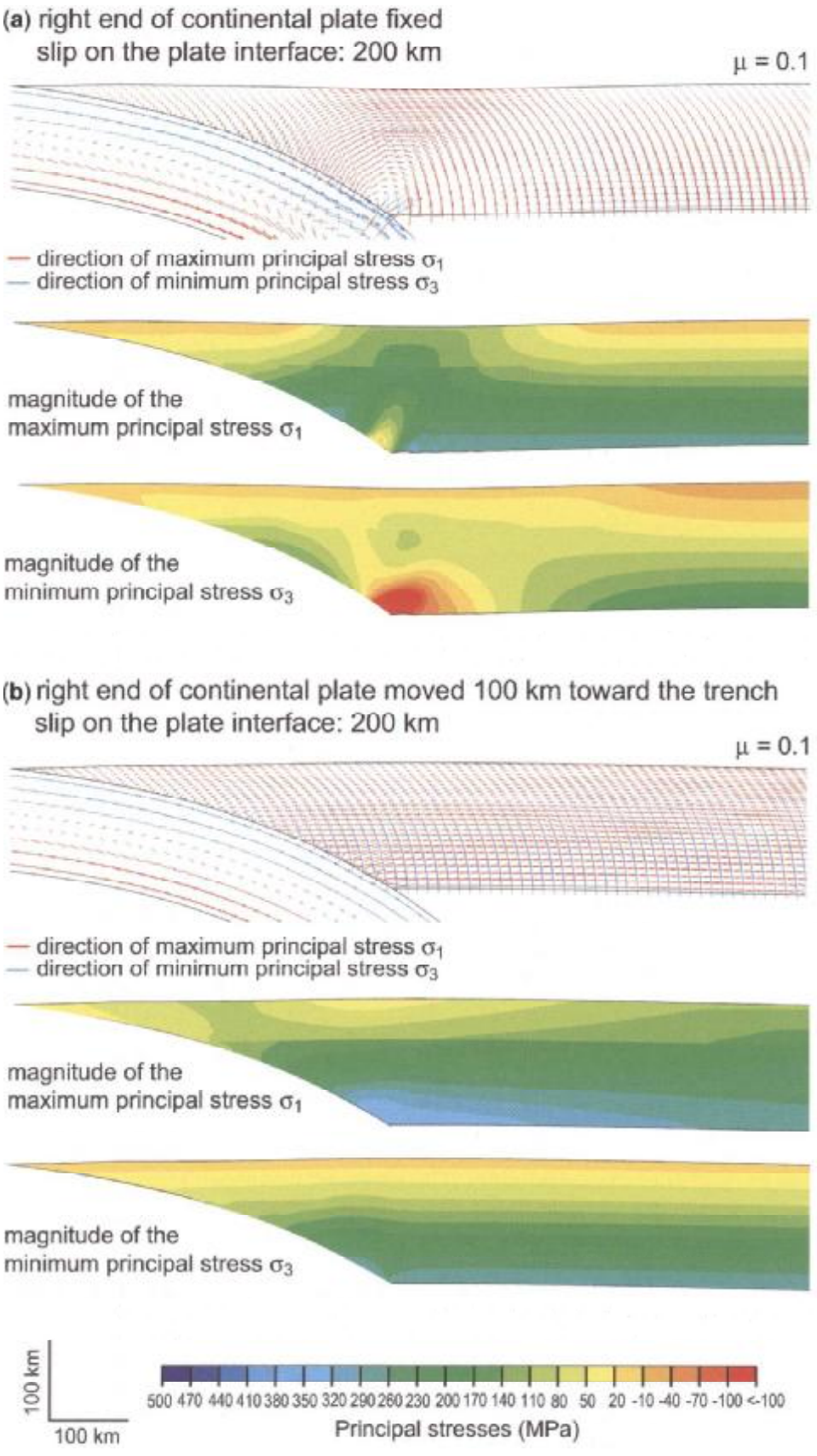


**Fig. 6.** Orientation and magnitude of the maximum and minimum principal stresses in the experiments with a friction coefficient of $\mu = 0.1$; (**a**) without and (**b**) with trenchward motion of the upper plate.

overcomes the downward drag exerted by the subducting plate, which is a combined effect of slab pull and interplate coupling. Thus the growth of high topography is promoted (Fig. 6b). Our model results imply an active role of the continental plate in the mountain-building process and are in general agreement with Cattin *et al.* (1997). These authors report, however, that friction coefficients of $\mu \leq 0.1$ lead to the development of unrealistically high topography, an effect that does not occur in our experiments (Fig. 4a, b). We interpret this significantly different behaviour as a result from the fact that we account for the pull of the slab, which acts against upward displacement of the overriding plate, whereas Cattin *et al.* (1997) did not include slab pull into their models.

With respect to the relationship between the degree of interplate coupling and a high topography, our experiments demonstrate that it may be misleading to infer a high coefficient of friction simply from the presence of high topography, without accounting for the motion of the upper plate. Such an approach was applied, for example, to the Andes (Lamb & Davis 2003). Although the occurrence of strong subduction earthquakes and the absence of a thick sedimentary cover on the oceanic plate in the central segments of the Andean margin support the conclusion of high interplate coupling, the Andes represent an example where the topography and the intracontinental deformation are not solely related to the motion and nature of the oceanic plate. Instead, geological evidence points to a close relationship between intraplate deformation and upper plate motion. For example, the kinematic analyses of fault populations in the central Andes suggest that temporal changes in the contraction directions reflect the *absolute South American* plate motions during the last 20.5 Ma (Marrett & Strecker 2000) rather than the Nazca–South American relative motion (e.g., Hindle *et al.* 2002; Riller & Oncken 2003), which is dominated by the absolute motion of the Nazca Plate. Faults in the Eastern Cordillera of northwestern Argentina and southern Bolivia indicate WNW–ESE shortening from the Miocene until the Pliocene (Marrett *et al.* 1994; Müller *et al.* 2002). During this time span, from 20.5 Ma to 3.2 Ma, South America moved west–northwestward (Pardo-Casas & Molnar 1987). Since 2–3 Ma, ENE–WSW shortening dominates on the faults (Marrett & Strecker 2000). At 3.2 Ma, South America changed to the west–southwestward direction still maintained today (Pardo-Casas & Molnar 1987; DeMets *et al.* 1990; Norabuena *et al.* 1998). This strongly suggests a causative relation between intraplate contraction and the westward advance of the South American plate, which has been faster than the rollback of the Nazca plate (Marrett & Strecker 2000). South America's absolute motion is primarily caused by the push of the South Atlantic ridge, which leads to a westward motion of both the mid-ocean ridge and South America relative to an approximately stable African Plate (Meijer & Wortel 1992; DeMets *et al.* 1990).

In conclusion, our model results indicate that the motion of the overriding plate plays a key role in the formation of mountain belts at convergent margins. Depending on the behaviour of the overriding plate, friction along the plate interface either leads to subsidence or amplifies crustal shortening and the growth of topography in the upper plate.

We wish to thank the editors, S. Buiter and G. Schreurs, who also co-organized the extremely stimulating GEOMOD 2004 conference in Emmetten at the Lake Lucerne, Switzerland, for their efforts. The thoughtful comments by S. Buiter and by the reviewers M. Gerbault, R. de Franco, and R. Govers improved the manuscript. A. H. thanks R. Hetzel for critical comments on earlier versions of the manuscript. Funding for the project was provided by the Swiss National Science Foundation (grant no. 2000-067952).

## References

ABAQUS/Standard User's Manual, 2002. Version 6.3, Hibbitt, Karlson and Sorenson, Inc., Pawtucket, RI, USA.

BEVIS, M., KENDRICK, E., SMALLEY, R., BROOKS, B., ALLMENDINGER, R. & ISACKS, B. 2001. On the strength of interplate coupling and the rate of backarc convergence in the central Andes: an analysis of the interseismic velocity field. *Geochemistry, Geophysics, Geosystems ($G^3$)*, **2**, 2001GC000198.

BILLEN, M. I. & GURNIS, M. 2001. A low viscosity wedge in subduction zones. *Earth and Planetary Science Letters*, **193**, 227–236.

BOTT, M. H. P., WAGHORN, G. D. & WHITTAKER, A. 1989. Plate boundary forces at subduction zones and trench-arc compression. *Tectonophysics*, **170**, 1–15.

BUITER, S. J. H., GOVERS, R. & WORTEL, M. J. R. 2001. A modelling study of vertical surface displacements at convergent plate margins. *Geophysical Journal International*, **147**, 415–427.

CATTIN, R., LYON-CAEN, H. & CHERY, J. 1997. Quantification of interplate coupling in subduction zones and forearc topography. *Geophysical Research Letters*, **24**, 13, 1563–1566.

CHASE, C. G. 1978. Extension behind islands arcs and motions relative to hot spots. *Journal of Geophysical Research*, **83**, 5385–5387.

CONRAD, C. P., BILEK, S. & LITHGOW-BERTELLONI, C. 2004. Great earthquakes and slab pull: interaction between seismic coupling and plate-slab coupling. *Earth and Planetary Science Letters*, **218**, 109–122.

DEMETS, C., GORDON, R. G., ARGUS, D. F. & STEIN, S. 1990. Current plate motions. *Geophysical Journal International*, **101**, 425–478.

DEWEY, J. F. & LAMB, S. H. 1992. Active tectonics of the Andes. *Tectonophysics*, **205**, 1–3, 79–95.

DMOWSKA, R., ZHENG, G. & RICE, J. R. 1996. Seismicity and deformation at convergent margins due to heterogeneous coupling. *Journal of Geophysical Research*, **101**, B2, 3015–3029.

ENGLAND, P. & WORTEL, R. 1980. Some consequences of the subduction of young slabs. *Earth and Planetary Science Letters*, **47**, 403–415.

FORSYTH, D. & UYEDA, S. 1975. On the relative importance of the driving forces of plate motion. *Geophysical Journal of the Royal Astronomical Society*, **43**, 163–200.

FUNICIELLO, F., MORRA, G., REGENAUER-LIEB, K. & GIARDINI, D. 2003. Dynamics of retreating slabs: 1. Insights from two-dimensional numerical experiments. *Journal of Geophysical Research*, **108**, B4, 2206, DOI 10.1029/2001JB000898.

GEPHART, J. 1994. Topography and subduction geometry in the central Andes: clues to the mechanics of a noncollisional orogen. *Journal of Geophysical Research*, **99**, 12279–12288.

HAMILTON, W. B. 1995. Subduction systems and magmatism. *In*: SMELLIE, J. L. (ed.) *Volcanism Associated with Extension at Consuming Plate Margins*, Geological Society Special Publications, **81**, 3–28.

HAMILTON, W. B. 2003. An alternative Earth. *GSA Today*, **13**, 11, 4–12, DOI 10.1130/1052-5173.

HASSANI, R., JONGMANS, D. & CHÉRY, J. 1997. Study of plate deformation and stress in subduction processes using two-dimensional numerical models. *Journal of Geophysical Research*, **108**, 17951–17965.

HINDLE, D., KLEY, J., KLOSKO, E., STEIN, S., DIXON, T. & NORABUENA, E. 2002. Consistency of geologic and geodetic displacements during Andean orogenesis. *Geophysical Research Letters*, **29**, 8, 2001GL013757.

HUANG, S. S., SACKS, I. S. & SNOKE, J. A. 1998. Compressional deformation of island-arc lithosphere in northeastern Japan resulting from long-term subduction-related tectonic forces: finite-element modeling. *Tectonophysics*, **287**, 1–4, 43–58.

HEURET, A. & LALLEMAND, S. 2005. Plate motions, slab dynamics and back-arc deformation. *Physics of the Earth and Planetary Interiors*, **149**, 31–51.

HUSSON, L. & RICARD, Y. 2004. Stress balance above subduction: application to the Andes. *Earth and Planetary Science Letters*, **222**, 1037–1050.

JARRARD, R. D. 1986. Relations among subduction parameters. *Reviews of Geophysics*, **24**, 217–284.

JORDAN, T. E., ISACKS, B. L., ALLMENDINGER, R. W., BREWER, J. A., RAMOS, V. A. & ANDO, C. J. 1983. Andean tectonics related to geometry of subducted Nazca Plate. *Geological Society of America Bulletin*, **94**, 3, 341–361.

KAO, H. & CHEN, W. P. 1991. Earthquakes along the Ryukyu-Kyushu arc: strain segmentation, lateral compression, and thermomechanical state of the plate interface. *Journal of Geophysical Research*, **96**, 21443–21485.

LAMB, S. & DAVIS, P. 2003. Cenozoic climate change as a possible cause for the rise of the Andes. *Nature*, **425**, 792–797.

MARRETT, R. & STRECKER, M. R. 2000. Response of intracontinental deformation in the central Andes to late Cenozoic reorganization of the South American Plate motions. *Tectonics*, **19**, 3, 452–467.

MARRETT, R., ALLMENDINGER, R. W., ALONSO, R. N. & DRAKE, R. E. 1994. Late Cenozoic tectonic evolution of the Puna Plateau and adjacent foreland, northwestern Argentine Andes. *Journal of South American Earth Sciences*, **7**, 179–207.

MEIJER, P. T. & WORTEL, M. J. R. 1992. The dynamics of motion of the South American Plate. *Journal of Geophysical Research*, **97**, 11915–11931.

MOLNAR, P. & ATWATER, T. 1978. Interarc spreading and cordilleran tectonics as alternates related to the age of subducted oceanic lithosphere. *Earth and Planetary Science Letters*, **41**, 330–340.

MOLNAR, P. & ENGLAND, P. 1990. Temperatures, heat flux, and frictional stress near major thrust faults. *Journal of Geophysical Research*, **95**, 4833–4856.

MÜLLER, J. P., KLEY, J. & JACOBSHAGEN, V. 2002. Structure and Cenozoic kinematics of the Eastern Cordillera, southern Bolivia (21°S). *Tectonics*, **21**, 5, 1037, DOI 10.1029/2001TC001340.

NICOL, A. & BEAVAN, J. 2003. Shortening of an overriding plate and its implications for slip on a subduction thrust, central Hikurangi Margin, New Zealand. *Tectonics*, **22**, 6, 1070.

NORABUENA, E., LEFFLER-GRIFFIN, L. *ET AL.* 1998. Space geodetic observations of Nazca-South American convergence across the central Andes. *Science*, **279**, 358–362.

PARDO-CASAS, F. & MOLNAR, P. 1987. Relative motion of the Nazca (Farallon) and South American Plates since Late Cretaceous time. *Tectonics*, **6**, 233–248.

RILLER, U. & ONCKEN, O. 2003. Growth of the Central Andean Plateau by tectonic segmentation is controlled by the gradient in crustal shortening. *Journal of Geology*, **111**, 367–384.

ROYDEN, L. H. 1993. The tectonic expression of slab pull at continental convergent plate boundaries. *Tectonics*, **12**, 303–325.

RUFF, L. & KANAMORI, H. 1980. Seismicity and the subduction process. *Physics of the Earth and Planetary Interiors*, **23**, 240–252.

SCHOLZ, C. H. & CAMPOS, J. 1995. On the mechanism of seismic decoupling and backarc spreading at subduction zones. *Journal of Geophysical Research*, **100**, B11, 22103–22115.

SHEMENDA, A. 1993. Subduction of the lithosphere and backarc dynamics: insights from physical modeling. *Journal of Geophysical Research*, **98**, B9, 16167–16185.

STERN, R. J. 2002. Subduction zones. *Reviews of Geophysics*, **40**, 4, 1012, DOI 10.1029/2001RG000108.

TICHELAAR, B. W. & RUFF, J. L. 1993. Depth of seismic coupling along subduction zones. *Journal of Geophysical Research*, **98**, 2017–3027.

TURCOTTE, D. L. & SCHUBERT, G. 2002. *Geodynamics*, Cambridge University Press, 2nd edition.

UYEDA, S. & KANAMORI, H. 1979. Backarc opening and the mode of subduction. *Journal of Geophysical Research*, **84**, 1049–1061.

WANG, K. L. & HE, J. H. 1999. Mechanics of low-stress forearcs: Nankai and Cascadia. *Journal of Geophysical Research*, **104**, B7, 15191–15205.

WDOWINSKI, S., O'CONNELL, R. J. & ENGLAND, P. 1989. A continuum model of continental deformation above subduction zones: application to the Andes and the Aegean. *Journal of Geophysical Research*, **94**, 10331– 10346.

WILLETT, S. D., BEAUMONT, C. & FULLSACK, P. 1993. Mechanical model for the tectonics of doubly vergent compressional orogens. *Geology*, **21**, 371–374.

YANEZ, G. & CEMBRANO, J. 2004. Role of viscous plate coupling in the late Tertiary Andean tectonics. *Journal of Geophysical Research*, **109**, B02407, 15191–15205, DOI 10.1029/2003JB002494.

# Deformation transfer in viscous detachments: comparison of sandbox models to the South Pyrenean Triangle Zone

HEMIN A. KOYI[1] & MAURA SANS[2]

[1]*Hans Ramberg Tectonic Laboratory, Department of Earth Sciences, Uppsala University, Uppsala, Sweden (e-mail: hemin.koyi@geo.uu.se)*

[2]*Universitat Autonoma Barcelona, Barcelona, Spain*

**Abstract:** Results of scaled sandbox models, containing three viscous layers located at different geographic and stratigraphic levels simulating three evaporitic units in the South Pyrenean Triangle Zone, and interpreted field data are presented here to explain structural variation and kinematics in shortened areas containing multiple weak horizons acting as detachments. In the Southern Pyrenean Triangle Zone, the Beuda, Cardona and Barbastro thrust fronts have similar geometric features to those developed in the models, suggesting that they could have formed and evolved in a similar way. These deformation fronts are not always perpendicular to the regional shortening direction. Instead, their direction is governed by the initial pinch-out of the viscous horizons. Model results show that triangle zones form when: (1) deformation is transferred to weak horizons located at higher stratigraphic levels, and (2) the deformation front reaches the pinch-out of the weak horizons. Model results also show that the rheology of the detachment horizons controls the geometry of the deformation front. Weak detachments (Cardona Formation, and pure silicone in the models) promote folding and back-vergent structures, and thus formation of triangle zones at the deformation front, irrespective of the location of the thrust front relative to the pinch-out of the viscous detachment. However, over strong (more viscous) detachments (Barbastro and Beuda formations, and impure silicone in the models), folds that eventually evolve to thrusts are dominant. In such cases, backthrusts form only at the pinch-out of the detachment layer. In cases where no viscous detachment is present, no backthrusts form, and therefore the thrust front does not develop a triangle zone geometry. Instead, a foreland-vergent piggyback sequence of thrusts forms. Model results show that the stratigraphic level of a detachment governs size, geometry and spacing of the imbricates formed above it.

The South Pyrenean Triangle Zone (SPTZ, Fig. 1) is an excellent area for studying the geometry of triangle zones because it fulfils two important requisites for formation and preservation of such zones: presence of ductile detachments (Cousenz-Schultz & Whiltscho 1996; Sans *et al.* 1996*a*, *b*) and moderate displacement along faults (Hatcher 1999). A triangle zone is defined as the strata between the basal blind thrust, the hinterland-vergent thrust and the most external of the foreland vergent thrusts to intersect the surface (Gordy *et al.* 1977; Charlesworth *et al.* 1987) irrespective of its internal structure. The presence of ductile detachments is fundamental to the formation of triangle zones. Moreover, the rheology and thickness of the mechanically weak layers control the style of deformation at the deformation front, and therefore at the tip line of the triangle zone (Sans *et al.* 1996*a*). Moderate displacement allows preservation of the triangle zone geometry after the triangle zone is abandoned and deformation progresses towards the foreland. Triangle zones have survived in only a few thrust systems with large displacements. In these cases the hinterland-vergent thrust was inverted. Displacement should therefore be considered a key factor for survival of triangle zones even if all the other attributes are present (Hatcher 1999).

Different aspects of the effect of multiple detachments have been studied using analogue models (e.g., Letouzey *et al.* 1995; Verschuren *et al.* 1996; Bonini 2001). However, in this paper, we present the results of two scaled analogue models prepared to study the formation and evolution of the Southern Pyrenean Triangle Zone, whose stratigraphy includes three evaporitic units located at different levels. In these models, three viscous layers were arranged in a lateral and frontal stepping-up order embedded within layers possessing Coulomb rheology in a similar way to that of the South Pyrenean

*From*: BUITER, S. J. H. & SCHREURS, G. (eds) 2006. *Analogue and Numerical Modelling of Crustal-Scale Processes.* Geological Society, London, Special Publications, **253**, 117–134.
0305-8719/06/$15.00 

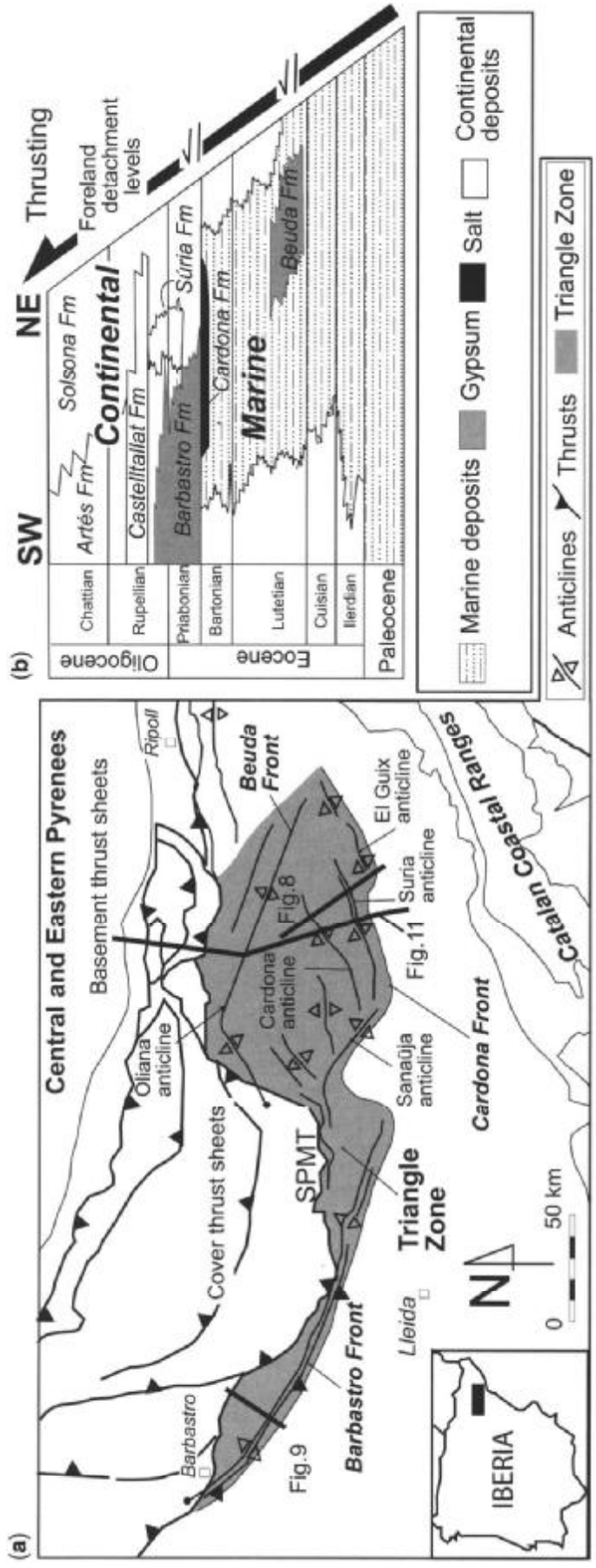


**Fig. 1.** (**a**) Structural map of the study area (inset shows location). The triangle zone (dark grey) is bounded by the South Pyrenean Main Thrust (SPMT) in the north and the most external structure in the foreland to the south. The triangle zone is internally deformed by anticlines with different orientations indicated in the map. (**b**) Stratigraphy of the Ebro foreland basin. The basin infill changed from marine to continental during thrusting. The three evaporitic levels outlined are the main detachments of the South Pyrenean Thrust System.

Triangle Zone. The purpose of these experiments was to understand the effect of multiple weak horizons in the deformation of a fold-thrust belt, investigate how deformation is transmitted between different detachment levels, study the effect of differences in thickness and rheology of the viscous layers on the geometry of triangle zones, and compare the results with the South Pyrenean Triangle Zone.

## South Pyrenean thrust front

The geometry of the South Pyrenean thrust front changes along strike from east to west (Fig. 1). Both in the eastern and the westernmost parts, where there are no evaporitic levels at depth, the front is represented by a foreland-vergent and emergent thrust which places cover rocks on top of the foreland sediments. In contrast, in the central and central eastern parts, where there are evaporitic levels in the stratigraphic section of the foreland sediments, deformation is transferred to the foreland and the thrust front is blind (Vergés *et al.* 1992). Moreover, in this area, the tilted beds of the southern limbs of the antiforms have been passively transported towards the hinterland along a backthrust. The South Pyrenean Triangle Zone is, thus, limited between the South Pyrenean main emergent thrust in the north (hinterland), a basal thrust and the most external of the hinterland vergent structures (Fig. 1) (Sans *et al.* 1996*a*, *b*). The internal structure of the Triangle Zone is characterized by the presence of folds and thrusts with three different orientations. In the northern part the folds are NW–SE, in the central part, they are NE–SW, and in the southern and more western parts they are WNW–ESE (Vergés *et al.* 1992). Each of these areas corresponds, at depth, with a different detachment horizon of the Triangle Zone. In the north the detachment is located in the Beuda formation; in the central part, in the Cardona formation; and in the southwestern part, in the Barbastro formation. These three evaporitic formations are arranged in a lateral and foreland stepping-up geometry (Fig. 1b) which produced a staircase geometry in the basal detachment of the Triangle Zone. Wide flats are located within the evaporitic formations and ramps connect them (Vergés *et al.* 1992; Sans & Vergés 1995; Sans *et al.* 1996*a*, *b*).

Three main thrust wedges have developed along the southern margins of the evaporitic units. The Beuda thrust wedge is located at the southern pinch-out of the Beuda Formation where the basal thrust steps up into the Cardona salt. The Beuda Formation consists of more than 1000 m of alternating shale and anhydrites with 100 m of salt in its middle-upper part (Martínez *et al.* 1989). The intermediate thrust wedge coincides at the surface with the Santa Maria d'Oló, Súria and Sanaüja anticlines and it is related to the southern and southwestern pinch-out of the Cardona formation which consists of a maximum 350 m of salt. At the southern pinch-out of the Cardona formation, a hinterland vergent double anticline has developed (Sans & Vergés 1995; Sans 1999, 2003) representing the southern limit of the Triangle Zone. In the southwestern pinch out, the ramp between the Cardona and the Barbastro Formation coincides at the surface with the Sanaüja anticline. In this anticline, the difference in behaviour between the Cardona Formation (consists mainly of halite) and the Barbastro formation (consists mainly of gypsum and whose thickness increases from east to west, about 1 km thick) can be seen in the different structure under both limbs of the anticline (Sans & Vergés 1995; Sans *et al.* 1996*a*). Whereas in the northeastern limb, the salt of the Cardona Formation flows into the anticline core, the Barbastro gypsums forms a backthrust system that thickens the southwest limb of the anticline. The southernmost thrust wedge is represented at the surface by the Barbastro anticline which formed at the blind tip line of the Barbastro Formation. These details are displayed on seismic data of the area (Gil & Jurado, 1998, fig. 3). The Barbastro anticline consists of a south-vergent antiformal stack of the gypsum levels which, in the southern limb, shows a hinterland-vergent thrust. This thrust may correspond to the reactivation of the previous foreland-vergent upper detachment of the antiformal stack (Sans *et al.* 1996*b*).

Syntectonic sediments related to these three thrust wedges allow dating the formation of the wedges to Late Eocene–Early Oligocene, Late Oligocene and Late Oligocene–Early Miocene, from north to south respectively (Pardo & Villena 1979; Riba *et al.* 1983; Sáez 1987; Burbank *et al.* 1992; Senz & Zamorano 1992; Meigs *et al.* 1996; Vergés & Burbank 1996). From these ages, the three wedges are considered to have been the successive frontal structures of the Triangle Zone during the tectonic evolution of the area (Sans *et al.* 1996*a*). These wedges represent relict thrust fronts abandoned as the basal thrust propagated southwestwards to more external areas.

## Modelling materials

Two basic materials have been used: a viscous silicone polymer (SGM36) and dry loose sand. SGM36 is a suitable material to simulate

ductile behaviour of evaporites or mudstones, whereas loose sand is appropriate for simulating the brittle behaviour of non-evaporitic sediments in the upper crust (Weijermars 1986; Ballard *et al.* 1987; Koyi *et al.* 1993; Weijermars *et al.* 1993; Bonini 2001). SGM36, manufactured by Dow Corning Ltd, is a Newtonian viscous silicone. We used two kinds of SMG36: pure SGM36, which has an effective viscosity of $5\times10^4$ Pa s (density 987 kg $m^{-3}$) and impure SGM36 (mixed with loose sand), which is one order of magnitude more viscous, i.e., $5 \times 10^5$ Pa s (density 1100 kg $m^{-3}$).

The angle of internal friction of rocks in the brittle upper crust ranges between $\phi_n = 31°–40°$ with a cohesive strength of about 50 MPa (Byerlee 1978; Brace & Kohlstedt 1980). Loose sand with the same internal frictional angle, $\phi_m = 36°$ (McClay & Ellis 1987; Mulugeta & Koyi 1987; Koyi *et al.* 1993; Weijermars *et al.* 1993) and a small cohesive strength is a nearly perfect Coulomb material to simulate the brittle behaviour of sedimentary cover (Krantz 1991).

Layers of overburden were constructed to the desired thickness by scraping alternating layers of loose sand (grain size $\geq 35$ μm). The bulk density of the loose sand is $\rho_m = 1700$ kg $m^{-3}$ with a cohesive strength of about 140 Pa (Cotton & Koyi 2000).

## Model set-up

Two models, referred to as model 1 and model 2 throughout this article, were designed to study the transfer of thin-skinned deformation between detachments at different levels. The models are based on the stratigraphic section shown in Figure 1 to simulate the effect of the three detachment horizons on the evolutionary history of the SPTZ. Each model consisted of three viscous layers (simulating the three detachment levels (Beuda Fm, Cardona Fm and Barbastro Fm in the SPTZ) interbedded with layers of loose sand (Fig. 2). The rheology, thickness and geometrical arrangement of each layer were similar in both experiments, and the minor differences (few millimetres to maximum 0.5 cm) in lateral dimension of the viscous layers between the two models, we believe were of minor significance (Fig. 2). The major difference between both experiments was the amount of bulk shortening: model 1 was shortened up to 15% and model 2 to 22%. Both values are in the range of shortening values achieved in the frontal part of the SPTZ (15–30%).

The brittle-viscous models, which were 30 × 47 cm, were shortened from one end perpendicular to their width at 2 cm/hr. The models consisted of three viscous layers of SGM36 embedded in sand layers. The viscous layers were smaller in dimension than the model and arranged in a lateral and frontal stepping-up order (Fig. 2). The bottom viscous, layer, which was of impure SGM36 (viscosity *c.* $5 \times 10^5$ Pa s), was 0.5 cm thick in both models and simulated the Beuda Formation. This viscous layer was located in the lower right-hand quadrangle of the model, adjacent to the rear wall representing the backstop. A second viscous layer (intermediate viscous layer) of pure SGM36 (viscosity *c.* $5 \times 10^4$ Pa s) simulated the Cardona Formation. This viscous layer was 0.5 cm thick in model 1 and 0.8 cm thick in model 2, was placed in the centre of the model and did not overlap with the lower viscous layer. The third and uppermost viscous layer, consisting of impure SGM36, simulated the Barbastro Formation. The top part of the model overlying the uppermost viscous layer consisted of a 1.5 cm thick layer of sand with colour markers at different levels. Initial heights of model 1 and 2 were 4.3 and 4.45 cm, respectively. A passive grid (1.2 cm × 1.2 cm) was placed on top of the models and twelve reference points (P1–P12) were printed in three longitudinal rows to monitor the horizontal displacement and vertical growth of the structures during shortening (Fig. 2).

## Scaling

Our models are geometrically, kinematically and dynamically scaled to a prototype according to the following parameters. In our models, length ratio is $6.6 \times 10^{-7}$, implying that 1 cm in the model simulates 1.5 km in nature.

The models presented here are intended to represent the structural evolution of the SPTZ. Therefore, kinematic similarity was fulfilled by assuming that shortening in model and prototype started after the deposition of all units. However, synkinematic erosion and/or sedimentation, likely to occur in the prototype, were not incorporated in our models.

By choosing modelling materials with relatively similar mechanical properties to that of rocks in the prototype, dynamic scaling was approached. The Mohr–Coulomb criterion, which predicts the rheological behaviour of brittle material, can be used to calculate ratios of the dynamic similarity between models and nature. The Coulomb–Mohr criterion contains

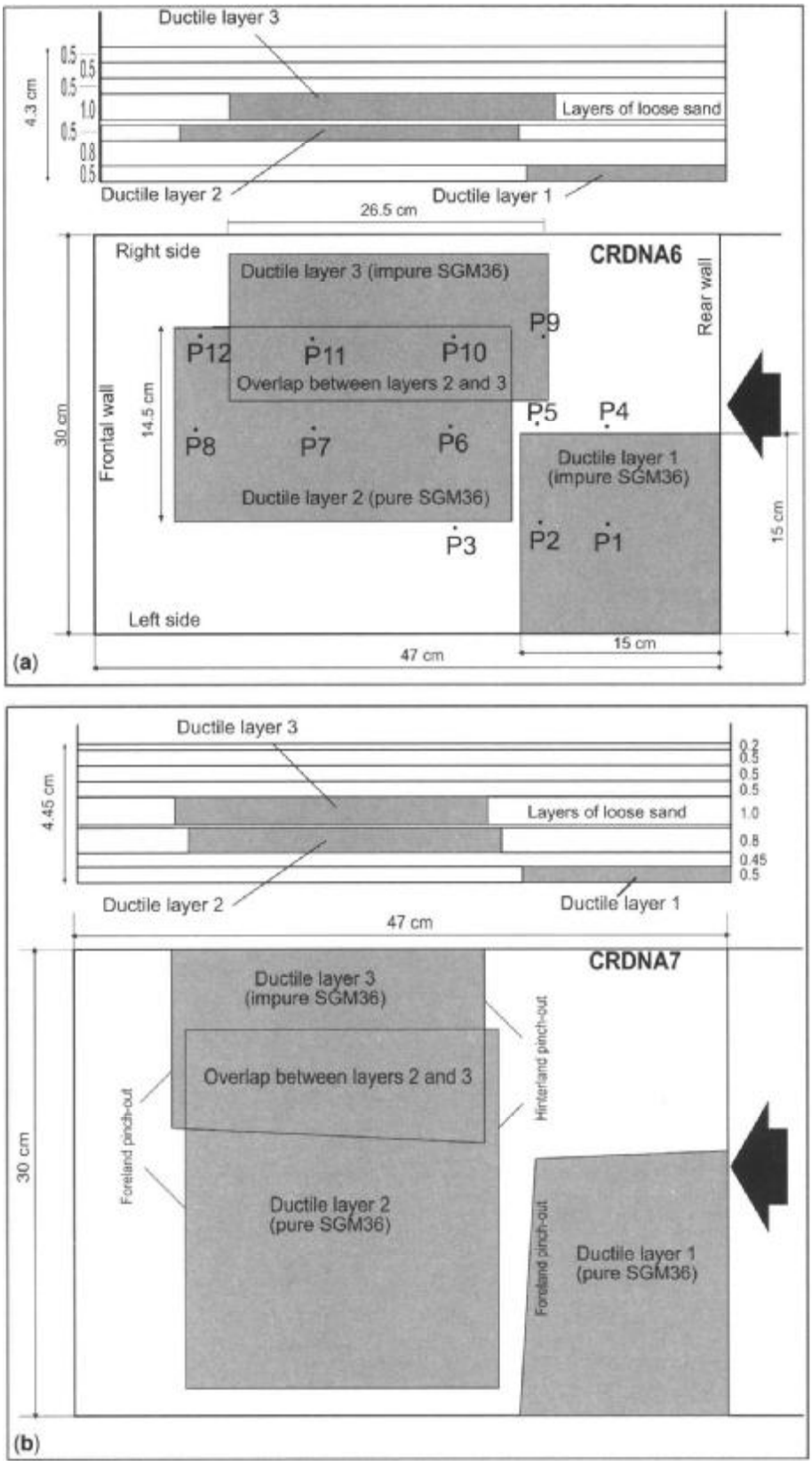


**Fig. 2.** Initial configuration of (**a**) model 1 (CRDNA6) and (**b**), model 2 (CRDNA7) showing both a schematic profile (top of a and b) and map view (bottom of a and b). The ductile layers are shaded in grey and the sand layers in white. Dimensions are in centimetres. Arrows indicate the shortening direction. In the map view in (a), the location of the marker points (P1 to P12) is indicated. These points were used to monitor deformation in the models.

some intrinsic material properties, for instance cohesive shear strength ($C_o$) and coefficient of internal friction ($\mu$), which need to be equal in model and nature in order to achieve dynamic similarity:

$$\tau = C_o + \sigma\mu \quad (1)$$

where $\tau$ and $\sigma$ are shear and normal stresses, $\mu = \tan \phi$ is the coefficient of internal friction and $\phi$ is the angle of the internal friction. For rocks in the upper crust, $\phi_n$ ranges between 31° and 40° (Byerlee 1978; Brace & Kohlstedt 1980) which give a coefficient of internal friction between 0.6 and 0.84. The angle of internal friction of loose sand used in the models is $\phi_m = 36°$ and gives a coefficient of internal friction $\mu_m = 0.73$, comparable to rocks in the brittle upper crust. To scale the model dynamically, the non-dimensional shear strength ($\tau/\sigma$ in model and prototype) also should be equal or within the same order of magnitude (Childs *et al.* 1993; Koyi *et al.* 1993; Weijermars *et al.* 1993). Dividing equation (1) by $\sigma$ gives:

$$\tau/\sigma = (\mu + C_o)/\sigma \quad (2)$$

Assuming dynamic similarity, the $\tau/\sigma$ ratio for the model (m) and nature (n) should be equal:

$$[(\mu + C_o)/\sigma]_m = [(\mu + C_o)/\sigma]_n \quad (3)$$

Since $\mu_m$ and $\mu_n$ are almost equal, they can be neglected in equation (3):

$$(C_o/\sigma)_m = (C_o/\sigma)_n \quad (4)$$

Normal stress $\sigma$ can be defined as

$$\sigma = \rho g l \quad (5)$$

where $\rho$ is density, g is the gravity acceleration and l is the length. Equation (4) can be rewritten as

$$(C_o/\rho g l)_m = (C_o/\rho g l)_n \quad (6)$$

Substituting the values in equation (5), the non-dimensional shear strength values will be $1.9\times10^{-1}$ and $8.9\times10^{-1}$ for nature and model respectively. These values, which are within the same order of magnitude, suggest that dynamic similarity between the models and nature is approached.

For the viscous layers, dynamic similarity was achieved by simulating the ductile behaviour of rock salt (effective viscosity ranging from $10^{17}$–$10^{18}$ Pa s) with a Newtonian viscous material (SGM36), whose effective viscosity at room temperature is $5\times10^4$ Pa s for the pure SGM36 and $5\times10^5$ Pa s for the impure SGM36, giving a scaling ratio of $5\times10^{-14}$ to $5\times10^{-12}$ for both the pure and impure viscous SGM36 layers, respectively.

## Results

After a total bulk shortening of 15% in model 1 and 22% in model 2, the surface geometry of the models showed that in model 1, deformation had not reached the pinch-out of the intermediate viscous layer in the foreland (Figs 3 and 4), whereas in model 2 some structures could be seen as far as the pinch-out of the intermediate and upper viscous layers. At the early stages of shortening, a large foreland-vergent structure developed near the backstop of both models across the width of the model coinciding with the frontal pinch-out of the lower viscous layer and with the rear pinch-out of the intermediate and upper viscous layers. With continuing shortening, structures usually developed in front of the frontal pinch out of the lower viscous layer. These structures were less continuous along strike, and displayed curved geometries close to the lateral pinch-outs of the different viscous layers (Figs 3 and 4). In the purely frictional area, where there was no basal viscous layer in the model stratigraphy, foreland-vergent structures were dominant, whereas in the area where there were one or several viscous layers at depth, both foreland and hinterland-vergent structures were formed (Figs 3 and 4).

### *Deformation sequence*

In the models presented here, it was possible to monitor deformation sequence not only qualitatively through the changes of the surface geometry, but also quantitatively through a continuous monitoring of the temporal and spatial change in the position of the marker points initially 'printed' on the surface of the models (Figs 3, 4 and 5).

In both models, deformation started at the rear part of the model, close to the moving wall, and advanced towards more frontal areas of the model (Figs 3 and 4). Propagation of deformation took place laterally in the direction of tectonic transport as well as across the stratigraphy to the upper and lateral detachments. The first visible fault formed above the frictional area (at 2% bulk shortening), where no viscous layer was present in the stratigraphy (Figs 3 and 4). This foreland-vergent fault was active throughout the whole deformation history, and its position coincided with the rear pinch-out of the upper and intermediate viscous layers. The

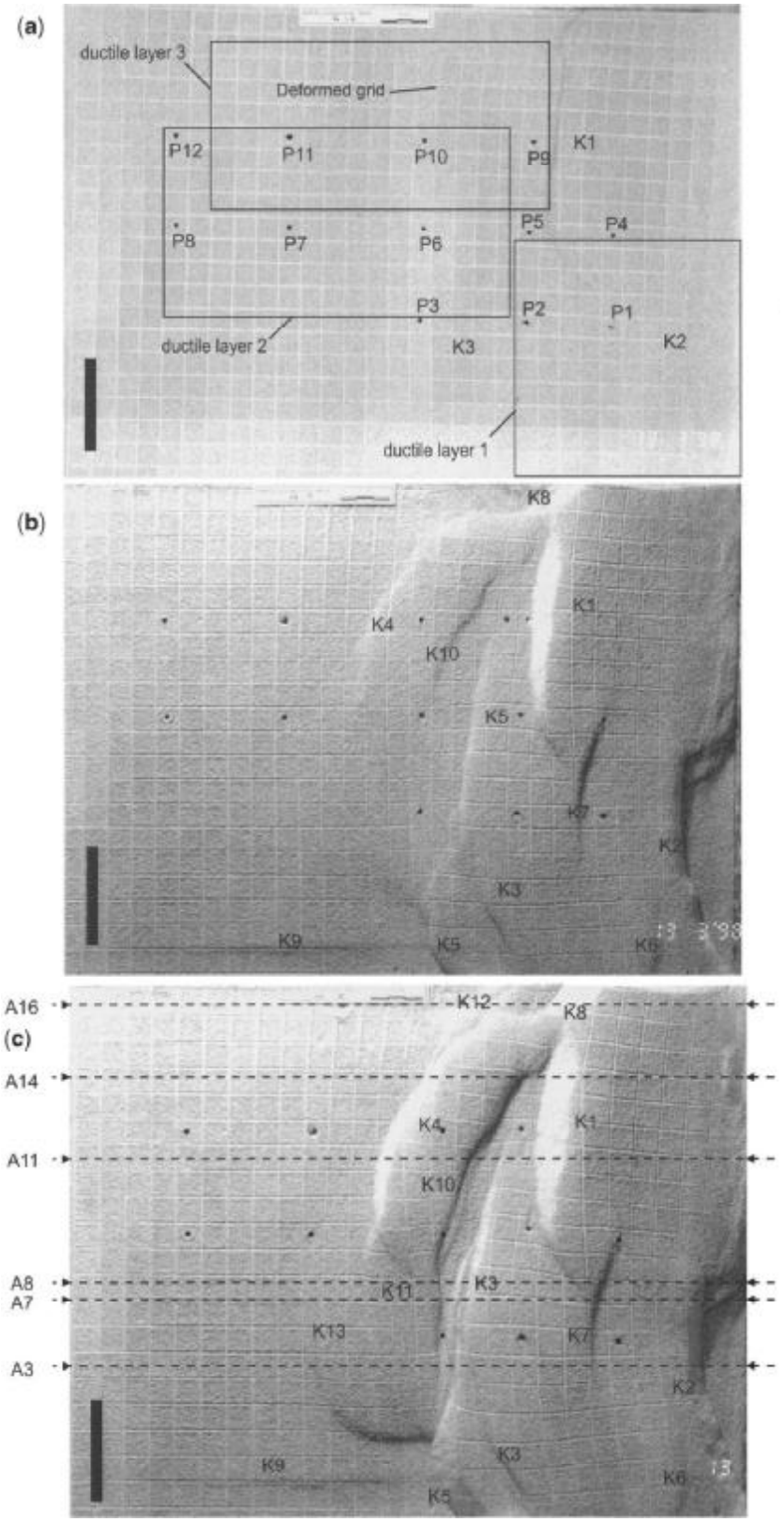


**Fig. 3.** Top views of model 1 (CRDNA6) during deformation: (**a**) at 4% shortening, (**b**) at 9% shortening, and (**c**) at 15% shortening. The boxes in A indicate the initial distribution of the three ductile layers. Note the irregular geometry and propagation mode of the deformation front and the individual thrusts/kinks (K1, K2, . . .) in different domains of the model. Location of sections is shown in (c) (see Fig. 6).

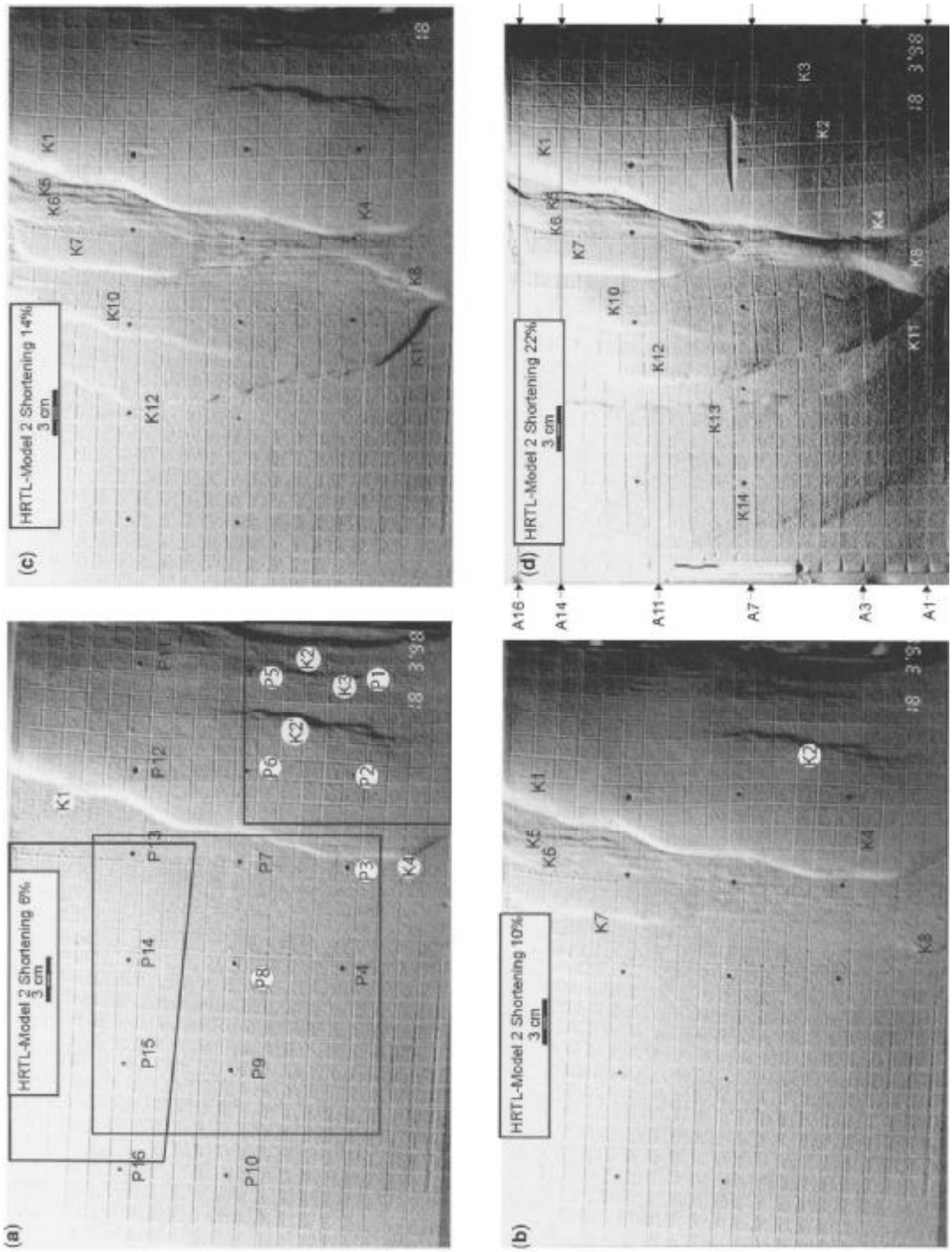


**Fig. 4.** Top views of model 2 (CRDNA7) during deformation: (**a**) at 6% shortening, (**b**) at 10% shortening, (**c**) at 14% shortening, and (**d**) at 22% shortening. The boxes in (a) indicate the initial distribution of the three ductile layers. Note the irregular geometry and propagation mode of the deformation front and the individual thrusts/kinks (K1, K2, . . .) in different domains of the model. Location of sections is shown in (d) (see Fig. 7).

fault grew along strike by merging with other fault segments that formed later at a similar distance from the backstop in areas where viscous layers were present.

In areas where viscous detachments were present, the first structures formed later (at 4% bulk shortening). Some of these structures, which were verging towards the hinterland of the models, were located close to the backstop, whereas others were foreland-verging and were located at the frontal pinch-out of the lower viscous layer. After the formation of these structures, deformation was transferred from the basal detachments (lower viscous layer and frictional detachment, relative to different parts of the models) to the intermediate and upper detachments (at 5% shortening, Figs 3 and 4). Between 6% and 10% of shortening, the ramp between the lower and the intermediate detachments was accommodating most of the shortening in the central part of the model, whereas in areas of the frictional detachment, new structures were developing towards the foreland (Figs 3 and 4).

After 10% shortening, propagation to the front of the model was achieved in a normal sequence in which deformation propagated progressively more to the frontal areas of the model (Fig. 4, K2, K7 and K10). Only when structures were nucleated above two different detachments did younger structures form in a break-back sequence (e.g., K5 formed behind K4 in Fig. 3). In general, all structures remained active, albeit with variable intensity, throughout the model deformation (Fig. 5). Highest displacements are recorded along the thrusts (ramps) which connected a lower detachment with one at a higher stratigraphic level (e.g., P2–P3 and P5–P6; Figs 3 and 5). Only in the model with 22% bulk shortening did the deformation front reach the foreland pinch-out of the intermediate and upper viscous layers.

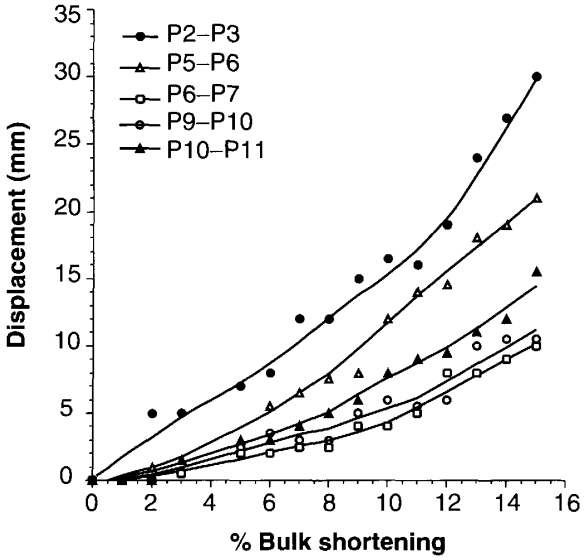


**Fig. 5.** Graphs of displacement along thrusts monitored through the change in lateral distance between adjacent points in model 1. Here, only five pairs of points are shown (for location of the points see Fig. 3). Note that all thrusts are active throughout model deformation, albeit with variable intensity.

### *Geometry of structures and their relation to the different viscous layers*

In map view and in cross-sections, three different domains could be identified in the models: (1) the external area of the model, where no deformation occurred; (2) the middle part of the model, which is the deformed area located above the intermediate and the upper detachment levels; and (3) the internal area of the model, which corresponds to the deformed area above the basal frictional and lower viscous detachments (lower viscous layer, Figs 3, 4, 6 and 7).

The undeformed external area was larger in model 1 because it was shortened only up to 15% and deformation did not reach the foreland pinch-out of the intermediate and/or upper viscous detachments. In map view, the deformation front, separating the external undeformed area from the intermediate area, was located at variable distances from the backstop; it had advanced furthest in the areas above the intermediate and upper viscous layers that acted as detachment levels (Figs 3 and 4). In model 1, the deformation front was 18 cm away from the backstop above the frictional detachment (Fig. 6a) and above the lower viscous layer (Fig. 6f), whereas it was around 27 cm away from the backstop above the intermediate and upper viscous layers (Figs 3 and 6). However, the major difference in the deformation front between these two areas was not in the position of the deformation front, but in its geometry. Above the intermediate viscous layer (consisting of pure SGM36) the most external structure was hinterland vergent, or backward dominated, irrespective of whether it had formed at the pinch-out of the layer (model 2) or had not reached the pinch-out (model 1). In contrast, above the upper viscous layer (impure SGM36), the frontal structure was foreland-vergent except when it developed at the pinch-out (Figs 7a, b, c and d).

The deformed area above the intermediate and upper viscous layers is characterized by the presence of folds with an initial wavelength of

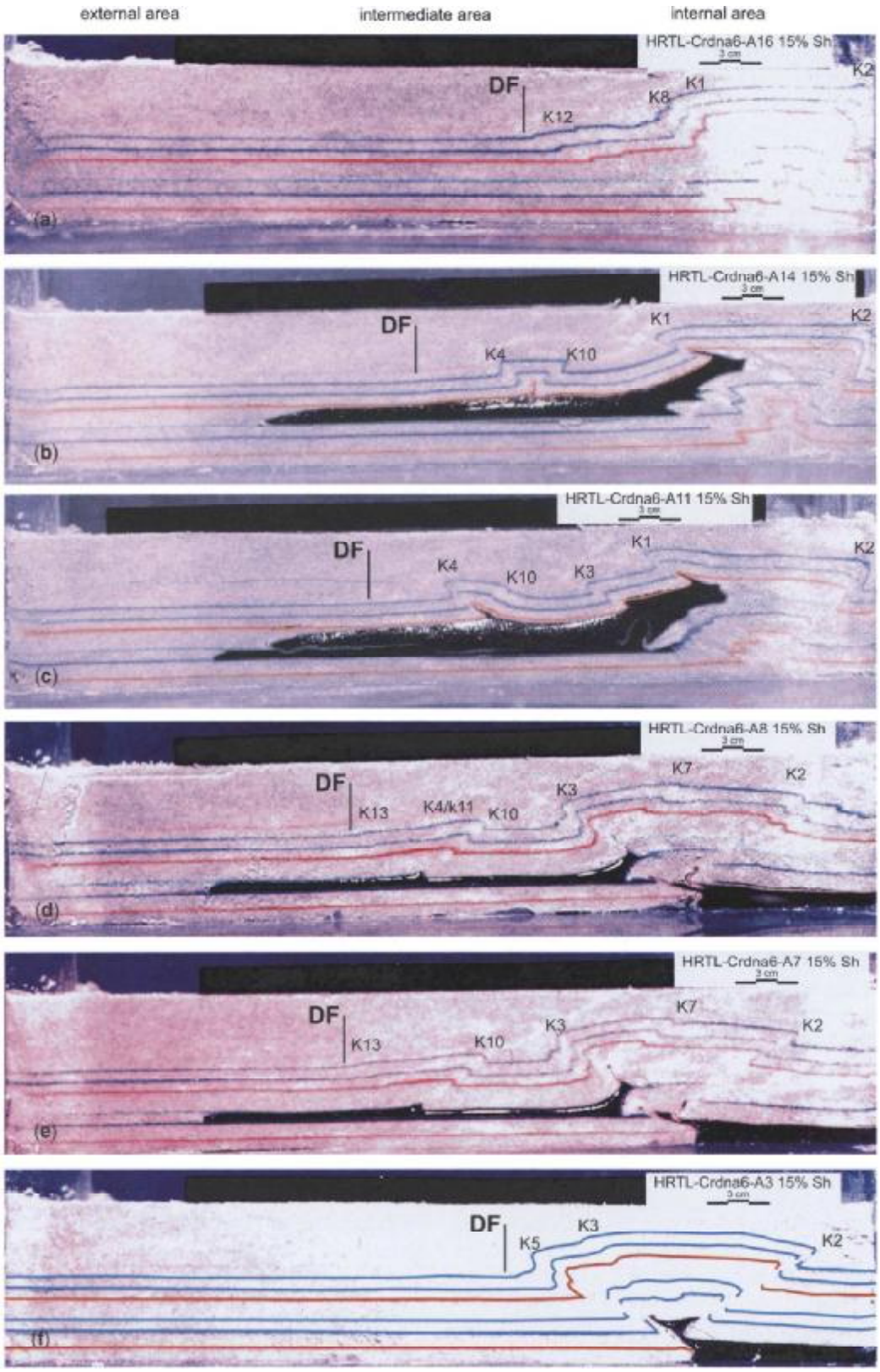


**Fig. 6.** Sections (**a**)–(**f**) (A3, A7, A8, A11, A14 and A16) of model 1 after 15% shortening. (See Fig. 3 for location.) The lower viscous layer is seen in sections (d), (e) and (f); the intermediate layer in sections (c), (d) and (e); the upper layer is seen in (b) and (c). Section a is taken of an area of the model without any viscous layers. K1, K2, ... indicate the sequence of the structures formed during shortening of the model. DF = deformation front.

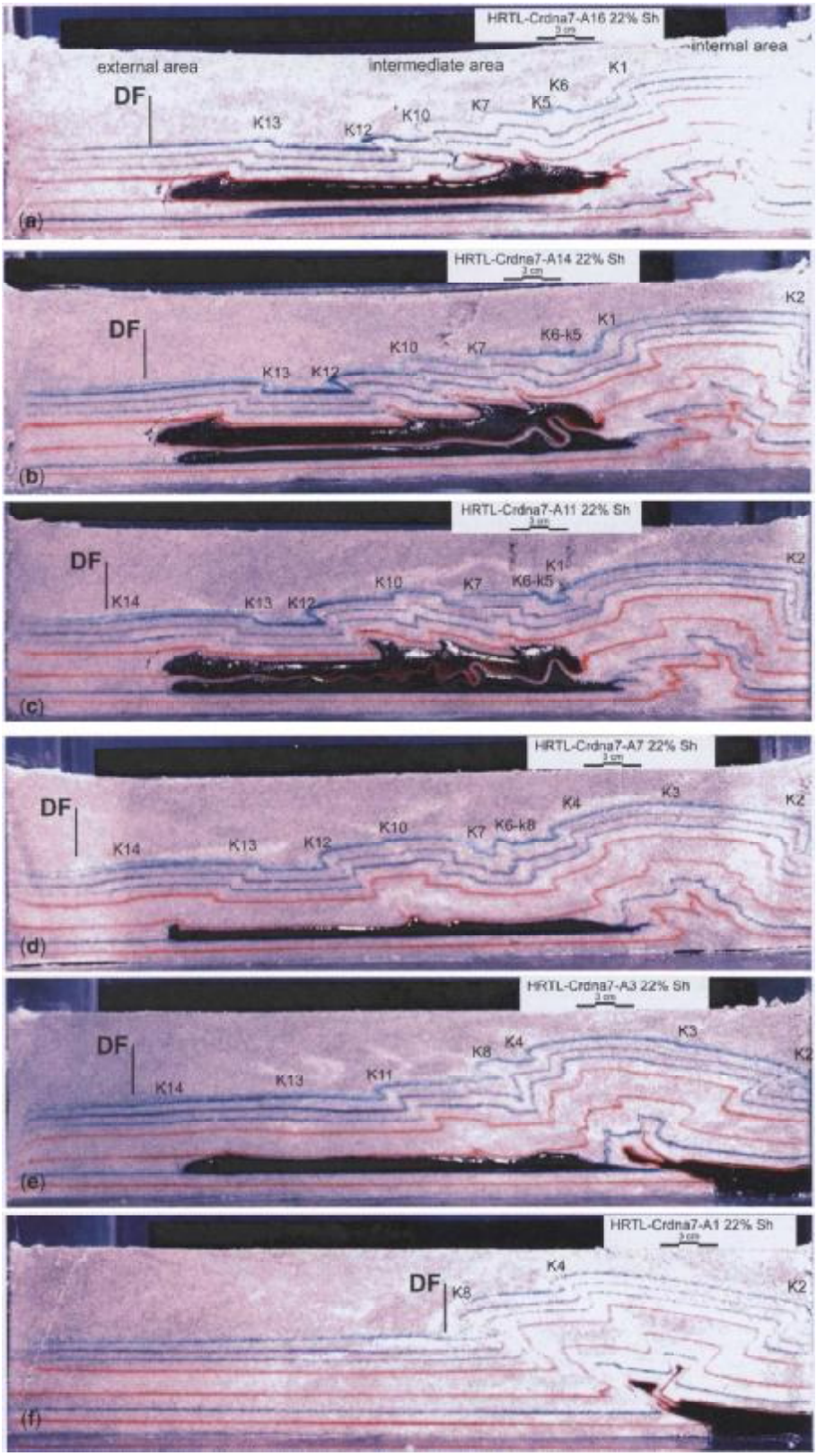


**Fig. 7.** Sections (**a**)–(**f**) (A1, A3, A7, A11, A14 and A16) of model 2 after 22% shortening. (See locations in Fig. 4.) The lower viscous layer is seen in sections (e) and (f); the intermediate layer in sections (b), (c), (d) and (e); and the upper layer is seen in (a), (b) and (c). K1, K2, ... indicate the sequence of the structures formed during shortening of the model. DF = deformation front.

10–12 cm and an uplift of 1 cm above the intermediate viscous layer; thrust faults have a spacing of 3.5 cm and vertical displacements of 1.25 cm above the upper viscous layer. These structures usually did not form across the entire width of the model; they branched with other structures and were curved along strike coinciding with the lateral pinch-out of the viscous layers (Figs 3 (K13) and 4 (K7)). Above the intermediate viscous layer, where the overburden layers are thicker, the structures have slightly larger wavelengths than above the upper viscous layer (Figs 3 and 6d; K10 and K13) (Figs 4 and 7d; K10 and K13). In cross-section, box folds outlined by a pair of kink-bands formed above the intermediate viscous layer. The kink-bands did not form simultaneously; one of them dominated, giving the general vergence to the fold. Above the intermediate viscous layer, the back-kinks dominate in both models, even though fore-kinks developed in model 2 (Figs 8d and 9d). This is supported by the sequence of formation of the different kinks (Fig. 3, structures K10 and K13). However, the structures behind these kinks may obscure this formation sequence in cross-section. In contrast in both models, foreland vergent structures were dominant above the upper viscous layer, except for the frontal box-fold which verges towards the hinterland (Fig. 6). Above this layer, thrusting, which is the dominant structure in the final stages of model deformation, follows folding.

The internal area of the models is characterized by a large stack of thrusts which extends across the entire width of the models (Figs 3, 4, 6 and 7). Above the frictional areas, the thrust stacks reach the maximum height. A ramp that developed between the lower and the intermediate viscous layers, transferred deformation to the frontal areas (Figs 3e and 4e). In areas where the intermediate detachment level was absent, deformation was not transferred to the front. Instead, the thrust emerged at the surface with a similar geometry to that of the frictional area (Figs 6f and 7f).

In the overburden layers located above the upper viscous layer the dominant deformation mechanism was thrusting, which was mainly foreland-vergent except at the deformation front (Figs 6c, and 7b, c). During shortening of the model, the upper viscous layer thickened in the hanging walls of the thrusts. No offset was seen in the sand layer located between the intermediate and upper viscous layers. This sand layer was folded (with ptygmatic signature) during the flow of the intermediate and upper viscous materials (Figs 6c, and 7b, c). Both the intensity and amplitude of the folds in this layer decreased towards the foreland as the wavelength of the folds increased. The vergence of the folds is not consistent and seems to be controlled by the drag of the upper viscous layer towards the hanging wall of the thrusted units.

## Discussion

### *Comparison of model results with the South Pyrenean Triangle Zone*

In the South Pyrenean Triangle Zone, deformation style in each of the three thrust fronts is different and depends on the mechanical behaviour of the overburden units and the detachment layers (salt and/or gypsum) (Sans *et al.* 1996*a*) and on the spatial distribution of the three detachment layers. The frontal wedges, being active during a certain period of time, were abandoned once the sole thrust climbed to a stratigraphically higher detachment level and propagated towards the foreland. The three fronts, despite evolving similarly, have different geometries. Salt-cored anticlines (e.g., Cardona, Suria, el Guix; Figs 1 and 8) formed above the salt detachment, whereas antiformal stacks (e.g., Sanaüja or Barbastro; Figs 1 and 9) formed above

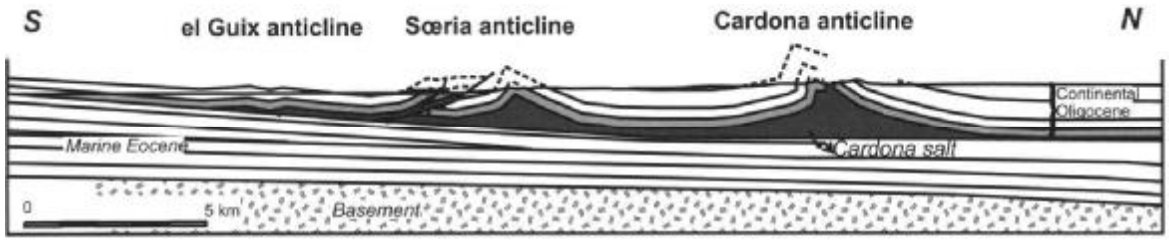


**Fig. 8.** A N–S section of the Cardona thrust front. Both frontal anticlines are double structures formed by a south-vergent forethrust in the north and a north-vergent backthrust in the south. In spite of the complexity of these structures, the frontalmost structure, which is at the pinch-out of the Cardona salt, is always hinterland-vergent. The Cardona anticline is located in a more internal position and is slightly foreland-vergent. Vertical scale is equal to the horizontal scale.

gypsum and shale detachments (Figs 8 and 9) (Sans *et al.* 1996*a*).

These types of detachments are simulated in the models presented here. Nevertheless, our models do not incorporate the effects of erosion or syntectonic deposition, which have a strong influence on the evolution of the structures in the SPTZ. Mugnier *et al.* (1997) used analogue models to outline the crucial effect of superficial mass-transport phenomena in the tectonic style of thrust belts. Using sandbox models, Storti & McClay (1995) showed that syncontractional sedimentation dramatically changes the shape of the Coulomb thrust wedge, the number of thrust slices, the internal shortening, and the critical taper of the wedge. Rapid, localized sedimentation may influence and even inhibit the development of emergent thrust faults (e.g., Willet *et al.* 1993; Storti & McClay 1995). Erosion may reactive and/or lead to increased displacement along thrusts in the internal areas, whereas sedimentation buries active thrusts and may render them inactive when a deformation front is transferred to the external areas (Koyi *et al.* 2003). Moreover, although the overall shortening in the South Pyrenean foreland was from the north, lateral ramps have formed in the area (Vergés 1993), which together with the irregular disposition of the evaporitic formation with respect to the shortening direction, have resulted in more complex geometries and rotation of the deformation fronts (Sans *et al.* 1996*a*). Similarly, in our models, which are a simplified version of the SPTZ, lateral ramps, discontinuous thrusts and thrusts inclined to the shortening direction have formed (Figs 3 and 4). However, even though the degree of rotation (around a vertical axis) observed in the SPTZ (*c.* 90°), is not entirely duplicated in our models (*c.* 55°), the experiments illustrate the irregular evolution of thrust fronts above multiple detachments. Similar to the natural prototype, lateral ramps formed at the lateral pinch-out of the viscous detachments (Figs 3 and 4).

The Cardona thrust front is characterized by the presence of a 350 m thick salt layer (Cardona Formation). In this area, shortening was in general accommodated by folding, with both fore and back-vergence and development of a counter-regional frontal structure (Fig. 8). This situation was simulated in the models by the intermediate viscous layer (pure SGM36). Structures formed above this layer show, at the end of the experiment, a back-vergent asymmetric box fold (Figs 6d and e). With increasing bulk shortening (model 2), the initially back-vergent structures may increase the displacement along the fore-kink resulting in the back kink being carried upwards and forming box folds with tilted crests towards the foreland (Fig. 7d; K12-K7 and K14-K13). This suggests that, above the intermediate detachment, folds that nucleated at the deformation front with an initial back-vergence that were modified with progressive shortening. As a result, above such type of detachments, subsequent triangle zones formed at the deformation front, regardless of their location relative to the pinch-out of the ductile layer. This type of triangle zones is dominated by folding and could be correlated with type I of triangle zones described by Couzens-Schultz & Wiltschko (1996).

Where the detachment horizon in the South Pyrenean Triangle Zone consists of gypsum (Barbastro and Beuda formations), deformation is mainly dominated by thrusting, with less folding (Sans *et al.* 1996*a*). At the Barbastro front (Fig. 9), back-vergent thrusts are only present at the pinch-out of the evaporitic layer (Barbastro thrust front). This situation was simulated by the upper viscous layer of the impure SGM36, which was one order of magnitude more viscous than the pure SGM36 used for the intermediate viscous layer. Although thrusted

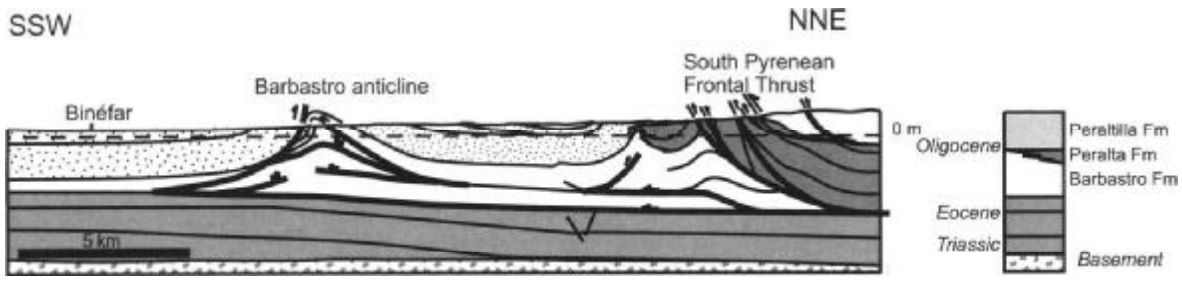


**Fig. 9.** Balanced cross-section of the Barbastro thrust front constructed at minimum shortening. Gypsum layers of the Barbastro Fm are thrust and piled to form a foreland-vergent antiformal stack. This structure is limited in the front by a hinterland-vergent thrust which defines the thrust wedge geometry of this frontal anticline. Structures more to the north all are foreland-vergent. The stratigraphic column is not to scale. Modified from Sans *et al.* (1996*a*).

folds dominate at the end of the experiment, initially symmetric box folds (Fig. 6b) formed above the upper detachment. As deformation progressed, these folds squeezed the viscous material out of their cores and evolved to foreland-vergent thrusts (Fig. 7a; K7, K10 and K12). However, at the pinch-out of the upper detachment, a back-vergent box fold was formed (Fig. 7a; K13). The asymmetry of the fold was maintained until the end of the experiment (Fig. 7a). As a result, above the upper detachment, triangle zones are formed only at the pinch-out of the viscous layer, and deformation style in the overburden was dominated by thrusting (Fig. 7a).

Finally, when the mechanical stratigraphy of the detachment is complex, with the presence of both rocksalt and gypsum (Cardona and Barbastro formations respectively), the features observed in the field (Sanaüja anticline in the Cardona thrust) indicate that salt and gypsum are folded disharmonically. The evolution of this thrust wedge is sketched in Figure 10 (Sans *et al.* 1996*a*). During the early stages of deformation, as the basal detachment propagated towards the foreland, the Barbastro gypsum, and presumably the Cardona salt, developed flow folds of short wavelength (tens of meters). These folds have generally southwestern vergence in both limbs of the Sanaüja anticline, which indicates that they are not diapiric or second order folds of the anticline (Sans *et al.* 1996*b*). Instead these folds are formed due to the ductile shear in the detachment levels as a result of flow of the Cardona salt during shortening. Further deformation was accommodated by folding and the flow of the Cardona salt from the NE syncline into the anticline. Increasing friction along the basal thrust due to the decrease in thickness of the Cardona Formation to the southwest, led to the development of a counter-regional thrust (northeast-vergent). Later, a foreland-dipping passive roof duplex developed in the forelimb of the anticline. The roof thrust is located a few meters below the upper contact of the gypsum, and also a detachment is present between the Cardona salt and Barbastro gypsum which allows the differential deformation of both lithologies.

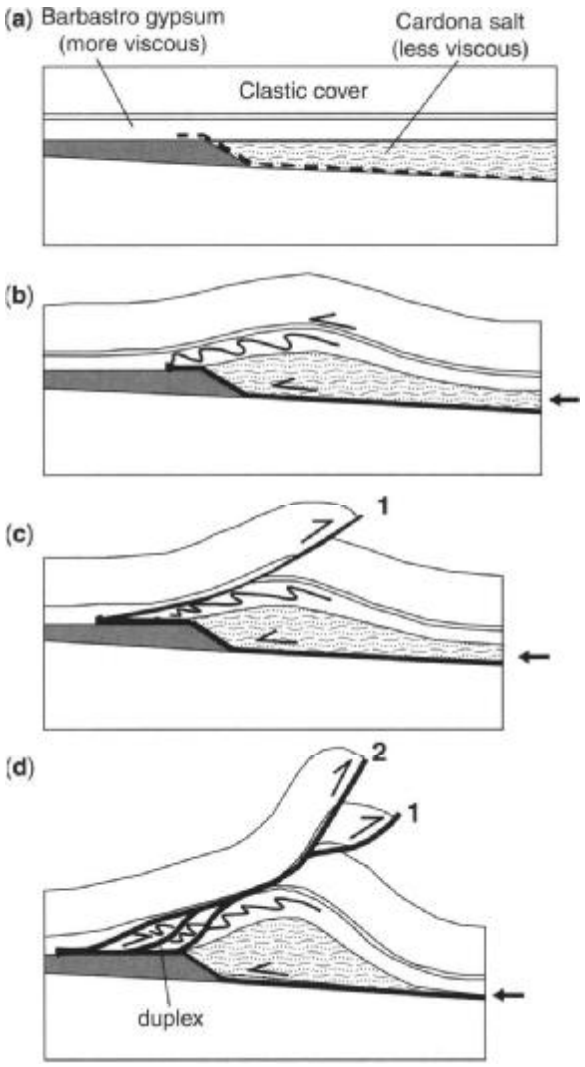


**Fig. 10.** Evolution of the Sanaüja anticline. (**a**) Initial geometry of the Cardona salt (light grey), the Barbastro gypsum and the clastic cover. (**b**) Cardona salt flowed from the northeast into the growing anticline and folds developed in the Barbastro gypsum related to the shear sense in the detachment. (**c**) A backthrust developed, reactivating previous foreland-vergent structures and separating folded gypsum layers from unfolded gypsum layers. (**d**) Salt flow from the northeastern limb continued at the same time as the development of a hinterland-vergent duplex in the Barbastro Formation. Not to scale.

Growth of the Sanaüja anticline ended with the complete withdrawal of the Cardona salt formation from the adjacent syncline to the NE. Some segments of the backthrust in the hanging wall of the roof backthrust became inactive due to the growth of the anticline and steepening of the limbs. In the models, this scenario was simulated by two viscous layers (intermediate and upper viscous layers) overlapping each other. Although the details of the evolution of the Sanaüja anticline have not been reproduced in our models, the main geometrical features can be observed. The first similarity is the location of the deformation front and its vergence. In model 2, deformation has reached the pinch-out of the intermediate viscous layer, and both the intermediate and upper viscous layers are deformed. The frontal counter-regional

thrusted fold is the equivalent structure of the Sanaüja anticline (Figs 7b and c).

*Deformation of transfer zones*

At the early stages of deformation, before any visible structures could be detected at the surface of the model (before 2% bulk shortening), the sand layers accommodated the push from the rear by penetrative deformation, which must have led to internal compaction of the sand layers. This penetrative strain was visible through the square grid, printed initially on top of the model, and which close to the backstop was deformed to rectangles with an aspect ratio of 1.1 at 2% bulk shortening. Also, as deformation proceeded, change in the elevation of the surface started sequentially from more internal to more external areas. Most of the structures grew in amplitude throughout the model shortening.

All three viscous layers acted as effective detachments that allowed deformation to be transmitted vertically from the lower to the upper levels, leaving the sand layers below them undeformed, and horizontally further from the rearwall. Model results show that at the presence of different detachment horizons, deformation is transferred from lower to upper detachment horizons. In this article, two situations are studied: (1) transfer from a lower less viscous detachment to an upper highly ductile detachment without overlap and, (2) transfer from a lower frictional detachment to a higher viscous detachment formed by two partially overlapping viscous layers of different rheologies. Below, we use model results to illustrate these two cases.

In the case where two detachments were present, one in front and at a higher stratigraphic position than the other, deformation was transferred from the lower detachment to the upper one through a ramp (Figs 6d and e, 7e and 11) forming a flat-ramp-flat (FRF) staircase. The basal detachment of the model thus had a flat in the lower viscous detachment, a ramp at its pinch-out and a flat in a higher detachment (intermediate viscous layer). In the lower detachment, a large pop-up formed above the pinch-out of the viscous layer (Figs 6e and f, 7e and f). This structure accommodated shortening until it was transferred to the intermediate detachment. Then the fold was transported above the ramp to the intermediate detachment. Above the ramp, which connected the lower and intermediate detachments, there was mainly a forelandward transport of the anticline (cored by the lower detachment), without any further vertical growth.

The geometry of the models is similar to the geometry of the ramp between the Beuda formation, which is the lower detachment and the Cardona Formation, which is the intermediate detachment in the South Pyrenean Triangle Zone (Figs 6d, e and 11). Above the ramp linking the lower Beuda detachment layer with the upper Cardona detachment, an anticline (Oliana anticline) has formed. This scenario was reproduced above the ramp linking the lower with the intermediate viscous layer, where an anticline formed. However, the models failed to reproduce some other details e.g., the antiformal stack coring the anticline and the geometry of the major backthrust present at the base of the Cardona detachment (Verges 1993), probably because not enough shortening was applied to the models.

In the case where displacement was transferred from a lower frictional detachment to a higher viscous detachment which consisted of two partially overlapping viscous layers of different rheologies (double viscous detachment), deformation was partitioned. Deformation was transmitted through a ramp from the lower frictional detachment to the upper viscous detachment (Figs 6b and c, 7b and c). No deformation is seen in the layers below the double viscous detachment. The sand layers located above the upper detachment were thrusted, with thrust surfaces soling into the upper detachment layer (Fig. 7). In contrast, the sand layer embedded between the upper and intermediate detachments underwent folding, suggesting that deformation between these two viscous layers is partitioned. This is in agreement with field observations reported by Sans & Vergés (1995) and Sans *et al.* (1996*a*), indicating that the top part of the Barbastro gypsum deforms conformably with its overburden unrelated to the Cardona Formation.

In model 1, shortening (15% bulk shortening) was stopped before deformation reached the frontal pinch-out of the intermediate and upper ductile layers. In model 2, shortening (22% bulk shortening) continued until deformation reached the frontal pinch-out. However, the pinch-out was only slightly deformed. It is thus not possible to document how deformation would have proceeded if the model had been shortened further. However, based on the sequence of deformation style above the lower viscous layer at the rear of the model, it is argued here that continued shortening would have been accommodated within the layers above the intermediate and upper viscous layers before propagating to the frictional areas in front of the viscous layers (Fig. 7f).

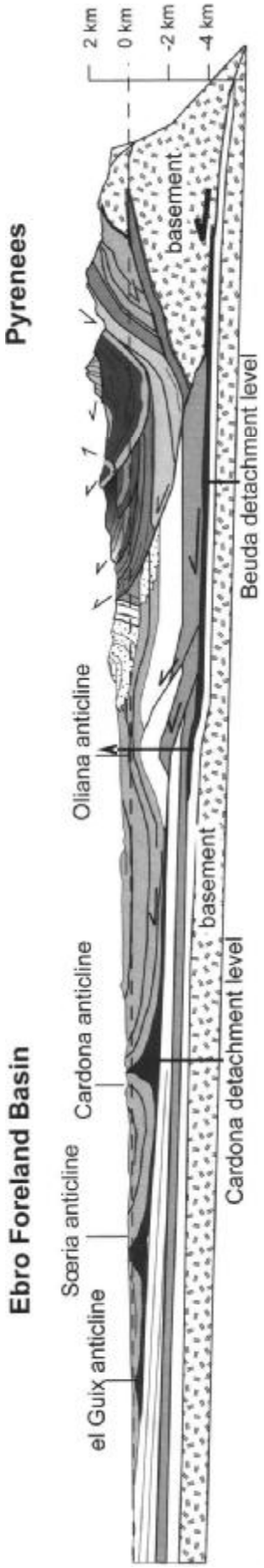


**Fig. 11.** Regional cross-section through the Beuda and Cardona thrust fronts, showing transfer of deformation from deeper detachments to shallower levels (from Vergés 1993). The Oliana anticline was initiated where the basal thrust ramps from the Beuda Formation (lower detachment) to the Cardona Formation (intermediate detachment) and has been transported over the Cardona flat.

## Conclusions

Results of analogue models show that triangle zones form when (1) deformation is transferred to weak horizons located at higher stratigraphic levels, and (2) the deformation front reaches the pinch-out of the weak horizons. In the models, transfer of deformation from lower to upper viscous detachments, which do not overlap, takes place through a connecting ramp. Structures in the lower detachment are highly controlled by the geometry of its foreland pinch-out. In the upper detachment, deformation is accommodated in front of and away from the ramp. Even in cases where a lower viscous detachment is absent, deformation from a frictional detachment is transferred to a viscous, but stratigraphically higher, detachment through a connecting ramp above which an anticline forms.

Model results also show that, in cases where two viscous layers (intermediate and upper layers) are partially overlapping, the two layers may act as one viscous unit above which the upper overburden layers decouple from the lower overburden layers. However, each of the viscous layers accommodate the shortening separately and hence deformation between them is partitioned; overburden layers above the upper viscous layer undergo thrusting, while the layers above the intermediate viscous layer accommodate the shortening by folding.

The models presented here have similar geometric features to those developed in the South Pyrenean Triangle Zone, the Beuda, Cardona and Barbastro thrust fronts, suggesting that they could have formed and evolved in a similar way; the initial distribution of the viscous layers and their pinch-out dictates the position and geometry of the deformation fronts.

J. Vergés kindly provided an electronic version of a regional cross-section of the Pyrenees. Thanks are due to A. Ravaglia and an anonymous reviewer for their thorough review and many insightful comments, which contributed to the improvement of the manuscript. Special thanks to G. Schreurs for useful comments and suggestions. H. A. Koyi acknowledges financial support from the Swedish Research Council (VR).

## References

BALLARD, J. F., BRUN, J-P., VAN DEN DRIESSCHE, J. & ALLEMAND, P. 1987. Propagation des chevauchements au-dessus des zones de décollement: modèles expérimentaux. *Comptes rendus de l'Académie des Sciences*, **305**, Série II, 1249–1253.

BONINI, M. 2001. Passive roof thrusting and forelandward fold propagation in scaled brittle-ductile physical models of thrust wedges. *Journal of Geophysical Research*, **106**, 2291–2311.

BRACE, W. F. & KOHLSTEDT, D. L. 1980. Limits on lithosphere stress imposed by laboratory experiments. *Journal of Geophysical Research*, **85**, 6248–6252.

BURBANK, D. W., PUIGDEFÁBREGAS, C. & MUÑOZ, J. A. 1992. The chronology of the Eocene tectonic and stratigraphic development of the eastern Pyrenean Foreland Basin, NE Spain. *Geological Society of America Bulletin*, **104**, 1101–1020.

BYERLEE, J. 1978. Friction of rocks. *Pure Applied Geophysics*, **116**, 615–625.

CHARLESWORTH, H. A. K., JOHNSTON, S. T. & GAGNON, L. G. 1987. Evolution of the triangle zone in the Rocky Mountain Foothills near Coalspur, Central Alberta. *Canadian Journal of Earth Science*, **24**, 1668–1678.

CHILDS, C., EASTON, S. J., VENDEVILLE, B. C., JACKSON, M. P. A., LIN, S. T., WALSH, J. J. & WATTERSON, J. 1993. Kinematic analysis of faults in a physical model of growth faulting above a viscous salt analogue. *Tectonophysics*, **228**, 313–329.

COTTON, J. T. & KOYI, H. A. 2000. Modelling of thrust fronts above ductile and frictional decollements: application to structures in the Salt Range and Potwar Plateau, Pakistan. *Geological Society of America Bulletin*, **112**, 351–363.

COUSENZ-SCHULTZ, B. A. & WILTCHSKO, D. V. 1996. The control of mechanical stratigraphy on the formation of triangle zones. *Bulletin Canadian Petroleum Geology*, **44**, 165–179.

GIL, J. A. & JURADO, M. J. 1998. A 3D geological interpretation and numerical modelling of salt movement in the Barbastro–Balaguer anticline (Southern Pyrenees), *Tectonophysics*, **293**, 141–155.

GORDY, P. L., FREY, F. R. & NORRIS, D. K. 1977. *Geological Guide for the Waterton-Glacier Park Field Conference, Calgary*. Canadian Society of Petroleum Geologists.

HATCHER, R. 1999. Development of triangle zones in the evolution of foreland fold-thrust belts. *American Association of Petroleum Geologists Annual Convention*. Abstracts with program, A56.

KOYI, A. H., JENYON, M. K. & PETERSEN, K. 1993. The effect of basement faulting on diapirism. *Journal of Petroleum Geology*, **16**, 285–312.

KOYI, H. A., HESSAMI, K. & TEIXELL, A. 2000. Epicenter distribution and magnitude of earthquakes in fold-thrust belts: insights from sandbox models. *Geophysical Research Letters*, **27**, 273–276.

KOYI, H. A., SANS, M., TEIXELL, A., COTTON, J. & ZEYEN, H. 2003. The significance of penetrative strain in confractional areas. *In*: MCCLAY, K. R. (ed.) *Thrust Tectonics and Petroleum Systems*. Memoir 8, **2**, American Association of Petroleum Geologists, Tulsa, OK, 207–222.

KRANTZ, R. W. 1991. Measurements of friction coefficients and cohesion for faulting and fault reactivation in laboratory models using sand and sand mixtures. *In*: COBBOLD, P. R. (ed.) Experimental and numerical modelling of continental deformation. *Tectonophysics*, **188**, 203–207.

LETOUZEY, J., COLLETTA, B., VIALLY, R. & CHERMETTE, J. C. 1995. Evolution of salt-related structures in compressional settings. *In*: JACKSON, M. P. A. *ET AL.* (eds) *Salt Tectonics. A Global Prespective*. American Association of Petroleum Geologists Memoir, **65**, 41–60.

MARTÍNEZ, A., VERGÉS, J., CLAVELL, E. & KENNEDY, J. 1989. Stratigraphic framework of the thrust geometry and structural inversion in the southeastern Pyrenees: La Garrotxa area. *Geodinamica Acta*, **3**, 185–194.

MCCLAY, K. R. & ELLIS, P. G. 1987. Geometries of extensional fault systems developed in model experiments. *Geology*, **15**, 341–344.

MEIGS, A. J., VERGÉS, J. & BURBANK, D. W. 1996. Ten million-year history of a thrust sheet. *Geological Society of America Bulletin*, **108**, 1608–1625.

MULUGETA, G. & KOYI, H. 1987. Three-dimensional geometry and kinematics of experimental piggyback thrusting. *Geology*, **15**, 1052–1056.

PARDO, G. & VILLENA, J. 1979. Aportación a la geología de la región de Barbastro. *Acta Geológica Hispánica*, Homenatge a Lluis Solé i Sabarís, **14**, 289–292.

RIBA, O., REGUANT, S. & VILLENA, J. 1983. Ensayo de síntesis estratigráfica y evolutiva de la cuenca terciaria del Ebro. Libro Jubilar J. M. Rios, *Geología de España*, **II**, 131–159.

SÁEZ, A. 1987. *Estratigrafía y sedimentología de las formaciones lacustres del tránsito Eoceno Oligoceno del NE de la Cuenca del Ebro*. Ph.D. thesis, Universitat de Barcelona.

SANS, M. 1999. *From thrust tectonics to diapirism: The role of evaporites in the kinematic evolution of the eastern south-Pyrenean front*. Ph.D. thesis, Universitat de Barcelona.

SANS, M. 2003. From thrust tectonics to diapirism. The role of evaporites in the kinematic evolution of the eastern South Pyrenean front. *Geologica Acta*, **1**, 239–259.

SANS, M. & VERGÉS, J. 1995. Fold development related to contractional salt tectonics: southeastern Pyrenean thrust front, Spain. *In*: JACKSON, M. P. A., ROBERTS, D. G. & SNELSON, S. (eds) *Salt Tectonics: a Global Perspective*. American Associaton of Petroleum Geologists Memoir, **65**, 369–378.

SANS, M., MUÑOZ, J. A. & VERGÉS, J. 1996*a*. Triangle zone and thrust wedge geometries related to evaportic horizons (southern Pyrenees). *Bulletin of Canadian Petroleum Geology*, **44**, 375–384.

SANS, M., SÁNCHEZ, A. & SANTANACH, P. 1996*b*. Internal structure of a detachment horizon in the most exernal part of the Pyrenean fold and thrust belt (northern Spain). *In*: ALSOP, G. I., BLUNDELL, D. J. & DAVISON, I. (eds) *Salt Tectonics*, Geological Society, London, Special Publications, **100**, 65–76.

SENZ, J. G. & ZAMORANO, M. 1992. Evolución tectónica y sedimentaria durante el Priaboniense superior-Mioceno inferior, en el frente de cabalgamientos de las Sierras Marginales occidentales. *Acta Geològica Hispànica*, **27**, 195–209.

STORTI, F. & MCCLAY, K. 1995. Influence of syntectonic sedimentation on thrust wedges in analogue models. *Geology*, **23**, 999–1002.

VERGÉS, J. 1993. *Estudi geològic del vessant sud del Pirineu oriental i central. Evolució cinemàtica en 3D*. Ph.D. thesis, Universitat de Barcelona.

VERGÉS, J. & BURBANK, D. K. 1996. Eocene-Oligocene thrusting and basin configuration in the eastern and central Pyrenees (Spain). *In*: FRIEND, P. F. & DABRIO, C. J. (eds) *Tertiary Basins of Spain*. Cambridge University Press, 120–133.

VERGÉS, J., MUÑOZ, J. A. & MARTÍNEZ, A. 1992. South Pyrenean fold-and-thrust belt: role of foreland evaporitic levels in thrust geometry. *In*: MCCLAY, K. R. (ed.) *Thrust Tectonics*. Chapman & Hall, London, 255–264.

VERSCHUREN, M., NIEUWLAND, D. A. & GAST, J. 1996. Multiple detachment levels in thrust tectonics: sandbox experiments and palinspastic reconstruction. *In*: BUCHANAN, P. G. & NIEUWLAND, D. A. (eds) *Modern Developments in Structural Interpretation, Validation and Modelling*. Geological Society, London, Special Publications, **99**, 227–234.

WEIJERMARS, R. 1986. Finite strain of laminar flows can be visualized in SGM36-polymer. *Naturwissenschaften*, **73**, 33–34.

WEIJERMARS, R., JACKSON, M. P. A. & VENDEVILLE, B. C. 1993. Rheological and tectonic modelling of salt provinces. *Tectonophysics*, **217**, 143–174.

WILLETT, S., BEAUMONT, C. & FULLSACK, P. 1993. Mechanical model for the tectonics of doubly vergent compressional orogens. *Geology*, **21**, 371–374.

# Analogue modelling of a reactivated, basement controlled strike-slip zone, Sierra de Albarracín, Spain: application of sandbox modelling to polyphase deformation

S. MERTEN[1], W. G. SMIT[1], D. A. NIEUWLAND[2] & H. E. RONDEEL[1]
[1]*Faculty of Earth and Life Sciences, Vrije Universiteit, de Boelelaan 1085, 1081 HV Amsterdam, The Netherlands (e-mail: sandra.merten@falw.vu.nl)*
[2]*4e Binnenvestgracht 13, 2311 NT Leiden, The Netherlands*

**Abstract:** This paper presents the results of an analogue modelling study on the reactivation of Riedel shears generated by basement-induced sinistral strike-slip faulting. It is based on a natural example in the Sierra de Albarracín, Iberian Range (Spain). The area has a polyphase deformation history, defined by the Variscan and Alpine orogenies. Late Variscan deformation was concentrated in a wide NW–SE shear zone with accompanying kilometre-scale E–W Riedel shears, which divided the Palaeozoic basement into large fault blocks. Alpine reactivation resulted in differential movements on the Riedel shears, as evidenced by a NW–SE chain of Palaeozoic inliers surrounded by a Mesozoic cover that generally shows minor deformations except near the E–W Riedel shears, where strata locally appear in near-vertical to overturned position.

Sandbox analogue modelling was applied to improve insight into the structural history. It focused on the kinematics of spontaneously developed en echelon Riedel shears, reactivated in a rotated stress field. Sand with a controlled added strength was used to form Riedel shears in a first deformation phase to act as weak zones for a second phase.

The modelling showed that in the first deformation phase large pop-up structures developed between the Riedel shears in a basement-induced sinistral strike-slip zone. Later reactivation in the N060°E and N135°E shortening directions was taken up respectively by sinistral-reverse and dextral-reverse shear along the pre-existing Riedel shears, but only if the sand on one side of the fault zone was allowed to move freely along the other. Scissor faulting along the Riedel shears with their complex 3D-geometry increased the height of the up-squeezed blocks. For experiments with fixed boundaries and no oil-water emulsion layer between the base plate and sand pack, thrusting at the backstop occurred rather than reactivation of the Riedel shears. This approach provided robust insights on the 4D development of the Sierra de Albarracín area.

Although the 3D geometry of strike-slip faults formed in the upper brittle crust is generally well understood, the kinematic and structural processes associated with the reactivation of these faults in rotated stress fields are poorly known. Sandbox analogue modelling offers an opportunity to systematically study the evolution of these faults, as it allows spontaneous growth of faults in three dimensions (Naylor *et al.* 1986). Several authors have described the complex pattern of en echelon curved faults associated with experimental basement-induced strike-slip faulting (e.g., Cloos 1928; Riedel 1929; Wilcox *et al.* 1973; Naylor *et al.* 1986; Richard 1991; Schellart & Nieuwland 2003). Schreurs & Colletta (2002) showed with a series of oblique-slip experiments that the early fault style in transpression experiments depends on the ratio of shear strain rate and shortening rate. For relatively high strain ratios, initial failure in brittle layers is accommodated by steep strike-slip faults; for lower strain ratios pairs of thrust faults develop. Additional deformation is mostly taken up by oblique-slip along favourably oriented faults, creating positive flower structures.

Several authors have carried out analogue sandbox experiments on the reactivation of pre-existing faults. Richard & Krantz (1991) showed that faults produced during initial dip-slip deformation strongly influence the patterns of superimposed strike-slip deformation. Dip-slip faults are reactivated as strike-slip faults at depth; reactivation at the surface is less common. They attributed this behaviour to a drop in cohesion associated with existing

*From*: BUITER, S. J. H. & SCHREURS, G. (eds) 2006. *Analogue and Numerical Modelling of Crustal-Scale Processes.* Geological Society, London, Special Publications, **253**, 135–152.
0305-8719/06/$15.00 

faults, which increases with depth where faults are generated. Reactivation experiments on the influence of pre-existing thrust faults on normal fault geometry were carried out by Facenna *et al.* (1995). They revealed that reactivation in brittle material only occurs when the dip of the pre-existing fault exceeds 40°, because of the drop in friction coefficient, and thus of the shear strength that occurs along the pre-existing fault zone. Buchanan & McClay (1991) and McClay & Buchanan (1992) showed that inversion of extensional fault systems is characterized by high-angle thrust systems that may be convex upwards, steepen downwards and join pre-existing extensional detachments. In these experiments the footwall of the normal fault consisted of a material that was too strong to be faulted in a sandbox model experiment. As a result, the final fault pattern was strongly model driven.

In all the reactivation experiments described above, second phase deformation is induced by movements of a base plate. In this contribution we present the results of sandbox analogue modelling focusing on the geometry and kinematics of spontaneously developed en echelon Riedel shears, reactivated in a rotated stress field. Riedel shears were formed in a first deformation phase induced by strike-slip faulting along a base plate. Sand with a controlled added strength (Mulugeta 1988; Lopes Cardozo *et al.* 2002; Van Mechelen 2004) enabled us to preserve these Riedels as weak zones for a second deformation phase, in which the base plate was fixed.

Mechanically, reactivation processes occur because existing fault zones are weaker than the non-deformed surrounding rocks. Important parameters controlling reactivation are a drop in cohesion between the fault zone and its surrounding rock (Donath & Cronwell 1981), and a drop in friction coefficient. These parameters result in a decrease of shear strength along the pre-existing faults, thus creating the possibility of reactivating faults that are properly oriented with respect to the principal stress directions (Mandl 1988). The boundary conditions for the sandbox models are based on geometries and principal stress directions obtained from a natural example in the Sierra de Albarracín (Spain). The polyphase deformation history of the area provided the opportunity to test different

consists of an extensively deformed Palaeozoic basement unconformably covered by Mesozoic and Tertiary sediments. Several Palaeozoic basement inliers crop out in NW–SE alignment (Fig. 1b). In this paper the main focus is on two of these inliers, the Macizo de Nevera and the Macizo del Tremedal (Fig. 2).

### *Geological evolution of the Iberian Range*

The Iberian Range is a NW–SE trending intraplate mountain range in the central-eastern part of the Iberian Peninsula. Its tectonic evolution is mainly defined by reactivation of Late Variscan strike-slip zones during several phases of Mesozoic extension and Alpine compression (Arche & López-Gómez 1996; Casas-Sainz & Maestro-González 1996). Early Variscan E–W compression led to the build-up of the Variscan orogen and induced N–S folding and thrusting. Late Variscan collapse of the orogen caused the development of conjugate strike-slip faults and of large-scale NW–SE orientated extensional shear zones (Doblas *et al.* 1994). These Late Variscan shear zones controlled the formation of the intracratonic Iberian Basin during Permian and Mesozoic extension (Arche & López-Gómez 1992, 1996; Salas & Casas 1993; Guimerà 1996), when rifting induced vertical movements on the Late Variscan faults, generating volcanic activity (Arthaud & Matte 1977; Alvaro *et al.* 1979) and the formation of local palaeohighs (Salas & Casas 1993). The Serranía de Cuenca Fault and the Molina–Teruel–Espadan Fault (Fig. 1b; SCF and MTEF) acted as basin boundary faults in the southeastern part of the Iberian Basin. These NW–SE normal fault systems are parallel to the fundamental Variscan structures and consist of 50 to 70 km long arcuate sequences, offset by transversal faults trending at high angles (Arche & López-Gómez 1992, 1996). Gravity modelling by Salas & Casas (1993) suggests that the faults go down beyond the Moho directly below the Sierra de Albarracín.

The Alpine orogeny caused the formation of the Iberian Range through inversion of the Iberian Basin (Arche & López-Gómez 1996). Several Alpine phases have been identified, starting with collision between Iberia and

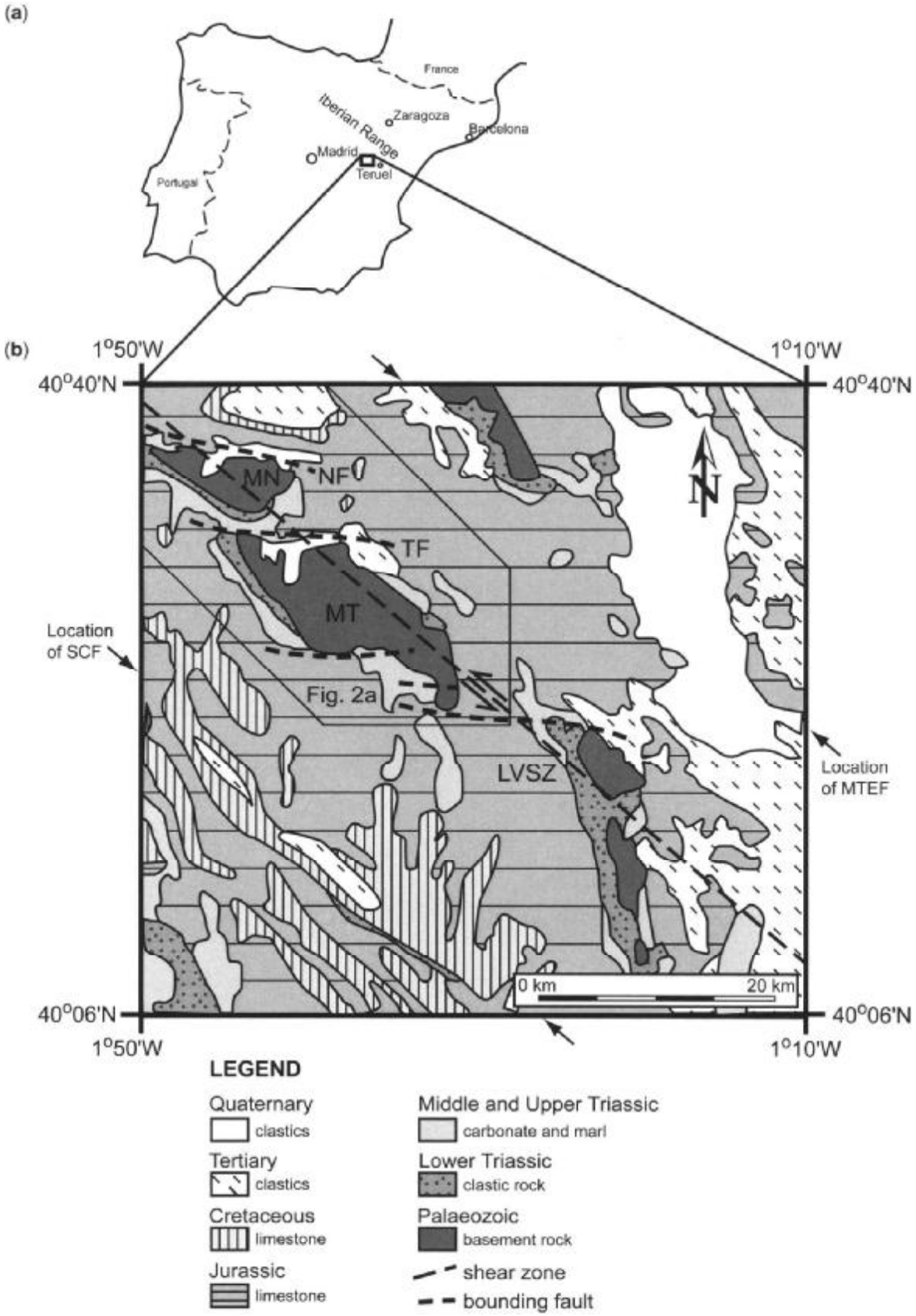


**Fig. 1.** (**a**) Location map of the Sierra de Albarracín (Spain). Inset shows the location of the study area. (**b**) Main geological features of the NW–SE trending Sierra de Albarracín: MN = Macizo de Nevera; MT = Macizo del Tremedal; LVSZ = Late Variscan shear zone; SCF = Serranía de Cuenca Fault; MTEF = Molina–Teruel–Espadan Fault. Inset shows the location of Fig. 2a.

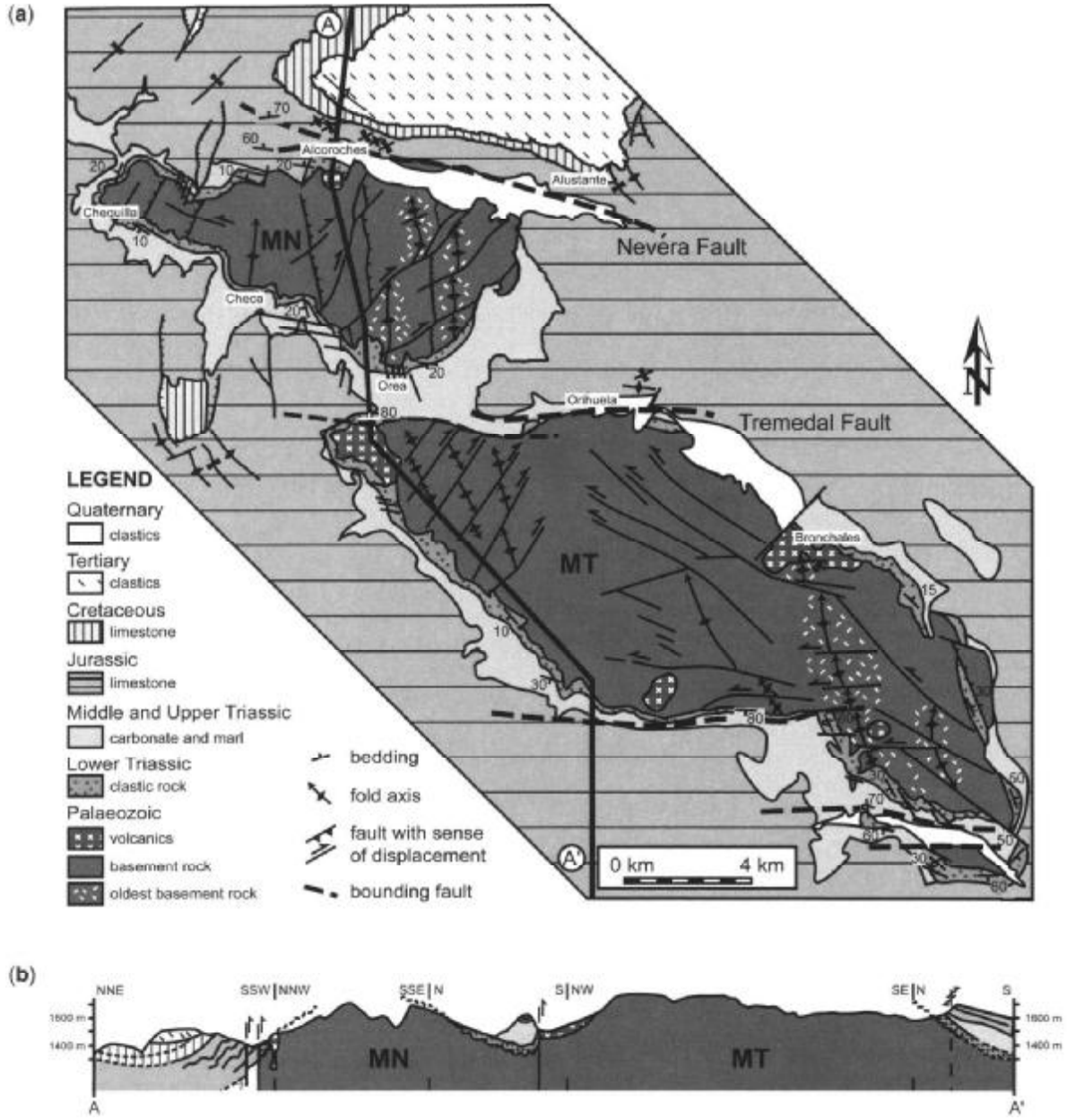


**Fig. 2.** (**a**) Structural map of the Macizo de Nevera (MN) and the Macizo del Tremedal (MT). The profile line A–A′ indicates the position of (**b**) schematic cross-section through the Macizo de Nevera and the Macizo del Tremedal. Only the main faults that divide the Palaeozoic basement into different blocks are indicated.

De Ruig *et al.* (1991) defined for the Early Eocene a NW–SE compressional stress regime west of the Sierra de Albarracín and a NNE–SSW compressional regime more to the east. From Early Oligocene to Early Miocene times a NE–SW compressional regime, $\sigma_1$ oriented at N060°E, reactivated Late Variscan basement faults and was responsible for NW–SE folding of the Mesozoic and Tertiary cover. This regime is considered the most important Alpine stress field in the Iberian Range (Simón-Gómez 1986; Rodriguez-Pascua *et al.* 1994; Muñoz-Martín *et al.* 1998). For the Middle Miocene a NNW–SSE compressional regime is identified, followed by a dominantly NW–SE regime with $\sigma_1$ oriented between N130°E and N150°E from the Late Miocene to present activating mainly strike-slip faults (Simón-Gómez 1986; Rodriguez-Pascua *et al.* 1994; De Vicente *et al.* 1996; Muñoz-Martín *et al.* 1998).

### *Stratigraphy of the Sierra de Albarracín*

The folded Palaeozoic rocks of the Sierra de Albarracín consist of a heterogeneous siliciclastic pelitic sequence of Ordovician to Silurian age.

Total thickness of this basement amounts to about 1 to 2 km, with about 400 m of shales at the base (Rondeel *et al.* 1984). It is locally transected and covered by Permian volcanics (Pérez-Arlucea & Sopeña 1983, 1985; Rondeel *et al.* 1984). The absence of Devonian and Carboniferous strata that appear elsewhere in the Iberian Range implies non-deposition and/or large-scale uplift and erosion.

The Palaeozoic is unconformably overlain by Upper Permian to Lower Triassic continental siliciclastics (Pérez-Arlucea & Sopeña 1983, 1985; Ramos *et al.* 1986; Arche & López-Gómez 1992; Muñoz *et al.* 1992), Middle Triassic dolomites alternating with clay-marl-gypsum levels (Hinkelbein 1969; Pérez-Arlucea & Sopeña 1983, 1985; López-Gómez *et al.* 1993), gypsum-rich Upper Triassic clays and marls (Hinkelbein 1969) and Jurassic limestones. The basal siliciclastics cover a palaeorelief of at least 60 m. They have a strongly variable thickness and are even absent in the eastern part of the Macizo de Nevera where higher units transgressively overlie Variscan rocks (Pérez-Arlucea & Sopeña 1983, 1985; Rondeel *et al.* 1984). These basal siliciclastics are mechanically attached to the basement. Thickness variations within the overlying Triassic are attributed to later décollement excision. The Jurassic limestones behaved as a rigid super-stratum relative to the Triassic (Rondeel *et al.* 1984).

Unconformably covering this sequence are Cretaceous limestones, characterized by relatively strong lateral and temporal shifts in depositional environments due to differential tectonic movements (Vilas *et al.* 1983; Salas & Casas 1993; Van Wees *et al.* 1998). In turn, the Cretaceous is unconformably covered by Tertiary and Quaternary detrital rocks.

### *Structural style of the Sierra de Albarracín*

The complex polyphase deformation history of the Sierra de Albarracín is evidenced by a wide variety of structures (Fig. 2a). In the following section the focus will be on the main faults that divide the Palaeozoic basement into different blocks and are responsible for the present-day structure (Viallard 1983; Pérez-Arlucea & Sopeña 1983, 1985; Ramos *et al.* 1986).

The Variscan fault system of the Macizo de Nevera is predominantly a NE–SW running dextral strike-slip system. This fault system cuts across N–S trending large scale folds with their accompanying axial plane cleavage (Weijermars & Rondeel 1984) and does not continue into the overlying Upper Permian and younger rocks. The situation within the Macizo del Tremedal is strikingly different. In its westernmost domain a great number of dextral NNE–SSW strike-slip faults displace the Variscan fold series. However, in the remainder of the Macizo NW–SE sinistral strike-slip faults are disrupting the folds.

The Variscan fold structure consistently runs NNW–SSE with deviations of no more than 10°, except in two domains in the southern part of the Macizo del Tremedal where E–W faults disrupt the continuity. Here, the folds and accompanying cleavage are sheared in a sinistral sense. The Lower Triassic siliciclastics unconformably cover this Variscan structure. The presence of these faults forms the argument to postulate major sinistral E–W shears of Variscan age to lie buried under the Mesozoic cover at the southern limit of the Macizo del Tremedal (Fig. 2b).

The thickness distribution of the Lower Triassic siliciclastics around the Macizo del Tremedal, being thick and only slightly dipping at western boundaries, but reduced in thickness and strongly inclined (even overturned) at southern boundaries, suggests a reactivation of the shears in vertical motion during and after the Triassic. On the south side of each of the faults delimiting the Macizo del Tremedal to the south, the Lower Triassic consistently shows a continuous change in attitude. Going from E to W the Lower Triassic has a slightly SE-dipping attitude, followed by a steeper S-dipping inclination, a vertical position and an overturned Lower Triassic dipping E to NE, locally even at 30° (Fig. 2a). The vergence of this structure is indicative of westward movement of the material to the south of the faults, thus indicating rejuvenation of the E–W faults in a dextral sense. In this movement the Variscan basement participated with its attached Lower Triassic siliciclastics. Decoupling over the clay-marl-gypsum levels of the Middle and Upper Triassic caused the Jurassic to behave independently as rigid 'floating' blocks (Viallard 1983; Rondeel *et al.* 1984). Amidst these incompetent levels, the dolomitic Middle Triassic folded and faulted passively and decoupled completely.

These observations in the southern part of the Macizo del Tremedal are the basis for the assumption of large E–W shears limiting the Macizos on two sides with sinistral movement in Variscan times and dextral movement in Alpine periods, with intermediate vertical motions. The indications for the occurrence of E–W faults, limiting the Macizos, are numerous. The location of the Tremedal fault is inferred from the non continuity of the Variscan structure between the Macizo de Nevera and the Macizo del Tremedal. In both Macizos, the folds are north plunging and still, the oldest rocks of the

Macizo de Nevera approach the youngest Variscan sediments of the Macizo del Tremedal within a distance of 2 km. A thin zone of vertical to overturned Lower Triassic siliciclastics shows up at the northwestern limit of the Macizo del Tremedal (Fig. 2), and is indicative of its uplift.

The Nevera fault is indicated by the appearance of Palaeozoic basement and strongly inclined Jurassic rocks north of the Macizo de Nevera. Furthermore, small-scale en echelon NE–SW folds within the Jurassic rocks might indicate dextral reactivation of the E–W faults (Fig. 2a). Volcanics occur along all major E–W shears and are probably related to Late Variscan orogenic extension (Doblas *et al.* 1994).

From the presence of the deep-seated Serranía de Cuenca Fault and the Molina–Teruel–Espadan Fault (Salas & Casas 1993) and their strike parallel to the Late Variscan lineaments, we infer a single deep-seated NW–SE Late Variscan shear zone below the Sierra de Albarracín along which major strike-slip faulting occurred during the Variscan orogeny, thus creating the Sierra de Albarracín pop-up structure. It is hypothesized that the major E–W faults bounding the Macizos originated as Riedel shears from this shear zone. The right-stepping Palaeozoic basement inliers are interpreted to represent up-squeezed blocks in an en echelon Riedel shear pattern (Naylor *et al.* 1986) induced by Late Variscan sinistral strike-slip faulting along the shear zone (Fig. 1b).

Later Alpine stress fields caused reverse and dextral reactivation of the E–W faults, evidenced by steeply inclined, overturned and overthrusted Lower Triassic rocks. Of the stress fields described for the Alpine orogeny, we expect the Oligocene-Miocene stress field with a N060°E oriented maximum principal stress (Simón-Gómez 1986; Rodriguez-Pascua *et al.* 1994; Casas-Sainz & Maestro-González 1996; Muñoz-Martín *et al.* 1998) and the Eocene and Late Miocene-present stress field with a N130°E to N150°E oriented maximum principal stress (De Ruig *et al.* 1991; De Vicente *et al.* 1996; Jabaloy *et al.* 2002), later referred to as N060°E and N135°E shortening directions, to be in the most favourable orientation to reactivate the E–W Riedel shears. This would result in sinistral-reverse and dextral-reverse reactivation respectively of the Riedel shears.

## Sandbox analogue modelling

### *Experimental set-up and procedure*

Analogue experiments were carried out in a sandbox with a rigid base plate divided in two halves (Table 1 and Fig. 3). This plate was covered by a 20 mm homogeneous pack of dry sand representing the Palaeozoic rocks before Variscan deformation. Coloured marker layers were added to assist structural interpretation of cross-sections at the end of the experiments. To reduce the friction between plate and sand pack, a 2 mm thick lubricant layer of oil-water emulsion (OWE) was spread on top of the base plate for experiments 2 and 4. In these experiments the OWE layer represents the shales at the base of the Palaeozoic rock pile. The ductile, weak elasto-plastic, non-viscous OWE does not flow and forms a localized shear zone. It is an analogue for clays and shales at shallow crustal levels, where the strength is essentially not strain-rate dependent. Silicone putty, commonly used in analogue model experiments to provide detachment levels, is viscous and not ideal for simulating ductile clays and shales. More accurate scaling is presently not possible due to a lack of data on the mechanical properties of décollement shales (Verschuren *et al.* 1996).

The sand was slowly sifted onto the base plate or onto the OWE layer from a container with openings of about 2 mm, followed by careful levelling. Four marker layers were sifted onto the levelled sand pack after every 4 mm of sand added. The horizontal dimensions of the sand pack were 72 cm × 85 cm for experiment 1, 46 cm × 71 cm for experiment 2, and 60 cm × 60 cm for experiments 3 and 4. North Sea sand (Oude Pekela, The Netherlands) was used for experiment 1, while Fontainebleau sand (France) was used for experiments 2, 3 and 4. For North Sea sand, grains are sub-angular with intermediate sphericity and a grain size range of 200–450 μm. The density is about 1.6 g/cm$^3$ with an internal friction angle of about 40° and a cohesion of 23 Pa. For Fontainebleau sand, grains are sub-rounded with intermediate sphericity and a grain size range of 100–400 μm. The density is about 1.5 g/cm$^3$ with an internal friction angle of about 40°–45° and a cohesion of 70 Pa (Van Mechelen 2004). Using a scaling factor of $10^{-4}$–$10^{-5}$ between cohesion values of natural crustal rock and analogue material (Horsfield 1977), these cohesion values proportionally conform to the cohesion values of natural rocks between 1 and 5 MPa (Byerlee 1978; Van Mechelen 2004).

In the first deformation phase, a sinistral strike-slip displacement was applied to the sand pack by slowly moving one half of the base plate past the other at a constant velocity using a stepping motor (Figs 3a and b). Movement continued until a clear Riedel shear pattern developed in the sand pack.

**Table 1.** *Experimental parameters*

| **Experiment number** | 1 | 2 | 3 | 4 |
|---|---|---|---|---|
| Layering | 20 mm sand | 2 mm OWE + 20 mm sand | 20 mm sand | 2 mm OWE + 20 mm sand |
| Horizontal dimensions (cm) | 72 × 85 | 46 × 71 | 60 × 60 | 60 × 60 |
| *Phase 1: sinistral strike-slip displacement* | | | | |
| Model set-up | Fig. 3a | Fig. 3a | Fig. 3b | Fig. 3b |
| Strike-slip direction of base plate | sinistral | sinistral | sinistral | sinistral |
| Velocity of base plate (mm/hr) (sinistral strike-slip component) | 36 | 18 | 18 | 18 |
| Total movement of baseplate (mm) (sinistral strike-slip displacement) | 8 | 18 | 8 | 15 |
| *Phase 2: shortening oblique to the Riedel shears* | | | | |
| Model set-up | Fig. 3c | Fig. 3c | Fig. 3d | Fig. 3d |
| Shortening direction | N060°E | N060°E | N135°E | N135°E |
| Theoretical angle (°) between shortening direction and Riedel shears (E–W faults) | 20–25 | 20–25 | 45–50 | 45–50 |
| Shortening velocity (mm/hr) | 27 | 18 | 18 | 18 |
| Total amount of shortening (mm) | 40 | 5 | 23 | 6 |
| **Material properties** | | | | |
| *Oil-water emulsion (OWE) (Verschuren et al. 1996)* | | | | |
| Rheology | – | elasto-plastic | – | elasto-plastic |
| Cohesion (Pa) | – | 30–40 | – | 30–40 |
| *Sand (Van Mechelen 2004)* | *North Sea* | *Fontainebleau* | *Fontainebleau* | *Fontainebleau* |
| Rheology | frictional-plastic | frictional-plastic | frictional-plastic | frictional-plastic |
| Grain size range (μm) | 200–450 | 100–400 | 100–400 | 100–400 |
| Grain shape | sub-angular | sub-rounded | sub-rounded | sub-rounded |
| Sphericity | intermediate | intermediate | intermediate | intermediate |
| *Dry sand (Van Mechelen 2004)* | | | | |
| Density (g/cm$^3$) | 1.59 | 1.63 | 1.63 | 1.63 |
| Angle of internal friction (°) | 40 | 40–45 | 40–45 | 40–45 |
| Cohesion (Pa) | 23 | 69 | 69 | 69 |
| *Damp sand (Mulugeta 1988; Van Mechelen 2004)* | | | | |
| Density (g/cm$^3$) | 1.77 | 1.69 | 1.69 | 1.69 |
| Angle of internal friction (°) | 28 | 28 | 28 | 28 |
| Cohesion (Pa) | 600–1814 | 600–2080 | 600–2080 | 600–2080 |

After this first deformation phase, a small amount of water was sprayed onto the sand to strengthen it, to better simulate the Palaeozoic basement rheology. The small amount of water causes a significant increase of the cohesion of the sand up to 600–2000 Pa, while the internal friction angle drops only slightly, to about 28° (Mulugeta 1988; Lopes Cardozo *et al.* 2002; Van Mechelen 2004). These cohesion values proportionally scale to the cohesion values of brittle basement rocks in the upper crust between 10 and 50 MPa (Byerlee 1978; Van Mechelen 2004). Fault zones are dilated zones in the sand and consequently have less grain-to-grain contact points with water bridges. The Riedel shears were therefore preserved as internal weakness zones, thus increasing the difference in strength between the strong sand and the relatively weak inherited faults, analogue to the strong Palaeozoic basement with the relatively weak Variscan faults. Using this technique allows the inherited faults to be reactivated in a

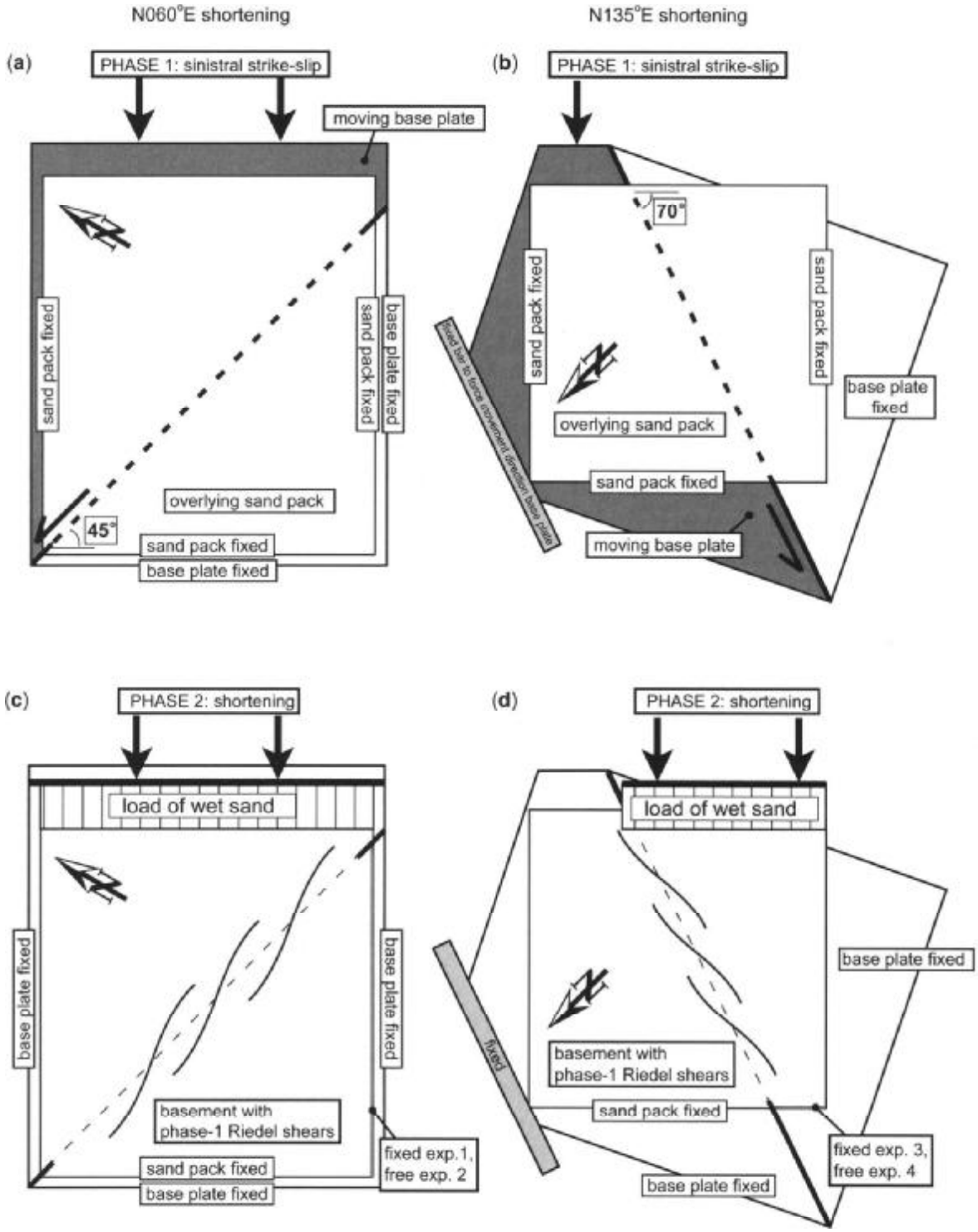


**Fig. 3.** Experimental set-up. (**a**) and (**b**) Set-up for the first deformation phase. One half of the base plate is laterally driven along the other fixed half using a stepping motor. Basement-induced sinistral strike-slip faulting is continued until a well developed Riedel shear pattern has formed in the overlying sand pack. (**c**) Set-up for the second deformation phase with N060°E shortening applied to the sand pack with the E–W Riedel shears. Both halves of the base plate are fixed. Boundaries of the sand pack are fixed for experiment 1 and free for experiment 2. An extra load of sand was applied at the backstop to force stresses to build up into the Riedel shear zone. (**d**) Set-up for the second deformation phase with N135°E shortening applied to the sand pack with the E–W Riedel shears. Again both halves of the base plate are fixed. Boundaries of the sand pack are fixed for experiment 3 and free for experiment 4.

second deformation phase in a favourable stress field and/or new faults to be formed. This is a critical step in connecting thin-skinned deformation with thick-skinned (deep seated) deformation processes. However, in our models we did not use a complete basement-cover model for the second phase as we started with the simplest approach to study the reactivation of Riedel shears.

In the second deformation phase the base plate was completely fixed and shortening was applied only to the sand pack above the OWE layer, in an attempt to reactivate the Riedel shears. In experiments 1 and 2, the movement direction of the vertical backstop was at 45° to the strike of the base fault, thus making a theoretical angle of about 20°–25° to the Riedel shears (Fig. 3c). In experiments 3 and 4, the movement direction of the vertical backstop was at 70° to the strike of the base fault, thus making a theoretical angle of about 45°–50° to the Riedel shears (Fig. 3d). These two models represented the E–W Riedel shears in second phase N060°E and N135°E shortening directions respectively. A load of sand was applied on top of the sand pack near the backstop, to allow stresses to build up in the Riedel shear zone. In experiments 1 and 3, the boundaries of the model were fixed. In experiments 2 and 4, only the backstop and its opposite side were fixed, thus allowing the sand pack to move freely along the Riedel shears (Figs 3c and d).

The top-views were photographed during the experiments. To study the internal structure of the models, cross-sections were made by vertically slicing the wetted sand pack at the end of the experiment. Before completely wetting the models, a protective additional sand layer was added to preserve the surface topography of the model.

### *Modelling results*

Table 2 and Figures 4 to 7 give an overview of the modelling results. First, the results of the sinistral strike-slip deformation phase will be discussed for all four experiments. Subsequently, the results of the second deformation phase will be discussed with respect to the response of the models to different boundary conditions and to reactivation in the two different stress fields.

**Table 2.** *Modelling results*

| **Experimental number** | 1 | 2 | 3 | 4 |
|---|---|---|---|---|
| *Phase 1: sinistral strike-slip displacement* | | | | |
| Development of first Riedel shears (mm of sinistral strike-slip displacement) | 6 | 8 | 6 | 8 |
| Termination of first phase after development of Riedel shears along the entire fault zone (mm of sinistral strike-slip displacement) | 8 | 18 | 8 | 15 |
| Angles of Riedel shears to the base fault (°) | 21–28 thrust component | 17–27 | 20–28 | 15–26 |
| Average angle of Riedel shears to the base fault (°) | ±25 | ±22 | ±25 | ±20 |
| Amount of horizontal displacement along Riedel shears (mm) | 4–7 | 4–8 | 4–6 | 4–8 |
| Relief after first phase (mm) | 2–3 | 1–3 | 2–4 | 3–5 |
| *Phase 2: shortening oblique to the Riedel shears* | | | | |
| Experimental angle (°) between shortening direction and Riedel shears | ±20 | ±23 | ±45 | ±40 |
| Reactivation of Riedel shears | only at the backstop | yes | only at the backstop | yes |
| Displacement along Riedel shears | thrusting at backstop | sinistral-reverse | thrusting at backstop | dextral-reverse |
| Total amount of shortening (mm) | 40 | 5 | 23 | 6 |
| Amount of horizontal displacement along Riedel shears (mm) | – | 2–4 | – | 2–5 |
| Dip of upper section of Riedel shears (°) | 35–50 | 40–50 | 40–45 | 40–50 |
| Dip of lower section of Riedel shears (°) | 60–80 | 70–85 | 75–85 | 55–75 |
| Total relief after second phase (mm) | 2–5 | 2–5 | 2–5 | 4–6 |

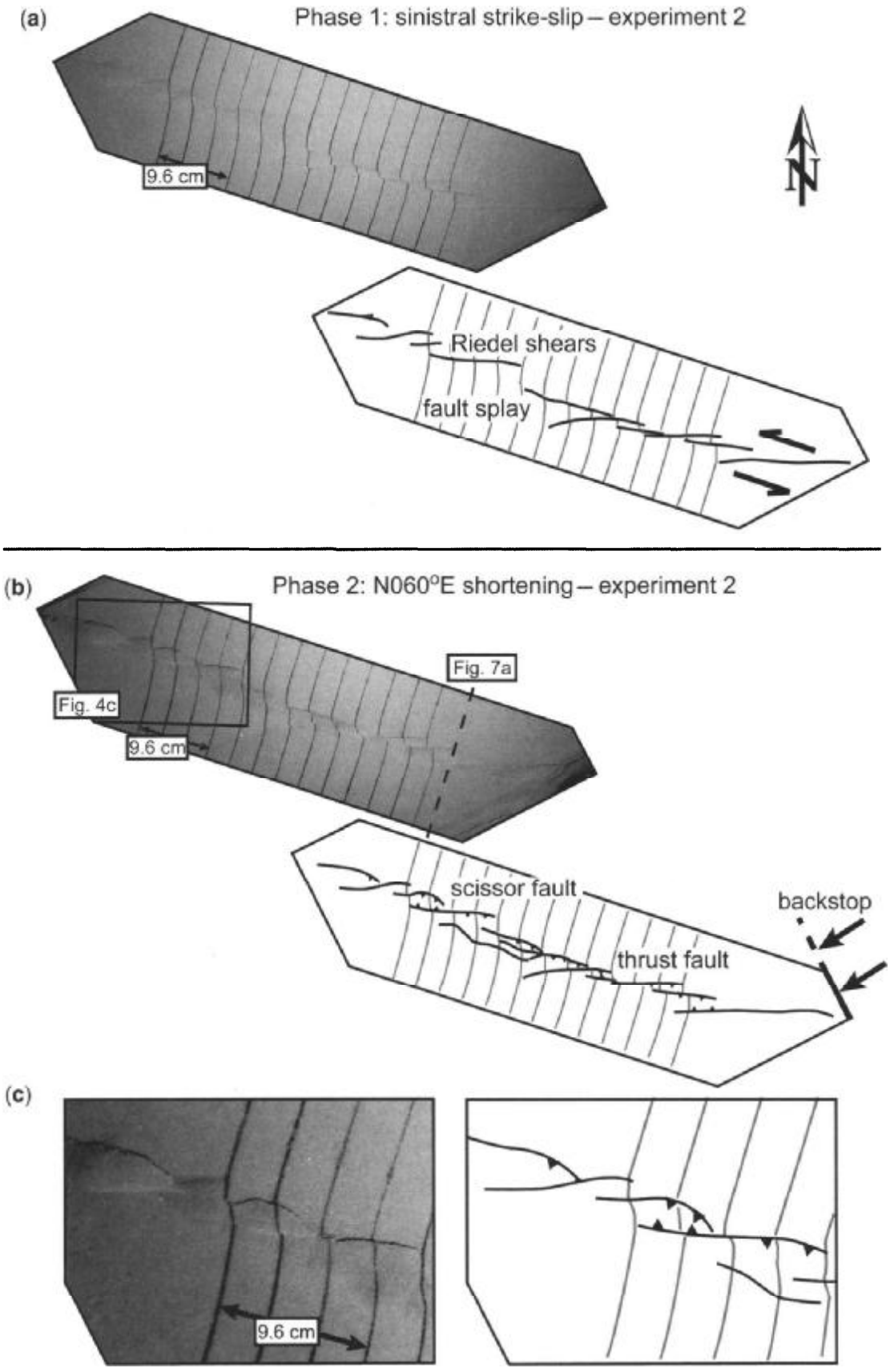


**Fig. 4.** Top-views and interpretations for reactivation in the N060°E shortening direction. (**a**) Pattern of en echelon Riedel shears induced by sinistral strike-slip faulting at the end of the first deformation phase (experiment 2). (**b**) Riedel shears reactivated by N060°E shortening at the end of the second deformation phase. Location of detailed top view (Fig. 4c) and cross-section (Fig. 7a) is shown. (**c**) Detailed top view of the final model.

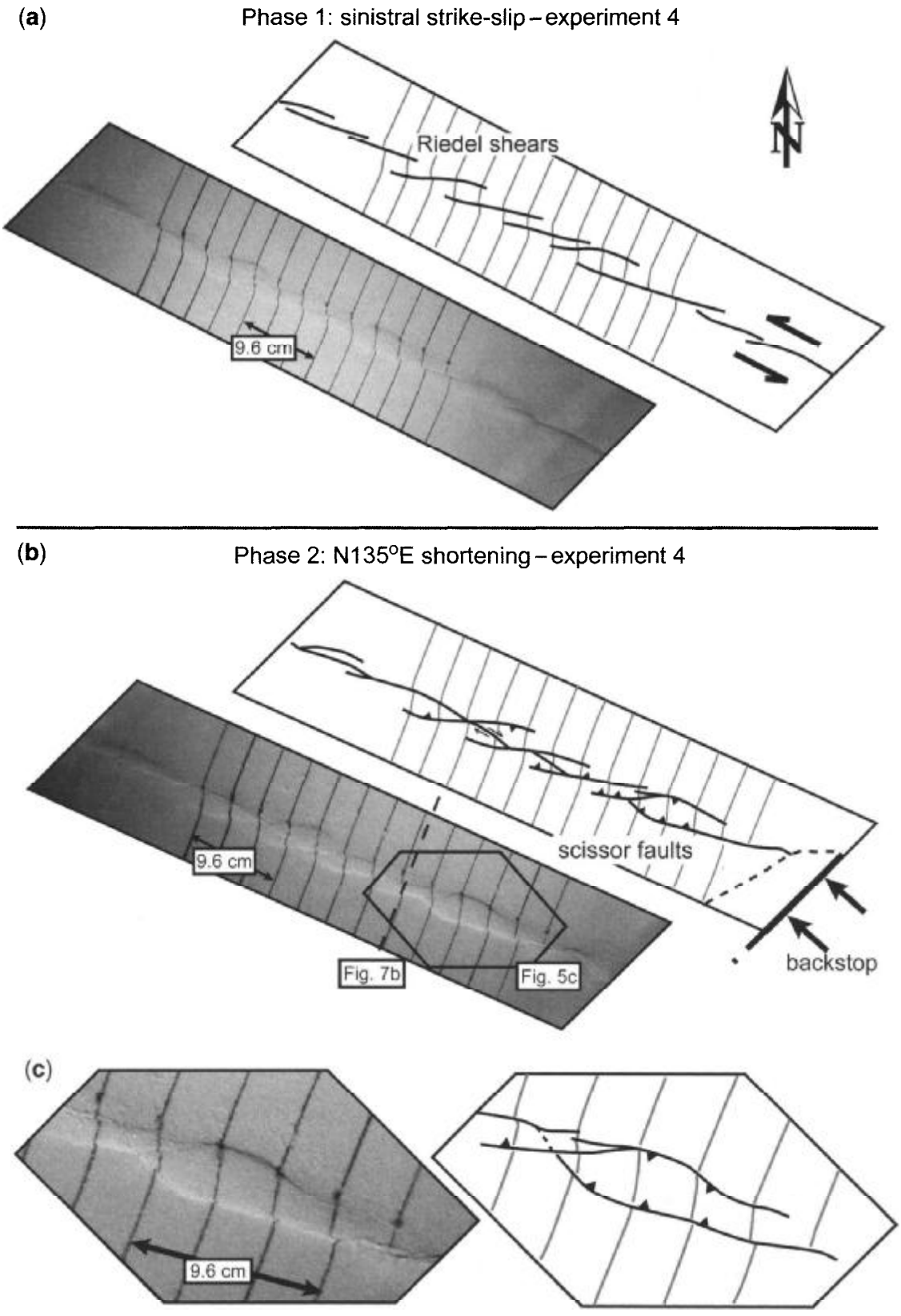


**Fig. 5.** Top-views and interpretations for reactivation in the N135°E shortening direction. (**a**) Pattern of en echelon Riedel shears induced by sinistral strike-slip faulting at the end of the first deformation phase (experiment 4). (**b**) Riedel shears are reactivated by N135°E shortening at the end of the second deformation phase, mainly by scissor faulting. An irregular fault partly cuts off the Riedel shears. Location of detailed top view (Fig. 5c) and cross-section (Fig. 7b) is shown. (**c**) Detailed top view of the final model.

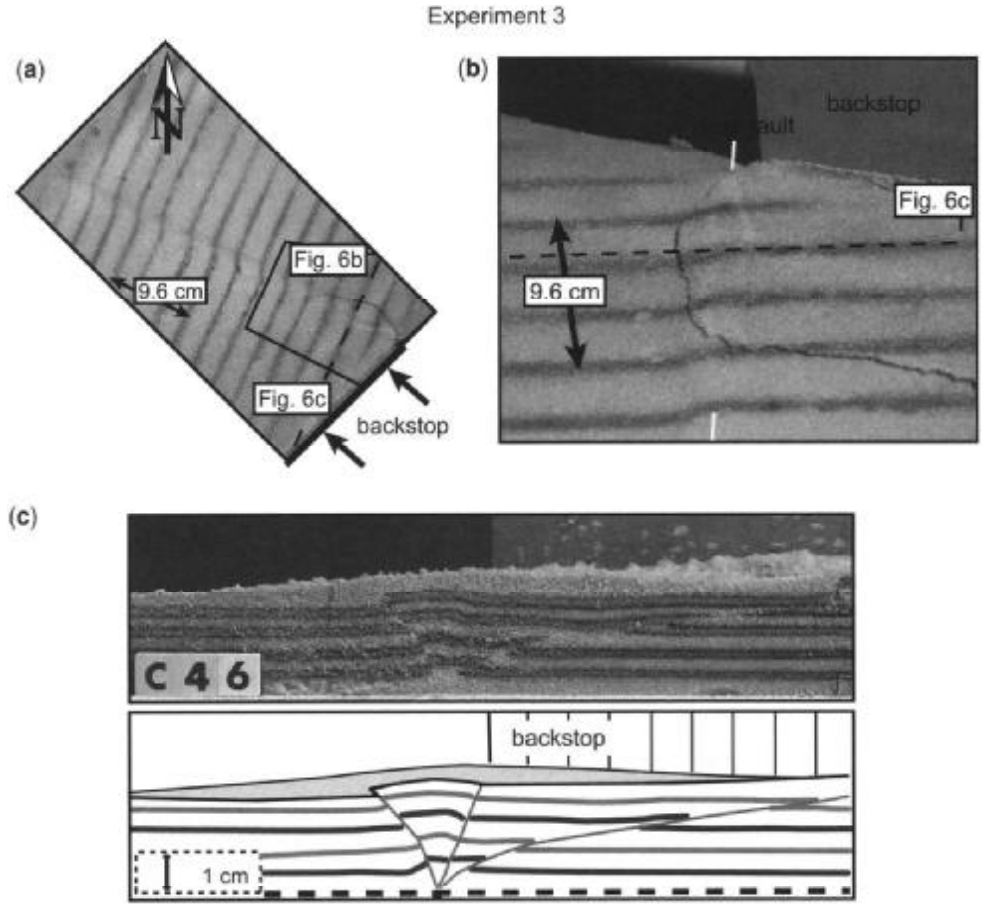


**Fig. 6.** Final model for second phase shortening in the N135°E direction with fixed boundaries (experiment 3). (**a**) Top view and (**b**) detailed top view showing thrusting in a short zone at the backstop limited to the width of the Riedel shear fault zone, thus only reactivating the Riedel shear close to the backstop. Location of cross-section (Fig. 6c) is indicated by a dashed line. (**c**) Cross-section shows that the newly formed thrust fault is limited by the Riedel shear.

*Phase 1: Sinistral strike-slip displacement.* In the first deformation phase, sinistral strike-slip faulting resulted in a typical right-stepping synthetic Riedel shear pattern (Figs 4a and 5a) with a zone of higher relief at early stages. Widely spaced Riedel shears started to form after 6 mm of strike-slip displacement in experiments 1 and 3 and a small thrust component developed at the backstop side of the shear zone in experiment 1. At the end of the first phase (8 mm of strike-slip displacement) a well-developed Riedel shear pattern characterized the two models. Riedel shears started to form after 8 mm of strike-slip displacement in experiments 2 and 4. However, a complete Riedel shear pattern above the entire length of the base fault developed only after 18 and 15 mm of strike-slip displacement respectively. At that stage, splay faults had already formed in experiment 2 at the tips of the Riedel shears near the backstop side. The difference in the amount of basal displacement needed to obtain a complete Riedel shear pattern might be due to slightly different model set-ups, such as layering (presence of OWE layer) and boundary conditions. After termination of the first phase, en echelon Riedel shears strike at angles between 20° and 28° to the base fault for experiments 1 and 3, with an average of about 25°. For experiments 2 and 4, Riedel shears strike at slightly lower angles between 15° and 27°, with an average of about 20°–22°.

The amount of horizontal sinistral displacement along the Riedel shears was between 4 and 8 mm, as obtained from the top views. Most Riedels display scissor faulting, with their sense of vertical displacement reversing at their mid-points above the base fault. The region between two Riedel shears is an up-squeezed block. The relief amounted to about 10%–25% of the original thickness of the sand pack (2 to 5 mm). Relief was slightly lower in experiment 2 (5%–15%).

*Phase 2: Shortening oblique to the Riedel shears.* Second phase deformation depended

(a) Experiment 2

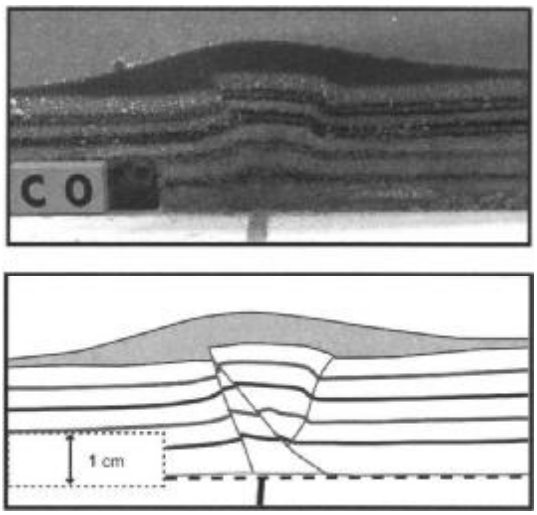


(b) Experiment 4

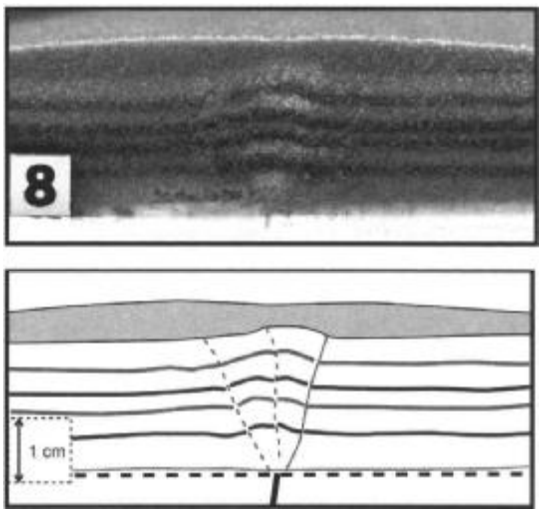


**Fig. 7.** Cross-sections of the final models for reactivation in the N060°E shortening direction (experiment 2) and N135°E shortening direction (experiment 4). (**a**) The cross-section clearly shows that scissor faulting occurred along the upper section of the Riedel shears. The lower steeper section of the Riedel shears has been cut off by a newly formed, less steep thrust. (**b**) The cross-section shows that clear evidence for second phase deformation cannot be deduced from the cross-sections.

greatly upon the boundary conditions. Riedel shears were not reactivated in the experiments with fixed boundaries and no OWE layer between base plate and sand pack (experiments 1 and 3 with N060°E and N135°E shortening directions respectively). In both these experiments initial shortening was accommodated by compaction (layer parallel shortening) and was followed with ongoing shortening by thrusting close to the backstop and limited to the width of the Riedel shear fault zone, thus only reactivating the Riedel shear near the backstop (Fig. 6). At the end of the second phase, after 40 and 23 mm of shortening in experiments 1 and 3 respectively, relief in the Riedel shear zone had only slightly increased, probably due to compaction of the sand pack.

In experiment 2, Riedel shears were reactivated for shortening at angles of 20°–25° to the Riedel shears (N060°E shortening direction). Reactivation resulted in a sinistral-reverse displacement on the Riedels (Figs 4b and c). Reactivation of Riedel shears near the backstop started after 1 mm of shortening. With ongoing shortening, Riedel shears at the opposite side of the model were reactivated first, and finally Riedel shears in the middle part, after 5 mm of shortening (Fig. 4b). Scissor faulting occurred along most Riedel shears, thus increasing the height of the up-squeezed blocks (Fig. 4c). Riedel shear segments NE of the base fault, in the actively moving part of the sand pack, mostly have a thrust component. The horizontal sinistral displacement along the Riedel shears at the end of the second phase was between 2 and 4 mm, as obtained from the top views. The total relief was about 10%–25% (2–5 mm) of the original thickness of the sand pack.

A cross-section through the pop-up structures displays mostly palm tree geometries with convex upward-shaped Riedel shears (Fig. 7a). Generally, only the upper section of the Riedel shears, which dips between 40° and 50°, appears to have been reactivated. Their steeper, lower part, dipping between 70° and 85°, failed and was cut off by a less steep fault that developed towards the base.

In experiment 4, Riedel shears were reactivated by shortening at angles of 40°–45° (N135°E shortening direction). Reactivation resulted in a dextral-reverse displacement along all shears from the onset of shortening. Ongoing shortening resulted in scissor faulting along the Riedel shears increasing the height of the almond-shaped up-squeezed blocks at the backstop side (Figs 5b and c). At the opposite side, Riedel shears were partly reactivated and partly cut off by an irregular fault roughly parallel to the base fault (Fig. 5b). The experiment was terminated after 6 mm of horizontal shortening. The horizontal dextral displacement along the Riedel shears at the end of the second phase was between 2 and 5 mm, as obtained from the top views. The total relief was about 20%–30% (4–6 mm) of the original thickness of the sand pack.

The cross-section through the pop-up structures displays mostly palm tree geometries with

convex upward-shaped Riedel shears (Fig. 7b). Evidence for second phase deformation cannot be deduced from the cross-sections. Syn-tectonic sedimentation might have made such a polyphase analysis possible.

### *Reactivation of Riedel shears in a rotated stress field*

The response of the curved Riedel shears to the second phase stress field is complex, but mechanically understandable. In the models with fixed boundaries (experiments 1 and 3), Riedel shears were not reactivated, probably due to stress build-up at right angles to the shortening direction. The sand on the two sides of the fault zone thus could only escape in a vertical direction. This is comparable to a situation in which the principal stresses in the horizontal plane are relatively large compared to the minimum principal stress, as illustrated with a Mohr diagram (Jaeger & Cook 1968; Sibson 1985; Mandl 1988; Fig. 8a: $\sigma_1 \approx \sigma_2 \gg \sigma_3$). Assuming $\sigma_3$ vertical, a plane with $2/3\ C_0$ (cohesion) of the intact rock, an internal friction angle ($\varphi$) of 30°, and a 20°–40° angle between $\sigma_1$ and the strike of the Riedel shears, a new thrust develops rather than pre-existing Riedel shears being reactivated.

In experiments 2 and 4, sinistral-reverse and dextral-reverse reactivation of the Riedel shears occurred respectively. This is attributed to the presence of the OWE layer reducing the basal friction, and to the fact that the sand on one side of the fault zone could freely move along the other side by horizontal movement along the pre-existing Riedel shears. This is comparable to a situation in which the two smaller principal stresses are relatively small compared to the maximum principal stress, as illustrated with a mohr diagram (Fig. 8a; $\sigma_1 \gg \sigma_2 \approx \sigma_3$). For these 'stress' conditions oblique-slip reactivation of the relatively weak Riedel shears may occur.

The upper section of the Riedel shears was clearly reactivated in experiments 2 and 4. In experiment 2 the lower sections of most Riedel shears were cut off by a less steep newly formed thrust and some were reactivated. Merging of strike-slip faults with obliquc-slip reverse faults at depth is also reported for transpressional models consisting of a basal shear component and a transverse shortening component (Schreurs & Colletta 2002). However, in the experiments of Schreurs & Colletta (2002) these oblique-slip reverse faults are older faults formed during initial stages of deformation, whereas in our experiments they developed with ongoing deformation from the upper shallower dipping sections of the Riedel shears. In experiment 4, Riedel shears were not cut off by a newly formed thrust towards the base. Instead, with ongoing deformation, an irregular fault developed throughout the fault zone, thus connecting individual Riedel shears.

The relationship between the fault dip and the likelihood of reactivation occurring is (semi) quantitatively analysed in the Mohr diagram of Figure 8b. In order to analyse the reactivation mechanisms for experiment 2, the curved fault planes were divided into two main sections: a steep lower section dipping about 80°, and a shallower upper section dipping 45° (Table 2). The angle between the strike of the Riedel shears and the maximum principal stress is between 20° and 30°. In these experiments with shortening oblique to the Riedel shears, the angle ($\alpha$) between $\sigma_1$ and the intersection of the pre-existing fault plane with the vertically oriented $\sigma_1$–$\sigma_3$ plane controls whether reactivation occurs. For the steep lower section, $\alpha$ ranges from 62° to 72°, and for the upper section it is between 18° and 26°. Plotting this in the Mohr diagram (Fig. 8b), again assuming $\sigma_3$ vertical, a plane with $2/3\ C_0$, and an internal friction angle of 30°, reveals that with increasing $\sigma_1$ reactivation occurs of fault planes with $\alpha$ between 12° and 48° instead of failure of the matrix rock. For the steep lower section $\alpha$ is too large, thus causing the matrix to fail before reactivation can take place. This explains the cut-off of the lower section of most Riedel shears and a new less steep fault towards the base. For the upper section, a small increase in $\sigma_1$ is sufficient to result in the conditions required for reactivation.

In experiment 4 the lower section of the Riedel shears was reactivated. This might possibly be explained in terms of a shallower dipping lower section of the Riedels in combination with a plane with extremely low cohesion. It appears that in this experiment some of the Riedel shears have a shallower dipping lower section compared to the other experiments, even as low as 55° (Table 2). In the case of a plane without cohesion, the range of fault dips that can be reactivated would reach from 3° to 62° (Fig. 8c), thus incorporating faults of the lower section of the Riedel shears observed in this model. A possible explanation for the presence of a relatively weaker plane towards the base is that the drop in cohesion increases with depth (Richard & Krantz 1991), where faults are generated during the first deformation phase. With a maximum fault dip of about 62° for reactivation to occur, this would explain why reactivation of the lower section occurs in experiment 4 (fault dips

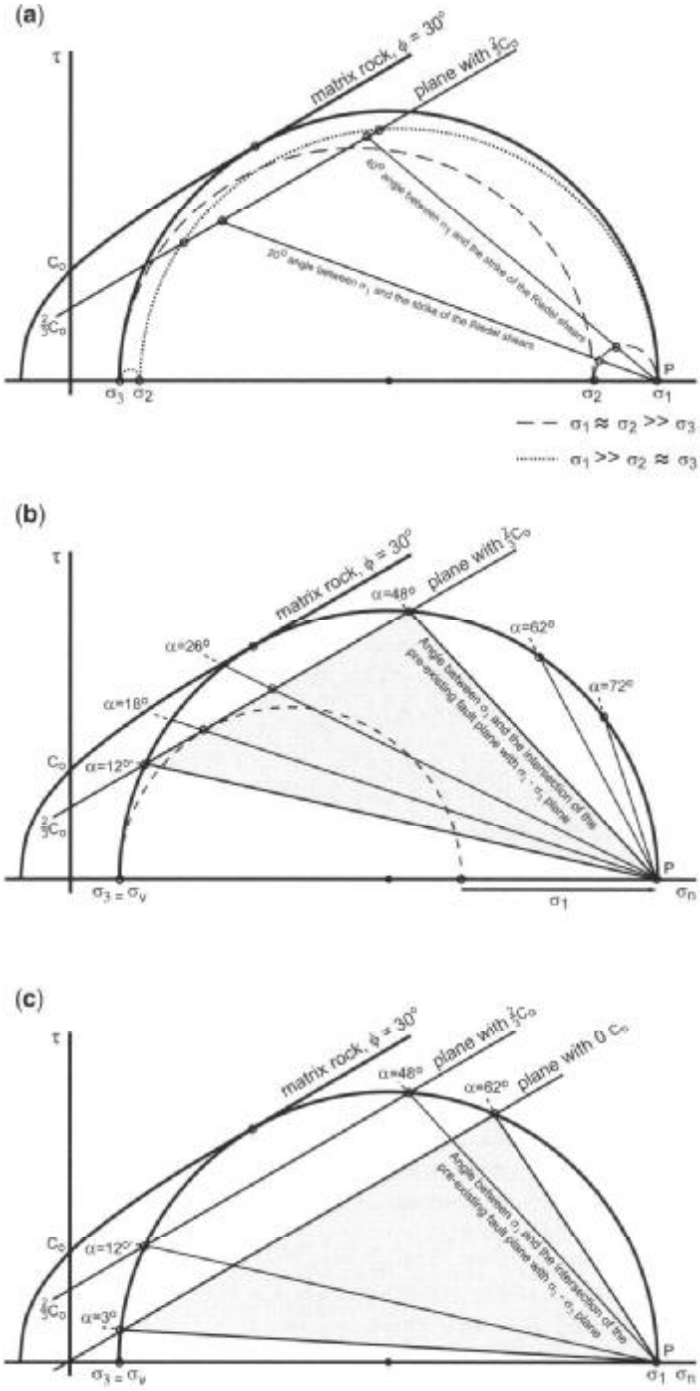


**Fig. 8.** Mohr diagrams explaining the response of the Riedel shears to reactivation in a second phase stress field. (**a**) Mohr diagram illustrating the effect of the relative size of the principal stresses on the likelihood for strike-slip reactivation to occur. For the condition where $\sigma_1 \approx \sigma_2 \gg \sigma_3$, assuming $\sigma_3$ in vertical direction, a plane with $\frac{2}{3}$ $C_0$ (cohesion) of the intact rock, an internal friction angle ($\varphi$) of 30°, and a 20° (experiment 1) to 40° (experiment 3) angle between $\sigma_1$ and the strike of the Riedel shears, a new thrust develops rather than strike-slip reactivation occurring (experiments 1 and 3). However, for the condition where $\sigma_1 \gg \sigma_2 \approx \sigma_3$, oblique-slip reactivation of the relatively weak Riedel shears may occur (experiments 2 and 4). (**b**) Mohr diagram illustrating why the steeper lower sections have been cut off and the upper shallower dipping sections were reactivated (experiment 2). Plotting the fault planes, again assuming $\sigma_3$ vertical, a plane with $\frac{2}{3}$ $C_0$, and an internal friction angle of 30°, reveals that with increasing $\sigma_1$, reactivation occurs of fault planes with $\alpha$ between 12° and 48° instead of failure of the matrix rock. For the steep lower section, $\alpha$ is too large (62°–72°), thus causing the matrix to fail instead of reactivation of the pre-existing fault planes. (**c**) In the case of a plane without cohesion, the range of fault dips that can be reactivated would reach from 3° to 62°, thus incorporating faults of the lower section of the Riedel shears observed in experiment 4.

between 55° and 75°) and only partly in experiment 2 (fault dips between 70° and 85°). It is however difficult to establish if, and if so why, the lower sections of the Riedel shears developed at lower dip angles in experiment 4.

## Discussion and conclusions

Based on structural and palaeostress data two types of models for the polyphase deformation history of the Sierra de Albarracín were tested with sandbox analogue modelling. Both types of models involved two phases of deformation to simulate Late Variscan sinistral shearing followed by shortening in an Alpine stress field with either a N060°E oriented $\sigma_1$ (first type of model: experiments 1 and 2) or a N135°E $\sigma_1$ (second type of model: experiments 3 and 4). In both types of models reactivation of first-phase Riedels during second phase shortening only occurred in experiment 2 and 4, in which an OWE layer was applied and in which sand on one side of the first phase fault zone could freely move along the other side.

In experiment 2, E–W Riedel shears originating from a Late Variscan sinistral shear zone were reactivated during Alpine N060°E shortening in a sinistral-reverse shear sense, whereas in experiment 4 reactivation of the Late Variscan E–W Riedels during Alpine N135°E shortening occurred in a dextral-reverse shear sense. Both experiments 2 and 4 show that the up-squeezed blocks in the en echelon Riedel shear pattern (Naylor *et al.* 1986) are comparable to the Palaeozoic basement inliers aligned in a NW–SE arrangement and bounded by E–W faults. This specific geometry and the observed sinistral displacement of the oldest Palaeozoic basement rocks can only be obtained by initial Late Variscan sinistral shearing.

For Alpine reactivation, modelling results reveal that the second phase deformation is taken up by oblique-slip along favourably oriented Riedel shears. In the N060°E reactivation model, the steep lower segments of most Riedel shears were cut off by newly formed thrusts, whereas the upper shallower dipping segments were reactivated by sinistral oblique-slip displacement. In the N135°E reactivation model, dextral oblique-reverse slip occurred along the complete Riedel shear segments. In contrast to experiment 2, the lower sections of the Riedel shears in experiment 4 were not cut off by thrust faults. This can be explained by slightly shallower dipping lower sections of the Riedel shears in experiment 4 compared to experiment 2 and an increasing drop in cohesion of pre-existing fault planes with depth (Richard & Krantz 1991).

Vertical displacements are observed along the E–W faults bordering the northern limit of the Macizo de Nevera, but it is unclear whether Alpine reactivation of these faults involved an oblique-slip component and if so, whether reactivation was dextral-reverse or sinistral-reverse. The orientation of these structures would fit both the N060°E and the N135°E reactivation model. The westward vergence of structures within the Lower Triassic south of the E–W faults bordering the Macizo del Tremedal corresponds with the dextral strike-slip movement along pre-existing Riedel shears in the N135°E reactivation model. Thus, the structures observed in the vicinity of the Macizo del Tremedal favour an Alpine N135°E reactivation model to explain the polyphase structure of the Sierra de Albarracín.

It is stressed that second phase reactivation only occurs in experiments 2 and 4, and requires that sand on one side of the fault zone can freely move along the other. This is comparable to a situation in which the maximum principal stress is horizontal and relatively large compared to the other principal stresses. Furthermore, a lubricant OWE layer has to be present between base plate and sand pack, analogous to decoupling of the Palaeozoic rock pile over the shales at its base.

A major advantage of the models is that they explain the present-day structure of the Sierra de Albarracín in terms of a single major Late Variscan megashear zone reactivated during Alpine shortening. This is consistent with the generally accepted idea that the Late Variscan lineaments controlled the evolution of the Iberian Range (e.g., Arche & López-Gómez 1992, 1996).

We thank F. Storti, D. Cunningham and G. Schreurs for constructive and helpful reviews that greatly improved this manuscript. Furthermore, our appreciation goes to our fellow students from the Vrije Universiteit, with whom we had interesting discussions during the Albarracín fieldwork. D. Sokoutis is thanked for the availability of the tectonic analogue modelling laboratory (TecLab) of the Vrije Universiteit. Furthermore, we would like to thank M. Papo and M. Corver for their assistance during the analogue modelling.

## References

ALVARO, M., CAPOTE, R. & VEGAS, R. 1979. Un modelo de evolución geotectónica para la cadena Celtibérica. *Acta Geologica Hispanica*, **14**, 172–177.

ARCHE, A. & LÓPEZ-GÓMEZ, J. 1992. Una nueva hipótesis sobre las primeras etapas de la evolución tectosedimentaria de la cuenca pérmico-triásica de SE de la Cordillera Ibérica. *Cuadernos de Geología Ibérica*, **16**, 115–143.

ARCHE, A. & LÓPEZ-GÓMEZ, J. 1996. Origin of the Permian-Triassic Iberian Basin, central-eastern Spain. *Tectonophysics*, **266**, 443–464.

ARTHAUD, F. & MATTE, P. 1977. Late Paleozoic strike-slip faulting in southern Europe and northern Africa: result of a right-lateral shear zone between the Appalachians and the Urals. *Geological Society of America Bulletin*, **88**, 1305–1320.

BUCHANAN, P. G. & MCCLAY, K. R. 1991. Sandbox experiments of inverted listric and planar fault systems. *Tectonophysics*, **188**, 97–115.

BYERLEE, J. 1978. Friction of rocks. *Pure and Applied Geophysics*, **116**, 615–626.

CASAS-SAINZ, A. M. & MAESTRO-GONZÁLEZ, A. 1996. Deflection of a compressional stress field by large-scale basement faults. A case study from the Tertiary Almazán basin (Spain). *Tectonophysics*, **255**, 135–156.

CLOOS, H. 1928. Experimenten zür Inneren Tektonik. *Zentralblatt für Mineralogie, Geologie, Paläeontologie*, **B**, 609–621.

DE RUIG, M. J., SMIT, J., GEEL, T. & KOOI, H. 1991. Effects of the Pyrenean collision on the Paleocene stratigraphic evolution of the southern Iberian margin (southeast Spain). *Geological Society of America Bulletin*, **103**, 1504–1512.

DE VICENTE, G., GINER, J. L., MUÑOZ-MARTÍN, A., GONZALEZ-CASADO, J. M. & LINDO, R. 1996. Determination of present-day stress tensor and neotectonic interval in the Spanish Central System and Madrid Basin, central Spain. *Tectonophysics*, **266**, 405–424.

DOBLAS, M. & LÓPEZ-RUIZ, J. *ET AL.* 1994. Extensional tectonics in the central Iberian Peninsula during the Variscan to Alpine transition. *Tectonophysics*, **238**, 95–116.

DONATH, F. P. & CRONWELL, R. M. 1981. Probabilistic treatment of faulting in geologic media. *In*: CARTER, N. L., FRIEDMAN, M., LOGAN, J. M. & STRARNS, D. W. (eds) *Mechanical Behaviour of Crustal Rocks*. American Geophysical Union Geophysical Monograms, **24**, 231–241.

FACENNA, C., NALPAS, T., BRUN, J.-P. & DAVY, P. 1995. The influence of pre-existing thrust faults on normal fault geometry in nature and in experiments. *Journal of Structural Geology*, **17**, 1139–1149.

GUIMERÀ, J. 1996. Cenozoic evolution of eastern Iberia: Structural data and dynamic model. *Acta Geologica Hispanica*, **29**, 57–66.

HINKELBEIN, K. 1969. El Triásico y el Jurásico de los alrededores de Albarracín. *Separata de Teruel*, Teruel, **41**.

HORSFIELD, W. T. 1997. An experimental approach to basement-controlled faulting. *Geologie & Mijnbouw*, **56**, 363–370.

JABALOY, A., GALINDO-ZALDÍVAR, F. & GONZÁLEZ-LODEIRO, F. 2002. Palaeostress evolution of the Iberian Peninsula (Late Carboniferous to present-day). *Tectonophysics*, **357**, 159–186.

JAEGER, J. C. & COOK, N. G. 1968. *Elasticity, Fracture and Flow: With Engineering and Geological Applications*. Science Paperbacks, Methuen & Co.

LOPES CARDOZO, G., BADA, G., LANKREIJER, A. C. & NIEUWLAND, D. A. 2002. Analogue modelling of a prograding strike-slip fault: the case study of the Balatonfö fault, western Hungary. *In*: CLOETINGH, S. A. P. L., HORVATH, F., BADA, G. & LANKREIJER, A. C. (eds) *Neotectonics and Surface Processes: the Pannonian Basin and Alpine/Carpathian System*. European Geoscience Union, Stephan Mueller Special Publication Series, **3**, 217–226.

LÓPEZ-GÓMEZ, J., MAS, R. & ARCHE, A. 1993. The evolution of the Middle Triassic (Muschelkalk) carbonate ramp in the SE Iberian Ranges, eastern Spain: sequence stratigraphy, dolomitization processes and dynamic controls. *Sedimentary Geology*, **87**, 165–193.

MANDL, G., 1988. Mechanics of tectonic faulting: models and basic concepts. *In*: H. J. ZWART (ed.) *Developments in Structural Geology*, **1**.

MCCLAY, K. R. & BUCHANAN, P. G. 1992. Thrust faults in inverted extensional basins. *In*: MCCLAY, K. R. (ed.) *Thrust Tectonics*. London Royal Holloway and Bedford New College, Chapman & Hall, 93–104.

MULUGETA, G. 1988. Squeeze box in a centrifuge. *Tectonophysics*, **148**, 323–335.

MUÑOZ, A., RAMOS, A., SÁNCHEZ-MOYA, Y. & SOPEÑA, A. 1992. Evolving fluvial architecture during a marine transgression: Upper Buntsandstein, Triassic, central Spain. *Sedimentary Geology*, **75**, 257–281.

MUÑOZ-MARTÍN, A., CLOETINGH, S., DE VICENTE, G. & ANDEWEG, B. 1998. Finite-element modelling of Tertiary palaeostress fields in the eastern part of the Tajo Basin (central Spain). *Tectonophysics*, **300**, 47–62.

NAYLOR, M. A., MANDL, G. & SIJPESTEIJN, C. H. K. 1986. Fault geometries in basement-induced wrench faulting under different initial stress states. *Journal of Structural Geology*, **8**, 737–752.

PÉREZ-ARLUCEA, M. & SOPEÑA, A. 1983. Estudio estratigrafico y sedimentologico de los materiales Permicos y Triasicos en el noroeste de la Sierra de Albarracín (Provincia de Guadalajara). *Estudios Geológicos*, **39**, 329–343.

PÉREZ-ARLUCEA, M. & SOPEÑA, A. 1985. Estratigrafía del Permico y Triasico en el sector central de la Rama Castellana de la Cordillera Iberica (Provincias de Guadalajara y Teruel). *Estudios Geológicos*, **41**, 207–222.

RAMOS, A., SOPEÑA, A. & PEREZ-ARLUCEA, M. 1986. Evolution of Buntsandstein fluvial sedimentation in the northwest Iberian Ranges (Central Spain). *Journal of Sedimentary Petrology*, **56** (6), 862–875.

RICHARD, P. 1991. Experiments on faulting in a two-layer cover sequence overlying a reactivated basement fault with oblique-slip. *Journal of Structural Geology*, **13**, 459–469.

RICHARD, P. & KRANTZ, R. W. 1991. Experiments on fault reactivation in strike-slip mode. *Tectonophysics*, **188**, 117–131.

RIEDEL, W. 1929. Zur Mechanik geologischer Brucherscheinungen. *Zentralblatt für Mineralogie, Geologie, Paläeontologie*, **B**, 354–368.

RODRIGUEZ-PASCUA, M. A., DE VICENTE, G. & GONZALEZ-CASADO, J. M. 1994. Kinematic and dynamic array of the Alpine deformations in alto Tajo area (Guadalajara). *Cuaderno Laboratorio Xeolóxico de Laxe*, Coruña, **19**, 163–174.

RONDEEL, H. E., WEIJERMARS, R. & VAN DORSSEN, H. G. 1984. Reactivation of early reverse faults

associated with oblique strike-slip faulting: A mechanism for crustal shortening (Macizo de Nevera, Sierra de Albarracín, Spain). *Geologie en Mijnbouw*, **63**, 387–398.

SALAS, R. & CASAS, A. 1993. Mesozoic extensional tectonics, stratigraphy and crustal evolution during the Alpine cycle of the eastern Iberian basin. *Tectonophysics*, **228**, 33–55.

SCHELLART, W. P. & NIEUWLAND, D. A. 2003. 3D evolution of a pop-up structure above a double basement strike-slip fault: some insights from analogue modelling. *In*: NIEUWLAND, D. A. (ed.) *New Insights Into Structural Interpretation and Modelling*. Geological Society, London, Special Publications, **212**, 169–179.

SCHREURS, G. & COLLETTA, B. 2002. Analogue modelling of continental transpression. *In*: SCHELLART, W.P. & PASSCHIER, C. (eds) *Analogue Modelling of Large-Scale Tectonic Processes*. Journal of the Virtual Explorer, **6**, 67–78.

SIBSON, R. H. 1985. A note on fault reactivation. *Journal of Structural Geology*, **7** (6), 751–754.

SIMÓN-GÓMEZ, J. L. 1986. Analysis of a gradual change in stress regime (example from the eastern Iberian Chain, Spain). *Tectonophysics*, **124**, 37–53.

VAN MECHELEN, J. L. M. 2004. Strength of moist sand controlled by surface tension for tectonic analogue modelling. *Tectonophysics*, **384**, 275–284.

VAN WEES, J. D., ARCHE, A., BEIJDORFF, C. G., LÓPEZ-GÓMEZ, J. & CLOETINGH, S. A. P. L. 1998. Temporal and spatial variations in tectonic subsidence in the Iberian Basin (eastern Spain): inferences from automated forward modelling of high-resolution stratigraphy (Permian-Mesozoic). *Tectonophysics*, **300**, 285–310.

VERSCHUREN, M., NIEUWLAND, D. & GAST, J. 1996. Multiple detachment levels in thrust tectonics: sandbox experiments and palinspastic reconstruction. *In*: BUCHANAN, P. G. & NIEUWLAND, D. A. (eds) *Modern Developments in Structural Interpretation, Validation and Modelling*. Geological Society, London, Special Publications, **99**, 227–234.

VIALLARD, P. 1983. Le décollement de couverture dans la Chaîne Ibérique méridionale (Espagne): effet de raccourcissements differentials entre substratum et couverture. *Bulletin de la Société Géologique de France*, **7** (3), 379–387.

VILAS, L., ALONSO, A., ARIAS, C., GARCÍA, A., MAS, R., RINCÓN, R. & MELÉNDEZ, N. 1983. The Cretaceous of the Southwestern Iberian Ranges (Spain). *Zitteliana*, **10**, 245–254.

WEIJERMARS, R. & RONDEEL, H. E. 1984. Shear band foliation as an indicator of sense of shear: field observations in central Spain. *Geology*, **12**, 603–606.

WILCOX, R. E., HARDING, T. P. & SEELY, D. R. 1973. Basic wrench tectonics. *Bulletin of the American Association of Petroleum Geologists*, **57**, 74–96.

# Lithospheric scale gravitational flow: the impact of body forces on orogenic processes from Archaean to Phanerozoic

PATRICE F. REY[1] & GREGORY HOUSEMAN[2]

[1]*School of Geosciences, The University of Sydney, NSW 2006 and Dept. de Géologie, UMR-CNRS 6524, Université Jean Monnet, St Etienne, F42023, France*

[2]*School of Earth and Environment, University of Leeds, Leeds, LS2 9JT, UK*

**Abstract:** In the Archaean, the combination of warmer continental geotherm with a lighter sub-continental lithospheric mantle suggests that gravitational forces played a more significant role in continental lithospheric deformation. To test this hypothesis, we compare the evolution of the deformation and the regional state of stress in 'Archaean-like' and 'Phanerozoic-like' lithospheres submitted to the same boundary conditions in a triaxial stress-field with imposed convergence in one direction. For plausible physical parameters, thickening of normal to cold Phanerozoic lithospheres produces relatively weak buoyancy forces, either extensional or compressional. In contrast, for Archaean continental lithospheres, or for anomalously warm Phanerozoic lithospheres, lateral gravitationally-driven flow prevents significant thickening. This conclusion is broadly consistent with: (1) the relative homogeneity of the erosional level now exposed at the surface of Archaean cratons, (2) the sub-aerial conditions that prevailed during the emplacement of up to 20 km of greenstone cover, (3) the relatively rare occurrence in the Archaean record of voluminous detrital sediments, (4) the near absence of significant tectonic, metamorphic and magmatic age gradients across Archaean cratons, (5) the relative homogeneity of strain across large areas, and (6) the ubiquitous presence of crustal-scale strike slip faults in many Late Archaean cratons.

One of the most contentious issues in Archaean geology is the significance of the particular features seen in the surface geology of most Archaean cratons. These involve the characteristic strain pattern of domes and basins; the ubiquity (in particular in Late-Archaean cratons) of strike-slip faults; the relative homogeneity at the craton scale of the finite strain field, the metamorphic facies and the erosion level; together with the particular timing of tectonics, magmatism, and metamorphism that seem to develop craton-wide within a very narrow time window (Binns *et al.* 1976; Choukroune *et al.* 1997; Galer & Mezger 1998; Hamilton 1998; Qiu *et al.* 1999; Rey *et al.* 2003). Based on the same field evidence, these features are interpreted by some authors as evidence of plate-tectonic processes (e.g., Snowden & Bickle 1976; Myers & Watkins 1985; Treloar & Blenkinsop 1995), and by others as evidence of gravitational instabilities (McGregor 1951; Collins 1989; Ramsay 1989; Jelsma *et al.* 1993; Bouhallier *et al.* 1993; Chardon *et al.* 1998) possibly related to plume activity (Choukroune *et al.* 1995; Warren & Ellis 1996). In this three-decade-long ongoing debate, the differences in mechanical behaviour of Phanerozoic and Archaean continental lithospheres have not been properly considered, yet regional finite strain fields depend significantly on the thermo-mechanical properties of the continental lithosphere. Consequently, the particular features observed in Archaean cratons could be related, in part, to contrasting lithospheric mechanical properties rather than to contrasting tectonic processes.

In this paper we aim to illustrate the relatively greater importance of gravitational forces in the tectonic evolution of ancient continental lithospheres. Based on triaxial numerical experiments that compare the evolution of Phanerozoic-like and Archaean-like lithospheres under horizontal convergence, we show that ancient continental lithospheres could have been under an increased stabilizing influence of gravitational forces that promoted homogeneous deformation and therefore impeded the development of strain localization along linear belts. If the buoyancy-derived stress were greater in the Archaean, then lateral escape (strike-slip faults and crustal-scale lateral crustal flow) rather than large-scale thrust and thickening could have become the primary response to tectonic convergence. We also suggest that the secular cooling

*From*: BUITER, S. J. H. & SCHREURS, G. (eds) 2006. *Analogue and Numerical Modelling of Crustal-Scale Processes.* Geological Society, London, Special Publications, **253**, 153–167.
0305-8719/06/$15.00 

of the continental geotherm, combined with the decrease in the buoyancy of the sub-continental lithospheric mantle (SCLM), have changed the thermo-mechanical properties of the continental lithosphere in such a way that the impact of gravitational forces on lithospheric deformation has decreased over geological time.

## Argand Ratio: assessing the impact of gravitational forces on modern and ancient continental lithospheres

Scaled models of orogenic systems depend on a few dimensionless parameters that describe the relative importance of different processes in the stress and thermal balance. Amongst these parameters the Argand Ratio characterizes the ability of gravitational forces to intervene in lithospheric deformation (Fig. 1). The Argand Ratio ($AR$) can be defined as the local ratio of the gravitational stress (arising from lateral variation of gravitational potential energy and thus of density) to the averaged lithospheric strength at a nominal strain rate (i.e., the stress-driving deformation). The ratio $AR$ may be compared with the Argand Number ($Ar$) of England & McKenzie (1982, 1983), a global parameter by which one can quantify the overall regional balance between gravitational stress and viscous stress in an indentation problem (see also Houseman & England 1986; Buck & Soukoutis 1994; Schmalholz *et al.* 2002, 2005). $AR$ is obtained from $Ar$ by replacing the nominal buoyant stress factor in $Ar$ with the locally variable buoyant stress (relative to a reference column), and similarly replacing the nominal viscous stress scale factor in $Ar$ with the locally variable strength of the lithosphere. The resulting Argand Ratio can be used to describe the evolution during deformation of the balance between buoyant stress and the strength of the lithosphere. The Argand Ratio measures the tendency of the lithosphere to deform in response to the variation of gravitational potential energy ($\Delta GPE$), and therefore is a measure of the ability of gravitational forces to intervene in lithospheric deformation.

In modern continental lithospheres, the Argand Ratio may reach values $\geq 1$ when large $\Delta GPE$ exists and/or when the orogenic system involves a weak lithosphere (i.e., a warmer geotherm). In Tibet as well as in the Basin and Range Province of the western USA, it has been argued that present-day crustal flow is strongly influenced by forces induced by large gradients in gravitational potential energy (England & Molnar 1997; Jones *et al.* 1996; Flesch *et al.* 2000). A warmer geotherm reduces the strength of the continental lithosphere and, as a rule of thumb, it is inferred that a thickened continental crust spreads under its own weight (i.e., Argand Ratio $\geq 1$ for a given effective strain rate) when the temperature at the Moho is above *c.* 700°C (e.g., Sonder *et al.* 1987).

In modern continental lithospheres, such a thermal condition is likely to be transient and associated with either crustal thickening or the rise of the lithosphere/asthenosphere interface under continental areas. In the Archaean however, the larger radiogenic heat production, possibly coupled with a stronger basal heat flow, would lead to warmer continental geotherms. For radiogenic-element contents compatible with the present-day average composition of Archaean cratons (Taylor & McLennan 1986) and plausible mantle heat flow, the steady state temperature at the Moho in the Late Archaean could have been close to 700°C (Rey *et al.* 2003). In fact, one can argue that this temperature could have buffered the thickness of the continental crust, since a thicker crust would have spread (Bailey 1999). Hence, the Archaean continental lithosphere would have been less likely to develop large gradients of crustal thickness. In addition, there is solid evidence that the buoyancy of Archaean continental lithosphere was enhanced by a sub-continental lithospheric mantle, more depleted, and therefore less dense, than that of Phanerozoic lithosphere (3310 kg $m^{-3}$ vs 3370 kg $m^{-3}$, Griffin *et al.* 1998). Upon lithospheric thickening, a more buoyant sub-continental lithospheric mantle would produce relatively greater extensional forces, and therefore a larger Argand Ratio. Figure 1a illustrates the consequences of a warmer geotherm on the integrated strength of the lithosphere (i.e., the denominator of $AR$). Figure 1b illustrates the effect of a more buoyant lithospheric mantle on the local gravitational stress (i.e., the numerator of $AR$). Both effects imply that local gravitational forces might have been more important relative to in-plane stresses arising from distant plate boundaries in the Archaean than in the Phanerozoic.

## Models: assumptions and simplifications

Keeping in mind that our objective is to illustrate the difference in lithospheric deformation due to contrasting buoyancy and thermal structure, we assume here that Archaean-like and Phanerozoic-like lithospheres are similar in all but two aspects: the density profile and the temperature profile. There are a number of problems when

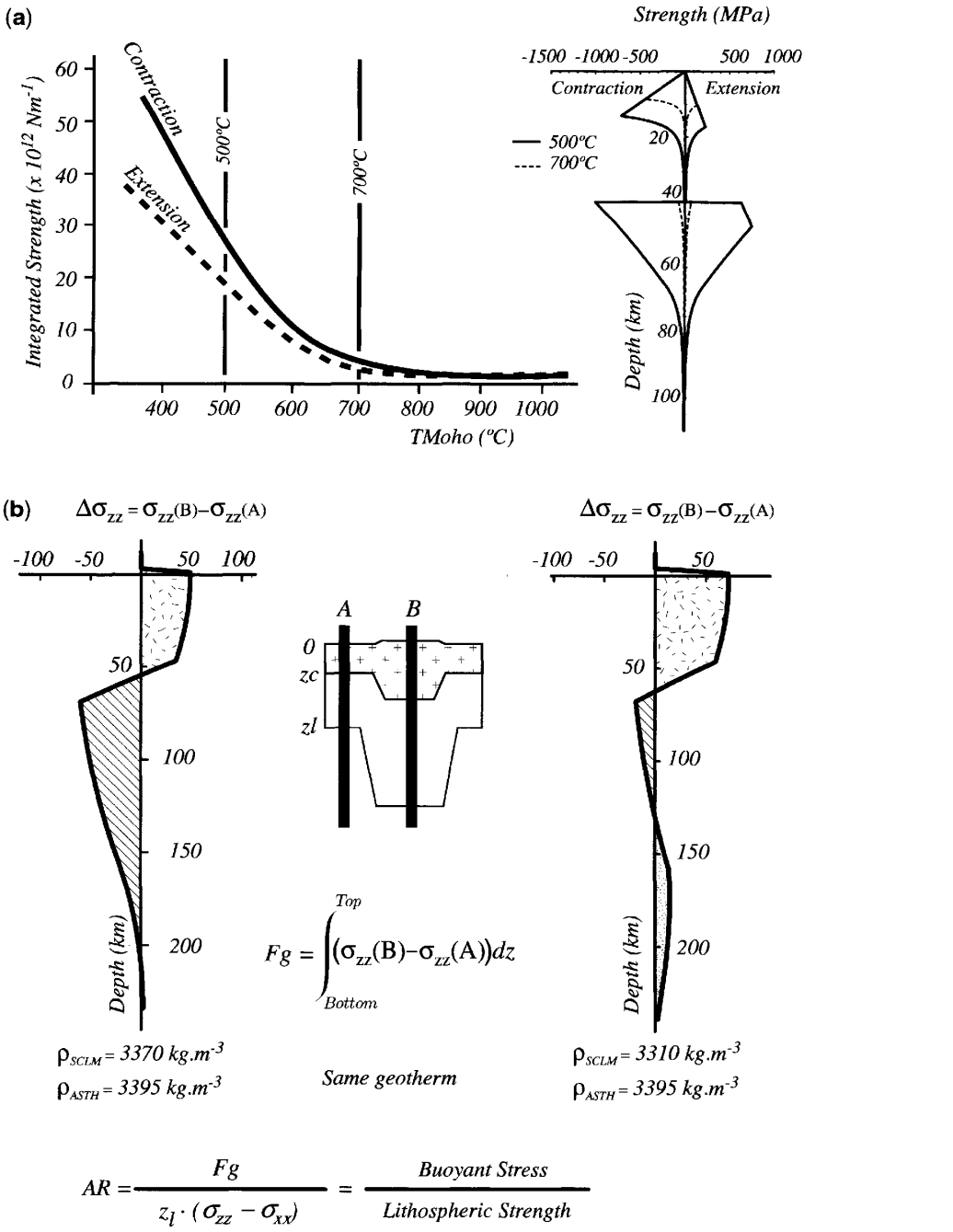


**Fig. 1.** (**a**) Consequences of a warmer geotherm on the strength of continental lithosphere and therefore on the *AR* denominator, and (**b**) consequences of a more buoyant sub-continental lithospheric mantle on the gravitational force related to homogeneous thickening and therefore on the *AR* numerator. (**a**) The temperature at the Moho is used as a proxy for the continental geotherm. As the temperature at the Moho increases, the integrated strength of the continental lithosphere (integration with depth of the rheological profile) decreases linearly until the Moho reaches *c.* 700°C. Above this temperature, the integrated strength does not change much as the strength of the upper crust, which is now the stronger layer of the lithosphere, is less sensitive to temperature. In inset, the rheological profiles for $T_{\mathrm{Moho}} =$ 500°C and 700°C showing the disappearance of the strong upper mantle in warm continental lithospheres. (**b**) Upon doubling the thickness of a lithospheric column via homogeneous thickening, a gravitational force is created. The gravitational force (*Fg*) is given by the integration with depth of the difference in the lithostatic pressure ($\Delta\sigma_{zz}$) between the deformed (column B) and the reference lithosphere (column A). Upon thickening, a heavy SCLM generates a deficit in gravitational potential energy (hatched areas in left profile) that balances the excess in gravitational potential energy (stippled areas) in the upper lithosphere. In contrast, a less dense SCLM reduces the gravitational force stored in the lower lithosphere (right profile) but increases the gravitational potential energy stored in the upper lithosphere. Hence, the overall gravitational force created by homogeneous thickening of a lithosphere with a buoyant lithospheric mantle is much larger than that created by the homogeneous thickening of a lithosphere with a denser lithospheric mantle.

trying to define average continental lithospheres representative of Archaean and Phanerozoic eons. Firstly, there is a much larger reduction in crustal radiogenic heat production within the Archaean Eon alone than from the end of the Archaean to now. Secondly, Phanerozoic lithospheres exist in a very large range of thermal regimes. We must account for variation in the properties of both Archaean and Phanerozoic continental lithospheres, for probable systematic differences between the average properties, and for significant overlap in the ranges of properties of the two types of lithosphere. Therefore, we define three Archaean and three Phanerozoic model lithospheres covering a plausible range of thermal regimes (Table 1). Table 2 summarizes the relevant thermo-mechanical parameters.

### *Density structure*

In all models, the continental crust has the same thickness, $z_c$ (40 km) and the same depth-dependent density structure, defined at 0°C. For the crust, the density is assumed to increase from the top of the crust ($\rho_a$) to the Moho ($\rho_b$) because of a compositional gradient. In addition, it is dependent on temperature ($\alpha_c$ is the coefficient of thermal expansion).

$$\rho_{\text{crust}}(z) = \left[\rho_a + \left(\frac{\rho_b - \rho_a}{z_c}\right) \cdot z\right] \times (1 - \alpha_c \cdot T(z)) \quad (1)$$

Because of a larger degree of depletion, the density of the sub-continental lithospheric mantle (SCLM) was most likely lower in the Archaean (Jordan 1975, 1997; Griffin *et al.* 1998). Following Griffin *et al.* (1998), the density at 0°C of the SCLM in the Archaean and Phanerozoic models are 3310 kg m$^{-3}$ and 3370 kg m$^{-3}$ respectively. We assume that the asthenospheric mantle acts as an infinite reservoir with constant density through time ($\rho_{ao} = 3395$ kg m$^{-3}$). Assumed pressure- and temperature-dependences for the lithospheric mantle density are defined by:

$$\rho_{lm}(z) = \rho_{lmo} \cdot (1 - \alpha_m \cdot T(z) + \chi_m \cdot P) \quad (2)$$

where $\chi_m$ is the coefficient of compressibility, $P$ is the pressure, and $\rho_{lmo}$ is the density of lithospheric mantle at 0°C. For the density profile in the asthenosphere, the density of the asthenosphere $\rho_{ao}$ at 0°C is substituted for $\rho_{lmo}$ in equation (2), with constant temperature equal to that at the base of the lithosphere, and the same value of $\chi_m$.

### *Continental geotherm*

The temperature profile is calculated from a two-layer model with no radiogenic heat production in the SCLM and a depth-independent radiogenic heat production in the crust of thickness $z_c$. The steady state and transient geotherms are derived from the one-dimensional diffusion-advection equation:

$$\frac{\partial T}{\partial t} = \kappa \cdot \frac{\partial^2 T}{\partial z^2} + \frac{H}{\rho \cdot cp} - v \cdot \frac{\partial T}{\partial z} \quad (3)$$

where $\kappa$ thermal diffusivity; $H$ is the radiogenic heat production; $\rho$ is the density; $cp$ is the heat capacity; and $v$ is the velocity of the medium relative to the upper surface. For boundary conditions we assume a constant mantle heat flow entering the base of the lithosphere, and a constant temperature (25°C) at the top of the crust. During deformation, the mantle heat flow remains constant and is applied to the base of the lithosphere, which is defined by the isotherm 1330°C.

For Archaean-like lithospheres, we conservatively choose a crustal radiogenic heat production representative of the Late Archaean. Using the average concentration in radiogenic elements for present-day Archaean cratons

**Table 1.** *Vertical geometry and thermal parameters for our models of Phanerozoic-like and Archaean-like continental lithospheres*

| | $z_c$ (km) | $H$ ($10^{-6}$ Wm$^{-3}$) | $Q_o$ ($10^{-3}$ Wm$^{-2}$) | $z_l$ (km) | $T_{\text{Moho}}$ (°C) |
|---|---|---|---|---|---|
| Phan160 | 40 | 0.48 | 18.7 | 160 | 447 |
| Phan120 | 40 | 0.48 | 24.95 | 120 | 546 |
| Phan80 | 40 | 0.48 | 37.4 | 80 | 741 |
| Arch160 | 40 | 0.99 | 16.2 | 160 | 566 |
| Arch120 | 40 | 0.99 | 21.6 | 120 | 652 |
| Arch80 | 40 | 0.99 | 32.3 | 80 | 820 |

Abbreviations: $z_c$: crustal thickness; $H$: Crustal radiogenic heat production (depth independent); $Q_o$: Basal heat flow; $z_l$: Depth of the isotherm 1330°C, base of the lithosphere; $T_{\text{Moho}}$: Temperature at the Moho.

**Table 2.** *List of parameter values*

| Parameters | Values | Units |
|---|---|---|
| Gravity: $g$ | 9.81 | $m\ s^{-2}$ |
| Crust thermal expansion: $\alpha_c$ | $3.5 \times 10^{-5}$ | $K^{-1}$ |
| Mantle thermal expansion: $\alpha_m = a_0 + a_1T + a_2T^{-2}$ | $a_0 = 2.697 \times 10^{-5}$<br>$a_1 = 1.0192 \times 10^{-8}$<br>$a_2 = -0.1282$ | $K^{-1}$ |
| Mantle bulk modulus: $\chi_m$ | 130 | GPa |
| Lithosphere thermal diffusivity: $\kappa$ | $0.97 \times 10^{-6}$ | $m^2\ s^{-1}$ |
| Crust volumetric heat production: $H_c$ | *cf.* Table 1 | $Wm^{-3}$ |
| Mantle volumetric heat production: $H_m$ | 0 | $Wm^{-3}$ |
| Heat capacity: $cp$ | 1000 | $J\ kg^{-1}\ K^{-1}$ |
| Surface temperature: $T_o$ | 293 | K |
| Temperature at the base of the lithosphere: $T_l$ | 1603 | K |
| Heat flow at the base of the lithosphere: $Q_o$ | *cf.* Table 1 | $Wm^{-2}$ |
| Crustal thickness: $z_c$ | *cf.* Table 1 | km |
| Lithosphere thickness: $z_l$ | *cf.* Table 1 | km |
| Lithospheric mantle density @ T = 0°C: $\rho_{lmo}$ | Arch: 3310, Phan: 3370 | $kg\ m^{-3}$ |
| Asthenospheric mantle density @ T = 0°C: $\rho_{ao}$ | 3395 | $kg\ m^{-3}$ |
| Upper crust mass density @ @ T = 0°C: $\rho_a$ | 2700 | $kg\ m^{-3}$ |
| Lower crust mass density @ @ T = 0°C: $\rho_b$ | 2900 | $kg\ m^{-3}$ |
| Water mass density: $\rho_w$ | 1030 | $kg\ m^{-3}$ |
| Ratio pore pressure to overburden stress: $\lambda$ | 0.36 | |
| Universal gas constant: $R$ | 8.3144 | $J\ mol^{-1}\ K^{-1}$ |
| Crust power law sensitivity: $n_c$ | 3 | |
| Crust power law activation enthalpy: $Q_c$ | 190000 | $J\ mol^{-1}$ |
| Crust power law pre-exponent: $A$ | $5 \times 10^{-6}$ | $MPa^{-n}\ s^{-1}$ |
| Mantle power law sensitivity: $n_m$ | 3 | |
| Mantle power law activation enthalpy: $Q_m$ | 520000 | $J\ mol^{-1}$ |
| Mantle power law pre-exponent: $A_m$ | $7 \times 10^4$ | $MPa^{-n}\ s^{-1}$ |
| Mantle Dorn plasticity activation enthalpy: $Q_d$ | 540000 | $J\ mol^{-1}$ |
| Mantle Dorn plasticity law stress threshold: $\sigma_d$ | 8500 | MPa |
| Mantle Dorn plasticity law strain rate: $\varepsilon_d$ | $3.05 \times 10^{11}$ | $s^{-1}$ |

(Taylor & McLennan 1986) one can work out the crustal radiogenic heat production 2.7 Ga ($0.99 \times 10^{-6}$ $Wm^{-3}$). For Phanerozoic-like lithospheres, we chose the present-day average crustal radiogenic heat content of Archaean crusts ($0.48 \times 10^{-6}$ $Wm^{-3}$). We assume for simplicity that the bases of the thermal, mechanical and compositional lithopheres are all coincident. The mantle heat flow controls, $z_l$ the thickness of the lithosphere (i.e., the depth of the isotherm 1330°C). This is highly variable in Phanerozoic lithospheres, and was most likely highly variable in the Archaean too (Lenardic & Moresi 2000). We chose mantle heat flows to get three Archaean-like models (Arch80, Arch120 and Arch160) and three Phanerozoic-like models (Phan80, Phan120 and Phan160) with nominal equilibrium lithospheric thicknesses of 80, 120, and 160 km respectively (Fig. 2, Table 1). Consequently, the Moho temperature for Phanerozoic-like lithosphere with assumed crustal thickness of 40 km ranges from 447°C (Phan160), to 546°C (Phan120), to 741°C (Phan80). Phan80 represents an anomalously warm and thin continental lithosphere, while Phan160 represents a cold and thick lithosphere. The Moho temperature of the Archaean-like models varies from 566°C (Arch160), to 652°C (Arch120), to 820°C (Arch80). Arch80 is clearly an anomalously hot and thin continental lithosphere with a Moho temperature in excess of what would be required for lower crustal flow.

### *Constitutive equations and rheological profile*

We consider here the thin viscous sheet equations in a triaxial situation in which we specify that the horizontal principal stresses, $\sigma_{xx}$ and $\sigma_{yy}$, are externally specified while the vertical stress component, $\sigma_{zz}$, is determined simply by gravity. All quantities represent vertical averages through the lithospheric column. Expressed in terms of differential stresses, and

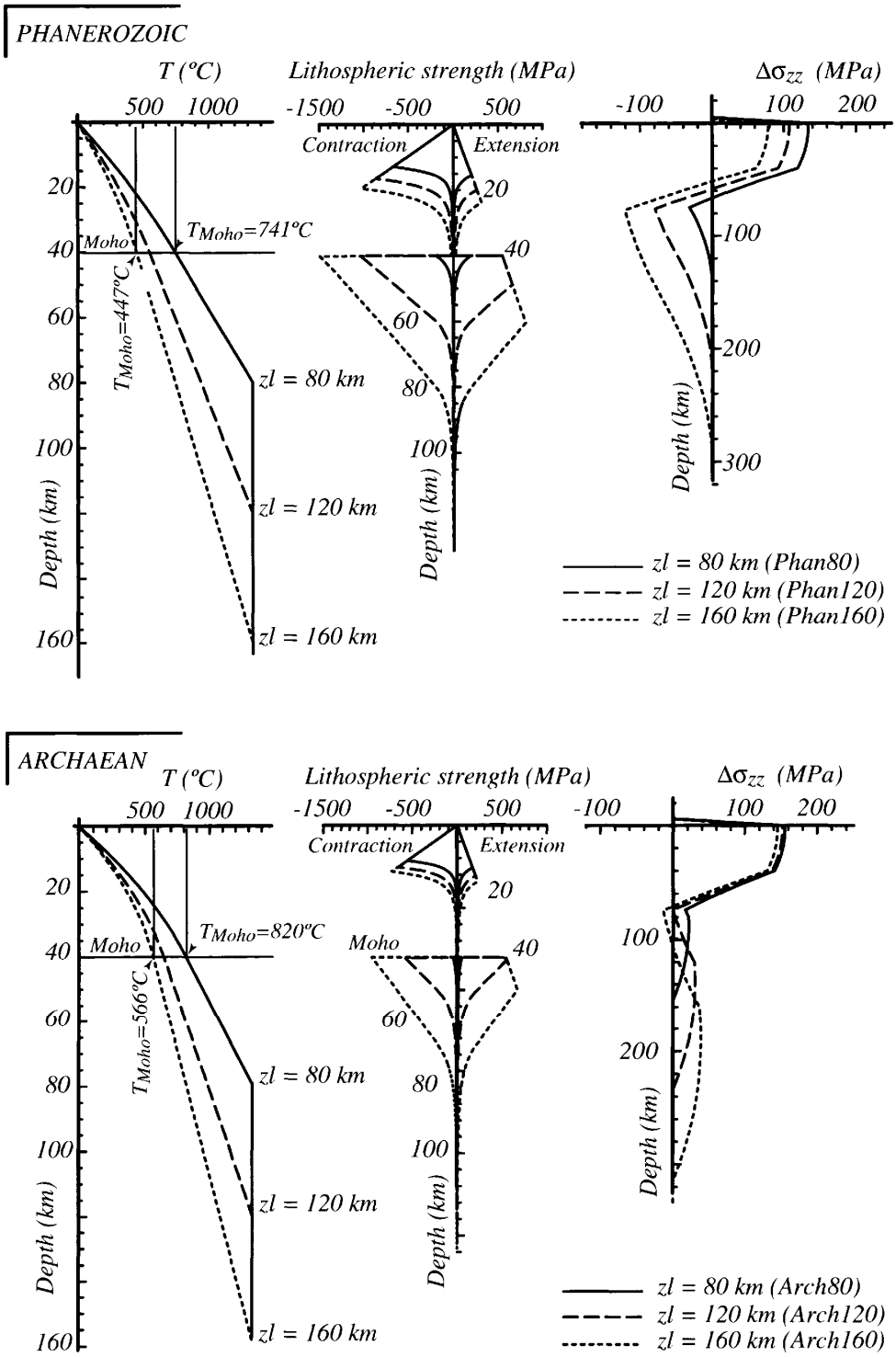


**Fig. 2.** Definition of Phanerozoic-like and Archaean-like lithosphere models. Moho temperatures of Archaean models are systematically greater by *c.* 100°C than Phanerozoic models (566–820°C vs 447–741°C). Hence, the Archaean models have a reduced strength when compared to the Phanerozoic models. Rheological profiles show that Phan160 and Arch120 have a strong upper mantle whereas Phan80 and Arch80 have a weak upper mantle. The contrasting density structure impacts on the gravitational force, as shown by plotting the $\Delta\sigma_{zz}$ profile for each model, assuming homogeneous doubling of the lithosphere thicknesses. In Archaean models, excesses in gravitational potential energy are stored in both crustal and mantle layers. For Phan80, the $\Delta\sigma_{zz}$ profile is similar to Archaean profiles in the sense that there is a large, unbalanced excess in gravitational potential energy (GPE) in the upper part of the lithosphere. In contrast, for the $\Delta\sigma_{zz}$ profile of Phan160, the deficit in gravitational energy in the lower lithosphere is greater than the excess in GPE in the upper lithosphere.

assuming isotropy for simplicity, the constitutive equations can be expressed as:

$$\sigma_{xx} - \sigma_{yy} = 2\eta \cdot (\dot{\varepsilon}_{xx} - \dot{\varepsilon}_{yy}) \quad (4)$$

$$\sigma_{zz} - \sigma_{yy} = 2\eta \cdot (\dot{\varepsilon}_{zz} - \dot{\varepsilon}_{yy}) \quad (5)$$

$$\sigma_{zz} - \sigma_{xx} = 2\eta \cdot (\dot{\varepsilon}_{zz} - \dot{\varepsilon}_{xx}) \quad (6)$$

where $\eta$ represents the depth-averaged effective isotropic viscosity, which includes the frictional Byerlee's law relation in the brittle layer and ductile stress laws in the lower layer as summarized below. Noting that the medium is effectively incompressible: $\dot{\varepsilon}_{xx} + \dot{\varepsilon}_{yy} + \dot{\varepsilon}_{zz} = 0$, then the three unknown strain-rates under the prescribed triaxial stress field are given by:

$$\dot{\varepsilon}_{zz} = \frac{1}{6\eta} \cdot (2\sigma_{zz} - \sigma_{xx} - \sigma_{yy}) \quad (7)$$

$$\dot{\varepsilon}_{yy} = \frac{1}{6\eta} \cdot (2\sigma_{yy} - \sigma_{zz} - \sigma_{xx}) \quad (8)$$

$$\dot{\varepsilon}_{xx} = \frac{1}{6\eta} \cdot (2\sigma_{xx} - \sigma_{zz} - \sigma_{yy}) \quad (9)$$

The effective viscosity is obtained by calculating the resistance to deformation at a specified strain-rate (assumed constant with depth) by evaluating the vertically integrated strength of the lithosphere:

$$\textit{Integrated Strength} = \int_{bottom}^{top} (\sigma_1(z) - \sigma_3(z)) \cdot dz \quad (10)$$

We use the standard rheological profile of Brace & Kohlstedt (1980) for the continental lithosphere, in which frictional sliding is the dominant failure mechanism at low temperature and high strain rate (in the upper crust and the upper mantle, Sibson 1974):

$$\sigma_1(z) - \sigma_3(z) = \beta \cdot \rho(z) \cdot g \cdot z \cdot (1 - \lambda) \quad (11)$$

where $g$ is the gravitational acceleration; $\lambda$ is the ratio of fluid pore pressure to the normal stress; and $\beta$ is a parameter dependent on the type of faulting, therefore dependent on the tectonic regime. It is given by:

$$\beta = \frac{R - 1}{1 + \delta \cdot (R - 1)} \quad (12)$$

with

$$R = \left(\sqrt{1 + \mu^2} + \mu\right)^{-2}$$

and

$$\delta = \frac{\sigma_{zz} - \sigma_3}{\sigma_1 - \sigma_3} \quad (13)$$

and $\mu$ the coefficient of internal friction (*cf.* Houseman & England 1986; Ranalli 1995). As the differential stress ratio $\delta$ varies from 0 (when $\sigma_{zz} = \sigma_3$) to 1 (when $\sigma_{zz} = \sigma_1$), $\beta$ varies from 3 (reverse faults) to 0.75 (normal faults) for $\mu = 0.75$. Intermediate $\beta$ values describe oblique slip faulting with $3 < \beta < 1.2$ for transpression, and $1.2 < \beta < 0.75$ for transtension. Strike-slip faulting occurs for $\beta = 1.2$ (when $\sigma_{zz} = (\sigma_1 + \sigma_3)/2$). Although different mechanisms (e.g., thrusting and strike-slip faulting) may occur simultaneously in a general triaxial stress-field, our calculation of the effective isotropic viscosity must assume a single value of $\beta$, which is determined from the current differential stress ratio $\delta$.

At high temperatures and differential stresses below 200 MPa, the viscous deformation of the crust and the mantle is modelled as power law creep (Evans & Goetze 1979). The creep is thermally activated (Ranalli 1995) and may be written in terms of the second invariant of the strain-rate tensor $\dot{E}^2 = (\sum_{i,j} (\dot{\varepsilon}_{ij} \cdot \dot{\varepsilon}_{ij}/2))$ as follows:

$$(\sigma_{ii} - \sigma_{jj}) = \left[ \left(\frac{2}{3}\right)^{(n+1)/2n} A^{-1/n} \dot{E}^{(1-n)/n} \times \exp\left(\frac{Q}{n \cdot R \cdot T}\right) \right] (\dot{\varepsilon}_{ii} - \dot{\varepsilon}_{jj}) \quad (14)$$

The numerical factor in (14) is introduced so that $A$ values determined for uniaxial compression experiments can be used in a general triaxial formulation which is independent of the orientation of the axes (Molnar *et al.* 1998).

Finally, at differential stresses larger than 200 MPa we use a Dorn flow law (Evans & Goetze 1979):

$$\sigma_{ii} - \sigma_{jj} = \sigma_d \left[ 1 - \sqrt{\frac{R \cdot T(z)}{Q_d} \cdot \ln\left(\frac{\dot{\varepsilon}_d}{\dot{\varepsilon}_{ii}}\right)} \right] \quad (15)$$

where $\sigma_d$, the so-called Peierls stress, is the yield stress needed to move crystal dislocations at $T = 0$ K. This experimental law limits the strength of the upper mantle to realistic values at high strain rates. We thus define an effective viscosity for the whole system by first integrating the stress difference as a function of depth through the lithosphere (using the different

deformation mechanisms that apply in the relevant depth ranges) and dividing by twice the strain-rate difference (compare Eqns 4–6).

### *Boundary conditions*

The model lithospheres are set up in dynamic equilibrium, assuming that the two horizontal principal stress components are initially equal to the vertical principal stress component as determined from the initial density column (each component depth-averaged). The tectonic effect of in-plane stress in the $x$-direction from a remote plate boundary is then simulated by adding to the stress component, $\sigma_{xx}$, an increment that is great enough to drive convergence at an initial strain rate of $5 \times 10^{-15}\,s^{-1}$. Under this tectonic driving force, thin sheet deformation (England & McKenzie 1982, 1983) occurs, and the tectonic stress balance changes with the thickness of the deforming lithosphere. Disregarding erosion and sedimentation, the lithospheric column changes under the action of (1) a triaxial state of stress, (2) local isostasy, and (3) thermal relaxation. These processes are integrated forward in time, using small increments of time whose duration is such that the incremental change in crustal thickness is kept below 250 m and that of the entire lithosphere to under 500 m. Calculation of transient geotherms uses a Crank-Nicholson finite differences scheme with a constant heat flow at the base of the lithosphere and no lateral heat transfer. Deformation strain rates are calculated using the thin sheet approximation, in which the vertically averaged stress-difference is related to the strain rates by the constitutive equations incorporated into Equation (10). The vertical stress-component is always evaluated directly from the current density profile. The two horizontal stress-components are set up as described above: $\sigma_{yy}$ is constant throughout the experiments and equal to its initial value; $\sigma_{xx}$ results from maintaining a constant plate boundary force against the vertical section of the deforming lithosphere normal to the $x$-direction. Therefore, $\sigma_{xx}$ is inversely proportional to the current thickness of the deforming lithosphere on which the force is applied.

## Presentation of the results

The evolution of our six model lithospheres, subject to the above boundary conditions, is presented in Figures 3 to 5. Figure 3 gives the position through time of the three main density interfaces: the surface, the Moho, and the base of the lithosphere (i.e., the isotherm 1330°C). Hence, it illustrates the evolution of the crustal and lithospheric thicknesses during convergence. Figure 4 shows the evolution of the magnitude of the differential stresses $(\sigma_{zz} - \sigma_{xx})$ versus $(\sigma_{zz} - \sigma_{yy})$. In this graph, four domains can be identified, a domain in which extension occurs in both horizontal directions $((\sigma_{zz} - \sigma_{xx}) > 0$ and $(\sigma_{zz} - \sigma_{yy}) > 0$, therefore $\sigma_{zz} = \sigma_1)$; a domain in which convergence occurs in both horizontal directions $((\sigma_{zz} - \sigma_{xx}) < 0$ and $(\sigma_{zz} - \sigma_{yy}) < 0$, hence $\sigma_{zz} = \sigma_3)$; and the two transcurrent domains in which there is a combination of extension in one direction and convergence in the other $(\sigma_{zz} = \sigma_2)$.

Figure 4 can also be contoured for the Argand Ratio. We have defined the Argand Ratio as the ratio of the gravitational stress to the depth-averaged strength of the lithosphere at a nominal strain rate. Assuming local isostatic compensation, and disregarding flexural stresses and shear tractions at the base of the lithosphere, the gravitational stress is the depth average of $(\sigma_{zz} - \sigma_{yy})$. It is the difference between the averaged lithostatic stress under the deformed lithosphere and the averaged lithostatic stress determined in the lowland region down to the same depth, i.e., to the base of the deforming lithosphere (Artyushkov 1973; Turcotte 1983; Molnar & Lyon-Caen 1988). The depth-averaged strength at the imposed nominal strain rate is $|\sigma_{zz} - \sigma_{xx}|$, the effective differential stress-driving convergence. Hence, the Argand Ratio is simply:

$$AR = \frac{\sigma_{zz} - \sigma_{yy}}{|\sigma_{zz} - \sigma_{xx}|} \qquad (16)$$

and constant values of $AR$ can therefore be mapped as straight lines onto the $(\sigma_{zz} - \sigma_{yy})$ – $(\sigma_{zz} - \sigma_{xx})$ plane, as shown in Figure 4. In the definition of the Argand Ratio, the absolute value of $(\sigma_{zz} - \sigma_{xx})$ is used so that its sign is consistent with prior use of the Argand Number ($Ar$), in which the positive Argand Number drives extension or resists convergence (England & McKenzie 1982; Houseman & England 1986). Figure 5 depicts the evolution of the Argand Ratio through time for our six model lithospheres.

The convergence history of all Archaean models and that of the Phanerozoic model with an anomalously warm geotherm (Phan80) unfolds in two stages (Fig. 3). In the first stage, convergence is accommodated by crustal and lithospheric thickening, with a monotonically decreasing rate of thickening. The duration of this first stage is proportional to the thickness of the initial lithosphere (Fig. 3). In the second

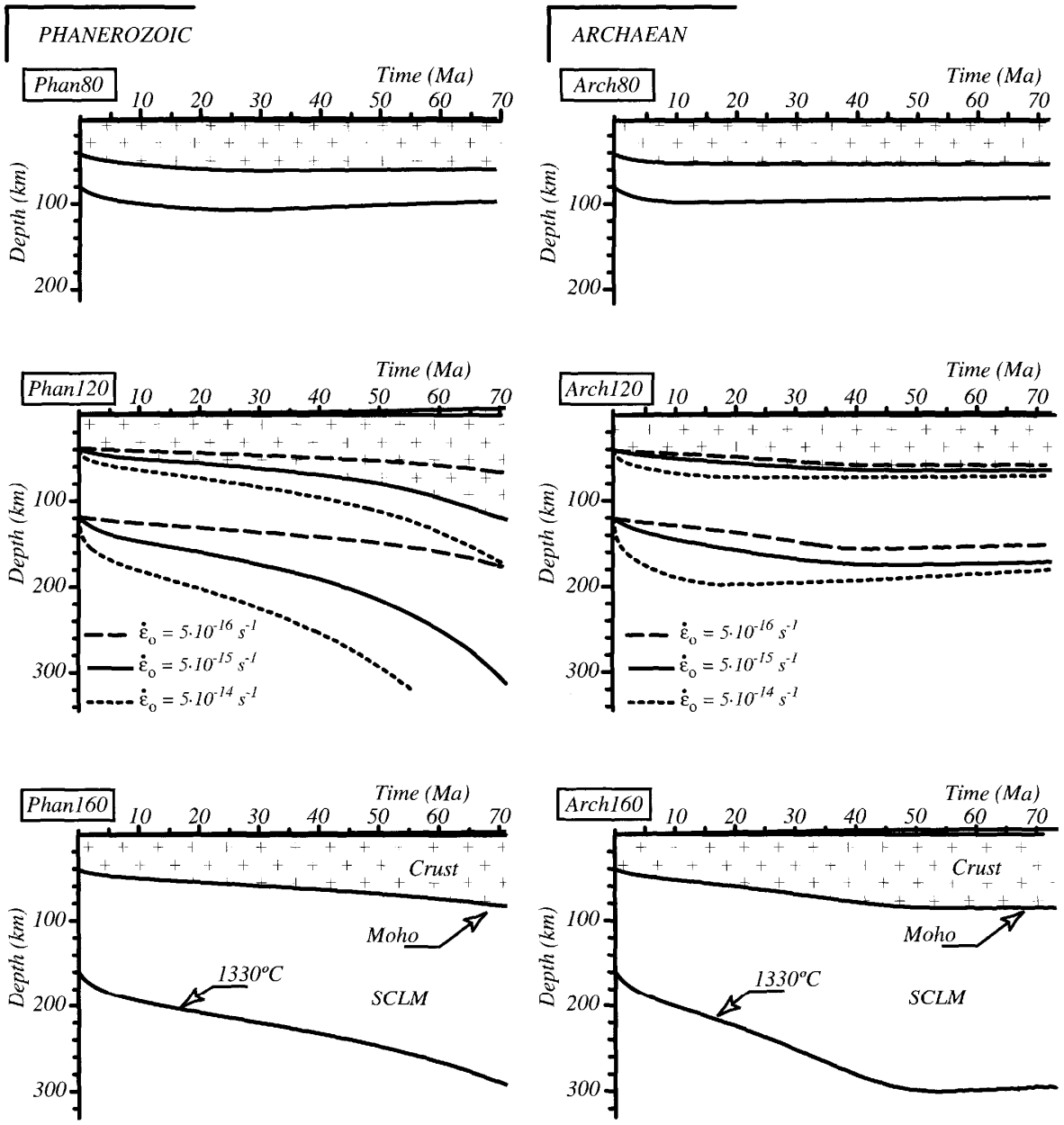


**Fig. 3.** Evolution of the position of the main density interfaces during convergence. In all Archaean models, the continental lithosphere reaches a plateau stage during which the depths of the density interfaces do not change much. The timescale at which this stage is reached is proportional to the initial thickness of the lithophere. A similar evolution is displayed by Phan80, which in many respects is like the Archaean models. In contrast, the depth of the density interfaces for Phan120 and Phan160 increases at an increasing rate. In these models, the thickening rate increases despite convergence being driven by a decreasing horizontal stress.

stage, convergence continues without significant thickening and even with a slight decrease in the thickness of the SCLM. This near steady-state evolution is maintained for the duration of the convergence. Since convergence is ongoing, shortening in the $x$-direction is balanced by extension in the direction perpendicular to convergence. Surface deformation at this stage would be primarily in the strike-slip mode. It is interesting to note that during convergence the ratio thickness of the crust to that of the SCLM increases only very slightly (Arch80: 0.5–0.56; Arch120: 0.33–0.363; and Arch160: 0.25–0.269) due to the thermal thinning of the SCLM. Therefore, the two-stage evolution described above cannot be the result of a change in the

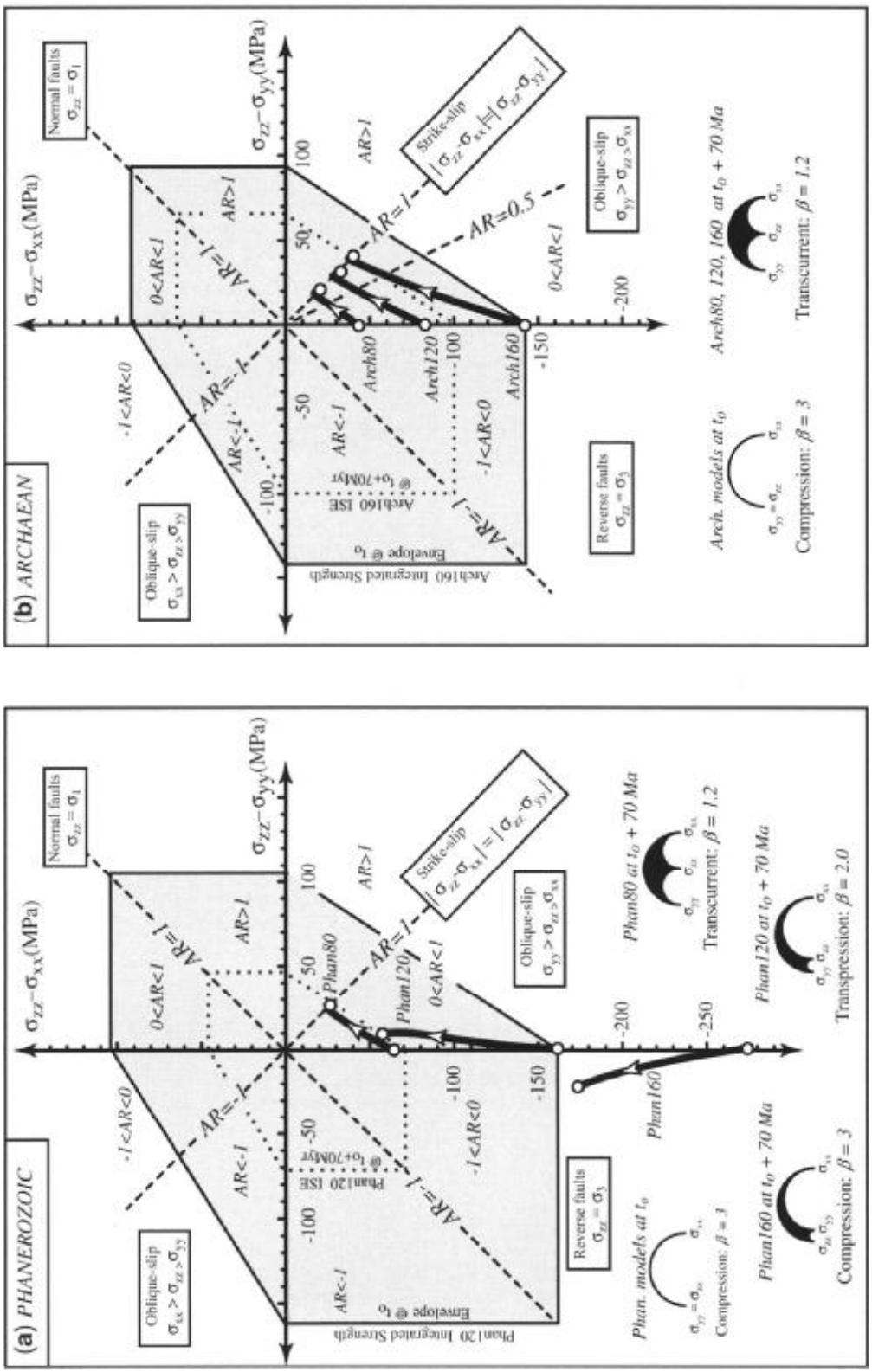


**Fig. 4.** Evolution of the state of stress during convergence is shown on a graph of $\sigma_{zz} - \sigma_{yy}$ against $\sigma_{zz} - \sigma_{xx}$. (**a**) The Phanerozoic model Phan160 follows a stress path within the domain of convergence in both horizontal directions (least principal stress vertical). For the models Phan120 and Phan80 the state of stress is transpressional. (**b**) The state of stress of all Archaean models becomes transpressional, reaching the transcurrent domain, where $|\sigma_{zz} - \sigma_{yy}| = |\sigma_{zz} - \sigma_{xx}|$. Contours parallel to the boundary of the shaded area define the stress differences required to drive deformation at a specified strain-rate. The Argand Ratio ($AR$) can be mapped into the $\sigma_{zz} - \sigma_{yy}/\sigma_{zz} - \sigma_{xx}$ plane. The stress state of all Archaean models evolves to an increasingly positive Argand Ratio, eventually reaching 1. At that stage, gravitational stress is equal to the stress that drives convergence.

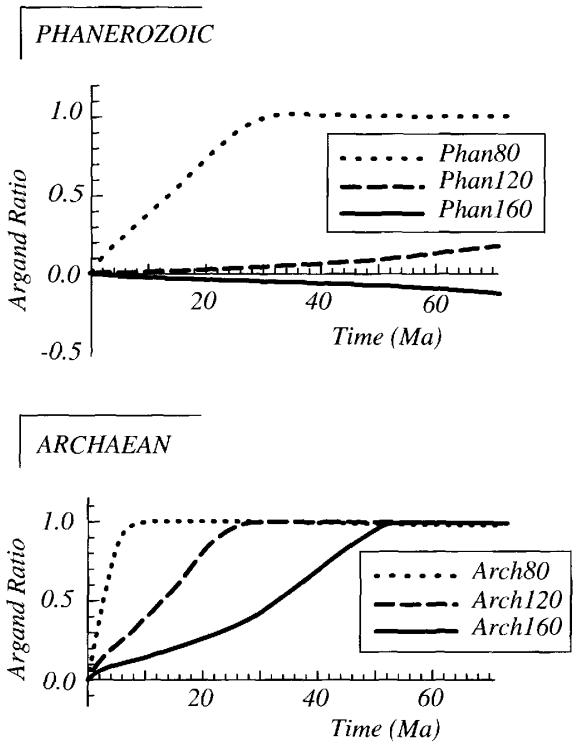


**Fig. 5.** Evolution of the Argand Ratio during convergence. *AR* for all Archaean models evolves toward 1. At that stage, a steady-state evolution is reached where convergence in one horizontal direction is balanced by extension in the orthogonal horizontal direction. Phanerozoic models show variable evolution of *AR*. For Phan60, the gravitational force enhances the tectonically driven convergence, whereas the gravitational force for Phan80 opposes it.

relative thickness of the crustal and the SCLM layers.

Convergence histories for the Phanerozoic models show large variations, that of model Phan80 being similar to that of Archaean models. Convergence histories for Phan120 and Phan160 models follow a different pattern. As shown in Figure 3, the thickening rate increases monotonically, as demonstrated by the progressive deepening of the Moho and that of the isotherm 1330°C. In these cases, the $y$-direction spreading is unable to keep pace with the imposed $x$-direction convergence (Phan120 in Fig. 4) and the increasing gravitational potential energy deficit caused by the thickened lithospheric root actually causes $y$-direction convergence as well (Phan160 in Fig. 4). Eventually this evolutionary path may lead to the initiation of a mechanical instability as the thickening rate increases exponentially, as suggested by Fleitout and Froidevaux (1982). However, as for the Archaean models, the ratio between the thickness of the crust and that of the SCLM increases very slightly (Phan80: 0.5–0.57; Phan120: 0.33–0.368; and Phan160: 0.25–0.267). The pull of the SCLM is therefore modest.

This contrasting evolution between Archaean and Phanerozoic models is the result of contrasting tectonic regimes that develop in response to an evolving stress balance. Figure 4 illustrates the differences. From its starting point on the biaxial compression axis ($\sigma_{xx} > \sigma_{zz} = \sigma_{yy}$, Fig. 4a), the state of stress for the model Phan160 moves into the domain in which both horizontal axes are convergent along a path where $\sigma_{xx} > \sigma_{yy} > \sigma_{zz}$. Along that path, the parameter $\beta = 3$ and the tectonic regime is in contraction. For such a state of stress, it is inferred that reverse faults and thickening would accommodate the convergence. The state of stress for Phan80 and Phan120 follows a path into the transpression domain where $\sigma_{xx} > \sigma_{zz} > \sigma_{yy}$. However, after 70 Ma of convergence the parameter $\beta$ for Phan120 is only 2 (oblique-slip faults), whereas it stabilizes at 1.2 (transcurrent tectonic regime with strike-slip faults) for Phan80. The crustal thickening factors $f_c$ increase at an increasing rate for Phan120 and Phan160 but stabilize at *ca.* 1.4 for Phan80. All Archaean lithospheres follow a state of stress history similar to that of model Phan80 (Fig. 4b). Their state of stress moves along a transpression path where $\sigma_{xx} > \sigma_{zz} > \sigma_{yy}$, and then stabilizes in the transcurrent tectonic regime where $(\sigma_{xx} - \sigma_{zz}) = (\sigma_{zz} - \sigma_{yy})$. When the steady-state transcurrent tectonic regime is reached, we infer that strike-slip faults in the upper crust and lateral viscous flow in the lower crust accommodate convergence. This overall lateral flow explains the limited thickening of Archaean lithospheres ($1.4 \leq f_c \leq 2$) and anomalously warm Phanerozoic lithopheres ($f_c \leq 1.4$).

This contrasting evolution is also illustrated by the evolution of the Argand Ratio (Fig. 5). For the Archaean models, and for Phan80, stage 1 of the convergence history leads to a positive Argand Ratio that increases approximately linearly with time (Fig. 5). As the differential stresses have opposite signs they promote opposing flows. Hence, when the Argand Ratio reaches unity (second stage), the tendency of the thickened crust to spread under gravity produces a lateral flow whose rate balances that of convergence, preventing further thickening. In contrast, convergence of the Phanerozoic model Phan160 produces a negative Argand Ratio that decreases at an increasing rate. The gravitational force in this example enhances the tectonic differential stress promoting convergence and thickening. In Phan160, the colder and denser SCLM keel

pulls on the deforming lithosphere, enhancing the compressive horizontal stress and promoting thickening. The role of the SCLM in this kind of instability has been proposed in a number of studies (e.g., Fleitout & Froideveaux 1982; Sun & Murrel 1994; Houseman & Molnar 1997, 2001; Conrad 2000), and England & Houseman (1989) noted that the question of whether increased thickening of the lithosphere leads to an increasingly negative or increasingly positive Argand Ratio depends sensitively on assumed density and thermal parameters. Based on the compositional buoyancy of surviving Archaean SCLM, such instabilities would be less likely in Archaean times, and orogeny would more likely lead to convergence in one direction being balanced by extension in the orthogonal direction.

## Discussion

Because of the secular cooling of the continental geotherm and the secular change in the composition of the SCLM (Griffin *et al.* 1998), continental thickening in modern and Phanerozoic lithospheres develops with typically lower Argand Ratios compared to those of Archaean times. For moderate to cold thermal regimes, prevalent in Phanerozoic and modern continental lithospheres, $AR$ is $\ll 1$, promoting strain localization necessary for the formation of linear orogens (i.e., mountain belts). During thickening, one could expect that high temperature transient continental geotherms (a response to crustal thickening) would lead to an increasing Argand Ratio. This is because warmer conditions increase the buoyancy of the lithosphere (i.e., increase the $AR$ numerator) while decreasing its integrated strength (i.e., decreasing $AR$ denominator). However, as shown by our experiments Phan120 and Phan160 (Fig. 3) this effect competes with the cooling of the geotherm induced by the downward heat advection driven by thickening. In Phanerozoic and modern continental lithospheres, Argand Ratios $\geq 1$, necessary for the development of extensional collapse, require a change in the external factors that affect the orogen. Such changes may be produced either by a decrease of the driving tectonic stresses (reduction of the $AR$ denominator), or by a sudden increase in gravitational potential energy induced by the convective thinning of the thermal boundary layer (England & Houseman 1988, 1989) and the establishment of higher transient continental geotherm (increase of $AR$ numerator). The Basin and Range Province (Jones *et al.* 1996; Flesch *et al.* 2000) and Tibet (England & Molnar 1997) confirm that, in present-day continental lithospheres, gravitational forces indeed play a significant role in the tectonic evolution of anomalously warm and/or buoyant lithospheres. The convergence experiment Phan80 (Fig. 3) illustrates the impact of gravitational force on an initially warm thin continental lithosphere.

Triaxial numerical experiments clearly point toward a more significant role for gravitational forces in lithospheric deformation during the Archaean. The gravitational forces determine the sustainable amount of thickening, the tectonic regime, and the spatial distribution of strain. The reduced ability of continental lithospheres in the Archaean to sustain significant contrast in gravitational potential energy has profound implications on the mode of deformation during both extensional and contractional deformation. In particular, our triaxial tests suggest that convergence involving warm and buoyant lithospheres would result in (1) less topographic relief, (2) more homogeneous lithospheric deformation distributed over broad regions (i.e., less prominent linear belts), and (3) an overall transcurrent tectonic regime where strike-slip faults and crustal-scale gravitational flow are the likely outcomes of sustained convergence. Experiments performed under driving tectonic forces that produce initial strain rates of $5 \times 10^{-16}$ s$^{-1}$ and $5 \times 10^{-14}$ s$^{-1}$ (Fig. 3) show that these conclusions are not affected by considering different level of tectonic forcing in the Archaean.

Archaean geological records provide plenty of observations consistent with the predictions made above. A low surface elevation and the absence of large gradients of crustal thickness in Archaean cratons are suggested by the rather low and homogeneous erosion level ($5 \pm 2$ km) across most Archaean cratons (Galer & Metzger 1998). In particular, the co-existence of very low-grade greenstones in close proximity with granitic domes suggests that in most cases only a few kilometres of supracrustal rocks have been removed by erosion. Hence, erosion does not reveal any deep orogenic zones, but instead reveals low to medium grade meta-sedimentary and meta-volcanic rocks. The evidence of Archaean high-grade terranes such as the Pikwitonei and Kapuskasing domains in the Superior Province, the granulite facies migmatite from the Limpopo belt, and the granulite gneisses of the Karelian craton in central Finland have sometimes been advanced as an argument that regional crustal thicknesses on the order of 60–80 km

were created by Archaean orogenies. These rocks, however, record pressures lower than 1100 MPa (*c.* <40 km) and have been exposed to the surface following Proterozoic exhumation (Percival & Peterman 1994; Kamber *et al.* 1995, 1996; Korsman *et al.* 1999), not during Archaean orogenesis involving crustal-scale thrusts. Crustal-scale gravitational flow is also suggested by the maintenance of a sub-aerial to shallow sub-aqueous surface topography during the accumulation of volcano-sedimentary sequences (greenstones), some up to 20 km thick, above mainly felsic basement (Arndt 1997; De Witt & Ashwal 1997). Despite their thickness, greenstone covers failed to thicken the continental crust sufficiently to raise its surface elevation above sea level. The gravitational flow of the lower continental crust during the loading of crust could explain why the accumulation of thick volcano-sedimentary sequences did not translate into significant crustal thickening or significant gradients in crustal thickness.

The triaxial tests presented here suggest that Archaean continental lithospheres reach the plateau stage, and an Argand Ratio close to one, for a smaller amount of thickening. How much smaller depends on the thickness of the SCLM relative to that of the crust. For Arch120 the plateau stage is reached for a crustal thickening factor of 1.5. Therefore, continental convergence in the Archaean, if sustained, should ultimately have led to orogenies being dominated by strike-slip faults and lateral flow. Crustal-scale thrusts of Archaean age appear absent, and have yet to be documented in Archaean cratons. In contrast, craton-scale strike-slip faults of Archaean age are ubiquitous in many Late Archaean cratons such as the Superior Province, the Yilgarn craton, the Dharwar craton, or the Karilian craton. In the Yilgarn craton for instance, they are typically 50–250 km long and 2–10 km in width (Whitaker 2001). These strike-slip faults develop in close temporal relationship with elliptical granitic intrusions whose long axes roughly parallel the trend of strike-slip faults (e.g., Gee 1979). This structural relationship has previously been used to argue for horizontal shortening accommodated by strike-slip faults and horizontal extension (e.g., Treloar & Blenkinsop 1995; Hamilton 1998; Davis & Maiden 2003). The relatively high spatial frequency of these faults (one to three *c.* 300 km long strike-slip fault every 50 km across strike in the Yilgarn craton) contrasts strongly with the few major faults that accommodate lateral escape tectonics in Phanerozoic and modern convergent orogens such as the Himalayas, the European Alps or the European Variscan belt. The relatively homogeneous deformation fields of the Archaean are more likely to have extended over greater areas than in Phaneozoic orogenies. With the possible exception of the Superior Province, many Archaean cratons record regional finite strain fields with similar characteristics over a length scale of hundred of kilometres (Choukroune *et al.* 1997; Hamilton 1998), with little or no metamorphic gradient, and little or no tectono-magmatic age gradient. This strongly contrasts with modern orogens where tectono-metamophic and magmatic events are known to migrate from hinterland to foreland over many tens of millions years.

## Conclusion

The steady-state thermal structure of continental lithospheres in the Archaean may have been similar to that of modern and thermally mature orogenic zones. Studies of present-day crustal flow in Tibet and in the Basin and Range Province argue that gravitational forces play a significant role. Both regions have a high Argand Ratio relative to a large anomaly in gravitational potential energy (particularly in Tibet) and a weak lithosphere (particularly in the Basin and Range Province). In ancient continental lithospheres, warmer steady-state thermal conditions combined with a more buoyant SCLM would have ensured the dominant role of the gravitational force in Archaean continental dynamics. Our numerical experiments show that, because of their contrasted thermo-mechanical properties, Archaean-like (warm and buoyant) and Phanerozoic-like (colder and heavier) continental lithospheres evolve along contrasted strain/stress paths when submitted to the same triaxial deformation conditions. In Archaean times, gravitational forces acted as a stabilizing agent by impeding thickening and promoting diffuse deformation over large areas through gravitational flow perpendicular to the direction of convergence. For moderate to cold thermal regimes, prevalent in Phanerozoic and modern times, the continental lithosphere may be too strong to be impacted by gravitational forces. Only when transient high-temperature geotherms are established do gravitational forces intervene in lithospheric deformation. Secular cooling of the continents has increased their strength while the secular increase in density of the subcontinental lithospheric mantle has reduced their buoyancy, both effects diminishing *AR* and therefore the relative importance of gravitational forces in continental dynamics.

Many thanks to Y. Poujdom Djomani, B. Griffin and S. O'Reilly for enlightening discussions on the evolution through time of the density of the SCLM. Thanks to S. Buiter, S. Costa, R. Pysklywec and M. Sandiford for their constructive comments of the first draft of this manuscript. Special thanks are due to K. Stüwe whose thorough review considerably improved its final version. This work was supported by ARC Large Grant N°: A10017138.

## References

ARNDT, N. 1997. Why was flood volcanism on submerged continental platforms so common in the Precambrian? *Precambrian Research*, **97**, 155–164.

ARTYUSHKOV, E. V. 1973. Stresses in the lithosphere caused by crustal thickness inhomogeneities. *Journal of Geophysical Research*, **78**, 7675–7708.

BAILEY, R. C. 1999. Gravity-driven continental overflow and Archaean tectonics. *Nature*, **398**, 413–415.

BINNS, R. A., GUNTHORPE, R. J. & GROVES, D. I. 1976. Metamorphic patterns and development of greenstone belts in the eastern Yilgarn Block, Western Australia. *In*: WINDLEY, B. F. (ed.) *The Early History of the Earth*. Wiley, New York, N.Y., 303–316.

BOUHALLIER, H., CHOUKROUNE, P. & BALLEVRE, M. 1993. Diapirism, bulk homogenous shortening and transcurrent shearing in the Archaean Dharwar craton: the Holenarsipur area. *Precambrian Research*, **63**, 43–58.

BRACE, W. F. & KOHLSTEDT, D. L. 1980. Limits on lithospheric stress imposed by laboratory experiments. *Journal of Geophysal Research*, **85**, 6248–6252.

BUCK, W. R. & SOKOUTIS, D. 1984. Analogue model of gravitational collapse and surface extension during continental convergence. *Nature*, **369**, 737–740.

CHARDON, D., CHOUKROUNE, P. & JAYANANDA, M. 1998. Sinking of the Dharwar Basin (South India); implications for Archaean tectonics. *Precambrian Research*, **91**, 15–39.

CHOUKROUNE, P., BOUHALLIER, H. & ARNDT, N. T. 1995. Soft lithosphere during periods of Archaean crustal growth or crustal reworking. *In*: COWARD, M. P. & RIES, A. C. (eds) *Early Precambrian Processes*. Geological Society, London, Special Publications, **95**, 67–86.

CHOUKROUNE, P., LUDDEN, J. N., CHARDON, D., CALVERT, A. J. & BOUHALLIER, H. 1997. Archaean crustal growth and tectonic processes: a comparison of the Superior Province, Canada and the Dharwar Craton, India. *In*: BURG, J. P. & FORD, M. *Orogeny Through Time*. Geological Society, London, Special Publications, **121**, 63–98.

COLLINS, W. J. 1989. Polydiapirism of the Archaean Mount Edgar Batholith, Pilbara Block, Western Australia. *Precambrian Research*, **43**, 41–62.

CONRAD, C. P. 2000. Convective instability of thickening mantle lithosphere, *Geophysics Journal International*, **143**, 52–70.

DAVIS, B. K. & MAIDEN, E. 2003. Archaean orogen-parallel extension: evidence from the northern Eastern Goldfields Province, Yilgarn Craton. *Precambrian Research*, **127**, 229–248.

DE WITT, M. & ASHWALL, L. D. 1997. Greenstone Belts. *Oxford Monographs on Geology and Geophysics*, **35**.

ENGLAND, P. C. & HOUSEMAN, G. A. 1988. The mechanics of the Tibetan plateau. *Philosophical Transaction of the Royal Society of London*, **326**, 301–320.

ENGLAND, P. C. & HOUSEMAN, G. A. 1989. Extension during continental convergence, with application to the Tibetan Plateau. *Journal of Geophysical Research*, **94**, 17561–17579.

ENGLAND, P. C. & MCKENZIE, D. P. 1982. A thin viscous sheet model for continental deformation. *Geophysical Journal of the Royal Astronomical Society*, **70**, 295–321.

ENGLAND, P. C. & MCKENZIE, D. P. 1983. Correction to: A thin viscous sheet model for continental deformation. *Geophysical Journal of the Royal Astronomical Society*, **73**, 523–532.

ENGLAND, PH. & MOLNAR, P. 1997. Active deformation of asia: from kinematics to dynamics. *Science*, **278**, 647–650.

EVANS, B. & GOETZE, C. 1979. The temperature variation of hardness of olivine and its implication for polycrystalline yield stress. *Journal of Geophysical Research*, **84**, 5505–5524.

FLEITOUT, L. & FROIDEVAUX, C. 1982. Tectonics and topography for a lithosphere containing density heterogeneities. *Tectonics*, **1**, 21–56.

FLESCH, L. M., HOLT, W. E., HAINES, A. J. & SHEN-TU, B. 2000. Dynamics of the Pacific-North American plate boundary in the western United States. *Science*, **287**, 834–836.

GALER, S. & METZGER, K. 1998. Metamorphism, denudation and sea level in the Archaean and cooling of the Earth. *Precambrian Research*, **92**, 389–412.

GEE, R. D. 1979. Structure and tectonic style of the Western Australia shield. *Precambrian Research*, **58**, 327–369.

GRIFFIN, W. L., O'REILLY, S. Y., RYAN, C. G., GAUL, O. & IONOV, D. 1998. Secular variation in the composition of the subcontinental lithospheric mantle. *In*: BRAUN, J. *ET AL.* (eds) *Structure and Evolution of the Australian Continent*, Geodynamics Series, **26**, American Geophysical Union, 1–25.

HAMILTON, W. B. 1998. Archean magmatism and deformation were not products of plate tectonics. *Precambrian Research*, **91**, 143–179.

HOUSEMAN, G. & ENGLAND, P. 1986. Finite strain calculations of continental deformation: 1. Method and general results for convergent zone. *Journal of Geophysical Research*, **91**, 3651–3663.

HOUSEMAN, G. & MOLNAR, P. 1997. Gravitational (Rayleigh-Taylor) instability of a layer with non-linear viscosity and convective thinning of continental lithosphere. *Geophysics Journal International*, **128**, 125–150.

HOUSEMAN, G. & MOLNAR, P. 2001. Mechanisms of lithospheric renewal associated with continental orogeny. *In*: MILLER, J. A., HOLDSWORTH, R. E., BUICK, I. S. & HAND, M. (eds) *Continental Reworking and Reactivation*. Geological Society, London, Special Publications, **184**, 13–37.

JELSMA, H. A., VAN DER BEEK, P. A. & VINYU, M. L. 1993. Tectonic evolution of the Bindura-Shamva greenstone belt (northern Zimbabwe): progressive deformation around diopiric batholiths. *Journal of Structural Geology*, **15**, 163–176.

JONES, C. H., UNRUH, J. R. & SONDER, L. J. 1996. The role of gravitational potential energy in active deformation in the southwestern United States. *Nature*, **381**, 37–41.

KAMBER, B. S., BIINO, G. G., WIJBRANS, J. R., DAVIES, G. R. & VILLA, G. 1996. Archaean granulites of the Limpopo Belt, zone of the Limpopo Belt, Zimbabwe: one slow exhumation or two rapid events? *Tectonics*, **15**, 1414–1430.

KAMBER, B. S., KRAMERS, J. D., NAPIER, R., CLIFF, R. A & ROLLINSON, H. R. 1995. The Triangle Shearzone, Zimbabwe, revisited: new data document an important event at 2.0 Ga in the Limpopo Belt. *Precambrian Research*, **70**, 191–213.

KORSMAN, K., KORJA, T., PAJUNEN, M., VIRRANSALO, P. & GGT/SVEKA WORKING GROUP, 1999. The GGT/SVEKA Transect – structure and evolution of the continental crust in the Palaeoproterozoic Svecofennian Orogen in Finland. *International Geology Review*, **41**, 287–298.

LENARDIC, A. & MORESI, L. 2000. A new class of equilibrium geotherms in the deep thermal lithosphere of continents. *Earth Planetary Science Letters*, **176**, 331–338.

MCGREGOR, A. M. 1951. Some milestones in the Precambrian of Southern Rhodesia. *Transactions of the Geological Society of South Africa*, **54**, 27–70.

MOLNAR, P. & LYON-CAEN, H. 1988. Some simple physical aspects of the support, structure and evolution of mountain belts. *In*: CLARK JR., S. P., BURCHFIELD, B. C. & SUPPE, J. (eds) *Processes in Continental Lithosphere Deformation*. Geological Society of America, Special Papers, **218**, 179–207.

MOLNAR, P., HOUSEMAN, G. A. & CONRAD, C. P. 1998. Rayleigh-Taylor instability and convective thinning of mechanically thickened lithosphere: effects of non-linear viscosity decreasing exponentially with depth and of horizontal shortening of the layer. *Geophysical Journal International*, **133**, 568–584.

MYERS, J. & WATKINS, K. P. 1985. Origin of granite-greenstone patterns, Yilgarn Block, Western Australia. *Geology*, **13**, 778–780.

PERCIVAL, J. A. & PETERMAN, Z. E. 1994. Rb–Sr biotite data from the Kapuskasing uplift and their bearing on the cooling and exhumation history. *Canadian Journal of Earth Sciences*, **31**, 1172–1181.

QIU, Y. M., MCNAUGHTON, N. J., GROVES, D. I. & DALSTRA, H. J. 1999. Ages of internal grantoids in the Southern Cross region, Yigarn Craton, Western Australia, and their crustal evolution and tectonic implications. *Australian Journal of Earth Sciences*, **46**, 971–981.

RAMSAY, J. G. 1989. Emplacement kinematics of a granite diapir: the Chindamora batholith, Zimbabwe. *Journal of Structural Geology*, **11**, 191–209.

RANALLI, G. 1995. *Rheology of the Earth*. Chapman & Hall, London.

REY, P., PHILIPPOT, P. & THÉBAUD, N. 2003. Contribution of mantle plume, crustal thickening, and greenstone blanketing to the 2.75–2.65 Ga global crisis. *Precambrian Research*, **127**, 43–60.

SCHMALHOLZ, S. M., PODLADCHIKOV, Y. Y. & BURG, J. P. 2002. Control of folding by gravity and matrix thickness: implications for large-scale folding. *Journal of Geophysical Research*, **107**, no B1, ETG-1–1, DOI 10.1029/2001JB000355.

SCHMALHOLZ, S. M., PODLADCHIKOV, Y. Y. & JAMVIET, B. 2005. Structural softening of the lithosphere. *Terra Nova*, **17**, 66–72.

SIBSON, R. H. 1974. Frictional constraints on thrust, wrench and normal faults, *Nature*, **249**, 542–544.

SONDER L. J., ENGLAND, P. C., WERNICKE, B. P. & CHRISTIANSEN, R. L. 1987. A physical model for Cenozoic extension of the western North America. *In*: COWARD, M. P., DEWEY, J. F. & HANCOCK, P. L. (eds) *Continental Extensional tectonics*. Geological Society, London, Special Publications, **28**, 187–201.

SNOWDEN, P. A. & BICKLE, M. J. 1976. The Chinamora Batholith; diapiric intrusion of interference fold? *Journal of the Geological Society, London*, **132**, 131–137.

SUN, J. & MURRELL, A. F. 1994. On the growth and collapse of wide orogenic belts. *Geophysical Journal International*, **118**, 255–268.

TAYLOR, S. R. & MCLENNAN, S. M. 1986. The chemical composition of the Archaean crust. *In*: DAWSON, J. B., CARSWELL, D. A., HALL, J. & WEDEPOHL, K. H. (eds) *The Nature of the Lower Continental Crust*. Geological Society, London, Special Publications, **24**, 173–178.

TREOLAR, P. J. & BLENKINSOP, T. G. 1995. Archaean deformation patterns in Zimbabwe: true indicators of Tibetan-style crustal extrusion or not? *In*: COWARD, M. P. & RIES, A. C. (eds) *Early Precambrian Processes*. Geological Society, London, Special Publications, **95**, 87–107.

TURCOTTE, D. L. 1983. Mechanisms of crustal deformation. *Journal of the Geological Society, London*, **140**, 701–724.

WARREN, R. G. & ELLIS, D. J. 1996. Mantle-underplating, granite tectonics, and metamorphic P-T-t paths. *Geology*, **24**, 663–666.

WHITAKER, A. J. 2001. Component and structure of the Yilgarn craton, as interpreted from aeromagnetic data. 4th International Archaean Symposium 2001, Extended Abstracts. *In*: CASSIDY, K. F. *ET AL.* (eds) 2001. AGSO–*Geoscience Australia, Record*, **37**, 536–538.

# Analogue and numerical modelling of accretionary prisms with a décollement in sediments

YASUHIRO YAMADA[1], KEI BABA[2] & TOSHIFUMI MATSUOKA[1]

[1]*Department of Civil and Earth Resources Engineering, Kyoto University, Kyoto 606-8501, Japan (e-mail: yama@electra.kumst.kyoto-u.ac.jp)*

[2]*JAPEX Research Center, Chiba 261-0025, Japan*

**Abstract:** Active accretionary prisms at subduction margins generally include a horizontal detachment, décollement, within the sedimentary pile. The décollement, and its extension to undeformed regions (i.e., proto-décollement), corresponds to a layer of high fluid pressure. The deformation of the prisms, including such an anomalous layer, can be modelled and examined using analogue experiments and numerical simulations. Both these methods approximate the material under deformation as an assembly of particles (grains). The décollement layer is found to be best modelled by intercalating a layer with smaller internal frictional coefficient than the surrounding materials corresponding to the sediments. Our analogue experiments with dry sand and microglass beads reproduce structural geometry similar to that of interpreted seismic profiles at the toe of the prisms. Thrust faults originate from the horizontal beads layer and propagate upward with a constant angle of about 30°. Each of the fault bends produces a series of minor back thrusts. A particle image velocimetry (PIV) analysis revealed that the fault activity is characterized by intermittent reactivation and segmentation. The numerical simulations based on the distinct element method (DEM) were performed with similar kinematic settings and material properties as the analogue experiments. The numerical simulation results not only reproduce similar geometries as in the analogue experiments, but also show that the particle assembly experiences temporal variations in the deformation velocity and stress field as deformation propagates. This might be related to stick-slip motion of the frictional fault surfaces, which is a common feature of faulting during accretionary processes at subduction margins.

Geological modelling using physical materials in scaled analogue experiments is an extremely useful technique for a detailed examination of the geometry and deformation process of accretionary prisms. Since the mechanics of the upper crust can be approximated by Navier-Coulomb brittle behaviour, granular materials such as dry sand are an appropriate material to model such brittle deformation (McClay 1990) with fulfillment of the scaling theory by Hubbert (1937). Analogue experiments with dry sand (sandbox experiments) have thus been widely applied to simulate a wide variety of geological structures (e.g., Mandl 1988; Cobbold & Castro 1999; Koyi & Mancktelow 2001; Yamada & McClay 2003*a*, 2003*b*, 2004; Yamada *et al.* 2005 and the references therein). Accretionary prism formation, as well as thrust-and-fold belts, has been investigated in detail by a number of analogue models (e.g., Colletta *et al.* 1991; Huiqi *et al.* 1992; Willet 1992; Lallemand *et al.* 1992; Mulugata & Koyi 1992; Gutscher *et al.* 1996; Nieuwland *et al.* 2000; Koyi & Vendeville 2003).

There are two types of model kinematics, either pushing a rigid backstop or pulling a sheet underneath sand, but the results are the same except for the boundary effects of sidewalls (see Schreurs *et al.* 2006). A typical result of these models shows that a foreland propagating (piggyback) sequence of thrusts form a Coulomb wedge with a taper mainly dependent upon the friction of the detachment fault. That is, higher basal friction leads to formation of a steeper slope prism, whereas low basal friction leads to formation of a gentler slope prism. This corresponds with the basic theory of non-cohesive critical Coulomb wedges (Davis *et al.* 1983; Dahlen 1984; Dahlen & Suppe 1984), assuming that an actively accreting wedge attains a critical taper, an internal state of stress on the verge of Coulomb failure throughout. Dahlen (1984) concluded that the surface slope of a critical taper is dependent on the internal and basal friction coefficients, internal and basal fluid pressure ratios, the dip of the basal detachment and the strength of the rock composing the wedge. The theory explains how basal

*From*: BUITER, S. J. H. & SCHREURS, G. (eds) 2006. *Analogue and Numerical Modelling of Crustal-Scale Processes.* Geological Society, London, Special Publications, **253**, 169–183.
0305-8719/06/$15.00 

friction or basal fluid pressure controls the structural styles, including subduction erosion, active accretion, subduction without accretion and normal faulting (Dahlen 1984).

Deformation of granular assemblies can also be simulated numerically using the distinct element method (DEM). The DEM calculates force and velocity in two (normal and shear) directions for all elements, which is repeated for the updated element relations at the next time increment (Cundall & Strack 1979). With significant advances in computing technology, the technique can now handle a large number of elements and be applied to a variety of research fields (e.g., Konietzky 2002; Shimizu *et al.* 2004). Application of the DEM to geological problems requires the geological body to be approximated as an assembly of elements (e.g., Finch *et al.* 2003); thus sandbox experiments are an ideal scenario (e.g., Saltzer 1993; Yamada *et al.* 2004). Numerical models using the DEM are, however, not scale models in the sense of physical models where typical Earth values are used as their input parameters (Strayer & Suppe 2002). Two significant advantages of the DEM are: (1) no need to predefine artificial parameters of discontinuity surfaces, and (2) ability to extract all information from each element during deformation in a quantitative way. The DEM therefore has high potential to be a numerical simulator that can incorporate discontinuity surfaces properly.

This paper shows selected sandbox experiments and DEM simulations for a simplified geological model of accretionary prisms. The results are analysed to investigate the detailed process of fault development.

## Accretionary prisms with a décollement in sediments

Recent investigations revealed that the accretion process at subduction margins generally develops a sub-horizontal detachment, décollement, within the sedimentary sequences accumulated in the trench area. This horizon is typically defined by a layer of anomalous high fluid pressure and can generally be easily traced with reverse polarity on seismic profiles (Tobin *et al.* 1994; DiLeonardo *et al.* 2002; Tsuji *et al.* 2004; Bangs *et al.* 2004). The sediments above the décollement are deformed by a series of imbricate thrusts that converge with the décollement surface, whereas those underneath it are subducted without internal deformation.

A typical example can be seen in the Nankai trough located offshore southwest Japan, where the Philippine Sea Plate is subducting underneath the Eurasian Plate at a rate of 4 cm/yr along an azimuth of 310–315° (Fig. 1; Seno *et al.* 1993). Extensive seismic surveys in this area reveal that a décollement is clearly located within the sediments, not at the top horizon of the volcanic basement (Fig. 2a; Bangs *et al.* 2004). The reverse polarity of the décollement suggests that the layer may have extremely high fluid pressure, even at the 'proto-décollement' region (Tsuji *et al.* 2005). The proto-décollement is an extension of the de'collement surface in the undeformed sediments, seaward of the deformation front. This clear identification of the proto-décollement on the profiles suggests that a preferred layer of décollement exists prior to initiation of the actual displacement. Geophysical logging and core analysis at Site 1174 of the Ocean Drilling Project Leg 196 showed that the décollement is located in a hemi-pelagic mudstone sequence at Nankai (Mikada *et al.* 2002).

Such features of décollement development are also observed in Barbados (DiLeonardo *et al.* 2002) and in Cascadia (Tobin *et al.* 1994). The décollement in the Barbados accretionary prism, where the Atlantic Plate is subducting underneath the Caribbean Plate, is located in a radiolarian mudstone of high porosity and low strength (Moore & Klaus 2000). This horizon also forms the proto-décollement. In Cascadia, a large scale accretionary prism develops due to the subduction of the Juan de Fuca Plate underneath the North American Plate, and the décollement (and its proto-décollement) is formed at a boundary horizon between upper turbidites and lower hemi-pelagic mudstones (Westbrook *et al.* 1994). The structural styles

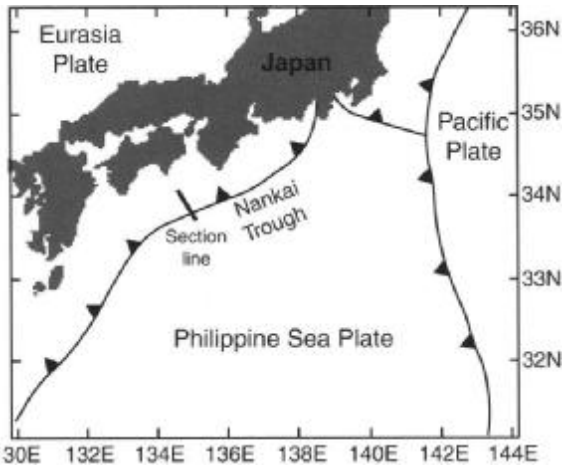


**Fig. 1.** Location map of the Nankai Trough and the section line.

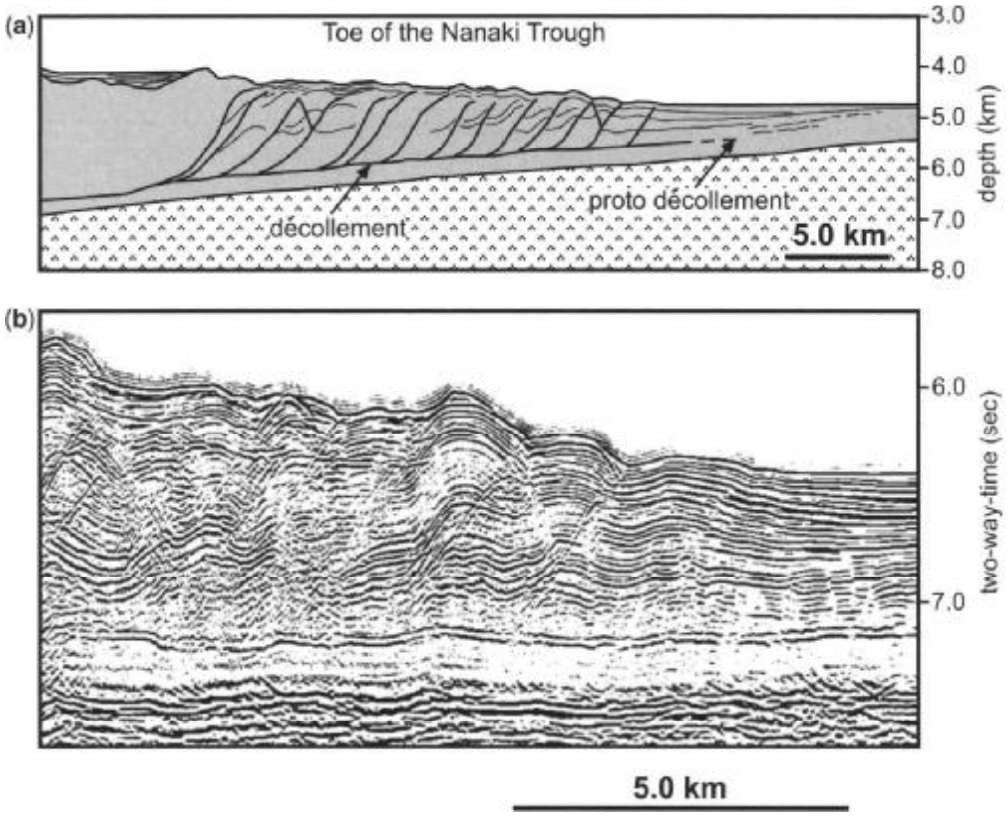


**Fig. 2.** Section geometry of the Nankai accretionary prism (see Fig. 1 for the location of the section line). (**a**) Schematic geological cross-section (Mikada *et al.* 2002). (**b**) A seismic profile at the toe of the wedge off Muroto Point (Bangs *et al.* 2004). Note that the décollement is not at the uppermost horizon of the volcanic basement (the strong reflector at 7.5 sec), but at the middle (*c.* 7.1 sec) of a thick mudstone sequence (low reflective sediments).

of these prisms are generally similar on seismic profiles.

The experiments and simulations aim to investigate the effects of the décollement within the sediments. Figure 2b is a seismic profile illustrating the characteristic structural style at the toe of the Nankai prism off Muroto Point. The thickness of the sediments above the décollement is *c.* 800 m, fault spacing at the toe is *c.* 1300 m, and the slope angle is *c.* 4°.

## Analogue experiments

### *Modelling set-up*

The experimental apparatus is an acrylic box (25 cm × 150 cm × 50 cm) underlain by a flat plastic sheet (Fig. 3). Layers of analogue material are piled on the sheet, which is then pulled by a motor at a constant speed of $1.67 \times 10^{-2}$ cm $sec^{-1}$ through a slit under the fixed end wall. This slit produces a décollement horizon within the analogue material. The scaling ratio is $4.0 \times 10^{-5}$, thus 1 cm in the experiments corresponds to 250 m in nature.

Selection of the modelling materials is an important factor of the analogue experiments. In this study, the effects of the anomalous high fluid pressure along the natural décollement must be considered. The high fluid pressure reduces strength, both in nature and in experiments. Low friction materials thus may be used to approximate the effects of the fluid pressure. In fact, a pioneering work by Cobbold *et al.* (2001) showed that an increase in the inter-granular pore pressure of a layer in their thrust-wedge-type sandbox experiments produced a decreased taper angle and widened fault spacing. These effects are similar to the experiments with a décollement of a smaller internal friction coefficient. Microbeads have been recently regarded as suitable materials for such weaker layers (e.g., Massoli *et al.* 2002; Lohrmann *et al.* 2003; Yamada *et al.* 2005). We used Toyoura dry quartz beach sand and glass microbeads as analogue materials. The average grain sizes are 200 μm and 50 μm respectively. Our shearing tests showed that the microbeads have a much smaller internal friction angle (25°) than Toyoura sand (34°, see Table 1).

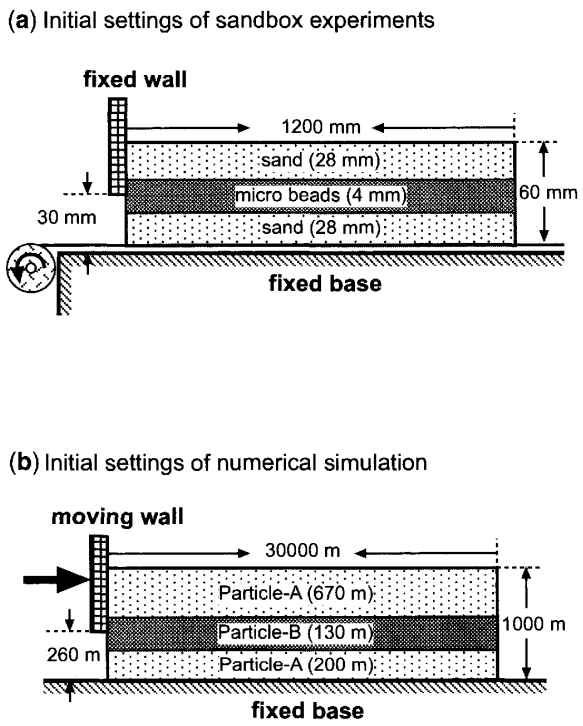


**Fig. 3.** Set-up for analogue and numerical models. (**a**) The analogue materials are piled on a plastic sheet which is then pulled by an electric motor. Note the slit between the fixed base and the bottom of the fixed end wall. (**b**) The model design for the numerical simulation. This is equivalent to the analogue experiments, including the slit underneath the fixed end-wall, but the polarity of shortening is opposite (i.e., a moving wall instead of a moving sheet).

This paper presents two representative results of sandbox experiments conducted for this study. Experiment I employs pure sand of 6.0 cm thickness, whereas Experiment II includes a layer of microbeads (0.4 cm thickness) midway up the sand pile (6.0 cm in total including the beads layer). The microbeads are white and the sand is naturally light brown, thus they can be easily distinguished. We also used dyed marker sand layers only adjacent to the transparent sidewalls. The marker sands have almost the same physical properties as the undyed sand. These are to maintain the homogeneity of the sand layers. During the experiments, photographs were taken through the sidewall after every 1 cm of displacement of the sheet. The structural style on the free surface suggests that the deformation of the experiments can be approximated as plane strain.

## *Experimental results*

*Experiment I.* The homogeneous dry sand model reproduced typical thrust-and-fold belt structures including a wedge geometry, and foreland vergent thrusts that propagated upward with a piggyback sequence from a sub-horizontal décollement produced within the sand pack (Fig. 4). The décollement connected to the frontal thrust without forming a bend. The angle of the prism surface (line linking the tips of the thrusts) is *c.* 18–24° and fault spacing near the frontal thrust is *c.* 6.0 cm (corresponds to 1.5 km).

*Experiment II.* The results of this model, which has a microbeads layer inserted into the sand, showed that the microbeads layer acted perfectly as a horizontal décollement (Fig. 5). Detailed observations revealed that the décollement surface was at the lower boundary of the microbeads layer. The analogue material below the décollement did not deform and was expelled from the experimental rig through the slit. From the décollement, the foreland vergent frontal thrust propagated upward, dipping *c.* 28°–34°. Thus, the active surface of the frontal thrust through the décollement has a bend where the frontal thrust is generated from the décollement. Above the bend, a series of minor back-thrusts was generated in a piggyback sequence, which was only active while the fault underneath was active. The foreland vergent thrusts also formed a piggyback sequence. In Experiment II, the angle of the prism surface (the slope of the line linking the tips of the thrusts) is gentler (*c.* 9–14°), and the fault spacing near the frontal thrust is wider (*c.* 8.3 cm, corresponding to 2.1 km), than in Experiment I (*cf.* Fig. 4).

## *PIV analysis*

In order to analyse the deformation process in detail, time-lapse digital pictures of the

**Table 1.** *Material properties and grain characteristics of analogue materials*

| Material | Density (kg m$^{-3}$) | C (Pa) | $\phi_{stable}$ (°) | Strain soft. (%) | Ave. grain size (μm) | Grain shape | Composition |
|---|---|---|---|---|---|---|---|
| Quartz sand | 1390 | n.d. | 34 | 9 | m = 200 | Angular | 93% $SiO_2$ 4% $Al_2O_3$ |
| Microbeads | 1420 | n.d. | 25 | 0 | m = 50 | Spherical | $Na_2O$–CaO–$SiO_2$ |

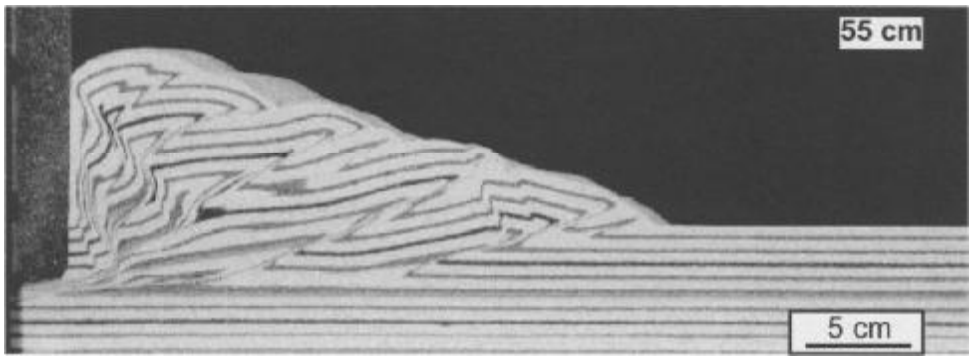


**Fig. 4.** Result of Experiment I. This pure sand model produces characteristic features of thrust wedges, including a piggyback sequence of thrusting. This picture is taken after 55 cm of shortening and the model has a surface slope of 18°.

experiments were evaluated with an image correlation technique called particle image velocimetry (PIV). This technique is commonly used for dynamic flow analysis and soil mechanics (e.g., Hryciw *et al.* 1997), but has recently also been applied to structural geology (Adam *et al.* 2002; Wolf *et al.* 2003; Adam *et al.* 2005). The method calculates the displacement field of the grains with a theoretical resolution of *c.* 0.5 mm. The displacement accuracy depends on the picture size and the resolution of the digital camera (Wolf *et al.* 2003). PIV data cover the complete range of structural evolution, as well as a major part of the stick-slip field, in experiments with a scaling factor of $10^5$–$10^6$ (Adam *et al.* 2005).

Figure 6a is an example of the photographs that have been taken after every 1 cm of displacement of the plastic sheet and that have been analyzed using PIV. The results are shown in Figure 6b, in which the fixed wall and the basal plate provide axes of a frame of reference for the kinematics of the model. Dark arrows correspond to large displacement, whereas light grey arrows correspond to minor displacement. White areas with no arrows correspond to regions where the software detects no correlation. These displacement distributions identify coherent blocks of active displacement, the discontinuities between such blocks indicating active faulting. The top diagram is the displacement distribution between the images taken after 38 and 39 cm of total displacement, showing that the hanging wall of the frontal thrust is moving to the upper-left relative to the fixed wall, whereas the rest of the regions only show minor displacement in other directions. This suggests that shortening is mainly accommodated by the frontal thrust. The displacement distribution between 39 and 40 cm of total displacement shows a similar pattern to the previous stage described above. However, minor differences can be found in regions of previous thrust sheets, suggesting that these thrusts are reactivated.

The displacement pattern then changes significantly after 40 cm of total displacement. According to the PIV calculations, the frontal area shows a similar displacement distribution between 40 and 42 cm of total displacement as between 39 and 40 cm displacement, but the adjacent area has a large displacement anomaly that drops sharply along the third thrust fault from the frontal thrust. This means that the third thrust fault reactivates between 40 and 42 cm of total displacement. The hanging wall of the thrust fault also shows such a discontinuity in displacement distribution, suggesting that a back thrust also reactivates at this stage. These thrust faults are inactive during the stages from 38 to 40 cm of total displacement.

The PIV results generally confirm the in-sequence thrust process, but each thrust sheet has an intermittent displacement distribution. Adam *et al.* (2005) also reported such temporal activity of faults, characterized by fault reactivation, in their thrust-and-fold type experiments.

## Numerical simulations

The distinct element method (DEM) was employed as the numerical simulation technique in this study. The model domain consists of discrete circular elements, and linear elasticity (force-displacement law; Cundall & Strack 1979) is incorporated through normal and shear forces at elemental contacts. The inter-element friction in the shear direction is determined by the normal force and a friction coefficient. The size of each element is preserved during deformation, thus volume change (i.e., dilation) is

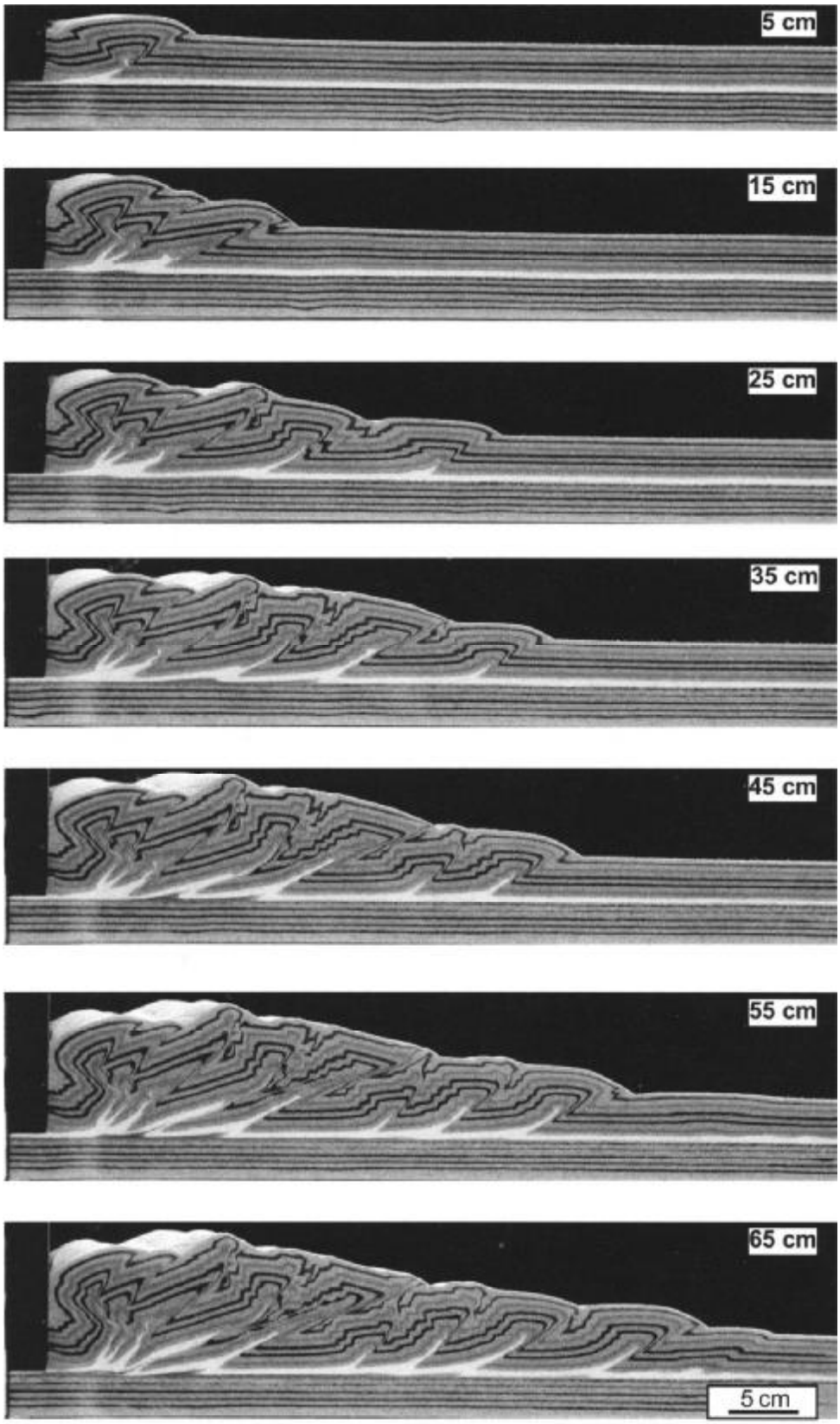


**Fig. 5.** Results of Experiment II (the length values are amounts of shortening). A layer of microbeads inserted into the sand pile acts as a horizontal décollement. Only the analogue material above this layer is shortened (see Fig. 3a). Thrusts propagate upward from the décollement, forming a piggyback sequence. Note that each thrust has a bend where a backthrust is initiated in its hanging wall. The surface slope of the wedge is about 12° at 65 cm of shortening.

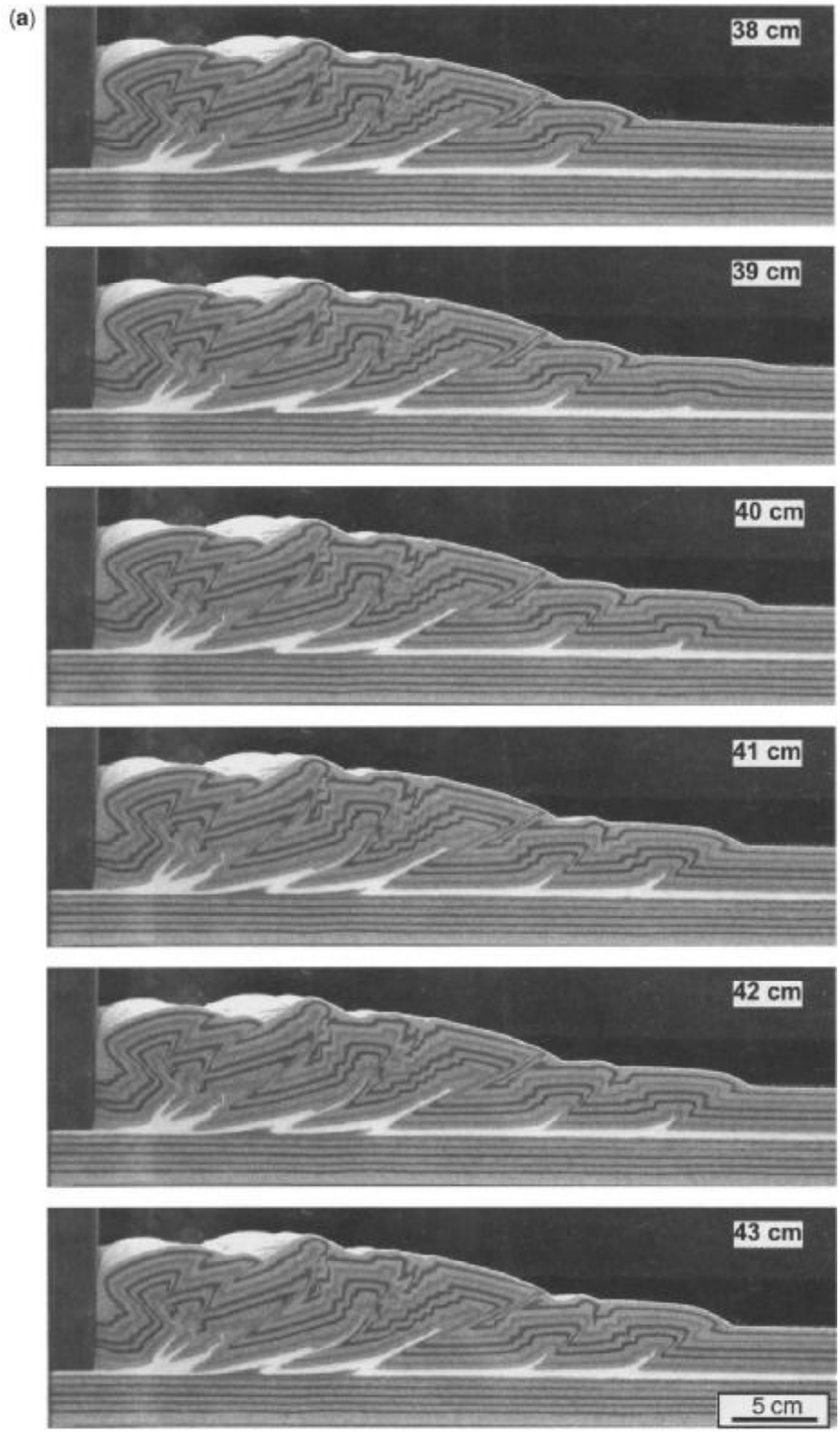


**Fig. 6.** Particle image velocimetry (PIV) analysis for analogue model II. (**a**) The images analysed are taken at every 1 cm of shortening (the length values are amounts of shortening). (**b**) The results of PIV analysis showing the velocity vectors during shortening. The fixed wall and the basal plate provide axes of a frame of reference for the kinematics of the model. Dark arrows correspond to large displacement, whereas light grey arrows correspond to minor displacement. White areas with no arrow correspond to a region where the software detects no correlation. Note that the velocity patterns suggest sequential fault reactivations.

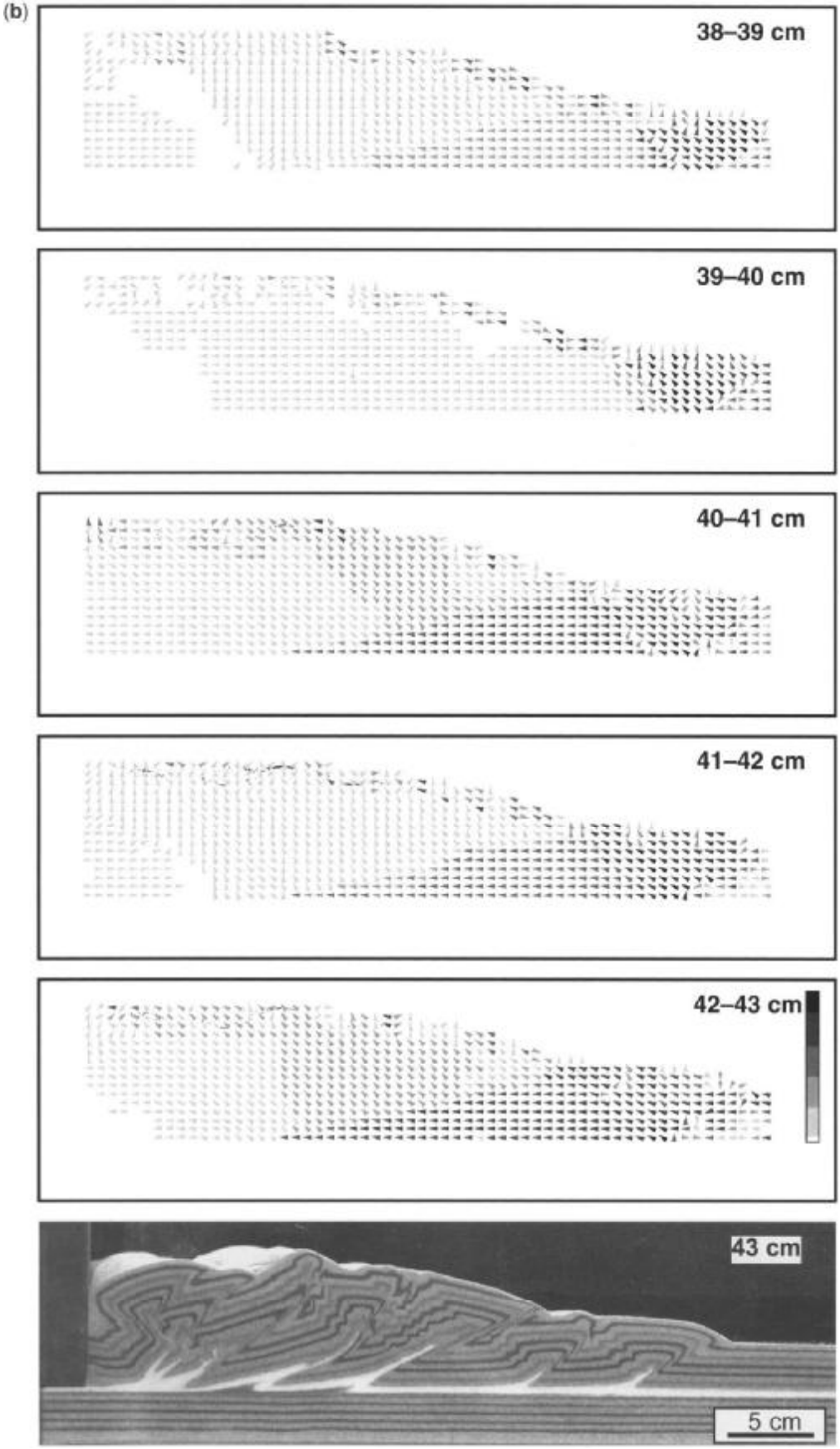


**Fig. 6.** *Continued.*

accommodated by the inter-element porosity. The method has two steps in each calculation cycle (time-step): the first step is to evaluate interaction forces for every element, and the second step is to move all elements according to numerical integration following Newton's equation of motion for the given external forces. The software employed in this study is PFC 2D developed by the ITASCA Corporation, Minneapolis, USA.

### *Input parameters*

The simulations aim to reproduce the two-dimensional structural style of the accretionary prism with a décollement in the sedimentary sequence. In order to make the initial conditions of the simulations similar to those of the analogue experiments, the input parameters are carefully determined after a series of compression test simulations. Since DEM describes only the parameters related to element contacts, such compression tests are necessary to measure the physical properties of the element assembly. Table 2 shows the physical characteristics of two particle types, which were obtained by bi-axial compression tests with a PFC-2D function called FISH-TANK. Particle A has an internal frictional angle of 35°, while particle B has an internal frictional angle of 25°. These particle types are selected to model the sand and the microbeads respectively in the analogue experiments (*cf.* Table 1). The friction coefficient between the wall and the particles is the same as that of particle A. Initial cohesion and bonding between elements are not introduced, due to the cohesionless nature of the analogue materials. The diameter of the elements has a variety of 20% from the average size to avoid formation of preferential weak planes in the initial arrangement of the element assembly.

The model kinematics is also designed after the sandbox experiments, but the polarity of shortening is opposite (Fig. 3b). In this two-dimensional simulation model, an assembly with a rectangular initial geometry is placed on a fixed base, and a horizontally moving wall pushes one side of the material from the left-hand side. The initial position of the moving wall is determined by the position of the décollement horizon. The displacement rate should be small enough to approximate the deformation as quasi-static. In this study, the rate is 0.9 cm for each calculation cycle. This is why DEM requires a few million time-steps to generate sandbox-type deformations.

The sizes of the elements in this study are larger than the equivalent material sizes of the analogue experiments. The use of the equivalent grain sizes requires the computer to be equipped with an extraordinary size of data storage and memory, and each calculation may also require an extremely long time (about a few months with a current workstation). This is why larger elements were generally used in previous research (e.g., Saltzer 1992; Finch *et al.* 2003; Strayer & Suppe 2002; Yamada *et al.* 2004). In this paper, two representative results of simulations are presented. Simulation I employs a layer of particle A of 670 m thickness without predefined décollement, whereas Simulation II has a layer of particle B (130 m thick) at the middle of a pile of particle A (1000 m in total including the particle B layer). These thicknesses have to be altered from the equivalent values of the analogue experiments, in order to obtain each calculation result within a month.

### *Simulation results*

*Simulation I.* The overall structural style is a wedge shape that increases in size as the displacement of the wall proceeds (Fig. 7). The simulation reproduces typical foreland vergent thrusts that propagate upward with a piggyback sequence from the basal décollement. The angle of the prism surface (line linking the tips of the thrusts) generally shows a gradual increase toward the deformation front. This value increases up to *c.* 48° adjacent to the frontal thrust after shortening of 6750 m (Fig. 7). The fault spacing around the frontal thrust is *c.* 0.7 km.

**Table 2.** *Material properties and element characteristics of numerical simulations*

| Material | Density (kg $m^{-3}$) | C (Pa) | $\phi_{stable}$ (°) | Strain soft. (%) | Ave. grain size (m) | Grain shape |
|---|---|---|---|---|---|---|
| Particle A | 1600 | n.d. | 35 | n.d. | m = 21 | Circular |
| Particle B | 1600 | n.d. | 25 | n.d. | m = 8 | Circular |

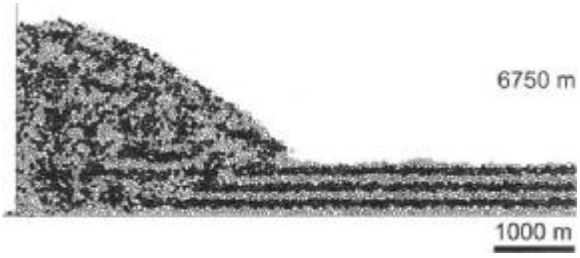


**Fig. 7.** Results of simulation I consisting of particle A only (the length values are amounts of shortening). The structural style of this particle assembly shows a steep slope angle.

*Simulation II.* The overall structural style is similar to Simulation I, but the surface slope of the wedge is 21°–22° and the fault spacing around the frontal thrust is *c.* 1.0–1.2 km (Fig. 8). Similar to the sandbox experiment II, these thrusts propagate upward from the décollement layer; thus the frontal thrust surface has a bend where the thrust originates from the décollement. Although backthrusts were also generated at the bend in the analogue experiments, they are unclear in the numerical simulations. Since the DEM calculates velocity and interaction forces of every element for every time-step, these can be extracted to examine the temporal variability of prism evolution. Snapshots of velocity distribution and interaction force, referenced to the fixed base, are shown in Figures 8b and 8c respectively. On the velocity distribution diagrams, a particle group with a same velocity vector behaves as a block and the boundaries of such coherent blocks are the faults. The velocity diagram thus shows the temporal variation of the faulting. For example, the frontal thrust at the 2250 m shortening stage shows a minor displacement rate in the deeper part of the prism with the rate greater in the shallower part, suggesting an interaction of the second thrust from the deformation front. The deeper part of this second thrust is active at the 4500 m shortening stage, but the entire fault surface of this thrust becomes inactive by 6750 m shortening. The deeper part of the frontal thrust at 4500 m shortening becomes active at 6750 m shortening, but the shallower part is inactive. At the 6750 m shortening stage, the frontal thrust is active only at the tip.

In the interaction force diagrams (Fig. 8c), the black lines are directions of maximum gross contact forces, indicating where, how much and in which direction the forces exist in the assembly. The forces initiated from the moving wall

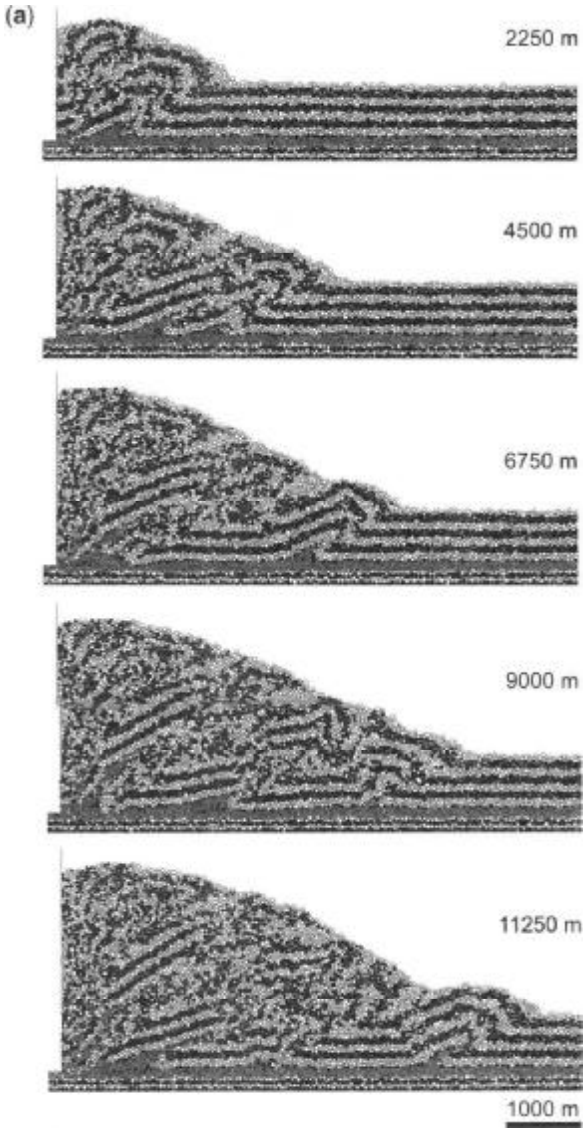


**Fig. 8.** Results of simulation II (the length values are amounts of shortening). (**a**) Structural style of the particle assembly during deformation. (**b**) Instantaneous velocity distributions of particles showing temporal variations during deformation. (**c**) Instantaneous distribution of maximum gross interaction forces. The curvature suggests that the force is affected by the décollement layer.

that pushes the elements, and can be traced downward to the base (down-to-the-right direction). Immediately above and underneath the décollement layer, the directions of the forces are generally sub-horizontal. This suggests that the layer with low internal friction coefficient acted as a décollement and affected the pattern of the interaction forces. Within the wedge, the interaction forces also show up-to-the-right directions, which may also correspond to the thrust fault activities.

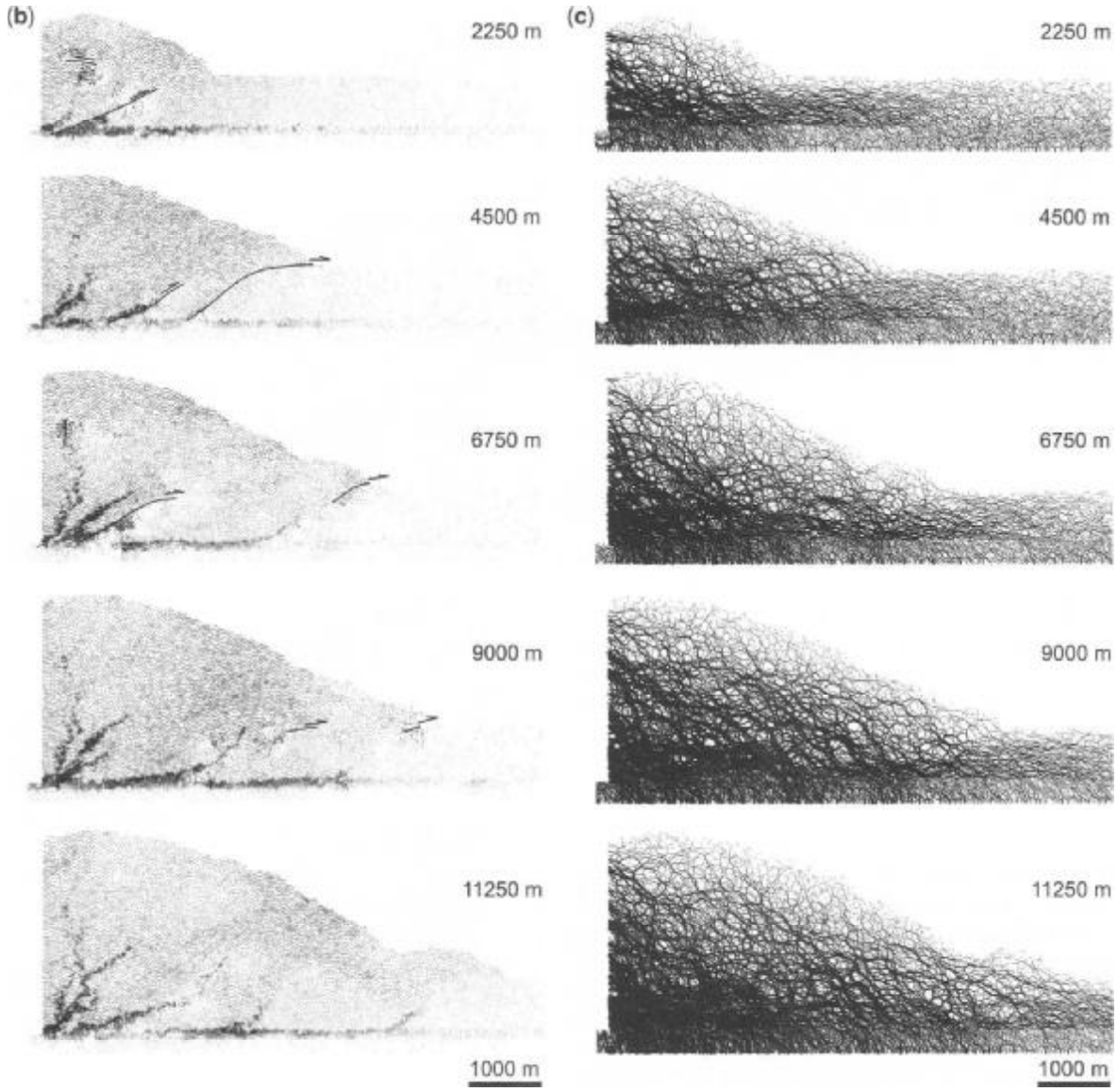


**Fig. 8.** *Continued.*

## Discussion

### *Effects of décollement and implications for accretionary prisms*

In both of the analogue experiments and numerical simulations, inserting the décollement, the layer of a lower frictional coefficient, reduces the slope angle (*c.* 18°–10° in analogue and 45°–23° in numerical; Fig. 9) and increases the fault spacing (*c.* 1.5–2.1 km in analogue and 0.7–1.1 km in numerical). This is in good agreement with the critical taper theory (Davis *et al.* 1983) arguing that the internal frictional coefficient along the décollement has a strong impact on the prism geometry. The internal friction angles of two materials (sand/particle A and microbeads/particle B) are almost the same in the analogue and numerical models. The resultant prism geometries are, however, significantly different. This is possibly caused by the smaller number of particles in the numerical simulations. Theoretically, the thickness of the décollement layer consists of 80 (or more) particles in the analogue models, whereas 16 (or more) are counted in the numerical models. This smaller number of numerical particles could not be enough to maintain the physical property of the layer, and the surrounding particle A could increase the internal friction of the décollement layer.

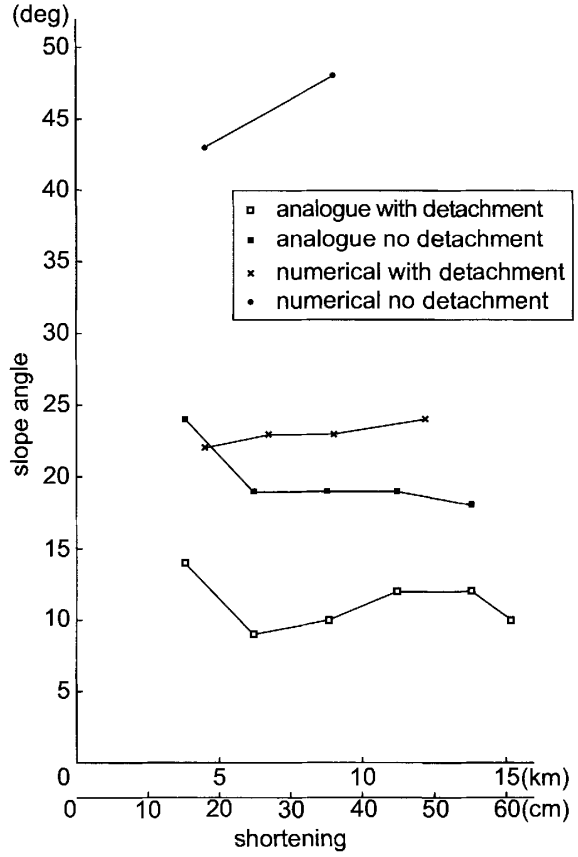


**Fig. 9.** Slope angles of analogue and numerical models. Inserting a décollement layer reduces the slope angle. Numerical models generally show steeper inclinations.

The effects of the low frictional layer in accretionary wedges can be identified in the prism geometry, the detachment geometry and the geometry of the frontal and backthrusts. The slope angle of the Nankai prism is *c.* 4° around the deformation front where the low friction décollement develops within the sediments, and is increased to *c.* 8° where the décollement is inactive. This may be a clear example showing the relationship between the slope angle and the frictional coefficient of the detachment. The detachment surfaces in the Nankai, Barbados and Cascadia wedges are characteristically flat (Bangs *et al.* 2004; Moore & Klaus 2000; Westbrook *et al.* 1994), similar to the experimental results. This suggests that the décollement geometry around the frontal thrust is strongly controlled by the pre-existing layers that have an anomalously low frictional coefficient. In experiment II, the active surface of the frontal thrust has a bend where the frontal thrust originates from the detachment. The bend produces a kink zone between the flat and the ramp, and compensation faults should be generated in the hanging wall that moves across the kink zone. These faults are observed as backthrusts. In Nankai, the detachment layer also generates a bend in the frontal thrust geometry and backthrusts in the overlaying sediments (*cf.* Fig. 2b).

### *Faulting and stresses*

The analogue and numerical models show variations in the slope angle during prism formation. Nieuwland *et al.* (2000) describe the dynamic equilibrium that is common to the development of critical tapers, the mechanical necessity of out-of-sequence thrusting and the systematically changing angle of a growing critical taper. That is, a new thrust fault lifts up the front of the taper, thereby reducing the angle, then existing thrust faults become reactivated to restore the critical angle. Our observed variations may be produced by a similar effect, and the process of the prism formation would be strongly controlled by sequential fault reactivations.

The directions of the maximum interaction force (Fig. 8a) presumably indicate the direction of the maximum principal stress, $\sigma_1$. This direction theoretically makes an angle of 27.5° with the direction of the active shear zone. Figure 10 shows an interpretation of such shear zone directions, based on the calculated stress orientations. It is predicted that the active shear zones would be steepened upward from the décollement and from the moving backstop. The velocity distributions (Fig. 8b) generally show similar directions, thus this prediction may be appropriate. The prediction also suggests that there may be normal faulting under the décollement. The stress measurements at Nankai accord with this extensional stress regime under the décollement (Mikada *et al.* 2002).

### *Temporal variations due to stick-slip behaviour of frictional faulting*

In the numerical results, the velocity and stress distributions show temporal variations during deformation. These distributions are calculated for 0.9 cm of displacement of the moving wall, thus they are regarded as instantaneous values. These variations should be closely related to the deformation behaviour of the particle assembly. Since no breakage of particles is observed during deformation, the shortening should be accommodated by a change of the particle arrangement. Thus, the grain boundaries in the particle assembly behave as displacement surfaces. Since the displacement along these surfaces is controlled by the normal force and frictional

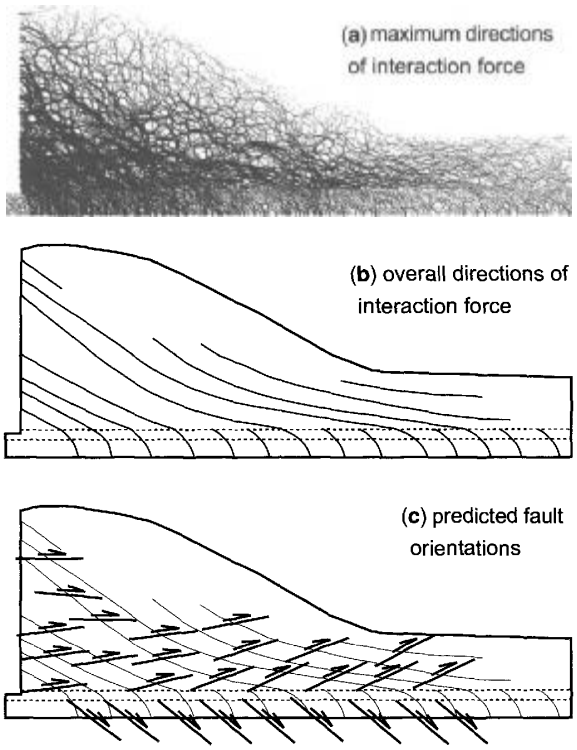


**Fig. 10.** Schematic diagram of possible active shear zone directions, based on the calculated stress orientations of the numerical model. (**a**) Directions of maximum interaction forces. (**b**) Schematic diagram of the overall direction of the maximum force. (**c**) Predicted active fault orientations. The internal friction angle is approximated as 35° from particle A's property.

coefficient acting on the surface, the displacement may be approximated as frictional gliding. This is grain-size independent and generally intermittent, causing so-called 'stick-slip' motion. Since the stick-slip motion occurs due to cycles of accumulation and release of elastic energy along the gliding surface, the force around the fault surface should be cyclically distorted. According to in-situ stress measurements by Nieuwland *et al.* (1999), low amplitude stress cycling after the initiation of a fault is observed in their thrust-and-fold belt sandbox experiments, interpreted as a stick-slip process in the fault zone. In cases where many faults exist, the distribution of the forces within the geological body will be affected by such distortion due to sequential fault events. The temporal variations in the particle velocity and forces are therefore presumably due to stick-slip behaviour along frictional surfaces.

Such temporal variations can be found in natural structures. Field and seismic observations clearly reveal that geological structures include many faults with a variety of directions even in a region that has been typically formed under a specific tectonic environment. Focal mechanism analysis of aftershocks also always shows such a variation even after one earthquake event (e.g., Shibazaki *et al.* 2002). This suggests that temporal variations of faulting are quite common in natural structures. The temporal variation may also be related to underground fluid flow. Sibson (1990) argues that the underground stress changes the permeability along fault surfaces, thus the variation in the force distributions may affect the fluid flow system in accretionary prisms. The pattern and the paths of the fluid flow in accretionary prisms may be important controls on the accumulation mechanism of methane hydrates. The temporal variations seen in the model results can thus be a key to understanding the heterogeneous distribution of methane hydrates in accretionary prisms (i.e., Baba & Yamada 2004).

Velocity and force variations in natural geological bodies due to stick-slip behaviour of faults are not yet well investigated. The models shown in this paper can be used to understand such natural instability in the geo-environment. This technique might be applied to prevent possible future geo-hazards (e.g., Ueta *et al.* 2000), provided that the models are properly scaled and the magnitude, place and timing of possible earthquakes and related deformations are properly understood from the modelling results.

## Conclusions

The analogue (sandbox) and numerical (distinct element method) models used to examine the effect of a décollement layer within sediments show that inserting a lower frictional coefficient layer reduces the slope angle and increases the fault spacing. This agrees with the critical taper theory (Davis *et al.* 1983). The geometric variations observed in the model prism may be explained by fault reactivations. The velocity and force directions extracted from numerical particles are instantaneous distributions and their temporal variations may be due to stick-slip behaviour of frictional gliding along grain boundaries. The active shear zone distributions interpreted from the stress directions of the numerical models predict possible fault curvatures within the prism, and agree with the numerical velocity vectors. The overall geometry of accretionary prisms with a décollement in the sedimentary pile is similar to the models, including the kinked geometry of the sequential thrust surfaces accompanied by backthrusting. The extensional stress regime under the décollement at Nankai is also explained by the numerical

stress distributions. This study shows that combinations of analogue and numerical models enable the extraction of more data from the results, that can be examined for detailed deformation characteristics.

This research is partly funded by the methane hydrate research consortium (MH-21) and their permission to publish this paper is gratefully acknowledged. S. Ueda and K. Kaneda assisted the numerical and experimental work respectively. The initial manuscript was greatly improved after constructive criticism by M. Seyferth and D. Nieuwland. The authors also appreciate comments and suggestions from the editors of this volume, G. Schreurs and S. Buiter.

## References

ADAM, J. & URAI, J. L. *ET AL.* 2005. Shear localization and strain distribution during tectonic faulting – new insights from granular-flow experiments and high-resolution optical image correlation techniques. *Journal of Structural Geology*, **27**, 283–301.

ADAM, J., LOHRMANN, J., HOTH, S., KUKOWSKI, N. & ONCKEN, O. 2002. Strain variation and partitioning in thrust wedges: High-resolution data from scaled sandbox experiments by 2D-3D PIV analysis. *Bolletino di Geofisica*, **42**, Supplement, 123–125.

BABA, K. & YAMADA, Y. 2004. BSRs and associated reflections as an indicator of gas hydrate and free gas accumulation – An example of accretionary prism and forearc basin system along the Nankai Trough, off central Japan. *Resource Geology*, **54**, 11–24.

BANGS, N. L. B., SHIPLEY, T. H., MOORE, G. F., GULICK, S. P. S. & NAKAMURA, Y. 2004. Evolution of the Nankai trough décollement from the trench into the seismogenic zone: inferences from 3-D seismic reflection imaging. *Geology*, **32**, 273–276.

COBBOLD, P. R. & CASTRO, L. 1999. Fluid pressure and effective stress in sandbox models. *Tectonophysics*, **301**, 1–19.

COBBOLD, P. R., DURAND, S. & MOURGUES, R. 2001. Sandbox modelling of thrust wedges with fluid-assisted detachments. *Tectonophysics*, **334**, 245–258.

COLLETTA, B., LETOUZEY, J., PINEDO, R., BALLARD, J. F. & BALE, P. 1991. Computerized X-ray tomography analysis of sandbox models: examples of thin-skinned thrust systems. *Geology*, **19**, 1063–1067.

CUNDALL, P. A. & STRACK, O. D. L. 1979. A discrete numerical model for granular assemblies. *Geotechnique*, **29**, 47–65.

DAVIS, D., SUPPE, J. & DAHLEN, F. A. 1983. Mechanics of fold-and-thrust belts and accretionary wedges: cohesive Coulomb theory. *Journal of Geophysical Research*, **88**, 1153–1172.

DAHLEN, F. A. 1984. Non-cohesive Critical Coulomb wedges: an exact solution. *Journal of Geophysical Research*, **89**, 10125–10133.

DAHLEN, F. A. & SUPPE, J. 1984. Mechanics of fold and thrust belts and accretionary wedges: cohesive Coulomb theory. *Journal of Geophysical Research*, **89**, 10087–10101.

DILEONARDO, C. G., MOORE, J. C., NISSEN, S. & BANGS, N. 2002. Control of internal structure and fluid migration pathways with the Barbados Ridge Décollement zone by strike-slip faulting: evidence from coherence and 3-D seismic amplitude imaging. *Bulletin of the Geological Society of America*, **114**, 51–63.

FINCH, E., HARDY, S. & GAWTHORPE, R. 2003. Discrete element modelling of contractional fault-propagation folding above rigid basement fault blocks. *Journal of Structural Geology*, **25**, 515–528.

GUTSCHER, M. A., KUKOWSKI, N., MALAVIELLE, J. & LALLEMAND, S. E. 1996. Cyclical behavior of thrust wedges: insight. from high basal friction sandbox experiments. *Geology*, **24**, 135–138.

HRYCIW, R. D., RASCHKE, S. A., GHALIB, A. M., HORNER, D. A. & PETERS, J. F. 1997. Video tracking for experimental validation of discrete element simulation of large discontinuous deformations. *Computers and Geotechnics*, **21**, 235–253.

HUBBERT, M. K. 1937. Theory of scaled models as applied to the study of geological structures. *Bulletin of Geological Society of America*, **48**, 1459–1520.

HUIQI, L., MCCLAY, K. R. & POWELL, D. 1992. Physical models of thrust wedges. *In*: MCCLAY, K. R. (ed.) *Thrust Tectonics*, London, Chapman and Hall, 71–81.

KONIETZKY, H. 2002. *Numerical Modeling in Micromechanics via Particle Methods*. Proceedings of the 1st International PFC Symposium, Gelsenkirchen, Germay, Rotterdam, Balkema Publishers.

KOYI, H. A. & MANCKTELOW, N. S. 2001. *Tectonic Modeling: A Volume in Honor of Hans Ramberg*. Geological Society of America Memoir 193.

KOYI, H. A. & VENDEVILLE, B. C. 2003. The effect of décollement dip on geometry and kinematics of model accretionary wedges. *Journal of Structural Geology*, **25**, 1445–1450.

LALLEMAND, S. E., MALAVIEILLE, J. & CALASSOU, S. 1992. Effects of oceanic ridge subduction on accretionary wedges: experimental modelling and marine observations. *Tectonics*, **11**, 1301–1313.

LOHRMANN, J., KUKOWSKI, N., ADAM, J. & ONCKEN, O. 2003. The impact of analogue material properties on the geometry, kinematics, and dynamics of convergent sand wedges. *Journal of Structural Geology*, **25**, 1691–1711.

MANDL, G. 1988. *Mechanics of Tectonic Faulting*. Elsevier, Amsterdam.

MASSOLI, D., KOYI, H. A., BARCHI, M. R. & ROGLEDI, S. 2002. Analogue modelling of the Po Plain: structural evolution of a fold thrust belt generated by multiple décollement. *Bollettino di Geofisica teorica ed applicata*, **42**, 1/2 supplement, 200–202.

MCCLAY, K. R. 1990. Deformation mechanics in analogue models of extensional fault systems.

*In*: KNIPE, R. J. (ed.) *Deformation Mechanisms, Rheology and Tectonics*, Geological Society of London Special Publications, **54**, 445–453.

MIKADA, H., BECKER, K. *ET AL.* 2002. *Proceedings of the Ocean Drilling Project Initial Reports*, **196**. Available from World Wide Web: http://www.odp.tamu.edu/publications/196_IR/196ir.htm.

MOORE, J. C. & KLAUS, A. 2000. *Proceedings of the Ocean Drilling Project Scientific Results*, **171A**. Available from World Wide Web: http://www.odp.tamu.edu/publications/171A_SR/171asr.htm.

MULUGETA, G. & KOYI, H. A. 1992. Episodic accretion and strain partitioning in a model sand wedge. *Tectonophysics*, **202**, 319–333.

NIEUWLAND, D. A., LEUTSCHER, J. H. & GAST, J. 2000. Wedge equilibrium in fold-and-thrust belts. Prediction of out-of-sequence thrusting, based on sandbox experiments and natural examples. *Netherlands Journal of Geoscience/Geologie en Mijnbouw*, **79**, 81–91.

NIEUWLAND, D. A., URAI, J. L & KNOOP, M. 1999. In-situ stress measurements in model experiments of tectonic faulting. *In*: LEHNER, F. K. & URAI, J. L. (eds) *Aspects of Tectonic Faulting*, Springer Verlag, 151–162.

SALTZER, S. D. 1993. Boundary conditions in sandbox models of crustal extension: an analysis using distinct elements. *Tectonophysics*, **215**, 349–362.

SCHREURS, G., BUITER, S. *ET AL.* 2005. Analogue benchmarking: results of shortening and extension experiments. *In*: SCHREURS, G. & BUITER, S. (eds) *Analogue and Numerical Modelling of Crustal Scale Processes*. Geological Society Special Publications, **253**, xx–yy.

SENO, T., STEIN, S. & GRIPP, A. E. 1993. A model for the motion of the Philippine Sea plate consistent with NUVEL-1 and geological data. *Journal of Geophysical Research*, **98**, 17941–17948.

SHIMIZU, Y., HART, R. D. & CUNDALL, P. 2004. *Numerical Modeling in Micromechanics Via Particle Methods*. Proceedings of the 2nd International PFC Symposium. Leiden, Balkema Publishers.

SHIBAZAKI, B., YOSHIDA, Y., NAKAMURA, M., NAKAMURA, M. & KATAO, H. 2002. Rupture nucleations in the 1995 Hyogo-ken Nanbu Earthquake and its large aftershocks. *Geophysical Journal International*, **149**, 572–588.

SIBSON, R. H. 1990. Conditions of fault-valve behavior. *In*: KNIPE, R. J. & RUTTER, E. H. (eds) *Deformation Mechanisms, Rheology and Tectonics*. Geological Society Special Publications, **54**, 15–28.

STRAYER, L. N. & SUPPE, J. 2002. Out-of-plane motion of a thrust sheet during along-strike propagation of a thrust ramp: a distinct-element approach. *Journal of Structural Geology*, **24**, 637–650.

TOBIN, H. J., MOORE, J. C. & MOORE, G. F. 1994. Fluid pressure in the frontal thrust of the Oregon accretionary prism: experimental constraints. *Geology*, **22**, 979–982.

TSUJI, T., MATSUOKA, T. *ET AL.* 2005. Initiation of plate boundary slip in the Nankai Trough off the Muroto peninsula, southwest Japan. *Geophysical Research Letters*, **32**, L12306.

UETA, K., TANI, K. & KATO, T. 2000. Computerized X-ray tomography analysis of three-dimensional fault geometries in basement-induced wrench faulting. *Engineering Geology*, **56**, 197–210.

WESTBROOK, G. K., CARSON, B., MUSGRAVE, R. J. & SHIPBOARD SCIENTISTS. 1994. *Proceedings of Ocean Drilling Program, Initial Reports*, **146**.

WOLF, H., KÖNIG, D. & TRIANTAFYLLIDIS, T. 2003. Experimental investigation of shear band patterns in granular material. *Journal of Structural Geology*, **25**, 1229–1240.

WILLETT, S. D. 1992. Dynamic and kinematic growth and change of a Coulomb wedge. *In*: MCCLAY, K. R. (ed.) *Thrust Tectonics*, London, Chapman and Hall, 19–31.

YAMADA, Y. & MCCLAY, K. R. 2003*a*. Application of geometric models to inverted listric fault systems in sandbox experiments. 1:2D hanging wall deformation and section restoration. *Journal of Structural Geology*, **25**, 1551–1560.

YAMADA, Y. & MCCLAY, K. R. 2003*b*. Application of geometric models to inverted listric fault systems in sandbox experiments. 2: Insights for possible along strike migration of material during 3D hanging wall deformation. *Journal of Structural Geology*, **25**, 1331–1336.

YAMADA, Y. & MCCLAY, K. R. 2004. 3-D analog modeling of inversion thrust structures. *In*: MCCLAY, K. R. (ed.) *Thrust Tectonics and Hydrocarbon Systems*. American Association of Petroleum Geologists (AAPG) Memoir **82**, 276–301.

YAMADA, Y., UEDA, S. & MATSUOKA, T. 2004. Simulation of accretionary prisms by distinct element method. *In*: SHIMIZU, Y., HART, R. & CUNDALL, P. (eds) *Numerical Modeling in Micromechanics via Particle Methods*. Balkema Publishers, The Netherlands, 187–190.

YAMADA, Y., OKAMURA, H., TAMURA, Y. & TSUNEYAMA, F. 2005. Analogue models of faults associated with salt doming and wrenching: application to offshore UAE. *In*: SORKHABI, R. & TSUJI, Y. (eds) *Faults, Fluid Flow and Petroleum Traps*. American Association of Petroleum Geologists (AAPG) Memoir **85**, 95–106.

# Integrated four-dimensional modelling of sedimentary basin architecture and hydrocarbon migration

S. M. CLARKE[1]*, S. D. BURLEY[1,2], G. D. WILLIAMS[1], A. J. RICHARDS[1]**, D. J. MEREDITH[1] & S. S. EGAN[1]

[1]*Basin Dynamics Research Group, School of Earth Sciences and Geography, Keele University, Staffordshire, ST5 5BG, England, UK (e-mail: smcl@bgs.ac.uk.)*

[2]*BG Exploration and Production India Ltd, Midas Building, Sahar Plaza, M.V. Road, East Andheri, Mumbai, 400 059, India*

**Current address: GLNB, British Geological Survey, Murchison House, West Mains Road, Edinburgh, EH9 3LA, Scotland, UK*

***Current address: Grid Operations Support Centre, CCLRC e-Science Centre, Rutherford Appleton Laboratory, Chilton, Didcot, Oxfordshire, England, UK*

**Abstract:** Structural geometries, faults and their movement histories, together with the petrophysical properties of flow units, are some of the major controls on hydrocarbon migration pathways within sedimentary basins. Currently, structural restoration, fault-seal analysis and hydrocarbon migration are treated as separate approaches to investigating basin geohistory and petroleum systems. Each of these separate modelling approaches in their own fields is advanced and sophisticated but they are not compatible with each other. Lack of integration produces incorrect palaeogeometries in basin models and inaccurate migration pathways.

A combined structural restoration and fault-seal analysis technique, integrated with fast hydrocarbon migration pathway modelling code based on invasion percolation (IP) methods, is described. These modelling methods are used to develop a 4D basin modelling workflow in which evolving basin geohistories and geometries form an integral part of the analysis of hydrocarbon migration and trapping. By combining structural restoration and 3D fault-seal analysis it is possible to investigate the evolution of structurally complex traps through time. Integration of these techniques with a numerically fast migration pathway modelling technique allows hydrocarbon migration pathways and accumulations to be modelled through the evolution of the basin with time. Additionally, the effects of uncertainties in structural geometry, fault seal or any of the model input parameters can be explored using a risk-driven approach to modelling.

These methods are demonstrated using synthetic, computer generated, 3D models and a well-constrained model of the Moab Fault, Utah, USA. Comparison of modelled structural geometries, fault-seal properties and predicted trapped hydrocarbons with outcrop data is used to validate the integrated modelling approach. The validated techniques are then applied to a seismically derived, 3D model from the southern North Sea, UK, to demonstrate how an integrated, risk-driven approach to modelling allows the effects of uncertainties in the distribution of hydrocarbon accumulations to be investigated.

Basin modelling is an established, powerful technique for predicting the timing of petroleum generation and the distribution of the hydrocarbon phase in the subsurface to reduce exploration risk (Iliffe & Dawson 1996; Welte *et al.* 1997; Burley *et al.* 2000). It is based on decompactional reverse modelling, from an understanding of the present day system, back to an initial depositional point, which is then used as a framework to forward model the basin and characteristics of the petroleum system. Commercial and research basin modelling tools enable many petroleum system processes to be modelled, including subsidence, temperature, compaction, maturation, secondary migration, and hydrocarbon phase (e.g., Mann *et al.* 1997; Wendebourg 2000). As a result, various case histories, 'calibrated' to present day known accumulations, have predicted

*From*: BUITER, S. J. H. & SCHREURS, G. (eds) 2006. *Analogue and Numerical Modelling of Crustal-Scale Processes*. Geological Society, London, Special Publications, **253**, 185–211.
0305-8719/06/$15.00 

hydrocarbon phase and distribution at the basin scale with varying degrees of success (e.g., Schroeder & Sylta 1993; Symington *et al.* 1998; Cowan *et al.* 1999; Johannesen *et al.* 2002).

Remarkably, few of these studies consider the structural evolution of basin geometry with time. Fluid flow conduits, and migration along them, constitute linked 3D networks defined by sediment fill and structural geometries, especially faults, throughout the basin. Accurate prediction of hydrocarbon accumulations therefore requires modelling in 4D, incorporating both 3D geometrical space, and how this geometry changes with time as the basin develops. However, incorporation of basin architecture and its evolution in basin models is at best simplistic. This is because hydrocarbon migration simulators employ an orthogonal grid data framework, suited to fluid flow calculations that conserve volumes, but unable to accommodate complex geometries (Wangen 1997). As a result, palaeogeometries and the effects of structuration on migration and entrapment are incorrect in current basin model realizations if migration pre-dates or is contiguous with structuration. Previous attempts at integrating the effects of faults into migration simulators have incorporated only vertical decompaction, backstripping and vertical shear on simple discontinuities in the orthogonal grid to represent faults and their properties. Methods are being developed to integrate structural restoration into migration simulators without requiring vertical grid alignment (e.g., Mello & Henderson 1997; Welte *et al.* 2000), and most recently, by using sequential time-step output from structurally restored horizons as input into a horizon-based migration simulator (Huggins *et al.* 2005).

The importance of structural restoration in determining basin geohistory for predictive petroleum system modelling is demonstrated in this paper. A new, integrated, modelling methodology is introduced, based on 3D fault restoration and fault-seal analysis software incorporating a hydrocarbon migration simulator employing *invasion percolation* (IP) techniques that enable migration pathways to be investigated through time as the basin geometry and architecture evolve. The fundamental features of the model are illustrated with a computer-generated 3D synthetic dataset, while a well constrained outcrop model of the Moab Fault, Utah, USA is used to demonstrate that accurate 3D restoration of basin geohistory and fault-zone gouge are critical to modelling hydrocarbon migration, and thus petroleum system analysis. This integrated technique also facilities rapid modelling of predicted accumulations, and allows a risk-driven approach to petroleum systems analysis in which multiple realizations can be used to rank the likelihood of migration and accumulation. Uncertainty in aspects of basin architecture, fault seal or petrophysical detail, and their effects on evolving migration pathways, can be assessed and specific accumulations risked accordingly. Application of the technique in a risk-driven scenario is demonstrated using a case study of seismically mapped fault blocks from the southern North Sea, UK.

Each of these models is provided to demonstrate aspects of the 4D modelling approach and to illustrate the effects of accurate restoration on migration pathways and trapping histories. Details of all the models and associated animations are available on the internet at http://www.bdrg.esci.keele.ac.uk/smcresearch.htm.

## Restoration, fault seal and migration in basin modelling

Structural restoration and basin modelling have traditionally addressed specialist problems within fields of structural validation and petroleum systems modelling. Appropriate tools for each approach have evolved in isolation from each other, with separate data requirements, assumptions and data structures. Structural modelling tools are based on geometric algorithms that describe rock deformation. By contrast, basin modelling techniques were developed from geochemical prediction of organic matter maturation and the need to calculate migration pathways and trapped volumes. Advances in computing power, visualization and the development of 3D modelling technology now enables the construction of high spatial resolution 3D models that can incorporate both structural restoration and hydrocarbon migration modelling. A more accurate numerical representation of the petroleum system of a basin and its evolution can be achieved by embedding structural modelling into hydrocarbon generation and migration modelling so that migration through palaeogeometries can be investigated. The key to incorporating structural restoration in basin simulators is to represent basin geometry as realistic structural and litho-stratigraphical surfaces (contacts) in 3D space. As faults and horizon discontinuities (such as unconformities) are important architectural components of a basin, these elements should *in principa* be the initial building blocks of the basin model if the basin geometry through time is to be represented.

### *Structural modelling*

Structural validation and modelling tools are based upon geometric algorithms that describe rock deformation, preserving area and/or

volumes. In 2D, conservation of volume simplifies to conservation of cross-sectional area, and/or bed length, assuming a section constructed parallel to the mass movement direction, plane strain deformation and a tectonic regime in which bed thickness is unaffected (Dahlstrom 1969; Gibbs 1983). Several 3D approaches have been developed, including strain trajectories (Cobbold 1979), iterative finite element methods (Gratier *et al.* 1991), best-fit unfolding and fault fitting (Rouby *et al.* 2000) and jigsaw fitting (Williams *et al.* 1997). All these techniques enable the restoration of complex faulted and folded structures. New algorithms, such as flexural flow, have been developed that consider out-of-plane movement of material for true 3D modelling (Williams *et al.* 1997).

Handling of complex geometries and deformations in 3D requires a flexible model representation in the form of irregular, triangulated meshes that can change topology (node pattern and connectivity) between modelling steps (Mello & Henderson 1997; Richards 2000). The geohistory of a basin is determined by reverse modelling of the present-day stratigraphical and structural architectures to restore palaeogeometries. Sediment layers are sequentially backstripped and decompacted (e.g., Van Hinte 1978; Bond & Kominz 1984). Differential compaction of layers, with variable thicknesses or discontinuity, has a major impact upon restored horizon palaeogeometries. Different compaction porosity-depth functions also affect restored palaeogeometries (Giles *et al.* 1998), though changes in structural amplitude rather than shape most commonly result.

Backstripping has traditionally been geometric, restoring horizons to an assumed depositional template, whereas latest research models are process-based, using lithospheric models to predict palaeogeometries (Kusznir *et al.* 1995). The simplest backstripping procedure restores the sediment depositional surface to a horizontal datum of a specified bathymetry, usually sea-level (Roberts *et al.* 1998) but can be enhanced by restoring to a palaeobathymetric template, defined from the stratigraphical architecture and biostratigraphy of the layer (Van Hinte 1978). Mechanical models predict basement geometry based upon lithospheric deformation and its isostatic response to basin infilling (Mckenzie 1978; Meredith & Egan 2002), defining evolving horizon geometries and palaeobathymetry.

Structural restoration through time involves a retro-deformational process in which sequential 'snapshots' of the basin evolution are portrayed. Observed or inferred displacement vector fields are combined with geometrical modelling methods that predict hanging wall geometries and define basin architecture with subsequent stages of deformation.

### *Fault-seal prediction*

Faults, their geometries, and their movement histories through time are important controlling elements of hydrocarbon migration and entrapment within sedimentary basins. When faults undergo displacement, their fluid transmissibility may change as a result of (1) juxtaposition of strata, (2) development of a damage zone, and (3) inclusion of material between faulted blocks. In addition, fault displacement modifies the geometry of faulted blocks. These effects have to be combined with 3D structural geometry modelling and incorporated into models of hydrocarbon migration for accurate migration pathways to be predicted.

The sealing properties of a fault can be approximated using 1D and 2D numerical methods (e.g., Allan 1989; Fristad *et al.* 1997) and may be applied to the fault in entirety or to a given stratigraphical sequence and deformational regime. In 3D, the structural geometries of faults and faulted blocks can be represented fully and the sealing properties determined at each spatial point on the fault surface from the interaction of the faulted stratigraphy, the deformation regime, the structural geometry of the fault blocks, and the properties of any fault-zone material (Clarke *et al.* 2005*a*) using 3D derivations of these techniques.

2D fault-surface projections can be constructed to analyse relative cross-fault juxtapositions for a given temporal stage in the deformational history of a fault. However, a fault that is curved along strike will not be represented correctly in the fault-surface section and, if a curved fault is resolved onto a flat plane, stratigraphical cut-off areas will not necessarily be preserved (Harper & Lundin 1997). Furthermore, fault representation as a fault-surface section does not allow investigation of the interaction of multiple faults on sealing capacity, nor analysis of lithology juxtaposition at other temporal stages in the evolution of the fault. These problems can be addressed by mapping properties of the faulted blocks to the footwall and hanging wall of the fault surface directly in 3D (Clarke *et al.* 2005*a*). Furthermore, the interaction of juxtaposition seal between multiple faults is revealed and, by examining relationships at other temporal stages, the evolution of cross-fault juxtaposition can be determined.

Argillaceous smearing is an example of a fault-zone process that can modify transmissibility. This process has attracted much attention due

to its particular relevance to mixed arenaceous and argillaceous sequences and the availability of field examples for calibration (e.g., Foxford *et al.* 1996). Many workers have produced 1D and 2D numerical and empirical models to quantify argillaceous smearing and, of these models, the *shale gouge ratio* or SGR (Fristad *et al.* 1997) is commonly employed for the analysis of fault transmissibility using the expression:

$$\mathrm{SGR} = \frac{\sum_{i=1}^{I} (\Delta z f_{cl})_i}{t} \quad (1)$$

where $\Delta z$ is interval or unit thickness of unit $i$, $f_{cl}$ is the argillaceous fraction of unit $i$, $t$ is fault throw, and $I$ is the total number of units that have passed a given point on the fault surface.

In general, an SGR value of *c.* 20% represents the threshold above which smear continuity is sufficient to cause sealing (Gibson 1994; Fristad *et al.* 1997; Yielding 2002), although this value is likely to be affected by case-specific geological factors such as host rock mineralogy and confining pressure. Despite such limitations, the SGR is an accepted technique for the analysis of fault seal potential. Use of the parameter 'throw' in the original published algorithm inherently defines this expression as 1D, although it can be applied repeatedly along the length of a fault to generate a 2D or pseudo-3D analysis. Modern methods project the derivation of throw into a slip-azimuth projection, thus reducing inaccuracy in settings where faults have a significant component of strike-slip. True 3D applications of the SGR, incorporating 3D structural displacement vectors and properties of the faulted sequence, allow fault-zone argillaceous content to be modelled in the full 3D environment and its effects on hydrocarbon migration and accumulation to be investigated in the context of the basin architecture (Clarke *et al.* 2005*a*).

### *Hydrocarbon migration*

Secondary hydrocarbon migration is a multiphase, water-oil-gas process (Schowalter 1979) driven by the balance between buoyancy and capillary forces, although in high permeability sediments pressure gradients, a function of compaction, play a role (Berg 1975). Current petroleum system concepts suggest that hydrocarbons migrate in focused stringers (less than a few metres high, a few tens of metres wide, but up to many kilometres long), at moderate saturations (20–40%; Sylta 2002). Focusing takes place because the permeability fabric of sediments is heterogeneous, so once critical saturations required for the flow condition are established, initial migration pathways are maintained. This 'fingering' dictates that only a small proportion of the basin-fill (in the order of 2%) is invaded by the migrating hydrocarbons, resulting in a highly efficient migration process (Larter *et al.* 1996). Laboratory simulations of hydrocarbon migration confirm that hydrocarbons move vertically under buoyancy until they encounter a permeability barrier, at which point they migrate laterally, or accumulate until the buoyancy pressure of the accumulation exceeds the capillary entry pressure of the confining barrier (Thomas & Clouse 1995).

Three different numerical approaches to modelling these aspects of migration are in widespread use: ray-path, Darcy flow and percolation (Hantschel *et al.* 2000; Carruthers 2003). In all cases, models are constructed from stacked horizon surface grids in which data nodes are vertically aligned. Simple fault geometries and their evolution are incorporated but are handled in a simplistic manner without discrete discontinuities in the grids, and without the complex geometries that can be derived from structural modelling techniques.

*Ray-path modelling* is a simple approach that allows vertical, buoyancy-driven migration until hydrocarbons impinge on surfaces bounded by low permeability seals, at which point they accumulate beneath the seal in topographical highs. This approach is very effective in reproducing aspects of the migration system, such as focused, high saturation flow in permeable carrier beds. The numerical simplicity of the approach results in very fast simulations, enabling statistical treatment of model results. However, ray-path modelling does not reproduce well migration through low permeability sediments, and is not representative of the whole migration process.

*Darcy flow geocellular-based models* calculate 3-phase flow as a function of sediment compaction and pressure gradients. Finite element and finite difference approximations are used to model hydrocarbon flow through and between regular or irregular shaped geo-cellular elements, each cell being assigned petrophysical properties. These methods predict the 'state' and direction of flow at each spatial and temporal point within the model in terms of physical and kinetic properties based on defined initial and boundary conditions. This approach honours the physics of matrix Darcy flow but assumes cells are filled with hydrocarbon to a given saturation before migration proceeds. As the

numbers of cells in the model is limited by computational power, shortcomings of this approach are dispersion of the migration front at coarse cell dimensions and long simulation times.

*Percolation-based models* use the principle of gradient invasion percolation, in which petroleum migrates under buoyancy into an opposing network of cells populated with capillarity pressures or permeabilities, pursuing the lowest entry pressure or highest permeability pathway. Computational times are extremely fast and capillary/permeability grids can be defined statistically, allowing enormously large models to be investigated directly from seismic data, and sensitivity studies to be rapidly conducted on model results. This contrasts with the long process times of Darcy flow-derived migration simulation, which renders a risk-driven approach to basin analysis and migration impractical. Over timescales associated with secondary hydrocarbon migration, percolation-based numerical approaches may be the most appropriate technique for modelling petroleum systems (Carruthers 2003).

## Modelling hydrocarbon migration through faulted structures

Here we introduce a combined approach to the modelling of sedimentary basin architecture, fault seal properties and hydrocarbon migration, based on percolation theory that enables a risk-driven analysis of hydrocarbon flow through faulted basins (Fig. 1). 3D structural restoration techniques are used to restore models, derive displacement vector fields and subsequently deform basin architecture to provide geometrically valid hanging wall structural geometries. Calculated displacement vectors are incorporated into 3D predictions of fault seal properties. True 3D juxtaposition and shale gouge effects are determined and percolation-based migration techniques are used to predict flow pathways and accumulations within these models. Percolation techniques are used because these provide a realistic representation of hydrocarbon migration and their numerical simplicity allows completion of many realizations (hundreds or thousands) in practical lengths of time. Multiple simulations can be run, having modified one or more input parameters to investigate the sensitivity of the petroleum system to a particular geological scenario. This approach can thus be used to filter low-risk prospects for use in more computationally intensive Darcy flow-based compositional flow simulators.

### *The structural basin model*

To model 3D structure, contacts between lithological and structural units of the sedimentary basin are represented as triangulated surfaces in 3D (Fig. 2a). Details of this methodology are described in Clarke *et al.* (2005*a*). The technique is computationally efficient, and allows structural restoration, as well as calculation and visualization of fault seal properties. However, it does not consider the rock volume between modelled surfaces; a necessary requirement for flow simulation.

To address this issue, we combine the surface model of Clarke *et al.* (2005*a*) with a 3D geocellular model. The rock volume between the surfaces is represented by a lattice in which each cell is populated by a node at its centre (Fig. 2b). Cell size may vary throughout the model, but it is assumed that the cell size at a given point adequately represents the heterogeneity in rock properties within the geological units. Cells adjacent to surfaces representing faults are representative of the fault zone and associated fault rocks. This requires that the cell size adjacent to such surfaces must be of the order of magnitude of the fault zone width and can be approximated from:

$$t_i \approx \frac{d_i}{66} \tag{2}$$

where $t_i$ is the fault zone thickness (in units of $d$) at point $i$ on the fault surface and $d_i$ is fault displacement at that point (Manzocchi *et al.* 1999).

The triangulated surfaces represent major structural or stratigraphical discontinuities and, as such, divide the geocelluar model into discrete blocks (Fig. 2b). This strong relationship between the surface and geocellular components controls data population of the model. Structural deformation and fault seal properties can be determined using the geometry of the surfaces and integrated with the properties of the geocellular model to control hydrocarbon migration.

### *Structural restoration and fault seal*

For integrated basin modeling, there are two overriding considerations in structural restoration: (1) The algorithm must predict the geometry of the hanging wall with differing degrees of deformation and, (2) the resultant deformation must volume balance. In some scenarios, fault displacement and hydrocarbon migration may occur concurrently. An iterative best-fit algorithm is used to derive the required displacement vector field that best restores the displaced

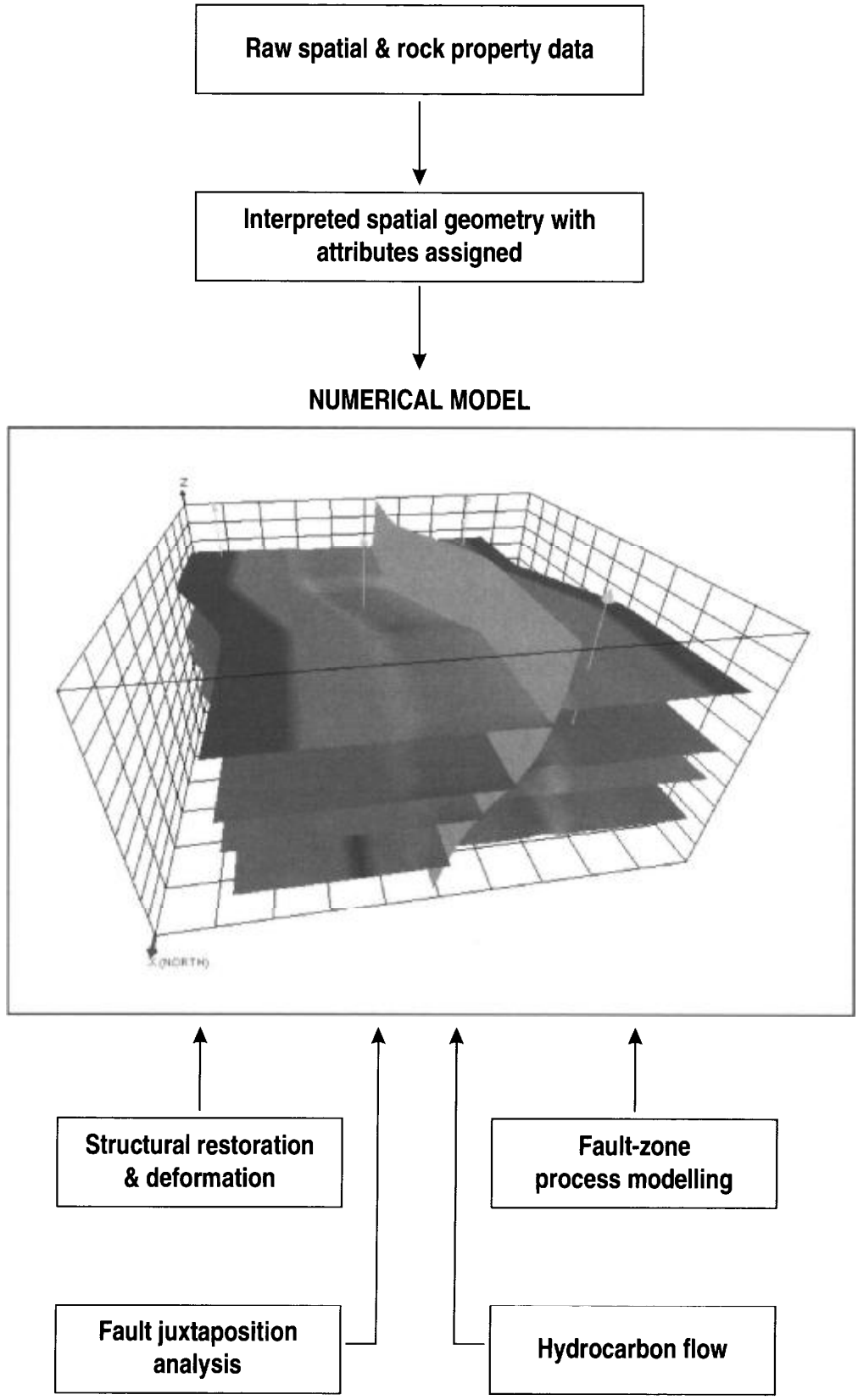


**Fig. 1.** The elements of the 4D model and workflow. Raw spatial and rock property data are used to interpret spatial geometry with assigned attributes. Structural restoration, fault-seal analysis and hydrocarbon flow modules operate on this model.

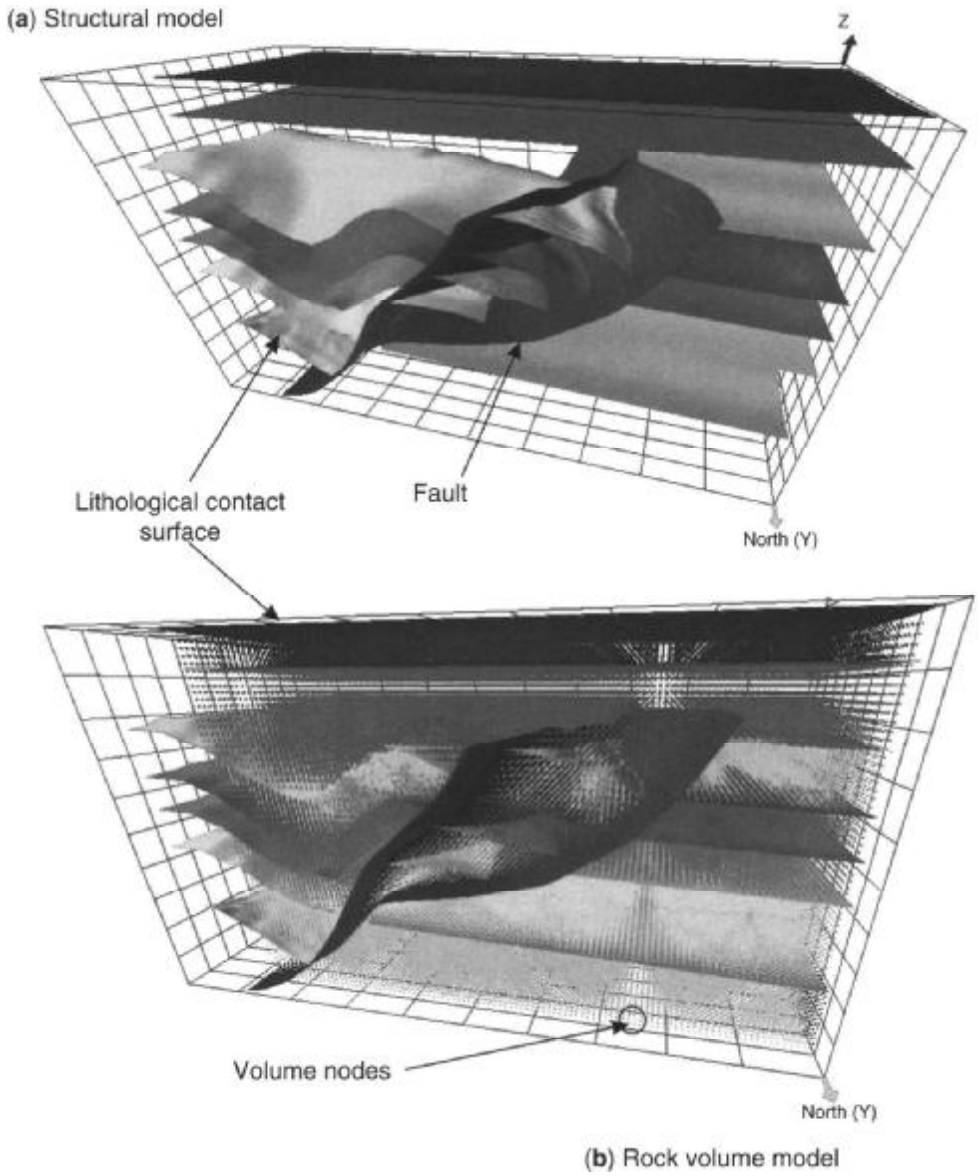


**Fig. 2.** The numerical model of a kilometre-scale basin. (**a**) Structural, stratigraphical and lithological contacts are represented as triangulated surfaces in 3D space. This modelling strategy allows efficient modelling of structural architecture, restoration and fault seal properties. (**b**) The rock volume between surfaces is represents by a geocellular lattice. Each cell is represented by a node at its centre. Nodes adjacent to faults represent the fault zone. The surfaces divide the rock volume into discrete blocks and constrain data interpolation to the volume.

geometry. First- and second-order derivatives of the map-plane geometry of respective footwall and hanging wall cut-offs are analysed to determine points of significant curvature along the cut-off, termed 'piercing points' (Fig. 3a). Each piercing point along the hanging wall cut-off is matched to a piercing point of the corresponding footwall cut-off in turn, generating a series of possible slip-azimuth vectors (Fig. 3a). The hanging wall cut-off is translated in the direction of each possible slip azimuth in turn and the amount of misfit with the footwall cut-off determined. The slip azimuth that produces the minimum amount of misfit is selected as the most likely restoration slip azimuth (Fig. 3b). The misfit between cut-offs with this slip azimuth is used to define a 'horizontal slip magnitude' gradient (distribution of the horizontal components of displacements in the slip-azimuth direction) for the hanging wall block (Fig. 3c) A 3D solution to the chevron/inclined shear construction (Clarke *et al.* 2005*a*) is used to restore the hanging wall and iteratively refine the slip magnitudes and define true 3D

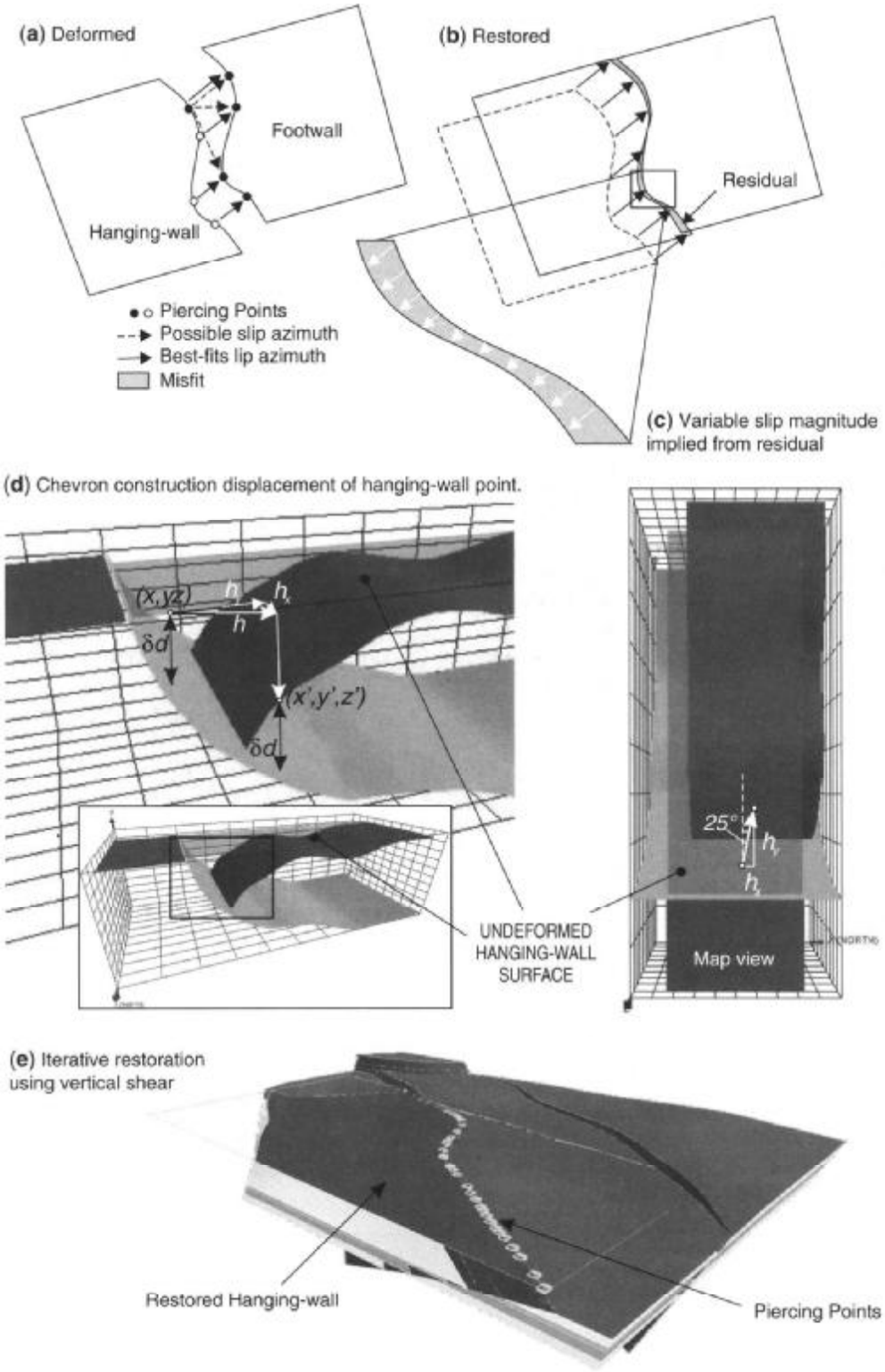


**Fig. 3.** Automated structural restoration. (**a**) First- and second-order derivatives of footwall and hanging wall cut-offs are used to derive 'piercing points'. The hanging wall cut-off is translated to match piercing points in turn. (**b**) The translation that produces the least misfit is considered the slip azimuth. (**c**) The misfit with this slip azimuth is used to derive the horizontal slip gradient. Iterative restoration using chevron or inclined shear is used to refine these vectors. (**d**) Hanging wall deformation can be achieved using these vectors and the chevron (shown) or inclined shear construction. Each point in the hanging wall is translated in the map plane by Cartesian components ($h_x$ and $h_y$) of the slip azimuth, and in the vertical plane such that original distances between the surface and the fault ($\delta d$) are maintained. (**e**) Hanging wall geometries can be predicted at given snapshots in time.

displacement vectors. Subsequently, the derived best-fit displacement vectors are used to deform hanging wall strata and generate required snapshots of basin evolution (Figs 3d and e). This approach maintains fault-block volumes with deformation. Given the strong relationship between the structural and geocellular components of the model, volume nodes representing the geocellular hanging wall volume are displaced in the same manner and their associated properties translated accordingly. Coherency between the structural and rock volume model is preserved.

Fault properties are modelled directly on the triangulated fault surfaces. Juxtaposition relationships across faults are modelled in 3D by comparing interpolated lithological and petrophysical properties of fault blocks bounded by fault surfaces. Fault-zone gouge is predicted using a 3D application of the SGR (Clarke *et al.* 2005*a*). The argillaceous contents of the faulted stratigraphy are interpolated to the fault surfaces and combined with the restoration-derived displacement vectors to determine gouge for each point on the fault using:

$$\mathrm{SGR} = \frac{\sum_{i=1}^{I} (\Delta a f_{cl})_i}{\sum_{i=1}^{I} \Delta a_j} \qquad (3)$$

where $\Delta a$ is a the area of a small, defined region $i$ of the fault surface, $f_{cl}$ is the shale fraction of the region and $I$ is the total number of regions, representative of the hanging wall cut-off, that have been displaced past the current fault point. In this way, the true 3D displacement of the hanging wall and the variation in argillaceous content of the footwall stratigraphy over which the hanging wall has moved, are incorporated into the prediction of gouge.

### *Hydrocarbon migration modelling: invasion percolation*

The invasion percolation (IP) approach to fluid flow has received much attention in applied physics (Wilkinson & Willemsen 1983; Meakin *et al.* 1992; Wagner *et al.* 1997; Schwarzer *et al.* 1999) and, more recently, it has been applied to hydrocarbon flow through geological structures (Paterson *et al.* 1996; Meakin *et al.* 2000; King *et al.* 2001; Carruthers 2003).

The technique is an iterative logical selection method that is orders of magnitude faster than numerical calculation (on the scale required for fluid flow simulation). Hence, in general, IP flow modelling is faster than ray-tracing and much faster than Darcy flow-based techniques. However, classical IP methods cannot predict temperature, pressure or associated properties within the flow regime, although advanced methods do facilitate secondary derivation of these properties.

IP theory is based on the concept of displacement of one fluid from a porous medium by another (Wilkinson & Willemsen 1983). The two fluids are immiscible and one fluid is assumed to show a greater affinity for the solid matrix and preferentially spread over the solid surface of the porous medium. This fluid is termed *wetting*; the other fluid is termed *non-wetting*. By considering the porous medium as a network of pores connected by narrower throats, capillary forces will be strongest at the throats and the fluid interface will move fastest through such points. Migration can be represented as a series of discrete 'jumps' in which one fluid displaces the other from the smallest available pore on the interface boundary. Accordingly, the principle of IP is that 'the interface between the two fluids will advance at the point of least resistance'. The general terms *invading fluid* and *defending fluid* are employed to describe the displacing and displaced fluids respectively (Meakin *et al.* 2000).

In an IP model, the porous medium is approximated by a regular, homogeneous, 3D matrix of 'sites' (representing the pores) with 'bonds' (representing pore throats) between them (Fig. 4a). To introduce heterogeneity, the sites and/or bonds are assigned numerical values representing their *ease of invasion*. At each iterative step, the invading fluid displaces the defending fluid from the *most easily invaded* pore space on the boundary of the invading volume. *Ease of invasion* is defined by the properties of the porous medium and the invading fluid. It is assumed that fluid migration is controlled by capillary forces (Wilkinson & Willemsen 1983). In hydrocarbon migration, the fluids have differing densities and the porous medium is heterogeneous and typically extremely anisotropic.

The effects of density differences between hydrocarbons and water can be incorporated into the invasion percolation algorithm by overprinting the ease of invasion of each site or bond with a depth-dependent factor (i.e., a gravity gradient). This concentrates the flow of the invading fluid into a *finger* or *string* within the porous medium and, with increasing gravity gradient, this string becomes more confined and concentrated (Meakin *et al.* 2000). Large-scale heterogeneities within a porous medium, such as those representing layering or structure, are represented by contrasts of ease of invasion

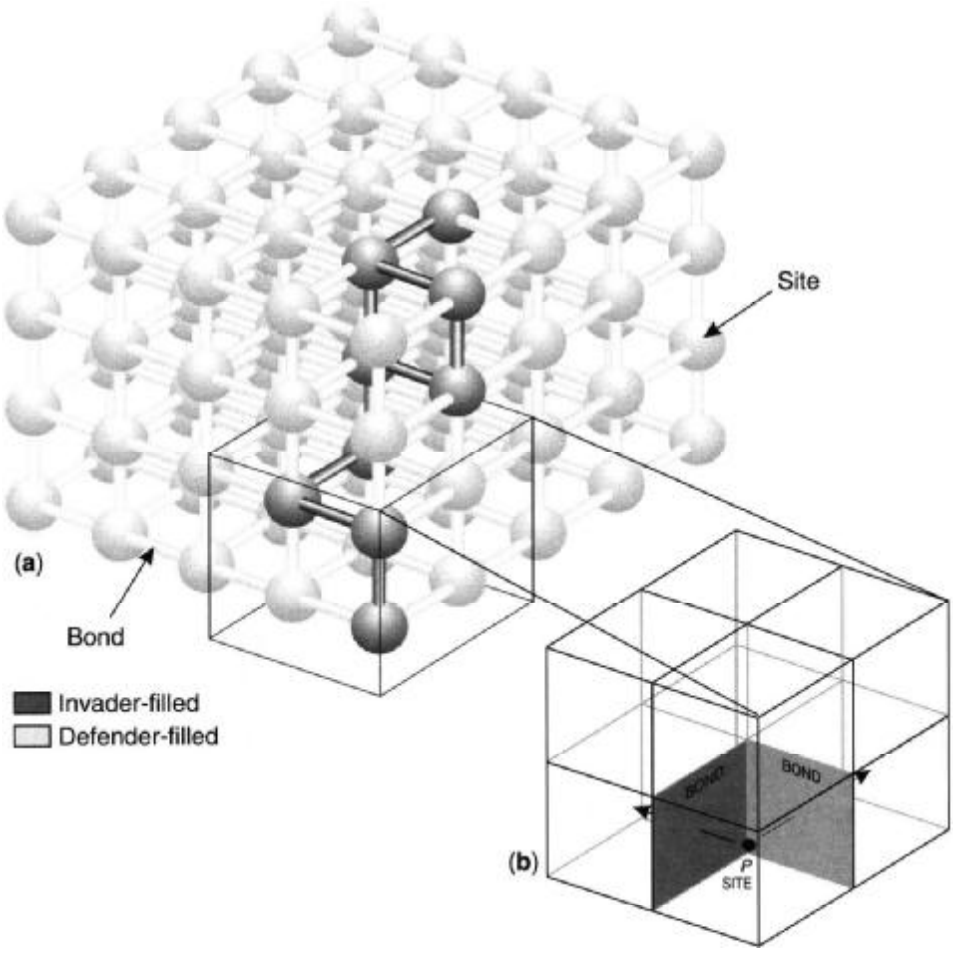


**Fig. 4.** The principles of invasion percolation. (**a**) Rock volume can be represented as an interconnected lattice of sites (pores) with bonds (pore throats) between them. The invader fluid follows the route of least resistance through the model. (**b**) In practice an exact model of pores of the rock volume is not possible and the lattice is approximated to a grid of cells with cell volumes representing the sites and cell interfaces representing the bonds.

between neighbouring sites or bonds. Such heterogeneities have a controlling influence on the large-scale pattern and pathways of the invading fluid.

In an ideal case, the site/bond matrix is an exact representation of the pores and connecting pore throats of the porous medium that it represents (Fig. 4a) and the value of ease of invasion is simply the size (volume) of each pore and each pore throat. In practice, the porous medium is approximated to a geocellular lattice in which sites and bonds are represented by cell volumes and cell interfaces respectively (Fig. 4b). This approach assumes that the size of the cells adequately reflects the heterogeneity of the porous medium. The low computational load of IP methods has the advantage of allowing many more cells than Darcy flow-based models and therefore a higher resolution model. Permeability (or capillary entry pressure) values are assigned to each cell volume. Values can be deterministically interpolated from available well data, using recognized spatial interpolation algorithms, or probabilistically populated using probability density functions if a comprehensive database is not available. Given the statistical nature of IP, the exact magnitude of permeability for a given cell is not significant. The migration pathways are controlled by the *relative* distribution of permeabilities throughout the model, and relative, dimensionless measures may be used.

In the simulations presented here the two fluids of interest are water and a single hydrocarbon phase. Multiphase flow is not considered since it presents additional theoretical considerations and increases the processing time. Water is always considered the defender and the hydrocarbon phase the invader fluid.

The IP model makes a number of assumptions:

(1) Both fluids are incompressible and homogeneous.
(2) The defending fluid always has a means of escape (withdrawal) when faced with the advance of the invader.
(3) There is an unlimited and constant supply of invading fluid into the model.
(4) Each site is assumed filled to capacity by either phase exclusively.
(5) Geological time is not integrated into the model. The number of iterations over which each realization is simulated is determined by the point at which hydrocarbons migrate out of one edge of the flow domain.

The ease of invasion from one cell to its neighbours is determined from their permeabilities using:

$$T_{AB} = \frac{2}{(1/k_A + 1/k_B)} \tag{4}$$

where $k_A$ is the permeability of cell $A$, $k_B$ is the permeability of neighbouring cell $B$, and $l$ is the distance between cell centres (Manzocci *et al.* 1999).

In settings where fault-zone gouge is predicted, the permeability of this material is derived from the predicted SGR (Manzocci *et al.* 1999) and used to populate the volume nodes immediately adjacent to fault surfaces representing the fault zone (Fig. 5). Transmissibility calculations (Eqn. 4) between these nodes and those representing the faulted blocks incorporate both the effects of cross-fault juxtaposition and cross-fault permeability reduction resulting from fault-zone gouge into the transmissibility distribution of the model (Fig. 5).

### *Populating the model with data*

Rock property values are interpolated to the surfaces and to the nodes, representing the geocellular model from high-resolution well data pertaining to wells that penetrate the fault blocks (Fig. 6). The geometry of the surfaces constrains interpolation of values to the geocellular model (Clarke *et al.* 2005*b*). In many simulations, particularly those that are data-poor, rock properties values are assigned from 'standard' ranges or estimated in bulk for a given sequence. IP-driven flow simulation has a significant advantage over more traditional methods in these scenarios. Pathway determination by the easiest route (ease of invasion) relies on relative values rather than absolute quantities. This reduces the error inherent in estimating bulk permeabilities. However, the IP methodology makes the assumption that an 'easiest route' exists. In scenarios where permeability values are estimated in bulk, a given geological unit will have homogeneous permeability, and the easiest route will be controlled by the algorithm rather than by the geology. Homogeneous units are conditioned randomly, with a normal distribution of data with a mean and modal value equal to the homogeneity and a variation over three standard deviations given by:

$$f(x) = \frac{1}{\sigma\sqrt{2\pi}} \exp\left[-\frac{(x-\mu)^2}{2\sigma^2}\right] \tag{5}$$

where $\sigma^2$ is variance, $\sigma$ is standard deviation, $\mu$ is mean and $(\mu - 3\sigma) < x < (\mu + 3\sigma)$.

This technique produces a heterogeneous but isotropic unit. On a unit-wide scale, flow pathways will progress evenly in all lateral directions. The value of standard deviation can be employed to express uncertainty in the homogeneity of the unit. Greater heterogeneity can be introduced by incorporating seismic reflection data and attribute volumes into the model to

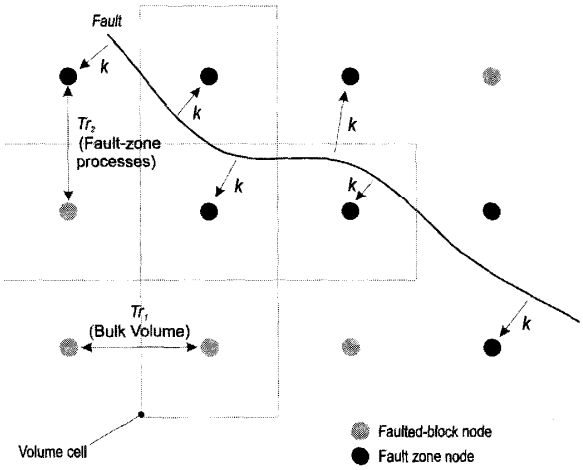


**Fig. 5.** The surfaces of the model divide up the volume cells (and nodes that represent them) into specific blocks. Those cells that are immediately adjacent to fault surfaces are used to represent the fault zone and populated with permeability values ($k$) derived from properties of the fault zone (such as gouge) predicted on the fault surfaces themselves. Transmissibility calculations between nodes of fault-block volume ($Tr_1$) incorporate heterogeneities of the fault blocks whereas transmissibility calculations between these nodes and fault-zone nodes ($Tr_2$) incorporate the effects of cross-fault juxtaposition and fault-zone properties into the flow model.

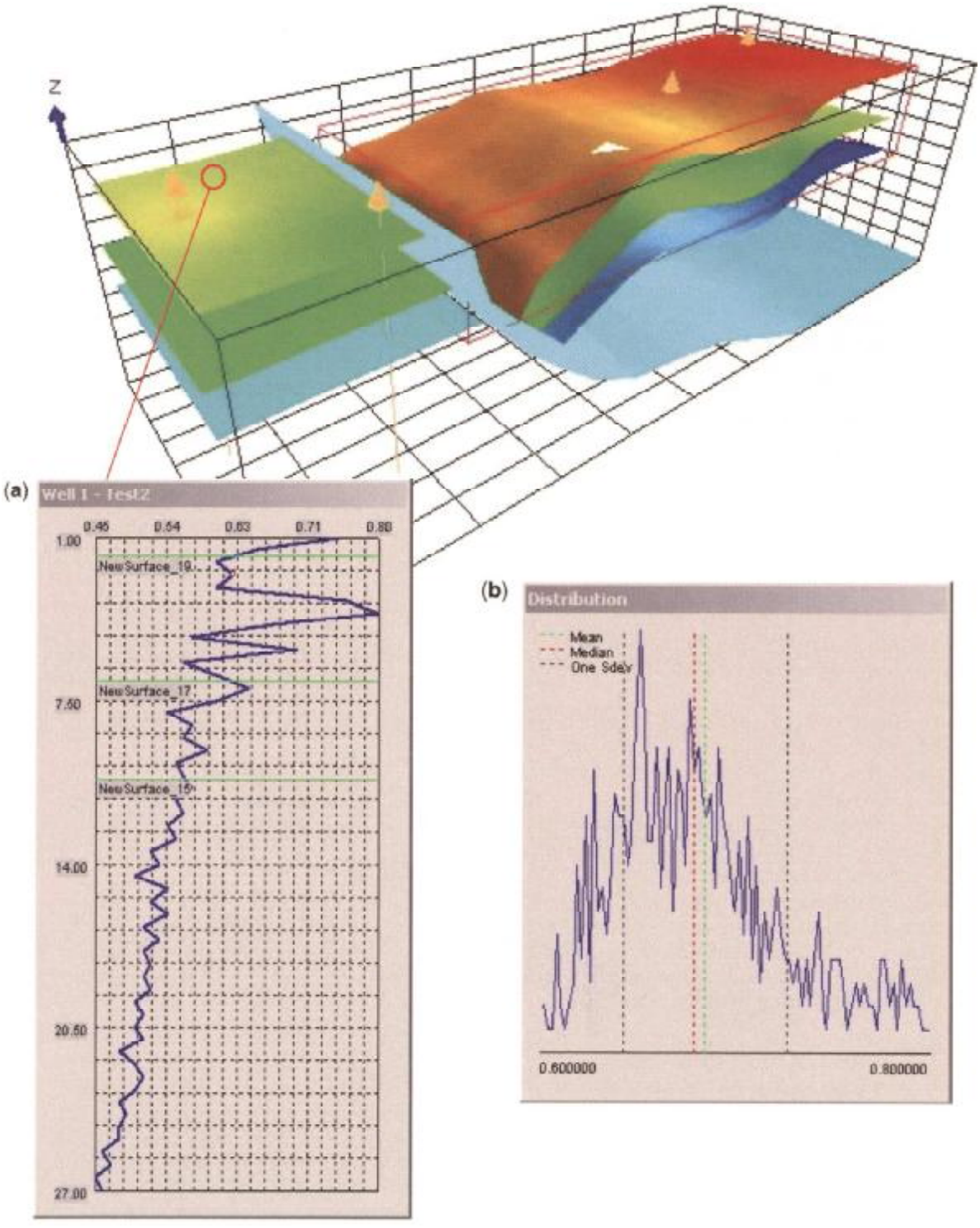


**Fig. 6.** Populating the model with data. (**a**) Detailed well logs are used to populate data to the modelled surfaces (shown) and volume, where such data are available. (**b**) In the absence of such data, statistical distributions may be used. Data interpolation is constrained by the geometry of the surfaces in 3D. Here, the surface colours show distribution of data interpolated from the wells shown.

'condition' the flow pathways. Finally, volume node permeability values are conditioned further by a depth-dependent buoyancy factor to facilitate upward migration within units.

The combined structural, fault seal and IP-driven hydrocarbon migration modelling approach is demonstrated using a series of computer generated synthetic 3D models (Figs 7 and 8).

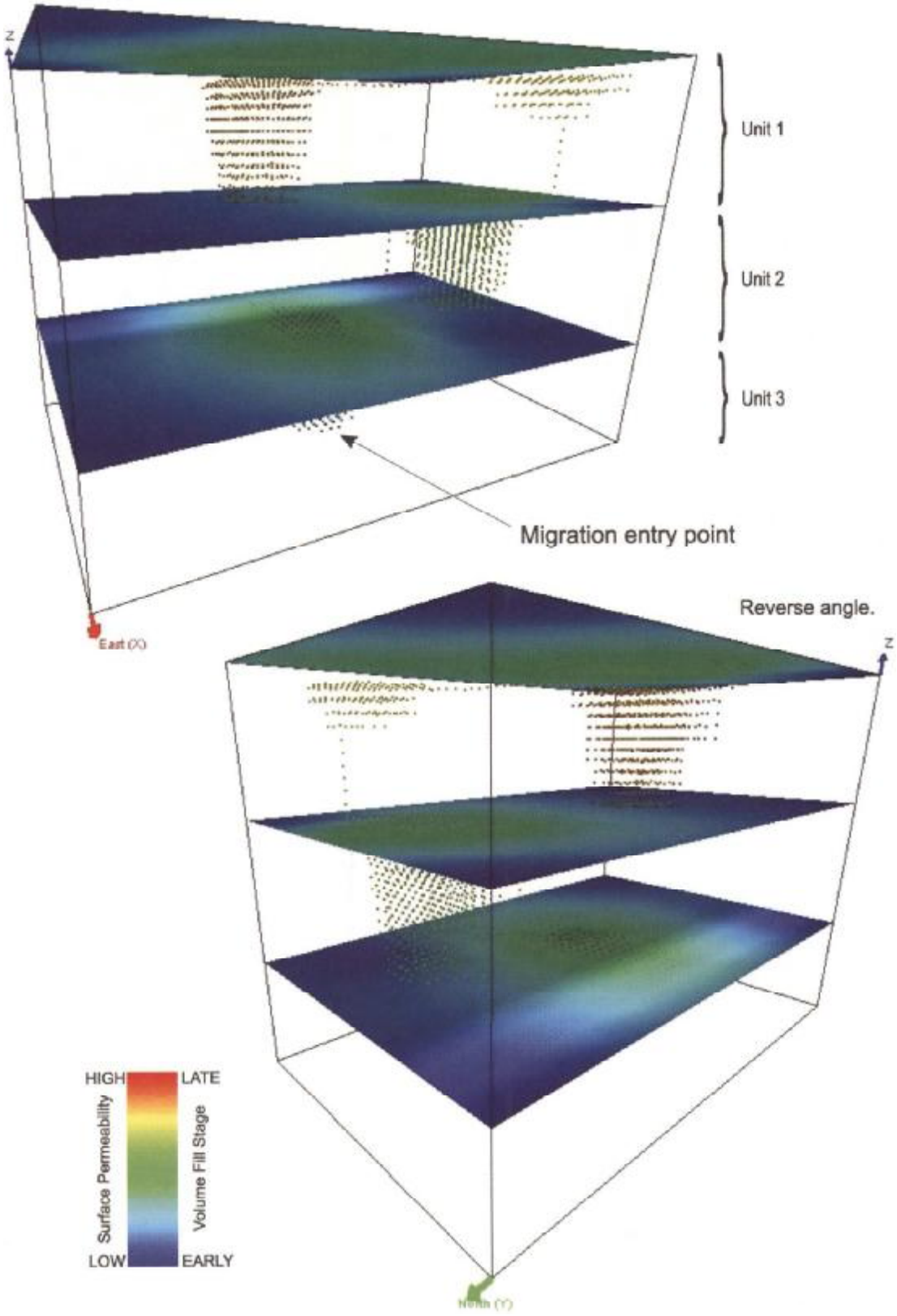


**Fig. 7.** A simple synthetic model of three lithological units represented by three surfaces. The model is designed to represent stratigraphy over several square kilometres and each unit shows variations in permeability (surface colours). This variation and the discontinuities in permeability at the unit surfaces control hydrocarbon flow through the model. Pooling occurs in highly permeable regions of each unit below each surface until a permeability contrast that represents an 'easiest route' is found through the surface into the unit above. Only filled volume nodes are shown, coloured by stage of fill.

The basic synthetic model contains three lithological units, the contacts between which are represented by three simple surfaces (Fig. 7) that represent major stratigraphical discontinuities. Synthetic values for permeability have been interpolated to the surfaces and to the volume nodes of the model, constrained by the position and geometry of the surfaces (see Fig. 6). Migration pathways from a defined migration entry point at the base of the model are controlled by both the permeability distribution within units and the discontinuities at the surfaces that bound them. Pooling of hydrocarbons takes place beneath each surface until a low permeability pathway is encountered that allows migration through to the overlying unit. Structural complexity is introduced in the form of a major normal fault and associated smaller synthetic fault (Fig. 8). Additionally, seven lithological units with varying permeabilites and shale content are represented by surfaces that bound them. The structural geometry constrains the interpolation of permeability from synthetic wells that penetrate the model to both the surfaces and cells. In Figure 8a migration pathways are predicted through the model based on the juxtaposition of permeabilities across the fault and demonstrate flow pathways up through the stratigraphy as a result of cross-fault migration in regions of juxtaposed high permeability units. Accumulation is predicted in the synthetic fault block and in a highly permeable unit at the top of the model. Figure 8b incorporates fault-zone gouge and demonstrates that the synthetic fault block and highly permeable unit at the top of the model are now sealed off from the flow pathway as a result of this gouge.

## Examples of integrated 4D structural modelling with fluid flow simulation

To demonstrate the effectiveness of the integrated methods presented here, the importance of structural geometries in hydrocarbon migration and significance of an integrated approach in risk-driven analysis, two models have been constructed from actual geological data. One model represents part of the Moab Fault, Utah, USA constructed primarily from field data, while the second represents a faulted Rotleigendes prospect from the southern North Sea, constructed from the interpretation of 3D seismic data to produce horizon and fault surfaces.

The model of the Moab Fault (Fig. 9) covers approximately 140 $km^2$ of the Paradox Basin, southeastern Utah, USA, includes 22 km of the Moab Fault and associated splay faults, and is based on detailed outcrop mapping. The gently folded succession cut by the Moab Fault is represented by contrasting lithological units of clean sands and consolidated shales. The model consists of 14 surfaces in all fault blocks of the Moab Fault and associated splay faults. For clarity, only representative surfaces are shown in Figure 9.

The model from the southern North Sea is an exploration prospect, covering approximately 10 $km^2$, in which there is significant uncertainty regarding the petrophysical properties of parts of the stratigraphical sequence associated with the main reservoir. Two surfaces are modelled: the top Rotleigendes reservoir and the top of the overlying Zechstein Formation (Fig. 10). One major fault is shown in the model, down-throwing to the west, with two minor faults forming a small antithetic fault block in the hanging wall.

### *Fault-controlled secondary migration pathways*

Field studies of the Moab Fault and associated faulted sequences indicate that the Moab Anticline and footwall closures to the Moab Fault are breached and subsequently exhumed hydrocarbon reservoirs (Garden *et al.* 2001). The widespread iron oxide reduction of sandstones is widely inferred to indicate the passage of a reducing hydrocarbon-related fluid (Chan *et al.* 2000; Garden *et al.* 2001).

1D, 2D and 3D analyses of the present day fault-seal capacity along the Moab Fault demonstrate that juxtaposition of lithologies across the fault and its associated splays provides an effective seal to hydrocarbons in reservoir sequences in both the footwall and hanging wall (Foxford *et al.* 1998; Clarke *et al.* 2005*a*). Furthermore, from study of the argillaceous fraction of the Moab Fault zone, Foxford *et al.* (1998) concluded that much of the fault zone, particularly the area around the Arches Anticline, contains sufficient argillaceous material (>20%) to provide a seal for hydrocarbons. Further north, as displacement decreases, insufficient gouge exists and potential sand-on-sand leak points indicated by juxtaposition are still present, especially in the vicinity of splay faults.

To demonstrate the effect of this complex fault zone geometry on present day and palaeomigration pathways around the Moab Fault, cross-fault juxtaposition and 3D SGR have been included in the model and bulk permeability values have been assigned to each unit,

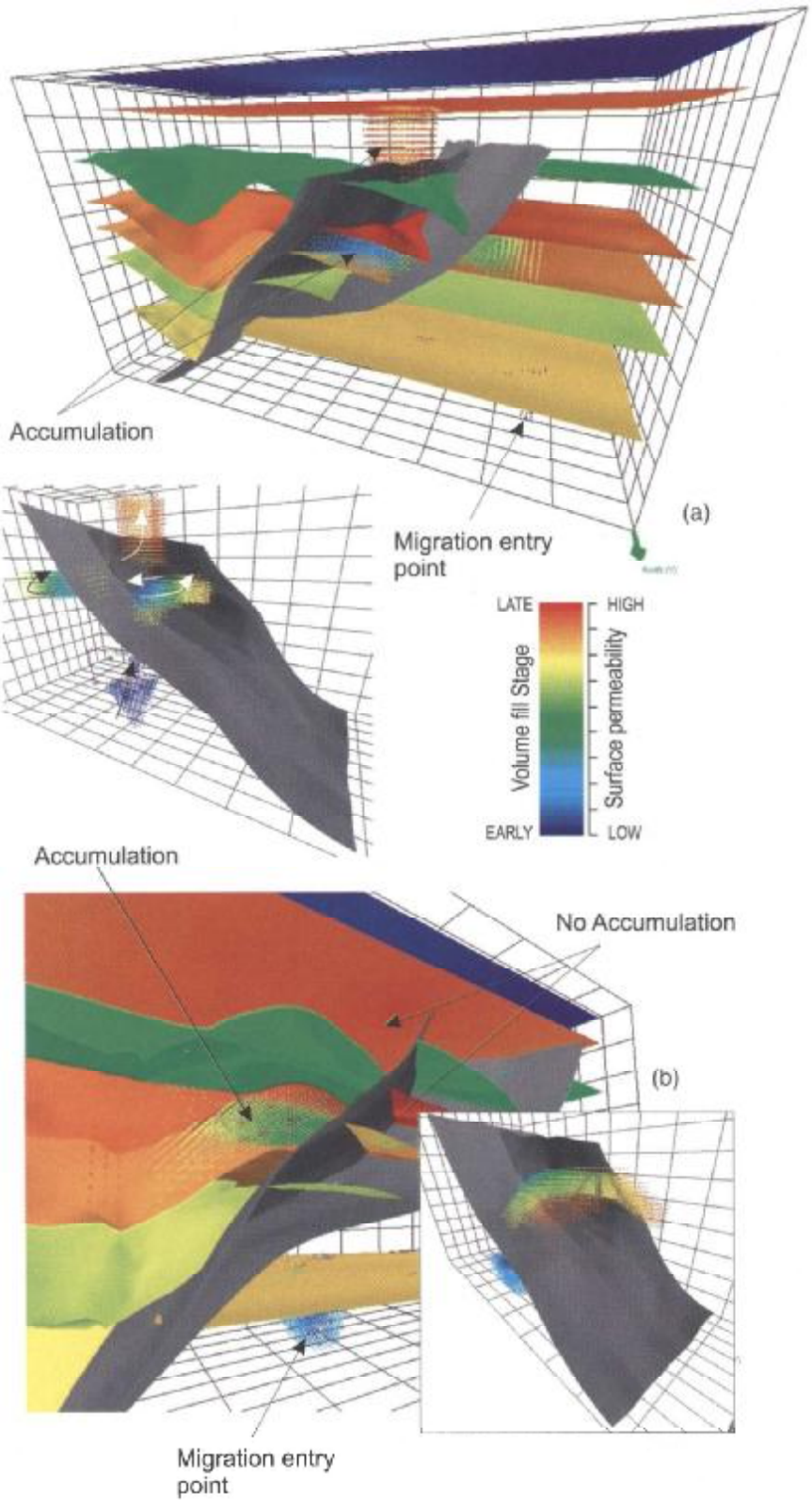


**Fig. 8.** A simple, synthetic model representing several square kilometres of seven lithological units and two faults. (**a**) Flow pathways are controlled by permeability variations within and between lithological units and juxtapositions across the faults. Migration through the succession is by repeated cross-fault and up-dip flow. Pooling occurs in one unit of the synthetic fault block and in the second highest unit. (**b**) Synthetic shale contents, and restoration-derived displacement vectors are used to calculate 3D shale gouge ratio and the effects of this are included in the flow model. Migration pathways bypass the synthetic fault block trap, which is sealed by fault zone gouge.

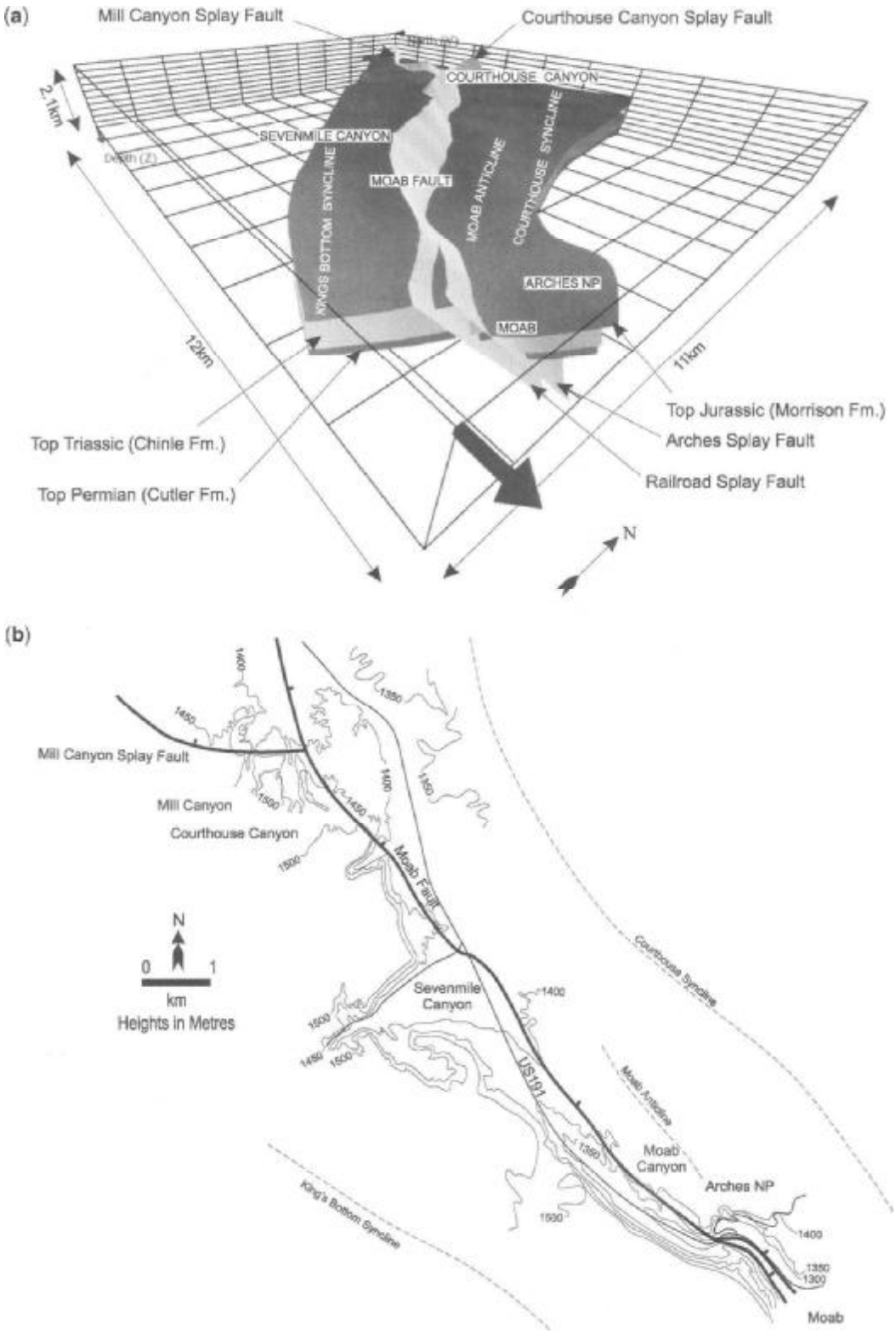


**Fig. 9.** (**a**) The numerical model of the Moab Fault. The full model consists of the fault surfaces and 14 stratigraphical surfaces in the footwall and hanging wall. For clarity only selected key surfaces are shown here. (**b**) Simplified topography and geology of the Moab region, Utah, USA, represented by the model.

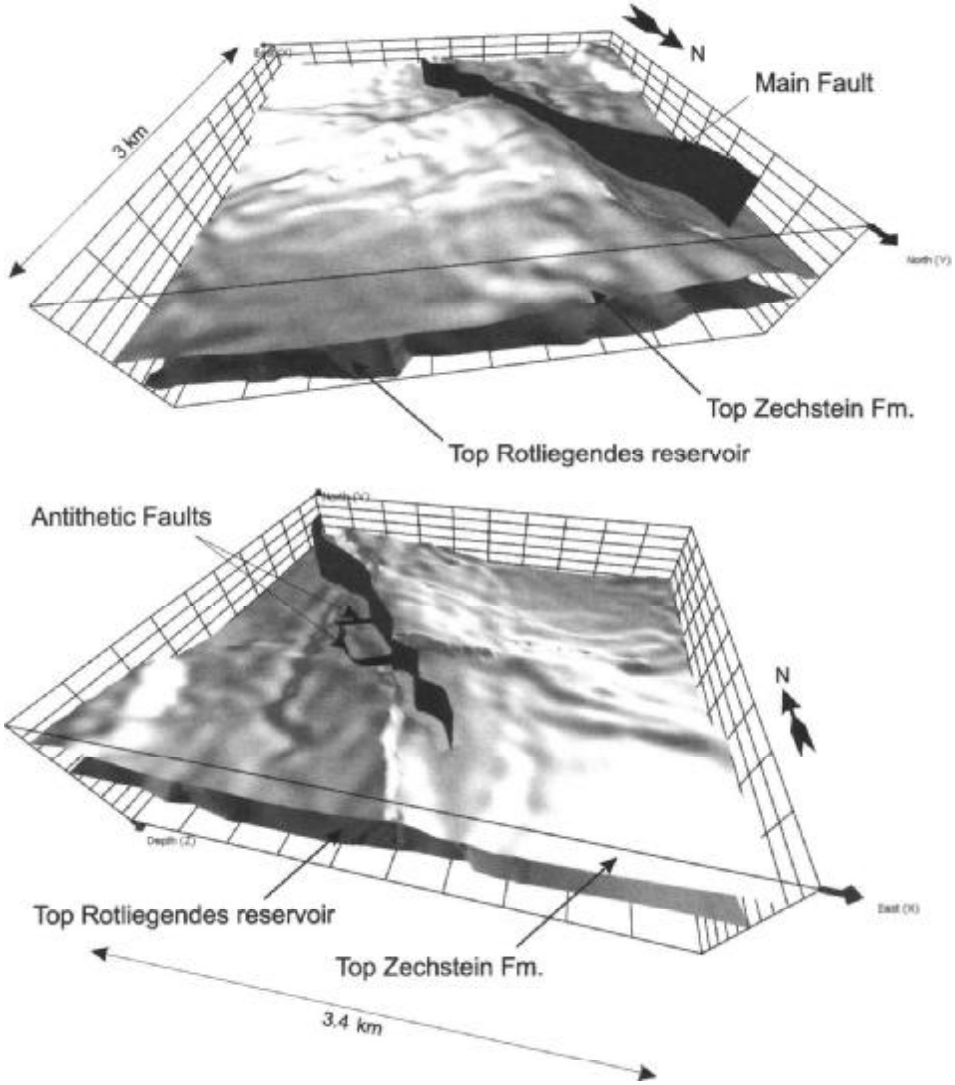


**Fig. 10.** The numerical model of the southern North Sea example. The model consists of two surfaces, representing the top of the Roteigendes reservoir and the top of the overlying Zechstein (seal) Formation. One major fault and two minor antithetic faults cut the model.

conditioned by normal distributions with standard deviations that reflect their heterogeneity. A series of realizations for both the present day and palaeostructural configurations (at 30 and 70% restoration) are modelled with different hydrocarbon migration entry points for each scenario.

The first series of present day realizations demonstrates migration pathways through the Moab Fault model in the absence of a fault zone, with migration pathways being controlled by cross-fault juxtapositions alone (Fig. 11). In these scenarios, flow pathways from a northeastern migration entry point encounter juxtaposed porous reservoir units in the region of Courthouse Canyon and leak across the fault towards the footwall high (Fig. 11a). Migration windows though the westerly splay are present in the absence of gouge and lead to an accumulation within the northern fault block (Fig. 11b). Choice of alternative migration entry points as an additional variable, results in flow pathways exploiting additional juxtaposed leakage windows. Figure 11c illustrates flow pathways from a migration entry point defined in the hanging wall around Sevenmile Canyon. The Moab Anticline trap spills to the south, and flow pathways develop across the fault to the footwall via juxtaposed reservoir units across the two synthetic splays.

For the second series of migration realizations based on present day structural geometries (Fig. 12), 3D shale gouge is incorporated into the model. Piercing-point restoration of the

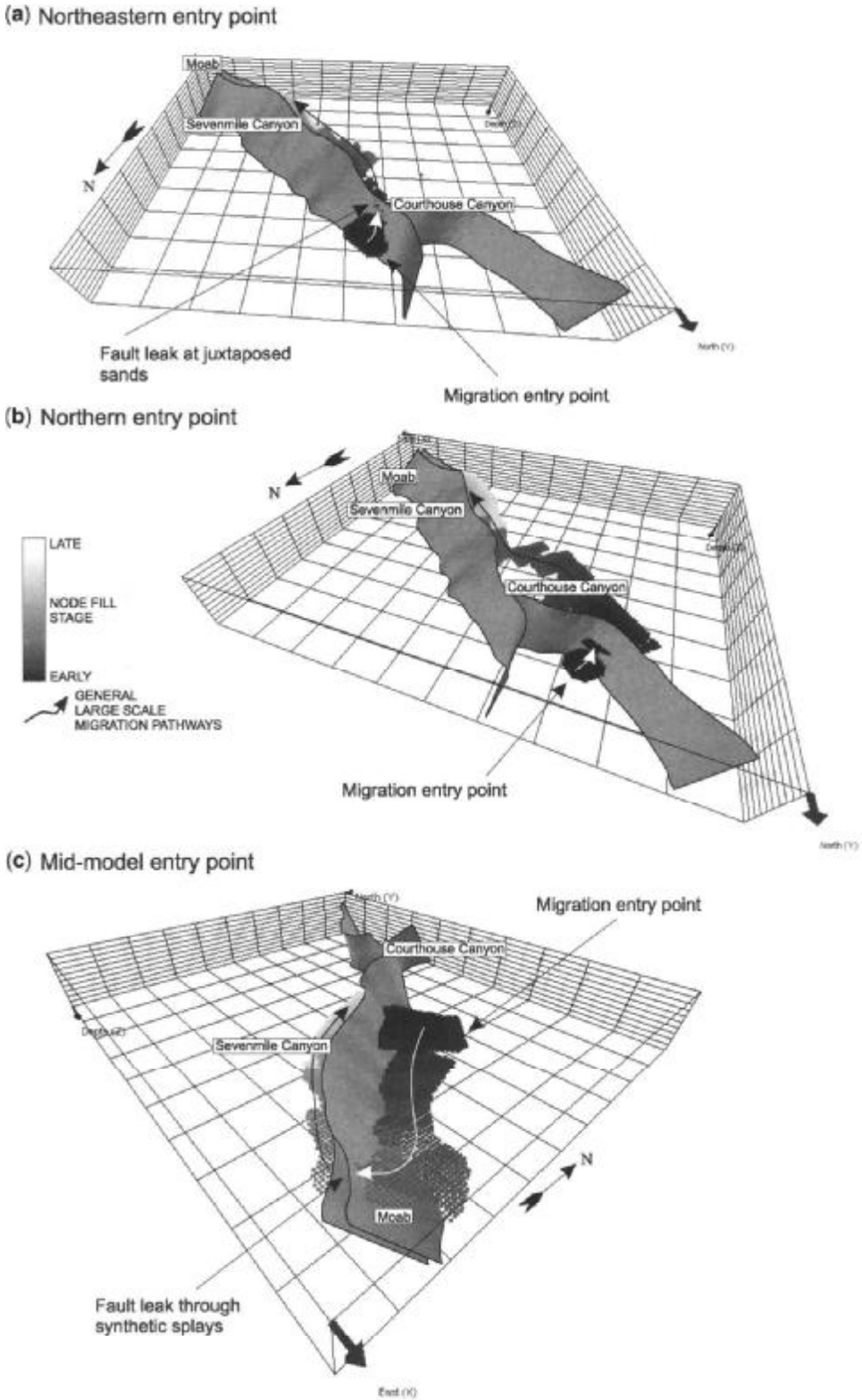


**Fig. 11.** Predicted migration pathways through the Moab Fault model controlled by cross-fault juxtaposition and present day structural geometries. (**a**) From a northeasterly migration entry point, juxtaposed porous sandstones at Courthouse Canyon provide migration pathways across the fault. (**b**) From a northern migration entry point pathways exist to the footwall across the westerly splay, and (**c**) from a migration entry point in the hanging wall, around Sevenmile Canyon, flow pathways exist to the south and across the fault via juxtaposed porous sandstones at the southern fault splays. Arrows show general trends of migration pathways.

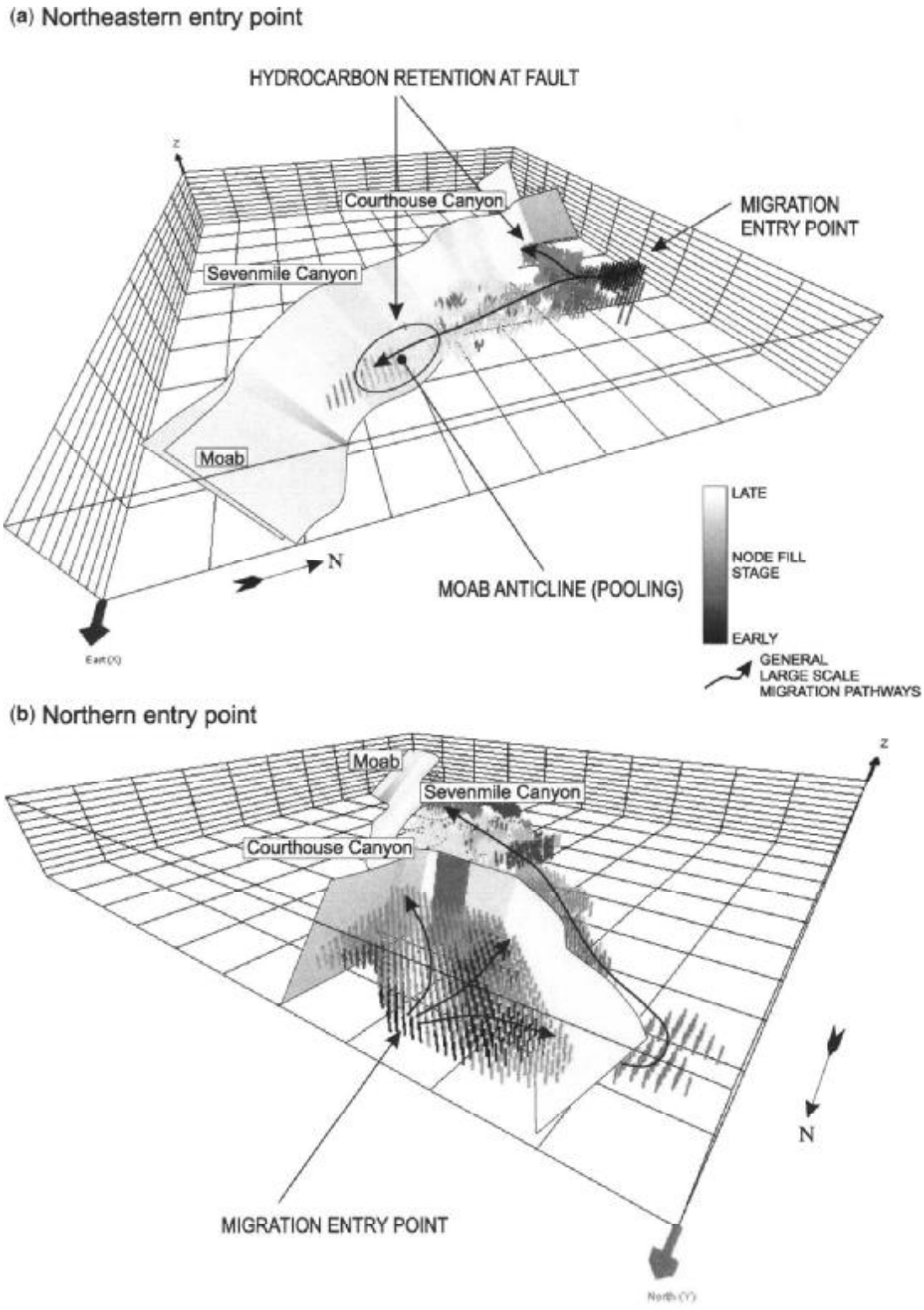


**Fig. 12.** Predicted migration pathways through the Moab Fault model for present day structural geometries and in the presence of a fault-zone gouge. (**a**) From a northeasterly migration entry point, migration pathways exist up-strata and up-dip to the structural high in the Moab Anticline, sealed at the fault by juxtaposition relationships and argillaceous gouge. (**b**) From a northerly migration entry point, the westerly splay of the Moab Fault still leaks and provides migration pathways to the structural high in the footwall around Sevenmile Canyon. Arrows show general trends of migration pathways.

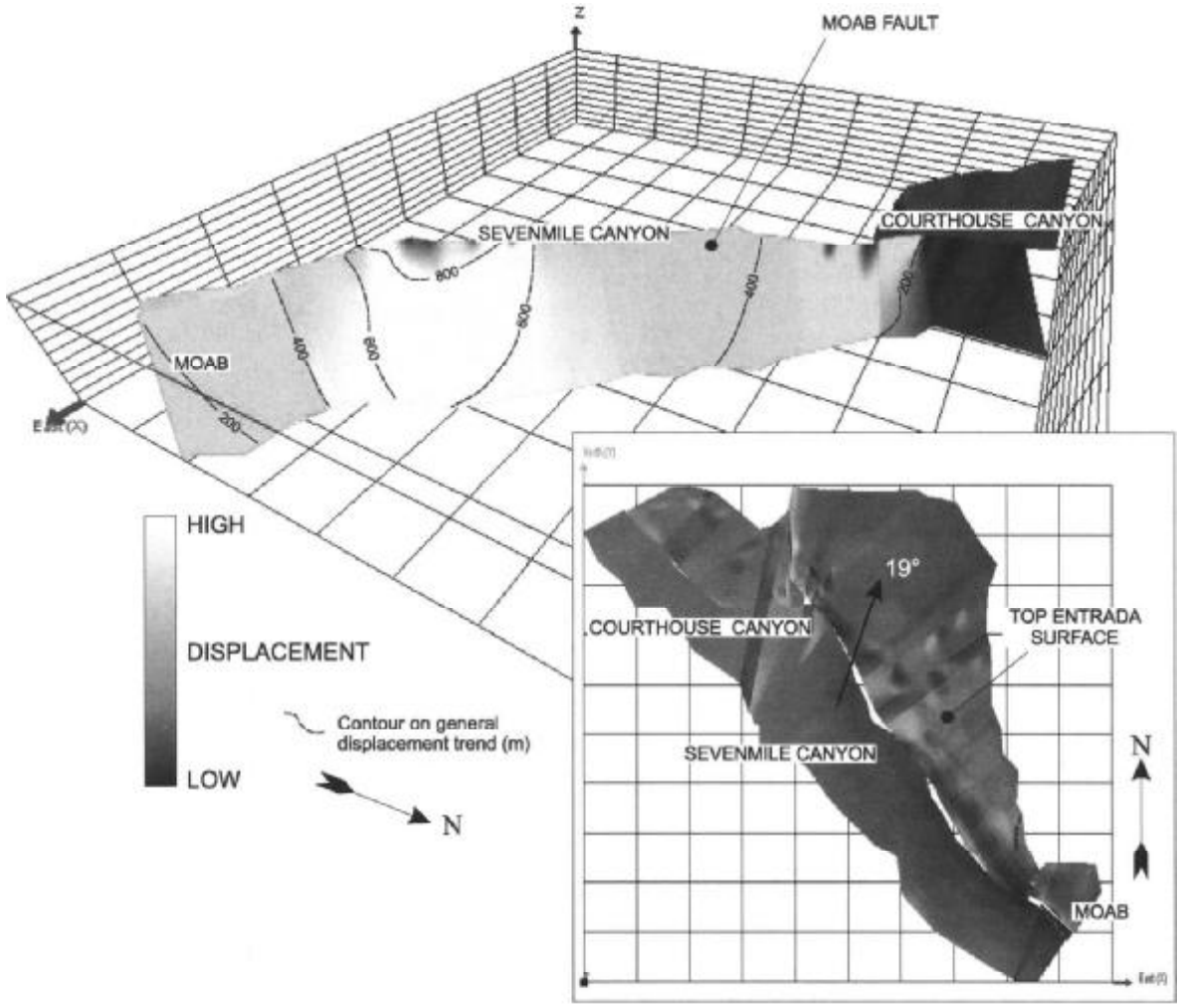


**Fig. 13.** (**a**) Predicted displacement gradient on the Moab Fault resulting from best-fit piercing point restoration. (**b**) Restored top Jurassic (Entrada Formation) surface using the piercing point-derived displacement gradient and predicted slip azimuth of 19°.

hanging wall (Fig. 13) indicates a slip azimuth of 19° and a displacement gradient that varies from a maximum around the footwall high at Sevenmile Canyon, reducing both northwards and southwards. Using these displacement vectors, the vertical shear chevron construction and the argillaceous contents of the faulted stratigraphy, the 3D distribution of argillaceous material within the fault zone has been predicted. From a northeastern entry point, an accumulation develops in the Moab Anticline, sealed to the east by the Moab Fault (Fig. 12a). This is consistent with field evidence (Garden *et al.* 2001), suggesting that the northeastern splay of the northern section of the Moab Fault, and the main fault around Sevenmile Canyon, have the capacity to seal cross-fault migration from a northeastern source and prevent flow into the footwall. To investigate whether the western splay of the fault has the capacity to seal cross-fault migration in the presence of gouge, another present day realization (Fig. 12b) was initialized from a northern migration entry point, within the fault block bounded by the two splays. Accumulation now takes place within the fault block until a leak point in the westerly splay is encountered. Migration progresses up-dip of the footwall to accumulate in the footwall high around Sevenmile Canyon, also consistent with field evidence of extensive iron oxide reduction. The presence of fault-zone gouge on the westerly splay is insufficient to cause total sealing of the fault.

In these two simulation scenarios flow pathways are controlled by the combined effects of cross-fault juxtapositions, fault zone properties and the structural geometries of the present day fault architecture. However, migration may have been contemporary with faulting, an uncertainty that can be investigated with structural

restoration. Using the derived displacement vectors, the hanging wall has been restored by 30% and 70% and potential flow pathways resulting from the interaction of restored palaeogeometries and cross-fault juxtaposition explored. A 30% restoration (Fig. 14a) is insufficient to juxtapose reservoir units around the footwall high and migration from a hanging wall entry point follows flow pathways defined by regional structural geometry (largely as described in Fig. 11c). However, at 70% restoration (Fig. 14b) juxtaposition of porous reservoir units across the fault in the region of the footwall high creates cross-fault pathways through the fault. Accumulations form in the hanging wall and leak to the footwall, eventually spilling back to the hanging wall to the south. The resulting migration pathways and accumulations are dramatically different from model realizations at full present day deformation, but in this case, not fully consistent with the migration pathways and accumulations inferred from field data (Chan *et al.* 2000; Garden *et al.* 2001). Moreover, the charging histories of the modelled accumulations are reversed from those predicted with both present day geometries and geometries predicted from lesser amounts of restoration.

### *Fault-controlled field-scale migration*

The exploration prospect model from the southern North Sea covers a much smaller area than the Moab Fault model. At this smaller scale, migration pathways are representative of intra-reservoir migration, charging histories and fault block compartmentalization. In this setting, integrated fault seal and hydrocarbon flow modelling can be used to risk specific accumulations within individual fault compartments in the light of uncertainties in the input data.

The geometry of the southern North Sea prospect suggests a potential trap in the footwall of the major fault, sealed by juxtaposition of the Rotliegend reservoir against the overlying Zechstein sequence across the fault. However, there is uncertainty concerning the extent of fracturing (and therefore the permeability) of the Zechstein sequence that is likely to affect the location and volume of hydrocarbon accumulations. Two realizations, integrating structural modelling, fault-seal analysis and hydrocarbon migration pathway prediction have been performed, with the Zechstein defined as either completely impermeable or completely permeable. The sealing capacity of the major fault is different in each scenario and accumulations of different sizes and locations are predicted for the two scenarios. With the unit defined as non-fractured (Fig. 15a), the footwall trap is sealed at the fault by lithological juxtaposition and accumulation takes place in the footwall high. With the unit defined as fractured (Fig. 15b), cross-fault flow results in a smaller footwall trap and additional hanging wall trap within the antithetic fault block. The speed and integrated nature of the approach presented can be exploited to further investigate this problem. In Figure 15c, 200 realizations, each with a different permeability (degree of fracturing) for the Zechstein unit, have been combined. Accumulations are ranked by the number of times each cell fills and therefore the risk associated with each trap location and volume.

## Discussion

The realizations presented here of synthetic and actual geological example models demonstrate both the viability and significance of an integrated approach to basin modelling that incorporates structural geometry, fault seal and hydrocarbon migration. In examples using real geological data, it is apparent that migration pathways, trapped hydrocarbon accumulations and their dependence on the 3D sealing properties of faults can become extremely complex, and difficult to interpret. Potential traps are often a result of the interaction of 3D sealing capacity on the fault surface and the structural geometry of the faulted blocks local to the fault surface contemporary with migration. It is not simple to visually determine potential seal and leak points or trapping geometries from an analysis of a fault seal map or fault plane projection alone. The ability to visualize fault geometries in 3D increases the ease of interpretation and is a major advantage of the true 3D approach to fault seal and migration modelling.

Secondly, the inclusion of structural restoration and deformation within an integrated 4D model allows flow pathways to be predicted at temporal stages other than present day. These pathways may be significantly different to those of the present day in terms of fault linkages, leakage points and the geometry of carrier beds. Earlier structural geometries may be critical to both migration pathways and the distribution of trapped hydrocarbons. The ability to model flow pathways through geologically realistic palaeogeometries (at least for normal faults) is a significant advance on current modelling capabilities.

In the models presented here we have employed 3D structural restoration techniques to determine best-fit deformation vectors and predict subsequent hanging wall geometries

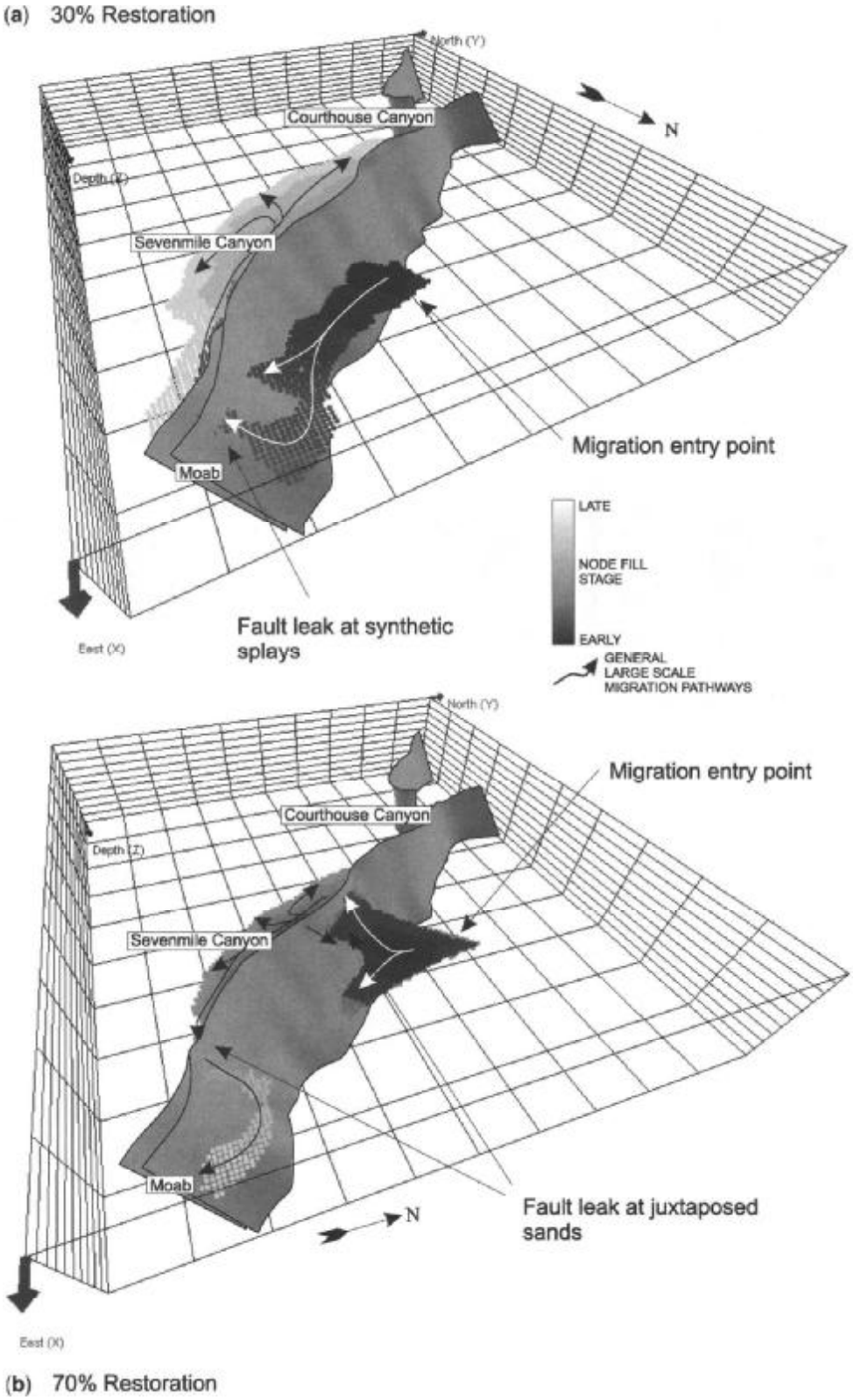


**Fig. 14.** Migration pathways through the Moab Fault at temporal stages representing (**a**) 30% restoration and (**b**) 70% restoration. At 30% restoration, pathways are similar to those at present day. At 70% restoration sandstones are juxtaposed across the fault and provide migration pathways from hanging wall to footwall and subsequently back to the hanging wall in the south of the model.

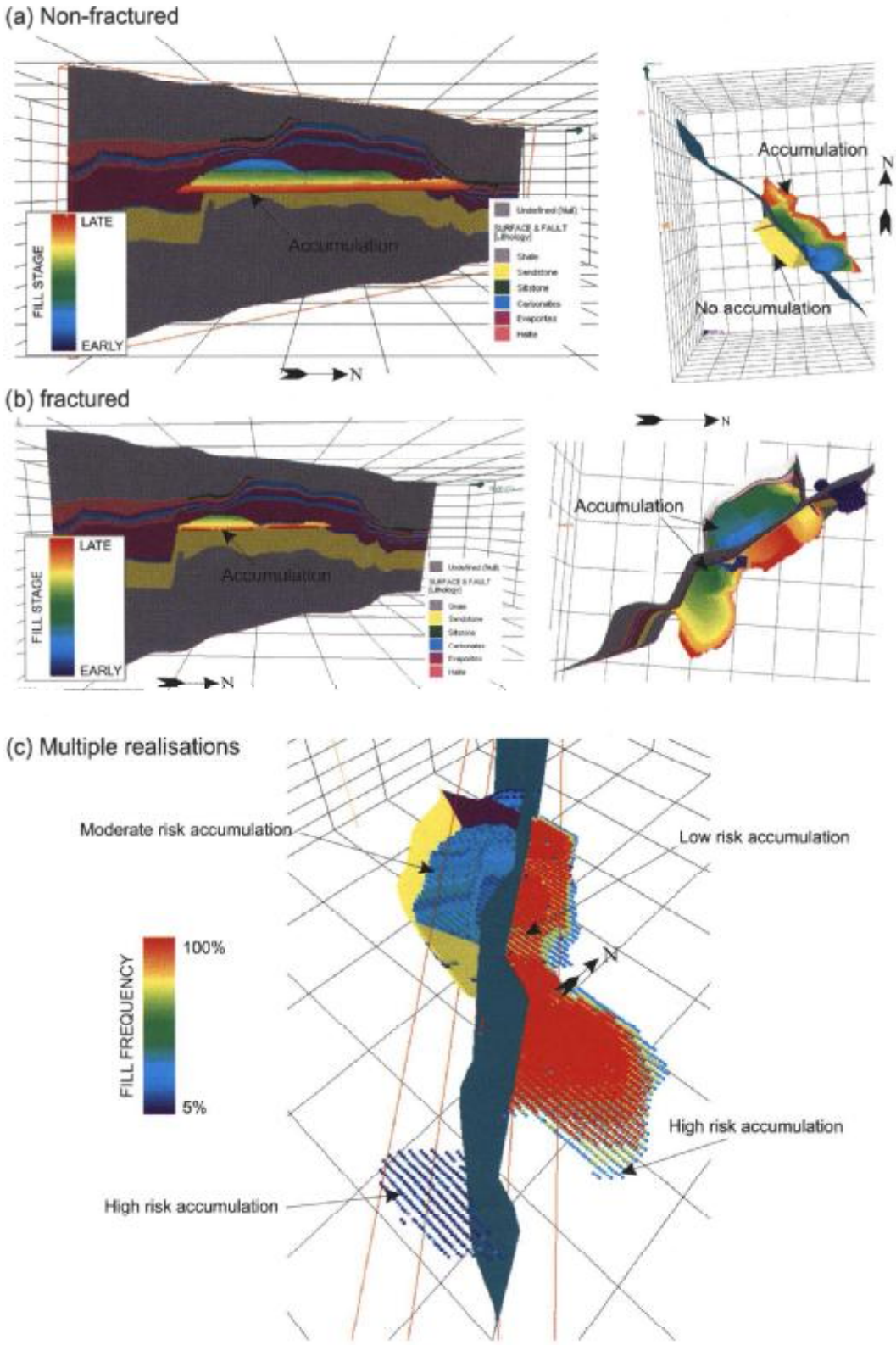


**Fig. 15.** Migration pathways through the southern North Sea model. (**a**) With the Zechstein defined as completely non-fractured, a large accumulation is predicted in the footwall. (**b**) With the Zechstein defined as completely fractured, cross-fault migration pathways exist to the small antithetic fault block and result in a smaller accumulation in the footwall and an accumulation in the antithetic fault block. (**c**) Comparison of 200 realizations of the southern North Sea model. In each realization the permeability of the Zechstein is slightly different. The resulting accumulations are coloured by their frequency of fill (likelihood of occurrence) and allow risking of the trap volumes and locations.

using fault-bend fold methodologies (chevron/inclined shear constructions). A third key point of the 4D integrated hydrocarbon flow modelling methodology presented is that it is independent of the structural restoration technique employed. Chevron and inclined shear constructions are particularly useful because they generate predictable hanging wall geometries that correlate well with observations of extensional regimes, and they also preserve rock volume with deformation. However, they rely on well-defined interpretations of structural geometry and they do not reproduce internal mechanisms that produce hanging wall deformation nor model subsequent strain effectively (Williams & Chapman 1983). These processes can affect the petrophysical properties of the rock mass and thus subsequent migration pathways. Furthermore, fault-bend-fold methodologies assume a static footwall and do not model isostatic changes in fault block geometry. It follows that the 3D restoration techniques employed here are applicable on the prospect, trap or similarly restricted spatial exploration scale, where isostatically-driven geometrical changes can be largely ignored, but at the larger basin scales (i.e., hundreds of $km^2$) these effects will be significant and are likely to impact migration pathways (Huggins *et al.* 2006).

Fourthly, by integrating fault seal and structural geology with a numerically fast migration modelling code in 4D, it is possible to test assumptions and uncertainties in the geological data or concept that is being developed. In the Moab Fault model presented here, for example, the presence or absence of fault zone gouge, the timing of migration with respect to deformation, and the assumed migration entry point significantly effect migration pathways. In the southern North Sea prospect, uncertainties related to the properties of the stratigraphical succession have a significant effect on flow and accumulations. The IP-driven approach to hydrocarbon migration through faulted structures is ideal for testing assumptions and uncertainties such as these. The Moab Fault model contains 950,000 volume cells and runs in *c.* 3 min whilst the southern North Sea model contains 5,000,000 cells and runs in *c.* 7 min. These short simulation times render risk-driven modelling approaches to hydrocarbon migration analysis practical. Multiple realizations, each with varied inputs (either deterministic or stochastic) can be used to determine the sensitivity of particular traps to uncertainties in poorly constrained input data. 'What if?' questions can thus be posed to investigate potential simulation outcomes or examine the sensitivity of the model to specific input variables. Comparison of results can be used to risk particular scenarios, and thus exploration prospects. In the southern North Sea model for example, the uncertain permeability of one particular unit has a significant impact on the location and size of predicted accumulations. By performing 200 realizations, each with a different permeability for this unit, it is possible to combine results and risk not only the location but also the potential size of each predicted trap. The combined realizations on this model indicate that a significant proportion of the volume of the footwall trap is very high risk as it depends on the Zechstein being completely impermeable (not fractured in this case); only the topmost fraction is low risk. By contrast, the antithetic fault block trap is moderate risk, as its occurrence and volume is largely independent of the permeable state of the Zechstein unit and the accumulation is only absent if the Zechstein is completely impermeable.

We have demonstrated the integrated 3D application of two aspects of fault seal: juxtaposition and argillaceous gouge. These are by no means the only seal characteristics of faults. Both factors are commonly the dominant sealing mechanisms, but other factors such as diagenetic alteration may contribute to fault seal. These factors have not been simulated in the examples shown here. Additionally, the sealing capacity of argillaceous gouge, predicted from SGR, does not account for entrained blocks within the fault zone and is likely to be affected by case-specific geological factors (e.g., host rock mineralogy and confining pressure). The statistical nature of the IP code implemented here does not facilitate modelling of these factors at present. Furthermore, the methods currently developed may not be appropriate for fault-seal analysis in high fluid pressure settings where mechanisms of seal failure and fluid migration are likely to be different (e.g., hydrocfracturing or seismic pumping/valving; Sibson 1981).

## Conclusions

The key to incorporating structural restoration in basin simulators is to represent basin geometry as realistic structural and litho-stratigraphical surfaces in 3D space. As faults and horizon discontinuities (such as unconformities) are the major architectural components of a basin, these elements should form the initial building blocks of the basin model if the basin geometry through time is to be represented. The integrated approach to restoration of basin architecture and hydrocarbon migration simulation presented here provides a fast method of determining flow pathways through structurally complex,

exploration prospect scale basins. It integrates 3D structural restoration techniques, 3D fault-seal analysis, the 3D geometry and variations in geology of a sedimentary basin, to predict potential seal and leak points at fault surfaces, highlighting potential trapping geometries in faulted sequences. This approach increases the resolution at which migration pathways can be analysed, and reduces the inherent assumptions in applying these techniques in isolation or with fewer dimensions (Harper & Lundin 1987). The integration of migration pathway prediction into the structural model provides a fast and effective tool for detecting and evaluating such seals, leak points and potential traps. Moreover, migration through restored palaeogeometries can be investigated.

The simplicity and thus speed of the technique makes it ideally suited to a risk-driven approach. Given a 3D model of the basin, structural geometries, fault seal and potential migration pathways and accumulations can be ascertained using this technique. The sensitivity of these potential traps to variations in geological parameters such as the stratigraphy (e.g., variations in sediment type), migration entry point locations, or petrophysical properties (e.g., clay content of sands, entry pressures or permeability) can be determined quickly from multiple realizations of the same model. 'What if?' questions can be posed to investigate potential simulation outcomes or examine the sensitivity of the model to specific input variables. Those potential traps or trap regions that show a high dependence on poorly constrained input parameters are high risk and can be discarded as potential prospects. In this way, the rapid simulation technique and integrated restoration-migration modelling approach presented forms a first pass to filter high-risk prospects prior to time-consuming Darcy flow-based simulation.

The authors wish to thank BG Group for permission to publish, and the Natural Environment Research Council and BG Group for funding this work (NERC grant reference GRC/98/280). S. Buiter, N. Cardozo and P. Nadeau all improved the manuscript with their valuable comments. The basin modelling, structural restoration, 3D fault seal and hydrocarbon migration simulations presented here were performed using software developed at Keele University. In addition to the authorship of this paper, the contributions of many other members of the School of Earth Sciences and Geography at Keele University, particularly P. Greatbatch and D. Wilde, are gratefully acknowledged.

## References

ALLAN, U. S. 1989. Model for hydrocarbon migration and entrapment within faulted structures. *AAPG Bulletin*, **73**, 803–811.

BERG, R. R. 1975. Capillary pressures in stratigraphic traps, *AAPG Bulletin*, **59**, 939–956.

BOND, G. C. & KOMINZ, M. A. 1984. Construction of tectonic subsidence curves for the early Paleozoic miogeocline, southern Canadian Rocky Mountains: implications for subsidence mechanisms, age of breakup, and crustal thinning. *Bulletin of the Geological Society of America*, **95**, 155–173.

BURLEY, S. D., CLARKE, S.M. *ET AL.* 2000. New insights on petroleum migration from the application of 4D basin modelling in oil and gas exploration. *Journal of Geochemistry Exploration*, **70**, 465–470.

CARRUTHERS, D. J. 2003. Modelling of secondary petroleum migration using invasion percolation techniques. *In*: DUPPENBECKER, S. & MARZI, R. (eds) Multi-dimensional basin modelling. *AAPG Discovery Series*, **7**, chpt 3.

CHAN, M. A., PARRY, W. T. & BOWMAN, J. R. 2000. Diagenetic oxides and fault-related fluid flow in Jurassic sandstones, southeastern Utah. *AAPG Bulletin*, **84**, 1281–1310.

CLARKE, S. M., WILLIAMS, G. D. & BURLEY, S. D. 2005*a*. A three-dimensional approach to fault seal analysis: fault block juxtaposition and argillaceous smear modelling. *Basin Research*, **17**, 269–288.

CLARKE, S. M., BURLEY, S. D. & WILLIAMS, G. D. 2005*b*. Dynamic fault seal analysis and flow pathway modelling in three-dimensional basin models. *In*: DORE, A. G. & VINING, B. A. (eds) *Petroleum Geology: North-west Europe and Global Perspectives* (PGC6), Geological Society, London, Miscellaneous Titles.

COBBOLD, P. R. 1979. Removal of finite strain using strain trajectories. *Journal of Structural Geology*, **1**, 67–72.

COWAN, G., BURLEY, S. D. *ET AL.* 1999. Oil and gas migration in the Sherwood Sandstone of the East Irish Sea Basin. *In*: FLEET, A. J. BOLDY & S. A. R. (eds) *Petroleum Geology of North West Europe*: Proceedings of the 5th Conference of the Geological Society, London.

DAHLSTROM, C. D. 1969. Balanced cross sections. *Canadian Journal of Earth Science*, **6**, 743–757.

FOXFORD, K. A., GARDEN, I. R., GUSCOTT, S. C., BURLEY, S. D., LEWIS, J. J. M., WALSH, J. J. & WATTERSON, J. 1996. The Field Geology of the Moab Fault. *In*: HUFFMAN, A. C., LUND, W. R. & GODWIN, L. H. (eds) *Geology and Resources of the Paradox Basin.* Special Symposium, Utah Geological Association and Four Corners Geological Society Guidebook, **25**.

FOXFORD, K. A., WALSH, J. J., WATTERSON, J., GARDEN, I. R., GUSCOTT, S. C. & BURLEY, S. D. 1998. Structure and Content of the Moab Fault Zone, Utah, USA and its Implications for fault seal prediction. *In:* JONES, G., FISHER, Q. J. & KNIPE, R. J. (eds) *Faulting, Fault Sealing and Fluid Flow in Hydrocarbon Reservoirs.* Geological Society, London, Special Publications, **147**, 87–103.

FRISTAD, T., GROTH, A., YEILDING, G. & FREEMAN, B. 1997. Quantitative fault seal prediction: a case study from Oseberg Sud. *In*: MOLLER, P. &

KOESTLER, A. G. (eds) *Hydrocarbon Seals: Importance for Exploration and Production.* NPF, Special Publications, **7**, 107–124.

GARDEN, R. C., GUSCOTT, S. C., BURLEY, S. D., FOXFORD, K. A., WALSH, J. J. & MARSHALL, J. 2001. An exhumed palaeo-hydrocarbon migration fairway in the Entrada Sandstone of SE Utah, USA. *Geofluids*, **1**, 195–213.

GIBBS, A. D. 1983. Balanced cross sections from seismic sections in areas of extensional tectonics. *Journal of Structural Geology*, **5**, 153–160.

GIBSON, R. G. 1994. Fault zone seals in siliclastic strata of the Columbus Basin, offshore Trinidad. *AAPG Bulletin*, **78**, 1372–1385.

GILES, M. R., INDRELID, S. L. & JAMES, D. M. D. 1998. Compaction – the great unknown in basin modelling. *In*: DUPPENBECKER, S. J. & ILIFFE, J. E. (eds) *Basin Modelling: Practice and Progress*, Geological Society, London, Special Publications, **141**, 15–43.

GRATIER, J. P., GUILLIER, B. & DELORME, A. 1991. Restoration and balance of a folded and faulted surface by best-fitting of finite elements: principle and applications. *Journal of Structural Geology*, **13**, 111–115.

HANTSCHEL, T., KAUERAUF, A. I. & WYGRALA, B. 2000. Finite element analysis and ray trace modelling of petroleum migration. *Marine and Petroleum Geology*, **17**, 815–820.

HARPER, T. R. & LUDIN, E. R. 1997. Fault seal analysis: reducing our dependence on empiricism. *In*: MOLLER, P. & KOESTLER, A. G. (eds) *Hydrocarbon Seals: Importance for Exploration and Production.* NPF, Special Publications, **7**, 149–165.

HUGGINS, P. BURLEY, S. D., SYLTA, O., TOMMERAS, A., Bland, S., KAPE, S. & KUSZNIR, N. 2006. Structural restoration techniques in 3D basin modelling: implications for hydrocarbon migration and accumulation. *Marine and Petroleum Geology*. In press.

ILLFE, J. E. & DAWSON, M. R. 1996. Basin modeling history and predictions. *In*: GLENNIE, K. & HURST, A. (eds) *AD1995: NW Europe's Hydrocarbon Industry*. Geological Society, London, Special Publications, 83–105.

JOHANNESEN, J., HAY, S. J., MILNE, J. K., JEBSEN, C., GUNNESDAL, S. C. & VAYSSAIRE, A. 2002. 3D oil migration modelling of the Jurassic petroleum system of the Statfjord area, Norwegian North Sea. *Petroleum Geoscience*, **8**, 37–50.

KING, P. R., BULDYREV, S. V. *ET AL.* 2001. Predicting oil recovery using percolation theory. *Petroleum Geoscience*, **7**, 105–107.

KUSZNIR, N. J., ROBERTS, A. M. & MORLEY, C. 1995. Forward and reverse modelling of rift basin formation. *In*: LAMBAISE J. (ed.) *The Hydrocarbon Habitat of Rift Basins*, Geological Society, London, Special Publications, **88**, 3–56.

LARTER, S. P., TAYLOR, M., CHEN, B., BOWLER, P., RINGROSE, P. & HORSTAAD, I. 1996. Secondary migration – visualizing the invisible – what can geochemistry do? *In*: GLENNIE, K. & HURST, A. R. *NW Europe's Hydrocarbon Industry*, Geological Society, London, Special Publications, 137–143.

MANN, U., HANTSCHEL, T., SCHAEFER, R. G., KROOS, B., LEYTHAEUSER, D., LITTKE, R. & SACHSENHOFER, R. F. 1997. Petroleum migration: mechanisms, pathways, efficiencies and numerical simulations. *In*: WELTE, D. H., HORSFIELD, B. & BAKER, D. R. (eds) *Petroleum and Basin Evolution.* Springer, 403–509.

MANZOCCHI, T., WALSH, J. J., NELL, P. & YEILDING, G. 1999. Fault transmissibility multipliers for flow simulation models. *Petroleum Geoscience*, **5**, 53–63.

MCKENZIE, D. P. 1978. Some remarks on the development of sedimentary basins. *Earth Planetary Science Letters*, **40**, 25–32.

MEAKIN, P., FEDER, J., FRETTE, V. & JOSSANG, T. 1992. Invasion percolation in a destabilizing gradient. *Physical Reviews* A, **46**(6), 3357–3368.

MEAKIN, P., WAGNER, G., VEDVIK, A., AMUNDSEN, H., FEDER, J. & JOSSANG, T. 2000. Invasion percolation and secondary migration: experiments and simulations. *Marine and Petroleum Geology*, **17**, 777–795.

MELLO, U.T. & HENDERSON, M. E. 1997. Techniques for including large deformations associated with salt and fault motion in basin modeling. *Marine and Petroleum Geology*, **14**, 551–564.

MEREDTIH, D. J. & EGAN, S. S. 2002. The geological and geodynamic evolution of the Eastern Black Sea Basin: insights from 2-D and 3-D tectonic modelling. *Tectonophysics*, **350**, 157–179.

PATERSON, L., PAINTER, S., KNACKSTEDT, M. A. & PINCZEWSKI, W. V. 1996. Patterns of fluid flow in naturally heterogeneous rocks. *Physica A*, **233**, 619–628.

RICHARDS, A. J. 2000. *An integrated approach to three-dimensional modelling of sedimentary basins.* PhD. thesis, Keele University.

ROBERTS, A. M., KUSZNIR, N. J., YIELDING, G. & STYLES, P. 1998. 2D flexural backstripping of extensional basins: the need for a sideways glance. *Petroleum Geoscience*, **4**, 327–338.

ROUBY, D., XIAO, H. & SUPPE, J. 2000. 3D restoration of complexly folded and faulted surfaces using multiple unfolding mechanisms. *AAPG Bulletin*, **84**, 805–829.

SCHOWALTER, T. T. 1979. Mechanics of secondary hydrocarbon migration and entrapment. *AAPG Bulletin*, **63**, 723–760.

SCHROEDER, F. W. & SYLTA, O. 1993. Modelling the hydrocarbon system of the North Viking Grabe. *In*: DORE *ET AL.* (eds) *Basin Modelling, Advances and Applications*, NPF Special Publication, **3**, 469–484.

SCHWARZER, S., HAVLIN, S. & BUNDE, A., 1999. Structural properties of invasion percolation with and without trapping: shortest path and distributions. *Physical Review*, E, **59**, 3262–3269.

SIBSON, R. H. 1981. Fluid flow accompanying faulting: field evidence and models. *In*: SIMPSON, D. W. & RICHARDS, P. G. (eds) *Earthquake Prediction: An Intenational Review*. American Geophysical Union, **4**, 593–603.

Sylta, Ø. 2002. Quantifying secondary migration efficiencies. *Geofluids*, **2**, 285–298.

SYMINGTON, W. A., GREEN, K. E., HUANG, J., POTTORF, R. J. & SUMMA, L. L. 1998. A multidisciplinary approach to modeling secondary migration: a Central North Sea example. *In*: DUPPENBECKER, S. J. & ILLIFE, J. E. *Basin Modelling, Practice and Progress.* Geological Society, London, Special Publications, **141**, 169–186.

THOMAS, M. M. & CLOUSE, J. A. 1995. Scaled physical model of secondary oil migration. *AAPG Bulletin*, **79**, 19–22.

VAN HINTE, J. E. 1978. Geohistory analysis-application of micropalaeontology in exploration geology. *AAPG Bulletin*, **62**, 201–222.

WAGNER, G., MEAKIN, P., FEDER, J. & JOSSANG, T. 1997. Buoyancy driven invasion percolation with migration and fragmentation. *Physica A*, **245**, 217–230.

WANGEN, M. 1997. Two-phase oil migration in compacting sedimentary basins modelled by the finite element method. *International Journal of Numerical and Analytical Methods in Geomechanics*, **21**, 91–120.

WELTE, D. H., HORSFIELD, B. & BAKER, D. R. 1997. *Petroleum and Basin Evolution – Insights From Petroleum Geochemistry, Geology and Basin Modelling.* Springer Verlag, Berlin, 535pp.

WELTE, D. S. H., Hantschel, T., WYGRALA, B. P., WEISSENBURGER, K. S. & CARRUTHERS, D. 2000. Aspects of petroleum migration modelling. *Journal of Geochemical Exploration*, **70**, 711–714.

WENDEBOURG, J. 2000. Modelling mulitcomponent petroleum migration in sedimentary basins. *Journal of Geochemical Exploration*, **70**, 651–656.

WILKINSON, D. & WILLEMSEN, J. F. 1983. Invasion percolation: a new form of percolation theory. *Journal Physics and Mathematics General*, **16**, 3365–3376.

WILLIAMS, G. D. & CHAPMAN, T. 1983. Strains developed in the hanging walls of thrusts due to their slip/propagation rate: a dislocation model. *Journal of Structural Geology*, **5**, 563–572.

WILLIAMS, G. D, KANE, S. J., BUDDIN, T. S. & RICHARDS, A. J. 1997. Restoration and balance of complex folded and faulted rock volumes: flexural flattening, jigsaw fitting and decompaction in three dimensions. *Tectonophysics*, **273**, 203–218.

YIELDING, G. 2002. Shale Gouge Ratio – calibration by geohistory. *In*: KOESTLER, A. G. H. & AMSTERDAM, R. (eds) *Hydrocarbon Seal Quantification.* Elsevier Science, 1–15.

# Rifting through a heterogeneous crust: insights from analogue models and application to the Gulf of Corinth

L. MATTIONI[1]*, L. LE POURHIET[1,2] & I. MORETTI[1]

[1]*Institut Français du Pétrole, Rueil Malmaison, France*

[2]*Laboratoire de Tectonique, Université Pierre et Marie Curie, Paris, France*

**Now at Beicip Franlab, Rueil Malmaison, France (luca.mattioni@beicip.fr)*

**Abstract:** We used analogue models to study the fault evolution produced by extension through a heterogeneous crust. In the experiments, the heterogeneous crust consisted of a gently dipping silicone layer surrounded by brittle material. The viscous silicone level simulates a weak, upper crustal nappe stack that formed during a previous phase of shortening. X-ray scanner facilities allowed us to acquire 3D images of the experimental models at regular time invervals and hence to study the fault pattern development and the location of the main depocenters during rifting. The experimental results show that the inherited weak nappe stack acts as a décollement and localizes deformation. In the early stages of extension a system of conjugate high-angle normal faults initiates close to the upper tip of the gently dipping silicone layer near the free surface and propagates upwards, resulting in an initial symmetrical graben configuration. Further extension results in (1) a progressive asymmetry of the rifted zone, due to migration of its right margin down the nappe, (2) a shift of the main depocentre downward along the décollement, and (3) the simultaneous activity of several normal faults within the rifted zone. When the pre-existing silicone layer is oblique to the extension, the normal faults develop in an en echelon array, with a strike intermediate between the azimuth of the gently dipping silicone layer and the extension direction. The experiments also show how rheological differences between areas with potential intracrustal weak layers and adjacent domains without décollement level can lead to significant differences in fault pattern, dimension and orientation of the rifted zone. Complete asymmetry of a rift and switches in fault dip direction between adjacent domains can be explained by the presence of pre-existing upper crustal heterogeneities.

In regions where extension affects a crust previously deformed by shortening, the recognition of the role exerted by inherited heterogeneities in controlling the subsequent crustal extensional deformation is now being increasingly appreciated (Stewart 1999).

Areas where extension has followed shortening are numerous: in eastern North America, for example, it is well documented that many Palaeozoic shortening-related structures were reactivated during subsequent northwest–southeast directed Triassic to Jurassic rifting (e.g., Olsen & Schlische 1990; Schlische *et al.* 2002, and references therein). In the Mediterranean area, the best examples of pre-existing orogens currently affected by extension are the central Apennines in Italy (e.g., Cooper & Burbi 1986; Lavecchia *et al.* 1987; Ghisetti *et al.* 1993) and the Hellenides in Greece (Jolivet 2001, and references therein).

Data from these and other areas clearly suggest that, among many important parameters, the thickness of weak layers and the inherited pre-rift structural architecture can play a pivotal role on the subsequent development of graben-structures (Stewart 1999).

Overall, the stacking of crustal slices during orogenesis results in a heterogeneous crustal strength profile. The influence of these pre-existing rheological variations on the geometry and kinematics of faulting during subsequent extension represents a key issue for a better understanding of the modes and styles of rifting processes. This problem has already been addressed with a thermomechanical approach by Le Pourhiet *et al.* (2004) using the Gulf of Corinth as an example. In this paper, we used analogue modelling techniques to investigate the influence of inherited heterogeneities on structures that form during rifting. We wish to stress that our modelling does not address fault reactivation, but rather investigates the influence of a pre-existing weak and dipping thrust sheet, embedded within more competent units,

*From*: BUITER, S. J. H. & SCHREURS, G. (eds) 2006. *Analogue and Numerical Modelling of Crustal-Scale Processes.* Geological Society, London, Special Publications, **253**, 213–231.
0305-8719/06/$15.00 

on fault development and evolution during rifting. Le Pourhiet *et al.* (2006) discuss the limits of these analogue models, which are especially related to the boundary conditions that can be imposed.

Although the boundary conditions in our analogue models have been chosen to provide insights into the fault pattern and evolution of the Gulf of Corinth, however our study does not intend to reach an ideal fit with the Gulf of Corinth data. In our opinion, the results of our analogue models can be applied to any natural example undergoing extension with a pre-existing upper crustal heterogeneity (a stratigraphic and/or structural one) that is mechanically weaker than the surrounding material.

## The Gulf of Corinth (Greece)

In the Gulf of Corinth, a system of roughly east–west normal faults (Moretti *et al.* 2003, and references therein) has been superimposed on the pre-existing structures of the Hellenides thrust belt since Quaternary times (Jolivet 2001) (Fig. 1a). The thrust belt comprises a series of structures striking roughly N150°E, which are therefore oblique to the subsequent north–south oriented extension. The different tectonic units making up the ancient Hellenides belt are best preserved and visible in outcrop in the western part of the Gulf of Corinth.

The Peloponnese, which forms the highlands of the rift to the south, includes uplifted syn-rift sediments. The possible cause of this general uplift may be associated with both the subduction of the Mediterranean plate and the rift opening (Moretti *et al.* 2003, and references therein).

The eastern part of the Gulf of Corinth is characterized by a few major faults that control the current syn-rift sedimentary deposits (Armijo *et al.* 1996) (Figs 1a, b). In its central part, the rift is rather symmetrical (Myriantis 1984; Stefatos *et al.* 2002; Moretti *et al.* 2003) and its marine part is about 30 km wide (Fig. 1a). In contrast, westward, the marine part of the rift is narrower (10 km) and the rift is characterized by several closely spaced normal faults that define a series of small fault-bounded blocks (see Fig. 1a). As shown in Figure 1a, the major faults belonging to the rift system show an average trend of N90°E to N100°E and are disposed en echelon. Furthermore, their age decreases towards the north (Flotté 2002; Micarelli *et al.* 2003, and references therein), but out-of-sequence structures also exist (Causse *et al.* 2004). Earthquakes located beneath the northern shore usually indicate extensional failure on east–west striking planes dipping N20°E–N40°E (Micarelli *et al.* 2003, and references therein). In outcrop these faults are planar, have a high dip angle and possibly root onto a gently dipping (roughly 10°–30° to the north) plane defined by a cluster of microseismicity (Fig. 1c) (Rigo *et al.* 1996).

The inherited thrust sheets of the Hellenides belt also include the Phyllades nappe, which crops out in a tectonic window south of the Gulf of Corinth (Flotté 2002). This nappe is made up mainly of weak phyllosilicates, showing extension lineations towards N30°E (Ghorbal 2002). In the eastern part of the Gulf of Corinth this nappe is absent, or at great depth. In contrast, subsurface data show its presence in all of the western part of the Gulf of Corinth. From a mechanical point of view, the Phyllades nappe represents a major rheological contrast to the surrounding rocks. Recently, Le Pourhiet *et al.* (2004) showed, by means of a thermo-mechanical numerical approach, that the presence of weak and anisotropic phyllosilicates results in an important mechanical weakening factor and influenced faulting during the early stages of the rifting in the Gulf of Corinth. In Le Pourhiet *et al.* (2006), new insights on the generation and development of the Gulf of Corinth have been gained by combining 3D numerical and analogue experiments.

## Previous analogue modelling of extension through a heterogeneous crust

Up to now, many sandbox models have been performed to investigate the influence of pre-existing heterogeneities on fault patterns and kinematics during extension (e.g., Brun *et al.* 1985; Vendeville 1987, 1988; Vendeville *et al.* 1987; Tron & Brun 1991; Richard 1991; Nalpas & Brun 1993; Higgins & Harris 1997; Withjack & Callaway 2000; Schreurs *et al.* 2002). More recently, Bahroudi *et al.* (2003) showed that the mechanical characteristics of weak layers play a significant role in controlling the mode and rate of deformation during extension. Experiments where extension has been applied to a brittle-viscous multilayer (Schreurs *et al.* 2002), showed that the shape and the position of a weak silicone level embedded within brittle strata has a major influence on the structural style that develops during extension. All these experiments consider a 'layer cake model', i.e., a model where extension is applied to a brittle sandpack resting above a flat basal layer, usually consisting of silicone. The mechanical aspects of interaction between normal faults and pre-existing thrust faults were studied by

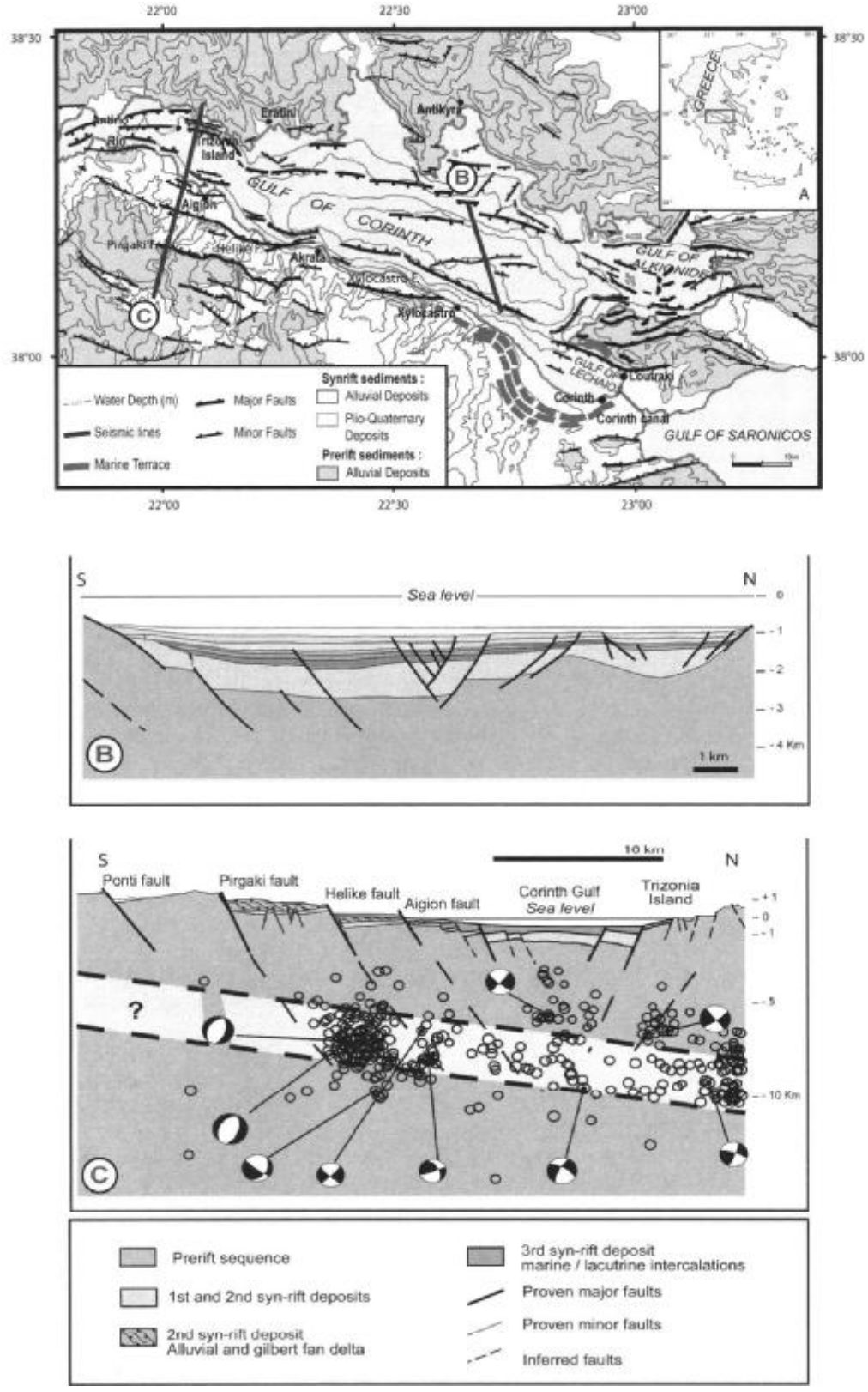


**Fig. 1.** (**a**) Structural map of the Gulf of Corinth area, modified from Moretti (2004). Water depth in metres. (**b**) Cross-section through the western part of the Gulf of Corinth, based on the interpretation of seismic lines from Hellenic Petroleum. Time-depth conversion is from Clément (2000) and interpretation from Moretti *et al.* (2003). (**c**) Cross-section through the western part of the rift (from Moretti 2004, slightly modified). The inferred seismogenic zone is represented in light green. The focal mechanisms and hypocenter locations of earthquakes are taken from Rigo *et al.* (1996).

Faccenna *et al.* (1995). Their models underwent first, shortening, resulting in thrust faults with variable dips, and then extension. For low-angle thrust faults ($<32^\circ \pm 1^\circ$), no interaction was observed, and normal faults developed independently. For thrust faults with a dip angle of $32^\circ \pm 1^\circ$, the new-formed normal faults branched at depth on the décollement level. Finally, for pre-existing thrust faults whose dip exceeded $41^\circ \pm 1^\circ$, normal reactivation of the thrust planes was observed. In experiments with a sand-pack above a stretching basement, McClay and Ellis (1987) showed that the extension above a rigid sloping basement resulted in faults dipping in the same direction as the basal detachment. More recently, Exadaktylos *et al.* (2003) performed experiments in which the base of the model is gently inclined. Their results showed that extension above a slightly sloping basal detachment leads first to the formation of a symmetrical graben and is followed by the formation of a family of secondary antithetic normal faults which cause an overall asymmetry of the rifted area.

In this context, our experiments are different: the original configuration (before extension) is characterized by the presence of a gently dipping silicone layer embedded within a flat, more competent brittle sand-cake. Our experiments aim to test the control exerted by the weak silicone layer on the style and kinematics of extensional deformation. Further specific parameters investigated in the course of our experiments include (1) the orientation of the embedded silicone layer with respect to the direction of the applied extension, (2) its position within the model, and (3) the role played by sedimentation during extension. The initial burial of the upper tip of the weak thrust sheet as well as its dip are important features for the final geometry; their influence has been discussed in Le Pourhiet *et al.* (2004). In our sandbox experiments, these parameters have been taken as constant.

## Analogue models

### *Experimental procedure*

The modelling techniques used for our purposes are similar to those commonly performed for experiments on brittle-ductile systems at the Laboratory of Analogue Modelling at Institut Français du Pétrole (IFP) (e.g., Colletta *et al.* 1991; Schreurs 1992; Mattioni *et al.* 2004). The experimental set-up is shown in Figure 2a and b and consists of a wooden box with two free sides. The other two sides of the box consist of two sliding backstops attached to two base plates, and driven by a double conveyor belt system that moves by means of computer-controlled stepper motors. The conveyor belt system allows the deformation to be localized at the base of the model near its central part (i.e., where the two base plates are in contact) where a velocity discontinuity occurs.

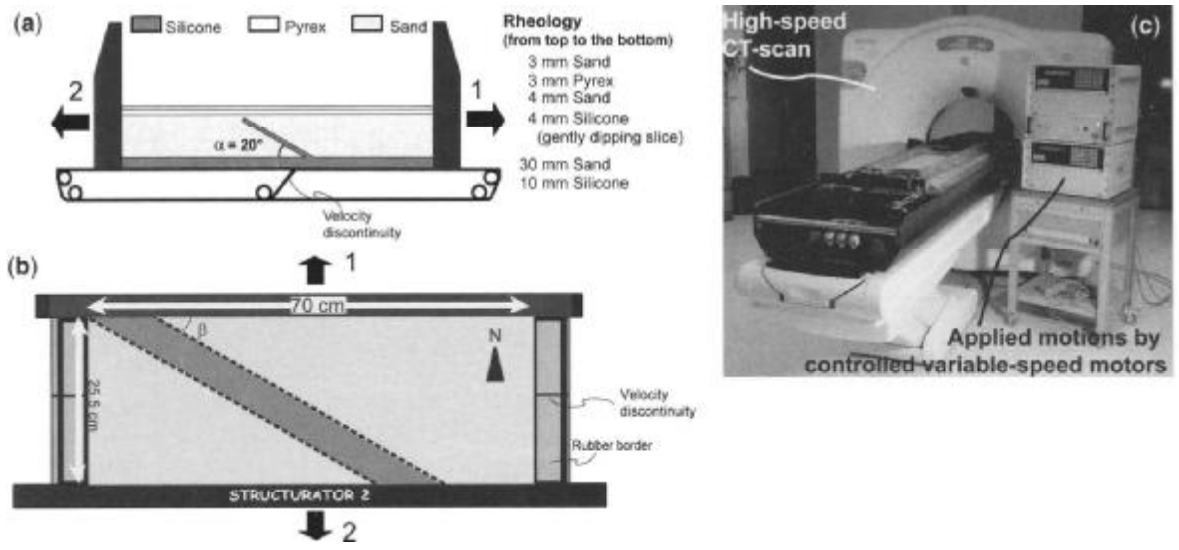


**Fig. 2.** (**a**) Schematic representation of the experimental apparatus and original configuration of each model before extension. (**b**) Schematic view of the experimental apparatus, showing the location (projected to the surface) of the embedded silicon layer. Note also that the conventional north direction has been fixed in our experiments as shown. (**c**) Photograph of CT scanner used for analysis of the experiments (IFP Laboratory).

During deformation, the central part of the sandbox was scanned by X-ray computerized tomography (Fig. 2c) (Hounsfield 1973; Mandl 1988; Colletta *et al.* 1991). This non-destructive technique generates a series of cross-sectional images through analogue models, thus allowing a detailed analysis of their internal geometry and kinematic evolution (e.g., Colletta *et al.* 1991). Attenuation of x-rays passing through a model depends on the materials used and is a function of density, effective atomic number and thickness. The difference in x-ray attenuation of sand, glass powder and silicone, allows us to visualize a stratified model. Furthermore, fault zones can be imaged in X-ray CT tomography, as they represent zones with lower densities and thus lower attenuation with respect to the unfaulted domains. The images obtained by the CT scanner were processed using specific software and then interpreted, more or less as 3D seismic images.

## *Materials and scaling*

In our experiments, we used granular materials (dry quartz sand and glass powder with an average grain size of *c.* 100 μm) and silicone (polydimethylsiloxane, PDMS). Angles of internal friction of quartz sand and glass powder (about 30° for sand and 39° for glass powder) are similar to those determined by Byerlee (1978) for upper-crustal rocks (40° for normal stresses <2 kbar and 31° for normal stresses between 2 and 20 kbar). Thus, quartz sand and glass powder are considered to be appropriate analogue materials for simulating brittle deformation in the upper crust (Horsfield 1977; Byerlee 1978). This has also been shown by Schellart (2000), who in addition stated that granular materials have negligible cohesion at very low normal stresses (<400 Pa). Lohrmann *et al.* (2003) and Ellis *et al.* (2004) have also pointed out a similarity in the mechanical behaviour of granular sifted materials and the behaviour exhibited by crustal rocks (Barnhoorn *et al.* 2004). In fact, sifted dry quartz sand and corundum sand are characterized by elastic-frictional plastic behaviour with an initial phase of strain-hardening preceding failure, which is followed by strain-softening until a stable dynamic value of strength is reached.

The ductile behaviour of rocks in the lower crust and/or of weak layers within the brittle upper crust is simulated by PDMS. Within the range of strain rates used in this study (lower than $10^{-2}$ $s^{-1}$), the silicone behaves as a Newtonian fluid and has a very low yield strength.

In our models, the model-to-prototype ratio for lengths, $L^*$, was $2.5 \times 10^{-6}$, thus implying that 1 cm in the model represents 4 km in nature. To simulate any natural process by analogue modelling, it is necessary to scale the model using the basic principles discussed in detail by Hubbert (1937), Ramberg (1981) and Vendeville *et al.* (1987). Thus, it must be (Table 1):

$$\sigma^* = \rho^* g^* L^* \quad (1)$$

where $\rho^*$ is the ratio for densities and $g^*$ is the ratio for gravity acceleration. As our models were deformed in a natural gravity field, $g^*$ was 1. The material density of materials used in our models was about half that of natural rocks, so that $\rho^*$ was 0.5. Hence, it follows that the stress ratio, $\sigma^*$, was $1.25 \times 10^{-6}$ (Table 1). For the velocity, we assumed that 1 cm/hr in our experiments corresponds to 1 cm/yr in nature. Because in our experiments we varied the velocity of extension from 1 cm/hr to 2 cm/hr, thus $V^*$ changed from $10^4$ (for Vmod = 1 cm/hr) to $2 \times 10^4$ (for Vmod = 2 cm/hr) (Table 1). Consequently, this implied that:

(1) for $V^* = 10^4$, $T^*$ was $2.5 \times 10^{-10}$ (i.e., 1 hr in the model corresponds to *c.* 456,000 years in nature), strain rate ratio $\varepsilon^*$ ($1/T^*$) was $0.4 \times 10^{10}$ and viscosity ratio $3 \times 10^{-16}$. As the measured viscosity of our own silicone was $2 \times 10^4$ Pa s (J. M. Daniel, pers.

**Table 1.** *Scaling values*

| Length ratio $L^* = Lmod/Lnat$ | | Gravity ratio $g^* = Gmod/Gnat$ | Density ratio $\rho^* = \rho mod/\rho nat$ | Stress ratio $\sigma^* = \rho^* g^* L^*$ |
|---|---|---|---|---|
| $2 \times 10^{-6}$ | | 1 | 0.5 | $1.25 \times 10^{-6}$ |
| Vmod (cm/hr) | Velocity ratio ($V^* = Vmod/Vnat$) | Time ratio ($T^* = Tmod/Tnat$) | Strain rate ratio ($\varepsilon^* = 1/T^*$) | Viscosity ratio ($\eta^* = \eta mod/\eta nat$) |
| 1 | $10^4$ | $2.5 \times 10^{-10}$ | $0.4 \times 10^{10}$ | $3 \times 10^{-16}$ |
| 2 | $2 \times 10^4$ | $1.25 \times 10^{-10}$ | $0.8 \times 10^{10}$ | $1.6 \times 10^{-16}$ |

comm.), it implies a natural viscosity of $0.64 \times 10^{20}$ Pa s.

(2) for $V^* = 2 \times 10^4$, $T^*$ was $1.25 \times 10^{-10}$ (i.e., 1 hr in the model corresponds to *c.* 913,000 years in nature), strain rate ratio $\varepsilon^*$ $(1/T^*)$ was $0.8 \times 10^{10}$ and viscosity ratio $1.6 \times 10^{-16}$ (thus implying a natural viscosity of $1.2 \times 10^{20}$ Pa s).

*Experimental set-up*

The initial configuration of all models consisted of a 1 cm-thick silicone layer directly above the base plates and covered by a 4 cm-thick sandpack (Fig. 2a). Within the sandpack, we placed a gently dipping silicone layer 0.4 cm-thick, which simulated a ductile level embedded within a more mechanically competent series. The angle $\alpha$ of apparent dip of the silicone layer (e.g., the angle measured along a vertical section perpendicular to the velocity discontinuity) was fixed at 20°, which is the dip angle of the seismogenic zone in the western part of the Gulf of Corinth. All the models were subjected to symmetrical extension, with a direction perpendicular to the longitudinal borders of the sandbox. The extension velocity varied between experiments and was either 1 cm/hr or 2 cm/hr (see Table 2).

The boundary conditions and experimental parameters are summarized in Table 2. In the first reference model (experiment 1) the strike of the embedded silicone layer was orthogonal to the direction of the applied extension. Thus, this experiment corresponds to a cylindrical 2D case, discussed in Le Pourhiet *et al.* (2006). In all other models, the strike of the embedded silicone layer was N120°E (Fig. 2b), which corresponds to the expected strike of the weak Phyllades nappe in the Gulf of Corinth. Hence, the angle between the trend of the silicone level and the longitudinal sidewalls of the sandbox ($\beta$ in Fig. 2b) is 30°. In the experiments we tested the influence of (i) the position of the weak silicone layer within the model (experiments 2 and 3), (ii) its geometry (experiment 4), and (iii) the role of syn-extensional sedimentation (experiment 5) on the resulting fault pattern. With the exception of experiment 1 (called 'reference model' in this paper), all the experiments were divided into two parts: one part with and one part without a dipping silicone layer, referred to as 'heterogeneous' and 'homogeneous' crust respectively. This particular configuration allowed us to compare the two different areas and to check the possible interactions between both areas.

## Experimental results

In the description of the experiments, we will call those faults dipping in the same dip direction as the silicone level 'synthetic faults' and all faults dipping in the opposite dip direction 'antithetic faults'. These names are used for convenience and do not mean that the antithetic faults are genetically linked to the synthetic ones. All the structures observed within the models have been orientated with respect to a conventional north direction, fixed as shown in Figure 2b. Thus, in the accompanying cross-sections south is on the left side and north on the right side. A thin layer of glass powder (pyrex) near the surface of each experiment acted as a stratigraphic marker, allowing to identify structures on cross-sections during

**Table 2.** *Experimental parameters and boundary conditions*

| Model number | Thickness of the embedded silicone layer (cm) | Velocity of extension (cm/hr) | Angle $\beta$ | Apparent dip of the embedded silicone layer (°) | % Bulk extension | Length of the upper border of the silicone layer (cm) | Remarks |
|---|---|---|---|---|---|---|---|
| 1 | 0.4 | 1 | 0 | 20 | 16 | 70 | |
| 2 | 0.4 | 1 | 30 | 20 | 15.6 | 24 | |
| 3 | 0.4 | 2 | 30 | 20 | 16 | 48 | |
| 4 | 0.4 | 2 | 30 | 20 | 16 | 34 | Silicone layer with a free lateral termination |
| 5 | 0.4 | 2 | 30 | 20 | 16 | 34 | Syn-rift sedimentation<br>Silicone layer with a free lateral termination |

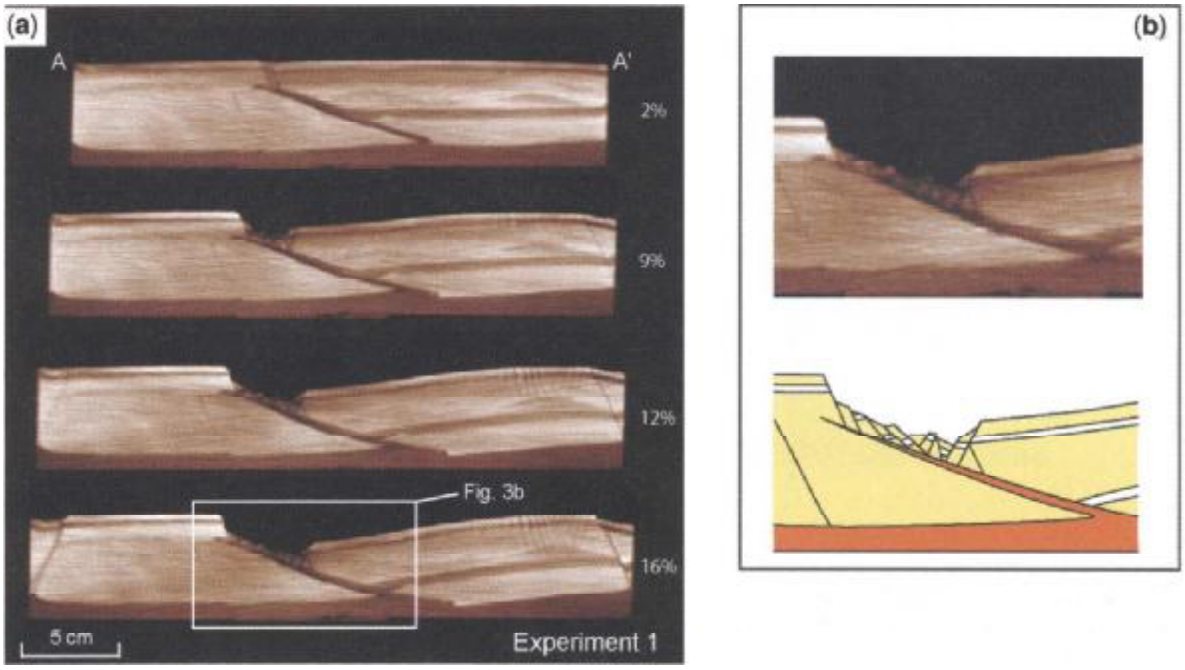


**Fig. 3.** Experiment 1. (**a**) Vertical section through the model showing fault evolution at four consecutive stages of extension. Location of cross-section is indicated in Fig. 4. The inset at stage 4 displays the location of Fig. 3b. (**b**) Enlargement of rift zone at the end of the experiment.

deformation. Only experiment 1 had a deeper thin layer of glass powder (Fig. 3). A square grid of coloured sand markers was traced on top of each model to monitor the surface evolution.

### *The reference model (experiment 1)*

In this model, a gently dipping embedded silicone layer strikes orthogonal to the extension direction. The initial geometry and boundary conditions therefore correspond to a 2D experiment with a constant east–west strike of the silicone layer. The evolution of this experiment at four consecutive stages of extension is illustrated in vertical sections in Figure 3a.

In the early stages of deformation, a system of conjugate high-angle normal faults initiates roughly at the upper tip of the gently dipping silicone layer near the free surface. The faults propagate upward with increasing displacement along the dipping silicone layer, thus resulting in a more or less symmetrical graben configuration. As deformation goes on, the footwall south of the initial graben does not move, whereas the more northern rift-bounding fault shifts down slightly along the silicone layer, which acts as a décollement level. This leads to a progressive asymmetrical widening of the basin. Increasing deformation results in a progressive large flexure of the entire northern block, with several east–west striking high-angle normal faults that develop far from the basin at the bulge of the flexure. They dip both northward and southward and have limited offset. In contrast, along the southern margin, the footwall of the synthetic rift-bounding fault rift remains essentially undeformed.

With increasing extension the border faults remain the same all along the experiment, but new faults appear within the rift. The main fault with the highest offset is the one bordering the southern side of the rifted zone. Several minor synthetic and antithetic faults develop within the rift and root on the gently dipping silicone layer. Further opening of the rift is accommodated by progressive, anticlockwise tilting of the minor synthetic faults (changing from an average initial dip of 70° to 45° at the end of extension) on the southern side of the rift. In contrast, the antithetic faults in the northern part of the rift maintain their original dip (around 60°) throughout the experiment. After 16% of bulk extension (Fig. 3b), the rift shows a very marked asymmetrical shape, with one main fault at its southern border showing larger displacement with respect to both minor synthetic and antithetic faults cutting through the rift. At the surface, the resultant rift is bordered to the south by the main east–west striking and north dipping fault (Fig. 4). The northern side is more complex and

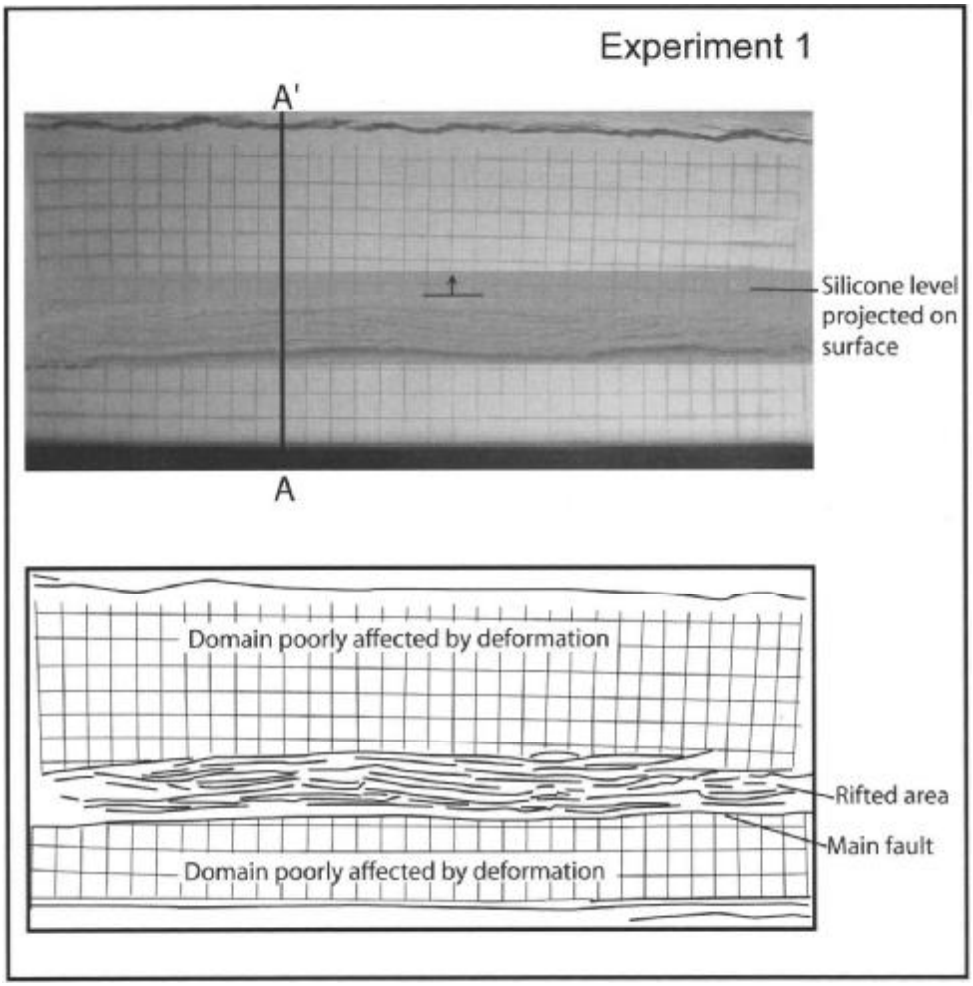


**Fig. 4.** Experiment 1. Line drawing after surface view at the end of the experiment (16% of bulk extension). The dark grey in the middle of the models displays the location (projected to the surface) of the interbedded gently dipping silicone layer. Arrow indicates its dip direction. Line A–A′ shows the location of the vertical section of Fig. 3.

defined by three east–west oriented and south dipping fault segments that overlap and link during the latest stages of deformation. Within the basin, minor synthetic and antithetic faults have a general east–west strike and are closely spaced. Their length and displacement are variable, and hence the dimension of the resulting fault-bounded blocks varies as well.

The top view allows us to highlight some other important features displayed on Figure 4, which corresponds to the surface fault pattern at the end of the extension. The rifted area is confined to a narrow zone within the model, with two adjacent broad domains showing only little deformation. Another important feature is the progressive migration of the depocentre of the basin in the dip direction of the silicone layer during the course of the experiment. Nevertheless, this does not mean that the active faults are restricted to the border of the depocentre; indeed, simultaneous activity of several normal faults located on both sides of the rift can be noted until the end of the experiment (Fig. 3).

### *Extension in zones with and without a pre-existing gently dipping silicone layer: a different style in fault genesis and evolution (experiments 2, 3 and 4)*

Three analogue experiments were performed in which the dipping silicone layer is only present in the western half of the model. This particular configuration allows us to compare the style of extension in the two areas and to study the structural style in the area of transition. The dipping silicone layer strikes N120°E in all three experiments and is oblique to the north–south oriented extension direction.

In experiments 2 and 3 the initial configuration is the same, with the northwestern and southeastern lateral terminations of the embedded

silicone layer being confined by the boundaries of the sandbox. Experiment 4 differs from the previous two as the southeastern lateral termination of the silicone layer ends within the sandpack. The fault evolution above the dipping silicone layer is quite similar for the three experiments, but the abrupt lateral termination of the silicone layer in experiment 4 strongly influences the fault pattern in the transition zone.

### *Experiments 2 and 3*

The initial configuration of these two experiments is the same (see Table 2) and consequently the observed fault evolution is very similar. Thus, for practical reasons, we will discuss only the results of experiment 3. Figures 5 and 6 illustrate the evolution of this experiment, as a cross-section and in map view. Both figures clearly show how the evolution of the normal fault pattern is closely related to the presence or absence of the dipping silicone level at depth. In the eastern half of the model (homogeneous domain), a system of conjugate faults develops in an almost symmetrical way at the early stages of extension (cross-section B–B′, Fig. 5). The normal faults extend down to the top of the basal silicone layer and the initial graben width reflects the depth to the basal silicone layer. With increasing extension, fault offset along existing faults progressively increases and new steep normal faults develop in the footwall of the previously formed normal faults, thus producing a wider graben. Further extension is accomodated by increasing displacement onto the main normal faults and by a progressive tilting of the fault-bounded blocks. Overall, this fault evolution is very similar to the ones previously described in analogue models (e.g., Allemand & Brun 1991; Schreurs *et al.* 2002) and in nature (e.g., the Gulf of Suez, Colletta *et al.* 1988; Moretti 2004).

In the western half of the model (heterogeneous domain), the style and mode of rifting is completely different (section A–A′, Fig. 5). The fault evolution in the vertical north–south sections is similar to the one described for the reference model. In fact, a conjugate system of high-angle normal faults initiates at the tip of the gently dipping silicone layer near the free surface and leads to an initial symmetrical graben. With continuing extension the rifted area widens by migration of its northeastern border down along the weak silicone layer. Progressive widening of the rift is accommodated by the formation of several closely spaced synthetic and antithetic faults that root on the dipping silicone layer. As for the reference model, further extension results in tilting of the synthetic faults cutting through the southern part of the basin, whereas the antithetic faults in the northwestern part of the rift maintain their original dip. At the end of the deformation, the rift becomes asymmetrical in shape (Fig. 5, vertical section A–A′).

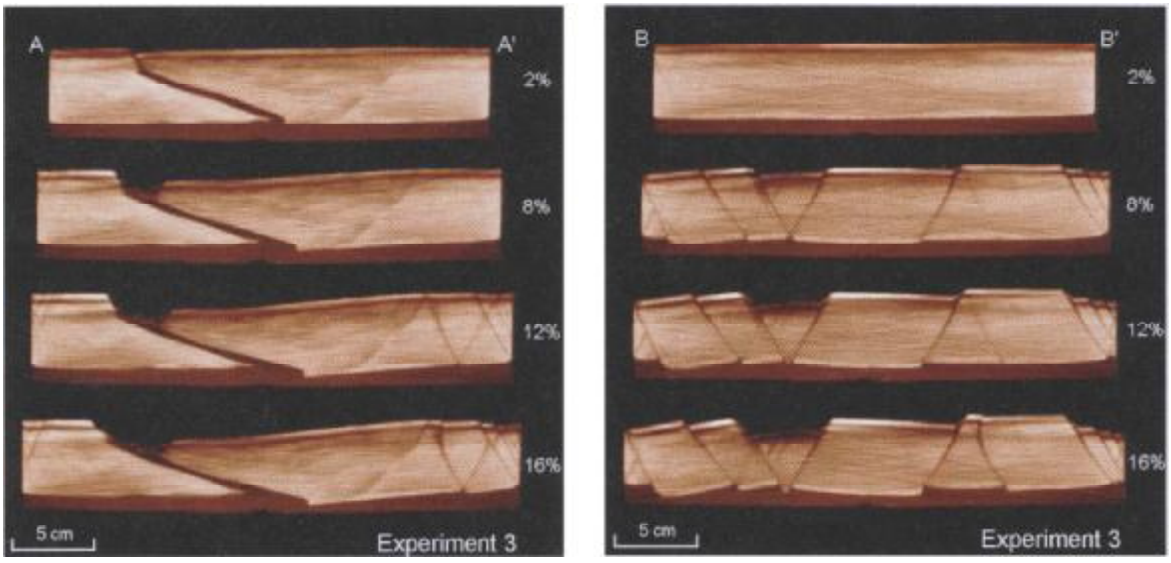


**Fig. 5.** Experiment 3. Vertical sections showing four consecutive stages of extension. The two cross-sections also display the different style of normal fault evolution within the model for the area where the gently dipping décollement level is present (A–A′) and where it is absent (B–B′). Location of these cross-sections within the model is shown in Fig. 6.

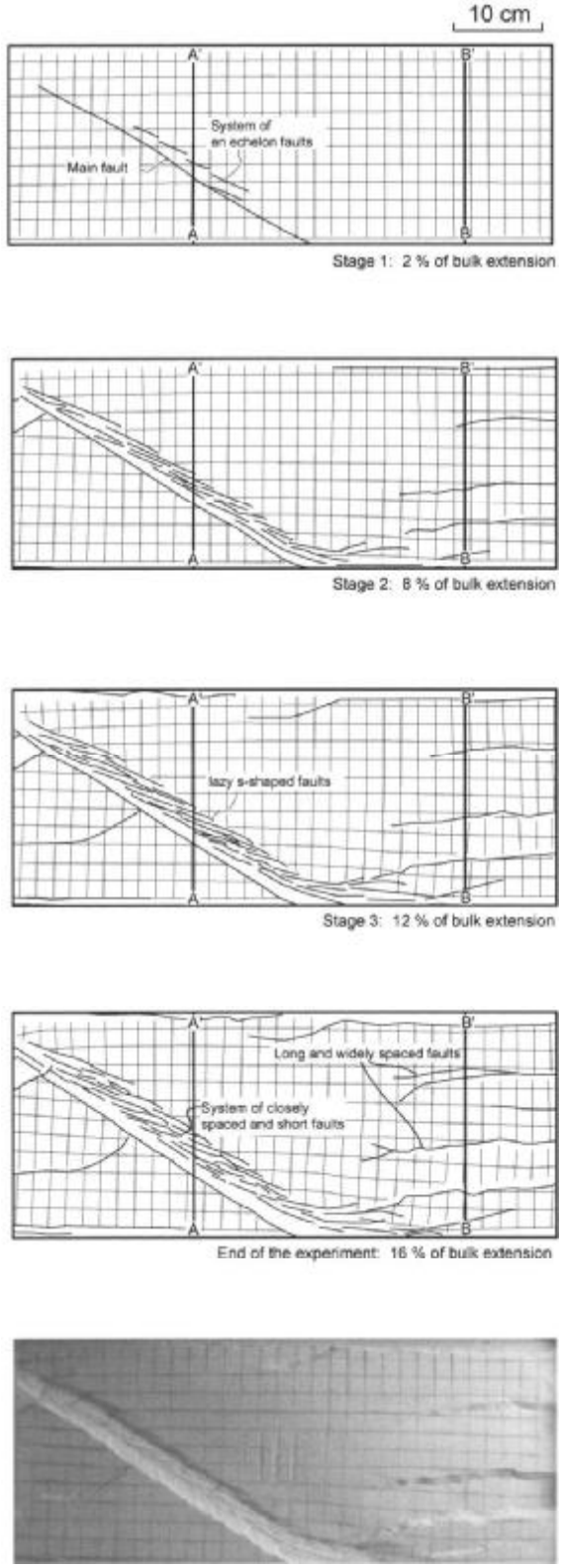


**Fig. 6.** Experiment 3. Line drawings after surface photographs showing four consecutive stages of extension. Lines A–A′ and B–B′ show the position of vertical sections of Fig. 5. The accompanying photo is representative of the end of the experiment. See text for further explanations.

The surface fault pattern that forms above the dipping silicone layer shows an en echelon pattern of normal faults. This evolution differs from the one described for the reference model and is clearly related to the difference in orientation of the dipping silicone layer with respect to the extension direction. The influence of this obliquity on the surface fault pattern will be discussed in more detail later on.

### *Experiment 4*

In this experiment, one lateral termination of the dipping silicone layer ends within the sandpack. This particular configuration allows us to better investigate the fault pattern in the transition zone between the areas with and without a dipping silicone layer. The experimental results are shown in Figures 7, 8 and 9. The evolution in vertical sections (Figs 7 and 8) is similar to the one described for experiment 3. In surface view (Fig. 9), the transition zone is characterized by the formation of several sub-vertical transfer faults that strike NE–SW, parallel to the lateral termination of the embedded silicone layer. Figure 9 also shows the change in orientation of the main east–west trending normal faults that developed in the western part of the model and propagated towards the embedded silicone layer. Their strike changes from N90°E to N65°E.

Figure 10 illustrates, by means of six serial vertical sections through the final stage of deformation, the drastic lateral changes in the structural style of extension between the homogeneous (i.e., the easternmost and westernmost parts of the model) and heterogeneous central domain. The transition zone between the two domains is marked by several sub-vertical extensional transfer faults, the location and orientation of which are closely linked to the geometry of the embedded silicone layer. These transfer faults have very large offsets, so the deepest part of the rift is located there (see cross-section E–E′ on Fig. 10). In this experiment, the N45°E oriented transfer faults link the N110°E asymmetrical oblique graben above the dipping silicone layer, with the N90°E symmetrical graben eastward. The N45°E transfer faults clearly correspond to the direction of the eastern lateral termination of the silicone level. The transfer faults appear during the early stages of extension, suggesting a strong control of the extremity of the silicone on their location and orientation (Fig. 9). In other words, the lateral tip of the silicone layer acts as a strong localizing factor of deformation. At the end of the experiment, the deformed square grid at the surface shows that no strike-slip displacement occurred along these transfer faults.

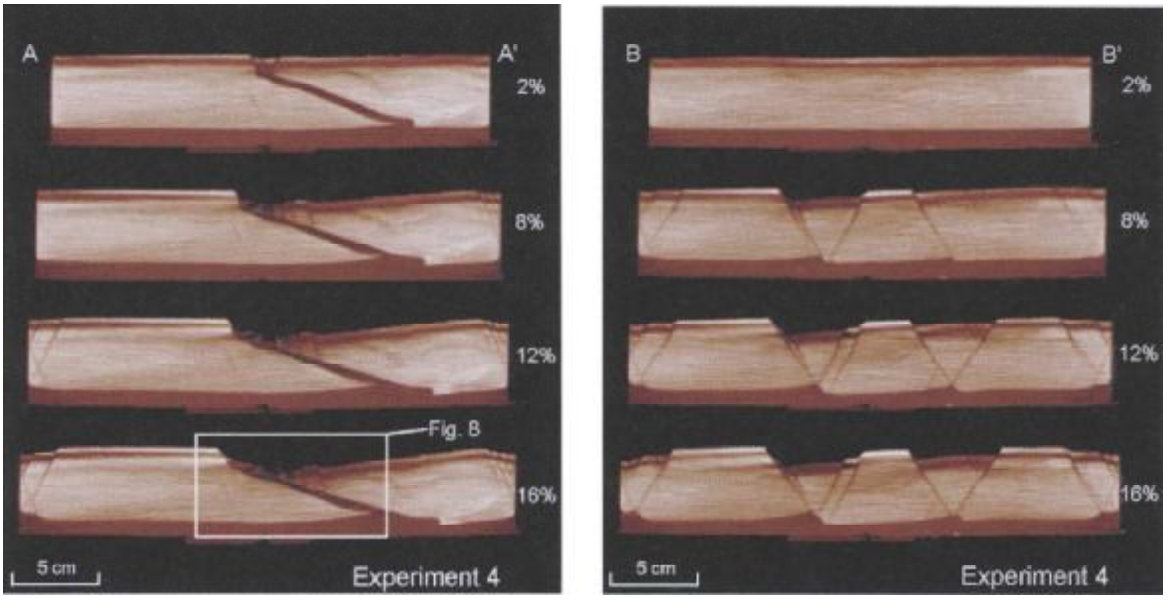


**Fig. 7.** Experiment 4. Vertical sections showing four consecutive stages of extension. Note the different fault style between areas where the gently dipping décollement level is present (A–A′) and where it is absent (B–B′). Location of cross-sections is shown in Fig. 9. The inset in A–A′ at stage 4 shows location of Fig. 8.

*Analysis of the fault pattern at the surface*

Figures 6 and 9 show the progressive evolution of structures at the surface of experiments 3 and 4, and illustrate the difference in fault pattern between the homogeneous and heterogeneous domains. In the former domain, faults develop orthogonal to the direction of the applied extension. They are few, straight and widely spaced, so that the resulting rift affects a large area of the model. In the heterogeneous domain, the general trend of the resulting rift is not necessarily orthogonal to the direction of the applied extension; rather, it is roughly N120°E oriented, corresponding to the trend of the underlying dipping silicone layer. Therefore, from the onset of extension a marked asymmetry exists in the orientation and distribution of faults at the two sides of the main rift. The southwestern rift boundary is characterized by one main fault striking N120°E, parallel to the underlying dipping silicone layer. This main fault and the minor synthetic faults that form very close to it, maintain their original trend parallel to that of the underlying silicone layer until the end of the experiment. In contrast, Figures 6 and 9 show that the northeastern border is structurally more complex. It consists of a system of en echelon antithetic faults, organized in a dextral stepping arrangement, that formed during the early stages of extension. Their strike of roughly N105°E is intermediate between the strike of the underlying gently dipping silicone layer and that of the applied extension. As extension continues, these antithetic faults become slightly sigmoidal in shape with their lateral terminations becoming progressively parallel to the strike of the silicone layer.

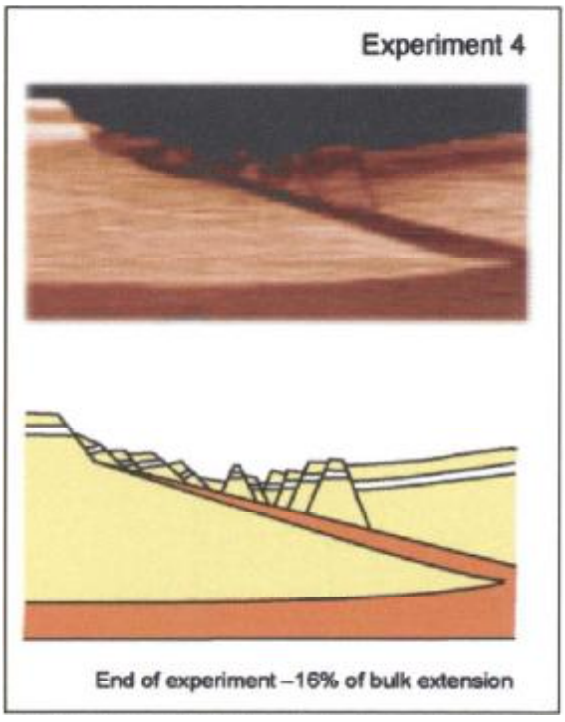


**Fig. 8.** Experiment 4. Enlargement of rift zone above the décollement level at the end of the experiment. Note the marked asymmetry of the rift with a main fault on the southwestern (left) side of the basin and several minor synthetic and antithetic faults cutting through the basin.

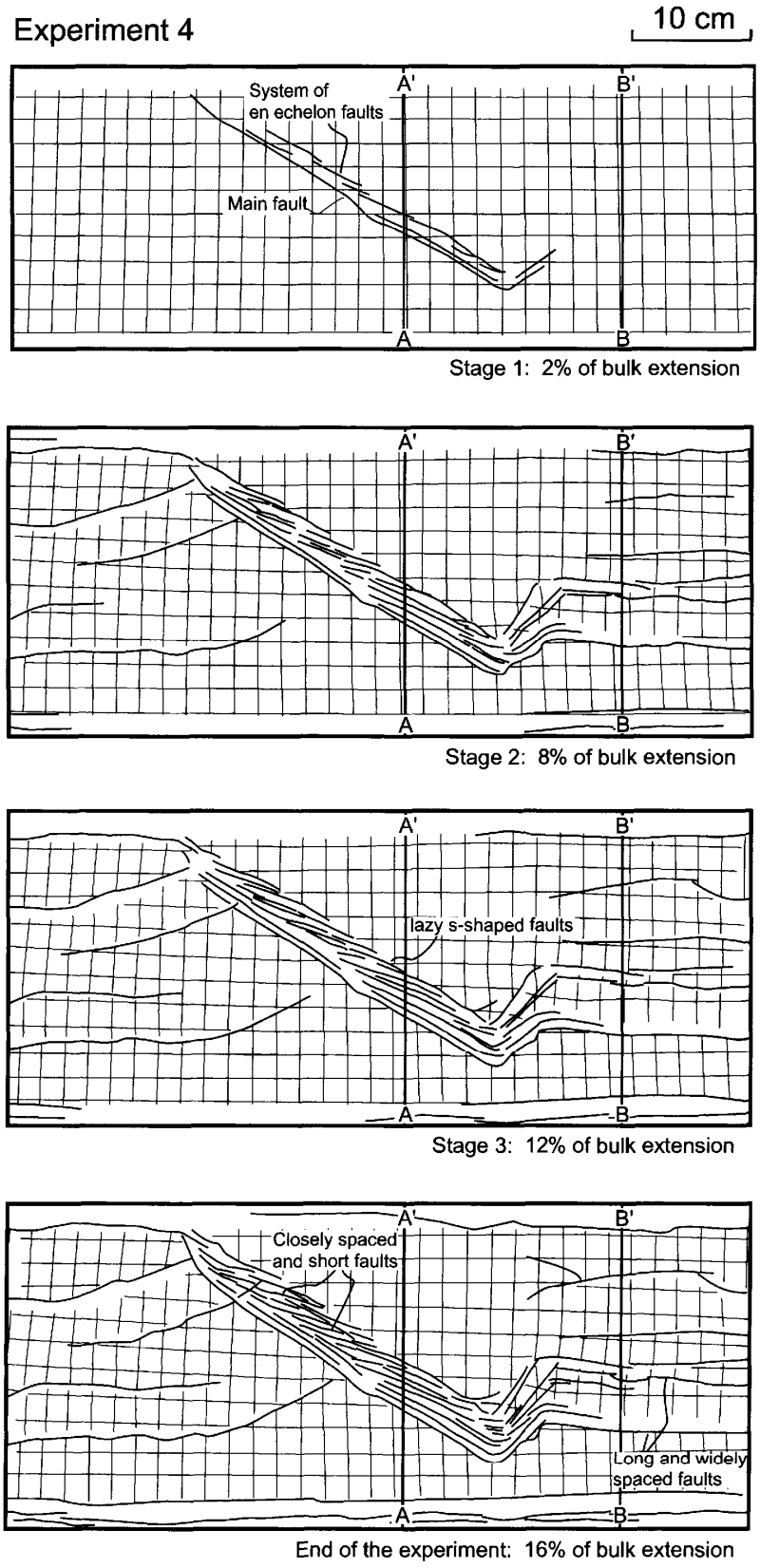


**Fig. 9.** Experiment 4. Line drawing after surface photographs at four consecutive stages of extension, showing the differences in fault pattern between the area underlain by a gently dipping silicone layer and the adjacent homogeneous areas. Lines A–A′ and B–B′ show the position of vertical sections of Fig. 7.

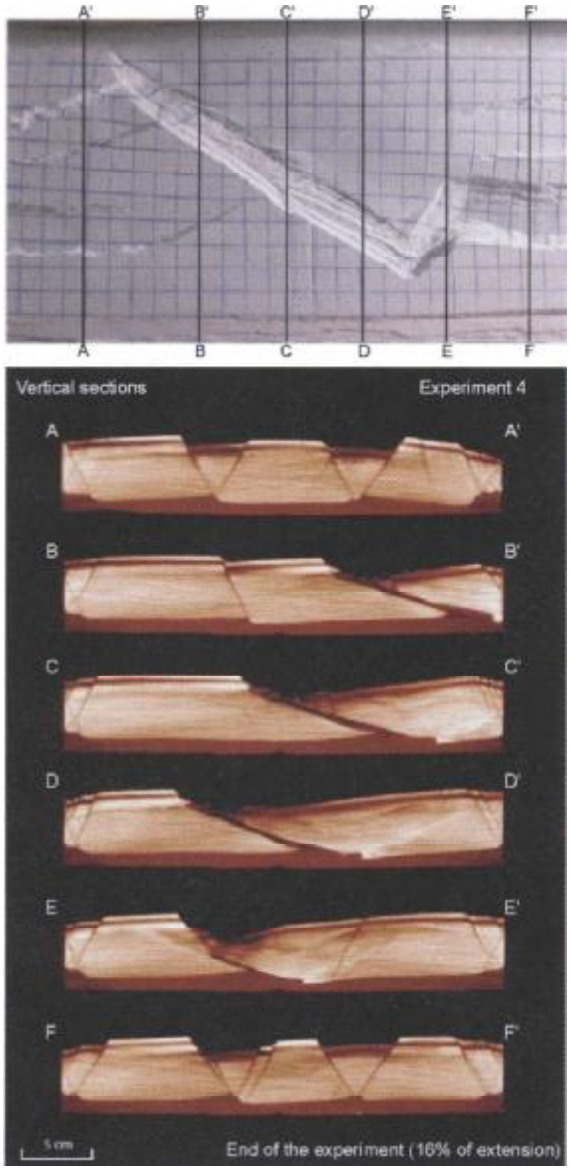


**Fig. 10.** Experiment 4. Cross-sections through the model at the end of extension, showing the fault pattern across the area where the gently dipping silicone layer is present (B–B′, C–C′ and D–D′) and where it is absent (see A–A′ and F–F′). Cross section E–E′ is representative of the boundary zone between the two areas.

At the end of the deformation (Figs 6 and 9), the surface fault pattern in the heterogeneous domain is clearly different from the one in the adjacent domains. The main rift zone in the heterogeneous domain is very narrow and characterized by several closely spaced and short faults. These faults are not orthogonal to the direction of the applied extension, but the general trend of the rift is roughly parallel to that of the underlying gently dipping silicone layer.

*Effect of syn-rift sedimentation (experiment 5)*

In this experiment, two cycles of syn-rift sedimentation were simulated: the first one (represented in green in Fig. 11) after 6% and a second one (light green in Fig. 11) after 12% of bulk extension. Figure 11 shows four consecutive stages of deformation through the domain with the gently dipping silicone layer. The initial model configuration is exactly the same as the one for experiment 4 (see Table 2) and the overall fault evolution was rather similar. Nevertheless, several important features are worth noting: for example, at the end of the deformation (Step 4 of Fig. 11), the faults within the rift propagated up to both the first and second cycle syn-rift deposits. These syn-rift deposits are clearly cut and offset, highlighting once again the contemporaneous activity of several faults. Another important feature is the location of the depocenter within the rift with respect to the location of the main fault of the system. The depocenter is located northward, since the graben is deeper in this area. Nevertheless the faults that have the larger offset are along the other margin.

## Discussion

Table 3 summarizes the main results from our analogue model experiments. Overall, the experiments show that rheological differences between areas with and without a dipping silicone layer ('heterogeneous' and 'homogeneous' crust, respectively) lead to marked differences in fault evolution.

The following differences between the two areas are evident from the analysis of the analogue experiments:

(1) Extension occurs in a deformation zone that is much wider in the area with homogenous crust than in the area with heterogeneous crust (see Figs 5, 6, 7 and 9).

(2) The extension through the homogenous crust is accommodated by relatively few normal faults in comparison to those developed above the heterogeneous crust. Faults in the homogeneous crust are straight, long, widely spaced and with large displacements, whereas in the heterogeneous crust they are more numerous, short and closely spaced. Furthermore, faults in regions of homogeneous crust sole out into the basal and flat weak silicone level without intersecting each other. In contrast, faults developed in regions of hetereogeneous crust root onto the dipping silicone layer, and some of them intersect each other.

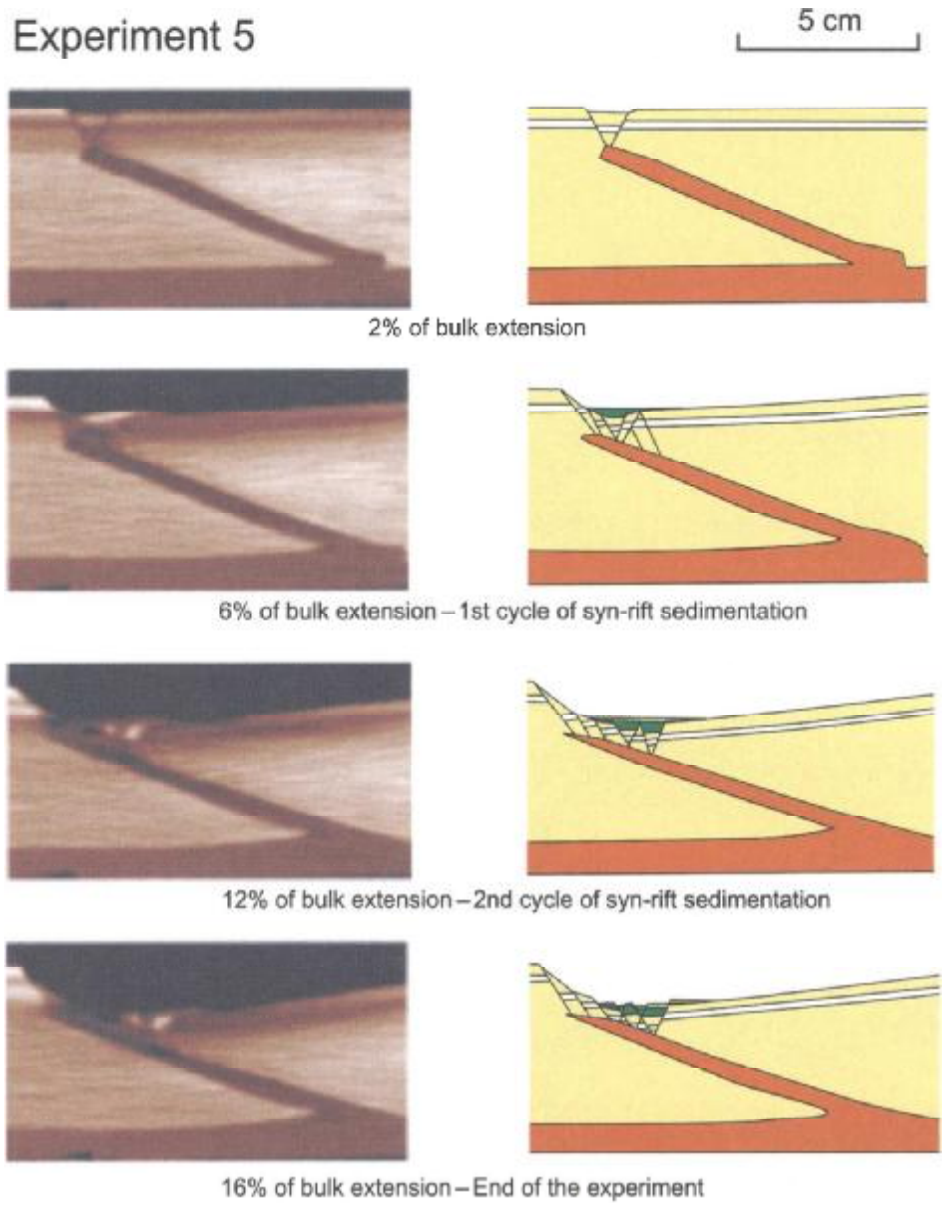


**Fig. 11.** Experiment 5. Enlargement of the stretched area above the gently dipping silicone level showing the evolution at four successive stages of extension. This experiment differs from the others since two cycles of syn-rift sedimentation have been carried out (the first one marked in green, the second one in light green).

From our models, a first major difference observed between the domains of homogeneous and heterogeneous crust concerns the shape and geometry of the resulting rift. In particular, rifting in regions of heterogeneous crust ultimately results in a marked asymmetry. In fact, from Figures 3b and 8, it may be seen that at the end of the deformation, the resulting basin is characterized by a major fault bordering its southern side and showing larger displacements with respect to those observed along the minor synthetic and antithetic faults cutting through the basin. This particular shape of the rift is not observed in domains where extension affected a homogeneous crust; here in fact, the extensional deformation affects a wider area and the resulting rift is characterized by a symmetrical shape. This symmetry is defined by a system of conjugate faults that develops at the early stages of deformation and extends down to the top of the basal silicone layer. In all experiments, the east–west orientation of faults in the homogeneous domain is consistent with the far-field applied stress system. At the surface, the spacing

**Table 3.** *Summary of model results*

| With an embedded dipping silicone layer ('hetereogenous crust') | Without an embedded dipping silicone layer ('homogeneous crust') |
|---|---|
| Narrow and asymmetric zone | Wide and symmetric deformation zone |
| Several normal faults | Few normal faults |
| Closely spaced, shorter and slightly s-shape normal faults | Widely spaced, longer and straighter normal faults |
| Irregular horsts and grabens | Regular horsts and grabens |
| Faults oblique to the direction of extension | Faults perpendicular to the direction of extension |
| Block rotation | |
| Simultaneous activity of several faults | |

of the faults reflects the brittle layer thickness, as already observed by Vendeville *et al.* (1987).

This particular fault genesis and evolution is markedly different from the one observed within the heterogeneous domain. In the latter domain, fault genesis and evolution is controlled to a large extent by the pre-existing embedded heterogeneity that is mechanically weaker than its surroundings. This heterogeneity results in a strong localization of the deformation in an area located above the silicone layer (Figs 3, 5 and 7). Only at the earliest stages of deformation is the developing rift more or less symmetrical, and is defined by a system of conjugate planar, normal faults. The normal faults extend down to the upper termination of the silicone layer, which acts as a décollement level. As deformation continues, the northernmost fault of this conjugate system progressively shifts down to the ductile level, and the graben gradually becomes asymmetrical. With increasing deformation, the formation of minor synthetic and antithetic faults and tilting of fault-bounded blocks accommodate further widening of the rift. These new faults develop at the hanging wall of the older ones and root on the gently dipping décollement level. Thus the oldest faults are those bordering the two sides of the rift.

The maximum depth and width (measured in sections through the central part of the graben) of the graben above the gently dipping silicone layer have been measured at different phases of bulk extension (Fig. 12). Both maximum graben depth and width increase roughly proportionally with increasing shear displacement along the gently inclined décollement level (see also Exadaktylos *et al.* 2003). The ratio between the maximum graben depth and width at different stages of the extension remains roughly constant, except during the initial phases of extension when this ratio is at its minimum value. This suggests that in the early stages of extension, the rift zone increases mainly in width rather than in depth, whereas with continuing extension, the amount of offset increases and the rift deepens quickly.

The analogue experiments indicate that fault orientation and fault pattern during extension can be profoundly controlled by the orientation and depth of a crustal heterogeneity. In fact, in experiments in which the gently dipping silicone layer strikes obliquely (with $\beta = 30^{\circ}$, Figs 6 and 9) to the direction of the applied extension, the strike of the normal faults forming above the heterogeneity is not necessarily orthogonal to the direction of extension. Rather, two groups of coeval normal fault orientations can be distinguished; a first group includes faults striking parallel to the direction of the underlying gently dipping silicone layer. These are mainly synthetic faults which form at the southern side of the rift where the silicone level is very shallow. The second group includes the antithetic faults that develop at the northeastern side of the rift, where the silicone layer is at a greater depth. These faults are arranged in a dextral en echelon arrangement with an orientation of N105°, i.e., intermediate between the trend of the underlying gently dipping silicone layer and that of the far-field applied stress regime.

On the other hand, the presence of a gently dipping silicone layer acting as a décollement level and oriented obliquely to the direction of the applied extension seems also to control the fault pattern of faults that formed far from it. Figure 9 shows how major east–west striking faults that developed in regions of homogenous crust deflect abruptly as they approach the embedded silicone layer.

## Applicability of the analogue models results to the Gulf of Corinth

Despite the inherent idealizations of analogue models and the fact that they are only partially

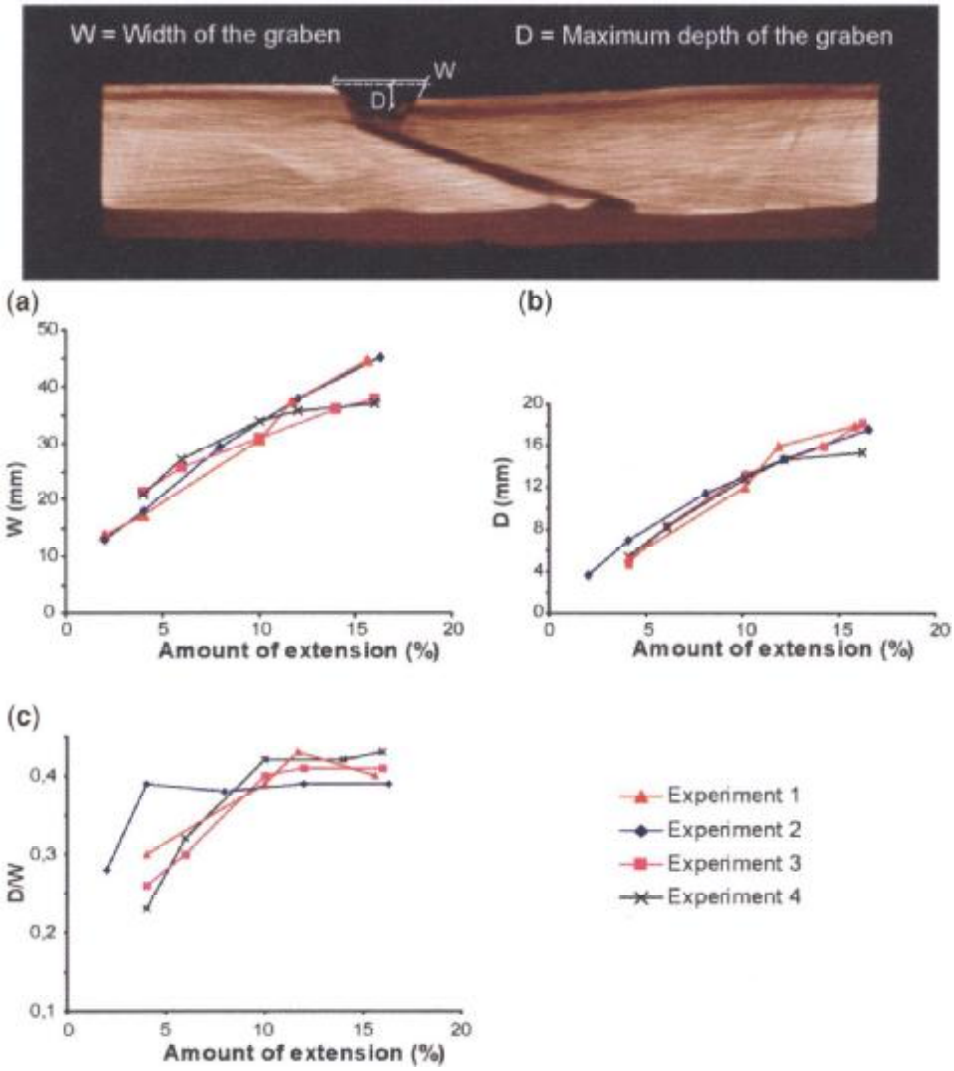


**Fig. 12.** Diagrams showing (**a**) the graben width (W) against the amount of extension, and (**b**) maximum graben depth at the free surface (D) against the amount of extension. (**c**) ratio D/W (maximal graben depth/graben width) against the amount of extension.

scaled, some important similarities can be observed with respect to the Gulf of Corinth. The west (left)–east (right) changes in fault pattern described in those models with a weak silicone layer oblique to the direction of the applied extension (e.g., experiment 4 in Figs 6 and 9), reflect very well the west–east variations observed in the Gulf of Corinth. There is also good agreement between the eastern homogeneous domain of experiments 3 and 4 (see Figs 6 and 9) and the eastern part of the Gulf of Corinth, where the weak Phyllades nappe is not present, or at least, is at great depth (see Fig. 1a, b). Here, both rifts (model and nature) are rather symmetrical, wide and with few and widely spaced major faults (see also Fig. 1b and cross section B–B′ in Figs 5 and 7). The trend of these faults is roughly east–west, which is clearly the expected direction if one considers the orientation of the present-day north–south extension. The western part of the Gulf of Corinth is characterized by several closely spaced normal faults that define a series of faulted blocks (see Fig. 1a). These faults show an average trend of N90°E–N100°E, which is rougly intermediate between the direction of the present-day extension and the strike of the underlying Phyllades nappe. This structural setting is very similar to the one observed in the western part of experiments 3 and 4 (Figs 6 and 9). From the analogue model results we infer that the en echelon structure observed in the western part of the Gulf of Corinth and the lack of field evidence for major transverse faults can be explained by the obliqueness between the present

direction of extension and the dip direction of the crustal heterogeneity presented by the Phyllades nappe.

In the Gulf of Corinth, the present depocenter in the western part is located near the northern shore, southward of the island of Trizonia (Stefatos *et al.* 2002; Moretti *et al.* 2003) (Fig. 1a). The island itself appears to be a horst. Similar features are observed in experiment 4, where horsts exist above the weak thrust sheet and are located either in the central part or near the northern margin (Fig. 8). In the western part of the Gulf of Corinth, the current depocenter is located in front of the Trizonia fault, i.e., near the northern shore of the rift as in experiment 5. However, the results of only one experiment performed with this particular configuration (sediments only deposited in the deepest part of the graben) have to be regarded with caution. Nevertheless, they might be of use for future experimental studies.

## Concluding remarks

The role played by inherited heterogeneities on normal fault genesis and evolution has been investigated by means of small-scale analogue model experiments. The experimental results indicate that the presence of structural heterogeneities within the brittle crust can profoundly influence the subsequent fault pattern and the distribution of deformation during a rifting episode. An embedded weak silicone layer simulating an inherited weak nappe behaves as a décollement level during extension, inducing a strong localization of faulting in a narrow area. Rheological differences between areas with intracrustal weak layers and adjacent domains of homogeneous crust can lead to remarkable differences in fault patterns and dimensions of the final rift. In the presence of an embedded gently dipping ductile layer, the resulting rift is completely asymmetrical, with one major border fault showing larger displacements and several other minor synthetic and antithetic faults cutting through the basin. These faults are closely spaced and short and the fault-bounded blocks are small. This fault pattern is markedly different from the one observed in domains of homogenous crust where the applied extension is spread over a wider zone. The resulting rift is symmetrical and the deformation is accommodated by means of a few, widely spaced and long faults. The produced horst-and-graben morphology is characterized by a series of large tilted fault-bounded blocks.

Our results document how the orientation of an interlayered gently dipping ductile layer can control the pattern and orientation of faults rooting on it and of faults that form further away from it. In fact, in experiments where the dipping silicone layer was oblique to the applied extension direction, the faults bordering the northeastern side of the rift above the gently dipping décollement level, form a dextral stepping en echelon arrangement, and their orientation is intermediate between the trend of the underlying gently dipping silicone layer and the far-field applied extension direction. On the other hand, major faults in regions of homogeneous crust also deflect their orientation as they approach the weak dipping silicone layer.

Rift asymmetry and along-strike changes of dominant fault dip in rifts occur frequently in nature (Bosworth 1985; Rosendahl 1987; Colletta *et al.* 1988; Moretti 2004). The analogue models presented here clearly indicate that an upper crustal heterogeneity may induce such an asymmetry.

There is a good agreement between our experiments and the Gulf of Corinth, especially as far as the change in fault pattern from west (presence of a dipping weak layer) to east (absence of a weak layer) is concerned. Our experimental approach may provide useful constraints for the understanding and the interpretation of complex geometries and kinematics in natural zones of extension through a heterogeneous crust.

The authors are grateful to B. Colletta, J. M. Daniel and L. Micarelli for their constructive comments and suggestions. J. M. Mengus and D. Pillot are thanked for their technical assistance in building the models and C. Fichen for her help in obtaining the CT-images. L. M. was partially funded during his stay at IFP by a CNR (Consiglio Nazionale delle Ricerche, Italy) grant (nr 203.22/2002). We thank C. Faccenna, G. Schreurs and an anonymous reviewer for improving the quality of the manuscript with their valuable comments and suggestions.

## References

ALLEMAND, P. & BRUN J. P. 1991. Width of continental rifts and rheological layering of the lithosphere. *Tectonophyiscs*, **188**, 63–69.

ARMIJO, R., MEYER, B., KING, G. C. P., RIGO, A. & PAPANASTASSIOU, A. 1996. Quaternary evolution of the Corinth rift and its implications for the late Cenozoic evolution of the Aegean. *Geophysical Journal International*, **126**, 11–53.

BAHROUDI, A., KOYI, H. A. & TALBOT, C. J. 2003. Effect of ductile and frictional décollements on style of extension. *Journal of Structural Geology*, **25**, 1401–1423.

BARNHOORN, A., BYSTRICKY, M., BURLINI, L. & KUNZE, K. 2004. The role of recrystallization on the deformation behaviour of calcite rocks: high strain torsion experiments on Carrara marble. *Journal of Structural Geology*, **26**, 885–903.

BOSWORTH, W. 1985. Geometry of continental propagating rift. *Nature*, **316**, 625–627.

BRUN, J. P., CHOUKROUNE, P. & FAUGERES, E. 1985. Les discontinuités significatives de l'amincissement crustal: application aux marges passives. *Bulletin de la Société Géologique de France*, **8**, 139–144.

BYERLEE, J. 1978. Friction of rocks. *Pure and Applied Geophysics*, **116**, 615–626.

CAUSSE, C., MORETTI, I., GHISETTI, F., ESCHARD, R., MICARELLI, L., GHALEB, B. & FRANK, N. 2004. Kinematics of the Corinth Gulf inferred from calcite dating and syntectonic sedimentary characteristics. *Comptes Rendues Académie des Sciences*, **336**, 281–290.

CLEMENT, C. 2000. *Imagerie sismique crustale de la subduction hellénnique et du golfe de Corinthe*. PhD thesis, University of Paris VII.

COLLETTA, B., BALÉ, P., BALLARD, J. F., LETOUZEY, J. & PINEDO, R. 1991. Computerized x-ray tomography analysis of sandbox models: examples of thin-skinned thrust systems. *Geology*, **19**, 1063–1067.

COLLETTA, B., LE QUELLEC, P., LETOUZEY, J. & MORETTI, I. 1988. Longitudinal evolution of the Suez rift structure (Egypt). *Tectonophysics*, **153**, 221–233.

COOPER, C. & BURBI, L. 1986. Geology of the Central Sibillini Mountains. *Memorie della Società Geologica Italiana*, **35**, 323–347.

ELLIS, S., SCHREURS, G. & PANIEN, M. 2004. Comparisons between analogue and numerical models of thrust wedge development. *Journal of Structural Geology*, **26**, 1659–1675.

EXADAKTYLOS, G. E., VARDOULAKIS, I., STAVROPOULOU, M. C. & TSOMBOS, P. 2003. Analogue and numerical modeling of normal fault patterns produced due to slip along a detachment zone. *Tectonophysics*, **376**, 117–134.

FACCENNA, C., NALPAS, T., BRUN, J. P., DAVY, P. & BOSI, V. 1995. The influence of pre-existing thrust faults on normal fault geometry in nature and experiments. *Journal of Structural Geology*, **17**, 1139–1149.

FLOTTÉ, N. 2002. *Caractérisation structurale et cinématique d'un rift sur détachement: le rift de Corinthe-Patras, Grèce*. PhD thesis, University of Paris South.

GHISETTI, F., BARCHI, M., BALLY, A. W., MORETTI, I. & VEZZANI, L. 1993. Conflicting balanced structural section across the Central Apennines (Italy): problems and implications. *In*: SPENCER, A. M. (ed.) *Generation, Accumulation and Production of Europe's Hydrocarbons III*, European Association of Petroleum Geoscience, Special Publication, **3**, 219–231.

GHORBAL, B. 2002. *Quels arguments en faveur d'un detachment Plio-Quaternaire au Sud du Golfe de Corinthe?: Etudes tectono-métamorphiques des Phyllades du Péloponnèse septentrionale*. MA thesis, Univerity of Paris Jussieu.

HIGGINS, R. I. & HARRIS, L. B. 1997. The effects of cover composition on extensional faulting above reactivated basement faults: results from analogue modeling. *Journal of Structural Geology*, **19**, 89–98.

HORSFIELD, W. D. 1977. An experimental approach to basement-controlled faulting. *Geologie en Mijnbouw*, **56**, 363–370.

HOUNSFIELD, G. N. 1973. Computerized transverse axial scanning (tomography). *British Journal of Radiology*, **46**, 1016–1022.

HUBBERT, M. K. 1937. Theory of scale models as applied to the study of geologic structures. *Geological Society of America Bulletin*, **48**, 1459–1520.

JOLIVET, L. 2001. A comparison of geodetic and finite strain pattern in the Aegean, geodynamic implications. *Earth Planetary Sciences Letters*, **187**, 95–104.

LAVECCHIA, G., MINELLI, G. & PIALLI, P. 1987. Contractional and extensional tectonics along the transect Trasimeno Lake-Pesaro (Central Italy). *In*: BORIANI, A., BONAFEDE, M., PICCARDO, G. B. & VAI, G. B. (eds) *The Lithosphere in Italy. Advances in Earth Science Research*, Atti Convegno Lincei, **80**, 139–142.

LE POURHIET, L., BUROV, E. & MORETTI, I. 2004. Rifting through a stack of inhomogeneous thrusts (the dipping pie concept). *Tectonics*, **23**, TC4005.

LE POURHIET, L., MATTIONI, L. & MORETTI, I. 2005. 3D modelling of rifting through a pre-existing stack of nappes in the Gulf of Corinth (Greece): a mixed analogue/numerical approach. *In*: BUITER, S. J. H. & SCHREURS, G. (eds) 2006. *Analogue and Numerical Modelling of Crustal-Scale Processes*. Geological Society, London, Special Publications, **253**, 233–252.

LOHRMANN, J., KUKOWSKY, N., ADAM, J. & ONCKEN, O. 2003. The impact of analogue material properties on the geometry, kinematics, and dynamics of convergent sand wedges. *Journal of Structural Geology*, **25**, 1691–1711.

MANDL, G. 1988. *Mechanisms of Tectonic Faulting*. Elsevier, Amsterdam.

MATTIONI, L., LE POURHIET, L. & MORETTI, I. 2004. Extension through a heterogeneous crust. The case of Gulf of Corinth (Greece). Part I: Analogue modelling. *Bollettino di Geofisica teorica ed applicata*, **45**, 237–241.

MCCLAY, K. R. & ELLIS, P. G. 1987. Geometries of extensional fault system in model experiments. *Geology*, **15**, 341–344.

MICARELLI, L., MORETTI, I. & DANIEL, J. M. 2003. Influence of depth and amount of displacement of the characteristics of normal faults, case study in the Gulf of Corinth – Greece. *Journal of Geodynamics*, **36**, 275–303.

MYRIANTHIS, M. L. 1984. Graben formation and associated seismicity in the Gulf of Korinth (Central Greece). *In*: DIXON, J. E. & ROBERTSON, A. H. F. (eds) *The Geological Evolution of the*

*Eastern Mediterranean*, Geological Society, London, Special Publications, **17**, 701–707.

MORETTI, I. 2004. Asymmetry of the early rift structures: a comparison between the Gulf of Suez and the Gulf of Corinth. *Studi Geologici Camerti*, Special Issue 2004, 105–111.

MORETTI, I., SAKELLARIOU, D., LYKOUSIS, V. & MICARELLI, L. 2003. The Gulf of Corinth: a half graben? *Journal of Geodynamics*, **36**, 323–340.

NALPAS, T. & BRUN, J. P. 1993. Salt flow and diapirism related to extension at crustal scale. *Tectonophysics*, **228**, 349–362.

OLSEN, P. & SCHLISCHE, R. W. 1990. Transtensional arm of the early Mesozoic Fundy rift basin: penecontemporaneous faulting and sedimentation. *Geology*, **18**, 695–698.

RAMBERG, H. 1981. *Gravity, Deformation and the Earth's Crust*. Academic Press, New York.

RICHARD, P. D. 1991. Experiments on faulting in a two-layer cover sequence overlying a reactivated basement fault with oblique (normal-wrench or reverse-wrench) slip. *Journal of Structural Geology*, **13**, 459–469.

RIGO, A. & LYON CAEN, H. *ET AL.* 1996. A microseismic study of the western part of the Gulf of Corinth (Greece): implications for the large-scale normal faulting mechanisms. *Geophysical Journal International*, **126**, 663–688.

ROSENDAHL, B. 1987. Architecture of continental rifts with special reference to east Africa. *Annual Review of Earth and Planetary Science*, **15**, 445–503.

SCHELLART, W. P. 2000. Shear test results for cohesion and friction coefficients for different granular materials: scaling implications for their usage in analogue modelling. *Tectonophysics*, **324**, 1–16.

SCHLISCHE, R. W., WITHJACK, M. O., EISENSTADT, G. 2002. An experimental study of the secondary deformation produced by oblique-slip normal faulting. *American Association of Petroleum Geologists*, **86**, 885–906.

SCHREURS, G. 1992. Analogue modelling using x-ray computed tomography analysis: experiments on distributed strike-slip shear deformation. *Institut Français du Pétrole Report* 39893.

SCHREURS, G., HÄNNI, R. & VOCK, P. 2002. The influence of brittle-viscous multilayers on faulting during rifting: an analogue modelling approach. *In*: SCHELLART, W. P. & PASSCHIER, C. (eds) *Analogue Modelling of Large-Scale Tectonic Processes*, Journal of Virtual Explorer, **6**, 89–97.

STEFATOS, A., PAPATHEODOROU, G., FERENTINOS, G., LEEDER, M. & COLLIER, R. 2002. Seismic reflection imaging of active offshore faults in the Gulf of Corinth; their seismotectonic significance. *Basin Research*, **14**(4), 487–491.

STEWART, S. A. 1999. Geometry of thin-skinned tectonic systems in relation to detachment layer thickness in sedimentary basins. *Tectonics*, **18**, 719–732.

TRON, V. & BRUN, J. P. 1991. Experiments on oblique rifting in brittle-ductile systems. *Tectonophysics*, **188**, 71–84.

VENDEVILLE, B. 1987. Champs de failles et tectonique en extension: modélisation expérimentale. PhD thesis, University of Rennes, France.

VENDEVILLE, B. 1988. Modèles expérimentaux de fracturation de la couverture contrôlée par des failles normales dans le socle. *Comptes rendus de l'Académie des Sciences*, **307**, 1013–1019.

VENDEVILLE, B. C., COBBOLD, P. R., DAVY, P., BRUN, J. P. & CHOUKROUNE, P. 1987. Physical models of extensional tectonics at various scale. *In*: COWARD, M. DEWEY, J. & HANCOCK, P. L. (eds) *Continental Extensional Tectonics*. Geological Society, London, Special Publications, **28**, 95–107.

WITHJACK, M. O. & CALLAWAY, S. 2000. Active normal faulting beneath a salt layer: an experimental study of deformation in the cover sequence. *American Association of Petroleum Geologists*, **84**, 627–651.

# 3D modelling of rifting through a pre-existing stack of nappes in the Gulf of Corinth (Greece): a mixed analogue/numerical approach

L. LE POURHIET[1,2*], L. MATTIONI[2**] & I. MORETTI[2]

[1]*Laboratoire de Tectonique, Université Pierre et Marie Curie, Paris, France (e-mail: laetitia@gps.caltech.edu)*

[2]*Institut Français du Pétrole, Rueil Malmaison, France*

**Now at Caltech, Pasadena, CA, USA*

***Now at Beicip Franlab, Rueil Malmaison, France*

**Abstract:** The Gulf of Corinth is a young (1 Ma) active rift currently extending N00, which displays significant contrasts in structural style along strike. A possible explanation for these variations is the presence of the Phyllades nappe in the basement of the western part of the Gulf. Previous 2D thermo-mechanical models have shown that a strong strength contrast between this metamorphic unit and the rest of the basement can explain the kinematics and the spacing of the faults in the western part. The rift, however, displays a wide variety of 3D features (e.g., en echelon faulting, N30 transverse normal faults) that cannot be taken into account using 2D modelling. To obtain 3D insights into the role of an inherited dipping weakness zone, analogue (sand and PDMS) experiments based on the results of the 2D numerical thermo-mechanical model have been performed. The analogue models show that a 30° discrepancy between the dipping direction of the weak nappe and the direction of extension leads to the formation of en echelon and N30 striking normal faults as observed in the Gulf of Corinth. However, fault spacing and graben width completely misfit both the data and the results of the thermo-mechanical models on which the analogue experiments were based. In order to understand those differences, numerical mechanical benchmarks of the analogue experiments have been run to test different factors (3D lateral displacements, values of the elastic parameters and bottom boundary conditions) that could have affected the dynamics of the analogue model. This approach highlights, for our case study, that the misfits are mostly related to the lack of isostatic compensation at the base of the analogue experiments.

## Geological setting

The area of the Gulf of Corinth has been in a continuous extensional regime since the middle Miocene (Jolivet *et al.* 1994; Jolivet & Faccenna 1999). This contribution deals with the last rifting event that has taken place for the last 1 to 1.5 Ma in the area, but as the long-term extension affects the structures, both the long-term and the neotectonic features will be briefly discussed in the following.

In the external zone of the Hellenides, long-term extension has led to the exhumation of metamorphic core complexes along ductile shear zones. In the Peloponnesus, the shear strain associated with these detachments is mainly localized inside the Phyllades nappe (Fig. 1). One of the core complexes crops out at the southern limit of the Gulf of Corinth in the Zarouchla tectonic window (outlined by strips in Fig. 1). The average strike of the stretching lineations affecting this dome structure is parallel to the Miocene direction of extension (i.e., N30 to N50). Hence, at the onset of the neotectonic rifting event, the Phyllades nappe was already retromorphosed from the lowest pressure in the blue schist metamorphic facies to the epimetamorphic facies.

The present day geometry of the shoreline of the Gulf of Corinth shows that the mean topography decreases eastwards. Moho depth follows the same trend (Makris 1978; Tiberi *et al.* 2001). This positive correlation, at the scale of the Gulf, suggests that the base of the crust is isostatically compensated and that the large-scale topographic gradient remains from long-term extension. The widening of the Gulf to the east is also compatible with a clockwise rotation of the Peloponnesus, as inferred from paleomagnetic data (e.g., Duermeijer *et al.* 2000), and reflects the fact that the finite extension has

*From*: BUITER, S. J. H. & SCHREURS, G. (eds) 2006. *Analogue and Numerical Modelling of Crustal-Scale Processes.* Geological Society, London, Special Publications, **253**, 233–252.
0305-8719/06/$15.00 

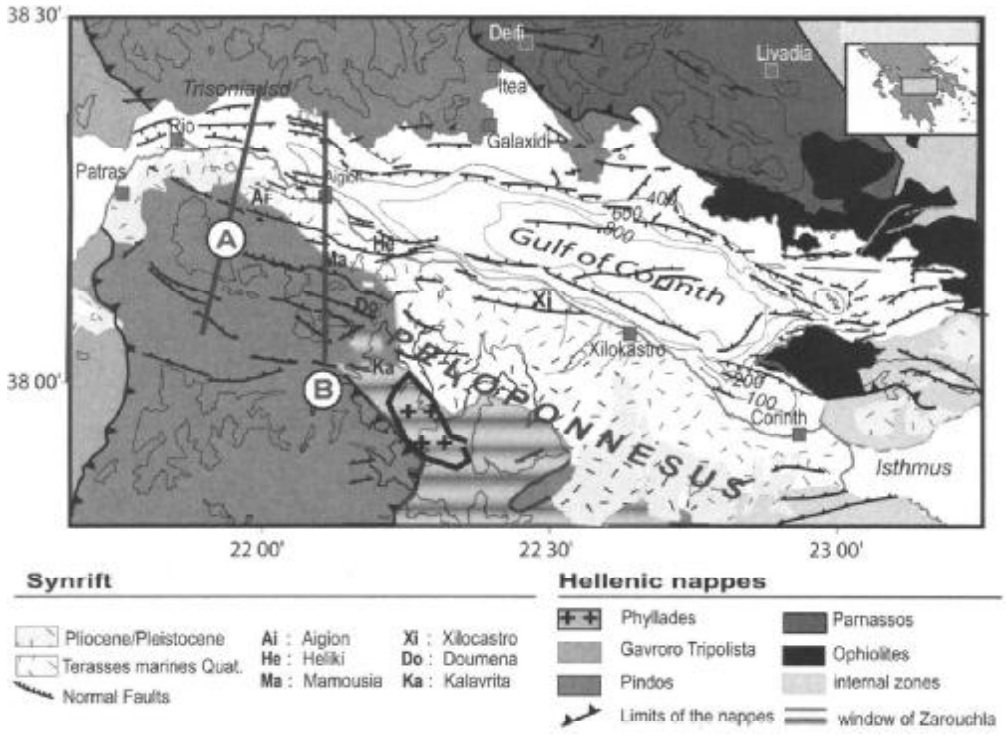


**Fig. 1.** Structural map of the Gulf of Corinth. Faults after Moretti (2004), limits of the nappes after Aubouin *et al.* (1970). A and B lines correspond, respectively, to the location of the geological cross-section (Moretti 2004) displayed in Fig. 5 and to the micro-seismic cross-section of Rigo (1996) used to constrain the validity of the thermo-mechanical models.

been much greater in the central Aegean domain than in the external part of the Hellenides.

At the onset of rifting, the eastern part of the rift was indeed connected to the Aegean Sea at the level of the Corinth Isthmus and Megara basin further east (Bentham *et al.* 1991). Because the western part of the current rift was still under compression until the Pliocene (Doutsos & Kokkalas 2001), the basin was closed by the Hellenides belt at the level of Patras and, therefore, has not been affected by long-term extension. The sediments from this side of the rift as well as the oldest dated calcite steps found along fault planes are early Pleistocene in age (i.e., $<1$ Ma; see Causse *et al.* 2004). This timing is compatible with the onset of dextral displacement on the Kefalonia fault (Cocard *et al.* 1999); a strike slip fault located further west. These data suggest a change in the regional kinematics by 1.5 Ma that could explain the discrepancies between geological observations and GPS measurements (Briole *et al.* 1999). GPS data indicates that the current direction of extension is N00 and that the rate of extension increases westward from 0.5 cm/yr at the level of the Corinth Isthmus to 1.5 cm/yr at the level of Patras. This anticlockwise rotation of the Peloponnesus with respect to the northern margin of the Gulf is not compatible with the paleomagnetic data. Therefore, given the short (60 km) length-scale of the Gulf of Corinth, the current rifting phase can be treated separately from the Neogene long-term extension.

From a structural point of view, the Quaternary rift is usually described as an asymmetric graben because the southern shore is covered by uplifted deposits of marine fan deltas and continental Guilbert's fan deltas (Ghisetti *et al.* 2001; Malartre *et al.* 2004), whereas, on the northern shore, the pre-rift basement crops out directly. Although some beach-rocks are locally uplifted, the northern shore is stable or slightly subsiding in general (Lykousis *et al.* 1998).

The Gulf of Corinth is segmented along strike (Ghisetti & Vezzani 2004). In the central-eastern part of the rift, the syn-rift deposits are located in one main graben in which faulting is roughly symmetrical (Stefatos *et al.* 2002). However, the marine terraces uplifted on the southern shore indicate a subsisting asymmetry of the shore (Armijo *et al.* 1996). At the eastern tip, the Gulf is divided into two grabens bordered by faults dipping 45° and branching at the base

of the seismogenic zone, which is located much deeper (i.e., 15 to 20 km) than in the west (Jackson *et al.* 1982). These faults have two main strike directions: N90° and N30°. The first ones were responsible for the 1981 earthquake. The last ones were responsible for the closure of the connection between the Gulf and the Aegean Sea during the Quaternary.

In the western part, the basin is elongated N120. The southern shore line reflects the en echelon disposition of the major faults. Their strikes are perpendicular to the current direction of extension (i.e., N90° to N110°, see Moretti *et al.* 2003). N30° normal faults are highlighted by microseismic events (Lyon Caen *et al.* 2004), micro-gravimetric survey (Mrlina 2004*a*, *b*) and seismic reflection data (Naville *et al.* 2004). These normal faults act as transfer between the N90 faults.

On the southern shore, sedimentation has been controlled by numerous and closely spaced faults forming a series of small isolated half grabens. The age of those grabens seems to decrease northward (Flotté 2002; Micarelli *et al.* 2003). Flotté (2002) used anticline deformation data of the syn-rift deposits to constrain kinematic reconstructions of the fault décollement level based on a roll-over model. His models imply that such a level deepens northwards. However, he was not able to propose a conceptual model explaining mechanically that fault spacing reduces from 8 km to 4–2 km in the direction of deepening of the inferred décollement level.

The microseismic and seismic events recorded in the western Gulf of Corinth also outline a northward dipping zone. Moreover, reconstruction of focal mechanisms of the earthquakes located inside this zone indicate very low angle nodal planes (i.e., 10°–30°, Rigo *et al.* 1996; Rietbrock *et al.* 1996) and thus favour the possibility for seismicity along shallow dipping fault(s). Seismologists tend now to agree on the fact that the outcropping major faults are planar up to the base of the seismogenic zone. Although the relation between the low-angle seismic events and the high-angle faults is not yet well understood, the low-angle dipping zone is clearly associated with the presence of fluids, as shown by anomalies in the Vp × Vs (velocity of P-wave × velocity of S-wave) tomography (Latorre *et al.* 2004) and in the magneto-telluric conductivity (Pham *et al.* 2000).

## Modelling approach

Based on the observations that (1) the spacing of the normal faults decreases in the same direction as the postulated décollement level deepens and that (2) the N120/N30 direction appears everywhere along this structure, Le Pourhiet *et al.* (2004) proposed that the N120° overall direction of the western part of the Gulf is inherited from the Neogene syn-orogenic extension. Their fully coupled 2D thermo-mechanical models include a weak dipping layer in the pre-rift basement, because:

(1) The southern fault of the zone affected by Quaternary rifting is observed to root at low angle on the Phyllades nappe, in the field (Flotté, 2002).
(2) The Phyllades tectonic unit was originally a pelitic deep basin deposit and was exhumed during the late Miocene (L. Jolivet, pers. comm. for the Gulf of Corinth; Trotet 2000 in the South Peloponesus). During its burial and exhumation, it has been enriched in anisotropic phyllosilicates known to be very weak in the ductile (Ranalli 1987) as in the plastic regime (Bos & Spiers 2002).
(3) Tiberi *et al.* (2001) evidence by means of gravity measurements, a very strong anomaly elongated N120, located at the place where the Phyllades crop out.

Once the presence of the weak dipping nappe in the basement of the Gulf of Corinth is established, thermo-mechanical models have been used to quantify the dynamic influences of the presence of a weak dipping nappe. The weakness of the heterogeneity has been set as a parameter and models have been computed for a wide range of competences. After comparing the kinematics and stress distribution in the model to the fault spacing, earthquakes distribution and fault kinematics in the Gulf of Corinth, it has been found that only a very weak nappe can explain the rotation of P and T axes for the relatively deep earthquakes, the shallow décollement level (inferred from rollover), and the fault spacing in the western part of the Gulf of Corinth.

As a step forward in the understanding of the Gulf of Corinth, this paper and Mattioni *et al.* (2006) aim to verify that the non co-linearity between the current direction of extension and the dipping direction of the weak nappe leads to the formation of en echelon structures similar to those observed in the Gulf of Corinth. 3D analogue models have been designed using the effective rheology (elasto-plastic v. viscous) obtained from the numerical thermo-mechanical computations. Despite this effort made in fitting the effective rheologies, major discrepancies exist in the shape of the graben (width, fault spacing).

Possible causes of these discrepancies fall into three categories: (1) The plane strain assumption in the thermo-mechanical model. (2) The rheological assumptions in the analogue models, e.g., neglecting the elastic effect in the overall model, neglecting plasticity in the weak layer. (3) The basal boundary conditions in the analogue models.

In order to explore the potential impact of these factors, numerical benchmarks of the analogue experiments have been carried out. This part of the study shows how a coupled approach using both 2D numerical modelling and 3D analogue modelling gives better insights into the validity of the models and their relevance for solving geodynamic issues.

After a description of the two modelling tools, the set-up and results of Le Pourhiet *et al.* (2004) are briefly described, as well as a similar thermo-mechanical experiment that will be used as reference for the present study. We then focus on the set-up of the analogue experiments and their results. After comparing the new coupled thermo-mechanical model with the analogue experiments, the paper will seek an explanation for the large discrepancies observed between both approaches, by computing numerical benchmarks of the analogue models and varying the different parameters listed above.

## Modelling techniques

### *Numerical approach*

We use Paravoz, a fast Lagrangian analysis of continua (FLAC)-based thermo-mechanical code (Cundall 1989; Poliakov *et al.* 1993). This code solves Newton's second law

$$\rho g_i + \frac{\partial \sigma_{ij}}{\partial x_j} = \rho \frac{\partial V_i}{\partial t} \tag{1}$$

and Fourier's law for heat transfer

$$\frac{DT}{Dt} = \frac{\partial}{\partial x_i}\left(\chi \frac{\partial T}{\partial x_i}\right) + \frac{H_r}{\rho C_p} \tag{2}$$

where $\rho$ = mean density, $g$ = gravity acceleration, $\sigma$ = stress tensor, $x$ = spatial coordinates, $V$ = velocity, $t$ = time, $\chi$ = thermal diffusivity, $T$ = temperature, $H_r$ = radiogenic heat production, $C_p$ = heat capacity. Einstein summation applies for repeated indices.

These partial differential equations are solved using a fully coupled (including thermal stress/shear heating) explicit scheme on a Lagrangian mesh using a mixed (element/nodes) discretization to avoid mesh locking (Cundall & Board 1988). Large strain computations are allowed by remeshing as soon as one of the corners of the triangular mesh reaches a critical minimum angle of 10°. As the remeshing process includes linear interpolation of nodal values (velocity, temperature) and closest neighbour redistribution of elementary values (stresses, physical properties including finite strain), it should be avoided as much as possible for the sake of precision.

Heat advection is implicitly solved considering the rate of deformation of the mesh as indicated by the objective time derivative $D$ in Fourier's equation. The explicit time-marching aspect of this numerical method implies very small time steps and thus enables various non-linear visco-elasto-plastic rheologies to be handled easily. In shear, each element behaves either as compressible an elasto-plastic or Maxwell visco-elastic body, depending on which of these two rheologies produces the lowest value of the second invariant of stress tensor.

Maxwell body behaviour can be written following an incremental rule:

$$\begin{cases} \sigma_{ij} = \sigma_{ij}^{\text{old}} + \dfrac{\partial \tau_{ij}}{\partial t}\Delta t + \delta_{ij}\dfrac{\partial \bar{\sigma}}{\partial t}\Delta t \\ \dfrac{\partial \tau_{ij}}{\partial t} = 2G\left(e_{ij} - \dfrac{\tau_{ij}}{2\mu_{\text{shear}}(T, e^{\text{II}})}\right) \\ \dfrac{\partial \bar{\sigma}}{\partial t} = K\nabla \cdot \mathbf{V} \end{cases} \tag{3}$$

where $\delta$ is the Kronecker delta, $G$ and K are respectively the shear and bulk modulus, and $e^{\text{II}}$ is the second invariant of the strain rate tensor $e$, while $\tau$ is the deviatoric part of the stress tensor, and $\bar{\sigma}$ is its trace divided by 3. $\mu_{\text{shear}}$ is the effective dynamic viscosity. It can be set as a constant or may depend on the second invariant of deviatoric strain-rate tensor following the 3D formulation of the power law creep flow rules described in Chen & Morgan 1990.

$$\mu_{\text{shear}}(T, e^{\text{II}}) = \frac{1}{4}(e^{\text{II}})^{((1/n)-1)}\left(\frac{3}{4}A\right)^{-1/n} \times \exp\left(\frac{E}{n\text{RT}}\right) \tag{4}$$

Here, $E$, $A$ and $n$ are the common non-Newtonian creep parameters obtained from uni-axial creep experiments; T and R are the absolute temperature and the gas constant respectively.

As the time steps are small, a simple elastic predictor/plastic corrector technique is used to

compute the non-associated Mohr–Coulomb elasto-plastic flow. This means that when the predicted elastic state of stress reaches the yield criterion $f^s$, which depends on the internal friction angle $\Phi$ of the material,

$$\begin{aligned} N_\Phi &= \frac{1+\sin\Phi}{1-\sin\Phi} \\ f^s &= \sigma 1 - \sigma 3 N_\Phi + 2C_0\sqrt{N_\Phi} \\ f^s &\le 0 \Rightarrow \text{rupture} \end{aligned} \tag{5}$$

The plastic strain $\varepsilon^{\text{plas}}$ is assumed to be proportional by a scalar factor $\lambda s$ to the derivative versus stress of plastic potential $Qs$. $Qs$ depends on the dilatancy angle $\Psi \ll \Phi$ for rocks.

$$\begin{aligned} N_\Psi &= \frac{1+\sin\Psi}{1-\sin\Psi} \\ Qs &= \sigma 1 - \sigma 3 N_\Psi \\ \varepsilon^{\text{plas}} &= \lambda s \frac{\partial Qs}{\partial \sigma} \end{aligned} \tag{6}$$

The plastic multiplier $\lambda s$ is found assuming that in a static yield regime, stresses stay on the yielding surface for consistency (Eqn. 7) reasons (for details see Vermeer & Deborst 1984).

$$\dot{f}^s = 0 \tag{7}$$

An explanation of the boundary conditions that are used in the numerical models is given in Figure 2.

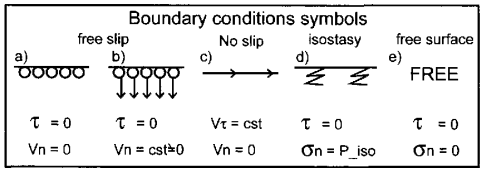


**Fig. 2.** Type of mechanical boundary conditions: (**a**) and (**b**) Free slip means that the orthogonal velocity is set to a constant (Vn) and the tangential stress ($\tau$) to zero. (**c**) No slip means that the tangential velocity is set to a constant (V$\tau$) and normal velocity (Vn) is set to zero. (**d**) Local isostasy means that shear stress ($\tau$) is set to zero and normal stress is ($\sigma$n) calculated with reference to a hypothetic isostatic compensation level at depth. (**e**) Free means that both normal ($\sigma$n) and shear stress ($\tau$) components are set to zero on the boundary. It constitutes a realistic boundary condition to model the Earth's surface and topography for Lagrangian mesh.

*Analogue approach*

The analogue experiments are described in further detail in Mattioni *et al.* (2006) and are only briefly described here.

The experiments are analysed by x-ray tomography (Colletta *et al.* 1991), a non-destructive technique that allows the 4D acquisition of the analogue model density (and thus material) distribution.

In the experiments, upper-crustal brittle rocks are simulated with sand and glass powder (Pyrex, usually used together with sand to get a better visualization of the results with the x-ray scanner). Their internal friction angles are 34° and 42°, respectively, while their densities range from 1500 to 1700 kg/m$^3$, depending on their compaction (note that the sand pile was not pre-compacted in the experiments). As dry granular media are dilatant in shear, the shear bands are easy to image by x-ray tomography as they represent narrow zones of reduced density.

In the present experiments, the Pyrex layer is 3 mm thick and is located 3 mm below the surface at the initial stage, approximately in the middle of the elasto-plastic layer that does not contain the weak dipping heterogeneity.

The ductile behaviour of rocks in the lower crust, and/or of weak layers within the brittle upper crust, is simulated by silicone putty (PDMS) presenting a much lower density than sand (965 kg/m$^3$) and therefore appearing darker on the cross-sections. PDMS behaves as a nearly Newtonian fluid with a viscosity of $2 \times 10^4$ Pa at room temperatures and at strain-rates below $3 \times 10^{-3}$ s$^{-1}$ (Weijermars 1986).

In order to be considered analogue to Earth, physical experiments have to be properly scaled. This means that the dimensionless physical properties that govern the modelled process must be equal in the analogue experiment and in nature (Ramberg 1981). In this study, the scaling of the physical experiments has followed classical rules for sand silicone experiments, thus neglecting the main governing factor for fault spacing, i.e., elasticity. However, the adjective 'analogue' is used instead of 'physical' to describe the experiments throughout our paper for consistency with other papers in this volume.

In the analogue experiments, extension is applied using diverging plastic sheets which are fixed to smooth diverging walls. Friction along those walls is taken to be negligible compared to the friction in the granular media. In the direction orthogonal to extension, the experiments are bordered by two rubber sheets which are used to simulate free slip boundaries.

### *Comparing numerical and analogue results*

Two main outputs have been chosen: topography and cumulative plastic strain. Although topography stands as a straightforward control parameter, one should note that (1) in the numerical scheme of Paravoz a slight diffusion is applied at the top of the models to reduce the occurrence of remeshing, and (2) as the Pyrex (which has a higher angle of internal friction) is not assigned any geological meaning, it has not been taken into account in the numerical model and will be considered as a possible factor introducing modelling artefact in the analogue approach. The numerical topographies are therefore always slightly smoother than those obtained by analogue modelling.

The second control parameter is cumulative plastic strain. It has been chosen because the dark strips, interpreted as faults in the analogue models, correspond in fact to a dilatation zone associated with plastic shear. For underconsolidated sand (as the case in the present analogue experiments), the dilation is theoretically supposed to be proportional to the plastic shear strain after 2% shear strain (Vermeer 1990). Before this critical strain, the shear bands compact slightly and thus will either not be visible by x-ray tomography or appear with lighter tones. It is thus predictable that some shear bands with low amounts of shear strain or diffuse plastic strain zones predicted by numerical modelling will not be visible through x-ray acquisition in the analogue models.

## From 2D thermo-mechanical to 3D analogue models

### *Thermo-mechanical experiments*

All thermo-mechanical experiments were run with Paravoz using a visco-elasto-plastic flow rule including non-Newtonian temperature-dependent viscosity and full thermal coupling. The space was discretized in quadrilateral elements which are initially 200 × 200 m. The mechanical parameters of the runs displayed in this paper are listed in Table 1. The thermal parameters $C_p$ and $\chi$ have been set constant for all materials (i.e., 1000 J kg$^{-1}$ K$^{-1}$ and 3 W m$^{-1}$ K$^{-1}$ respectively) as well as $H_r$, which decreases exponentially with depth according to characteristic decay of $1/e$ for 12 km, taking $H_0 = 10^{-9}$ W kg$^{-1}$ at the surface for all the materials.

Le Pourhiet *et al.* (2004) aimed at getting a better understanding of the impact of a pre-existing weak dipping nappe on the kinematics of faulting during the early stages of rifting. The weak nappe was introduced in the model as a shallow dipping layer (20°) possessing different mechanical properties. The thickness of the nappe (1.5 km), the size of the experiments (60 × 15 km) and the boundary condition were kept constant in the study (Fig. 3a), while two parameters were raised: (1) the contrast in Maxwell relaxation time between the weak dipping nappe and the rest of the pre-rift basement, (2) the pre-rift basement relaxation time. The contrast was obtained by keeping the elastic properties constant as well as the activation energy $E$ and the coefficient $n$ in the creep power law, and by varying the pre-exponential parameter $A$ for the different lithologies. These experiments show that the presence of a weak dipping nappe in the upper crust leads to a local reduction of the integrated strength of the upper crust (Fig. 3b). Consequently, strain localization occurs at a very specific location, the brittle-ductile transition (BDT) of the weak dipping heterogeneity. The parametric study has led to the conclusion that a very weak nappe was indeed needed to avoid the localization on one main decollement level (Fig. 3c) and hence to reproduce the fault spacing, the kinematics and the micro-seismicity depth distribution of the western part of the Gulf of Corinth.

However, to reduce the boundary effects in the analogue models, it was not possible to set the initial geometry of the analogue experiments to the same initial width as in Le Pourhiet *et al.* (2004). Therefore, a new thermo-mechanical run was performed using 102 km instead

**Table 1.** *Mechanical parameters of the thermo-mechanical experiment*

| Material | Density, $\rho$ (kg m$^{-3}$) | $A^{\ddagger}$ (MPa$^{-n}$) | $n^{\ddagger}$ | $E^{\ddagger}$ (J mol$^{-1}$) | Young's modulus, $E$ (Pa) | Cohesion (Pa), $C_0$ | Friction angle, $\Phi$ (°) |
|---|---|---|---|---|---|---|---|
| WN* | 2600 | $5 \times 10^{3}$ | 3 | $1.9 \times 10^{5}$ | $7.5 \times 10^{10}$ | $2 \times 10^{7}$ | 30° |
| SB† | 2600 | $5 \times 10^{-6}$ | 3 | $1.9 \times 10^{5}$ | $7.5 \times 10^{10}$ | $2 \times 10^{7}$ | 30° |

*WN: weak nappe.
†SB: strong basement.
‡Coefficients for non Newtonian creep law are taken from Le Pourhiet *et al.* (2004).

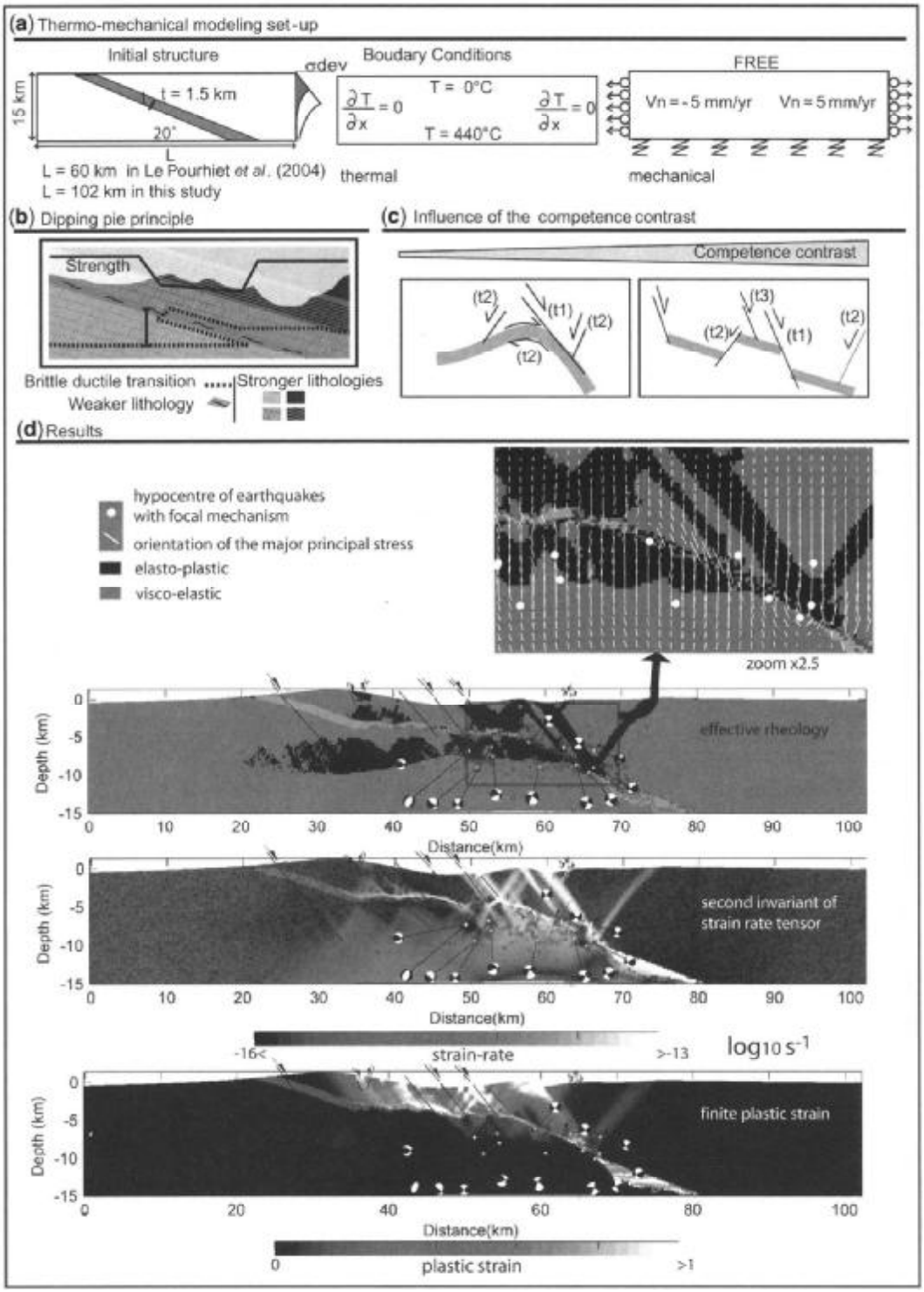


**Fig. 3.** (**a**) Initial geometry of the thermo-mechanical models; a unique weak nappe is represented in grey. Schematic yield strength envelope for the weak heterogeneity and the strong surrounding are drawn on the right. t is the thickness of the weak nappe. The brittle ductile transition of the weak nappe and background white material are the parameters of the study. The last two boxes display the boundary conditions of the thermo-mechanical models for the thermal and the mechanical parts, respectively. (**b**) The dipping pie conceptualizes a layered media on which stress is not applied parallel to the layers but with a slight angle. It applies to any stack of inhomogeneous units and implies local reduction of the strength (thick black line) of the upper crust associated with lateral variations of the depth of the brittle ductile transition (BDT = dashed line). (**c**) Resulting fault kinematics and distribution as a function of competence contrast. Numbers in brackets indicate the relative timing of faulting. (**d**) Comparison between the results of a thermo-mechanical run and the fault pattern and micro-seismic data from the Gulf of Corinth (Rigo *et al.* 1996).

of 60 km as initial width in the stretching direction, the rest of the parameters remaining unchanged.

The results of the new experiment are shown in Figure 3d. Although the strain rate is now slightly lower, the results obtained with this wider version are similar to those obtained in the previous study in terms of fault spacing and kinematics of faulting, i.e., some of the faults cross the weak nappe and root at the BDT of the upper crust, while the first fault and some out-of-sequence faults root at lower depth on the weak heterogeneity. After 1.5 Ma of extension, there is a good agreement with the fault spacing (i.e., finite plastic strain), the distribution of active faults, the depth distribution of the micro-seismicity, as well as the orientation of the principal stress direction at depth as inferred in the western part of the present day Gulf of Corinth.

### *Analogue experiments*

*Set-up.* The dimension of the sandbox is determined by the size of the medical scanner (i.e., $0.7 \times 0.255$ m). In order to be able to compare numerical and analogue models, the material distribution (i.e., granular or PDMS) in the analogue experiments should reflect the effective rheology (i.e., elasto-plastic or viscous) of the thermo-mechanical experiments. *Sandbox* experiments, unlike numerical experiments, do not enable the temperature dependence of the viscosity to be taken into account. Therefore, an arbitrary limit between the effectively brittle and effectively viscous domain has to be introduced. In order to set this limit, a comparison between the Maxwell relaxation time and the characteristic timescale of our control parameter (i.e., the fault formation and migration relevant for the Gulf of Corinth) has been made. We arbitrarily decided that the part of the thermo-mechanical models having a Maxwell characteristic time five times lower than the time needed to create a new fault, are considered to behave viscously while the rest is considered to behave as an elasto-plastic body. As the faulting timescale is 100 ka, the limit we are seeking corresponds to a Maxwell characteristic time of 20 ka. Taking into account the shear modulus $G = 3 \times 10^{10}$ Pa, this limit corresponds to an effective viscosity of $10^{22}$ Pa in the thermo-mechanical models.

Because the aim of the study is to get insight into the 3D structure of the Gulf of Corinth, the initial material distribution of the analogue models (Mattioni *et al.* 2006) has been determined using the effective viscosity computed for the best fitting thermo-mechanical model (see top of Fig. 4).

For comparison, we have chosen two analogue experiments presented in Mattioni *et al.* (2006): a 3D cylindrical experiment (PH1), in which the weak nappe dipping direction is in the direction of stretching (i.e., $\beta = 0°$ in Fig. 4), and a non-cylindrical experiment (PH4), in which the dipping direction is not co-linear with the stretching direction (i.e., $\beta = 30°$ in Fig. 4).

The dip of the weak nappe in the analogue experiments depends on its strike, $\beta$, and on its apparent dip in the stretching direction, which is set constant, i.e., $\alpha = 20°$. The two analogue experiments have different scaling because they were run with different velocities of extension. As our final goal is to study the Gulf of Corinth, we have arbitrarily chosen that, at nature scale, the velocity of extension is the same but the viscosities of the viscous layers are different. The rest of the scaling parameters are summarised in Table 2.

*Results of the analogue experiments.* The results of the experiments PH1 and PH4 are described in the companion paper by Mattioni *et al.* (2006) but are summarized here to allow for comparison. In both experiments, the dipping slab of silicone putty (where it exists) allows for the formation of a rift zone rooted above the silicone, which localizes most of the extension in the elasto-plastic domain. In the early stages of deformation, a system of conjugate high-angle normal faults initiates at the upper tip of the dipping layer and propagates to the free surface as the horizontal offset increases at the level of the dipping slab of silicone. As a result, a roughly symmetrical graben is created. As deformation increases, the first synthetic fault remains fixed with respect to the tip of the silicone slab, whereas the rifted zone slightly propagates in the down-dip direction of the silicone level. This leads to a progressive asymmetrical widening of the basin in which the faults rotate passively to a lower angle. As horizontal strain increases, a large downward flexure progressively deforms the hanging wall of the décollement level but no fault seems to form in this area (see cross-section in Fig. 5).

In the non-cylindrical experiment (PH4), the silicone dipping slab is not present everywhere along the strike. This experiment is thus divided into three structural zones (see Mattioni *et al.* 2006), a first one where the slab is present (left side of the surface view experiment in Fig. 5), a second one where the silicone is not present (right side of the surface view experiment in Fig. 5) and a third one which corresponds to the transition zone.

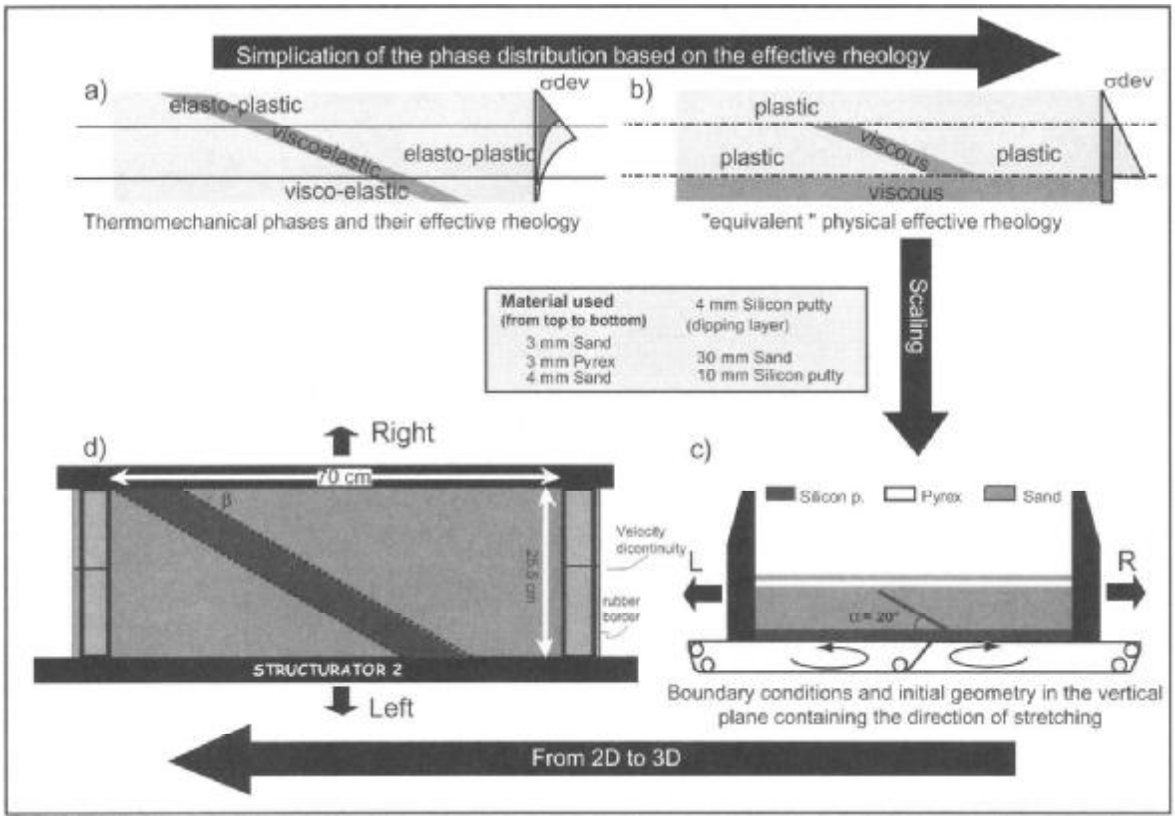


**Fig. 4.** From thermo-mechanical to analogue modeling: (**a**) Previous thermo-mechanical model and its yield strength envelopes. (**b**) Effective rheology is used to obtain the distribution of viscous and elasto-plastic analogue materials in the analogue experiment. (**c**) Final cross-section of the analogue model in the direction of extension. The apparent dip of the silicone putty in this direction is the same as in the thermo-mechanical model, but the boundary conditions at the base include a velocity discontinuity that is not present in the thermo-mechanical experiment. (**d**) Top view of experiment 4, $\beta = 30°$.

In the first structural zone, the overall trend of the modelled rift is parallel to the strike of the silicone slab. The first fault forming at the tip of the silicone putty maintains its original orientation during the course of the experiments (i.e., parallel to the strike of the underlying viscous layer). The faults forming in the later stage of the experiments are structurally more complex. They nucleate as a system of en echelon faults roughly oriented N105. As the deformation

**Table 2.** *Scaling parameters for the analogue models PH1 and PH4*

| Dimension | Scaling | Nature | Model |
|---|---|---|---|
| $L^*$ | $2.5 \times 10^{-6}$ | $4 \times 10^3$ m | $10^{-2}$ m |
| $g^*$ | 1 | 9.8 $ms^{-2}$ | 9.8 $ms^{-2}$ |
| $\rho^*$ | ~0.5 | 2600 $kg/m^3$ | 1000–1500 $kg/m^3$ |
| $V^{*(1)}$ | $10^4$ | 1 cm/yr | 1 cm/hr |
| $V^{*(4)}$ | $10^4$ | 1 cm/yr | 2 cm/hr |
| | | | formula |
| $\sigma^*$ | $1.25 \times 10^{-6}$ | | $\rho^* \times g^* \times L^*$ |
| $t^{*(1)}$ | $2.50 \times 10^{-10}$ | | $L^*/V^*$ |
| $\eta^{*(1)}$ | $3.13 \times 10^{-16}$ | | $\sigma^* \times T^*$ |
| $T^{*(4)}$ | $1.25 \times 10^{-10}$ | | $L^*/V^*$ |
| $\eta^{*(4)}$ | $1.56 \times 10^{-16}$ | | $\sigma^* \times T^*$ |

(1) and (4) refer respectively to the analogue experiments PH1 and PH4.

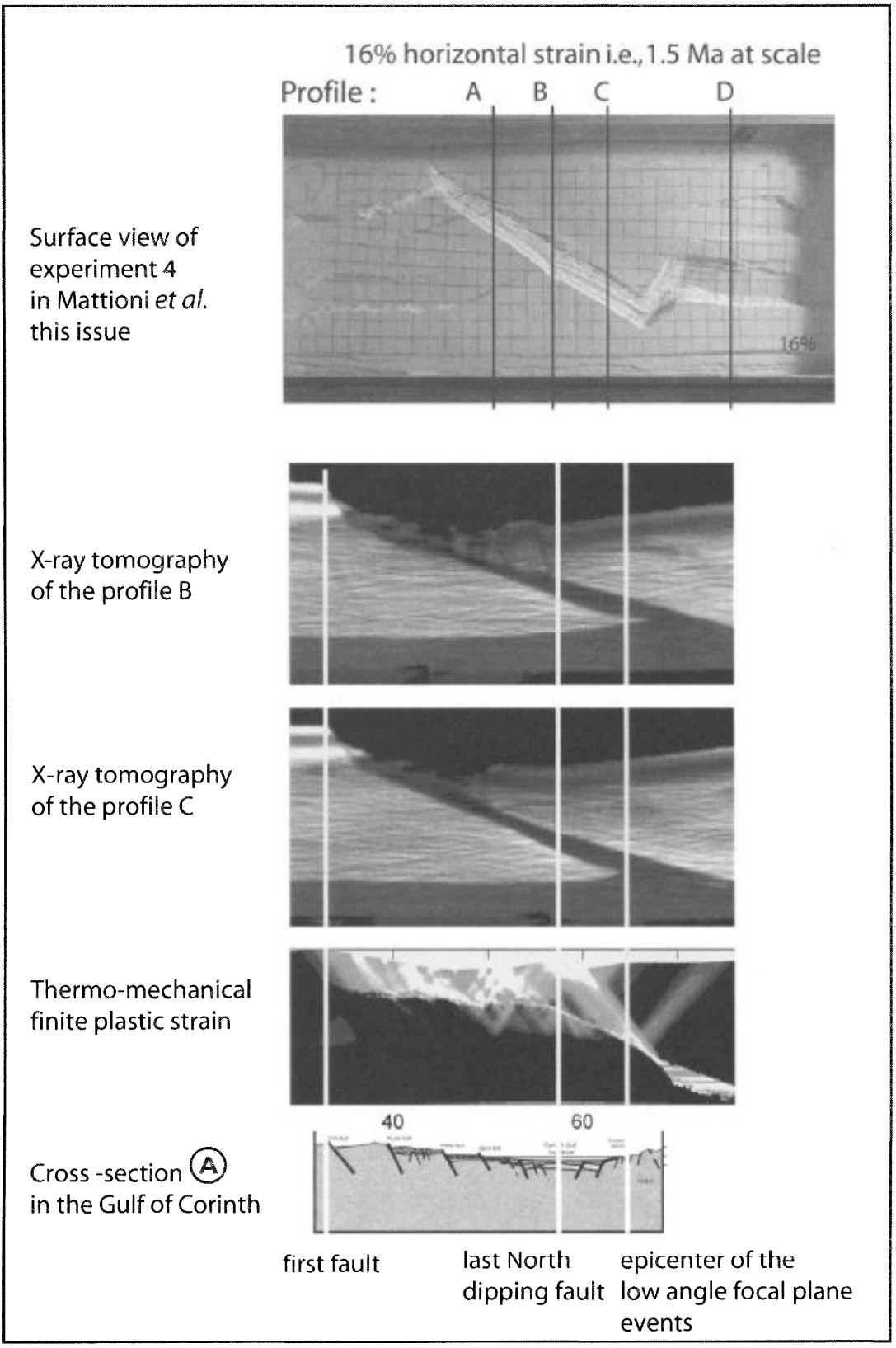


**Fig. 5.** A comparison between analogue model (PH4), the thermo-mechanical model and a cross-section in the Gulf of Corinth. Top: surface view of experiment PH4 after 16% strain showing the location of the 4 profiles used for comparison. Bottom: All the models are at the same scale, only details of the rifts are displayed. No vertical exaggeration.

progresses, their lateral terminations become progressively parallel to the strike of the viscous layer whereas their central segment remains orthogonal to the direction of extension. This rotation about the vertical axis gives them a roughly sigmoid shape (see surface photography in Fig. 5).

In the second structural zone, rifting is localized in wider grabens striking orthogonal to the direction of extension. Their size reflects the larger thickness of the sand pile. In the third structural zone (i.e., the transition zone), the geometry of the faults depends mostly on the initial geometry of the silicone slab termination (see experiments 2, 3 and 4 in Mattioni *et al.* 2006). However, it is worth noting that in every experiment, the existence of the silicone slab laterally in the model affects the location of the wider grabens in the second structural zone. As soon as the normal faults which border those grabens propagate laterally in the transition zone and further in the first structural zone, their strikes rotate and become perpendicular to the strike of the silicone slab (see surface view in Fig. 5). The strike rotation also occurs for the grabens which nucleate at the rear of the silicone slab (i.e., bottom/left of the surface view in Fig. 5). This rotation does not occur in the cylindrical model and thus cannot be related to border effects. This rotation of the horizontal stress field around the silicone slab suggests that the heterogeneity behaves like an elastic dislocation in the analogue model.

*Comparison between thermo-mechanical and analogue experiments (PH 4).* Figure 5 shows that the width of the rift as well as the fault spacing obtained in the sandbox experiments is much smaller than in the thermo-mechanical experiment and thus than observed in the Gulf of Corinth. How can those discrepancies be explained?

Some differences are certainly related to the simplifications that had to be done in terms of rheology and boundary conditions for the analogue modelling technique. Rheological assumptions fall into two main groups: (1) the elastic parameters of sand and PDMS are not scaled to the dimension of the model. In other words, elasticity is assumed to be negligible in the problem, and (2) there is no possibility of breaking the silicone putty layer because the transition from brittle to ductile behaviour is abrupt.

Concerning the boundary conditions, two major differences exist between analogue and thermo-mechanical models. Firstly, our 2D numerical models assume plane strain conditions (i.e., no strain occurs in the out-of-plane direction of the numerical model) whereas analogue experiments are 3D. Secondly, bottom boundary conditions differ between the two modelling techniques. The numerical thermo-mechanical models involve isostatic compensation at their base, whereas the analogue models have fixed velocities at their base in both horizontal and vertical direction and display a velocity discontinuity midway between their lateral boundaries where the underlying plastic sheets diverge.

In order to explore the potential effects of contrasting rheology and boundary conditions existing between the two modelling techniques, numerical benchmark tests have been conducted.

## Relevance of 2D numerical benchmarks for 3D analogue models

In all the numerical mechanical models, the initial element size is $250 \times 250$ m and the thermal coupling is disabled because (1) it is not needed to calculate the viscosity (which is set as constant) and (2) thermal stresses or other Boussinesq terms may only have a little effect on the results but may obscure the comparison with the analogue results.

### *Setting the numerical benchmarks: the REF and REFSLOW models*

In the analogue experiments, silicone behaves as a viscous body and sand as an elasto-plastic body. The same rheological laws are used to compute their numerical benchmarks except that for numerical reasons, the weak silicone slab has been replaced by a Maxwell visco-elastic body with a high shear modulus to ensure that it will always behave as an effectively viscous body. Sand and Pyrex have been replaced by a single elasto-plastic body (see Table 3 for the mechanical constants).

The first aim of the simplified numerical experiments is to reproduce the results of the analogue experiments. The second aim is to use them in order to get a better understanding of the discrepancies existing between the analogue and the thermo-mechanical experiments by varying in the numerical benchmarks the parameters that cannot be varied with the sandbox approach.

In order to simulate analogue experiments, numerical boundary conditions have been set as closely as possible to their analogue counterparts except that the sharp velocity discontinuity at the base has been enlarged to a zone of 10 km in order to limit repeated remeshing which leads to numerical diffusion when computing large strains with a Lagrangian strategy. Paravoz is numerically optimized to enter parameters related to lithospheric processes without previous scaling. Hence, the parameters of the

benchmarks are similar to the parameters of the sandbox but at nature scale. Some parameters are not used to scale the analogue experiments, (e.g., elastic moduli), but are needed for numerical computations. To compute the reference numerical benchmarks, they are set to their most accepted values in nature.

Because the experiments PH1 and PH4 were made with two different stretching velocities and thus two different viscosities at nature scale, two reference benchmarks had to be set up. Their initial and boundary conditions are described in Figure 6. REFSLOW is similar to the 3D cylindrical experiment PH1, while REF is the closest 2D approximation of a cross-section located at profile B in the analogue model PH4.

### *Results of the numerical benchmarks*

*REFSLOW and PH1.* The first benchmark test compares the 3D cylindrical analogue experiment PH1 with REFSLOW. Figure 7 displays a comparison between their topographic profiles, and highlights that conceivable differences in amplitude and width exist between the numerical experiments and the analogue experiments. Moreover, the first fault is much steeper in the analogue experiment. This analogue modelling artefact is probably due to the presence of a layer of Pyrex, which possesses a higher friction angle than sand and thus leads to a steeper (Coulombs) fault dip angle.

However, the faulting patterns are quite similar. For example, the number of faults present in the main graben as well as their spacing correlate well between the two models. This shows that the resolution used for the numerical benchmark is sufficient to distinguish between plastic shear bands at the same length-scale as those visualized by x-ray tomography.

*Testing the relevance of the 2D plane strain assumption for REF and PH4.* The first issue concerning the use of a mixed 2D numerical/3D analogue approach is to check the validity of the plane strain assumption through a series of cross-sections. This is important to validate the results of previous thermo-mechanical models as well as the benchmark approach. Four cross-sections oriented in the direction of extension have been chosen in the analogue experiments. Three of them (A to C) cross the weak nappe and the last profile (D) is located in an area where the weak nappe is not present. Their precise location is indicated on a surface picture of experiment PH4 at the top of Figure 5. For 30° of obliquity between the weak nappe and the direction of extension, analogue experiments clearly show two kinds of 3D structures at the surface: en echelon structures at small length scale, and sand-pile-scaled normal faults propagating from the domain where the weak nappe does not exist towards the weak nappe.

Using topography as a control parameter, profiles A, B and C have been compared to three numerical experiments in which the position of the weak nappe varies relative to the border of the model (Fig. 8). The topographic profiles obtained with these 2D plain strain numerical models are different from each other. As in the test with REFSLOW, the numerical experiments slightly underestimate the amplitudes of topography. However, the variation of width of the faulted zone in the numerical benchmarks is consistent with profiles taken in the direction of extension of the analogue model. This suggests that the variation of width of the rift along the strike of the weak nappe in the analogue experiments is not related to out-of-plane propagating structures but to the mean strain rate affecting the hanging wall of the nappe (i.e., where the rift forms). This rate depends on its position relative to the velocity discontinuity and the diverging wall. The results confirm that the weak nappe controls the depth and the location of localization and show that the topography is largely controlled by the dip of the weak nappe in the direction of extension.

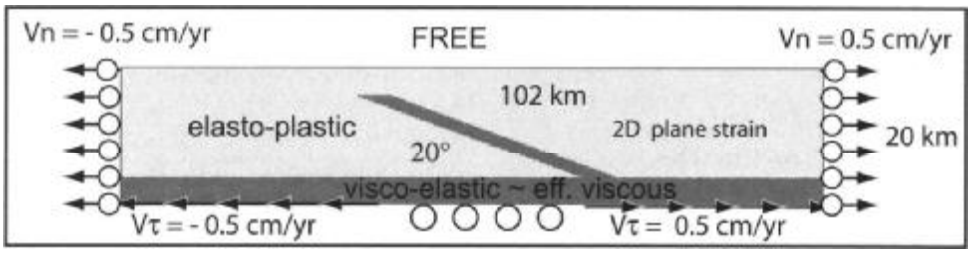


**Fig. 6.** The distribution of materials in the reference benchmark test, i.e., REF and REFSLOW models, is the same as in the analogue model. The velocity discontinuity at the base has been enlarged to reduce the occurrence of remeshing during computation.

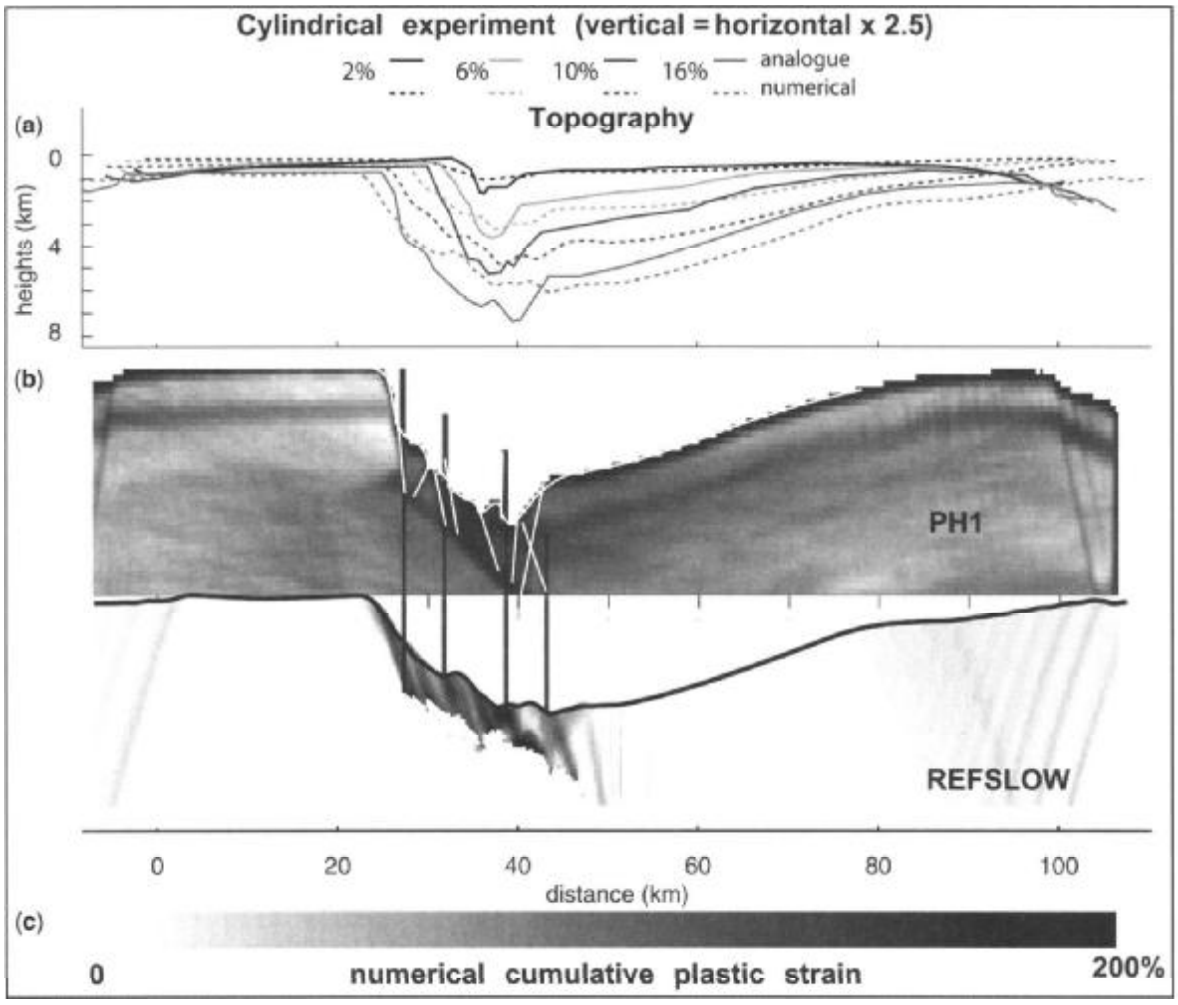


**Fig. 7.** (**a**): Topographic profiles of the 3D cylindrical experiment PH1 and of the numerical model REFSLOW for different finite stretching. (**b**) Tomographic vertical cross-section of PH1 at 16% stretching with faults and topography interpreted with white lines. (**c**) Cumulative plastic strain at 16% stretching for REFSLOW. The vertical black lines correlate faults between the numerical and the analogue experiments.

A comparison of the x-ray tomographic profile D (at the location where the nappe does not exist) and the cumulative plastic strain in the equivalent numerical model shows that the fault spacing is consistent. However, the location of the grabens differs and suggests that in the analogue model, the location of faults is laterally controlled by the presence of the weak nappe whereas, in the numerical model, it is controlled by boundary effects (Fig. 9).

## Testing the effect of rheological assumptions on the benchmarks

### *Effect of visco-elasto-plasticity in the weak nappe*

In the thermo-mechanical experiments, the weak nappe is broken into smaller segments during down dip migration of the subsidence. This phenomenon allows out-of-sequence faults to form at the rear of the major active faults. In the analogue experiments, the weak nappe has a purely viscous behaviour which may prevent the formation of those faults as well as the propagation of faults into the footwall of the weak nappe. To check this possibility, a visco-elasto-plastic (VEP) benchmark test has been computed. By visco-elasto-plastic, we mean that the visco-elastic part of the model has been replaced by a visco-elasto-plastic body with a similar viscosity to that in REF. The comparison between REF and VEP (Fig. 10) shows that a visco-elasto-plastic weak nappe does not affect the width of the faulted zone, but amplifies the effect of the velocity discontinuity by localizing strain rate above it.

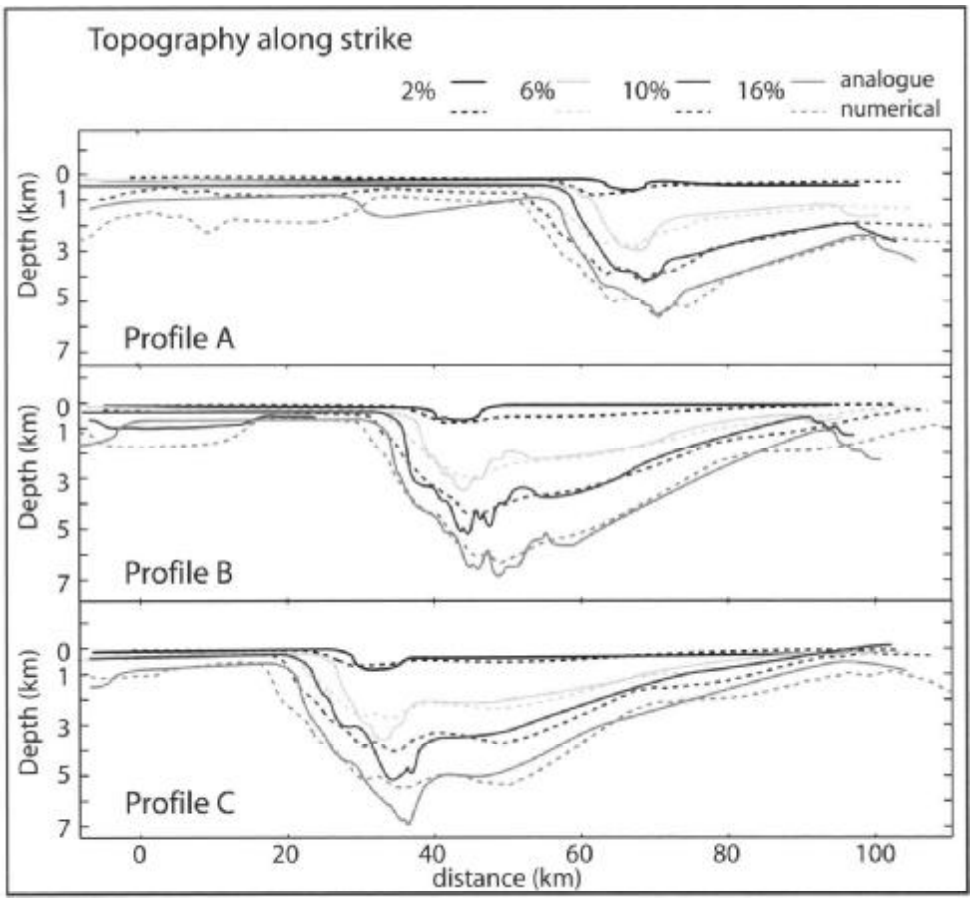


**Fig. 8.** Analogue model topographies of PH4 experiment are scaled up and shown with dashed lines while their equivalent numerical topographies are represented by plain lines.

### *Effect of elastic moduli in the elasto-plastic layer*

Elastic moduli values are usually not taken into account to scale sandbox experiments. Pa unit parameters are usually scaled following the experimental constrains related to Earth's gravity field, the density of the analogue material, cohesion and dimension of the modelling box.

$$\begin{aligned}\sigma^* &= \rho^* \times L^{*2} \times T^{*-2} \\ &= \rho^* \times L^* \times g^*\end{aligned} \tag{8}$$

where $\sigma^*$, $\rho^*$, $g^*$ and $T^*$ stand respectively for non-dimensional values of stress, density, gravitational acceleration ($g^* = 1$) and time.

Taking an accepted value of $10^7$ Pa (e.g., Vermeer 1990) for the shear modulus of sand and the scaling parameters of experiment 4, the shear modulus $G$ at Earth scale becomes:

$$\begin{aligned}G^{\text{at scale}} &= \frac{G^{\text{sand}}}{\sigma^*} \\ A.N.{:}G^{\text{at scale}} &= 8 \times 10^{12}\ \text{Pa}\end{aligned} \tag{9}$$

This value is far higher than values obtained from the PREM model (Poirier 2000) where the highest value is $2.9 \times 10^{11}$ Pa at the core mantle boundary. Moreover, it differs by two orders of magnitude from the values obtained

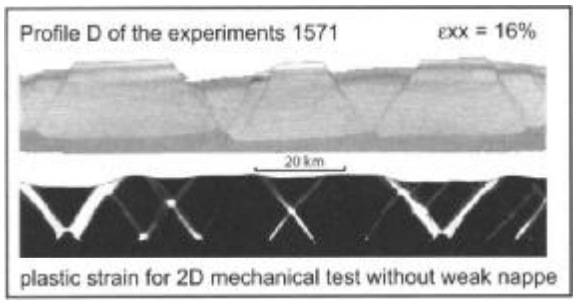


**Fig. 9.** Cumulative plastic strain without the weak nappe (bottom) is compared with profile D of exp. PH4 (top). In the numerical results, white stripes correspond to localized plastic strain.

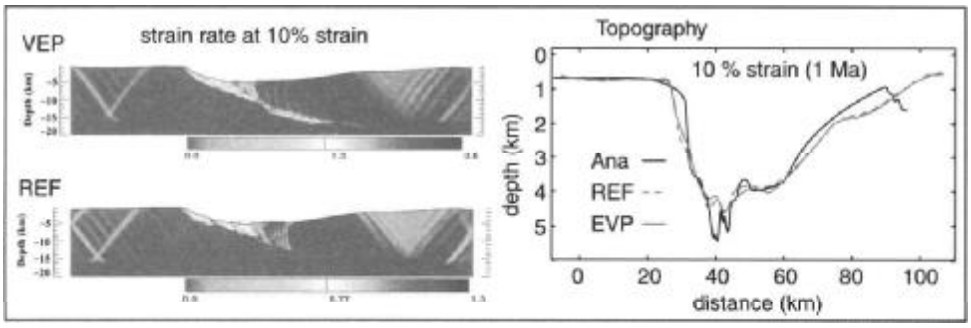


**Fig. 10.** The effect of a visco-elastic-plastic rheology for the weak nappe. VEP: visco-elasto-plastic; REF: reference model; ANA: experiment PH4 profile B.

for the crust, e.g., $2 \times 10^{10}$ Pa (Turcotte & Schubert 2002).

However, mechanical codes based on continuum mechanics (e.g., Paravoz) account for an elasto-plastic rheology, and the elastic moduli need to be set. In the REF experiments, elastic moduli are set to values that are relevant for rocks. To test the effects of mis-scaling elastic moduli, we vary their values by one order of magnitude above and below the commonly accepted value for Earth. The resulting topographies for different finite strains are plotted in Figure 11. They suggest that increasing elastic moduli values in the elasto-plastic layer leads to an increase of the topographic amplitudes for a given finite strain.

The misfit between REF and $\times 0.1$ experiments is bigger than between REF and $\times 10$ experiments because the faults (see cumulative plastic strain on Fig. 11) do not propagate down to the basal viscous layer in the model ($\times 0.1$). However, numerical results obtained with an over-estimated elastic coefficient fit much better with the topography of analogue experiments. This means that one should properly scale the elastic properties of sand by adjusting the density or the dimension of the box as much as possible. However, it is very difficult to determine the elastic properties of granular media like sand as they are very sensitive to damage and strain-rate (e.g., Lyakhovsky *et al.* 1993). This misfit highlights a more general problem: is the sand a good analogue for crust? How far do sand and silicone interact elastically? It is beyond the scope of this study to answer those questions because the set-up, dedicated to the Gulf of Corinth, is too complicated to get quantitative insights into these problems and this kind of study should be done by carefully checking the elastic properties of the sand used for the experiments, especially its Poisson coefficient. However, it seems that benchmarks with numerical codes may be helpful in solving this problem.

## Testing boundary conditions

### *Type of boundary conditions*

Boundary conditions in the analogue experiments are characterized by a horizontal velocity discontinuity where the underlying sheets diverge and by a vertical velocity set to zero at the base of the models. This differs significantly from the isostatic conditions that were imposed in the thermo-mechanical experiments and leads to the observation that the footwall of the weak nappe hardly rotates in the analogue experiments.

In order to explore the effects of a larger range of boundary conditions, several benchmarks have been run. One of them reproduces the exact boundary conditions of the coupled thermo-mechanical computations (i.e., B4 in Fig. 12) but, as this kind of basement is not available in the analogue experimental device, intermediate boundary conditions available in the lab have been tested. One way to simulate local isostasy is to use a thicker layer of silicone putty at the base of the model. As it is not possible to increase the vertical size of the analogue model, the thickness of the basal layer has been multiplied only by a factor 2. The effect of the basal velocity discontinuity on the results has also been investigated by changing it into free slip boundary conditions in the numerical model.

## Results

The strain rates resulting from a wide range of boundary conditions after 10% of bulk extension (Fig. 12) show that the velocity discontinuities, at the base and at the level of the weak nappe, interact to form some parasitic synthetic (almost vertical) faulting at the front of the basin. Such faults are sometimes observed in the analogue results.

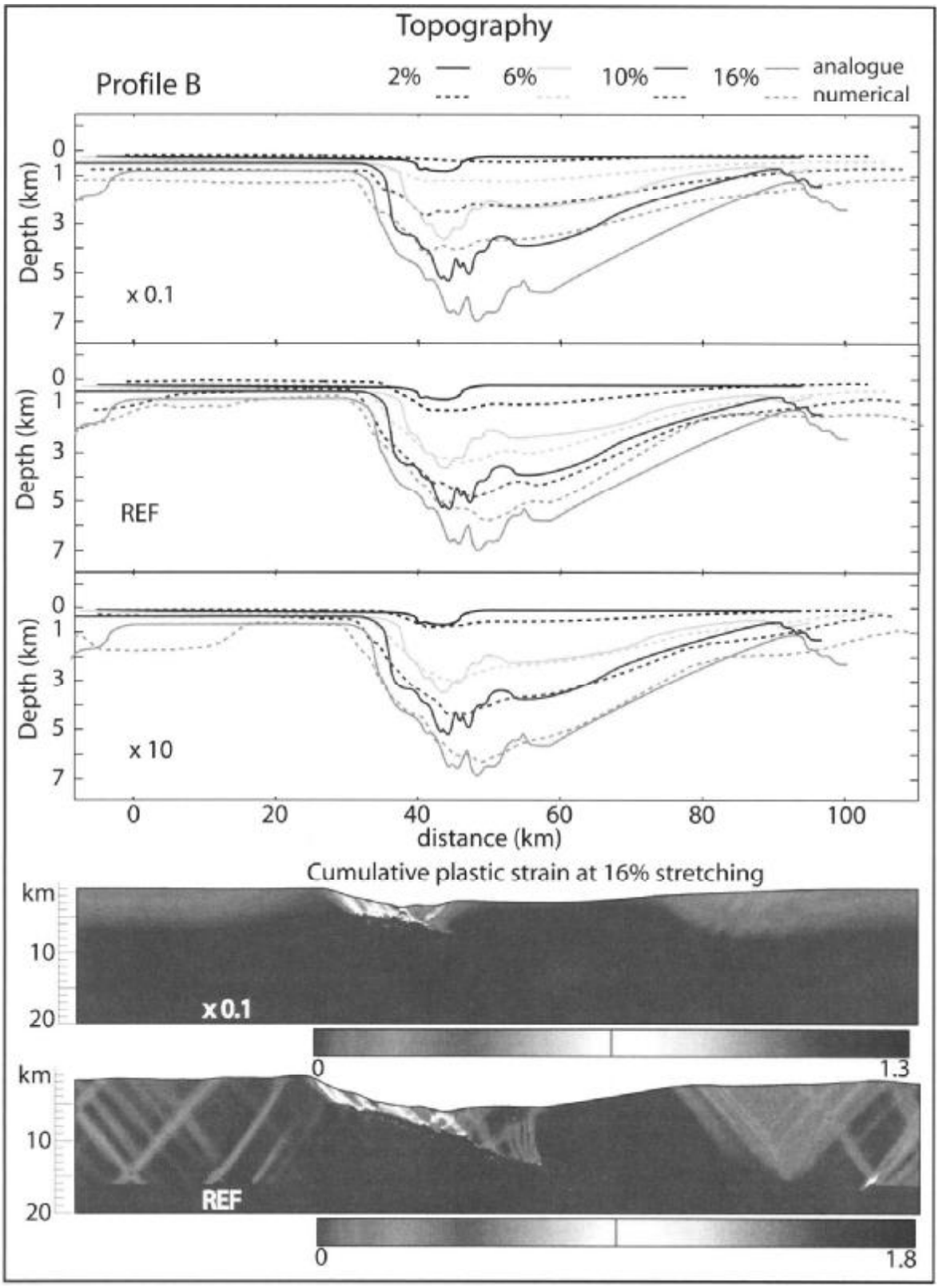


**Fig. 11.** The effect of misscaling of the elastic parameters. Dashed lines show topography at the level of profile B in analogue experiment PH4. Drawn lines represent the topography computed for three different value of shear modulus (Poisson coefficient kept constant at 0.25). A better fit is obtained for over-estimation of the shear modulus.

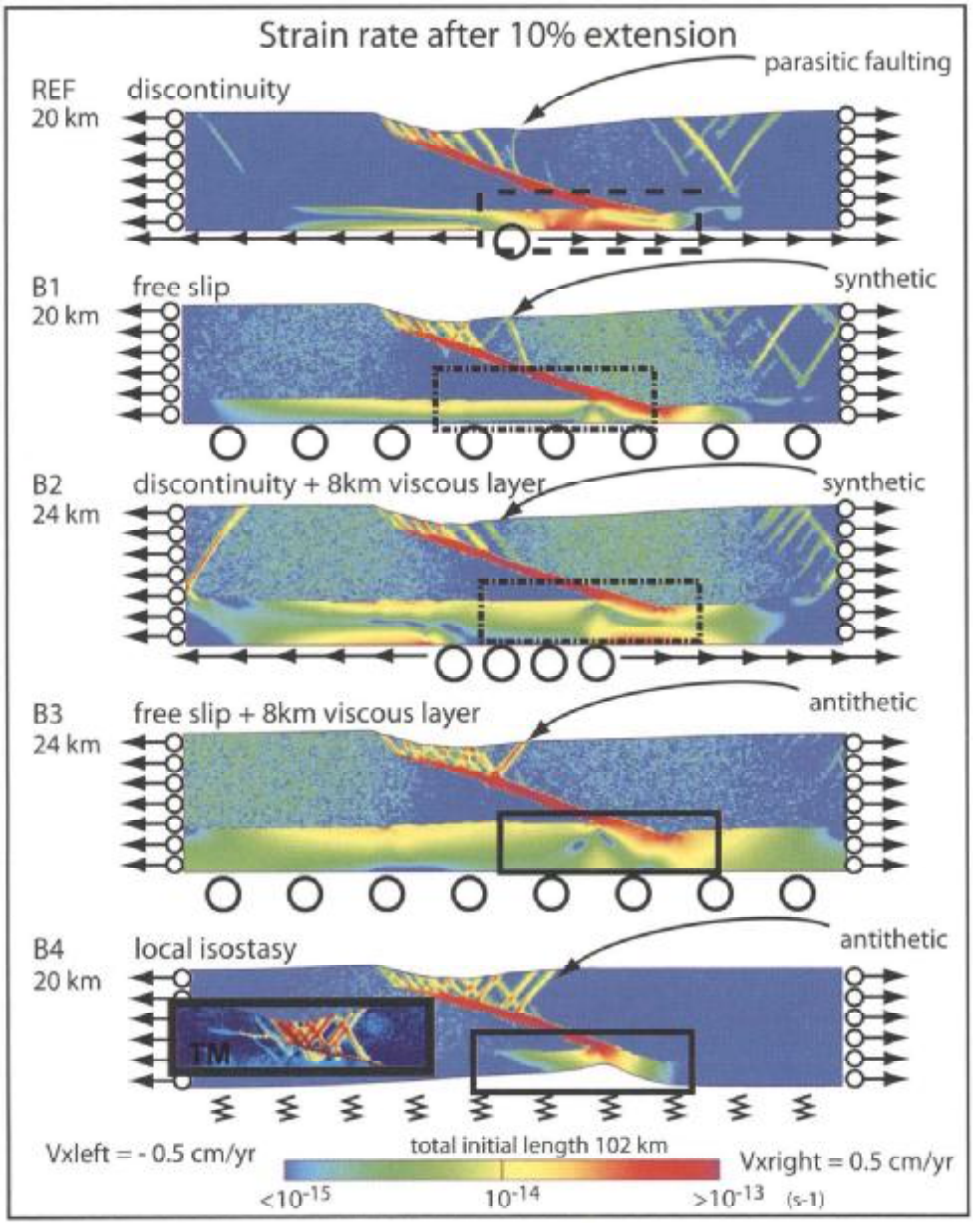


**Fig. 12.** Strain rate after 10% of bulk extension for a range of boundary conditions at the base: REF: Boundary conditions include a sharp velocity discontinuity in the centre. The base of the model is made of 4 km of viscous body (i.e., 1 cm of silicone putty). B1: Same geometry and vertical velocity to REF model but the base of the model is a free slip surface. B2: Same boundary conditions to REF but 4 km (equivalent to 1 cm of silicone putty) has been added at the base. B3: Same geometry to B2 with the boundary condition of B1. B4: Winkler basement equivalent to the boundary condition of the thermo-mechanical model in Le Pourhiet *et al.* (2004).

For comparison, we also add at the edge of the isostatic case in Figure 12, a detail of strain rate in the thermo-mechanical model for the same amount of bulk extension. It outlines that antithetic faults are active during the formation of the graben. These faults are only present in the B3 and B4 models. These models have their basal boundary conditions closest to those of the thermo-mechanical experiments. However, this detail of the thermo-mechanical results also shows discrepancies with the benchmarks. There are much less active faults in this more realistic experiment. This inactivity of the oldest fault is caused by the presence of faults crossing the footwall which annihilate the shear on the weak nappe and thus relate to the discussed rheological simplifications.

**Table 3.** *Mechanical properties of the mechanical benchmark test materials*

| Properties mat. | Density ($kg/m^3$) | Shear modulus (Pa) | Poisson ratio | Viscosity (Pa s) | Friction angle | Dilatation angle |
|---|---|---|---|---|---|---|
| Elasto-plastic | 2700 | $3 \times 10^{10}$ | 0.25 | no | 34° | 0° |
| Visco-elastic | | $3 \times 10^{11}$ | 0.25 | $1.25 \times 10^{20}$ | no | no |

Comparing REF and B2 with the other experiments suggests that the removal of the discontinuity at the base permits the antithetic faults to form. However, increasing the thickness of the basal silicone layer is a major factor in widening the rift, because it is the only one that permits the weak layer to flatten by rotation of the footwall (exp. B4). This phenomenon was shown by Le Pourhiet *et al.* (2004) to be one of the effective mechanisms for migration of the basin in the thermo-mechanical models, because upward flexure of the footwall favours faulting (Buck 1988). The annihilation of this flexure in the analogue experiments causes (1) all the faults to remain active, (2) the suppression of the synthetic out-of-sequence faults growth, and (3) the formation of a single basin instead of multiple half-grabens. All dynamic features observed in the thermo-mechanical model thus disappear in favour of a fully kinematically constrained model.

### *Conclusion on the methodology*

Our benchmark tests have shown that for our set-up: (1) The fact that the elastic coefficients are not correctly scaled with nature in the analogue experiments affects the models. However, in this special setting, the boundary conditions at the base and the weak nappe completely control the kinematics and it is difficult to evaluate quantitatively the effect of this mis-scaling. (2) The 2D plane strain approximation used in the thermo-mechanical experiments is valid as long as the weak nappe is present.

Analogue models give insights into expected fault patterns for a real 3D setting which, for software and hardware reasons, cannot be modelled with current numerical tools, but are very limited in terms of available boundary conditions, scaling, and/or acquisition of the results. The sharp rheological contrasts inside the model, as well as the scaling limitation, cause some parasitic phenomena which can easily be isolated using numerical benchmarks of the analogue models. In the present study these benchmark tests have shown that:

(1) The velocity discontinuity at the base of the models interferes with the discontinuity created by the rheological contrast of the weak nappe and leads to the formation of parasitic faults responsible for artefact topographic heights observed in both numerical and analogue models (profile B in Fig. 8).
(2) The vertical dimension of the modelling box, which is constrained by the size of the medical scanner used for the acquisition, does not allow us to put a thick viscous layer at the base of the experiments. The boundary conditions at the base lead to the annihilation of the formation of some of the principal structural features, i.e., faulting in the footwall and migration of the basin by flexural flattening of the weak nappe.

Thus, mixed methodology is a very useful tool because it leads to a better understanding of the features observed in the analogue models. This approach also helps to save time and money for 3D case studies because it enables some analogue experiments to be skipped.

### *Is the 3D model valid for the Gulf of Corinth?*

The 3D analogue and 2D numerical experiments have outlined that:

(1) The results of our previous thermo-mechanical study are only valid if local isostatic compensation occurs at the scale of the upper crust; i.e., the thickness of the elasto-plastic layer should be rather small compared to the thickness of the effectively viscous lower crust. In the case of the Gulf of Corinth, this hypothesis is acceptable, because the elasto-plastic layer extends down to the brittle ductile-transition, i.e., approximately 10–12 km (Rietbrock *et al.* 1996; Rigo *et al.* 1996; Pham *et al.* 2000; Lyon Caen *et al.* 2004), and because the crust is thick enough (40–45 km, according to Makris (1978) and Tiberi *et al.* (2001) to allow for the lower crust to diffuse in short times any displacements at small length scales (5–10 km).
(2) The en echelon structure and the lack of field evidence for major transverse faults can be explained by the discrepancy between the current direction of extension and the dipping direction of the weak heterogeneity.

(3) The seismic events relocated on SW/NE trending faults may not take place on inherited faults as suggested by Lyon Caen *et al.* (2004) but rather on newly-formed transverse normal faults.

(4) The comparison between analogue models and their mechanical numerical benchmarks suggest that the presence of a weak heterogeneity acts as a localizing factor even laterally where the Phyllades nappe does not exist, e.g., in the internal zone of the Hellenides corresponding to the eastern part of the rift.

However, these 3D analogue models and their mechanical benchmarks were not able to reproduce the kinematics (in and out-of-sequence faulting) and the geometry (multiple half-grabens) of the faults in the western part of the Gulf which is obtained with the 2D thermo-mechanical models.

Neither of the two modelling techniques taken separately would have been able to propose an explanation for the 3D dynamics of faulting in the Gulf of Corinth because (1) the boundary conditions imposed by technical limitations of the analogue method do not give full access to the dynamics of the problem, and (2) 3D numerical methods are not efficient enough yet (memory and CPU) to get insights into 3D mechanically consistent shear banding with large strains.

Our study has shown that, by using a mixed approached with a large set of geological data, it is possible to overcome these limitations. The results obtained by this type of approach are, however, case sensitive, because data are needed to test the models at each stage before making new assumptions or approximations. In our study, the dip and the burial depth to the sheet of silicone putty did not change during the analogue experimentation. These two parameters were deduced from systematic numerical modelling results to reduce the number of analogue experiments.

Thanks to E. Burov for helpful discussion and free use of his version of Paravoz (a Podladchickov & Poliakov[ltd] code). J. P. Brun and J. Smit are thanked for their useful comments during the meeting as well as S. Buiter, O. Dauteuil, C. Pascal and an anonymous reviewer for their careful, time-consuming but very useful reviews.

## References

ARMIJO, R., MEYER, B. *ET AL.* 1996. Quaternary evolution of the Corinth rift and its implications for the late Cenozoic evolution of the Aegean. *Geophysical Journal International*, **126**, 11–53.

AUBOUIN, J., BONNEAU, M. *ET AL.* 1970. Contribution à la géologie des Hellènides: le Gavrovo, le Pinde et la zone ophiolitique subpélagonienne. *Annales Société Geologique du Nord*, **90**, 277–306.

BENTHAM P., COLLIER, R. E. L. *ET AL.* 1991. Tectono-sedimentary development of an extensional basin: the Neogene Megara Basin, Greece. *Journal of the Geological Society*, **148**, 923–934.

BOS, B. & SPIERS, (2002). Frictional-viscous flow of phyllosilicate-bearing fault rock: Microphysical model and implications for crustal strength profiles. *Journal of Geophysical Research*, **107**, 2028, DOI: 10.1029/2001JB000301.

BRIOLE, P., RIGO, A. *ET AL.* 1999. Active deformation, of the Gulf of Korinthos, Greece: results from repeated GPS surveys between 1990 and 1995. *Journal of Geophysical Research*, **105**, 25605–25625.

BUCK, W. R. 1988: Flexural rotation of normal faults. *Tectonics*, **7**, 959–993.

CHEN, Y. & MORGAN, J. 1990. A non-linear rheology model for mid-ocean ridge axis topography. *Journal of Geophysical Research*, **95**, 17583–17604.

CAUSSE, C., MORETTI, I. *ET AL.* 2004. Kinematics of the Corinth Gulf inferred from calcite dating and syntectonic sedimentary characteristics. *Comptes Rendus Geoscience*, **336**, 281–290.

COCARD, M., KHALE, H. *ET AL.* 1999. New Constraints on the rapid motion of the Aegean region: recent results inferred from GPS measurements (1993) across the West Hellenic Arc, Greece. *Earth and Planetary Science Letters*, **172**, 39–47.

COLLETTA B., BALÉ, P. *ET AL.* 1991. Computerized x-ray tomography analysis of sandbox models: examples of thin-skinned thrust systems. *Geology*, **19**, 1063–1067.

CUNDALL, P. A. 1989. Numerical experiments on localization in frictional materials. *Ingenieur Archiv*, **59**, 148–159.

CUNDALL, P. A. & BOARD, M. 1988. A microcomputer program for modelling large-strain plasticity problems. *In*: SWOBODA, C. (ed.) *Numerical Methods in Geomechanics*, Balkema, Brookfield, 2101–2108.

DUERMEIJER, C. E., NYST, M. *ET AL.* 2000. Neogene evolution of the Aegean arc: palaeomagnetic and geodetic evidence for a rapid and young rotation phase. *Earth and Planetary Science Letters*, **176**, 509–525.

DOUTSOS, T. & KOKKALAS, S. 2001. Stress and deformation patterns in the Aegean region. *Journal of Structural Geology*, **23**, 455–472.

FLOTTÉ, N. 2002. Caractérisation structurale et cinématique d'un rift sur détachement: le rift de Corinthe-Patras, Grèce. PhD thesis, Université Paris Sud.

GHISETTI, F. & VEZZANI, L. 2004. Plio–Pleistocene sedimentation and fault segmentation in the Gulf of Corinth (Greece) controlled by inherited structural fabric. *Comptes Rendus Geoscience*, **336**, 243–249.

GHISETTI, F., VEZZANI, L. *ET AL.* 2001. Tectonic setting and sedimentary evolution of the south-west margin of the Corinth rift (Aigion-Xylocastro area). Public vol. 56207.

JACKSON, J. A., GAGNEPAIN, J. *ET AL.* 1982. Seismicity, normal faulting and the geomorphological development of the Gulf of Corinth (Greece): the Corinth earthquakes of February and March 1981. *Earth and Planetary Science Letters*, **57**, 377–397.

JOLIVET, L. & FACCENNA, C. 1999. The kinematics of back arc basins, examples from Tyrrhenian, Aegean and Japan seas. *In*: MACNIOCAILL, C. & RAYAN, P. D. (eds), *Continental Tectonics*, Geologial Society, London, Special Publications, 21–53.

JOLIVET, L., BRUN, J. P. *ET AL.* 1994. 3D kinematics of extension in the Aegean region from the early Miocene to the present, insights from the ductile crust. *Buletin Société Geologique France*, **165**, 195–209.

LATORRE, D., VIRIEUX, J. *ET AL.* (2004). Converted seismic wave investigation in the Gulf of Corinth from local earthquakes. *Comptes Rendus Geoscience*, **336**(4–5), 259–267.

LE POURHIET, L. 2004. Modélisation thermomécanique de l'extension continentale: developpement theorique et applications au golfe de Corinthe (Grèce), Laboratoire de Tectonique, UPMC, 241.

LE POURHIET, L., BUROV, E. B. *ET AL.* 2004. Rifting through a stack of inhomogeneous thrusts (study case in the Gulf of Corinth). *Tectonics*, **23**, TC4005.

LYKOUSIS, V., SAKELLARIOU, D. *ET AL.* 1998. Sequence stratigraphy in the N. margin of the Gulf of Corinth: implication to upper Quaternary basin evolution. *Bulletin of the Geological Society of Greece*, **XXX**, 157–164.

LYON CAEN, H., PAPADIMITRIOU, P. *ET AL.* 2004. On the seismicity of the Corinth Rift laboratory area. *Comptes Rendus Geoscience*, **336**.

LYAKHOVSKY, V., PODLADCHIKOV, Y. *ET AL.* (1993). A rheological model of a fractured solid. *Tectonophysics*, **226**, 187–198.

MAKRIS, J. 1978. the crust and upper mantle of the Aegean from deep seismic soundings. *Tectonophysics*, **46**, 269–284.

MALARTRE, F., FORD, M. *ET AL.* 2004. Preliminary biostratigraphy and 3D geometry of the Vouraikos Gilbert-type fan delta, Gulf of Corinth, Greece. *Comptes Rendus Geoscience*, **336**, 269–280.

MATTIONI, L., LE POURHIET, L. *ET AL.* 2006. Fault pattern produced by extension through a heterogeneous crust: new insights from analogue models. *In*: BRUITER, S. J. H. & SCHREURS, G. (eds), *Analogue and Numerical Modelling of Crustal Processes*. Geological Society, London, Special Publications.

MICARELLI, L., MORETTI, I. *ET AL.* 2003. Influence of depth and amount of displacement of the characteristics of normal faults, case study in the Gulf of Corinth–Greece. *Journal of Geodynamics*, **36**, 275–303.

MORETTI, I. 2004. Asymetry of the early rift structures: a comparison between the Gulf of Suez and the Gulf of Corinth. *In: COST-ACTION 625: Actives Faults: Analysis, Processes and Monitoring*, Camerino, Italy, EDIMOND, 105–111.

MORETTI, I., SAKELLARIOU, D. *ET AL.* 2003. The Gulf of Corinth: a half graben? *Journal of Geodynamics*, **36**, 323–340.

MRLINA, J. 2004*a*. Complex gravimetric investigation of active faults around Aigion, Gulf of Corinth, Greece. *Extended Abstracts, 66th EAGE Conference and Exhibition*, Paris.

MRLINA, J. 2004*b*. Structures and tectonics derived from gravity survey around Aigion, Gulf of Corinth, Greece. *Proceedings 5th International Symposium on Eastern Mediterranean Geology*, Thessaloniki, Greece, **1**, 138–140.

NAVILLE, C., SERBUTOVIEZ, S. *ET AL.* 2004. Pre-drill surface seismic in the vicinity of the AIG-10 well and post-drill VSP. *Comptes Rendus Geoscience* **336**(4–5), 407–414.

PHAM, V. N., BERNARD, P. *ET AL.* 2000. Electrical conductivity and crustal structure beneath the central Hellenides around the Gulf of Corinth (Greece) and their relationship with the seismotectonics. *Geophysical Journal International*, **142**, 948.

POIRIER, J. P. 2000. *Introduction to the Physics of the Earth's interior*. 2nd edn, Cambridge University Press.

POLIAKOV, A. N. B., PODLADCHIKOV, Y. Y. *ET AL.* 1993. Initiation of salt diapirs with frictional overburden: Numerical experiments. *Tectonophysics*, **228**, 199–210.

RAMBERG, H. 1981. *Gravity, Deformation and the Earth's Crust*. Academic Press, New York.

RANALLI, G. 1987. *Rheology of the Earth: Deformation and Flow Processes in Geophysics and Geodynamics*, Allen and Unwin, Boston.

RIETBROCK, A., TIBERI, C. *ET AL.* 1996. Seismic slip on a low angle normal fault in the Gulf of Corinth: evidence from high resolution cluster analysis of microearthquakes. *Geophysical Research Letters*, **14**, 1817–1820.

RIGO, A., LYON-CAEN, H. *ET AL.* 1996. A microseismic study in the western part of the Gulf of Corinth (Greece) implications for large-scale normal faulting mechanisms. *Geophysical Journal International*, **126**, 663–688.

STEFATOS, A., PAPATHEODOROU, G. *ET AL.* 2002. Seismic reflection imaging of active offshore faults in the Gulf of Corinth; their seismotectonic significance. *Basin Research*, **14**, 487–502.

TIBERI, C., DIAMENT, M. *ET AL.* 2001. Moho topography beneath the Corinth Rift area (Greece) from inversion of gravity data. *Geophysical Journal International*, **145**, 797–808.

TROTET, F. 2000. Exhumation des roches de haute pression- basse temperature le long d'un transect des Cyclades au Péloponnèse (Grèce). Implications géodynamiques. PhD thesis?, Université Paris XI.

TURCOTTE, D. L. & SCHUBERT, G. 2002. *Geodynamics*; 2nd edn, Cambridge University Press.

VERMEER, P. A. 1990. The orientation of shear bands in biaxial tests. *Geotechnique*, **40**, 223–236.

VERMEER, P. A. & DE BORST, R. (1984). Non-associated plasticity for soil, concrete and rock. *HERON*, **29**(3), 1–64.

WEIJERMARS, R. 1986. Flow behaviour and physical chemistry of bouncing putties and related polymers in view of tectonic laboratory applications. *Tectonophysics*, **124**, 325–358.

# Inversion of a symmetric basin: insights from a comparison between analogue and numerical experiments

M. PANIEN[1], S. J. H. BUITER[2], G. SCHREURS[1] & O. A. PFIFFNER[1]
[1]*Institute of Geological Sciences, University of Bern, Baltzerstrasse 1–3, CH-3012 Bern, Switzerland*
[2]*Centre for Geodynamics, Geological Survey of Norway, Trondheim, Norway (e-mail: susanne.buiter@ngu.no)*

**Abstract:** We use both analogue and numerical experiments to study the inversion by shortening of a symmetric sedimentary basin. The combination of the two modelling techniques uses the strengths of each method to provide insight into basin-inversion processes. The experiments start with a pre-existing basin filled, in part, with weak layers simulating weak sedimentary rocks. Both footwall and hanging wall can deform freely. The physical properties of the materials used in the analogue experiments (sand and microbeads) and the numerical experiments are appropriately scaled to represent upper crustal rocks. We present a systematic study of the effects of basin infill, basin width and basin location and a sensitivity analysis to understand the effects of the boundary conditions. The results of both methods show that the graben fill accommodates most shortening. Weak layers play an important role in localising shortening with limited reactivation of pre-existing (but weakened) faults. In general, forward thrusts and back thrusts nucleate at the lateral contrast of strong and weak materials and cut across the graben-bounding faults. Weak basal detachments are required to transfer shortening to the basin region. The overall evolution of the analogue and numerical models is encouragingly similar.

Analogue and numerical modelling are used in geology to investigate the mechanisms controlling the evolution of basins and orogens. By combining these approaches, it is possible to overcome the weaknesses inherent in each and to gain insight into natural processes (see, for example, Ellis *et al.* 2004). Advantages of numerical methods include: (1) the easy quantification of results, including the possibility of tracking stresses and strains during the evolution of the model, and (2) the relatively large freedom in choice of material properties and boundary conditions. Advantages of analogue approaches include: (1) the low time consumption and expense in model construction, and (2) the relative ease of building 3D models. The two modelling techniques are, therefore, complementary, and comparisons of the modelling results can increase the credibility of the results of each technique (Koyi 1997).

In this study, we present results of analogue and numerical models of inversion of a symmetric sedimentary basin. Basin inversion is the process of shortening a sedimentary basin which was created in extension (Fig. 1). The term 'inversion', introduced by Glennie & Boegner (1981) and used by several authors (Cooper & Williams 1989; Williams *et al.* 1989; Bishop & Buchanan 1995), describes a switch in tectonic mode from extension to shortening. The shortening results in uplift of the basin fill and the reverse reactivation of normal faults (Cooper *et al.* 2001). Many previous analogue experiments on basin inversion focused on hanging wall deformation and have, therefore, used rigid footwalls (e.g., McClay 1989, 1995; Buchanan & McClay 1991; McClay & Buchanan 1992; Keller & McClay 1995; Yamada & McClay 2003). In this type of experiment, inversion results in both the reactivation of the main detachment along the rigid footwall block and the initiation of new thrust faults. Inversion has also been modelled by uplift and rotation of a single rigid 'basement' block (Koopman *et al.* 1987) or by a series of rigid metal plates simulating strong domino fault blocks (Buchanan & McClay 1992; McClay & Buchanan 1991; Mitra 1993; Vially *et al.* 1994; Roure & Colletta 1996). In these cases, the movement of the rigid blocks strongly influences the reactivation of the normal faults.

Experiments where both footwall and hanging wall are able to deform allow the study of the evolution of structures in extension and inversion in a less restricted manner. In the clay models of Mitra & Islam (1994), initial shortening results in

*From*: BUITER, S. J. H. & SCHREURS, G. (eds) 2006. *Analogue and Numerical Modelling of Crustal-Scale Processes*. Geological Society, London, Special Publications, **253**, 253–270.
0305-8719/06/$15.00 

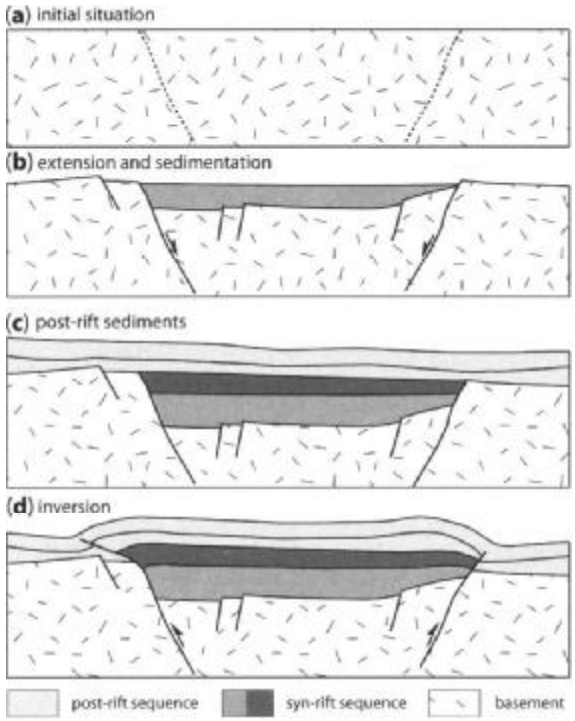


**Fig. 1.** Cartoon illustrating the formation and inversion of a symmetric sedimentary basin. (**a**) Basement block before extension (future normal faults are indicated). (**b**) During the initial stages of extension weak sediments (such as salt or shales) may be deposited in the shallow basin. (**c**) After extension, the syn-rift sequence is overlain by post-rift sediments. (**d**) Inversion leads to uplift of the basin fill and to reactivation of the major faults that propagate upward into the previously unfaulted post-rift sequence.

the uplift of the graben boundaries and in footwall deformation, but no fault reactivation occurs. The main normal faults in the wet clay models of Eisenstadt and Withjack (1995) are reversely reactivated in the early stages of shortening. During further shortening, low-angle thrust faults cut these reactivated normal faults. Fault reactivation is also observed in the brittle and/or viscous analogue models of basin inversion made by Dubois *et al.* (2002). In their models, Brun and Nalpas (1996) assess the effects of obliquity between the direction of shortening and the graben axis and show that the obliquity has to be less than 45° for graben inversion with fault reactivation to occur.

In our previous numerical experiments (Buiter & Pfiffner 2003) we focused on the inversion of a series of pre-defined half-graben basins. Although these experiments are not scaled equivalents of analogue studies, we could already notice some similarities in the resulting deformational structures to published analogue examples. Nielsen and Hansen (2000) and Hansen and Nielsen (2003) give examples of basin inversion in models on a lithospheric scale, which show the effect of an elastic component in material behaviour.

The focus of our study lies on the comparison of analogue modelling results of inversion of a symmetric basin with results from equivalent two-dimensional numerical models. We built the analogue experiments with granular materials sieved in a sandbox with glass sides and one mobile wall. For the numerical experiments we used a two-dimensional viscous-plastic finite element code. The experiments start with a pre-existing basin, whose bounding faults dip at 60°. We consider a setting in which part of the sedimentary deposits in the basin are weaker than adjacent rocks (Fig. 1). There are examples of inverted basins in nature, where, prior to inversion, less competent sediments are confined largely within the main graben and do not occur outside of it, e.g., in the Broad Fourteenth Basin in the North Sea and in parts of the Atlas foldbelt in northern Africa (Letouzey *et al.* 1995). In our models, therefore, part of the graben fill consists of granular materials which are weaker (microbeads) than the surrounding material (sand). Both footwall and hanging wall can deform freely. The main motivation for a pre-existing basin is to have the same starting geometry for analogue and numerical experiments, which would be difficult to achieve if we also modelled the precursor basin formation phase. We constrain the physical properties of the analogue materials through measurements. This allows us to use the equivalent (but scaled) material properties in the numerical experiments.

We investigate the inversion of symmetric basins with the aim of determining factors controlling the evolution of structures during inversion. We identify such key factors through (1) sensitivity analyses, which study the effect of variations in basal friction in analogue and numerical experiments, the effect of smoothing the velocity applied to the mobile wall and the addition of a strain-hardening phase in the numerical experiments and, (2) systematic studies of geometric parameters in both analogue and numerical experiments, i.e., location and width of the graben, and of the material infilling the basin.

## Analogue models

### *Modelling materials*

In our experiments, we used quartz sand (80–200 μm), corundum sand (88–125 μm) and microbeads (70–110 μm) as frictional analogue materials. Table 1 describes the shape of

**Table 1.** *Grain characteristics and material properties of quartz sand, corundum sand and microbeads*

| | Quartz sand | Corundum sand | Microbeads |
|---|---|---|---|
| Grain size | 80–200 μm | 88–125 μm | 70–110 μm |
| Shape | | | |
| –surface texture | irregularly rounded | conchoidal fractures | regular and smooth |
| –roundness | angular | angular | well-rounded |
| –form (elongation†) | 1.63 | 2.00 | 1.04 |
| –sphericity | low | low | high |
| Density (sieved) in g/cm$^3$ | 1.56 | 1.89 | 1.48 |
| Coefficient of internal peak friction* | 0.71 | 0.75 | 0.41 |
| Coefficient of dynamic-stable friction* | 0.61 | 0.63 | 0.37 |
| Angle of internal peak friction* | 35.5° | 37° | 22° |
| Angle of dynamic-stable friction* | 31° | 32° | 20.5° |
| Strain-softening‡ | 14% | 16% | 9.7% |
| Cohesion | 21 ± 18 Pa | 39 ± 10 Pa | 25 ± 4 Pa |

*The values for coefficient and angle of friction have been rounded off.
†Elongation is ratio between longest and shortest diameter.
‡Strain softening is the difference between the coefficients of peak strength and dynamic-stable strength divided by peak strength.

the grains of these materials, i.e., their surface texture, roundness, elongation and sphericity. The density strongly depends on the handling technique used to build the models. In our experiments, we sieved the materials from a height of 30 cm. Using this handling technique the density of quartz sand is 1.56 g/cm$^3$, of corundum sand 1.89 g/cm$^3$ and of microbeads 1.48 g/cm$^3$.

We measured the mechanical properties of the analogue materials with a ring-shear tester (Schulze 1994). The results show that granular materials have an elastic frictional-plastic behaviour. An initial strain-hardening phase precedes failure at peak strength and is followed by a transitional phase of strain-softening until stable sliding (dynamic-stable strength) is reached (Lohrmann *et al.* 2003; Ellis *et al.* 2004; Panien 2004). Angles of internal peak friction and dynamic-stable friction are 35.5° and 31° for quartz sand, 37° and 32° for corundum sand, and 22° and 20.5° for microbeads, respectively. All materials have a low cohesion, the value of which is poorly constrained at very low normal stresses.

### *Analogue model set-up and experimental procedure*

We built the models in a sandbox, 40 cm long, 15 cm wide and 15 cm high, with glass side panels, a plastic bottom and a mobile wall. The models consisted of alternating layers of quartz and corundum sand that were sieved in the sandbox to obtain three horizontal layers of 1 cm thick each (Fig. 2). The experiments do not include a phase of extension. A graben structure is created by means of two tilted metallic plates (each 1 mm thick) which are driven at a dip angle of 60° into the layered model. The material between the plates is carefully removed and replaced with brittle layers of alternating strength. The metallic plates are subsequently pulled out, which causes some disturbance of the normal arrangement of the grains along narrow 'fault areas'. The thickness of the disturbed zones is about 2 mm and similar to the initial thickness of faults (as seen in X-ray CT images in analogue experiments using the same granular materials). As the grains are less densely packed in these zones, they represent potential weak zones similar to a fault in a natural environment. To simulate a post-rift sequence, we sieved an additional 0.5 cm thick layer of sand on top of the model. The models are shortened by moving the right vertical wall of the sandbox directly over the base of the model with a hand-driven worm screw.

For ease of description, we refer to parts of the model situated on either side of the graben as 'right or left graben-bounding block', and the disturbed granular zones as 'graben-bounding faults' or 'graben sides'. To track the evolution of the structures, we used marker particles consisting of coloured sand at layer interfaces. These particles do not influence the properties of the surrounding granular material. Our reference model is 27.5 cm long, 15 cm wide and 3.5 cm thick. At the base of this model, the graben is 3.5 cm wide and located at 11 cm from the initial position of the mobile wall (A-ref, Fig. 2). The graben fill consists of a basal layer of weak microbeads overlain by two layers of strong quartz and corundum sand. A basal décollement layer at the base of the sandbox ensures stress transmission during shortening

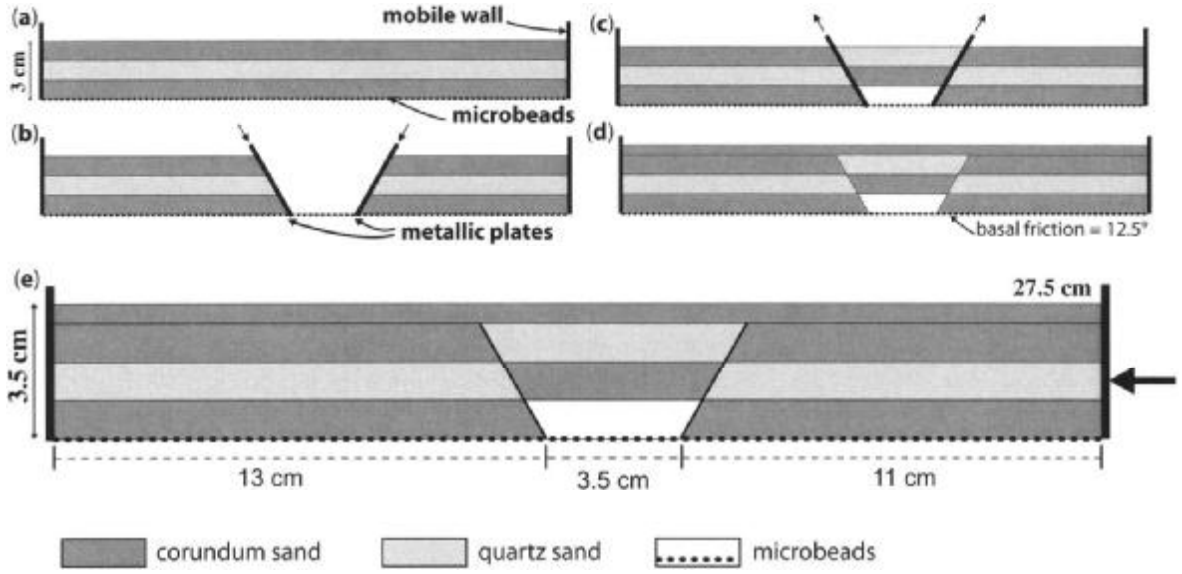


**Fig. 2.** Set-up of the analogue reference model. (**a**) Three layers of quartz and corundum sand are sieved in the sandbox over a thin layer of microbeads (0.5 mm thick). (**b**) Two tilted metallic plates are then driven at a dip angle of 60° into the model. The layers between the plates are removed and (**c**) replaced with alternating strength brittle layers. The metallic plates are subsequently pulled out and (**d**) an additional 0.5 cm thick layer of corundum sand is sieved on top of the model to simulate a post-rift sequence. (**e**) Analogue reference model showing width and location of graben. The layers in the graben, which are vertically offset from the layers in the left and right graben-bounding blocks, have not experienced any reverse displacement.

as in thin-skinned fold and thrust belts. The décollement layer consists of a thin layer of microbeads (0.5 mm thick) sieved over the plastic base of the sandbox. It reduces the basal friction from originally 28° to 12.5°. We tested the impact of the lateral boundary conditions (the glass side-panels) on the deformation by comparing the reference model to a model with free lateral edges made in a larger sandbox. At the end of shortening, the similarity of the two models shows that the lateral effects are negligible in our models. Table 2 lists all analogue experiments.

## Numerical modelling procedure and set-up

We used a two-dimensional plane-strain finite element model (Sopale) (Fullsack, 1995) for the numerical experiments. The model is arbitrary Lagrangian Eulerian (ALE): the equations of mechanical equilibrium are solved on an Eulerian grid to which material properties are assigned using Lagrangian tracking points. The rheology of materials is viscous-plastic. To simulate the brittle behaviour of the analogue granular materials, we use a frictional-plastic Coulomb criterion:

$$(J_2')^{1/2} = p_e \sin(\phi) + C\cos(\phi)$$

where $J_2'$ is the second invariant of the deviatoric stress tensor, $p_e$ the dynamic pressure, $C$ the cohesion, and $\phi$ the angle of internal friction. The viscosity is chosen high enough to ensure that the materials effectively deform in a rigid-plastic manner. Elastic behaviour is not included. As support for the latter assumption we note that in general, elastic deformation of granular materials such as those used in the analogue experiments seems to be minor (J. Adam, pers. comm.).

We scaled the numerical models such that similarity with the analogue models is as close as possible. One kilometre in the numerical model corresponds to one centimetre in the analogue model. The values for density and angle of internal friction are the same as those of the analogue materials (Table 1). A small amount of strain-softening of the angle of internal friction mimics the strain-softening which has been measured for the analogue materials. Softening occurs in a simple linear manner over a finite strain interval of 0.5 to 1.0 (finite strain is measured as total accumulated effective strain which is defined by the square root of the second invariant of the strain tensor). We scale the cohesion values in the numerical models by requiring that the ratio of frictional strength over gravitational force is equal for the numerical and the analogue models (Hubbert 1937; Ramberg 1981; see also Ellis *et al.* 2004).

**Table 2.** *List of experiments and related figures*

| | | Analogue model | Numerical model | Figure |
|---|---|---|---|---|
| Reference model | | A-ref | N-ref | 2, 3, 4 |
| Basal friction | | A-BF30 | N-BF30 | 5 |
| | | A-BF13 (A-ref) | N-BF13 | – |
| | | | N-BF11 (N-ref) | – |
| | | | N-BF5 | – |
| Velocity boundary condition | | | N-ref | 6 |
| | | | N-VPw | – |
| | | | N-VPx | – |
| | | | N-VPy | – |
| | | | N-VPz | – |
| Strain-hardening | | | N-SH | 7 |
| Graben width | | A-GW2 | N-GW2 | 8 |
| | | A-GW3.5 (A-ref) | N-GW3.5 (N-ref) | – |
| | | A-GW5 | N-GW5 | – |
| | | A-GW6.5 | N-GW6.5 | – |
| | | A-GW8 | N-GW8 | |
| Graben fill | all strong | A-GFas | N-GFas | 9a |
| | all weak | A-GFaw | N-GFaw | 9b |
| | weak at base | A-GF1b (A-ref) | N-GF1b (N-ref) | 9c |
| | | A-GF0.5bb | | 9d |
| | | A-GF0.5bt | | 9d |
| | weak in the middle | A-GF1 m | N-GF1m | 9c |
| | | A-GF0.5mb | | 9d |
| | | A-GF0.5mt | | 9d |
| | weak at top | A-GF1t | N-GF1t | 9c |
| | | A-GF0.5tb | | 9d |
| | | A-GF0.5tt | | 9d |
| Graben location | | A-GL9 | N-GL9 | 10 |
| | | A-GL11 (A-ref) | N-GL11 (N-ref) | – |
| | | A-GL13 | N-GL13 | – |
| | | A-GL14 | N-GL14 | – |

A cohesion of 1 Pa in the analogue models is then equivalent to 0.1 MPa in the numerical models. The cohesion is 5 MPa for 'quartz sand' and 'corundum sand' and 2.5 MPa for 'microbeads'. A model with a cohesion of 4 MPa for all materials showed that the structures in the reference model are not sensitive to small variations in cohesion.

The boundary conditions of the numerical model follow the analogue model as closely as possible (Fig. 3). The numerical reference model has 360 × 88 Eulerian elements (width × height, with an average normalized element size, as measured by the square root of element area, of 58.5 m) and a minimum of 280833 Lagrangian tracking points. Thin layers at the sides and base of the model provide boundary friction (4 Eulerian elements wide (312.5 m) or high (300 m), respectively, corresponding to around 3 mm on the sandbox scale). They are Eulerian only and are prevented from changing their overall shape. The basal frictional layer has an angle of internal friction of 11° to simulate the microbeads on plastic/wood friction, whereas the two vertical bars at the left and right side of the model have an angle of internal friction of 28° to simulate sand-wood friction. The left vertical side and the base of the model are held fixed. The right vertical side is moving with a velocity V of 1 cm/yr to the left. We smoothen the velocity at the lower part of the moving side by extrapolating it from V to zero over the height of the microbeads layer (4 elements high corresponding to 50 m in the model and to 0.5 mm on the sandbox scale, note that the vertical element size is variable) and the frictional boundary layer. This avoids numerical instabilities associated with a large velocity contrast over a too small distance. We examine and discuss the effects of this approach further below (in 'Sensitivity Analyses'). The surface of the model is a free surface to which a small amount of diffusive erosion is applied, with a diffusion coefficient of $10^{-8}$ $m^2/s$. This simulates the small amount of sand redistribution along

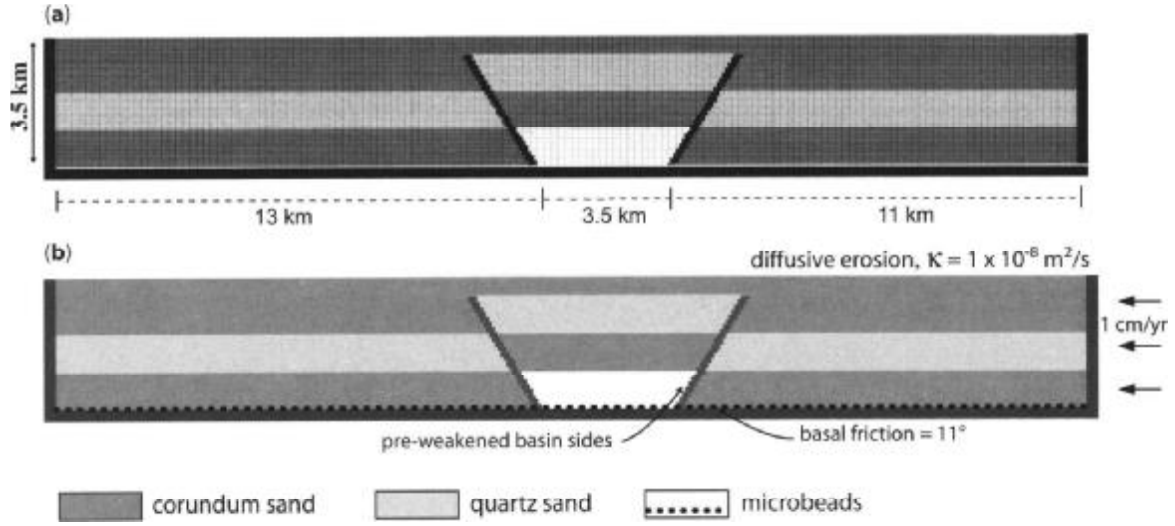


**Fig. 3.** Set-up of the numerical reference model. (**a**) Dimensions of the model. The grid is a subset of the Lagragian tracking grid (initial tracking grid is 6 times denser). (**b**) Boundary conditions. Thick black lines surrounding the model represent boundary friction layers.

the surface that occurs in the analogue models. We have verified that lower or higher values for the diffusion coefficient ($5 \times 10^{-9}$ to $5 \times 10^{-8}$) do not influence the inversion structures we observe in the numerical reference model. Even lower values for the diffusion coefficient cause surface instabilities, where corundum sand slides down when trying to attain its critical taper.

To take into account the disturbance of the graben sides when building the analogue models, we pre-weaken the basin sides of the numerical models by defining bands of quartz and corundum sand with a low (strain-softened) value for the angle of internal friction. The width of these bands is on the order of 3 Eulerian elements (around 240 m, corresponding to 2.4 mm on the sandbox scale). The basin sides and their parallel zone of weakness dip at 60° and do not extend into the post-rift layer.

The basal friction angle is the main exception to the attempted similarity between the numerical and the analogue model, as it needs to have a lower value in the numerical models. When using the friction angle measured in the ring-shear tester for the friction between microbeads and a basal plastic sheet (12.5°), more thrusts localize near the moving wall, as will be discussed later ('Sensitivity Analyses'). The reference model presented here, therefore, has a basal friction angle of 11°. With these parameters the results of numerical models seem to be in good agreement with the analogue experiments.

Caution is required when comparing results of continuum type numerical experiments with those of sandbox experiments. Due to its manual set-up, an analogue model will intrinsically have more heterogeneities than a numerical model (i.e., bedding planes always contain small irregularities). Furthermore, our numerical models do not include elasticity and dilatancy, whereas the analogue model materials do have these properties. As a consequence, shear zones in the numerical model initially develop at angles of around 45°. Table 2 lists all numerical experiments.

## Evolution of analogue and numerical reference models

### *Analogue reference model (A-ref)*

During the early stages of shortening, the horizontal displacement produced by the mobile wall propagates leftwards through a detachment at the base of the model. This displacement is accommodated between the mobile wall and the left graben-bounding fault. Stresses transmitted across the model decrease with distance from the mobile wall, resulting in compaction and diffuse deformation of both the right-hand graben-bounding block and graben fill. As a consequence, the width of the graben decreases (with 9% (0.3 cm) after 0.75 cm shortening), the graben fill bulges, the right graben-bounding block thickens and the basin sides steepen. Just prior to 1 cm of shortening, deformation localizes in a narrow zone, leading to the formation of a thrust fault (A in Fig. 4a) that nucleates at the basal transition from strong footwall to weak graben fill and attains a dip of *c.* 30°. This forward thrust accommodates most of the

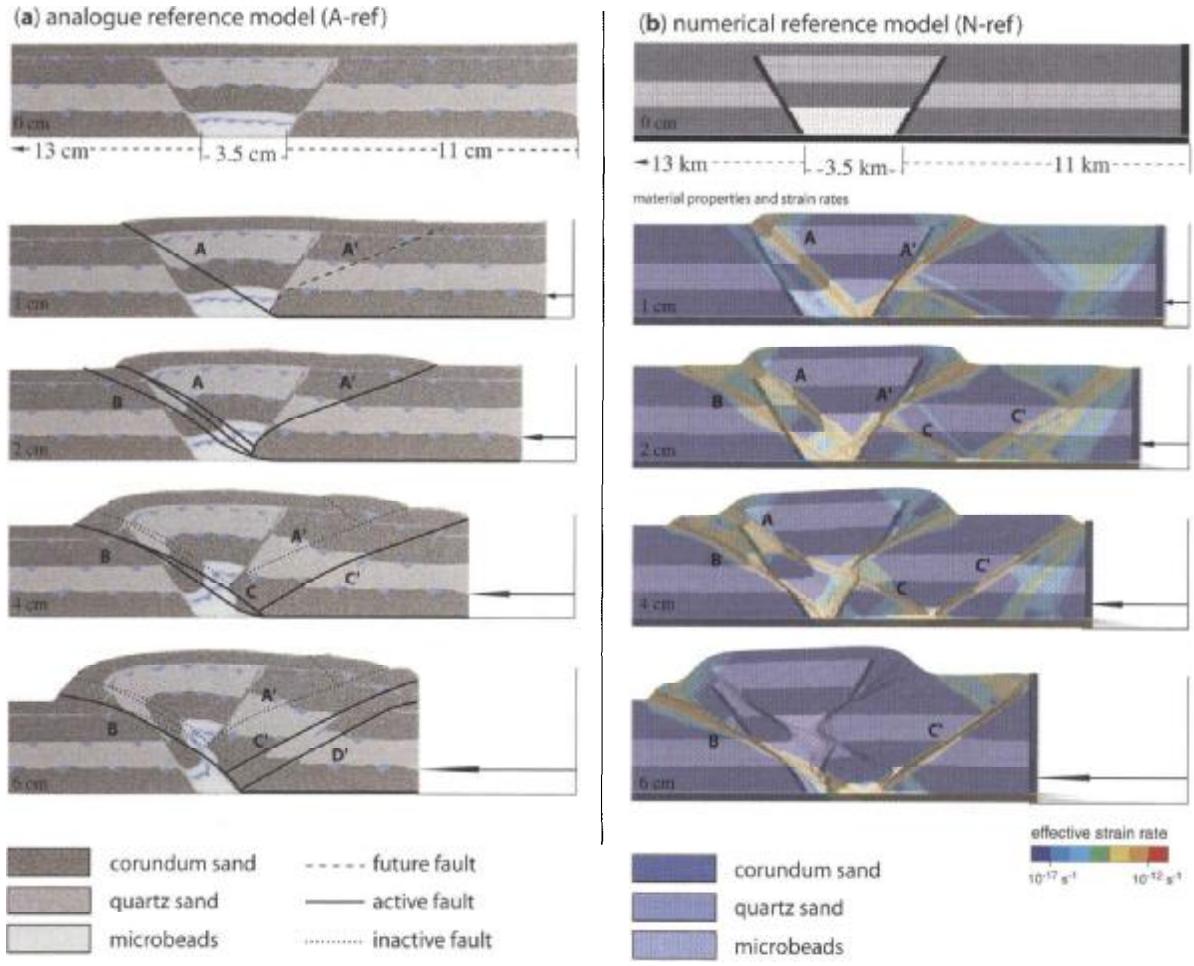


**Fig. 4.** Analogue and numerical reference models showing the evolution in 5 steps from the initial state until 6 cm of shortening. Note that the left side of the models is not shown completely. Transparent strain-rate plots are superimposed on the numerical models.

bulk shortening and propagates through the graben to the left graben-bounding fault and into the post-rift sediments. It connects more or less with the top of the left basin side. With increasing shortening a conjugate back thrust A′ forms in the weak microbeads. It follows the deeper part of the right graben-bounding weak zone, dipping at 60° (closest to the mobile wall), but propagates upward at a shallower dip into the footwall of the graben and the post-rift sediments. The back thrust A′ displaces the forward thrust A upward. After 2 cm of shortening, thrust A becomes inactive and a new forward thrust B forms at the base of the graben. With further convergence, new conjugate thrust faults (C and C′) nucleate outside the graben, in the hanging wall of thrust B. Forward thrust C cuts the graben-bounding fault and connects with forward thrust B. As back thrust C′ is advected along the forward thrust B, an additional back thrust D′ forms in its footwall. Most displacement takes place along the forward thrust B. The back thrusts are tilted and cease to be active one after the other as they are passively displaced along the forward thrusts C and D. During shortening, the graben fill is progressively uplifted, reaching a stable surface slope dipping at 35°, after which sand slides down along the slope. The stable slope corresponds to the angle of repose of quartz sand and corundum sand (as calculated for our set-up; Zhao *et al.* 1986; Dahlen & Suppe 1988).

### *Numerical reference model (N-ref)*

The dynamics of the numerical model are broadly consistent with those of the analogue model, showing the same general features (Fig. 4b). The formation of strain-softened shear zones, which are comparable to the visible faults in the analogue models, accommodates deformation. A forward thrust A initiates in the right part of the graben at the basal transition

from strong footwall block to weak graben fill and propagates through the graben and the post-rift layer. At the same time, a conjugate back thrust A′ forms in the weak microbeads, which follows the right basin-bounding side and then cuts through it. These conjugate thrusts resemble A and A′ in the analogue models and their activity leads to uplift of the basin fill. The initial stages in the numerical model are not characterized by overall thickening of the right graben-bounding block or by bulging of the graben fill as observed in the analogue results. Further shortening leads to the initiation of two new forward thrusts: one (B) in the left part of the model, the other (C) in the right part of the model. The short thrust C connects with the top right corner of the graben microbeads layer and later links up with A. A conjugate back thrust C′ is present in the right-hand graben-bounding block. We find that the conjugate thrusts C and C′ are quite stable features, which are neither related to the piling up of microbeads which are moving up from the basal microbeads layer, nor to the moving wall. The alignment of the former forward thrust A with the newly formed thrust C causes its reactivation after a convergence of 4 km, cutting through the still active back thrust A′. Back thrust C′ progressively displaces thrust AC, which then ceases to be active. After 6 km of shortening, only forward thrust B and back thrust C′ are active. Fewer back thrusts form in the numerical model in comparison with the analogue reference model.

Contrary to the resolution of the analogue models that makes small strains very difficult to observe, strain concentrations in numerical models can easily be observed in strain-rate plots. The strain-rate plots show which shear zones are active at different stages. They also show how deformation is often more distributed before localizing in shear zones (e.g., C′).

## Sensitivity analyses

### *Basal friction*

One of the features of the reference analogue model is the presence of a 0.5 mm thick basal layer of weak microbeads. This weak layer reduces the basal friction to 12.5° and allows the transmission of most of the shortening to the graben (A-BF13 in Fig. 5a). In the absence of such a décollement layer, the basal friction is higher (28°, i.e., basal friction between corundum sand and the plastic bottom of the sandbox) and initial deformation occurs closer to the mobile wall (A-BF30 in Fig. 5b). In this case, a

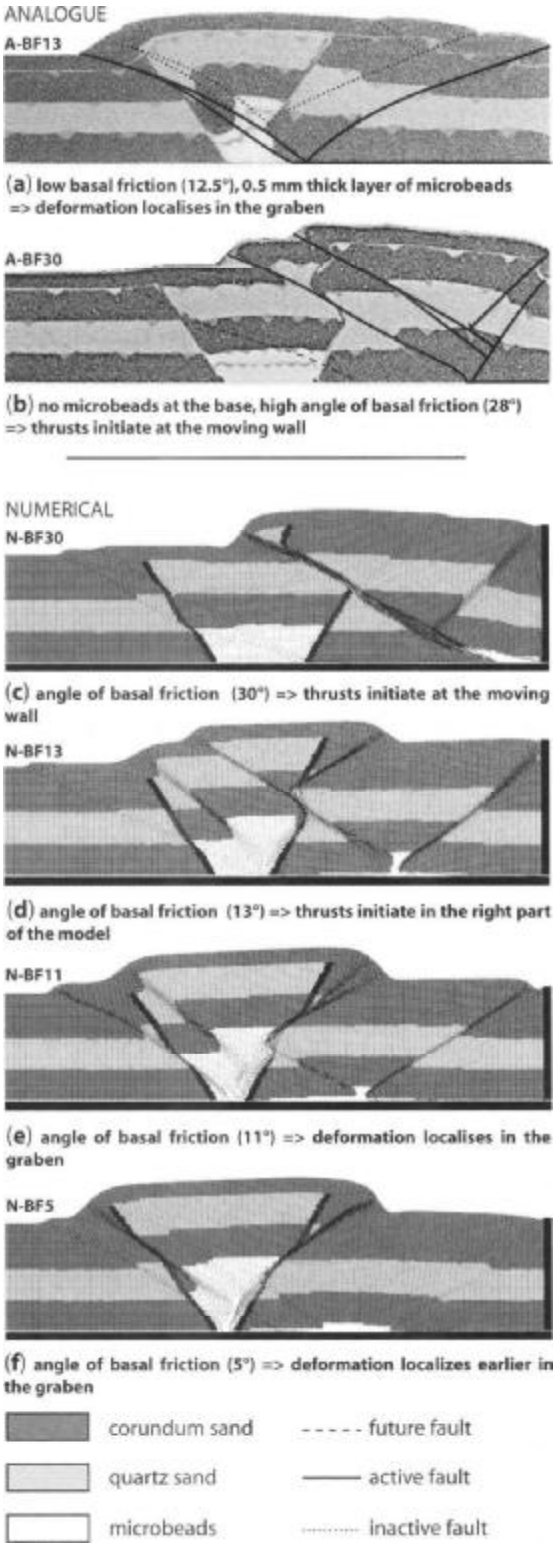


**Fig. 5.** Sensitivity study on the effect of basal friction. Cross-sections of analogue and numerical experiments after 4 cm and 4 km of shortening, respectively. Low friction favours graben inversion whereas high friction results in stronger effects of the boundary conditions (mobile wall). The left side of the model is not shown completely.

detachment initiates and propagates along the base of the model in the corundum layer. Conjugate thrust faults develop in the right-hand part of the model, with the forward thrust dipping shallower (30°) than the back thrust (between 45° and 55°). As shortening increases, a second and a third in-sequence thrust develop. The numerical model (N-BF30) with a high value of basal friction (30°) shows similar structures (Fig. 5c). The second in-sequence forward thrust forms from the base of the right graben side, whereas in the analogue model (A-BF30, Fig. 5b) the second (and third) thrust is located in the right graben-bounding block.

We first applied a basal friction of 13° in the numerical model (N-BF13, Fig. 5d). After 4 cm of shortening, two sets of conjugate thrusts form in the graben and in the right-hand part of the model. Contrary to the analogue model, the rightmost forward thrust does not link up with the forward thrust situated in the graben, but cuts the graben-bounding fault at the level of the corundum sand layer filling the graben. We tested lower basal frictions to examine the sequence of deformation in the graben and in the right graben-bounding block. With a basal friction of 11° (N-BF11 in Fig. 5e), deformation is initiated in the graben from the start. Thrust faults nucleate at the basal transition from strong footwall to weak graben fill. In this case, the numerical and analogue experiments are similar. Therefore, to obtain comparable results, the basal friction in the numerical models needed to be slightly weaker (11°) than in the analogue models. This small difference is interesting in itself. We speculate that it may either be caused by numerical artefacts, e.g., the way basal friction is implemented, or by a difference in the measured value of the analogue friction in the ring-shear tester and its actual value in the sandbox. In the numerical models it can be seen how microbeads from the basal layer migrate up a shear zone and facilitate further deformation on that shear zone. An even lower value for basal friction (5°) shows how deformation remains mainly focussed on the graben fill during shortening (N-BF5 in Fig. 5f).

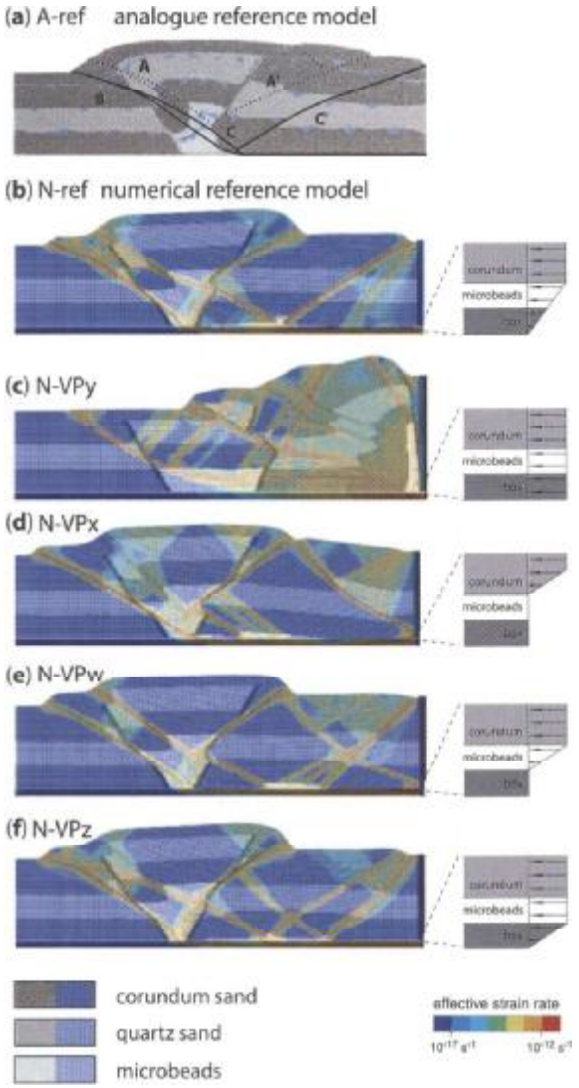


**Fig. 6.** Analysis of the effect of variations in implementation of the mobile wall velocity profile in the numerical reference model. A-ref, analogue model after 4 cm of shortening for comparison. Numerical models after 4 km of shortening. Sketches of the different applied velocity profiles are given on the right-hand side. 'Box' is short for frictional boundary layer. The left side of the model is not shown completely. Prefixes A and N indicate analogue and numerical models, respectively.

*Velocity boundary conditions*

We tried to design the boundary conditions of the numerical model such that they follow the analogue model as closely as possible, but the analogue set-up gives a relatively large freedom in the choice of appropriate velocity profile to apply to the mobile wall. In the reference numerical model (Fig. 6b), we applied a velocity V at a uniform rate along the right vertical wall and smoothened it to 0 over the layer of microbeads and the frictional boundary layer at the base. The velocity applied to the side of the frictional boundary layer allows a shear to build up near the side boundary of the model.

Figures 6b–f show model deformation after 4 km of shortening in numerical experiments in which the velocity profile at the right side boundary is varied. When we apply V to the complete right-hand sidewall (including microbeads and frictional boundary layer), thrusts form at the

exit slot of the mobile wall and propagate upward to the left (N-VPy model, Fig. 6c). In case only the mobile wall itself is pushed, smoothening the applied velocity to 0 in the layer of corundum sand (model N-Vpx, Fig. 6d), a thrust fault rooting at the basal right corner of the mobile wall is initiated. A similar feature can be seen when we extrapolate the velocity to 0 over the layer of microbeads (N-VPw model, Fig. 6e). This model has difficulties in converging and requires many iterations for every timestep. The N-VPz model (Fig. 6f) is a small variation on the reference model in which the velocity V is applied not only to the wall, but also to the layer of microbeads and then extrapolated to 0 over the frictional boundary layer. After 4 km of shortening, the model is quite similar to the reference model except that two sets of conjugate thrusts are initiated in the right graben-bounding block while only one forms in the reference model.

These tests show that models are very sensitive to the velocity profile applied at the moving wall, and especially to the velocity applied at the interface between the frictional boundary layer and the basal microbeads layer. To prevent the formation of a thrust rooting at the basal corner of the mobile wall, the velocity profile needs to be smoothened and the basal microbeads do not have to be decoupled from the frictional boundary layer.

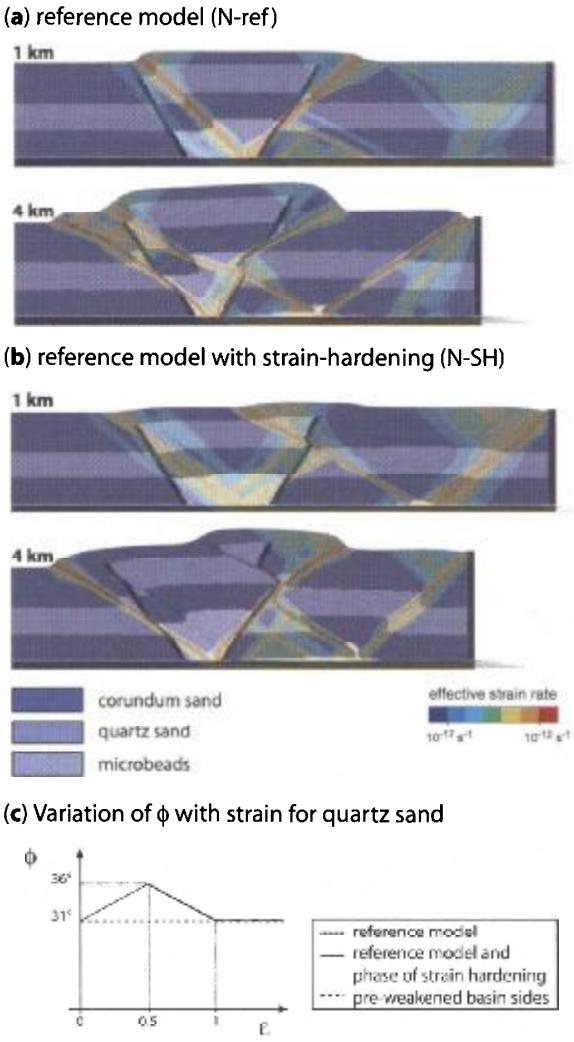


**Fig. 7.** Effect of a precursory strain-hardening phase in the numerical reference model. N-ref (**a**) and N-SH (**b**) models shown after 1 km and 4 km of shortening. (**c**) Example of the numerical implementation of strain-hardening and strain-softening for quartz sand. $\varepsilon$ denotes effective strain. The left side of the model is not shown completely.

*Strain-hardening*

Shear tests show that the granular materials we use to build the analogue models do not have constant frictional properties. They are characterized by elastic/frictional plastic behaviour, with strain-hardening preceding failure and subsequent strain-softening until a stable value is reached (Lohrmann *et al.* 2003; Ellis *et al.* 2004; Panien 2004). In the N-SH model, we test the effect of a phase of strain-hardening that precedes softening for the numerical reference model (Fig. 7b). Both strain-hardening and softening occur in a simple linear manner, over a finite strain interval of 0–0.5 for hardening and 0.5–1 for softening (Fig. 7c). This maximizes the strain-hardening phase, which in reality might be less in magnitude and/or occur over a smaller strain interval. All microbeads, quartz and corundum sand harden first and then soften. The frictional boundary layers at the sides and the base remain at 28° and 11° respectively, whereas the pre-weakened basin sides remain at their low value for the angle of internal friction. This means that initially there is no strength contrast between the pre-weakened basin sides and the corundum and quartz sand layers. In the N-SH model, deformation first localizes mainly in the right graben-bounding block and later in the basin, while deformation in the reference model initially concentrates in the graben. Deformation is initially more diffuse than in the reference model, as lower internal friction values of quartz and corundum sand layers make the initiation of thrust faults easier.

The introduction of a phase of strain-hardening reduces the initial strength contrast between the layers constituting the model and the weak zones, represented by microbeads and pre-weakened basin sides. The influence of basin

sides and microbeads on the deformation of the model is smaller in the first stages of shortening and causes more deformation in the right-hand part of the model in earlier phases than in the reference model.

## Effect of geometric parameters

### *Influence of graben-bounding sides*

The basin sides represent potential weak zones that can be partially activated during shortening. In both analogue and numerical reference models, a first forward thrust is initiated at the basal transition from strong footwall block to weak graben fill. It propagates through the graben with a dip angle of about 30° and connects with the basin top in the analogue model. The dip of the line joining the right bottom edge and the left top edge of the graben (called 'reference line' in the following) is around 30° and thus coincides with the forward thrust. We ran additional analogue and numerical experiments with varying graben widths (Figs 8a, b) to determine whether the position of the left graben side influences the orientation of the forward thrust. The dip of the thrusts is measured and compared to that of the reference line in both analogue and numerical experiments (Fig. 8c). In the analogue experiments, thrust faults dip around $30 \pm 2°$ irrespective of the graben width. It follows that the top left basin side of the graben does not influence the forward thrust dip. On the other hand, in the numerical models the graben width influences thrust dip in some cases. In models N-GW5 and N-GW6.5, the dip of the forward thrust is lower (33° and 30°, respectively) than in the other models ($\pm 43°$). When the basin becomes wider (N-GW8) or narrower (N-GW2 and N-GW3.5) the dip of the forward thrust has a 'stable' value (i.e., thrusts initially develop at angles of 45° in the numerical models). The graben shoulder is either too far away or too close to influence the fault dip.

For both analogue and numerical models, we observe that forward propagation of the thrusts is more clearly developed for the wider graben (GW8), where initially these faults form entirely within the graben.

### *Influence of the mechanical stratigraphy of the graben fill*

In both analogue and numerical reference experiments, the first forward thrust roots at the base in the right-hand part of the graben. It has a dip of $\pm 30°$ in the analogue and $\pm 43°$ in the numerical models. The location of this thrust is linked to the

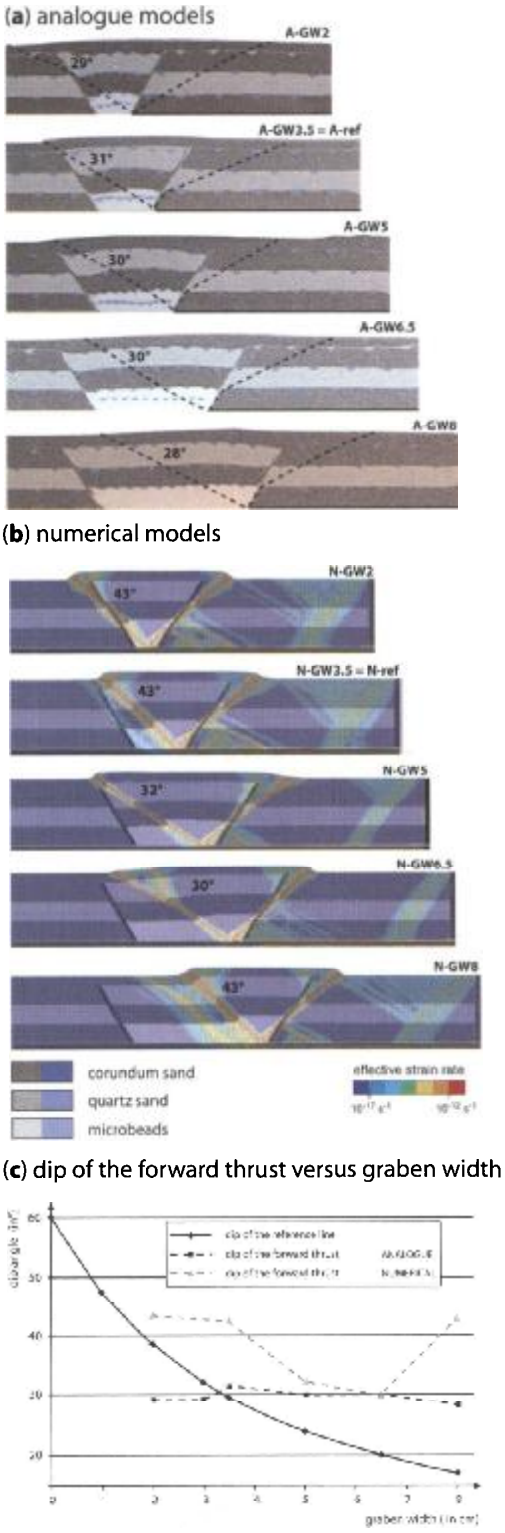


**Fig. 8.** Influence of the graben-bounding sides. (**a**, **b**) Analogue and numerical experiments for different graben widths. (**c**) The dip of the first forward thrust is measured after 1 cm/km of shortening and compared to that of the reference line (joining right bottom edge of the graben to its top left edge). Graben width is measured along the base of the models and is indicated in the name of the models (e.g., A-GW2 has a 2 cm wide graben). The left side of the model is not shown completely.

weak zone represented by (1) the graben side and/or by (2) the horizontal transition from strong corundum sand to weak microbeads filling the base of the graben. To test the influence of these two factors, we conducted experiments with varying graben fill. Apart from graben fill, the set-up of these models is the same as for the reference model. In the first two experiments, the graben is solely filled with either strong layers GFas (all strong) made of quartz and corundum sand or with weak microbeads layers GFaw (all weak) (Figs 9a, b). In the other three types of experiments, the position of the weak microbeads layer is at the base (GFb), in the middle (GFm) or at the top (GFt) of the graben. The weak layer is either 0.5 or 1.0 cm thick in the analogue experiments (Figs 9c, d) and 1 km thick in the numerical models. The overall evolution of the models during shortening is similar to the extent that a basal detachment and the formation of conjugate thrust faults accommodate shortening. However, the location of the forward thrusts varies between the models.

In GFas experiments (Fig. 9a), conjugate thrusts form in the right-hand part of the model. During further shortening, activity along the first forward thrust ceases and a second in-sequence forward thrust forms in the analogue model. In the numerical model further shortening is accommodated first by passive transportation of the forward thrust along the back thrust and then by the development of a new in-sequence forward thrust, whose orientation seems related to the top left pre-weakened basin side. In both analogue and numerical models, no faults form at the base of the basin sides. On the other hand, in the GFaw experiments (Fig. 9b), deformation is concentrated within the basin, and conjugate faults are clearly initiated in the graben fill in both analogue and numerical models. In the numerical model, a back thrust develops in the microbeads, parallel to the basin side. The forward thrust is tilted as it is transported by the back thrust during shortening. This leads to bifurcation of the thrust at its base in order to regain a more suitable dip. These two experiments (GFas and GFaw) indicate that the role of the microbeads in the basin is more important in localizing thrusts than the pre-weakened basin sides. Forward and back thrusts develop in the microbeads rather than using the basin side. Moreover, the basin side is not weak enough to influence the initiation of forward thrusts when the graben is only filled with strong materials.

Conjugate thrust faults also form in models where the graben is filled with both weak and strong layers (Figs 9c, d) and in each analogue and numerical experiment the forward thrusts propagate through the weak microbeads layer that partly fills the graben. Although the overall results are basically similar, some details are different in the analogue and numerical experiments. After 4 cm/km of shortening, analogue and numerical models A/N-GF1m and A/N-GF1t differ. In N-GF1m, a new forward thrust forms after 4 km shortening. It partly re-uses the former forward thrust, bifurcates into the microbeads layer at a lower dip, and continues to the surface. In this case, a single set of conjugate thrusts in the analogue model (A-GF1 m) entirely accommodates deformation. In A-GF1t, a second forward thrust forms once the first thrust has been displaced by the back thrust, whereas in the N-GF1t model, only one forward thrust passively transports successive back thrusts and bifurcates at a lower dip into the microbeads layer. Nevertheless, in both analogue and numerical experiments, the weak microbeads layer that partly fills the graben determines the location of the first forward thrust, irrespective of its depth and thickness. The transition from weak microbeads to quartz and corundum sand creates a strong lateral mechanical heterogeneity. During shortening, this heterogeneity causes the initiation of a fault that propagates backward and forward and ultimately connects with the basal detachment and breaks to the surface. This clearly shows that the location of the forward thrust strongly depends on the position of the weak layer inside the graben.

### *Influence of the graben location*

In order to test the effect of the location of the graben in the model, we conducted several experiments in which the base of the graben is 3.5 cm/km wide and located either at 9 cm/km (GL9), 11 cm/km (GL11, reference model), 13 cm/km (GL13) or 14 cm/km (GL14) from the mobile wall.

In the numerical models (Fig. 10b), the deformation of the graben fill is similar. A set of conjugate thrust faults forms at the right-hand side base of the graben. With increasing shortening, the back thrust displaces the forward thrust, leading to the formation of a new forward thrust in the graben. In the N-GL13 and N-GL14 another set of conjugate thrusts is located far away from the graben, almost in the middle of the right graben-bounding block. In the reference model (N-GL11), a set of conjugate thrusts also forms in the right graben-bounding block, but closer to the graben. Moreover, its forward

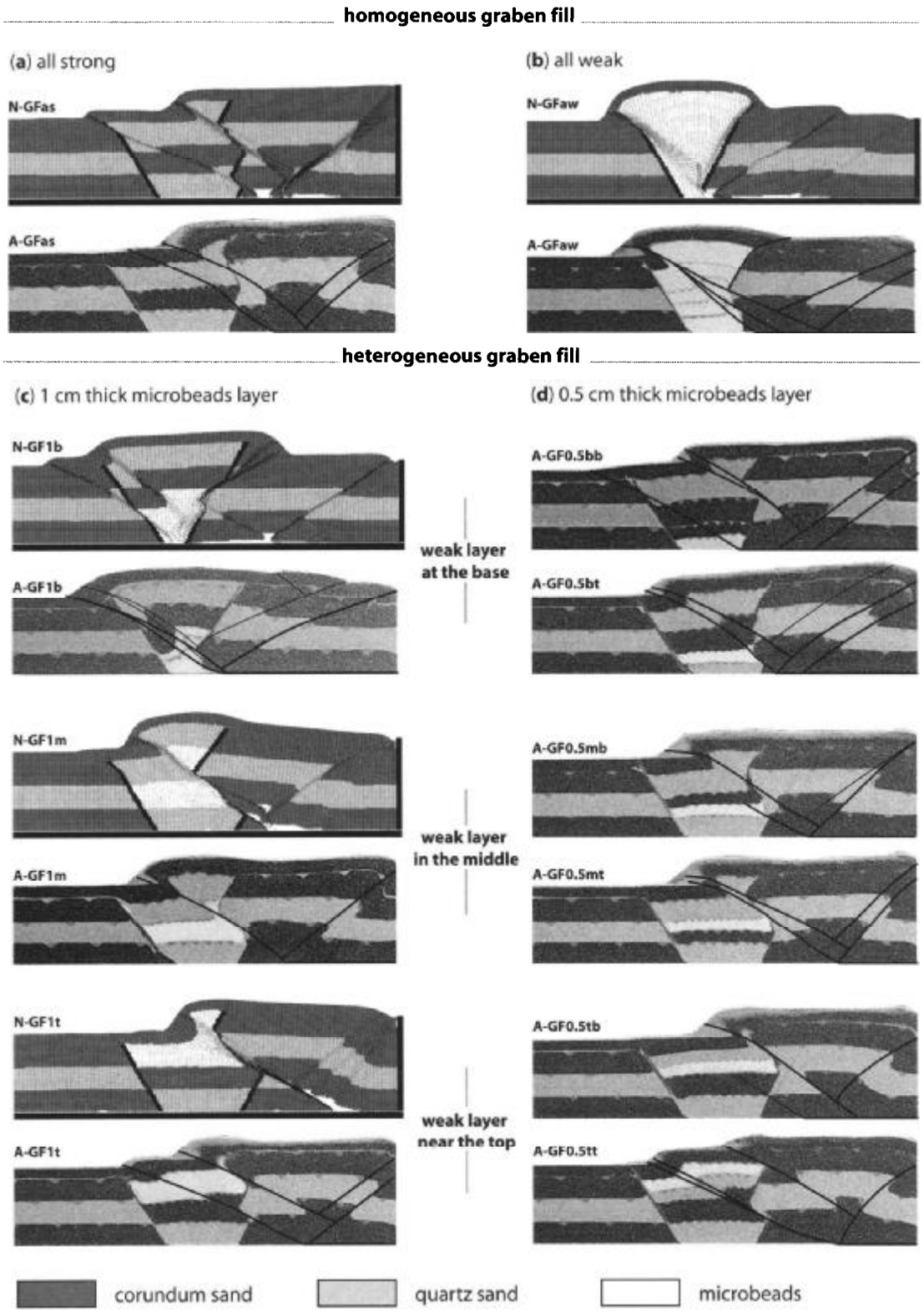


**Fig. 9.** The influence of varying graben fill on resulting structures during shortening. All experiments shown after 4 cm/km shortening. The left side of the model is not shown completely. Prefixes A and N indicate analogue and numerical models, respectively.

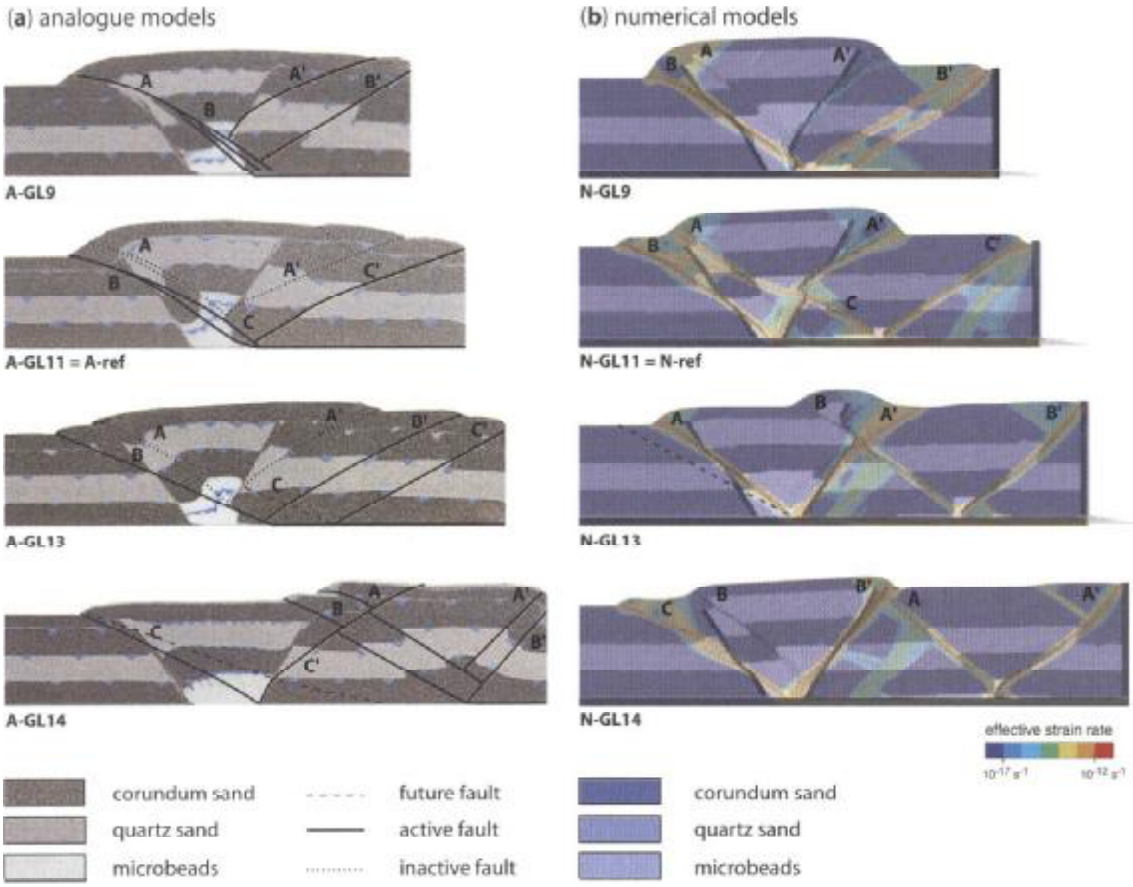


**Fig. 10.** Test of the influence of graben location. Analogue and numerical experiments are shown after 4 cm/km of shortening. The distance between the mobile wall and the right-bottom edge of the graben is 9 cm/km (GL9), 11 cm/km (GL11 = reference model), 13 cm/km (GL13) or 14 cm/km (GL14). The left side of the model is not shown completely.

thrust aligns with the first forward thrust that is thus reactivated.

In the analogue models A-GL9, A-GL11 and A-GL13 (Fig. 10a), the same mechanism of successive sets of conjugate thrusts accommodates shortening. In the A-GL9 model, the second forward thrust is superimposed on the first one. In the A-GL11 and A-GL13 models, the second set of conjugate thrusts propagates on both sides below the first set, and in the A-GL13 model, a third set of conjugate thrusts appears in the right part of the model. In the A-GL14 model, two sets of conjugate thrusts form in the right graben-bounding block, close to the mobile wall.

In the analogue and numerical GL9, GL11 and GL13 models, deformation localizes first in the graben, prior to localizing in the right part of the model, irrespective of the distance between the graben and the mobile wall. In case of a short right-hand graben-bounding block (GL9), deformation is concentrated in the graben, leading to enhanced bulging and inversion of the graben fill. In contrast, when the right graben-bounding block is longer (GL13), it undergoes internal deformation. As a consequence, less graben fill is expulsed at identical stages of shortening. Moreover, in case of a wider model (A-GL14 and N-GL14), deformation localizes first in the right part of the model.

It results from these experiments that the length of the right graben-bounding block does have an effect on the resulting structures during shortening: the amount of displacement and uplift of the graben varies as a function of its distance from the mobile wall for a certain amount of shortening. Clearly shortening is more effectively transferred to the graben along the basal frictional detachment for short distances. In case of a wider model, deformation takes longer to reach the basin and part of the shortening is taken up by thrusts, which form in the right part of the model. Nevertheless, the inversion of the basin itself is very similar between all these analogue and numerical models.

## Discussion

The geometry of the models (i.e., graben width and location), the graben fill, the basal friction, and the velocity boundary condition and strain-hardening phase (for the numerical models) influence to a higher or lesser degree the structures observed in our basin inversion experiments. The effect of these parameters on the structures allows the identification of key factors and points of preferential strain concentration shared by both analogue and numerical experiments.

### *Identification of key parameters*

Our sensitivity study shows that a low value for basal friction is essential for the transmission of deformation through the model. A low basal friction allows the basal detachment to propagate until it reaches a weaker zone (i.e., the weak graben fill). In case of higher basal friction, thrust faults initiate closer to the mobile wall before localizing in the graben of the numerical model or before propagating leftwards in the analogue model. Deformation also strongly depends on the velocity boundary condition applied at the mobile wall. It appears from the numerical tests that the velocity profile needs to be smoothened toward the base of the model to allow the propagation of a basal detachment and avoid thrusts propagating upward from the base of the mobile wall. The addition of a phase of strain-hardening prior to the phase of strain-softening leads to a decrease in the initial strength contrast between the graben-bounding blocks and the weak zones formed by the microbeads layer or the pre-weakened basin sides. Deformation in the reference model initially concentrates in the graben while in the strain-hardening model, deformation localizes first in the right graben-bounding block and later in the graben. The numerical model is not sensitive to small variations in cohesion and amount of surface diffusive erosion.

Analogue and numerical experiments demonstrate that the location of initiation of the forward thrust in the graben is independent of the graben width. Contrary to analogue models, the top left graben-bounding fault in numerical models clearly influences the dip of the forward thrust (N-GW3.5 and N-GW5). For both analogue and numerical models, forward propagation of the thrusts is more clearly developed for the wider graben (GW8), where initially these faults form entirely within the graben. Both analogue and numerical models are sensitive to the mechanical stratigraphy of the graben fill. The experiments demonstrate that the initiation of the first forward thrust strongly depends on the location of the weak layer of microbeads inside the graben. The overall geometry of the analogue and numerical models are similar after 4 cm/km of shortening. The geometry of the graben after inversion hardly depends on graben location in the model. Shortening of the basin is accommodated by the initiation of a set of conjugate thrusts rooted at the base of the right graben-bounding fault, irrespective of the distance of the graben from the moving wall. For large graben-mobile wall distances (GL-14), deformation first localizes in the right part of the model before reaching the graben. Results of analogue and numerical experiments for varying length of the right graben-bounding block are overall in good agreement.

From these observations, it appears that basin fill, basal friction and velocity boundary conditions are key parameters. The weak basin fill is important in localizing shortening in the sedimentary basin, while the basal friction and the velocity boundary condition applied to the mobile wall control the transmission of the deformation to the graben. The pre-weakened basin sides seem to play a less important role than the weak basin fill, but they nevertheless influence the dip of the forward thrust in some numerical models. Basin width and graben location do not control basin inversion structures, but do influence the amount of inversion.

### *Identification of points of preferential strain concentration*

In several experiments, thrust faults seem to initiate at similar locations. This observation seems to indicate that there are points of preferential strain concentration in the models, which are the loci of fault initiation. These 'points of weakness' are shared by several experiments and can be identified thanks to models of varied graben width, infill and location.

In the experiments of varied graben fill, the location for the forward thrust totally depends on the position of the weak microbeads layer inside the graben. The layer of microbeads constitutes the main point of weakness for both analogue and numerical experiments. This is not the case for the pre-weakened basin sides, which are not weak enough to be responsible for the initiation of thrust faults. On the other hand, the top edge of the left basin side may influence the dip of the propagating thrust faults and therefore is considered to be a point

of weakness. Its influence is less obvious in the analogue models.

We define two additional points of strain concentration in the numerical experiments, related to the upper corners of the layer of microbeads that form a weak polygon. These points are activated at different stages of shortening. In several numerical experiments, a second and a third forward thrust form in the graben, cutting the graben sides and going through the left and the right top microbeads layer, respectively. The analogue experiments only rarely use these points of weakness.

### *Comparison of analogue and numerical results*

In general the results of the analogue and numerical experiments are in good agreement. We do not observe reactivation of normal faults in the models. The back thrust initiated in the graben propagates parallel and close to the basin sides as the initiation of a thrust in the microbeads is easier than reactivation of the graben-bounding faults. The formation of forward thrusts that initiate at the basal transition from strong footwall to weak graben fill and propagate through the graben and into the post-rift sediments accommodates most of the shortening. The fact that weak sedimentary layers tend to localize deformation during shortening was previously found in numerical models (Buiter & Pfiffner 2003), in analogue models (Brun & Nalpas 1996) and described in natural examples (e.g., Vially *et al.* 1994; Roure & Colletta 1996). Brun and Nalpas (1996) compare their analogue models, in which a ductile layer allows décollement of the cover during inversion, to the Broad Fourteens basin, where the Zechstein salt layer facilitates decoupling of the sedimentary cover from its basement and thrusting of the graben fill onto the basement. Along the North African margin, a layer of Triassic salt constitutes the main décollement level during shortening (Vially *et al.* 1994), whereas in the Alps a weak Triassic layer partly controls the location of thrusts faults (Roure & Colletta 1996).

Despite the overall agreement between analogue and numerical model results, some discrepancies can be found between the two modelling techniques. Analogue models with low basal friction (12.5°) and a weak basal layer of microbeads in the graben show initial bulging of graben fill and cover, and thickening of right graben-bounding block, in contrast to equivalent numerical models. Bulging of graben fill during initial stages of shortening has been described in previous analogue experiments on basin inversion (Panien *et al.* 2005) and in southern England (Chadwick 1993) where the inversion of the Wessex Basin occurred by bulk shortening of the graben-fill and produced a regional upwarp. Chadwick (1993) suggests that bulging takes place by a combination of pure-shear shortening and localized minor reverse faulting in the young, poorly lithified and therefore relatively weak graben-fill sediments and that horizontal shortening at depth is progressively transformed into predominantly vertical motion in the shallower parts of the basin. In the analogue models, diffuse deformation initially accommodates shortening, whereas in the numerical models shortening seems to localize already in early stages along shear zones. In addition, lateral compaction could also play a role in the analogue model. The compaction of the granular material during the initial stages of deformation precedes its decompaction along shear zones during further shortening (Lohrmann *et al.* 2003). Dilation could already have occurred before failure along future shear zones. This dilation could lead to bulging prior to the development of throughgoing shear zones.

Another discrepancy is the influence of the position of the graben-bounding faults on the dip of the first-formed thrust faults in some numerical models, which is not apparent in the analogue models. This discrepancy could imply that the numerical model is more sensitive to lateral heterogeneities, as is the case for the graben-bounding faults.

The overall evolution of the analogue and numerical models is encouragingly similar, which increases faith in the robustness of these models. The combination of the analogue modelling technique, which is relatively simple, inexpensive and not very time consuming, with the numerical technique, in which the results are easily quantified and the input parameters easily modified, is really effective and fruitful as it allows to overcome the weakness inherent in each of the methods and thus to get more insight into the natural processes.

## Concluding remarks

Our results of analogue and numerical experiments of inversion of a symmetric basin document a similar structural evolution. The two modelling techniques show that weak layers strongly control the development of thrust zones. The approximations made in the reference numerical experiment (smoothening of the velocity profile toward the base of the model,

slightly lower basal friction, absence of strain-hardening phase, pre-weakening of the basin sides) are thus considered to be reasonable. The fact that the basal layer of microbeads needs to be weaker to obtain comparable results and the fact that there are more zones of weakness in the numerical models suggests that numerical models are more sensitive to small parameter changes than analogue models. The comparison of the two modelling techniques brings additional information about the mechanisms of deformation involved in analogue models and can be seen as a validation of numerical codes. The positive results of such a comparison enhance the credibility of modelling results and underlines the accuracy and applicability of both modelling techniques.

The numerical calculations used software (Sopale) developed by P. Fullsack. S. B. thanks C. Beaumont for helpful discussions on the numerical sandbox. A. Liechti is thanked for technical assistance. Funding by the Swiss National Science Foundation (project number 2000-067952.02) is gratefully acknowledged. We thank Martha Withjack and Hemin Koyi for their constructive reviews.

## References

BISHOP, D. J. & BUCHANAN, P. G. 1995. Development of structurally inverted basins: a case study from the West Coast, South Island, New Zealand. *In*: BUCHANAN, J. G. B. & BUCHANAN, P. G. (eds) *Basin Inversion*. Geological Society, London, Special Publications, **88**, 549–585.

BRUN, J. P. & NALPAS, T. 1996. Graben inversion in nature and experiments. *Tectonics*, **15**, 677–687.

BUCHANAN, P. G. & MCCLAY, K. R. 1991. Sandbox experiments of inverted listric and planar fault systems. *Tectonophysics*, **188**, 97–115.

BUITER, S. J. H. & PFIFFNER, O. A. 2003. Numerical models of the inversion of half-graben basins. *Tectonics*, **22**, 11–1/11–16.

CHADWICK, R. A. 1993. Aspects of basin inversion in southern Britain. *Journal of the Geological Society*, **150**, 331–322.

COOPER, M. A. & WILLIAMS, G. D. 1989. *Inversion tectonics*. Geological Society, London, Special Publications, **44**.

COOPER, M., WEISSENBERGER, J. *ET AL.* 2001. Basin evolution in Western Newfoundland: new insights from hydrocarbon exploration. *American Association of Petroleum Geologists*, **85**, 393–418.

DAHLEN, F. A. & SUPPE, J. 1988. Mechanics, growth, and erosion of mountain belts. *Geological Society of America Special Paper*, **218**, 161–178.

DUBOIS, A., ODONNE, F., MASSONNAT, G., LEBOURG, T. & FABRE, R. 2002. Analogue modelling of fault reactivation: tectonic inversion and oblique remobilisation of grabens. *Journal of Structural Geology*, **24**, 1741–1752.

EISENSTADT, G. & WITHJACK, M. O. 1995. Estimating inversion: results from clay models *In*: BUCHANAN, J. G. B. & BUCHANAN, P. G. (eds) *Basin Inversion*. Geological Society, London, Special Publications, **88**, 119–136.

ELLIS, S., SCHREURS, G. & PANIEN, M. 2004. Comparisons between analogue and numerical models of thrust wedge development. *Journal of Structural Geology*, **26**, 1659–1675.

FULLSACK, P. 1995. An arbitrary Lagrangian-Eulerian formulation for creeping flows and its application in tectonic models. *Geophysical Journal International*, **120**, 1–23.

GLENNIE, K. W. & BOEGNER, P. L. E. 1981. Sole Pit inversion tectonics. *In*: ILLING, L. V. & HOBSON, G. D. (eds) *Petroleum Geology of the Continental Shelf of North-West Europe; Proceedings of the Second Conference*. London, 110–120.

HANSEN, D. L. & NIELSEN, S. B. 2003. Why rifts invert in compression. *Tectonophysics*, **373**, 5–24.

HUBBERT, M. K. 1937. Theory of scale models as applied to the study of geologic structures. *Bulletin of the Geological Society of America*, **48**, 1459–1520.

KELLER, J. V. A. & MCCLAY, K. R. 1995. 3D sandbox models of positive inversion. *In*: BUCHANAN, J. G. B. & BUCHANAN, P. G. (eds) *Basin Inversion*. Geological Society, London, Special Publications, **88**, 137–146.

KOOPMAN, A., SPEKSNIJDER, A. & HORSFIELD, W. T. 1987. Sandbox model studies of inversion tectonics. *Tectonophysics*, **137**, 379–388.

KOYI, H. 1997. Analogue modelling: from a qualitative to a quantitative technique: a historical outline. *Journal of Petroleum Geology*, **20**, 223–238.

LETOUZEY, J., COLLETTA, B., VIALLY, R. & CHERMETTE, J. C. 1995. Evolution of salt-related structures in compressional settings. *In*: JACKSON, M. P. A., ROBERTS, D. G. & SNELSON, S. (eds) *Salt Tectonics: a Global Perspective*. AAPG Memoir, **65**, 41–60.

LOHRMANN, J., KUKOWSKI, N., ADAM, J. & ONCKEN, O. 2003. The impact of analogue material properties on the geometry, kinematics and dynamics of convergent sand wedges. *Journal of Structural Geology*, **25**, 1691–1711.

MCCLAY, K. R. 1989. Analogue models of inversion tectonics. *In*: COOPER, M. A. & WILLIAMS, G. D. (eds) *Inversion Tectonics*. Geological Society, London, Special Publications, **44**, 41–59.

MCCLAY, K. R. 1995. The geometries and kinematics of inverted fault systems: a review of analogue model studies, *In*: BUCHANAN, J. G. B. & BUCHANAN, P. G. (eds) *Basin Inversion*. Geological Society, London, Special Publications, **88**, 97–118.

MCCLAY, K. R. & BUCHANAN, P. G. 1992. Thrust faults in inverted extensional basins. *In*: MCCLAY, K. R. (ed.) *Thrust Tectonics*. London, 93–104.

MITRA, S. 1993. Geometry and kinematic evolution of inversion structures. *American Association of Petroleum Geologists Bulletin*, **77**, 1159–1191.

MITRA, S. & ISLAM, Q. T. 1994. Experimental (clay) models of inversion structures. *Tectonophysics*, **230**, 211–222.

NIELSEN, S. B. & HANSEN, D. L. 2000. Physical explanation of the formation and evolution of inversion zones and marginal troughs. *Geological Society of America*, **28**, 875–878.

PANIEN, M. 2004. *Analogue modelling experiments of basin inversion using well-characterised granular materials and comparisons with numerical models*. Ph.D. thesis, University of Berne.

PANIEN, M., SCHREURS, G. & PFIFFNER, O. A. 2005. Sandbox experiments on basin inversion: testing the influence of basin orientation and basin fill. *Journal of Structural Geology*, **27**, 433–445.

RAMBERG, H. 1981. The role of gravity in orogenic belts. *In*: MCCLAY, K. R. P. & PRICE, N. J. (eds) *Thrust and Nappe Tectonic*. Geological Society, London, Special Publications, **9**, 125–140.

ROURE, F. & COLLETTA, B. 1996. Cenozoic inversion structures in the foreland of the Pyrenees and Alps. *In*: ZIEGLER, P. A. H. & HORVATH, F. (eds) *Peri-Tethys Memoir 2: Structure and Prospects of Alpine Basins and Forelands*, Paris, Mémoire du Muséum National d'Histoire Naturelle, 173–209.

SCHULZE, D. 1994. Entwicklung und Anwendung eines neuartigen Ringschergerätes. *Aufbereitungs-Technik*, **35**, 524–535.

VIALLY, R., LETOUZEY, J., BENARD, F., HADDADI, N., DESFORGES, G., ASKRI, H. & BOUDJEMA, A. 1994. Basin inversion along the North African margin: the Saharan Atlas (Algeria). *In*: ROURE, F. (ed.) *Peri-Tethyan Platforms*. Paris, Technip, 79–118.

WILLIAMS, G. D., POWELL, C. M. & COOPER, M. A. 1989. Geometry and kinematics of inversion tectonics. *In*: COOPER, M. A. & WILLIAMS, G. D. (eds) *Inversion Tectonics*. Geological Society, London, Special Publications, **44**, 3–15.

YAMADA, Y. & MCCLAY, K. 2003. Application of geometric models to inverted listric fault systems in sandbox experiments. Paper 1: 2D hanging wall deformation and section restoration. *Journal of Structural Geology*, **25**, 1551–1560.

ZHAO, W. L., DAVIS, D. M., DAHLEN, F. A. & SUPPE, J. 1986. Origin of convex accretionary wedges: evidence from Barbados. *Journal of Geophysical Research B*, **91**, 10246–10258.

# Lower crustal rheological expression in inverted basins

MIKE SANDIFORD[1], DAVID L. HANSEN[2] & SANDRA N. MCLAREN[3]
[1]*School of Earth Sciences, University of Melbourne, Victoria, 3010, Australia*
*(e-mail: mikes@unimelb.edu.au)*
[2]*Department of Earth Sciences, University of Aarhus, Finlandsgade 6-8, DK-8200, Aarhus, Denmark*
[3]*Research School of Earth Sciences, Australian National University, ACT, Australia*

**Abstract:** Although lithospheric modelling has provided extraordinary insights into the processes that shape the continental crust, considerable uncertainty surrounds the basic rheology that governs behaviour at geological timescales. In part, this is because it has proved difficult to identify the geological observations that might discriminate, or unify, models of lithospheric rheology. In particular, the relative strength of lower crust and upper mantle remains a contentious aspect of continental lithospheric rheology. We show that various models for lower crustal rheology may produce distinct patterns of inversion in extensional sedimentary basins, consistent with some of the observed natural variability of inversion styles. Inversion of basin interiors, as is common in European Mesozoic basins, is favoured by a lithospheric rheology more sensitive to lateral thermal structure than to changes in the depth of the Moho, consistent with there being little strength contrast between the lower crust and upper mantle in these settings. In contrast, inversion of basin margins, particularly involving basinward verging structures, is consistent with a rheological sensitivity to the depth of Moho as would apply for a lower crust much weaker than the upper mantle. We use an example from central Australia to demonstrate this latter response, together with thermochronologic data that suggests that a relatively weak lower crust in this setting may reflect abnormally high geothermal gradients.

At the continental scale, meaningful predictions about the length-scales of deformation have been derived from models treating the lithosphere in terms of vertically averaged rheology (England & Houseman 1986). While these provide an important framework for understanding the long-wavelength deformation of continental interiors they do not provide much insight into the geometry of deformation at sub-lithospheric scales, where a more explicit treatment of the rheological and compositional stratification of the lithosphere is required (e.g., Beaumont *et al.* 2000). There is general consensus that rheological stratification of the lithosphere arises because of competition between pressure- and temperature-sensitive deformation mechanisms on the one hand, and compositional and mineralogical stratification of the lithosphere on the other (Brace & Kholstedt 1980). However, the distribution of strength remains controversial (Jackson 2002; Afonso & Ranalli 2004), as is the extent to which the strength distribution imposes on the resulting distribution of strain.

The Moho is the most important compositional boundary within the lithosphere, with the associated density contrast providing a fundamental control on the mechanics of crustal deformation. In many rheological models the strength contrast across the Moho (from weak lower crust to strong mantle) is so strongly expressed that the depth (and temperature) of the Moho is the dominant parameter controlling the rheological response of the lithosphere (Sonder & England 1986). This so-called 'jelly sandwich' model has been questioned (Jackson 2002) because it appears at odds with observations that imply that the lower crust is seismically active and capable of sustaining elastic stresses over geological timescales (Maggi *et al.* 2000). Indeed, Jackson (2002) has argued that the lower crust may be as strong as, if not stronger than, the upper mantle beneath, with the implication that the Moho has little relevance to the mechanical behaviour of the continental lithosphere (Fig. 1).

In numerical simulations, we might expect that the 'jelly sandwich' and 'stiff crust' (end-member) rheologies lead to qualitative differences in the styles and patterns of lithospheric deformation, especially for regions characterized by lateral variations in crustal thickness and

*From*: BUITER, S. J. H. & SCHREURS, G. (eds) 2006. *Analogue and Numerical Modelling of Crustal-Scale Processes.* Geological Society, London, Special Publications, **253**, 271–283.
0305-8719/06/$15.00 

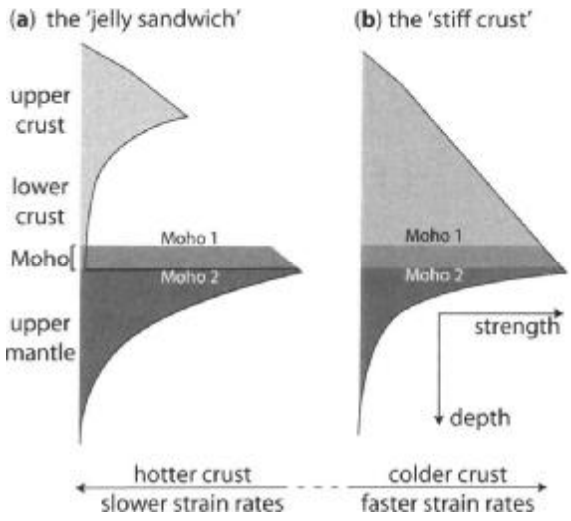


**Fig. 1.** Schematic illustration of vertical distribution of strength (at depth independent strain rate) in the (**a**) 'jelly sandwich' and (**b**) 'stiff crust' rheological models. An important difference between these models is the greater sensitivity of the 'jelly sandwich' rheology to the depth of the Moho, as indicated by the effect of changing Moho depth (i.e., Moho 1 to Moho 2) on the vertically integrated strength (i.e., the area under a given strength-depth profile). Such hypothetical models are sensitive to the geothermal and strain rate regimes.

thermal regime. The objective of this paper is to explore such qualitative differences by using forward numerical models for the inversion of extensional sedimentary basins. The classic setting showing such lateral structure is old, extended continental crust where the isostatic response to stretching has resulted in the development and filling of sedimentary basins (McKenzie 1978). Here, we consider the way inversion operates on thermally equilibrated extended lithosphere, adopting the assumption that sufficient time has elapsed since extension that all thermal transients associated with the extensional deformation and basin-filling have dissipated.

Many factors have been postulated to influence the style inversion of sedimentary basins, as evidenced by the extensive body of literature dedicated to this very subject (e.g., Cooper & Williams 1989; Buchanan & Buchanan 1995; Turner & Williams 2004). Our objective here is not to provide a comprehensive assessment of all factors that contribute to, and control, inversion, but rather to explore how the two end-member lower crustal rheologies might express themselves in terms of inversion styles. Thus we make a number of simplifying assumptions such as ignoring the anisotropy introduced by basin-forming faulting. This helps to isolate the specific consequences of differing lower crustal rheology and is not meant to imply that these other factors are not equally, if not more, important.

Of course, it is important to evaluate the results of forward models against observations from the real world, and so we begin with some basic observations pertinent to variability in the style of basin inversion in nature. This is followed by an analysis of simple thermo-mechanical models of basin evolution using the end-member rheologies that reproduce some of the essential elements of this natural variation. As summarized by Turner & Williams (2004), a particular problem highlighted in previous analyses of basin inversion has been the mechanical problem of inverting basin interiors where the lithosphere is assumed to have been strengthened by isostatically compensated reductions in Moho depth. This study directly relates to this problem, with our analysis suggesting that, to a large degree, the variation of inversion styles observed in nature may be explicable in terms of variability in lower crustal rheological state.

## Styles of inversion in nature

In nature there is a significant variation in the style and distribution of inversion within inverted basins (e.g., Turner & Williams 2004). Here we make some brief remarks about two distinct styles of inversion relevant to our later analysis of numerical modelling results.

The classic style of basin inversion, as evident in numerous examples from Europe (Fig. 2) is characterized by a central zone of basin floor uplift and intense deformation accommodated by reverse faults. The inverted zones coincide with the depocentres of the precursor rift basin and as such the deeper sediments experienced the most uplift. The basin flanks typically subsided and syn-inversion marginal troughs developed. The latter effect reflects the flexural isostatic response to the crustal thickening of the inversion zones (Nielsen & Hansen 2000). In Europe, in the Alpine foreland, the marginal troughs are consistently filled with late Cretaceous chalks, of which only a small fraction is reworked material, signalling the relative simultaneity of the main compressive inversion phases. Here, the time interval between basin formation and inversion is largely set by the phases of rifting, relating to the Mesozoic break-up of Pangea, and the phases of Late Cretaceous and Cenozoic compression relating to the collision of the African and European plates. As this time interval generally compares to the lithospheric thermal time constant, the localization

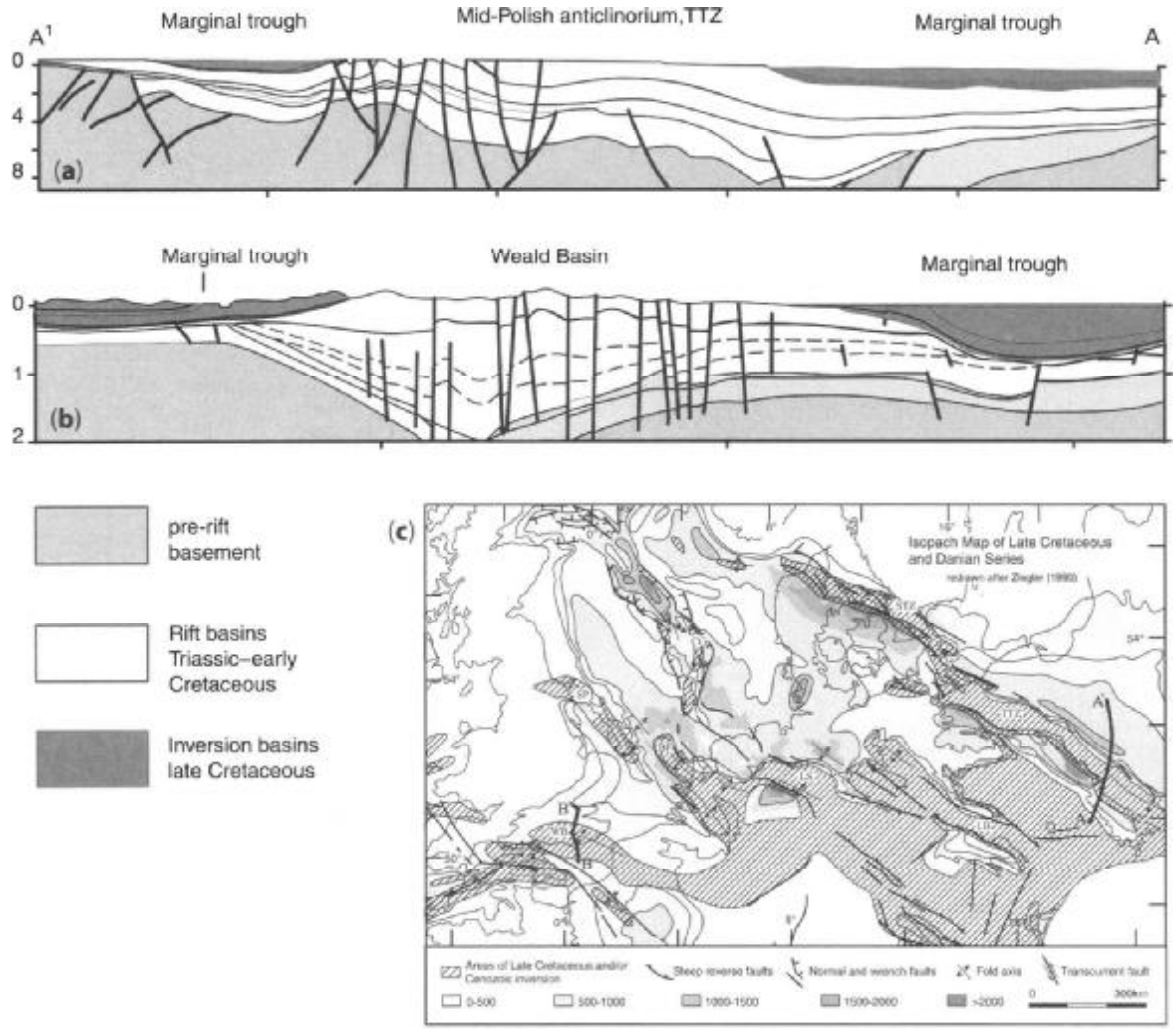


**Fig. 2.** Cross-section of typical inverted basins (upper panel: Polish trough *c.* 230 km across; lower panel: Weald Basin, SE England, *c.* 160 km across), adapted from Nielsen & Hansen (2000). The locus of maximum inversion intensity typically occurs in the interior of the precursor rift basins. During inversion reworked sediment is shed to marginal troughs that extend across the precursor basin margin towards the foreland. In these cases, inversion occurred at time intervals that preclude localization due to thermal transients associated with the initial rifting. In the case of the Polish Trough, rifting took place from 255 Ma to 152 Ma while the inversion occurred from 85 Ma to 55 Ma. For the Weald Basin, rifting took place from 210 Ma to 130 Ma and inversion from 60 Ma 13. TTZ: Tornquist-Teisseyre zone.

of deformation during inversion cannot be attributed to the thermal perturbations associated with the earlier rifting.

Palaeozoic inverted basins in central Australia show a rather different style of inversion (Fig. 3). Central Australia comprises a mosaic of structurally remnant Neoproterozoic basins initiated at around 800 Ma (e.g., Amadeus, Officer, Georgina and Ngalia basins). These basins are typically several hundred kilometres wide and bounded by basin verging structures that formed at various times through the Palaeozoic, many hundreds of million years after initial basin formation. These inversion structures now expose basement-cored Proterozoic gneissic complexes in their hanging wall (Figs 3 and 4). The distribution of sediment fill and underlying causes controlling the distribution of Neoproterozoic depocentres in the primary basins has been the subject of controversy warranting some discussion of their geodynamic setting. To this end we briefly summarize some salient ideas about these basins. The interested reader can find more comprehensive accounts in Lambeck (1983), Lindsay *et al.* (1987), Korsch and Lindsay (1989), Lindsay and Korsch (1991), Shaw *et al.* (1991), Walter and Gorter (1994), Walter *et al.* (1995) and Sandiford *et al.* (2001).

In one of the earliest accounts (Lambeck 1983) the formation of the central Australia basins was attributed to long high amplitude (*c.*10 km) lithospheric-scale buckling, largely on the basis of the

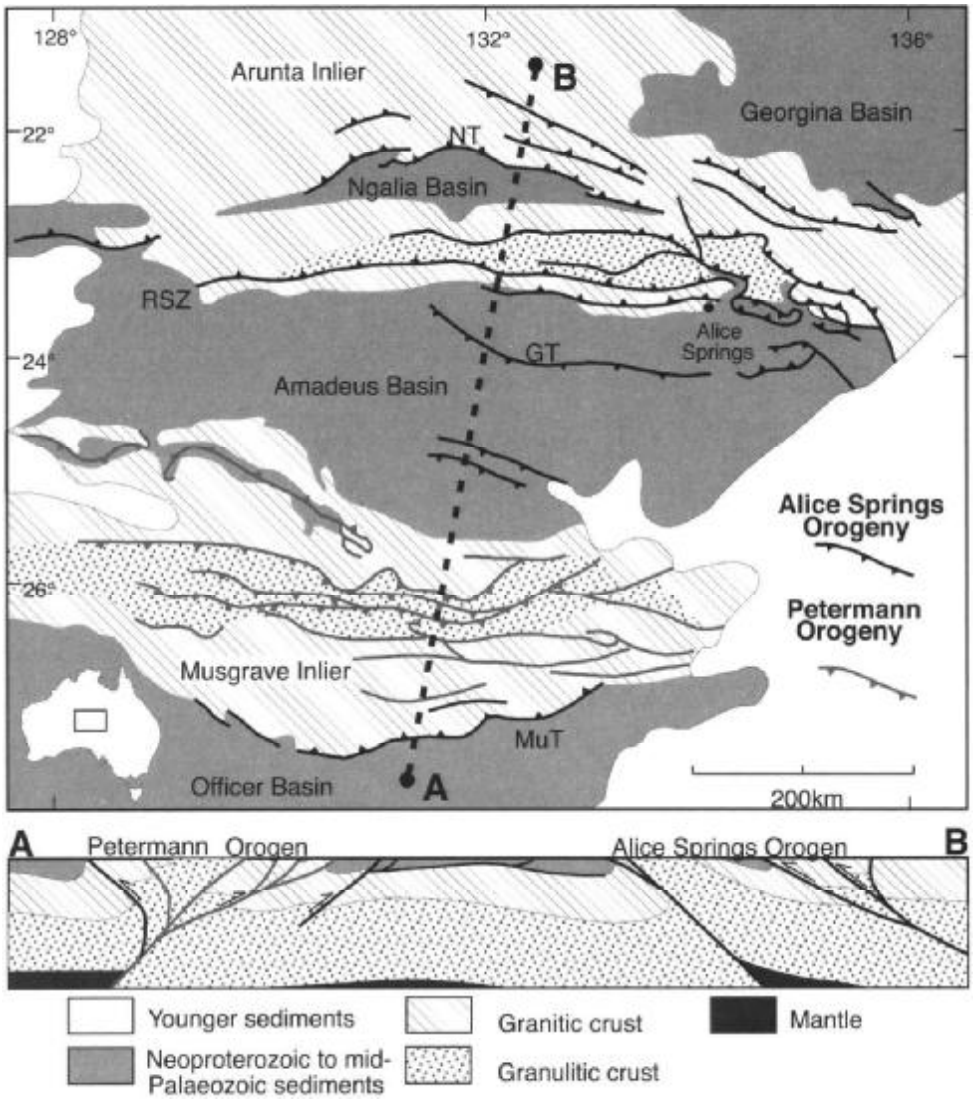


**Fig. 3.** Geological map of the central Australian region, showing the structurally remnant Neoproterozoic basins (the Officer, Amadeus, Ngalia and Georgina Basins), separated by basement inliers (the Musgrave and Arunta Inliers), adapted from Sandiford *et al.* (2001). Within the basement inliers we can distinguish two distinct types of terrane: (1) gneissic granite terranes that form the peripheral regions of the inliers and which are unconformably overlain by the sediments in the basins; (2) depleted granulite terranes that define the cores of the inliers and which are tectonically juxtaposed with the gneissic granite terranes. This juxtaposition reflects, in part, the strain associated with intraplate orogeny accumulated during the exhumation of the basement inliers from beneath a formerly more or less continuous intracratonic basin. In the Arunta Inlier this intraplate deformation was principally associated with the 450–300 Ma Alice Springs Orogeny, while in the Musgrave Inlier it was associated with the 550–500 Ma Petermann Orogeny. GT: Gardiner Thrust; MuT: Munyari Thrust; NT: Napperby Thrust; RSZ: Redbank Shear Zone.

distinctive gravity pattern of the region (see also Stephenson & Cloetingh 1991). However, subsequent workers (e.g., Teyssier 1985) have demonstrated that the gravity pattern largely reflects late structuring of the basin during inversion (Shaw *et al.* 1991; Sandiford 2002) and therefore does not provide an unequivocal constraint on the earlier basin-forming process. Consequently almost all subsequent analyses have emphasized the role of extensional processes in basin formation (e.g., Lindsay *et al.* 1987; Korsch & Lindsay 1989; Shaw *et al.* 1991; Walter & Gorter 1994; Walter *et al.* 1995; Sandiford *et al.* 2001). The current consensus is that the main rifting associated with basin-initiation stage occurred at >800 Ma. Subsidiary, milder extensional episodes are reflected in changes in the depocentres up until the early Ordovician (e.g., Shaw *et al.* 1991). Relatively new data from sediment provenance studies (Comacho *et al.* 2002) shed important further light on the original extent of these extensional

basins. These data demand proximal exposure of basement throughout basin evolution (implying that the present-day distribution of structurally remnant basins mirrors the original pattern of extensional basins). Moreover, from the point of view of our analysis, the findings of Comacho *et al.* (2002) imply that the style of inversion in central Australia must have involved marginal inversion, rather than inversion along a central basin axis as typifies the European Mesozoic basins, with the sediment generated during inversion redistributed towards the original basin centres. Further, the basin-verging asymmetry of the main structures that accommodate basin inversion in central Australia makes them geometrically incompatible with reactivation of plausible primary basin forming, extensional structures that would be expected to dip southwards towards the basin interior (Fig. 4). This is an important inference, since it implies that the existence of basin-forming structures is not likely to be the primary determinant in localizing crustal shortening during inversion in this setting. However, it is necessary to provide a word of caution about this interpretation since the geometry of the primary, basin-forming structures in central Australia is not well understood. This is partly due to the intensity of the subsequent inversion in which large thrust sheets and nappe structures developed as part of a crustal-scale deformation event (e.g., Teyssier 1985; Golbey *et al.* 1989; Sandiford 2002), thereby obscuring earlier formed structures.

One potentially important distinction between the European and Australian basins may relate to the crustal thermal regime at the time of inversion. Heat flows in the Tornquist zone in the Polish Basin (Fig. 2a) are *c.* 65–70 $mWm^{-2}$ (Balling 1995), which are only slightly greater than average continental crustal heat flows. Unfortunately heat flow data from central Australia is sparse, with no available data from the central Australian basins. However, the central Australian crust on which the basin is formed is characterized by unusually high radiogenic element concentrations (Sandiford *et al.* 2001, Fig. 4), as is much of the Australian Proterozoic, where the average heat flow is 85 $mWm^{-2}$ (see McLaren *et al.* 2003 for a full account). Bottom-hole temperatures from exploration wells in the northern half of the Amadeus Basin suggest modern-day thermal gradients of *c.* 25°C/km and locally as high as 35°C/km (Gorter 1984). Using our own unpublished thermal conductivity data (which yield average basin sediment conductivities of *c.* 2.7 W/m/K), these thermal gradients are consistent with heat flows of *c.* 65–95 $mWm^{-2}$. The existence of

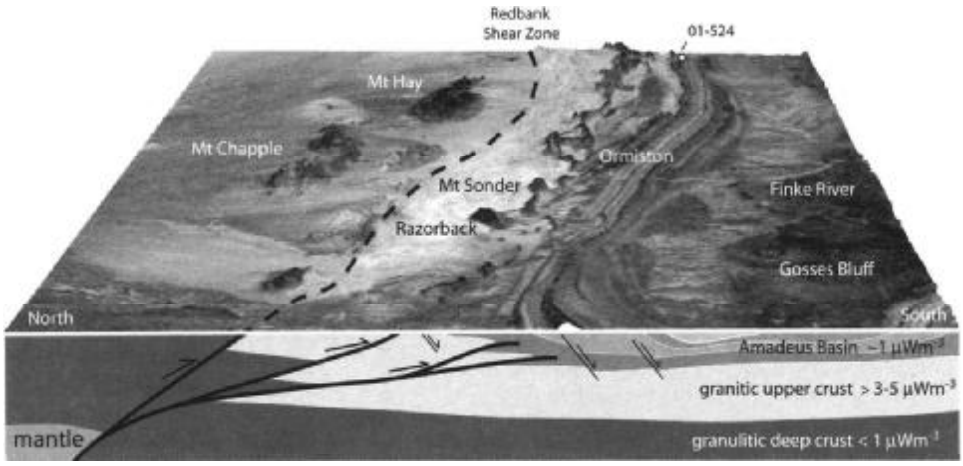


**Fig. 4.** Airborne radiometric image, data courtesy of Northern Territory Geological Survey, draped over a digital elevation model of the western Macdonnell ranges along the inverted boundary between the Arunta Inlier and the Amadeus basin, with crustal scale cross-section showing the main crustal elements associated with Proterozoic basin formation and Palaeozoic inversion. Note the basin-verging (southward) inversion structures associated with the Redbank shear zone (thick black lines) are geometrically incompatible with the schematically illustrated basin-forming structures (thin black lines). Sample site 01-524 shows the location of the K-feldspars used to constrain thermal regimes during basin inversion. In terms of radioelement concentrations, three distinct elements can be identified (Sandiford *et al.* 2002): (1) the sediments of the Amadeus basin that have heat production rates of *c.*1 $\mu Wm^{-3}$, (2) the granites and gneisses that immediately underlie the Amadeus Basin and have heat production rates of $>3$ $\mu Wm^{-3}$ (locally up to *c.* 10 $\mu Wm^{-3}$), and (3) the deep crustal mafic granulites that outcrop as isolated monadnocks (e.g., Mount Chapple and Mount Hay) in the desert to the north of the Redbank shear zone with heat production rates $<1$ $\mu Wm^{-3}$.

elevated thermal gradients in the central Australian basins prior to inversion is implied by thermochronological data of detrital K-feldspar from a granite boulder in glaciogenic sediments in the lower part of the basin (Fig. 5a). These data (are available online at http://www.geolsoc.org.uk/SUP18240. A hardcopy can be obtained from the Society Library.) show partial resetting of $^{40}Ar/^{39}Ar$ spectra and are believed to reflect the thermal conditions representative of the northern margin of the basin (see Appendix 1 for further elaboration). Importantly, the preservation of pre-basin formation $^{40}Ar/^{39}Ar$ ages (up to 1100 Ma) implies that temperatures *never* exceeded *c.* 230°C during the evolution of this part of the basin (i.e., in the interval 400–800 Ma). Similarly, the fact that the partial resetting of the $^{40}Ar/^{39}Ar$ spectra has demonstrably occurred during the basin-forming interval requires that temperatures must have exceeded 150°C (Fig. 5). Albeit subject to somewhat contentious vagaries of the method, our modelling of the spectra achieves best fits with peak temperatures in the range 170–190°C at the time when inversion commenced (*c.* 400 Ma) followed by cooling to *c.* 330 Ma, coincident with the inversion of the basin at this time (Haines *et al.* 2001). Assuming a surface temperature of about 20°C at the time of inversion then we derive average thermal gradients in the basin of about 28–38°C/km. Using our unpublished conductivity measurements cited above, these data yield heat flows of *c.* 75–100 $mWm^{-2}$ during the late stages of basin evolution, comparable with the range of modern thermal gradients and somewhat higher than in the Tornquist zone in western Europe (Balling 1995).

In terms of potential variations in Moho temperature for the different settings we need to make certain assumptions about the source of the heat flow variation. If we are correct in attributing the differences in heat flow to variations in the heat production of the crust underlying the basin

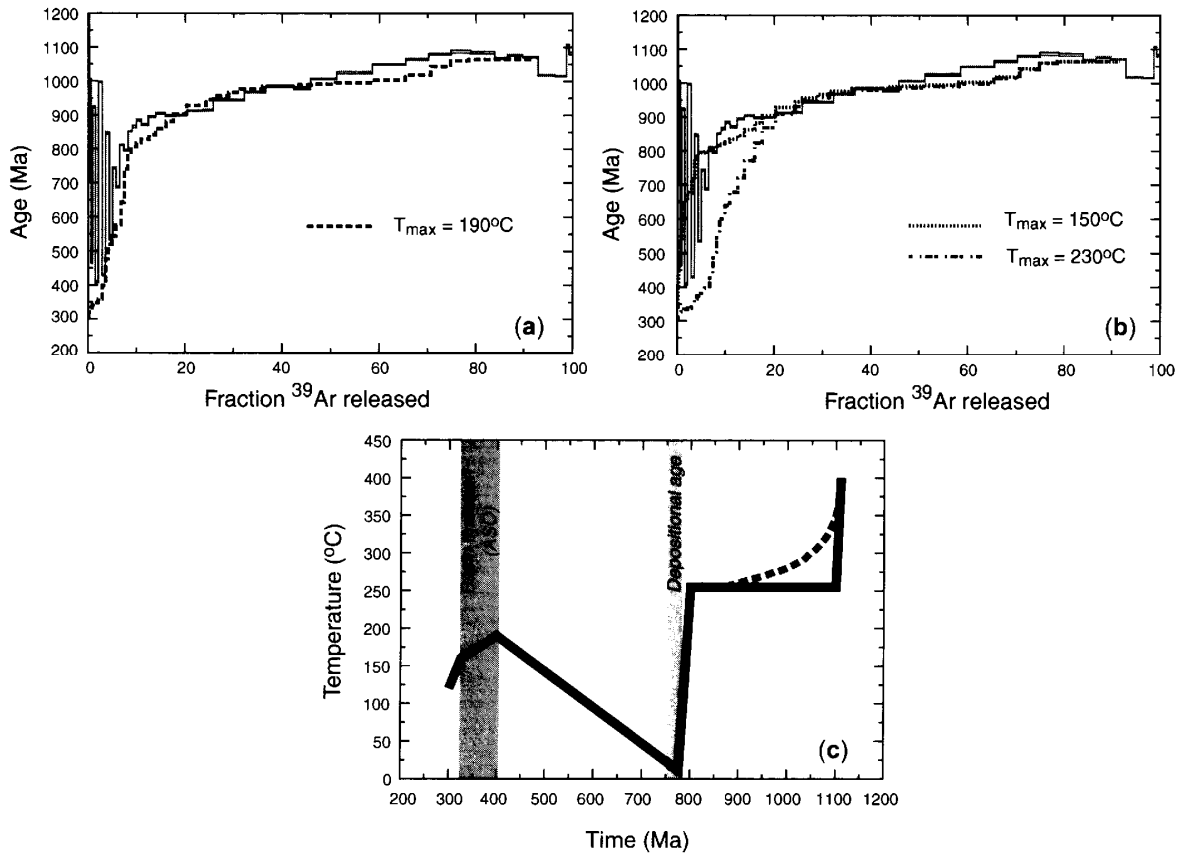


**Fig. 5.** $^{40}Ar/^{39}Ar$ age spectrum for K-feldspar 01-524 (**a**) laboratory age spectrum with best-fit model age spectrum, (**b**) laboratory age spectrum and model age spectra for post-depositional temperature maxima of 230°C and 150°C. The poor fit to the laboratory data provides robust constraints on this portion of the cooling history. (**c**) Best-fit temperature time history corresponding to a maximum post-depositional temperature of 190°C. Dashed line indicates alternative best-fit history for the higher temperature history. See Fig. 4 for the sample site and Appendix 1 for details of analytical methods and interpretation.

then, following the simple formula introduced by Sandiford and McLaren (2002), the difference in temperature at or beneath the Moho is given by

$$\Delta T_m = \frac{\Delta q_c\, h}{k} \qquad (1)$$

where $\Delta q_c$ is the difference in the integrated heat production of the crust (as, e.g., reflected in the surface heat flows), $h$ is the mean depth of the heat production and $k$ the thermal conductivity. Assuming a difference in heat production ($\Delta q_c$) equivalent to 15 $\mathrm{mWm}^{-2}$ (as suggested by the analysis above), $h = 10$ kms (as is typical of the continents), and $k = 2.7\ \mathrm{Wm}^{-1}\ \mathrm{K}^{-1}$ (as indicated by the above quoted conductivity), then we anticipate that temperatures at Moho depths might be as much as 50°C hotter beneath the Amadeus basin compared to the Tornquist zone. The effect of such temperature difference is significant, as in the temperature range 500–600°C, a 10° temperature rise results in approximately 10% reduction in bulk lithospheric strength at a given strain rate (Sonder & England 1986).

## Thermal and compositional controls on rheological structuring of rifted crust

At the lithospheric scale the long-term mechanical consequences of extension are potentially influenced by two distinct thermal and compositional effects (Fig. 6, see Sandiford 1999). Firstly, due to density contrasts between basin-filling sediments and extended crust there

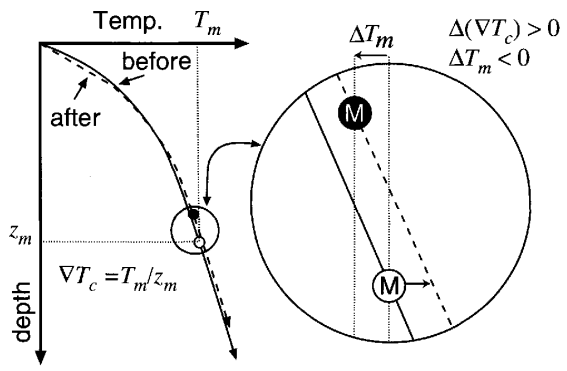


**Fig. 6.** Schematic illustration of the long-term thermal effects of crustal extension and basin formation (adapted from Sandiford 1999). Long-term Moho temperature changes ($\Delta T_m$) occur primarily due to Moho shallowing while changes in the thermal property structure of the overlying crust (mostly in the basin-fill), lead to changes in the average thermal gradient ($\nabla T_c = T_m/z_m$). See text for further discussion. As is shown in Fig. 7, the characteristic long-term thermal response to basin formation ($\Delta T_m < 0$ and $\Delta(\nabla T_c) > 0$ (see also Hansen & Nielsen 2002).

is a long-term reduction in the depth of the Moho following extension, with attendant Moho cooling ($\Delta T_m$) dependant mainly on the steady-state thermal gradient in the deep crust (typically estimated at 5–10°C/km). The second effect relates to changes in the average crustal thermal gradient ($\nabla T_c$) due to the thermal property structure (heat production and thermal conductivity) of the extended crust and associated basin-fill. The attenuation of heat production in the pre-existing crust during extension leads to long-term reductions in $\nabla T_c$, while the burial of this heat production beneath the basin-fill leads to increases in $\nabla T_c$ (Sandiford 1999; Hansen & Nielsen 2002; Sandiford *et al.* 2003).

There is a considerable range in the plausible thermal property structure of continental crust and basin-fill (Sandiford 1999). The large number of parameters that influence the thermal structure of continental crust implies there can be no unique thermal response of the continental crust to extension. Consequently, in order to demonstrate the plausible long-term thermal response, we use a Monte Carlo approach based on the thermal property parameter ranges outlined by Hansen and Nielsen (2002) and Sandiford *et al.* (2003), wherein further details can be found. Figure 7 shows the results of a Monte Carlo simulation (*c.* 4500 individual parameter sets) of thermally-mature extensional basins. The great proportion (*c.* 86%) of modelled parameter sets result in an increase in thermal gradient beneath basins ($\Delta(\nabla T_c) > 0$), with the median value of ($\Delta(\nabla T_c) \sim 1$°C/km) implying that the upper mantle beneath the basin is significantly hotter (by around 30–40°C) than the upper mantle at similar depths outside the basin. Despite this characteristic long-term increase in thermal gradient beneath basin centres, the great majority (76%) of modelled parameter sets result in long-term Moho cooling ($\Delta T_m < 0$) reflecting the significant reduction in Moho depth accompanying the isostatic compensation of low-density sediment fill. Long-term changes in the thermal gradient ($\nabla T_c$) beneath basins necessarily result in lateral heat flow, typically directed away from the basin centre because of the increase in the average thermal gradients beneath the basin. For $\Delta(\nabla T_c) > 0$ such lateral heat flow directed away from basin centres results in Moho temperature maxima beneath basin margins (Hansen & Nielsen 2002), where the Moho temperatures may be elevated by up to 20°C, although typically by less than 5°C.

The modelling results summarized in Figure 7 provide an important insight into the thermal structure beneath old, sediment-filled extensional basins. In particular, the lower crust and upper

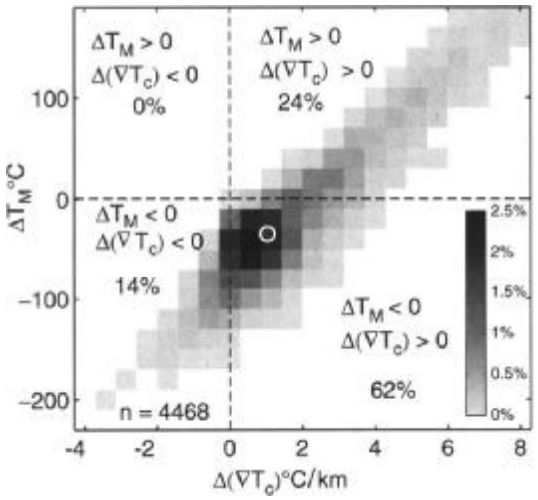


**Fig. 7.** Monte Carlo simulation of the long-term changes in thermal structure of extended continental crust on which a sedimentary basin has developed. The thermal structure is expressed in terms of the changes in Moho temperature ($\Delta T_M$) and average crustal thermal gradient ($\Delta(\nabla T_c)$). The parameter ranges for the 4468 individual parameter sets are the same as those employed by Hansen & Nielsen (2002). Data are presented as a proportion of the total, binned in 20°C × 0.57°C/km boxes. The median value is illustrated by the circle, with $\Delta T_M = -34$°C and $\Delta(\nabla T_c) = +1$°C/km.

mantle beneath the basin centres is likely to be several tens of degrees hotter than material at identical depths outside the basin, while the Moho is likely to be several tens of degrees cooler beneath the basin. The hottest Moho temperatures are expected at the margin of the stretched crust, where the Moho is deep but close enough to the warm basin interior to 'feel' the effects of lateral heat flow.

## Lower crustal rheological expression in inverted basins: thermal-mechanical modelling

### *Background*

The characteristic thermal and compositional structure of old, stretched continental crust (i.e., $\Delta T_m < 0$ and $\Delta(\nabla T_c) > 0$) arguably provides a useful natural experiment for testing models of lower crustal rheology against natural patterns of deformation observed in inverted basins. We use a thermal property set that is close to the median configuration produced by the Monte Carlo simulation (with $\Delta T_m = -34$°C, $\Delta(\nabla T_c) = +1$°C/km), and contrast the style of inversion produced with rheological models appropriate to a 'jelly sandwich' and 'stiff crust' schematically represented in Figure 1. For the 'jelly sandwich' model the lower crust and mantle are characterized by a rheology appropriate to wet anorthosite (Shelton & Tullis 1981) and wet dunite (Chopra & Paterson 1981), respectively, while for the 'stiff crust' model the lower crust and mantle both have the rheological properties of wet dunite (but with densities appropriate to crust and mantle, respectively). In both cases, the upper crust is assumed to have a rheology appropriate to wet quartzite (Paterson & Luan 1990). The response of basins to inversion is modelled using a coupled elasto-plasto-viscous rheology implemented in a thermo-mechanical fully Lagrangian finite element code using 4620 linear triangular elements. Details of the modelling approach are outlined below.

### *Modelling methodology*

A two-dimensional thermo-mechanical continuum model is used to investigate the lithospheric response to compression. The lithospheric profile is initially 300 km long and 120 km deep, consisting of three different mineralogical layers of upper crust (wet quartzite), lower crust (wet anorthosite) and mantle (wet dunite). In the right half of the model the elsewhere 40 km thick crust is thinned to 24 km, with 8 km of sediments resting on top (Fig. 8). The mechanical part of the model is founded on a fully Lagrangian formulation of the principle of virtual work (Green & Zerna 1968; Budiansky 1969; Malvern 1969). The principle of virtual work is complemented by a set of constitutive relations enabling visco-elastic and plastic deformation. The visco-elastic deformation form simulates temperature and time-dependent ductile creep of solid rock mass and is based on a Maxwell relation stating additivity of elastic and viscous strain rates (Jaeger & Cook 1969). While the elastic strain rates satisfy Hooke's law (Ranalli 1995), with Young's modulus at $10^{11}$ Pa and Poisson's ratio at 0.25, the viscous strain rates satisfy the empirical Dorn equation relating effective strain rates and stress levels for steady state creep (Ranalli 1995). In this case, the associated viscosity, $\vartheta$, may be calculated by

$$\vartheta = B\dot{\varepsilon}^{1/n-1} \exp\left(\frac{Q}{nRT}\right) \qquad (2)$$

where $\dot{\varepsilon}$ is the effective visco-elastic strain rate, $T$ is absolute temperature, and $R = 8.31$ J/(mol K) is the ideal gas constant. $n$, $Q$, $B$, are experimentally derived creep parameters

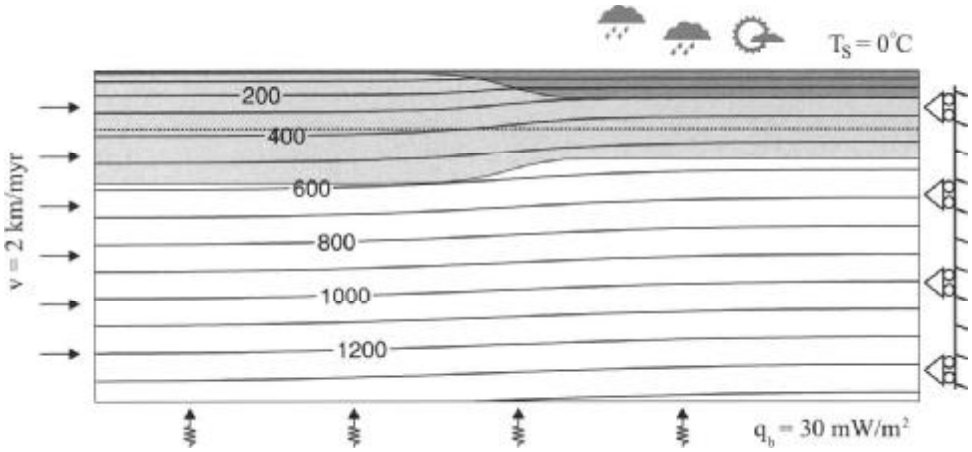


**Fig. 8.** Schematic of initial model conditions prior to inversion. The modelled domain is initially 300 km wide and 120 km deep. Inversion is imposed on the initial geometry with a thermally mature sedimentary basin above a constant thickness lithosphere. The dashed line indicates the approximate scale of the lithospheric stretching that would be needed to generate the initial basin.

(Chopra & Patterson 1981; Shelton & Tullis 1981) assumed only to depend on mineralogy.

When the yield stress of rocks is reached, the deformation form becomes visco-elastic-plastic, simulating brittle failure. The yield stress is derived from the pressure dependent Drucker-Prager yield function (Khan & Huang 1995):

$$\sqrt{J_2} + (1 - \lambda_v)\alpha(\phi)I_1 = 0 \qquad (3)$$

approximating the conditions under which frictional Coulomb type materials fail (Byerlee 1978). Here $I_1$ is the first invariant of the Cauchy stress tensor and $J_2$ the second invariant of its deviatoric part. $\alpha(\phi)$ is a function of the angle of internal friction, $\phi$ (Khan & Huang 1995):

$$\alpha(\phi) = \frac{2\sin(\phi)}{\sqrt{3}(3 - \sin(\phi))}$$

In Equation (3), $\lambda_v = 0.4$ is the pore-fluid factor of near hydrostatic conditions (Sibson 1990). A non-associated plasticity model (Vermeer & De Borst 1984), where incompressible plastic strain rates $\hat{\eta}^p$ are derived from the plastic potential, $\Omega$, is adopted:

$$\hat{\eta}^p = \frac{\partial \Omega}{\partial \sigma} \quad \text{where} \quad \Omega = \sqrt{J_2} + const. \qquad (4)$$

The displacement and temperature fields are coupled through the temperature dependence of viscosity (Eqn. 2) and density. The latter is given by

$$\rho = \rho_0(1 - a_v T) \qquad (5)$$

where $\rho_0$ is density at 0°C. $a_v = 3.2 \times 10^{-5}$ K$^{-1}$ is the volumetric expansion coefficient and $T$ is Celsius temperature.

In each model time step the temperature field is found by solving the transient heat transfer equation

$$\rho c\dot{T} = \nabla \cdot (k\nabla T) - \rho c v \cdot \nabla T + A + W \qquad (6)$$

where $c$ is specific heat capacity, $k$ is conductivity, $A$ is radiogenic heat production rate, and $W$ is the viscous shear heating rate (Ranalli 1995; Regenauer-Lieb & Yuen 1998). Material advection is represented by the relative velocity between material and grid points. On the mechanical model the temperature field is tracked using the same Lagrangian mesh and hence, here $v = 0$. However, above the mechanical model the thermal mesh is extended to account for the deposition/erosion of sediments and, as such, the thermal mesh follows the topography formed by the changing sediment distribution. The relative velocity then represents the passive flow of material across the model surface (Hansen & Nielsen 2003). The surface temperature is 0°C, whilst at the model base the vertical heat flow is 30 mW/m$^2$. At the base of the mechanical model pressure conditions are imposed, allowing the entire model to move vertically under the influence of buoyancy forces. At the left vertical axis a constant kinematic boundary condition (2 km/Ma) is imposed, compressing the model profile as the right vertical axis is fixed.

During the entire model evolution surface processes act to re-distribute sediments. These processes are modelled by a diffusion equation, with a source term enabling the transport of

sediments to and from the model profile. The transport equation is written

$$\dot{h} = \nabla \cdot (\kappa \nabla h) + \dot{s}(w) \quad (7)$$

$\kappa = 200\ \mathrm{km}^2/\mathrm{Ma}$ is the diffusivity of topography, $h$, and $\dot{s}(w)$ is a linear function of water depth. In the present study the last term is chosen so that any accommodation space created is immediately filled by sediments. Isochron markers record the chronological evolution of the basin fill by effectively representing stratigraphic boundaries. The porosity of sediment decreases with burial according to $\phi = \phi_0 \exp(z/2\,\mathrm{km})$, where $\phi_0$ is surface porosity and $z$ is maximal burial depth. All other parameters are listed in Table 1. The bulk of the sediment, which is present at the post-rift stage of the model start, is included in the thermo-mechanical model, whilst the sediment accumulating during the model evolution is directly included in the thermal model only. However, the redistribution of sediments during the model evolution influences the mechanical model as passive vertical loads.

### *Modelling results*

In the 'jelly sandwich' lithosphere, lateral variations in the strength of the lithosphere are governed primarily by the temperature of the uppermost mantle, immediately below the Moho (Sonder & England 1986). Because vertical thermal gradients are much greater than lateral gradients, variations in Moho depth are therefore crucial, with bulk lithospheric strength varying inversely with crustal thickness. With regard to a characteristic old extensional basin geometry with Moho shallowed beneath the centre of the basin, the lithosphere is strongest beneath the basin centre, and weakest along the outer margin of the basin. Consequently, in-plane compression will localize inversion in the vicinity of the basin margin (Fig. 9a). Deformation occurs in a confined zone that shows distinct localization in a zone propagating up through the crust as a basin verging ramp. Erosion focused on this marginal uplift sheds reworked sediment towards the basin interior, as well as away from the basin margin into the hinterland. Reworked sediment trapped within the basin interior produces a distinctive off-lapping succession progressively restricted towards the internal zones of the underlying rift basin.

In our 'stiff crust' lithosphere, the depth and temperature of the Moho is irrelevant to the rheological response of the lithosphere, and the thermal gradient is the primary control on the bulk lithospheric strength distribution. Because the modelled basin has higher average thermal gradients beneath the basin centre, in-plane compression necessarily localizes deformation beneath basin centres. The numerical simulation (Fig. 9b) produces diffuse strain rate gradients around a broad zone of distributed inversion. Erosion of the inverted domain sheds reworked sediment towards the basin foreland, potentially producing secondary marginal basins, outboard of the primary extensional basin. Structural asymmetry, albeit weak, verges from the basin centre towards the foreland. While not explicitly considered in the models shown here, localization phenomenon due to plastic instabilities should be expected to localize deformation in basin interiors and show a more abrupt transition between the inverted domain and the surrounding crust.

## Discussion

Given the extraordinary temperature and mineralogical sensitivity of rheological flow laws pertinent to lithospheric deformation, it seems entirely reasonable that the mechanical response of the lithosphere will vary significantly as a function of its thermal regime and composition. It would therefore be unwise to suggest that the inversion of continental lithosphere can be characterized by the one uniform mode. Indeed, one of the paramount challenges in geodynamics is the understanding of how variations in the mechanical response to external forcing affect the final form and architecture of deformed continental crust. With this in mind, our models for

**Table 1.** *Rheological and thermal parameters used in numerical models*

| Parameter | Symbol [units] | Upper crust | Lower crust | Upper mantle | Sediment |
|---|---|---|---|---|---|
| Angle of internal friction | $\phi$ | 30 | 30 | 30 | 30 |
| Thermal conductivity | $k$ [W/m/K] | 3.0 | 2.3 | 4.0 | 2.0 |
| Specific heat | $c$ [J/kg/K] | 850 | 900 | 1000 | 900 |
| Heat production rate | $A$ [$\mu$W/m$^3$] | 1.3 | 0.3 | 0.01 | 1.0 |
| Creep parameter | n | 3.10 | 3.20 | 4.48 | 3.10 |
| Creep parameter | B [MPa s$^{1/n}$] | 208.0 | 12.28 | 0.2628 | 208.0 |
| Creep parameter | Q [kJ/mol] | 135 | 239 | 498 | 135 |
| Density | $\rho_0$ [kg/m$^3$] | 2800 | 2900 | 3400 | 2300 |

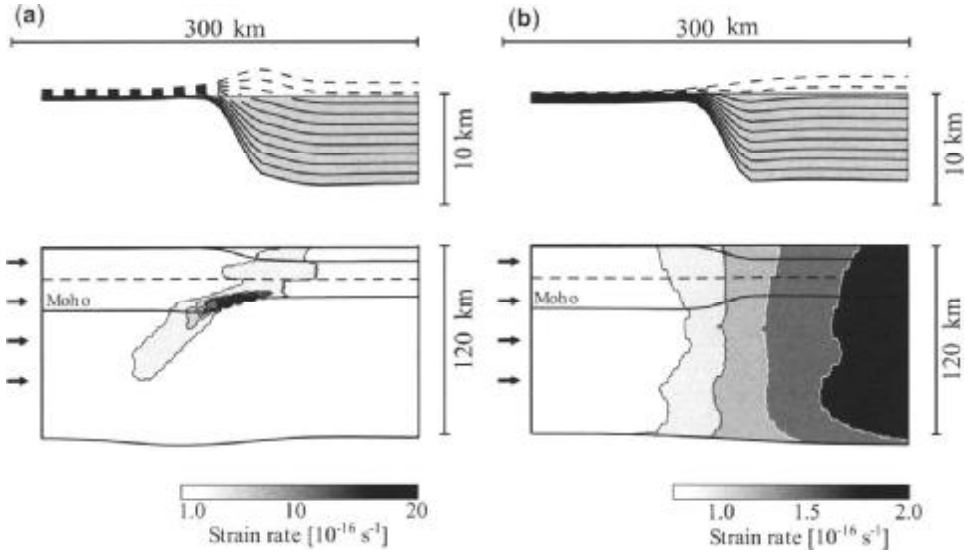


**Fig. 9.** Models of basin inversion styles predicted for different lower crustal rheology after 20 km of shortening. Upper panels show rift basin stratigraphy after inversion, while lower panels show the mean strain rate during the period of inversion. (**a**) The distribution of deformation for the 'jelly-sandwich' model. The weak lower crust and strong contrast across the Moho make the depth and temperature of the Moho critical determinants to the mechanical response. (**b**) Identical modelling scenario but with a 'stiff crust' rheology (i.e., a relatively strong lower crust, with no contrast in strength across the Moho). Modelling techniques are based on a fully Langrangian elasto-plasto-viscous deformation code, as detailed in the text.

two end-member scenarios of lower crustal rheology provide an intriguing insight into some of the observed variations in the style of inversion in natural inverted basins. Our modelling suggests that the characteristic response of basins in inversion, producing inversion along the central basin axis (Figs 2 and 9b), is consistent with there being little rheological sensitivity to the position of the Moho. For standard thermal regimes, where steady-state Moho temperatures are expected to be no greater than *c.* 500°C, this may therefore reflect the characteristic strong lower crustal rheological mode.

However, it is conceivable that, under different thermal regimes, the rheological contrast across the Moho plays a more prominent role. In support of this notion we can cite the unusual inversion record of Neoproterozoic basins in central Australia (Figs 3 and 4), where Palaeozoic inversion was at least partly localized along the margins of much older (>200 Ma) extensional basins. Here, the inversion structures verge towards basin interiors, similar to Figure 9a, with reworked sediment shed towards the interior of the inverted basins. As such, this central Australian style of inversion is consistent with a more prominent rheological contrast across the Moho. This analysis suggests that the thermal regime provides a principal control on the rheological structure of the lower crust, with the observed natural variation in inversion styles reflecting, at least in part, variations in the rheological state of the lower crust.

The model results we have presented show how thermal and compositional structuring of the lithosphere can lead to distinctive patterns of strain localization at the lithospheric scale, without appealing to strain-dependent weakening mechanisms. Many studies have shown that strain-dependent weakening is of fundamental importance to the behaviour of the continental lithosphere, and an important challenge is to establish the relative importance of the various localization mechanisms. With regard to this, our analysis suggests that the rheological structuring of the lithosphere associated with changes in Moho temperature of order 10°C is comparable to, if not more significant than, the rheological structuring associated with strain-dependent weakening processes during basin formation.

## Appendix 1. $^{40}Ar/^{39}Ar$ thermochronology

K-feldspar 01-524 was irradiated for 480 hours in the Australian Nuclear Science and Technology Organization HIFAR reactor, NSW. The sample was subject to a series of 43 steps between 450°C and 1450°C. The gas released was analyzed using a VG Isotech MM3600 gas source mass spectrometer with a sensitivity of $3.5 \times 10^{-17}$ mol/mV (This data is available online at http://www.geolsoc.org.uk/SUP18240. A hardcopy can be obtained from the Society Library.). The resultant $^{40}Ar/^{39}Ar$ age spectrum was interpreted using the multiple-diffusion-domain method assuming

that argon release is by a thermally activated diffusion process (Lovera *et al.* 1989; Richter *et al.* 1991). We computed a distribution of activation energies and domain length scales (volume fraction and effective size) using eight slab-shaped domains (This data is available online at http://www.geolsoc.org.uk/SUP18240. A hardcopy can be obtained from the Society Library.). The geological setting explicitly requires a reheating history associated with basin formation and we are able to calculate the best-fit temperature-time paths by inputting trial thermal histories and minimizing the differences between the laboratory and modelled-age spectra by iteration. Elsewhere (McLaren *et al.* 2002) we have shown that K-feldspar MDD modelling can be used to recover robust thermal histories from Australian Neoproterozoic basins, and that paper contains a rigorous discussion of our approach and the problems that need to be addressed to demonstrate that this approach yields meaningful results. The $^{40}Ar/^{39}Ar$ age spectrum of the sample (from estimated palaeodepths of $5.1 \pm 0.2$ kms in the Areyonga formation; see location in Fig. 4) shows a distinctive monotonically increasing age gradient, which suggests that the sample started to accumulate argon around 1100 Ma, with final closure to argon loss occurring in the Palaeozoic (Fig. 5). The preservation of Neoproterozoic ages provides an important constraint on the post-depositional temperatures in the basin. Modelling produces good fits with slow cooling from 1100 Ma until at least 900 Ma (as indicated by the broad range of ages in this interval). A period of rapid cooling at around 900–800 Ma is required to generate the sedimentary detritus by the inferred depositional age of the sediment (*c.* 780 Ma, Lindsay 1989). While excess argon in the early released gas precludes a robust reconstruction of the reheating history in the depositional interval 780–400 Ma, we are able to constrain the range of temperature experienced during this interval. The age spectrum requires a period of slow reheating from 780 Ma to between 170 and 190°C at 400 Ma at *c.* 0.5°C/Ma at broadly consistent with the depositional history of the overlying sedimentary pile (e.g., Haines *et al.* 2001).

This work was supported by ARC grants DP0209157 and F10020050 and by the ACcESS MNRF. Constructive comments from L. Gemmer, R. Stephenson and E. Eide, and S. Buiter have helped our preparation of the manuscript. Irradiation of K-feldspar 01-524 was undertaken by the Australian Nuclear Science and Technology Organization through the Australian Institute of Nuclear Science and Engineering.

## References

AFONSO, J. C. & RANALLI, G. 2004. Crustal and mantle strengths in continental lithosphere: is the jelly sandwich model obsolete? *Tectonophysics*, **394**, 221–232.

BALLING, N. 1995. Heat flow and thermal structure of the lithosphere across the Baltic Shield and northern Tornquist Zone. *Tectonophysics*, **244**, 13–50.

BEAUMONT, C., MUNOZ, J. A., HAMILTON, J. & FULLSACK, P. 2000. Factors controlling the Alpine evolution of the central Pyrenees inferred from a comparison of observations and geodynamical models. *Journal of Geophysical Research*, **105**, 8121–8145.

BRACE, W. F. & KOHLSTEDT, D. L. 1980. Limits on lithospheric strength imposed by laboratory experiments. *Journal of Geophysical Research*, **85**, 6248–6252.

BUCHANAN, J. G. & BUCHANAN, P. G. 1995. *Basin Inversion*. Geological Society, London, Special Publications, **88**.

BUDIANSKY, B. 1969. Remarks on theories of solid and structural mechanics. *In*: LAVRENT'EV, M. (ed.) *Problems of Hydrodynamics and Continuum Mechanics*. SIAM, Philadelphia, 77–83.

BYERLEE, J. D. 1978. Friction of rocks. *Pure and Applied Geophysics*, **116**, 615–626.

CAMACHO, A., HENSEN, B. J. & ARMSTRONG, R. 2002. Isotopic test of a thermally driven intraplate orogenic model, Australia. *Geology*, **30**, 887–890.

CHOPRA, P. N. & PATERSON, M. S. 1981. The experimental deformation of dunite. *Tectonophysics*, **78**, 453–473.

COOPER, M. A. & WILLIAMS, G. D. 1989. *Inversion Tectonics*. Geological Society, London, Special Publications, **44**.

ENGLAND, P. & HOUSEMAN, G. 1986. Finite strain calculations of continental deformation II: comparison with the India-Asia collision zone. *Journal of Geophysical Research*, **91**, 3664–3676.

GOLEBY, B. R., SHAW, R. D., WRIGHT, C., KENNETT, B. L. N. & LAMBECK, K. 1989. Geophysical evidence for 'thick-skinned' crustal deformation in central Australia. *Nature*, **337**, 325–330.

GORTER, J. D. 1984. Source potential of the Horn Valley Siltstone, Amadeus basin. *Australian Petroleum Exploration Association Journal*, **24**, 66–90.

GREEN, A. E. & ZERNA, W. 1968. *Theoretical Elasticity*. Oxford University Press, New York.

HAINES, P., HAND, M. & SANDIFORD, M. 2001. Palaeozoic syn-orogenic sedimentation in central and northern Australia: a review of distribution and timing with implications for the evolution of intracontinental orogens. *Australian Journal of Earth Sciences*, **48**, 911–928.

HANSEN, D. L. & NIELSEN, S. B. 2002. Does thermal weakening explain basin inversion, stochastic modelling of the thermal structure of sedimentary basins. *Earth and Planetary Science Letters*, **198**, 112–127.

HANSEN, D. L. & NIELSEN, S. B. 2003. Why rifts invert in compression. *Tectonophysics*, **373**, 5–24.

JACKSON, J. A. 2002. Strength of the continental lithosphere: time to abandon the jelly sandwich? *GSA Today*, **12**, 1–4.

JAEGER, J. C. & COOK, N. G. W. 1969. *Fundamentals of Rock Mechanics*. Chapman and Hall Ltd., London.

KHAN, A. S. & HUANG, A. 1995. *Continuum Theory of Plasticity*. John Wiley & Sons Inc., New York.

KORSCH, R. J. & LINDSAY, J. F. 1989. Relationships between deformation and basin evolution in the intracratonic Amadeus Basin. *Tectonophysics*, **158**, 5–22.

LAMBECK, K. 1983. Structure and evolution of the intracratonic basins of central Australia, *Journal of the Royal Astronomical Society*, **74**, 843–866.

LINDSAY, J. F. 1989. Depositional controls on glacial facies associations in a basinal setting, late Proterozoic, Amadeus Basin, central Australia. *Palaeogeography, Palaeoclimatology, Palaeoecology*, **73**, 205–232.

LINDSAY, J. F. & KORSCH, R. J. 1991. The evolution of the Amadeus Basin, central Australia. *In*: KORSCH, R. J. & KENNARD, J. M. (eds) *Geological and Geophysical Studies in the Amadeus Basin, Central Australia*. Bureau of Mineral Resources, Geology and Geophysics Australia Bulletin, **236**, 7–32.

LINDSAY, J. F., KORSCH, R. J. & WILFORD, J. R. 1987. Timing the breakup of a Proterozoic supercontinent: evidence from Australian intracratonic basins. *Geology*, **15**, 1061–1064.

LOVERA, O. M., RICHTER, F. M. & HARRISON, T. M. 1989. The $^{40}Ar/^{39}Ar$ thermochronometry for slowly cooled samples having a distribution of diffusion domain sizes. *Journal of Geophysical Research*, **94**, 17917–17935.

MAGGI, A., JACKSON, J. A., MCKENZIE, D. & PRIESTLEY, K. 2000. Earthquake focal depths, effective elastic thickness, and the strength of the continental lithosphere. *Geology*, **28**, 495–598.

MALVERN, L. E. 1969. *Introduction to the Mechanics of a Continuous Medium*. Prentice-Hall, Inc., New Jersey.

MCKENZIE, D. 1978. Some remarks on the development of sedimentary basins. *Earth and Planetary Science Letters*, **40**, 25–32.

MCLAREN, S., DUNLAP, J., SANDIFORD, M. & MCDOUGALL, I. 2002. The thermochronological record of extraordinary heat production at Mount Painter, South Australia: implications for tectonic reactivation of continental interiors. *Tectonics*, 10.1029/2000TC001275.

MCLAREN, S., SANDIFORD, M., HAND, M., NEUMANN, N., WYBORN, L. & BASTRAKOVA, I. 2003. *The Hot Southern Continent: Heat Flow and Heat Production in Australian Proterozoic Terranes*. Geological Society, Australia, Special Publications, **22**, 157–167.

NIELSEN, S. B. & HANSEN, D. L. 2000. Physical explanation of the formation and evolution of inversion zones and marginal troughs. *Geology*, **28**, 875–878.

PATERSON, M. S. & LUAN, F. C. 1990. Quartize rheology under geological conditions. *In*: KNIPE, R. & RUTTER, E. (eds) *Deformation Mechanisms, Rheology and Tectonics*. Geological Society, London, Special Publications, **54**, 299–307.

RANALLI, G. 1995. *Rheology of the Earth*. Chapman & Hall, London.

REGENAUER-LIEB, K. & YUEN, D. 1998. Rapid conversion of elastic energy into shear heating during incipient necking of the lithosphere. *Geophysical Research Letters*, **25**, 2737–2740.

RICHTER, F. M., LOVERA, O. M., HARRISON, T. M. & COPELAND, P. 1991. Tibetan tectonics from $^{40}Ar/^{39}Ar$ analysis of a single K-feldspar samples. *Earth and Planetary Science Letters*, **105**, 266–278.

SANDIFORD, M. 1999. Mechanics of basin inversion. *Tectonophysics*, **305**, 100–120.

SANDIFORD, M. 2002. Low thermal Peclet number intraplate orogeny in central Australia. *Earth and Planetary Science Letters*, **201**, 309–320.

SANDIFORD, M. & MCLAREN, S. 2002. Tectonic feedback and the ordering of heat producing elements within the continental lithosphere. *Earth and Planetary Science Letters*, **204**, 133–150.

SANDIFORD, M., FREDERIKSEN, S. & BRAUN, J. 2003. The long-term thermal consequences of rifting: implications for basin reactivation. *Basin Research*, **15**, 23–24.

SANDIFORD, M., HAND, M. & MCLAREN, S. 2001. Tectonic feedback, intraplate orogeny and the geochemical structure of the crust: a central Australian perspective. *In*: MILLER, J., HOLDSWORTH, R., BUICK, I. & HAND, M. (eds) *Continental Reactivation and Reworking*. Geological Society, London, Special Publications, **184**, 195–218.

SHAW, R. D., ETHERIDGE, M. A. & LAMBECK, K. 1991. Development of the late Proterozoic to mid-Palaeozoic intracratonic Amadeus Basin in central Australia: a key to understanding tectonic forces in plate interiors. *Tectonics*, **10**, 688–721.

SHELTON, G. & TULLIS, J. 1981. Experimental flow laws for crustal rocks. *EOS (Transactions), American Geophysical Union*, **62**, 396.

SIBSON, R. 1990. Conditions for fault-value behaviour. *In*: KNIPE, R. J. & RUTTER, E. H. (eds) *Deformation Mechanisms, Rheology and Tectonics*. Geological Society, London, Special Publications, **54**, 143–165.

SONDER, L. & ENGLAND, P. 1986. Vertical averages of rheology of the continental lithosphere; relation to thin sheet parameters. *Earth and Planetary Science Letters*, **77**, 81–90.

STEPHENSON, R. A. & CLOETINGH, S. 1991. Some examples and mechanical aspects of continental lithosphere folding. *Tectonophysics*, **188**, 27–27.

TEYSSIER, C. 1985. A crustal thrust system in an intracratonic environment. *Journal of Structural Geology*, **7**, 689–700.

TURNER, J. P. & WILLIAMS, G. A. 2004. Sedimentary basin inversion and intraplate shortening. *Tectonophysics*, **65**, 277–304.

VERMEER, P. A. & DE BORST, R. 1984. Non-associated plasticity for soils, concrete and rock. *Heron*, **29**, 1–62.

WALTER, M. R. & GORTER, J. D. 1994. The Neoproterozoic Centralian Superbasin in Western Australia: the Savory and Officer Basins. *In*: PURCELL, P. G. & PURCELL, R. R. (eds) *The Sedimentary Basins of Western Australia*. Proceedings Petroleum Exploration Society Australia Symposium, Perth, 851–864.

WALTER, M. R., VEEVERS, J. J., CALVER, C. R. & GREY, K. 1995. Neoproterozoic stratigraphy of the Centralian Superbasin, Australia. *Precambrian Research*, **73**, 173–195.

# Geometric and experimental models of extensional fault-bend folds

MARTHA O. WITHJACK & ROY W. SCHLISCHE
*Department of Geological Sciences, Rutgers University, Piscataway, New Jersey, 08854, USA*
*(e-mail: drmeow3@yahoo.com)*

**Abstract:** We use geometric and experimental models to study the development of extensional fault-bend folds. The geometric models show that fault shape, fault displacement, and patterns of aggradation/erosion profoundly affect the distribution of growth beds, the magnitude and direction of dip of pregrowth and growth beds, and the location and dip of the outer limit of folding in pregrowth and growth beds. Complex structural and stratigraphic patterns develop if the rate of aggradation/erosion relative to the rate of fault displacement changes through time. The experimental models (with dry sand and wet clay) show that several deformational styles can accommodate extensional fault-bend folding. In sand models, a few, relatively major, secondary antithetic normal faults accommodate most hanging wall deformation. Pregrowth layers, although faulted, remain flat. The effective shear direction parallels the antithetic normal faults, and the shear angle is about 60°–65°. In clay models, numerous, relatively minor, secondary normal faults (antithetic and synthetic) and cataclastic flow accommodate most hanging wall deformation. The deformed pregrowth and growth layers dip gently toward the main fault. The effective shear angle (35°–50°) is considerably less than the dip of the antithetic normal faults. In the sand models and geometric models with a large shear angle (60°), more displacement occurs on the main normal fault and the hanging wall collapses in a relatively narrow zone. In the clay models and geometric models with a small shear angle (35°), less displacement occurs on the main normal fault. Instead, the hanging wall stretches substantially and collapses in a relatively wide zone.

Normal faults have a great variety of shapes in cross-sectional view. Some are listric (i.e., concave upward), either dipping (Fig. 1a) or flattening at depth (Figs 1b–d). Others steepen with depth (Fig. 1c). Still others have complex ramp-flat-ramp geometries (Fig. 1f). Movement on nonplanar normal faults causes the hanging wall to deform, typically by extensional fault-bend folding. Several researchers have used experimental and geometric models to study the development of extensional fault-bend folds. Experimental studies with wet clay (e.g., H. Cloos 1928, 1930; E. Cloos 1968; Withjack *et al.* 1995) and dry sand (e.g., McClay & Ellis 1987*a*, *b*; Ellis & McClay 1988; McClay & Scott 1991) have simulated the secondary faulting and folding associated with movement on nonplanar normal faults. Geometric studies (e.g., White *et al.* 1986; Dula 1991; White & Yielding 1991; Kerr & White 1992; Xiao & Suppe 1992; Withjack & Peterson 1993) have examined how fault shape, fault displacement and depositional patterns affect hanging wall geometries and tested the applicability of geometric modelling.

Each modelling approach has strengths and weaknesses. With geometric models, it is easy to vary fault shape, fault displacement and depositional/erosional patterns. It is necessary, however, to prescribe a hanging wall deformation mechanism, typically layer-parallel shear in compressional settings or inclined simple shear in extensional settings (Fig. 2). With experimental models, it is difficult to vary fault shape without imposing unrealistic boundary conditions (e.g., Withjack *et al.* 1995; Hauge & Gray 1996). The hanging wall, however, can deform by a range of deformation mechanisms that can vary spatially and temporally. In this paper, we use these complementary modelling approaches to better understand the development of extensional fault-bend folds. Specifically, we use the geometric models to document how fault shape, fault displacement, depositional and erosional patterns, and multiple episodes of faulting affect the geometry of extensional fault-bends folds. We use experimental models with dry sand and wet clay to study the hanging wall deformation that accommodates extensional fault-bend folding.

*From*: BUITER, S. J. H. & SCHREURS, G. (eds) 2006. *Analogue and Numerical Modelling of Crustal-Scale Processes*. Geological Society, London, Special Publications, **253**, 285–305.
0305-8719/06/$15.00 

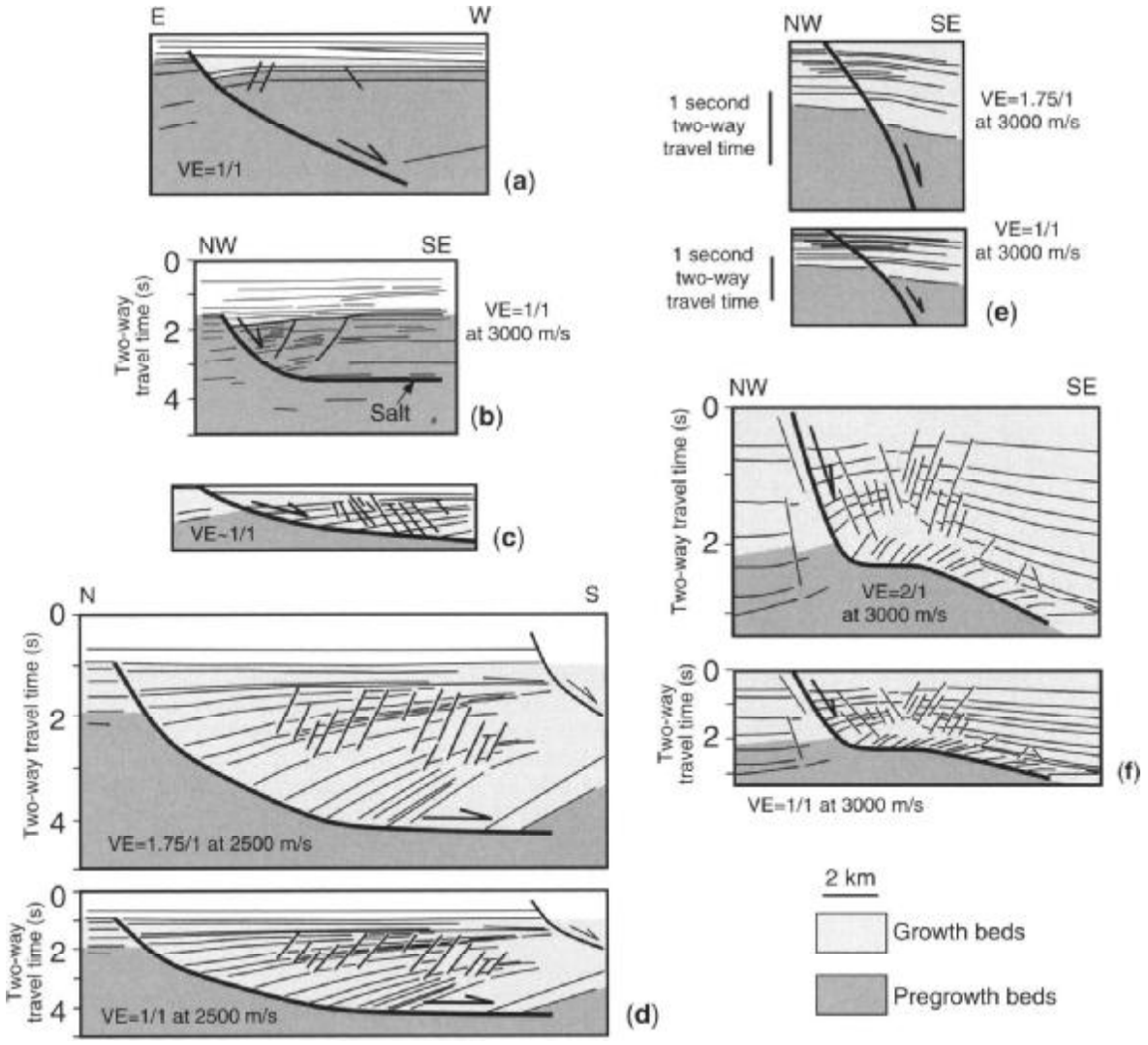


**Fig. 1.** Examples of normal faults and extensional fault-bend folds. (**a**) Line drawing of seismic line from offshore Norway (converted to depth) showing listric normal dipping at depth, rollover fold and secondary normal faults (Yielding *et al.* 1991). (**b**) Line drawing of migrated seismic line from offshore Norway showing listric normal fault flattening at depth in salt, rollover fold and antithetic secondary normal faults (after Withjack & Peterson 1990). (**c**) Line drawing of seismic line from Gulf of Oman with listric normal fault flattening at depth, rollover fold and synthetic secondary normal faults (after Wernicke & Burchfiel 1982; Hauge & Gray 1996). The line is displayed with approximately no vertical exaggeration. (**d**) Line drawing of migrated seismic line from Gulf of Mexico with listric normal fault flattening at depth, rollover fold and antithetic secondary normal faults. (**e**) Line drawing of migrated seismic line from offshore Australia (Northwest Shelf) showing normal fault that steepens with depth and associated hanging wall fold. (**f**) Line drawing of migrated seismic line from Gulf of Mexico showing normal fault (Brazos fault) with ramp-flat-ramp geometry, hanging wall folding, and complex pattern of secondary normal faulting. The line drawings in panels d–f are displayed with (top) and without (bottom) vertical exaggeration.

## Geometric modelling

Movement on a nonplanar fault surface creates a potential gap between the footwall and hanging wall (Fig. 2a). In our geometric models, we assume that deformation of the hanging wall by inclined simple shear closes this gap, forming an extensional fault-bend fold. Numerous case studies have shown that inclined simple shear is a reasonable approximation of the bulk deformation in the hanging walls of nonplanar normal faults (e.g., White & Yielding 1991; Kerr & White 1992; White 1992; Xiao & Suppe 1992; Withjack & Peterson 1993; Withjack *et al.* 1995; Hauge & Gray 1996). For simplicity, we assume that the inclined shear direction dips 70° toward the main normal fault. We also assume that the footwall remains rigid, that

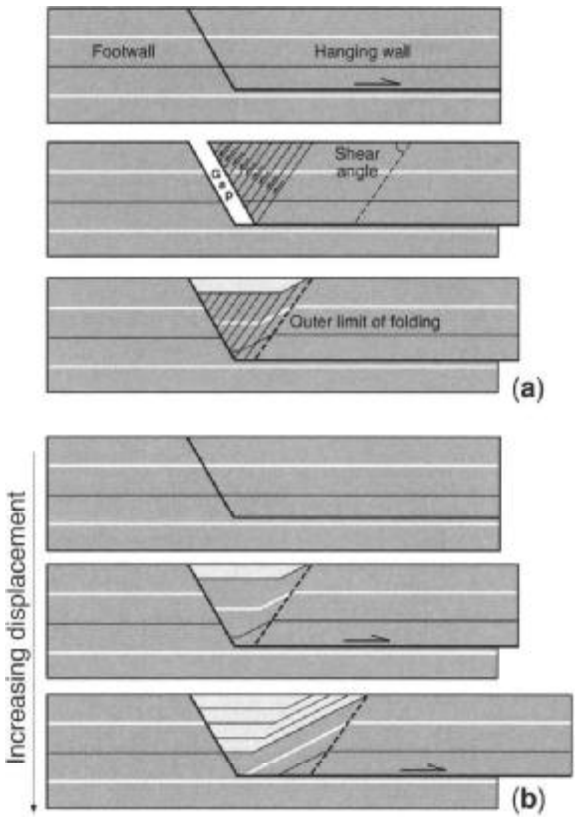


**Fig. 2.** Geometric modelling technique. (**a**) Movement on a nonplanar normal fault creates a potential gap between the footwall and hanging wall. Deformation of the hanging wall by inclined shear closes the gap and forms an extensional fault-bend fold. A growth bed fills the depression above the fold. (**b**) As fault displacement increases, fault-bend folding continues and new growth beds fill the resultant depressions above the fold. The pregrowth and growth beds deform as fault displacement increases.

compaction is negligible, and that growth beds completely fill any depressions that develop during faulting up to a prescribed regional datum (Fig. 2b). Although these factors certainly affect the geometry of extensional fault-bend folds (e.g., White & Yielding 1991; Xiao & Suppe 1992), the focus of this paper is to systematically study the effects of fault shape, fault displacement, and patterns of deposition and erosion for one or more episodes of normal faulting.

## Experimental modelling

In our experimental models, either dry sand or wet clay represents the sedimentary overburden. The dry sand is composed of quartz grains with diameters of less than 0.5 mm (Withjack & Callaway 2000). Its density is about 1600 kg $m^{-3}$. It has a negligible cohesion, and a coefficient of internal friction of about 0.6. Localized cataclastic faulting (e.g., Rutter 1986) is the primary deformation style, even when strains are small. Thus, the dry sand has a negligible ductility as defined by Rutter (1986). The wet clay is composed predominantly of kaolinite and water (*c.* 40% by weight) (Withjack & Callaway 2000). Its density is about 1600 kg $m^{-3}$. It has a low cohesion (*c.* 50 Pa) and a coefficient of internal friction of about 0.5. Distributed cataclasis (e.g., Rutter 1986) is the primary deformation style in the wet clay when strains are small. With increasing strain, however, deformation becomes localized and cataclastic faulting is the primary deformation style. Thus, the wet clay has a greater ductility than that of the dry sand. The cohesion and coefficient of internal friction of the dry sand and wet clay are appropriate to ensure dynamic similarity between the models and natural prototypes (see Appendix). The sand and clay, however, simulate different types of rocks. The dry sand, with its negligible cohesion and ductility, represents rock that deforms primarily by localized cataclastic faulting (e.g., granite that deforms into large fault blocks with little internal deformation). The wet clay, with its greater cohesion and ductility, represents rock that deforms by distributed cataclasis and localized cataclastic faulting (e.g., interbedded sandstone and shale that deforms into fault blocks with considerable internal deformation).

Our experimental models have two different set-ups. One set-up has two overlapping metal plates beneath a 4 cm-thick layer of dry sand or wet clay (Fig. 3a). During the experiments, the lower plate slides outward at 4 cm $hr^{-1}$. In response, a normal fault propagates upward from the edge of the fixed, upper plate through the overlying sand or clay layer. The second set-up, originally described in Withjack and Callaway (2000), has two juxtaposed metal blocks beneath a 4 cm-thick layer of dry sand or wet clay (Fig. 3b). The 45°-dipping boundary between the metal blocks represents a dipping normal fault. During the experiments, the hanging wall block slides down the normal fault at 0.25 cm $hr^{-1}$. In response, a normal fault propagates upward from the edge of the footwall block through the overlying sand or clay layer. During the experiments, we fill subsiding areas with either dry sand or wet clay to simulate deposition during deformation. Also, we photograph the top surface of the models to document the surface deformation through time. After the experiments, we vertically slice the models, creating serial cross sections that

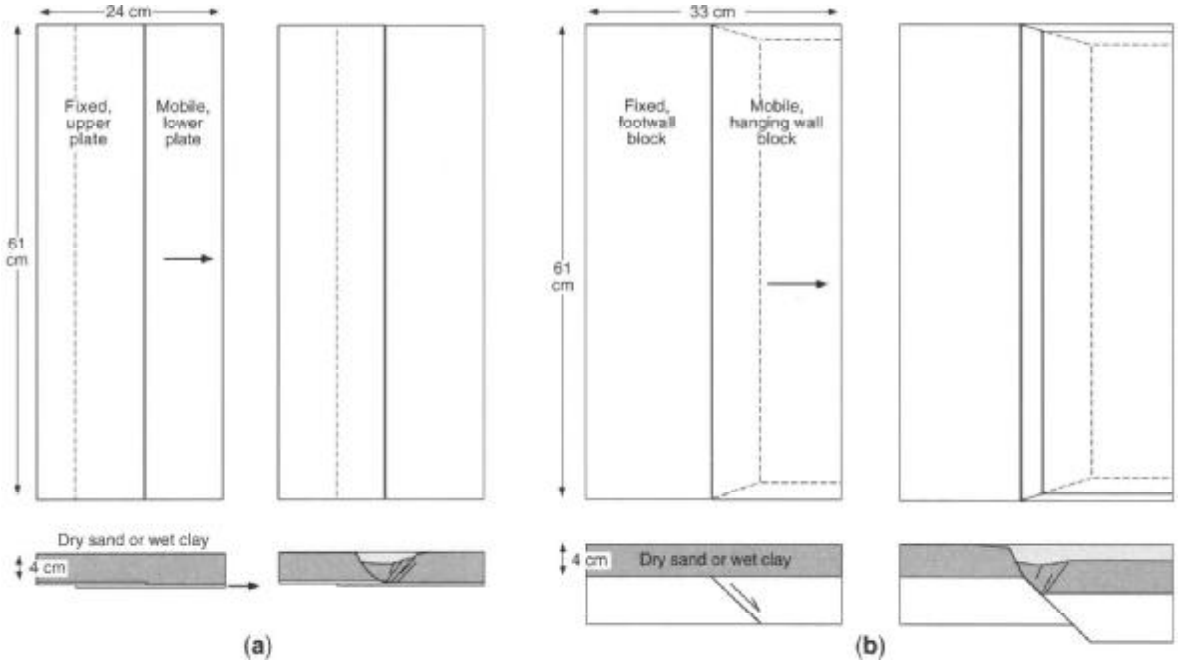


**Fig. 3.** Experimental modelling technique. (**a**) Experimental set-up with two overlapping metal plates beneath a layer of dry sand or wet clay. During the experiments, the lower plate slides away from the upper plate. (**b**) Experimental setup with two juxtaposed metal blocks beneath a layer of dry sand or wet clay. The 45°-dipping boundary between the blocks represents a dipping normal fault. During the experiments, the hanging wall block slides downward.

record the final deformation throughout the models. Colored (but mechanically identical) sub-layers within the sand and clay help identify faults and folds.

## Results of geometric modelling

### *Fault shape*

Our geometric models, like those of White *et al.* (1986), Dula (1991), White and Yielding (1991), Kerr and White (1992), Xiao and Suppe (1992) and Withjack and Peterson (1993), show that fault shape profoundly affects the shape of an extensional fault-bend fold.

If a normal fault flattens/detaches at depth (Fig. 4, left column), then growth beds have a limited lateral distribution, provided no aggradation occurs during faulting. Far from the fault, pregrowth beds in the hanging wall rise to the level of their footwall counterparts. If the upper fault segment is planar (Fig. 4a), then a triangular panel of undeformed, flat-lying beds exists near the fault. Adjacent to this triangular panel, the deformed pregrowth and growth beds dip uniformly toward the normal fault. If the upper fault segment is listric (Fig. 4b), then pregrowth and growth beds dip toward the fault. The dip of the growth beds systematically increases with depth, creating a fanning geometry.

If a normal fault dips at depth (Fig. 4, right column), then growth beds have a wide lateral distribution. All hanging wall beds are below the level of their footwall counterparts. The outer limit of the folding in the growth beds parallels the lowest fault segment, provided no aggradation or erosion occurs during faulting. If the upper fault segment is planar, then a triangular panel of undeformed, flat-lying beds exists near the fault. If the planar segment dips more steeply than the lower fault segment (Fig. 4c), then the tilted pregrowth and growth beds dip uniformly toward the main normal fault. If the planar segment dips more gently than the lower fault segment (Fig. 4d), then the tilted pregrowth and growth beds dip uniformly away from the main normal fault. If the upper fault segment is concave-upward (Fig. 4e), then the pregrowth and growth beds near the fault dip toward the fault. The dip of the growth beds systematically increases with depth, creating a fanning geometry. If the upper fault segment is convex-upward (Fig. 4f), then the pregrowth and growth beds near the fault dip away from the fault. Dips systematically increase

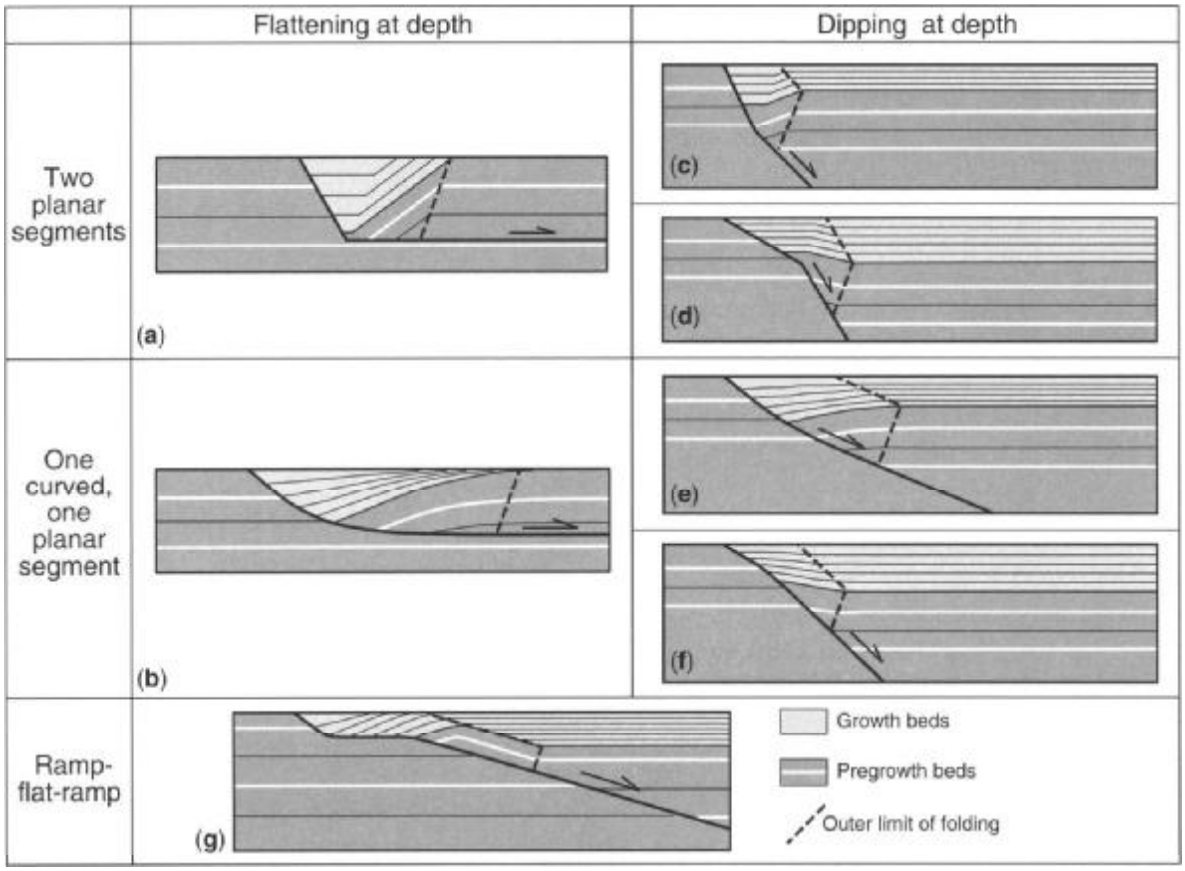


**Fig. 4.** Geometric models showing the effect of fault shape on the geometry of an extensional fault-bend fold. No aggradation or erosion occurs during faulting. Fault shape affects the lateral distribution of growth beds and the direction and magnitude of bedding dip. See text for further discussion.

with depth. This latter type of extensional fault-bend fold resembles a fault-propagation fold or a compaction-related fold.

If a normal fault has a ramp-flat-ramp geometry (Fig. 4g), then an anticline develops in the pregrowth beds. Growth beds near the fault dip and thicken toward the fault. Growth beds far from the fault are flat-lying. The outer limit of the folding in the growth beds parallels the lower ramp, provided no aggradation or erosion occurs during faulting.

### *Fault displacement and fold evolution*

The geometry of an extensional fault-bend fold changes through time as fault displacement increases. If a fault has two planar segments (Fig. 2b), then fault displacement affects the distribution, but not the dip, of the deformed pregrowth and growth beds. As displacement increases, more of the pregrowth and growth beds deform. The dip of the deformed pregrowth and growth beds, however, remains constant. For a listric normal fault that flattens at depth (Fig. 5a), the dip of the pregrowth beds increases as fault displacement increases. Growth beds develop a pronounced fanning geometry, and pregrowth and growth beds become thinner and longer. When fault displacements are very large, the oldest growth beds are substantially thinned and lengthened. Their fanning geometry becomes subtle, making it difficult to distinguish between growth and pregrowth layers.

For a normal fault with a ramp-flat-ramp geometry (Fig. 5b), a wide anticline initially forms in the pregrowth beds above the flat. Near the fault, growth beds dip and thicken toward the fault. Far from the fault, growth beds are flat-lying. No deposition occurs above the central part of the flat across the crest of the anticline. As fault displacement increases, the anticline narrows and moves down the lower ramp. Growth beds continue to accumulate near and far from the fault, but not above the central part of the flat. With additional fault displacement, the site of no deposition moves down the lower ramp, producing a dipping, diachronous unconformity. Correlative beds are offset across

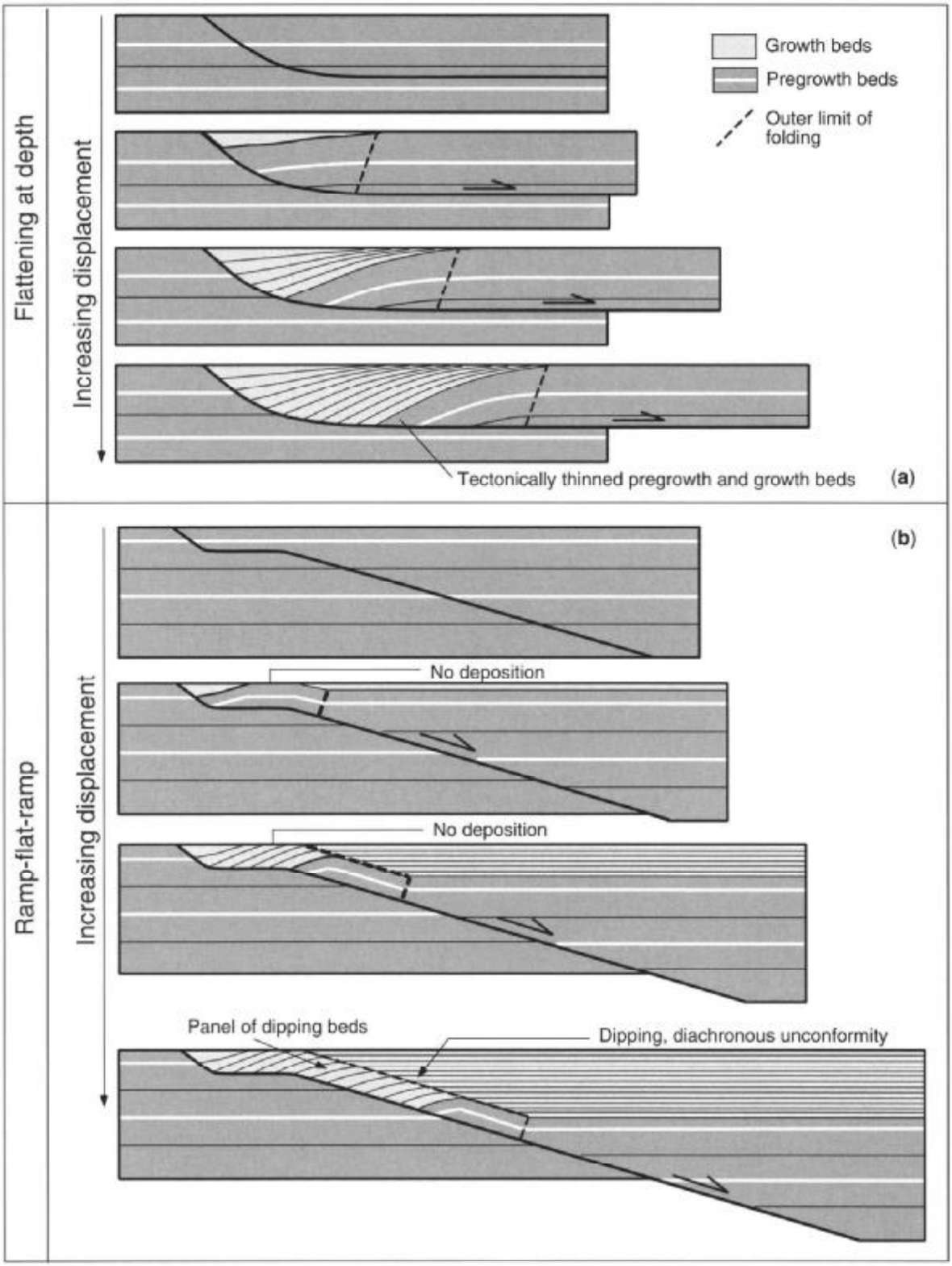


**Fig. 5.** Geometric models showing the effect of fault displacement on the geometry and evolution of an extensional fault-bend fold. No aggradation or erosion occurs during faulting. (**a**) Listric fault that flattens at depth. (**b**) Fault with ramp-flat-ramp geometry. See text for further discussion.

the unconformity. Thus, the unconformity resembles a normal fault that parallels the lower ramp. A panel of dipping growth beds develops directly above the lower ramp.

### *Aggradation and erosion*

In many extensional settings, regional subsidence, regional uplift, and fluctuations in sediment supply or sea level lead to aggradation or erosion during normal faulting. Our geometric models (Figs 6 and 7) support the conclusion of Xiao and Suppe (1992) that the rate of aggradation relative to the rate of fault displacement profoundly affects the shape of an extensional fault-bend fold. Additionally, our geometric models show that the rate of erosion relative to the rate of fault displacement also profoundly affects the shape of an extensional fault-bend fold.

For a listric fault that flattens at depth (Fig. 6a), growth beds have a wide lateral distribution with aggradation and a very limited lateral distribution with erosion. With erosion, growth beds have a more subtle fanning geometry and can, in fact, closely resemble pregrowth beds. For a fault that dips at depth (Fig. 6b), the dip of the outer limit of the folding in the growth beds depends on the amount of aggradation or erosion that occurs during faulting. As mentioned previously, the outer limit of the folding in the growth beds parallels the lower fault segment, if no aggradation or erosion occurs (Fig. 4). With aggradation, the outer limit of the folding dips more steeply than the lower fault segment. The greater the amount of aggradation, the steeper the dip. With erosion, the outer limit of the folding dips more gently than the lower fault segment. The greater the amount of erosion, the gentler the dip. For a normal fault with a ramp-flat-ramp geometry (Fig. 7), a panel of dipping growth beds develops above the lower ramp with aggradation and with

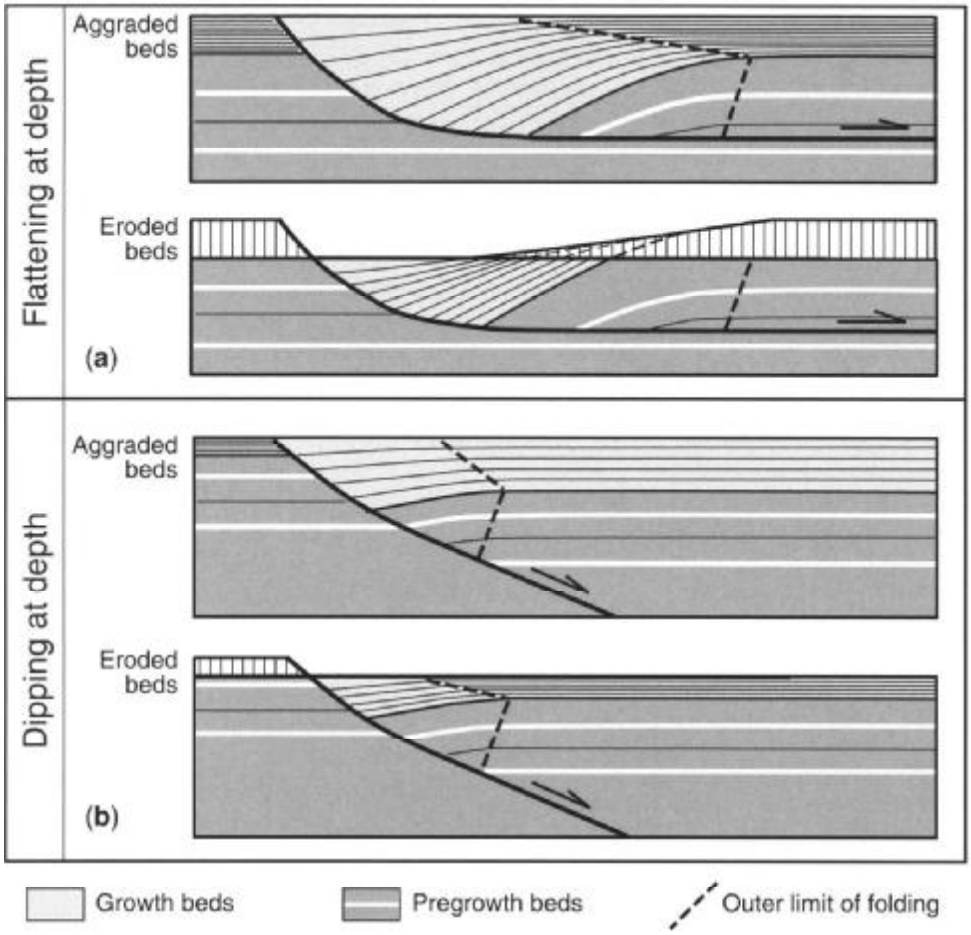


**Fig. 6.** Geometric models showing the effect of aggradation and erosion on the geometry of an extensional fault-bend fold. (**a**) Fault that flattens at depth. (**b**) Fault that dips at depth. The occurrence of aggradation/erosion affects the lateral distribution of growth beds, the dip of the growth beds, and the outer limit of the folding. See text for further discussion.

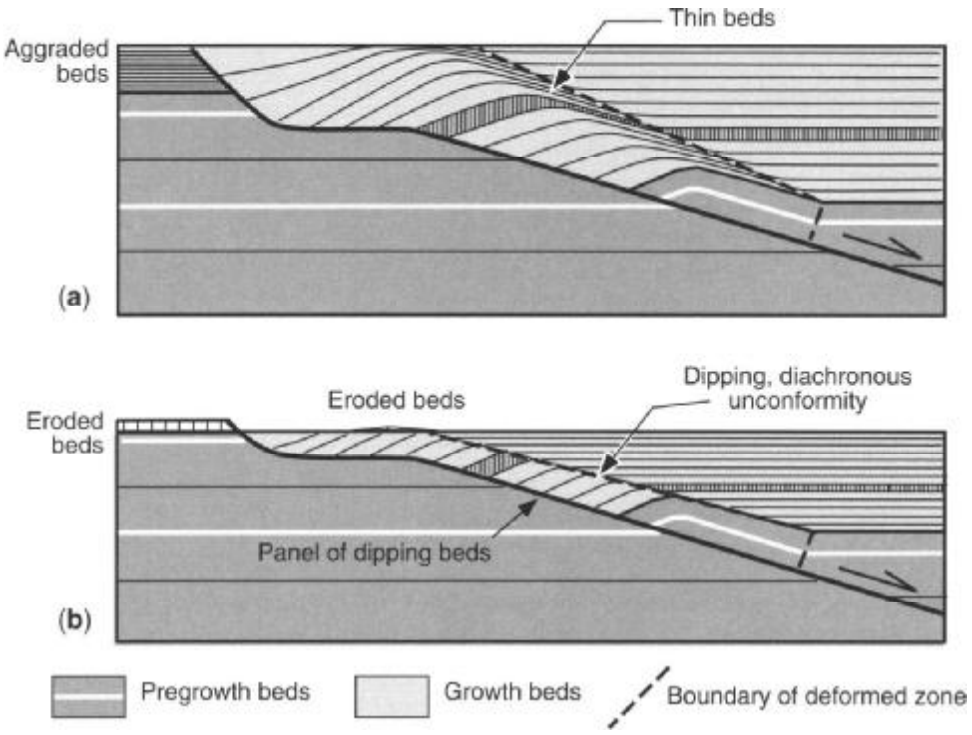


**Fig. 7.** Geometric models of faults with ramp-flat-ramp geometry showing the effect of (**a**) aggradation and (**b**) erosion on the geometry of an extensional fault-bend fold. The occurrence of aggradation/erosion affects the lateral distribution of growth beds, the dip of the growth beds, and the outer limit of the folding. See text for further discussion.

erosion. With aggradation, the panel widens upward, and thin growth beds dipping away from the fault overlie the panel (Fig. 7a). With erosion, the panel narrows upward, and a dipping, diachronous unconformity overlies the panel. The unconformity dips more gently than the lower ramp (Fig. 7b).

### *Multiple episodes of faulting*

Complex structural and stratigraphic patterns develop with multiple episodes of normal faulting if the rate of aggradation/erosion relative to the rate of fault displacement changes through time (Fig. 8). In Figures 8a–c, the normal fault is listric and flattens at depth. In Figure 8a, aggradation occurs during the second episode of faulting but not during the first episode. The distribution and geometry of the growth beds associated with each faulting episode differ substantially. The outer limit of the folding is not planar. It parallels the inclined shear direction in the pregrowth beds, it flattens above the growth beds associated with the first faulting episode, and it dips away from the fault in the growth beds associated with the second faulting episode. In Figure 8b, widespread deposition occurs between episodes of normal faulting. The outer limit of the folding parallels the inclined shear direction in the pregrowth beds. It flattens above the growth beds associated with the first faulting episode, and it parallels the inclined shear direction in the beds deposited between the faulting episodes. In Figure 8c, erosion occurs between the episodes of normal faulting. The growth beds associated with the first faulting episode have a very subtle fanning geometry. In fact, they closely resemble the underlying pregrowth beds. In Figure 8d, the normal fault has a ramp-flat-ramp geometry. If significant aggradation occurs during the second episode of faulting but not during the first episode, then the distribution and geometry of the growth beds associated with each faulting episode differ substantially. The outer limit of the folding is not planar. It parallels the lower ramp in the growth beds associated with the first faulting episode, and it dips toward the fault in the growth beds associated with the second faulting episode.

## Results of experimental modelling

As discussed below, the sand and clay models provide information about the styles of deformation associated with extensional fault-bend folding (Figs 9–11).

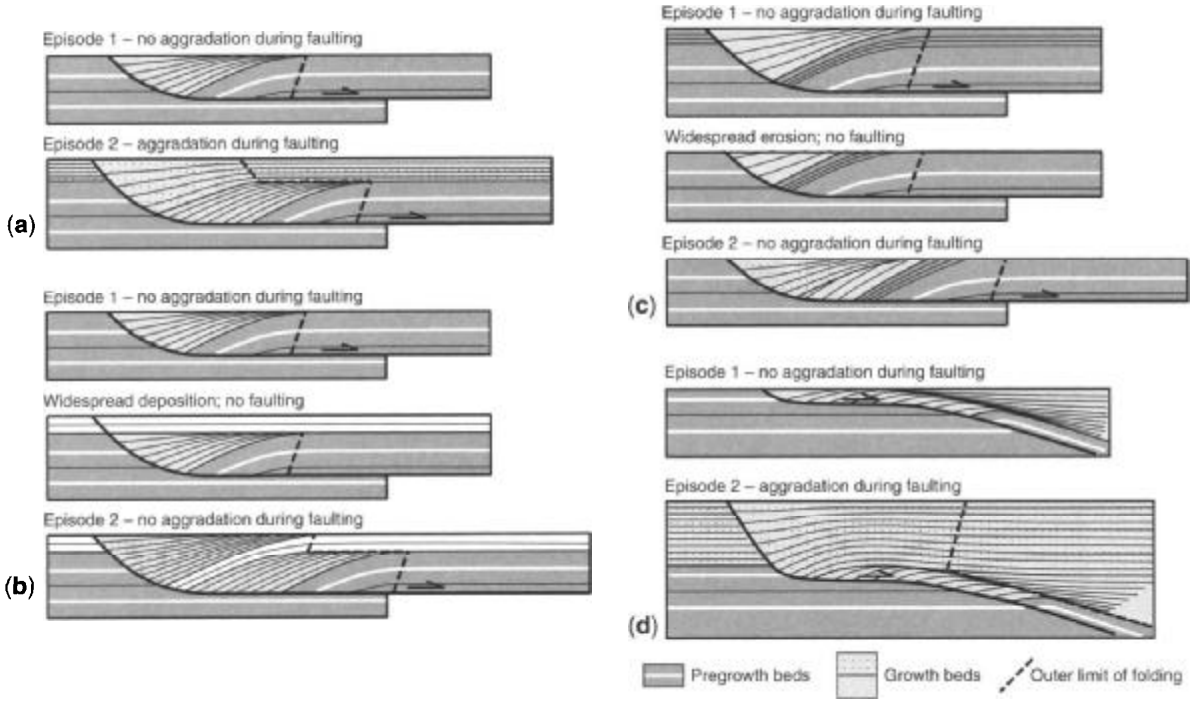


**Fig. 8.** Geometric models showing the effect of multiple episodes of faulting on the geometry of an extensional fault-bend fold. The rates of aggradation/erosion relative to the rates of fault displacement vary during the faulting episodes. See text for further discussion.

### *Models with overlapping plates: horizontal detachment at depth*

In the sand model with the overlapping plates (Fig. 9a), a fault propagates upward from the edge of the fixed upper plate. The fault is planar and dips steeply, about 60°–65°. This steep fault and the horizontal mobile plate, together represent a normal fault that flattens/detaches at depth. A fault bend separates the steep and horizontal segments. As the deformation progresses, a series of steeply dipping antithetic faults develops in the hanging wall. Each antithetic fault forms near the fault bend, moves with the mobile plate past the fault bend, and becomes inactive. Thus, the antithetic faults become progressively older the farther from the fault bend. The antithetic faults have relatively large displacements and accommodate most of the hanging wall deformation, accounting for about 40% of the imposed displacement of the mobile plate (Fig. 9c). The upper segment of the main normal fault accounts for another 45% of the imposed displacement. The remainder (15%) is internal deformation within the fault blocks. Kautz and Sclater (1988) determined similar amounts of internal deformation in their extensional sand models. The effective shear direction in the sand model (based on the outer limit of the folding) is subparallel to the antithetic normal faults. Thus, the inclined shear angle in the sand model is about 60°–65°, agreeing with the value obtained by Xiao and Suppe (1992) for a similar sand model published by McClay and Ellis (1987*a*).

In the clay models with the overlapping plates (Figs 9b and 11a–d), a fault propagates upward from the edge of the fixed upper plate. Unlike the sand models, fault-propagation folding and secondary faulting precede the development of the through-going normal fault. The fault is listric, steeply dipping (*c.* 75°) near the surface and gently dipping (*c.* 35°) near the base of the clay layer. This steep fault and the horizontal mobile plate, together, represent a normal fault that flattens/detaches at depth. A fault bend separates the steep and horizontal segments. As displacement increases, an upward-widening zone of deformation develops, emanating from the fault bend (Fig. 11a). Deformation includes secondary normal faulting (antithetic and synthetic) and fault-bend folding (layers dip toward the main normal fault). The deformation zone moves with the mobile plate, passing the fault bend. Eventually, it becomes inactive and a new deformation zone replaces it (Figs 11b, c). Thus, deformation becomes progressively older

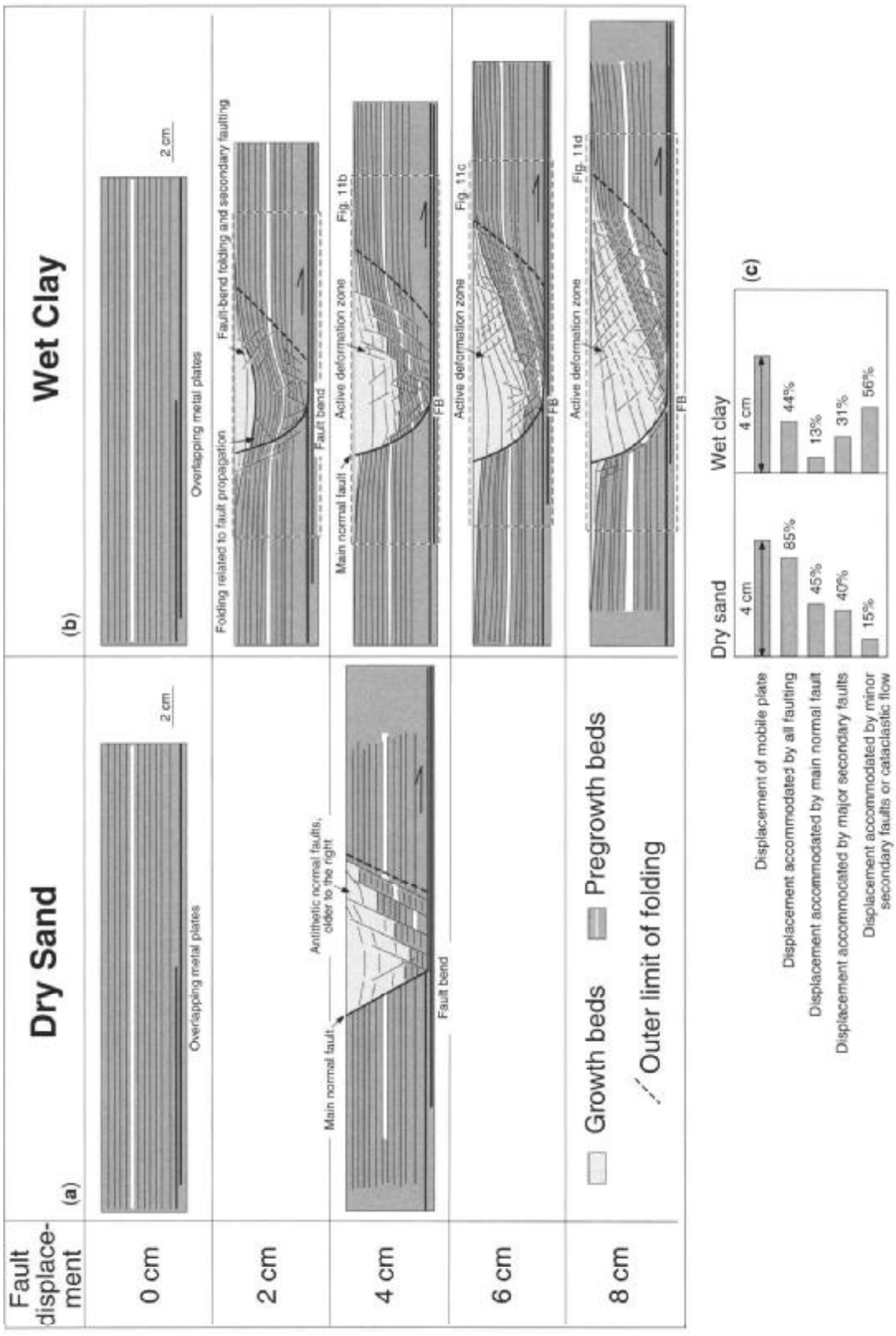


**Fig. 9.** Line drawings of cross sections through (**a**) experimental model with dry sand and (**b**) four experimental models with wet clay. The sand or clay layer overlies overlapping metal plates. During the experiments, the lower plate moves to the right by a prescribed displacement. The experimental models simulate fault-bend folding associated with a normal fault that flattens at depth. The boxes show the locations of the photographs in Fig. 11. FB is fault bend (**c**) Accommodation of imposed displacement (4 cm) in the sand and clay models.

the farther from the fault bend. By 8 cm of displacement of the mobile plate (Fig. 11d), most pregrowth and growth layers are faulted and dip gently (*c.* 20°) toward the main fault. Fault-bend folding rotates many of the secondary faults. Thus, synthetic faults dip more gently and antithetic faults dip more steeply through time. The pregrowth beds and the oldest growth beds have thinned and lengthened significantly. In fact, many of the oldest growth beds lack an obvious fanning geometry and resemble pregrowth beds (Fig. 11d).

In the clay models, cataclastic faulting, cataclastic flow and rigid-body rotation accommodate the fault-bend folding. For example, in the model with 4 cm of displacement of the mobile plate, the major secondary faults account for about 31% of the imposed displacement (Fig. 9c). The upper segment of the main normal fault accounts for another 13% of the imposed displacement. Minor faulting, cataclastic flow, and rigid-body rotation account for 56% of the imposed displacement. Kautz and Sclater (1988) determined similar amounts of internal deformation within their extensional clay models. The effective shear angle is about 35°–50° (based on the average dip of the outer limit of the folding), considerably less than the dip of the antithetic faults. White and Yielding (1991) calculated a similar value (49°) for a published clay model by E. Cloos (1968), and Withjack *et al.* (1995) obtained similar values (50°–55°) for their clay-model experiments.

### *Models with juxtaposed blocks: dipping fault at depth*

In the sand model with the juxtaposed blocks (Withjack & Callaway 2000), a normal fault propagates upward from the edge of the fixed block (Fig. 10a). It is planar, and dips steeply, about 65°. This steep fault segment and the 45°-dipping boundary between the juxtaposed blocks represent a normal fault that dips at depth. A steeply dipping antithetic fault forms near the fault bend between the fault segments. It moves downward with the mobile block as fault displacement increases. Pregrowth and growth layers near the main fault dip gently toward the fault. The effective shear direction in the sand model (based on the dip of the outer limit of the folding) is subparallel to the antithetic normal fault. Thus, the inclined shear angle is about 65°.

In the clay model with the juxtaposed blocks (Withjack & Callaway 2000), a normal fault propagates upward from the edge of the fixed block (Figs 10b and 11e). Fault-propagation folding and secondary faulting precede the development of the through-going normal fault. The fault is listric, steeply dipping (*c.* 90°) near the surface and gently dipping (*c.* 45°) near the base of the clay layer. This fault segment and the 45°-dipping boundary between the juxtaposed blocks represent a normal fault that dips at depth. An upward-widening zone of deformation develops in the hanging wall of the main normal fault. The zone, emanating from the fault bend, moves downward with the mobile block as fault displacement increases. Deformation within the zone includes secondary faulting (mostly antithetic normal faults) and fault-bend folding with pregrowth and growth layers dipping gently toward the main fault. The effective shear angle (based on the average dip of the outer limit of the folding in the pregrowth layers) is about 50°.

## Discussion and applications

### *Comparisons of geometric and experimental models*

The style of hanging wall deformation varies considerably in the experimental models, reflecting the differences in the cohesion and ductility of the dry sand and wet clay. In the sand models, a few, relatively large, secondary antithetic normal faults accommodate most of the hanging wall deformation. Pregrowth layers, although faulted, are flat-lying. The effective shear direction parallels the antithetic normal faults, and the shear angle is about 60°–65°. In the clay models, secondary faulting (antithetic and synthetic) and cataclastic flow accommodate most of the hanging wall deformation. The deformed pregrowth and growth layers dip gently toward the main normal fault. The effective shear angle (35°–50°) is considerably less than the dip of the antithetic normal faults.

The style of deformation in the sand models differs from that in the geometric models in several ways. Deformation is focused on a few, relatively large, antithetic normal faults in the sand models, not uniformly distributed as it is in the geometric models. Pregrowth layers are nearly flat-lying in the sand models, not dipping at they are in the geometric models. Although the distributed style of deformation in the clay models is similar to that in the geometric models, the clay models also differ from the geometric models in several ways. Fault-propagation folding precedes the development of through-going normal faults in

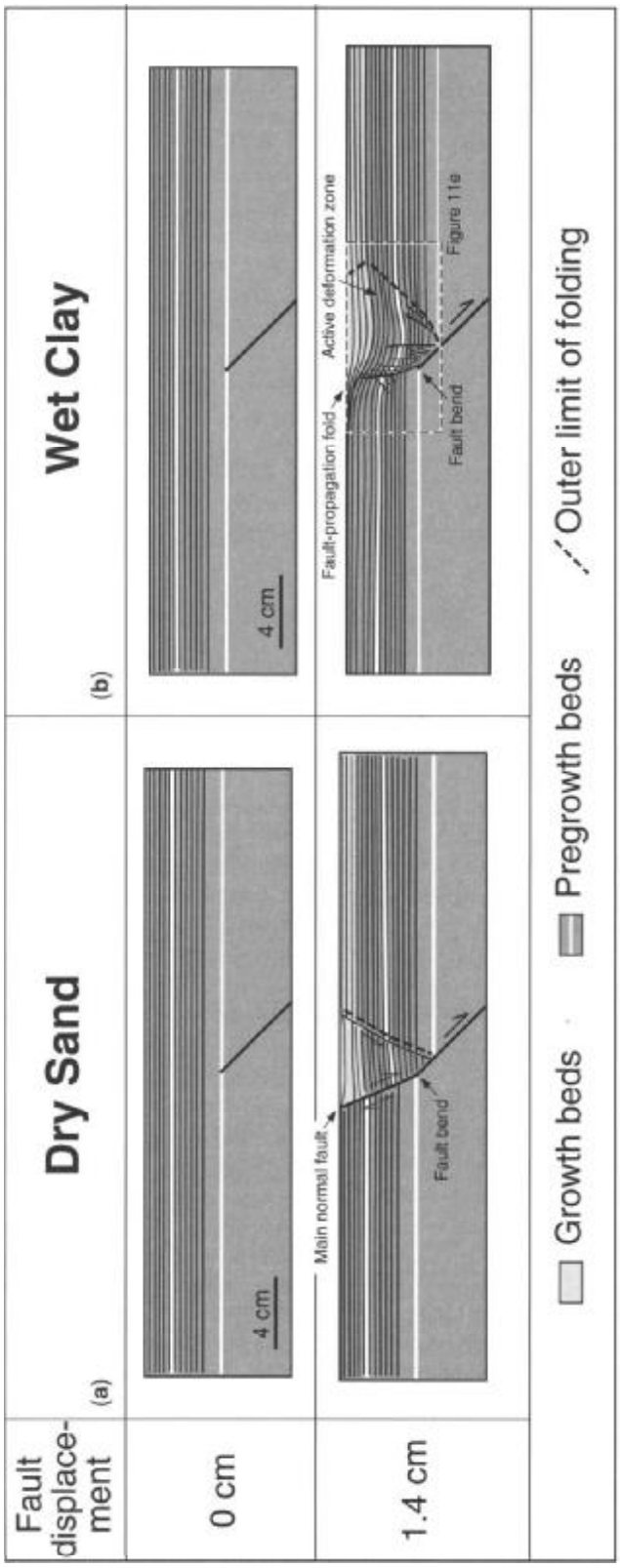


**Fig. 10.** Line drawings of cross sections through experimental models with dry sand and wet clay (after Withjack & Callaway 2000). The sand or clay layer overlies juxtaposed metal blocks. During the experiments, the hanging wall block moves downward by a prescribed displacement. The experimental models simulate fault-bend folding associated with a normal fault that dips at depth. The box shows the location of the photograph in Fig. 11e.

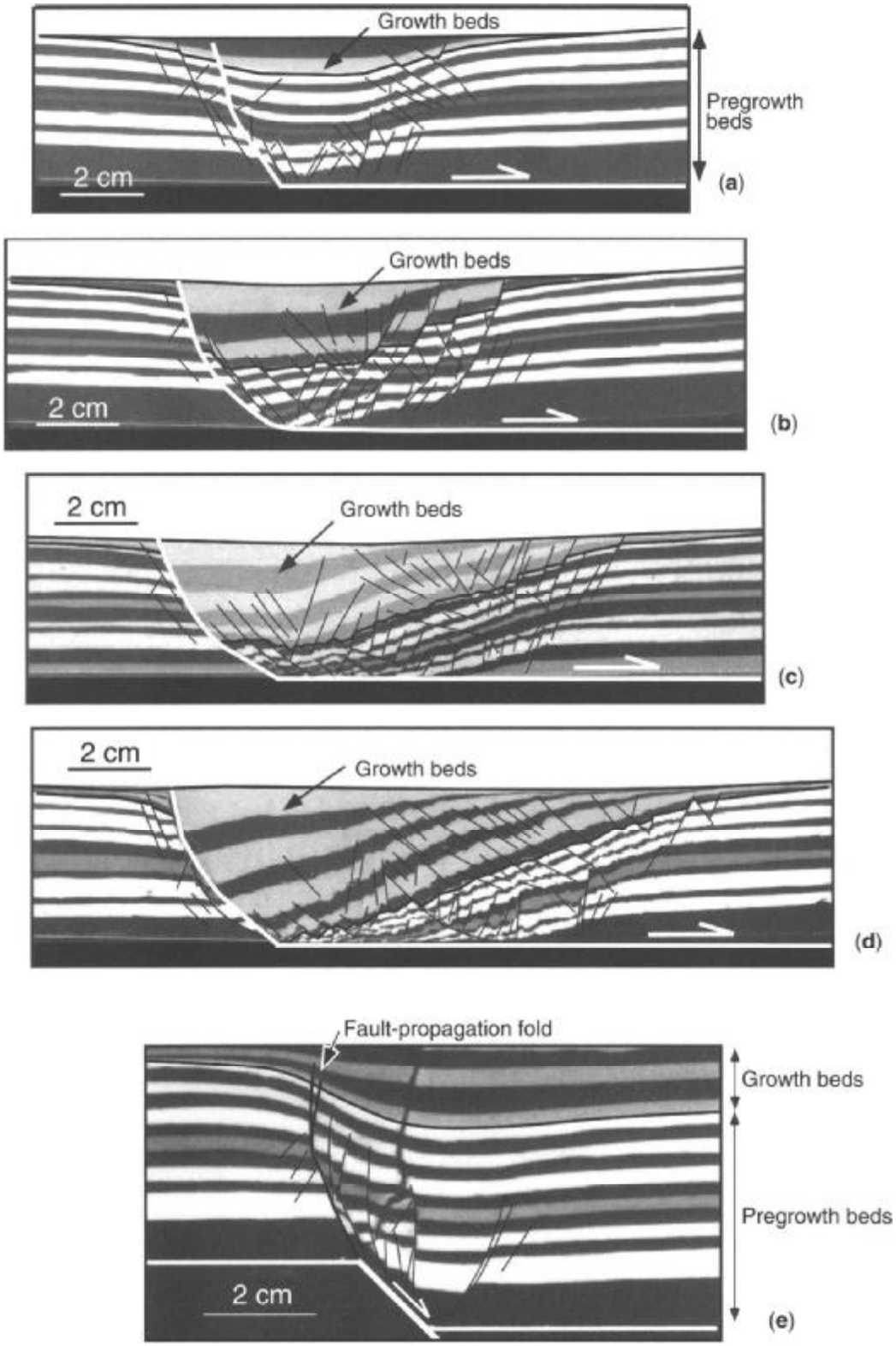


**Fig. 11.** Photographs of cross sections through five clay models. Major secondary faults are shown in black. (**a**) Cross section through model with 2 cm displacement of mobile plate. (**b**) Cross section through model with 4 cm displacement of mobile plate. (**c**) Cross section through model with 6 cm displacement of mobile plate. (**d**) Cross section through model with 8 cm displacement of mobile plate. (**e**) Cross section through model with 1.4 cm of displacement on mobile block.

the clay models. Thus, not all deformation in the clay models is related to fault-bend folding. Also, deformation zones in the pregrowth layers widen upward in the clay models. In geometric models with inclined shear, the width of the deformation zones in the pregrowth layers remains constant with depth (Withjack *et al.* 1995).

Despite differences in the styles of deformation, the geometric and experimental modelling approaches yield similar results for the overall shape and evolution of an extensional fault-bend fold. Specifically, in models with a normal fault that flattens at depth, growth beds have a limited lateral distribution. In models with a normal fault that dips at depth, growth beds have a wide lateral distribution. Both the geometric and experimental models show that rollover folds develop in the hanging walls of normal faults whose dip decreases with depth. The geometric and clay models with a listric, upper fault segment show that the dip of the growth beds increases with depth, creating a fanning geometry. If fault displacements are large, then pregrowth and growth beds thin and lengthen significantly during extensional fault-bend folding.

Figure 12 compares sand and clay models (with 4 cm of displacement of the mobile plate) with similar geometric models with shear angles of 60° and 35°, respectively. The distribution of deformation in the experimental models closely resembles that in the geometric models. In the sand model and the geometric model with the 60° shear angle, more displacement occurs on the upper segment of the main normal fault than in the clay model and the geometric model with the 35° shear angle. The hanging wall collapses in a relatively narrow zone in the sand model and the geometric model with the 60° shear angle. The hanging wall stretches substantially and collapses in a relatively wide zone in the clay model and the geometric model with the 35° shear angle.

Figure 13 compares a geometric model with a shear angle of 35° with the cross section from the clay model with 8 cm of displacement of the mobile plate. The clay model closely resembles the geometric model. Specifically, the location of the hanging wall cutoffs, the dip of the deformed hanging wall beds (*c.* 20°), and the displacement distribution for the pregrowth and growth beds are similar in both models. In the clay model and the geometric model, the hanging wall stretches considerably, requiring less displacement on the upper segment of the main normal fault. In the clay model, the youngest growth beds near the main normal fault dip and thicken toward the fault. In the geometric model, the growth beds near the main normal fault are flat-lying. This difference reflects the listric shape of the upper fault segment in the clay model and the planar shape of the upper fault segment in the geometric model.

### *Geological examples*

Observed hanging wall folds in many natural examples resemble those in the geometric and experimental models. Rollover folds develop in the hanging wall of normal faults that flatten at depth (Figs 1b, c and d). Growth beds dip and thicken toward the main fault, and the oldest growth beds commonly have subtle fanning geometries. Normal faults with convex-up bends (Fig. 1e) have hanging wall beds that dip away from the main fault. Normal faults with ramp-flat-ramp geometries (Fig. 1f) have complex hanging wall deformation. Beds dip toward the fault near the main fault, and a dipping unconformity that parallels the lower ramp commonly develops above the ramp. The secondary normal faults in many natural examples resemble those in the experimental models. Many secondary normal faults are antithetic to the main fault (Figs 1a, b and d). Some, however, are synthetic to the main normal fault (Fig. 1c), like those in the clay models (Figs 9b and 11). Most secondary normal faults have relatively small displacements (Figs 1, 14 and 15), like those in the clay models (Figs 9b and 11). Calculated inclined shear angles for geological examples of extensional fault-bend folds (Hauge & Gray 1996) range from about 45°–70°, similar to those in the experimental models.

The Blackberry fault from the Gulf of Mexico (Fig. 14) has up to 10 km of normal displacement. It is listric, flattening within shales. Two small fault bends are present at shallow levels. Secondary normal faults in the hanging wall are antithetic to the Blackberry fault and have relatively small displacements. As predicted by the geometric and experimental models, a large rollover fold affects its hanging wall. Growth beds dip and thicken toward the fault. Second-order fault-bend folding occurs near the small fault bends. This folding, with beds dipping away from the Blackberry fault, resembles fault-propagation folding. It is, however, associated with beds passing through a convex-upward fault bend. Similar second-order fault-bend folds develop in our clay models (Fig. 14d). Xiao and Suppe (1992) have reported similar folds elsewhere in the Gulf of Mexico.

The Brazos fault from the Gulf of Mexico (Fig. 15) has two major fault bends, a northwest

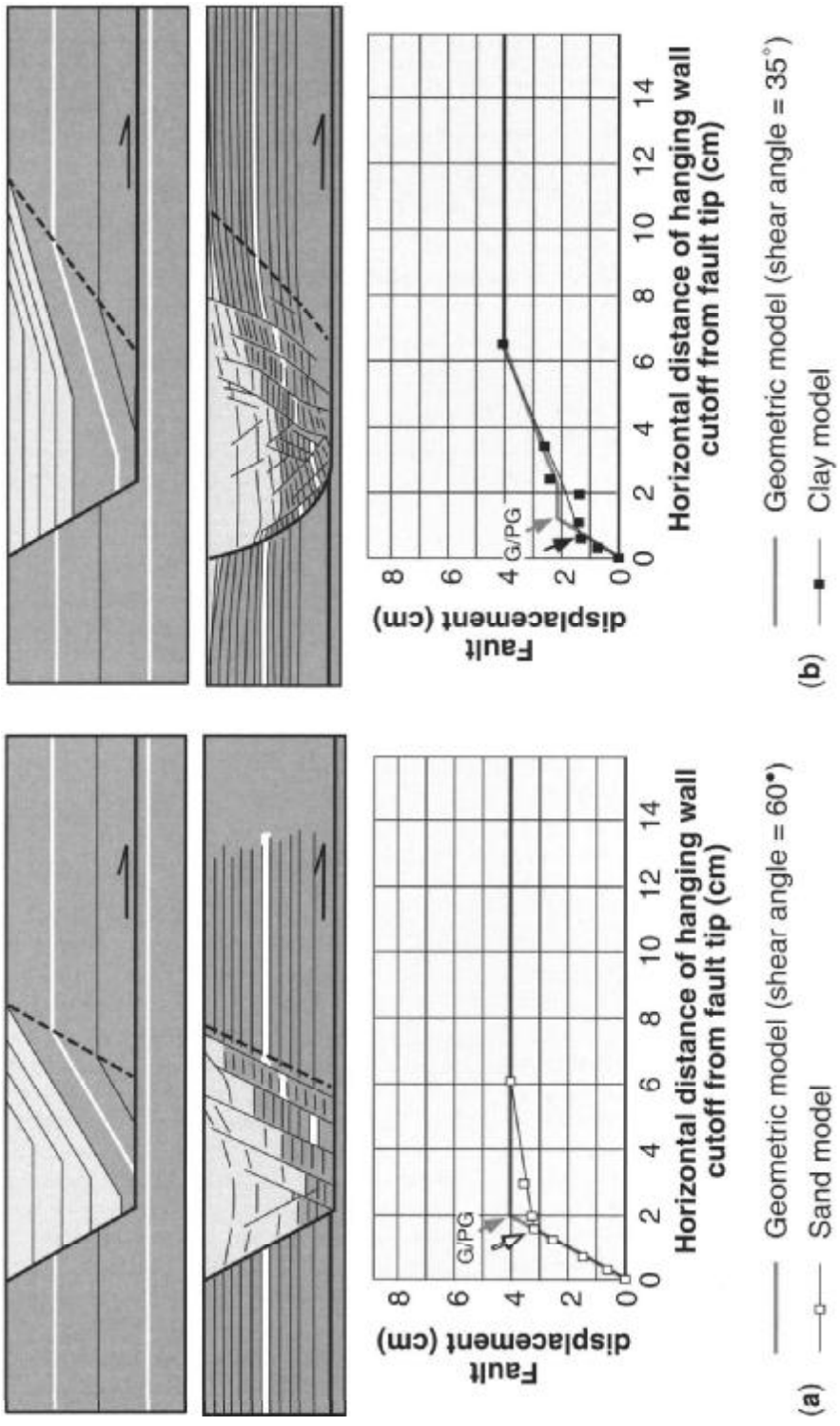


**Fig. 12.** (**a**) Line drawing of sand model (4 cm displacement of the mobile plate) and geometric model with 4 units of displacement and inclined shear angle of 60°. Plot of fault displacement versus horizontal distance of hanging wall cutoffs from fault tip for sand model and geometric model. (**b**) Line drawing of clay model (4 cm displacement of the mobile plate) and geometric model with 4 units of displacement and inclined shear angle of 35°. Plot of fault displacement versus horizontal distance of hanging wall cutoffs from fault tip for clay model and geometric model. G/PG indicates the boundary between the growth and pregrowth beds.

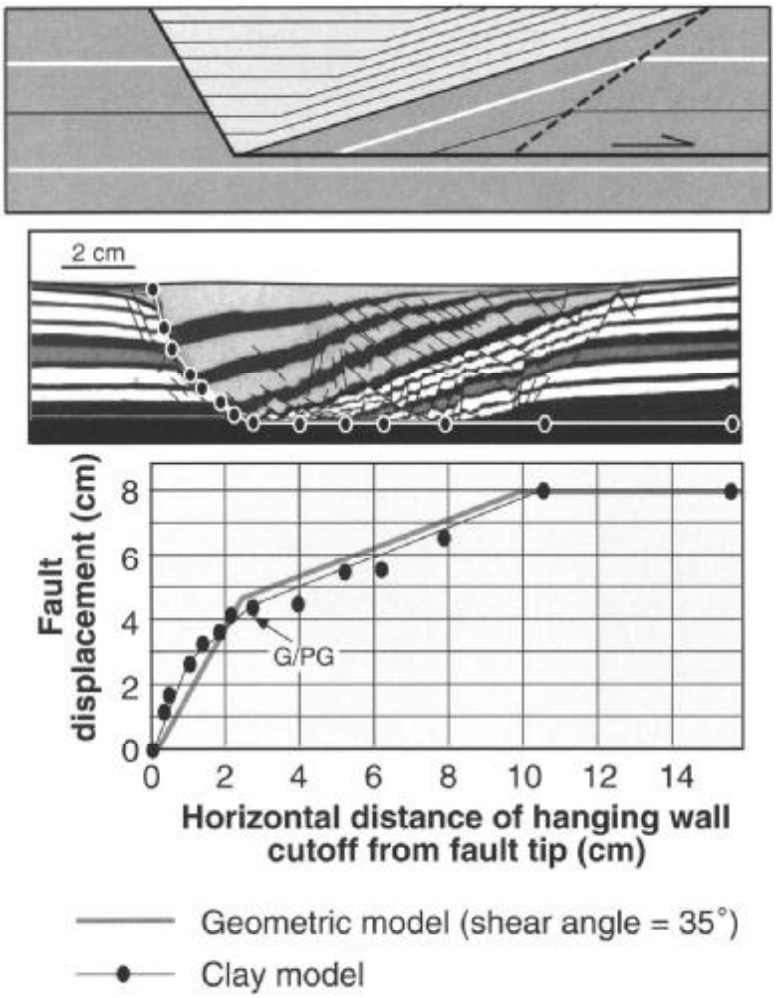


**Fig. 13.** Geometric model of fault-bend fold with 8 units of displacement (top). Inclined shear angle is 35°. Photograph of cross section of clay model after 8 cm of displacement (centre). Circles show locations of hanging wall cutoffs for key growth and pregrowth beds. Plot of fault displacement versus horizontal distance of hanging wall cutoffs from fault tip for clay model and geometric model (bottom). G/PG indicates the boundary between the growth and pregrowth beds.

concave-up bend and a southeast convex-up bend. The geometry of the fault changes considerably along strike (Vogler & Robinson 1987). On parts of the Brazos fault, the segment between the fault bends dips gently to the southeast (Figs 15a–c). On other parts of the Brazos fault, the segment between the fault bends is nearly horizontal (Fig. 15d). The hanging wall deformation closely resembles the deformation in the geometric models with the ramp-flat-ramp geometry (Figs 4g, 5b, 7 and 8d). Near the fault, growth beds dip toward the fault. Farther from the fault, growth beds dip gently away from the fault. A panel of dipping growth beds develops directly above the lower ramp. The geometry of the extensional fault-bend fold varies depending on the dip of the central segment. Where the segment is flat (Fig. 15d), the growth beds directly above the panel of dipping growth beds are very thin. In fact, Vogler and Robinson (1987) report that a dipping unconformity locally overlies the panel of dipping growth beds. Where the segment is dipping (Fig. 15c), the growth beds directly above the panel of dipping growth beds are slightly thicker. The abrupt change in the style of the fault-bend folding with depth (i.e., tight folding at depth; broad folding at shallow levels) probably reflects significant aggradation during the latter stages of faulting and folding (Fig. 8d).

The low-angle, east-dipping Vicksburg fault underlies the Slick Ranch field in southern Texas (Fig. 16) (Erxleben & Carnahan 1983). The deformation in the hanging wall of the Vicksburg fault resembles that in the hanging

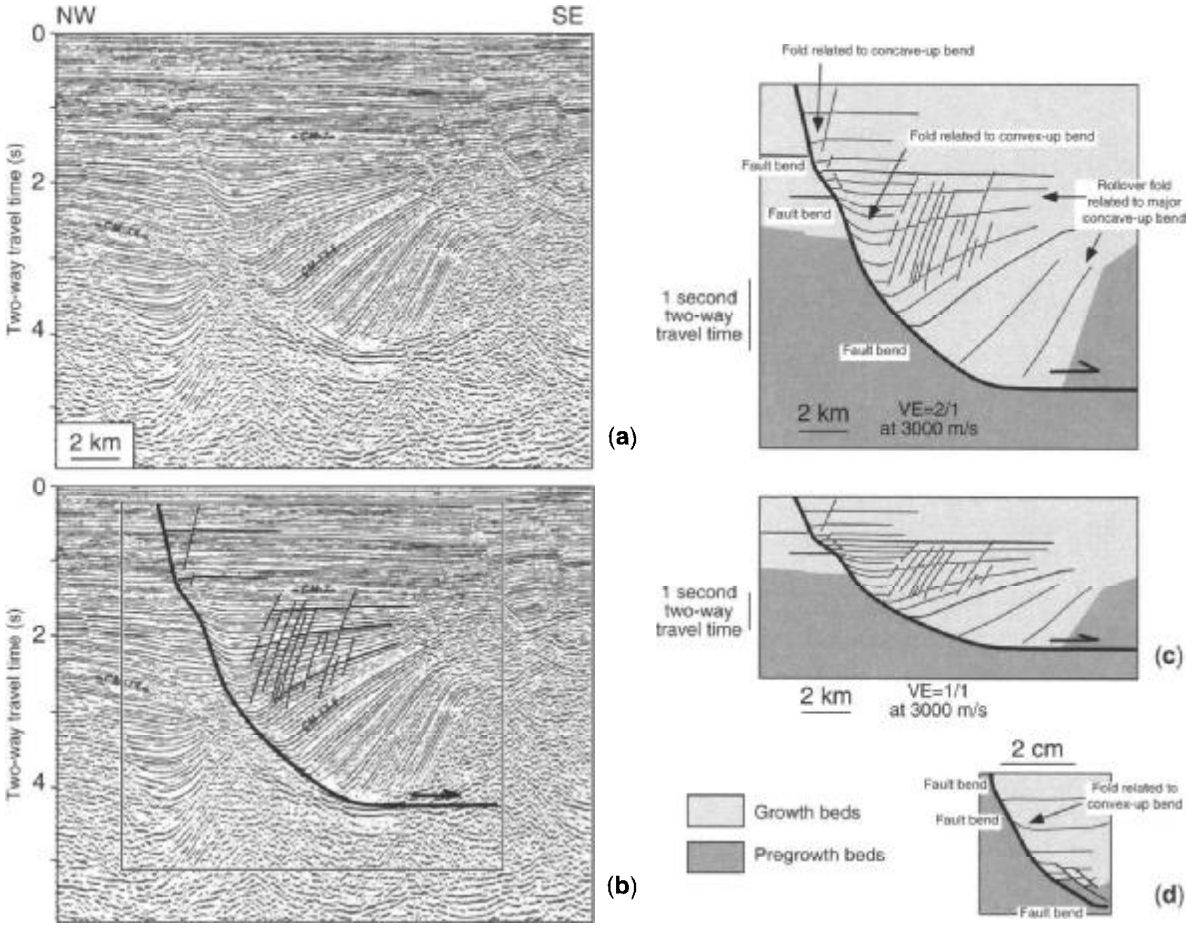


**Fig. 14.** Blackberry normal fault, offshore Texas, Gulf of Mexico. (**a**) Time-migrated seismic line (after Bally *et al.* 1991). CM-7 and CM-12.5 represent strata that are about 7 Ma and 12.5 Ma, respectively. (**b**) Interpreted seismic data. Black box shows location of line drawing. (**c**) Interpreted line drawing with (top) and without (bottom) vertical exaggeration. Second-order fault-bend folding occurs near small fault bends. (**d**) Second-order fault-bend fold in clay model with overlapping metal plates and 6 cm displacement.

wall of the Brazos fault in terms of geometry and dimensions (Fig. 15e). A panel of dipping growth beds overlies the low-angle fault. A dipping unconformity overlies the panel of dipping growth beds. As in the case of the Brazos fault, this deformation probably reflects movement on a fault with a ramp-flat-ramp geometry.

## Conclusions

We have used geometric and experimental models to better understand the development of extensional fault-bend folds. The geometric models show that:

(1) The shape of a normal fault controls the distribution of growth beds, the magnitude and direction of dip of the pregrowth and growth beds, the outer limit of folding in the pregrowth and growth beds, and the level of hanging wall beds relative to their footwall counterparts (Fig. 4).

(2) If a fault has two planar segments, then fault displacement controls the distribution, but not the dip, of the deformed pregrowth and growth beds (Fig. 2b). If a fault has a curved segment, then fault displacement controls the dip, thickness, and distribution of the deformed pregrowth and growth beds (Fig. 5).

(3) Aggradation and erosion control the distribution of growth beds, the dip of the pregrowth and growth beds, and the outer limit of folding in the pregrowth and growth beds (Figs 6 and 7). The outer limit of the folding in the growth beds parallels the lower fault segment, if no aggradation or erosion occur (Fig. 5). With aggradation, the outer limit of the folding dips more steeply than the lower fault segment. With erosion, the outer limit of the folding dips more gently than the lower fault segment.

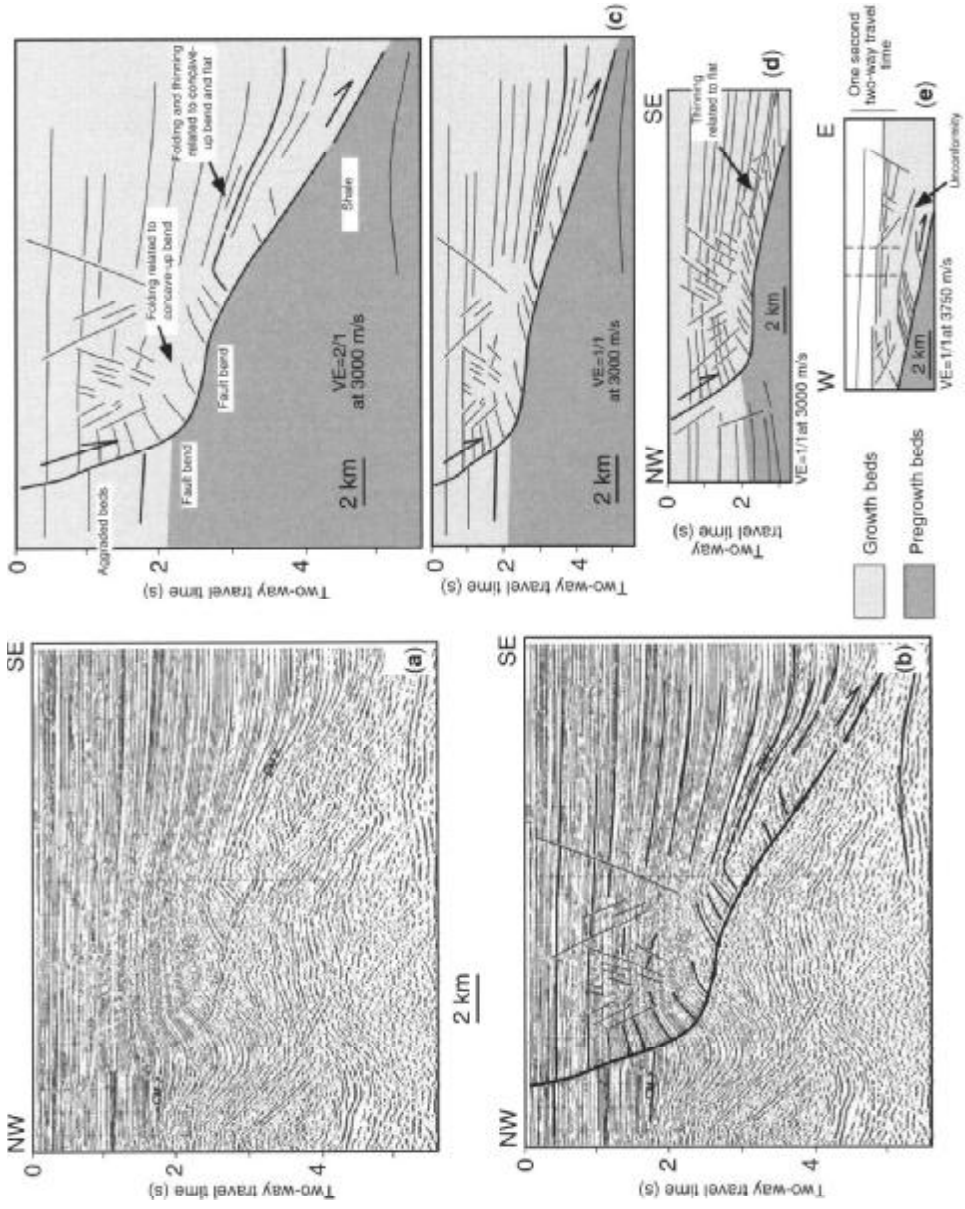


**Fig. 15.** (**a**) Time-migrated seismic line of Brazos fault, offshore Texas, Gulf of Mexico (after Bally *et al.* 1991). CM-7 represents strata that are about 7 Ma. (**b**) Interpreted seismic data. (**c**) Interpreted line drawing with (top) and without (bottom) vertical exaggeration. This part of the Brazos fault has two major fault bends. The intervening fault segment dips gently to the southeast. Beds near the fault dip toward the fault. Beds slightly farther from the fault dip away from the fault. Antithetic and synthetic normal faults affect the hanging wall. (**d**) Interpreted line drawing of seismic line from different part of the Brazos fault. This part also has two major fault bends. The intervening fault segment is flat-lying. (**e**) Vicksburg fault near Slick Ranch field, southern Texas. Hanging wall deformation resembles that of Brazos fault in terms of geometry and dimension. Vertical dashed lines show well locations. See also Fig. 16.

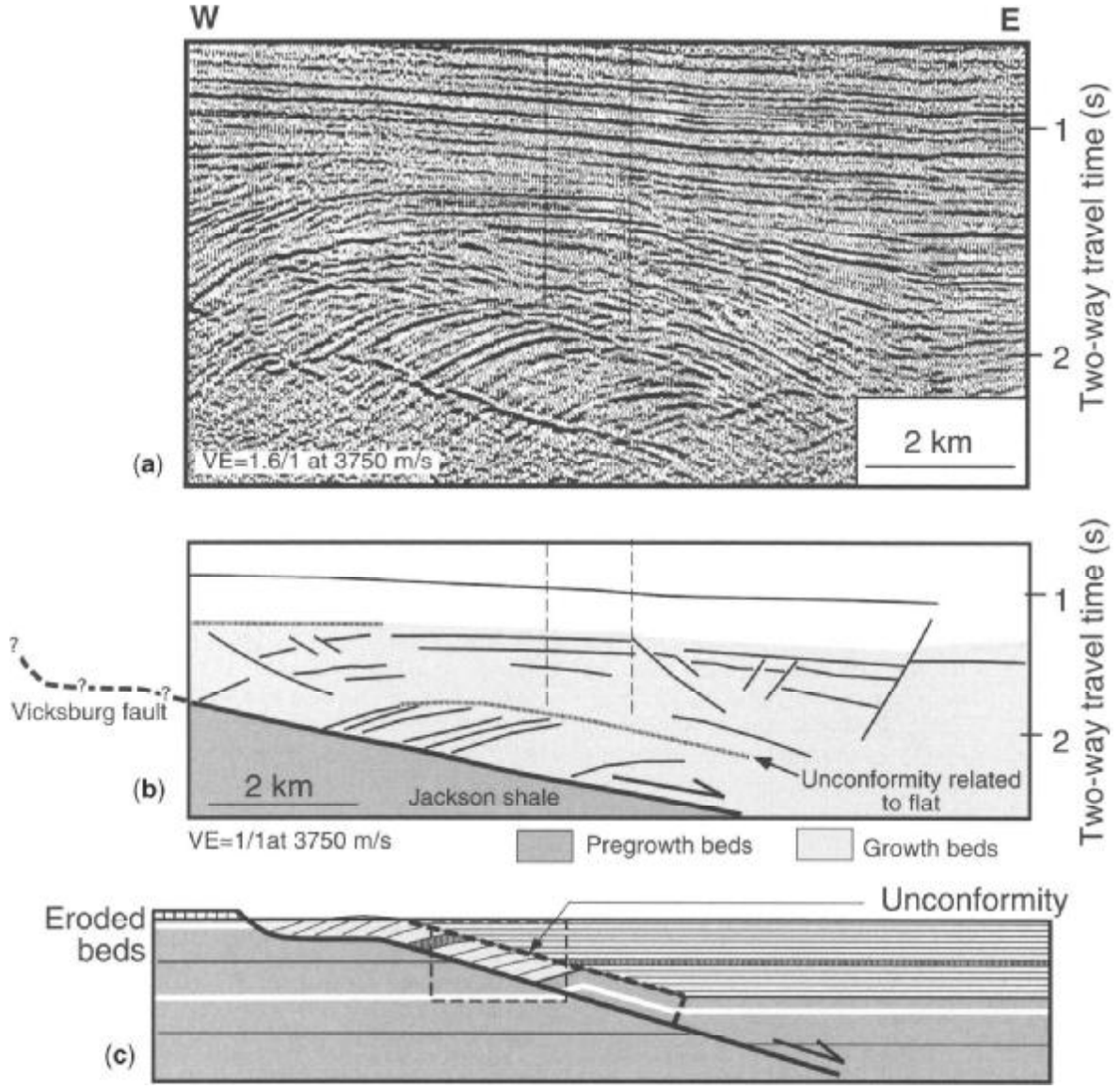


**Fig. 16.** Vicksburg fault near Slick Ranch field, southern Texas. Vertical dashed lines show well locations. (**a**) Uninterpreted seismic line with vertical exaggeration (after Erxleben & Carnahan 1983). (**b**) Interpreted line drawing of time-migrated seismic line displayed with approximately no vertical exaggeration (after Erxleben & Carnahan 1983). An unconformity separates a lower panel of growth beds dipping toward the fault from an upper panel dipping away from the fault. (**c**) Geometric model of ramp-flat-ramp fault showing unconformity similar to that in (b).

(4) Complex structural and stratigraphic patterns develop with multiple episodes of normal faulting if the rate of aggradation/erosion relative to the rate of fault displacement changes through time (Fig. 8). The outer limit of the folding dips more gently for growth packages associated with episodes of normal faulting without aggradation and more steeply for growth packages associated with episodes of normal faulting with aggradation. If erosion occurs between episodes of normal faulting, then growth beds associated with the first faulting episode can have a subtle fanning geometry and closely resemble pregrowth beds.

The experimental models indicate that the style of hanging wall deformation can vary considerably.

(1) In sand models, a few, relatively large secondary antithetic normal faults accommodate most hanging wall deformation. Pregrowth layers, although faulted, remain flat. The effective shear direction parallels the antithetic normal faults, and the shear angle is about 60°–65°.

(2) In clay models, secondary faulting (antithetic and synthetic) and cataclastic flow accommodate most of the hanging wall deformation. The deformed pregrowth and growth layers dip gently toward the main normal fault. The

effective shear angle (35°–50°) is considerably less than the dip of the antithetic normal faults.

(3) The sand and clay models resemble geometric models with large (*c.* 60°) and small (*c.* 35°) shear angles, respectively. In the sand models and the geometric models with large shear angles, more displacement occurs on the main normal fault and the hanging wall collapses in a relatively narrow zone. In the clay models and the geometric models with small shear angles, less displacement occurs on the main normal fault. Instead, the hanging wall stretches substantially and collapses in a relatively wide zone.

Observed hanging wall folds in nature resemble those in the geometric and experimental models. Rollover folds develop in the hanging wall of normal faults that flatten at depth. Normal faults with convex-up bends have hanging wall beds that dip away from the main fault. Normal faults with ramp-flat-ramp geometries have complex hanging wall deformation; beds dip toward the fault near the main fault, and a dipping unconformity that parallels the lower ramp commonly develops above the ramp. Observed secondary normal faults in nature resemble those in the experimental models, especially the clay models. Many secondary normal faults are antithetic to the main fault, but some are synthetic to the main normal fault. Most secondary normal faults have relatively small displacements.

## Appendix: scaling

The strength of most upper crustal rocks increases with depth, obeying a Mohr-Coulomb criterion of failure (e.g., Byerlee 1978). According to this criterion,

$$\tau = c + \mu \cdot \sigma_n, \qquad (1)$$

where $\tau$ and $\sigma_n$ are, respectively, the shear and normal stresses on a potential fault surface, $c$ is the cohesion, and $\mu$ is the coefficient of internal friction. This empirical criterion of failure describes the initiation of new faults rather than the frictional reactivation of existing faults. For most sedimentary rocks, $\mu$ ranges from about 0.55–0.85 (e.g., Handin 1966; Byerlee 1978). For intact sedimentary rocks, $c$ is about 10–20 MPa (Handin 1966), whereas for highly fractured sedimentary rocks, $c$ is significantly less (e.g., Byerlee 1978; Brace & Kohlstedt 1980). To ensure dynamic similarity between the models and natural prototypes, two conditions must be satisfied (e.g., Hubbert 1937; Weijermars *et al.* 1993; Vendeville *et al.* 1995). First, the modelling materials and the rocks in nature must have similar coefficients of internal friction. This condition is satisfied with either dry sand or wet clay as the modelling material. Second,

$$c^* = \rho^* \cdot g^* \cdot l^*, \qquad (2)$$

where $c^*$, $\rho^*$, $g^*$ and $l^*$ are model-to-natural prototype ratios for cohesion, density, gravity and length, respectively. In our models, the values of $\rho^*$ and $g^*$ are about 0.7 and 1, respectively, and $l^*$ is about $10^{-5}$ (i.e., 1 cm in the models equals about 1 km in nature). Thus, to ensure dynamic similarity between the models and natural prototypes, the cohesion of rock must be about $10^5$ greater than that of the modelling materials. This condition is satisfied with either dry sand or wet clay as the modelling material.

We thank E. Peterson for his assistance with the geometric modelling, and S. Callaway, S. Dixon, G. Eisenstadt and D. Sims for their help with the experimental models. We also wish to thank G. Corti, T. Dooley and B. Vendeville for their helpful reviews of the manuscript. The research was partially supported by NSF grant EAR-0408878.

## References

Bally, A., Withjack, M., Meisling, K. & Fisher, D. 1991. *Seismic expression of structural styles*. Geological Society of America, Short Course Notes, 1991 National Meeting.

Brace, W. F. & Kohlstedt, D. L. 1980. Limits on lithospheric stress imposed by laboratory experiments. *Journal of Geophysical Research*, **85**, 6248–6252.

Byerlee, J. 1978. Friction of rocks. *Pure Applied Geophysics*, **116**, 615–626.

Cloos, E. 1968. Experimental analysis of Gulf Coast fracture patterns. *American Association of Petroleum Geologists Bulletin*, **52**, 420–444.

Cloos, H. 1928. Experimente zur inneren tektonik. *Centralblatt für Mineralogie*, **B**, 609–621.

Cloos, H. 1930. Kunstliche gebirge, II. *Natur und Museum*, **60**, 258–269.

Dula, W. F. 1991. Geometric models of listric normal faults and rollover folds. *American Association of Petroleum Geologists Bulletin*, **75**, 1609–1625.

Ellis, P. G. & McClay, K. R. 1988. Listric extensional fault systems – results of analogue model experiments. *Journal of Basin Research*, **1**, 55–70.

Erxleben, A. W. & Carnahan, G. 1983. Slick Ranch area, Starr County, Texas. *In*: Bally, A. W. (ed.) *Seismic Expression of Structural Styles*. American Association of Petroleum Geologists, Studies in Geology, **15**, 2.3.1, 22–26.

HANDIN, J. 1966. Strength and ductility. *In*: CLARK, S. P. Jr. (ed.) *Handbook of Physical Constants*. Geological Society of America, **Memoir 97**, 223–289.

HAUGE, T. A. & GRAY, G. G. 1996. A critique of techniques for modelling normal-fault and rollover geometries. *In*: BUCHANAN, P. G. & NIEUWLAND, D. A. (eds) *Modern Developments in Structural Interpretation, Validation and Modelling*. Geological Society, London, Special Publications, **99**, 89–97.

HUBBERT, M. K. 1937. Theory of scale models as applied to the study of geologic structures. *Geological Society of America Bulletin*, **48**, 1459–1520.

KAUTZ, S. A. & SCLATER, J. G. 1988. Internal deformation in clay models of extension by block faulting. *Tectonics*, **7**, 823–832.

KERR, H. G. & WHITE, N. 1992. Laboratory testing of an automatic method for determining normal fault geometry at depth. *Journal of Structural Geology*, **14**, 873–885.

MCCLAY, K. R. & ELLIS, P. G. 1987*a*. Analogue models of extensional fault geometries. *In*: COWARD, M. P. DEWEY, J. F. & HANCOCK, P. L. (eds) *Continental Extensional Tectonics*. Geological Society, London, Special Publications, **28**, 109–125.

MCCLAY, K. R. & ELLIS, P. G. 1987*b*. Geometries of extensional fault systems developed in model experiments. *Geology*, **15**, 341–344.

MCCLAY, K. R. & SCOTT, A. D. 1991. Experimental models of hangingwall deformation in ramp-flat listric extensional fault systems. *Tectonophysics*, **188**, 85–96.

RUTTER, E. H. 1986. On the nomenclature of mode of failure transition in rocks. *Tectonophysics*, **122**, 381–387.

VENDEVILLE, B., HONGXING, G. & JACKSON, M. P. A. 1995. Scale models of salt tectonics during basement-involved extension. *Petroleum Geoscience*, **1**, 179–183.

VOGLER, H. A. & ROBINSON, B. A. 1987. Exploration for deep geopressured gas–Corsair trend, offshore Texas. *American Association of Petroleum Geologists Bulletin*, **71**, 777–787.

WEIJERMARS, R., JACKSON, M. P. A. & VENDEVILLE, B. 1993. Rheological and tectonic modeling of salt provinces. *Tectonophysics*, **217**, 143–174.

WERNICKE, B. P. & BURCHFIEL, B. C. 1982. Modes of extensional tectonics. *Journal of Structural Geology*, **4**, 105–115.

WHITE, N. 1992. A method for automatically determining normal fault geometry at depth. *Journal of Geophysical Research*, **97**, 1715–1733.

WHITE, N. J. & YIELDING, G. 1991. Calculating normal fault geometries at depth: theory and examples. *In*: ROBERTS, A. M., YIELDING, G. & FREEMAN, B. (eds) *The Geometry of Normal Faults*. Geological Society, London, Special Publications, **56**, 251–260.

WHITE, N. J., JACKSON, J. A. & MCKENZIE, D. P. 1986. The relationship between the geometry of normal faults and that of the sedimentary layers in their hanging walls. *Journal of Structural Geology*, **8**, 897–909.

WITHJACK, M. O. & CALLAWAY, J. S. 2000. Active normal faulting beneath a salt layer – an experimental study of deformation in the cover sequence. *American Association of Petroleum Geologists Bulletin*, **84**, 627–651.

WITHJACK, M. O. & PETERSON, E. T. 1993. Prediction of normal-fault geometries – a sensitivity analysis. *American Association of Petroleum Geologists Bulletin*, **77**, 1860–1873.

WITHJACK, M. O., ISLAM, Q. & LAPOINTE, P. 1995. Normal faults and their hanging-wall deformation – an experimental study. *American Association of Petroleum Geologists Bulletin*, **79**, 1–18.

XIAO, H. & SUPPE, J. 1992. Origin of rollover. *American Association of Petroleum Geologists Bulletin*, **76**, 509–529.

YIELDING, G., BADLEY, M. E. & FREEMAN, B., 1991, Seismic reflections from normal faults in the northern North Sea. *In*: ROBERTS, A. M., YIELDING, G. & FREEMAN, B. (eds) *The Geometry of Normal Faults*. Geological Society, London, Special Publications, **56**, 79–89.

# Recent advances and current problems in modelling surface processes and their interaction with crustal deformation

JEAN BRAUN
*Géosciences Rennes, Université de Rennes 1, Rennes, France*
*(e-mail: Jean.Braun@univ-rennes1.fr)*

**Abstract:** I present a brief summary of recent advances in the field of computational geomorphology and various attempts to couple numerical models of landscape evolution to models of crustal/lithospheric deformation. The most commonly used formulations for the various physical processes at play during surface erosion, transport and deposition are presented, as well as an outline of how they have been incorporated in a variety of numerical schemes. I also explain how the coupling between erosion and tectonics has been performed under various simplifying assumptions. Determining the rate constants for each of the proposed landforming mechanisms remains a difficult challenge that has recently been helped by the advent of new low temperature thermochronometers and exposure dating by cosmogenic radionuclides. I demonstrate how the information contained in the relationship between age and elevation can be used to provide constraints on the 'age' of a landscape, as well as how important rate information can be extracted from various datasets by using simple modelling techniques. This paper demonstrates why the field of computational geomorphology needs to harmonize the various parameterizations (often the legacy of empirical relationships derived from observations at the human scale), quantitative estimates of the value of the numerous rate parameters and improvement of the numerical techniques.

In recent years, much work has been devoted to understanding the coupling between tectonics, erosion and climate (Molnar & England 1990; Koons 1994; Beaumont *et al.* 1999; see also Burbank & Pinter (1999) for an introduction to this subject). We know that tectonic movements create topography at the Earth's surface by which atmospheric circulation can be perturbed, thereby creating a first-order interaction between tectonics and climate. This perturbation often takes the form of enhanced precipitation on the windward side of a mountain belt which, in turn, can be responsible for enhanced rates of erosion. This feedback is less obvious to demonstrate but may be responsible for much of the morphological variety that is observed among active and ancient mountain belts.

The Southern Alps of New Zealand are often presented as a classical example of a tectonic feature which has perturbed atmospheric circulation: it rains on average ten times more on the west coast of the South Island of New Zealand than on the east coast. It is also often taken as an example of an area where the feedback has been extreme: rocks are preferentially exhumed from a much larger depth along the western front of the orogen (Wellman 1979; Koons 1990; Beaumont *et al.* 1996). Thus the first-order features of an orogen, such as the surface distribution of metamorphic rocks, or the geometry and location of large structures, may be dictated by patterns in the local climate.

At the larger scale, it has been postulated that the Tibetan Plateau is the result of ongoing continental shortening and thickening, unbalanced by erosion, principally due to the lack of rainfall in the region (Royden 1996; Beaumont *et al.* 2001). Once a proto-plateau formed, potentially as early as 35 Ma, rainfall was even more perturbed, and dry conditions established themselves on the plateau and most of its flanks, limiting erosion to the Himalayan front, the only plateau boundary facing an open body of water.

At an even larger scale, Molnar and England (1990) postulated that the apparent increase in global erosion rates since the beginning of the Cenozoic is the product of a strong feedback between tectonics and climate. According to this hypothesis, higher erosion rates resulting from the colder climatic conditions experienced by the Earth over the past 65 Ma leads to local relief production which, by flexural isostasy, results in mountain peak uplift and further perturbs the climate; this perturbation would ultimately lead to more efficient erosion in regions of high elevation.

*From*: BUITER, S. J. H. & SCHREURS, G. (eds) 2006. *Analogue and Numerical Modelling of Crustal-Scale Processes.* Geological Society, London, Special Publications, **253**, 307–325.
0305-8719/06/$15.00 

## Numerical modelling of the coupling between tectonics, erosion and climate

The links between tectonics, climate and erosion have been demonstrated by many numerical models of the coupled lithosphere–hydrosphere system in which varying erosional conditions have led to clear modifications in tectonic regime. In particular, in active orogenic settings, it has been demonstrated that the large-scale morphology of a mountain belt can be modified by perturbing the dominant wind direction (Willett *et al.* 1993; Willett 1999). As an example, I show the results of a series of computations in which a thermo-mechanical model of the continental lithosphere has been coupled to a simple, one-dimensional model of surface erosion, transport and deposition (Fig. 1). The crust is assumed to be shortened by the subduction of the underlying lithospheric mantle. Rock rheology is a combination of pressure-dependent brittle failure and temperature-dependent creep. The heat transport equation is also solved and the resulting temperature used to calculate the viscosity of rocks. The results show that the behaviour of the system is strongly controlled by the efficiency of the surface processes. It has been assumed that, as it evolves, the orogen is abruptly subjected to an increase in erosion rate, potentially corresponding to a change in climatic

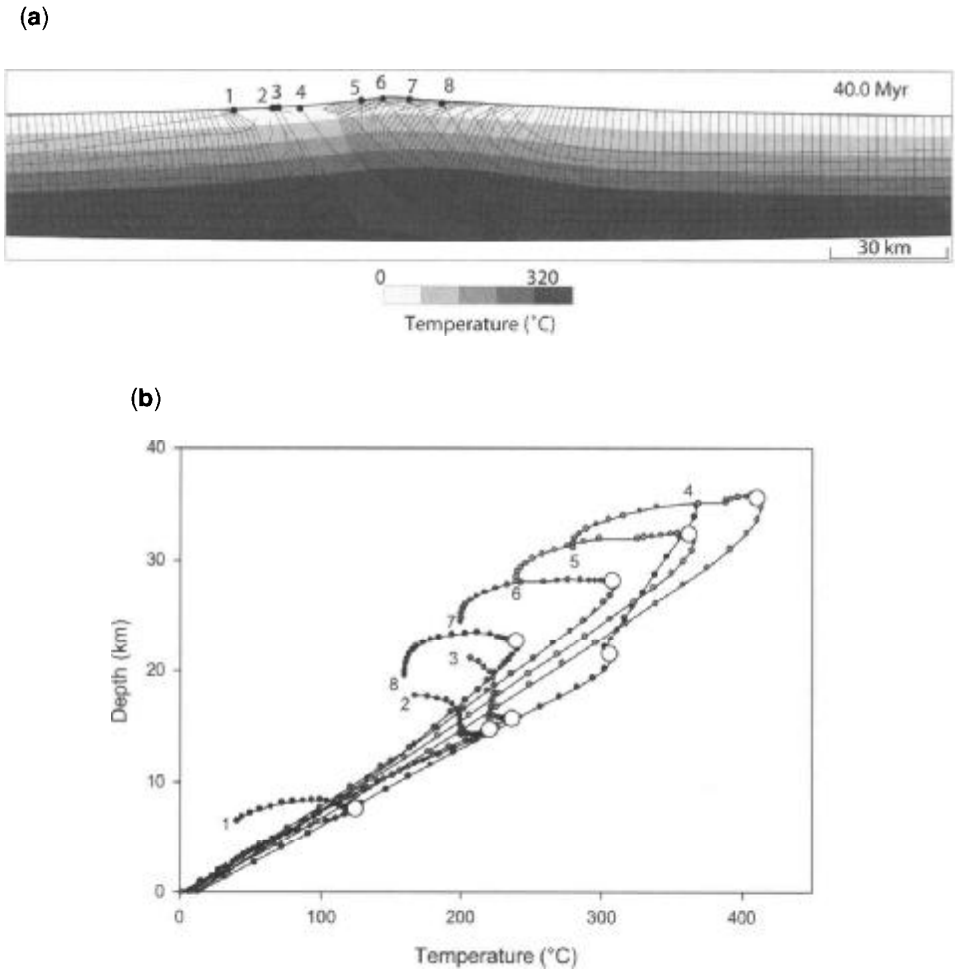


**Fig. 1.** Results of a numerical model of crustal deformation coupled to surface erosion; see Braun and Sambridge (1994) for details of the numerical method. Deformation is driven by an imposed velocity discontinuity at the base of the crust; a uniform heat flow is imposed at the base of the model. Erosion rate is assumed proportional to (1) local slope and drained area (fluvial erosion) and (2) curvature of the topography (hillslope processes). At 20 Ma in the evolution of the model, fluvial and diffusive erosion parameters are increased by a factor 2 to represent an increase in erosion rate. (**a**) Temperature and geometry of an initially rectangular grid; the dark circles are Lagrangian markers advected towards the surface by the computed velocity field. (**b**) Depth-temperature-time paths of the 8 particles tracked in panel (**a**). The small circles are time markers at 1 Ma intervals in the evolution of the model; the large white circle corresponds to the 20 Ma time step.

conditions or to its emergence above sea level. When erosion increases (Fig. 1a), the orogen is rapidly transformed; it evolves from a state of lateral growth to a phase of rapid and localized exhumation, steepening of the structures controlling the deformation, and the exhumation and, subsequently, narrowing of the mountain belt.

In another series of numerical experiments in which a tectonic model was coupled to a surface processes model through a simplified representation of orographic precipitation, Beaumont *et al.* (1992) and later Batt and Braun (1999) illustrated the complete feedback between local climate and tectonics (Fig. 2). During the early stages of development of a mountain belt, erosion is relatively uniform as little or no orographic control exists on precipitation. As the mountain grows, the local wind circulation is affected by the rising topography and precipitation becomes focused on the windward side of the orogen, leading to an asymmetric erosion pattern across the orogen. The 'wet' side of the orogen is characterized by much steeper topography than the 'dry' side. Further growth of the orogen enhances the orographic effect and the asymmetry of the resulting topography.

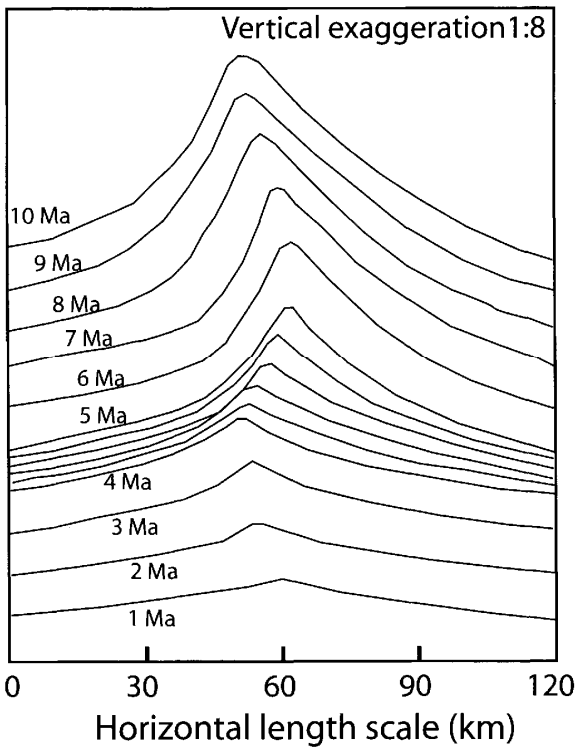


**Fig. 2.** Simulated evolution of the topography across an active mountain belt, from the time of onset of collision until 10 Ma in the evolution of the orogen. Model set-up is similar to that shown in Fig. 1 but precipitation is orographically controlled. Dominant wind direction is from left to right. As topography grows, orographic control on precipitation leads to asymmetric erosion patterns which leads to an asymmetric topography and a further enhancement of the orographic control on precipitation. Modified from Batt and Braun (1999).

Through the results of numerical simulations, Beaumont *et al.* (2001, 2004) and Jamieson *et al.* (2004) have shown that the dynamic evolution of the Himalayan orogen and the adjacent Tibetan Plateau are causatively linked and that the strong rainfall along the Himalayan front is the main driving mechanism for the exhumation of a mobile lower crust that formed in response to thickening of the Plateau (Fig. 3). As shown by Royden (1996) and Clark and Royden (2000), it is the difference in potential energy between the Plateau and the adjacent Indian continent that provides the pressure gradient necessary to mobilize the lower crust, but it is the focused erosion along the Himalayas that causes it to be exhumed so rapidly, and, in doing so, creates the tallest mountain range at the Earth's surface (Beaumont *et al.* 2001; Hodges *et al.* 2001).

This coupling between erosion and tectonics arises from the very strong density gradient that exists at the interface between the lithosphere and the overlying hydrosphere. Indeed, small vertical deflections of that interface can create very large horizontal pressure (stress) gradients in the underlying lithosphere that can strongly affect the force balance and enhance or inhibit deformation (Fig. 4). Recently, it has been postulated that the pressure change caused by the rapid incision of a deep river valley may be sufficient to cause localization of the deformation in the area just beneath the valley. This scenario has been formulated by Zeitler *et al.* (2001*a*, *b*) and Koons *et al.* (2002) to explain the apparent 'pinning' of the Himalayan front at its two syntaxes.

Finally, it must also be noted that the recent technological and algorithmic developments that have made possible the coupling between models of lithospheric deformation and models of surface erosion and transport, have also made it possible to greatly improve the prediction capabilities of these models and their ability to reproduce geological observations/data. Indeed, it is erosion that is responsible for the exhumation of rocks towards the surface where they are observed and collected by geologists. An important consequence of this development has been the further realization that tectonic processes, combining with spatially variable erosional processes, are not only responsible for the vertical movement of rocks towards the surface but also for very large horizontal transport. As they 'travel' through an orogen, the temperature and pressure history of exhumed rocks will be strongly affected by this lateral transport component.

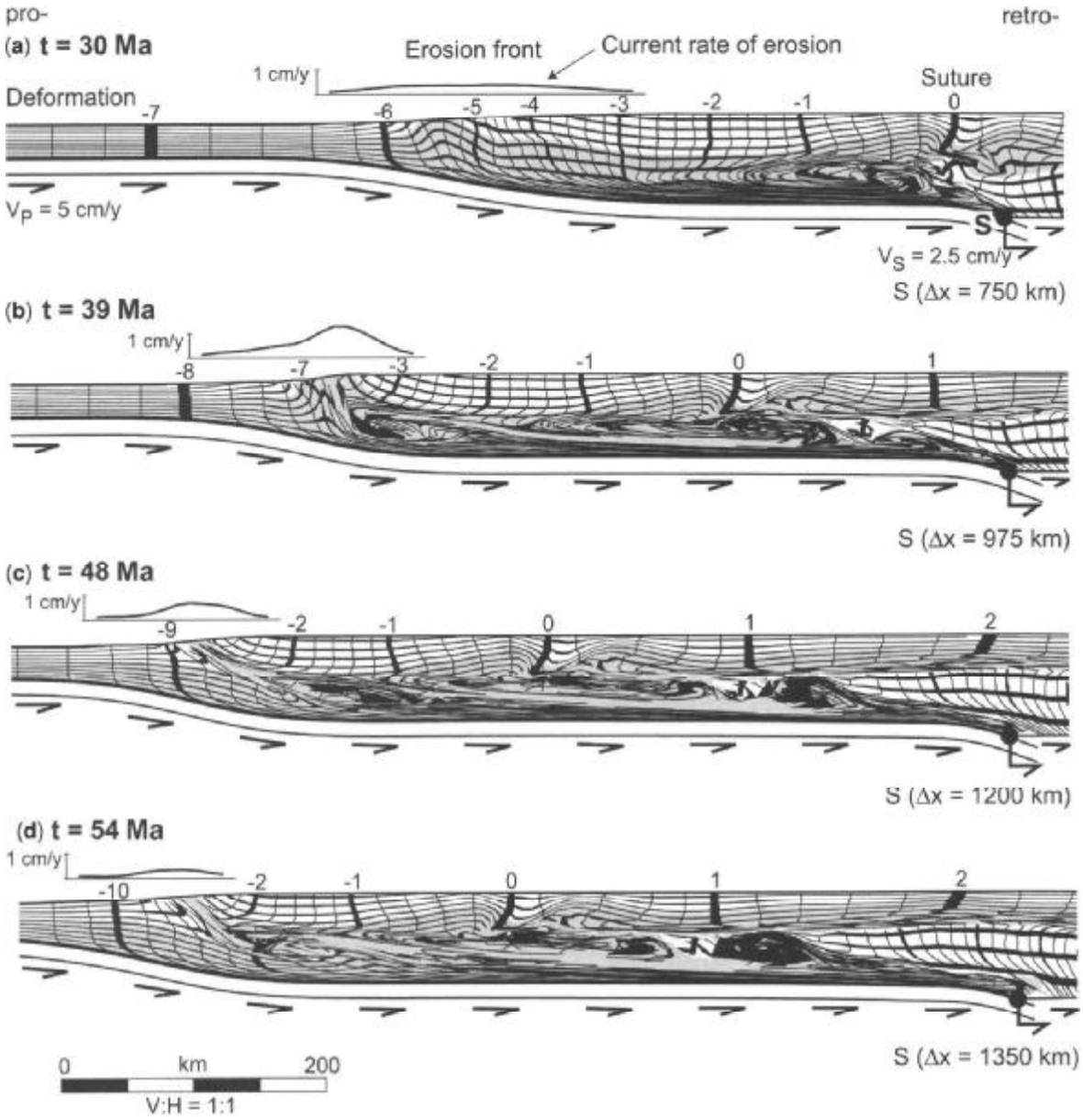


**Fig. 3.** Numerical model of the tectonic development of the Tibetan Plateau and Himalayan front. Convergence is driven by imposed subduction of the pro- (Indian) side of the orogen beneath the retro- (Eurasian) side. Extrusion of the lower crust is driven by a horizontal pressure gradient caused by the elevated topography of the Tibetan Plateau with respect to the Indian continent and made possible by efficient erosion along the Himalayan front. The four panels correspond to four different stages of evolution of the model showing the formation of a mobile lower crust and a focusing of the erosion along the Himalayan 'erosional front'. Total convergence is (**a**) 1500 km, (**b**) 1950 km, (**c**) 2400 km and (**d**) 2700 km, respectively. Modified from Beaumont *et al.* (2004).

The results presented in Figure 1 illustrate this point: a series of rock particles originating from a range of locations, both in the horizontal and vertical dimensions, are brought together towards their final surface position during the tectonic event. Each particle also experiences a clear change in its pressure and temperature evolution at the time of increase in erosional conditions at the surface (the large white circles in Fig. 1b), but the amplitude and sign of this pressure/temperature change will be different in various parts of the orogen, therefore affecting each rock particle differently.

## Parameterization of landform evolution

To quantify the coupling between tectonics, erosion and climate, many numerical models of

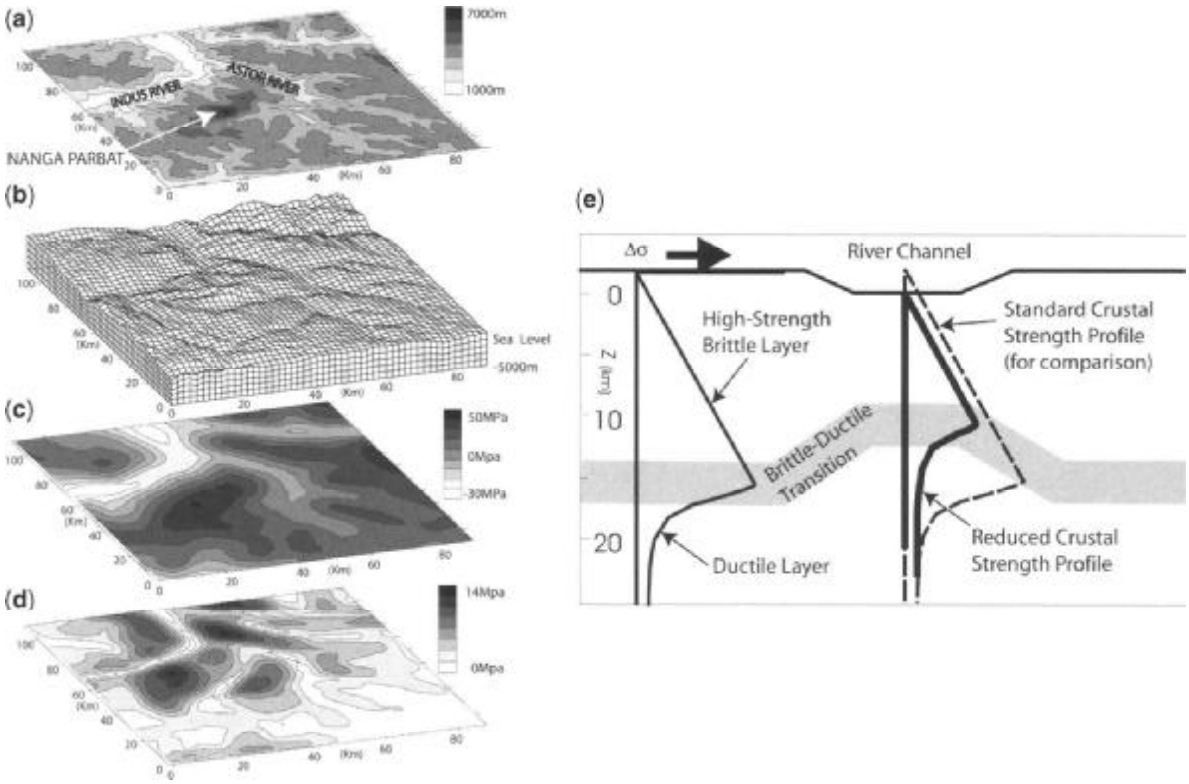


**Fig. 4.** Large gradient in surface topography (**a**) and (**b**) caused by the incision of a river channel may lead to perturbation in the underlying state of stress (**c**) and (**d**). (**c**) Topographic contribution to the vertical normal stress as represented by the departure of the vertical normal stress ($\sigma_{zz}$) at 5 km below sea level from that predicted by a constant 2 km elevation over the region. (**d**) Vertical shear stress component $(\tau_{xz}^2 + \tau_{yz}^2)^{1/2}$ generated by topography at 5 km below sea level. As shown in the right panel (**e**), two factors contribute to strength reduction beneath a deeply incised river channel: the erosional unloading and the thermal perturbation caused by rapid advection of heat towards the surface. Modified from Koons *et al.* (2002).

surface processes, often called Surface Processes Models (SPMs) or Landscape Evolution Models (LEMs), have been developed in recent years. It is not possible here to cite all the models. Instead, I will try to summarize the most common algorithms that have been used, often based on an extrapolation of observations made at the human scale to the scale of tectonic processes, both in space and time. Apart from a few examples (Stock & Montgomery 1999; van der Beek & Bishop 2003; Tomkin *et al.* 2003), this extrapolation is often not tested and the first-order match between model predictions and large-scale features of natural landscapes is taken as proof of the appropriateness of the extrapolation.

Landform evolution is determined by a wide range of processes that have been parameters in a variety of ways (Dietrich *et al.* 2003). In general, one tries to express the rate of change of topography, $h$, as a function of parameters and quantities that can either be computed from the shape of the landscape (local slope, drained area, etc.) or determined empirically. In most LEMs, the landscape is divided into small cells in which the elevation is commonly assumed to be uniform or vary linearly; a notable exception is the continuum approach developed by Simpson and Schlunegger (2003). One then introduces a rule for local erosion/deposition and, combining it with a form of the continuity equation, one obtains a law that encompasses erosion, sedimentation and transport.

### *Stream-power law*

Water channels (rivers or streams) are often regarded as the controlling elements of many land surfaces, where the interaction between the hydrosphere and the lithosphere is focused. Stream incision is commonly parameterized by the *stream-power law*:

$$\frac{\partial h}{\partial t} = K_f S^n A^m \qquad (1)$$

in which incision rate is assumed to be proportional to the product of the local slope, $S = \|\overrightarrow{\text{grad}}\, h\|$, and water discharge. Drainage area, $A$, is commonly used as a proxy for discharge (this is appropriate if one assumes that precipitation, evaporation and infiltration are uniform over the catchment), $K_f$ is a constant that depends on local precipitation, rock type and other factors such as vegetation, $n$ and $m$ are power-law exponents. The value of $n$ is assumed to vary between $\frac{2}{3}$ and $\frac{5}{3}$ (Whipple & Tucker 1999), but a commonly used value is 1. The value of $m$ is less well known. If one assumes steady-state, the ratio $m/n$ can be determined by the downstream rate of increase of channel slope with drainage area (Whipple & Tucker 1999). This ratio is often referred to as the *concavity* of a river profile and has a value that is typically around $\frac{1}{2}$ (Whipple 2001).

River incision may be limited by the mechanical strength of the substratum, in which case a threshold, $C_0$, needs to be introduced (Tucker & Slingerland 1994)

$$\frac{\partial h}{\partial t} = K_f S^n A^m - C_0 \tag{2}$$

Note, however, that if a threshold is used, the stochastic nature of many quantities, such as precipitation or bedrock resistance to incision, will play an important role in determining the time-integrated behaviour of the system (Tucker 2004).

### *Transport-limited incision*

One can also assume that it is not the rate of incision that controls the rate of landform evolution but the rate at which material can be transported away from its source by the channel. To model this behaviour, one introduces a quantity called the *carrying capacity* of the river, $Q_{eq}$, that is the flux of sediment (volume per unit time) that a river can transport for a given slope, $S$, and catchment area, $A$:

$$Q_{eq} = K_t S^{n'} A^{m'} \tag{3}$$

where $K_t$ is a proportionality constant. $n'$ and $m'$ are poorly known and commonly assumed to be similar to $n$ and $m$ in Equation 1. Assuming that a river is always carrying sediment at capacity, the rate of evolution of the surface is given by the continuity equation (Willgoose *et al.* 1991):

$$\frac{\partial h}{\partial t} = -\frac{1}{W}\frac{\partial Q_{eq}}{\partial x} \tag{4}$$

where $x$ is the downstream direction and $W$ is the width of the river channel.

Sediments can have two effects in a river channel: when they are in motion within the water column, they can be regarded as tools to abrade the substratum (Sklar & Dietrich 1998); when they are at the bottom of the channel, they can protect it. This latter role of sediments has been introduced in an alternate formulation for river incision that also incorporates transport and deposition/sedimentation (Kooi & Beaumont 1994) in which the rate of incision/deposition is assumed to be proportional to the disequilibrium between carrying capacity and local sediment flux, $Q_{sed}$:

$$\frac{\partial h}{\partial t} = -\frac{1}{WL_f}(Q_{eq} - Q_{sed}) \tag{5}$$

where $L_f$ is an erosion/deposition length scale required for disequilibrium to be reduced by a factor of $(e)$ when $Q_{eq}$ is constant (Kooi & Beaumont 1994). Sediment flux can be calculated by integrating the erosion/deposition flux over the upstream part of the catchment.

### *Hill-slope processes*

Stream incision leads to a local increase in surface slope along the sides of the valley carved by the stream. The other type of processes that will control the long-term evolution of the landscape is thus the transport along hill/valley slopes. In rapidly uplifting, tectonically active regions, landslide is the process dominating mass transport (Hovius *et al.* 1997), in lower relief, tectonically inactive regions, soil creep controls hill slope transport (Anhert 1967).

On soil-mantled hill-slopes, the rate of landform evolution is controlled by the rate at which soil is produced, transported and/or deposited:

$$\frac{\partial h}{\partial t} = -\frac{\partial Q_S}{\partial x} + (\kappa - 1)P \tag{6}$$

where $Q_S$ is the soil flux, $x$ is the downhill direction, $\kappa$ is the ratio of bedrock to soil density, and $P$ is the rate of soil production (Braun *et al.* 2001).

Soil production is often regarded as proportional to soil thickness, as the chemical alteration of bedrock to form soil is dependent on the availability and thus penetration of water into the soil. Based on cosmogenic isotope measurements at the bedrock/saporolite interface at a few sites worldwide, Heimsath *et al.* (2000, 2001) have proposed a soil production function,

$P$, that varies as the negative exponential of soil thickness:

$$P = P_0 e^{-\xi/\xi_0} \tag{7}$$

where $\xi$ is soil thickness, $P_0$ is the production rate at zero soil thickness and $\xi_0$ is the production $e$-folding depth, that is, the soil thickness necessary to reduce production by a factor $e$.

Soil transport is a complex physical process that is likely to involve more than one mechanism. These commonly include simple soil creep, for which soil flux, $Q_S$, is linearly related to local slope, $S$ (Anhert 1967):

$$Q_S = -K_d S \tag{8}$$

Martin (2000) suggests a range of values for $K_d$, the linear diffusion coefficient, that are suited to the long-term evolution of soil-mantled hill slopes. Because soil flux is the product of soil thickness by vertically-integrated soil velocity, this commonly used law implies that mean soil velocity is inversely proportional to soil thickness. Furthermore, a linear transport law predicts that, at steady state, all hill slopes should be convex, not straight as is often observed in moderately active tectonic settings (Roering *et al.* 1999). To resolve these problems, depth-dependent soil transport has been used and is represented by:

$$Q_S = -K_v \xi^{m''} S^{n''} \tag{9}$$

where $K_v$ is a proportionality constant that varies with soil type, climate and vegetation. If soil flow conforms to Manning's equation for liquid flow (Olson 1973), $m''$ and $n''$ are 1.67 and 0.5, respectively which is also compatible with *in situ* measurements (Clarke *et al.* 1999). Finally, soil may be transported by overland flow, in which case soil flux can be expressed as (Moore & Burch 1986):

$$Q_S = -K_w A^k S^p \tag{10}$$

The exponents $k$ and $p$ have values between 1 and 2 (Prosser & Rustomji 2000). The proportionality constant $K_w$ is poorly known and depends mostly on soil type and vegetation (Prosser & Rustomji 2000).

In situations where river incision is fast (mm/yr or more), due, for example, to a very large rate of tectonic uplift and/or base level drop, important slopes develop and landsliding can play a dominant role in the transport of material from hill slopes to river channels (Hovius *et al.* 1997, 2000; Montgomery & Brandon 2002). Proper parameters of the conditions for slope instability and of the volume and rate of transport of individual landslides is difficult to include in landform evolution models, principally due to their lack of spatial resolution. Indeed, critical slope angles for landsliding are of the order of 30° or more, which would require a spatial resolution of the order of a few tens of meters, well below what is commonly used (typically 100 m to 1 km) in most large-scale LEMs.

One can either assume an artificially low critical angle for soil movement by sliding (Champel *et al.* 2002) or that a simple linear transport equation is adequate to represent all hill-slope processes, including landsliding (Kooi & Beaumont 1994). This latter approach is, however, not consistent with the observation that at high uplift rate, erosion rates adjust primarily through changes in the frequency of landsliding rather than by increased hill-slope steepness (Montgomery & Brandon 2002). This implies that a non-linear form of the diffusion equation (Martin 2000) or a threshold must be introduced (Roering *et al.* 2000; Densmore *et al.* 1998).

### *Glacial erosion*

In the recent geological past, the Earth's climate has been characterized by fluctuations on a time scale of a few tens to a hundred thousand years during which conditions in most mountainous regions of the world have oscillated between fluviatile and glaciated. In fact, over the past 3 million years, mountains in temperate to cold regions of the globe have experienced glaciated conditions more often than not. It is thus unfortunate that the effect of glacial erosion on landform evolution in tectonically active areas has been neglected in most landscape evolution models (Braun *et al.* 1999).

Assuming that abrasion, glacial plucking or quarrying are the dominant mechanisms responsible for glacial erosion, the rate of surface lowering by glaciers can be shown to be linearly related to ice sliding velocity, $u_s$ (Hallett 1979), through the following relationship:

$$\frac{\partial h}{\partial t} = -K_g u_s \tag{11}$$

where $K_g$ is a proportionality constant that depends on rock type. The sliding velocity must be computed from the solution of the ice dynamics equation which may be obtained by combining the force balance equation (Newton's first and second laws), mass conservation and a rheological law that relates ice

deformation to local stress conditions. In cases where variations in ice thickness take place over length scales that are much greater than the thickness of the ice, the thin-ice approximation can be used to compute the basal sliding velocity (Hutter 1981). A simple climatological model must also be introduced to estimate where ice accumulation and ablation takes place. Finally the temperature distribution at the base of the ice must also be estimated to determine where the ice is sliding on the bedrock or whether it is frozen (Braun *et al.* 1999). Such an approach has been used to simulate the effect of varying climatic conditions, and thus landforming mechanisms, on the evolution of a high relief, tectonically active mountain range in two dimensions (Braun *et al.* 1999), or the formation of high-relief steps and overdeepenings in longitudinal glacial valley profiles generated at the confluence of tributary glaciers (MacGregor *et al.* 2000).

### *Chemical weathering*

In regions where bedrock lithology is dominated by calcareous rocks, chemical erosion must be taken into account. A large-scale representation of the processes of karst formation and their relationship to surface runoff, and the evolution of the surface landform is still to be developed. Combining a simple law for chemical weathering and the consequent downstream evolution of carbon dioxide pressure in a flowing river, Kauffman and Braun (2001) have shown that incision rate in a karst-dominated limestone landform may simply be related to discharge, or drainage area.

## Numerical models of landform evolution

Many landform evolution models exist. Of interest to us are those aimed at studying the evolution of landforms at the time scale of orogenic processes and at the length scale of a small to medium size orogen, or at least a large catchment. These include SIBERIA (Willgoose *et al.* 1991), PRECIPITON (Chase 1992), DRAINAL (Beaumont *et al.* 1992), the detachment-limited model of Howard (1994), GOLEM (Tucker & Slingerland 1994), CASCADE (Braun & Sambridge 1997), CAESAR (Coulthard *et al.* 1997), ICE-CASCADE (Braun *et al.* 1999), ZSCAPE Densmore *et al.* 1998), LAPSUS (Schoorl *et al.* 2000), CHILD (Tucker *et al.* 2001), HEXSOIL (Braun *et al.* 2001) and EROS (Crave & Davy 2001). A good description of these various numerical methods up to 2001 is given in Coulthard (2001). In broad terms, they differ by the type of spatial discretization used to represent the landscape (rectangular, hexagonal, irregular), whether the channels are treated on a separate network, and the combination of equations/processes used.

To illustrate the purpose of a typical landform evolution model, I show in Figure 5 the results of computations made by Tomkin (2000) using the ICE-CASCADE model which combines fluvial, hill-slope and glacial erosion laws. These computations (Tomkin & Braun 2002) confirmed the suggestion of Whipple *et al.* (1999) that glaciations do not increase catchment-scale relief unless temperature is sufficiently low for ice to be frozen to and protect mountain peaks. In another study, Braun *et al.* (1999) used ICE-CASCADE to demonstrate that the rate of mountain erosion is, in most cases, more efficient under cyclic climatic conditions during which the dominant landforming process switches between fluvial and glacial erosion, with such a frequency (100 ka) that the shape of the landscape is continuously out of balance with the dominant process. During ice-free periods, near-vertical glacial valley walls are gravitationally unstable and prone to landslides (Hovius *et al.* 1997). In actively uplifting regions, this process combines with others to rapidly transform glacial landforms into graded, V-shaped fluvial valleys. Once the ice returns, these valleys are filled with fast-flowing glaciers and are rapidly reshaped into glacial troughs (Harbor 1992). Braun *et al.* (1999) demonstrated that this continuous imbalance leads to a more efficient rate of erosion than if the conditions were stable in one of the two states. This process is thought to occur in the South Island of New Zealand, with a partial or complete reshaping of the landform on a time scale of a few tens of thousands of years (Whitehouse 1987).

It is worth mentioning the recent development of laboratory set-ups in which landforming processes are studied using analog materials (Crave *et al.* 2000; Lague *et al.* 2003). Scaling of the geomorphological laws to the size of the experimental apparatus is difficult, especially due to the finite size of the material grains. Despite these limitations, the method is useful in studying the scaling properties of channelized systems.

## Coupling with tectonics

The most commonly used, zeroth-order approach to 'couple' tectonics to a landscape evolution model is through the definition of a purely kinematic uplift function to which the landscape

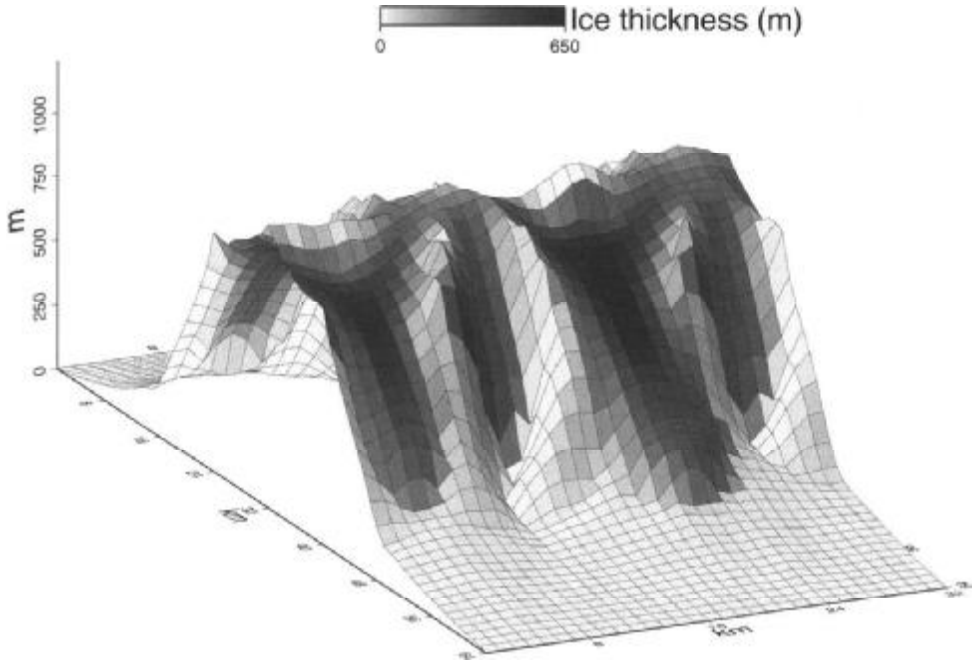


**Fig. 5.** Ice draped over topography. Ice thickness and landform computed by ICE-CASCADE (Tomkin *et al.* 2003) assuming a simple mass balance between precipitation, ablation and transport, that ice deforms as a power-law viscous fluid and that glacial erosion is linearly proportional to ice basal sliding velocity. Note that where the ice is frozen to the landscape, no erosion takes place.

evolution model reacts. There is no feedback from the erosional system onto the tectonic forcing.

The first-order coupling is to calculate the isostatic rebound associated with the redistribution of mass caused at the Earth's surface by erosional and depositional processes. In practice, the change in surface topography over a time step of the LEM is converted into an equivalent surface load (positive where deposition took place, negative where erosion took place) that is then applied to an isostatic foundation, under the assumption of local or regional/flexural isostasy. In most cases where flexural isostasy is considered, a simple linear, thin elastic plate foundation is used (Beaumont *et al.* 1999; Braun & Sambridge 1997; Braun *et al.* 1999). Under this strategy there is a feedback between surface processes and the tectonic forcing but only on its amplitude, not its geometry.

Second-order coupling, i.e., involving a feedback that will affect the distribution of forces within the underlying lithosphere, has been achieved in many different ways. The simplest is to use the predictions of the LEM to determine the parameters (angles) of the analytical solution to the critical wedge problem (Dahlen 1984). This approach was originally used by Johnson and Beaumont (1995) and, more recently, further developed by Hilley and Strecker (2004), Whipple and Meade (2004) and Roe *et al.* (2005).

Coupling to fully dynamic models of tectonic deformation is performed under the assumption of two dimensionality, either by using a plane-form, thin-sheet model of lithospheric/crustal deformation to which an LEM can be directly connected (Ellis 1995; Braun & Shaw 2001; Simpson 2004), or by using a 2D (vertical cross-section) tectonic model which requires a strike average of the results of the LEM (Beaumont *et al.* 1992; Stolar *et al.* 2005) or coupling to a one dimensional LEM (Batt & Braun 1999). Examples of these approaches (thin-sheet approximation and coupling with a 1D LEM) are shown in Figure 6.

Deformation of the crust/lithosphere during a tectonic event leads to uplift but also horizontal deformation. A proper coupling between an LEM and a tectonic model must incorporate both effects which, unfortunately, may lead to numerical problems. Indeed, most LEMs are based on a regular discretization of space which prevents them from incorporating a horizontal advection term of the landform unless some sort of spatial interpolation of the landform is made (Densmore *et al.* 2004), or the coupling between tectonics and erosion is made at strategically chosen time intervals at which parts of the landscape are moving by an amount exactly equal to

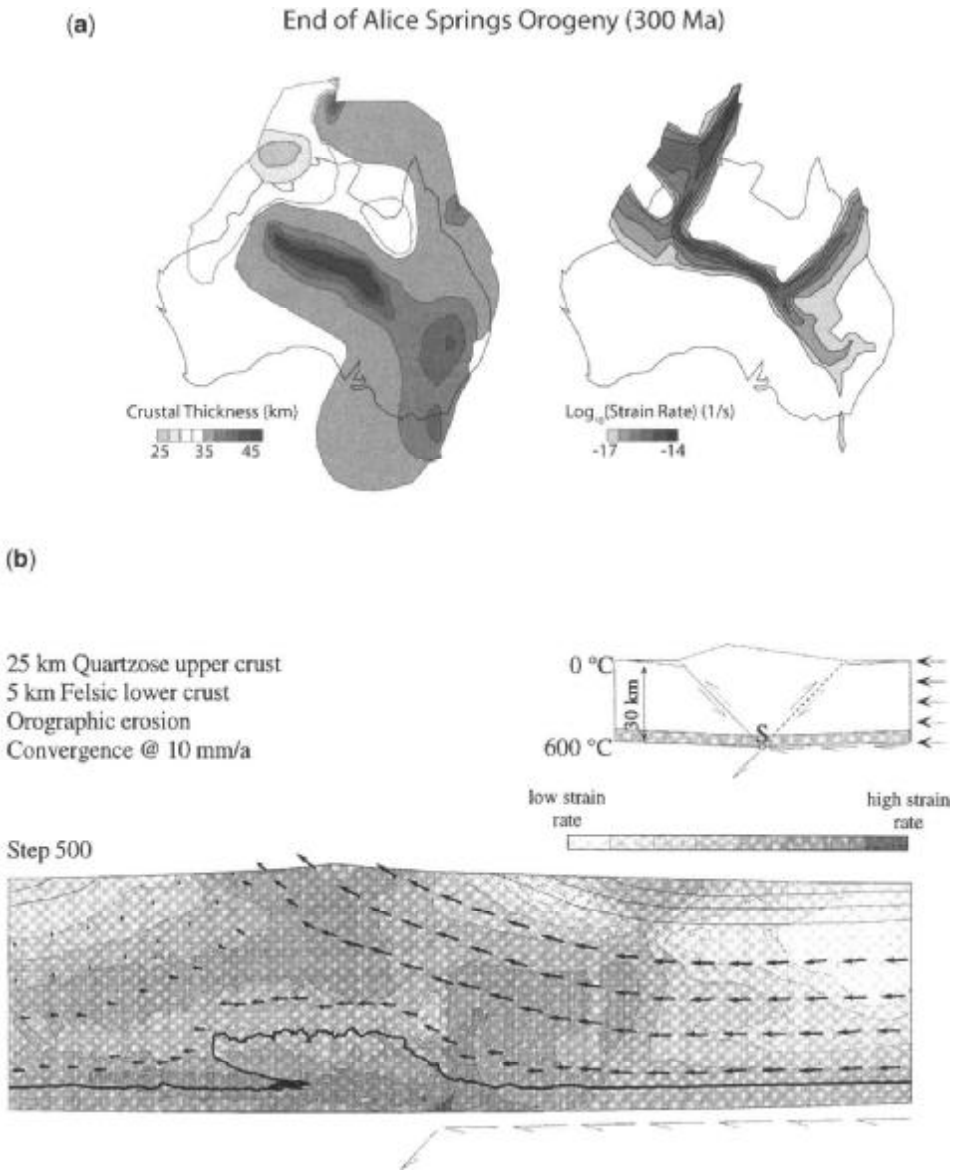


**Fig. 6.** Results of fully coupled erosion-tectonic models. (**a**) A model for the Palaeozoic deformation of the Australian continent based on thin sheet approximation and coupled to a LEM; the feedback from erosion to tectonics is through variations in pressure and temperature within the lithosphere that lead to variations in strength (from Braun & Shaw 2001); at this scale, it is assumed that surface mass transport is linearly related to slope; variations in crustal thickness are the result of the time-integrated deformation of the lithosphere whereas strain rate is a measure of instantaneous deformation; the predictions of the model are shown near the end of the Palaeozoic Alice Springs Orogeny. (**b**) A sophisticated 2D vertical tectonic model in which the solution of the equation of force balance in a visco-elasto-plastic material is used to predict horizontal and vertical tectonic transport; it has been linked to a 1D LEM in which river incision and hill slope diffusion have been incorporated; an orographically-controlled precipitation function can also be activated to include the feedback from tectonics unto local climate; at this stage in the evolution of the model total convergence is 50 km, i.e., approximately twice the thickness of the crust (from Batt & Braun 1999).

the spatial discretization (Garcia-Castellanos 2002). In models where an irregular discretization of space is used, this problem can easily be overcome (Braun & Sambridge 1997; Willett *et al.* 2001).

Finally, it is worth mentioning here a recent attempt at coupling a numerical model of landscape evolution with an analogue model of crustal deformation (Persson *et al.* 2004). In this later approach, a 'sandbox' analog model is used to represent the internal deformation of the Earth's crust under the forcing of imposed displacements along its side or bottom boundaries. The geometry of the deformed surface is

carefully measured and used to determine an uplift function that is then introduced in a landscape evolution model. The LEM is used to compute the evolution of the surface over an interval of time equivalent to the scaled time step of the laboratory experiment by a combination of fluvial and hill-slope processes. The resulting change in surface topography is imposed onto the surface of the sandbox model by carefully removing sand grains with a small vacuum pump.

## Constraining the rate of landscape evolution

One of the major issues facing LEMs concerns their prediction capability: we do not know the value of the rate parameters entering the geomorphological laws (e.g., $K_f$, $K_t$, $K_d$, $K_v$, $K_w$ and $K_g$) with enough accuracy to ensure that the model predictions can be trusted in absolute terms. In Table 1, I give a range of values derived by selected authors for some of these rate constants, demonstrating how poorly constrained they commonly are. In fact, we still lack a basic understanding of the long-term processes at play during the carving of a landform to state with confidence the time it takes to achieve it. Commonly, parameter values are chosen from empirical considerations, from rate measurements at the human scale or in such a way that the LEMs predictions compare well to first-order rate observations, like catchment integrated erosion rates (Summerfield & Hulton 1994). These approaches require an extrapolation in space and time that is often difficult to justify.

Several recent studies (Stock & Montgomery 1999; van der Beek & Bishop 2003; Tomkin *et al.* 2003) have attempted to provide quantitative constraints on the rate of landscape evolution on geological time scales with the use of a variety of geochronological methods. Notably, Stock and Montgomery (1999) and, more recently, van der Beek and Bishop (2003), used well dated basaltic flows to define the initial geometry of the present-day landform in southeastern Australia (Stock & Montgomery 1999; van der Beek & Bishop 2003), Hawaii, Japan and California (Stock & Montgomery 1999) and, from it, a first-order estimate of the rate at which the system evolved. van der Beek and Bishop (2003) provided estimates of the fluvial incision constants in agreement with a previous study in the same area (van der Beek & Braun 1998). Similarly, Tomkin *et al.* (2003) combined a study of fluvial terraces with low temperature thermochronological data to obtain a good estimate of incision rates along the Clearwater River in the northwestern USA. They provided some constraints on the value of fluvial incision parameters but also concluded that many of the parameterizations were incapable of describing the evolution of the landform within realistic bounds.

The advent of the low-temperature apatite (U-Th)/He chronometer has driven a series of studies to determine the age of a variety of landforms (House *et al.* 1998, 2001; Reiners *et al.* 2003*a*, *b*). Good summaries of how the thermochronometer can be used to constrain the rate of landform evolution can be found in Braun (2002*b*, 2005) and Ehlers and Farley (2003). The use of cosmogenic isotopes has also flourished to determine current, instantaneous rate of erosion (Cerling & Craig 1994). In the following sections I provide two examples of how these dating methods have been used to derive quantitative constraints on the rate of landform evolution.

### *Low-T thermochronology*

The perturbation caused by a finite amplitude topography on the thermal structure of the

**Table 1.** *Values of the constants appearing in the equations*

| Parameter | Value | Reference |
|---|---|---|
| $K_f$ | $10^{-7} - 10^{-2}$ m$^{0.2}$/yr (for $m = 0.3$–$0.5$ and $n = 1$) | Stock & Montgomery 1999 |
| $l_f$ | 5–30 km | van der Beek & Bishop 2003 |
| $K_d$ | $10^{-4} - 1$ m$^2$/yr | Martin 2000; Braun *et al.* 2001 |
| $K_v$ | $1 - 3 \times 10^{-3}$ m$^{2-m'}$/yr | Braun *et al.* 2001 |
| $K_w$ | $1 - 3 \times 10^{-2}$ m$^{2-2k}$/yr | Braun *et al.* 2001 |
| $K_g$ | 0.01 – ? (poorly constrained) | Tomkin & Braun 2002 |
| $P_0$ | 50–200 m/Ma | Heimsath *et al.* 1999, 2000; Dietrich *et al.* 1995 |
| $\xi_f$ | 45–50 cm | Heimsath *et al.* 1999, 2000 |

Values from a limited number of sources, demonstrating how variable and/or poorly constrained these values are.

underlying crust is a function of the wavelength of the topography. More precisely, the perturbation decreases exponentially with depth over a depth range that is equal to the wavelength of the topography (Turcotte & Schubert 1982). Braun (2002*a*) demonstrated that by considering the relationship between age and elevation as a function of wavelength, one can extract independent information on the mean rate of rock exhumation and the rate of landform evolution.

For most thermochronological systems, the 'age' of a rock corresponds to the time in the past when the rock cooled through the so-called 'closure temperature'. This temperature is different for each dating method; for example, it ranges from 65° to 85°C for (U-Th)/He dating in apatite. Considering an age-elevation profile at short wavelength, one can assume that, because the depth of the isotherm corresponding to the closure temperature is constant across the profile, the variation in age is directly proportional to the rate of rock exhumation and cooling through the closure temperature isotherm. Conversely, at long wavelength, isotherms should perfectly follow the shape of the landscape and there should be no variation of age with elevation, unless the shape of the landform has changed since the rocks cooled through the closure temperature isotherm. Any variation of age with elevation at long wavelength can thus be interpreted as an indication that the relief has increased (in the case of a positive age-elevation slope) or decreased (in the case of a negative slope) (Braun 2002*a*).

Accurate estimates of both mean exhumation rate and rate of landform evolution can be derived from appropriately sampled age-elevation profiles by performing a spectral analysis on the datasets. A so-called 'gain function' can be calculated as the complex ratio between the age and elevation spectra. At short wavelength, the inverse of the gain function value is directly proportional to the mean exhumation rate. The ratio of short to long wavelength gain values provides an estimate of the change in relief between the time corresponding to the mean age along the profile and today (Braun 2002*a*).

This method has been used to derive estimates of the amount of relief loss in the Sierra Nevada since the end of the Laramide Orogeny (Braun 2002*a*), based on (U-Th)/He datasets collected in the area by House *et al.* (1998). The results clearly demonstrated that the larger features of the landscape, including the 30 km-wide Kings Canyon, are indeed very old (60–70 Ma) and that, since the end of the Laramide Orogeny, relief amplitude has decreased by a factor of approximately 2. Plotting the age and elevation datasets along the profile (Fig. 7) clearly demonstrates that there is a strong positive correlation between the two at short wavelength and a clear anti-correlation at longer wavelength. The method was also used to determine the rate of relief evolution in the Dabie Shan of Eastern China (Braun & Robert 2005), confirming that the present-day relief in the area is also relatively old and results from the isostatically-compensated, erosional decay of a late Cretaceous mountain belt.

Braun and van der Beek (2004) also used low-temperature thermochronological data from a transect across the marginal escarpment of south-eastern Australia to demonstrate that this geomorphic feature formed very rapidly to reach its present-day position within 15 Ma of the onset of rifting, some 90 Ma ago and has since remained relatively stable. Braun and van der Beek (2004) also demonstrated that the existing thermochronological data cannot be used to differentiate between competing scenarios for the evolution of the escarpment.

More recently, Herman and Braun (2005) and Herman *et al.* (2005) have used (U-Th)/He dating in zircon and apatite to determine the rate of landform evolution in an extremely active tectonic environment, along the west coast of the South Island, New Zealand. They demonstrated that the high relief glaciated landscape that forms on the east side of the main divide is tectonically advected towards the west coast where it is

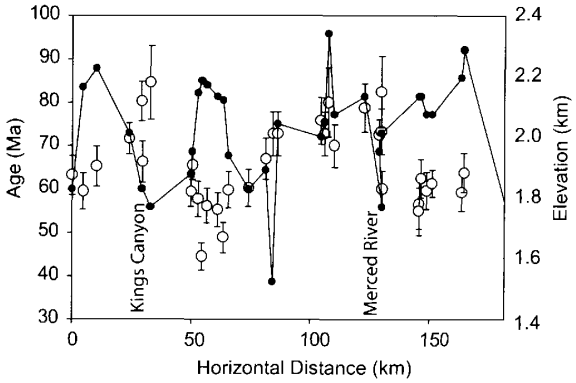


**Fig. 7.** Age and elevation along a linear profile in the Sierra Nevada, California (from House *et al.* 1998) clearly showing a positive correlation between (U-Th)/He apatite age (white circles) and elevation (black circles) along the narrow features of the landform and a negative correlation across the broader features. This data can be interpreted to demonstrate that the large-scale features of the landform are very old and that relief amplitude has decreased by a factor 2 over the past 60 Ma (Braun 2002*a*).

rapidly transformed into its present-day form. The very young ages and their relationship to elevation suggest that the reshaping of the landform from long, linear, flat-bottom glacial troughs into V-shaped graded river valleys is a relatively rapid process that takes place on a scale of less than 100 thousand years.

These various studies have further demonstrated that there exists a wide range of rates at which landforming processes operate and that the main factor controlling this rate is clearly related to tectonic uplift. Indeed, in regions of low tectonic activity, such as in the Sierra Nevada (House *et al.* 1998; Braun 2002*a*), the Dabie Shan (Reiners *et al.* 2003*b*; Braun & Robert 2005) or along the escarpments of southeastern Australia (Persano *et al.* 2002; Braun & van der Beek 2004) or southern Africa (Brown *et al.* 2002; van der Beek *et al.* 2002), very old landforms, i.e., 10 to 100 Ma old, are preserved. Despite their age, they can be characterized by very large local relief – several thousand meters in the Sierra Nevada. At the other end of the spectrum, in regions of high tectonic uplift, erosion processes can rejuvenate a landform on a much smaller time scale (Herman *et al.* 2005), i.e., of the order of 1 Ma or less. This implies that erosional systems must be characterized by a threshold beyond which their efficiency is greatly enhanced. This threshold could take the form of a mean critical slope beyond which the frequency of landslides increases (Montgomery & Brandon 2002).

### *Cosmogenic isotopes*

Cosmogenic isotopes ($^{10}$Be, $^{26}$Al in quartz, $^{36}$Cl in calcite, Kfeldspar and whole rock samples, and $^{3}$He and $^{21}$Ne in olivine and feldspar) are formed by high energy cosmic ray reactions in the uppermost 1–2 m of the crust (Cerling & Craig 1994). Isotope production rates depend strongly on depth, hence isotope accumulation reflects a sample's shielding history in the uppermost crust. Where a sample's exposure geometry was altered instantaneously by a geomorphic event (a landslide, fault rupture, etc.), cosmogenic isotopes provide age information. Where a geomorphic process continuously alters a sample's depth, the process rate can be determined from cosmogenic isotope data via a model of the balance between local erosion rate and *in situ* isotope production (Cerling & Craig 1994; Bierman 1994).

*In situ* cosmogenic isotope concentrations have thus been used to determine the rate of soil production (Heimsath *et al.* 2000). Combining such data with morphometric measurements at two locations (southwestern California and southeastern Australia), Braun *et al.* (2001) have provided constraints on the various parameters entering the laws controlling soil transport. In their study, Braun *et al.* (2001) used a two-dimensional finite volume model to predict the relationship between soil thickness and topographic surface curvature, using the cosmogenic data to constrain a production function, in which production decreases exponentially with soil thickness (Heimsath *et al.* 2000). The results were compared to measurements of soil thickness and surface curvature to provide direct constraints on the efficiency of each of the mechanisms assumed to be efficient at transporting soil on soil-mantled hill slopes, on the residence time of the soil on the landscape, and on the response time of the system to rapidly changing environmental conditions.

Cosmogenic isotopes have been used to constrain the rate of landform evolution in a range of settings, including, for example, glaciated landscapes (Stroeven *et al.* 2002). They are commonly used to date fluvial terraces (Hancock *et al.* 1999). See Duller (2000) for a short review of the method and its application to geomorphology.

## Current and outstanding problems

### *Parameterization and scaling*

The most pressing problem in the development and use of landscape evolution models is the formulation of a widely accepted parameterization of the basic processes at play during erosion, transport and deposition. Unlike tectonic models that are based on the solution of Newton's laws of force balance, there is no consensus in the field of geomorphology about the fundamental equations that should be used to represent, for example, the physical processes of fluvial erosion. Should we use the stream power law? Should we include a carrying capacity term or introduce a threshold to represent the strength of the bedrock? What form of the soil transport law should we use? How do we parameterize landsliding, chemical erosion, or eolian transport? Note that it is not just the value of the various parameters that is unknown, it is also the form of the equations to solve that remains uncertain.

Potentially, this lack of simple or uniformally accepted parameterization is a reflection of the wide range of processes involved in the formation of landforms. Which is most important certainly depends on environmental conditions including climate, vegetation, tectonic setting,

etc. It might therefore be utopian to believe that a single parameterization could ever represent all processes efficiently and/or accurately. On the other hand, this state of affairs may also be the result of how the field of quantitative or predictive geomorphology has evolved from its observational and empirical beginnings. Most of the laws we use have been constructed to represent physical processes at the human scale. The extrapolation to longer scales has been done with little justification. Thankfully, work is already under way (e.g., see Davy & Crave 2000; or Martin & Church 2004) to understand how this scaling may be done with more rigour, which, ultimately, may lead to the formulation of equations that have only little resemblance to the 'classical' geomorphic laws but are more appropriate to describe the system over long timescales. Of particular interest in the formulation of these more fundamental parameterizations, are the effects of infrequent but significant (large) events such as floods or mega-size landslides on the long-term evolution of the landform (Lague *et al.* 2003).

### *Thermochronology: sampling strategy*

Geochronology, and in particular thermochronology, are the most widely used tools to determine the rate of Earth processes. The use of these techniques was, until recently, confined to the field of tectonics. The development of accurate low-temperature thermochronometers has opened the door to a broader use of these techniques and, potentially, will permit the quantification of the rate of landform evolution. Unfortunately, as shown by Braun (2002*a*) and Braun and van der Beek (2004), sampling strategies developed to study tectonic processes are usually incompatible with those necessary to document erosional processes. Typically, to constrain tectonic systems, rocks are collected along transects that run perpendicular to the main controlling structure, whereas to estimate the rate of river incision in an active tectonic setting, rocks need to be collected along a profile parallel to the main controlling structure to ensure not only that the mean exhumation rate is uniform along the transect, but also to sample the relief at the most meaningful wavelengths. To date, very few datasets exist that satisfy this requirement.

## Future work

### *More efficient algorithms*

Despite ever-increasing computer power, there is a need to continue developing efficient algorithms to solve the complex geomorphic equations for the following two reasons: (1) to test the validity of scaled laws and the importance of critical but rare events requires a very fine spatial and temporal discretization; (2) to determine the sensitivity of LEMs behaviour to variations in relatively poorly constrained parameters requires that large numbers of model runs be performed. Ideally, in cases where thermochronological and morphometric datasets exist and are used to constrain the value of model parameters, a proper inversion procedure should be used (van der Beek & Braun 1998; van der Beek & Bishop 2003; Tomkin *et al.* 2003; Braun & van der Beek 2004); it commonly requires that thousands to tens of thousands of LEM runs be executed, in order to adequately sample parameter space in all directions.

The most challenging part of these computations is to calculate the geometry of catchments and compute sediment flux by integration of upstream erosion/sedimentation rate. Ranking of the discrete topographic heights is the most commonly used algorithm (Beaumont *et al.* 1992), but it becomes rather inefficient for very large problems. Others have opted for a stochastic approach that does not require the explicit computation of catchment geometry (Chase 1992; Crave & Davy 2001) but cannot be used to estimate upstream sediment flux. With the increase availability of parallel computers, there is a need to develop a parallelized version of a dynamic network routing algorithm to compute drainage networks and the geometry of catchments.

### *3D tectonic models*

The study of the coupling between erosion and tectonics has been limited so far by the simplifying assumption of two dimensionality in the vertical or horizontal direction. To fully comprehend the complex interactions between surface processes and tectonics requires the solution of the force balance equation in three dimensions. Surface processes are strongly affected by subtle variations in the distribution of uplift. Long-range interaction mechanisms, such as channel incision and fluvial transport, may lead to efficient mass redistribution on the landscape, which will produce important pressure gradients in the underlying lithosphere. Thus the feedback or coupling between erosion and tectonics cannot, in principle, be averaged in any particular direction.

Because most thrust faults have a gentle dip, horizontal advection must play as important a role as tectonic uplift in regions of continental

convergence. Horizontal advection of landforms by tectonic movement across faults or drainage divides has so far been neglected or treated empirically. The accuracy of the methods used needs first to be established. Most would agree that, in nature, the processes involved are discrete: a drainage divide may be redefined during a landslide and drainage reorganization may take place during a single slip event on a fault. The behaviour of these systems will therefore depend on the stochastic nature of these processes, which needs to be better defined.

### *Define target areas where the efficiency of the coupling can be estimated*

Finally, one must be reminded that the demonstration that a coupling between erosion and tectonics exists has so far been limited to the results of computer modelling of the system. As amply demonstrated in a collection of jointly published papers (Reiners *et al.* 2003*a*; Burbank *et al.* 2003; Dadson *et al.* 2003), our efforts to document this coupling in nature have been rather inconclusive. The most pressing development to improve our understanding of the lithosphere–hydrosphere system might be the definition of a natural situation where the efficiency of the mechanisms we invoke can be measured or estimated independently. For example, a good situation to document might be a long compressional orogen in which one of the two driving mechanisms (erosion or tectonics) is clearly uniform and constant and where the other varies along strike. The two key elements in the selection of such a natural laboratory will be (1) the ability to discern between causes and effects and (2) the ability to describe a system that is not at steady-state.

The author wishes to thank Y. Martin, D. Stolar and an anonymous reviewer for very constructive comments on an earlier version of this manuscript.

## References

ANHERT, F. 1967. The role of the equilibrium concept in the interpretation of landforms of fluvial erosion and deposition. *In*: MACAR, P. (ed.) *L'Evolution des versants*. Université de Liège, Belgium, 22–41.

BATT, G. E. & BRAUN, J. 1999. The tectonic evolution of the Southern Alps, New Zealand: insights from fully thermally coupled dynamical modelling. *Geophysical Journal International*, **136**, 403–420.

BEAUMONT, C., FULLSACK, P. & HAMILTON, J. 1992. Erosional control of active compressional orogens. *In*: MCCLAY, K. R. (ed.) *Thrust Tectonics*. Chapman and Hall, New York, 1–18.

BEAUMONT, C., JAMIESON, R., NGUYEN, M. & LEE, B. 2001. Himalayan tectonics explained by extrusion of a low-viscosity crustal channel coupled to focused surface denudation. *Nature*, **414**, 738–742.

BEAUMONT, C., JAMIESON, R., NGUYEN, M. & MEDVEDEV, S. 2004. Crustal channel flows: 1. Numerical models with applications to the tectonics of the Himalayan-Tibetan orogen. *Journal of Geophysical Research*, **109**(B06406): DOI 10.1029/2003JB002809.

BEAUMONT, C., KAMP, P., HAMILTON, J. & FULLSACK, P. 1996. The continental collision zone, South Island, New Zealand: comparison of geodynamical models and observations. *Journal of Geophysical Research*, **101**, 3333–3359.

BEAUMONT, C., KOOI, H. & WILLETT, S. 1999. Coupled tectonic-surface process models with applications to rifted margins and collisional orogens. *In*: SUMMERFIELD, M. (ed.) *Geomorphology and Global Tectonics*. John Wiley and Sons Ltd, New York, 29–55.

BIERMAN, P. 1994. Using in situ produced cosmogenic isotopes to estimate rates of landscape evolution: a review from the geomorphic perspective. *Journal of Geophysical Research*, **99**, 13885–13896.

BRAUN, J. 2002*a*. Estimating exhumation rate and relief evolution by spectral analysis of age-elevation datasets. *Terra Nova*, **14**, 210–214.

BRAUN, J. 2002*b*. Quantifying the effect of recent relief changes on age-elevation relationships. *Earth and Planetary Sciences Letters*, **200**, 331–343.

BRAUN, J. 2005. *Thermochronology*, MSA-RiMG, in press.

BRAUN, J. & ROBERT, X. 2005. Constraints on the rate of post-orogenic erosional decay from thermochronological data: example from the Dabie Shan, China. *Earth Surface Processes and Landforms*, **30**, 1203–1225.

BRAUN, J. & SAMBRIDGE, M. 1994. Dynamical Lagrangian remeshing (DLR): a new algorithm for solving large strain deformation problems and its application to fault-propagation folding. *Earth and Planetary Sciences Letters*, **124**, 211–220.

BRAUN, J. & SAMBRIDGE, M. 1997. Modelling landscape evolution on geological time scales: a new method based on irregular spatial discretization. *Basin Research*, **9**, 27–52.

BRAUN, J. & SHAW, R. 2001. A thin-plate model of Palaeozoic deformation of the Australian lithosphere: implications for understanding the dynamics of intracratonic deformation. *In*: MILLER, J., HOLDSWORTH, R., BUICK, I. & HAND, M. (eds) *Continental Reactivation and Reworking*. Geological Society, London, Special Publications **184**, 165–193.

BRAUN, J. & VAN DER BEEK, P. 2004. Evolution of passive margin escarpments: what can we learn from low-temperature thermochronology? *Journal of Geophysical Research*, **109**, F04009, DOI 10.1029/2004JF000147.

BRAUN, J., HEIMSATH, A. & CHAPPELL, J. 2001. Sediment transport mechanisms on soil-mantled hillslopes. *Geology*, **29**, 683–686.

BRAUN, J., ZWARTZ, D. & TOMKIN, J. 1999. A new surface processes model combining glacial and fluvial erosion. *Annals of Glaciology*, **28**, 282–290.

BROWN, R., SUMMERFIELD, M. & GLEADOW, A. 2002. Denudational history along a transect across the Drakensberg Escarpment of southern Africa derived from apatite fission track thermochronology. *Journal of Geophysical Research*, **107**, 2350, DOI 10.1029/2001JB000745.

BURBANK, D. & PINTER, N. 1999. Landscape evolution: the interactions of tectonics and surface processes. *Basin Research*, **11**, 1–6.

BURBANK, D., BLYTHE, A. *ET AL.* 2003. Decoupling of erosion and precipitation in the Himalayas. *Nature*, **426**, 652–655.

CERLING, T. & CRAIG, H. 1994. Geomorphology and in-situ cosmogenic isotopes. *Annual Review of Earth and Planetary Sciences*, **22**, 273–317.

CHAMPEL, B., VAN DER BEEK, P., MUGNIER, J. & LETURMY, P. 2002. Uplift and lateral propagation of fault-related folds in the Siwalik foothills, Nepal Himalaya: rates, mechanisms, and geomorphic signature. *Journal of Geophysical Research*, **107**, 2111, DOI 10.1029/2001JB000578.

CHASE, C. 1992. Fluvial landscuplting and the fractal dimension of topography. *Geomorphology*, **5**, 39–57.

CLARK, M. & ROYDEN, L. 2000. Topographic ooze: Building the eastern margin of Tibet by lower crustal flow. *Geology*, **28**, 703–706.

CLARKE, M., WILLIAMS, M. & STOKES, T. 1999. Soil creep: problems raised by a 23 year study in Australia. *Earth Surface Processes and Landforms*, **24**, 151–175.

COULTHARD, T. J. 2001. Landscape evolution models: a software review. *Hydrological Processes (HP Today)*, **15**, 165–173.

COULTHARD, T., KIRKBY, M. & MACKLIN, M. G. 1997. Modelling hydraulic, sediment transport and slope processes, at a catchment scale, using a cellular automaton approach. *In*: PASCOE, R. (ed.) *Proceedings of the Second Annual Conference: GeoComputation 97*. University of Otago, Dunedin, New Zealand, 309–318.

CRAVE, A. & DAVY, P. 2001. A stochastic 'precipiton' model for simulating erosion/sedimentation dynamics. *Computers and Geosciences*, **27**, 815–827.

CRAVE, A., LAGUE, D., DAVY, P., KERMARREC, J.-J., SOKOUTIS, D., BODET, L. & COMPAGNON, R. 2000. Analogue modelling of relief dynamics. *Physics and Chemistry of the Earth*, **6–7**, 549–553.

DADSON, S., HOVIUS, N. *ET AL.* 2003. Links between erosion, runoff variability and seismicity in the Taiwan orogen. *Nature*, **426**, 648–651.

DAHLEN, F. 1984. Noncohesive critical Coulomb wedges: an exact solution. *Journal of Geophysical Research*, **89**, 10125–10133.

DAVY, P. & CRAVE, A. 2000. Upscaling local-scale transport processes in large-scale relief dynamics. *Physics and Chemistry of the Earth*, **25**, 533–541.

DENSMORE, A., DAWERS, N., GUPTA, S., GUIDON, R. & GOLDIN, T. 2004. Footwall topographic development during continental extension. *Journal of Geophysical Research*, **109**, F03001, DOI 10.1029/2003JF000115.

DENSMORE, A., ELLIS, M. & ANDERSON, R. 1998. Landsliding and the evolution of normal-fault-bounded mountains. *Journal of Geophysical Research*, **103**, 15203–15219.

DIETRICH, W., BELLUGI, D., SKLAR, L., STOCK, J., HEIMSATH, A. & ROERING, J. 2003. Geomorphic transport laws for predicting landscape form and dynamics. *In*: WILCOCK, P. & IVERSON, R. (eds) *Prediction in Geomorphology. Geophysical Monograph*, American Geophysical Union, Washington, DC, **135**, DOI 10.1029/135GM09.

DIETRICH, W., REISS, R., HSU, M.-L. & MONTGOMERY, D. 1995. A process-based model for colluvial soil depth and shallow landsliding using digital elevation data. *Hydrological Processes*, **9**, 383–400.

DULLER, G. 2000. Dating methods: geochronology and landscape evolution. *Progress in Physical Geography*, **24**, 111–116.

EHLERS, T. & FARLEY, K. 2003. Apatite (U-Th)/He thermochronometry: methods and applications to problems in tectonic and surface processes. *Earth and Planetary Sciences Letters*, **206**, 1–14.

ELLIS, S. 1995. *Continental convergence: length scales, aspect ratios, and styles of crustal deformation*. PhD thesis, Dalhousie University, HALIFAX, NS, Canada.

GARCIA-CASTELLANOS, D. 2002. Interplay between lithospheric flexure and river transport in foreland basins. *Basin Research*, **14**, 89–104.

HALLETT, B. 1979. A theoretical model of glacial abrasion. *Journal of Glaciology*, **89**, 39–50.

HANCOCK, G., ANDERSON, R., CHADWICK, O. & FINKEL, R. 1999. Dating fluvial terraces with $^{10}$Be and $^{26}$Al profiles: application to the Wind River, Wyoming. *Geomorphology*, **27**, 41–60.

HARBOR, J. 1992. Numerical modelling of the development of U-shaped valleys by glacial erosion. *Geological Society of America Bulletin*, **104**, 1364–1375.

HEIMSATH, A., CHAPPELL, J., DIETRICH, W., NISHIIZUMI, K. & FINKEL, R. 2000. Soil production on a retreating escarpment in southeastern Australia. *Geology*, **28(9)**, 787–790.

HEIMSATH, A., CHAPPELL, J., DIETRICH, W., NISHIIZUMI, K. & FINKEL, R. 2001. Late Quaternary erosion in southeastern Australia: a field example using cosmogenic nuclides. *Quaternary International*, **83(5)**, 169–185.

HEIMSATH, A., DIETRICH, W., NISHIIZUMI, K. & FINKEL, R. 1999. Cosmogenic nuclides, topography, and the spatial variation of soil depth. *Geomorphology*, **27**, 151–172.

HERMAN, F. & BRAUN, J. 2005. Fluvial response to horizontal shortening and glaciations: a study in the Southern Alps of New Zealand. *Journal of Geophysical Research*, in press.

HERMAN, F., BRAUN, J. & DUNLAP, W. 2005. Low temperature themochronology to constrain the tectono-morphic evolution of the Southern Alps

of New Zealand. *Journal of Geophysical Research*, in press.

HILLEY, G. & STRECKER, M. 2004. Steady-state erosion of critical Coulomb wedges with application to Taiwan and the Himalaya. *Journal of Geophysical Research*, **109**, B01411-10.1029/2002JB002284.

HODGES, K., HURTADO, J. & WHIPPLE, K. 2001. Southward extrusion of Tibetan crust and its effect on Himalayan tectonics. *Tectonics*, **20**, 799–809.

HOUSE, M., WERNICKE, B. & FARLEY, K. 1998. Dating topography of the Sierra Nevada, California, using apatite (U-Th)/He ages. *Nature*, **396**, 66–69.

HOUSE, M., WERNICKE, B. & FARLEY, K. 2001. Paleogeomorphology of the Sierra Nevada, California, from (U-Th)/He ages in apatite. *American Journal of Science*, **301**, 77–102.

HOVIUS, N., STARK, C. & ALLEN, P. 1997. Sediment flux from a mountain belt derived from landslide mapping. *Geology*, **25(3)**, 231–234.

HOVIUS, N., STARK, C., HAO-TSU, C. & JIUM-CHUAN, L. 2000. Supply and removal of sediment in a landslide-dominated mountain belt: Central Range, Taiwan. *Journal of Geology*, **108**, 73–89.

HOWARD, A. 1994. A detachment–limited model of drainage basin evolution. *Water Resources Research*, **30(7)**, 2261–2285.

HUTTER, K. 1981. The effect of longitudinal stress on the shear stress of an ice sheet: in defence of using stretched co-ordinates. *Journal of Geology*, **27**, 39–56.

JAMIESON, R., BEAUMONT, C., MEDVEDEV, S. & NGUYEN, M. 2004. Crustal channel flows: 1. Numerical models with implications for metamorphism in the Himalayan-Tibetan orogen. *Journal of Geophysical Research*, **109** (B06407): DOI 10.1029/2003JB002811.

JOHNSON, D. & BEAUMONT, C. 1995. Preliminary results from a planform kinematic model of orogen evolution, surface processes, and the development of clastic foreland basin stratigraphy. *In*: DOROBEK, S. & ROSS, G. (eds) *SEPM Special Publication on Stratigraphic Evolution of Foreland Basins*, 3–24.

KAUFFMAN, G. & BRAUN, J. 2001. Modelling karst denudation on a synthetic landscape. *Terra Nova*, **36**, 1381–1391.

KOOI, H. & BEAUMONT, C. 1994. Escarpment evolution on high-elevation rifted margins: insights derived from a surface processes model that combines diffusion, advection and reaction. *Journal of Geophysical Research*, **99**, 12191–12209.

KOONS, P. 1990. Two-sided orogen: collision and erosion from the sandbox to the Southern Alps, New Zealand. *Geology*, **18**, 679–682.

KOONS, P. 1994. Three-dimensional critical wedges: Tectonics and topography in oblique collisional orogens. *Journal of Geophysical Research*, **99**, 12301–12315.

KOONS, P., ZEITLER, P., CHAMBERLAIN, C., CRAW, D. & MELZER, A. 2002. Mechanical links between erosion and metamorphism in Nanga Parbat, Pakistan Himalaya. *American Journal of Science*, **302**, 749–773.

LAGUE, D., CRAVE, A. & DAVY, P. 2003. Laboratory experiments simulating the geomorphic response to tectonic uplift. *Journal of Geophysical Research*, **108**, 10.1029/2002JB001785.

MACGREGOR, K., ANDERSON, R., ANDERSON, S. & WADDINGTON, E. 2000. Numerical simulations of glacial-valley longitudinal profile evolution. *Geology*, **28**, 1031–1034.

MARTIN, Y. 2000. Modelling hillslope evolution: linear and nonlinear transport relations. *Geomorphology*, **34**, 1–21.

MARTIN, Y. & CHURCH, M. 2004. Numerical modelling of landscape evolution: geomorphological perspectives. *Progress in Physical Geography*, **28**, 317–339.

MOLNAR, P. & ENGLAND, P. 1990. Late Cenozoic uplift of mountain ranges and global climate change: chicken and egg? *Nature*, **346**, 29–34.

MONTGOMERY, D. & BRANDON, M. 2002. Topographic control on erosion rates in tectonically active mountain ranges. *Earth and Planetary Sciences Letters*, **201**, 481–489.

MOORE, I. & BURCH, G. 1986. Sediment transport capacity of sheet and rill flow: application of unit stream power theory. *Water Resources Research*, **22**, 1350–1360.

OLSON, R. 1973. *Essentials of Engineering Fluid Mechanics*. 3rd edn, Feefer and Simons International University Editions, New York.

PERSANO, C., STUART, F., BISHOP, P. & BARFORD, D. 2002. Apatite (U-Th)/He age constraints on the development of the Great Escarpment on the southeastern Australian passive margin. *Earth and Planetary Sciences Letters*, **200**, 79–90.

PERSSON, K., GARCIA-CASTELLANOS, D. & SOKOUTIS, D. 2004. River transport effects on compressional belts: first results from an integrated analogue-numerical model. *Journal of Geophysical Research*, **109**, DOI 10.1029/2002JB002274.

PROSSER, I. & RUSTOMJI, P. 2000. Sediment transport capacity relations for overland flow. *Progress in Physical Geography*, **24**, 179–193.

REINERS, P., EHLERS, T., MITCHELL, S. & MONTGOMERY, D. 2003*a*. Coupled spatial variations in precipitation and long-term erosion rates across the Washington Cascades. *Nature*, **426**, 645–647.

REINERS, P., ZHOU, Z., EHLERS, T., XU, C., BRANDON, M., DONELICK, R. & NICOLESCU, S. 2003*b*. Post-orogenic evolution of the Dabie Shan, eastern China, from (U-Th)/He and fission-track thermochronology. *American Journal of Science*, **303**, 489–518.

ROE, G., STOLAR, D. & WILLETT, S. 2005. The sensitivity of a critical wedge orogen to climatic and tectonic forcing. *In*: WILLETT, S., HOVIUS, N., BRANDON, M. & FISHER, D. (eds) *Tectonics, Climate, and Landscape Evolution*, Geological Society of America, Special Publication.

ROERING, J., KIRCHNER, J. & DIETRICH, W. 1999. Evidence for a non-linear, diffusive sediment transport on hillslopes and implications for landscape

evolution. *Water Resources Research*, **35(3)**, 853–870.

ROERING, J., KIRCHNER, L., SKLAR, J. & DIETRICH, W. 2000. Hillslope evolution by nonlinear creep and landsliding: an experimental study. *Geology*, **29(2)**, 143–146.

ROYDEN, L. 1996. Coupling and decoupling of crust and mantle in convergent orogens: implications for strain partitioning in the crust. *Journal of Geophysical Research*, **101**, 17679–17705.

SCHOORL, J., SONNEVELD, M. & VELDKAMP, A. 2000. Three-dimensional landscape process modelling: the effect of DEM resolution. *Earth Surface Processes and Landforms*, **25**, 1025–1034.

SIMPSON, G. 2004. A dynamic model to investigate coupling between erosion, deposition, and three-dimensional (thin-plate) deformation. *Journal of Geophysical Research*, **109**, F02006. DOI 10.1029/2003JF000078.

SIMPSON, G. & SCHLUNEGGER, F. 2003. Topographic evolution and morphology of surfaces evolving in response to coupled fluvial and hillslope sediment transport. *Journal of Geophysical Research*, **108**, F02300, DOI 10.1029/2002JB002162.

SKLAR, L. & DIETRICH, W. 1998. River longitudinal profiles and bedrock incision models: stream power and the influence of sediment supply. *In*: TINKLER, K. & WOHL, E. (eds) *Rivers over Rock: Fluvial Processes in Bedrock Channels*. Geophysical Monograph, American Geophysical Union, Washington, D.C., 237–260.

STOCK, J. & MONTGOMERY, D. 1999. Geologic constraints on bedrock river incision using the stream power law. *Journal of Geophysical Research*, **104**, 4983–4993.

STOLAR, D., ROE, G. & WILLETT, S. 2005. Evolution of a critical orogen under various forcing scenarios: findings from a numerical sandbox. *In*: WILLETT, S., HOVIUS, N., BRANDON, M. & FISHER, D. (eds) *Tectonics, Climate, and Landscape Evolution*. Geological Society of America, Special Publication.

STROEVEN, A., FABEL, D., HATTESTRAND, C. & HARBOR, J. 2002. A relict landscape in the centre of Fennoscandian glaciation: cosmogenic radionuclide evidence of tors preserved through multiple glacial cycles. *Geomorphology*, **44**, 145–154.

SUMMERFIELD, M. & HULTON, N. 1994. Natural controls of fluvial denudation rates in major world drainage basins. *Journal of Geophysical Research*, **99**, 13871–13883.

TOMKIN, J. 2000. *Landforming processes in glaciated orogens: a numerical study*. PhD thesis, the Australian National University, Canberra, ACT, Australia.

TOMKIN, J. & BRAUN, J. 2002. The effect glaciation has on the relief of a fast growing orogen: a numerical modelling study. *American Journal of Science*, **302**, 169–190.

TOMKIN, J., BRANDON, M., PAZZAGLIA, F., BARBOUR, J. & WILLETT, S. 2003. Quantitative testing of bedrock incision models, Clearwater River, WA. *Journal of Geophysical Research*, **108**, 2308, DOI 10.1029/2001JB000862.

TUCKER, G. 2004. Drainage basin sensitivity to tectonic and climatic forcing: implications of a stochastic model for the role of entrainment and erosion thresholds. *Earth Surface Processes and Landforms*, **29**, 185–205.

TUCKER, G. & SLINGERLAND, R. 1994. Erosional dynamics, flexural isostacy, and long-lived escarpments: a numerical modeling study. *Journal of Geophysical Research*, **99**, 12229–12243.

TUCKER, G., LANCASTER, S., GASPARINI, N. & BRAS, R. 2001. The Channel-Hillslope Integrated Landscape Development (CHILD) Model. *In*: HARMON, R. & DOE III, W. W. (eds) *Landscape Erosion and Evolution Modeling*. Kluwer Academic/Plenum Publishers, 349–388.

TURCOTTE, D. & SCHUBERT, G. 1982. *Geodynamics: Applications of Continuum Physics to Geological Problems*. 1st edn, John Wiley and Sons, New York.

VAN DER BEEK, P. & BISHOP, P. 2003. Cenozoic river profile development in the Upper Lachlan catchment (SE Australia) as a test of quantitative fluvial incision models. *Journal of Geophysical Research*, **1108**, 2309, DOI 10.1029/2002JB002125.

VAN DER BEEK, P. & BRAUN, J. 1998. Numerical modelling of landscape evolution on geological time scales: a parameter analysis and comparison with the southeastern highlands of Australia. *Basin Research*, **10**, 49–68.

VAN DER BEEK, P., SUMMERFIELD, M., BRAUN, J., BROWN, R. & FLEMING, A. 2002. Modelling post-breakup landscape development and denudational history across the southeast African (Drakensberg Escarpment) margin. *Journal of Geophysical Research*, **107**, 2351, DOI 10.1029/2001JB000744.

WELLMAN, H. 1979. An uplift map for the South Island of New Zealand, and a model for uplift of the Southern Alps. *In*: WALCOTT, R. I. & CRESSWELL, M. M. (eds) *The Origin of the Southern Alps*. Bulletin, Royal Society of New Zealand, 13–20.

WHIPPLE, K. 2001. Geomorphic limits to climate-induced increases in topographic relief. *American Journal of Science*, **301**, 313–325.

WHIPPLE, K. & MEADE, B. 2004. Controls on the strength of coupling among climate, erosion, and deformation in two-sided, frictional orogenic wedges at steady state. *Journal of Geophysical Research*, **109**, F01011, DOI 10.1029/2003JF000019.

WHIPPLE, K. & TUCKER, G. 1999. Dynamics of the stream-power incision model: implications for height limits of mountain ranges, landscape response timescales and research needs. *Journal of Geophysical Research*, **104**, 17661–17674.

WHIPPLE, K., KIRBY, E. & BROCKLEHURST, S. 1999. Geomorphic limits to climate-induced increases in topographic relief. *Nature*, **401**, 39–43.

WHITEHOUSE, I. 1987. Geomorphology of a compressional plate boundary: Southern Alps, New Zealand. *International Geomorphology*, **1**, 897–924.

WILLETT, S. 1999. Orogeny and orography: the effects of erosion on the structure of mountain belts. *Journal of Geophysical Research*, **104**, 28957–28981.

WILLETT, S., BEAUMONT, C. & FULLSACK, P. 1993. Mechanical model for the tectonics of doubly-vergent compressional orogens. *Geology*, **21**, 371–374.

WILLETT, S., SLINGERLAND, R. & HOVIUS, N. 2001. Uplift, shortening, and steady state topography in active mountain belts. *American Journal of Science*, **301**, 455–485.

WILLGOOSE, G., BRAS, R. & RODRIGUEZ-ITURBE, I. 1991. A physically based coupled network growth and hillslope evolution model: 1. Theory. *Water Resources Research*, **27**, 1671–1684.

ZEITLER, P. & MELTZER, A. *ET AL.* 2001*a*. Erosion, Himalayan geodynamics, and the Geomorphology of Metamorphism. *GSA Today*, **11**, 4–9.

ZEITLER, P. K. & KOONS, P. O. *ET AL.* 2001*b*. Crustal reworking at Nanga Parbat, Pakistan: evidence for erosional focusing of crustal strain. *Tectonics*, **20**, 712–728.

# Macroscale dynamics of experimental landscapes

STEPHANE BONNET & ALAIN CRAVE
*Géosciences Rennes, UMR 6118 CNRS/Université de Rennes 1, 35042 Rennes cedex, France*
*(e-mail: sbonnet@univ-rennes1.fr)*

**Abstract:** We review results from laboratory-scale modelling of erosion and relief dynamics under variable uplift and rainfall rates. Under constant values of these forcing parameters an experimental landscape typically evolves towards a steady-state between uplift and erosion, and we show how the geometry of the steady-state landscape adjusts to the rates of uplift and rainfall. The comparison between these laboratory-scale landscapes and the natural ones is not straightforward because contrary to analogue modelling in tectonics, natural conditions of relief evolution cannot be downscaled to the laboratory without any scale distortions. Laboratory-scale modelling in geomorphology is therefore only experimental, not analogue. Despite these limitations, experimental models may be used to provide physical tests for numerical models and they give insights into first-order behaviours and directions for future research.

The recognition of the importance of erosion in geodynamics (Beaumont *et al.* 1991, 2001; Avouac & Burov 1996; Horton 1999; Willett 1999; Montgomery *et al.* 2001; Zeitler *et al.* 2001; Finlayson *et al.* 2002; Wobus *et al.* 2003; Simpson 2004; Thiede *et al.* 2004; Vannay *et al.* 2004) has led to a need for a better understanding of topographic evolution at geological timescales. However the changing form of the landscape with time is a long-standing question (Davis 1859; Penck 1953; Hack 1960) that is difficult to assess because of the timescale of the processes involved. Numerous recent theoretical advances have been made regarding the physical description of erosional processes (e.g., Howard 1994) and their incorporation into numerical models of erosion and landscape dynamics at geological timescales. Recent experimental models in geomorphology have been primarly built to provide physical tests for numerical models of erosion (Hasbargen & Paola 2000; Hancock & Willgoose 2001; Lague *et al.* 2003). Experimental dynamics have been successfully reproduced by some numerical models (e.g., EROS code: Crave & Davy 2001) given the use of appropriate parameters of the erosion law (e.g., Lague *et al.* 2003). Experimental modelling in geomorphology has been widely developed for the study of erosional/depositional processes such as hillslope erosion and landsliding (Densmore *et al.* 1997; Roering *et al.* 2001; Gabet 2003), bedrock abrasion (Sklar & Dietrich 2001), sediment transport (Paola *et al.* 1992), or channel dynamics (Shepherd & Schumm 1974; Holland & Pickup 1976; Ashmore 1982; Gardner, 1983; Schumm *et al.* 1987; Meunier & Métivier 2000). Some other experiments have also focused on drainage network growth (Schumm *et al.* 1987; Pelletier, 2003) and on the dynamics of landscape (Crave *et al.* 2000; Hasbargen & Paola 2000; Hancock & Willgoose 2001; Bonnet & Crave 2003; Lague *et al.* 2003; Babault *et al.* 2005). We use here a selection of experiments to illustrate how experimental landscapes adjust to the applied uplift and rainfall rates. We discuss the meaning of the experiments regarding scaling problems and how they give insights into controls on, and dynamics of, relief generation.

## Experimental modelling in geomorphology

### *Principle*

The basic principle of modelling in geomorphology is very simple, and consists of surface erosion and sediment transport by runoff of water. However, differences between models arise from many aspects: the material; the size of the model; the device used to generate rainfall, which controls the rate of rainfall and/or the size of raindrops; the mechanism of applying uplift or base-level change; and the measurement of the experimental results; by photographs, digitization of the topography, and/or measurement of the eroded flux. Because of this diversity, model experiments performed in different laboratories (e.g., University

*From*: BUITER, S. J. H. & SCHREURS, G. (eds) 2006. *Analogue and Numerical Modelling of Crustal-Scale Processes*. Geological Society, London, Special Publications, **253**, 327–339.
0305-8719/06/$15.00 

of Minnesota: Hasbargen & Paola 2000; University of Rennes1/CNRS: Crave *et al.* 2000; University of Newcastle: Hancock & Willgoose 2001), even if simple in principle, are very difficult to compare with each other. For example, the experiments developed at Rennes are the only ones where erosion may act to compensate an applied uplift of the model. The basic data generated by these experiments consist of topographic measurements through time, whereas in other experiments, for example, by Hasbargen and Paola (2000), the data consist of flux measurements (weight of eroded material through time).

We only detail herein results of experiments made in Rennes over the last six years. In a first step, an innovative experimental design was built and successfully used in different studies (Crave *et al.* 2000; Bonnet & Crave 2003; Lague *et al.* 2003; Crave *et al.* 2005). However the use of this system revealed some defects that have led to different improvements and the development of a new device (Fig. 1) that is presently in use (Babault *et al.* 2005). These experimental set-ups were designed to study the dynamics of small-scale systems under simple conditions of erosion, uplift and rainfall rates. Rainfall and uplift rates are totally independent and set by the operator. No feedback loops exist between the surface uplift of the model and the rainfall rate (orographic effect) or between the pattern of erosion of the model and the uplift rate (isostatic effect). These simplifications of the natural conditions are not solely due to technical problems but are also deliberate, mainly for two reasons. Firstly, the complexity of geomorphological processes is still poorly understood so we prefer to minimize the parameters involved, instead of adding hypothetical analogue processes in the experiments. Secondly, simple case studies are necessary to define a baseline of experimental observations to help the interpretation of results from more complex experimental set-ups.

Whatever the simplifications of the geomorphological processes, the experimental device offers the possibility of studying a large open field of questions on relief dynamics that are not yet physically explored. The main assumption of this set-up is to reduce all the processes of erosion to the sole action of runoff. Other erosion processes like eolian transport or slope instability are certainly important in sculpting topography, but we believe that runoff is the major erosion vector at the global scale and is responsible for the drainage organization of most continental surfaces.

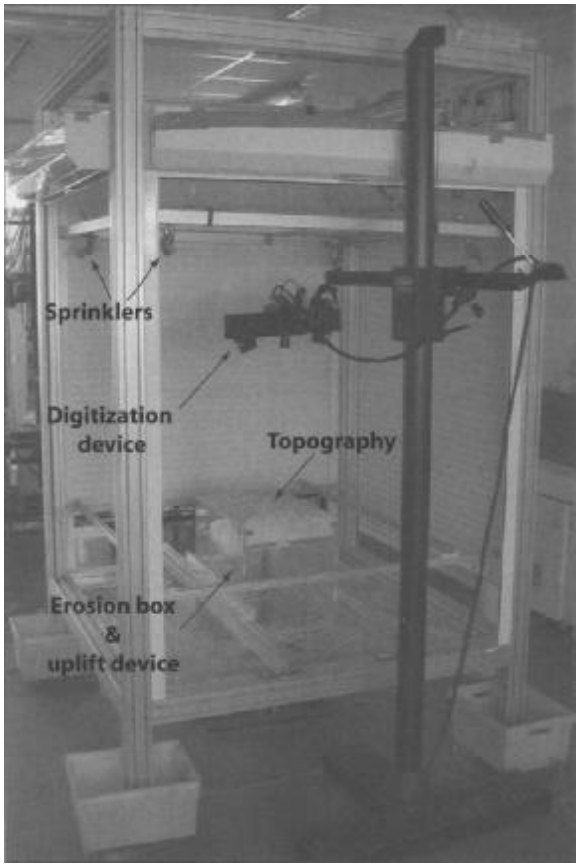


**Fig. 1.** Experimental device in use at Geosciences Rennes since 2003. Experiments are run within a rainfall simulator (size: 2 m × 2 m) whose four walls consist of roll shutters. Four sprinklers are positioned in the top corners. The erosion box is filled with the material to be eroded. Base movements are driven by a screw and a computer-controlled stepping motor. During an experiment, the base moves upward at a constant rate and pushes the material relative to the top of the erosion box at a rate defined as the uplift rate.

## *Experimental set-up*

*Eroded material.* The main material used is a paste made by mixing a granular silica powder (median grain size of between 10 and 20 μm) with water. Some experiments have also been made with loess, as in the study by Lague *et al.* (2003). Adding water during the preparation of the material leads to pore saturation so infiltration is negligible during the subsequent erosion of the model. Silica has been chosen to avoid any chemical reaction with water. Because of the small grain size, small shear stresses are needed for particle transportation, and cohesion allows for the development of a fine network of topographic incisions with steep slopes. The resistance of the material to erosion is partially due to the angular shape of the silica grains

we use. The addition of rounded grains of silica with the same size as the angular ones increases the erosion rates (Fig. 2) because of the decrease of material resistance to erosion.

*Erosion box and uplift device.* Tectonic uplift is one of the main parameters that controls erosion and relief dynamics at the Earth's surface at geological timescales, so the incorporation of an uplift device is essential for modelling purpose. We built an erosion box (Fig. 1) that we use for experiments where erosion acts to compensate an uplift applied to the model. It consists of a plexiglas box that is filled with the material to be eroded. It is open at its top side while its base can move upwards or downwards within the box. The movements of the base are driven by a screw and a computer-controlled stepping motor. During an experiment, the base moves upward at a constant rate. It pushes the silica paste relative to the top of the erosion box uniformly at a rate defined as the uplift rate, usually between 1 and 50 mm/hr. The four walls of the erosion box act as the constant-elevation base level for the eroding system. Erosion boxes of several different sizes have been used: $14 \times 20$ cm (Bonnet & Crave 2003; Crave *et al.* 2005), $20 \times 30$ cm (Lague *et al.* 2003) and $40 \times 60$ cm (Babault *et al.* 2005). The influence of the size of the erosion box on the experimental topography is discussed below.

*Rainfall simulator.* Experiments are run within a simulator that produces rain, whose kinetic energy is low enough to avoid the detachment effect of raindrop impacts (splash effect). In a first step (Crave *et al.* 2000; Bonnet & Crave 2003; Lague *et al.* 2003; Crave *et al.* 2005), we produced an artificial fog by atomization of a high-pressure water flow through as many as 44 sprinklers. With this system the raindrop size was less than 10 μm and the possible rates of rainfall varied between 50 to 350 mm/hr depending on the number of active sprinklers, their orientation and configuration, and the water pressure. However the spatial variability was often high (around 20%) because the high pressure induced a 3D circulation of the fog. The variability of rainfall rate in time was also high, between 5 and 10%. In a second step (Babault *et al.* 2005) we have built a new rainfall simulator in which rainfall is produced by using four sprinklers that deliver a mixture of water and pressurized air (Fig. 1). This yields less spatial and temporal variability of rainfall (around 5% and 3% respectively) over the same range of rainfall rates.

Before each experimental run, we measure the spatial variability of rainfall rate by collecting water in pans that are regularly spaced within the rainfall simulator at the erosion box location. During the run, it is not possible to measure the rainfall rate at the erosion box location so we collect rainfall in four pans located at the corners of the erosion box to avoid any perturbation of rainfall above the model.

### *Digitization of the topography*

The acquisition of high-resolution digital elevation models (DEMs) of the experimental topography is of first importance in experimental geomorphology. Firstly, as explained below, during an experimental run we follow the steps of development of a relief by computing its mean elevation from the produced DEMs. To track the development of topography during an experiment, we need a topographic acquisition facility that allows for the fast acquisition and computation of surfaces that are possibly rugged. The resulting DEMs must have a high resolution (less than 1 mm) in order to characterize the geometry of the landscape.

Two main devices have been used in our experiments. The first consisted of five telemetric lasers mounted on a rack whose displacements on the horizontal axis were controlled precisely by two stepping motors. This allowed the digitization of the topography with a vertical accuracy of 40 μm and a horizontal accuracy of 500 μm. The second device (Fig. 1) is an industrial stereo-photography device, the Advanced TOpometric Sensor (ATOS) developed by the gOm Company. This device allows the quick digitization of complex topography with near vertical slopes with an accuracy of 30 μm. By using these two systems we produce high-resolution DEMs (usually 0.5–1 mm square-grid DEMs Fig. 3).

The production of the DEMs requires the momentary cessation of the experiment because of the opacity within the rainfall simulator and of the vulnerability of the measurement devices to rainfall. Consequently we regularly stop the uplift and rainfall devices, usually for 10 to 30 minutes of erosion, to digitize the model topography and generate a DEM. The interruption of erosion for an interval of less than 30 minutes does not significantly modify the surface of the topography (due to drying of the surface and formation of a solid crust) and its subsequent evolution. The digitization of a small model (area around 300 $cm^2$) took around 5 minutes with the first device and less than 5 minutes with the second one. However for larger models (area $> 2000$ $cm^2$) the acquisition time using the first device is too long, more than

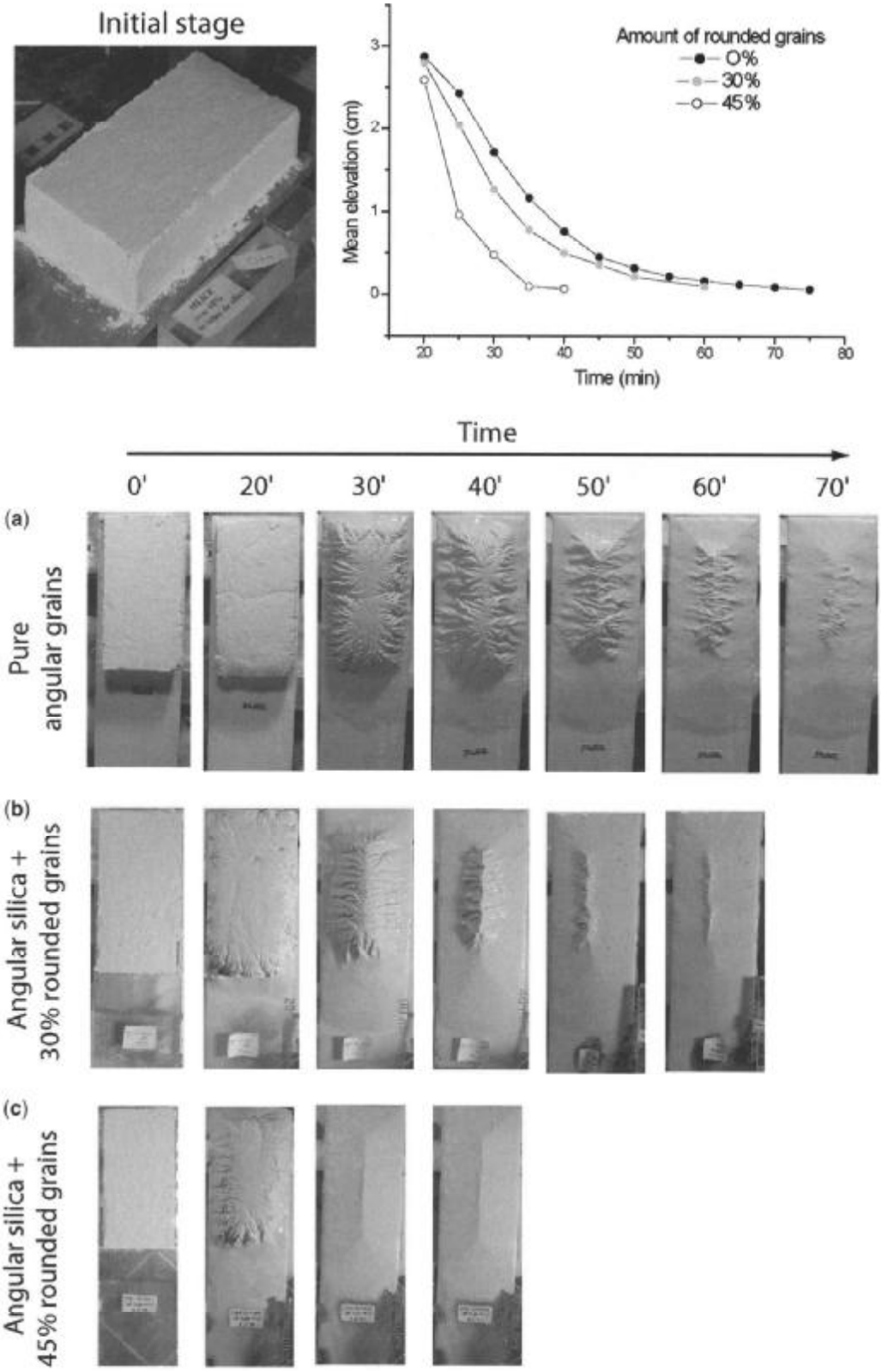


**Fig. 2.** Erosional decay of silica blocks (initial size 20 × 10 cm; height 3 cm) made of pure angular grains of silica or of a mixture of angular and rounded grains of silica (30 and 45% of rounded grains are shown). No uplift is applied during erosion. Rainfall rate is 60 mm/hr. The graph shows the decrease of the mean elevation of the blocks during erosion and illustrates that the addition of rounded grains accelerates the rate of elevation decay. The addition of rounded grains then decreases the resistance to erosion of the material as illustrated qualitatively by the sequence of photos. (**a**) 0% of rounded grains. (**b**) 30% of rounded grains. (**c**) 45% of rounded grains.

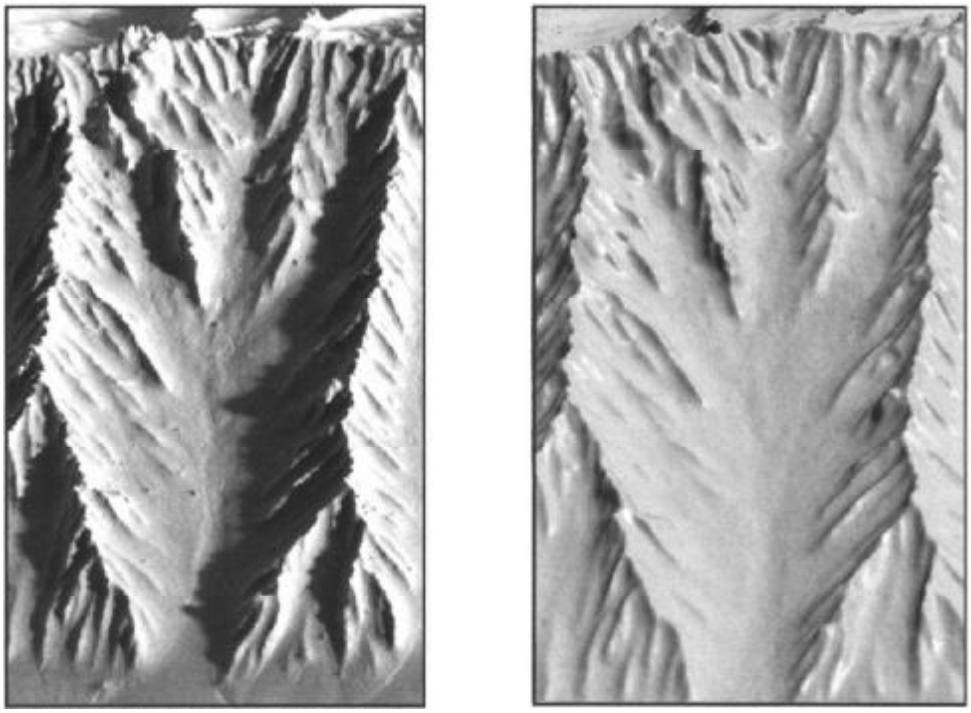

**Fig. 3.** Photograph (left) and 3D view of the corresponding DEM (right; 0.5 mm square grid) of an experimental drainage basin. The width of the view is around 5 cm.

1 hour, whereas it takes around 10–15 minutes using the ATOS. During an experimental run, we follow the relief dynamics by computing the mean and maximum elevations of the topography at each step of the digitization (Fig. 4). The difference between two successive DEMs is used to measure the output sediment flux and to elaborate denudation maps of the landscape.

## Results

### *Typical evolution of an experimental landscape*

Most of the experiments begin with the erosion box filled with the silica paste up to the top of the erosion box so the initial stage of a run corresponds to the uplift of a plateau (Fig. 4). An experiment begins when we start the uplift and rainfall devices. For constant uplift and rainfall rates a topography typically involves a growth phase and a steady-state phase (Fig. 4). When the initial plateau begins to be uplifted, some topographic incisions form along the four borders of the model (Fig. 4). As uplift continues, incisions propagate inward until there is complete dissection of the initial plateau. This growth phase is characterized by an increase in both the mean and maximum elevations (Fig. 4). In a second step, both the mean and maximum elevations stabilize with time (Fig. 4), while the applied uplift is still active. This indicates that erosion fully balances uplift at the scale of the model, that is, the output eroded flux equals the input uplift flux (flux steady-state: Willet & Bradon 2002). The repetition of some experiments shows that for a given rainfall and uplift rate the elevation curves are highly reproducible, with a variability of the stabilization value of the mean elevation of less than 10%.

A constant mean elevation with time is one criterion that can be used to define a steady state of the topography (e.g., Willett & Brandon 2002). At topographic steady state (Willett & Brandon 2002) the elevation of all the points of the topography does not change with time and hillcrests erode at the same rate as the valley floors. It should be noticed that a constant mean elevation is not a sufficient criterion to infer a topographic steady state. The shape of the relief could vary while its mean elevation remained constant, if, for example, uplift of summits is compensated by valley lowering. This is the reason why we also follow the maximum elevation during an experiment and we use the stability of this criterion together with the mean elevation to infer that an experimental relief approachs a topographic steady state (Fig. 4). Note that as also observed in other experimental models by Hasbargen and Paola (2000), our experimental

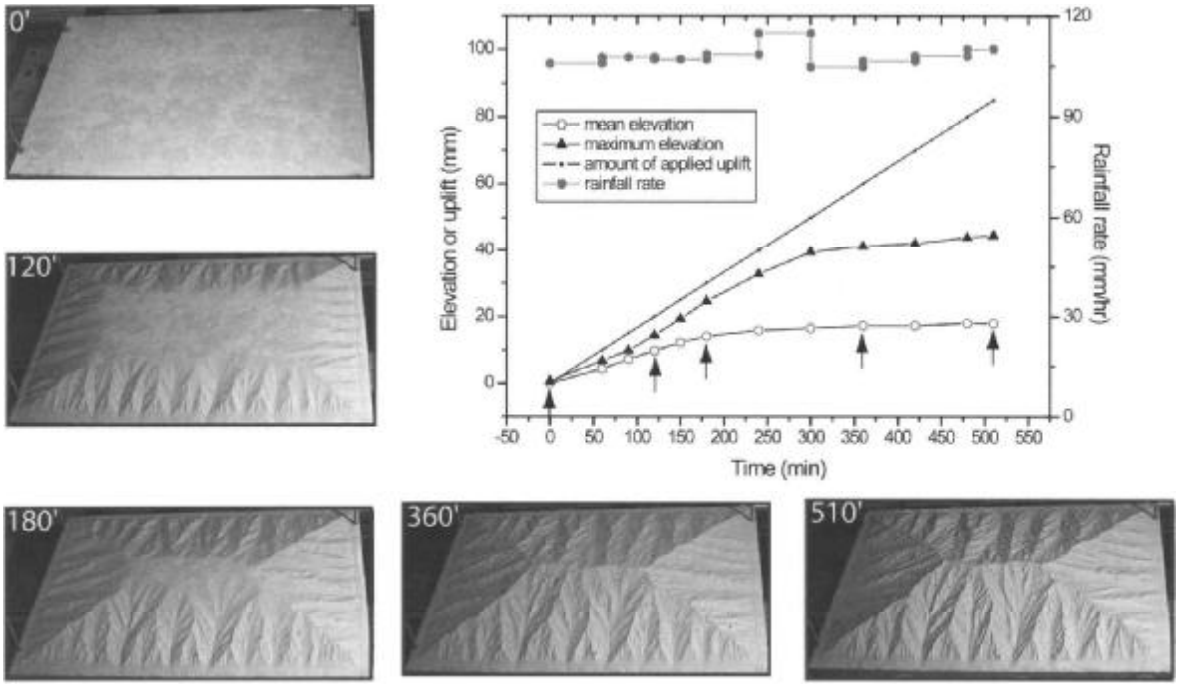


**Fig. 4.** Evolution of mean and maximum elevation of an experiment under constant rates of uplift (10 mm/hr) and rainfall (110 mm/hr) up to steady state, calculated from high-resolution DEMs (0.5 mm square grid) taken at different time intervals. Photos show the topography during the growth phase (photos taken at 0, 120 and 180 min) and during steady state (photos taken at 360 and 510 min), and correspond to arrows on the time-elevation plot. The size of the model is 40 × 60 cm.

landscapes never reach a pure topographic steady state. We usually observe a spatial migration of ridges and rivers at the local scale (less than 1 cm) that we assume to come from small uncontrolled spatial variations in the rainfall rate. The steady-state landscapes we characterized are then mostly at flux steady state.

### *Influence of the rainfall rate*

We report here results from experiments made under the same uplift rate of 20 mm/hr but different rainfall rates, ranging from 100 to 300 mm/hr. Figure 5 shows the dependency between mean elevation of the steady-state topographies and the rainfall rate. Steady-state elevations show a clear inverse dependency with the rainfall rate (Fig. 5): the higher the rainfall rate, the lower the steady-state topography (Bonnet & Crave 2003). Figure 6 shows three experimental landscapes at steady state under different rainfall rates which illustrate this outcome. Note that these three landscapes experience the same uplift rate (20 mm/hr) so they all denude at the same rate of 20 mm/hr. It is commonly accepted that the erosion rate at any point in a landscape is set by the product of the local slope and the water discharge coming from upstream (Howard & Kerby 1983), this latter being approximated by the product of the rainfall rate and the drainage area. Steady state then corresponds to a combination of low rainfall plus high slope or high rainfall plus low slope. Therefore, low mean

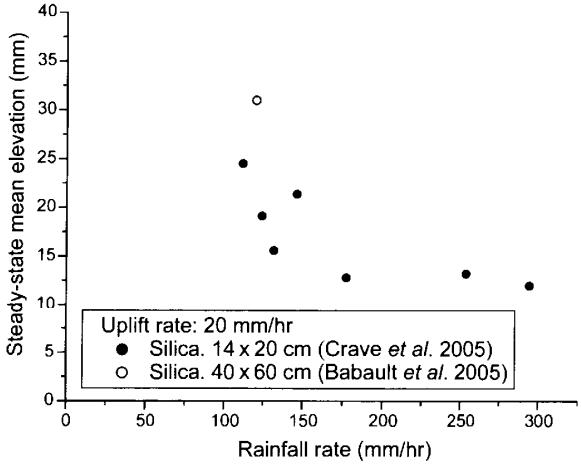


**Fig. 5.** Mean elevation of experimental landscapes at steady state against rainfall rate. The uplift rate is 20 mm/hr in all experiments.

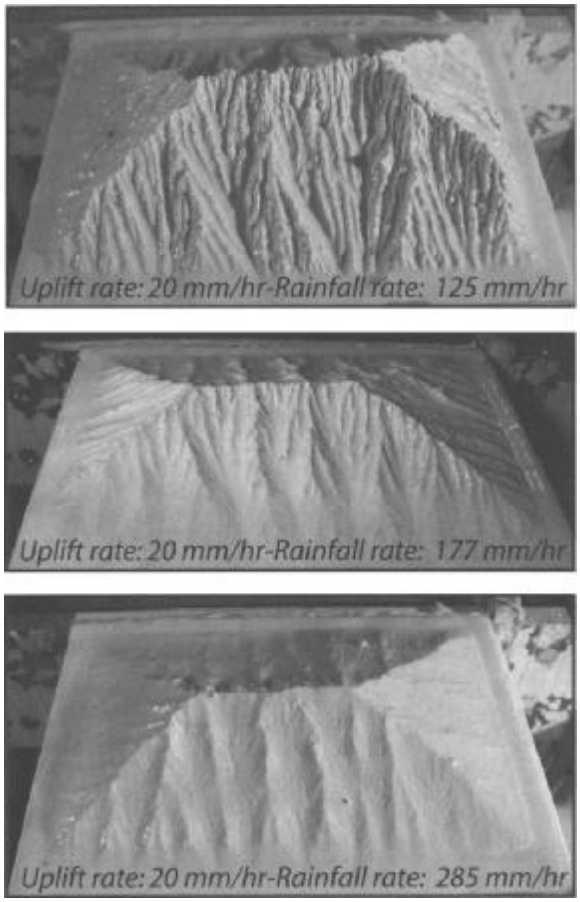


**Fig. 6.** Photos of steady-state topographies (model size: 14 × 20 cm) under a similar uplift rate of 20 mm/hr but different rainfall rates of 125 (upper), 177 (middle) and 285 (lower) mm/hr. Note that because erosion and uplift rates are balanced, denudation rates are the same in all three experiments.

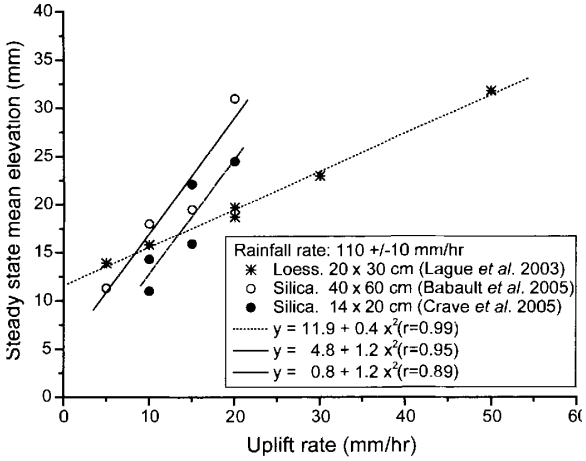


**Fig. 7.** Mean elevation of experimental landscapes at steady state against uplift rate. The rainfall rate is around 110 mm/hr in all experiments. Experiments made with loess are shown by stars, those with silica are shown by circles. Note that the system varies between 14 × 20 cm (solid circles) and 40 × 60 cm (open circles) for the latter set of experiments.

elevation and slopes do not imply a low uplift rate. Montgomery *et al.* (2001) argued that climate exerts a strong control on the large-scale morphology of the Andes. They suggested that the low elevations of the northern Andes could result from high precipitation rather than lower rates of crustal shortening and rock uplift. This phenomenon is plausible in view of our results (Bonnet & Crave 2003).

Given the present set of data we cannot properly fit the trend of mean elevations against rainfall rate with a well-defined function (see Crave *et al.* 2005 for a full discussion). From theoretical considerations (Whipple & Tucker 1999; Lague *et al.* 2003) this function should be a power law whose exponent would depend on the exponent on the drainage area of the transport law, but its determination is presently limited by the range of possible rainfall rates within the rainfall simulator.

### *Influence of the uplift rate*

We report results from experiments made under the same rainfall rate of 110 ± 10 mm/hr but different uplift rates. Figure 7 shows the dependency between the mean elevation at steady state and the uplift rate for three sets of experiments: models made of loess with a size of 20 × 30 cm (Lague *et al.* 2003), and models made of silica with a size of 14 × 20 cm (Crave *et al.* 2005) and 40 × 60 cm (Babault *et al.* 2005). Each individual data set shows a positive linear correlation between the mean elevation at steady state and the uplift rate (Fig. 7). It should be noticed that the slope of the linear fits clearly depends on the material used in the experiments (Fig. 7). As all the other parameters are similar, this could be directly linked to their difference in erodibility. Also, each data set shows a non-zero intercept of the linear fit that implies a positive elevation of the landscape in the absence of uplift. This value corresponds to the non-zero mean elevation reached by a relaxing landscape (i.e., one that evolves without uplift) after a long time period of erosion, and is interpreted as the signature of an erosion threshold (Lague *et al.* 2003).

### *Influence of the model size*

Experiments with silica have been made with two sizes of the erosion box that span almost a tenfold difference in the eroded area: 280 $cm^2$

(14 × 20 cm: Bonnet & Crave 2003; Crave *et al.* 2005) against 2400 $cm^2$ (40 × 60 cm: Babault *et al.* 2005). As erosion depends on the aggregation of the water flux coming from upstream, our aim in increasing the experiment size was to explore the possibility of more complex erosional dynamics in larger experiments compared to the smaller ones. Surprisingly, their steady state mean elevation versus uplift rate trends are very similar in terms of the slope of the linear fits, the only difference being a small offset between the two trends (Fig. 7). Because of the small number of experiments and the small range of uplift rates that has been investigated, one can ask if these results are significant or not. Analysis of the relationships between local slopes and their corresponding drainage area (Fig. 8) allows us to go deeper into this problem.

It is well known that slope and drainage area correlate (Hack 1957) and these correlations have been used to characterize the local shapes

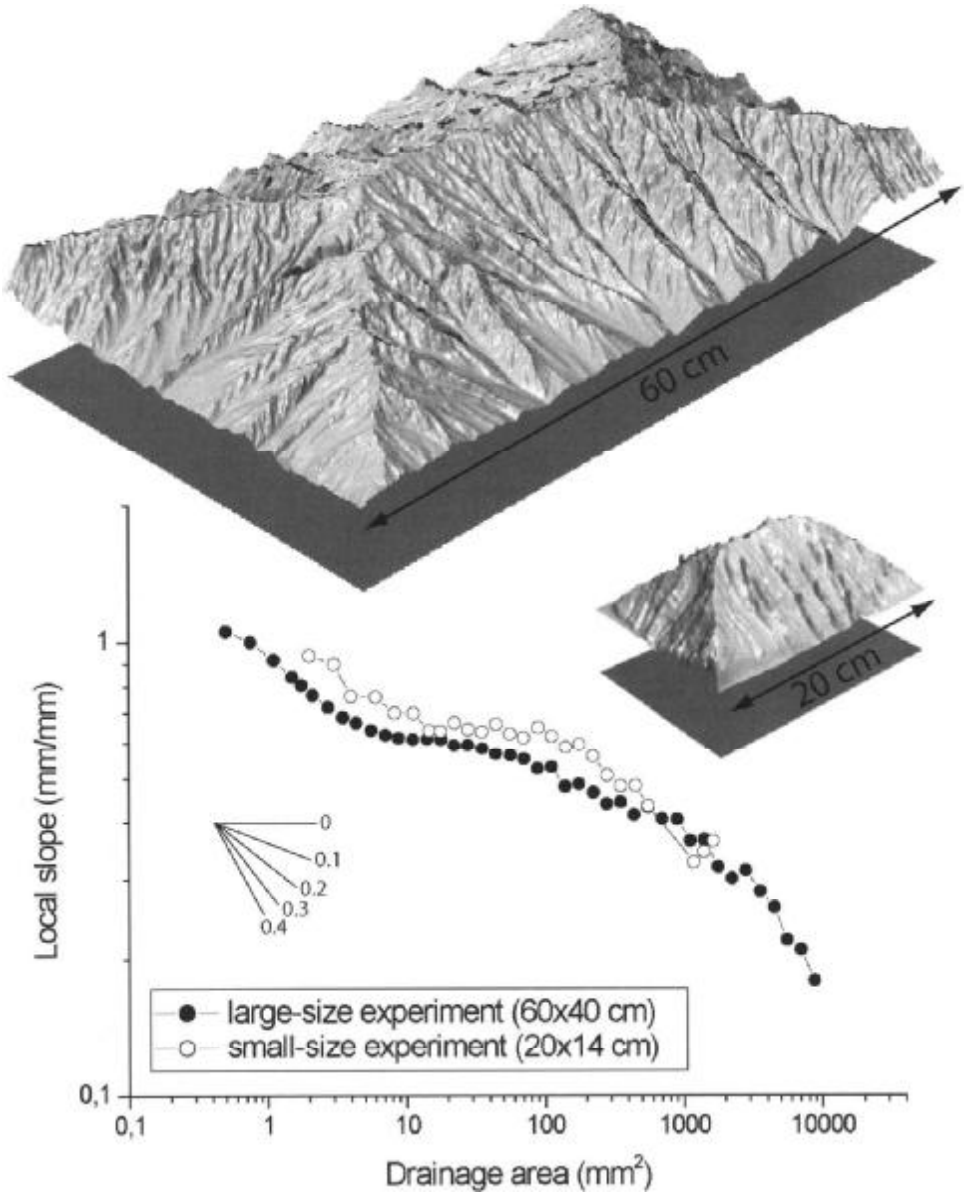


**Fig. 8.** Plot of local slope against drainage area for two experiments made with silica and at steady state under the same uplift (20 mm/hr) and rainfall (110 mm/hr) rates. The two experiments differ by their size (14 × 20 cm and 40 × 60 cm). The data are the logarithm bin averages of raw data for the entire surfaces. Note that the offset between the two curves is not relevant with regard to standard deviation (not shown for visibility). Also shown are 3D views of the corresponding DEMs (0.5 mm square grid) represented at the same scale.

of the landscapes with regard to erosional processes (e.g., Montgomery & Foufoula-Georgiou 1993). Note that in this kind of analysis, drainage area is used as a surrogate for water discharge. A log-log plot of the local slope against the drainage area allows the definition of linear trends whose slope parameter is a measure of the concavity of the topography (concavity exponent: Snyder *et al.* 2000), which could depend on the erosional processes. For example a river typically shows a negative trend that indicates a decrease of its local slope with increasing drainage area (i.e., a concave-up shape) with a concavity exponent that is typically between 0.3 and 0.7 (Whipple & Tucker 1999). The determination of the concavity exponent of a landscape over a given range of drainage areas could help to define the prevailing erosional process over this range, by the sole analysis of the topography. Note that even if widely used, intepretation of slope-area data must be done with great caution as it has been recently demonstrated that slope-area dependence can be entirely unrelated to erosional processes (Schorghofer & Rotham 2002).

Figure 8 shows the slope/area relationships of two topographies that developed under the same conditions of uplift and rainfall rates but whose size is different. The two curves have a very similar shape and show three main domains of slope reduction for increasing drainage area: a first domain with a concavity exponent around 0.2–0.3, a second domain with an exponent less than 0.1, and a third domain with an exponent of 0.3–0.4 (see Crave *et al.* 2005 for a full discussion of the significance of these domains). The visual inspection of the experimental landscapes confirms the existence of three topographic domains characterized by different shapes that we believe to result from different action of the running water, possibly because of different hydraulic regimes. The identification of these three domains over roughly the same ranges of drainage area on both landscape would indicate that despite the difference in system size, the two models evolved under the same set of erosional processes, as defined using slope/area relationships. It would imply that these two kind of models probably behave the same way regarding external parameters and that the similarity between the two trends defined on Figure 7 would probably not be an artefact. It appears that a tenfold increase in the size of the experiments is not sufficient to change the erosional dynamics of the experimental landscapes.

## Discussion and conclusions

### *Scaling and analogy*

The systems we study are deliberately oversimplified and do not take into account many processes that may play a role in natural landscapes (for example vegetation, weathering, etc.). Our objective is to understand first how individual external parameters influence a simple physical system. Nevertheless, a major unsolved problem lies in the scaling of the experiments. Unlike some laboratory experiments in tectonics (e.g., Davy & Cobbold 1991), experiments in geomorphology are not analogous to natural systems. The main reason is that it is quite impossible to downscale natural conditions to the laboratory without any scale distortions, so the ratios of significant dimensions and forces are not equal to those in nature. Processes involved in the formation of natural landscapes span a very wide range of timescales, from hydraulical (hours) to geological (millions of years), and the reduction of the geomorphic systems to the laboratory does not preserve their ratio. Similarly the ratio between the size of the experimental drainage basins and the grain size is much smaller than in natural conditions and its preservation would need the use of materials with a granulometry at least ten to a hundred fold smaller than the one we use. These two examples illustrate some of the reasons that make modelling in geomorphology experimental instead of analogue (Schumm *et al.* 1987).

Despite these scaling problems one of the most striking feature of experimental reliefs is that they often look very much like natural landscapes, and they obey some fundamental geometric laws deduced from natural systems, such as Hack's law or slope/area relationships (Hack 1957). As explained above, the study of the local shape of a topography through analysis of its slope/area relationship may give information about the processes responsible for the sculpting of its relief (Howard & Kerby 1983; Montgomery & Foufoula-Georgiou 1993). The detailed analysis of slope/area relationships on experimental landscapes (Lague *et al.* 2003; Crave *et al.* 2005) reveals that their concavity exponent is never higher than 0.4 whatever the material used, the size of the model or the topographic domain considered (Fig. 8). This has important implications because in nature, rivers are often characterized by a high concavity, with values of the slope/area exponent near 0.3–0.7 (Whipple & Tucker 1999). Thus the erosional processes within our experiments never form topographic incisions with

concave shapes as observed for natural rivers. Consequently our experimental reliefs cannot be viewed as systems whose dynamics is equivalent to fluvial-driven landscapes. In contrast, large areas of the experimental landscapes are characterized by a low value of the slope/area exponent, near 0.1 (central domain on Fig. 8), comparable to those seen in debris-flow dominated colluvial channels (Montgomery & Foufoula-Georgiou 1993). Consequently, rather than simulating all the landscape components of a mountain range, our experiments can be better viewed as an equivalent of the landmass that is between the main streams of the landscape, including debris flow-dominated channels. In this scheme, the four borders of the erosion box can be viewed as streams at equilibrium in which all the material eroded from the landscape is transferred outside the system.

### *Relief dynamics: insights from experimental models and research needs*

The development of numerical models of erosion and relief dynamics has stimulated a drive for tools and criteria to test their validity. Some geometric criteria obeyed by natural landscapes, like Horton's laws (Horton 1945), have been used but it has been demonstrated that these relations are independent of the origin or structure of landscapes (Kirchner 1993). Their use for testing numerical models is thus limited and experimental models of relief dynamics have been built first to provide some physical tests for numerical models (Hasbargen & Paola 2000; Hancock & Willgoose 2001; Lague *et al.* 2003). The SIBERIA (Willgoose & Bras 1991) and EROS (Crave & Davy 2001) codes have for example successfully reproduced the form and the macroscale dynamics of some experimental landscapes given an appropriate erosion law (Hancock & Willgoose 2001; Lague *et al.* 2003).

As pointed out by Hooke (quoted in Schumm *et al.* 1987, p. 5) it can be logically assumed that a process which produces a characteristic behaviour in experiments has the same effect on natural systems. If correct, this implies that despite scaling problems some macroscale experimental dynamics are probably partly relevant to natural systems evolution, so modelling can be used to emphasize general concepts of landscape behaviour. Our experiments demonstrated, for example, a positive correlation between the mean elevation of steady-state landscapes and the uplift rate (Fig. 7), in agreement with theoretical formulations (e.g., Whipple & Tucker 1999) and inferences from natural systems (Snyder *et al.* 2000; Lague & Davy 2003), as long as landsliding is not the main process of hillslope erosion in response to river incision (Schmidt & Montgomery 1995; Burbank *et al.* 1996). Experimental landscape response to uplift is therefore partly analogous to natural systems and the main problem lies in the representativeness of the linear relationship observed in experiments.

From a detailed analysis of experimental steady-state landscapes, Lague *et al.* (2003) demonstrated that this linear relationship results from a linear dependency between the erosion rate and the local slope of the experimental landscapes. No consensus exists about the nature of this relationship in natural systems. Some studies support, for example, a linear relationship for hillslope erosion (Small *et al.* 1999; Lague & Davy 2003), whereas others argue for a non-linear one (Roering *et al.* 1999), and the same discrepancy exists about erosion at the drainage or continental scale (Ahnert 1970; Pinet & Souriau 1988; Montgomery & Brandon 2002). The lack of knowledge of natural systems makes the representativeness of the experimental landscape dynamics with regard to uplift difficult to fully assess. Note that the question of the nature of the relationship between erosion rate and local slope is crucial with respect to the tectonic/erosion problem because analytical developments predict that the degree of non-linearity of this relationship controls the response time of the topography with respect to the uplift rate (Whipple & Tucker 1999). One important outcome is the prediction that the timescale to steady state would be independent of the uplift rate in the case of linearity between erosion rate and slope (Whipple & Tucker 1999), which is effectively observed in our experiments (Lague *et al.* 2003; Babault *et al.* 2005).

Experimental models also give insights into general concepts of landscape behaviour relative to climate through rainfall. Gabet *et al.* (2004) observed a decrease in the mean hillslope angles with increasing rainfall rate in the Himalayas, in agreement with the decrease in the mean elevation with increasing rainfall rate we observed in the experiments (Fig. 5) and with theoretical formulations (Willgoose *et al.* 1991; Tucker & Bras 1998). As in our experiments, Gabet *et al.* (2004) cannot propose a fit to their data, but of interest for our purpose here is the qualitative similarity of behaviour between this natural system and our experiments. As a consequence of the inverse correlation between mean steady-state elevation and the

rainfall rate, Bonnet and Crave (2003) demonstrated experimentally a shift from high to low rainfall rate induces surface uplift of the landscape, even with constant uplift rate. This phenomenon is defined as a climatically induced surface uplift (Bonnet & Crave 2003), as opposed to a tectonically induced surface uplift, and corresponds to a specific dynamic of denudation, so that it is theoretically possible to differentiate between the climatic or tectonic causes of surface uplift from records of output sediment fluxes (Bonnet & Crave 2003). If we assume that the experimental landscape response to rainfall variations is qualitatively relevant to natural systems, this raises the question of the sensibility of landforms (in terms of magnitude and timescale of response) to climatic perturbations (Whipple 2001), with important issues regarding the origin of continental surface uplifts.

One of the primary values of experimental modelling in geomorphology is to generate hypotheses which can be tested by reference to natural lanscapes (Schumm *et al.* 1987; Bonnet & Crave 2003; Babault *et al.* 2005). Even under constant external forcing, experimental models are also more dynamic than numerical models would suggest (Hasbargen & Paola 2000), so they can potentially improve our understanding of landscape sculpting by erosional processes. Recent field studies have demonstrated a discrepancy between measured erosion rates and some theoretical parameters of erosion efficiency such as stream power (Dadson *et al.* 2003; Reiners *et al.* 2003), which implies an inadequancy of the current theory to describe and predict erosion (Molnar 2003). Experimental modelling could also be a valuable tool for improving the theory of erosion, given the possibility of directly evaluating the erosion law of the models.

We thank A. Densmore for a constructive review that greatly helped improve this paper. We also thank P. Davy, D. Lague, J. Van den Driessche and J. Babault for helpful discussions and J.-J. Kermarrec, whose technical assistance made this work possible. This study was funded by CNRS-INSU.

## References

AHNERT, J. 1980. Contemporary uplift and erosion of the southern Alps, New Zealand: summary. *Geological Society of America Bulletin*, **91**, 2–4.

ASHMORE, P. E. 1982. Laboratory modelling of gravel braided stream morphology. *Earth Surface Processes and Landforms*, **7**, 201–225.

AVOUAC, J.-P. & BUROV, E. B. 1996. Erosion as a driving mechanism of intracontinental mountain growth. *Journal of Geophysical Research*, **101**, 17747–17769.

BABAULT, J., BONNET, S., CRAVE, A. & VAN DEN DRIESSCHE, J. 2005. Influence of Piedmont sedimentation on erosion dynamics of an uplifting landscape: an experimental approach. *Geology*, **33**, 301–304.

BEAUMONT, C., FULSACK, J. & HAMILTON, J. 1991. Erosional control of active compressional orogens. *In*: MCCLAY, K. R. (ed.) *Thrust Tectonics*. Chapman and Hall, New York, 1–18.

BEAUMONT, C., JAMIESON, R. A., NGUYEN, M. H. & LEE, B. 2001. Himalayan tectonics explained by extrusion of low-viscosity crustal channel coupled to focused surface denudation. *Nature*, **414**, 738–742.

BONNET, S. & CRAVE, A. 2003. Landscape response to climate change: insights from experimental modelling and implications for tectonic versus climatic uplift of topography. *Geology*, **31**, 123–126.

BURBANK, D. W. *ET AL.* 1996. Bedrock incision, rock uplift, and threshold hillslopes in the northwestern Himalaya. *Nature*, **379**, 505–510.

CRAVE, A. & DAVY, P. 2001. A stochastic 'precipiton' model for simulating erosion/sedimentation dynamics. *Computers & Geosciences*, **28**, 815–827.

CRAVE, A., BONNET S. & LAGUE, D. 2005. Influence of rainfall rate on laboratory-scale reliefs. *Journal of Geophysical Research*, under review.

CRAVE, A., LAGUE, D., DAVY, P., KERMARREC, J.-J., SOKOUTIS, D., BODET, L. & COMPAGNON, R. 2000. Analogue modelling of relief dynamics. *Physics and Chemistry of the Earth*, **25**, 549–553.

DADSON, S. J. *ET AL.* 2003. Links between erosion, runoff variability and seismicity in the Taiwan orogen. *Nature*, **426**, 648–651.

DAVIS, W. M. 1899. The geographical cycle. *Geographical Journal*, **14**, 481–504.

DAVY, P. & COBBOLD, P. R. 1991. Experiments on shortening of a 4-layer model of continental lithosphere. *Tectonophysics*, **188**, 1–25.

DENSMORE, A. L., ANDERSON, R. S., MCADOO, B. G. & ELLIS, M. A. 1997. Hillslope evolution by bedrock landslides. *Science*, **275**, 369–372.

FINLAYSON, D. P., MONTGOMERY, D. R. & HALLET, B. 2002. Spatial coincidence of rapid inferred erosion with young metamorphic massifs in the Himalayas. *Geology*, **30**, 219–222.

GABET, E. J. 2003. Sediment transport by dry ravel. *Journal of Geophysical Research*, **108**, 2049, DOI 10.1029/2001JB001686.

GABET, E. J., PRATT-SITAULA, B. A. & BURBANK, D. W. 2004. Climatic controls on hillslope angle and relief in the Himalayas. *Geology*, **32**, 629–632.

GARDNER, T. W. 1983. Experimental study of knickpoint and longitudinal profile evolution in cohesive, homogeneous material. *Geological Society of America Bulletin*, **94**, 664–672.

HACK, J. T. 1957. Studies of longitudinal stream profiles in Virginia and Maryland. *United States Geological Survey Professional Paper*, **294B**, 45–94.

HACK, J. T. 1960. Interpretation of of erosional topography in humid temperate region. *American Journal of Science*, **258**, 80–97.

HANCOCK, G. & WILLGOOSE, G. 2001. Use of a landscape simulator in the validation of the Siberia catchment evolution model: declining equilibrium landforms. *Water Resource Research*, **37**, 1981–1992.

HASBARGEN, E. L. & PAOLA, C. 2000. Landscape instability in an experimental drainage basin. *Geology*, **28**, 1067–1070.

HOLLAND, W. N. & PICKUP, G. 1976. Flume study of knickpoint development in stratified sediment. *Geological Society of America Bulletin*, **87**, 76–82.

HORTON, B. K. 1999. Erosional control on the geometry and kinematics of thrust belt development in the central Andes. *Tectonics*, **18**, 1292–1304.

HORTON, R. E. 1945. Erosional development of streams and their drainage basins: hydrophysical approach to quantitative morphology. *Geological Society of America Bulletin*, **56**, 275–370.

HOWARD, A. D. 1994. A detachment-limited model of drainage basin evolution. *Water Resource Research*, **30**, 2261–2285.

HOWARD, A. D. & KERBY, G. 1983. Channel changes in badlands. *Geological Society of America Bulletin*, **94**, 739–752.

KIRCHNER, J. W. 1993. Statistical invevitability of Horton's laws and the apparent randomness of stream channel networks. *Geology*, **21**, 591–594.

LAGUE, D. & DAVY, P. 2003. Constraints on the long-term colluvial erosion law from the analyzis of slope-area relationships at various tectonic uplift rates in the Siwaliks Hills (Nepal). *Journal of Geophysical Research*, **108**, 2129, DOI 10.1029/2002JB001893.

LAGUE, D., CRAVE, A. & DAVY, P. 2003. Laboratory experiments simulating the geomorphic response to tectonic uplift. *Journal of Geophysical Research*, **108**, 2008, DOI 0.1029/2002JB001785.

MOLNAR, P. 2003. Nature, nurture and landscape. *Nature*, **426**, 613–614.

MEUNIER, P. & MÉTIVIER, F. 2000. Permanence des flux de masse d'une rivière en tresses expérimentales. *Compte Rendu de l'Académie des Sciences*, **331**, 105–110.

MONTGOMERY, D. R. & BRANDON, M. T. 2002. Topographic controls on erosion rates in tectonically active mountain ranges. *Earth and Planetary Science Letters*, **201**, 481–489.

MONTGOMERY, D. R. & FOUFOULA-GEORGIOU, E. 1993. Channel network source representation using digital elevation models. *Water Resource Research*, **29**, 3925–3934.

MONTGOMERY, D. R., BALCO, G. & WILLET, S. D. 2001. Climate, tectonics, and the morphology of the Andes. *Geology*, **29**, 579–582.

PELLETIER, J. D. 2003. Drainage basin evolution in the rainfall erosion facility: dependence on initial conditions. *Geomorphology*, **53**, 183–196.

PAOLA, C., PARKER, G., SEAL, R., SINHA, S. K., SOUTHARD, J. B. & WILCOCK, P. R. 1992. Downstream fining by selective deposition in a laboratory flume. *Science*, **258**, 1757–1760.

PENCK, W. 1953. *Morphological Analysis of Land Forms*. Macmillan, London.

PINET, P. & SOURIAU, M. 1988. Continental erosion and large-scale relief. *Tectonics*, **7**, 563–582.

REINERS, P. W., EHLERS, T. A., MITCHELL, S. G. & MONTGOMERY, D. R. 2003. Coupled spatial variations in precipitation and long-term erosion rates across the Washington Cascades. *Nature*, **426**, 645–647.

ROERING, J. J., KIRCHNER, J. W. & DIETRICH, W. E. 1999. Evidence for nonlinear, diffusive sediment transport on hillslopes and implications for landscape morphology. *Water Resource Research*, **35**, 853–870.

ROERING, J. J., KIRCHNER, J. W., SKLAR, L. S. & DIETRICH, W. E. 2001. Hillslope evolution by non linear creep and landsliding: an experimental study. *Geology*, **29**, 143–146.

SCHMIDT, K. M. & MONTGOMERY, D. R. 1995. Limits to relief. *Science*, **270**, 617–620.

SCHORGHOFER, N. & ROTHMAN, D. H. 2002. Acausal relations between topographic slope and drainage area. *Geophysical Research Letters*, **29**, 1–5.

SCHUMM, S. A., MOSLEY, M. P. & WEAVER, W. E. 1987. *Experimental Fluvial Geomorphology*. John Wiley, New York.

SHEPHERD, R. G. & SCHUMM, S. A. 1974. Experimental study of river incision. *Geological Society of America Bulletin*, **85**, 257–268.

SIMPSON, G. 2004. Dynamic interactions between erosion, deposition, and three-dimensional deformation in compressional fold belt setting. *Journal of Geophysical Research*, **109**, F03007, DOI 10.1029/2003JF000111.

SKLAR, L. S. & DIETRICH, W. E. 2001. Sediment and rock strength controls on river incision into bedrock. *Geology*, **29**, 1087–1090.

SMALL, E. E., ANDERSON, R. S., HANCOCK, G. S. & FINKEL, R. S. 1999. Estimates of regolith production from $^{10}$Be and $^{26}$Al: evidence for steady state alpine hillslopes. *Geomorphology*, **27**, 131–150.

SNYDER, N. P., WHIPPLE, K. X., TUCKER, G. E. & MERRITTS, D. J. 2000. Landscape response to tectonic forcing: DEM analysis of stream profiles in the Mendocino triple junction region, northern California. *Geological Society of America Bulletin*, **112**, 1250–1263.

THIEDE, R. C., BOOKHAGEN, B., ARROWSMITH, J. R., SOBEL, E. R. & STRECKER, M. R. 2004. Climatic control on rapid exhumation along the Southern Himalayan front. *Earth and Planetary Science Letters*, **222**, 791–806.

TUCKER, G. E. & BRAS, R. L. 1998. Hillslope processes, drainage density, and landscape morphology. *Water Resources Research*, **34**, 2751–2764.

VANNAY, J.-C., GRASEMANN, B., RAHN, M., FRANK, W., CARTER, A., BAUDRAZ, V. & COSCA, M. 2004. Miocene to Holocene exhumation crustal wedges in the NW Himalaya: evidence for tectonic extrusion coupled to fluvial erosion. *Tectonics*, **23**, TC1014, DOI 10.1029/2002TC001429.

WHIPPLE, K. X. 2001. Fluvial landscape response time: How plausible is steady-state denudation? *American Journal of Science*, **301**, 313–325.

WHIPPLE, K. X. & TUCKER, G. E. 1999. Dynamics of the stream-power incision model: implications for the height limits of mountain ranges, landscape response timescales, and research needs. *Journal of Geophysical Research*, **104**, 17761–17674.

WILLET, S. D. 1999. Orogeny and orography: The effects of erosion on the structure of mountain belts. *Journal of Geophysical Research*, **104**, 28957–28981.

WILLET, S. D. & BRANDON, M. T. 2002. On steady states in mountain belts. *Geology*, **30**, 175–178.

WILLGOOSE, G. R. & BRAS, R. L. 1991. Results from a new model of river basin evolution. *Earth Surface Processes & Landforms*, **16**, 237–254.

WILLGOOSE, G. R., BRAS, R. L. & RODRIGUEZ-ITURBE I. 1991. A physically based coupled network growth and hillslope evolution model, 1: theory. *Water Resource Research*, **27**, 1671–1684.

WOBUS, C. W., HODGES, K. V. & WHIPPLE, K. X. 2003. Has focused denudation sustained active thrusting at the Himalayan topographic front? *Geology*, **31**, 861–864.

ZEITLER, P. K. & MELTZER, A. M. *ET AL.* 2001. Erosion, Himalayan geodynamics and the geomorphology of metamorphism. *GSA Today*, **11**, 4–9.

# Numerical modelling of erosion processes in the Himalayas of Nepal: effects of spatial variations of rock strength and precipitation

V. GODARD[1], J. LAVÉ[2] & R. CATTIN[1]

[1]*Laboratoire de Géologie, Ecole Normale Supérieure, 24, rue Lhomond, 75005 Paris, France (e-mail: godard@geologie.ens.fr)*

[2]*Laboratoire de Géodynamique des Chaînes Alpines, CNRS, 1381, rue de la Piscine, 38400 St-Martin d'Hères, France*

**Abstract:** The interplay between tectonics and erosion has a predominant control on the evolution of the morphology of mountain belts. Here we investigate the modalities of deformation in Central Nepal on a *c.* 100 ka time scale in response to tectonic and external forcings, through the use of a finite-element thermomechanical model coupled with an integrative denudation formulation that accounts for fluvial incision and hillslope landsliding. We study the complex coupling existing between tectonics and erosion, with special emphasis on the influences of rock strength and rainfall distributions. Our results underline the key role played by lithologic variations in the elevation of both rivers and mean topography. We show that the location of the Main Frontal Thrust is mainly controlled by the low erodability of the unconsolidated sandstone in the Siwaliks Hills. As previously suspected (Burbank *et al.* 2003), our simulations demonstrate that the pattern of uplift in Nepal is mainly dependent on both erodability and fault geometry, rather than on rainfall distribution.

It has long been understood that the landscape of mountain belts is the result of the balance between tectonic uplift and surface processes, as modulated by denudation and sedimentation (Molnar 2003). Outside glaciated regions, river incision into bedrock has been recognized as a primary agent in both landscape evolution and large-scale surface mass transport (e.g., Burbank *et al.* 1996; Willett 1999; Whipple & Tucker 1999; Lavé & Avouac 2001). Erosion influences tectonics by modifying the mass distribution in the orogen, which controls the isostatic response and the strain localization. On the other hand, tectonic uplift or subsidence is related to the distribution of erosion and sedimentation zones.

Over the last fifteen years many numerical models have been developed to study feedbacks and interactions between tectonics and denudation in mountainous areas. However, in most of these models, transport of mass at the surface is either reduced to a diffusion law (Avouac & Burov 1996; Cattin & Avouac 2000), to a linear function of the local slope (Beaumont *et al.* 2001), or to a simple fluvial incision law where the mean topographic profile is represented by a river profile (Willett 1999). Those approaches do not take into account the dual nature of denudation in mountain ranges, which combines river bedrock incision and hillslope landsliding.

Here we explore how patterns of precipitation and rock strength affect both river and topographic profiles across the range of the Himalayas and southern Tibet. Following the approach of Godard *et al.* (2004) we have coupled a 2D thermomechanical model, which includes localization of deformation through frictional faults, to a surface process model based on a detachment-limited fluvial incision law. In contrast with Willett (1999), the mean topographic profile is computed using both the calculated trans-Himalayan river profile and an implicit description of the tributaries and hillslopes (Lavé 2005). Our purpose here is to evaluate the importance of rainfall and rock strength distributions in controlling the modalities of landscape denudation. We investigate the response of the mechanical model to forcings corresponding to variations of those two parameters. We first review the geodynamic and hydrological setting of the study area that encompasses the Himalayas of Nepal from the Gangetic Plain to the southern edge of the Tibetan Plateau. Next, we describe the modelling approach and the surface processes formulation introduced as a boundary condition at the surface of the model. Then, we present the behaviour of a reference

*From*: BUITER, S. J. H. & SCHREURS, G. (eds) 2006. *Analogue and Numerical Modelling of Crustal-Scale Processes.* Geological Society, London, Special Publications, **253**, 341–358.
0305-8719/06/$15.00 

model which closely mimics the main features of the Himalayan–Tibetan system. Starting from this reference model, the sensitivity of the results to rock strength and rainfall distribution is investigated.

## Geodynamical setting

### *Himalayan tectonics*

The Himalaya results from the collision between India and the southern edge of Eurasia. Since *c.* 20 Ma, tectonic and erosive processes have built an impressive landscape characterized by a steep topographic front from the 5000 m elevation Tibetan Plateau down to the Gangetic plain. Four major morphotectonic domains are usually recognized from north to south: the low-relief South Tibetan plateau, the High Himalaya (HH) with deep gorges and *c.* 8000 m summits, the mountainous to hilly relief of the Lesser Himalaya (LH), and the frontal low elevation relief of the Siwalik Hills (Fig. 1). The Himalayan range results from the successive activation of major thrust zones: the main central thrust (MCT) and the main boundary thrust (MBT) (Le Fort 1986). These two faults are presumed to branch upward from a major mid-crustal décollement, the main Himalayan thrust (MHT) (Schelling & Arita 1991; Zhao *et al.* 1993; Pandey *et al.* 1995; Lavé & Avouac 2001). Coeval with thrusting, the Indo-Gangetic foredeep formed in front of the rising Himalaya and accumulated several kilometres of Cenozoic molasse deposits, material eroded from the areas of high relief. Thin-skinned thrust-faulting has incorporated these sediments into the hanging walls of several thrusts, now expressed as the Siwaliks Hills. These frontal faults branch from the MHT, which roots at a depth of 30–40 km beneath the South Tibet (Zhao *et al.* 1993), and displays a ramp-and-flat geometry beneath the HH and LH domains (Schelling & Arita 1991; Pandey *et al.* 1995; Lavé & Avouac 2001). The long-term shortening rate across the range is *c.* 20 mm $yr^{-1}$ (Lyon Caen & Molnar 1985; Armijo *et al.* 1986) and is similar to present convergence imaged by GPS (Bilham *et al.* 1997). In central Nepal, geomorphic evidence

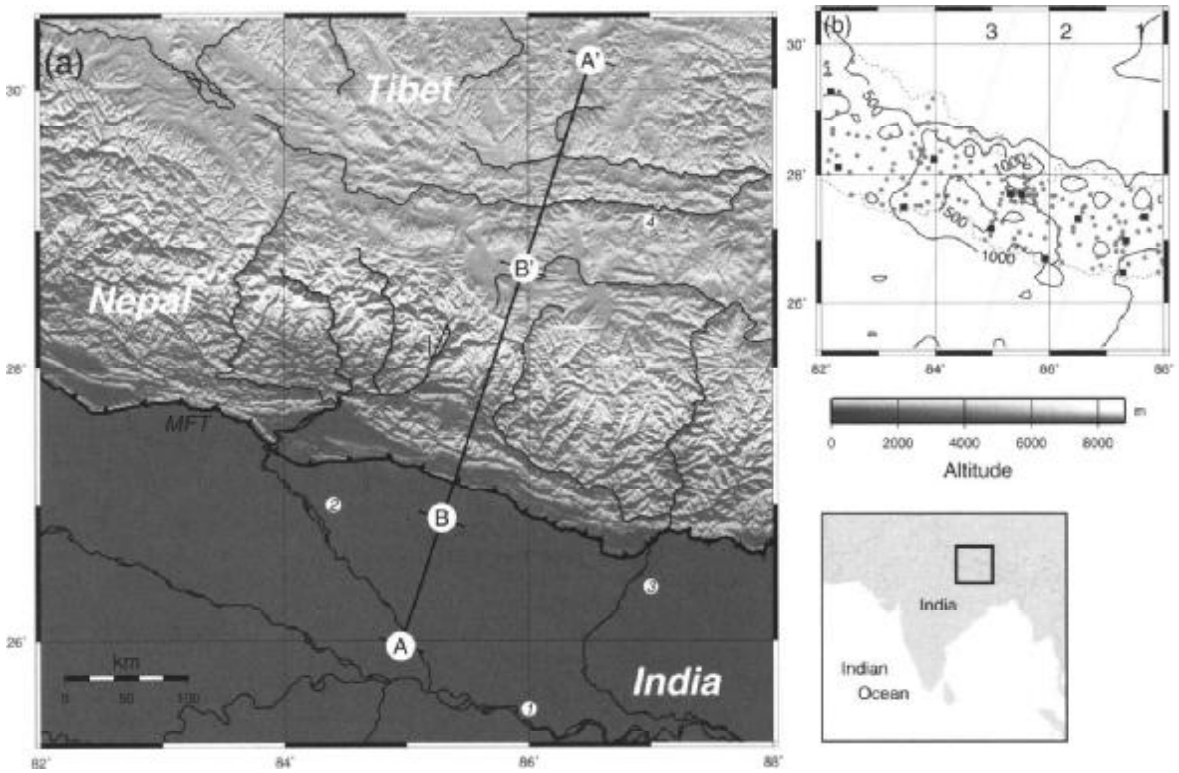


**Fig. 1.** Situation. (**a**) Topographic map of the study region (GTOPO30 DEM), showing the principal hydrographic features, the position of the main frontal thrust, and the cross sections AA′ (Fig. 3) used in the modelling and BB′ presented on Fig. 8. 1 – Ganga, 2 – Narayani, 3 – Sapt Kosi, 4 – Tsangpo. (**b**) Rainfall map derived from NOAA (2005) estimates. The position of the 3 cross-sections of Fig. 2 is indicated. Light grey dots and dark grey squares represent the rain gauges of GAME (2005) and NMFD (2005) networks, respectively.

suggests in addition that most of the present shortening across the Himalayas is transferred toward the main frontal thrust (MFT) (Lavé & Avouac 2000).

### *Precipitation, hydrology and erosive processes*

Precipitation in Nepal is mainly controlled by the barrier of the Himalayas, with a brutal condensation against the HH of the wet air coming from the Indian Ocean during the monsoon. Whereas a marked rain shadow develops on the northern flank of the HH, the prominent fluvial network of the southern flank, fed by intense rainfall, is deeply entrenched in the topography and actively contributes to the denudation of the orogen. Important lateral variations of the distribution of rainfall exist in Nepal (Figs 1 and 2), but, despite the amplitude of change, the consistent main patterns are the increasing precipitation from the Gangetic plain to the HH, the orographic barrier of the HH, and the low precipitation on the Tibetan Plateau. Several major north-south rivers drain the Himalayas of Nepal from southern Tibet down to the Indo-Gangetic plain. In Central and East Nepal, across the HH, those trans-Himalayan rivers are on average *c.* 50 km apart before joining, in the southern part of the LH, two major rivers systems, the Narayani and

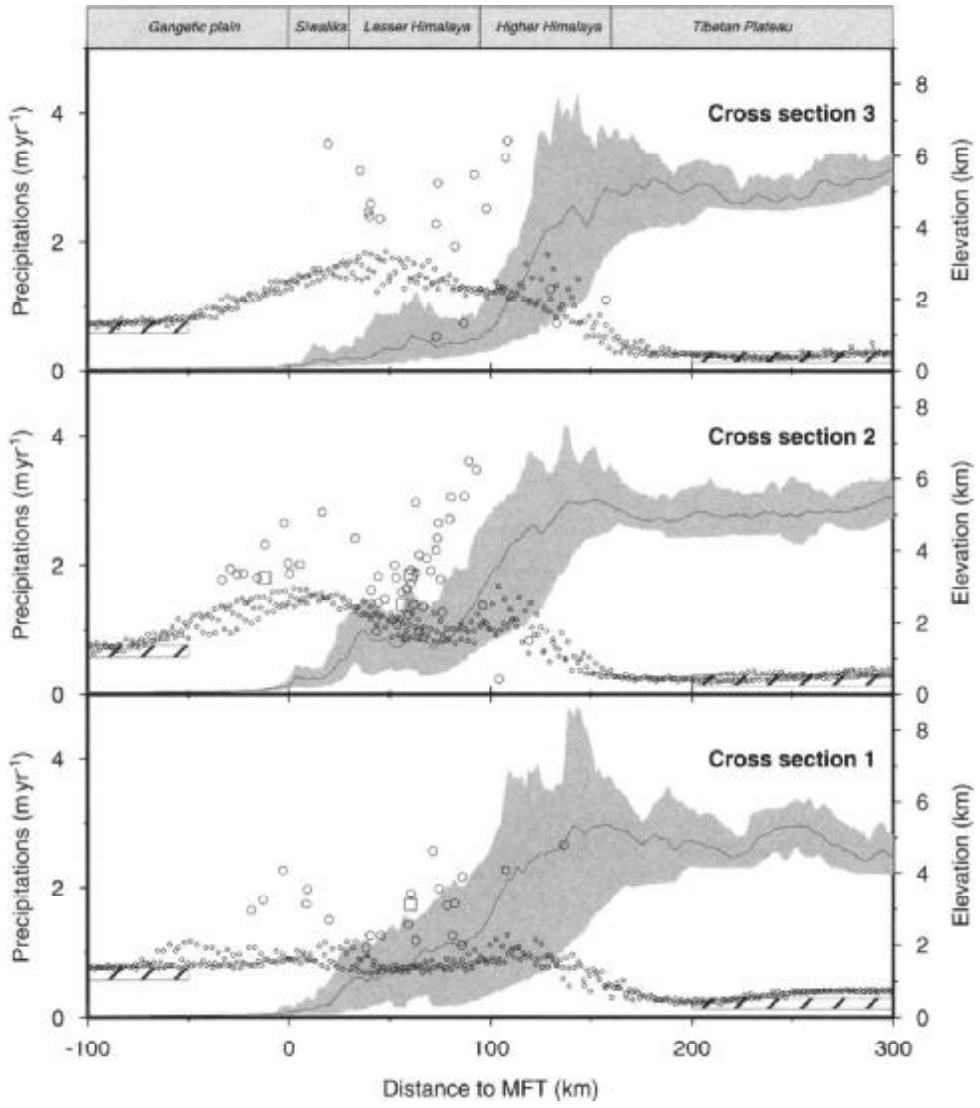


**Fig. 2.** Projection of the precipitation data on the three swathe profiles presented in Fig. 1, with corresponding mean elevation from GTOPO30 DEM (grey area indicates minimal and maximal values). Dots derive from NOAA dataset and circles and squares refers to measurements from GAME (2005) and NMFD (2005) gauge networks, respectively. Dashed boxes in Tibet and India represent compilation of data from GAME (2005) and IITM (2005), respectively. All swathes are 100 km wide.

Sapt Kosi basins. Both rivers are tributaries of the Ganga (Fig. 1). Trans-Himalayan rivers and fluvial terraces profiles in Nepal (Lavé & Avouac 2000, 2001), and cosmogenic data in India (Vance *et al.* 2003) suggest that erosion is maximal across the Siwaliks and the HH, lower in the LH, and minimal in South Tibet.

## Modelling approach

### *Geometry of the system*

Our model is based on a 700 km long N18°E cross-section perpendicular to the range, from the Gangetic Plain to the Tibetan Plateau (see Fig. 1 for the location). The principal geometric characteristics of our model are similar to Cattin and Avouac's model (2000) and our previous work (Godard *et al.* 2004) and are presented in Figure 3. The geometry of the Moho beneath South Tibet is derived from INDEPTH seismic profile (Zhao *et al.* 1993) and from gravity data (Cattin *et al.* 2001). The initial elevation for both river and mean topography mimics the main features of the present day topography.

### *Rheology*

We use a 2D Lagrangian finite element code (Hassani *et al.* 1997) that allows us to solve the constitutive rheological equations expressing the relationships between stress and strain tensors ($\underline{\underline{\sigma}}$ and $\underline{\underline{\varepsilon}}$, respectively). The behaviour of the materials is considered elasto-visco-plastic. The elasticity is expressed by Hooke's law (see specification of parameters in Table 1),

$$\varepsilon_{ij} = \frac{1+\nu}{E}\sigma_{ij} - \frac{\nu}{E}\mathrm{trace}(\underline{\underline{\sigma}})\delta_{ij} \qquad (1)$$

while the non-Newtonian viscous behaviour, dependent on temperature $T$, is controlled by the following relationship between deviatoric stress and strain rate $\dot{\varepsilon}$,

$$\dot{\varepsilon} = \gamma_0(\sigma_1 - \sigma_3)^n e^{E_a/RT} \qquad (2)$$

where $\sigma_1$ and $\sigma_3$ are the maximum and minimum principal stresses, respectively. The limit between the visco-elastic and the plastic domains is defined by a Drucker-Prager failure

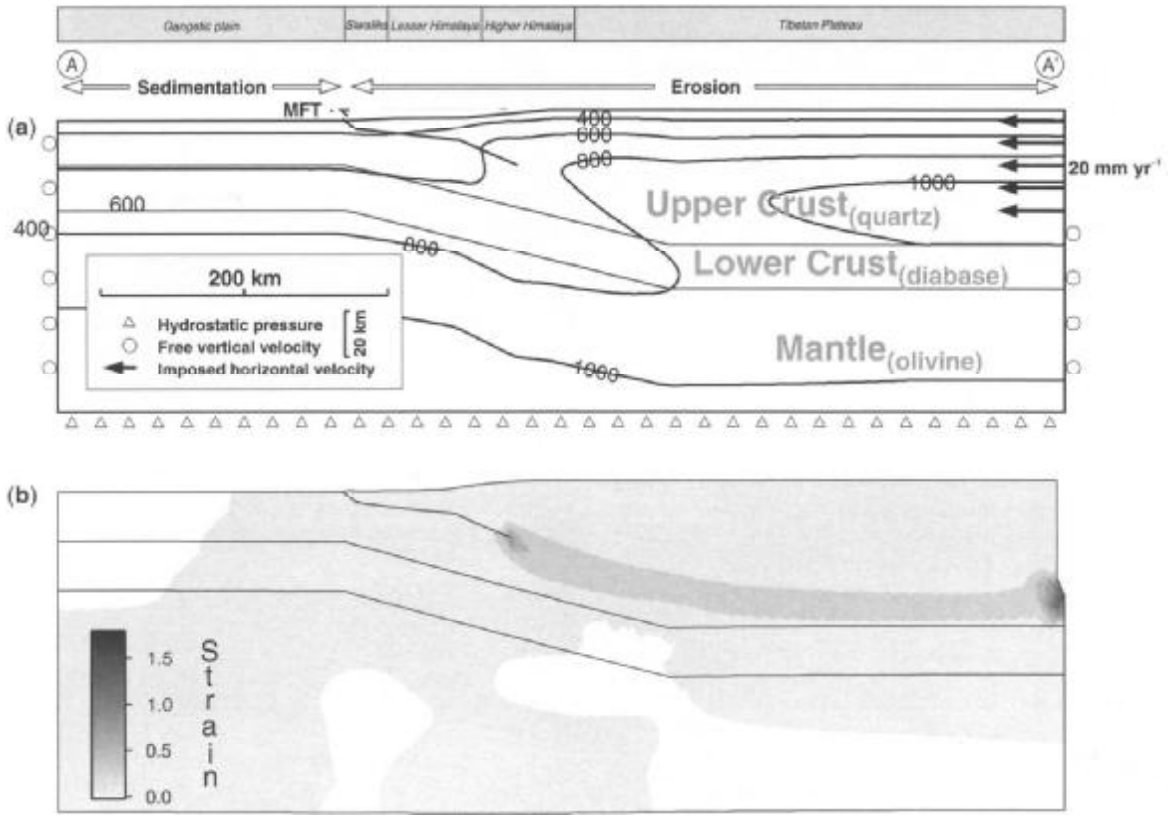


**Fig. 3.** Main features of the model. (**a**) Geometry of the system, temperature field ($K$), rheological units, and boundary conditions used for the modelling. In the foreland sedimentation balances subsidence. In the range, landscape evolution is controlled by the fluvial incision law. (**b**) Second invariant of the deviatoric strain tensor at the end of the simulation. Horizontal and vertical dimensions of model are 700 km and 130 km, respectively.

**Table 1.** *Rheological parameters used for the mechanical model*

| | Quartzite | Diabase | Olivine |
|---|---|---|---|
| Density, $\rho$ (kg m$^{-3}$) | 2900 | 2900 | 3300 |
| Young modulus, $E$ (Gpa) | 20 | 20 | 70 |
| Poisson's ratio, $\nu$ | 0.25 | 0.25 | 0.25 |
| Cohesion, $c$ (Mpa) | 10 | 10 | 10 |
| Internal friction angle, $\phi$ | 30° | 30° | 30° |
| Standard fluidity, $\gamma_0$ (Pa$^{-n}$ s$^{-1}$) | $6.03 \times 10^{-24}$ | $6.31 \times 10^{-20}$ | $7.00 \times 10^{-14}$ |
| Power law exponent, $n$ | 2.72 | 3.05 | 3.0 |
| Activation energy, $E_a$ (kJ mol$^{-1}$) | 134 | 276 | 510 |

Parameters from Carter & Tsenn 1987; Tsenn & Carter 1987; Kirby & Kronenberg 1987. Universal gas constant $R = 8.314$ J mol$^{-1}$ K$^{-1}$.

criterion, according to,

$$\frac{1}{2}(\sigma_1 - \sigma_3) = \left(c(\cot\phi) + \frac{1}{2}(\sigma_1 + \sigma_3)\right) \times \sin\phi \quad (3)$$

Godard *et al.* (2004) have shown that a composite quartz-diabase rheology associated with a fluvial incision law is required to explain both erosion rate and topographic profile in the Himalayas. Three layers are distinguished for the lithosphere: the upper and lower crusts, and the upper mantle. Each layer has specific mechanical properties. We use the empirical rheological equations and laboratory-derived material properties for quartz, diabase and dry olivine (Table 1). The temperature field from Henry *et al.* (1997) (Fig. 3) is used to compute the viscosity of the material. Considering the typical duration (*c.* 100 ka) of our simulations, we do not solve the heat equation. This temperature field is thus considered stable, relative to the mesh, over the run.

### *Boundary conditions*

The boundary conditions applied to the system are constrained by geodynamical data. Most of the observations available in this area (see Fig. 8 caption), including GPS measurements (Bilham *et al.* 1997; Larson *et al.* 1999) estimate a shortening rate of 20 mm yr$^{-1}$. Recently, Chen *et al.* (2004) suggested velocities closer to 13 mm yr$^{-1}$. A variation of this magnitude in convergence rate does not modify significantly our conclusions. We apply, therefore, a 20 mm yr$^{-1}$ horizontal velocity on the northern vertical face to a depth of 40 km, which is the depth of the high temperature and low viscosity zone under Tibet, used as a decoupling level in the crust. Vertical velocities on the other vertical faces are left free. The structure is supported by hydrostatic pressure at its base, which allows isostatic compensation and thus generates a coupling between rock-uplift and denudation.

A fault with a simple Coulomb friction law is introduced and follows the ramp-and-flat geometry proposed for the MHT. Due to the duration of our simulations we consider long-term deformation, which integrates a large number of seismic cycles, and slip on a low friction MHT ($\mu = 0.01$) is considered as continuous (Cattin & Avouac 2000). This low frictional surface connects to a mid-crustal high temperature zone that allows the localization of a narrow ductile deformation zone corresponding to the continuation of the MHT (Fig. 3), imaged by the INDEPTH experiment (Zhao *et al.* 1993).

The main purpose of this study is to focus on the influence of the surface processes applied to the topography as a boundary condition. We distinguish two domains in term of surface processes: the foreland south of the MFT ($x < 0$), with active sedimentation, and the mountain range north of the MFT, dominated by active erosional processes. The first domain, the Indo-Gangetic basin is classically described as a low elevation over-filled basin (Lyon-Caen & Molnar 1985): we thus assume in the following a constant *c.* 0 m elevation for it. The characteristics of the fluvial incision formulation used in the range are described further down.

### *Numerical method*

The approach used here for simulating tectonic processes employs the dynamic relaxation method (Underwood 1983) coupled with the finite element method. The dynamic relaxation (DR) method is an explicit iterative method for the static solution of mechanical problems. The method can easily take into account large deformations of materials with non-linear behaviour. It is based on the fact that the static solution is the steady-state part of the transient response

for a temporal load,

$$M\ddot{q} + C\dot{q} + Kq = F_e \tag{4}$$

with $q$, $\dot{q}$ and $\ddot{q}$ the displacement, velocity and acceleration vectors, respectively. $C$ is the damping matrix, $K$ the stiffness matrix, and $F_e$ the external forces applied on the system, respectively. $M$ is the fictitious mass matrix, which can be chosen to be non-singular. The DR algorithm evaluates in each time step the unbalanced forces, that is, the acceleration $\ddot{q}$ due to the disequilibrium between external and internal forces,

$$\ddot{q} = M^{-1}(-C\dot{q} - Kq + F_e) \tag{5}$$

The quantity $C\dot{q}$ represents a numerical viscosity introduced for stabilization purposes, and $Kq$ is the internal forces computed from the integration of the constitutive material laws (Eqns 1, 2 and 3).

The time integration scheme computes velocity and displacement using an explicit (forward in time) finite difference method. The explicit algorithm is conditionally stable, the condition being

$$\Delta t \leq \frac{2}{\omega_{\max}} \tag{6}$$

where $\lambda_{\max} = \omega^2_{\max}$ is the highest eigenvalue of the matrix $M^{-1}K$.

## Time scenario and stability

The total duration of the simulations is *c.* 320 ka, with an effective simulation duration (Fig. 4) of 80 ka and a time step of 1.5 yr. The elements are triangular with a typical size (diameter of circumscribing circle) of 3 km.

The convergence of the algorithm is associated with the minimization of unbalanced forces (i.e., acceleration); the different processes acting on the system are thus introduced gradually (Fig. 4). The simulation is divided into two steps: (1) a stabilization period where tectonics and denudation are introduced

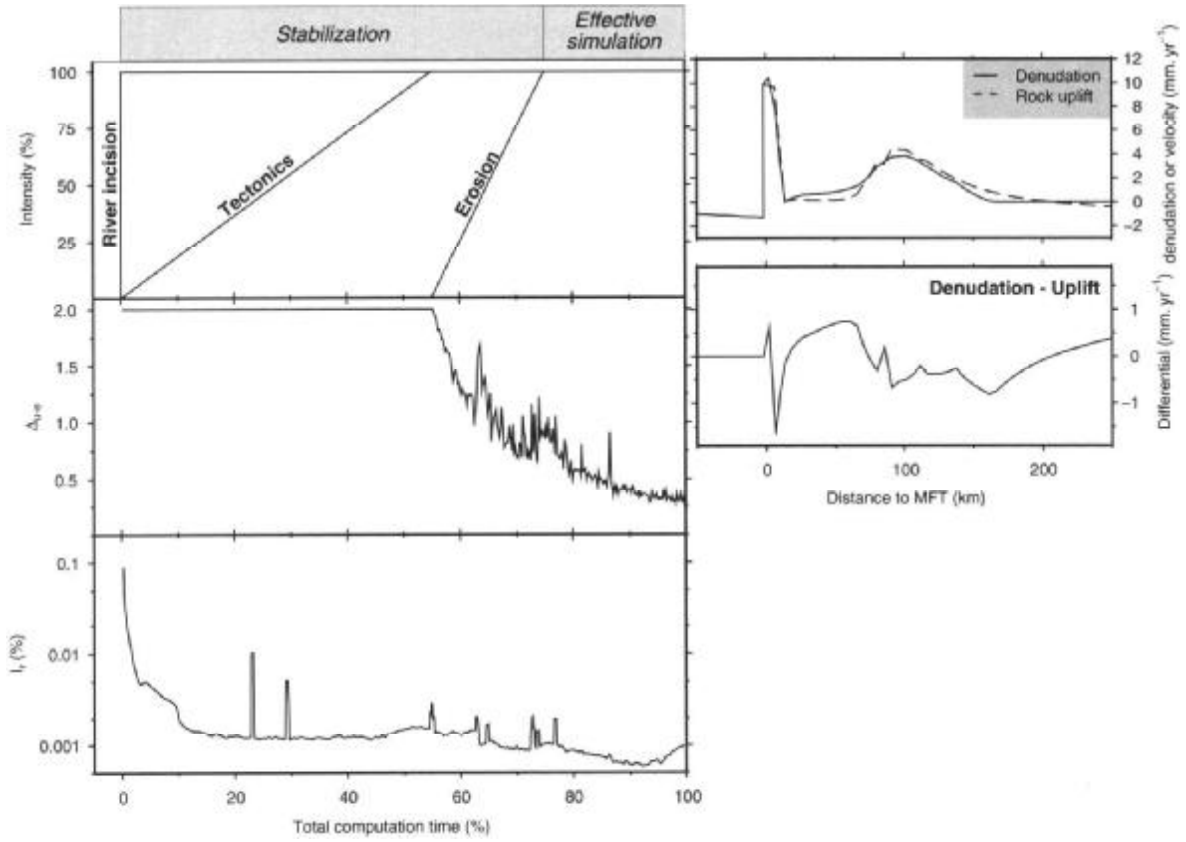


**Fig. 4.** Time scenario of boundary conditions (see Fig. 6 for details on the relationship between the tectonic computation and the surface processes), evolutions of the inertial ratio ($I_r$, Eqn 7) and of the difference between uplift and denudation ($\Delta_{u-e}$, Eqn 8). See text for details. The uplift and denudation profiles at the end of the computation, and their difference, are also plotted.

progressively, (2) an effective simulation period, when all the processes act at full intensity. The initial river profile is the same as the initial mean topographic profile. Starting fluvial incision before topographic denudation is thus necessary to promote the stabilization of the river (i.e., convergence toward the steady-state profile) and to allow a significant entrenchment to exist at the beginning of the effective simulation period, thereby initiating topographic denudation. To evaluate the stability of the computation, we use the inertial ratio, $I_r$ computed as,

$$I_r = \frac{\|\vec{F_e} + \vec{F_i} + \vec{F_c}\|}{\|\vec{F_e}\| + \|\vec{F_i}\| + \|\vec{F_c}\|} \quad (7)$$

where $\|\vec{F_e}\|$, $\|\vec{F_i}\|$ and $\|\vec{F_c}\|$ are respectively the external, internal and reaction forces acting on the system. The mechanical steady state is defined as an average equilibrium between uplift and denudation rates, which is computed as the average, at each point along the profile, of the normalized difference between denudation, $e_i$, and rock-uplift, $u_i$,

$$\Delta_{u-e} = \frac{\sum_{i=1}^{N_p} |u_i - e_i|}{\sum_{i=1}^{N_p} (u_i + e_i)/2} \quad (8)$$

The time limit of the simulations is imposed by distortions of the mesh in high erosion areas (Siwaliks foothills).

Figure 4 shows that the inertial ratio $I_r$ is lower than 0.01% during the effective simulation period, which attests to the overall numerical stability of the model. The slight increase of the ratio at the end of the run is associated with the reduction of the size of the elements due to erosive processes. During the effective simulation period, $\Delta_{u-e}$ converges toward a constant value of $c.$ 0.3 which indicates a slight degree of disequilibrium. Part of the mismatch between uplift and erosion corresponds to the contribution of horizontal velocity to uplift. Our main concern is to reach a relative equilibrium that allows inter-model comparison.

## Surface processes

### *Fluvial incision*

Recent studies have underlined the key role played by fluvial incision in driving unglaciated landscape denudation (Whipple & Tucker 1999). Whereas different functional forms have been proposed to model fluvial incision (Whipple & Tucker 2002), in an attempt to develop a simple approach, we have used a detachment-limited relation that provides satisfying first-order results in the Subhimalaya (Lavé & Avouac 2001). This approach states that the bedrock incision rate of a river, at abscissa $x$, is proportional to the fluvial shear stress $\tau_x$ in excess of some threshold $\tau_c$:

$$\left(\frac{\partial h_{\text{riv}}}{\partial t}\right)_x = K_x(\tau_x - \tau_c) \quad (9)$$

with $\tau_x = \rho \cdot g \cdot H_x \cdot S_x$, $\rho$ the density of water, $S_x$ the river slope, $H_x$ the flow depth and $K_x$ an erodability coefficient that primarily depends on rock strength with respect to abrasion (Lavé & Avouac 2001), but which could mask hidden dependencies on sediment flux and flood distribution. For the sake of simplicity, we will ignore the two latter variables. The shear stress $\tau$ represents the force exerted by the flowing water on an area unit of the channel bottom, and is derived from energy expenditure equation. Assuming Manning's equation to describe mean water flow velocity, and employing a scaling law between river width and discharge, it can be shown (Howard *et al.* 1994) that shear stress can reduce to an expression of channel slope and drainage area. The central Himalaya, like many other mountain ranges, displays a relative cylindrical structure and linear drainage systems perpendicular to the range axis. Along these linear drainage systems, 50 km apart, the drainage area is linearly related to the cross-range distance (Fig. 5). Shear stress can then be expressed by:

$$\tau_x = k_1(\bar{P}_x - P_r)^{\gamma}(L(X - x))^{\beta}\left(\frac{S_x}{s_0}\right)^{\alpha} \quad (10)$$

where $k_1$ is a coefficient that depends on the river network geometry and sediment size, $L$ the width of the watershed, $s_0$ the average sinuosity of the main stream (Fig. 5) and $\alpha$, $\beta$, $\gamma$ are constant exponents. $\bar{P}$ is the average precipitation on the watershed and $P_r$ some threshold runoff. $X$ is the abscissa of the drainage divide. The values of these parameters are given in Table 2.

## Landscape denudation by fluvial incision and landslides

Many numerical models (e.g., Willett 1999) compute the denudation rates applied to topography directly from Equation 9. However, despite their prominent role, the main rivers do not account for the mean topography, which is the pertinent variable for the upper boundary

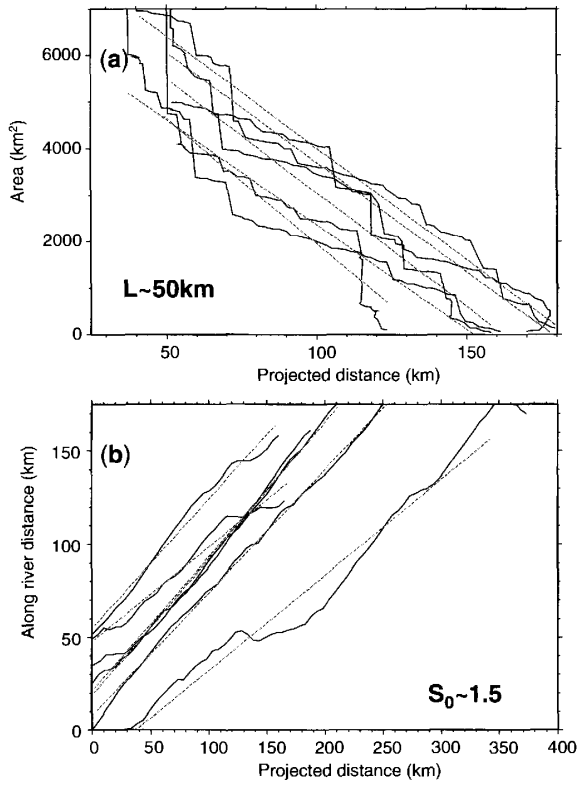


**Fig. 5.** Two examples of parameter determination for the fluvial incision formalism. (**a**) Evolution of the area of the watershed of some major Trans-Himalayan rivers as a function of projected distance (abscissa on a N18° trending line) illustrating the existence of a linear relationship between those two parameters. The slope of the fit (dashed line) gives the width $L$ of the watershed, ranging from 45 to 53 km. (**b**) Evaluation of the sinuosity for some major Trans-Himalayan rivers through the relation between projected distance (N18°) and along river distance (measured along the river path). The slope of the fit (dashed line) gives the inverse of sinuosity $1/s_0$, sinuosity ranges from 1.4 to 1.9. Fluvial network and watersheds extracted from a 90 m DEM.

**Table 2.** *Denudation law parameters*

| Parameter | Value |
|---|---|
| Hillslope angle of repose, $\theta_c$ (degrees) | 40 |
| Himalayan valley width, $L$ (km) | 50 |
| Sinuosity, $s_0$ | 1.5 |
| Slope exponent, $\alpha$ | 0.7 |
| Area exponent, $\beta$ | 0.27 |
| Precipitation exponent, $\gamma$ | 0.33 |
| Critical shear stress, $\tau_c$ (Pa) | 30 |
| $k_1$ (Pa $m^{-0.87}$ $s^{0.33}$) | 5677 |
| $k_2$ (Pa $m^{-1.03}$ $s^{0.33}$) | 2400 |
| Threshold runoff, $P_r$ (m) | 0.2 |

From Lavé & Avouac (2001) or Himalayan river measurements (e.g., Fig. 5).

condition of mechanical modelling. The elevation profile of the trans-Himalayan rivers in fact represents the base level for the network of tributaries that are draining the whole topography, from their sources at the base of the hillslopes to their confluence with the trunk stream. At a given abscissa, the mean elevation of the topography $\bar{h}$ is therefore the sum of three contributions: (1) the elevation of the main river $h_{\text{riv}}$, (2) the fluvial relief associated to the tributaries $\Delta h_{\text{trib}}$ that we assume to be controlled by the same incision law as the main river, and (3) the mean relief of the hillslope from the fluvial network to the crest, $\Delta h_{\text{hill}}$. In active orogens, hillslopes are dominated by landslides (Hovius *et al.* 1997); we thus assume that they display a critical slope angle of repose $\theta_c$ and that they react instantaneously to any local base-level drop. A new formulation to integrate the fluvial relief associated with the tributary network (Lavé 2005) enables computation at each time step of the changes of the elevation of the trunk stream from Equation 10 and the changes in mean topography according to

$$\left(\frac{\partial \bar{h}}{\partial t}\right)_x = \left(\frac{\partial h_{\text{riv}}}{\partial t}\right)_x + K_x(k_2(P_x - P_r)^{\gamma} \times \Delta h_{\text{trib}_x}^{\alpha} - \tau_c) \quad (11)$$

with,

$$\Delta h_{\text{trib}} = \Delta h_{\text{total}} - \Delta h_{\text{hill}} = \Delta h_{\text{total}} - \frac{\Delta l}{2}\tan\theta_c \quad (12)$$

where $k_2$ is a coefficient which depends on the tributary network geometry and $\Delta l$ is the horizontal distance between the crest and the base of the hillslope.

The solving scheme is based on the interplay between two profiles: the mean elevation profile and the river profile (Fig. 6). The river profile is advected with the tectonic velocity field computed by the mechanical solver and the incision rates computed from Equation 10. The mean topographic profile constitutes the upper boundary of the mechanical model. Feedback between tectonics and erosion is achieved by this dynamic interface: (1) the mean topography is advected with the tectonic velocity field and the denudation rates from Equation 11, and (2) the internal stress field is affected by mass removal from the mean topography by denudation processes.

The above formulation does not satisfy, strictly speaking, the mass conservation equation and could be viewed as incomplete. However, in

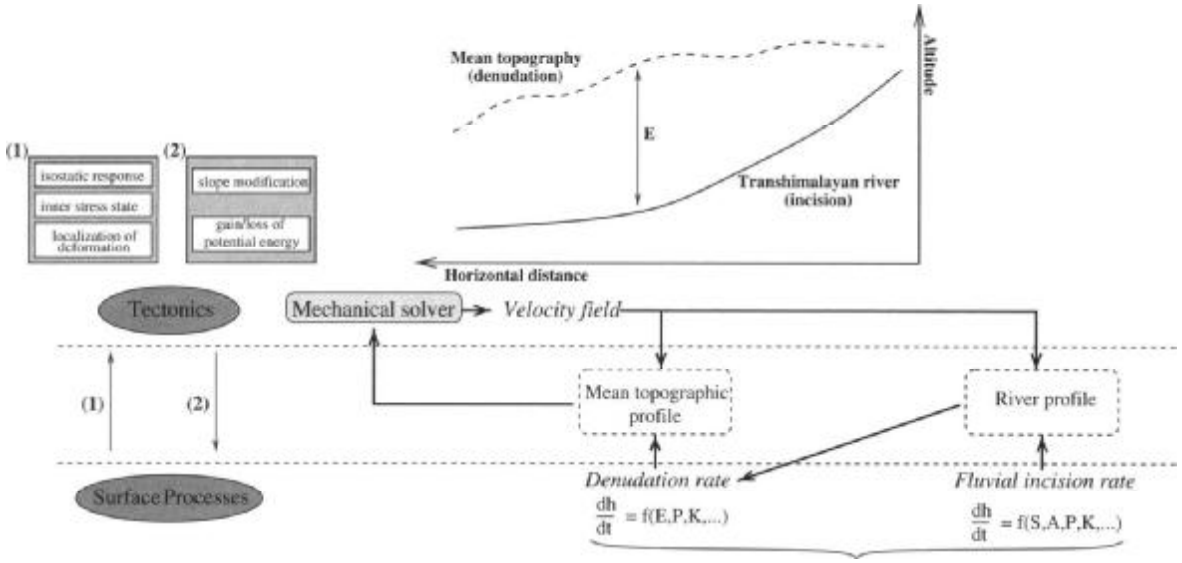


**Fig. 6.** Relationship between the mechanical solver and the surface processes computation. S: slope of the river, A: area of the watershed, P: precipitation over the watershed, K: erodability, E: entrenchment.

a detachment-limited system, the required hydraulic energy to incise bedrock is considered to be much higher than the energy required to transport the eroded sediments toward the foreland basin. In the above formalism, the sediments are systematically and efficiently evacuated from the range and do not play any explicit role in erosion processes, so mass conservation is not strictly required.

## Controlling parameters in fluvial incision and landscape denudation

The threshold $\tau_c$ of the incision law is close to the threshold of pebble motion in rivers and, in steep mountains, much lower than average shear stress. Neglecting this threshold term in Equations 9 and 11 provides two simple expressions for river incision and landscape denudation, as the products of a local stream or regional topographic gradient ($\Delta h$ and $S$ respectively) and of a coefficient which depends on several factors. The denudation term depends on local precipitation, local erodability and valley width $L$ (embedded in $k_2$). The main trans-Himalayan river incision depends not only on local erodability and valley width, but also on regional precipitation as averaged over the length of its contributing area. For a mountain range subjected to uniform erodability conditions and precipitation, the study of coupling between erosion and tectonics can be reduced to an investigation of the role of a single erosion parameter, $E^* = f(P, K)$. Depending on the precipitation exponent $\gamma$, the sensitivity of the system to precipitation can be viewed as weak relative to the sensitivity to abrasion rock strength. For a precipitation exponent $\gamma = 0.33$ and according to Equations 9 and 11, increasing the precipitation by a factor 8 is equivalent to increasing the erodability by a factor 2.

However, the Himalayas display large cross-range variations in precipitation and rock types. Because of these variations, and because tributary denudation and main river incision depend on local and integrated precipitation respectively, the above non-dimensional analysis and reliance on a single erosive parameter loose their validity. To investigate these complexities in the interaction between landscape denudation, main river incision and tectonics, we consider different case studies in which the erodability and precipitation profiles are varied independently. To illustrate lateral (Fig. 1) and cross-range variations in precipitation, a series of profiles representing the lateral amplitude variation of rainfalls in Nepal will first be tested.

Rock types across the Himalayan range display strong variation, from poorly cemented sandstones in the Siwalik Hills, to schists, quartzite and sandstones in the LH, or gneissic units in the HH, or sedimentary units in the South Tibetan series (Fig. 7). A recent study (Attal & Lavé 2006) has shown that these lithologic variations can lead to differences up to 3 orders of magnitude in pebble abrasion rates. Similarly, the bedrock erodability of the Siwalik units represents an erodability coefficient 15 times larger than the LH units: $K_{\mathrm{siw}} = 1.05 \times 10^{-1}$ mm yr$^{-1}$ Pa$^{-1}$ and $K_{\mathrm{LH}} = 0.76 \times 10^{-2}$ mm yr$^{-1}$ Pa$^{-1}$, respectively

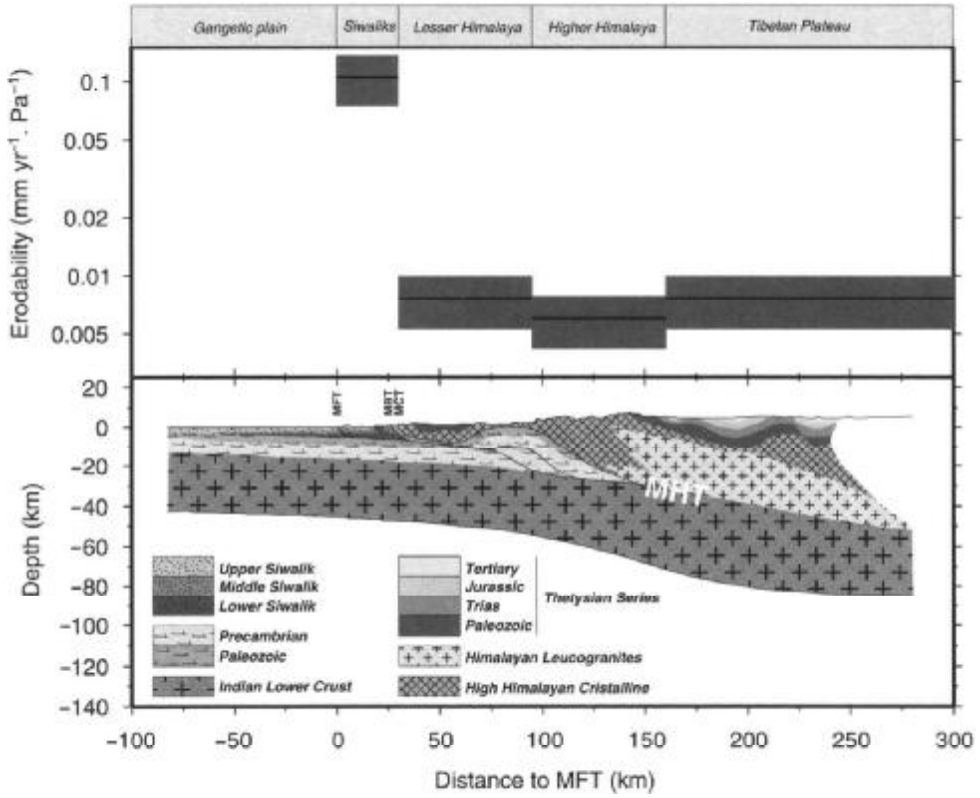


**Fig. 7.** Erodability values determinated across Central Nepal (Lavé & Avouac 2001) and corresponding geological cross-section modified from Lavé & Avouac (2001). MBT: Main Boundary Thrust; MCT: Main Central Thrust.

(Lavé & Avouac 2001). In order to evaluate the sensitivity of our model to this parameter, we test different kinds of profiles. First we consider that erodability in the Siwalik Hills is $K_{siw}$ while the erodability of the Lesser Himalaya ($K_{LH}$) is applied to the entire range north of the frontal foothills. Then, we consider homogeneous profiles across the range, where no variation of erodability is considered, with erodability ranging from $0.5 \times 10^{-2}$ mm yr$^{-1}$ Pa$^{-1}$ to $2 \times 10^{-2}$ mm yr$^{-1}$ Pa$^{-1}$. Finally, considering that the erodability in the HH has been evaluated by Lavé and Avouac (2001) such that $K_{HH}$ *c.* 0.8 $K_{LH}$, we introduce this variation to evaluate the influence of slight changes in erodability.

## Reference model

From the observations of Figures 2 and 7, two reference profiles are defined for both precipitation and erodability. These two profiles are used as an input for the modelling. The results obtained with this model (Fig. 8, hereafter refered to as the reference model) are in good agreement with the available data sets in the study area (Fig. 1).

The horizontal velocity profile (relative to India) shows that the 20 mm yr$^{-1}$ of convergence applied as a boundary condition are transferred to the MFT. This is related to the low-friction coefficient of the fault, which allows free slip on it. The calculated convergence rate across the range is in agreement with the data, including (1) the horizontal shortening deduced from the uplift of fluvial terraces in the Siwalik foothills (Lavé & Avouac 2001), (2) the progradation of the Gangetic Plain sediments associated with the flexure of the Indian plate (Lyon-Caen & Molnar 1985), and (3) South Tibet Quaternary grabens extension (Armijo *et al.* 1986). Due to gravitational collapse of the range, the horizontal velocity is slightly higher than 20 mm yr$^{-1}$ in the Lesser Himalaya.

This gravitational collapse also accounts for the offset of the calculated topographic profile, which is shifted southward relative to the present-day topography. However, it still preserves both the clear slope transition between the HH and the LH, and the respective average values of slopes in those areas. The present-day topography is used as initial profile for both the mean topography and the main trans-Himalayan river. To allow a significant entrenchment to be created before the beginning of the effective simulation period, the incision of the main

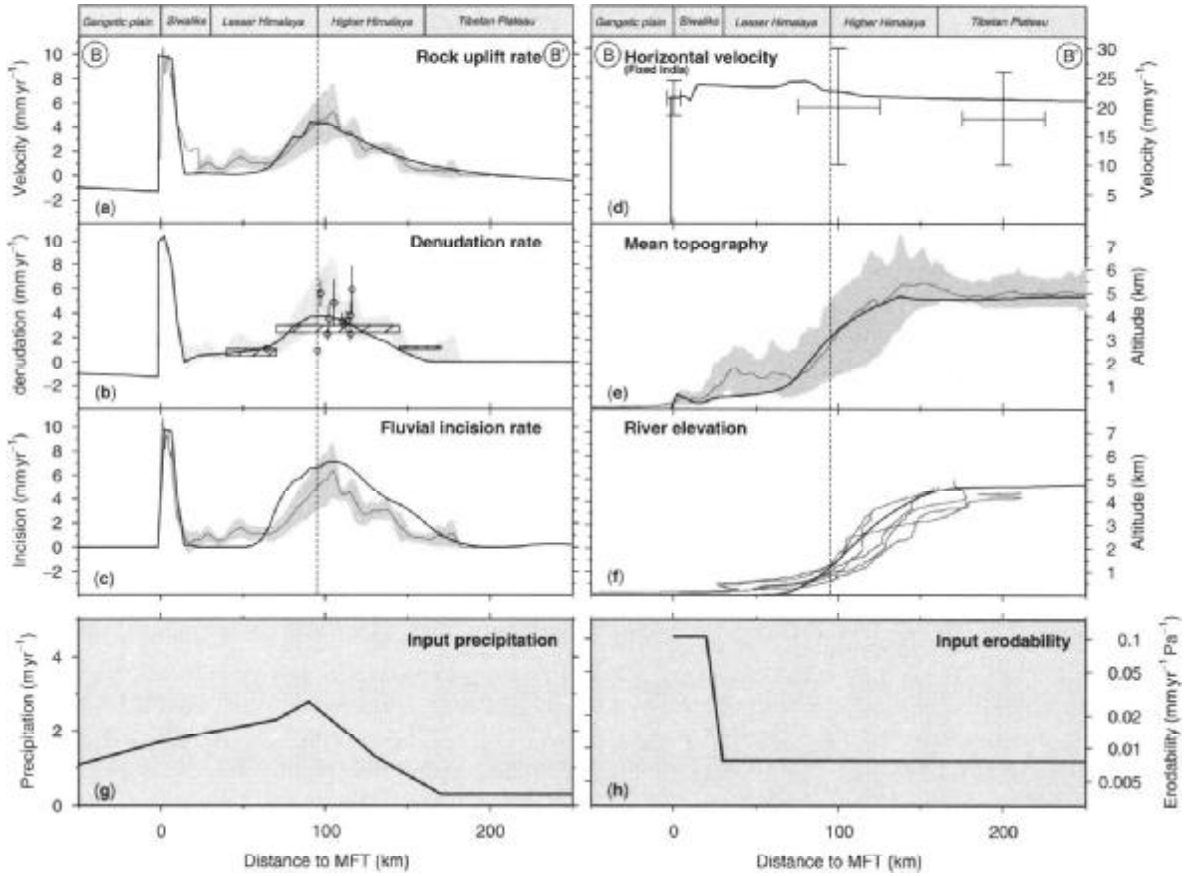


**Fig. 8.** Reference model. Thick black lines represents model outputs averaged on the last 1% of computation time. The data used to constrain the model outputs are listed below, see text for details. (**a**) Uplift profile, data from Lavé and Avouac (2001): mean value (solid thin line) and $1\sigma$ confidence interval (grey area). (**b**) Denudation profile, fission track data from Burbank *et al.* (2003) and averaged cosmogenic denudation rates from Vance *et al.* (2003) (dashed boxes). (**c**) Fluvial incision profile, data from Lavé & Avouac (2001): mean value (solid thin line) and $1\sigma$ confidence interval (grey area). (**d**) Horizontal velocity profile, control points from Lavé and Avouac (2000), Lyon-Caen & Molnar (1985) and Armijo *et al.* (1986) (north to south). (**e**) Topographic profile, data derived from GTOPO30 DEM mean (solid thin line) and extreme values (grey area). (**f**) River profile, trans-Himalayan river profiles from Lavé and Avouac (2001). (**g**) and (**h**) present rainfall and erodability profiles used as an input in the modelling. Note that time parameterization is different than that used by Godard *et al.* (2004).

trans-Himalayan river starts at the beginning of the simulation, while the denudation of topography begins later (Fig. 4). Even though the river profile does not reach a strict steady state, it tends to stabilize at the end of the run (Fig. 9). The modelled river profile displays a shape which is in the range of that observed for the main rivers crossing the range.

Fluvial incision rates across the range were calculated by Lavé and Avouac (2001) from a detachment-limited fluvial incision law calibrated in the Siwaliks and the LH. The incision rates on the main trans-Himalayan river computed from Equation 10 give values slightly higher than the data. However, the wavelength and position of the extrema in the Siwaliks and at the LH-HH boundary are consistent with observations.

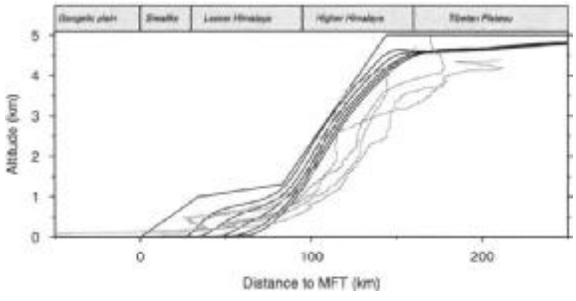


**Fig. 9.** Evolution of the river profile during the reference run (black lines). The time interval between each profile is *c.* 60 ka. The grey lines represent observed trans-Himalayan river profiles.

Denudation is compared with exhumation rates deduced from apatite fission-track ages in the HH (Burbank *et al.* 2003) and cosmogenic dating of river sediments, which provide an estimation of short-term denudation rate on the watershed (Vance *et al.* 2002). An estimation of uplift rates across the range was deduced from the fluvial incision profile (Lavé & Avouac 2001). This data set indicates that denudation and uplift reach a maximum in the Siwaliks and at the boundary between the Lesser and Higher Himalaya and decrease to a minimum in the LH and South Tibet. Computed denudation and vertical velocity profiles from the model display similar patterns, which are consistent in amplitude and wavelength with what is observed in Central Nepal.

A maximum for uplift, denudation and incision can be observed in the Siwaliks; its presence is mainly due to the high erodability value assigned to this area. The localization of another maximum at the LH-HH boundary can be associated with three mechanisms: (1) presence of a high precipitation zone in the HH, (2) localization of high river slopes in this area, implying high incision rates and, as a result, high entrenchment and denudation, and (3) existence of a ramp for the MHT below the HH. The relative importance of those three contributions is examined in the two next sections.

## Sensitivity to precipitation patterns

### *Influence of rainfall amplitude*

The precipitation (collected by the hydrographic network) directly influences the incision on the main trans-Himalayan river according to Equations 10 and 11. The response of the system was tested for various rainfall profiles (Fig. 10), which differ in the amplitude of precipitation in the high range. The erodability profile is the same as for the reference model (Fig. 8).

The increase of precipitation at the LH-HH transition leads to higher denudation rates in this area, whereas the changes in rainfall have no significant effects on denudation in the southern part of the LH. This can be related to the fact that the rock-uplift is close to 0 in the LH, which reduces the sensitivity of the river to the variations of discharge. Fluvial incision of the trans-Himalayan rivers is much less affected than the local incision along tributaries (inferred from the denudation profile) and is, therefore, less than the topographic denudation. This is because discharge along the trans-Himalayan rivers reflects the integration of precipitation along the whole profile and because precipitation is kept constant in South Tibet. Furthermore the variability of incision in the HH leads to important variations of entrenchment (i.e., difference of elevation between the topographic and river profiles, $\Delta h_{\text{total}}$ in Eqn 12), which propagates to the denudation rates in this area.

The near steady-state topographic profile is relatively insensitive to variations in precipitation at the timescale of our study. The increase in denudation near the LH-HH boundary is thus correlated to an increase in the uplift in this area. This highlights a level of coupling between tectonics and erosion, where increased precipitation induces more denudation and more uplift as an isostatic response. As a counterbalance, the uplift, by increasing topographic gradients and tributary relief, will favour an increase in landscape denudation.

### *Constant precipitation rates over the range*

In order to quantify the effects of the rainfall distribution, the behaviour of the model is tested for a set of profiles where precipitation rates are constant between the MFT and southern Tibet. This constant precipitation rate ranges from 0.3 m $yr^{-1}$ to 3.5 m $yr^{-1}$. On the Tibetan Plateau the precipitation rate falls to 0.3 m $yr^{-1}$ for all the profiles (Fig. 11), to take into account the orographic barrier of the HH. The results reveal that the model is relatively insensitive to the existence of a maximum in precipitation at the LH-HH transition.

When comparing simulations with constant rainfall over the range to what is obtained with the reference model, it appears that the existence of a high precipitation zone between the HH and the LH does not have a noticeable consequence, in our model, on the position of the maximum for denudation, incision or uplift. However the amplitude of this maximum depends directly on the amount of precipitation provided to the system.

The uplift pattern stays unchanged whatever the rainfall profiles, with a maximum at the transition between the HH and the LH. Part of this is due to the rather low value of the precipitation exponent ($\gamma = 0.33$) in the detachment limited incision law (Eqns 10 and 11). In area/slope analysis (Whipple & Tucker 2002), the discharge/area or precipitation exponents cannot be measured, but only estimated relative to the slope exponent. Some studies along rivers draining regions with variable uplift rates (Tomkin *et al.* 2003; Van der Beek & Bishop 2003) have, however, proposed absolute values for the discharge/area exponent, but with large uncertainties. According to Lavé & Avouac's study (2001) in the Siwaliks, and based also on

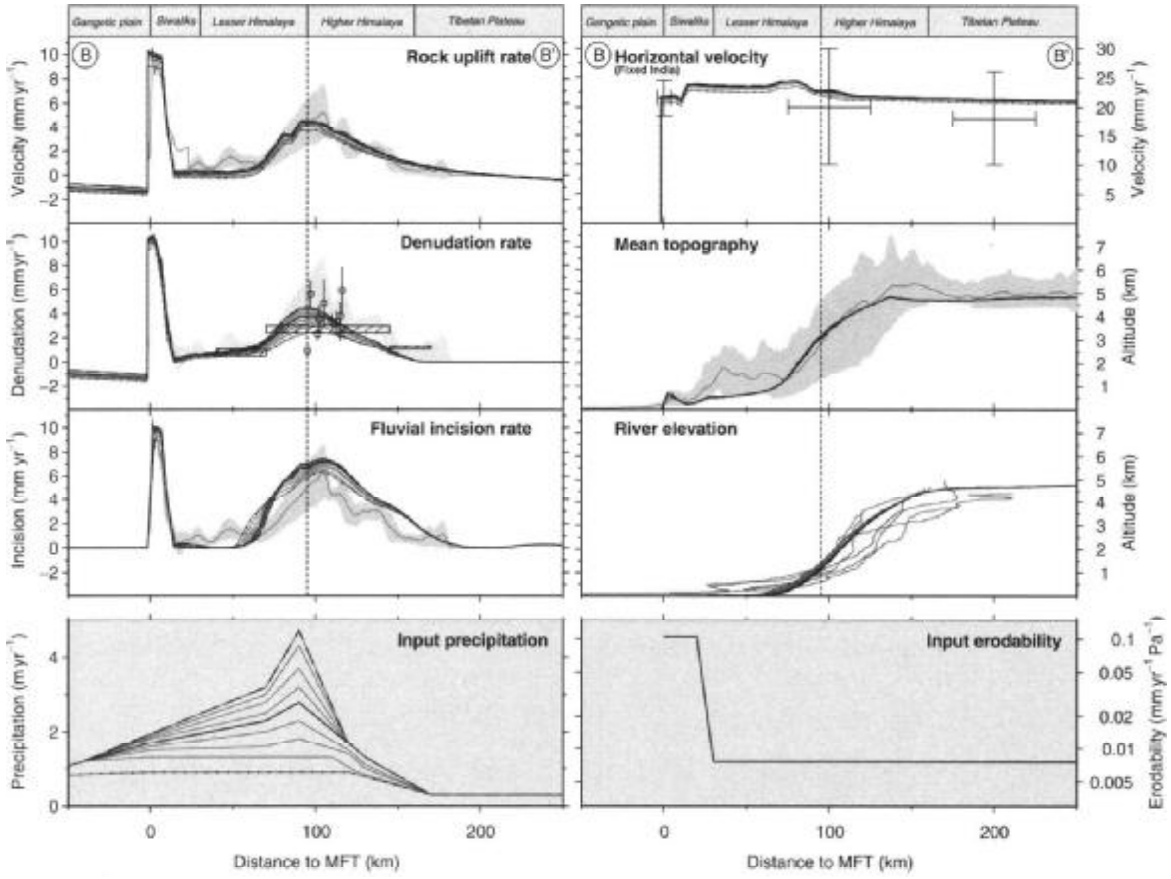


**Fig. 10.** Results of the simulations with various rainfall profiles. Dashed and dotted lines refer to the maximum and minimum rainfall profiles respectively. The solid bold line is the reference model presented in Fig. 8. The data sets used to compare with the model outputs are the same as in Fig. 8.

a larger data set of worldwide rivers, Lavé and Attal (2003) suggest that the shear stress exponent in the detachment limited incision law is ranging between 0.7 and 1.3. Consequently, the precipitation exponent would range between 0.23 and 0.43. Even though more work is still required to better assess the physical expression of bedrock incision laws, we hypothesize that the sensitivity of incision to precipitation is relatively low. In contrast with previous studies (Thiede *et al.* 2004), it brings the idea that the maximum for rock uplift at $x \sim 100$ km, observed both in the model outputs and the data from Lavé and Avouac (2001), is mainly related, in our model, to the ramp-flat geometry of the MHT rather than to the location of the peak of precipitation.

## Sensitivity to erodability

### *Constant erodability*

A set of profiles with constant erodability from the MFT to the Tibetan Plateau, ranging from $2.5 \times 10^{-3}$ mm yr$^{-1}$ Pa$^{-1}$ to $2 \times 10^{-2}$ mm yr$^{-1}$ Pa$^{-1}$ were tested (Fig. 12). Due to the linear relationship between erodability and both incision and denudation rates (Eqns 10 and 11), a slight increase in erodability has important implications on the global behaviour of the model.

Increasing erodability leads to higher incision and denudation rates and a coincident augmentation in the uplift rate. The sensitivity is maximum in the HH, where the use of an erodability of $2 \times 10^{-2}$ mm yr$^{-1}$ Pa$^{-1}$ leads to denudation rates up to 10 mm yr$^{-1}$ in the HH, which far exceed the values of the denudation rate estimated in this area. Erodabilities in the $0.5-1 \times 10^{-2}$ mm yr$^{-1}$ Pa$^{-1}$ range gives values for denudation and uplift in much better agreement with the observations.

Variations of erodability strongly influence both the amplitude and the location of the maximum of fluvial incision rate. This can be related to the regressive incision of the main trans-Himalayan river in response to increasing erodability, which offsets both the maximum for

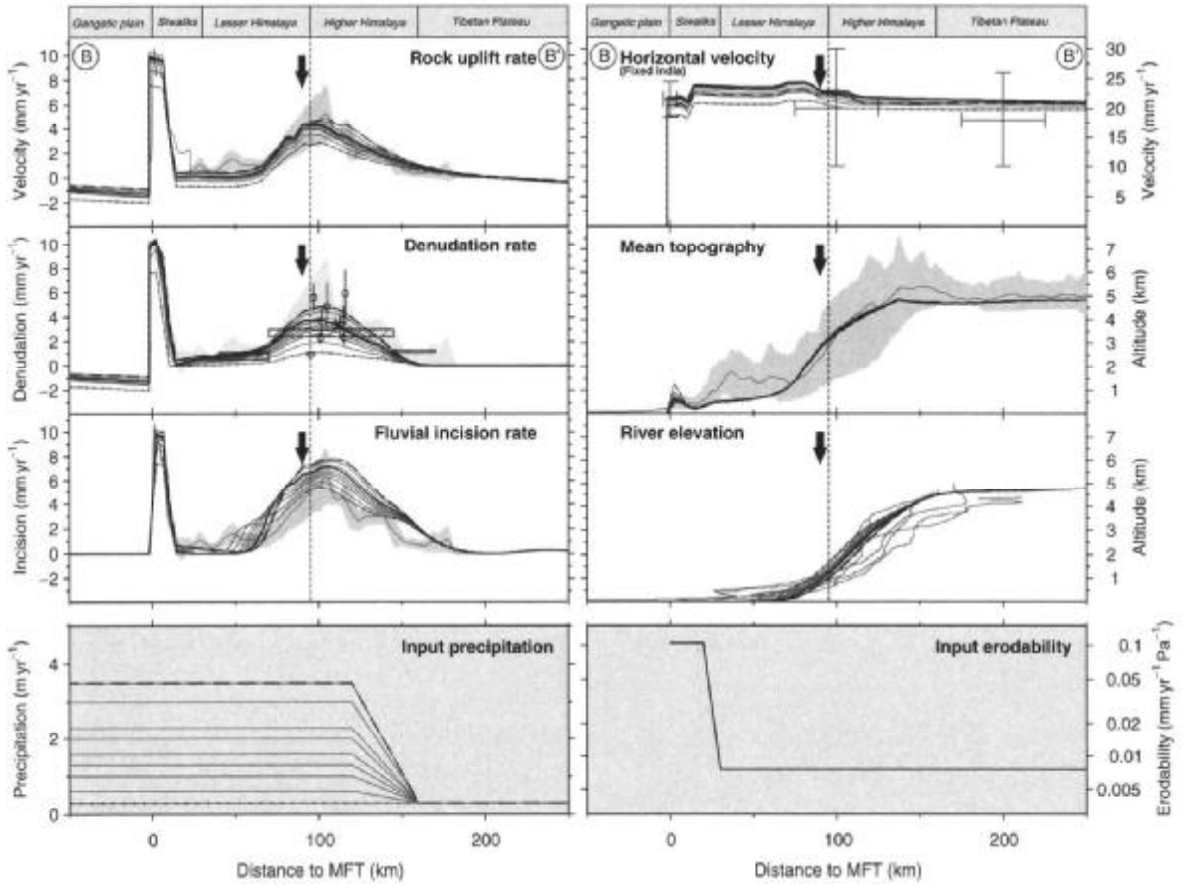


**Fig. 11.** Results of simulations where the precipitation rate is assumed to be constant from the MFT to southern Tibet, ranging from 0.3 m $yr^{-1}$ to 3.5 m $yr^{-1}$. Dashed and dotted lines refer to the maximum and minimum rainfall profiles, respectively. The solid bold line is the reference model presented in Fig. 8. The black arrow indicates the maximum of the reference rainfall profile (Fig. 8). The data sets used to compare with the model outputs are the same as in Fig. 8.

the slope of the river and the maximum in incision northward, in accordance with Equation 10. The topographic profile exhibits a lower sensitivity to erodability than does the river profile. More surprisingly, horizontal velocities are significantly affected by the variations of erodability. The rate of convergence in the frontal foothills, like the uplift rates, decreases with increasing rock strength (i.e., with erodability decrease). This phenomenon appears to reflect the role of erosion in stripping crustal material and in favouring the full transfer of the convergence toward the frontal structures.

### *Changes of erodability along the transect*

The models presented in the previous section assume relatively low erodabilities in the Siwaliks foothills, in comparison with the value calculated by Lavé and Avouac (2001) of $1.05 \times 10^{-1}$ mm $yr^{-1}$ $Pa^{-1}$. This leads to the development of an unrealistic *c.* 2000 m-high topographic front that cannot be counterbalanced by erosion (the run duration does not permit the equilibrium topography to be reached so this value represents a minimum value). The introduction of a high erodability zone in the Siwalik associated with the unconsolidated sandstones of the foothills, is thus required, first, to obtain a reasonable topographic front in this area, and second, to be able to localize deformation and a very high uplift rate without propagating the deformation southward.

Finally, a more refined erodability profile (dash-dot line, Fig. 12), which imposes slightly lower erodability at the LH-HH boundary in comparison with the southern LH ($6 \times 10^{-3}$ mm $yr^{-1}$ $Pa^{-1}$ instead of $7.6 \times 10^{-3}$ mm $yr^{-1}$ $Pa^{-1}$ in the reference model), is tested. This low variation of erodability does not have noticeable effects on horizontal shortening and topography. However, the calculated river profile is significantly less entrenched than in the reference case, and it induces a decrease of 1–2 mm $yr^{-1}$ for incision, denudation and uplift rates in the HH. One noteworthy point is

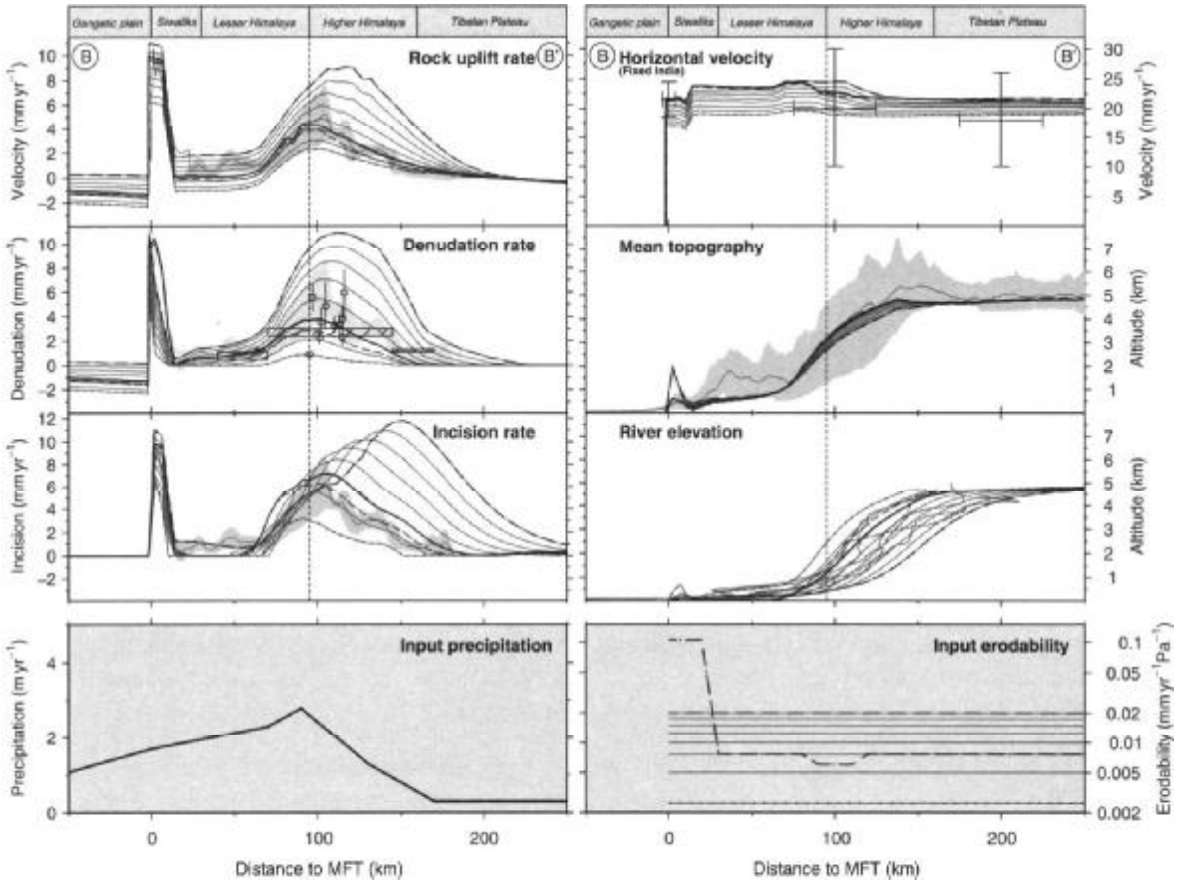


**Fig. 12.** Results of the simulations for various erodability profiles. Dashed and dotted lines refer to the maximum and minimum erodability profiles, respectively. The solid thick line is the reference model presented in Fig. 8. Dot dashed black line represents the case where a distinction of erodability is made between the different units of the range. The data sets used to compare with the model outputs are the same as in Fig. 8.

that the area affected by this modification (in comparison to the reference profiles) is wider and extends farther north than the defined low erodability area (*c.* 60 km against *c.* 30 km). This is interpreted as a response to an upstream adjustment of the main river near-equilibrium profile, which tends to be less steep. It leads to less entrenchment and, as a consequence, to a relative diminution of denudation and rock-uplift in an area wider than just the low erodability zone.

## Discussion and conclusions

Godard *et al.* (2004) have shown that the choice of the erosion law in the modelling of an orogenic system can strongly influence the results of the models and the associated interpretations. Using a fluvial incision formulation, instead of, for example, a classical diffusion law, brings some significant improvements. In particular, an incision-driven model allows the use of external parameters in modelling, measurable on the field, such as precipitation and erodability. The goal of this study was to test the behaviour of the system in response to variations of those two quantities in terms of both amplitude and spatial distribution.

Erodability is a relatively poorly constrained parameter, and even if its importance in orogenic evolution has been recognized (Schlunegger & Simpson 2002) in most modelling, it is considered as uniform. The results presented in this study clearly reveal that rock strength has a first-order control on the evolution of an orogenic wedge and that lithologic considerations really matter when introducing a denudation formulation in a mechanical model. Furthermore, this study demonstrates the predominant role of the high erodability of the Siwalik sediment in the localization of the deformation front and in the regulation of topography.

Moreover, it appears that small variations in erodability (for example between the HH and the LH), may have small, but significant, consequences on the amplitude of denudation and

uplift. As significant uncertainties are often associated with the quantification of the erodability coefficient, it appears that systematic study of the relationship between lithology and erodability is required to develop realistic coupled modelling of tectonics and surface processes. This perspective is certainly influenced by the way denudation processes are formulated in this study and is perhaps particularly relevant to our area of interest. Nevertheless the erodability parameter may still have a predominant control on the modalities of landscape denudation, as observed with the almost linear relationship existing between this parameter and the total sediment flux (Fig. 13).

Due to the values of the parameters used in the fluvial incision formulation, our modelling is less sensitive to rainfall than to erodability (exponent $\gamma = 0.33$ for precipitation, linear dependency for erodability). Precipitation is far better documented than erodability, but the spatial and temporal variabilities of both parameters are extremely important. The approach used in this study was to consider only first-order long-wavelength features characterizing the spatial distribution of precipitation, as, for example, the rain shadow between the HH and Tibetan Plateau (Fig. 2). The amplitude of precipitation directly controls the amplitude of denudation and uplift (Figs 10 and 11). However, the spatial distribution of rainfall seems to have a limited impact on the behaviour of the system, given that the presence or absence of a localized high-precipitation area at the LH-HH boundary does not induce noticeable modifications of the uplift pattern in this area, although it clearly affects the magnitude of denudation. The important variable to take into account is the global volume of water provided to the system by precipitation (Fig. 14). The relative distribution of that precipitation in the range has second order effects and does not modify the global amount of sediment eroded from the system (Fig. 14). Short-wavelength variations exist (Fig. 1) but the results presented in this study show that their relative influence on the tectonics of the system is limited. Our study demonstrates that the existence of localized high denudation and uplift rates can be related to lithology (high erodability in the Siwaliks) or structural and morphological features (ramp-flat geometry of the MHT, high slopes in the HH), rather than to a particular high precipitation area, as suggested by Thiede *et al.* (2004). In a mechanically coupled system, the tectonic behaviour is mostly sensitive to the global amount of precipitation and not to small-scale variations: in the case of the Himalayas, looking for spatial correlation between denudation and precipitation at a wavelength smaller than 20–40 km is not likely to be justified.

Such phenomena and the general low sensitivity of the chosen fluvial incision law to precipitation could explain the recent data along the Marsyandi river in Central Nepal (Burbank *et al.* 2003). This study displays a zone across the HH with uniform values of the FT closure

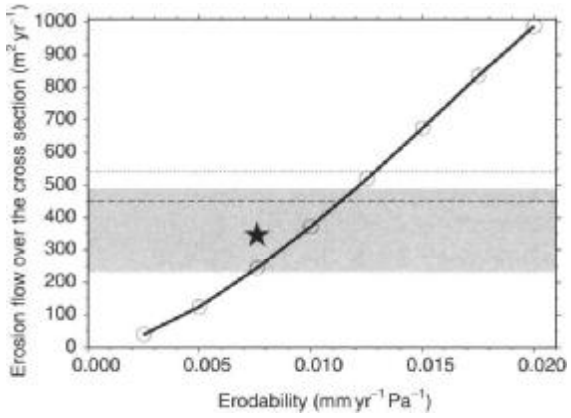


**Fig. 13.** Erodability versus outcoming flux of sediments for the constant erodability simulations (Fig. 12). The grey area, the dashed and dotted bold lines represent the erosion flux estimated by Métivier *et al.* (1999), Pinet and Souriau (1988) and Summerfield and Hutton (1994), respectively. The position of the reference model (Fig. 8) is indicated by the black star. The mean erodability associated with the reference model takes into account the variations of this parameter along the studied profile.

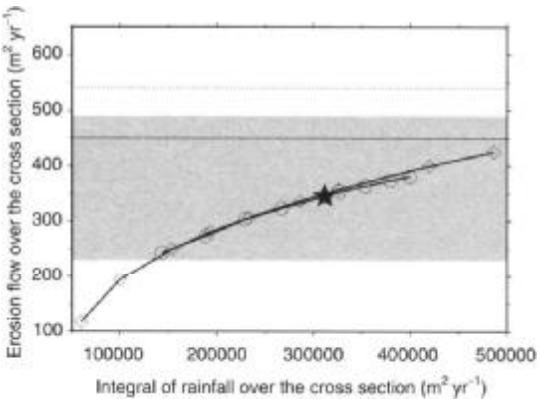


**Fig. 14.** Integrated precipitations over the cross-section versus outcoming flux of sediments (integration of the denudation profile). Circles and diamonds represent outputs for runs from Figs 10 and 11, respectively (variable precipitation and constant erodability). The black star indicates the position of the reference model (Fig. 8). The data are the same as in Fig. 13.

ages in apatite, and probably of the denudation rates, despite a three to four fold drop of the rainfall profile across the HH. These ages would primarily reflect the underlying uniform tectonic uplift associated with the mid-crustal ramp, and the lower sensitivity of the trans-Himalayan rivers to the local precipitation. This illustrates the difficulties or, perhaps, the systematic bias in trying to correlate local rainfall with local denudation to demonstrate or invalidate coupling between tectonics and climate.

Our assumption that applied present-day observed rainfall amplitudes to the timescale of the Quaternary in our simulations could be questioned. In particular, the influence of short to middle term evolution of climatic variables (e.g., monsoon, glaciations) on the tectonics of mountain ranges is still unclear and is worth investigating.

Most of the illustrations of this paper were prepared using GMT (Wessel & Smith 1991). We are grateful to J. Chéry and R. Hassani for providing the finite element code and Y. Dramais for corrections on the manuscript. Constructive reviews by F. Schlunegger, D. W. Burbank and one anonymous reviewer contributed to improve the manuscript. This work is supported by a RELIEF grant from the Centre National de la Recherche Scientifique.

## References

ARMIJO, R., TAPPONIER, P., MERCIER, J. L. & TONGLIN, H. 1986. Quaternary extension in southern Tibet. *Journal of Geophysical Research*, **91**, 13803–13872.

ATTAL, M. & LAVÉ, J. 2006. Changes of bedload characteristics along the Marsyandi River (central Nepal): Implications for understanding hillslope sediment supply, sediment load evolution along fluvial networks and denudation in active orogenic belts. *In*: WILLETT, S. D., HOVIUS, N., BRANDON, M. T. & FISHER, D. (eds), *Tectonics Climate, and Landscape Evolution*, Geological Society of America Special Paper, **398**, p. 143–171, DOI: 10.1130/2006.2398(09).

AVOUAC, J. P. & BUROV, E. B. 1996. Erosion as a driving mechanism of intracontinental mountain growth. *Journal of Geophysical Research*, **101**, 17747–17769.

BEAUMONT, C., JAMIESON, R. A., NGUYEN, M. H. & LEE, B. 2001. Himalayan tectonics explained by extrusion of a low-viscosity crustal channel coupled to focused surface denudation. *Nature*, **414**, 738–742.

BILHAM, R. K., LARSON, K., FREYMULLER, J. & PROJECT IDYLHIM MEMBERS, 1997. Indo-Asian convergence rates in the Nepal Himalayas. *Nature*, **386**, 61–64.

BURBANK, D. W., LELAND, J., FIELDING, E., ANDERSON, R. S., BROZOVIC, N., REID, M. R. & DUNCAN, C. 1996. Bedrock incision, rock uplift and threshold hillslopes in the northwestern Himalayas. *Nature*, **379**, 505–510.

BURBANK, D. W., BLYTHE, A. E. *ET AL.* 2003. Decoupling of erosion and precipitation in the Himalayas. *Nature*, **426**, 652–655.

CARTER, N. L. & TSENN, M. C. 1987. Flow properties of continental lithosphere. *Tectonophysics*, **136**, 27–63.

CATTIN, R. & AVOUAC, J. P. 2000. Modelling moutain building and the seismic cycle in the Himalaya of Nepal. *Journal of Geophysical Research*, **105**, 13389–13407.

CATTIN, R., MARTELET, G., HENRY, P., AVOUAC, J. P., DIAMENT, M. & SHAKYA, T. R. 2001. Gravity anomalies, crustal structure and thermo-mechanical support of the Himalayas of Central Nepal. *Geophysical Journal International*, **147**, 381–392.

CHEN, Q., FREYMUELLER, J. T., YANG, Z., XU, C., JIAN, W., WANG, Q. & LIU, J. 2004. Spatially variable extension in southern Tibet based on GPS measurements. *Journal of Geophysical Research*, **109**, DOI 10.1029/2002JB002350.

GAME DATA CENTRE. 2005. World Wide Web address: ftp://ftpprd.ncep.noaa.gov/pub/cpc/fews/S.Asia/

GODARD, V., CATTIN, R. & LAVÉ, J. 2004. Numerical modelling of mountain building: interplay between erosion law and crustal rheology. *Geophysical Research Letters*, **31**, DOI 10.1029/2004GL021006.

HASSANI, R., JONGMANS, D. & CHÉRY, J. 1997. Study of plate deformation and stress in subduction processes using two-dimensional numerical models. *Journal of Geophysical Research*, **102**, 17951–17965.

HENRY, P., LE PICHON, X. & GOFFÉ, B. 1997. Kinematic, thermal and petrological model of the Himalayas: constraints related to metamorphism within the underthrust Indian crust and topographic elevation. *Tectonophysics*, **273**, 31–56.

HOVIUS, N., STARK, C. P. & ALLEN, P. A. 1997. Sediment flux from a mountain belt derived from landslide mapping. *Geology*, **25**, 231–234.

HOWARD, A. D., DIETRICH, W. E. & SEIDL, M. A. 1994. Modelling fluvial erosion on regional to continental scales. *Journal of Geophysical Research*, **99**, 13971–13986.

INDIAN INSTITUTE OF TROPICAL METEOROLOGY (IITM). 2005. World Wide Web address: http://www.tropmet.res.in/

KIRBY, S. H. & KRONENBERG, A. K. 1987. Rheology of the lithosphere: Selected topics. *Reviews of Geophysics*, **25**, 1219–1244.

LARSON, K. M., BURGMANN, R., BILHAM, R. & FREYMULLER, J. 1999. Kinematics of the India-Eurasia collision zone from GPS measurements. *Journal of Geophysical Research*, **104**, 1077–1094, DOI 10.1029/1998JB900043.

LAVÉ, J. 2005. Analytic solution of the mean elevation of a watershed dominated by fluvial incision and hillslopes landslides. *Geophysical Research Letters*, **32**, L11403, DOI 10.1029/2005GL022482.

LAVÉ, J. & ATTAL, M. 2003. Landscape evolution due to river incision in active mountains. *Geophysical Research Abstracts*, **5**.

LAVÉ, J. & AVOUAC, J. P. 2000. Active folding of fluvial terraces across the Siwaliks Hills, Himalayas of central Nepal. *Journal of Geophysical Research*, **105**, 5735–5770.

LAVÉ, J. & AVOUAC, J. P. 2001. Fluvial incision and tectonic uplift across the Himalayas of central Nepal. *Journal of Geophysical Research*, **106**, 26561–26591.

LE FORT, P. 1986. Metamorphism and magmatism during the Himalayan collision. *In*: COWARD, M. P. & RIES, A. C. (eds) *Collision Tectonics*. Geological Society Special Publications, **19**, 159–172.

LYON-CAEN, H. & MOLNAR, P. 1985. Gravity anomalies, flexure of the Indian plate, and the structure support and evolution of the Himalaya and Ganga basin. *Tectonics*, **4**, 513–538.

MÉTIVIER, F., GAUDEMER, Y., TAPPONIER, P. & KLEIN, M. 1999. Mass accumulation rates in Asia during the Cenozoic. *Geophysical Journal International*, **137**, 280–318.

MOLNAR, P. 2003. Nature, nurture and landscape. *Nature*, **426**, 612–614.

NEPALESE METEOROLOGICAL FORECASTING DIVISON (NMFD). 2005. World Wide Web address: http://www.mfd.gov.np.table.php

NOAA CLIMATE PREDICTION CENTRE. 2005. World Wide Web address: http://hydro//iis.u-tokyo.ac.jp/GAME-T.GAIN-T/routine/Nepal

PANDEY, M. R., TANDUKAR, R. P., AVOUAC, J. P., LAVÉ, J. & MASSOT, J. P. 1995. Interseismic strain accumulation on the Himalayan crustal ramp (Nepal). *Geophysical Research Letters*, **22**, 751–754.

PINET, P. & SOURIAU, M. 1988. Continental erosion and large scale relief. *Tectonics*, **7**, 563–582.

SCHELLING, D. & ARITA, K. 1991. Thrust tectonics, crustal shortening and the structure of the Far Eastern Nepal Himalaya. *Tectonics*, **10**, 851–862.

SCHLUNEGGER, F. & SIMPSON, G. 2002. Possible erosional control on lateral growth of the European Central Alps. *Geology*, **30**, 907–910.

SUMMERFIELD, M. A. & HUTTON, N. J. 1994. Natural control of fluvial denudation rates in major world drainage basins. *Journal of Geophysical Research*, **99**, 13871–13883.

THIEDE, R. C., BOOKHAGEN, B., ARROWSMITH, J. R., SOBEL, E. R. & STRECKER, M. R. 2004. Climatic control on rapid exhumation along the Southern Himalayan Front. *Earth and Planetary Science Letters*, **222**, 791–806.

TOMKIN, J. H., BRANDON, M. T., PAZZAGLIA, F. J., BARBOUR, J. R. & WILLETT, S. D. 2003. Quantitative testing of bedrock incision models for the Clearwater River, NW Washington State. *Journal of Geophysical Research*, **108**, 2308, DOI 10.1029/2001JB000862.

TSENN, M. C. & CARTER, N. L. 1987. Upper limits of power law creep of rocks. *Tectonophysics*, **136**, 1–26.

UNDERWOOD, P. 1983. *Dynamic Relaxation. Computational Methods for Transient Analysis*. Elsevier, Amsterdam, 245–265.

VANCE, D., BICKLE, M., IVY-OCHS, S. & KUBIK, P. W. 2003. Erosion and exhumation in the Himalaya from cosmogenic isotope inventories of river sediments. *Earth and Planetary Science Letters*, **206**, 273–288.

VAN DER BEEK, P. A. & BISHOP, P. 2003. Cenozoic river profile development in the Upper Lachlan catchment (SE Australia) as a test of quantitative fluvial incision models. *Journal of Geophysical Research*, **108**, 2309, DOI 10.1029/2002JB002125.

WESSEL, P. & SMITH, W. H. F. 1991. Free software helps map and display data. *EOS Transactions AGU*, **72**, 441, 445–446.

WHIPPLE, K. X. & TUCKER, G. E. 1999. Dynamics of the stream-power river incision model: implications for height limits of mountain ranges, landscape response timescales, and research needs. *Journal of Geophysical Research*, **104**, 17661–17674.

WHIPPLE, K. X. & TUCKER, G. E. 2002. Topographic outcomes predicted by stream erosion models: sensitivity analysis and intermodel comparison. *Journal of Geophysical Research*, **107**, 2179, DOI 10.1029/2001JB000162.

WILLETT, S. D. 1999. Orogeny and orography: The effects of erosion on the structure of mountain belts. *Journal of Geophysical Research*, **104**, 28957–28981.

ZHAO, W., NELSON, K. D. & PROJECT INDEPTH TEAM. 1993. Deep seismic-reflection evidence continental underthrusting beneath southern Tibet. *Nature*, **366**, 557–559.

# Effects of compaction processes on stresses, faults, and fluid flow in sedimentary basins: examples from the Norwegian margin

KNUT BJØRLYKKE
*Department of Geosciences, Box 1047, University of Oslo, 0316 Oslo, Norway (e-mail: knut.bjorlykke@geo.uio.no)*

**Abstract:** Modelling of sediment compaction requires that the rate limiting processes are understood. The compaction of uncemented sediments at relatively shallow burial depths should be modelled as a function of effective stress following soil mechanical principles and using experimental compaction data for calibration. In siliceous rocks chemical compaction is dominant at depths greater than 2–3 km (80–100°C). Chemical compaction should be modelled as a function of the temperature history and the mineralogical and textural composition of the sediments. The rate of chemical compaction for siliceous sediments is to a large extent a function of the quartz cementation, which is an exponential function of temperature, while the effective stress plays a minor role. In the case of carbonate sediments the kinetics of precipitation of cement is much faster and the effective stress is more important than temperature.

The magnitude and distribution of effective *in situ* stresses is a complex function of external tectonic stresses, gravitational forces and fluid pressures. Sediments undergo mechanical compaction when subjected to high effective stress and are much more compressible than basement rocks. Chemical compaction also results in a reduction in rock volume and this has a strong feedback on the *in situ* stresses. If the horizontal stress is greater than the vertical stress, both mechanical compaction and chemical compaction will also occur in the horizontal direction, thus relaxing *in situ* stresses unless there is significant basin shortening. Calculations show that relatively large *in situ* stress anomalies (10 MPa) may be relaxed in 5–10 ka by chemical compaction during basin subsidence. Chemical compaction may also continue during uplift; it is fundamentally different from mechanical compaction and must be modelled separately.

Faults may be conduits or barriers to fluid flow in sedimentary basins. In basins like the North Sea they tend to be barriers (Fisher *et al.* 2003). The formation of faults and their properties with respect to fluid flow depends on the nature and magnitude of stress and on the physical properties of the rocks responding to the imposed stress. Compaction processes determine the rocks' mechanical properties at the time of deformation and, therefore, the properties of the fault zone. The permeabilities of faults are subsequently modified by mechanical stress and cementation along the fault zone.

The compaction of sediments in sedimentary basins involves very complex mechanical and chemical processes. Modelling sediment compaction and fluid flow requires that we can identify the rate-limiting processes and then attempt to quantify these. Compaction processes cause a reduction in fluid volume, which is defined as the porosity, and an increase in rock density. Mechanical compaction is a function of the effective stress ($\sigma_e$):

$$\sigma_e = \sigma_t - P_f \quad (1)$$

where $\sigma_t$ is the total stress which may the weight of the sedimentary overburden and $P_f$ is the pressure in the fluid phase (pore pressure). The volume change of the solid phase is negligible due to the low compressibility of the mineral phases. The change in rock volume is then almost exclusively due to the change in fluid content, which is the porosity ($\varphi$), and the fluids must be expelled for compaction to continue. Equation (1), which is the Terzagi equation, has been modified to include a factor $\alpha_B$, the Biot constant (Biot 1955) which modifies the effect of the pore pressure:

$$\sigma_e = \sigma_t - \alpha_B P_f \quad (2)$$

For sandstones and other relatively permeable sediments the Biot constant is close to 1 but it is

*From*: BUITER, S. J. H. & SCHREURS, G. (eds) 2006. *Analogue and Numerical Modelling of Crustal-Scale Processes.* Geological Society, London, Special Publications, **253**, 359–379.
0305-8719/06/$15.00 

difficult to determine this constant in fine grained rocks like shales where it may be lower. (For discussions see Lothe *et al.* 2004.) Compaction of sediments can be modelled by the rules of soil mechanics (Lambe & Whitman 1979) as long as there is no chemical process involved such as dissolution and precipitation of minerals. This however requires accurate input about the effective stresses as a function of time and the sediment composition, determining the mechanical compressibility.

Chemical compaction involves dissolution and precipitation of solids (mostly minerals) and these processes are controlled by the thermodynamic stability of the mineral phases and by the kinetics of the reactions. The degree to which the system is open or closed with respect to solid transport is critical for basin modelling. On a 1–10 m scale the chemical composition of the sediments may be assumed to remain nearly constant during burial so that cementation equals dissolution, except near the surface or on large permeable fractures. The amount of solids dissolved in the pore water is determined by the solubility of the minerals and is in most cases very small. Precipitation or dissolution due to advection is a function of the fluid flux and the solubility/temperature gradient. Calculations show, however, that in silicates transport of solids in solution by compaction-driven fluid flow is in most cases insignificant due to the low solubility of silicate minerals and the low fluid fluxes (Bjørlykke 1994). The volume of cement ($V_c$) precipitated is (Bjørlykke 1994):

$$V_c = Ft\nabla T\alpha_T\rho^{-1} \quad (3)$$

Here $F$ is the vertical component of the fluid flux, $t$ is time, $\nabla T$ is geothermal gradient, $\alpha_T$ is the solubility/temperature gradient of a mineral phase and $\rho$ is the mineral density. Modelling shows that it requires about $10^9$ volumes of water to precipitate one volume of quartz, assuming normal geothermal gradients (Bjørlykke 1994). Also in the case of carbonates the fluid transport is limited in compacting sedimentary basins due to low solubility gradients which are retrograde with respect to temperature (Wood 1994). The solubility gradients imply that if quartz is precipitated by advective flow, 30 to 100 times more calcite will dissolve and the presence of calcite is therefore evidence of limited quartz precipitation (Bjørlykke & Egeberg 1993). The distribution of cement is therefore in most cases controlled by local diffusion rather than by advective transport, except near the surface and along permeable faults. Pore water is normally in equilibrium with calcite which is nearly always present, at least in marine sediments. The volume of the solid phase may, however, be reduced by mineral dehydration and by diffusion over shorter distances. The generation of petroleum also represents a phase transformation of solids (kerogen) to fluids.

Sedimentary rocks in subsiding sedimentary basins differ in very important aspects from metamorphic and igneous basement rocks. Sedimentary rocks with significant porosity (>5%) may shrink significantly by chemical compaction, while this is not the case for well-cemented sedimentary rocks and metamorphic rocks.

By studying well exposed outcrops the geometrical distribution of faults and fractures can be mapped in great detail (e.g., Antonellini & Aydin 1995). In sedimentary basins the composition of faults can only be studied when sampled by cores, but the subsidence and temperature history is mostly well constrained by well logs. In many cases the rocks are presently at their maximum burial depth compared to their previous burial history. The response to external stress depends on the timing of the deformation in relation to compaction and diagenesis during subsidence. It is very important to distinguish between deformation occurring during subsidence when sediments may be normally consolidated, and during uplift when the rocks are mostly over-consolidated and brittle (Figs 1 and 2). In subsiding sedimentary basins mechanical compaction will normally occur under increasing effective stress. The sediments are then normally consolidated and have ductile properties. This means that these sediments

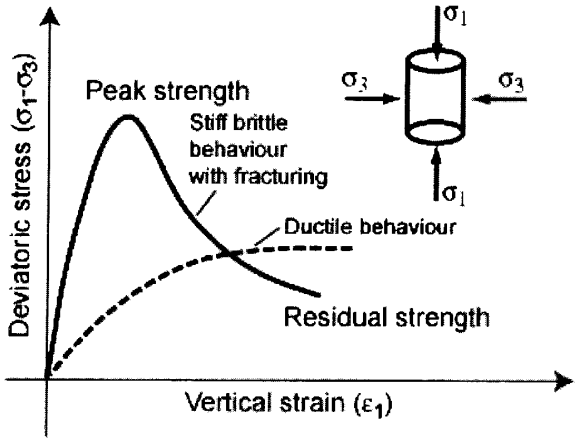


**Fig. 1.** Principal difference between brittle and ductile response to deviatoric stresses. Normally consolidated rocks will tend to show a ductile response while over-consolidated rocks are brittle. Modified from Bjørlykke and Høeg (1997).

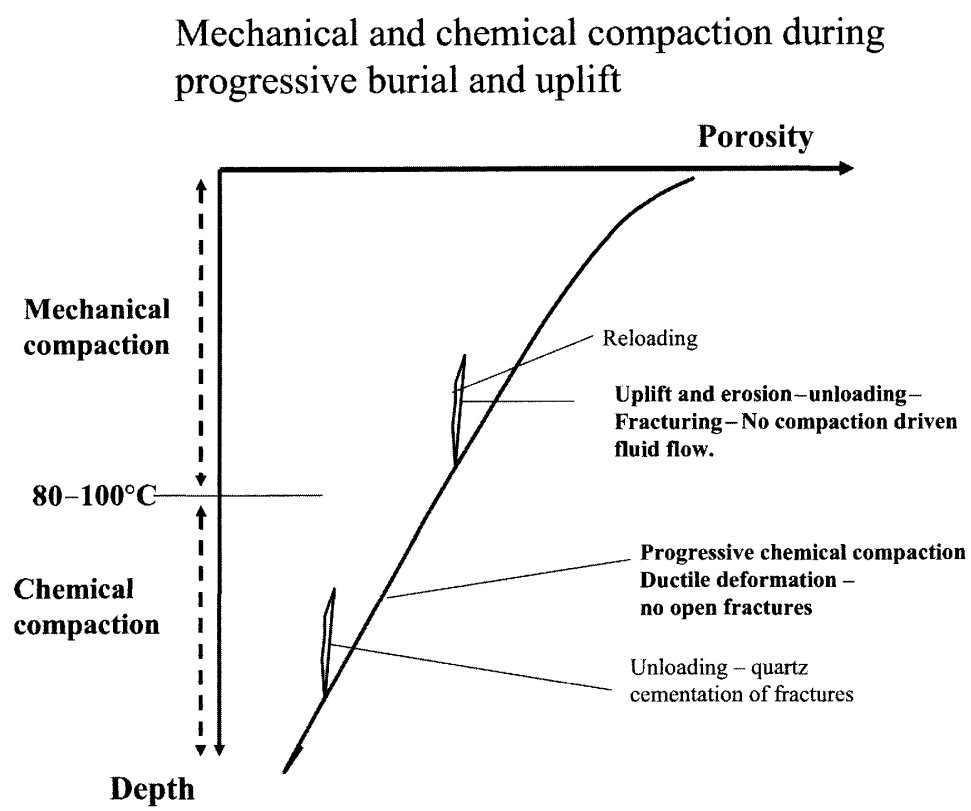


**Fig. 2.** Rock properties as a function of progressive burial and uplift (exhumation). Reduced overburden stress causes extension and brittle behaviour. No compaction-driven flow then occurs, because there is no porosity loss and lower than hydrostatic pressures may develop due to the extension because of a slight increase in porosity. Chemical compaction due to quartz cementation may, however, continue during exhumation for temperatures >80–100°C, because it is driven by temperature rather than effective stress.

have no peak strength (Fig. 1), are ductile and do not deform by brittle fracturing. They then fall on the solid line for compaction during progressive burial and increasing stress (Fig. 2) (Bjørlykke & Høeg 1997; Bjørlykke 1999). Open fractures can then not exist. Uplift and erosion will, however, reduce the effective vertical stress and cause the sediments to be over-consolidated and brittle. Open fractures are then likely to develop, due to high differential stresses and extension. A build up of overpressure may also reduce the effective stress despite deeper burial and cause sediments to become over-consolidated.

When discussing fluid flow in sedimentary basins we must always consider the source of the fluids and maintain a mass balance. In subsiding sedimentary basins water is expelled upwards at an average rate which is constrained by the porosity loss of the underlying sedimentary sequences. This porosity reduction may be due to mechanical compaction caused by increased effective stress or chemical compaction due to dissolution and precipitation of minerals. In addition water is released by dehydration of minerals, mostly clay and evaporite minerals. Although the average water flow is upwards in relation to the subsiding sedimentary layers, it can be shown to be downwards in relation to the sea floor (Bjørlykke 1994). The actual flow rates are controlled by the distribution of permeabilities in the sedimentary sequences. During uplift (exhumation) there is very little compaction of the sedimentary sequence and if extension and fracturing occurs the pore volume increases, resulting in lower than hydrostatic pressure and a slight downwards flow of meteoric water.

The distribution of stress is critical for both the generation of faults and the properties of the fault zones, and it is important to understand the processes controlling the distribution and magnitude of stresses in sedimentary basins. The present paper will discuss the effect of mechanical and chemical compaction on stresses in sedimentary basins and how this affects the properties of fault zones with respect to fluid flow. The North Sea and Haltenbanken basins of offshore Norway provide good field datasets for studying the effects of compaction processes during

subsidence. These principles will apply also to other basins that have been subjected to recent subsidence and where the sedimentary layers are presently at their maximum depth and stress. Examples are basins in a passive margin setting which are formed during rifting and subject to post-rift cooling and subsidence.

The principles discussed in this study are of direct importance for basin modelling studies. Modelling of sediment compaction, distribution of stresses and fluid flow should for shallow depths and cold temperatures be based on soil and rock mechanical principles. For the deeper parts (<80°C–100°C) the principles of chemical compaction apply in siliceous sediments where the rate of compaction is an exponential function of temperature integrated over time (Walderhaug *et al.* 2001; Bjørkum & Nadeau 1998; Bjørkum *et al.* 1998*a*). Failure to distinguish between these two very different processes in basin modelling may produce rather erroneous results. Mechanical compaction will stop or continue at a very slow rate due to creep when the effective stress is constant, while chemical compaction may continue at constant or even much reduced stress. Chemical compaction will also continue at reduced temperature during uplift, but at a slower rate if the temperature is above 80°C in siliceous sediments. The rate of chemical compaction can be modelled as an exponential function of temperature, grain size and other textural parameters controlling the surface area available for quartz cementation, following Walderhaug (1996), Perez *et al.* (1999), Walderhaug *et al.* (2001) and Lander *et al.* (2003). The principles involved in such modelling are relatively well understood, but the main difficulty is to estimate the input parameters for the modelling, particularly the textural parameters such as grain size and the presence of clay coatings.

## Distribution of stresses during mechanical compaction

We must distinguish between stresses generated by gravitational forces internally within the basins and stresses imposed by external tectonic forces. In a sedimentary basin the total vertical stress ($\sigma_v$) is a function of the weight of the overburden. The effective stress ($\sigma_{ve}$) transmitted to the solid phase (mostly minerals) is $\sigma_{ve} = \sigma_v - p_p$, where $p_p$ is the pressure in the fluid phase.

Mechanical compaction of sand as a function of increasing effective stress can be tested in the laboratory. The mechanical compressibility is a function of the composition and sorting of the sand. Well-sorted coarse grained sands are significantly more compressible than fine grained sand, due to grain crushing (Chuhan *et al.* 2002, 2003). At an effective stress of 20–30 MPa (corresponding to 2–3 km of overburden and hydrostatic fluid pressure) coarse grained sand is reduced to 26–30% porosity while fine grained sand has 36–38% porosity. The porosity prior to uniaxial loading was in both cases 42% (Chuhan *et al.* 2002, 2003).The rate of compaction in mudstones varies greatly and smectitic mudstones compact much less and at much lower rates than other types of mudstones. This results in much lower log velocities (Storvoll *et al.* 2005).

In a uniform horizontal sedimentary sequence the horizontal stress should be expected to be the same in all directions. If the horizontal stress is higher than the vertical stress, compaction will also occur in the horizontal direction. A gradual tectonic shortening of the basin is then required to maintain differential stresses. On passive margins horizontal stresses are produced by the ridge push effect (Grollimund *et al.* 2001; Gölke & Coblentz 1996), but these stresses will mainly be transmitted through the basement which is much stiffer (higher modulus) than the overlying sedimentary sequence (Kjeldstad *et al.* 2003). The elevation of basement rocks on a margin mainland will also generate a horizontal stress component similar to ridge push, but this is also mainly transmitted through the basement rather than through the sedimentary sequence (Fig. 3). Across mid Norway and the northern North Sea, some reverse faults can be related to compression in the underlying basement (Dore *et al.* 2002; Faleide *et al.* 2002; Dore & Lundin 1996). Most of the Cretaceous and Cenozoic sedimentary sequence in the North Sea and Haltenbanken (offshore Norway) show, however, no evidence of horizontal compression. The small shortening of the basin indicated by the reverse faults is taken up by compaction of the overlying sedimentary sequence. The late tertiary sequence was probably deposited after the compression which may have been of Miocene age (Dore & Lundin 1996). In the North Sea and Haltenbanken brittle faulting is mostly associated with late Jurassic rifting when much of the basin was uplifted (Gabrielsen *et al.* 2001). Few of the faults extend far into the Cretaceous sequence which was deposited during continued subsidence (Fig. 4).

In this passive margin setting basement faults may still be reactivated because they represent zones of weakness which have lower shear strength than the rest of the basement. In the

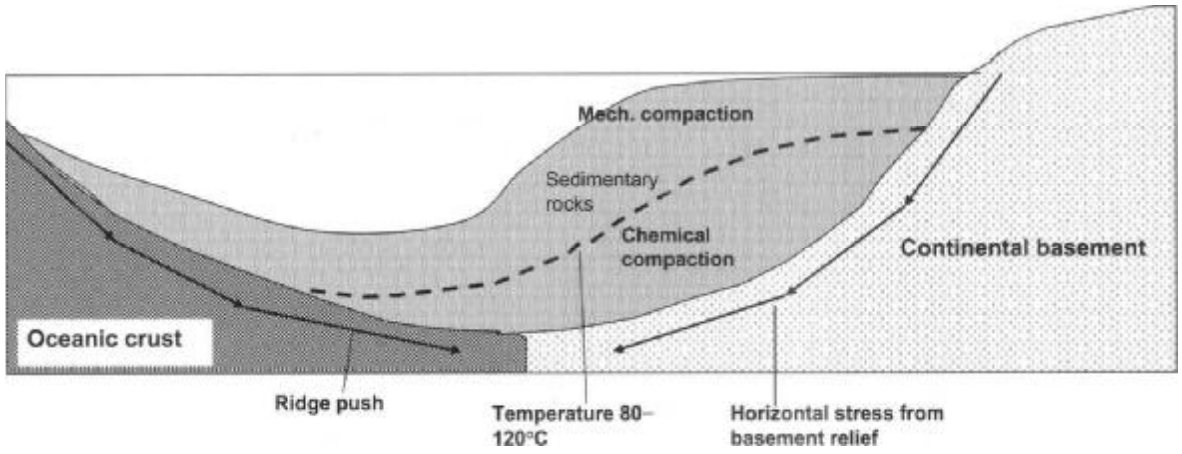


**Fig. 3.** Schematic presentation of a sedimentary basin in a passive margin setting. The horizontal stress component, resulting from the topography of the spreading ridges (ridge push) and the relief of the continental basement, is transmitted mostly through the basement rocks. Only a small part of this stress is transmitted though the sediments in a subsiding basin where the sedimentary rocks are undergoing mechanical and chemical compaction because of their higher compressibility both mechanically and chemically.

late Mesozoic and Tertiary sequence offshore Norway few faults have formed (Fig. 4) and they are in most cases not reactivation of older faults. Faults in Jurassic reservoirs in the North Sea and Haltenbanken nearly always have lower porosity and permeability than the rock matrix and are often preferentially cemented by quartz cement or carbonate cement (Fisher & Knipe 2001; Fisher *et al.* 2003). They have higher shear strength than the rock matrix and are not zones of weakness which are likely to be reactivated. Based on very extensive studies of faults undertaken at the University of Leeds, Quentin Fisher states: 'One of the best pieces of evidence that indicates fault reactivation has not lead to leakage is that despite all of the numerous analyses we have conducted on faults from within cores of the reservoirs on Haltenbanken and the North Sea (including those from Visund) – we have never found faults that have shown evidence of being formed at depths greater than 500 m below the seafloor or containing extra-formational cements precipitated by localized fluid flow. This is unlike examples where there is clear seismic evidence of late-stage fault reactivation, where there are often numerous examples of such features' (Q. Fisher, pers. comm. 2005). There are also few evidences of late faulting on seismic sections (Fig. 4).

In many of the over-pressured fields in the northern North Sea and the Central Graben (offshore Norway) the present day overpressures agree well with the measured fracture pressure (Moss *et al.* 2003). This is certainly also true for the Gullfaks Field (Heum 1996) which is leaking and draining large parts of the Tampen area. Leakage below fracture pressure has been attributed to high horizontal stresses caused by glacial loading (Wiprut & Zoback 2000; Grollimund & Zoback 2003). There is, however, no evidence for glacio-tectonic deformation on seismic sections (Faleide *et al.* 2002). High horizontal effective stress (up to 60 MPa) at about 3 km depth has been inferred from Haltenbanken based on bore hole breakouts (Norgaard Bolås & Hermandrud 2002), but this would have resulted in significant horizontal compaction and grain breakage. This could not have been possible without a shortening of the basement (and the basin) corresponding to the horizontal compaction.

Seabed topography and dipping sedimentary layers of different density will produce gravity-driven differences in the horizontal stresses (Bjørlykke & Høeg 1997). The overall bathymetric relief of the continental slope west of Haltenbanken exceeds 1 km, producing a lateral variation in vertical effective stress of $>10$ MPa at the same depth. When the horizontal stress is a function of the vertical stress this sea floor topography will set up a corresponding horizontal stress. The slope will produce extension near the top and compression near the base.

When modelling compaction and stresses in sedimentary basins, normally consolidated and over-consolidated sedimentary rocks must be treated differently since they have different compressibilities (Fig. 2). Normally consolidated sediments fall on the continuous stress/strain curve. At hydrostatic pressures the effective stress increases with depth as a function of the sediment density. When sediments are subjected

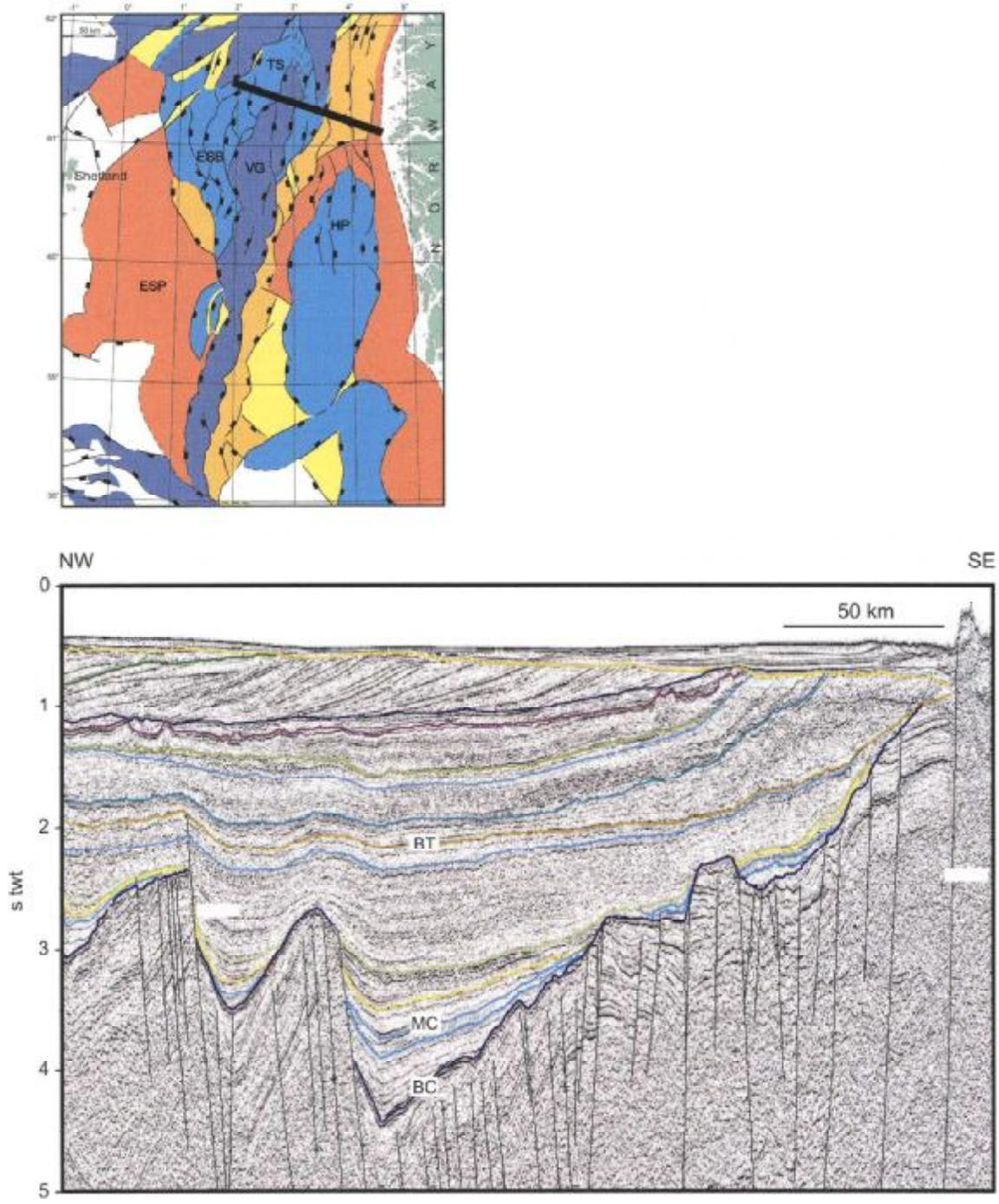


**Fig. 4.** Top: Main structural elements of the northern North Sea and location of regional seismic line. VG: Viking Graben; HP: Horda Platform; ESP: East Shetland Platform; ESB: East Shetland; TS: Tampen Spur Basin (modified from Faleide *et al.* 2002). Below: Regional seismic profile across the northern North Sea. BT: Base Tertiary; MC: Mid Cretaceous; BC: Base Cretaceous (Modified from Faleide *et al.* 2002).

to increasing effective stress during burial they are normally consolidated and behave in a ductile manner (Fig. 2). After uplift and exhumation the stress is reduced and sediments become mechanically over-consolidated. If they are then subjected to reloading, they have a much lower compressibility (Fig. 2). Where the sediments have earlier been subjected to higher effective stresses before they are over-consolidated, very little compaction will take place. When reloading over-consolidated sedimentary rocks, compaction is partly elastic and also due to closing of open extensional fractures. The stress/strain curve follows the hysteresis loop on the

unloading-reloading curve (Fig. 2) and the compressibility is much lower than for normally consolidated sediments. In sedimentary basins, renewed sedimentation after a period of erosion will cause reloading, and normal compaction will resume once the previous maximum effective stress has been exceeded (Fig. 2). In the North Sea brittle faulting occurred during rifting associated with uplift and extension (Færseth 1996), but there is little evidence for that in the Cretaceous and younger sediments. Cementation of the grain framework (e.g., by carbonate or quartz cement) increases the rocks strength and makes the rocks over-consolidated (Fig. 5). Build up of overpressure may also reduce the effective stress and cause over-consolidation.

Erosion reduces the overburden and thus the vertical stress, causing elastic expansion of the sedimentary layers in the vertical direction. Horizontal expansion, however, is usually limited in the horizontal dimensions and the horizontal stresses are, therefore, normally not relaxed to the same extent, resulting in high ratios of horizontal to vertical stress. When sedimentary rocks are normally consolidated they will yield (compact) in response to any increase in the effective stress, following the normal compaction curve (Fig. 2). In extensional stress regimes the highest effective stress will be in the vertical direction due to the weight of the overburden. The horizontal stress is then a function of the vertical stress. Should the horizontal stress be higher than the vertical stress, compaction would result in shortening in the horizontal direction as long as the horizontal stresses are greater than the vertical stresses. If there is no shortening of the underlying basement during continued subsidence, to maintain the high horizontal stress it must, therefore, be lower than the vertical stress. When the vertical gravity-generated stress is the maximum effective stress ($\sigma_{ve}$), the horizontal effective stress $\sigma_{he} = K_0 \cdot \sigma_{ve}$ related to the Poisson's ratio ($\nu$). For isotropic uniaxial elastic deformation $K_0 = \nu/(1 - \nu)$ (Jaeger & Cook 1979).

In the North Sea, the ratio between the total horizontal and vertical stresses ($\sigma_h/\sigma_v$) measured by leak off tests (LOT) may typically be between 0.8–0.95, approaching 1.0 (Moss *et al.* 2003). The relation between the effective horizontal and vertical stresses, particularly in over-pressured rocks may be significantly lower. The values measured by leak-off tests (LOT) may be too high because of the drop in pressure across low permeability mud cakes next to the formation (Raaen *et al.* 2001). Even when taking this into account the stress ratios ($\sigma_h/\sigma_v$) in basins like the North Sea are relatively high. The may be the result of mechanical creep as well as chemical compaction, which will tend to make the stress distribution more isotropic and the ratio between the horizontal and vertical directions closer to 1.0.

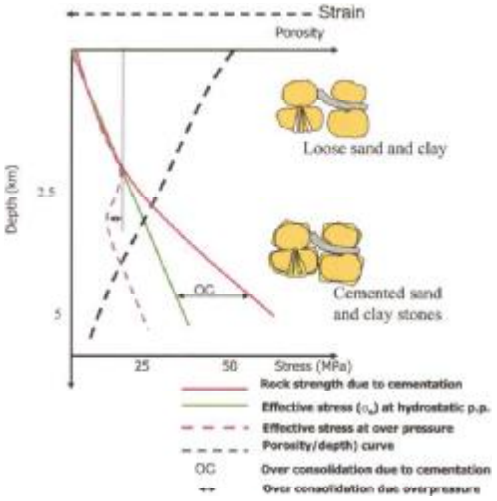


**Fig. 5.** Changes in stress and rock properties of a sediment layer as a function of increasing burial. Over-consolidation may be produced by overpressure or by cementation. A build up of overpressure may reduce the effective stress so that the rock becomes over-consolidated. At hydrostatic pore pressure the effective stress will increase as a function of depth causing the sedimentary rocks to be normally consolidated. However the rocks may become 'pseudo-over consolidated' due to cementation at shallow depth by carbonate and at greater depth (>80–100°C) by quartz cement.

## Chemical compaction

Chemical compaction involves dissolution at grain contacts which are load bearing and precipitation of cements in open pores where there is no effective stress, a process resulting in reduced rock volume. Strain rates during chemical compaction are controlled by the rate of dissolution of grains and precipitation of cements. Quartz dissolution and cementation is one of the main processes in siliceous sediments, but dissolution and precipitation of clay minerals and feldspars may also play a role. In the deeper parts of sedimentary basins the compaction of siliceous sandstones is mainly chemical and controlled by temperature (Bjørkum 1996; Walderhaug 1996; Walderhaug *et al.* 2001). In sandstones and other siliceous sediments the precipitation of quartz is assumed to be the rate-limiting step and this is a function of temperature rather than stress (Bjørkum 1996; Oelkers *et al.* 1996; Walderhaug 1996; Walderhaug *et al.* 2001). The rate of porosity loss and vertical

shortening as a function of time and temperature has been modelled by the authors listed above. The rate of compaction is an exponential function of temperature integrated over time and of the grain surface area available for quartz cementation. The rate of quartz cementation per unit area (available grain surface) ($r$) can be calculated from (Walderhaug *et al.* 2001):

$$r = Ae^{E_a/RT} \quad (4)$$

Here $A$ is a constant with units of mol cm$^{-2}$ s$^{-1}$, $E_a$ is the activation energy in J mol$^{-1}$, $R$ is the universal gas constant and $T$ is temperature in degrees Kelvin. The rate of compaction as function of temperature and time can then be modelled (Fig. 6).

Clastic mica and also clay minerals have a catalytic effect on the dissolution of quartz (Bjørkum 1996) determining where dissolution occurs, but the precipitation stage may still be rate limiting. The quartz dissolution rates in pure water increase by a factor of about $10^5$ from 20°C to 100°C (Palandri & Kharaka 2004) and surface controlled precipitation may speed up by a factor up to $10^7$ for the same temperature interval (Giles 1997). The precipitation of quartz cement increases the degree of consolidation and rock strength of the sediments in a way which is nearly independent of stress and this is often referred to as pseudo-overconsolidation (Fig. 5).

Compaction of siliceous mudstones is mostly mechanical at temperatures below about 80°C. At higher temperatures (80–110°C) smectite become thermally unstable and opal A and Opal CT is dissolved and the silica reprecipitated as quartz. Both mechanical and chemical compaction of mudstones varies greatly with the mineral composition and particularly with the smectite content. Chemical compaction of mudstones is more difficult to model than sandstones because of the uncertainty about textural parameters, but here also quartz cementation is one of the main controls in addition to the stability of the clay minerals. Carbonate cement in shales strongly influences the compaction behaviour of mudstones. They become overconsolidated and much less compressible than uncemented mudstones even at relatively shallow depth (Nygård *et al.* 2004).

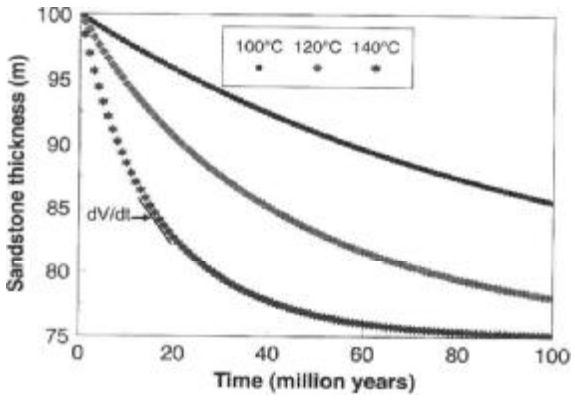


**Fig. 6.** Results from numerical modelling of chemical compaction of sandstones due to quartz cementation at constant temperatures. Modified from Walderhaug *et al.* (2001). The rate of compaction ($d\varphi/dt$ or $dV/dt$) at a given time is the derivative of this compaction curve and is an expression of the rate of rock volume reduction.

In the case of carbonates compaction is more sensitive to stress and to a lesser degree to temperature, compared with siliceous sediments (Giles 1997). The kinetics of carbonate mineral dissolution and precipitation is relatively fast, also at low temperatures. For calcite the activation energy for dissolution and precipitation is much lower than for quartz (Palandri & Kharaka 2004). Increasing effective stress at grain contacts or along stylolites increases the solubility of carbonate minerals like calcite. This provides a thermodynamic drive for chemical compaction. The dissolution step is, therefore, probably rate-limiting for what is often referred to as pressure solution in carbonates, but here also clay plays an important role in the dissolution process. Clay minerals also increase the rate of dissolution and they become concentrated along stylolites where much of the dissolution occurs.

Chemical compaction may also involve the dissolution of hydrous minerals like smectite and kaolinite and precipitation of less hydrous minerals like illite, thus reducing the volume of the solid phase (Fig. 2). The principles of chemical compaction due to diagenetic processes apply also to progressive metamorphism where the increased density of less hydrous minerals accounts for most of the loss of rock volume. This could also potentially reduce *in situ* stresses, but the boundary conditions in terms of tectonic stress may be very different than for sedimentary basins on passive margins.

In summary, chemical compaction is driven by thermodynamics and kinetics, while mechanical compaction is a result of effective stress and rock strength.

## Fluid flow in sedimentary basins

In a sedimentary basin water will always be the continuous phase on a large scale and hence control the overall fluid potential. The pressure in the hydrocarbon phase will be controlled by

the thickness of the hydrocarbon columns, and the difference in pressure is balanced against the water pressure by the capillary forces.

The flow of water can be modelled using the simple Darcy equation (Verruijt 1982):

$$F = k\frac{\nabla P}{\mu} \quad (5)$$

The fluid flux ($F$), however, can in most cases not be modelled from these parameters because the pressure gradient ($\nabla P$) and the distribution of permeability, $k$, are not sufficiently well known within a sedimentary basin. The viscosity ($\mu$) of the fluids is better constrained. To predict the fluid flow in a sedimentary basin the three-dimensional distributions of permeability must be known over large distances and this is generally not possible. The flow in permeable sandstones in the deeper parts of a sedimentary basin depends only to a small degree on the permeability of the sandstones but mainly on the permeability of the surrounding tight shales. The compaction driven fluid flux ($F$) in the Darcy equation is a function of the rate of compaction and the viscosity, which may be relatively constant over a limited period of geological time. The pressure gradient ($\nabla P$) is then a function of the permeability ($k$).

It is important to note that in the case of chemical compaction in siliceous sedimentary rocks the rate of compaction and fluid flow is a function of temperature and nearly independent of stress and degree of overpressure. The actual flow rate is a function of the distribution of permeabilities. The main factor controlling the degree of overpressure is the minimum permeability along a pathway all the way to the surface. The distribution of pressure is also very difficult to predict because it depends on the distribution of permeabilities in three dimensions. From the Halten Terrace, offshore Mid-Norway, the presence of high overpressure can be shown to depend on the lateral drainage rather than on the permeability of the overburden (Olstad *et al.* 1997). Also in the northern North Sea the pressure compartments are controlled by faults restricting the lateral drainage (Moss *et al.* 2003) which implies that the overpressure is not primarily a function of the permeability of the overlying shale (seal) but of the drainage in three dimensions.

If all input parameters in the Darcy equation were known on a local and regional scale the pressure distribution would already be known and modelling of fluid fluxes would become circular. The main constraint on fluid flow in sedimentary basins is the source of the fluids. Both the meteoric water flowing into the basin and the water flux released by compaction can be quantified or at least constrained. The compaction-driven flux is a direct function of the reduction in porosity in the underlying sediments and the water released by mineral reactions. The contribution from each layer to the compaction-driven water flux is the derivative of the porosity/depth curve, $d\varphi/dz$ (Fig. 2), but this curve is different for each lithology. The upward flow of water is always lower than the sedimentation (subsidence) rate except where there is a very high degree of focussing (Bjørlykke 1993). Assuming a given porosity/depth curve the compaction-driven flux can be calculated as a function of the sedimentation rate.

## The effect of faults on fluid flow in sedimentary basins

A clear distinction must be made between flow perpendicular to faults in sandstones and flow along faults. Faults in sandstone reservoirs may be important barriers for fluid flow and the permeability across the fault is controlled both by the mechanical shearing and the subsequent diagenetic reactions. The type of fracture depends both on the magnitude and distribution of effective stresses and the shear strength of the rocks (Fig. 7). Shear deformation in soft (uncemented) sediments at shallow depth is likely to cause compaction (negative dilation, Fig. 7a) while well-cemented sedimentary rocks and metamorphic rocks will tend to develop dilation and increased permeability (Fig. 7b).

Shear deformation in uncemented sand depends on the normal stress and on the composition and size of the grains. This can be tested experimentally. For quartz-rich sand, significant grain crushing starts at 5–10 MPa for coarse to medium grade, while fine-grained sand requires normal stresses exceeding 10 MPa, corresponding to at least 1 km of overburden, for significant grain crushing to occur (Kjeldstad 2002) (Fig. 8). Shear deformation of relatively well-sorted sand produces a dense, interlocking grain fabric and strain hardening (Wong et al. 1997) and reduced permeability even before grain crushing. Because of strain hardening the zone of shear deformation will tend to shift, resulting in a broad zone of shear deformation without a well-defined shear plane. This type of shear deformation in clean sand is not likely to introduce clay smear from adjacent clay layers because the offset will be small.

Diagenetic reactions, particularly quartz cementation, cause a reduction in porosity and

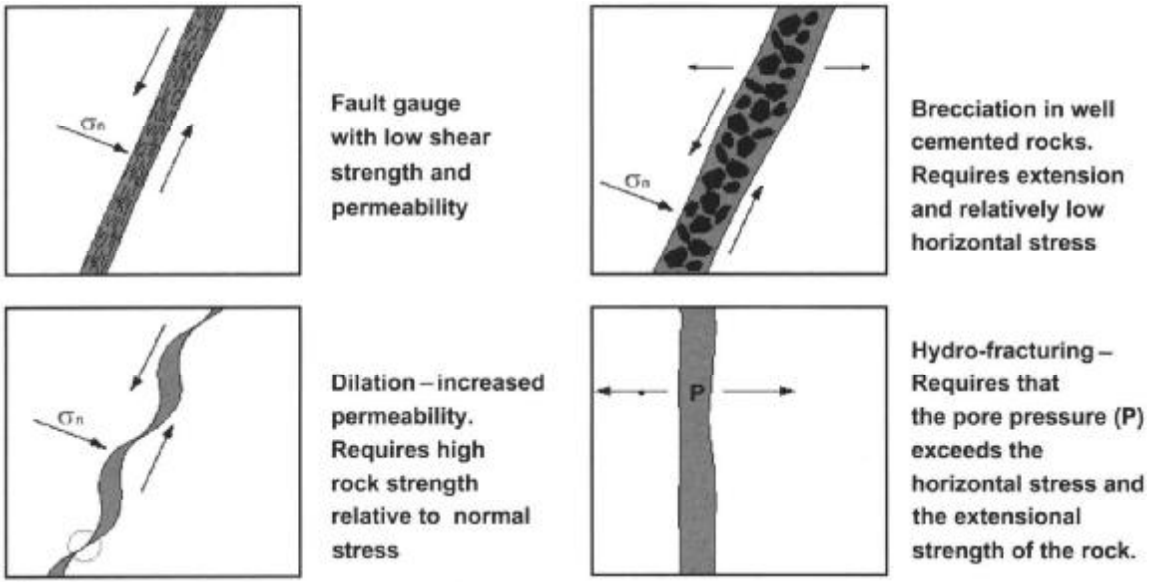


**Fig. 7.** Different types of fractures. In soft sediments (low shear strength) a fault gauge with negative dilation may develop at relatively low normal stresses (6a). In well cemented rocks and metamorphic rocks shear deformation may result in brecciation (6c) and dilation (6b), causing increased permeability. When the pore pressure exceeds the minimum stress, normally the horizontal stress, hydro-fracturing occur (6d).

permeability as a function of time and temperature during burial. This process can be modelled numerically (Walderhaug 1996; Walderhaug *et al.* 2001) and such modelling is done on a commercial basis in most major oil companies. The porosity in the shear zone at the onset of quartz cementation is one of the most critical factors determining the final porosity and permeability (Fisher *et al.* 2003). If the shearing occurs after the precipitation of clay coating, grain crushing will expose fresh quartz surfaces, promoting higher rates of quartz cementation within the fault plane (Fisher & Knipe 2001; Chuhan *et al.* 2002; Hesthammer *et al.* 2002; Fisher *et al.* 2003). Diagenetic healing of faults may change their permeability and capacity to serve as pressure barriers through time as shown by examples from the Haltenbanken area (Olstad *et al.* 1997; Karlsen *et al.* 2004). Small amounts of clay, like mica and kaolinite, present in the sand will be concentrated along the fault plane and may later develop into stylolites which have a strong effect on the flow properties, reducing the permeability and increasing the capillary entry pressure. The effective permeability of shear zones is difficult to predict when the fault zone is broad and diffuse and contains numerous discontinuous shear zones.

In the Haltenbanken basin and also the North Sea basin, faulting occurred during Late Jurassic rifting (Corfield & Sharp 2002) (Fig. 9). Most of the faults seem to end near the base Cretacous reflector. Even so the permeability is relatively low due to dense grain packing (Fisher & Knipe 2001). This implies that the faults intersecting Middle Jurassic reservoir rocks were active at a time when the reservoir sand was buried at a depth of only a few hundred metres. Faults from the Kristin Field at Haltenbanken show shear bands which have probably formed during strain hardening in relatively clean sand. This has resulted in a dense packing of small and coarse grains giving relatively low porosity and permeability compared to the matrix (Fig. 10). Here the shearing has occurred before the precipitation of grain-coating chlorite and illite. The grain coating is therefore well preserved and consequently there is little quartz cementation in the shear zones (Fig. 11). At burial depths less than 600–700 m the vertical stress may have been 5–6 MPa and the horizontal stress would have been less than 5 MPa. This is insufficient horizontal stress to cause grain crushing in medium to fine grained sand (Kjeldstad *et al.* 2003) (Fig. 7).

In metamorphic rocks, fractures account for nearly all the porosity and changes in the apertures of faults and fractures provide a mechanism for seismic pumping, as described by Sibson (1981). In sedimentary basins, however, most of the fluids are stored in the pores, even in well-cemented sandstones, and the effects of fractures are very different. Well cemented sedimentary rocks and basement rocks may cause dilation when sheared (Fig. 7), while in poorly cemented weak rocks shearing is likely to

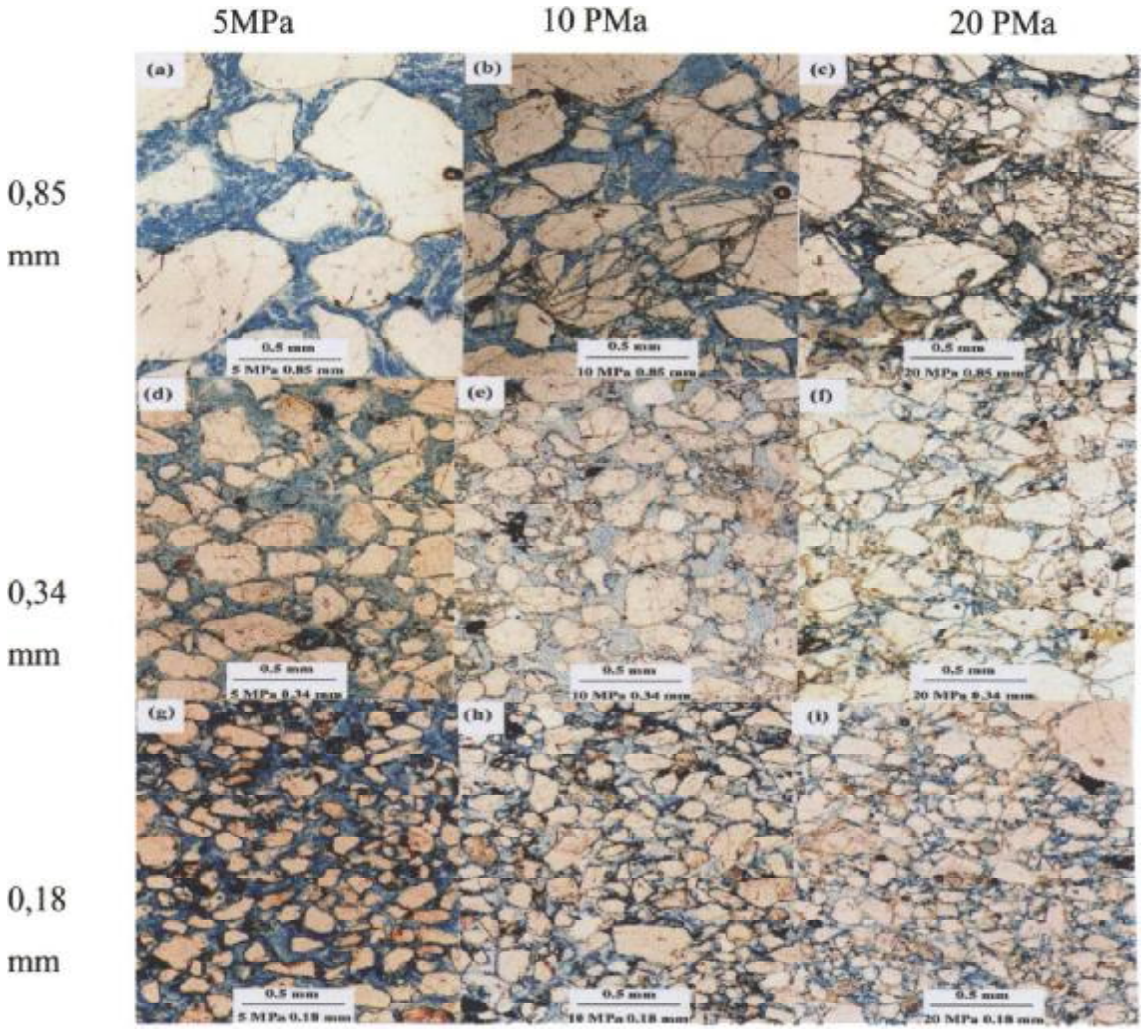


**Fig. 8.** Experimental shearing of sand with different grain sizes (from Kjeldstad 2002). Coarse grained sand (0.85 mm) becomes more fractured than fine grained (0.18 mm) sand subjected to the same stress. At normal stresses below 10 MPa there is little grain crushing in fine to medium grained sand. At 20 MPa there is significant grain crushing in coarse grained sand.

cause compaction or negative dilation, as shown by experimental shearing (Fig. 8).

Extensional faulting due to rifting is often associated with uplift and erosion of the margin. This will stop mechanical compaction because of the reduced effective stress and it will reduce the rate of chemical compaction by quartz cementation. There will therefore be little porosity reduction or no compaction-driven fluid flow to fill the fractures. The increase in porosity caused by fracturing may lower the pore pressure below hydrostatic levels and provide a potentiometric gradient for a drawdown of meteoric water from above (Bjørlykke 1999).

Permeable faults and fractures are rarely filled with cement precipitated from advective water flow along the fractures. Quartz cementation requires temperatures above 70–100°C and much higher fluid fluxes than can realistically be obtained, while calcite will dissolve when upward-flowing water is cooled (Bjørlykke & Egeberg 1993). Modelling of fluid flow in sedimentary basins shows that precipitation of one unit volume of quartz by upwards flow of cooling water will cause dissolution of 30–100 unit volumes of calcite, depending on the pH and the geothermal gradient (Bjørlykke & Egeberg 1993). This means that the presence of calcite precludes significant introduction of quartz by advection. Fractures are most likely to be filled by crystal growth sourced by diffusion from the adjacent rocks (Egeberg & Saigal 1991; Hesthammer *et al.* 2002). Fractured grains provide good nucleation sites for quartz overgrowth, and fault zones, therefore, often have more quartz cement than the matrix

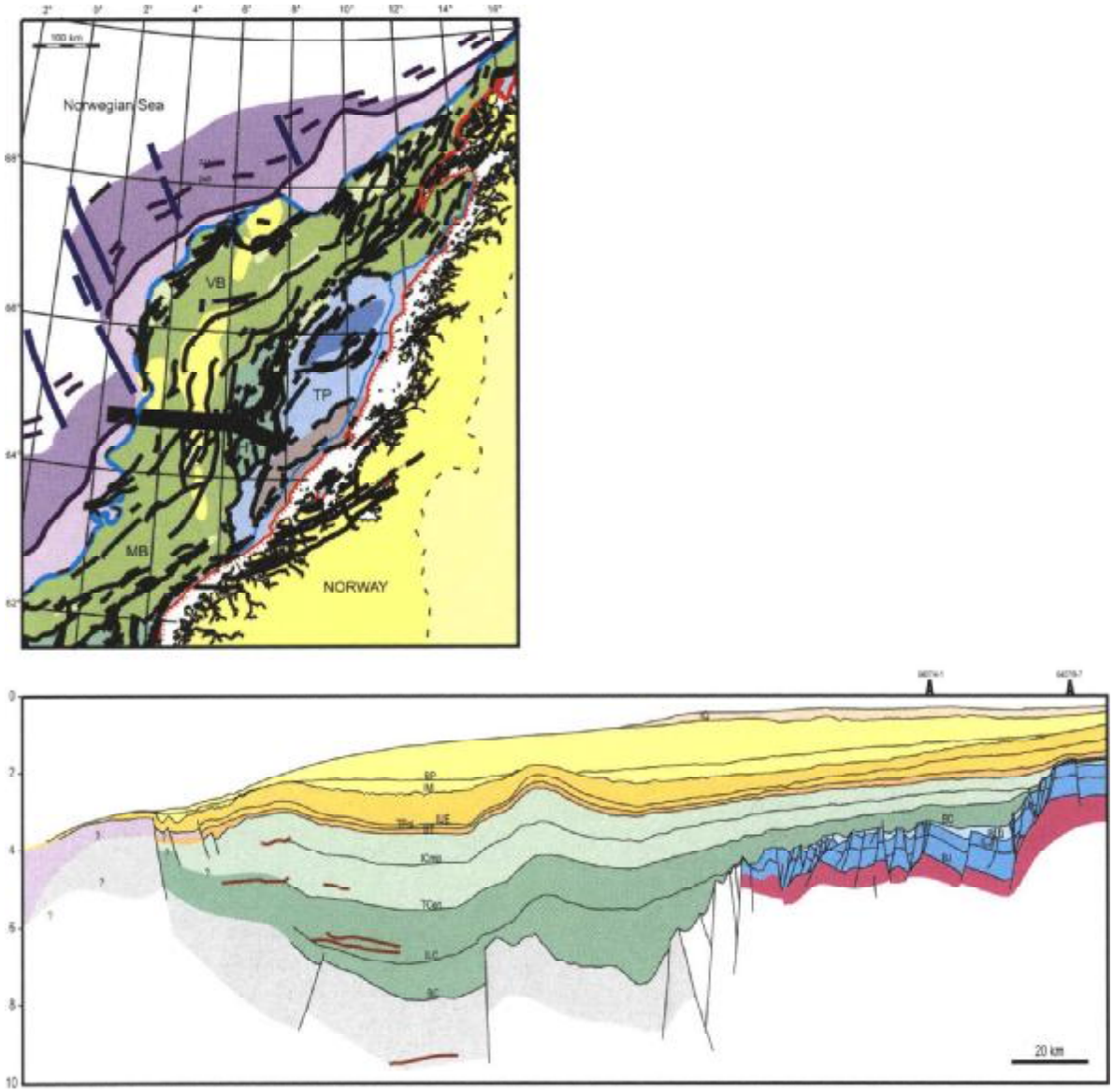


**Fig. 9.** Main structural elements of the continental shelf and margin off mid-Norway (top) and interpreted regional seismic profile (below). MB: Møre Basin; VB: Vøring Basin; HT: Halten Terrace; TP: Trøndelag Platform. The thick solid line in the top figure indicates the location of the regional profile. (modified from Blystad *et al.* 1995).

(Fisher & Knipe 2001). They are therefore unlikely to be reactivated, because the fault plane has acquired higher shear strength than the matrix. Reactivation of basement faults and differential compaction and stress along juxtaposed lithologies may, however, produce new faults close to older cemented faults. In this case failure is not due to reduced shear strength along pre-existing faults. The rate of cementation of fractures depends on the porosity and diffusion constant in the rock matrix adjacent to the fracture.

Fractures in well-cemented sedimentary rocks and in metamorphic rocks may remain open longer than in porous sandstones. In these rocks, faulting produces a plane of weakness (reduced shear strength) and when subjected to repeated shear stresses the shearing tends to follow existing shear planes. Clay-rich sediments may develop a clay smear along fault planes which results in strain softening, and these faults may therefore be reactivated. During burial, however, the shear strength of clayey sediments may also change, due to increased compaction or diagenetic alteration. Studies in the North Sea faults show that burial depth and temperature have a major effect on the permeability of faults (Fisher & Knipe 2001).

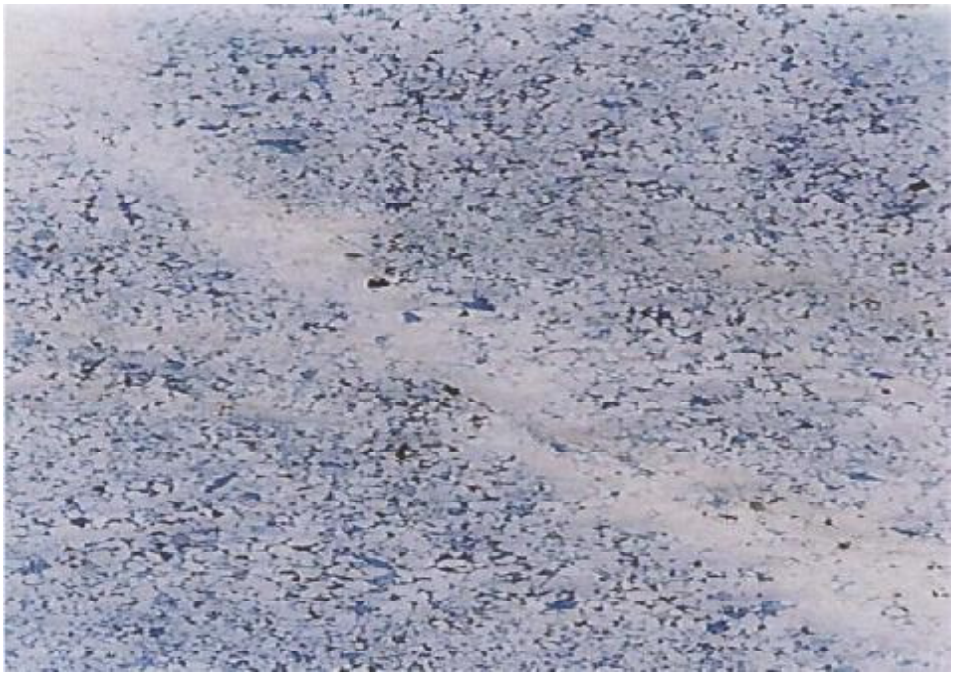


**Fig. 10.** Scanned image of thin section (3 cm), impregnated with blue epoxy. From the Middle Jurassic Garn Formation, Kristin Field, 5 km depth. Note that the shear zone produced by strain hardening has low porosity.

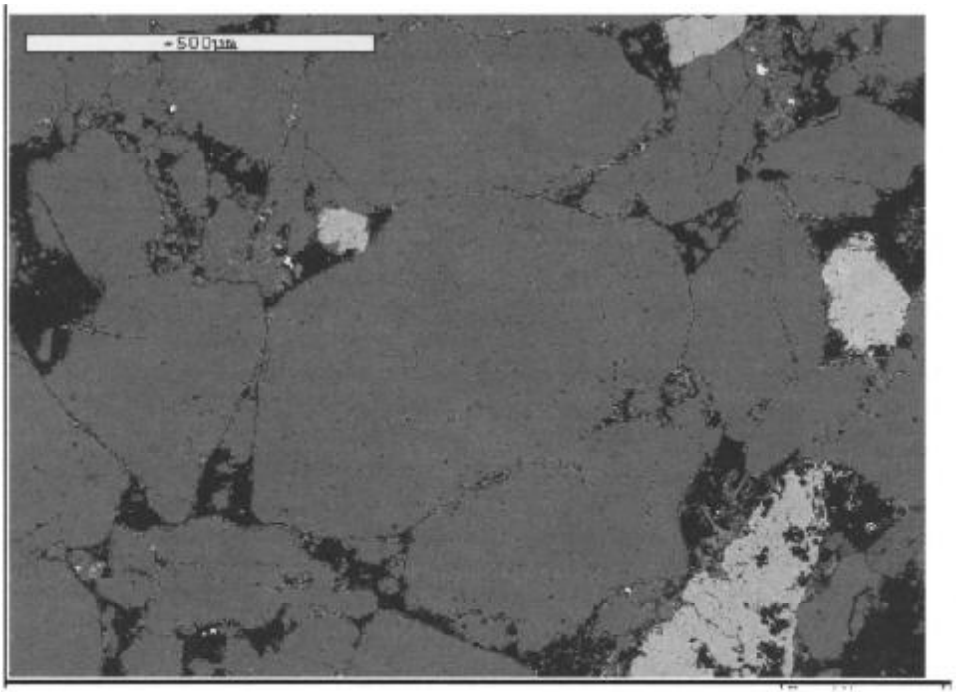

**Fig. 11.** SEM picture of shear zone in the Kristin Field produced by dense packing of grains resulting in strain hardening, but very little grain breakage. The grains were subsequently coated with chlorite coating which has prevented quartz overgrowth, preserving much of the remaining porosity.

Recrystallization of clay, such as the illitization of smectite, and precipitation of quartz along the fault plane, can increase the shear strength of the fault gouge so that it becomes stronger than the matrix. Carbonate cementation along the fault plane may also increase the shear strength.

Even if faults have sufficient permeability not to be pressure barriers for water over geological time, they may be sealing for oil and gas in water-wet reservoirs. During production the sealing capacity becomes even higher than in a static setting and at the Snorrre Field in the northern North Sea sealing capacities up to 15 bar (1.5 MPa) for hydrocarbon flow across some faults (Sverdrup *et al.* 2003).

## Cap rock integrity and leakage

Cap rock may leak due to intergranular flow when the capillary entry pressure for the hydrocarbons is exceeded, or due to hydro-fracturing. The North Sea Basin provides good examples of over-pressuring and hydro-fracturing (Gaarenstroom *et al.* 1993; Leonard 1993; Heum 1996; Isaksen 2004). Shales are in most cases impermeable for oil and fracturing is, therefore, required before leakage can take place. The permeability in mudstones may be low at relatively shallow depth due to carbonate cementation, but clay mineral reaction and quartz cementation are important in the making of a tight seal. Fracturing occurs when the pore pressure ($P_p$) exceeds the least principal stress. In subsiding sedimentary basins this is normally the horizontal stress ($\sigma_h$). The requirement for hydrofracturing is that $P_p > \sigma_h + \tau$. The tensional strength ($\tau$) is assumed to be small compared to $\sigma_h$.

The formation or reactivation of brittle faults and fractures may cause leakage at pressures below the normal fracture pressure (Sibson 2003). Chemical compaction involving the cementation of faults and fractures reduces the probability of fault reactivation. Even if high overpressure makes cap rocks brittle in a mechanical sense, chemical compaction will produce a ductile response to low strain rates as discussed above. Furthermore, shear failure will not necessarily cause leakage since it may also result in negative dilation if the normal stress is high compared to the rock strength.

The thickness of the hydrocarbon column determines the pressure difference between the hydrocarbon phase and the water phase, but this difference is accommodated by the capillary pressure. If the cap rock is water-wet, fracturing of the cap rock will occur when the pressure in the water phase exceeds the fracture pressure, because it is the water phase which is critical for fracturing in a water-wet cap rock. Thus if the capillary entry pressure for oil or gas of the cap rock is not exceeded, the thickness of the hydrocarbon column has little effect on the risk for leakage by hydro-fracturing (Bjørkum *et al.* 1998*b*).

The effects of uplift and erosion on pore pressure have been modelled (Luo & Vaseur 1995) based on assumptions about mechanical compaction, but these models do not take the effects of chemical compaction into account. In the case of hydrostatic pressure erosion will cause an overpressure which takes time to bleed off (Luo & Vaseur 1995). Parts of basins which are under high overpressure may upon uplift and leakage continue to compact due to increasing effective stress, and behave as normally consolidated rocks in a ductile manner for a period when the effective stress increases during deformation.

High overpressures occur most commonly in pressure compartments with limited lateral drainage. If the pore pressure approaches the fracture pressure, the strength of the cap rock cannot prevent fracturing. The compaction-driven water flux in siliceous sediments at temperatures above about 80–100°C is primarily controlled by temperature and time (Walderhaug 1996). The underlying sediments will therefore continue to compact and provide water flux even if the effective stress is reduced.

## Calculation of relaxation of tectonic stresses by mechanical and chemical compaction

During progressive burial in sedimentary basins, sediments are usually subjected to increasing effective stresses and, if there is limited cementation (chemical compaction), are normally consolidated. The sedimentary rocks will then compact and yield to any increase in the effective stress, potentially in both the vertical and horizontal directions. High lateral stress resulting from ridge push will primarily be transmitted through oceanic crust and continental basement (Fig. 3). Also, well cemented sedimentary rocks with low porosity and negligible potential for further compaction could transmit stress over long distances.

High horizontal (tectonic) stresses in subsiding sedimentary rocks will gradually be relaxed by the compaction process unless there is additional shortening of the basement across the basin. For normally consolidated sediments, increases in the effective stress will cause compaction and this then reduces the stress if there is no basin shortening. The vertical stress $\sigma_v$ is

driven by the weight of the overburden and is usually the direction of maximum stress.

Without significant shortening of the underlying basement rocks, imposed horizontal stresses, e.g., from ridge push, will be relaxed by the compaction process. If there was a net shortening of the basin and the sedimentary layers, the sediments would still be normally consolidated with respect to the horizontal stress, and compact horizontally. Experimental compaction (Chuhan *et al.* 2002, 2003) shows that well sorted medium to fine grained sands with an initial porosity of about 42% have been compacted to 30–37% at 20 MPa effective stress ($\sigma_{ve}$), corresponding to about 2 km burial depth where there is little quartz cement. In the North Sea, reservoirs at 2–2.5 km depth have maximum porosities between 30 and 35% (Ramm & Bjørlykke 1994). A 20 MPa increase in effective stress ($\sigma_{ve}$) results in a porosity reduction of 5–12% (0.05–0.12). This is equal to a compression modulus of $B = \sigma_{ve}/\varepsilon_v = 400$–150 MPa.

If the width of the basin remains constant, nearly all the compaction (strain) is in the vertical direction. When subjected to increased horizontal stress exceeding the vertical stress, the basement must be shortened to compensate for the strain in the horizontal direction. Horizontal stresses exceeding the vertical stress are therefore only possible in over-consolidated sediments, because normally consolidated sediments would compact mechanically and produce a significant inelastic horizontal strain which could also involve significant grain crushing (Figs 2 and 8). The maximum horizontal stress is therefore governed by the degree of over-consolidation reducing mechanical compaction. For chemical compaction the precipitation of quartz is assumed to be the rate-limiting step and is controlled by kinetics (temperature) (Bjørkum 1996; Walderhaug *et al.* 2001). Even though the dissolution at grain contacts requires some stress, the rate of dissolution is mainly a function of the rate of precipitation and therefore nearly independent of the effective stress. The compaction processes involve a reduction in rock volume (shrinkage) and this will relax *in situ* stresses. This is a very slow process which may determine the *in situ* stress in the rocks for slow strain rates. The rate of deformation is controlled by the temperature and the grain surface area available for precipitation (Walderhaug 1996). In well-cemented sandstones with little porosity the potential for chemical compaction is limited by the small surface area for precipitation of cement.

Even if the rate of dissolution is controlled by the rate of precipitation in the open pores, it requires some effective stress and is probably also favoured by the presence of clay and mica (Bjørkum 1996). Dissolution at grain contacts and also along stylolites results in a shortening in the vertical direction, but may also result in a shortening in the horizontal direction when subjected to tectonic stress with a horizontal component. Thus chemical compaction will result in ductile properties with an approximately isotropic distribution of stress for low strain rates.

Only a small fraction of the total strain ($\Delta\varepsilon$) is elastic and reversible (Fig. 12) and chemical compaction corresponding to the elastic strain ($\varepsilon_{el}$) is required to relax a tectonic stress, assuming no additional basin shortening. Thus the change in rock volume due to chemical compaction ($\Delta V/V$) will cause a reduction in stress ($\Delta\sigma$). The rate of stress relaxation ($\Delta\sigma$) can be calculated as a function of the chemical compaction and Young's modulus (E) for elastic deformation:

$$E = \frac{\Delta\sigma}{\Delta\varepsilon_{el}} \tag{6}$$

The volumetric strain $\Delta\varepsilon$ is the change in rock volume $\Delta V/V$ due to compaction and can in the case of sandstones be modelled as a function of temperature and sediment composition (Walderhaug 1996) or estimated from porosity/depth curves ($d\varphi/dz$) and changes in

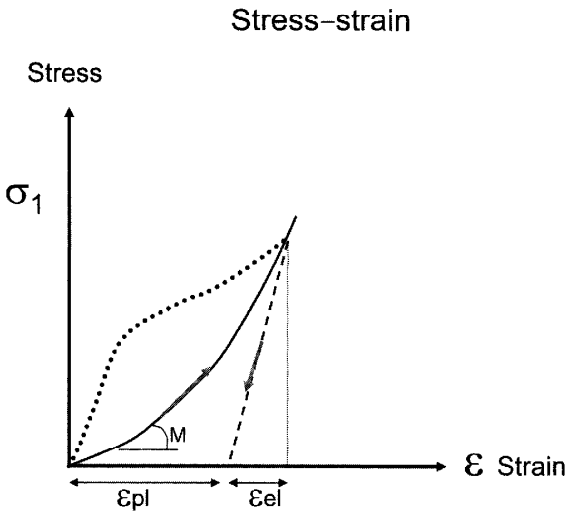


**Fig. 12.** Stress–strain diagram illustrating that the elastic strain which can be measured after unloading is only a small fraction of the total strain. Chemical compaction corresponding to the elastic strain will however relax *in situ* stresses. M is the modulus which is the ratio between the stress ($\sigma$) and the strain ($\varepsilon$).

the rock volume of the solid phase ($dV_s/dz$):

$$\frac{dV}{dz} = \frac{dV_s}{dz} + \frac{dV_\varphi}{dz} \quad (7)$$

Based on the sedimentation (subsidence) rate ($dz/dt$) the rate of compaction as a function of time can be calculated:

$$\frac{dV}{dt} = \frac{dV}{dz} \times \frac{dz}{dt} \quad (8)$$

Integrating the volumetric strain ($dV/dt$) as a function of time and temperature we obtain the total strain ($\Delta\varepsilon$) over a certain or time or depth interval depending on the subsidence rate. Even if this deformation is ductile, the total strain will relax *in situ* stress according to Equation (6) for elastic deformation (Fig. 12). If the elastic Young's modulus E for quartz is 90 GPa ($9.10^{10}$ Pa) (Karner *et al.* 2003), a strain ($\Delta\varepsilon$) of $10^{-4}$ would cause a reduction in stress ($\Delta\sigma$) of 9 MPa ($9.10^6$ Pa). The time (t) required to obtain a strain ($\Delta\varepsilon$) of $10^{-4}$ can then be calculated from the rate of porosity loss $dV_\varphi/dz$ and the subsidence rate ($dz/dt$). If the density and volume ($dV_s/dz$) of solid phase (minerals) remains constant, the reduction in volume $dV/dz$ is equal to the porosity loss $dV_\varphi/dz$ (Eqn. 7). Mineral reactions involving dehydration such as the dissolution of smectite and kaolinite and the precipitation of illite increase the density of the solid phase and represent compaction in addition to the porosity loss.

The porosity gradient in the North Sea basin is typically 1–2%/100 m (Ramm & Bjørlykke 1994). If the sedimentation rate is $10^{-4}$ m/yr, the rate of volume loss ($dV/dt$) is 1–2 × $10^{-8}$/yr. In porous sediments the change in bulk volume is mostly due to porosity loss ($dV_\phi$), and the change in solid phase ($dV_s$) is small except due to mineral dehydration. The time (t) required to obtain a strain of $10^{-4}$ is then 5000–10,000 years (Fig. 13) and this will relax the *in situ* stress correspondingly. This means that excess horizontal stresses ($\Delta\sigma$ = 10–20 MPa) in basins like the North Sea and Haltenbanken may be relaxed by chemical compaction in 5000–20,000 years. For cemented sandstones the value of E may be lower than for pure quartz and the time required for stress relaxation would be correspondingly longer.

Compaction of mudstones is more complex than the compaction of sandstones. If there is no carbonate cement, mudstones compact mechanically at temperatures up to about 80°C. At higher temperatures chemical compaction may occur due to dissolution and precipitation of clay minerals, mainly dissolution of smectite and precipitation of illite and quartz (80–100°C), and dissolution of kaolinite and K-feldspar and precipitation of illite and quartz (130°C) (Bjørlykke *et al.* 1995). In addition, quartz cementation sourced by amorphous silica and also dissolution of clastic quartz may be important for the compaction process in mudstones turning into shales. The compaction of mudstones is therefore to a large extent controlled by temperature.

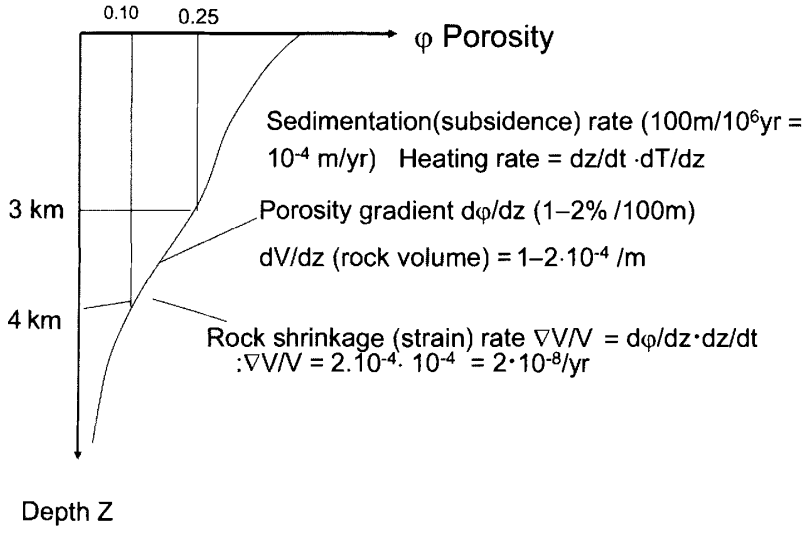


**Fig. 13.** Calculations showing the rate of stress relaxation due to chemical compaction. If the porosity gradient and the sedimentation (subsidence) rate are known, the rate of volume shrinkage $dV/dt$ can be calculated. In $10^4$ years the total strain ($\Delta\varepsilon$) will be $10^{-4}$, assuming an annual strain of $10^{-8}$. Using the elastic modulus (E) for quartz (90 GPa) the stress will be relaxed by 9 MPa in 10000 years. See discussions in the text.

Carbonate-cemented mudstones and sandstones reach a high stiffness and already have a low compressibility at shallow depth and thus have a smaller potential to relax tectonic stress.

If it is assumed that there is no shortening of the basin due to tectonics, the horizontal stress cannot exceed the vertical stress in subsiding sedimentary basins like the North Sea and Haltenbanken. Mechanical compaction requires continued subsidence and increase in effective stress to produce the shrinkage in rock volume which relaxes the differential stresses. Chemical compaction in siliceous sediments will, however, continue without progressive subsidence or heating and will also occur during uplift and cooling, as long as the temperature is above 80–100°C and the porosity is high enough to accommodate it. The shrinkage of the rock volume resulting from chemical compaction would relax tectonically-produced *in situ* lateral stresses also during uplift.

We may therefore conclude that as long as sedimentary rocks are subsiding and being subjected to compaction, horizontal stresses cannot be higher than the vertical stress in the situation where there is no shortening of the basement. Even if there should be some basement shortening, horizontal stresses would still be reduced by horizontal compaction. The *in situ* stresses would then be a function of the rate of horizontal shortening, i.e., due to tectonic stress, the mechanical compressibility of the rocks and the rate of chemical compaction. The minimum horizontal stress ($\sigma_{vmin}$) in both the northern North Sea and Haltenbanken, as measured by the fracture pressure, is close to the overburden stress ($\sigma_v$) (Moss *et al.* 2003). If the maximum horizontal stress cannot exceed the vertical stress it follows that ($\sigma_{hmax}/(\sigma_{hmin}$) must be close to 1.0.

Horizontal stress anomalies may, however, be produced by a component of the gravitational force due to sloping sea floors or dipping sedimentary layers of different density. In sedimentary basins subjected to uplift and erosion, reduction of the vertical stress due to unloading may lead to a situation where the horizontal stresses exceed the vertical stress if the former are not reduced to the same extent due to lack of expansion in the horizontal direction for extensive layered rocks. While mechanical compaction will stop, chemical compaction will continue and reduce the horizontal stress after uplift if the temperatures still are high enough for significant quartz cementation (>80–90°C).

Chemical compaction may, as shown above, relax differential stress produced tectonically and reduce the build-up of *in situ* stresses which can cause brittle deformation and earthquakes. Focal depths are reported to be deep in the southern North Sea, northern North Sea and offshore Mid-Norway, while they are shallow in onshore western Norway, onshore mid-Norway and in Finnmark, Northern Norway (Hicks *et al.* 2000). It is clear that the brittle basement rocks of onshore Norway have shallow epicentres compared to areas where there are 5–10 km or more of sedimentary rocks. This is probably because basements rocks have very limited potential for both mechanical and chemical compaction and external stress may then result in brittle failure.

Stress orientations based on bore hole breakouts in the North Sea and Haltenbanken have been interpreted to be due to plate tectonics stress (ridge push) (Lindholm *et al.* 1995; Hicks *et al.* 2000). The ridge push stress is transmitted through oceanic crust into continental crust and it is difficult to see how much of this stress should be transmitted into the more compressible sediments. The sediments in the uppermost 2–3 km burial depth undergo compaction, mostly due to mechanical compaction, and that can also occur in the horizontal directions. The deeper part of the basin will be dominated by chemical compaction which also can have a horizontal component if there are high horizontal stresses (Fig. 13). Even if there should be some shortening in the basement, high compressibility in the overlying sedimentary rocks may prevent the build up of high *in situ* stresses. The orientation of stresses indicated by earthquakes, bore hole breakouts and over-coring shows that the stress anomalies are not a direct result of the ridge push effect (Byrkjeland *et al.* 2000).

The basement rock underlying the North Sea and Haltenbanken consists of metamorphic rocks, mostly formed at depths exceeding 20–30 km, and subsidence of up to 10 km will not result in significant compaction and reduction of *in situ* stresses. Shear stress may therefore build up to reach failure while the stress in the sedimentary sequence above may be relaxed by chemical compaction. Well-cemented sedimentary rocks with low porosity have limited potential for further compaction and will be able to sustain stresses nearly to the same degree as the basement.

## Implications for basin modelling

Modelling of sediment compaction is an important part of basin analyses because it affects the sediment density and rock properties and, therefore, the distribution of stress. This study has shown that sediments compact by very different processes and any modelling must first identify the critical and rate-limiting processes.

Mechanical compaction of sedimentary rocks is in principle well understood as described in rock and soil mechanics. The main problem is to predict the highly variable physical properties of sedimentary rocks and the processes responsible for the stresses. It is important to distinguish between external tectonic stress and gravitational stress generated within the basins. Mechanical compaction is dominant in uncemented sand and in mudstones without significant carbonate cement.

At depths greater than 2–3 km (>80–100°C) both sandstones and mudstones tend to become mechanically 'pseudo over-consolidated' due to cementation, and further compaction is controlled mostly by chemical processes. Carbonate cements in sandstones and mudstones at shallow depth drastically reduce the mechanical compressibility upon further subsidence. Chemical compaction follows completely different principles compared to mechanical compaction. In the case of siliceous sediments dissolution and precipitation of quartz exerts the main control on the rate of compaction. As discussed above, chemical compaction can be modelled as an exponential function of temperature and time (Walderhaug 1996; Bjørkum & Nadeau 1998; Walderhaug *et al.* 2001; Lander *et al.* 2003). The main problem is to predict the initial sediment composition, including parameters such as grain size and grain coatings. Using the observed amounts of quartz cement in sandstones the burial (temperature) history can be modelled using, for example, the EXEMPLAR model (Perez *et al.* 1999). When modelling compaction of mudstones the thermodynamic stability of the clay minerals, such as smectite and kaolinite, are important because the solid phase is dissolved and reprecipitated as less hydrous minerals. In carbonate rocks the kinetics of mineral reactions are much faster than in siliceous rocks, implying that dissolution at grain contacts (pressure solution) rather than precipitation may be rate limiting. Compaction of carbonate rocks is therefore more sensitive to effective stress and not very sensitive to temperature.

Both mechanical compaction and chemical compaction are sensitive to the primary rock composition. Modelling of sediment compaction and fluid flow on a regional scale in a sedimentary basin requires knowledge of the distribution of sedimentary facies and also of provenance. Basin modelling must therefore be linked to facies analyses and sequence stratigraphy. The properties of shear zones depend not only on the stress distribution, but also substantially on the timing relative to mechanical and chemical compaction processes (diagenesis). Studies of outcrops may be a good basis for mapping out fault zones, but they provide very poor constraints on the rock properties at the time of deformation. In subsiding basins the burial history relative to deformation episodes is much better constrained, thus providing a better basis for realistic basin modelling in combination with experimental compaction data.

Hydraulic leakage by pressure and stress simulations have been modelled using examples offshore Mid-Norway (Lothe *et al.* 2004). Simulations of the build up of pore pressures are, however, very difficult because of the poorly defined permeability distributions in the shales (seals). Even if the temperature history of the sediments can be relatively well constrained, the rate of chemical compaction in shales and sandstone, and thereby the fluid flux, will also to a large degree depend on mineralogical and textural parameters which are poorly known. This is also the case for the degree of focusing of the fluids and lateral drainage. The distribution of stresses may influence the fracture pressure, but the rate of chemical compaction and the build up of pore pressure by chemical compaction is nearly independent of the effective stresses. It is very difficult to model the build up of pore pressures and the timing for hydrofracturing because of the poorly constrained variables and the variable sediment composition. In particular the distribution of permeabilities in three dimensions will vary greatly.

## Conclusions

Realistic modelling of sediment compaction and rock properties requires that the rate-limiting processes are identified and then quantified. The properties of faults and fractures with respect to fluid flow must be predicted based on rock and soil mechanical principles and on chemical processes including mineral precipitation and dissolution. These are very different processes that must be modelled separately. Mechanical compaction should be based on the principles of soil mechanics when the sediments are mostly uncemented. In calcareous sediments chemical compaction may start at relatively shallow depth. In siliceous sediments quartz dissolution and cementation is controlling much of the chemical compaction and this starts at 2–3 km (>80–100°C) and must be modelled mainly as a function of temperature and sediment composition.

Faults rarely serve as conduits for fluid flow during continued subsidence and compaction in sedimentary basins. When fracture pressure is reached, leakage will occur by hydro-fracturing independently of the faults. During uplift and

extension fractures tend to be open, but there is little compaction-driven fluid flow along fractures because the sediments are not compacting. The horizontal stresses must be lower than the vertical stress in a basin that is subsiding without significant shortening.

Compaction in siliceous sedimentary rocks can be modelled as a function of the rate of quartz cementation which is controlled by temperature and time. Chemical compaction causing reduced porosity and reduced rock volume will then occur both during subsidence and uplift as long as the temperature is high enough for quartz cementation to continue. Shrinkage of the rock volume represents a strain which will also reduce the elastic *in situ* stress in the horizontal direction, which may then occur both during subsidence and uplift as long as the chemical compaction continues. In the case of well-cemented sedimentary sandstones and shales the porosity may be too low for significant continued chemical compaction and this is also usually the case for metamorphic rocks. High horizontal stress may then be preserved during exhumation and reduction of the vertical stress, resulting in high ratios between horizontal and vertical stress. During subsidence of reservoir rocks the *in situ* lateral stresses at deeper burial are to a large extent controlled by chemical compaction. During petroleum production, however, increased effective stress due to reduced fluid pressure will cause a purely mechanical response at least in siliceous sedimentary rocks, changing the ratio between the horizontal and the vertical stresses.

The principles involved in sediment compaction are relatively well known and may be modelled as functions of effective stresses, temperature and time. Such models are however very sensitive to variations in the primary sediment composition, and basin modelling therefore requires input from facies analyses and studies of sediment provenance.

The author would like to thank K. Høeg, J. Jahren and A. Read for comments on the manuscript and J. I. Faleide and P. Aagaard for discussions. Thanks are also due to the reviewers K. Heffer and A. Aydin. The editor S. Buiter has helped to improve the manuscript and to make it more accessible to readers from other disciplines. This contribution was based on projects funded by NFR and Statoil (Vista).

## References

ANTONELLINI, M. & AYDIN, A. 1995. Effect of faulting on fluid flow in porous sandstones: geometry and spatial distribution. *American Association of Petroleum Geologists Bulletin*, **79**, 642–671.

BIOT, M. A. 1955. Theory of elasticity and consolidation for a porous anisotropic solid. *Journal of Applied Physics*, **26**, 182–185.

BJØRKUM, P. A. 1996. How important is pressure in causing dissolution of quartz in sandstones? *Journal of Sedimentary Research*, **66**, 147–154.

BJØRKUM, P. A. & NADEAU, P. H. 1998. Temperature controlled porosity/permeability reduction fluid migration, and petroleum exploration in sedimentary basins. *Australian Petroleum Production and Exploration Association Journal*, **38**, 453–465.

BJØRKUM, P. A., OELKERS, E. H., NADEAU, P. H., WALDERHAUG, O. & MURPHY, W. M. 1998*a*. Porosity prediction in quartzose sandstones as a function of time, temperature, depth, stylolite frequency, and hydrocarbon saturation. *American Association of Petroleum Geologists Bulletin*, **82**, 637–648.

BJØRKUM, P. A., WALDERHAUG, O. & NADEAU, P. H., 1998*b*. Physical constraints on hydrocarbon leakage and trapping revisited. *Petroleum Geoscience*, **4**, 237–239.

BJØRLYKKE, K. 1993. Fluid flow in sedimentary basin. *Sedimentary Geology*, **86**, 137–158.

BJØRLYKKE, K. 1994. Fluid flow and diagenesis in sedimentary basins. *In*: PARNELL, J. (ed.) *Geofluid: Origin, Migration and Evolution of Fluids in Sedimentary Basins*. Geological Society, London, Special Publications, **78**, 127–140.

BJØRLYKKE, K. 1999. An overview of factors controlling rates of compaction and fluid flow in sedimentary basins. *In*: JAMTVEIT, B. & MEAKIN, P. (eds) *Growth, Dissolution and Pattern Formation in Geosystems*. Kluwer Akademic Publishers, 381–404.

BJØRLYKKE, K. & EGEBERG, K. 1993. Quartz cementation in sedimentary basins. *American Association of Petroleum Geologists Bulletin*, **77**, 1538–1548.

BJØRLYKKE, K. & HØEG, K. 1997. Effects of burial diagenesis on stresses, compaction and fluid flow in sedimentary basins. *Marine and Petroleum Geology*, **14**, 267–276.

BJØRLYKKE, K., AAGAARD, P., EGEBERG, P. K. & SIMMONS, S. P. 1995. Geochemical constraints from formation water analyses from the North Sea and Gulf Coast Basin on quartz, feldspar and illite precipitation in reservoir rocks. *In*: CUBITT, J. M. & ENGLAND, W. A. (eds) *The Geochemistry of Reservoirs*. Geological Society, London, Special Publications, **86**, 33–50.

BLYSTAD, P., BREKKE, H., FÆRSETH, R. B., LARSEN, B. T., SKOGSEID, J. & TØRUDBAKKEN, B. 1995. Structural elements of the Norwegian continental shelf: Part II. The Norwegian Sea region. *Norwegian Petroleum Directorate Bulletin*, **8**.

BYRKJELAND, U., BUNGUM, H. & ELDHOLM, O. 2000. Seismotectonics of the Norwegian continental margin. *Journal of Geophysical Research*, **105**, 6221–6236.

CHUHAN, F. A., KJELDSTAD, A., BJØRLYKKE, K. & HØEG, K. 2002. Porosity loss in sand by grain crushing. Experimental evidence and relevance to reservoir quality. *Marine and Petroleum Geology*, **19**, 39–53.

CHUHAN, F. A., KJELDSTAD, A., BJØRLYKKE, K. & HØEG, K. 2003 Experimental compression of loose sands simulating porosity reduction in petroleum reservoirs during burial. *Canadian Geotechnical Journal*, **40**, 995–10011.

CORFIELD, S. & SHARP, I. R. 2000. Structural style and stratigraphic architecture of fault propagation folding in extensional settings: a seismic example from the Smorbukk area, Halten Terrace, Mid-Norway. *Basin Research*, **12**, 329–341.

DORE, A. G. & LUNDIN, E. R. 1996. Cenozoic compressional structures on the NE Atlantic margin; nature, origin and potential significance for hydrocarbon exploration. *Petroleum Geoscience*, **2**, 299–311.

Dore, A. G., CARTWRIGHT, J. A., STOCKER, M. S., TURNER, J. P. & WHITE, N. 2002. *Exhumation of the North Atlantic margin; timing, mechanism and implications for petroleum exploration*, Geological Society, London, Special Publications, **196**.

EGEBERG, P. K. & SAIGAL, G. 1991. North Sea chalk diagenesis – cementation of chalks and healing of fractures. *Chemical Geology*, **92**, 339–354.

FALEIDE, J. I., KYRKEBØ, R., KJENNERUD, T., GABRIELSEN, R. H., JORDT, H., FANAVOLL, S. & BJERKE, M. D. 2002. Tectonic impact on sedimentary processes during Cenozoic evolution of the northern North Sea and surrounding areas. *In*: DORE, A. G., CARTWRIGHT, J. A., STOKER, M. S., TURNER, J. P. & WHITE, N. (eds) *Exhumation and Implications for Petroleum Exploration.* Geological Society, London, Special Publications, **196**, 235–269.

FÆRSETH, R. B. 1996. Interaction of Permo-Triassic and Jurassic extensional fault-blocks during the development of the northern North Sea. *Journal of the Geological Society*, London, **153**, 931–944.

FISHER, Q. J. & KNIPE, R. J. 2001. The permeability of faults within siliclastic petroleum reservoirs of the North Sea and Norwegian Continental Shelf. *Marine and Petroleum Geology*, **18**, 1063–1081.

FISHER, Q. J., CASEY, M., HARRIS, X. & KNIPE, R. J. 2003. Fluid-flow properties of faults in sandstones: the importance of temperature history. *Geology*, **31**, 965–968.

GAARENSTROOM, L. R., TROMP, A. J., DE JONG, M. C. & BRANDENBURG 1993. Over-pressures in the Central North Sea. Implications for trap integrity and drilling safety. *In*: PARKER, J. R. (ed.) *Petroleum Geology of Northwest Europe*. Proceedings from the 4th Conference. Geological Society, London, 1305–1313.

GABRIELSEN, R. H., KYRKJEBØ, R., FALEIDE, J. I., FELDSKAR, W. & KJENNERUD, T. 2001. The Cretaceous post-rift development in the northern North Sea. *Petroleum Geoscience*, **7**, 137–154.

GILES, M. R. 1997. *Diagenesis: A Quantitative Perspective*. Kluwer.

GROLLIMUND, B. & ZOBACK, M. D. 2003. Impact of glacially induced stress changes on fault-seal integrity offshore Norway. *American Association of Petroleum Geologists Bulletin*, **87**, 493–506.

GROLLIMUND, B., ZOBACK, M. D., WRIPUT, D. J. & ARNESEN, L. 2001. Stress orientation, pore pressure and least principal stress in the Norwegian sector of the North Sea. *Petroleum Geoscience*, **7**, 173–180.

GÖLKE, M. & COBLENTZ, D. 1996. Origins of the European regional stress field. *Tectonophysics*, **266**, 11–24.

HESTHAMMER, J., BJORKUM, P. A. & WATTS, L. 2002. The effect of temperature on sealing capacity of faults in sandstone reservoirs: Example from the Gullfaks Field. *American Association of Petroleum Geologists Bulletin*, **86**, 1733–1751.

HEUM, O. R. 1996. A fluid dynamic classification of hydrocarbon entrapment. *Petroleum Geoscience*, **2**, 145–158.

HICKS, E. C., BUNGUM, H. & LINDHOLM, C. D. 2000. Stress inversion of earthquake focal mechanism solutions from onshore and offshore Norway. *Norsk Geologisk Tidskrift*, **80**, 235–250.

ISAKSEN, G. H. 2004. Central North Sea hydrocarbon systems: generation, migration, entrapment and thermal degradation of oil and gas. *American Association of Petroleum Geologists Bulletin*, **8**, 1545–1572.

JAEGER, J. C. & COOK, N. G. W. 1979. *Fundamentals of Rock Mechanics*. Chapman and Hall, London.

KARLSEN, D. A., SKEIE, J. E. *ET AL.* 2004. Petroleum migration, faults and over pressure. Part II. Case history. The Haltenbanken Petroleum Province, offshore Norway. *In*: CUBITT, J. M., ENGLAND, W. A. & LARTER, S (eds) *Understanding of Petroleum Reservoirs; Towards an Integrated Reservoir Engineering Approach.* Geological Society, London, Special Publications, **237**, 305–372.

KARNER, S. L., CHESTER, F. M., KRONENBERG, A. K. & CHESTER, J. S. 2003. Subcritical compaction of granular sand. *Tectonophysics*, **377**, 357–381.

KJELDSTAD, A. 2002. *Compaction and shear deformation in sedimentary basins*. Ph.D. thesis, University of Oslo.

KJELDSTAD, A. J., SKOGSEID, J., LANGTANGEN, H. P., BJØRLYKKE, K. & HØEG, K. 2003. Differential loading by prograding sedimentary wedges on continental margins: an arch forming mechanism. *Journal of Geophysical Research*, **108**, 2036, DOI 10.1029/2001 JB001145.

LAMBE, T. W. & WHITMAN, R. V. 1979. *Soil Mechanics, SI Version*. John Wiley, New York.

LANDER, R. H., HELSET, H. M., MATHEWS, J. C. & BONELL, L. M. 2003. Can sandsteons diagenesis induce overpressure? *In*: DUEPPENBECKER, S. J. & MARZI, R. W. (eds) *Multidimensional Basin Modelling. American Association Petroleum Geologists of Discovery Series*, 352–353.

LEONARD, R. C. 1993. Distribution of sub-surface pressure in the Norwegian Central Graben and applications for exploration. *In*: PARKER J. R. (ed.) *Petroleum Geology of Northwest Europe. Proceedings of the 4th Conference.* The Geological Society, 1295–13003.

LINDHOLM, C. D., BUNGUM, H., BRATLI, R. K., AADNØY, B. S., DAHL, N. T., RUDBAKKEN, B. & ATAKAN, K. 1995. Crustal stress in the northern North Sea as inferred from borehole breakouts and earthquake focal mechanisms. *Terra Nova*, **7**, 51–59.

LOTHE, A. E., BORGE, H. & GABRIELSEN, R. H. 2004. Modelling of hydraulic leakage by pressure and stress simulations and implications for Biot's constant: an example from the Halten Terrace, offshore Mid Norway. *Petroleum Geoscience*, **10**, 199–213.

LUO, X. & VASSEUR, G. 1995. Modelling of pore pressure evolution associated with sedimentation and uplift in sedimentary basins. *Basin Research*, **7**, 35–52.

MOSS, B., BARSON, D., RAKHUT, K., DENNIS, H. & SWARBRICK, R. 2003. Formation pressure and formation water. *In*: EVANS, D., GRAHAM, C., ARMOUR, A. & BATHURST, P. (eds) *The Millennium Atlas: Petroleum Geology of the Central and Northern North Sea*. Geological Society, London, 317–329.

NORDGAARD BOLÅS, H. M. & HERMANDRUD, C. 2002. Rock stress in sedimentary basins – implication for trap integrity. *In*: KOESTLER, A. G. & HUNSDALE, R. (eds) *Hydrocarbon Seal Quantification* Norwegian *Petroleum Society*, Special Publication, **11**, 17–35.

NYGÅRD, R., GUTTIERREZ, M., HØEG, K. & BJØRLYKKE, K. 2004. Influence of burial history on microstructure and compaction behaviour of Kimmeridge Clay. *Petroleum Geoscience*, **10**, 269–270.

OELKERS, E. H., BJØRKUM, P. A. & MURPHY, W. M. 1996. A petrographic and computational investigation of quartz cementation and porosity reduction in North Sea sandstones: *American Journal of Science*, **296**, 420–452.

OLSTAD, R., BJØRLYKKE, K. & KARLSEN, D. K. 1997. Pore water flow and petroleum migration in the Smørbukk Field area, offshore Norway. *In*: MØLLER-PEDERSEN, P. & KOESTLER, A. G. (eds) *Hydrocarbon Seals – Importance for Exploration and Production. Norwegian Petroleum Society*, Special Publication, **7**, 201–216.

PALANDRI, J. L. & KHARAKA, Y. K. U. 2004. A compilation of rate parameters of water-mineral interaction kinetics to geochemical modelling. *U.S. Geological Survey Report*, 2004–1068.

PEREZ, R. J., CHATELLIER, J. I. & LANDER, R. H. 1999. Use of quartz cementation kinetic modeling to constrain burial histories; examples from the Maracaibo Basin, Venezuela. *Revista Latino-Americana de Geoquimica Organica*, **5**, 39–46.

RAAEN, A. M., SKOMEDAL, E., KJØRHOLT, H., MARKESTAD, P. & ØKLAND, D. 2001. Stress determination from hydraulic fracturing tests: the system stiffness approach. *International Journal of Rock Mechanics and Mining Sciences*, **38**, 529–541.

RAMM, M. & BJØRLYKKE, K. 1994. Porosity/depth trends in reservoir sandstones: assessing the quantitative effects of varying pore – pressure, temperature history and mineralogy. Norwegian Shelf data. *Clay Minerals*, **29**, 475–490.

SIBSON, R. H. 1981. Fluid flow accompanying faulting. Field evidence and models. *In*: SIMPSON, D. W. & RICHARDS, P. G. (eds) *Earthquake Prediction: An International Review*. American Geophysical Union, Maurice Ewing Series, **4**, 593–603.

SIBSON, R. H. 2003. Brittle-failure controls on maximum sustainable overpressure in different tectonic regimes. *American Association of Petroleum Geologists Bulletin*, **87**, 901–908.

STORVOLL, V., BJØRLYKKE, K. & MONDOL, N. H. 2005. Velocity-depth trends in Mesozoic and Cenozoic sediments from the Norwegian Shelf. *American Association of Petroleum Geologists Bulletin*, **89**, 359–381.

SVERDRUP, E., HELGESEN, J. & VOLD, J. 2003. Sealing properties of faults and their influence on water-alternating-gas injection efficiency in the Snorre field, northern North Sea. *American Association of Petroleum Geologists Bulletin*, **87**, 1437–1458.

VERRUIJT, A. 1982. *Ground Water Flow*. Macmillan Press, London.

WALDERHAUG, O. 1996. Kinetic modelling of quartz cementation and porosity loss in deeply buried sandstone reservoirs. *American Association of Petroleum Geologists Bulletin*, **80**, 731–745.

WALDERHAUG, O., BJØRKUM, P. A., NADEAU, P. H. & LANGNES, O. 2001. Quantitative modelling of basin subsidence caused by temperature-driven silica dissolution and precipitation. *Petroleum Geoscience*, **7**, 107–113.

WIPRUT, D. & ZOBACK, M. D. 2000. Fault reactivation and fluid flow along a previously dormant normal fault in the northern North Sea. *Geology*, **28**, 595–598.

WONG, T.-F., DAVID, C. & ZHU, W. 1997. The transition from brittle faulting to cataclastic flow in porous sandstones. Mechanical deformation. *Journal of Geophysical Research*, **102**, 3009–3025.

WOOD, J. R. 1994. Chemical Diagenesis. *In*: WILSON, M. D. (ed.) *Reservoir Quality Assessment and Prediction in Clastic Rocks. SEPM Short Course*, **30**, 119–136.

# Multiple faults in ductile simple shear: analogue models of flanking structure systems

ULRIKE EXNER[1,*], BERNHARD GRASEMANN[2] & NEIL S. MANCKTELOW[1]
[1]*Geologisches Institut, ETH-Zentrum, CH-8092 Zürich, Switzerland*
[2]*Institut für Geologische Wissenschaften, University of Vienna, A-1090 Vienna, Austria*
**Current address: University of Vienna, Althanstrasse 14, 1090 Vienna, Austria*
*(e-mail: ulrike.exner@univie.ac.at)*

**Abstract:** Rotational behaviour and deformation around multiple faults was investigated in analogue experiments using a linear viscous matrix material under simple shear boundary conditions. Previous analogue and numerical studies have shown that, for single faults, characteristic deformation geometries are produced in initially straight marker lines parallel to the shear zone boundary (flanking structures). Observations from several natural shear zones suggest that not only single faults, but often several parallel or conjugate fault planes are subjected to progressive shear resulting in distinctive deflection geometries. If the distance between faults is on the order of their length, or less, then the perturbation flow fields interfere and coalescence, and finite deflection structures develop that are distinctly different from those around single fractures. In particular, coeval contractional and extensional geometries may develop across conjugate faults, although for bulk simple shear the total length of marker lines parallel to the shear zone boundary cannot change. This advises caution in inferring shear-zone parallel contraction or extension from secondary slip surfaces. In contrast to single flanking structures, conjugate flanking structure systems occurring in natural shear zones are reliable shear sense indicators due to their triclinic symmetry.

Planar discontinuities, such as fractures, veins or dykes, may be subjected to progressive deformation in ductile shear zones. Depending on the flow geometry of the shear zone and the initial orientation of the discontinuity with respect to the shear zone boundary (SZB), various deflection geometries of passive, initially planar, markers may develop. The resulting structures have been collectively called flanking structures (Passchier 2001). Several studies (Grasemann & Stüwe 2001; Grasemann *et al.* 2003; Exner *et al.* 2004; Wiesmayr & Grasemann 2005) have systematically investigated the formation of such structures around single, isolated discontinuities, termed cross-cutting elements (CE; Fig. 1), embedded in linear viscous materials under isochoric plane strain boundary conditions. Flanking structures are the geometric consequence of a perturbation of the homogeneous flow field induced by planar discontinuities, recorded by planar markers in the surrounding material. This effect is referred to as perturbation strain (e.g., Cobbold 1975; Mancktelow 1991).

In all orientations other than parallel to the eigenvector of the flow, CEs co-rotate with respect to the bulk shear sense in simple shear. Nevertheless, the sense of movement along the CE with respect to the bulk shear sense, the type of offset of a marker line, as well as the sense of deflection of the marker line in the immediate vicinity of the CE, may vary. Furthermore, the deflection of marker lines changes along the length of a CE, and the characteristic geometric features are ideally observed along the central marker line (CML; Fig. 1). In simple shear, six different geometries of flanking structures are possible at small strains (Fig. 2; Grasemann *et al.* 2003). These geometries can be characterized in terms of the offset of the CML along the CE relative to the bulk shear (s = synthetic or co-shearing, a = antithetic or counter-shearing), the drag of the CML against the CE (normal or reverse, *cf.* Hamblin 1965), and whether there is locally extension or contraction along the CML across the CE. This classification requires knowledge of the bulk shear sense, which is given for experimental models and may be independently established in field examples.

In this study, we apply the definition of flanking structures as introduced by Grasemann & Stüwe (2001), where a pinned slip surface (or an elliptical

*From*: BUITER, S. J. H. & SCHREURS, G. (eds) 2006. *Analogue and Numerical Modelling of Crustal-Scale Processes.* Geological Society, London, Special Publications, **253**, 381–395.
0305-8719/06/$15.00 

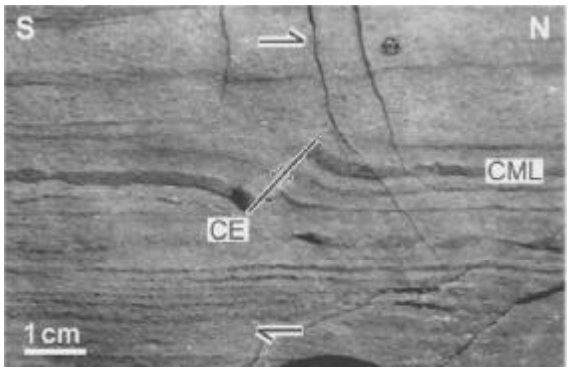


**Fig. 1.** Natural example of a flanking fold with extensional, antithetic offset and reverse drag in mylonitic marble with known shear sense (arrows) on Naxos, Greece (N37°11′23.6″, E25°30′55.1″). The central marker line (CML) is located in the approximate symmetry centre of the structure; at a distance to the structure, marker lines above and below the tips of the cross-cutting element (CE) are straight and continuous.

low-viscosity inclusion) embedded in a linear viscous matrix accounts for the formation of a confined flanking structure with monoclinic symmetry. Shear bands are a particularly common, but special example, that develop at low angles with the SZB (0–45°), showing extensional, synthetic offset of the CML (Fig. 2). At medium angles (45–135°), flanking folds with antithetic displacement along the CE are formed, having either contractional or extensional offset of the CML. Above 135°, flanking folds with synthetic, but now contractional, offset can be observed.

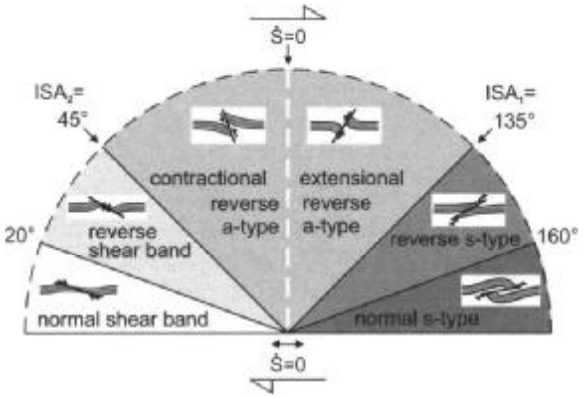


**Fig. 2.** Instantaneous structure development of flanking structures in dextral simple shear, depending on the initial orientation of the CE to the shear zone boundary (after Exner *et al.* 2004). Instantaneous stretching axes (ISA) delimit sectors of synthetic and antithetic sense of shear along the CE; lines of zero stretch ($\dot{S} = 0$) are at 0° and 90° to the SZB in simple shear, separating contractional and extensional structures within the syn/antithetic sectors.

With progressive deformation, it is also possible for one type of flanking structures to evolve into another (Exner *et al.* 2004).

Observations from natural shear zones suggest that not only single discontinuities, but also sets of parallel or conjugate features are commonly affected by subsequent ductile deformation. Multiple (sub)parallel shear bands in mylonite zones are a well known example, but other combinations of multiple flanking structures are, although quite common in natural rocks, completely unstudied. We want to introduce the term *flanking structure system*, defining a complex structure resulting from the interference of perturbation strains in a set of two or more CEs. Perturbation strains of CEs overlap when the distance between the CEs roughly equals the length of the CE (Pollard & Segall 1987).

In this study we present a series of analogue experiments, which were designed to examine the systematics of deformation around conjugate or parallel planar features within a homogeneous ductile matrix. A major advantage of analogue experiments over numerical models is that it is relatively simple to introduce more than one fault surface. Moreover, the amount of finite shear strain is unlimited in the ring shear apparatus employed in this study, permitting the observation of structure development to large strains. Although the basic principles of flanking structures can easily be applied to a series of parallel or conjugate discontinuities, there are some major differences in structural evolution and finite geometries, especially if the perturbation strains induced by different CEs in the host rock interfere.

The aim of this paper is to investigate analogue models of parallel and, in more detail, conjugate flanking structure systems by means of finite perturbation fields and to compare the results with natural examples. The study has important consequences for: (1) the coexistence and simultaneous activity of contractional and extensional faults; (2) the development of triclinic flanking structure systems; and (3) the correct interpretation of shear sense derived from flanking structure systems.

## Experimental procedure

The analogue experiments were conducted in a ring shear apparatus (Arbaret *et al.* 2001). This analogue rig consists of two concentric vertical cylinders rotating in opposite directions at the same velocity. The volume between the two cylinders is filled with a linear viscous polymer, PDMS (polydimethylsiloxane SGM 36, manufactured by Dow Corning), resting on

a lubricant glycerine layer. Isochoric plane strain cylindrical shear flow is produced in the analogue material between the counter-rotating cylinders, with increasing strain rate from the outer to the inner cylinder.

The setup of the analogue experiments closely follows the procedure described in Exner *et al.* (2004). At the centre of the model shear zone, 'faults' were cut into the PDMS and filled with soap or silicone oil. A passive marker grid was imprinted on top of the model surface using partially fixed photocopies (Dixon & Summers 1985).

The distance between the CEs was chosen to accord with that observed in natural examples, avoiding direct connection of the fault surfaces, yet allowing the perturbations around the faults to produce combined geometries instead of two completely independent structures. Whether interference occurs depends on the spacing and initial orientation of the faults relative to their length. This relationship was also investigated in the current experiments.

## Results of analogue experiments

Pinned (non-propagating) slip surfaces embedded in a linear viscous matrix produce flanking structures if subjected to further deformation (e.g., Grasemann & Stüwe 2001). The main feature of flanking structures, apart from a more or less significant offset of initially straight markers along the CE, is the deflection of these markers as they approach the CE. This deflection, especially the phenomenon of reverse drag, was first described by Hamblin (1965), and extended by, e.g., Reches and Eidelman (1995) and Grasemann *et al.* (2003). In contrast to all previous interpretations, the main conclusion of the most recent work is that fault drag is not produced by the frictional resistance along the CE, but by the perturbation field induced by slip along the CE (Passchier *et al.* 2005). The slip along the CE causes a localized strain that differs from the imposed bulk strain, and this difference must be compensated in the immediate vicinity of the fault. This results in the development of four open perturbation loops (Mancktelow 1991), which represent an inhomogeneous vector field with highest magnitudes adjacent to the fault, decreasing to zero at some distance into the matrix (Passchier *et al.* 2005).

The finite perturbation fields presented in this study are constructed by subtracting the heterogeneously deformed finite grid from the deformed grid not influenced by the presence of a CE. Under ideal simple shear this part, which is not influenced by the CE, would be the homogeneous part of the finite deformation, sometimes called the background strain (Weijermars 1992). However, because in our experiments the strain rate is a function of the radius of the rig, our background strain is in fact also heterogeneous. An intuitive approach for investigating perturbation fields is that these vector fields represent the deflections of straight marker lines in the vicinity of heterogeneities (e.g., fault drag along a CE), because in a homogeneous strain field, initially straight passive marker lines remain straight. Note that these finite perturbation fields are the same as the 'finite vector displacement field of the heterogeneous component of deformation' of Mancktelow (1991, Fig. 5), but different from the instantaneous perturbation velocity fields discussed by Passchier *et al.* (2005).

The present analogue study was designed to investigate (1) the shape and variation of the perturbation loops, (2) the rotational behaviour of multiple CEs in simple shear, and (3) the deflection geometries of planar makers around multiple conjugate or parallel CEs resulting from the combination of perturbation flow and fault rotation.

### *Mechanisms*

Generally, there are two different mechanisms responsible for the finite geometries of markers around planar discontinuities: (1) the existence of an instantaneous perturbation velocity field, and (2) the progressive rotation of the CEs with respect to the SZB, which causes the perturbation velocity field to change with time.

*Perturbation displacement fields.* Perturbation flow accounts for the deflection of markers around the CEs. Following the concept of Passchier *et al.* (2005), perturbation flow can be visualized as a vector field. Vector fields can generally be divided into a series of open or (in special cases) closed loops separated by lines where the polarity of flow changes, and points of no perturbation flow.

For single CEs, there exist four instantaneous perturbation loops, which are variably developed depending on the orientation of the CE. When the CE is parallel to one of the instantaneous stretching axes (ISA), the polarity of the loops is inverted. CE orientations symmetrical about the ISA have identical instantaneous perturbation velocity fields except for a reversal in polarity (Passchier *et al.* 2005, Fig. 7c,g).

Parallel flanking structure systems exhibit a coalescence of the intermediate perturbation loops. Figure 3 shows the perturbation field

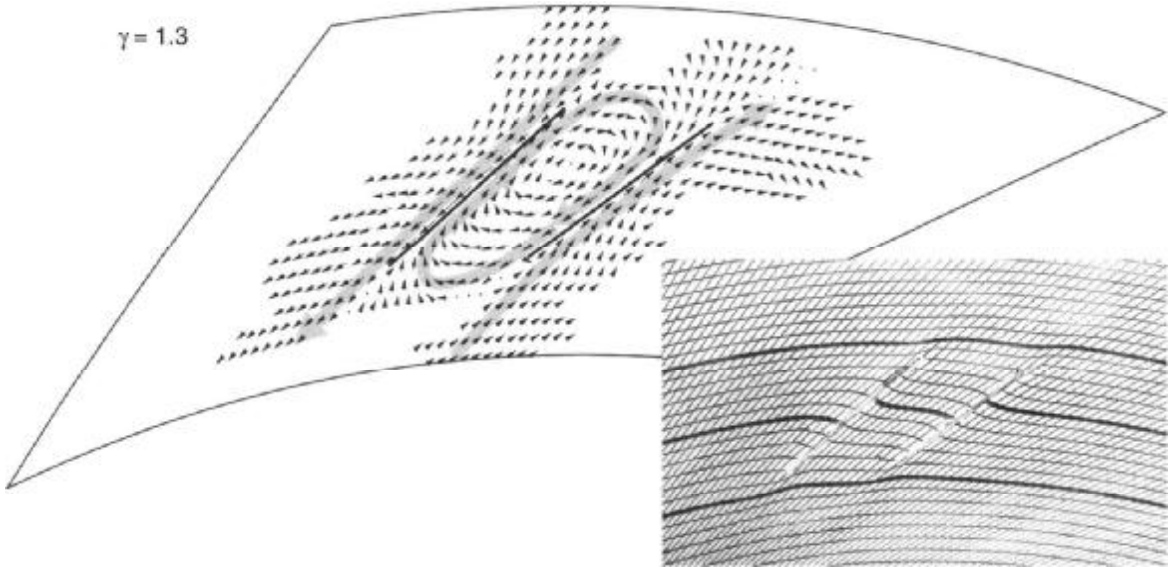


**Fig. 3.** Finite perturbation displacement field and image of analogue experiment of a parallel flanking structure system with initial orientation of the CEs at 90° to the SZB at $\gamma = 1.3$. A concentric perturbation loop accounts for the clockwise rotation and reverse drag of the CML between the CEs.

around two parallel reverse a-type flanking fold geometries, where the intermediate region is defined by a clockwise closed circular loop, which is explicitly separated from the two external, anti-clockwise open loops. Because the CEs have the same orientation within the flow field, they also have the same rotation sense and rate. Therefore, the whole finite structure shows a monoclinic symmetry, even when several CEs with the same orientation are arranged en echelon. A natural example of parallel flanking structure systems are asymmetric boudinage structures, which have been classified as Type I forward rotating and Type II backward-rotating shear geometries (Swanson 1992), depending on the orientations of the CEs and thus the sense of the coalescent perturbation loops. A complete geometric description of boudin geometries was discussed in detail by Goscombe *et al.* (2004).

Conjugate flanking structure systems are controlled by a more complex arrangement of perturbation loops. Here, the loops are no longer monoclinic. Although the configuration for separate isolated CEs with the same orientation consists of four independent loops around each CE, in combined systems the neighbouring cells between the two CEs immediately merge to form a common vector field, where boundaries between distinct loops cannot be distinguished (see Fig. 7).

Perturbation loops are characterized by a flow field deviating significantly from the bulk flow field. Hence, lines initially already parallel to the bulk fabric attractor (in simple shear also a line of no finite elongation) may nonetheless experience rotation away from this orientation and consequently, significant extension and/or contraction during progressive deformation. Passive markers record the finite sum of all previous (instantaneous) perturbation fields. Their heterogeneous deformation is a direct consequence of the finite perturbation field, which may deviate strongly from the instantaneous perturbation field. Deformed marker lines, both in experiment and nature, provide a visualization of the finite effects of perturbation flow and thus a practical basis for comparison and classification.

*Fault rotation.* It is important to note that rotation of a fault (or CE) is not a prerequisite for producing drag effects in adjacent marker layers. Faults that are stable or meta-stable in orientation may also produce flanking structures (*cf.* Fig. 7a of Passchier *et al.* 2005). Nevertheless, the sense and rate of rotation is critical in controlling the progressive deformation and finite geometry of flanking structures (Exner *et al.* 2004), especially if they rotate into a different field of instantaneous flanking structure development. This effect is particularly important in conjugate flanking structure systems.

A comparison between the rotation rate of passive markers and CEs (i.e., active slip surfaces) shows that, within experimental error, they have the same rotational behaviour. Kocher and Mancktelow (2004) came to the same conclusion when comparing analytical solutions

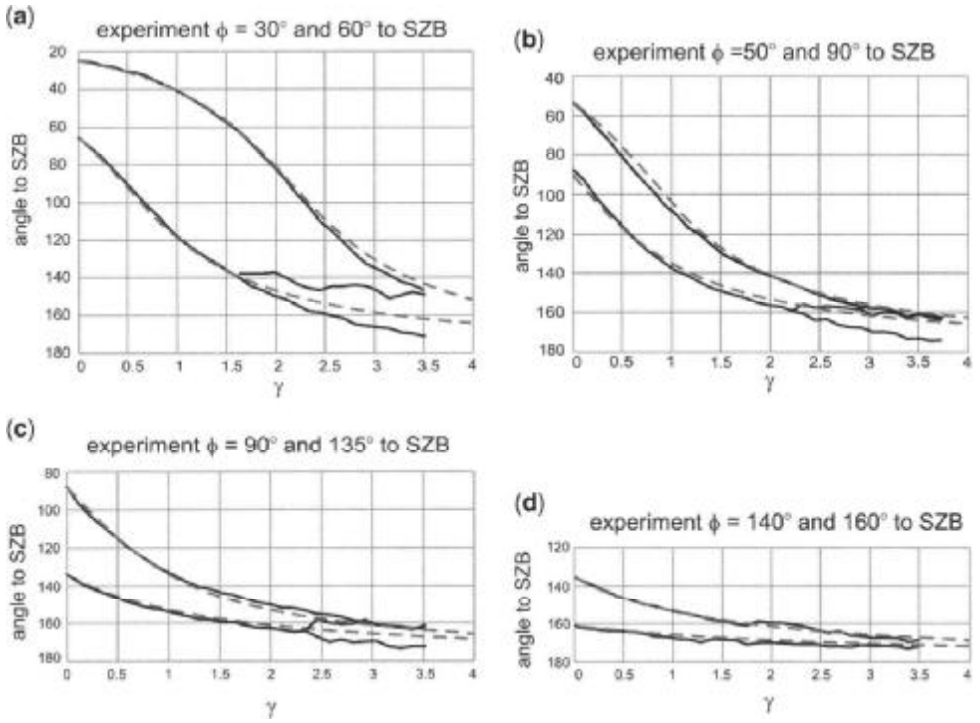


**Fig. 4.** Rotation of CEs measured from experiments (continuous lines) and theoretical rates of passive markers (dashed lines) in simple shear calculated with Eqn (2). Corresponding to Fig. 7, experiments with initial angles of CEs at (**a**) 30° and 60°, (**b**) 50° and 90°, (**c**) 90° and 135° and (**d**) 140° and 160° are shown. Note the excellent match of the model with theory, even though the model set-up clearly differs from the geometrical constraints of the theory.

and finite element models of rotating ellipses with theoretical curves for passive marker line rotation. This is quite general: any elongate inclusion ($R > c$. 10) will effectively rotate as a passive line whether the inclusion is weaker or stronger than the matrix (e.g., see the analytical solutions of Schmid & Podladchikov 2003). In Figure 4a–d, experimental data for rotating CEs are compared to the corresponding theoretical curves for purely passive markers in simple shear. Following Ramsay (1967), the rotation rate $\dot{\omega}$ of passive markers can be calculated using

$$\dot{\omega} = (\dot{\gamma}/2)(1 - \cos 2\alpha) \qquad (1)$$

Alternatively, the orientation of passive markers can be determined using the trigonometric relationship

$$\cot \alpha' = \cot \alpha + \gamma \qquad (2)$$

Any difference between the experimentally observed values for CEs and the theoretical values for a passive line can be attributed to the inherent heterogeneity in strain that occurs in the ring shear machine. The shear strain rate (and therefore rotation rate) is greater toward the inner cylinder, so that initially straight CEs (and marker lines) become curved at higher shear strain values.

An important corollary of these experimental results is that, even though CEs induce a complex perturbation flow field, their rotational behaviour is not affected. Even when the perturbation fields of neighbouring CEs interfere, the rotation rates are unaffected and they still behave like passive marker lines. This finding is consistent with observations from analogue experiments on rigid particles in simple shear, whose rotational behaviour is not changed unless the distance between them is shorter than their own length (Ildefonse *et al.* 1992). It follows that the only stable orientation of CEs in simple shear is the eigenvector, or fabric attractor (Passchier 1997), parallel to the shear direction (Fig. 5).

### *Geometry of passive marker lines*

Deflection and offset of passive marker lines around multiple CEs is controlled by (1) the bulk flow geometry of the shear zone, (2) the initial orientation of the CEs with respect to the SZB, (3) the initial angle of the CEs with

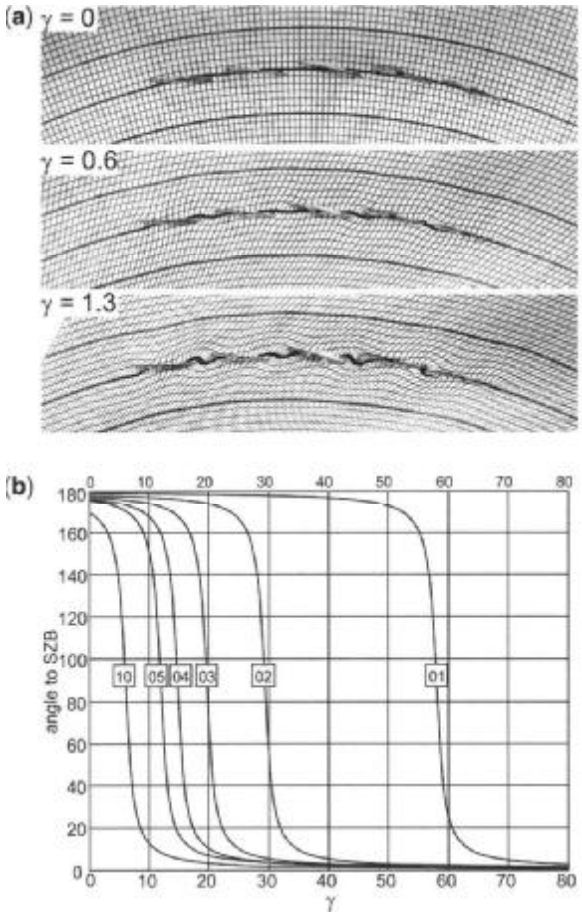


**Fig. 5.** (**a**) Analogue experiment with 5 CEs initially oriented at *c.* 10° to SZB at $\gamma = 0$, 0.6 and 1.3. Development of pronounced flanking structures can be observed, whereas the rotation rate of the CEs is rather insignificant. (**b**) Rotational behaviour of passive markers at low angles (between 1° and 10°) to SZB. Small variations in the initial orientation result in major differences of the value of shear strain, at which the markers start to rotate significantly into the shear direction.

respect to each other, and (4) the distance between the CEs relative to their length.

*Conjugate flanking structure systems.* For simple shear flow considered here, all initially horizontal marker lines (i.e., parallel to the SZB) remain straight and parallel and maintain the same spacing in the far field of flanking structures around single discontinuities. In contrast, marker lines in the area between closely spaced conjugate CEs are subjected to a combination of two (unequal or even opposed) perturbation fields. The mutual interference between these different vector fields results in a combined perturbation flow field that may involve the coalescence of loops or even the formation of new loops. Thus, due to the small distance between the CEs (relative to their length), initially SZB-parallel markers in the space between the two CEs are not only deflected, but may be translated (either upwards or downwards) and/or rotated with respect to their initial position.

Figure 6 shows a selection of five possible combinations of initial conjugate CE orientations. The amount of finite shear strain is small for all structures (between 0.6 and 1.3), allowing a comparison at a similar stage in their evolution. Corresponding to the concept of flanking structures around single CEs, the drag and sense of offset along the two CEs depends on the initial orientation of the CE with respect to the SZB. More specifically, special combinations of CE orientations with respect to the SZB result in special rotation and drag geometries of the marker lines between the CEs. Interestingly, instantaneous geometries may develop that are quite unexpected for simple shear flow. For example, not only co- and counter-rotation of the inter-CE marker lines can be observed, but also apparently extensional (Fig. 6b) and contractional (Fig. 6d) geometries. Such geometries are only possible if the distance between the CEs is small enough to allow the two perturbation fields to interfere. Note that some of the model results have striking similarities with large-scale fault bounded structures like horst and graben (Fig. 6b), domino- or bookshelf-type halfgraben (Fig. 6c), extruding-wedge geometries (Fig. 6d) or pop-up structures. Therefore, we speculate that the concept of interfering perturbation fields also work on scales which are several orders of magnitude larger than our models.

Finite conjugate flanking structure systems generally have triclinic symmetry, even if the initial orientation of the conjugate CEs was monoclinic. This is an effect of the induced simple shear flow forcing differently oriented CEs to rotate with different rates (Fig. 4). As an important consequence, one CE might be in an orientation of synthetic (or co-) shearing, while the other CE might be in an orientation of antithetic (or counter-) shearing. From a detailed investigation of natural examples on all scales, it can be seen that triclinic conjugate flanking structure systems are more the rule than the exception.

As an example, Figure 7a shows the perturbation displacement field around two CEs initially oriented at an angle of 30° and 60° to the SZB, respectively, at $\gamma = 0.6$. As can be seen in the inset photograph of the analogue experiment, the CEs have already rotated to higher angles, and the initially straight (or more precisely, concentric) marker lines show a distinct offset and deflection. The finite perturbation

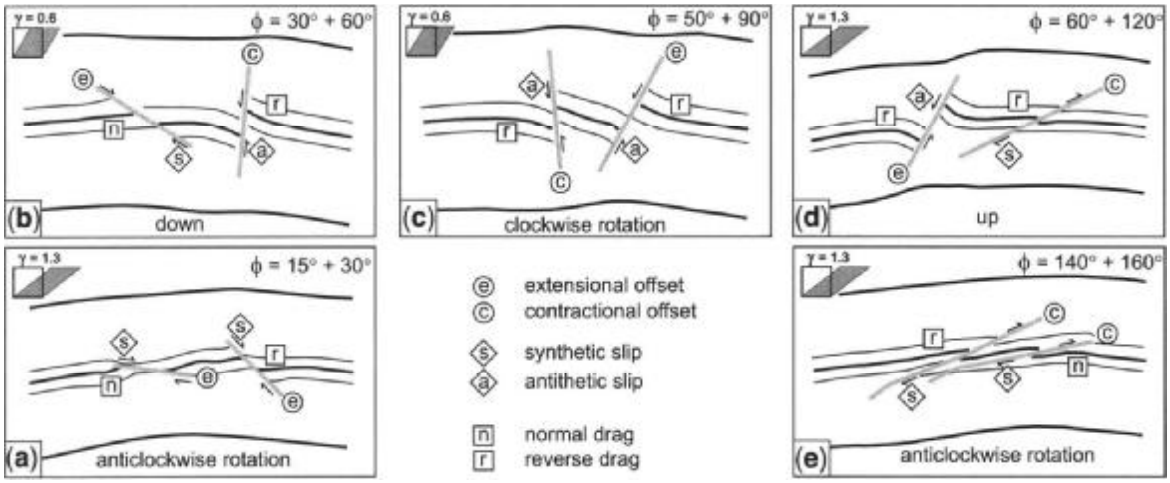


**Fig. 6.** Five possible combinations of conjugate flanking structure systems. Various initial conjugate angles result in different geometries. Note the variation in rotation/relative position of CML between the CEs, resulting from different combinations of syn/antithetic slip, extensional/contractional offset and normal/reverse drag. Some of the model results resemble tectonic structures, which occur in nature at much larger scales compared to the size of our model: e.g., (**a**) high and low angle normal faults, (**b**) graben, (**c**) half-graben, (**d**) extruding wedge, (**e**) duplex.

field has developed two distinct external perturbation loops, whereas the intermediate loops form a common, more or less homogeneously oriented vector field. Although it is not immediately evident in the photograph of the experiment, the perturbation arrows show a larger offset in the internal area between the CEs, especially for the left (less steeply inclined) CE.

At larger shear strain ($\gamma = 1.3$), the picture becomes more complex (Fig. 7b). Now, only the external perturbation loop on the right side of the conjugate CEs displays a simple concentric vector field. The central and left perturbation loops are connected by a zone of short, upwards pointing arrows. Here, the vectors transform from a downwards-directed field into a left-directed movement. Moreover, the perturbation direction along the right margin of the left CE is separated into two diverging, oppositely directed loops, approximately in the centre of the CE. Consequently, marker lines above this divergence point show a normal, below it a reverse, drag. The finite perturbation field is to some extent counter-intuitive, but this is a consequence of the procedure by which it is determined. Tracing the relative movement of marker points follows the finite displacement paths and represents an integration of instantaneous perturbation flow fields that change as the individual CEs rotate during progressive deformation. Thus, areas with low initial perturbation will show the finite effects of a reversal in the instantaneous sense of movement much earlier than areas with initially high perturbation.

Figure 7c–f presents two experiments with initial angles of the conjugate CEs at 50° and 90° (Fig. 7c,d) or 90° and 135° (Fig. 7e,f) to the SZB, respectively. Both experiments are shown at two different stages ($\gamma = 0.6$ and 1.3), to allow comparison of the different evolution of the perturbation loops, and especially of the direction of the perturbation displacement fields between the CEs with different initial angles. It can be seen that the perturbation loops change their orientation, size and also magnitude, while the CEs rotate at different rates according to their orientation with respect to the SZB (Fig. 4).

*Parallel flanking structure systems.* For parallel flanking structure systems, the midpoint of the CML between two CEs always maintains the same position relative to the SZB. This reflects the monoclinic symmetry of both the initial geometry and the imposed simple shear boundary conditions. Even for complex progressive histories, where the sense of rotation (counterclockwise/clockwise) and offset direction (antithetic vs. synthetic) of the CML changes with time, the symmetry is maintained (e.g., Figs 3 and 5). In contrast, flanking structure systems where the CEs were initially conjugate have an initial triclinic symmetry, which is also maintained during deformation (Fig. 7).

A special type of parallel flanking structure system is represented by parallel shear bands, SCC' or ECC fabrics. They are frequently observed in anisotropic rocks (micaschists or

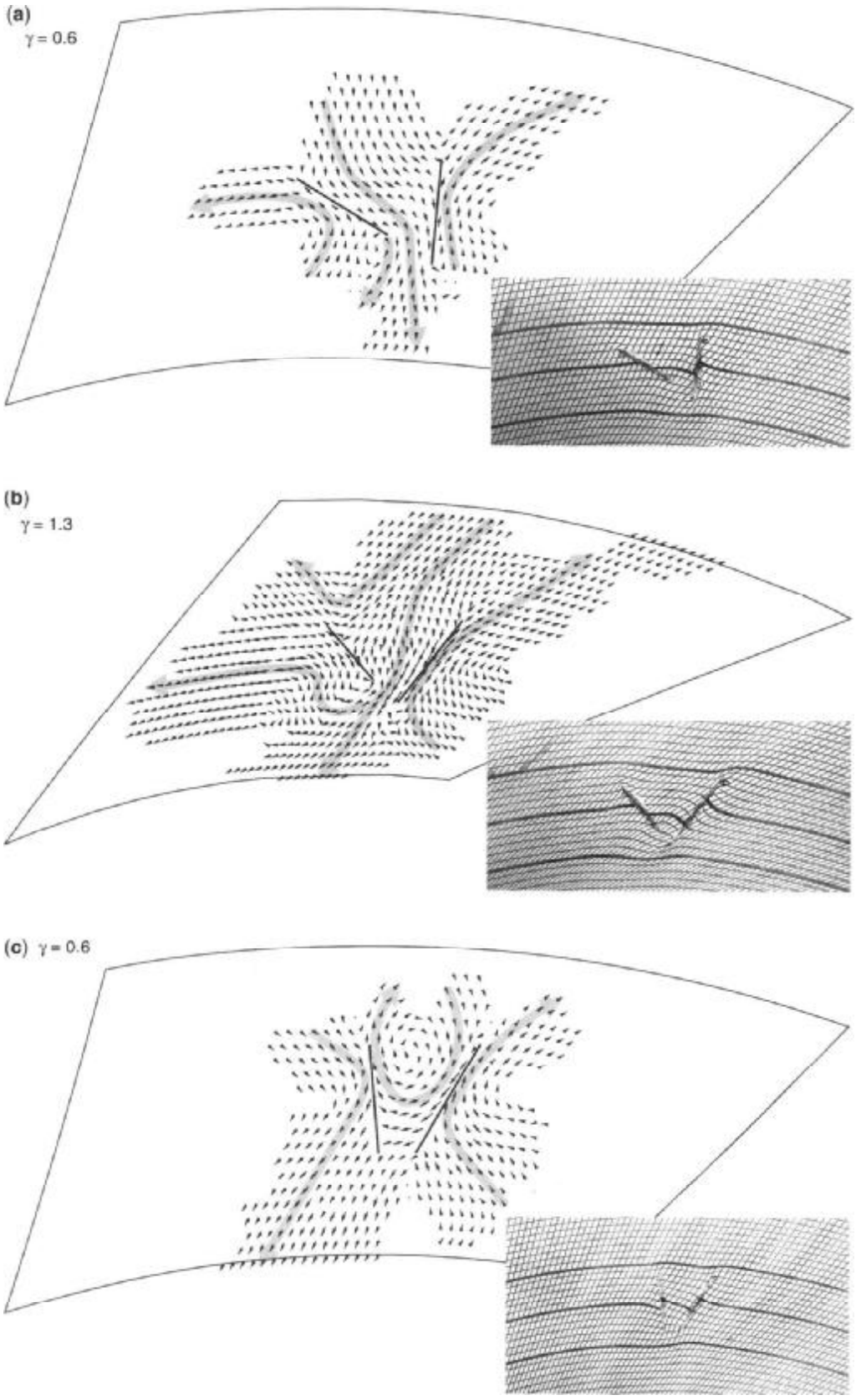


**Fig. 7.** Perturbation displacement fields of selected experiments of conjugate flanking structure systems. Initial orientations of the CEs are at 30° and 60° for (**a**) and (**b**), at 50° and 90° for (**c**) and (**d**) and at 90° and 135° for (**e**) and (**f**). Each experiment is shown at $\gamma$ of 0.6 and 1.3. The large grey arrows drawn in the background should help to highlight trajectories of the perturbation flow field. Note that this is not identical to a particle flow field. Images of analogue experiments are provided for comparison of the perturbation fields with the actual geometry of the marker lines.

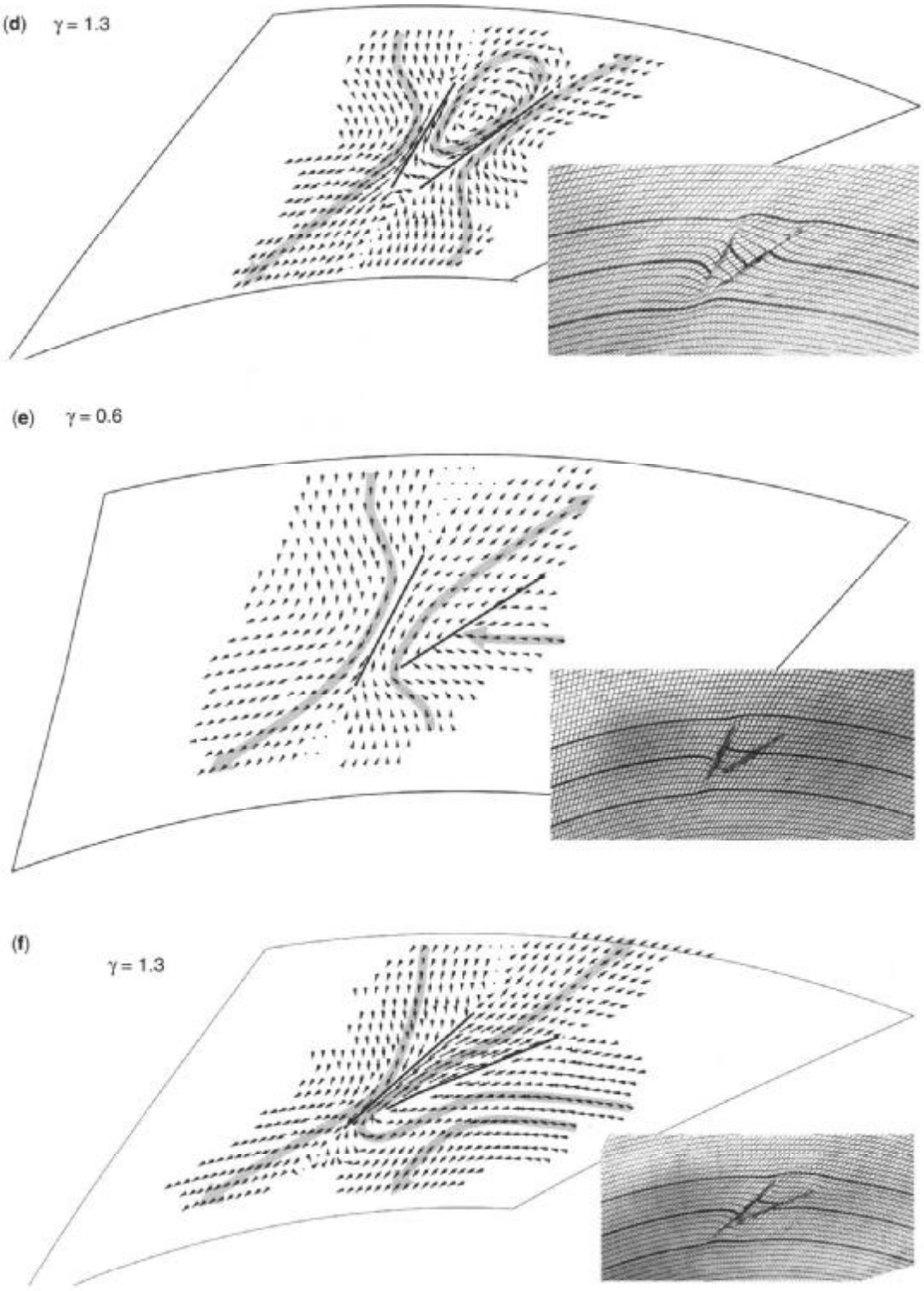


**Fig. 7.** *Continued.*

paragneisses). Even though the mechanism of formation of the CEs is not investigated in the present study, the geometric result of synthetic shearing along moderately inclined secondary CEs is identical to the one observed in our analogue experiments. For example, in an experiment with five CEs initially oriented at 10° to the SZB (Fig. 5a), the fault orientation changes very little up to (very) large $\gamma$. For an even smaller initial angle to the SZB, CEs retain their 'stable' position even longer, up to $\gamma \sim 50$ for an angle of 1° to the SZB (Fig. 5b).

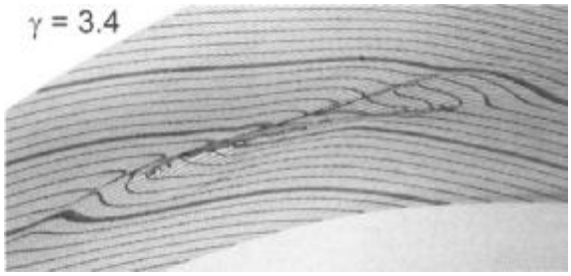


**Fig. 8.** Analogue experiment with initial orientations of CEs at 90° and 135°, at $\gamma = 3.4$. With increasing strain, some markers develop tight folds along the CE.

## Discussion

As outlined above, parallel flanking structure systems maintain their monoclinic symmetry during progressive deformation. En echelon arrangement of parallel flanking structure systems, including natural examples, have been extensively studied in several papers on boudinage in layered and foliated rocks (e.g., Platt & Vissers 1980; Swanson 1992; Goscombe & Passchier 2003). Figures 9a and b show two photographs of natural parallel flanking structure systems with CEs at low and high angles to the SZB, respectively. It can be seen that the finite geometries of CMLs are strongly dependent on the distance between the CEs. Recent geometric studies of parallel flanking structure systems in high-grade rocks have proposed several different mechanisms for the phenomenon of 'back-rotation' of the foliation between parallel shear zones or faults (e.g., Harris 2003). We suggest that most of the effects reported are a direct consequence of the perturbation strains induced by these CEs and that the concept of flanking structure systems is also applicable to the description of marker rotation between shear zones (Blenkinsop 2004). In this study, we focus on the discussion of conjugate flanking structure systems, which (1) may develop complex triclinic geometries, (2) can show contemporaneous extensional and contractional faults, and (3) may allow determination of the bulk shear sense. Figure 9 comprises natural examples of flanking structures with monoclinic and triclinic symmetry from Naxos, Greece, where a strong non-coaxial component of flow is well documented (e.g., Urai *et al.* 1990), thus allowing qualitative comparison with our simple shear analogue experiments.

### *Flanking structure systems with triclinic symmetry*

The concept of an ideal isolated fault ellipse (Walsh & Watterson 1989), which rotates during progressive deformation to produce a single monoclinic flanking structure, is probably more the exception than the rule in nature, although beautiful examples have been described (e.g., Passchier 2001; Grasemann *et al.* 2003). The simple analogue models of two conjugate CEs deforming in plane strain, as presented here, provide some important insights into the development of interfering perturbations caused by CEs, but natural three-dimensional examples of conjugate fault systems may be considerably more complex.

Figure 6 shows five of our modelled triclinic flanking structure systems, which represent a subset of the wide range of structures that could develop from a set of two CEs with differing initial orientations. Here, we focus on the possible instantaneous structures that may form in simple shear from a combination of the initial orientation of the CEs relative to the six fields of instantaneous flanking structure development (Fig. 1). Considering two CE orientations with six deformation sectors gives 15 different combinations. Including the possibility that both CEs could be also located in the same field with only slightly different orientations results in $15 + 6 = 21$ different instantaneous conjugate flanking structure systems. In fact, the number of possible finite structures is even greater, because during progressive deformation the CEs will rotate with different rates into the next field or even the field after that (Exner *et al.* 2004). The range of potential structures is further increased in general shear compared to simple shear, because CEs may not only co-, but also counter-rotate (Grasemann *et al.* 2003; Wiesmayr & Grasemann 2005). The natural examples in Figure 9 highlight this potential complexity in real systems.

### *Coeval extension and contraction in conjugate flanking structure systems*

In the following, we focus on contemporaneous contractional and extensional CEs and their transient development. It should be emphasized that these geometries develop despite the fact that all structures were modelled under simple shear boundary conditions, where in the far field flow there is no extension or contraction parallel to the shear zone.

In simple shear, the instantaneous stretching axes (ISA) and principal stress directions are oriented at 45° and 135° to the SZB. By definition, these directions experience no instantaneous shear and separate fields of synthetic (or co-) and antithetic (or counter-) shearing. In the fields $<45°$ and $>135°$, CEs show synthetic shearing, whereas CEs oriented between 45° and

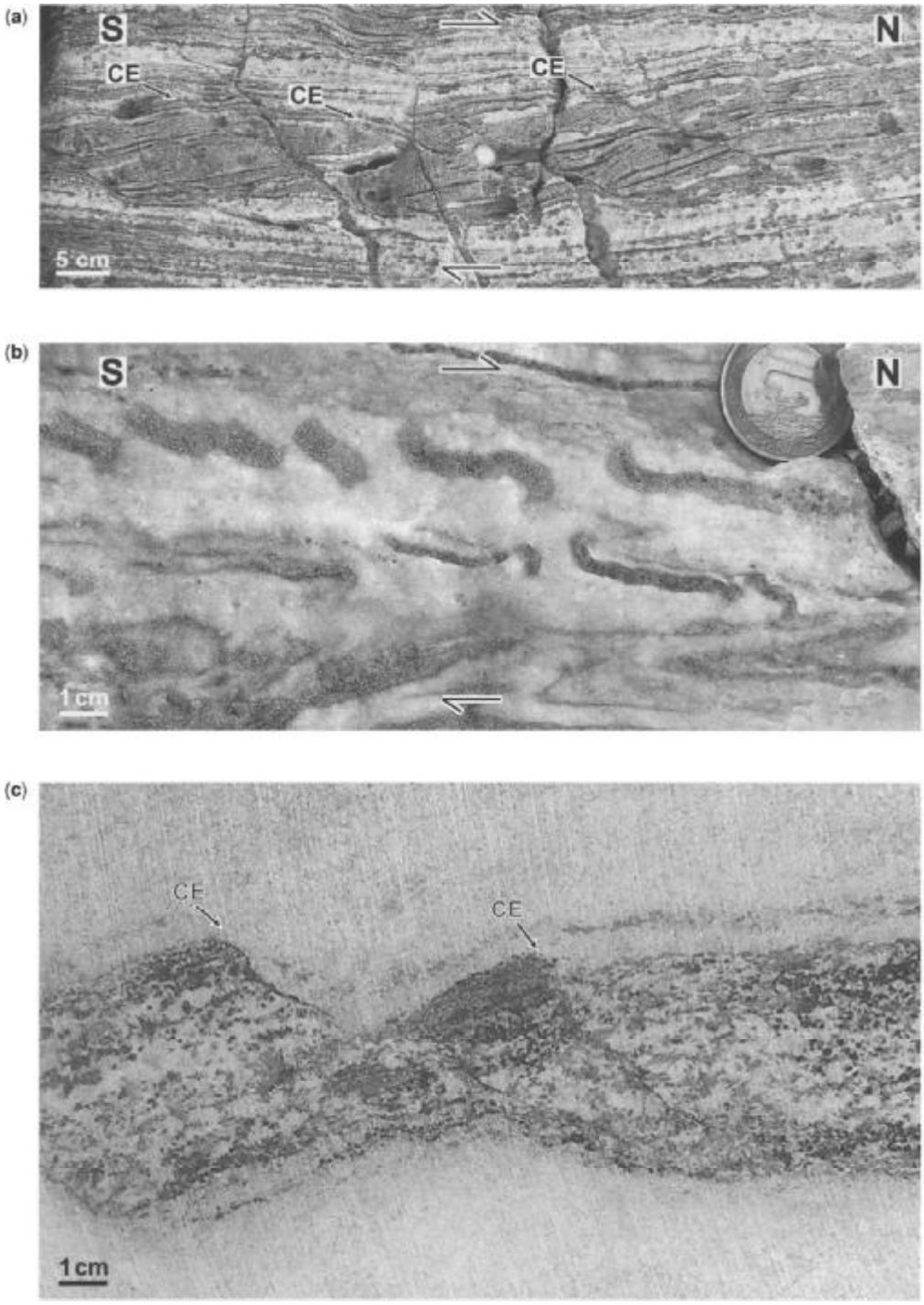


**Fig. 9.** Natural examples of flanking structure systems. (**a**) Parallel flanking structure system at low angle to SZB, showing synthetic, extensional offset of markers in a calcite marble with dolomitic layers from Naxos, Greece, along a vertical section with a top to the north sense of shear in the core of the Naxos dome (N37°11′26.2″, E025°30′48.8″); (**b**) parallel flanking structure system with CEs at high angles to the layering, taken from a similar lithology at the same location as (a); (**c**) amphibolite layer in a block from a marble quarry in Kinidaros (Naxos, Greece), with a low-angle conjugate flanking structure system producing a triclinic geometry of the marker layers; (**d**) conjugate flanking structure system from the same location as (a), combining a contractional with an extensional CE, resulting in a clockwise rotation of the CML between the CEs; (**e**) conjugate flanking structure system with several CEs at high angles to the layering, on the southern coast of Naxos, Greece, along a horizontal section at the western limb of the Naxos dome with bulk dextral shear sense (N36°58′22.9″, E25°24′21.6″); (**f**) at the same location as the structure in (e), two CEs oriented at high angles to the SZB form a conjugate flanking structure system. Drag effects of the marker lines between them vary significantly, from convex in the central parts of the structure to sigmoidal shapes in the upper right area, strongly resembling the geometry of markers in the experiment shown in Fig. 8.

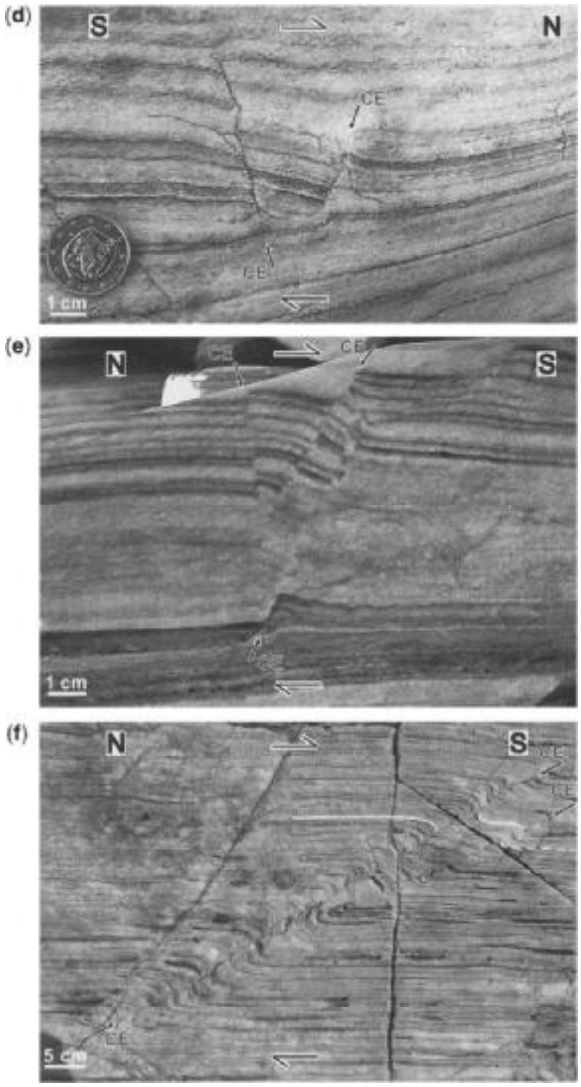


**Fig. 9.** *Continued.*

135° show antithetic shearing. Furthermore, the lines of zero instantaneous stretch oriented at 0 and 90° to the SZB separate alternate quadrants of instantaneous extension and contraction. Depending on the initial orientation of the conjugate CEs and their progressive rotation and shearing, complicated conjugate flanking structure systems with extensional and contractional offsets may coexist.

An amphibolite layer in a marble from Naxos, Greece (Fig. 9c), is cut by a low-angle CE with extensional offset and reverse drag, which is pronounced on the right side of the structure. On closer inspection, a second CE at a slightly steeper angle to the layering can be identified at the right side of the prominent CE. Hence, the triclinic symmetry of the structure can be attributed to the conjugate flanking structure system with two slightly oblique CEs, comparable to Figure 6a.

Another conjugate flanking structure system developed in a layered marble from Naxos, Greece (Fig. 9e). Several CEs with variable lengths and angles are developed, each featuring a different drag, amount of slip and, in some cases, even a different sense of offset. In this case, a sequential initiation of the CEs may also be possible.

A conjugate flanking structure system also from Naxos, Greece, with CEs oriented at high angles to the SZB is presented in Figure 9f. Variable drag effects identical to those in Figure 8 can be observed along the two CEs, which merge into a single CE toward the bottom left. These examples suggest caution in using secondary slip surfaces in shear zones to imply overall shear zone parallel extension or contraction in natural examples. Contraction of a shear zone parallel marker across a thrust, which repeats the marker in a section normal to the shear direction, does not necessarily imply contraction parallel to the shear zone in the far field. For example s-type flanking structures can develop in our analogue models while there is no extension or contraction parallel to the SZB (*cf.* Fig. 1; Exner *et al.* 2004). Similarly, extension of a shear zone parallel marker across a normal fault (e.g., shear bands, C′ fabric) does not necessarily represent an extension of the whole shear zone in the far field. Thus, the expression 'extensional crenulation cleavage' (Platt 1979), used to describe synthetic, low-angle, parallel flanking structure systems occurring as a dominant fabric element, can be misleading, by suggesting an extensional component parallel to the shear zone boundary. In fact, these kind of parallel flanking structure systems are possible not only under simple shear boundary conditions, but also in transtensive flow where there is even a component of contraction parallel to the SZB (Wiesmayr & Grasemann 2005).

### *Shear sense derived from conjugate flanking structure systems*

Finite element modelling and natural examples suggest that single flanking structures may be ambiguous shear sense indicators, because mirror symmetries exist for all structures (Grasemann *et al.* 2003). Similarly, parallel flanking structure systems, which maintain their monoclinic symmetry, are also ambiguous. However, the analogue models presented in Figure 6 show that simple shear conjugate flanking structure systems are very reliable shear sense indicators due to their triclinic symmetry.

For instance, the natural example in Figure 9d demonstrates how a triclinic flanking structure

system can be used as kinematic indicator. The marker lines are cut by two conjugate CEs: the left one shows a thrust geometry, while a normal offset is recognizable in the right one. Although the normal fault could be kinematically compatible with top-to-south shear, an anti-clockwise rotation of the left CE would require extensional offset, which is incompatible with the observed contractional offset. Thus, overall this geometry clearly indicates bulk top-to-north shear sense.

### *Strain estimates from conjugate flanking structure systems*

Comparing geometries of the experimental conjugate flanking structure systems with natural examples allows a tentative estimate of the amount of shear strain that was accommodated by the specific structure, and thus the approximate degree of rotation of the CE. Figure 9d provides a natural example of a conjugate flanking structure, which represents the combination of a contractional and an extensional reverse a-type flanking fold. The comparable analogue experiment (Fig. 7c) suggests a shear strain of $\gamma \sim 1$. In the experiment, the CEs rotated about 30°–35° from their initial positions at *c.* 50° and 90° to the SZB. Reverse numerical modelling of specific natural conjugate flanking structure systems has potential for constraining both the bulk strain and flow type during their development. The analogue experiments suggest that this constraint may be tighter than for single flanking structures, which are already capable of providing quantitative results in well-defined natural examples (Kocher & Mancktelow 2004).

### *Application to large-scale structures*

Even though our simple physical models do not account for rheological contrasts, isostasy, flexural loading/unloading or gravity, there are nevertheless clear similarities between the small-scale models and some natural large-scale structures, suggesting that the basic geometric effects induced by planar discontinuities are valid at all scales. Deflections of the regional foliation or bedding planes near low- and high-angle faults are well known from natural examples. Low-angle normal faults are normally described in association with a regional-scale normal drag, whereas reverse drag is frequently associated with high-angle normal faults (e.g., Hamblin 1965; Tearpock & Bischke 2003). The geometric similarities between such natural regional scale faults and our model results are remarkable (e.g., compare Fig. 6b and c to the Cinderhill Fault in Figs 7 and 8 of Barnett *et al.* 1987).

The geometry of the set of conjugate normal faults in Figure 6b, with the resulting normal offset of the central part of the structure, is directly comparable to graben structures in rift systems (e.g., Hills 1963) and to the flank uplift and subsidence observed at rifted continental margins (Sclater & Célérier 1987). Similarly, Figure 6c would commonly be interpreted as a steep normal fault with a roll-over antiform, which is crosscut by a conjugate reverse fault acting as accommodation structure in the hanging wall (e.g., McClay & Scott 1991). However, our experiments make it clear that this geometry can also be explained as a conjugate flanking structure system.

Furthermore, some model results show extruding wedge geometries (e.g., Fig. 6d), with a thrust fault at the base and a normal fault at the top. In our models, there is large offset along the faults and decreasing strain towards the centre of the wedge. There is also a background regional strain that results in a rotation of the bounding faults, particularly the upper, more steeply inclined normal faults. In contrast, current models of extruding wedges assume that the bounding blocks are basically rigid and the limiting faults are therefore fixed in their orientation, and explain the observed geometry with wedge-normal shortening and general shear extrusion along stretching faults (e.g., Grujic *et al.* 1996; Vannay & Grasemann 2001). Nevertheless, fault analyses, e.g., in the Buthan Himalayas (Wiesmayr *et al.* 2002) indicate progressive rotation of the normal faults at the upper margin of the extruding wedge (i.e. the Higher Himalaya Crystalline), which is in line with the observations from our analogue experiments (e.g., Figs 7e, f and 8). Finally, the structure shown in Figure 6e is geometrically similar to natural imbricate thrust systems (e.g., Butler 1982), in spite of the fact that there is no shear zone parallel contraction in our analogue models.

Although there may be fundamental differences between the mechanics of our models and the natural examples, the effects of flow perturbations caused by variable slip along faults are scale independent and these effects can also be significant for large-scale structures. It may be argued that linear viscous material and brittle rocks in the upper crust have quite different rheologies. Nevertheless, the resulting perturbations in the velocity field are a purely geometric effect, which can also develop in brittle and/or anisotropic materials. This is confirmed by the analogue scale models of Brun *et al.* (1994) and Koyi and Skelton (2001), which consist of a brittle upper layer above a viscous

lower layer. Both these layers develop drag geometries that are very similar to those of our experiments. These analogue experiments were scaled to model large-scale geodynamic processes, involving both gravity and a free upper surface, yet still show the same perturbation effects.

## Conclusions

Perturbations of the homogeneous flow field around discontinuities cause flanking structures. Intersection of perturbations preconditions the development of conjugate and parallel flanking structure systems. Due to the perturbation of the homogeneous bulk simple shear flow field, lines initially parallel to the fabric attractor (in simple shear a line of no finite elongation) may (1) rotate in any direction away from this orientation, and (2) may experience elongation or contraction during progressive deformation. The sense and rate of rotation of faults is the same as for passive marker lines. Perturbation fields around conjugate (and parallel) flanking structure systems are markedly different from the simpler patterns developed around single discontinuities. During progressive deformation and coeval rotation of the faults, geometry, size and direction of the perturbation cells may change significantly, thus resulting in a complex evolution of the geometry of initially planar markers. Various combinations of fault orientations can produce geometric results that would not intuitively be attributed to simple shear boundary conditions: extensional horst and graben-like and contractional extruding wedge geometries can develop simultaneously in simple shear without layer-parallel deformation. The amount of background strain and fault rotation necessary to produce significant offset and deflection of marker layers is remarkably low ($\gamma \sim 1$). Conjugate flanking structure systems are suitable as shear sense indicators, because in simple shear they produce characteristic geometries depending on their orientation relative to the shear zone boundary. Geometries from analogue models can be used as a rough estimate of the amount of shear strain in natural examples. The only relevant scale factor of flanking structures is the length of the CE, which controls the size of the perturbation loops and thus the area and amount of deflection of passive markers.

The authors gratefully acknowledge financial support from ETH project 0-020998-02 and Austrian Science Foundation FWF project P-15668-Geo. Collaborative field work with G. Wiesmayr and T. Kocher and comments on an earlier version of the manuscript by J. P. Burg are highly appreciated. Reviews by F. Odonne and P. Bons and editorial comments by G. Schreurs also helped to improve the quality of the manuscript.

## References

ARBARET, L., MANCKTELOW, N. S. & BURG, J.-P. 2001. Effect of shape and orientation on rigid particle rotation and matrix deformation in simple shear flow. *Journal of Structural Geology*, **23**, 113–125.

BARNETT, J. A. M., MORTIMER, J., RIPPON, J. H., WALSH, J. J. & WATTERSON, J. 1987. Displacement geometry in the volume containing a single normal fault. *American Association of Petroleum Geologists Bulletin*, **71**, 925–937.

BLENKINSOP, T. 2004. Comment on 'Folding in high-grade rocks due to back-rotation between shear zones' by Lyal B. Harris. *Journal of Structural Geology*, **26**, 601–602.

BRUN, J. P., SOKOUTIS, D. & VAN DEN DRIESSCHE, J. 1994. Analogue modeling of detachment fault systems and core complex. *Geology*, **22**, 319–322.

BUTLER, R. W. H. 1982. The terminology of structures in thrust belts. *Journal of Structural Geology*, **4**, 239–245.

COBBOLD, P. R. 1975. Fold propagation in single embedded layers. *Tectonophysics*, **27**, 333–351.

DIXON, J. M. & SUMMERS, J. M. 1985. Recent developments in centrifuge modelling of tectonic processes: equipment, model construction techniques and rheology of model materials. *Journal of Structural Geology*, **7**, 83–102.

EXNER, U., MANCKTELOW, N. S. & GRASEMANN, B. 2004. Progressive development of s-type flanking folds in simple shear. *Journal of Structural Geology*, **26**, 2191–2201.

GOSCOMBE, B. D. & PASSCHIER, C. W. 2003. Asymmetric boudins as shear sense indicators – an assessment from field data. *Journal of Structural Geology*, **25**, 575–589.

GOSCOMBE, B. D., PASSCHIER, C. W. & HAND, M. 2004. Boudinage classification: end-member boudin types and modified boudin structures. *Journal of Structural Geology*, **26**, 739–763.

GRASEMANN, B. & STÜWE, K. 2001. The development of flanking folds during simple shear and their use as kinematic indicators. *Journal of Structural Geology*, **23**, 715–724.

GRASEMANN, B., STÜWE, K. & VANNAY, J.-C. 2003. Sense and non-sense of shear in flanking structures. *Journal of Structural Geology*, **25**, 19–34.

GRUJIC, D., CASEY, M., DAVIDSON, C., HOLLISTER, L. S., KÜNDIG, R., PAVLIS, T. & SCHMID, S. 1996. Ductile extrusion of the Higher Himalayan Crystalline in Bhutan: evidence from quartz microfabrics. *Tectonophysics*, **260**, 21–43.

HAMBLIN, W. K. 1965. Origin of 'reverse drag' on the downthrown side of normal faults. *Geological Society of America Bulletin*, **76**, 1145–1164.

HARRIS, L. B. 2003. Folding in high-grade rocks due to back-rotation between shear zones. *Journal of Structural Geology*, **25**, 223–240.

HILLS, E. S. 1963. *Elements of Structural Geology*. Methuen and Co., London.

ILDEFONSE, B., SOKOUTIS, D. & MANCKTELOW, N. S. 1992. Mechanical interactions between rigid particles in a deforming ductile matirx. Analogue experiments in simple shear flow. *Journal of Structural Geology*, **14**, 1253–1266.

KOCHER, T. & MANCKTELOW, N. S. 2004. Numerical modelling of progressive evolution of flanking structures. *Bollettino di Geofisica*, **45**, 304.

KOYI, H. A. & SKELTON, A. 2001. Centrifuge modelling of the evolution of low-angle detachment faults from high-angle normal faults. *Journal of Structural Geology*, **23**, 1179–1185.

MANCKTELOW, N. S. 1991. The analysis of progressive deformation form an inscribed grid. *Journal of Structural Geology*, **13**, 853–864.

MCCLAY, K. R. & SCOTT, A. D. 1991. Experimental-models of hanging wall deformation in ramp flat listric extensional fault systems. *Tectonophysics*, **188**, 85–96.

PASSCHIER, C. W. 1997. The fabric attractor. *Journal of Structural Geology*, **19**, 113–127.

PASSCHIER, C. W. 2001. Flanking structures. *Journal of Structural Geology*, **23**, 951–962.

PASSCHIER, C. W., MANCKTELOW, N. S. & GRASEMANN, B. 2005. Flow perturbations: a tool to study and characterize heterogeneous deformation. *Journal of Structural Geology*, **27**, 1011–1026.

PLATT, J. P. 1979. Extensional crenulation cleavage. *Journal of Structural Geology*, **1**, 95.

PLATT, J. P. & VISSERS, R. L. M. 1980. Extensional structures in anisotropic rocks. *Journal of Structural Geology*, **2**, 397–410.

POLLARD, D. D. & SEGALL, P. 1987. Theoretical displacements and stresses near fractures in rocks. *In*: ATKINSON, B. K. (ed.) *Fracture Mechanics of Rock*. Academic Press, London, 277–349.

RAMSAY, J. G. 1967. *Folding and Fracturing of Rocks*. New York, McGraw-Hill.

RECHES, Z. & EIDELMAN, A. 1995. Drag along faults. *Tectonophysics*, **247**, 145–156.

SCHMID, D. W. & PODLADCHIKOV, Y. Y. 2003. Analytical solutions for deformable elliptical inclusions in general shear. *Geophysical Journal International*, **155**, 269–288.

SCLATER, J. G. & CÉLÉRIER, B. 1987. Extensional models for the formation of sedimentary basins and continental margins. *Norsk Geologisk Tidsskrift*, **67**, 253–267.

SWANSON, M. T. 1992. Late Acadian – Alleghenian transpressional deformation: evidence from asymmetric boudinage in the Casco Bay area, coastal Maine. *Journal of Structural Geology*, **14**, 323–341.

TEARPOCK, D. J. & BISCHKE, R. E. 2003. *Applied Subsurface Geological Mapping*. Prentice Hall, New Jersey.

URAI, J. L., SCHUILING, R. D. & JANSEN, J. B. H. 1990. Alpine deformation on Naxos (Greece). *In*: KNIPE, R. J. & RUTTER, E. H. (eds) *Deformation Mechanisms, Rheology and Tectonics*. Geological Society, London, Special Publications, **54**, 509–522.

VANNAY, J.-C. & GRASEMANN, B. 2001. Himalayan inverted metamorphism and syn-convergence extension as a consequence of a general shear extrusion. *Geological Magazine*, **138**, 253–276.

WALSH, J. J. & WATTERSON, J. 1989. Displacement gradients on fault surfaces. *Journal of Structural Geology*, **11**, 307–316.

WEIJERMARS, R. 1992. Progressive deformation in anisotropic rocks. *Journal of Structural Geology*, **14**, 723–742.

WIESMAYR, G. & GRASEMANN, B. 2005. Sense and non-sense of shear in flanking structures with layer-parallel shortening: implications for fault-related folds. *Journal of Structural Geology*, **27**, 249–264.

WIESMAYR, G., EDWARDS, M. A., MEYER, M., KIDD, W. S. F. LEBER, D., HÄUSLER, H. & WANGDA, D. 2002. Evidence for steady fault-accommodated strain in the High Himalaya; progressive fault rotation of the southern Tibet detachment system in NW Bhutan. *In*: DE MEER, S., DRURY, M. R., DE BRESSER, J. H. P. & PENNOCK, G. M. (eds) *Deformation Mechanisms, Rheology and Tectonics: Current Status and Future Perspectives*. Special Publications **200**, Geological Society, London, 371–386.

# Using an elastic dislocation model to investigate static Coulomb stress change scenarios for earthquake ruptures in the eastern Marmara Sea region, Turkey

JORDAN R. MULLER[1,2], ATILLA AYDIN[1] & TIM J. WRIGHT[3]
[1]*Department of Geological and Environmental Sciences, Stanford University, 450 Serra Mall, Bldg. 320, Stanford, CA, 94305, USA*
[2]*Present address: NASA Goddard Space Flight Center, Geodynamics Branch, Mail Code 921, Greenbelt, MD, 20771, USA (e-mail: jmuller@core2.gsfc.nasa.gov)*
[3]*Department of Earth Sciences, Oxford University, Parks Road, Oxford OX1 3PR, UK*

**Abstract:** Using an elastic dislocation model, we incorporate a historical earthquake catalog, mapped Marmara Sea fault traces, and fault slip distributions for the 1999 Izmit earthquake inferred from InSAR and GPS data to determine various stress change scenarios crucial for evaluating future earthquake potential in the eastern Marmara Sea. We have tested six plausible past rupture configurations arising from the uncertainty in the location of the western termination of 1999 Izmit earthquake rupture and the location of the 1963 Yalova earthquake rupture. Coulomb stresses calculated are increased on the Princes' Islands, Çinarcik, and Armutlu fault segments in each case. In four of the six plausible configurations of previous ruptures, the Çinarcik fault receives the greatest average stress change. In one other configuration, the average stress increase on the Princes' Islands fault is greatest. In another, the stress changes on the Çinarcik and Princes' Islands faults are comparable. Moreover, we show that rupture initiating on either the Princes' Islands or Armutlu faults would be favoured to propagate onto the Central Marmara, or Imrali fault, respectively, based on the favourable geometries of the respective fault intersections. Rupture initiating on the Çinarcik fault, however would be limited to a much shorter length based on its mapped western termination. Therefore, while the earthquake-induced stress changes may, in most cases, be greatest on the Çinarcik fault, an earthquake initiating on this fault segment may produce a shorter cumulative rupture compared to rupture initiated on the two other major eastern Marmara Sea fault segments. These results are encouraging for the use of geomechanical modelling tools in addressing uncertainties inherent in most geological and geophysical data applied to earthquake-related problems.

The cascading sequence of large earthquakes progressing along the North Anatolian fault from 1912 to 1999 has led scientists to an intuitive, yet troubling, conclusion: the next large earthquake is most likely to rupture along the northern portion of the Sea of Marmara and within tens of kilometres of Istanbul, a city of 14 million inhabitants (Fig. 1) (Le Pichon *et al.* 1999; Hubbert-Ferrari *et al.* 2000; Parsons *et al.* 2000). To address this threat, earth scientists aim to provide geologically constrained probabilities of future rupture scenarios (e.g., Stein *et al.* 1997). Following the 1999 Izmit earthquake, Parsons *et al.* (2000) combined earthquake records over the past several centuries, earthquake recurrence intervals and computed stress changes associated with recent earthquakes, to estimate that there is a $62 \pm 15\%$ probability for strong shaking to occur in Istanbul before 2030. The contribution of the computed static stress changes to this probability estimate is large – without the stress changes associated with the 1999 Izmit earthquake, the probability is reduced by *c.* 15%. Realistic future rupture scenarios and effective incorporation of earthquake interaction in probability studies therefore require accurate calculation of stress changes on a well-constrained Marmara Sea fault geometry.

Several recent studies have calculated stress changes on vertical faults with uniform or smoothly varying strike directions throughout the Sea of Marmara due to large earthquakes within the 20th century (Nalbant *et al.* 1998; Hubert-Ferrari *et al.* 2000; Parsons *et al.* 2000; Pinar *et al.* 2001; Cakir *et al.* 2003). This

*From*: BUITER, S. J. H. & SCHREURS, G. (eds) 2006. *Analogue and Numerical Modelling of Crustal-Scale Processes.* Geological Society, London, Special Publications, **253**, 397–414.
0305-8719/06/$15.00 

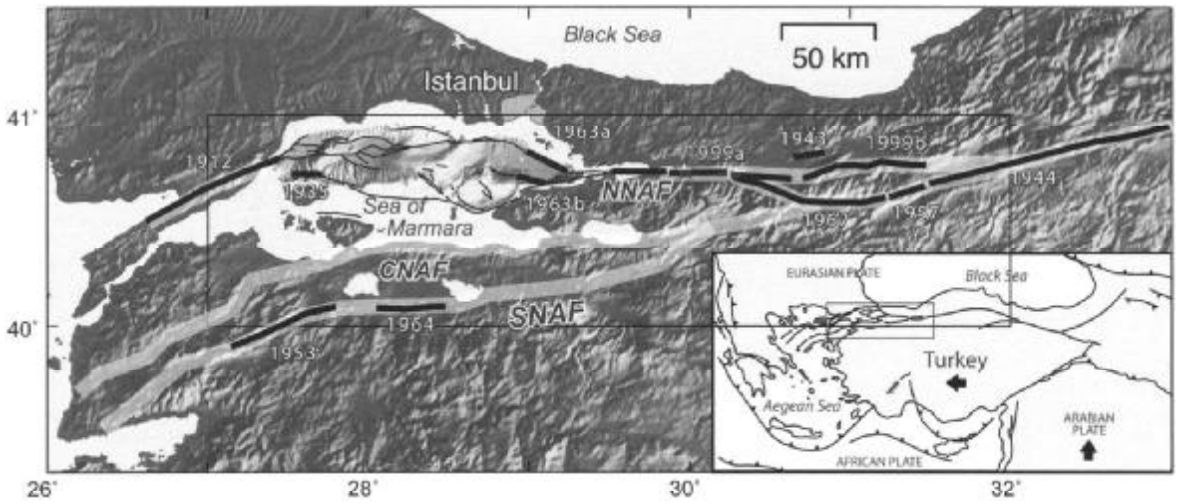


**Fig. 1.** Seismotectonic setting of the Marmara Sea and surrounding region. Surface traces of $M_s > 6.4$ earthquakes since 1900 are plotted in black. The ruptures 1963a and 1963b refer to the same event on September 18 but show the different rupture locations interpreted in other publications. Thick light gray lines show the locations of the northern (NNAF), central (CNAF) and southern (SNAF) strands of the NAF. Marmara Sea fault geometry is modified from Armijo *et al.* (2002). Inset figure shows the regional setting of the larger figure. Large rectangle in larger figure shows boundaries of Fig. 2a.

'optimally oriented fault' approach is only accurate to the degree that the local fault orientation in the Sea of Marmara matches the assumed regional fault orientation in the model. This approach therefore introduces inaccuracies in regions such as the eastern Sea of Marmara, where faults that bound the Çinarcik basin dip 60° or shallower and deviate in strike from the assumed plate boundary by up to 30°. Others have computed stress changes resolved onto individual Sea of Marmara fault segments (Hubert-Ferrari *et al.* 2000; Pinar *et al.* 2001). In general, the calculated stress increases range from 0.01 to 0.5 MPa depending on the proximity of the fault segment to the nearby modelled earthquake ruptures. Not surprisingly, the greatest stress increases are located in the eastern Sea of Marmara region, to the west of the presumed termination of the 1999 Izmit earthquake. In this region, the northern North Anatolian fault (NNAF) splits into three strands (Fig. 2), and Pinar *et al.* (2001) suggest that the Yalova-Hersek fault segment (0.45 MPa) was subjected to a greater stress change due to the Izmit earthquake than either the Princes' Islands (0.18 MPa) or Çinarcik-Yalova (0.09 MPa) fault segments.

The recent earthquakes in this region, however, have ambiguous rupture configurations, making it difficult to constrain a single stress-change scenario. The locations of both the western termination of the 1999 Izmit earthquake rupture and the rupture of the 1963 eastern Marmara earthquake (commonly referred to as the 'Yalova' earthquake) are debated within the literature. Various authors have suggested that the 1999 Izmit earthquake has either terminated east of the Hersek Delta within the Bay of Izmit, or propagated anywhere between 12 and 33 km further west (Fig. 2b). The 1963 earthquake has been thought to occur on either the NW-trending Princes' Islands fault (Taymaz *et al.* 1991; Parsons *et al.* 2000) or the WNW-trending southern Çinarcik fault (Jackson & McKenzie 1988; Nalbant *et al.* 1998). The stress changes that are calculated within the eastern Sea of Marmara will depend significantly on the configurations of these ruptures.

Using geomechanical models, we aim to evaluate how future rupture scenarios, in terms of Coulomb stress changes, depend on the locations of these recent eastern Sea of Marmara earthquake ruptures. We argue that future rupture is most favoured along either the southern Çinarcik fault or the Princes' Islands fault, depending on the location of earlier ruptures. The difference between these two scenarios has important implications for the potential hazard posed to the region by a future earthquake due to the proximity of the faults to Istanbul. The rupture lengths that may develop for an earthquake initiating on either fault are likely to be different. The Çinarcik fault is mapped to have an abrupt western termination whereas the Princes' Island fault may more effectively transfer slip as it links with the

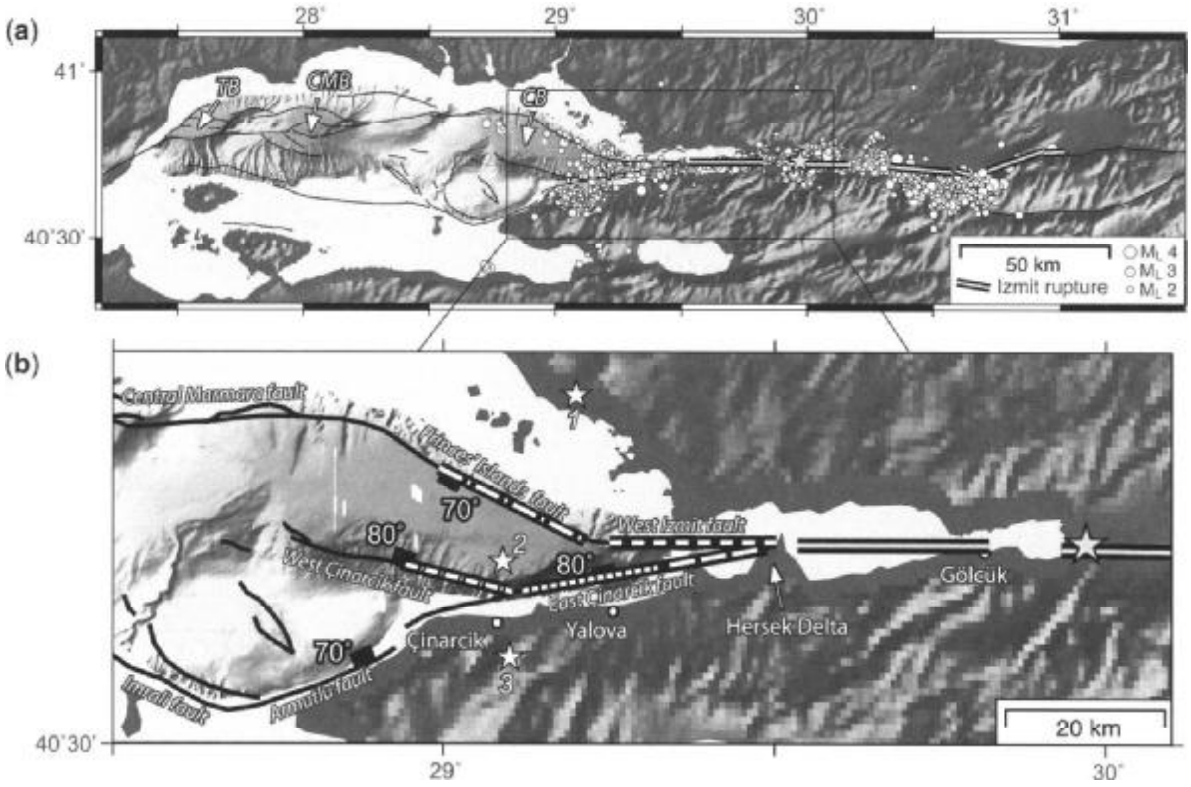


**Fig. 2.** (**a**) Location of major 1999 Izmit earthquake rupture segments (white bounded by black) and epicentre (star), Izmit earthquake aftershocks (Özalaybey *et al.* 2002), and faults within the Sea of Marmara (thin black) (Armijo *et al.* 2002). TB: Tekirdag basin; CMB: Central Marmara basin; CB: Çinarcik basin. (**b**) Configuration of eastern Sea of Marmara faults and the three different westernmost Izmit earthquake rupture segment geometries (white, dashed) and two different 1963 earthquake rupture locations (white, dot-dashed) tested in our study. Small stars indicate epicentral locations of 1963 Yalova earthquake proposed by (1) Taymaz *et al.* (1991), (2) Jackson and McKenzie (1988), and (3) Ambraseys and Finkel (1988).

Central Marmara fault that continues tens of kilometres further west.

## 1963 earthquake location

The size of the $M_s = 6.2–6.4$ 1963 earthquake (Table 1) suggests that the fault segment ruptured in this earthquake released at least several decades of stress accumulation; therefore, the local distribution of stress change on the eastern Sea of Marmara fault segments depends significantly on the location of this event. Seismological studies have determined epicentral locations up to tens of kilometres apart (Fig. 2b) (Ambraseys & Finkel 1988; Jackson & McKenzie 1988; Taymaz *et al.* 1991). Relative to the locations of the Princes' Islands and Çinarcik faults (Fig. 2b), Taymaz *et al.* (1991) determine the event to be to north of both faults, Jackson & McKenzie (1988) place it between the faults, and Ambraseys & Finkel (1988) provide a location south of both faults. Based on the ambiguity of these locations, previous stress change studies have modelled the 1963 rupture either on the SW-dipping Princes' Islands fault (Parsons *et al.* 2000) or

**Table 1.** *Location of the 1963 earthquake in seismological and stress modelling studies*

| Long (°) | Lat (°) | Strike (°) | Dip (°) | Rake (°) | Reference |
|---|---|---|---|---|---|
| 29.1 | 40.7 | 268 | 70 | 235 | Jackson & McKenzie (1988) |
| 29.1 | 40.6 | – | – | – | Ambraseys (1988) |
| Princes' Islands fault | | 296 | ~60 | – | Parsons *et al.* (2000) |
| 29.2 | 40.9 | 304 | ~56 | −82 | Taymaz *et al.* (1991) |
| Çinarcik fault | | 304 | ~56 | −82 | Nalbant *et al.* (1998) |

the north-dipping southern Çinarcik fault (Nalbant *et al.* 1998; Hubert-Ferrari *et al.* 2000).

Taymaz *et al.* (1991) provide the most comprehensive source determination and compute almost pure normal slip on south- and north-dipping nodal planes that approximately matches the orientations of the Princes' Islands and southern Çinarcik faults, respectively. However, their resolved epicentral location is not near to the major faults in the region (Fig. 2a), it is *c.* 15 km northeast of the Princes' Islands fault and *c.* 25 northeast of the southern Çinarcik fault. Damage from the earthquake was localized on the southern coast of the Sea of Marmara, leading Nalbant *et al.* (1998) to attribute the earthquake to rupture of the southern Çinarcik fault, and the north-dipping nodal plane of Taymaz *et al.* (1991). Parsons *et al.* (2000) have attributed the event to rupture of the Princes' Island fault, presumably based on its closer proximity to the epicentre location, and the southwest-dipping nodal plane of Taymaz *et al.* (1991). The combination of epicentral location, nodal plane solutions and damage reports does not clearly define which fault ruptured in 1963. Therefore, we test and evaluate separate scenarios of rupture associated with the 1963 event on both the Princes' Islands and the southern Çinarcik faults.

## Possible locations for the western termination of the 1999 Izmit rupture

### *Previous slip inversions*

Since most of the Izmit surface rupture west of the epicentre occurred underwater within the Bay of Izmit, we rely upon a variety of geophysical data sets in constraining the rupture location. These include GPS and InSAR geodetic data, seismic waveform data, and aftershock locations. Inverting for Izmit earthquake fault slip, Reilinger *et al.* (2000) show that GPS geodetic measurements do not account for slip in excess of 0.6 m more than 10 to 15 km west of the Hersek Delta along the Yalova segment of the Izmit rupture. Synthetic aperture radar interferometry (InSAR) indicates that the best-fitting length of rupture beyond the Hersek Delta is 12 km, with good fits to the interferograms for fault lengths between 9 and 18 km (Wright *et al.* 2001*b*). At fault lengths beyond 12 km west of the Hersek Delta, the increase in misfit is reduced, allowing for the possibility that rupture extended further than 12 or even 18 km west of the Hersek Delta. However, the small increases in misfit may be attributed to the lack of InSAR data coverage west of the Hersek Delta, reduced data coverage as the Gulf of Izmit widens, and a lack of coherence on the southern shore of the Gulf of Izmit in the interferograms (Wright *et al.* 2001*b*).

Seismic waveform data reveals different interpretations of the western rupture termination depending on the data set and processing method. Yagi and Kikuchi (2000) use near-field strong motion data and teleseismic body wave data to invert for the slip distribution, and show that subsurface slip extended no further than 25 km west of the epicentre near Gölcük (15 km east of the Hersek Delta). Gülen *et al.* (2002) invert teleseismic body waves from 25 seismic stations, and when they include the latter phases of the seismograms (60–100s) in their inversion they find a rupture sub-event west of the Hersek delta corresponding to 1.3 m of slip approximately 10 km west of the Hersek Delta. They propose that this sub-event corresponds to rupture of the Yalova segment and is responsible for the lineation of surface cracking nearby onshore, and the alignment of aftershocks extending along the coast and into the Marmara Sea. Aydin and Kalafat (2002) argued for a similar southwest extension of the rupture based on the field observation of earthquake-related faults and increased damage in the Yalova region. Based primarily on a lineation of aftershocks, Gülen *et al.* (2002) also suggest the possibility that the Izmit rupture propagated west along a more northerly fault segment extending from the Hersek Delta to the southern portion of the Princes' Islands fault. However, this rupture scenario is hard to constrain because it is well within the Sea of Marmara, placing it further from coastal sites and geodetic measurements.

Based on the ground motion from five near-fault accelerometers, Bouchon *et al.* (2002) compute fault slip that sharply decreases from a local surface slip maximum of 2 m near the Hersek Delta on a fault that trends east–west into the Marmara Sea. Also using near-fault strong motion waveforms, Sekiguchi and Iwata (2002) suggest that slip extended west of the Hersek Delta for at least 5 km. Several authors use joint inversion of different types of geodetic data (Feigl *et al.* 2002), or combined geodetic and seismic data (Delouis *et al.* 2002) to constrain the western rupture termination. Similar to the Bouchon *et al.* (2002) results, the solutions of both Delouis *et al.* (2002) and Feigl *et al.* (2002) include less than a metre of slip about 50 km west of the epicentre that decays to zero about 15 km west of the Hersek Delta.

In summary, the various slip inversion studies suggest that the western termination of the 1999 Izmit earthquake rupture is located 10–20 km west of the Hersek Delta (50–60 km west of the epicentre), although the latitudinal position is not well constrained because the inversion models presuppose a fault trend.

### *Aftershock location studies*

The distribution of aftershocks following the Izmit earthquake extend approximately 75 km west of the epicentre (Karabulut *et al.* 2002; Özalaybey *et al.* 2002) and are clustered in three general regions within and west of the Bay of Izmit (Fig. 2a). One cluster is a linear trend of aftershocks that extend about 35 km west of Hersek with an uninterrupted east–west trend parallel to the axis of Izmit Bay. The vast majority of the hypocentres occurred at 5–17 km depth (Karabulut *et al.* 2002; Özalaybey *et al.* 2002) and have predominantly strike-slip focal mechanisms (Karabulut *et al.* 2002).

Further west, the second cluster branches to the NW and extends to within 10 km south of the Princes Islands. Coseismic slip in this region is not confirmed or ruled out by the geodetic or strong motion inversions and may be suggested by teleseismic body wave inversion (Gülen *et al.* 2002). Focal mechanisms of three $M_L \geq 4.0$ events that occurred along this lineation show right-lateral strike-slip mechanisms along WNW-trending fault planes (Özalaybey *et al.* 2002), while many smaller events show normal faulting mechanisms (Karabulut *et al.* 2002).

In contrast, the third cluster of aftershocks, mostly onshore and near the city of Yalova, show 45°–60° north-dipping normal faulting mechanisms (Özalaybey *et al.* 2002) that cluster along a N50°-dipping zone of seismicity. The number of aftershocks within the Yalova cluster significantly increases two days after the mainshock. This delayed onset, together with the dip-slip focal mechanisms, indicate that this cluster represents triggered seismicity and is not likely to be part of the mainshock rupture; however, the localized cluster suggests a local stress concentration that could be related to nearby termination of the Izmit rupture.

Pinar *et al.* (2001) concluded that the Izmit rupture terminated east of 29.6°E. They argue that this rupture termination location, as opposed to one further west at 29.1°E, places a greater number of aftershocks within regions of increased Coulomb stresses. Several observations complicate this approach. First, the vertical faults with an optimally oriented strike direction along which Coulomb stress were calculated in their model is less accurate in view of the variation of the focal mechanism nodal planes in this region. Second, in addition to regions beyond the lateral fault tips, aftershocks can be triggered along the upper and lower tiplines of ruptures. In map view, the aftershocks along the upper or lower tiplines would plot along the main trace of the rupture, resulting in a rather continuous lineation of aftershocks along the fault and well past its tips. This makes it difficult to clearly discern where within this linear cluster the lateral terminations of the rupture are located. Indeed, there are aftershocks all along the rupture trace for both locations of western termination that Pinar *et al.* (2001) evaluate, suggesting that aftershocks are a poor constraint for determining the lateral limits of this rupture.

Review of the geophysical data and other investigations suggests four possible western termination locations for the Izmit rupture (Fig. 2b): (1) Rupture continuing 15 km WSW of the Hersek Delta along the southern strand of the NNAF within the Bay of Izmit, as suggested by slip inversions from seismic and geodetic data. (2) Rupture continuing 20 km west of the Hersek Delta along the northern strand of the NNAF towards the Princes' Islands fault as suggested by aftershocks and slip inversions by Gülen *et al.* (2002). (3) Rupture continuing 30 km WSW of the Hersek Delta along the southern strand of the NNAF as suggested by aftershock clustering and strong shaking in Çinarcik and Yalova (Özalaybey *et al.* 2002). (4) Rupture terminating just east of the Hersek Delta as suggested by Pinar *et al.* (2001). We note that the available data cannot rule out the possibility that several of these faults strands ruptured simultaneously during the earthquake; however, we choose to investigate single-strand rupture geometries which should produce the end-member magnitudes of possible stress changes on the eastern Marmara faults.

## Investigated Izmit earthquake rupture scenarios

To evaluate the stress changes that each of these different rupture scenarios would produce on faults in the eastern Sea of Marmara, we invert InSAR (Wright *et al.* 2001*a*, *b*) and GPS (Reilinger *et al.* 2000) ground surface displacement data to solve for the Izmit earthquake slip distributions for each of the four different

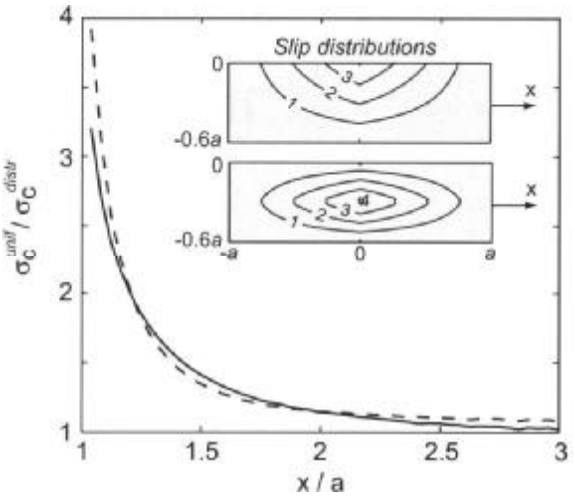


**Fig. 3.** Comparison of stress change magnitudes as a function of distance from the fault edge for uniform versus distributed slip. Uniform slip produces Coulomb stress changes that are several times greater than stress changes from distributions with either maximum slip at the surface (solid) or at depth (dashed). Faults (grey shaded) with slip distributions are shown in inset with the average slip in both cases (1 m) matching the case of uniform slip.

fault configurations. Solving for the distributed slip, rather than simply applying a uniform slip magnitude to an entire fault surface, is important because faults with uniform slip produce stress changes up to several times greater than that of tapered slip within a half-length of the ruptured fault (Fig. 3). Using well-constrained distributed slip solutions will be particularly important for the faults in the eastern Sea of Marmara because the NNAF splits into three different strands within a half-length of the major fault segments of the Izmit rupture (Fig. 2a).

We solve for a distribution of Izmit earthquake fault slip that provides the best fit to ground surface displacements from InSAR interferometry (Wright *et al.* 2001*a*) and GPS data (Reilinger *et al.* 2000) in a least squares sense. We use an ERS-2 ascending interferogram computed from satellite passes on 13 August and 17 September 1999. The western edge of the interferogram is located about 25 km west of the Hersek Delta. The computed fault slip values will therefore be less well constrained, approaching or exceeding the western edge of the interferogram. The GPS data were acquired within the first two months of the earthquake and were recorded at 51 sites (Reilinger *et al.* 2000).

The fault segments used in our inversion are rectangular and we fix their geometry (Fig. 4, Table 2). Surface displacements for each slip solution are calculated, with each fault patch modelled as a rectangular dislocation in a homogeneous, isotropic elastic medium. We assume pure right-lateral fault slip on the fault segments and determine its distribution using a standard linear least squares inversion procedure (e.g., Jónsson *et al.* 2002; Wright *et al.* 2004). We use a smoothing parameter, based on the finite difference approximation to the Laplacian operator, to constrain the variation in slip between each slip patch and its neighbours. The relative weight of the smoothing is chosen by plotting the slip roughness against data misfit: the value selected gives the smoothest solution that still has a satisfactory fit to the data. A positivity constraint is also applied to ensure that slip within each entire fault segment is right-lateral. A zero-slip boundary condition is prescribed along the lateral and bottom edges of the fault. Following the method of Wright *et al.* (2004), we weighted the GPS and InSAR data using weight matrices, **W**, the Cholesky decompositions of the respective data variance-covariance matrices, $\Sigma$ ($\mathbf{W}^T\mathbf{W} = \Sigma^{-1}$). Because we include off-diagonal terms for the variance-covariance matrix of the InSAR data, to account for the high degree of spatial correlation, the InSAR data do not swamp the GPS data. The final slip solution is that which provides the minimum misfit between the observed geodetic surface displacements and those computed using the model slip solution (Wright *et al.* 2004).

The misfits between the modelled and observed InSAR and GPS surface displacements indicate that the scenario with no faulting west of the Hersek Delta (scenario 4) cannot reproduce observed displacements as well as cases with slip extending further west (Fig. 5, Table 3), so this scenario is not considered for use in the stress change calculations. The multi-segment slip distributions for the three cases where slip extends west of the Hersek Delta, projected onto a single fault only for display, are shown in Figure 4. For the most part, they are very similar, with a slip maximum of 6.7–6.8 m located west of the epicentre, along the eastern portion of the Bay of Izmit. Slip decreases to less than 3 m within 10 km of the east Hersek Delta and just west of Lake Sapanca. These three cases, however, all fit the data equally well. This is likely to be due to the proximity of the western edge of the InSAR interferogram and the lack of data within the Bay of Izmit. This means that the three scenarios with rupture extending west of the Hersek Delta are equally justified based on the available InSAR and GPS data. This uncertainty motivates our modelling approach and requires

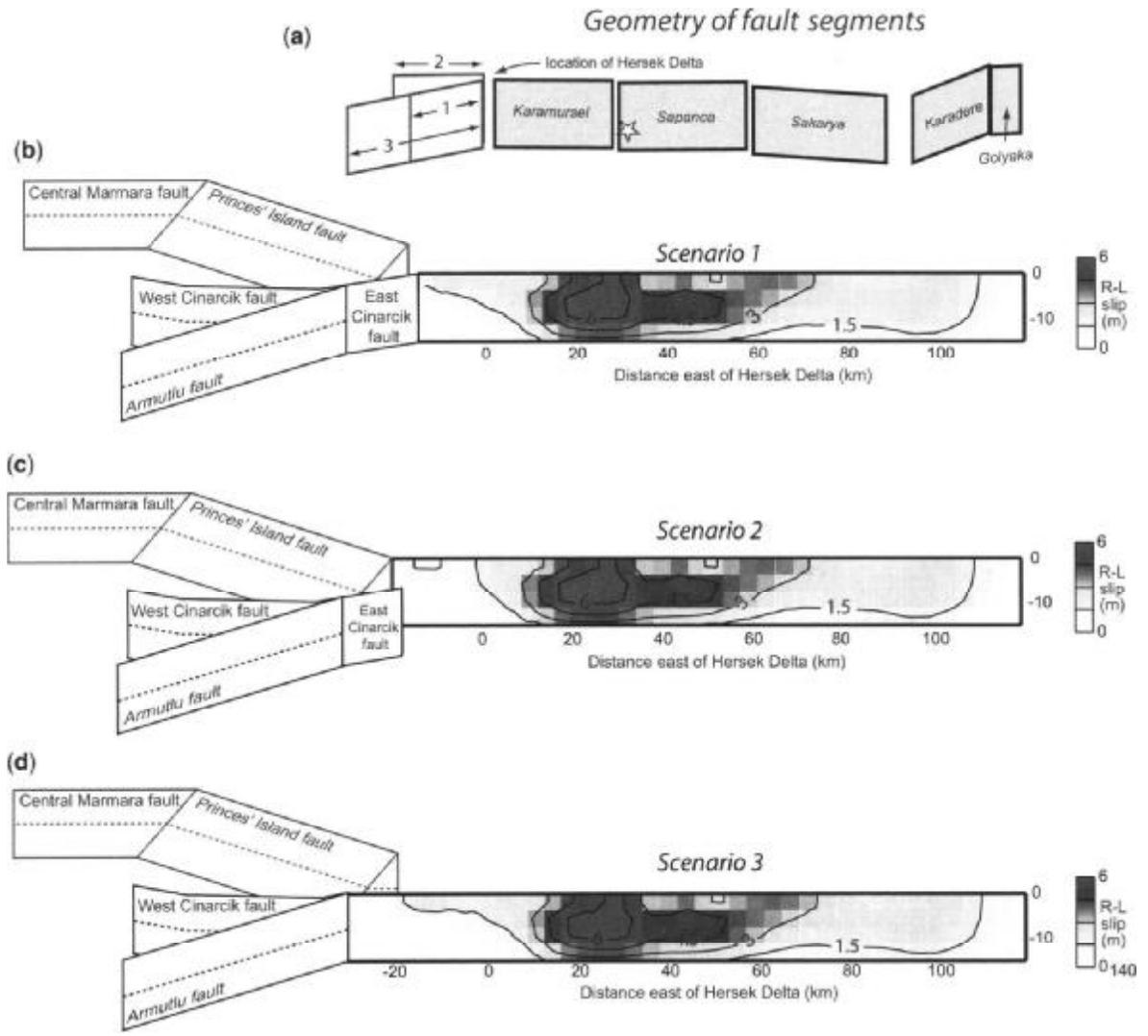


**Fig. 4.** (**a**) 3-D geometry of Izmit earthquake rupture segments used for slip inversion showing the three different western termination geometries where slip extends west of the Hersek Delta. Segment parameters are given in Table 2. The named grey segments with black outline are the same for all inversions. The star indicates the location of the Izmit earthquake hypocentre. The three different westernmost segments outlined in red and numerically labelled correspond to the segments included for inversion in scenarios 1, 2, and 3. The inversion smoothes slip across the discontinuous segment boundaries. (**b**) Computed slip distribution for scenario 1 (fault extends 15 km southwest of Hersek Delta, along the Bay of Izmit coast). Slip values are projected onto a planar surface for presentation only. (**c**) Slip distribution for scenario 2 (fault extends 20 km west towards Princes' Islands fault). (**d**) Slip distribution for scenario 3 (fault extends 30 km southwest along Yalova/Çinarcik coast to intersect Armutlu fault).

us to test these three different Izmit rupture configurations.

## Stress changes after 1999

To gain an accurate measure of the Coulomb stress change in the eastern Marmara Sea for each scenario, we resolve the shear and normal stress on the fault surfaces at a depth of 7.5 km. This depth is half of the approximate 15 km thickness of the seismogenic crust based on the lower depth of aftershocks following the 1999 Izmit earthquake (Karabulut *et al.* 2002; Özalaybey *et al.* 2002). The surface traces of the model faults (Fig. 2b) are those of Armijo *et al.* (2002) and the dips and dip directions are based on seismic reflection data (Parke *et al.* 1999; Okay *et al.* 2000; Le Pichon *et al.* 2001) and the modelling analysis of different proposed Marmara Sea fault geometries (Muller & Aydin 2005).

The Coulomb stress change is defined as

$$\sigma_c = |\Delta\tau| + \mu'\Delta\sigma$$

**Table 2.** *Fault segment parameters*

| Izmit rupture segment | Strike (°) | Dip (°) | Rake (°) | Length (km) | Depth (km) | Marmara Sea fault segment | Strike (°) | Dip (°) |
|---|---|---|---|---|---|---|---|---|
| *Scenario 1* | | | | | | | | |
| Westernmost segment | 77 | 90 | 180 | 17.0 | 15 | West Izmit | 270 | 90 |
| *Scenario 2* | | | | | | Princes' Islands | 116 | 70 |
| Westernmost segment | 88 | 90 | 180 | 21.7 | 15 | East Çinarcik | 260 | 80 |
| *Scenario 3* | | | | | | West Çinarcik | 284 | 80 |
| Westernmost segment | 77 | 90 | 180 | 33.1 | 15 | Armutlu | 245 | 70 |
| Karamursel | 89 | 90 | 180 | 28.4 | 15 | | | |
| Sapanca | 88 | 90 | 180 | 30.6 | 15 | | | |
| Sakarya | 92 | 90 | 180 | 32.0 | 15 | | | |
| Karadere | 64 | 90 | 180 | 19.8 | 15 | | | |
| Golyaka | 84 | 90 | 180 | 7.2 | 15 | | | |

where $\Delta\tau$ is the change in the shear traction on the fault surface due to a neighbouring earthquake, $\Delta\sigma$ is the change in the normal traction (compression is negative), and $\mu'$ is the effective coefficient of friction. It is necessary to keep track of the sign of $\tau$ (traction inducing right-lateral slip being positive) because shear tractions of different sign, but equal magnitude, on adjacent areas of a fault surface could produce a uniform positive Coulomb stress change, while this situation would not physically lead to failure in any given direction. Such a scenario is unlikely to occur, but should be considered in the eastern Marmara Sea region where perturbations from dip-slip and strike-slip earthquakes in close proximity are modelled.

The effective coefficient of friction $\mu'$ is used to relate pore pressure to the normal stress acting on the fault surface and can be defined as $\mu' = \mu(1 - B)$ where Skempton's coefficient $B$

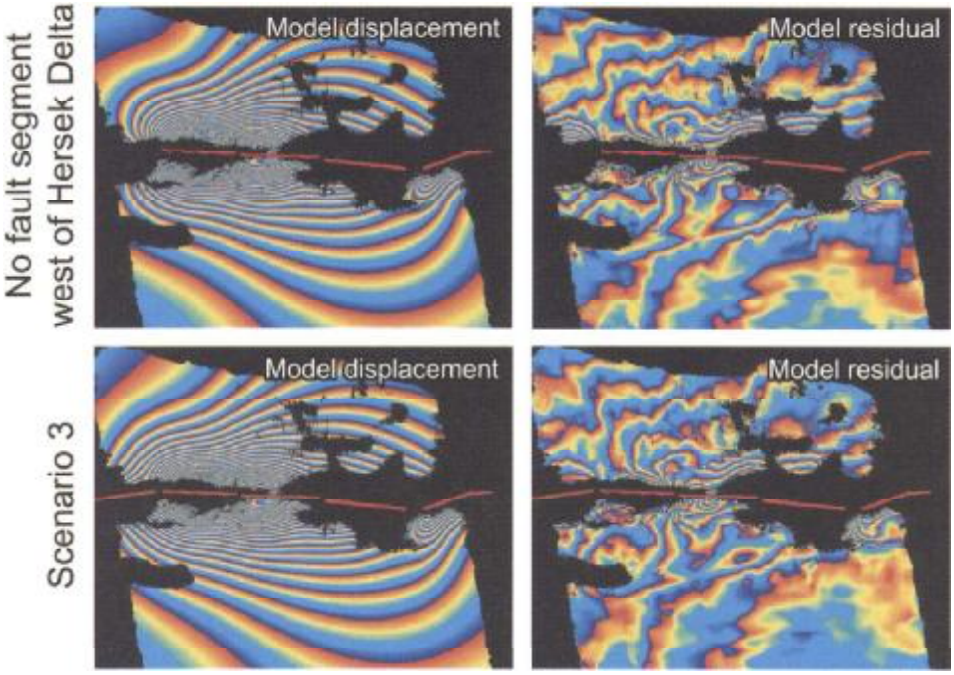


**Fig. 5.** Computed satellite line-of-sight surface displacement interferograms (left column) and residual interferograms (right column) for endmember Izmit fault geometries. Residuals are calculated by subtracting the model interferogram from the actual interferogram. In upper panels, there is no Izmit rupture segment west of the Hersek Delta. In the lower panels, the fault geometry corresponds to scenario 3 in Fig. 4. Note the concentration of fringes indicating large residuals in the western end of the Izmit rupture when there is no fault segment west of the Hersek Delta (upper right panel).

**Table 3.** *Root-mean-squared misfits between modelled and observed InSAR and GPS data*

| Scenario | Western termination of Izmit rupture | InSAR residual (cm) | GPS residual (cm) |
|---|---|---|---|
| 1 | 15 km west of the Hersek Delta, along southern coast of Bay of Izmit | 3.29 | 4.59 |
| 2 | 20 km west of the Hersek Delta, at intersection with Princes' Islands fault | 3.30 | 4.50 |
| 3 | 30 km west of the Hersek Delta, along southern coast of Bay of Izmit | 3.27 | 4.60 |
| 4 | Hersek Delta | 3.45 | 4.99 |

theoretically ranges from 0 for fully drained conditions to 1 for fully saturated conditions (Harris 1998). However, $\mu'$ is not physically well-constrained because we commonly do not know the appropriate value of $B$ to employ for the fault rocks in the seismogenic zone and because pore pressures can change with time (Scholz 2002). Studies of stress changes produced by earthquakes suggest that $\mu'$ can range from 0 to 0.75, with values of $\mu' = 0.4–0.5$ appropriate in earthquake-triggering investigations (e.g., Harris *et al.* 1995; Harris & Simpson 1996; Stein *et al.* 1997). We set $\mu' = 0.4$, for direct comparison with other Coulomb stress change studies along the NAF (e.g., Stein *et al.* 1997; Hubert-Ferrari *et al.* 2000; Pinar *et al.* 2001).

## Modelling method

We compute stress changes using Poly3D (Thomas 1993), a boundary element code that provides quasi-static stress changes at any point in an isotropic and homogeneous linear elastic half-space due to slip on dislocation surfaces. The boundary element method is computationally efficient for dislocation modelling because only the dislocations, and not the surrounding body, require discretization. The dislocation, or fault, surfaces embedded in the model half-space consist of multiple planar, triangular elements. Each triangular element is composed of six superposed angular dislocations (Comninou & Dunders 1975) arranged in such a way that a discontinuity in displacement exists only in a desired triangular region (Jeyakumaran *et al.* 1992). The full derivation of the solution for the stress at any point within the elastic half-space due to prescribed displacement discontinuity boundary conditions on one, or many, triangular elements is given in Thomas (1993, appendix A). The displacement discontinuity is constant on each element, but multiple elements can be used to model an arbitrary number of mechanically interacting fractures or faults with non-uniform slip distributions (Crouch & Starfield 1983). Unlike rectangular fault elements used in many dislocation models (e.g., those based on the solution of Okada 1985), the triangular fault elements in Poly3D allow for three-dimensional curved fault surfaces and tiplines without introducing artificial gaps and overlaps among elements (Resor 2004). In our models, the average element size is approximately 7 $km^2$. The stresses calculated within our model are static in that time-dependent, or dynamic, stresses that are associated with the propagation of seismic waves during earthquake rupture are not considered.

The slip distributions computed from the InSAR and GPS inversions (Fig. 4) are applied as the displacement discontinuity boundary conditions on the Izmit fault segments in our six test cases. We test permutations of the three different western terminations of the 1999 Izmit rupture and the two possible locations of the 1963 Yalova earthquake, for a total of six different eastern Marmara rupture scenarios (Fig. 6a–f, col. 1).

In addition to the 1963 Yalova and 1999 Izmit earthquakes, we include in our models all $M_s \geq 6.4$ earthquakes in the Sea of Marmara region since 1900 (Fig. 1; Table 4). Besides the 1963 Yalova and 1999 Izmit events, these earthquakes contribute stress changes of the order of 0.01–0.02 MPa to the faults in the eastern region of the Sea of Marmara, which represent *c.* 5–10% of the total stress changes when the 1963 Yalova and 1999 Izmit earthquakes are included in the model. For all earthquakes besides the 1999 Izmit event, a constant displacement discontinuity is applied on the entire fault surface, with slip magnitude rake and direction given in Table 4.

Stress increases associated with secular plate motion, commonly incorporated in stress change calculations, are hard to accurately constrain in the Marmara Sea region. Due to the lack of GPS survey measurements close to the fault strands, it is unclear how the multiple upper crustal fault strands in this region connect with deep plate motion beneath the locked seismogenic portion of the lithosphere. Studies suggest different locking depths and

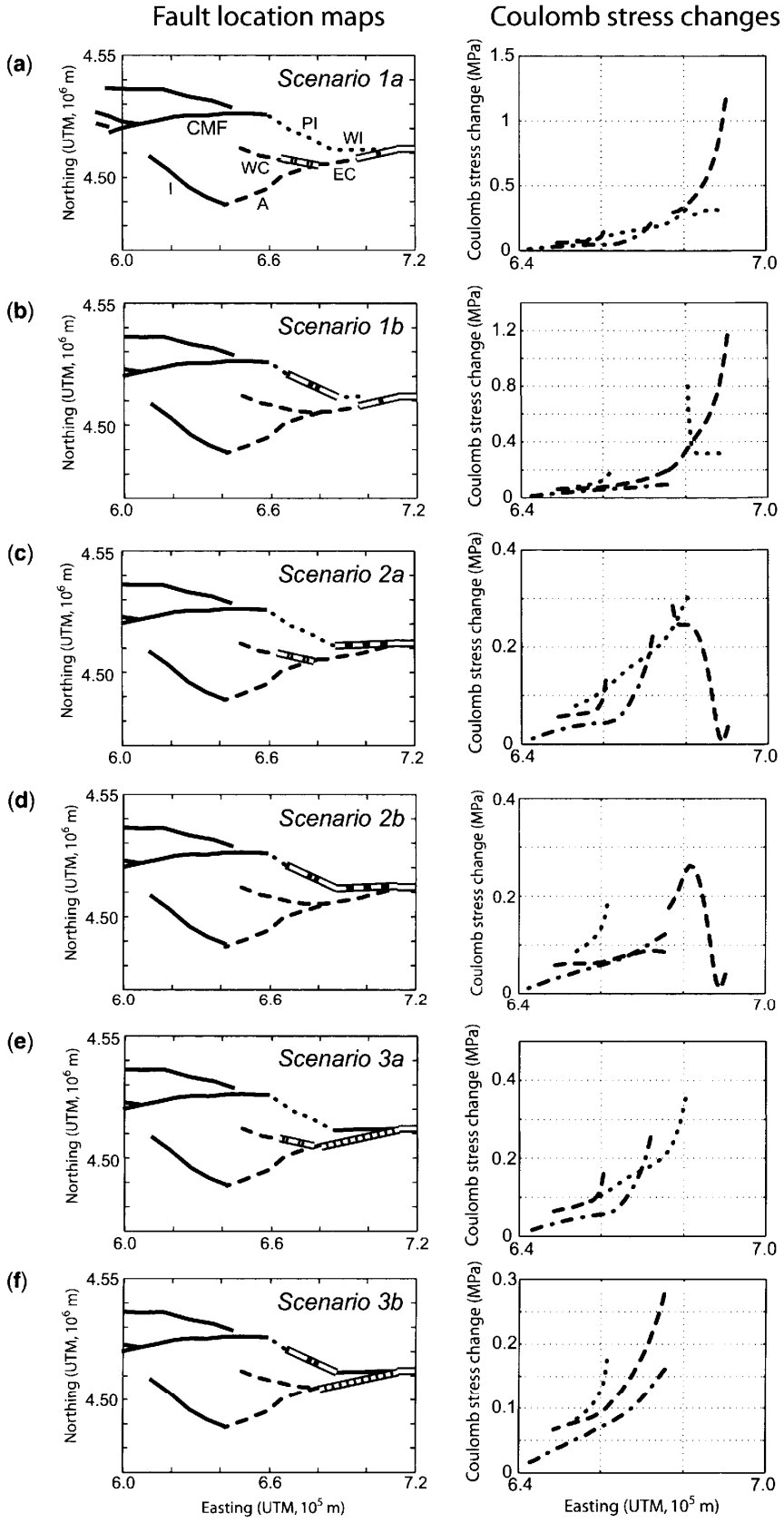


**Fig. 6.** Rupture scenarios (left column) and Coulomb stress changes (right column) for the eastern Marmara Sea faults. WI: West Izmit fault (dotted); PI: Princes' Islands fault (dotted); EC: East Çinarcik fault (dashed); WC: West Çinarcik fault (dashed); A: Armutlu fault (dot-dashed); I: Imrali fault (solid); CMF: Central Marmara fault (solid). Western segment of Izmit earthquake rupture is shown as thick dashed white line corresponding to Fig. 2b. 1963 earthquake rupture is shown as thick dot-dashed white line corresponding to Fig. 2b.

**Table 4.** *Earthquakes since 1900 included in the stress change model*

| Date | $M_s$ | $M_o$ ($10^{19}$ Nm) | Area of model fault[6] ($10^8$ m$^2$) | Dip of model fault (°) | Slip[7] (m) | Rake on model fault[8] (°) |
|---|---|---|---|---|---|---|
| Jan. 19, 1912 | 7.4 | 12.6[1] | 11.7 | 90 | 3.60 | 180 |
| Feb. 4, 1935 | 6.4 | 0.4[1] | 3.4 | 60N | 0.39 | −90 |
| June 20, 1943 | 6.4 | 0.4[1] | 2.4 | 90 | 0.54 | 180 |
| Feb. 1, 1944 | 7.3 | 8.9[1] | 19.4 | 90 | 1.53 | 180 |
| March 18, 1953 | 7.2 | 6.3[1] | 9.0 | 90 | 2.35 | 180 |
| May 26, 1957 | 7.0 | 3.2[1] | 3.0 | 90 | 3.57 | 180 |
| Sept. 18, 1963 | 6.4 | 0.1[2] | 3.0[4] | 70S[4] | 0.10[4] | −90 |
| | | | 2.1[5] | 80N[5] | 0.15[5] | −90 |
| Oct. 6, 1964 | 6.9 | 0.4[2] | 7.8 | 60N | 0.18 | −90 |
| July 22, 1967 | 7.1 | 11.0[3] | 1.2 | 90 | 2.96 | 180 |
| Nov. 12, 1999 | 7.2 | 6.3[1] | 7.8 | 60N | 2.69 | 180 |

[1]Scalar seismic moment computed by assuming $M_w = M_s$ and using the relationship $M_o = 10^{(1.5*M_w+9)}$ (Shearer 1999).
[2]Scalar seismic moment from Taymaz *et al.* (1991).
[3]Scalar seismic moment from Pinar *et al.* (1996).
[4]Rupture on the Princes' Islands fault (e.g., Parsons *et al.* 2000).
[5]Rupture on the Çinarcik fault (e.g., Nalbant *et al.* 1998).
[6]Faults have lengths shown in Fig. 1, dips in column 5, and extend to 15 km depth.
[7]Average slip, $u = M_o/(\mu A)$, where $\mu = 30$ GPa, and A is fault area (Shearer 1999).
[8]Rake assumed to be pure dip-slip or strike-slip.

plate boundary locations in the Marmara Sea (Hubert-Ferrari *et al.* 2000; Meade *et al.* 2002). In addition, due to uncertainties in the rupture location, it is unclear if the 1719, 1754, or 1766 event was the last major earthquake in this region (Hubert-Ferrari *et al.* 2000; Parsons *et al.* 2000). Regardless of this, based on these dates and the slip rate of the NNAF it is clear that the eastern Marmara Sea is in the late stages of an interseismic cycle and the secular stress accumulation should be large. Using the most conservative penultimate earthquake date of 1766 and estimates of secular stress loading in these faults for a conservative locking depth of 15 km, the Princes' Islands and Çinarcik faults will have accumulated at least 3–4 MPa of tectonic stress (Muller & Aydin 2005). Since this accumulated stress is an order of magnitude greater than the stress changes due to nearby earthquakes, the location, orientation, and locking depth of deep plate boundary slip are important factors in determining the absolute stress conditions in the eastern Marmara faults. However, we are focusing solely on the stress changes due to recent earthquakes because (1) the true location of the plate boundary structure beneath the eastern Marmara Sea, and hence the amount of stress transfers onto the shallow eastern Marmara faults, is not precisely resolvable, and (2) the additional stress perturbation from preceding earthquakes is commonly the trigger for subsequent earthquakes along the North Anatolian fault (e.g., Stein *et al.* 1997).

## Stress changes

The results show that, in all cases, all of the Marmara faults receive increases in Coulomb stress due to the combined effects of all earthquakes since 1999. However, the fault segment receiving the greatest stress change is not the same for each scenario (Fig. 6, col. 2, Table 5). In four of the six scenarios, the Çinarcik fault receives the greatest stress change (Figs. 6a, b, d, f). In one scenario, the Çinarcik and Princes' Islands faults receive approximately equal stress increases (Fig. 6c), and in another the Princes' Islands fault receives the greatest increase (Fig. 6e). In all tests, the maximum stress increase on the Armutlu fault is less than those on the Çinarcik and Princes' Islands faults, but of the same order of magnitude. The direction of the maximum shear stress vector along the faults, in all cases, never deviates by more than $\pm 20°$ from pure right-lateral shear.

### *Scenario 1a and 1b*

If the Izmit earthquake ruptured 15 km SW of the Hersek Delta along the southern coast of the Bay of Izmit, and the 1963 earthquake ruptured along the Çinarcik fault (scenario 1a, Fig. 6a), the East Çinarcik segment receives the greatest stress change, with a maximum of over 1 MPa. This magnitude of Coulomb stress change is greater than the average increase of 0.4 MPa calculated at the epicentres of large earthquakes triggered during the 1939–1992 earthquake sequence along the NAF (Stein

**Table 5.** *Maximum and average Coulomb stress changes on eastern Marmara Sea faults*

| Scenario | 1a | | 1b | | 2a | | 2b | | 3a | | 3b |
|---|---|---|---|---|---|---|---|---|---|---|---|
| Izmit rupture western termination | 15 km west of Hersek Delta, along coast | | 15 km west of Hersek Delta, along coast | | 20 km west of Hersek Delta, to Princes' Islands fault | | 20 km west of Hersek Delta, to Princes' Islands fault | | 30 km west of Hersek Delta, along coast | | 30 m west of Hersek Delta, along coast |
| Fault ruptured in 1963 event | Çinarcik | | Princes' Islands | | Çinarcik | | Princes' Islands | | Çinarcik | | Princes' Islands |
| | Coulomb stress change (MPa) | | | | | | | | | | |
| Fault segment | Max. | Av. | Max. | Av. | Max. | Av. | Max. | Av. | Max. | Av. | Max. | Av. |
| West Izmit | 0.32 | 0.29 | 0.81 | 0.38 | – | – | – | – | – | – | – | – |
| Princes' Islands | 0.32 | 0.16 | 0.17 | 0.11 | 0.30 | 0.16 | 0.18 | 0.11 | 0.35 | 0.16 | 0.18 | 0.11 |
| East Çinarcik | 1.16 | 0.54 | 1.17 | 0.50 | 0.29 | 0.17 | 0.26 | 0.16 | – | – | – | – |
| West Çinarcik | 0.14 | 0.07 | 0.19 | 0.10 | 0.13 | 0.07 | 0.09 | 0.07 | 0.16 | 0.08 | 0.28 | 0.13 |
| Amutlu | 0.21 | 0.06 | 0.09 | 0.06 | 0.22 | 0.06 | 0.12 | 0.06 | 0.25 | 0.07 | 0.16 | 0.07 |

*et al.* 1997). The next largest average increases occur on the West Izmit and Princes' Islands fault segments. Based on these results, it is difficult to assess which future rupture scenario is more likely due solely to stress changes from previous earthquakes. To produce an earthquake rupture of at least 40 km, westward propagating rupture on the East Çinarcik fault would have to either propagate through the portion of the fault assumed to have ruptured in 1963, or it would have to propagate onto the Armutlu fault. Therefore, throughgoing rupture along the West Izmit and Princes' Islands faults or initial slip on the East Çinarcik segment that branches onto the Armutlu fault may be more plausible rupture scenarios than rupture west along the Çinarcik fault.

If instead the 1963 earthquake occurred on the Princes' Islands fault (scenario 1b, Fig. 6b), the East Çinarcik fault receives the greatest stress change. In this case, there is no impediment to throughgoing rupture on the Çinarcik fault because the fault hasn't ruptured recently, so complete rupture of the Çinarcik fault is possible. In this case, although the West Izmit fault segment has a 30% greater average stress increase than that in scenario 1a, the location of the 1963 rupture would be likely to impede throughgoing rupture along this fault segment.

### *Scenario 2a and 2b*

If the Izmit earthquake ruptured 20 km directly west of the Hersek Delta to the intersection with the Princes' Islands fault segment, and the 1963 earthquake was on the Çinarcik fault, the East Çinarcik and Princes' Islands faults receive comparable maximum and average Coulomb stress increases (scenario 2a, Fig. 6c). Following earlier arguments, while the stress changes equally advance the likelihood of rupture initiation on either segment, throughgoing rupture seems more likely on the Princes' Islands fault because, in this case, it is not assumed to have ruptured in 1963. Branching rupture onto the Armutlu fault is again plausible, but the average stress increase on the Princes' Islands fault is at least twice as large as that on the Armutlu fault.

If the 1963 earthquake ruptured the Princes' Islands fault (scenario 2b, Fig. 6d), the East Çinarcik fault again receives the greatest stress changes. The stress changes on the West Çinarcik and Armutlu faults are comparable, which suggests that rupture initiating on the East Çinarcik fault could be equally likely to propagate onto either segment.

*Scenario 3a and 3b*

If the Izmit earthquake ruptured 30 km west of the Hersek Delta along the southern coast of the Bay of Izmit, and the 1963 earthquake ruptured along the Çinarcik fault (scenario 3a, Fig. 6e), the Princes' Islands fault receives the greatest stress change, with a maximum of 0.3 MPa. Unlike what we found in this case, the alignment of the western part of the Izmit rupture with the Armutlu fault could intuitively suggest that the Armutlu fault should receive the greatest Coulomb stress changes due to the large shear stress concentrations ahead of the Izmit rupture tip. However, it must be noted that although the rupture extends 30 km west of the Hersek Delta, the amount of slip resolved in the slip inversion is less than 20 cm within several kilometres of the western edge of the Izmit rupture. This, combined with the reduced normal stresses acting on the Princes' Islands fault due to its location within the extensional deformation quadrant of the Izmit rupture, are the likely causes for the greatest Coulomb stress increases being located on the Princes' Islands fault. This results contradicts the singular prediction by Pinar *et al.* (2001) that the Yalova-Hersek fault segment received the greatest stress change after the Izmit earthquake. Following our stress change result, if the Princes' Islands fault ruptured in the 1963 earthquake (scenario 3b, Fig. 6f), thereby releasing stresses, stress changes must increase the likelihood of initiation and continued westward rupture along the Çinarcik fault.

## Future westward rupture propagation

Having analysed which of the faults in the eastern Marmara Sea have an increased likelihood of rupture for each scenario, we now focus on the potential for the initial rupture to extend further west within the Marmara Sea. We consider geometry of the faults mapped further west and calculate Coulomb stress changes produced by the scenarios of rupture in Figure 6 that most favour failure of each of the three different major eastern Marmara Sea fault segments (Princes' Islands, Çinarcik and Armutlu faults). In the future failure scenario for each eastern Marmara fault, we apply uniform slip from 0 to 15 km depth with a magnitude derived from an empirical relationship between surface rupture length and moment magnitude (Table 6) (Wells & Coppersmith 1994).

The potential rupture length of an earthquake rupture initiating on the Princes' Islands fault segment would depend on the ability of the rupture to continue onto the vertical, nearly east–west trending Central Marmara fault (Muller & Aydin 2004). Coulomb stress changes on the Central Marmara fault, calculated for either a strike-slip or normal-slip earthquake on the Princes' Islands fault (see Table 6), are greatly increased near the intersection of this fault with the Princes' Islands fault and are positive for the entire fault segment (Fig. 7a). For this hypothetical scenario, the uniform slip on the Princes' Islands fault exaggerates the magnitudes of the stress change close to the fault intersection, therefore, we consider the results to be qualitative. Nevertheless, it is clear that the relative orientations of the Princes' Islands fault and the Central Marmara fault favour throughgoing rupture from the standpoint of static stress change.

The length of rupture associated with a Çinarcik fault earthquake would strongly depend on the accuracy of the fault configuration; specifically, the connection or lack thereof between this fault and the Central Marmara fault further west (Parke *et al.* 1999; Okay *et al.* 2000; Le Pichon *et al.* 2001; Armijo *et al.* 2002). Strike-slip earthquake ruptures have not been known to jump between fault segments

**Table 6.** *Rupture parameters for the eastern Marmara faults used in potential future rupture scenarios*

| Fault | Area* ($km^2$) | $M_w^{\dagger}$ | $M_o^{\ddagger}$ (1019 Nm) | Av. slip[§] (m) | Rake (°) |
|---|---|---|---|---|---|
| Princes' Islands (SS) | 507 | 6.74[a] | 1.29 | 0.85 | 180 |
| Princes' Islands (NS) | 507 | 6.69[b] | 1.08 | 0.71 | −90 |
| Çinarcik | 1230 | 7.13[a] | 4.95 | 1.34 | 180 |
| Armutlu | 588 | 6.80[a] | 1.58 | 0.90 | 180 |

*Faults extend from surface to 15 km depth along surface traces in Fig. 7. Fault dips are given in Fig. 2b.

†[a]Calculated from empirical relationship for strike-slip earthquakes $M_w = 3.98 + 1.02^{*}\log(A)$, where $A$ is rupture area (Wells & Coppersmith 1994).

†[b]Calculated from empirical relationship for normal-slip earthquakes $M_w = 3.93 + 1.02^{*}\log(A)$ (Wells & Coppersmith 1994).

‡Scalar seismic moment, $M_o = 10^{(1.5^{*}M_w+9)}$ (Shearer 1999).

§Average fault slip, $u = M_o/(\mu A)$ (Shearer 1999).

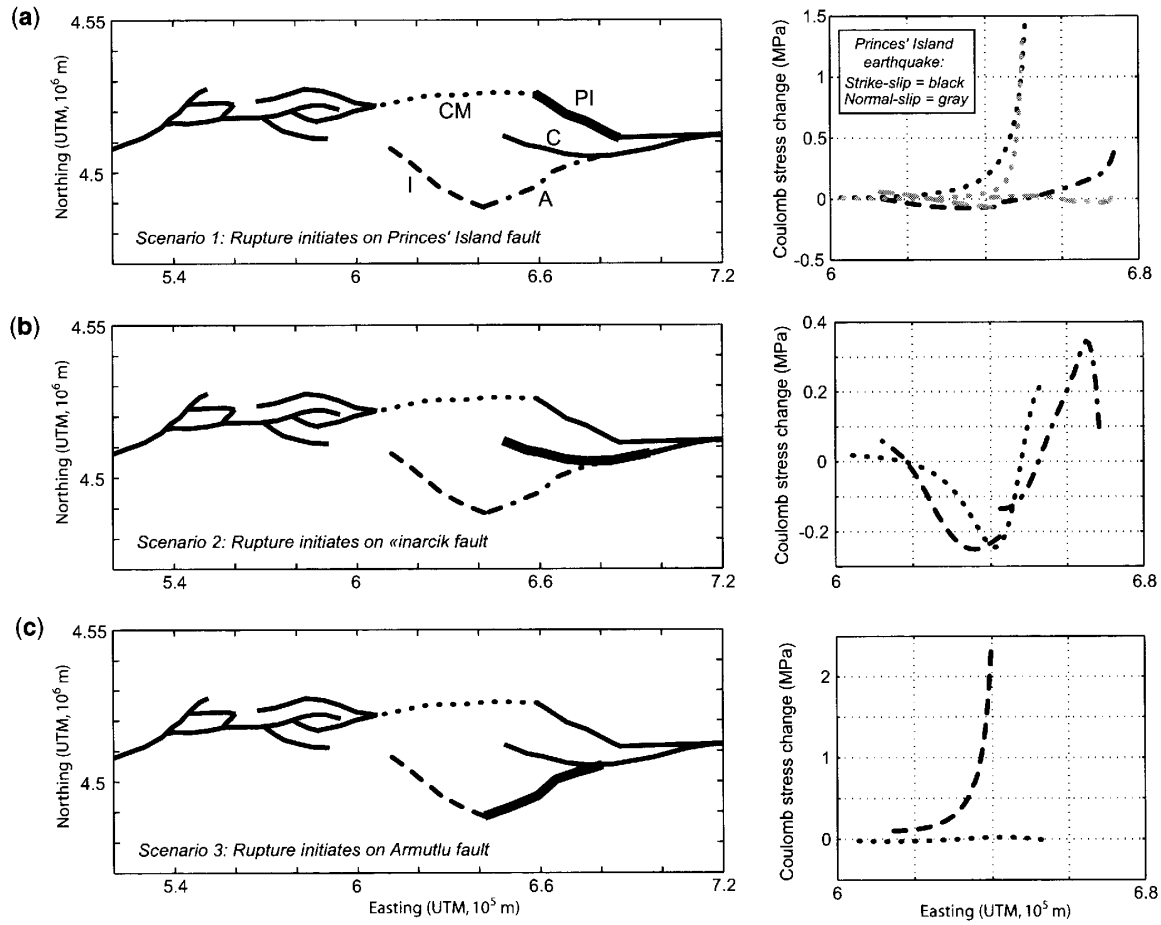


**Fig. 7.** Coulomb stress changes (right column) on faults in the central Marmara Sea due to potential initial eastern Marmara ruptures (left column). PI: Princes' Islands fault (solid); C: Çinarcik fault (solid); A: Armutlu fault (dot-dashed); I: Imrali fault (dashed); CM: Central Marmara fault (dotted). (**a**) A case in which the initial future rupture (thick black line) occurs on the Princes' Islands fault. Stress plot on right shows stress changes for either a strike-slip or dip-slip Princes' Islands earthquake. Black patterned lines show results for the strike-slip mechanism and gray patterned lines for a normal dip-slip mechanism (Table 6). (**b**) A case in which the initial future rupture occurs on the Çinarcik fault. (**c**) A case in which the initial future rupture occurs on the Armutlu fault.

separated by more than 5–10 km (Harris & Day 1993), so it would be unlikely to propagate further west. Rupture of this Çinarcik fault geometry would also decrease the Coulomb stresses acting on the Central Marmara and Imrali fault further west (Fig. 7b; Table 7), perhaps impeding or delaying the continued migration of slip through the central and western portions of the NNAF within the Marmara Sea.

In many of our stress change scenarios, the Armutlu fault receives stress changes greater than 0.2 MPa, even though in no case is it the segment with the greatest stress increase. The scenario in which Izmit rupture has propagated along the coast past Yalova (Fig. 6e) shows the greatest possibility for future failure along the Armutlu fault. Despite the large change in fault strike, the Coulomb stress is significantly increased along the Imrali fault (Fig. 7c). This is primarily because the fault is located in what would be the extensional quadrant of the Armutlu rupture segment. Transition of slip between these fault segments would produce a rupture with a combined length exceeding 80 km.

## Discussion

By considering the uncertainties in the rupture geometries of the 1963 Yalova earthquake and the western termination of the 1999 Izmit earthquake, our analysis represents a systematic investigation of the Coulomb stress changes for the most plausible scenarios involving the eastern Marmara Sea faults. Assuming that static stress changes do provide a measure of the future failure tendency for large earthquakes (e.g., King *et al.* 1994; Stein *et al.* 1997), our

**Table 7.** *Maximum and average Coulomb stress changes on Marmara Sea faults west of potential eastern Marmara Sea ruptures*

| Scenario | 1 | | 1 | | 2 | | 3 | |
|---|---|---|---|---|---|---|---|---|
| Future rupture segment | Princes' Islands fault (strike-slip offset) | | Princes' Islands fault (normal-slip offset) | | Çinarcik fault | | Armutlu fault | |
| | Coulomb stress change (MPa) | | | | | | | |
| Fault segment | Max. | Av. | Max. | Av. | Max. | Av. | Max. | Av. |
| Central Marmara | 1.42 | 0.15 | 1.28 | 0.06 | 0.21 | −0.05 | 0.02 | −0.01 |
| Armutlu | 0.38 | 0.08 | 0.02 | 0.00 | 0.34 | 0.08 | – | – |
| Imrali | 0.01 | −0.05 | 0.06 | 0.00 | 0.06 | −0.13 | 2.31 | 0.40 |

results show that predicting future rupture scenarios depends on accurately constraining the recent earthquake configurations and slip distributions (Muller *et al.* 2003). For the majority of our stress change scenarios, the Çinarcik fault receives a greater stress increase than the Princes' Islands fault segment. In an analysis of the stress changes from the Izmit earthquake alone, Pinar *et al.* (2001) reach the same conclusion. This result does not support the notion that combined failure along the Princes' Islands and Central Marmara faults is the only, or most likely future rupture scenario (e.g., Le Pichon *et al.* 1999) or the suggestion that the stress changes on the Princes' Islands and Çinarcik fault are essentially identical (e.g., Hubert-Ferrari *et al.* 2000). Our results instead show that several future scenarios are possible and that, in the case of the Çinarcik fault rupture, a future earthquake may not be as hazardous because of the limited length of such a rupture if the fault is not connected to other Marmara Sea fault strands further west.

One way to evaluate the effects of different stress change magnitudes on different faults is to compare the magnitude of the stress change with the long-term stress loading rate on each fault due to plate motion. GPS measurements (Reilinger *et al.* 1997) and elastic modelling (Flerit *et al.* 2003; Muller & Aydin 2005) of slip along the plate boundary structures in NW Turkey suggests that 30 mm/yr of right-lateral slip on the NAF east of the Marmara Sea and 24 mm/yr on the NNAF and 6 mm/yr on the central strand of the NAF (CNAF) within the Marmara Sea region are appropriate long-term slip rates. These slip rates applied to plate boundary with a locking depth of 15 km (Muller & Aydin 2005) provide approximate stressing rates of *c.* $1.5 \times 10^{-2}$ MPa/yr at 7.5 km depth on the faults of interest. The average stress changes from scenarios 1a and 1b have therefore advanced the rupture time by approximately 30 years for the East Çinarcik fault. In the other scenarios, the averages stress changes shorten the time until rupture on the Princes' Islands and West Çinarcik fault by approximately a decade relative to their long-term stressing rate. These time advances toward rupture are comparable to the 25 year average advance calculated by Stein *et al.* (1997) for the sequence of large earthquakes along the eastern and central portions of the NAF from 1939–1992; therefore, the progression of rupture into the Marmara Sea seems likely within the next several decades.

Several factors that we have not included in our model could affect the future rupture scenario in the eastern Marmara Sea. First, the location of the 1894 earthquake that caused widespread damage in the Bay of Izmit between the cities of Yalova and Sapanca is not very well constrained. From extensive review of historical damage reports, Ambraseys & Finkel (1991) suggest that the rupture occurred in the Bay of Izmit and further east. Hubert-Ferrari *et al.* (2000) support this location and suggest the event ruptured the mountainfront fault between the 1967 Mudurnu Valley earthquake and the 1999 Izmit earthquake. Parsons *et al.* (2000) suggest, however, that the rupture occurred within the Bay of Izmit and extended further west along the Armutlu fault. The latter interpretation would have relieved some of the long-term stress accumulation in the eastern Marmara Sea, whereas the earlier interpretation would have added an increased stress perturbation. The locations of damage reported in this earthquake, including Istanbul, are similar to those reported in the Izmit earthquake; therefore, it does not appear that rupture extending far along the Armutlu fault is necessary to explain the

damage pattern. We therefore hesitate to rule out the Armutlu fault as a potential candidate for future rupture based on the 1894 rupture location interpreted by Parsons *et al.* (2000).

Second, the partitioning of loading from deep slip along the plate boundary onto the shallower eastern Marmara Sea faults is not well-constrained. GPS data is able to show that slip below the locked shallow faults is several times greater along the NNAF than along the CNAF (Straub *et al.* 1997), but within the shallow NNAF strands themselves, it is unclear if certain faults are being loaded with a greater stressing rate. A shallow fault preferentially aligned above the deep plate boundary shear zone would be likely to fail more frequently than faults further from the plate boundary.

In this paper we do not investigate the stress changes resolved on the fault geometry in the western Marmara Sea. In focusing on the eastern Marmara Sea region, we are by no means implying that the next large earthquake in the Marmara Sea could not occur further west, in the region of increased Coulomb stress east of the 1912 Ganos earthquake. We recognize that the stress change scenario in this region will be affected by uncertainty in the location of the eastern termination of the Ganos earthquake. This $M_s = 7.4$ earthquake ruptured only 40 km on land before entering the Gulf of Saros to the west and the Marmara Sea to the east, suggesting that a significant portion of its rupture occurred offshore to the east or west. Armijo *et al.* (2003) suggest that a set of surface breaks extending 60 km east in to the Marmara Sea from the onshore rupture, as observed from a submarine remote-operated vehicle, may be associated with the 1912 rupture. Evaluation of earthquake-induced stress changes in the western Marmara Sea region would therefore need to consider the ambiguities in the 1912 rupture geometry as well as the complex fault geometries bounding the Tekirdag and Central Marmara basins (Fig. 2a). To this end, the methodology in this study can be used to assess each potential scenario involving the past rupture locations and fault configurations.

## Conclusions

Using a geomechanical modelling tool, we find that earthquake-induced stress changes of several tenths of an MPa load faults in the eastern Marmara Sea for each possible different location of the 1963 Yalova earthquake and western termination of the 1999 Izmit earthquake. In four of the six permutations of these past rupture locations that we test, a portion of the Çinarcik fault receives the greatest average stress change. In one case, when Izmit earthquake slip extending up to 30 km west of the Hersek Delta and the 1963 rupture occurred on the Çinarcik fault, the Princes' Islands fault receives the greatest stress increase. For the case where the Izmit rupture propagated straight west and the 1963 event was on the Çinarcik fault, the stress increases on the Princes' Islands and portions of the Çinarcik fault are comparable. The magnitudes of the stress increases due to the recent perturbations relative to the long-term tectonic stressing rate, suggest that the time before future rupture is advanced by approximately 10–30 years.

Based on the mapped fault configuration extending west from the initial failure of these faults, an earthquake along the Princes' Islands fault is likely to be the most hazardous due to its proximity to Istanbul and because its intersection geometry with the Central Marmara fault favours continuous propagation of westward rupture. This scenario would result in a cumulative rupture length of at least 80 km before the rupture intersected the Central Marmara basin. In contrast, rupture of the Çinarcik fault would not be likely to exceed 50–60 km, based on its isolated western termination and therefore, although it may represent the scenario most likely in terms of stress change, it may present slightly less hazard to Istanbul. Earthquake-induced average stress changes on the Armutlu fault, while positive, do not exceed those on the other eastern Marmara faults for any tests. If, however, rupture were to initiate on this segment, then static stress changes would favour the transition of westward rupture onto the NW-trending Imrali fault segment, thereby producing a combined rupture length exceeding 80 km.

Our results show that identification of the fault segment receiving the greatest earthquake-induced stress increase can vary depending on minor changes in local rupture geometry and slip distribution, thus highlighting the need for accurate surface mapping or active fault and earthquake rupture geometries as well as quality geodetic or seismological data for modelling earthquake slip distributions. Given that uncertainties in these parameters are unavoidable, geomechanical modelling provides a unique tool to test the significance of each case and its resulting realization.

Izmit earthquake aftershock data was generously provided by T. Taymaz and S. Özalaybey. Several figures were plotted with GMT software (Wessel & Smith 1998). The Stanford Rock Fracture Project provided partial financial

support of this work. T. Wright is funded by a Royal Society University Research Fellowship. The authors thank reviewers K. Johnson and M. Belardinelli and editor S. Buiter for constructive criticism that improved this manuscript.

## References

AMBRASEYS, N. & FINKEL, C. 1988. The Anatolian earthquake of 17 August 1668. *In*: LEE, W. H. K., MEYERS, H. & SHIMIZAKI, K. (eds) *Historical Seismograms and Earthquakes of the World*. Academic Press, 173–180.

AMBRASEYS, N. N. & FINKEL, C. F. 1991. Long-term seismicity of Istanbul and of the Marmara Sea region. *Terra Nova*, **3**, 527–539.

ARMIJO, R., MEYER, B., NAVARRO, S., KING, G. & BARKA, A. 2002. Asymmetric slip partitioning in the Sea of Marmara pull-apart: a clue to propagation processes of the North Anatolian Fault? *Terra Nova*, **14(2)**, 80–86.

ARMIJO, R. & THE MARMARASCARPS CRUISE PARTY 2003. Young earthquake breaks in the Sea of Marmara floor: a possible underwater extension of the 1912 earthquake rupture? *In*: *International Workshop on the North Anatolian, East Anatolian, and Dead Sea Fault Systems*, Middle East Technical University, 27.

AYDIN, A. & KALAFAT, D. 2002. Surface ruptures of the August 17 and November 12, 1999, Izmit and Düzce earthquakes in NW Anatolia, Turkey: their tectonic and kinematic significance and the associated damage. *Bulletin of the Seismological Society of America*, **92**, 95–106.

BOUCHON, M., TOKSÖZ, M. N., KARABULUT, H., BOUIN, M., DIETRICH, M., AKTAR, M. & EDIE, M. 2002. Space and time evolution of rupture and faulting during the 1999 Izmit earthquake. *Bulletin of the Seismological Society of America*, **92**, 256–266.

ÇAKIR, Z., BARKA, A. & EVREN, E. 2003. Coulomb stress interactions and the 1999 Marmara earthquakes. *Turkish Journal of Earth Sciences*, **12**, 91–103.

COMNINOU, M. A. & DUNDERS, J. 1975. The angular dislocation in a half-space. *Journal of Elasticity*, **5**, 203–216.

CROUCH, S. L. & STARFIELD, A. M. 1983. *Boundary Element Methods in Solid Mechanics*. Allen and Unwin, London.

DELOUIS, B., GIARDINI, D., LUNDGREN, P. & SALICHON, J. 2002. Joint inversion of InSAR, GPS, teleseismic, and strong-motion data for the spatial and temporal distribution of earthquake slip: application to the 1999 Izmit mainshock. *Bulletin of the Seismological Society of America*, **92**, 278–299.

FEIGL, K. L., SARTI, F. *ET AL.* 2002. Estimating slip distribution for the Izmit mainshock from coseismic GPS, ERS-1, RADARSAT, and SPOT measurements. *Bulletin of the Seismological Society of America*, **92**, 138–160.

FLERIT, F., ARMIJO, R., KING, G. C. P., MEYER, B. & BARKA, A. 2003. Slip partitioning in the Sea of Marmara pull-apart determined from GPS velocity vectors. *Geophysical Journal International*, **154**, 1–7.

GÜLEN, L., PINAR, A., KALAFAT, D., ÖZEL, N., HORASAN, G., YILMAZER, M. & ISIKARA, A. M. 2002. Surface fault breaks, aftershock distribution, and rupture process of the 17 August 1999 Izmit, Turkey, earthquake. *Bulletin of the Seismological Society of America*, **92**, 230–244.

HARRIS, R. A. 1998. Introduction to special section: stress triggers, stress shadows, and implications for seismic hazard. *Journal of Geophysical Research*, **103**, 24347–24358.

HARRIS, R. A. & DAY, S. M. 1993. Dynamics of fault interaction: parallel strike-slip faults. *Journal of Geophysical Research*, **98**, 4461–4472.

HARRIS, R. & SIMPSON, R. W. 1996. In the shadow of 1857 – the effect of the great Ft. Tejon earthquake on subsequent earthquakes in southern California. *Geophysical Research Letters*, **23**, 229–232.

HARRIS, R. A., SIMPSON, R. W. & REASENBERG, P. A. 1995. Influence of static stress changes on earthquake locations in southern California. *Nature*, **375**, 221–224.

HUBERT-FERRARI, A., BARKA, A. *ET AL.* 2000. Seismic hazard in the Marmara Sea region following the 17 August 1999 Izmit earthquake. *Nature*, **404 (6775)**, 269–273.

JACKSON, J. & MCKENZIE, D. P. 1988. The relationship between plate motions and seismic moment tensors, and the rates of active deformation in the Mediterranean and Middle East. *Geophysical Journal of the Royal Astronomical Society*, **93**, 45–73.

JEYAKUMARAN, M., RUDNICKI, J. W. & KEER, L. M. 1992. Modeling slip zones with triangular dislocation elements. *Bulletin of the Seismological Society of America*, **82**, 2153–2169.

JÓNSSON, S., ZEBKER, H., SEGALL, P. & AMELUNG, F. 2002. Fault slip distribution of the 1999 Mw 7.1 Hector Mine earthquake, California, estimated from satellite radar and GPS measurements, *Bulletin of the Seismological Society of America*, **92**, 1377–1389.

KARABULUT, H., BOUIN, M., BOUCHON, M., DIETRICH, M., CORNOU, C. & AKTAR, M. 2002. The seismicity in the eastern Marmara Sea after the 17 August 1999 Izmit earthquake. *Bulletin of the Seismological Society of America*, **92**, 387–393.

KING, G. C. P., STEIN, R. S. & LIN, J. 1994. Static stress changes and the triggering of earthquakes. *Bulletin of the Seismological Society of America*, **84(3)**, 935–953.

LE PICHON, X., SENGÖR, A. M. C. *ET AL.* 2001. The active Main Marmara Fault. *Earth and Planetary Science Letters*, **192**, 595–616.

LE PICHON, X., TAYMAZ, T. & SENGOR, C. 1999. The Marmara fault and the future Istanbul earthquake. *In*: KARACA, M. & URAL, D. N. (eds) *ITU-IAHS International conference on the Kocaele Earthquake 17 August 1999*, Istanbul Technical University, 41–54.

MEADE, B. J., HAGER, B. H. *ET AL.* 2002. Estimates of seismic potential in the Marmara Sea region from block models of secular deformation constrained

by global positioning system measurements. *Bulletin of the Seismological Society of America*, **92**, 208–215.

MULLER, J. & AYDIN, A. 2004. Rupture progression along discontinuous oblique fault sets: implications for the Karadere rupture segment of the 1999 Izmit earthquake, and future rupture in the Marmara Sea. *Tectonophysics*, **391**, 283–302.

MULLER, J. R. & AYDIN, A. 2005. Using mechanical modelling to constrain fault geometries proposed for the northern Marmara Sea. *Journal of Geophysical Research*, **110**, B03407, DOI: 10.1029/2004JB003226.

MULLER, J., AYDIN, A. & MAERTEN, F. 2003. Investigating the transition between the 1967 Mudurnu Valley and 1999 Izmit earthquakes along the North Anatolian fault with static stress changes. *Geophysical Journal International*, **154**, 471–482.

NALBANT, S. S., HUBERT, A. & KING, G. C. P. 1998. Stress coupling between earthquakes in northwest Turkey and the north Aegean Sea. *Journal of Geophysical Research*, **103**, 24469–24486.

OKADA, Y. 1985. Surface deformation due to shear and tensile faults in a half-space. *Bulletin of the Seismological Society of America*, **75**, 1135–1154.

OKAY, A. I., KASLILAR-OZCAN, A., IMREN, C., BOZTEPE-GUNEY, A., DEMIRBAG, E. & KUSCU, I. 2000. Active faults and evolving strike-slip basins in the Marmara Sea, Northwest Turkey; a multichannel seismic reflection study. *Tectonophysics*, **321(2)**, 189–218.

ÖZALAYBEY, S., ERGIN, M., AKTAR, M., TAPIRDAMAZ, C., BICMEN, F. & YÖRÜK, A. 2002. The 1999 Izmit earthquake sequence in Turkey: seismological and tectonic aspects. *Bulletin of the Seismological Society of America*, **92**, 376–386.

PARKE, J. R., MINSHULL, T. A. *ET AL.* 1999. Active faults in the Sea of Marmara, Western Turkey, imaged by seismic reflection profiles. *Terra Nova*, **11**, 223–227.

PARSONS, T., TODA, S., STEIN, R. S., BARKA, A. & DIETERICH, J. H. 2000. Heightened odds of large earthquakes near Istanbul: an interaction-based probability calculation. *Science*, **288(5466)**, 661–665.

PINAR, A., HONKURA, Y. & KIKUCHI, M. 1996. A rupture model for the 1967 Mudurnu Valley, Turkey earthquake and its implications for seismotectonics in the western part of the North Anatolian fault zone. *Geophysical Research Letters*, **23(1)**, 29–32.

PINAR, A., HONKURA, Y. & KUGE, K. 2001. Seismic activity triggered by the 1999 Izmit earthquake and its implications for the assessment of future seismic risk. *Geophysical Journal International*, **146**, F1–F7.

REILINGER, R. E., ERGINTAV, S. *ET AL.* 2000. Coseismic and postseismic fault slip for the 17 August 1999, M = 7.5, Izmit, Turkey earthquake. *Science*, **289**, 1519–1524.

REILINGER, R. E. & MCCLUSKY, S. C. 1997. Global positioning system measurement of the present-day crustal movements in the Arabia-Africa-Eurasia plate-collision zone. *Journal of Geophysical Research*, **102**, 9983–9999.

RESOR, P. 2004. *Deformation associated with continental normal faults.* PhD thesis, Stanford University.

SCHOLZ, C. H. 2002. *The Mechanics of Earthquakes and Faulting*. Cambridge University Press, New York.

SEKIGUCHI, H. & IWATA, T. 2002. Rupture process of the 1999 Kocaeli, Turkey, earthquake estimated from strong-motion waveforms. *Bulletin of the Seismological Society of America*, **92**, 300–311.

SHEARER, P. M. 1999. *Introduction to Seismology*. Cambridge University Press, New York.

STEIN, R. S., BARKA, A. A. & DIETERICH, J. H. 1997. Progressive failure on the North Anatolian fault since 1939 by earthquake stress triggering. *Geophysical Journal International*, **128**, 594–604.

STRAUB, C., KAHLE, H.-G. & SCHINDLER, C. 1997. GPS and geological estimates of the tectonic activity in the Marmara Sea region, NW Anatolia. *Journal of Geophysical Research*, **102(12)**, 27587–27601.

TAYMAZ, T., JACKSON, J. & MCKENZIE, D. 1991. Active tectonics of the north and central Aegean Sea. *Geophysical Journal International*, **106**, 433–490.

THOMAS, A. L. 1993. *Poly3D: a three-dimensional, polygonal element, displacement discontinuity boundary element computer program with applications to fractures, faults, and cavities in the earth's crust.* MS Thesis, Stanford University.

WELLS, D. L. & COPPERSMITH, K. J. 1994. New empirical relationships among magnitude, rupture length, rupture width, rupture area, and surface displacement. *Bulletin of the Seismological Society of America*, **84(4)**, 974–1002.

WESSEL, P. & SMITH, W. H. F. 1998. New, improved version of generic mapping tools released. *EOS*, **79(47)**, 579.

WRIGHT, T., FIELDING, E. & PARSONS, B. 2001*a*. Triggered slip: observations of the 17 August 1999 Izmit (Turkey) earthquake using radar interferometry. *Geophysical Research Letters*, **28(6)**, 1079–1082.

WRIGHT, T., PARSONS, B. & FIELDING, E. 2001*b*. The 1999 Turkish earthquakes: source parameters from InSAR and observations of triggered slip. *In*: TAYMAZ, T. (ed.) *Symposia on Seismotectonics of the North-Western Anatolia–Aegean and Recent Turkish* Earthquakes, Istanbul Technical University, 54–71.

WRIGHT, T., LU, Z. & WICKS, C. 2004. Constraining the slip distribution and fault geometry of the Mw 7.9, 3 November 2002, Denali fault earthquake with interferometric synthetic aperture radar and global positioning system data. *Bulletin of the Seismological Society of America*, **94(6B)**, S175–189.

YAGI, Y. & KIKUCHI, M. 2000. Source rupture process of the Kocaeli, Turkey, earthquake of August 17, 1999, obtained by joint inversion of near-field data and teleseismic data. *Geophysical Research Letters*, **27(13)**, 1969–1972.

# Oil reservoirs in foreland basins charged by thrustbelt source rocks: insights from numerical stress modelling and geometric balancing in the West Carpathians

MICHAL NEMČOK[1] & ANDREAS HENK[2]

[1]*Energy & Geoscience Institute, University of Utah, 423 Wakara Way, Suite 300, Salt Lake City, UT 84108, USA*

[2]*Geologisches Institut, Universität Freiburg, Albertstrasse 23b, D-79104 Freiburg, Germany (e-mail: henk@uni-freiburg.de)*

**Abstract:** The West Carpathian thrustbelt advanced northeastwards over the European Platform. Its thrust sheets comprise sediments of the Early Cretaceous rifts that evolved on a passive margin of the European Platform, the Late Cretaceous–Paleocene basins formed by rift inversion, and the Eocene-Oligocene flexural basin. Geochemical analyses established a clear link between pooled oils in the foreland and the Oligocene Menilite Formation inside the thrustbelt. In order to understand the driving forces for this oil migration scenario, finite-element models of fault-propagation and fold-bend folds are used to study the mean stress distribution in the thrust sheets and the foreland. Mean stress has a profound control on the pore fluid pressure through the relationship affected by sediment porosity, and sediment skeleton and fluid compressibilities. Modelling results suggest that only fault-propagation folds are capable of generating foreland-directed mean stress gradients as they are characterized by a large foreland area of decreased mean stress, by coupled increased/decreased mean stress areas on advancing/receding sides of the ramp tip, and an overall mean stress decrease inside the thrust sheet in the direction towards the foreland. This interpretation is in accordance with the dominant fold-and-thrust style in the Western Carpathians inferred from balanced cross-section restoration. It shows that frontal fault-propagation folding was active during the late Oligocene–Early Miocene, providing an effective tectonic driving force for hydrocarbon migration from source rocks inside the thrustbelt towards reservoirs in the foreland.

The West Carpathian thrustbelt (Fig. 1a) formed during the Tertiary by a NE- and eastward accretion and advance over the European passive margin and adjacent oceanic crust (e.g., Royden & Báldi 1988). It developed in front of the advancing Carpathian microplates (e.g., Balla 1984; Kovács *et al.* 1989; Csontos *et al.* 1992). The development was driven by subduction roll-back (e.g., Royden *et al.* 1982) with some influence from the eastward lateral mass extrusion from the Eastern Alps (Neubauer & Genser 1990; Ratschbacher *et al.* 1991). Subduction placed the remnant Carpathian Flysch Basin between the Carpathian microplates and the European Platform and floored by oceanic and thinned continental crust (e.g., Nemčok *et al.* 1998). The thrustbelt itself comprises sediments deposited in Early Cretaceous rifts evolved on the European margin (e.g., Książkiewicz 1977), in Late Cretaceous–Paleocene basins formed by an inversion of Early Cretaceous rifts (e.g., Suk *et al.* 1984 and references therein; Roca *et al.* 1995), and in Eocene–Oligocene foreland basins (Winkler & Ślączka, 1992; Roure *et al.* 1993). The European Platform underneath and in front of the thrustbelt shows Palaeozoic–Triassic sediments related to combined effects of Palaeozoic rifting, late Palaeozoic contraction and Mesozoic rifting. Jurassic sediments evolved in Mesozoic rifts, Upper Cretaceous sediments related to contraction and, finally, Lower-Middle Miocene molasse sediments of the flexural foreland basin.

Apart from fields in the thrustbelt, there are about 67 producing hydrocarbon fields in various stratigraphies of the foreland close to the thrustbelt (Karnkowski 1999). Of these, 13 contain oil, allowing oil/source rock correlations. Oils in these fields are very similar to thrustbelt oils, having a light to medium character, with densities of 810–860 kg $m^{-3}$ and paraffin content of 2.32–9.37% (Weil *et al.* 1998). Based on total

*From*: BUITER, S. J. H. & SCHREURS, G. (eds) 2006. *Analogue and Numerical Modelling of Crustal-Scale Processes*. Geological Society, London, Special Publications, **253**, 415–428.
0305-8719/06/$15.00 

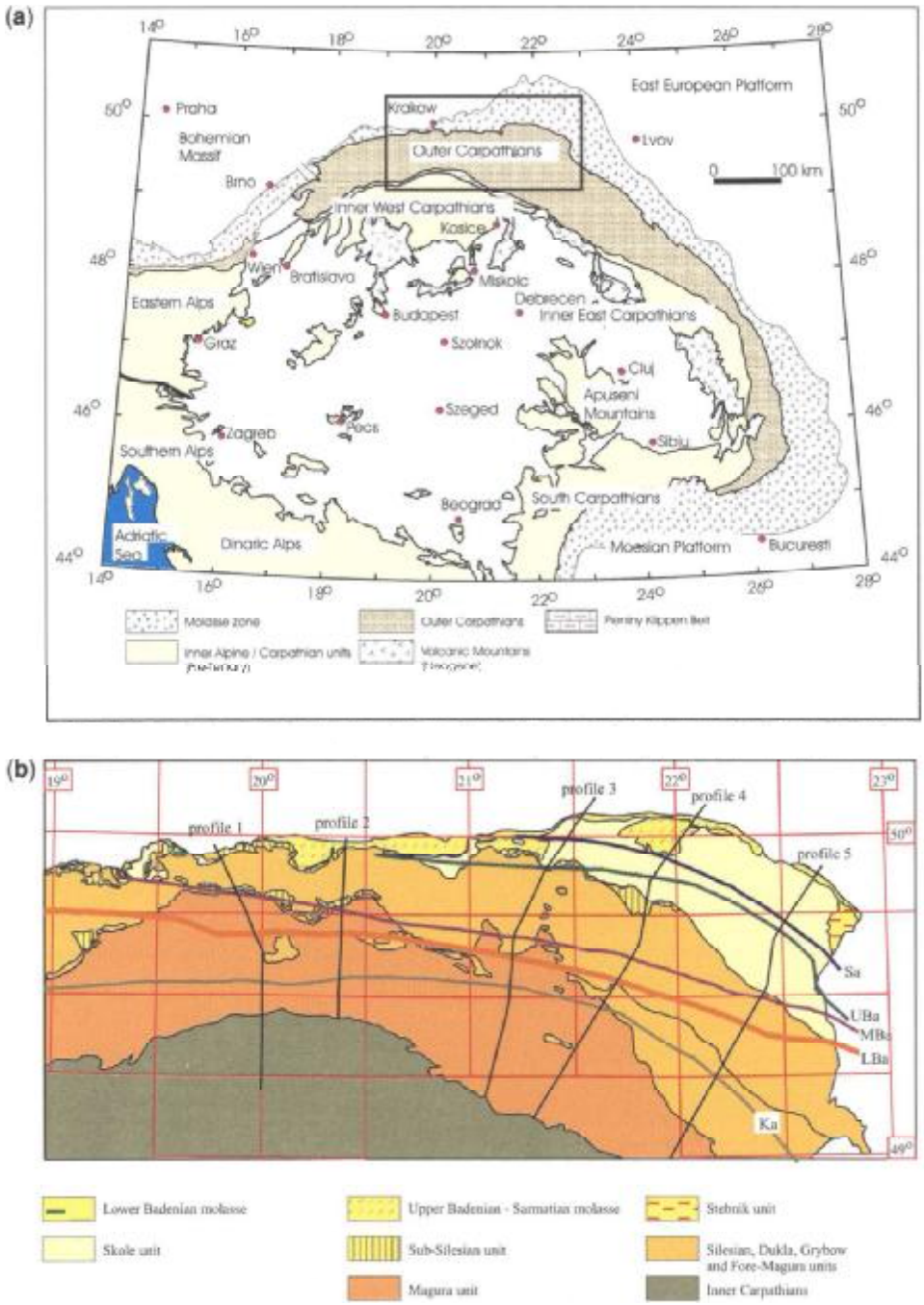


**Fig. 1.** (**a**) Map of the Carpathians with major tectonic units (modified after Krs & Roth 1977; Krs & Potfaj 1991; Krs *et al.* 1993; Koráb *et al.* 1981; Royden & Báldi 1988; Sandulescu 1988; Márton & Márton 1989; Túnyi & Kováč 1991; Patrascu *et al.* 1994). Rectangle indicates location of figure (b). (**b**) Portion of the West Carpathians with location of balanced cross-sections (after Nemčok *et al.* 1999). Coloured lines indicate southernmost extent of the various autochthonous molasse sediments below the accretionary wedge (Ka: Karpatian, Lba: Lower Badenian, Mba: Middle Badenian, UBa: Upper Badenian, Sa: Sarmatian).

organic carbon content and other source rock characteristics, initial source rock candidates for described fields in the orogenic foreland are: Lower Carboniferous and Miocene formations of the foreland, and Lower Cretaceous and Oligocene thrustbelt formations (Bessereau *et al.* 1996; Ślączka 1996; PUGzG Geopol 1998). Geochemical data and angiosperm-derived biological markers from oils of the autochthonous foreland (Grobla, Partynia-Podborze and Tarnów fields; Ten Haven *et al.* 1993; Bessereau *et al.* 1996) indicate that the source rock has Late

Cretaceous-Tertiary age (Moldowan *et al.* 1991). This excludes Lower Carboniferous sediments of the foreland and Lower Cretaceous thrustbelt sediments from being a source rock for fields in the autochthonous foreland. Miocene sediments of the foreland are not mature enough to be considered (Kotarba *et al.* 1987). A combination of the various arguments outlined above allows determination of the source rock for the foreland reservoirs. The only candidate matching all constraints is the Oligocene thrustbelt formation, the Menilite shale (Bessereau *et al.* 1996), indicating that source rock for oils in the autochthonous foreland was located inside the thrustbelt. The age of oil migration is Late Oligocene and younger (Ten Haven *et al.* 1993; Bessereau *et al.* 1996).

How was it possible for oils to migrate from the thrustbelt into its foreland? Which migration driving forces could have an effect on this special scenario? This paper tries to address these questions by studying thrustbelt structures by balancing and simulating migration controls by finite-element modelling. While several authors have focused on different numerical techniques to model fold-and-thrust structures (e.g., Sassi & Faure 1996; Salvini *et al.* 2001; Burbidge & Braun 2002; Kwon & Mitra 2004), we attempt a coupled geometric-mechanical approach to document the incidence of thrusting and related palaeostress evolution as a driving mechanism for fluid transfer out of a thrustbelt.

## Methods

### *Balancing*

In order to determine the geometries and kinematics of the thrust sheets in the Western Carpathians at the time of oil migration, we have constructed five balanced cross-sections from the West European Platform to the Inner Carpathians (Fig. 1b). Details for cross-section construction are partly described in Nemčok *et al.* (1999, 2000, 2001) and further information is given below. Data constraints for balancing were provided by:

(1) magnetotelluric data (e.g., Ryłko & Tomas, 1995) that helped to determine the basement top;
(2) reflection seismic profiles (e.g., profiles 5-3-73K, 5-1-78K, 5A-1-78K; Nemčok *et al.* 1999, 2000) that imaged thrust sheet geometries;
(3) bore holes that provided thicknesses of thrust sheets and thicknesses of involved sediments; and
(4) our own outcrop data and data from available geological maps that provided thrust sheet geometries and thicknesses of sediments.

Dip domain and kink band analyses of planar data were made manually, in order to exclude local complexities such as small-scale folding. Small-scale complexities were filtered out from large-scale geometries of thrust sheets, constructed without either small-scale faulting or complex deformation zones, which were smaller than the resolution of regional balanced cross-sections. Obtained fold geometries cleaned from small-scale complexities comprise fault-bend folds (Suppe 1983), fault-propagation folds (Suppe & Medwedeff 1984) and their evolutional combinations (e.g., Mitra 1990), providing an exact understanding of their mechanisms and interactions. Cross-sections were constructed using the program GeoSec 2D® (Paradigm Geophysical Ltd., Houston, USA). Surface level and well profiles provided the best constraints. The construction downward was less precisely controlled by the wedge base line interpreted from seismics and magnetotellurics. Pin lines for the Magura and Silesian Units were located in their fronts. Volume preservation was simulated by the area preservation within the cross-section. Deformed cross-sections were validated by restoration to undeformed state, made by the same software, using the flexural slip algorithm.

### *Numerical modelling*

In order to understand oil migration driven by mean stress gradients, we study a set of 2D finite-element models of fault-propagation and fault-bend folds. Model geometries describing different stages of fold development were made by forward balancing from undeformed to most mature folding stages using programs GeoSec 2D® and Move 2D® (Midland Valley Exploration Ltd., Glasgow, UK) (Fig. 2). Rock mechanics were added by transferring the various balancing stages into the finite-element program ANSYS® (Ansys Inc., Houston, USA), analyzing for stress field perturbations and strain localization during fold growth.

Modelled profiles comprise 2 km thick pretectonic sediments composed of three lithologic layers. The upper one is 620 m thick, the middle one is 710 m thick and the lower one is 670 m thick (Fig. 2). Ramp angles for fault-propagation and fault-bend folds are 28° and 26°, respectively. The pre-tectonic section of the siliciclastic scenario is composed of a sandstone–shale–sandstonesuccessionmimicking

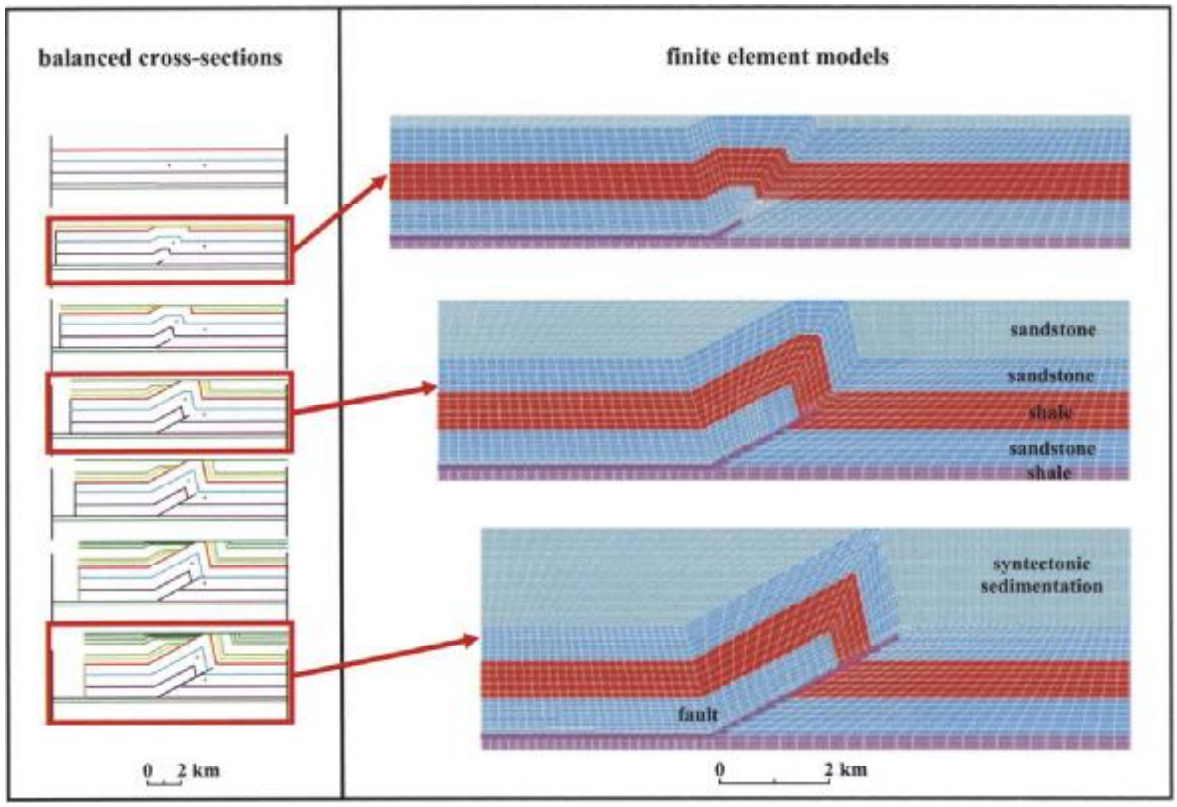


**Fig. 2.** Finite element models based on balanced sections representing different growth stages of fault-propagation folds. Thickness of the pre-tectonic thrust sheet is 2 km. Vertical scale equals horizontal scale.

the conditions in the West Carpathian thrust belt. For comparison, a more brittle dolomite–limestone–dolomite succession is also studied. Both scenarios experienced either 50% erosion of the evolving folds or deposition keeping up with the growth structure during simulated shortening, in order to test both continental and marine settings. Syn-tectonic sediments are either shale or sandstone.

Each of the finite-element models describes a cross-section through the folded sedimentary sequence, which is broken by planes of weakness, i.e., faults. ANSYS® uses a Lagrangian formulation to simulate plane strain deformation using four-node isotropic elements to represent the individual pre- and syn-tectonic sediment layers. Their mechanical behaviour in the elastic domain is described by the generalized Hooke's law, relating strains to stresses via Young's modulus and Poisson's ratio (e.g., Mandl 1988). Brittle failure is governed by the Coulomb criterion according to Jaeger and Cook (1979):

$$\tau_{crit} = c + \mu\sigma_n, \qquad (1)$$

where $\tau_{crit}$ is the critical shear stress, $c$ is the cohesion, $\mu$ is the coefficient of internal friction and $\sigma_n$ is the stress normal to the shear fracture. The various physical properties of the lithologies used in the numerical models are summarized in Table 1.

Faults are described by so-called contact elements. This approach handles large differential movements between parts of the model, but does not describe cracking, i.e., the fault propagation itself. Contact elements are defined at opposing sides of the pre-assigned fault and stiffness values similar to the Young's moduli of the rocks in contact are used to enforce compatibility between adjacent fault surfaces. Contact elements are also capable of describing frictional sliding, so that the influence of different friction coefficients can be studied. Depending on the restoration stage, up to 2100 planar elements and 900 contact elements were used to represent the model geometry.

Boundary conditions for the fault-propagation fold models are a fixed base and right side, while the top is a free surface. Displacement constraints are applied to the nodes on the left side of the hanging wall to simulate compression. Boundary conditions for the fault-bend fold models differ in one only aspect: a lithostatic pressure boundary condition is applied to the

**Table 1.** *Physical properties of rocks used in the finite-element models*

| Rock | Angle of internal friction (degree) | Coefficient of internal friction | Cohesion (MPa) | Young's modulus (GPa) | Poisson's ratio | Density ($kgm^{-3}$) |
|---|---|---|---|---|---|---|
| Sandstone | 28.8 | 0.55 | 27.2 | 18.30 | 0.38 | 2180 |
| Shale | 21.0 | 0.38 | 0.69 | 5.52 | 0.25 | 2470 |
| Limestone | 26.4 | 0.50 | 26.8 | 77.40 | 0.26 | 2720 |
| Dolomite | 39.0 | 0.81 | 35.9 | 106.00 | 0.29 | 2840 |

Values are taken from Clark (1966); Lama & Vutukuri (1978); Čermák & Rybach (1982); Ibrmajer *et al.* (1989); Cloetingh *et al.* (1995).

part of the left model side representing the syntectonic sediments. The displacement boundary condition is 2.3 mm $a^{-1}$. Models are run until excessive mesh distortion and/or mesh penetration at the contact elements cause an instable numerical solution. This typically occurs after 50–60 m of total convergence.

Stresses in our models were built up by block motions, i.e., movement of the hanging wall relative to the footwall. Special focus is on the mean stress distribution and stress field orientation during the various restoration stages. However, as only an approximate description of the real sediment rheology is used, we do not attempt to predict absolute values but concentrate on the relative patterns of mean stress in relation to different thrust geometries and their kinematics. Mean stress has a profound control on the forces driving and opposing fluid migration. Driving forces are (e.g., Vandenbroucke 1993):

$$\text{buoyant force} = (\rho_w - \rho_o)g \sin(\phi)\, l \quad (2)$$

where $\rho_w$ and $\rho_o$ are water and oil densities, $g$ is the acceleration of gravity, $\varphi$ is the angle between migration and horizontal directions, l is the oil column length; and (e.g., Mandl 1988)

$$\text{hydraulic head} = h_p + h_e \quad (3)$$

where $h_p$ and $h_e$ are pressure and elevation heads. $h_e$ represents the potential energy of a fluid due to its elevation above a reference level, while

$$h_p = \Delta p/(\rho g) \quad (4)$$

where $\Delta p$ is pore fluid pressure difference and $\rho$ is fluid density.

Opposing forces are (e.g., Winter 1987):

$$\text{capillary pressure} = 2\gamma \cos(\theta)/r \quad (5)$$

where $\gamma$ is the interfacial tension between oil and water, $\theta$ is the wettability expressed as the contact angle of the oil–water interface against the rock surface, and $r$ is the average radius of the interconnected pore space; and (e.g., Mandl 1988)

$$\text{frictional resistivity force} = -\eta\, u/k \quad (6)$$

where $\eta$ is the fluid viscosity, $u$ is the filtration velocity and $k$ is the permeability.

Loading of the thrust sheet by tectonic stress generated by block motions affects fluid migration forces in various ways. In the case of the buoyant force, the shortening would result in a growth of the fold structure, increasing the angle between migration and horizontal directions. This effect is not directly coupled to mean stress and, therefore, remains effective even after the end of the thrustbelt shortening. We call this control passive because it is effective even after shortening.

In the case of the hydraulic head, the shortening affects both elevation and pressure heads. The elevation head changes with growth of the fold structure. Remaining changed after the end of shortening in the thrustbelt, the elevation head also qualifies for being a passive control. The pressure head is coupled with mean stress development via its effect on the pore fluid pressure (e.g., Shi & Wang 1986; Ge & Garven 1992):

$$\Delta p = (a_n/[a_n + nb(1-n))]\Delta\sigma_m \quad (7)$$

where $\Delta p$ is the change in pore fluid pressure, $a_n$ is the porosity compressibility, $n$ is the porosity, $b$ is the fluid compressibility, and $\Delta\sigma_m$ is the change in mean stress. Because mean stress perturbations develop in each stress build-up cycle, they qualify for an active control, as they vanish after the end of thrustbelt shortening.

In the case of the capillary pressure, the mean stress controls the average radius of the interconnected pore space via its effect on the pore space (e.g., Zimmerman *et al.* 1986). Because the pore space decreases both elastically, being able to return to its earlier volume after loading release, and plastically, undergoing permanent

pore space changes, this control has passive and active components.

In the case of the frictional resistivity, the permeability and filtration velocity reacts to the mean stress (Vandenbroucke 1993; Brown *et al.* 1994; R. Sigal 1998, pers. comm.) both temporally and permanently; this control has both passive and active components.

## Results

### *Balancing results*

All balanced cross-sections are pinned on the European Platform and end at the Pieniny Klippen Belt (Fig. 1b), except profile 1, which goes further to the Inner Carpathians. As profiles 1 and 2 have already been discussed in detail in Nemčok *et al.* (1999, 2000, 2001), this paper focuses on the description of the remaining profiles 3 to 5 (Fig. 3). The general style of deformation and the dominant fold-and-thrust style are similar in all five sections.

The frontal half of the thrustbelt along profile 3 accreted small volumes of the Neogene molasse sediments (Fig. 3a). The youngest of them are of Badenian-Lower Sarmatian age. The frontal half of the wedge comprises a Silesian sediment section accreted in 4.3–18.6 km wide thrust sheets. This width, increased in comparison with profile 4 and roughly comparable to profile 5, is caused by the dramatic thickness increase of the Cretaceous portion of the sedimentary section in the unit defined as the Skole Unit, which caused a strength increase of the accreted sedimentary package. The maximum thickness of the package is 3.6 km. Thrust sheets were formed by fault-propagation folding, as indicated not only by our balancing but also by available reflection seismics. They were thrust over incompetent formations of the autochthonous molasse. Two preserved ramp tips are located inside the Upper Cretaceous–Paleocene inversion-related section, one at the base of the Oligocene–Lower Miocene syn-tectonic sediments. Syn-tectonic sediments show large thickness variations, which are due to erosion of shortened structures and the existence of complex topography during their deposition.

The frontal third of the accretionary wedge along profile 4 incorporates a small volume of the Neogene molasse, Lower Sarmatian being the youngest (Fig. 3b). Thrust sheet widths are affected by thickness changes of the pre-Eocene portion of the sedimentary section. The thick section, which has a thickness of about

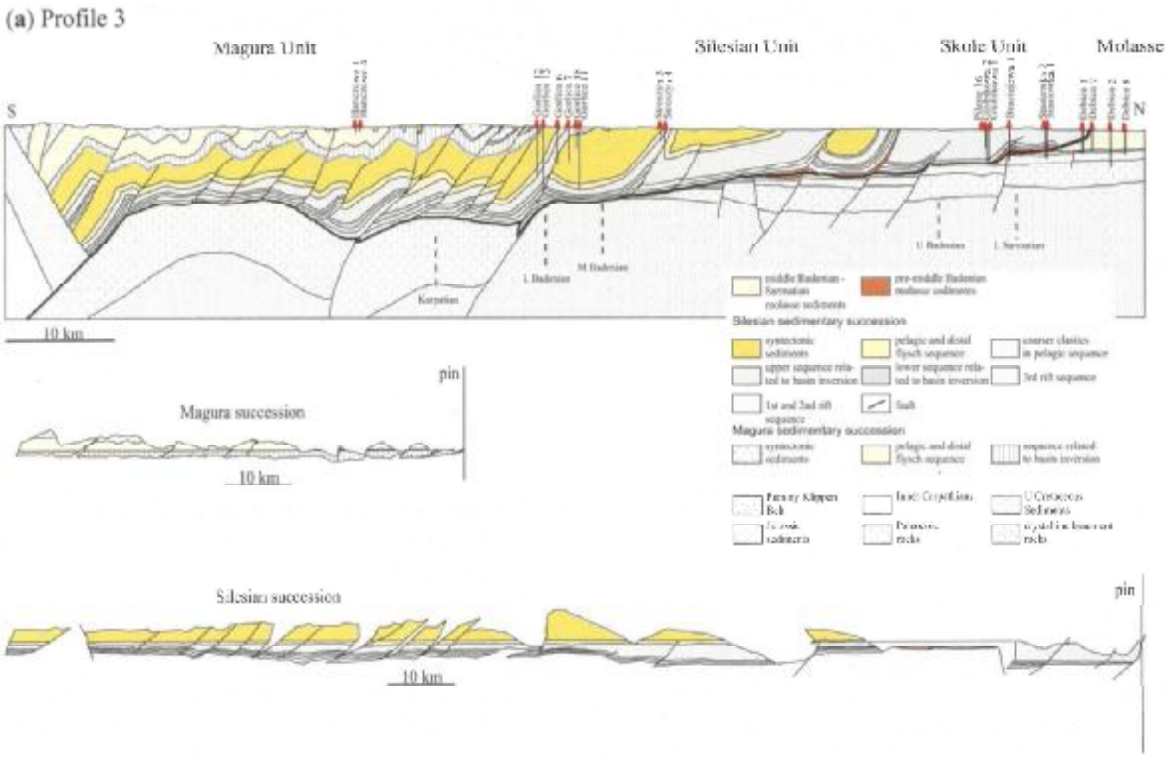


**Fig. 3.** Balanced deformed and restored cross sections through the Western Carpathians (see Fig. 1b for location). Vertical scale equals horizontal scale. The thick dashed lines indicate the southernmost extent of autochthonous molasse sediments of indicated age below the accretionary wedge. The thrustbelt incorporates sediments of two main units; Magura and Silesian Units.

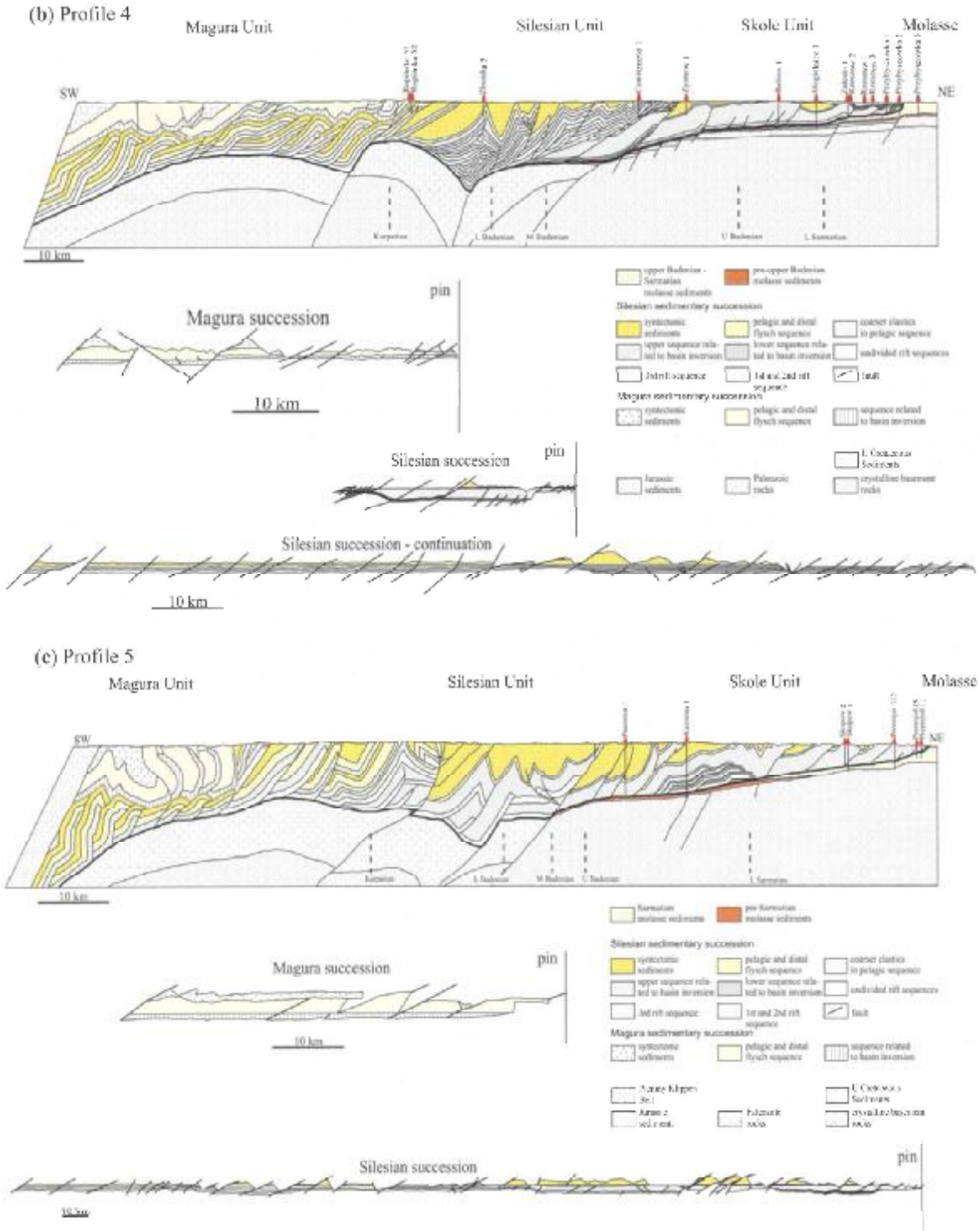


**Fig. 3.** *Continued.*

1.92 km, forms thrust sheets 5.5–7.1 km wide. The thin section, located at both southern and northern sides of the thick section, which has a thickness of about 0.5 km, forms thrust sheets only 0.55–1.65 km wide. Most of these thrust sheets are formed by fault-propagation folding, thrust over incompetent Neogene molasse sediments. Four ramp tips are located in the middle of the upper sequence related to basin inversion. One ramp tip is located inside the Eocene pelagic and distal flysch sequence. The frontal six ramps propagated upward into Neogene molasse sediments deposited in a pig-gyback basin carried on top of the frontal thrust

sheets. This is the only profile with preserved geometries of frontal thrust sheets. Profiles 3 and 5 have their frontal structures deeply eroded.

The frontal half of the thrustbelt along profile 5 comprises a Silesian sediment section imbricated in 2.1–26.4 km wide thrust sheets (Fig. 3c). This increased width in comparison with profile 4 and roughly comparable to profile 3, is caused by the thickness increase of the Cretaceous sedimentary section in the Skole Unit, which increased its strength. Its maximum thickness, comparable to profile 3, is 3.6 km. The frontal part of the wedge was thrust over less competent middle Badenian–Sarmatian facies of the autochthonous molasse. Due to the deep erosional level, only three of the frontal thrust sheets show the evidence of fault-propagation folding. Two preserved ramp tips are located at the base of the Eocene section. Variable thickness of the thrust sheets controls the thrust sheet widths. Thrust sheets with a width of 7.1–26.4 km have a thickness close to its maximum value, containing both Lower and Upper Cretaceous sections. The thickness of 2.1–8.6 km wide thrust sheets ranges between 1.4 and 2.1 km. These thrust sheets do not contain the Lower Cretaceous section and the thickness of the Upper Cretaceous section is frequently reduced.

Rear portions of the described profiles are not composed of simple fault-propagation fold structures. The rear half of the thrustbelt along profile 3 has a complex structure, which includes thick-skin tectonics, buried Silesian duplexes and the overlying Magura Unit (Fig. 3a). The rear two-thirds of the thrustbelt along profile 4 includes thick-skin tectonics, two levels of buried duplexes in the Czarnorzeki area, an antiformal stack and two triangle zones with back-thrusting in the Zboiska area and the Magura Unit above Silesian buried duplexes (Fig. 3b). The rear portion of the wedge along profile 5 contains thick-skin tectonics, several triangle zones and back-thrusts in the Silesian section (Fig. 3c).

Results of our balancing demonstrate that fault-propagation folding developed large frontal portions of the West Carpathians. This observation is in accordance with observations made from our profiles 1 and 2 (Nemčok *et al.* 1999, 2000, 2001).

### *Finite-element modelling results*

Analysis of the finite-element modelling results focused on the mean stress distribution in relation to different fold-and-thrust geometries and balancing stages, respectively, in order to assess the driving forces for fluid migration. Figures show the mean stress distribution for various growth stages of a fault-propagation fold with syn-tectonic sedimentation (Fig. 4) and with syn-tectonic erosion (Fig. 5). Similarly, mean stresses for two growth stages of a fault-bend fold are shown in Figure 6.

Fault-propagation fold scenarios with syn-tectonic deposition (Fig. 4) indicate the following features of the mean stress perturbation:

(1) Maximum mean stress anomaly in the advancing side of the propagating ramp tip, whereas minimum mean stress anomaly exists in the receding side of the propagating ramp tip.
(2) Minimum mean stress anomaly in the anticline during early stages of the stress build-up.
(3) Maximum mean stress anomaly in the hanging wall in the bend area above the flat/ramp transition. The whole lower beam unit (sandstone) above the flat experiences a mean stress increase, which diminishes in direction toward the ramp tip.
(4) Medium mean stress anomaly in the anticline.
(5) Distinct minimum mean stress anomaly in the footwall in front of the upper portion of the ramp.
(6) The footwall underneath the flat is characterized by mean stress increase during all stages of the stress build-up.
(7) The footwall in front of the lowermost portion of the ramp progressively develops mean stress increase by the end of the fold growth during last stages of the stress build-up.

Fault-propagation fold scenarios with syn-tectonic erosion (Fig. 5) show the following mean stress distribution: (1) Only slightly increased mean stress in the advancing side of the propagating ramp tip and a minimum mean stress anomaly in the receding side of the propagating ramp tip during the last stages of the fold growth and last stages of the stress build-up. (2) A broad minimum mean stress anomaly in the upper parts of the anticline and in the foreland in front of the upper half of the ramp. (3) Slightly increased mean stress in the hanging wall in the bend area above the flat/ramp transition.

Fault-bend fold scenarios are depicted in Figure 6 for the dolomite–limestone–dolomite succession with syn-tectonic shale deposition, which shows a more variable mean stress pattern than the corresponding siliciclastic

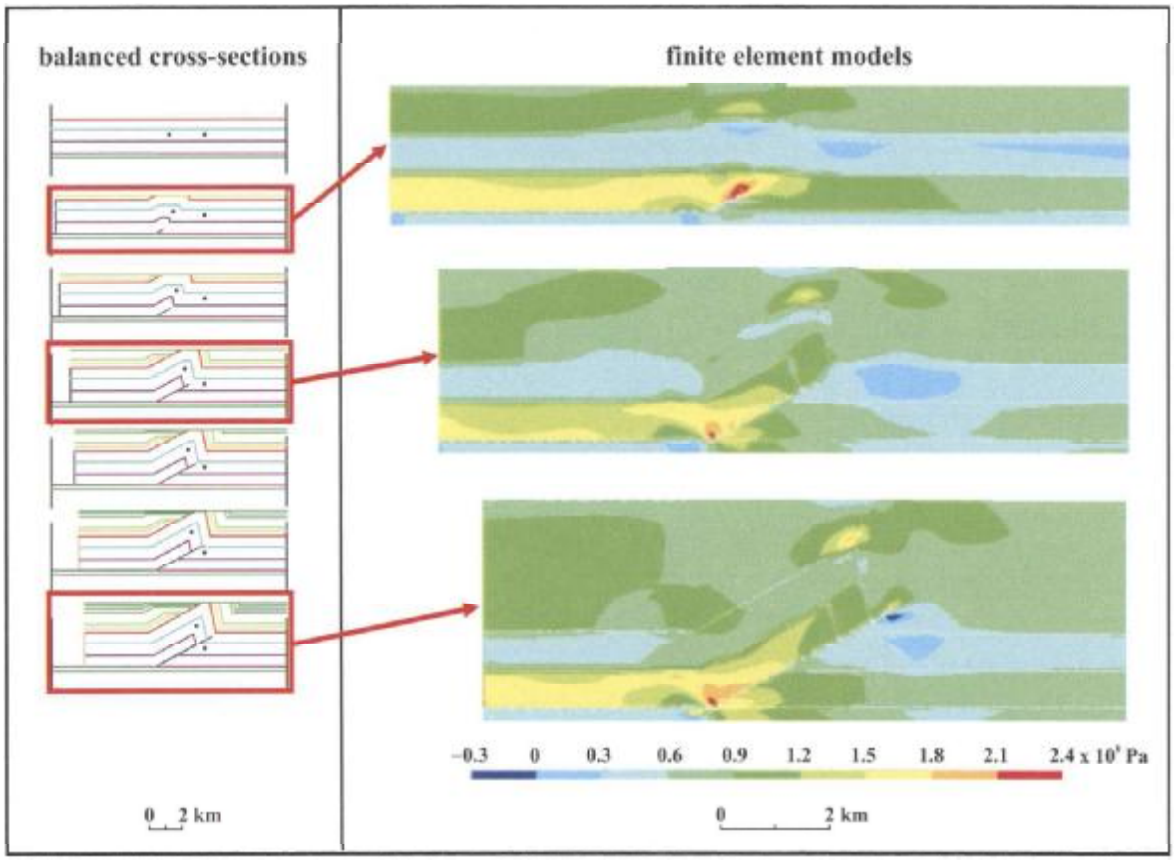


**Fig. 4.** Finite-element models of mean stress perturbations during various development stages of the fault-propagation fold scenario with syn-tectonic sedimentation. Models show the siliciclastic scenario represented by an upper sandstone, a middle shale and a lower sandstone layer of the pre-tectonic section. The syn-tectonic sediment keeping up with growing structure is sandstone. Colour scale is in Pa.

scenario. They indicate the following features for the mean stress perturbation: (1) Maximum mean stress anomaly is developed in the foreland in front of the lowermost portion of the ramp. It develops during the last stress build-up stages, but only in carbonate scenarios, which are 'more brittle' than siliciclastic ones. (2) A broad minimum mean stress anomaly in the anticline, which is developed in both carbonate and siliciclastic scenarios. Carbonate scenarios generate

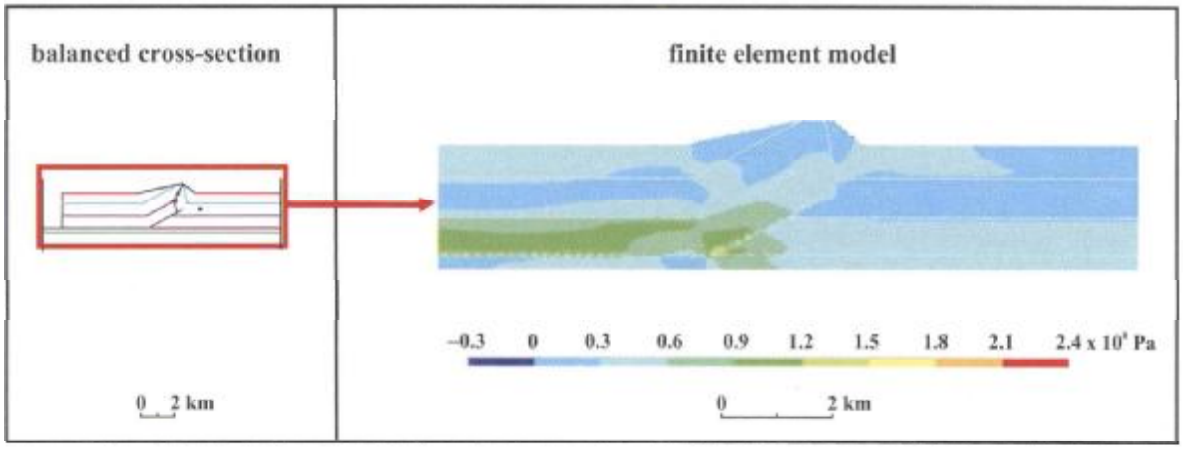


**Fig. 5.** Mean stress distribution of fault-propagation fold scenario with syn-tectonic erosion. Colour scale is in Pa. A corresponding scenario with syn-tectonic sedimentation is shown in Fig. 4 middle.

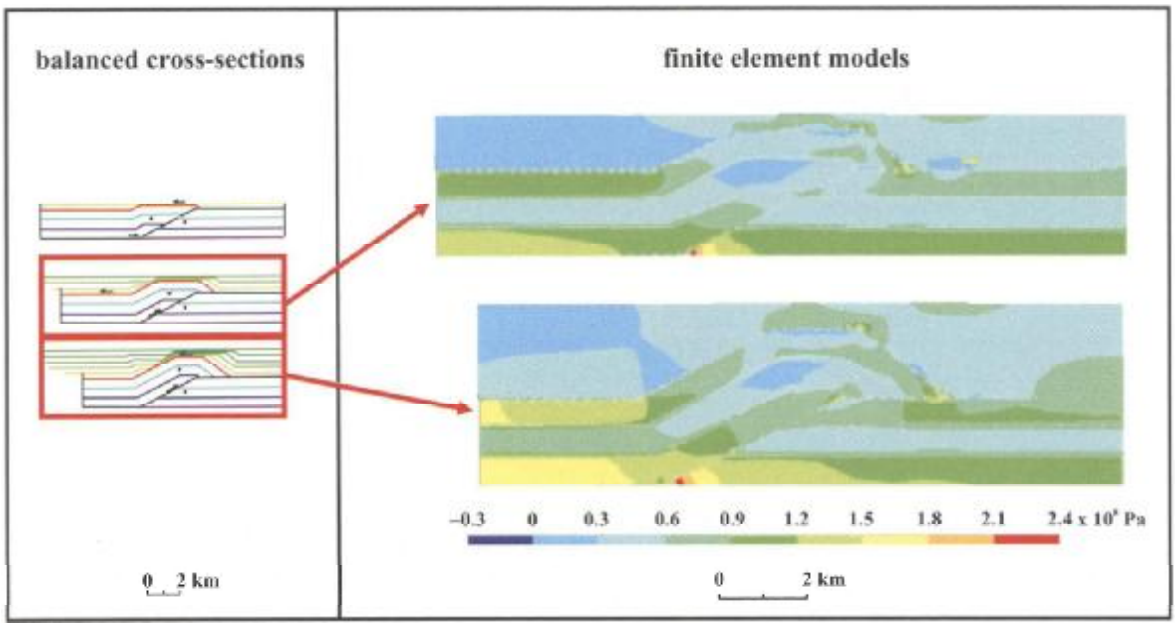


**Fig. 6.** Finite-element models of mean stress during mature development stages of the fault-bend fold type. Models show the carbonate scenario represented by upper dolomite, middle limestone and lower dolomite layers of the pre-tectonic section. The syn-tectonic sediment keeping up with growing structure is shale. Colour scale is in Pa.

stronger anomalies. (3) A slight minimum mean stress anomaly in the foreland in front of the central portion of the ramp.

During growth of the fault-bend fold, continuing block movements build up a new stress cycle ultimately leading to failure and rapid stress release. A very early stage of this build-up is captured in Figure 7b. This figure shows that several areas of the profile do not 'feel' loaded by tectonic stress yet. In these areas the maximum principal stress $\sigma_1$ is still oriented vertically and has not yet changed into sub-horizontally oriented compression. An advanced stage of the build-up is shown in Figure 7c. This is the time when the whole profile affected by block movements experiences loading by sub-horizontally and sub-vertically oriented maximum and minimum principal compressional stresses $\sigma_1$ and $\sigma_3$, typical for thrusting regime. Several areas of the profile experience various stress perturbations caused by complexities added by the frictional resistance of fault planes, flexure, internal deformation of the thrust sheet and uneven distribution of gravity forces. Stress perturbations are not only characterized by changes in orientations of principal stresses but also by changes in their magnitudes. The last stress build-up stage, before the failure of the model, is captured in Figure 7d. The stress regime is similar to that of Figure 7c but stress perturbations are more pronounced.

## Discussion

Our finite element modelling results indicate that each fold type has its own typical stress distribution during each stress build-up and growth stage. The straining, which controls the stress transfer, differs among various fold types (compare Figs 4 and 6), because their different geometries and fault constellations also control what portions of the stress generated by the driving force would be spent on overcoming the frictional resistance of pre-existing faults, internal deformation of the thrust sheet, overcoming gravity forces, and deformation of the foreland.

Mean stress in various portions of fault-bend fold models is affected by the complex stress perturbations described earlier. The whole anticline is the place where the mean stress decreases below the regional level (Fig. 6). This observed mean stress decrease, together with an anticline being the morphologically highest feature of the thrust sheet, causes a match of favourable elevation and pressure terms of the hydraulic gradient, which would have a strong tendency to drive fluids from broader hanging wall to hanging wall anticline in all tested fault-bend scenarios. The drive will be strongest in the carbonate case with sealing syn-tectonic shale. Figure 6 indicates that practically the whole anticline serves as a

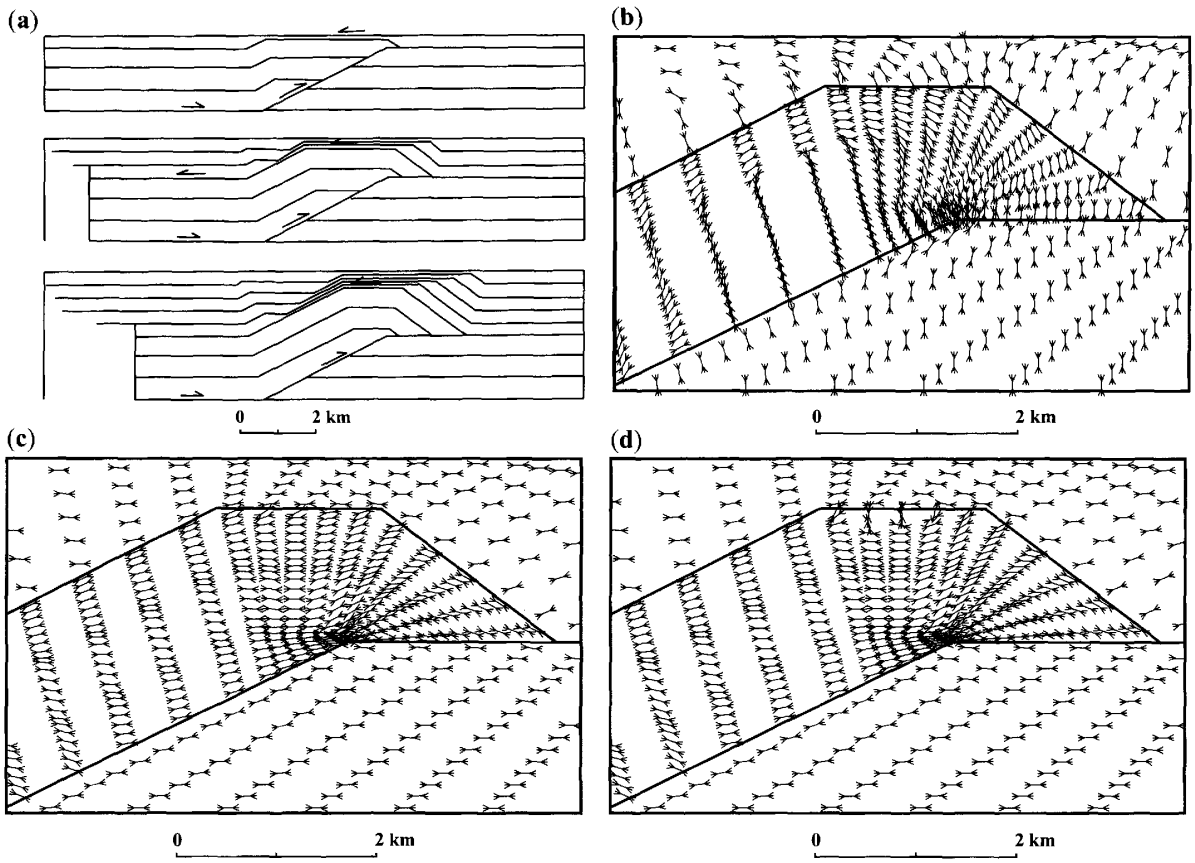


**Fig. 7.** (a) Forward model of the fault-bend fold (passive roof duplex). Roof thrust is formed by syn-tectonic sandstone, the deposition rate of which was faster than uplift of the growth structure during simulated shortening. (**b–d**) Finite-element models capturing the orientation of the maximum principal stress during a stress build-up cycle within the passive-roof duplex in its mature growth stage shown in Fig. 7a bottom. Arrows indicate orientation of the largest principal stress $\sigma_1$ after 4.6 m (b), 26.3 m and 39.1 m (d) of horizontal convergence.

fluid sink. A comparison of Figure 6 with Figure 4 indicates that the fault-bend fold is not capable of generating large-scale mean stress perturbations and can be defined as 'low energy' structure.

The fault-propagation fold is characterized by: coupled mean stress increase and decrease on hanging wall and footwall sides of the ramp tip; mean stress decrease in the initial anticline followed by increase during later anticline growth; progressive mean stress increase in the broader hanging wall; and progressive mean stress decrease in the foreland.

Observed mean stress features indicate hydraulic gradients, which can potentially drive fluids (Fig. 4): from hanging wall to footwall by tip-tapping mechanism in the ramp tip region; from the advancing to the receding side of the ramp tip; thus acting as a source-sink mechanism between anticline and foreland.

These modelling results strongly suggest that only the fault-propagation folds can generate mean stress perturbations, which would drive fluids into their foreland if any other fluid-migration driving and opposing forces were ignored. The Carpathian data indicate that the mean-stress controlled fluid drive into the foreland dominated over the fluid drive into growing anticlines created by fault-propagation folding. The fluid drive into anticlines would be controlled by (1) a buoyant force enhanced by the shortening-controlled angle between migration and horizontal directions; and (2) the elevation head enhanced by shortening.

The additional enhancement of the forelandward fluid drive was provided by active portions of the mean stress control over the pore volume gradients (i.e., capillary pressure gradients) and permeability gradients, which provided an additional fluid pumping mechanism from more compacted to less compacted, or less permeable to more permeable, areas. In doing this, fault-propagation folds are dynamically different from any other fold types, as discussed earlier.

Separation of various fluid-drive controls into passive and active provides an understanding of which controls remain effective or vanish after the end of the thrustbelt shortening. Fault-propagation folds are capable of modifying both pressure and elevation portions of the hydraulic head when they are active. They can modify the elevation head when they are both active or passive. The pressure head controlled by mean stress perturbations in active fault-propagation folds creates pore fluid pressure gradients that act in addition to the elevation head effect. The changing structural geometry forms elevation controls. When folds are passive, the hydraulic head is controlled only by the structural architecture developed earlier during the active thrusting. Therefore, the answer whether folds were active during hydrocarbon migration becomes very important, because that is the only time when fault-propagation folds can pump fluids into their forelands. When they are passive they become accumulators just like any other fold types. Mean stress perturbations in the modelled folds just make the oil accumulation in the anticline stronger when folds are active. Other active controls affected by mean stress perturbations in growing fault-propagation folds over fluid migration forces are effects on pore space, permeability and filtration velocity.

## Conclusions

The combination of geochemical results (Ten Haven *et al.* 1993; Bessereau *et al.* 1996) with our balancing data indicate that oil migration from the Oligocene Menilite source shale inside the West Carpathian thrustbelt to fields in its autochthonous foreland took place during the Late Oligocene–Early Miocene. This was the time when the thrustbelt underwent shortening and its frontal structures adjacent to the autochthonous foreland developed by fault-propagation folding. The source-reservoir correlation and the dominant tectonic style inferred from geometric balancing are in accordance with the predictions made by the numerical simulations. Only the fault-propagation folds are characterized by a large foreland area of decreased mean stress, by a coupled increased/decreased mean stress areas on advancing/receding sides of the ramp tip and the overall mean stress decrease inside the thrust sheet in the foreland direction. These mean stresses and related hydraulic gradients provided an effective fluid pumping mechanism from frontal fault-propagation folds into their footwalls. It can operate when the influence of the pressure head on the fluid migration dominates over the influence of elevation head and buoyant force, and becomes enhanced by advantageous distribution of capillary pressure and frictional resistivity gradients that further enhance fluid flow from the thrust sheet into its foreland.

Numerical modelling portion of the study was made within the project 'Systematics of hydrocarbon exploration and production in thrustbelts' sponsored by Elf, Enterprise, Occidental, Repsol YPF and Texaco. The balancing portion of the study was sponsored by Amoco. B. Welker and C. Christensen helped with figures. S. Buiter, F. Roure and B. Sperner are thanked for their helpful comments on an earlier version of the manuscript.

## References

BALLA, Z. 1984. The Carpathian loop and the Pannonian basin: a kinematic analysis. *Geophysical Transactions*, **30(4)**, 313–353.

BESSEREAU, G., ROURE, F., KOTARBA, A., KUSMIEREK, J. & STRZETELSKI, W. 1996. Structure and hydrocarbon habitat of the Polish Carpathians. *In*: ZIEGLER, P. A. & HORVATH, F. (eds) Peri-Tethys Memoir 2: Structure and prospects of Alpine basins and forelands. *Memoires du Museum National & Histoire Naturelle*, **170**, 343–373.

BROWN, K. M., BEKINS, B., CLENNELL, B., DEWHURST, D. & WESTBROOK, G. 1994. Heterogeneous hydrofracture development and accretionary fault dynamics. *Geology*, **22**, 259–262.

BURBIDGE, D. R. & BRAUN, J. 2002. Numerical models of the evolution of accretionary wedges and fold-and-thrust belts using the distinct element method. *Geophysical Journal International*, **148**, 542–561.

ČERMÁK, V. & RYBACH, L. 1982. Thermal conductivity and specific heat of minerals and rocks. *In*: G. Angenheister (ed.) *Landolt-Bornstein Numerical Data and Functional Relationships in Science and Technology*. New Series, 16, Springer Verlag, Berlin.

CLARK, S. P. Jr. 1966. *Handbook of Physical Constants*. GSA Memoir, New York, **97**.

CLOETINGH, S. A. P. L., ZOETEMEIJER, R. & VAN WEES, J. D. 1995. *Tectonics I. Tectonics and basin formation in convergent settings; thermomechanical evolution of the lithosphere and basin evolution in compressive tectonic regimes*. Short course, Vrije University, Amsterdam.

CSONTOS, L., NAGYMAROSY, A., HORVÁTH, F. & KOVÁČ, M. 1992. Tertiary evolution of the intracarpathian area: a model. *Tectonophysics*, **208**, 221–241.

GE, S. & GARVEN, G. 1992. Hydromechanical modelling of tectonically driven groundwater flow with application to the Arkoma foreland basin. *Journal of Geophysical Research*, **97**, 9119–9144.

IBRMAJER, J., SUK, M. *ET AL.* 1989. *Geophyiscal Image of the CSSR* (in Czech). ÚÚG Praha.

JAEGER, J. C. & COOK, N. G. W. 1979. *Fundamentals of Rock Mechanics*. Chapman & Hall, London.

KARNKOWSKI, P. 1999. *Oil and Gas Deposits in Poland*. The Geosynoptics Society 'GEOS', Cracow.

KORÁB, T., KRS, M., KRSOVÁ, M. & PAGÁČ, P. 1981. Palaeomagnetic investigations of Albian (?) – Paleocene to Lower Oligocene sediments from the Dukla unit, East Slovakian Flysch, Czechoslovakia. *Západné Karpaty, Séria Geológia*, **7**, 127–149.

KOTARBA, M., SZAFRAN, S. & ESPITALIE, J. 1987. A study of organic matter and natural gases of the Miocene in the Polish part of the Carpathian Foredeep. *Chemical Geology*, **64**, 197–207.

KOVÁCS, S., CSASZAR, G., GALACZ, A., HAAS, J., NAGY, E. &VOROS, A. 1989. The Tisza superunit was originally part of the northern (European) margin of Tethys. *In*: RAKÚS, M., DERCOURT, J. & NAIRN, A. E. M. (eds) *Evolution of the Northern Margin of Tethys*. Memoires de la Société Geologique de France, Nouvelle Serie, Paris, 81–100.

KRS, M. & POTFAJ, M. 1991. Palaeo-magnetic investigations of the flysch belt in the Orava region, Magura unit, Czechoslovak Western Carpathians. *Geologické Práce*, Správy, **92**, 125–151.

KRS, M. & ROTH, Z. 1977. A paleomagnetic study of Cenomanian–Lower Turonian sediments in the Moravskoslezké Beskydy Mts (in Czech). *Věstník ÚÚG*, **52(6)**, 323–332.

KRS, M., KRSOVÁ, M. & CHVOJKA, R. 1993. Palaeomagnetic investigations in the Biele Karpaty mountains, flysch belt of the West Carpathians. *Geologica Carpathica*, **45(1)**, 35–43.

KSIĄŻKIEWICZ, M. 1977. Plate motion hypothesis and Carpathian development (in Polish). *Annales de la Société Geologique de Pologne*, **47**, 321–353.

KWON, S. & MITRA, G. 2004. Three-dimensional finite element modelling of a thin-skinned fold-thrust belt wedge; Provo Salient, Sevier Belt, Utah. *Geology*, **32**, 561–564.

LAMA, R. D. & VUTUKURI, V. S. 1978. *Handbook on Mechanical Properties of Rocks*. Transtech Publications, Bay Village, 2.

MANDL, G. 1988. *Mechanics of Tectonic Faulting. Models and Basic Concepts*. Elsevier, Amsterdam.

MÁRTON, E. & MÁRTON, P. 1989. A compilation of paleomagnetic results from Hungary. *Geophysical Transactions*, **35**, 117–133.

MITRA, S. 1990. Fault-propagation folds: geometry, kinematic evolution, and hydrocarbon traps. *American Association of Petroleum Geologists Bulletin*, **74**, 921–945.

MOLDOWAN, J. M., FAGO, F. J., HUIZINGA, B. J. & JACOBSON, S. R. 1991. Analysis of oleanane and its occurrence in upper Cretaceous rocks. *In*: MANNING, D. A. C. (ed.) *Advances and Applications in Energy and the Natural Environment. Organic Geochemistry*. Manchester University Press, Manchester, 195–197.

NEMČOK, M., COWARD, M. P., SERCOMBE, W. J. & KLECKER, R. A. 1999. Structure of the West Carpathian accretionary wedge: insights from cross-section construction and sandbox validation. *Physics and Chemistry of the Earth*, **24**, 659–665.

NEMČOK, M., NEMČOK, J. *ET AL.* 2000. Results of 2D balancing along 20° and 21° longitude and pseudo-3D in the Smilno tectonic window: implications for shortening mechanisms of the West Carpathian accretionary wedge. *Geologica Carpathica*, **51**, 281–300.

NEMČOK, M., NEMČOK, J. *ET AL.* 2001. Reconstruction of Cretaceous rifts incorporated in the Outer West Carpathian wedge by balancing. *In*: CLOETINGH, S., NEMČOK, M., NEUBAUER, F., HORVÁTH, F. & SEIFERT, P. (eds) *The Hydrocarbon Potential of the Carpathian–Pannonian Region*. Marine and Petroleum Geology, **18**, 39–64.

NEMČOK, M., POSPÍŠIL, L., LEXA, J. & DONELICK, R. A. 1998. Tertiary subduction and slab break-off model of the Carpathian–Pannonian region. *Tectonophysics*, **295**, 307–340.

NEUBAUER, F. & GENSER, J. 1990. Architektur und Kinematik der östlichen Zentralalpen: eine Übersicht. *Mitteilungen des Naturwissenschaftlichen Vereines für Steiermark*, **120**, 203–219.

PATRASCU, S., PANAIOTU, C., SECLAMAN, M. & PANAIOTU, C. E. 1994. Timing of rotational motion of Apuseni Mountains (Romania): paleomagnetic data from Tertiary magmatic rocks. *Tectonophysics*, **233**, 163–176.

PUGZG GEOPOL 1998. *Poland Petroleum Opportunities*. Geopol, Warsaw.

RATSCHBACHER, L., FRISCH, W., LINZER, H. G. & MERLE, O. 1991. Lateral extrusion in the Eastern Alps, part 2: structural analysis. *Tectonics*, **10(2)**, 257–271.

ROCA, E., BESSEREAU, G., JAWOR, E., KOTARBA, M. & ROURE, F. 1995. Pre-Neogene evolution of the Western Carpathians: constraints from the Bochnia–Tatra Mountains section (Polish Western Carpathians). *Tectonics*, **14**, 855–873.

ROURE, F., ROCA, E. & SASSI, W. 1993. The Neogene evolution of the outer Carpathian flysch units (Poland, Ukraine and Romania): kinematics of a foreland/fold-and-thrust belt system. *Sedimentary Geology*, **86**, 177–201.

ROYDEN, L. H. & BÁLDI, T. 1988. Early Cenozoic tectonics and paleogeography of the Pannonian and surrounding regions. *In*: ROYDEN, L. H. & HORVÁTH, F. (eds) *The Pannonian Basin. A Study in Basin Evolution*. American Association of Petroleum Geologists Memoir, Tulsa, 1–16.

ROYDEN, L. H., HORVÁTH, F. & BURCHFIELD, B. C. 1982. Transform faulting, extension and subduction in the Carpathian-Pannonian region. *Geological Society of America Bulletin*, **73**, 717–725.

RYLKO, W. & TOMAS, A. 1995. Morphology of the consolidated basement of the Polish Carpathians in the light of magnetotelluric data. *Geological Quarterly*, **39**, 1–16.

SALVINI, F., STORTI, F. & MCCLAY, K. 2001. Self-determing numerical modelling of compressional fault-bend folding. *Geology*, **29**, 839–842.

SANDULESCU, M. 1988. Cenozoic tectonic history of the Carpathians. *In*: ROYDEN, L. H., HORVÁTH, F. (eds) *The Pannonian Basin. A Study in Basin Evolution*. (American Association of Petroleum Geologist Memoir), **45**, 17–26.

SASSI, W. & FAURE, J. L. 1996. Role of faults and layer interfaces on the spatial variation of stress

regimes in basins; inferences from numerical modelling. *Tectonophysics*, **266**, 101–119.

SHI, Y. & WANG, C. Y. 1986. Pore pressure generation in sedimentary basins: overloading versus aquathermal. *Journal of Geophysical Research*, **91**, 2153–2162.

SLACZKA, A. 1996. Oil and gas in the Northern Carpathians. *In*: WESELY, G. & LIEBL, W. (eds) *Oil and Gas in Alpidic Thrustbelts and Basins of Central and Eastern Europe*. EAGE Special Publication, **5**, 187–195.

SUK, M., BLÍŽKOVSKÝ, M. *ET AL*. 1984. *Geological History of the Territory of the Czech Socialist Republic*. Czech Geological Survey, Prague.

SUPPE, J. 1983. Geometry and kinematics of fault-bend folding. *American Journal of Science*, **283**, 684–721.

SUPPE, J. & MEDWEDEFF, D. A. 1984. Fault-propagation folding. *GSA Bulletin*, Abstracts with Programs, **16**, 670.

TEN HAVEN, H. L., LAFARGUE, E. & KOTARBA, M. 1993. Oil/oil and oil/source rock correlations in the Carpathian Foredeep and overthrust, south-east Poland. *Organic Geochemistry*, **20**(**7**), 935–959.

TÚNYI, I. & M. KOVÁČ. 1991. Paleomagnetic investigation of the Neogene sediments from the Little Carpathians. *Contributions of Geophysical Institute of Slovak Academy of Sciences*, **21**, 125–146.

VANDENBROUCKE, M. 1993. Migration of Hydrocarbons. *In*: BORDENAVE, M. L. (ed.) *Applied Petroleum Geochemistry*. Paris, Technip, 125–148.

WEIL, W., GORECKI, W., KRUCEK, J. & KARNKOWSKI, P. 1998. Discoveries of petroleum deposits in the years 1987–96 and current reserves of oil and gas in Poland. *Oil and Gas News*, **8**, 19–33.

WINKLER, W. & SLACZKA, A. 1992. Sediment dispersal and provenance in the Silesian, Dukla and Magura flysch nappes (Outer Carpathians, Poland). *Geologische Rundschau*, **81**, 371–382.

WINTER, A. 1987. Percolative aspects of hydrocarbon migration. *In*: DOLIGEZ, B. (ed.) *Migration of Hydrocarbons in Sedimentary Basins*. Editions Technip, Paris, 237–255.

ZIMMERMAN, R. W., SOMERTON, W. H. & KING, M. S. 1986. Compressibility of porous rocks. *Journal of Geophysical Research*, **91**, 12765–12777.

# Relation between effective friction and fault slip rate across the Northern San Andreas fault system

ANN-SOPHIE PROVOST & JEAN CHÉRY
*Laboratoire Dynamique de la Lithosphère, Université Montpellier 2, cc. 060, Place E. Bataillon, 34095 Montpellier cedex 5, France*
*(e-mail: jean@dstu.univ-montp2.fr)*

**Abstract:** The San Andreas Fault system is a complex tectonic ensemble that accommodates most of the relative plate motion between the Pacific and the North American plates. The structure and rheological properties of the faults vary along the plate boundary and lead to the distribution of deformation that we observe today. In order to learn more about the mechanical behaviour of such a fault system, a model of the northern California fault system is built, constrained by heat flow data, GPS and palaeoseismological measurements of slip rates (on the San Andreas, the Maacama and Bartlett Springfaults), and stress orientations. Our basic assumption is that the upper crust has a high frictional strength and that major faults represent weak zones with a lower effective friction. Several combinations of effective fault frictions on the three major faults of the system in the model are tested. We find that slight variations of the effective friction angle on one of the three active strands lead to an important redistribution of slip rates through the system. If present in nature, this fault behaviour could explain why fault slip rates vary in time, as suggested by slip rate variations over geological scales in intracontinental fault systems.

The San Andreas Fault system, slipping at a rate of 39 mm/yr, accommodates 80% of the relative plate motion between the Pacific plate and the North American plate (Freymueller *et al.* 1999; Argus & Gordon 2001). The distribution of the deformation varies largely along the fault zone. In central California south of 36.5° latitude, 90% of the differential motion between the Sierra Nevada and the Pacific plate is concentrated on a single strand of the San Andreas Fault, with a geodetic slip rate of 34 mm/yr (Lisowski *et al.* 1991). The fault system north of San Francisco is more complex than in the central region (Fig. 1). Slip rate is distributed over three major fault zones, including the San Andreas Fault to the west, the Maacama fault just to the east of the San Andreas, and farther to the east the Bartlett Springs fault (Castillo & Ellsworth 1993). The two latter zones are the northward continuations of the Hayward and the Calaveras faults in the San Francisco Bay area, and dip at 60° to 70° toward the NE. Here we attempt to quantify the slip distribution over the faults in order to understand fault interactions.

Because the kinematic boundary conditions of the system remain almost the same from central to northern California, it has been proposed that the broader distribution of deformation over different fault strands in Northern California should be related to differences in fault zone properties between Northern and Central California (Chéry *et al.* 2001). Indeed, a variation of the effective fault friction on a fault results in a change in the slip velocity of the fault system. The deformation is also dependent on the thermal state of the lithosphere, which is believed to strongly influence the lithospheric rheology (Kirby 1985). We quantify the distribution of the long-term deformation on the fault system (i.e., averaged over several seismic cycles) by means of numerical modelling and we sort out the factors that determine the activity of the three major fault zones of northern California.

Both geodetical and geological observations of the deformation have been made in the region. Based on GPS measurements corrected for elastic loading (Freymueller *et al.* 1999) the long-term slip rate is 17.4, 13.9 and 8.2 mm/yr for the San Andreas, Maacama and Bartlett Spring faults respectively, at latitude 39°N. On a longer time scale, palae oseismological studies are consistent with slip rates of 20–25 mm/yr for the San Andreas fault (Prentice 1989; Niemi & Hall 1992), *c.* 6.4–10.4 mm/yr for the Rogers Creek fault just south of the Maacama fault (Schwarz *et al.* 1992), and

*From*: BUITER, S. J. H. & SCHREURS, G. (eds) 2006. *Analogue and Numerical Modelling of Crustal-Scale Processes.* Geological Society, London, Special Publications, **253**, 429–436.
0305-8719/06/$15.00 

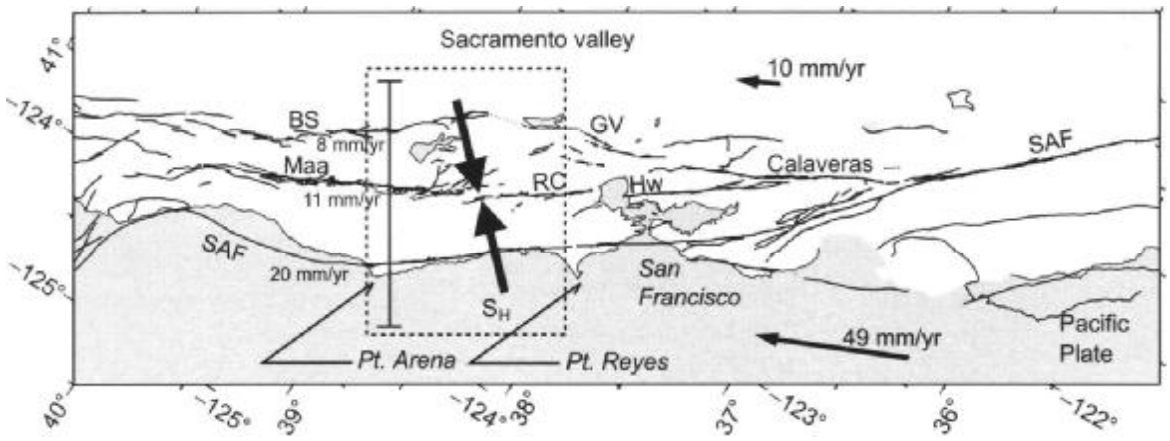


**Fig. 1.** Map of northern California fault system (Jennings 1992). The vectors show the relative plate motion of the Pacific plate (49 mm/yr) and the Sacramento valley (10 mm/yr) relative to North America. The estimated slip rates on the three major faults of the system are; 20, 11 and 8 mm/yr for the San Andreas, the Maacama and the Bartlett Spring faults respectively (see text for details). The maximum horizontal compression $S_H$ is found to be at *c.* 60° of the strike of major faults in this area (Provost & Houston 2003) as indicated by the facing arrows. The area studied is delimited by the line across the fault system. The zone of interest for modelling corresponds to the dashed rectangle. BS: Bartlett Spring fault; GV: Green Valley fault; Hw: Hayward fault; Maa: Maacama fault; Pt. Arena: Point Arena; RC: Rogers Creek fault; SAF: San Andreas fault.

*c.* 5 mm/yr for the Green Valley fault just south of the Bartlett Spring fault (Frizell & Brown 1976). Although short-term (geodetical) and long-term (geological) fault slip rate estimates may not necessarily coincide (Friedrich *et al.* 2003), we develop our analysis with combining these slip rates, which allows us to build a simplified deformation field across the fault system. We define an area close to Point Arena (latitude 39°), extending 180 km inland and stack our data on a cross-section perpendicular to the average fault system orientation (Fig. 1). Assuming that most of the strain is accommodated by a three-fault system, we choose the following slip rates: 20, 11, and 8 mm/yr for the San Andreas, Maacama and Bartlett Spring faults respectively and we use this information to constrain our model.

## Mechanical model

As mentioned earlier, the San Andreas Fault system has a different mechanical behaviour in northern and central California. The central segment of the San Andreas fault displays a maximum horizontal compression $S_H$ oriented at very high angles (*c.* 84°) to the fault (Mount & Suppe 1987; Zoback *et al.* 1987; Provost & Houston 2001), while the compression is more oblique (60°) in the northern San Andreas fault system (Provost & Houston 2003). The distribution of the deformation in northern California has been explained as an increase of the effective fault friction with respect to the central California segment (Chéry *et al.* 2001). Alternatively, it has been proposed that the viscosity of the lower crust has a dominant effect on the distribution of the deformation in the upper crust (Roy 1998). Also, the surface geological fault slip rate could be entirely controlled by the averaged velocity of the lower lithosphere underneath these crustal blocks (Bourne *et al.* 1998). In this view the influence of the brittle crust would be negligible. With a thermomechanical model we investigate the effect of the effective fault friction and of the lateral variation of the temperature field on the slip rate of a multistrand fault system.

We build our model using a 3D Lagrangian finite element code, ADELI3D (Chéry *et al.* 2001; Provost *et al.* 2003). We solve a system of equations formed by the momentum equation, the constitutive law of the medium, and static and kinematical boundary conditions. The numerical experiments are conducted with meshes having 9918 tetrahedral elements corresponding to a typical element size of *c.* 2 km. The entire model is subject to gravitational forces (g in Fig. 2) and a density of 2800 kg/m$^3$ is assumed. Geometry and boundary conditions of our model are shown in Figure 2. The model is 180 km long (x) perpendicular to the strike of the faults, and 30 km deep (z). We assume here no variation of deformation and stress along strike (y). Because this hypothesis is enforced by means of boundary conditions on

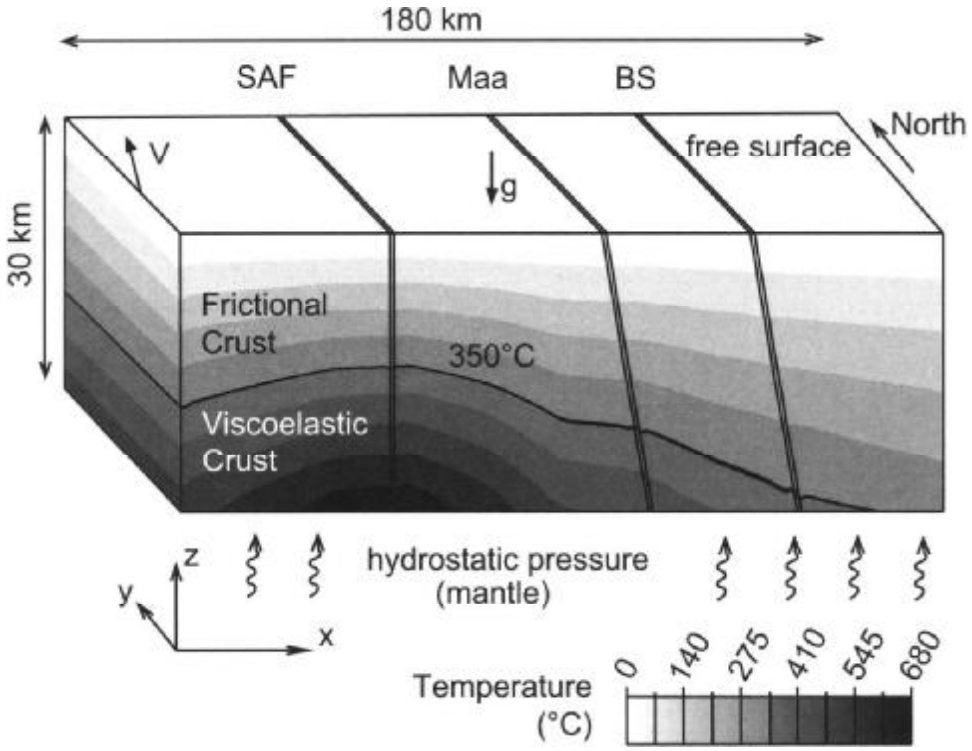


**Fig. 2.** Geometry and boundary conditions of the 3D mechanical model used in this analysis. The north is along the y-axis. The model is 30 km deep (z-axis) and 180 km long (x-axis). On the model The dip of the Maacama and Bartlett Spring faults is 65°. The vector V indicates the velocity (Vx; Vy) imposed on the western part of the model, and g is the gravitational force applied on it. Abbreviations are as in Fig. 1.

x-z planes, the mesh width in the y-direction is arbitrary. Our resulting model is therefore between a 2D and a 3D model, the non-zero components of the strain tensor $\varepsilon$ being $\varepsilon_{xx}$, $\varepsilon_{xy}$, $\varepsilon_{xz}$, $\varepsilon_{yz}$, $\varepsilon_{zz}$.

The velocity of the eastern part of the model (Sacramento Valley) is fixed to zero, and we impose a velocity on the western part of the model (Pacific plate) of 39 mm/yr along strike (Vy) and of 3.5 mm/yr perpendicular to it (Vx) in order to simulate the transpressive stress state occurring in central and northern California. However, this perpendicular value could be somewhat inaccurate and rely on geological (Thompson 1999) and geodetical (Gordon & Argus 1998; Argus & Gordon 2001) estimates. Because the fault zone corresponds to a hot lithospheric region (based on seismic tomography), the uppermost mantle viscosity is probably low (Furlong *et al.* 1989) and we assume that the lithospheric strength is located mainly in the crust. Therefore, we incorporate the buoyancy effect of the underlying mantle as a hydrostatic pressure applied at the base of the crust. As temperature measurements in wells have shown (Lachenbruch & Sass 1980), the heat flow is much higher close to the San Andreas Fault (*c.* 80 $mW/m^2$) than farther east in the Sacramento Valley (*c.* 30 $mW/m^2$).

We solve explicitly the 1D conductive heat flow equation in order to derivate a steady-state temperature field in agreement with these observations (Fig. 2). To do so, we use standard values of thermal parameters for the continental crust (conductivity of 3 $Wm^{-1}K^{-1}$, radiogenic crustal heating of 1 $\mu W/m^3$) and we adjust the mantle heat flow at the base of the model. As a result, the San Andreas Fault area corresponds to a hot geotherm where the 350°C isotherm is at 12 km depth. Cooler crustal temperatures occur towards the east and the 350°C temperature is found at 30 km depth in the Bartlett Spring area.

The crustal rheology is modelled using a viscoelastoplastic law according to pressure and temperature variations within the crust. Elastic parameters correspond to a Young's modulus of $10^{11}$ Pa and to a Poisson's coefficient of 0.25 in the whole medium. At low P-T, we assume a elastic-frictional behaviour for the crust for which we use a Drucker-Prager model (Leroy & Ortiz 1989). We adopt an effective friction angle $\phi$ of 15°. Because the Drucker-Prager model involves the intermediate stress, this

friction angle is not directly comparable to the one involved in the Mohr-Coulomb criterion, which depends on minimum and maximum principal stresses only. However, the value of $\phi$ of 15° would be compatible with a Mohr-Coulomb friction coefficient of 0.51 and a hydrostatic pore pressure for the surrounding crust. We set the cohesion to a low value of $10^6$ Pa for both the crust and the faults. Assuming that faults are weaker than the surrounding crust (Bird & Kong 1994), we define active faults with a distinct material behaviour and we use lower effective friction angles for the fault zones (from 3° to 12° which correspond to effective friction coefficients ranging from 0.1 to 0.44). At high P-T a viscoelastic behaviour is assumed and a temperature-dependent, linear Maxwell model is used in order to reproduce the ductile behaviour of quartzo-feldspathic rocks (Kirby 1985). The thermal dependence is controlled by the fluidity $\gamma = \gamma_0 \exp(-E/RT)$, $\gamma_0$ is a pre-exponential constant, $E$ the activation energy, $R$ the gas constant ($R = 8.32$), and $T$ the temperature in K. The viscous parameters are determined by assuming an effective viscosity of $10^{23}$ Pa s at 350 °C and of $10^{20}$ Pa s at 650 °C, leading to $\gamma_0 = 8.49 \times 10^{-15}$ Pa s and E = 110 KJ/mol.

## Results

We run five tests in which we vary the angle of friction, $\phi$, on the San Andreas (SAF), the Maacama (Maa) and the Bartlett Spring (BS) faults, as well as the temperature field distribution. Our first tests are run with the temperature field described as in Figure 2 and with the same effective friction angle on the three faults. We start with a very low friction on the fault system, with $\phi$ (SAF, Maa, BS) = (3°,3°,3°), increase it up to $\phi = (8°,8°,8°)$ and then to $\phi = (12°,12°,12°)$. We list in Table 1 the velocities obtained for each of these three tests, across the faults and in between them (off-fault regions), as well as the percentage of deformation absorbed on-fault and off-fault, and the average orientation of the maximum horizontal compression $S_H$ with respect to the strike of the faults. These results lead to a dramatic variation of the distribution of the deformation across the fault system with effective friction angle changes.

*Case 1* with $\phi = (3°,3°,3°)$ shows that the distribution of the deformation is mostly on-fault (98%) with a slip rate on the San Andreas fault of 28.8 mm/yr that is much larger than the slip rate on the two other faults: 6.2 and 3.3 mm/yr on the Maacama and Bartlett Spring faults respectively. These slip rates are not in agreement with the observed ones of 20, 11, and 8 mm/yr respectively. When the angle of friction $\phi$ increases by equal amounts on the three faults, the slip rate on the San Andreas fault remains largest, but some deformation appears off-fault, 30% for *case 2* with $\phi = (8°,8°,8°)$ and up to 75% for *case 3* where $\phi = (12°,12°,12°)$. The latter case is extreme, because almost all the deformation imposed on the model is accommodated by the San Andreas Fault and its surroundings, leaving the eastern and cooler regions almost not affected by the deformation. One can notice that for these three cases, even though the effective friction angle $\phi$ is the same on the three faults, the slip rate on the San Andreas fault is always much larger than those found for the Maacama and Bartlett Spring faults. This is caused by the influence of the temperature field on the mechanical behaviour of the crust: the lower crust in the vicinity of the San Andreas Fault is warmer than for the other faults at the same depth, thus less viscous than in the eastern regions of the model. Consequently, the viscous lithosphere surrounding the San Andreas Fault at depth is more compliant than the one surrounding the other faults and can accumulate more strain.

Because the slip rates computed by our previous three tests are not in agreement with the estimated ones, we run several tests in which we applied different angles of friction to the faults. In Table 1 we list the results for a model (*case 4*) that reasonably satisfies the geological and geodetical slip rates. Starting from *case 1*

**Table 1.** *Differential velocities (mm/yr) across the faults and off-faults for cases 1 to 5*

| Case number | $\phi$ SAF, Maa, BS | $V_{off1}$ | $V_{SAF}$ | $V_{off2}$ | $V_{Maa}$ | $V_{off3}$ | $V_{BS}$ | $V_{off4}$ | $V_{on\text{-}faults}$ (%) | $V_{off\text{-}faults}$ (%) | $S_H$ (SAF) | $S_H$ (far-field) |
|---|---|---|---|---|---|---|---|---|---|---|---|---|
| 1 | 3, 3, 3 | 0.2 | 28.8 | 0.2 | 6.2 | 0.1 | 3.3 | 0.1 | 98.5 | 1.5 | 61° | 75° |
| 2 | 8, 8, 8 | 6.9 | 25.0 | 1.7 | 1.7 | 0.3 | 0.3 | 0.2 | 69.3 | 30.7 | 52° | 56° |
| 3 | 12, 12, 12 | 16.7 | 8.7 | 0.7 | 0.7 | 0.8 | 0.1 | 0.3 | 24.4 | 75.6 | 48° | 49° |
| 4 | 4, 3, 3 | 0.3 | 18.1 | 10.8 | 10.8 | 0.1 | 9.3 | 0.2 | 98.0 | 2.0 | 62° | 76° |
| 5 | 4, 3, 3 | 0.2 | 3.6 | 17.3 | 17.3 | 0.1 | 17.3 | 0.4 | 97.8 | 2.1 | 59° | 69° |

with $\phi = (3°,3°,3°)$, a slight increase of $\phi$ on the San Andreas fault to 4° leads to a drastically reduced slip rate down to 18.1 mm/yr, inducing a slip rate increase on the Maacama and the Bartlett Spring faults to 10.8 and 9.3 mm/yr respectively. Profiles of the velocity along strike (in the y-direction) are shown in Figure 3a. The black line shows the velocity at the surface while the dashed line represents the velocity at 25 km depth. Surface deformation in this case occurs mainly on faults, while at depth only warmer regions (under the San Andreas Fault) allow the deformation to spread off-fault. This broadening of the deformation is clearly visible on the cross-section of Figure 3b showing the strain rate for *case 4*. Between 15 and 30 km depth, under the San Andreas Fault, a wide zone (*c.* 20 km) is deforming viscously at strain rates above $1.3 \times 10^{-15}\,s^{-1}$. Such strain rates are visible only below 20 km depth

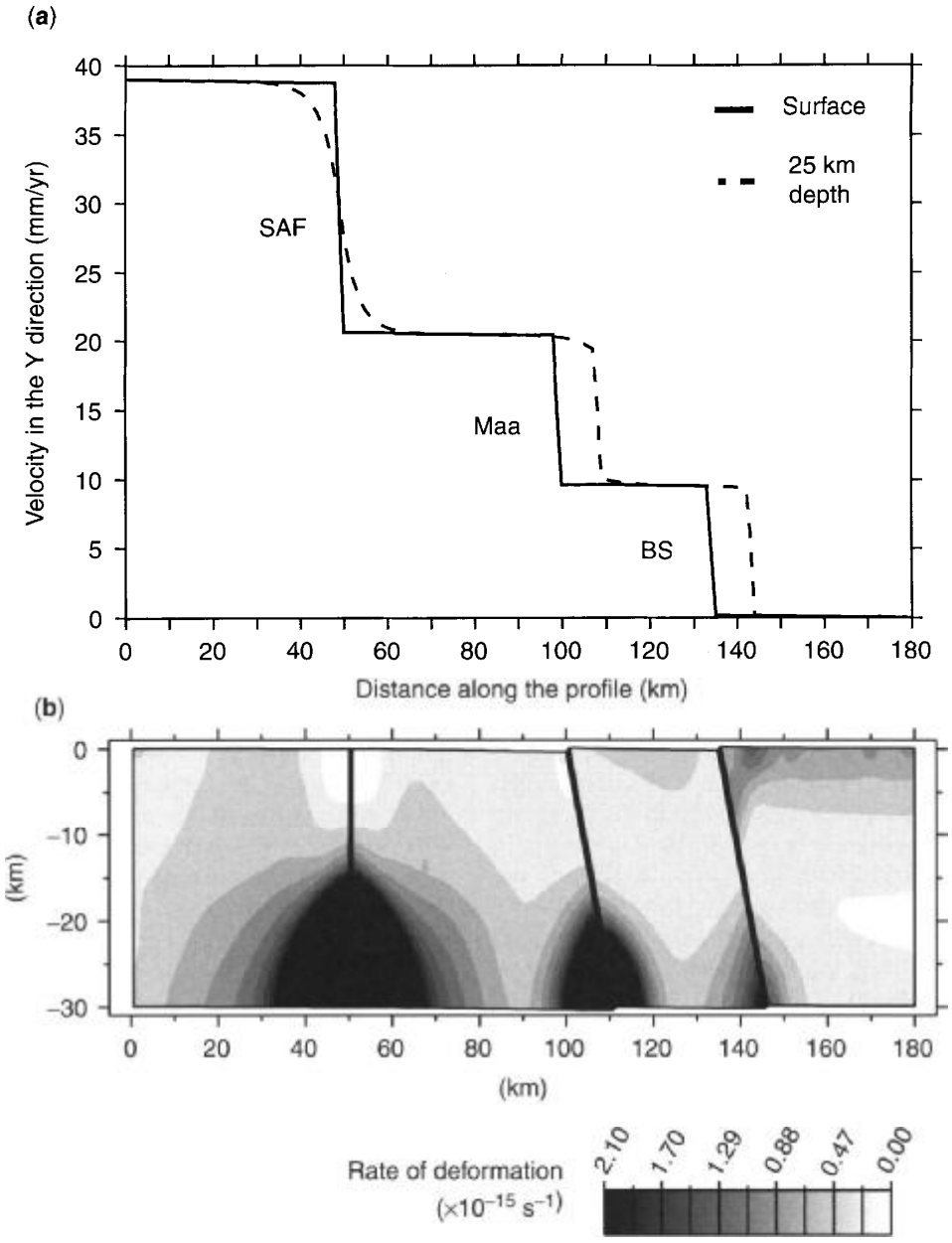


**Fig. 3.** Velocity profiles and distribution of the deformation across the model for the case $\phi = (4°, 3°, 3°)$. (**a**) Profiles across the fault system of the velocity along strike (y-direction) at the surface (black line) and at 25 km depth (dashed line). The shift of the dashed line at the location of the Maacama and Bartlett Spring faults is due to their dipping planes. (**b**) Distribution of strain rate deduced from the model. Here the strain rate is expressed as the quadratic invariant of the strain rate tensor. Abbreviations are as in Fig. 1.

over a 10 km wide zone at Maacama and correspond to a very limited area under the Bartlett Spring fault.

In order to clarify the role of temperature on the fault slip rate, we present a last test (*case 5*) with $\phi = (4°,3°,3°)$ as for *case 4* but having a constant surface heat flow of 80 $mW/m^2$, corresponding to a 350 °C isotherm at 15 km. This run leads to very different slip rate values with respect to *case 4*. The San Andreas Fault slips at a low rate of 3.6 mm/yr whereas the Maacama and Bartlett Spring faults slip rates increase up to 17.3 mm/yr for both. These values are obviously in agreement with field observations of recent fault activity. Clearly, it should be possible to obtain a better agreement of measured slip rate using a constant heat flow model with *slightly* decaying the friction angle of the San Andreas Fault. Although we do not perform this exercise here, we point out that a trade-off exists between the a priori thermal model and the set of friction angles to be used. Similarly, the optimal friction angle set may also depend on the viscous flow laws. The exploration of this effect is beyond the scope of this paper. However, we found through numerical experiments that the influence of the flow law remains small for values typical of the continental crust (Kirby 1985).

## Discussion

As already mentioned, the average orientation of the maximum horizontal compression $S_H$ is at about 60° from the strike of major faults in Northern California (Provost & Houston 2003), with a little variation (10°) between orientations very close to and far from the main faults. Because our modelling involves a velocity boundary condition between the two vertical sides, $S_H$ orientations are not initially set but depend on the solution of the momentum equation. We obtain similar values (56° to 76°) for *cases 2, 4* and *5* (i.e., low friction cases). $S_H$ appears to strongly depend on the effective friction. For large $\phi$ values (12° as for *case 3*), $S_H$ is oriented at smaller angles to the faults (49°). Therefore, our best kinematical model (*case 4*) with $\phi = (4°,3°,3°)$ also satisfies the seismological observations. Interestingly, we remark that even if $S_H$ is oriented at smaller angles to the faults in this region (compared to Central California where $S_H$ is *c.* 84°), this does not necessarily imply that the fault zone's frictional strength is higher. This finding is somewhat different than the one obtained for a one-strand strike-slip fault model (Chéry *et al.* 2001). For such a tectonic setting, these authors demonstrate that a decrease of the effective fault friction angle always corresponds to an increase in the value for $S_H$.

We find that the mechanical rules that hold for a single strike-slip fault (Rice 1992) may not be directly applicable to a multistrand fault system. Our analysis shows that a fault system composed of more than one strand does not behave as one single fault. Indeed, communication between the faults balances the overall distribution of the deformation in the system. We have shown that the slip rate can vary largely from one fault to the other if rheological or thermal parameters are changed. Perhaps the most striking feature of our model is that a variation as small as 1° of the effective friction angle on one fault profoundly influences the slip distribution of the whole fault system. Because a multi-fault system (such as the San Andreas Fault in northern California) has more degrees of freedom than a single-strand fault (the San Andreas Fault in central California), we suggest that it is thus more sensitive to the variation of the friction angle on one fault, resulting in the variation of the fault velocities. This behaviour is due to the coupling between frictional and viscous deformation in the fault zone. The strength of the fault plane (here the y-z plane) corresponds to the sum of a frictional stress, which is rate independent, and a viscous stress, which increases with the strain rate. For a constant slip rate, a decrease of the effective friction on one fault of the system brings the system out of equilibrium due to a decrease of the strength of the fault. As a quasi-static equilibrium is required for a slowly evolving geological system (as is our model), the fault must adapt by increasing its viscous strength and therefore its slip rate.

On a global scale, plate tectonics display a good agreement of differential plate motion over geodetical and geological time scales (Sella *et al.* 2002). On a smaller spatial scale, it has often been postulated that fault slip rates slowly evolve over geological times. That would explain why geodetic strain rates may coincide with geological estimates. This view appears correct for the Central San Andreas Fault where geological and geodetical slip rates are coincident (Sieh & Jahns 1984; Lisowski *et al.* 1991). However, a growing geological data archive for California also shows that fault slip rates vary largely over various time scales (0.01–10 Ma). For the northern San Andreas Fault system, a spatial and temporal slip distribution analysis leads to a fault model in which slip rates vary on short geological time periods (Wakabayashi 1999). This author suggests that the fastest slipping group of faults has shifted

several times during the northward migration of the Mendocino triple junction. The western faults were more active than the eastern ones from 18 to 16 Ma and from 12 to 8 Ma, but from 16 to 12 Ma this trend was reversed. In southern California, the slip rates of San Andreas and the San Jacinto faults have also evolved largely during the Quaternary (Kendrick *et al.* 2002; Bennett *et al.* 2004). Other evidence for rapid fault slip rate variation has recently been discovered in other continental zones such as the Basin and Range in the western United States (Wallace 1987; Friedrich *et al.* 2003) and in Mongolia (Ritz *et al.* 2003).

Because our modelling indicates that a small change of effective friction strongly affects the slip rate of a group of faults, this behaviour may provide a mechanical basis for rapid temporal changes. As a result, comparing Quaternary and geodetically determined slip rates could be not as straightforward as we postulated in the introduction of this paper. Indeed, we demonstrate that a variation of 1° of the friction angle drastically affects the slip rate on a fault embedded in a multistrand fault system and one can compute that the equivalent shear stress change on the fault plane is *c.* 5 MPa for a seismogenic depth of 10 km. This change is a small fraction of the total differential stress that can be accommodated by crustal rocks (*c.* 100 MPa). Therefore, 5% change of the differential stress could lead to a slip rate variation of 30%, as shown by the comparison between cases 1 and 4.

As most of large intracontinental faults are earthquake prone, it is plausible that effective friction variations on fault planes in nature are related to earthquake mechanics and seismic cycle. Because our model is based on a steady-state approximation, we cannot directly model the effect of repeated earthquakes on the averaged fault friction. However, one can remark that the stress change we mention (5 MPa) is close to the mean stress drop of 3 MPa associated with continental earthquakes (Hanks 1977). Combined with the fact that earthquakes do not regularly occur on large faults (Grant & Sieh 1994), the occurrence of a few earthquakes clustered in time may be an indication that the maximum stress sustainable by the fault is dropping by a few MPa. Consequently, the interseismic fault slip rate could increase dramatically, while other faults slow down according to constant plate boundary conditions. This feedback process may lead low slip rate faults to cease their activity and heal, while the accelerating fault accommodates most of the differential plate motion, as in central California. As relative plate motion slowly evolves over a few million years, the remaining active fault should slip with a constant velocity for this corresponding time period.

We thank M. Nyst, F. Pollitz and S. Buiter for their constructive reviews. This work has been supported by the research program ACI 'prevention des catastrophes naturelles' of the French ministry of Research.

## References

ARGUS, D. F. & GORDON, D. 2001. Present tectonic motion across the Coast Ranges and San Andreas fault system in central California. *Geological Society of America Bulletin*, **113(12)**, 1580–1592.

BENNETT, R., FRIEDRICH, A. M. & FURLONG, K. P. 2004. Codependent histories of the San Andreas and San Jacinto fault zones from inversion of fault displacement rates. *Geology*, **32**, 961–964.

BIRD, P. & KONG, X. 1994. Computer simulations of California tectonics confirm very low strength of major faults. *Geological Society of America Bulletin*, **106**, 159–174.

BOURNE, S. J., ENGLAND, P. C. & PARSONS, B. 1998. The motion of crustal blocks driven by flow of the lower lithosphere: implications for slip rates of faults in the south island of New Zealand and Southern California. *Nature*, **391**, 655–659.

CASTILLO, D. A. & ELLSWORTH, W. L. 1993. Seismotectonics of the San Andreas Fault System between Point Arena and Cape Mendocino in northern California: implication for the development and evolution of a young transform. *Journal of Geophysical Research*, **98(B4)**, 6543–6560.

CHÉRY, J., ZOBACK, M. D. & HASSANI, R. 2001. An integrated mechanical model of the San Andreas Fault in central and northern California. *Journal of Geophysical Research*, **106(B10)**, 22051–22066.

FREYMUELLER, J. T., MURRAY, M. H., SEGALL, P. & CASTILLO, D. 1999. Kinematics of the Pacific-North America plate boundary zone, northern California. *Journal of Geophysical Research*, **104(B4)**, 7419–7441.

FRIZELI, V. A. J. & BROWN, R. D. Jr. 1976. *Map showing recently active breaks along the Green Valley fault, Napa and Sonoma Counties*, California, M(200) MF no. 743, US Geological Survey.

FRIEDRICH, A. M., WERNICKE, B. P., NIEMI, N. A., BENNETT, R. A. & DAVIS, J. L. 2003. Comparison of geodetic and geologic data from the Wasatch region, UTAH, and implications for the spectral character of Earth deformation at periods of 10 to 10 million years. *Journal of Geophysical Research*, **108(B4)**, DOI 10.10292001JB000682.

FURLONG, K. P., HUGO, W. D. & ZANDT, G. 1989. Geometry and evolution of the San Andreas fault zone in northern California. *Journal of Geophysical Research*, **94(B3)**, 3100–3110.

JENNINGS, C. W. 1992. *Preliminary fault activity map of California*. California Division of Mines and Geology, Sacramento.

GORDON, R. G. & ARGUS, D. F. 1998. Present tectonic motion across the Coast Ranges and San Andreas Fault System in central California. *EOS Transaction AGU*, **79(95)**, S204.

GRANT, L. B. & SIEH, K. 1994. Paleoseismic evidence of clustered earthquakes on the San Andreas fault in the Carrizo plain, California. *Journal of Geophysical Research*, **99**, 6819–6841.

HANKS, T. 1977. Earthquake stress drop, ambient tectonic stress, and stress that drives plate motions. *Pageoph*, **115**, 441–458.

KENDRICK, K. J., MORTON, D. M., WELLS, S. G. & SIMPSON, R. W. 2002. Spatial and temporal deformation along the Northern San Jacinto Fault, Southern California: Implications for slip rates. *Bulletin of the Seismological Society of America*, **92**, 2782–2802.

KIRBY, S. H. 1985. Rocks mechanics observations pertinent to the rheology of the lithosphere and the localization of strain along shear zones. *Tectonophysics*, **119**, 1–27.

LACHENBRUCH, A. H. & SASS, J. H. 1980. Heat flow and energetics of the San Andreas fault zone. *Journal of Geophysical Research*, **85(B11)**, 6185–6222.

LEROY, Y. & ORTIZ, M. 1989. Finite element analysis of strain localization in frictional materials. *International Journal for Numerical and Analysis Methods in Geomechanics*, **13**, 53–74.

LISOWSKI, M., SAVAGE, J. C. & PRESCOTT, W. H. 1991. The velocity field along the San Andreas fault in central and southern California. *Journal of Geophysical Research*, **96(5)**, 8369–8389.

MOUNT, V. S. & SUPPE, J. 1987. State of stress near the San Andreas fault: implications for wrench tectonics. *Geology*, **15**, 1143–1146.

NIEMI, T. M. & HALL, N. T. 1992. Late Holocence slip rate and recurrence of great earthquakes on the San Andreas fault in northern California. *Geology*, **20**, 195–198.

PRENTICE, C. 1989. *Earthquake geology of the northern San Andreas fault near Point Arena, California*. Ph.D. thesis, California Institute of Technology Pasadena.

PROVOST, A.-S. & HOUSTON, H. 2001. Orientation of the stress field surrounding the creeping section of the San Andreas fault: evidence for a narrow mechanically-weak fault zone. *Journal of Geophysical Research*, **106(B6)**, 11373–11386.

PROVOST, A.-S. & HOUSTON, H. 2003. Stress orientations in northern and central California: evidence for the evolution of frictional strength along the San Andreas Plate boundary system. *Journal of Geophysical Research*, **108(B3)**, 2175, DOI 10.1029/2001JB001123.

PROVOST, A.-S., CHÉRY, J. & HASSANI, R. 2003. 3D mechanical modeling of the GPS velocity field along the North Anatolian fault. *Earth and Planetary Science Letters*, **209**, 361–377.

RICE, J. R. 1992. Fault stress states, pore pressure distributions, and the weakness of the San Andreas fault. *In*: B. EVANS and T.-F. WONG (eds) *Fault Mechanics and Transport Properties of Rock*, Academic Press, London, 475–503.

RITZ, J.-F., BOURLES, D., BROWN, E. T. *ET AL.* 2003. Analysing the uplift rate along the Gurvan Bulag thrust fault (Gobi-Altag, Mongolia) during the past 130,000 yrs using surface-exposure 10Be datings. *Journal of Geophysical Research*, **108**(B3), 2162, DOI: 10.1029/2001JB000553, 2003.

ROY, M. 1998. Evolution of fault system at a strike-slip plate boundary: a viscoelastic model. *Geophysical Research Letters*, **25(15)**, 2881–2884.

SCHWARZ, D. P., PANTOSTI, D., HECKER, S., OKUMURA, K., BUDDING, K. E. & POWERS, T. 1992. Late Holocence behavior and seismogenic potential of the Rogers Creek fault zone. *The second Conference on Earthquake Hazards in the Eastern San Francisco Bay Area*, 393–398.

SELLA, G. F., DIXON, T. H. & MAO, A. 2002. REVEL: A model for recent plate velocities from space geodesy. *Journal of Geophysical Research*, **107(B4)**, ETG 11-1,11-32.

SIEH, K. & JAHNS, R. H. 1984. Holocence activity of the San Andreas Fault at Wallace Creek, California. *Geological Society of America Bulletin*, **95(8)**, 883–896.

THOMPSON, G. A. 1999. California coast ranges tectonics in the light of geophysical constraints: A tribute to Ben Page. *International Geology Review*, **41**, 383–390.

WAKABAYASHI, J. 1999. Distribution of displacement on and evolution of a young transform fault system: the northern San Andreas fault system, California. *Tectonics*, **18(6)**, 1245–1274.

WALLACE, R. E. 1987. Grouping and migration of surface faulting and variations in slip rates on faults in the Great Basin province. *Bulletin of the Seismological Society of America*, **77**, 868–876.

ZOBACK, M. D., ZOBACK, M. L. *ET AL.* 1987. New evidence on the state of stress of the San Andreas fault system. *Science*, **238**, 1105–1111.

# Index

Page numbers in italic, e.g. *45*, refer to figures. Page numbers in bold, e.g. **35**, signify entries in tables.

# Analogue and Numerical Modelling of Crustal-Scale Processes

Edited by
**S. J. H. Buiter and G. Schreurs**

The crust of the Earth records the deformational processes of the inner Earth and the influence of the overlying atmosphere. The state of the Earth's crust at any time is therefore the result of internal and external processes, which occur on different time and spatial scales. In recent years important steps forward in the understanding of such complex processes have been made by integrating theory and observations with experimental and computer models. This volume presents state-of-the-art analogue and numerical models of processes that alter the Earth's crust. It shows the application of models in a broad range of geological problems with careful documentation of the modelling approach used. This volume contains contributions on analogue and numerical sandbox models, models of orogenic processes, models of sedimentary basins, models of surface processes and deformation, and models of faults and fluid flow.

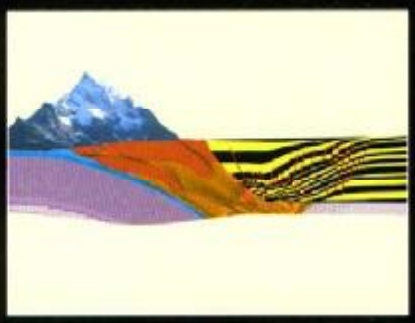

**Visit our online bookshop:** http://www.geolsoc.org.uk/bookshop

**Geological Society web site:** http://www.geolsoc.org.uk

Midland Valley

The cost of colour figures in this book was in part sponsored by Midland Valley. Their support is kindly acknowledged

ISBN 1-86239-191-2

**Cover illustration:**

Composite image schematically portraying some of the geological structures and processes described in this volume.

Illustration courtesy of M. Panien, M. Withjack, S. Buiter and G. Schreurs.